

IntechOpen

Advances in Spacecraft Technologies

Edited by Jason Hall



ADVANCES IN SPACECRAFT TECHNOLOGIES

Edited by **Jason Hall**

Advances in Spacecraft Technologies

<http://dx.doi.org/10.5772/568>

Edited by Jason Hall

Contributors

Charles Reynerson, Sathyan Krishnan, Sang-Heon Lee, Hung-Yao Hsu, Gopinath Konchady, Ka Wai Lee, Hirohisa Kojima, Pavel M. Trivailo, Rune Schlanbusch, Per Johan Nicklasson, Abdulrahman H. Bajodah, Mahmut Reyhanoglu, Herman J. Mosquera Cuesta, Tongli Chang, Michele Coletti, Angelo Grubisic, Cheryl Collingwood, Stephen Gabriel, Taihua Zhang, Xian hong Meng, Xing Zhang, Malcolm Macdonald, Anders Larsson, Niklas Wingborg, Kezhao Li, Qin Zhang, Jianping Yuan, Siliang Yang, Akihisa Matsubara, Atsushi Tomiki, Tomoaki Toda, Takehiko Kobayashi, José M. Sánchez-Pena, Carlos Marcos, Alberto Carrasco, Ricardo Vergaz, Ramón Zaera, Zhi-Hui Li, Ki-Lyuk Yong, Hyun-Sam Myung, Hyochoong Bang, Yuichi Ikeda, Takashi Kida, Tomoyuki Nagashio, Nikolay Semena, Georgi Smirnov, Anna Guerman, Susana Dias, Akira Iwasaki, Jonghee Bae, Youdan Kim, Seungho Yoon, Shifeng Zhang, Lijun Zhang, Mario Garcia-Sanz, Irene Eguinoa, Marta Barreras, Yechiel Crispin, Dongeun Seo

© The Editor(s) and the Author(s) 2011

The moral rights of the and the author(s) have been asserted.

All rights to the book as a whole are reserved by INTECH. The book as a whole (compilation) cannot be reproduced, distributed or used for commercial or non-commercial purposes without INTECH's written permission.

Enquiries concerning the use of the book should be directed to INTECH rights and permissions department (permissions@intechopen.com).

Violations are liable to prosecution under the governing Copyright Law.



Individual chapters of this publication are distributed under the terms of the Creative Commons Attribution 3.0 Unported License which permits commercial use, distribution and reproduction of the individual chapters, provided the original author(s) and source publication are appropriately acknowledged. If so indicated, certain images may not be included under the Creative Commons license. In such cases users will need to obtain permission from the license holder to reproduce the material. More details and guidelines concerning content reuse and adaptation can be found at <http://www.intechopen.com/copyright-policy.html>.

Notice

Statements and opinions expressed in the chapters are these of the individual contributors and not necessarily those of the editors or publisher. No responsibility is accepted for the accuracy of information contained in the published chapters. The publisher assumes no responsibility for any damage or injury to persons or property arising out of the use of any materials, instructions, methods or ideas contained in the book.

First published in Croatia, 2011 by INTECH d.o.o.

eBook (PDF) Published by IN TECH d.o.o.

Place and year of publication of eBook (PDF): Rijeka, 2019.

IntechOpen is the global imprint of IN TECH d.o.o.

Printed in Croatia

Legal deposit, Croatia: National and University Library in Zagreb

Additional hard and PDF copies can be obtained from orders@intechopen.com

Advances in Spacecraft Technologies

Edited by Jason Hall

p. cm.

ISBN 978-953-307-551-8

eBook (PDF) ISBN 978-953-51-5973-5

We are IntechOpen, the world's leading publisher of Open Access books Built by scientists, for scientists

4,000+

Open access books available

116,000+

International authors and editors

120M+

Downloads

151

Countries delivered to

Our authors are among the
Top 1%

most cited scientists

12.2%

Contributors from top 500 universities



WEB OF SCIENCE™

Selection of our books indexed in the Book Citation Index
in Web of Science™ Core Collection (BKCI)

Interested in publishing with us?
Contact book.department@intechopen.com

Numbers displayed above are based on latest data collected.
For more information visit www.intechopen.com



Meet the editor



Dr. Jason Hall is a U.S. Naval officer specializing in space systems acquisition. His research interests include dynamics and guidance and control of spacecraft and robotic systems. He has worked on control system design for proximity operations and docking of autonomous spacecraft for the Spacecraft Robotics Laboratory at the Naval Postgraduate School and developed a novel algorithm to effect three axis control of a spacecraft with only two control actuators such as reaction wheels. He earned his B.S. degree in Systems Engineering from the U.S. Naval Academy, his M.S. degree in Astronautical Engineering and PhD in Mechanical Engineering, each from the Naval Postgraduate School.

Contents

Preface XIII

Part 1 Innovative Hardware Technologies 1

- Chapter 1 **Hardware-In-the Loop Simulation System Construction for Spacecraft On-orbit Docking Dynamics, Ideas, Procedural and Validation 3**
Tongli Chang
- Chapter 2 **Solar Sailing: Applications and Technology Advancement 35**
Malcolm Macdonald
- Chapter 3 **Measurements and Characterization of Ultra Wideband Propagation within Spacecrafts- Proposal of Wireless Transmission for Replacing Wired Interface Buses 61**
Akihisa Matsubara, Atsushi Tomiki,
Tomoaki Toda and Takehiko Kobayashi
- Chapter 4 **Lubrication of Attitude Control Systems 75**
Sathyan Krishnan, Sang-Heon Lee
Hung-Yao Hsu and Gopinath Konchady
- Chapter 5 **Development of Optoelectronic Sensors and Transceivers for Spacecraft Applications 99**
José M. Sánchez-Pena, Carlos Marcos, Alberto Carrasco,
Ricardo Vergaz and Ramón Zaera
- Chapter 6 **Solar Electric Propulsion Subsystem Architecture for an All Electric Spacecraft 123**
Michele Coletti, Angelo Grubisic,
Cheryl Collingwood and Stephen Gabriel
- Chapter 7 **Green Propellants Based on Ammonium Dinitramide (ADN) 139**
Anders Larsson and Niklas Wingborg

- Chapter 8 **Use of Space Thermal Factors by Spacecraft** 157
N. Semena
- Chapter 9 **The Mechanics Analysis of Desquamation for Thermal Protection System (TPS) Tiles of Spacecraft** 175
Zhang Taihua, Meng Xianhong and Zhang Xing
- Part 2 Cutting Edge State Estimation Techniques** 195
- Chapter 10 **Unscented Kalman Filtering for Hybrid Estimation of Spacecraft Attitude Dynamics and Rate Sensor Alignment** 197
Hyun-Sam Myung, Ki-Kyuk Yong and Hyochoong Bang
- Chapter 11 **Fault-Tolerant Attitude Estimation for Satellite using Federated Unscented Kalman Filter** 213
Jonghee Bae, Seungho Yoon, and Youdan Kim
- Chapter 12 **Nonlinear Electrodynamics: Alternative Field Theory for Featuring Photon Propagation Over Weak Background Electromagnetic Fields and what Earth Receivers Read off Radio Signals from Interplanetary Spacecraft Transponders** 233
Herman J. Mosquera Cuesta
- Chapter 13 **Detection and Estimation of Satellite Attitude Jitter Using Remote Sensing Imagery** 257
Akira Iwasaki
- Chapter 14 **Gas-Kinetic Unified Algorithm for Re-Entering Complex Flows Covering Various Flow Regimes by Solving Boltzmann Model Equation** 273
Zhi-Hui Li
- Chapter 15 **Aerodynamic Disturbance Force and Torque Estimation For Spacecraft and Simple Shapes Using Finite Plate Elements – Part I: Drag Coefficient** 333
Charles Reynerson
- Chapter 16 **State Feature Extraction and Relative Navigation Algorithms for Spacecraft** 353
Kezhao Li, Qin Zhang and Jianping Yuan
- Part 3 Novel Control Methods** 383
- Chapter 17 **Inertia-Independent Generalized Dynamic Inversion Control of Spacecraft Attitude Maneuvers** 385
Abdulrahman Bajodah

- Chapter 18 **Tracking Control of Spacecraft by Dynamic Output Feedback - Passivity- Based Approach - 405**
Yuichi Ikeda, Takashi Kida and Tomoyuki Nagashio
- Chapter 19 **Linear Differential Games and High Precision Attitude Stabilization of Spacecrafts With Large Flexible Elements 423**
Georgi V. Smirnov, Anna D. Guerman and Susana Dias
- Chapter 20 **Advanced Attitude and Position MIMO Robust Control Strategies for Telescope-Type Spacecraft with Large Flexible Appendages 443**
Mario Garcia-Sanz, Irene Eguinoa and Marta Barreras
- Chapter 21 **Fuzzy Attitude Control of Flexible Multi-Body Spacecraft 471**
Siliang Yang and Jianli Qin
- Chapter 22 **Applications of Optimal Trajectory Planning and Invariant Manifold Based Control for Robotic Systems in Space 497**
Ka Wai Lee, Hirohisa Kojima and Pavel M. Trivailo
- Chapter 23 **Optimal Control Techniques for Spacecraft Attitude Maneuvers 523**
Shifeng Zhang, Shan Qian and Lijun Zhang
- Chapter 24 **Modeling and Control of Space Vehicles with Fuel Slosh Dynamics 549**
Mahmut Reyhanoglu
- Chapter 25 **Synchronization of Target Tracking Cascaded Leader-Follower Spacecraft Formation 563**
Rune Schlanbusch and Per Johan Nicklasson
- Chapter 26 **Rendezvous Between Two Active Spacecraft with Continuous Low Thrust 585**
Yecheil Crispin and Dongeun Seo

Preface

The development and launch of the first artificial satellite Sputnik more than five decades ago, propelled both the scientific and engineering communities to new heights as they worked together to develop novel solutions to the challenges of spacecraft system design. This symbiotic relationship has brought significant technological advances that have enabled the design of systems that can withstand the rigors of space without significant maintenance while continuing to provide valuable space-based services such as telecommunication, television and radio broadcasting, weather forecasting, navigation assistance and natural disaster assistance. Most recently, these advances have led to the design and launch of spacecraft systems that are autonomous in nature, such as the Progress and the Automated Transfer Vehicle, which rely on precise sensors and actuators as well as accurate and timely state estimation and control to effect safe proximity navigation and docking operations with little or no human interaction. With its 26 chapters divided into three sections, this book brings together critical contributions from renowned international researchers to provide an outstanding survey of recent advances in spacecraft technologies that can be used to design the next generation of spacecraft.

The book is divided into three sections that are focused on the key aspects of spacecraft design. The first section is composed of nine chapters that focus on innovative hardware technologies. Chapter 1 presents a Hardware-In-the-Loop system design for development and validation of on-orbit docking requirements. This unique simulator provides realistic on-orbit working conditions for a proposed docking mechanism. Chapter 2 surveys the state of solar sail technologies. Through an excellent review of past and current solar sail programs, the missions where solar sail structures may prove most useful are succinctly analyzed. Chapter 3 deals with the measurement and characterization of radio propagation with a goal of replacing certain portions of the wired onboard bus with wireless technology. By substituting a wireless bus for the traditional wired, several advantages have the potential to be realized to include reduction in overall spacecraft weight, more flexibility in spacecraft design and more reliable connections. In Chapter 4, the key fundamentals regarding the lubrication requirements of today's attitude control systems are studied. Chapter 5 presents several optoelectrical sensor and transceiver applications to enable more precise measurement of projectile velocities and optimize free space optical communications systems. A solar electric propulsion subsystem is analyzed in Chapter 6 with the goal of designing an all electric spacecraft. All electric designs have the unique benefits of eliminating the requirements for working with the traditional highly caustic propellants used in main and attitude control propulsion systems while additionally reducing the control

complexities levied by propellant slosh. Chapter 7 presents a green propellant solution for traditional propulsion systems that is based on Ammonium Dinitramide (ADN). Current propellants, such as Ammonium Perchlorate and Hydrazine, have excellent performance qualities but are both highly toxic and thus require special handling while ADN has the ability to provide nearly the same performance without the inherent operational limitations. In Chapter 8, a thermal control subsystem is presented that is both capable of being used to determine the orientation of the spacecraft but is also independent of the other subsystems and variation of thermal factors due to the space environment. Chapter 9 closes out this first section by considering the problem of Thermal Protection System (TPS) tiles becoming debonded from spacecraft, potentially causing catastrophic failure as in the case of the Space Shuttle *Columbia* in 2003.

The second section of the book is composed of seven chapters that center on cutting-edge state estimation techniques. Chapter 10 begins the section by defining an Unscented Kalman Filter (UKF) methodology to estimate the attitude dynamics and align rate sensors. In framing the benefits of the UKF based filtering algorithm, which is designed to approximate the nonlinear dynamics to the second order, a simulation based comparison is made to a typical first-order approximating Extended Kalman Filter. Chapter 11 presents a fault-tolerant state estimation technique by using a federated UKF. By employing a federated UKF, which is based on a decentralized KF, several advantages that include consideration of increased data and simpler fault detection and isolation can be gained. In Chapter 12, an analysis of the nonlinear electrodynamic effects on interplanetary spacecraft is presented. In this analysis, an alternative field theory is formulated to help explain anomalous measurements on interplanetary spacecraft. Chapter 13 studies the use of satellite imagery to provide feedback based detection and estimation for an imaging spacecraft's attitude jitter. By adding an additional image sensor on the focal plane, the anomalous disturbances caused by vibration originating from such mechanical devices as tracking solar arrays, reaction wheels and high gain antennas can be more accurately measured and subsequently, a more precise state can be determined. In Chapter 14, the complex gas dynamic flow issues surrounding atmospheric re-entry and its subsequent effect on proper state estimation are addressed and a solution is presented by means of the Boltzmann equation. In Chapter 15, a unique method of estimating the aerodynamic force and torque on low earth orbiting spacecraft by means of finite plate elements is presented. Through this method, a more accurate prediction of the drag coefficient for an orbiting spacecraft can be gained with the goal of producing a higher fidelity state estimation. Chapter 16 closes out the second section by presenting a shape and state feature based algorithm that is based on Mathematical Morphology (MM) to more accurately estimate the state of an orbiting spacecraft. MM, which is an emerging discipline focused on imaging analysis and processing, possesses several inherent advantages such as its ability to conduct fast and parallel processing while being simple and easy to operate and thus makes it desirable for automation and intelligence object detection.

The final section contains ten chapters that present a series of novel control methods for spacecraft orbit and attitude control. Chapter 17 begins this section by presenting a unique and highly promising methodology to provide three-axis stabilization using dynamic inversion. By inverting the desired attitude error dynamics for the control variables that realize the attitude dynamics instead of the inverting the mathematical model, a global transformation is directly gained without the issues arriving from

deriving the inverse equations of motions. In Chapter 18, a feedback controller similar to a Proportional-Derivative (PD) based controller is demonstrated for a potential on-orbit servicing mission. This PD-like feedback controller is based on the passive system derived by transforming the full six-Degrees Of Freedom (DOF) relative equations of motion through coordinate and feedback transformation and proper parameter selection. Chapter 19 investigates using linear differential games and high precision attitude stabilization schemes to control spacecraft with large flexible appendages. Chapter 20 presents a multi-input multi-output control methodology to simultaneously regulate the six-DOF spacecraft state for a potential imagining spacecraft with flexible appendages. Fuzzy control logic is applied to the control problem of a spacecraft with flexible structures in Chapter 21. By treating the inherently nonlinear and not precisely mathematically defined spacecraft model as a “black box”, the relationship between the inputs and the outputs and the behavior represented from this process, called fuzzy control, is investigated. Chapter 22 studies the application of optimal trajectory planning and invariant manifold control for on-orbit robotic systems. Given the inherent nature of these systems with their power and space limitations, coupled with the requirement for real-time trajectory deconfliction of any manipulator movement, optimal trajectory planning has the potential to provide a proper solution. In Chapter 23, an excellent survey of recent advances in optimal control methods for attitude control is presented. This survey shines light specifically on three specific aspects: the minimal energy maneuvering control problem for rigid spacecraft, an attitude determination algorithm based on the improved gyro-drift model, and the three-axis stabilized control problem given a momentum wheel control actuator based system. In Chapter 24, a novel set of control laws are presented to stabilize the vehicle dynamics in the presence of fuel slosh. These control laws are specifically unique due to their modeling of the complete nonlinear translational and rotational vehicle dynamics. Chapter 25 presents a real-time control solution to effect leader-follower synchronization for the formation flying control problem. Chapter 26 closes out this section and the book by proposing a novel genetic algorithm based optimal control solution for a given cooperative rendezvous problem. The results of this control algorithm are further compared to an optimal control solution based on simulated annealing.

Jason Hall
Naval Postgraduate School
Spacecraft Robotics Laboratory
Monterey,
USA

Part 1

Innovative Hardware Technologies

Hardware-In-the Loop Simulation System Construction for Spacecraft On-orbit Docking Dynamics, Ideas, Procedural and Validation

Tongli Chang

*School of Electrical and Mechanical Engineering, Northeast Forestry University,
School of Electrical and Mechanical Engineering, Harbin Institute of Technology,
P. R. China*

1. Introduction

The Hardware-In-the-Loop (HIL) simulation system for on-orbit docking dynamics is a large-scale complex test equipment. It establishes working conditions for the docking mechanism similar with those on orbit. The kernel of above dynamics HIL simulation system is a mechanical force and movement actions simulator. Besides the mechanical force and movement actions simulator, it also includes an environmental simulator, a micro-gravity simulator and so on.

In a narrow mind, the HIL simulation system for on-orbit docking dynamics refers to the mechanical force and movement action simulator. It is a feedback system which consists of the dynamics simulation model and real-time simlaton computer, the hardwares under test, the force and torque sensor, the motion simulator. The research topic of this paper is limited in above narrow mind.

The HIL simulation system for on-orbit docking dynamics is a key technology that played important roles in the lunar excursion of America and in the assembling and re-supplying of Russian MIR space station. Morden space programme enhance the requirements to the HIL simulation for spacecraft docking dynamics. International Space Station (ISS) program also required that the ISS Common Berthing Mechanism (CBM) testing on ground simulator should be performed under operational vacuum and thermal conditions (Office of NRBMP, 1999).

In the early days, the physical simulators played main roles in docking dyniamics tests. Because of the development of computer and the complexity of modern docking mechanism, the HIL simulation technology is applied in the docking dynamics simulation. The dynamic docking test system (DDTS) is setup in US (Gates & Graves, 1974), and the integated testing system for docking mechanism was built in former Soviet (Peng et al., 1992). In1980s, docking dynamic test facility (DDTF) was created for testing the handles-latch docking mechanism (Crimbert & Marchal, 1987). National space development agency of Japan built the rendezvous and docking operation test system (RDOTS) testing three-points handles-latch docking mechanism (Lange & Martin, 2002).

The HIL simulation for spacecraft on-orbit docking is a attractive and promising research field. Lim et al. (1989) modeled and simulated the Stewart platform of DDTS. They pointed

out the inertia matrix has tendency to decouple when the mass of the legs increasing, for purpose of increasing the rigidity, and relative to the platform. But the inertia power matrix does not show any noticeable general tendency. Ananthakrishnan et al. (1996) developed a prediction based feed forward filter to enhance the simulation of contact forces and rebound velocities during the space docking. They used the off-line acquisition and least-squares procedure to define the pre-filter. But the characteristic of the simulation/hardware interface with the pre-filter is not clearly discussed. Zhang (1999) presented the scheme of 6-DOF HIL simulation system for docking. Guan (2001) simulated the spacecraft docking dynamics with mathematic simulation and pointed out that rigid-body model of spacecraft could meet the demand of the research on docking dynamics. Kawabe et al. (2001) adopted a high speed zero gravity motion simulator, whose frequency response is higher than 40Hz, to setup a HIL simulation system to research the collision and impact dynamics under zero gravity. They also validated the HIL simulation system with a drop shaft test. Huang et al. (2005) presented the spacecraft docking simulation using HIL simulator with Stewart platform and spring-mass payload. Yan et al. (2007) established a Space docking hybrid simulation prototype experiment system and stabilized it through adding superfluity digital damp. The docking dynamics calculation method was setup with spacecrafts docking in space. Tian et al. (2007) simulated the movement simulator in integrate test platform for docking mechanism. Zhao et al. (2007) analyzed the dynamometry scheme for semi-physical simulation platform of space docking mechanism and simulated with single-sensor and double-sensor schemes separately. The mathematic motion model of two spacecrafts was set up with two-spacecraft docking model. Zhao & Zhang (2008) analyzed the stability of the whole system of space docking dynamics simulation with simplified HIL simulation system based on mass-spring-damp simulated object. Under the proportion controller condition, the stability of the HIL simulation is analyzed. Wu et al. (2008) took the electro-hydraulic Stewart of the HIL simulation for on-orbit docking dynamics as a research object, designed a fuzzy-immune PID control of a 6-DOF parallel platform for docking simulation.

This paper will summarize the research results of author in the HIL simulation for on-orbit docking dynamics, and present a novel HIL simulation system construction idea based on simulation/hardware interface. Then, the HIL simulation system building procedurals based on it are developed. At last, validations of them are done with experimental test.

Even though the HIL simulation system design procedural discussed in this paper is based on the spacecraft on-orbit docking dynamics, it can meet the demands of other applications.

2. Aim and task of HIL simulation for spacecraft on-orbit docking dynamics

The aim of the HIL simulation for spacecraft on-orbit docking dynamics is to re-emerge the dynamic process of two spacecrafts on-orbit docking on the earth surface.

The tasks of the HIL simulation for spacecraft on-orbit docking dynamics include testing docking mechanism, checking buffer characteristics, simulating the dynamic process of two spacecrafts docking on orbit, defining parameters of docking mechanism, re-emerging troubles of actual spacecraft docking to help finding solution, checking the initial docking conditions of spacecraft docking process, testing the action and counteraction of spacecraft docking process, and so on.

As a large-scale experimental equipment, the HIL simulation system for spacecraft on-orbit docking dynamics should meet the following requirements to complete its simulation task:

1. Ability to simulate the docking process of various spacecrafts.

2. Ability to check or test various docking mechanisms.
3. Ability to test the actual physical docking mechanism and evaluate its performance.
4. Possibility to output and record necessary process parameters of the experimental test.
5. Feasibility to permit human being participates in the simulation.

Then, four attributes of system design of HIL simulation for spacecraft on-orbit docking dynamics are brought forward, they are the stability of the dynamics feedback system, the accuracy of re-emerging the dynamic process, the robust ability of the delay compensator and the adaptability to the docking mechanism and to the spacecraft. In another words, they are four fundamental problems of system design of HIL simulation for spacecraft on-orbit docking dynamics (Chang et al., 2008).

3. Analysis on spacecraft on-orbit docking dynamics

3.1 Initial conditions of on-orbit docking

The initial capturing conditions of two on-orbit docking spacecrafts are shown below

Axial approaching velocity	+0.35 m/sec ;
Radial approaching velocity	-0.10 ~ +0.10 m/sec ;
Radial deflection	-0.30 ~ +0.30 m ;
Pitch and yaw deflection	-7.0 ~ +7.0° ;
Roll deflection	-15.0 ~ +15.0 ° ;
Pose angle velocity	-1.0 ~ +1.0 °/sec .

Since the dynamic process of the spacecraft on-orbit docking does always converge, the initial conditions of on-orbit docking are often the utmost working conditions of the HIL simulation system for spacecraft on-orbit docking dynamics. Usually, 6DOF's operational capabilities of the HIL simulation system (Office of NRBMP, 1999):

- Positional tolerance of $\pm 1.27\text{mm}$ and $\pm 0.10\text{degrees}$.
- Motion range of ± 5 degrees for roll, pitch, and yaw; $\pm 0.15\text{m}$ for translation in the horizontal plane; and 0.61m for vertical travel.
- Payload weight of 1135kg .

3.2 Segmentation of simulated system

Since the hard wares under test in the HIL simulation system are docking mechanisms, then the spacecraft on-orbit docking system can be segmented into two parts, shown in Figure 1. The active docking mechanism on chaser vehicle and the passive docking mechanism on target vehicle is classified as the hardwares under test, which is simulated with physical model. And the rest of the simulated system which consists of two spacecraft bodies are described with the mathematical model, which is translated into a programme which runs on a real-time simulation computer.

3.3 Dynamics model of on-orbit docking spacecraft bodis

The reference frame $e(OXYZ)$ is set on the ground, it is inertia reference frame. Chaser vehicle body frame $e_1(O_1X_1Y_1Z_1)$ is set at the mass centre of the chaser vehicle, and target vehicle body frame $e_2(O_2X_2Y_2Z_2)$ is set at the mass centre of the target vehicle. $e_3(O_3X_3Y_3Z_3)$ and $e_4(O_4X_4Y_4Z_4)$ are at the geometry centre of the assembling surface between docking mechanism and spacecraft body. The directions of the reference frames are shown in Figure 2. The position and pose of spacecraft is defined in Figure 3. Euler angles are defined in Figure 4.

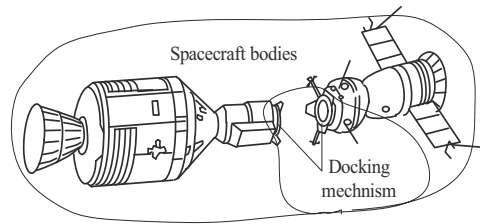


Fig. 1. Segmentation of simulated system

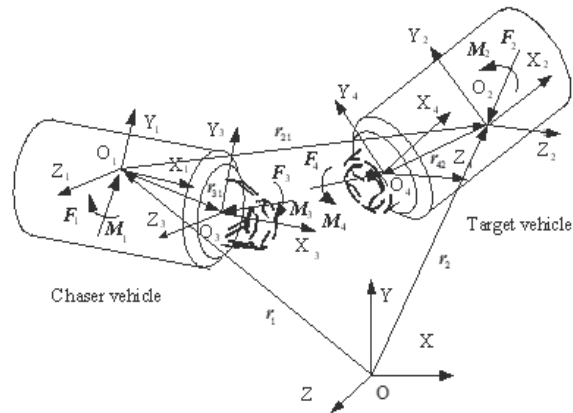


Fig. 2. On-orbit docking spacecraft bodies

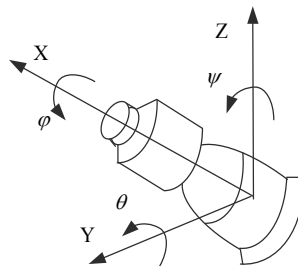


Fig. 3. Definition of position and pose

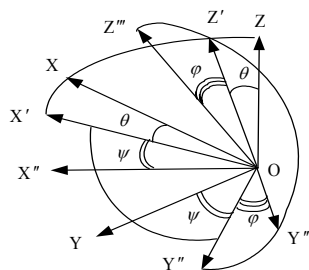


Fig. 4. Definition of Euler angle

When A stands for the transferring matrix from reference frame (OXYZ) to frame (OX''Y'''Z'''), then

$$\mathbf{A} = \begin{bmatrix} c\theta \cdot c\psi & s\varphi \cdot s\theta - c\varphi \cdot c\theta \cdot s\psi & c\varphi \cdot s\theta + s\varphi \cdot c\theta \cdot s\psi \\ s\psi & c\varphi \cdot c\psi & -s\varphi \cdot c\psi \\ -s\theta \cdot c\psi & s\varphi \cdot c\theta + c\varphi \cdot s\theta \cdot s\psi & c\varphi \cdot c\theta - s\varphi \cdot s\theta \cdot s\psi \end{bmatrix}. \quad (1)$$

Where $s(\cdot) = \sin(\cdot)$; $c(\cdot) = \cos(\cdot)$.

The roll, yaw and pitch angles of vehicle i can be work out with angle velocities of its pose.

$$\begin{pmatrix} \dot{\psi}_i \\ \dot{\theta}_i \\ \dot{\varphi}_i \end{pmatrix} = \begin{pmatrix} 0 & \cos(\varphi_i) / \cos(\theta_i) & -\sin(\varphi_i) / \cos(\theta_i) \\ 0 & \sin(\varphi_i) & \cos(\varphi_i) \\ 1 & -\cos(\varphi_i) \tan(\theta_i) & \sin(\varphi_i) \tan(\theta_i) \end{pmatrix} \begin{pmatrix} \omega_{ix} \\ \omega_{iy} \\ \omega_{iz} \end{pmatrix} = \mathbf{N} \begin{pmatrix} \omega_{ix} \\ \omega_{iy} \\ \omega_{iz} \end{pmatrix}. \quad (2)$$

The force F_3 and torque M_3 come from active docking mechanism to the chaser vehicle are defined in $\mathbf{e}_3(O_3X_3Y_3Z_3)$, the other equivalent force F_1 and torque M_1 acting on chaser vehicle are defined in $\mathbf{e}_1(O_1X_1Y_1Z_1)$. The control signals to the chaser vehicle can be included in F_1 and M_1 .

As well, the force F_4 and torque M_4 come from passive docking mechanism to the target vehicle are defined in $\mathbf{e}_4(O_4X_4Y_4Z_4)$, the other equivalent force F_2 and torque M_2 acting on chaser vehicle are defined in $\mathbf{e}_2(O_2X_2Y_2Z_2)$. The control signals to the target vehicle can be included in F_2 and M_2 .

Through equation derivation (Chang et al., 2007e), the docking dynamics model of spacecraft body is gained, it can be describe with Figure 5.

\mathbf{R}_1 stands for the direction cosine matrix of frame $\mathbf{e}_1(O_1X_1Y_1Z_1)$ to frame $\mathbf{e}(OXYZ)$, \mathbf{R}_2 is the direction cosine matrix of frame $\mathbf{e}_2(O_2X_2Y_2Z_2)$ to frame $\mathbf{e}(OXYZ)$, \mathbf{R}_{21} is the direction cosine matrix of frame $\mathbf{e}_2(O_2X_2Y_2Z_2)$ to frame $\mathbf{e}_1(O_1X_1Y_1Z_1)$. And some symbols are defined as:

$$\left(\overset{\circ}{\cdot} \right) = \frac{\Delta^b d}{dt} \left(\cdot \right), \left(\overset{\bullet}{\cdot} \right) = \frac{\Delta^r d}{dt} \left(\cdot \right), \left(\overset{\infty}{\cdot} \right) = \frac{\Delta^b d^2}{dt^2} \left(\cdot \right), \left(\overset{\bullet\bullet}{\cdot} \right) = \frac{\Delta^r d^2}{dt^2} \left(\cdot \right).$$

3.4 Dynamic characteristics of docking mechanism

The docking mechanism is an important constituent of the HIL simulation system and of the simulated object system. The dynamic characteristic of docking mechanism plays important roles in the dynamic characteristic of the spacecraft on-orbit docking.

For an example, the APAS 89 docking mechanism is an inner guided petal androgynous peripheral assembly system, whose mechanical structure is Stewart platform. But the motions of six actuators of the Stewart platform are differential and not stand-alone (Kang, 1999). So the rigidity and damp characteristics of APAS 89 is very complicate.

Yu et al.(2004) set up the model of the APAS 89 docking mechanism with Adams software, which is a dynamics simulation and analysis software tool kit. Dynamics characteristics of the docking mechanism can be tested with its Adams model.

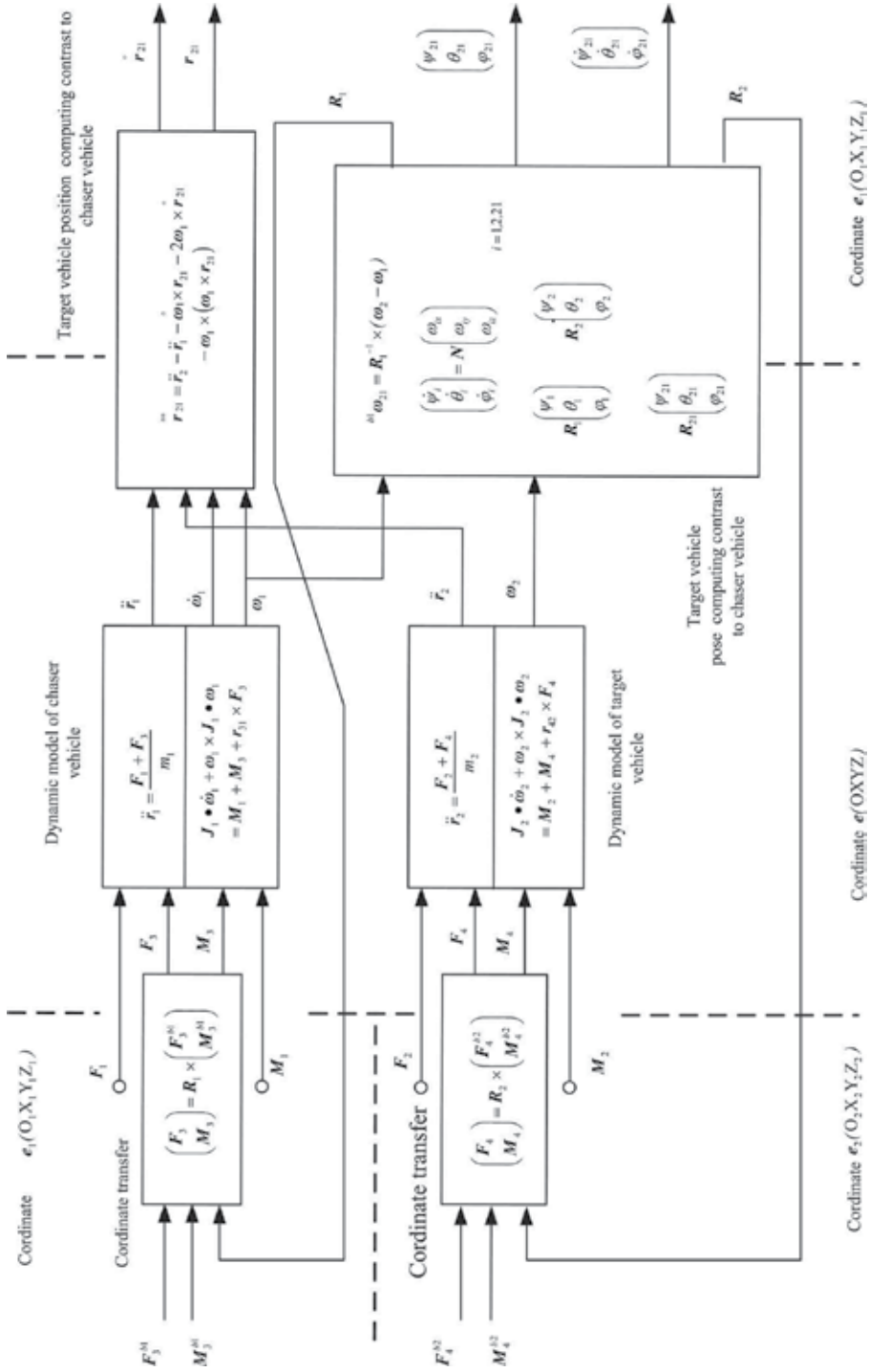


Fig. 5. Mathematic model of on-orbit docking spacecraft bodies

The displacement and force relationship of the docking mechanism in the X direction can be shown in Figure 6. The displacement and force relationship of the docking mechanism in the Y or in Z direction are nearly same, shown in Figure 7. The relationships between torque and yaw angle or pitch angle of the docking mechanism are nearly same, they are shown in Figure 8. The relationship between torque and roll angle of the docking mechanism are shown in Figure 9. Above figures indicates the complexity of the dynamics characteristics of docking mechanism.

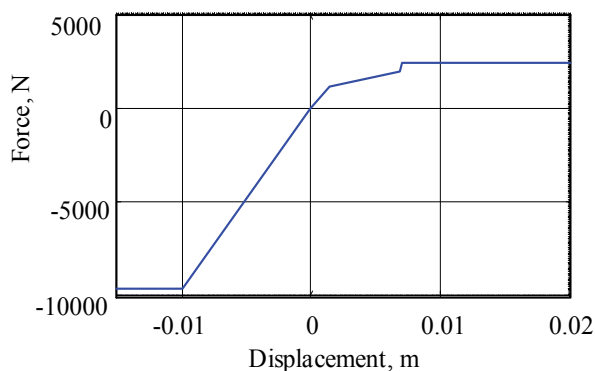


Fig. 6. Force and displacement in X direction

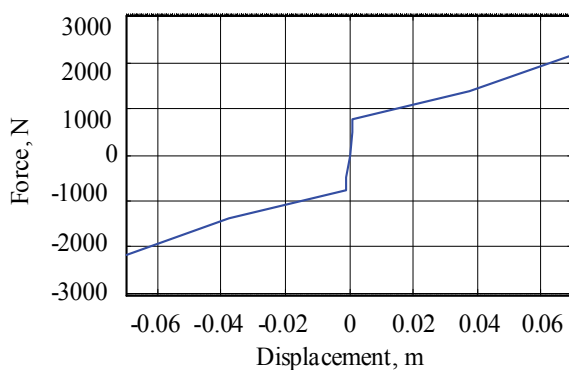


Fig. 7. Force and displacement Y or Z direction

The capturing and the impact absorbing are two main successive on-orbit docking phases for the on-ground HIL simulation (Peng et al., 1992). During the impact-absorbing phase, the docking mechanism shows strong coupling and nonlinearity and its parameters vary in large scale. During the capturing phase, the active docking mechanism on the chase vehicle collisions with the passive docking mechanism mounted on the target vehicle and the contact cases are very complicate (Guan, 2001). So it is difficult to describe the actual docking mechanism with the mathematical model, or it will abate the credence of the simulation. Thus, it is proper to use the physical model of docking mechanism, especially use full scale to docking/berthing hardware as the physical model participating in the simulation.

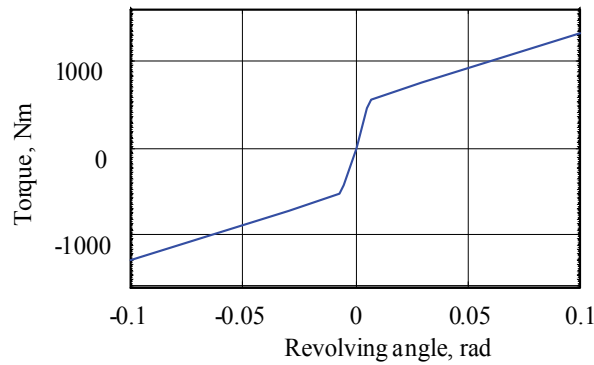


Fig. 8. Torque and angle in yaw and pitch

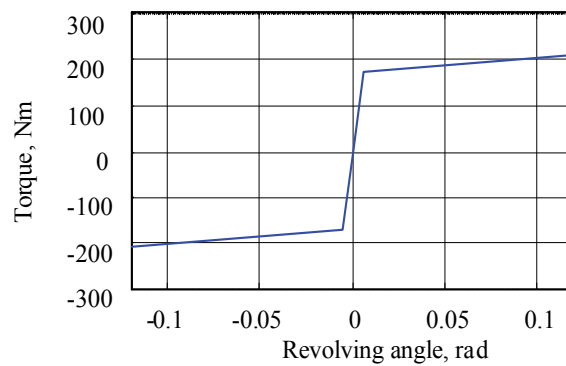


Fig. 9. Torque and angle in roll

3.5 Dynamics model of simulated system

If the mathematic model of the docking mechanism is established, its block diagram can connect with the block diagram of the docking dynamics model of spacecraft body. Then the dynamics model of simulated system is established, shown in Figure 11. Its reference frame is the body coordinate $e_1(O_1X_1Y_1Z_1)$.

The mathematic model of the simulated system can be used to validate the correction of real-time simulation model of the HIL simulation system.

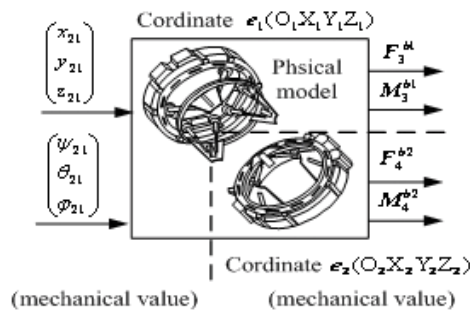


Fig. 10. Block diagram of docking mechanism

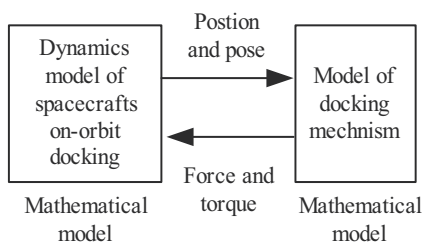


Fig. 11. Simulated system model

3.6 Frequency band width of docking dynamics

The rigidity in the longitudinal direction of the APAS 89 is bigger than that in other directions. The value of the rigidity is not a constant, it varies in large-scale. But it can be roughly divided as contacting rigidity and impact absorbing rigidity. The contacting rigidity is nearly 10^6 N/m. Considering the mass of the spacecrafts, the frequency of the main dynamic process needed to be re-emerging by the HIL simulation is finite. The upper frequency bound is called as docking frequency, signed as ω_d and ω_d is usually no larger than 5 Hz. The dynamic process of spacecraft on-orbit docking is a high frequency response process, it requires that the motion simulator and the F/T sensor should have high frequency response ability.

4. System construction ideas of HIL simulation for spacecraft on-orbit docking dynamics

The dynamics model of spacecraft on-orbit docking and the actual body of docking mechanism are two components of the HIL simulation. They come from the simulated system, shown in Figure 12. Before the constructing of HIL simulation system, the correction of the dynamic model of spacecrafts on-orbit docking should be verified.

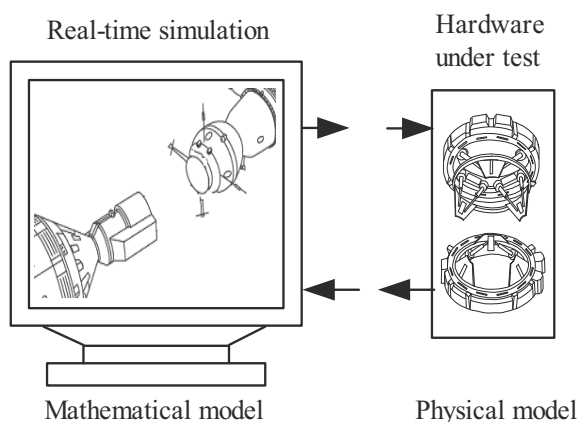


Fig. 12. Simulated system

The mathematic model of spacecraft on-orbit docking dynamics can run on real-time simulation computer, but it is not stand alone. The input signals of the real-time simulation

computer are the forces and torques values created by the docking mechanism, mean while the real-time simulation computer outputs the movement values of the spacecraft bodies.

Obviously, the actual docking mechanisms or their physical models can not be drive by the electrical signals created by the real-time simulation computer, and they can not provide the electrical signals of force and torque needed by the real-time computer either.

Here, a generalized interface concept is presented. The simulation/hardware interface is a complex system, not an electrical interface. It connects the real-time simulation with the hard wares under test and sets up the HIL simulation system, shown in Figure 13. It may include electro-hydraulic system, electro-mechanical system, parallel manipulator, various sensors, and so on.

The simulation/hardware interface of the HIL simulation system for spacecraft on-orbit docking dynamics consists of the motion simulator and the force and torque sensors. The motion simulator accepts the motion command signals created by the real-time simulation computer and outputs mechanical movements which can drive the docking mechanism. Then, the active dock mechanism and passive docking mechanism can collide with each other and produce force and torque. The force and torque sensor which is mounted on the rack picks up the force and torque acted by the active docking mechanism. This force and torque sensor can be imaged having been mounted between the passive docking mechanism and the target vehicle body. The force and torque sensor which is mounted on the moving plate of the Stewart platform picks up the force and torque acted by the passive docking mechanism. This force and torque sensor can be imaged having been mounted between the active docking mechanism and the chaser vehicle body. The actual forces and torques are transformed into the digital signals which can be collected by the real-time simulation computer. Now, the main feedback loop of the HIL simulation system is established. It is called two force and torque sensor scheme.

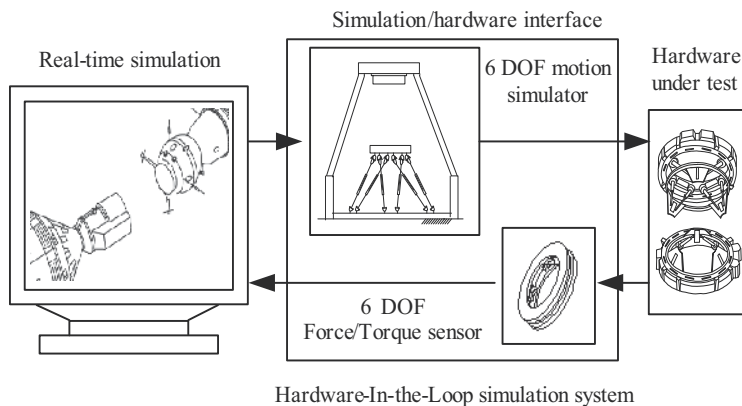


Fig. 13. HIL simulation system

The dynamic characteristics of the feedback system of the HIL simulation system are required to be similar with those of the simulated system. But unfortunately the dynamic characteristics of the simulation/hardware interface distort the similarity, especially for the high frequency response dynamics simulation. If the dynamic characteristics of the feedback system are not properly rebuilt, the dynamic characteristics of the HIL simulation system are quietly different with those of simulated system. For an example, the simulated system is always stable, but its HIL simulation may be unstable. This is the fundamental reason of the system design problem or system integrated problem. So the system design problems or

system integrated problems (Chang et al., 2007a) are put forward. But the system construction of the HIL simulation for the spacecraft on-orbit docking dynamics is difficult. The main part of the motion simulator of the simulation/hardware interface is a Stewart platform driven by six electro-hydraulic servo systems, it is a nonlinear and strong coupling multi-input multi-output (MIMO) system. The dynamic model of spacecrafts on-orbit docking is also a nonlinear and strong coupling MIMO system. Further more, the actual docking mechanism is included into the HIL simulation, the docking mechanism is a very complex electro-mechanical system. It may be controlled or operated by a human. So the HIL simulation system is too complex to study as a whole system. That is why the ideas of simulation/hardware interface of HIL simulation system for spacecraft on-orbit docking is put forward.

The system design procedure based on the concept of the simulation/hardware interface is illustrated in Figure 14. It is expected to find the criterion or guideline to the design of the simulation/hardware interface, through analyzing the HIL simulation system. The guide line of the simulation/hardware interface design can be gained through analyzing the guide line of the HIL simulation. During system design period, design problem of the complex HIL simulation system is simplified as a comparatively simple design problem of simulation/hardware interface.

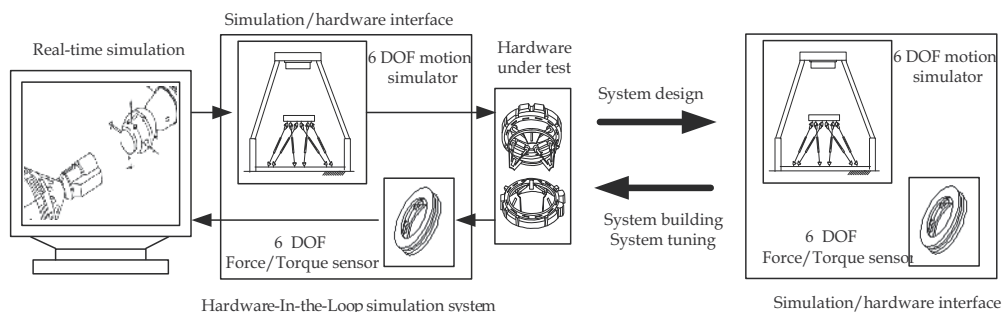


Fig. 14. HIL simulation system design, system building and system tuning

During system tuning or system building period, the object of the system tuning is simulation/hardware interface. Through tuning the dynamic characteristics of the simulation/hardware interface, the dynamic characteristics of the whole HIL simulation system can be adjusted to meet the requirements of simulation.

If un-modelled dynamic characteristics are omitted, the real-time simulation and the hardware under test do little to the authenticity of the HIL simulation based on above system construction ideas, because they are the components of the simulated system. In another word, above system construction ideas ensure the adaptability of the HIL simulation system to the docking mechanism and to the spacecraft.

And this is the fundamental base that a simplified docking mechanism can be used to validate the HIL simulation system. This is another merit of above HIL simulation system construction ideas.

The initial capture condition and locus planning model block is added into above HIL simulation, the basic system structure of HIL simulation for on-orbit docking is shown in Figure 15. The locus planning programme drives the motion simulator to make the passive docking mechanism to collide with active docking mechanism mounted on the rack with the initial test conditions. And just before capturing, the feed back loop of the dynamics control is closed.

5. Research procedure to technology of HIL simulation for spacecraft on-orbit docking dynamics

Because of the complexity of the HIL simulation system construction for spacecraft on-orbit docking dynamics, the analysis and synthesis of the HIL simulation system for on-orbit docking is still difficult today yet, because there are many obstacles involving in them. The main obstacles that are brought into the HIL simulation system design by the hardware under test are strong nonlinearity and strong coupling of the docking mechanism, the high equivalent rigidity of the docking mechanism and the large-scale varying of the rigidity. The high-speed response dynamic process of on-orbit docking and the high accuracy of the simulation requirement make the HIL simulation design even more difficult. Furthermore, the nonlinear and the coupling of mathematic model of the spacecraft on-orbit dynamics, the nonlinear and the coupling of motion simulator further hinder people to analyze or to synthesize the HIL simulation system with theoretical method.

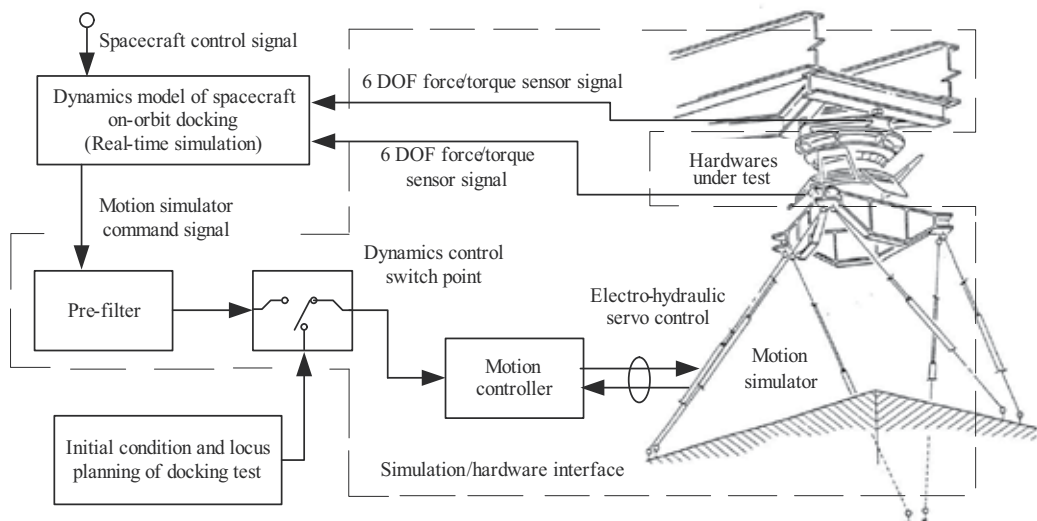


Fig. 15. Basic system structure of HIL simulation for on-orbit docking

Obviously, it is an easy to research the design guideline of the HIL simulation system with single degree-of-freedom (DOF) model, which is the simplified model of the actual spacecraft on-orbit docking.

So the first step of the research procedural is to research design guideline of the HIL simulation system with the single DOF model, then the results of the single DOF model can be extended to the MIMO HIL simulation system case through theoretical analysis and experimental validation.

6. System construction procedure to HIL simulation for single-degree-of-freedom spacecraft on-orbit docking dynamics

The single DOF HIL simulation system is a single-input single-output (SISO) system. Since ultimate aim of the SISO system research is helping find the design guideline of MIMO system. Even though it is not difficult to analyze or synthesize the single HIL simulation

system as the whole system, the research on single DOF model will strictly follow the ideas of simulation/hardware interface.

6.1 Single DOF HIL simulation system model

The actual spacecrafts on-orbit docking are simplified as a single DOF spacecraft on-orbit docking, which is two single DOF spacecrafts docking with a simplified docking mechanism model. Under the idea of simulation/hardware interface, the single DOF spacecrafts docking with a simplified docking mechanism model is segmented into two parts shown in Figure 16.

Then the model of HIL simulation system of a single DOF spacecraft on-orbit docking dynamics is set forth, it is illustrated with Figure 17. The force sensor and an electro-hydraulic servo-system driving actuator make up the simulation/hardware interface.

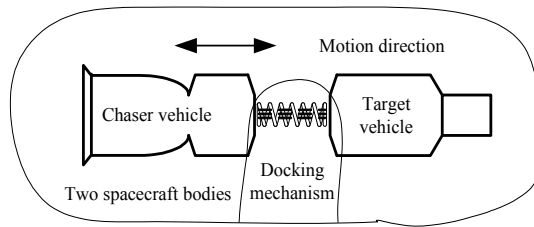


Fig. 16. Single DOF simulated system

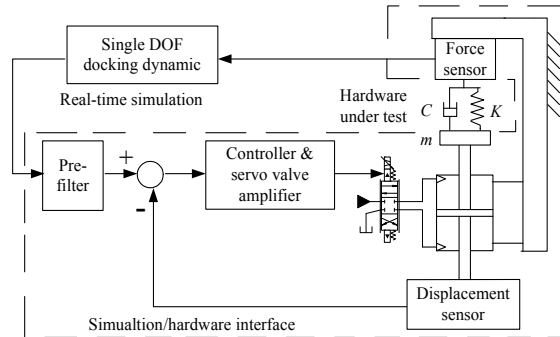


Fig. 17. Single DOF HIL simulation system

The single DOF spacecraft bodies are shown in Figure 18. x is defined as the relative displacement between the two spacecrafts, then

$$x = x_2 - x_1 . \quad (3)$$

The mathematic model for the real-time numerical simulation of the HIL simulation is the dynamics model of the two rigid bodies driven by a pair of acting and counteracting forces in the conditions of zero gravity and vacuum. By simple deriving, the dynamics model can be written as

$$G_{DDyn}(s) = \frac{X(s)}{F(s)} = \frac{m_1 + m_2}{m_1 m_2} \times \frac{1}{s^2} . \quad (4)$$

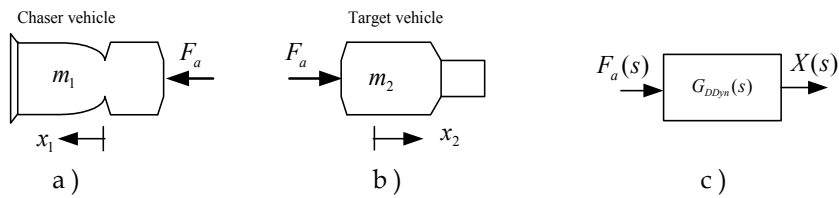


Fig. 18. Single-DOF spacecraft bodies

Above dynamics model is also a simplified version of the dynamics model actual spacecraft bodies shown in Figure 5.

The docking mechanism of the single DOF can be simplified as a spring and a damper, shown in Figure 19. Its mathematic model of the docking mechanism can be written as

$$G_{DMech}(s) = \frac{F(s)}{X(s)} = -Cs - K \tag{5}$$

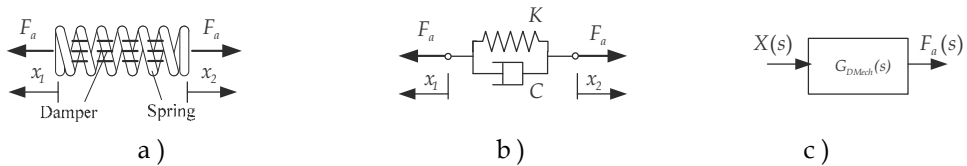


Fig. 19. Single-DOF docking mechanism

6.2 Ideas on simulation/hardware interface and control strategy on HIL simulation

When the docking mechanism is simplified as a spring-damp device, the single DOF simulated object system can be used to research the dynamic process of the face-to-face collision and impact absorbing process during spacecraft docking.

The dynamics characteristics of the simulated object system can be described by a feedback system shown in Figure 20, even though the mechanical structure of the simulated object system is open chain structure. The feedback characteristics are intrinsic and not obvious. Then

$$\frac{X_{mech}(s)}{F_r(s)} = \frac{G_{DDyn}(s)G_{DMech}(s)}{1 + G_{DDyn}(s)G_{DMech}(s)} \tag{6}$$

The HIL simulation system for on-orbit docking can be shown in Figure 21. The force sensor and the motion simulator are called as simulation/hardware interface. It is the simplified version of the system shown in Figure 13.

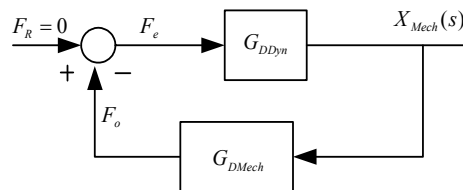


Fig. 20. Block diagram of simulated system

$$\frac{X_{mech}(s)}{F_r(s)} = \frac{G_{DDyn}(s)G_{DMech}(s)G_{FSensor}(s)G_{MSim}(s)}{1 + G_{DDyn}(s)G_{DMech}(s)G_{FSensor}(s)G_{MSim}(s)} \quad (7)$$

Comparing Equation (6) and Equation (7), The dynamic characteristics of the HIL simulation system and those of the simulated system are the same when $G_{FSensor}(s)G_{MSim}(s) = 1$.

Based on the idea of the simulation/hardware interface, the function of the simulation/hardware interface is to establish the connection between the physical model and the real-time simulation. The design guideline of HIL simulation system should be

$$G_I(s) = G_{FSensor}(s)G_{MSim}(s) \approx 1. \quad (8)$$

Where $s = j\omega$, for $0 \leq \omega \leq \omega_s$. ω_s is called as HIL simulation frequency in this paper.

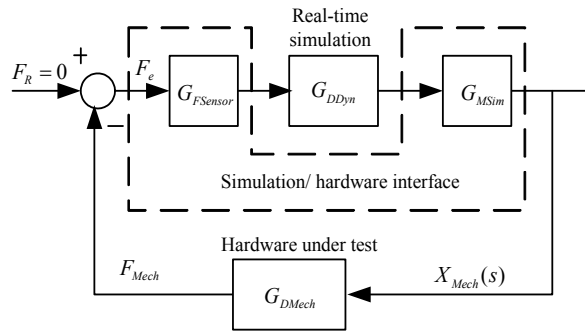


Fig. 21. Block diagram of HIL simulation system

To adapt to the characteristics of the docking mechanism, the HIL simulation frequency band is needed to cover the docking frequency band. That is $\omega_s \geq \omega_d$.

Above are the desired performances of the simulation/hardware interface. Its realization is a control problem. Many control strategies can meet above demand. These solutions scheme can be summarized up as two-degree-of-freedom control structure, shown in Figure 22.

$$G_{MSim}(s) = Y_M(s)/X_M(s) = G_{prefilter}G_{Controller}G_{Actuator} / (1 + G_{Controller}G_{Actuator}). \quad (9)$$

In two-degree-of-freedom control structure, $G_{Controller}$ is controller of feedback system, which help to reduce the variation of the plant output, while $G_{prefilter}$ is used as a filter to tailor the response of the simulation/hardware interface to meet the specification of the HIL simulation system. The precondition of the compensation with $G_{prefilter}$ is that the sensitivity of the dynamic characteristics of the electro-hydraulic system to the variation of factors such as payload rigidity is lower in the docking frequency. In another word, the sensitivity of the pole positions in S domain of the close-loop transfer function of the motion simulator to the large-scale variation of payload stiffness is lower.

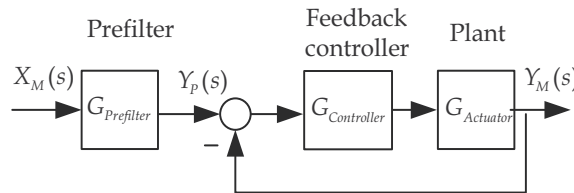


Fig. 22. Two-degree-of-freedom control structure

Once the control structure is made certain, the other control problems are the skills or methods to fulfill it.

To ensure the stability and the performance of the HIL simulation system, the error between $G_I(s)$ and 1 must be sufficiently small in the docking frequency band. The relationship between the distortion of the HIL simulation and above errors can guide the HIL system tuning (Chang et al., 2007d).

6.3 The key problems of the simulation/hardware interface design

The attribute of the simulation/hardware interface requires that the motion simulator of the HIL simulation system should be with high accuracy and high response. The electro-hydraulic actuator helps the motion simulator achieve high speed response and high rigidity. Zhang (2006) presents that the amplitude error of the electro-hydraulic system of motion simulator at the middle position is no larger than 2 dB and the lag is no larger than 70 degrees when the frequency of input signal is 10 Hz.

The hardware (docking mechanism) under test is the load of simulation/hardware interface. The large-scale variation of the rigidity of docking mechanism requires that the simulation/hardware interface should be insensitive to them. This is the precondition of the HIL simulation system synthesis using the two-degree-of-freedom control structure. The method to solve above problems is tried to increase hydraulic spring rate of the electro-hydraulic actuator to make the natural frequency of the hydraulic actuator approximate to the hydraulic undamped natural frequency.

Here we only make a brief explanation on it.

The displacement output of the hydraulic power element of the motion simulator can be expressed as:

$$Y = \frac{\frac{K_q}{A} X_v - \frac{K_{ce}}{A^2} \left(\frac{V_t}{4\beta_e K_{ce}} s + 1 \right) F}{\frac{V_t m}{4\beta_e A^2} s^3 + \left(\frac{m K_{ce}}{A^2} + \frac{B_c V_t}{4\beta_e A^2} \right) s^2 + \left(\frac{K V_t}{4\beta_e A^2} + \frac{B_e K_{ce}}{A^2} + 1 \right) s + \frac{K K_{ce}}{A^2}} \quad (10)$$

The symbols used here is as same as those in Merrit's book (Merrit, 1967). From equation (10), it can be known dynamic characteristics of the electro-hydraulic system will change when the stiffness of the payload is varying.

The hydraulic actuators could be designed to make the hydraulic spring rate of the hydraulic actuators much greater than the equivalent rigidity of the docking mechanism. That is to satisfy the following inequality by enlarging the effective area A of the hydraulic cylinder.

$$K / K_h \ll 1 \quad (11)$$

Where $K_h = 4\beta_e A^2 / V_t$. Then, the positions of the loop transfer function poles of the hydraulic power element are less sensitive to the rigidity variation of the payload. The positions of the close-loop poles of the electro-hydraulic system of the motion simulator are less sensitive to the rigidity variation of the docking mechanism (Chang et al., 2007c).

If working substance (oil) in the hydraulic system is done vacuum pumping, the bulk module of the working substance will be enlarged, K/K_h will be even smaller and the dynamic performance of the motion simulator will be less sensitive to the rigidity variation of the docking mechanism.

The force sensor adopted for the HIL simulation system is piezocrystal, which has higher rigidity. It can still achieve high natural frequency when it is attached on the docking mechanism. And the natural frequency of force sensor is possible to be higher than 350 Hz.

6.4 Validation with simulation

The simulation research is aim at verifying the design ideas of the simulation/hardware interface, design guideline of the HIL simulation system and the simulation/hardware interface, as well as the methods and skills for the system tuning. Single DOF spacecraft on-orbit docking is the simulated object.

The mathematic model of the single HIL simulation system for on-orbit docking dynamics is established with Matlab/Simulink. The parameters of the motion simulator are shown in Table 1.

Symbol	Nomenclature	Value
A	Effective area of actuator	0.06m ²
V_t	Total compressed volume of actuator	0.36m ³
m	Mass load of motion simulator	2500kg
β_e	Bulk module of oil	6.9×10^8 Pa
B_c	Viscous damping coefficient of motion simulator	20N/(m·s-1)
K_{ce}	Total flow-pressure coefficient	9×10^{-12} m ³ /(s·Pa)

Table 1. Parameters for single DOF motion simulator

The control structure of the motion simulator is shown in Figure 22. By tuning the controller $G_{prefilter}$, the performance of the motion simulator can be described as: when the frequency of the input signal is 10Hz, the amplitude error is not larger than 2dB and the phase error is no larger than 70 degrees.

Then $G_{Controller}$ is defined to make the simulation/hardware interface transfer function $G_I(s) \approx 1$ when $0 \leq \omega \leq \omega_s$, the Bode diagram of the simulation/hardware interface is shown in Figure 23.

The Table 2 shows the parameters of the on-orbit docking spacecrafts. If the linear model of the docking mechanism is adopted by the simulated object system, and its parameters are shown in Table3, the dynamic characteristics of the HIL simulation system are described by curve a in the Bode diagram, shown in Figure 24. The dynamic characteristics of the simulated object system are described by curve b. The curve a and curve b superpose with each other at lower frequency.

Symbol	Nomenclature	Value
m_1	Mass of chaser vehicle	8000kg
m_2	Mass of target vehicle	12000kg

Table 2. Parameters of single DOF spacecrafts

The simulated object adopted the nonlinear docking mechanism model, its characteristics are shown in Figure 6, and the results of simulation are shown in Figure 25 and Figure 26. The damp model of the docking mechanism is simplified as the viscous damp and its value is 4000Ns/m. In each figure, the curve a is the simulation result to the HIL simulation

system; the curve b is the ideal result of the simulated object system model shown in Figure 16 but with the nonlinear docking mechanism model.

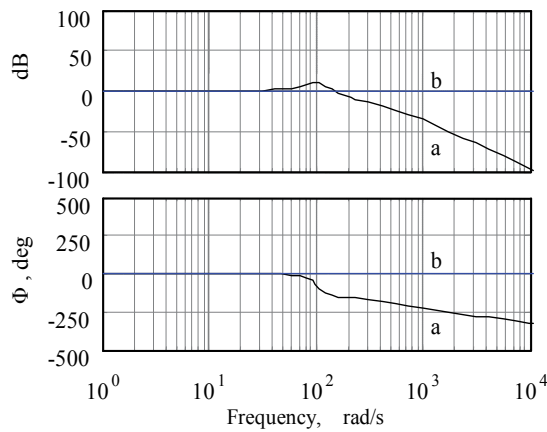


Fig. 23. Bode diagram of simulation/hardware interface

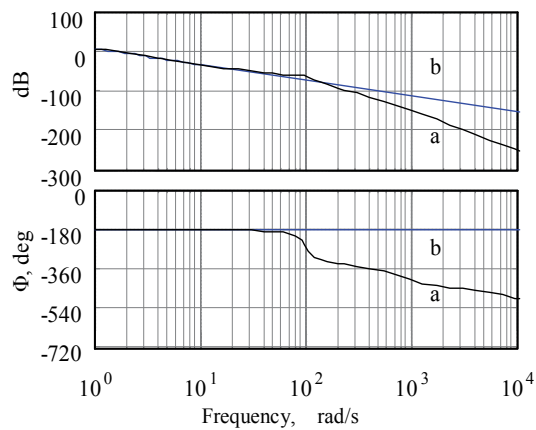


Fig. 24. Bode diagram of HIL simulation system

Symbol	Nomenclature	Value
K	Rigidity of docking mechanism	1000000N/m
C	Viscous damping coefficient of docking mechanism	0 N/(m·s-1)

Table 3. Parameters for single DOF linear docking mechanism

7. System construction procedure to HIL simulation for multi-degree-of-freedom spacecraft on-orbit docking dynamics

7.1 Actual HIL simulation system for spacecraft on-orbit docking dynamics

Since the simulated system is segmented in two parts, and they all take part into the HIL simulation system in different forms. The actual docking mechanisms are the hardwares

under test. The mathematic model of the real-time simulation is established with the spacecraft bodies, it can be described by Figure 27.

Based on the experience of the system construction of the single DOF spacecraft docking dynamics, the piezoelectricity 6-DOF force and torque sensors are adopted as the interface from the hardware to the real-time simulation. To drive the passive docking mechanism, a Stewart platform and a fixed rack are used as the motion simulator, it is the interface from real-time simulation to hardware. The six legs of the Stewart platform are driven by six electro-hydraulic servo control system. The response speed and rigidity of the motion simulator are all high.

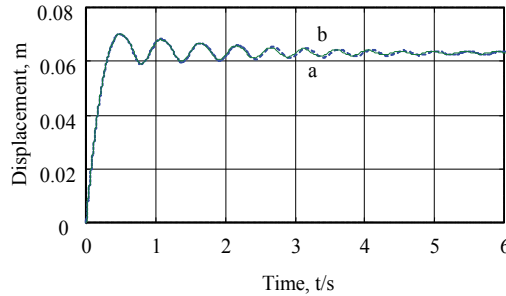


Fig. 25. Displacement curves

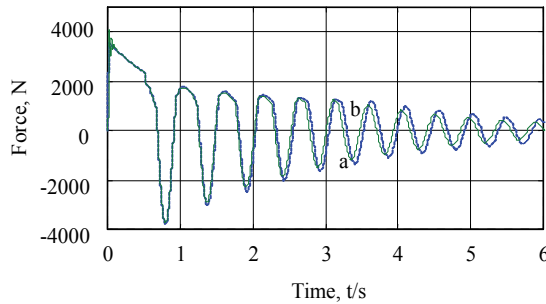


Fig. 26. Force curves

The reference frame $e_b(O_bX_bY_bZ_b)$ is set on the ground. $e_0(O_0X_0Y_0Z_0)$ is set on the fixed rack, and $e_p(O_pX_pY_pZ_p)$ is set on the moving plate of the Stewart platform. Their directions are shown in Figure 27.

Figure 28. shows the relationship between the reference frame of the motion simulator and the reference frame of spacecrafts bodies. It shows the transform from the position and pose signal of the spacecraft bodies of real-time simulation model to the command signal of the motion simulator.

In engineering, the two force and torque sensor scheme of the HIL simulation system bring some difficult in system tuning. When the mass of moving part of the active docking mechanism is relatively small, the force and torque sensor can be calculated out with signals from the force and torque sensor fixed on the rack by Equation (12) and Equation (13). The force and torque sensor mounted on the moving plate of the motion simulator can be omitted. And this is called single force and torque sensor scheme.

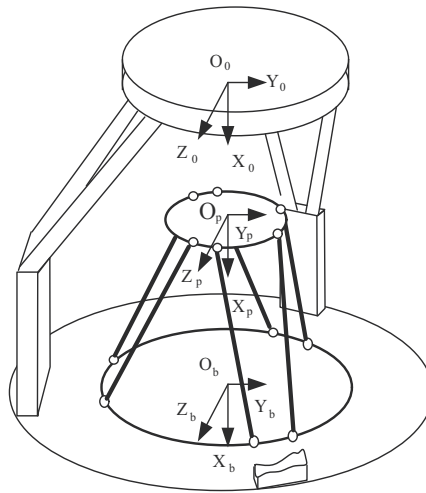


Fig. 27. Reference frame of motion simulator

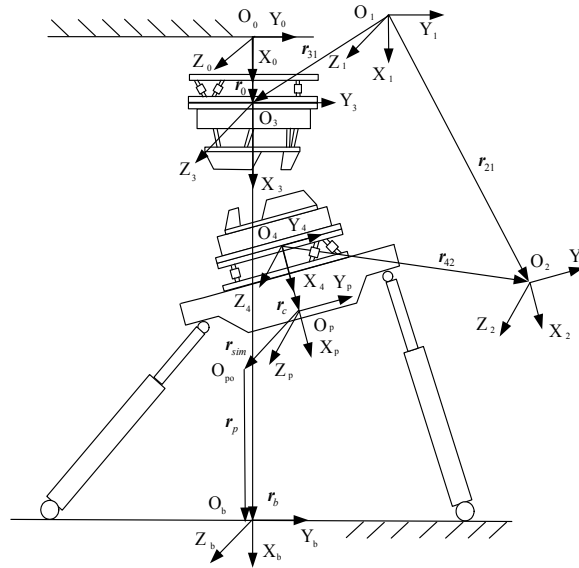


Fig. 28. Reference frame of HIL simulation

$$F_4 = -F_3 = F' = -F \quad (12)$$

$$M_4 = (r_{21} + r_{42} - r_{31}) \times F_4 - M_3 \quad (13)$$

7.2 Design issues on simulation/hardware interface

The natural frequency can be used as an index to evaluate the dynamic performance of a mechanical system. The natural frequency of the force and torque sensor is much higher than that of the motion simulator. So the dynamic characteristics of the simulation/hardware

interface are limited by the Stewart platform of motion simulator. The Stewart platform is a typical parallel manipulator, the design of the Stewart platform is relative complex. Because of the limitation of pages, the design of the Stewart platform isn't discussed in detail, and only some research conclusions are listed here. By the way, some literatures (Lim et al., 1989; Merlet, 2000; He, 2007) can provide more detail information on this topic.

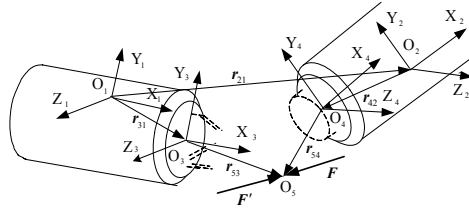


Fig. 29. Action and counteraction between spacecraft

From former research results, it is reasonable to expect that the MIMO simulation/hardware interface is decoupled and its dynamic performance is robust. Unfortunately, the research on the Stewart platform shows that it can not full decoupled, the dynamic characteristics of each degree of freedom of the Stewart platform will change when its position and pose is changing. How ever the variation of the dynamic characteristics of each degree of freedom of the Stewart can be reduced through its structure design.

Some research conclusions about the simulation/hardware interface design are listed here.

- Large-dimension Stewart platform is adopted to improve the decoupling and robust ability of dynamic performance of the Stewart platform. The docking work space is much smaller than the reachable work space of the Stewart platform.
- Stewart platform is driven by electro-hydraulic servo control systems to gain high-peed performance and high-rigidity.
- Single rode symmetry electro hydraulic cylinder is used to enhance the robust ability of dynamic performance.
- The effective areas of the hydraulic actuator are enlarged to reduce the sensitivity of the electro-hydraulic system to the large-scale variation of the payload ridigity. (the same as the issues on single-DOF model)
- The working substance (oil) in the hydraulic system is done vacuum pumping to enhance the bulk module of the working substance will be enlarged and to further reduce the sensitive of dynamic performance of the motion simulator to the large-scale variation of rigidity of the docking mechanism.

Under above conditions, the coupling between the degrees of freedom can be treated as the un-modelled dynamic characteristics. Then the research results of single DOF HIL simulation can be used on each degree of freedom of the MIMO HIL simulation system for spacecraft on-orbit docking.

7.3 Analysis on motion simulator

The chief part of the motion simulator is a hydraulic driven Stewart platform. With the parameters of DDTS, the reachable space of the motion simulator is shown in Figure 30. Mean while the docking work space can also be drawn in same reference frame. Obviously the docking work space is the small space at the core of the reachable space of the Stewart

platform. This feature of Stewart platform structure is help to reduce the variation of the dynamic characteristics of each degree of freedom of the Stewart platform in the docking work space.

By checking the natural frequency of the degree of freedom of the Stewart platform, the changing of its dynamic characteristics can be verified to meet the demands of the synthesis of HIL simulation system. In the upmost area of the docking work space, natural frequency of the degree of freedom of the Stewart platform is show in Figure 31, 32, 33, 34, 35 and 36.

7.4 Validation with experimental test

Base on the VV&A (Verification, Validation, and Accreditation) principles of system modeling and simulation, especially the priority objective principle and necessary but insufficient principle, the validation model used to check the authenticity of the HIL simulation results for spacecraft on-orbit docking dynamics is established. The validation model is a simplified spacecraft on-orbit docking model.

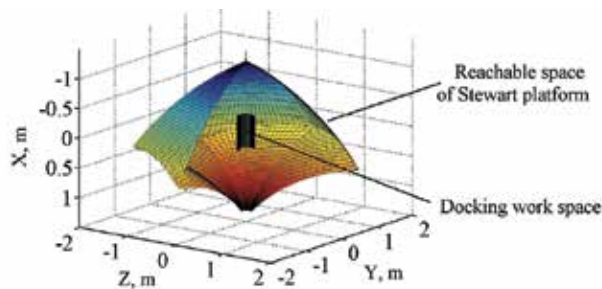


Fig. 30. Docking working space and reachable space of Stewart platform

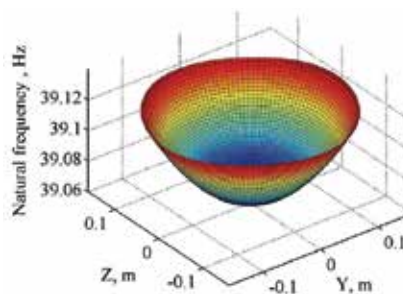


Fig. 31. Natural frequency in X direction

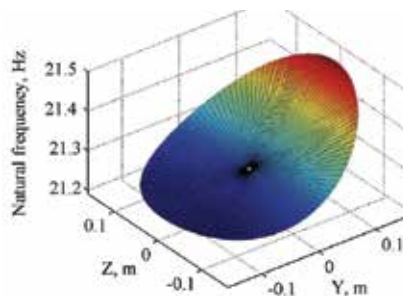


Fig. 32. Natural frequency in Y direction

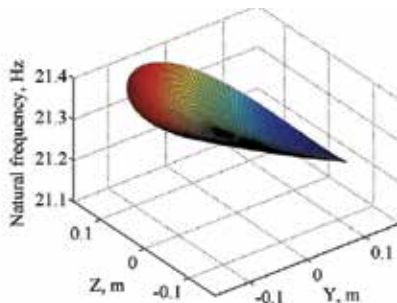


Fig. 33. Natural frequency in Z direction

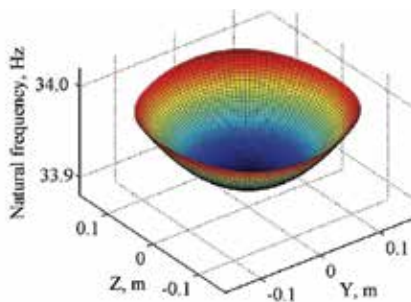


Fig. 34. Natural frequency in roll

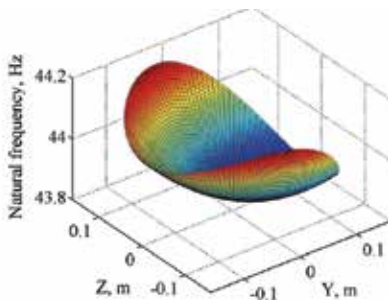


Fig. 35. Natural frequency in yaw

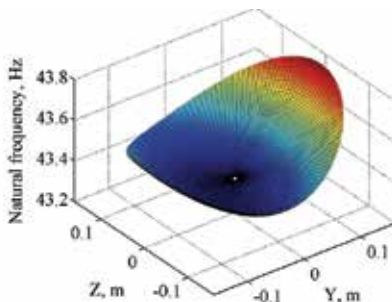


Fig. 36. Natural frequency in pitch

The validation model which can be simulated with the HIL simulation system is the simplified model of the simulated object system. The similarity between key parameters of the collision created by the hardwares of HIL simulation system and by the validation

model can be used to check the dynamic characteristics of the closed-loop HIL simulation system.

Figure 37 shows the validation model of the HIL simulation system of on-orbit docking dynamics. The collision created by non-damping spring stick and a rigid frame is used to simulate the collision between the two spacecrafts. The spring stick is a cantilever, and its deformation is small. Since the collision is happened at the same point on the spring stick, the spring stick can be regarded as a spring and its spring rate K can be worked out by Equation (14).

$$K = 3\pi E d^4 / (64l^3) \quad (14)$$

where E is the bulk module of material, N/mm^2 ; l is the nominal length of the spring stick; d is the diameter of the spring stick.

Omitting the damping of the spring stick caused by deformation (such as material damping, structural damping, etc.), the force relationship between elastic collision devices of the validation model is expressed in Equation (15).

$$F(x) = \begin{cases} -K(x - h/2 + d/2), & x > h/2 - d/2 \\ 0, & h/2 - d/2 \geq x \geq -h/2 + d/2 \\ -K(x + h/2 - d/2), & x < -h/2 + d/2 \end{cases} \quad (15)$$

where $F(x)$ stands for the collision force between the two spacecrafts, N ; x stands for the relative displacement between the two spacecrafts, m ; h see Figure 37, m .

The dynamics model of the mass bodies of the validation model is shown in Equation (16).

$$\ddot{x} = F(x) / [m_1 m_2 / (m_1 + m_2)] \quad (16)$$

where m_1 and m_2 are the mass of the mass bodies, kg .

Then the collision contact time of the validation model can be work out by Equation (17).

$$T_v = \pi \sqrt{m_1 m_2 / ((m_1 + m_2) K)} \quad (17)$$

While, T_h is the contact time of the collision created by the HIL simulation system. The similar ratio between the collision contact time R_T can be worked out by Equation (18).

$$R_T = T_h / T_v = T_h \sqrt{(m_1 + m_2) K / (m_1 m_2)} / \pi \quad (18)$$

If the damp of the validation model is omitted, the velocity recovery coefficient of the collision described by validation model e_v equals 1. The similarity ratio of the speed recovery coefficient R_e can be work out by Equation (19).

$$R_e = e_h / e_v = |v_1| / |v_0| \quad (19)$$

Where v_0 is the initial velocity, v_1 is bounce velocity, they can be read out from the velocity curve of the experimental results of the HIL simulation.

Obviously, if there is no distortion in the HIL simulation result, then $R_e = 1$, $R_T = 1$.

The experimental system of the HIL simulation system for spacecraft on-orbit docking dynamics is shown in Figure 38. The mathematical dynamics model run on the real time computer is the dynamics model of the actual spacecraft bodies which are docking on orbit, but its parameters should be set according to the specific freedom degree under test.

The validation mechanism, which is used as a testing device to check the performance of the HIL simulation system, can be installed into the HIL simulation system as the hardware under test instead of the docking mechanism.

The validation mechanism should be designed under direction of the HIL simulation system construction ideas and the validation model.

Figure 36 shows the HIL simulation system with the validation mechanism. All parts of the validation mechanism but the spring stick can be regard as the rigid bodies. The spring stick is used as a buffer device. Because the validation mechanism is the payload of the simulation/hardware interface of the HIL simulation system, its mass, inertia, mass center should comfort to the actual docking mechanism.

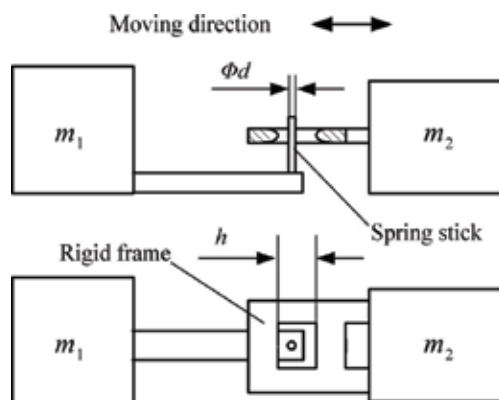


Fig. 37. Vibro-impact HIL simulation test



Fig. 38. Experimental validation system

Figure 39 and Figure 40 are Bode diagrams of motion simulator are tested in X direction and in Y direction respectively.

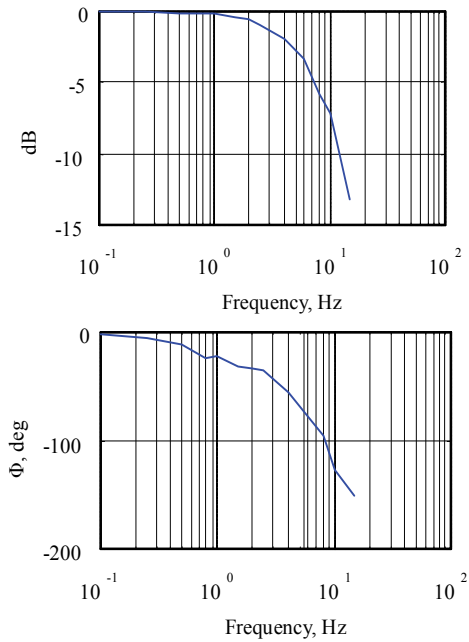


Fig. 39. Bode diagram in X direction

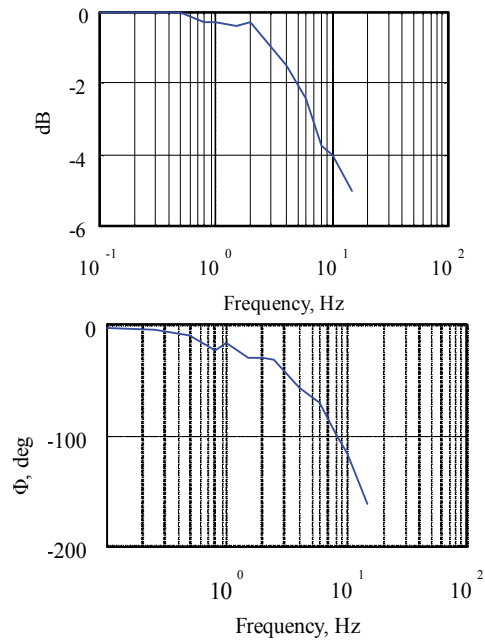


Fig. 40. Bode diagram in Y direction

If the dynamic characteristics of the HIL simulation system is not properly reconstructed with the time delay compensator, then if it is used to simulate the validation model (shown in Figure 37), the dynamic process of the HIL simulation system is divergent, shown in Figure 41 and Figure 42. By the way, above test is under control of the safe protection of the HIL system.

If the HIL simulation is over compensated, its dynamic process is not correct either, shown in Figure 43 and Figure 44.

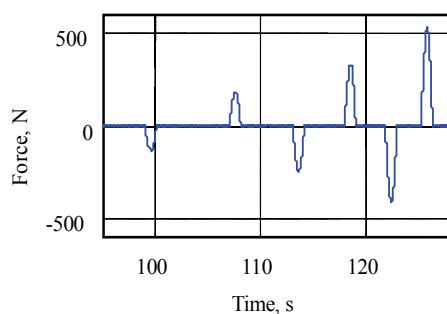


Fig. 41. Force curve

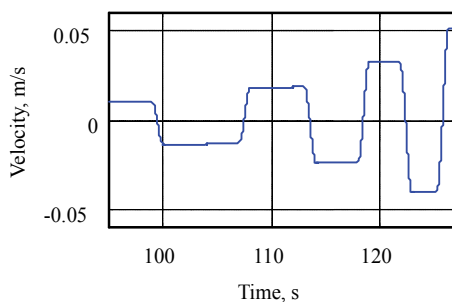


Fig. 42. Velocity curve

Test parameters			Test results			
Frequency (Hz)	l (m)	$m_1 = m_2$ (kg)	X direction		Y direction	
			R_e	R_T	R_e	R_T
0.235	0.140	32423	0.985	1.005	0.9725	1.019
0.471	0.140	8106	0.987	1.007	0.973	1.019
0.941	0.140	2026	0.95	0.988	0.96	1.016
1.731	0.100	1597	0.992	0.975	0.96	1.051
2.308	0.100	898	0.99	1.034	0.95	1.045
2.884	0.100	575	0.975	1.005	0.983	1.032

Table 4. Testing parameters & testing results

All above demonstrate that the HIL simulation system can not be used to simulate the spacecraft on-orbit docking dynamic process unless the dynamic characteristic of the HIL simulation system is properly reconstructed with the time delay and time lag of the compensator (Chang et al, 2007b).

After tuning the HIL simulation system, a set of tests are done in X direction and in Y direction respectively. The test parameters and the test results are shown in Table 4. Figure 45 and Figure 46 show the force curve and the velocity curve at 0.471Hz in X direction, while Figure 47 and Figure 48 show the force curve and the velocity curve at 0.471Hz in Y direction the test parameters. (Chang, 2010)

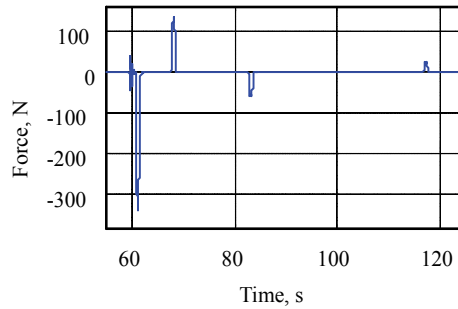


Fig. 43. Force curve

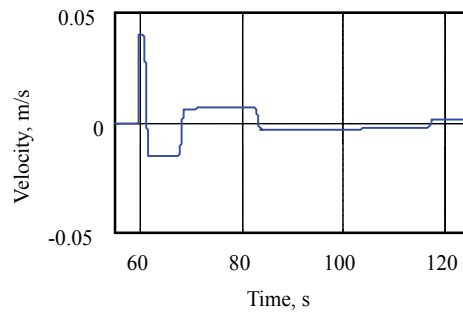


Fig. 44. Velocity curve

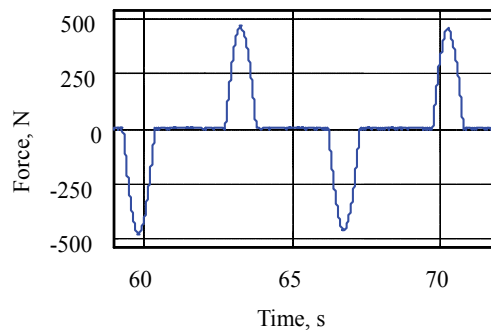


Fig. 45. Force curve

8. Conclusion

The ideas on the simulation/hardware interface are presented. The simulation/hardware interface is a complex mechnronics system, it connects the real-time simulation with the hard wares under test and sets up the HIL simulation system.

The ideas of the simulation/hardware interface simplified the HIL system design and system building. The design problem of the complex HIL simulation system is simplified as a comparatively simple design problem of simulation/hardware interface. Through tuning the dynamic characteristics of the simulation/hardware interface, the dynamic characteristics of the whole HIL simulation system can be rebuilt.

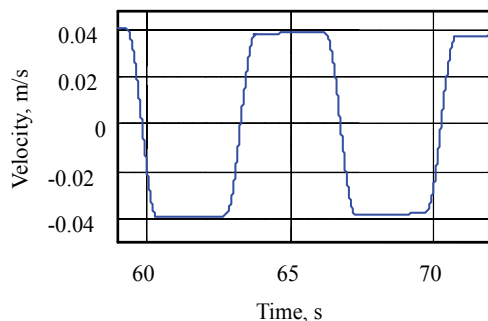


Fig. 46. Velocity curve

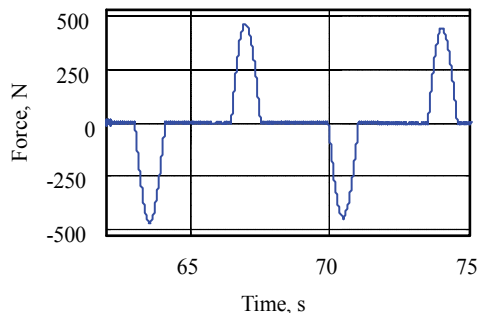


Fig. 47. Force curve

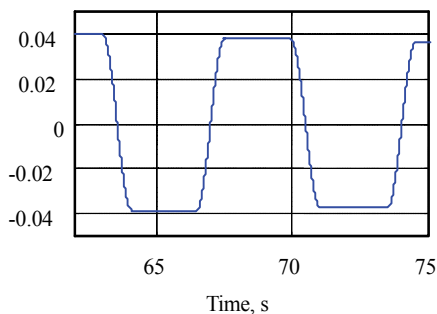


Fig. 48. Velocity curve

Based on the ideas on the simulation/hardware interface, the design procedural of the HIL simulation can be divided into following steps: the segmentation of the simulated system, the establishing of the mathematic model, the design of the simulation/hardware interface and the building of the whole system of HIL simulation.

The research on the single DOF HIL simulation system for spacecraft on-orbit docking dynamics verified the correction and feasibility of the ideas and procedural of the HIL

simulation system construction. Then the research results of single DOF HIL simulation can be used on each degree of freedom of the MIMO HIL simulation system for spacecraft on-orbit docking. And its validation was done on an experimental system.

Further research work may be focused on the system building theory or system synthesis theory of multi-DOF HIL simulation for spacecraft on-orbit docking. It is a promising research field.

9. References

- Ananthakrishnan, S.; Teders, R. & Alder, K. (1996). Role of estimation in real-time contact dynamics enhancement of space station engineering facility. *IEEE Robotics & Automation Magazine*, Sep. 1996, pp.20-27
- Chang, T. L.; Cong, D. C.; Ye, Z. M. & Han, J. W. (2007a). A new procedural for the integration of the HIL simulation system for on-orbit docking. *Proceedings of the 2007 IEEE International Conference on Integration Technology*, pp.769-773, ISBN Shenzhen Institute of Advanced Technology, Mar. 2007, IEEE, Shenzhen, China.
- Chang, T. L.; Cong, D. C.; Ye, Z. M. & Han, J. W. (2007b). Time problems in HIL simulation for on-orbit docking and compensation. *Proceedings of the 2nd IEEE Conference on Industrial Electronics and Applications (IEEE ICIEA 2007)*, pp.841-846. *IEEE Industrial Electronics (IE) Chapter & Harbin Institute of Technology*, Ma. 2007, Harbin, China
- Chang, T. L.; Cong, D. C.; Ye, Z. M. & Han, J. W. (2007c). Electro-hydraulic servo control system design of HIL simulator for spacecraft on-orbit docking. *Proceedings of the Fifth International Symposium on Fluid Power Transmission and Control (ISFP2007)*, Yansan University, Beidaihe, China, Jul. 2007: 580~584.
- Chang, T. L.; Cong, D. C.; Ye, Z. M. & Han, J. W. (2007d). Interface issues in Hardware-In-the-Loop simulation for spacecraft on-orbit docking. *Proceedings of the Sixth IEEE International Conference on Control and Automation (IEEE ICCA 2007)*, *IEEE Control Systems Chapter (Singapore) & IEEE Control Systems Chapter (Guangzhou)*, Guangzhou, China, Jun. 2007: 2584-2590.
- Chang, T. L.; Cong, D. C.; Ye, Z. M. & Han, J. W. (2007e). Simulation on HIL ground experimental simulator for on-orbit docking dynamics. *Acta Aeronautica et Astronautica*. Vol.28, No.4, Jul. 2007, pp.975-980(in Chinese)
- Chang, T. L.; Cong, D. C.; Ye, Z. M. & Han, J. W. (2008). Research on fundamental problems and the solutions of HIL simulation for on-orbit docking dynamics. *Journal of Astronautics*. Vol.29, No.1, Jan. 2008, pp.53-55(in Chinese)
- Chang, T. L. (2010). Research on verification of authenticity of HIL simulation using vibro-impact model. *Journal of Vibration and Shock*. Vol.29, No.1, Jan. 2010, pp.22-25 (in Chinese)
- Gates, R. M. & Graves, D. L. (1974). Mathematical model for the simulation of dynamic docking test system (DDTS) active table motion. N74-33776, pp.1-3
- Grimbert, D. & Marchal, P. (1987). Dynamic testing of a docking system. N88-19516, pp.281-288

- Guan, Y. Z.(2001). Research on dynamics and simulation technique of spacecraft docking process. Ph. D. thesis. Harbin, China: Harbin Institute of Technology, Aug. 2001, pp.8-12 (in Chinese)
- He, J. F.(2007). Analysis and control of hydraulically driven 6-DOF parallel manipulator. Ph. D. thesis. Harbin, China: Harbin Institute of Technology, Feb. 2007, pp.89-98 (in Chinese)
- Huang, Q. T.; Jiang, H. Z.; Zhang, S. Y. & Han, J. W. (2005). Spacecraft docking simulation using HIL simulator with Stewart platform. *Journal of Chinese Mechanical Engineering*. Vol.18, No.3, Mar. 2005, pp.415-418
- Kang, J.; Guan, H. H. & Song, J.(1999). Study on dynamics of mechano-electronic spring-damper system with differential connections. *J. Tsinghua Univ. (Sci. & Tech.)* Vol.39, No.8, Aug. 1999, pp.68-71
- Kawabe, H.; Inohira, E.; Kubota, T.; Uchiyama, M. (2001). Analytical and experimental evaluation of impact dynamics on a high-speed zero G motion simulator. *Proceedings of the 2001 IEEE/RSJ International Conference on Intelligent Robots and Systems*. Hawaii, USA, Oct. 2001, pp.39~45.
- Lange, C.; Martin, E.; Piedboeuf, J. C.; Kovacs, J. (2002). Towards Docking Emulation Using Hardware in the Loop Simulation with Parallel Platform. *Proceedings of the Workshop on Fundamental Issues and Future Directions for Parallel Mechanisms and Manipulators*. Quebec, Canada, Oct. 2002, pp.1-4
- Lim, G. K.; Freeman, R. A.; Tesar, D. (1989). Modelling and Simulation of a Stewart Platform Type Parallel Structure Robot. *The University of Texas at Austin*, 1989, pp.1-151
- Merlet, J. P. (2000). *Parallel robots*. Dordrecht: Kluwer Academic Publishers, 2000.
- Merrit, H.E. (1967). *Hydraulic control systems*. New York: Wiley, 1967
- Monti, A.; Figueroa, H.; Lentijo, S.; Wu, X. & Dougal, R. (2005). Interface issues in Hardware-in-the-Loop simulation. *Proceedings of the 2005 IEEE Ship Technologies Symposium*, Jul. 2005, pp.39-45
- Office of Naval Research's Best Manufacturing Practices. (1999). Report of survey conducted at NASA Marshall Space Flight Center. Best Manufacturing Practice Center of Excellence. Huntsville, USA, Apr. 1999, pp.12-13
- Peng, C. R.; Qu, G. J.; Ma, Z. C. & Yu, J. Y. (1992). Russia large spacecraft dynamics and its testing technology. *Spacecraft Engineering*, No.3, Mar.1992, pp.1-7 (in Chinese)
- Tian, H.; Zhao, Y. & Zhang, D. W. (2007). Movement simulator modelling and simulation in integrate test platform for docking mechanism. *Journal of Astronautics*. Vol.28, No.4, July 2007, pp.996-1001(in Chinese)
- Wu, L. B.; Wang, X. Y. & Li, Q. (2008). Fuzzy-immune PID control of a 6-DOF parallel platform for docking simulation. *Journal of Zhejiang University (Engineering Science)*. Vol.42, No.3, Mar.2008, pp.387-391(in Chinese)
- Yan, H.; Ye, Z. M.; Cong, D. C.; Han, J. W. & Li, H. R. (2007). Space docking hybrid simulation prototype experiment system. *Chinese Journal of Mechanical Engineering*. Vol.43, No.9, Sep.2007, pp.51-56(in Chinese)
- Yu, W.; Yang, L. & Qu, G. J. (2004). Dynamics analysis and simulation of spacecraft docking mechanism. *Journal of Dynamic and Control*, Vol.2, No.2, Feb.2004, pp. 38-42 (in Chinese)

- Zhang, C. F. (1999). Study on Six-Degree-of-Freedom simulation for docking. *Aerospace Control*, No.1, Jan. 1999, pp.70-74 (in Chinese)
- Zhang, S. Y. (2006). Research on force control of hydraulic driven 6-DOF parallel robot. Ph. D. thesis. Harbin, China: Harbin Institute of Technology, Apr. 2006, pp.6-7 (in Chinese)
- Zhao, H. & Zhang, S. Y. (2008). Stability analysis of the whole dynamics simulation system of space docking. *J. of Wuhan Uni. of Sci. & Tech. (Natural Science Edition)* Vol.31, No.1, Feb.2008, pp.87-97(in Chinese)
- Zhao, Y; Tian, H. & Wang, Q. S. (2007). Analysis of dynamometry scheme for semi-physical simulation platform of space docking mechanism. *Advances in Engineering Software*. Vol.38, 2007, pp.710-716

Solar Sailing: Applications and Technology Advancement

Malcolm Macdonald
*Advanced Space Concepts Laboratory
University of Strathclyde, Glasgow
Scotland, E.U.*

1. Introduction

Harnessing the power of the Sun to propel a spacecraft may appear somewhat ambitious and the observation that light exerts a force contradicts everyday experiences. However, it is an accepted phenomenon that the quantum packets of energy which compose Sunlight, that is to say photons, perturb the orbit attitude of spacecraft through conservation of momentum; this perturbation is known as solar radiation pressure (SRP). To be exact, the momentum of the electromagnetic energy from the Sun pushes the spacecraft and from Newton's second law momentum is transferred when the energy strikes and when it is reflected. The concept of solar sailing is thus the use of these quantum packets of energy, i.e. SRP, to propel a spacecraft, potentially providing a continuous acceleration limited only by the lifetime of the sail materials in the space environment. The momentum carried by individual photons is extremely small; at best a solar sail will experience 9 N of force per square kilometre of sail located in Earth orbit (McInnes, 1999), thus to provide a suitably large momentum transfer the sail is required to have a large surface area while maintaining as low a mass as possible. Adding the impulse due to incident and reflected photons it is found that the idealised thrust vector is directed normal to the surface of the sail, hence by controlling the orientation of the sail relative to the Sun orbital angular momentum can be gained or reduced. Using momentum change through reflecting such quantum packets of energy the sail slowly but continuously accelerates to accomplish a wide-range of potential missions.

1.1 An historical perspective

In 1873 James Clerk Maxwell predicted the existence of radiation pressure as a consequence of his unified theory of electromagnetic radiation (Maxwell, 1873). Apparently independent of Maxwell, in 1876 Bartoli demonstrated the existence of radiation pressure as a consequence of the second law of thermodynamics.

The first experimental verification of the existence of radiation pressure and the verification of Maxwell's results came in 1900. At the University of Moscow, Peter Lebedew succeeded in isolating radiation pressure using a series of torsion balance experiments (Lebedew, 1902). Nichols and Hull at Dartmouth College, New Hampshire, obtained independent verification in 1901 (Nichols & Hull, 1901, 1903). Around this period a number of science fiction authors wrote of spaceships propelled by mirrors, notably the French authors Faure and Graffigny in 1889. However, it was not until the early 20th century that the idea of a

solar sail was accurately articulated. Solar sailing as an engineering principle can be traced back to the Father of Astronautics, Ciołkowski (translated as Tsiolkovsky) and Canders (translated as Zander or Tsander) (Ciołkowski, 1936; Tsander, 1924). There is some uncertainty regarding the dates of Ciołkowski's writings on the potential use of photonic pressure for space propulsion. However, it is known that he received a government pension in 1920 and continued to work and write about space. It is within the early part of this period of his life, in 1921 perhaps, which he first conceived of space propulsion using light. Upon the publication of the works of Herman Oberth in 1923, Ciołkowski's works were revised and published more widely, enabling him to gain his due international recognition. Inspired by Ciołkowski, Canders in 1924 wrote "*For flight in interplanetary space I am working on the idea of flying, using tremendous mirrors of very thin sheets, capable of achieving favourable results.*" (Tsander, 1924). Today this statement is widely, though not universally, bestowed the credit as the beginning of solar sailing as an engineering principle.

In 1923 the German rocket pioneer Herman Julius Oberth proposed the concept of reflectors in Earth orbit (Spiegelrakete, or Mirror rocket) to illuminate northern regions of Earth and for influencing weather patterns (Oberth, 1923). It was this work which caused the works of Ciołkowski to be revised and published more widely. In 1929 Oberth extended his earlier concept for several applications of orbit transfer, manoeuvring and attitude control (Spiegelführung, or Mirror guidance) using mirrors in Earth orbit (Oberth, 1929). This work has a clear parallel with that of Canders' from 1924. However, it is also of interest that in this work Oberth noted solar radiation pressure would displace the reflector in a polar orbit in the anti-Sun direction. Thus, with the central mass, i.e. Earth, displaced from the orbit plane Oberth had, in-effect, noted the application of solar sailing to what we now call Highly Non-Keplerian Orbits and which will be discussed later in Section 3.1.2.

Following the initial work by Ciołkowski, Canders and Oberth the concept of solar sailing appears to have remained largely dormant for over thirty years. In the 1950s the concept was re-invigorated and published once again in popular literature, this time in North America. The first American author to propose solar sailing appears to have been the aeronautical engineer Carl Wiley, writing under the pseudonym Russell Sanders to protect his professional credibility (Wiley, 1951). Wiley discussed the design of a feasible solar sail and strategies for orbit raising in some technical detail. In particular he noted that solar sails could be "*tacked*" allowing a spiral inwards towards the Sun. In 1958 Richard Garwin, then at the IBM Watson laboratory of Columbia University, authored a solar sail paper in the journal *Jet Propulsion* where he coined the term "*solar sailing*" (Garwin, 1958).

Subsequent to the discussion of solar sailing by Garwin, more detailed studies of the orbits of solar sails were undertaken during the late 1950s and early 1960s (Birnbaum, 1968; Cotter, 1959; Fimple, 1962; Gordon, 1961; London, 1960; Norem, 1969; Sands, 1961; Tsu, 1959). For a fixed sail orientation several authors have shown that solar sail heliocentric orbits are of the form of logarithmic spirals (Bacon, 1959; London, 1960).

Early comparisons of solar sailing with chemical and ion propulsion systems showed that solar sails could match or out perform these systems for a range of mission applications, though of course the level of assumed technology status is crucial in such comparisons (MacNeal, 1972). These early studies explored the fundamental problems and benefits of solar sailing, but lacked a specific mission to drive detailed analyses and to act as a focus for future utilisation. In the early 1970's the development of the Space Shuttle and the technological advances associated with deployable structures and thin films suggested that perhaps solar sailing was ready to move beyond paper studies (Cotter, 1973; Grinevitskaia;

1973; Lippman, 1972; MIT Student Project, 1972). In 1974 NASA funded a low-level study of solar sailing at the Battelle laboratories in Ohio which gave positive recommendations for further investigation (Wright, 1974). The Battelle laboratories recommendations were acted upon at NASA-JPL in an Advanced Mission Concepts Study for Office of Aeronautics and Space Technology (OAST) in FY1976 (Uphoff, 1975). During the continuation of the Battelle laboratories study Jerome Wright discovered a trajectory that would allow a relatively high-performance solar sail to rendezvous with comet Halley at its perihelion in the mid-1980's by spiralling towards the Sun and then changing the orbit inclination by almost 180 deg (Wright & Warmke, 1976). The flight time of four years would allow for a late 1981 or early 1982 launch, however the required level of solar sail¹ performance suggests the study was always over optimistic. Furthermore, as it turns out the first operational space shuttle flight did not occur until the November of 1982 (STS-5); as such, the shuttle could not have acted as the Comet Halley solar sail launch vehicle as had been originally envisaged. A seven to eight year mission had been envisaged using solar-electric ion propulsion, requiring a launch as early as 1977. These positive results prompted NASA-JPL to initiate an engineering assessment study of the potential readiness of solar sailing, following which a formal proposal was put to NASA management on 30 September 1976. At the same time a companion study and technology development program for Advanced Solar Electric Propulsion was initiated in order to allow it to be evaluated as a competitor for the Halley mission. During the initial design study an 800-m per side, three-axis stabilised, square solar sail configuration was envisaged, but then dropped in May 1977 due to the high risks associated with deployment of such a massive structure. The design work progressed to focus on a spin stabilised heliogyro configuration. The heliogyro concept, which was to use twelve 7.5 km long blades of film rather than a single sheet of sail film, had been developed by Richard MacNeal and John Hedgepath (Hedgepath & Benton, 1968; MacNeal, 1967). The heliogyro could be more easily deployed than the square solar sail by simply unrolling the individual blades of the spinning structure. As a result of this design study the structural dynamics and control of the heliogyro were characterised and potential sail films manufactured and evaluated (Friedman et al, 1978; MacNeal, 1971). As a result of the Advanced Solar Electric Propulsion companion study NASA selected the Solar Electric Propulsion (SEP) system in September 1977 upon its merits of being a less, but still considerable risk for a comet Halley rendezvous (Sauer, 1977). A short time later the SEP rendezvous mission was also dropped due to escalating cost estimates (Logsdon, 1989).

1.2 Recent technology developments and activities

Following the Comet Halley studies solar sailing entered a hiatus until the early 1990's when further advances in spacecraft technology led to renewed interest in the concept. The first ever ground deployment of a solar sail was performed in Köln in December 1999 by the German space agency, DLR, in association with ESA and INVENT GmbH when they deployed a square 20-m solar sail, shown in Fig. 1 (Leipold et al, 2000; Sebolt et al, 2000). This ground deployment and the associated technology developed by DLR and ESA has struggled to progress to flight, initially an in-orbit deployment was planned for 2006 however this project floundered, with a similar, but smaller, demonstration now planned for 2013 as part of a three-step solar sail technology development program (Lura et al, 2010).

¹ The comet Halley solar sail had a required characteristic acceleration of 1.05 mm s^{-2} ; see Wright, 1992 (pp. 42).

In 2005 NASA completed dual solar sail development programs, funding a solar sail design by ATK and another by L'Garde Inc. who used the inflatable boom technology developed under the IAE program. Both solar sail systems were deployed to 20-m (side length) in the large vacuum chamber at NASA Glenn Research Center's Space Power Facility at Plum Brook Station in Sandusky, Ohio, U.S.A, the world's largest vacuum chamber (Lichodziejewski et al, 2003; Murphy et al, 2003 & 2004). Following the deployment demonstrations the L'Garde design was down-selected due to its perceived scalability to much larger sail sizes for the subsequent NASA New Millennium Space Technology 9 (ST-9) proposal, prior to the ST-9 program being cancelled. However, it should be noted that the ATK sail was considered a lower risk option. The intention of the NASA funding was to develop solar sail technology to Technology Readiness Level (TRL) six, however a subsequent assessment found that actually both the L'Garde and ATK sail failed to fully achieve either TRL 5 or 6, with the ATK sail achieving 89% and 86%, respectively and the L'Garde sail reaching 84 % and 78 %, respectively (Young et al, 2007).

In May 2010 the first spacecraft to use solar radiation pressure as its primary form of propulsion was launched by the Japanese space agency, JAXA, onboard an H-IIA launch vehicle from the Tanegashima Space Center as an auxiliary payload alongside the Japanese Venus orbiter Akatsuki, formerly known as the Venus Climate Orbiter (VCO) and Planet-C, and four micro-spacecraft. The solar sail spacecraft is called IKAROS (Interplanetary Kite-craft Accelerated by Radiation Of the Sun) and like the Akatsuki spacecraft was launched onto a near-Venus transfer trajectory. The IKAROS is a square solar sail, deployed using spinning motion and 0.5 kg tip masses, the polyimide film used for solar sailing also has thin-film solar arrays embedded in the film for power generation and liquid crystal devices which can, using electrical power, be switched from diffusely to specularly reflective for attitude control (Mori et al, 2010). IKAROS has demonstrated a propulsive force of 1.12mN (Mori et al, 2010) and is shown in Fig. 3. The IKAROS mission is envisaged as a technology demonstrator towards a power sail spacecraft, using the large deployable structure to host thin-film solar cells to generate large volumes of power to drive a SEP system (Kawaguchi, 2010).

In addition to the traditional view of solar sailing as a very large structure several organisations, including NASA and the Planetary Society, are developing CubeSat based solar sails. Indeed, NASA flew the first CubeSat solar sails on board the third SpaceX Falcon 1 launch on 2 August 2008 which failed approximately 2 minutes after launch. It is however unclear how such CubeSail programs will complement traditional solar sailing and whether they will provide sufficient confidence in the technology to enable larger, more advanced solar sail demonstrator missions. It is clear that the technology of solar sailing is beginning to emerge from the drawing board. Additionally, since the NASA Comet Halley mission studies a large number of solar sail mission concepts have been devised and promoted by solar sail proponents. As such, this range of mission applications and concepts enables technology requirements derivation and a technology application pull roadmap to be developed based on the key features of missions which are enabled, or significantly enhance, through solar sail propulsion. This book chapter will thus attempt to link the technology application pull to the current technology developments and to establish a new vision for the future of solar sailing.

2. Performance metrics

To compare solar sail mission applications and concepts standard performance metrics will be used. The most common metric is the characteristic acceleration which is the idealised SRP

acceleration experienced by the solar sail facing the Sun at a distance of 1 au. An ideal or perfect sail facing the Sun at a distance of 1 au will experience a pressure of $9.126 \mu\text{N m}^{-2}$; however, in practise an efficiency factor must be added to this to account for non-ideal performance (Wright, 1992). The sail characteristic acceleration offers an excellent performance metric unsullied by difficulties in hardware development and implementation of the theory.

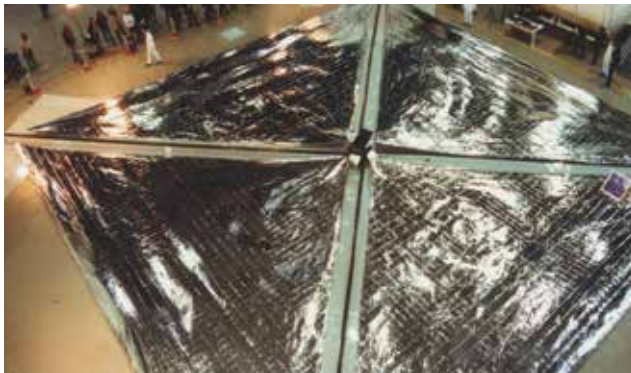


Fig. 1. DLR solar sail ground deployment test. Image credit DLR

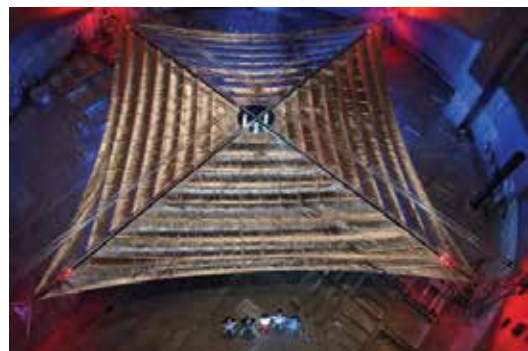
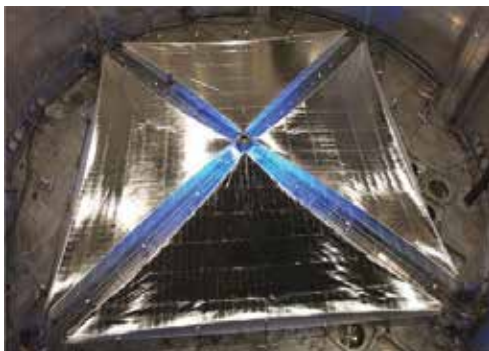


Fig. 2. 20-m solar sail deployment tests by ATK (left) and L'Garde (right) at NASA Glenn Research Center's Space Power Facility at Plum Brook Station. Image credit NASA

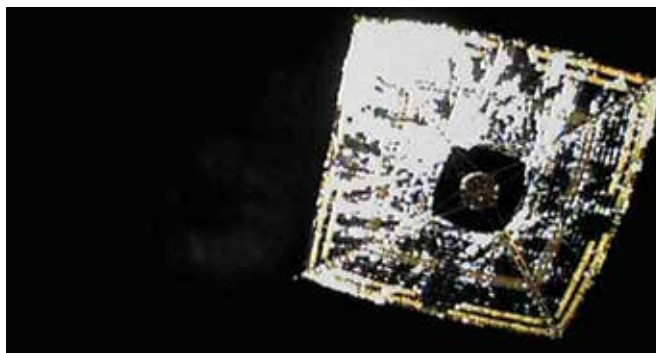


Fig. 3. IKAROS solar sail, imaged by free flying camera. Image credit JAXA

The sail assembly loading is the primary hardware performance metric for a solar sail, allowing a measure of the performance of the sail film and the efficiency of the solar sail architectural and structural design. The sail characteristic acceleration and assembly loading are defined as,

$$a_{S_c} = \frac{2P}{\sigma_S + (m_a / A)}, \quad \sigma_S = \frac{m_S}{A} \quad (1)$$

where, P is SRP acting on the solar sail, m_a is mass attached to the solar sail, m_S is mass of the solar sail and A is the reflective surface area of the solar sail, typically assumed simply as the sail film area.

3. Solar sail mission catalogue

In the final quarter of the 20th century and opening decade of the 21st century solar sail propulsion has been proposed for a diverse range of mission applications ranging throughout the solar system. However, in-order to develop an application-pull technology development roadmap the concepts which are truly enabled or significantly enhance by solar sail propulsion must be identified. As such the mission catalogue will initially consider a wide range of mission concepts to allow definition of key characteristics of missions which are truly enabled or significantly enhance by solar sail propulsion. Subsequently critical missions which can act as facilitators to later, more technologically complex missions will be discussed in further detail. Through these considerations a solar sail application-pull technology development roadmap is established, using each mission as a technology stepping-stone to the next.

3.1 Identification of key characteristics

To aid the identification of key characteristics solar sail applications are divided into the seven categories below.

3.1.1 Planet-centred and other short orbit period applications

This category is essentially planet, minor-planet and small body centred trajectories. Planet-centred trajectory design has been largely restricted to escape manoeuvres or relatively simplistic orbit manoeuvring, such as lunar fly-by's or orbit inclination change (Eguchi et al, 1993; Fekete et al, 1992; Fimple, 1962; Green, 1977; Irving 1959; Lawden, 1958; Leipold, 1999; Macdonald, 2005a, 2005b; Morgan, 1979; Pagel, 2002; Sackett, 1977; Sackett & Edelbaum, 1978; Sands, 1961). Such trajectories place significant technology demands on the solar sail architecture, for example a locally optimal energy gain control profile for an Earth-centred orbit requires the sail to be rotated through 180 degrees once per orbit and then rapidly reset to maximise energy gain; as the sail size grows clearly this becomes an increasingly demanding technology requirement. It is noted that other simplistic orbit manoeuvres require similarly agile sail technology, for example an orbit plane-change require the sail to be rotated approximately 70.5 deg. twice per orbit (Macdonald, 2005a). This technology requirement for an agile sail is a significant disadvantage to the majority of short orbit period solar sail applications; however it should not be considered a blockage on the roadmap.

Two highly significant planet-centred solar sail applications have been identified which do not require, but may in-practise desire, active sail control and hence do not require an agile

sail; these are the GeoSail concept (Leipold et al, 2010; Macdonald & McInnes, 2000; Macdonald et al, 2007a) and the Mercury Sun-Synchronous Orbiter (Leipold et al, 1996a, 1996b). These two solar sail mission concepts are very similar, both using a solar sail with fixed attitude to independently vary a single orbit parameter due to the orbits shape and alignment with the primary body, and the alignment to the Sun, creating a non-inertial orbit. GeoSail rotates the argument of perigee of an eccentric orbit within the ecliptic plane at approximately 1 deg per day such that orbit apogee remains within the Earth's magnetotail. The Mercury Sun-Synchronous Orbiter meanwhile rotates the ascending node of an eccentric orbit whose orbit plane is at right-angles to the ecliptic plane such that the orbit plane remains perpendicular to the Sun-planet line, therefore enabling a sun-synchronous orbit at Mercury which is not possible naturally due to the high reciprocal of flattening of the planet.

3.1.2 Highly non-keplerian orbit applications

This category is, in some regards, an extension of the concept embodied by non-inertial orbits, with the sail providing a small but continuous acceleration to enable an otherwise unattainable or unsustainable observation outpost to be maintained.

Interestingly, as early as 1929 Oberth, in a study of Earth orbiting reflectors for surface illumination (Oberth, 1929), noted that solar radiation pressure will displace a reflector in a polar orbit in the anti-Sun direction. Since then a significant volume of work has been performed in this area; a comprehensive review of Highly Non-Keplerian Orbits (NKO) has recently been completed by McKay et al (2010) in which a range of orbits and applications are presented. Highly NKOs are typically characterised as requiring a small but continuous acceleration in a fixed direction, in this case provided by a solar sail with fixed attitude to provide the thrust required to compensate for the differences in gravitation and rotational force (gravity gradient) to displace the spacecraft to an artificial equilibrium point at a location some distance from a natural libration point.

Two primary solar sail applications of Highly NKOs are found in the literature; Geostorm and Polesitter (also called Polar Observer) (Biggs & McInnes, 2009; Chen-wan, 2004; Driver, 1980; Forward, 1991; Matloff, 2004; McInnes et al, 1994; Sauer, Jr., 2004; Waters & McInnes, 2007; West, 1996, 2000, 2004). The Geostorm mission concept provides real-time monitoring of solar activity; the spacecraft would operate sunward of the Earth's L_1 point, thus increasing the warning time for geomagnetic storms. By imparting a radial outward force from the Sun the solar radiation pressure *in-effect* reduces solar gravity and allows the L_1 point to be moved sunward. As sail performance is increased solar gravity is further '*reduced*', thus providing enhanced solar storm warning.

The Polesitter concept extends the Geostorm concept from a singular equilibrium point to derive equilibrium surfaces which extend out of the ecliptic plane and are again parameterised by the sail performance (McInnes et al, 1994). By extending the artificial equilibrium points out of the ecliptic plane, the small but continuous acceleration allows a spacecraft to be stationed above, or below, the second body within the 3-body problem. A further example of a highly non-keplerian orbit application is the Statite proposed by Forward (1991), which would use a high-performance solar sail to directly balance the solar gravity to hover stationary over the poles of the Sun.

The conceptually simple nature of the Geostorm and Polesitter missions is complicated by mission requirements, risk and budget factors and by the unstable nature of artificial equilibrium points. Although station-keeping should be possible (Biggs & McInnes, 2009;

Chen-wan, 2004; Sauer, Jr., 2004; Waters & McInnes, 2007) the requirement to station-keep increases the minimum level of technology requirement of the mission beyond, for example, the GeoSail mission discussed previously.

3.1.3 Inner solar system rendezvous missions

This category covers missions which use the solar sail to rendezvous, and perhaps bound the orbit to, a body in the inner solar system; defined as all bodies from the asteroid belt inwards, specifically excluding bodies which are, in-effect, part of the Jupiter system, for example the Hilda and Jupiter Trojan asteroids.

The use of solar sails for high-energy sample return missions to the inner planets has been discussed extensively within the literature (Garner et al, 2001; Hughes, 2006; Leipold, 1999; McInnes et al, 2002; Sauer, Jr., 1976; Tsu, 1959; Vulpetti et al 2008; Wright, 1992; Wright & Warmke, 1976) often without presenting the trajectory as part of a larger system-level trade on the propulsion selection criteria. Solar sailing, like other forms of low-thrust propulsion, requires that if a bound orbit about the target body is desired then at arrival the spacecraft must have, in-effect, zero hyperbolic excess velocity. Therefore, any wholly low-thrust interplanetary mission is required, unlike high-thrust missions, to *slow-down* prior to arrival at the target body and subsequently the transfer duration is typically significantly increased; this is especially true for bodies which can be relatively easily reached by high-thrust, chemical propulsion systems such as Mars and Venus. Furthermore, once the solar sail has been captured into a bound-orbit about the target body it then has the typical disadvantages discussed previously for planet-centred solar sail applications.

A sequence of assessment studies was previously conducted by the Authors and Hughes looking at solar sail sample return missions to Mars (McInnes et al, 2003a), Venus (McInnes et al, 2003b), Mercury (Hughes, 2006; McInnes et al, 2003c), and a small-body (McInnes et al, 2003d), with the specific objective of enabling a system-level trade on the propulsion selection criteria within each mission. Within each of these a complete system level analysis was performed, considering a range of mission architectures, attempting to define the most preferential solar sail architecture. The identified preferential solar sail architecture was then compared against alternative propulsion systems conducting a similar mission.

In all Mars Sample Return mission architectures it was found to be very difficult to justify the use of a solar sail due to the significantly increased mission duration (McInnes et al, 2003a). The "*grab-and-go*" architecture, identified as the most preferential for solar sailing required a mission duration of 5 - 6 years depending on the launch vehicle, while a similar all chemical propulsion mission could be completed in only 2 years, although requiring a slightly larger launch vehicle (McInnes et al, 2003a). A very similar scenario was found in the analysis of the Venus Sample Return mission (McInnes et al, 2003b). However, it was found that due to the increased launch mass sensitivity to returned mass the use of a solar sail for the Earth return stage offered potential real benefits; note the solar sail attached mass for this scenario was 323 kg requiring a sail of less than 100-m side length at an assembly loading of 6 gm⁻², with 20 % design margin. It was found that using a solar sail for the Earth return stage of a Venus Sample Return mission reduced the launch mass by approximately 700 kg, enabling a smaller, hence lower cost, launch vehicle to be used without notably impacting mission duration. Such a scenario does however have the typical disadvantages discussed previously for planet-centred solar sail applications when using the sail to escape the Venus gravity-well.

Considering both the Mercury and Small Body Sample Return missions it was found that due to the high-energy nature of the transfer trajectories only low-thrust propulsion systems offered viable mission concepts, with solar sailing offering potential benefits (Hughes, 2006; McInnes et al, 2003c, 2003d). Note the small-body target was asteroid 2001 QP153, with an orbit inclination of 50 deg. The Mercury Sample Return mission would have the typical disadvantages discussed previously for Short Orbit Period solar sail applications, however it was found that a large, high-performance solar sail would offer some potential benefits to such a mission (Hughes, 2006). It is of note that missions to small bodies, such as asteroid 2001 QP153, could negate the disadvantages discussed previously for short orbit period solar sail applications as the sail may not be required to enter a bound orbit about the small-body, if indeed a stable orbit could even be found.

3.1.4 Outer solar system rendezvous missions

The use of solar sails for outer solar system rendezvous missions has been long discussed within the literature (Garner et al, 2001; Leipold, 1999; Wright, 1992; Wright & Warmke, 1976). Furthermore, an assessment study was previously conducted by the Authors and Hughes looking at a range of solar sail Jupiter missions (McInnes et al, 2003e, 2004a), including concepts for exploration of the Galilean moons. As with low-thrust inner solar system rendezvous missions the hyperbolic excess velocity at the target outer solar system body must be lower than high-thrust missions. The inverse squared variation in SRP with solar distance however means that the sail performance is significantly reduced over the same sail at Earth. As such the requirement to reduce the hyperbolic excess velocity prior to arrival at the outer solar system body leads to prolonged transfer durations. Note however that due to the large moons within both the Jupiter and Saturn planetary systems capture can be performed using gravity assist manoeuvres to enable the hyperbolic excess velocity to be significantly greater than zero (Macdonald, 2005c). Furthermore, the duration required to reduce the orbit altitude following capture is also significantly prolonged due to the inverse squared variation in SRP with solar distance. Clearly, this class of mission becomes increasingly unattractive as the target body moves further from the Sun.

Outer solar system rendezvous missions are concluded to be unsuitable for solar sail propulsion due to the inverse squared variation in SRP with solar distance.

3.1.5 Outer solar system flyby missions

Outer solar system fly-by missions remove the requirement to reduce the hyperbolic excess velocity prior to arrival at the target body and as such negate much of the negative elements of solar sail outer solar system rendezvous missions. A Jupiter atmospheric probe mission was considered by the Authors and Hughes (McInnes et al, 2003e) as a potential Jupiter flyby mission. It was concluded that due to the mass of the atmospheric probes, of which three were required, and the relative ease of such a mission with chemical propulsion that solar sail propulsion offered little to such a mission. It is of note that as the target flyby body moves further from the Sun, and hence the difficulty of such a mission with chemical or SEP increases, solar sail propulsion becomes increasingly beneficial; ultimately leading to a peak in solar sail benefits for such missions in the Beyond Neptune category which will be discussed later.

3.1.6 Solar missions

Most previous missions to study the Sun have been restricted to observations from within the ecliptic. The Ulysses spacecraft used a Jupiter gravity assist to pass over the solar poles,

obtaining field and particle measurements but no images of the poles. Furthermore, the Ulysses orbit is highly elliptical, with a pole revisit time of approximately 6 years. It is desired that future solar analysis be performed much closer to the sun, as well as from an out-of-ecliptic perspective. The Cosmic Visions mission concept Solar Orbiter intends to deliver a science suite of order 180 kg to a maximum inclination of order 35 deg with respect to the solar equator and to a minimum solar approach radius of 0.22 au using SEP. The inability of the Solar Orbiter mission to attain a solar polar orbit highlights the difficulty of such a goal with conventional propulsion. It has however been shown that a mid-term solar sail can be used to deliver a spacecraft to a true solar polar orbit in approximately five-years (Goldstein et al, 1998; Macdonald et al, 2006). The Solar Polar Orbiter (SPO) mission concept is a good example of the type of high-energy inner-solar system mission which is enabled by solar sail propulsion.

3.1.7 Beyond Neptune

A significant quantity of work in the past decade has been performed to assess the problem of trajectory and system design of a solar sail mission beyond Neptune (Colasurdo & Casalino, 2001; Dachwald, 2004a, 2004b, 2005; Garner et al, 2000, 2001; Leipold & Wagner, 1998; Leipold, 1999; Leipold et al, 2006, 2010b; Lyngvi et al, 2003, 2005a, 2005b; Macdonald et al, 2007b, 2010; McInnes, 2004b; Sauer, Jr., 2000; Sharma & Scheeres, 2004; Sweetser & Sauer, Jr., 2001; Vulpetti, 1997, 2002; Wallace, 1999; Wallace et al, 2000; West, 1998; Yen, 2001). It has been shown that solar sail propulsion offers significant benefits to missions concepts which aim to deliver a spacecraft beyond Neptune, for either a Kuiper Belt or Interstellar Heliopause (at approximately 200 au) mission. Such outer solar system missions initially exploit the inverse squared variation in SRP with solar distance by approaching the Sun to gain a rapid energy boost which generates a hyperbolic trajectory and allows the spacecraft to rapidly escape the solar system.

Solar sails mission concepts significantly beyond the Interstellar Heliopause were considered by Macdonald et al (2010). In-order to determine the limit of the solar sail concept an Oort cloud mission was examined using solely SRP to propel the spacecraft. It was found that although no fundamental reason existed why such a mission may not be possible the practicalities were such that the Interstellar Heliopause Probe (IHP) mission concept could be considered representative of the upper limiting bound of the solar sail concept.

3.1.8 Key characteristics

Solar sailing has traditionally been perceived as an enabling technology for high-energy missions; however, as has been shown in the preceding sections the key characteristics of a mission which is enabled, or significantly enhanced by solar sailing are more complex than simply this.

Solar sailing is, due to the lack of propellant mass, often noted as reducing the launch mass of an equivalent chemical or SEP concept, which is in-turn noted as reducing launch and mission cost. However, while it is accurate that the launch mass is typically reduced this does not directly result in a reduced launch vehicle cost as the reduction may not be sufficient to allow the use of a less capable, and hence lower cost, launch vehicle. As such the launch cost is only reduced if the reduced launch mass allows a smaller launch vehicle to be used, meaning that launch cost varies as a step function while launch mass linearly increases. Finally, it should be noted that if the total mission cost is high, say, 500+ M€ then

reducing the launch mass cost by 10 – 20 M€ is a cost saving of order 2 – 4 %, which may not be considered a good cost/risk ratio for the project and indeed, the cost saving may be insufficient to pay for the additional development of the technology. Thus for the reduction in launch mass to be an enabling, or significantly enhancing aspect of a solar sail mission concept the cost saving must also be a significant percentage of the total mission cost.

All solar sail mission concepts can be sub-divided into two classes, these are:

- Class One
 - Where the solar sail is used to reach a high-energy target and after which the sail can be jettisoned by the spacecraft, for example the Solar Polar Orbiter mission.
- Class Two
 - Where the solar sail is required to maintain a novel or otherwise unsustainable observation outpost, for example, highly non-keplerian or non-inertial orbit applications, such as Geostorm and GeoSail.

This distinction is important as the later compares very favourably against most other propulsion systems, especially as the mission duration and hence reaction mass is increased. However, a solar sail is a very large structure and could adversely impact the mission objectives either through a characteristically low pointing accuracy due to low frequency structural flexing, or due to the solar sail interfering with the local environment in, for example, particle and field measurements. Thus, a critical requirement on early solar sail demonstration missions must be to validate the simulated pointing accuracy of the platform and the effect of the sail on the local space environment.

From the mission catalogue it is seen that solar sail propulsion has been considered for a large range of mission applications, some of which it is more suitable for than others. Each of the solar sail applications within the mission catalogue are sub-divided by the level of enhancement offered by solar sail propulsion in Table 1. From Table 1 the key positive and negative characteristics of solar sail missions are defined in Table 2.

Enabled or Significantly Enhance	Marginal benefit	No benefit
Non-Inertial Orbits, such as GeoSail or a Mercury Sun-Synchronous Orbiter	Venus escape at end of sample return mission	Planetary escape at start of mission
Highly Non-Keplerian Orbits such as Geostorm and Polesitter	Mercury and high-energy small body Sample Return missions	Mars missions
Kuiper-Belt fly-through	Outer solar system planet fly-by	Outer solar system rendezvous and centred trajectories
Solar Polar Orbiter	Transit of Gravitational Lens region	Loiter at the Gravitational Lens
Interstellar Heliopause Probe	Oort Cloud	

Table 1. Solar sail missions by benefit

Positive Characteristic	Negative Characteristic
Very High Energy transfer trajectory	Mars and Venus rendezvous
Inner Solar System	Outer Solar System rendezvous
Highly Non-Keplerian and Non-Inertial orbits	Short orbit period with rapid slew manoeuvres
Final stage in a multi-stage system	High radiation environment
Fly-by beyond the orbit of Neptune	High pointing stability required
	Required to rendezvous with a passive body
	Fly-by beyond solar gravitational lens

Table 2. Solar sail mission key characteristics

3.2 Key missions

Three key mission will be briefly discussed, one from each of near, mid and far term.

3.2.1 Near-term: GeoSail

The GeoSail mission concept is motivated by the desire to achieve long residence times in the Earth's magnetotail, enabling high resolution statistical characterisation of the plasma in a region subject to a variety of external solar wind conditions (Alexander et al, 2002; Leipold et al, 2010a; Macdonald et al, 2000, 2003, 2007a; McInnes et al, 2001). This is accomplished by the novel application of a solar sail propulsion system to precess an elliptical Earth-centred orbit, interior to the lunar orbit, at a rate designed to match the rotation of the geomagnetic tail, the orientation of which is governed by the Sun-Earth line. The GeoSail mission concept is one of the earliest possible solar sail missions which can satisfy a clearly defined science requirement while also acting as a pathfinder to later, more technically demanding missions. The first true solar sail mission must not be an experiment but a demonstration which, through its heritage, enables more technically demanding missions. Considering GeoSail as a potential technology demonstration mission it is required to resolve known issues and validate simulations and prior experiments. In particular, measurement and analysis must be performed as to the effect of the sail on the local space environment. This is a key mission goal. The final engineering goal of GeoSail, or any sail demonstration mission, must be the successful demonstration of a sail jettison and separation manoeuvre; a key requirement of several solar sail missions such as the Solar Polar Orbiter and the Interstellar Heliopause Probe.

The GeoSail orbit has a perigee located above the planetary dayside at approximately 11 Earth radii (R_E), corresponding to alignment with the magnetopause. Apogee is aligned with the geomagnetic tail reconnection region on the night-side of the Earth, at 23 R_E . The orbit plane is within the ecliptic plane. With the spacecraft located in the ecliptic plane the sail normal is fixed at zero pitch, i.e. the sail is face-on to the Sun at all times, to induce the desired independent secular variation in the argument of pericentre (McInnes et al, 2001). Thus, by varying the sail thrust magnitude the rate of change of argument of pericentre can

be varied. The required sail characteristic acceleration is found to be $0.09985 \text{ mm s}^{-2}$; note the defined sail characteristic acceleration is adjusted to account for the prolonged shadow event each orbit. It is found that a square solar sail of order forty metres per side is required to conduct the GeoSail mission at an assembly loading of 34 g m^{-2} , using $3.5 \mu\text{m}$ Teonex® film and a boom specific mass of 40 gm^{-1} (Macdonald et al, 2007a). However, it was also found that for the GeoSail mission to provide sufficient heritage to later, more technically demanding missions, the design point was required to be more demanding than should the GeoSail mission be conducted in isolation. It is noted finally that the GeoSail orbit is well suited to a technology demonstration mission due to its proximity to Earth, allowing extended observation of the system from Earth.

In direct comparison of solar sail, SEP and chemical variants of the GeoSail concept it is found that a high-thrust mission has an annual Δv requirement of over 2 km s^{-1} , resulting in significant difficulties when attempting to perform mission durations of longer than approximately one-year. Conversely it is found that a SEP variant is rather attractive as the required thrust level is easily attainable with current technology. It is of note that the exhaust gases would need to be neutralised, especially for a geomagnetic tail mission, as the ionised particles would interfere with science measurements and spacecraft subsystems, this adversely impacts the propellant mass required. It is found that a SEP variant of GeoSail could have a nominal duration of at least two-years (Macdonald et al, 2007a). Therefore, the solar sail mission is increasingly attractive for increased mission durations. It is also of note that the solar sail mission was found to fit with a Vega launch vehicle, while the SEP variant just tipped into a Soyuz vehicle, hence incurring a notable launch cost increase.

3.2.2 Medium-term: solar [olar orbiter

The Solar Polar Orbiter (SPO) mission concept is motivated by the desire to achieve high latitude, close proximity observations of the Sun. Terrestrial observations of the Sun are restricted to the ecliptic plane and within the solar limb, thus restricting observations to within ± 7.25 deg of the solar equator. As discussed earlier the Ulysses spacecraft used a Jupiter gravity assist to pass over the solar poles, obtaining field and particle measurements but no images of the poles, however the orbit is highly elliptical, with a pole revisit time of approximately 6 years. It is desired that future solar analysis be performed much closer to the sun, as well as from an out-of-ecliptic perspective, this is the goal of the Cosmic Visions mission concept Solar Orbiter. However, the inability of the Solar Orbiter mission to attain a solar polar orbit highlights the difficulty of such a goal with conventional propulsion. The SPO mission uses a solar sail to place a spacecraft into an orbit at 90 deg inclination with respect to the solar equator (82.75 deg with respect to the ecliptic plane) and interior to the Earth's orbit. Additionally, the spacecraft orbit is phased such that it will remain near to the solar limb from a terrestrial perspective which eliminates solar conjunctions and hence loss of telemetry. Once the solar sail has delivered the spacecraft to the solar polar orbit it is jettisoned to allow the science phase of the mission to begin (Goldstein et al, 1998; Macdonald et al, 2006).

The third resonant orbit is defined as the target orbit as this places the spacecraft close to the Sun, while also being in a relatively benign thermal environment compared to higher order resonant orbits.

Macdonald et al (2006) conducted an analysis to determine the minimum required slew rate of the solar sail within the SPO mission. It was considered that during the orbit inclination increase phase of the trajectory, or the cranking phase, the sail pitch is fixed at $\arctan(1/\sqrt{2})$,

while the sail clock angle flips from 0 deg to 180 deg, however it is clear that the sail thrust vector cannot be rotated through approximately 70.5 deg instantaneously. Thus, the effect of variations in the sail slew rate on the cranking phase were quantified, concluding that a sail slew rate of 10 deg per day (10^{-4} deg s^{-1}) resulted in a performance degradation from the instantaneous slew of less than 0.5 %. A required sail slew rate of 10 deg per day was thus defined for the mission.

It is found that a square solar sail of order one-hundred and fifty metres per side is required to conduct the SPO mission at an assembly loading of 8 g m^{-2} and characteristic acceleration 0.5 $mm\ s^{-2}$ (Macdonald et al, 2006).

Macdonald et al (2006) concluded that both conventional SEP and chemical propulsion could not be considered viable alternatives to solar sailing for an SPO mission. As such a comparison against new and novel propulsion systems was conducted, such as nuclear electric propulsion (NEP), radioisotope electric propulsion (REP) and Mini-Magnetospheric Plasma Propulsion (M2P2). It was expected that any NEP system will require a large launch vehicle due to the inherent nature of the system. Meanwhile, the use of a REP system would require extremely advanced radioisotope power sources to compete with solar power. M2P2 could potentially provide the required change in velocity needed to attain a true solar polar orbit. This concept is akin to solar sails, but has the advantage of not requiring large structures to be deployed. The drawback to this propulsion method is that the magnetic field generating system mass may be quite high. The lack of viable competing propulsion systems serves to highlight the potential of solar sailing for a solar polar mission concept. It is thus concluded that solar sailing offers great potential for this mission concept and indeed may represent the first useful deep space application of solar sail propulsion.

3.2.3 Far-term: interstellar heliopause probe

As previously discussed a significant quantity of work in the past decade has been performed to assess the problem of trajectory and system design of a solar sail mission beyond Neptune. A specific example of this class of mission is the Interstellar Heliopause Probe (IHP) concept which exploits the inverse squared variation in SRP with solar distance by approaching the Sun to gain a rapid energy boost which generates a hyperbolic trajectory and allows the spacecraft to rapidly transit the inner solar system prior to sail jettison at 5 au.

The IHP mission concept typically envisages the spacecraft arriving at a solar distance of 200 au in 15 - 25 years. The issue of an upper feasible limit on mission duration is difficult to quantify. For example, the Voyager spacecraft remain operational over three-decades since launch, yet the primary mission of these spacecraft was, approximately, three and twelve years for Voyager 1 and 2 respectively. However, both spacecraft have continued to provide scientifically interesting data and as such operations have continued. Typically any IHP mission would provide continuous science data from 5 au onwards, i.e. post-sail jettison, thus it is anticipated that the spacecraft will provide scientifically interesting data from an early stage. However, the primary goal of the mission is measurement of the interstellar medium, which therefore necessitates a funding commitment over a much longer period than originally envisaged for the Voyager spacecraft. Clearly the perceived upper feasible limit on mission duration has a significant impact on the required technology of the mission concept. It is of interest that previous NASA led activities have targeted a solar distance of 200 au in 15 years (Garner et al, 2000; Wallace, 1999; Wallace et al, 2000), while recent ESA and European activities have typically targeted a solar distance of 200 au in 25 years (Leipold et al, 2010b; Lyngvi et al, 2003, 2005a, 2005b; Macdonald et al, 2007b, 2010). The

NASA led activities clearly determine that a conventional square solar sail will not suffice for the short mission duration and that a spinning disc sail, or some other equally low sail assembly loading sail architecture, is required. However, the European studies exhibit some ambiguity on the required sail technology level which was recently considered by Macdonald et al who concluded that the ambiguity was perhaps due to a slight relaxation in the mission duration requirement (2010).

It is found that a disc solar sail of order one-hundred and fifty to two-hundred metres radius is required to conduct the IHP mission at an assembly loading of $1.5 - 2 \text{ g m}^{-2}$, delivering a characteristic acceleration of $1.5 - 3 \text{ mm s}^{-2}$ (Macdonald et al, 2010; Wallace et al, 2000). It can be shown that a chemical IHP mission is feasible, however to provide a similar trip time it requires a heavy-lift launch vehicle and an Earth-Jupiter gravity assist trajectory which significantly limits the launch window opportunities. Note, the solar sail launch window repeats annually. Conventional chemical propulsion for the IHP mission appears unattractive from this concept, however should a specific impulse of over 450 seconds be achieved then such a variant, with a large burn at 4 solar radius may be possible from a Soyuz-like launch vehicle (McInnes et al, 2004b). The use of SEP is possible, again using a gravity assist trajectory; however, it is unlikely that a solar power system would be sufficient for an IHP mission. NEP is however an attractive option for the IHP mission and could be used to reduce trip time and launch mass over most other options, there will however be a limit to this launch mass reduction as the smallest fission reactor and engine size is likely to be of order 1200 kg (McInnes et al, 2004b). A major advantage of using NEP is that the reactor can be used to provide a power-rich spacecraft at 200 au and so provide high data rates through a modest high-gain antenna. The primary disadvantage of the NEP concept, beyond the attendant political issues, is that the spacecraft may be required to continue thrusting beyond the orbit of Jupiter to reach 200 au in the required timeframe. Continued thrusting may adversely impact the science objectives of the mission with a direct consequence for funding. Finally, M2P2 and electric sail technology may both offer interesting alternatives to solar sailing (Janhunen, 2008; Winglee et al, 2000).

4. Application pull technology development route

Considering the IHP mission as typical of the culmination of any solar sail application roadmap it is important that the technology requirements of this mission application be enabled by previous milestones on the roadmap, that is to say, previous missions. Hence, as the IHP mission requires a low sail assembly loading sail architecture it is critical that previous applications of solar sailing provide suitable heritage to this mission. The top-level technology requirements of each of the missions from within the catalogue, which satisfy the positive criteria detailed in Table 2, are shown in Fig. 4. It should be noted that Fig. 4., is independent of sail architecture as it simply relates the required sail surface area to the required sail assembly loading.

Each of the key missions discussed in Section 3.2 can be seen within Fig. 4. It is noted that despite, as discussed in Section 3.2.1, the GeoSail system analysis being over-engineered if the mission were conducted in isolation, rather than as part of a technology development roadmap, the GeoSail technology requirements still do not clearly fit within the application technology requirement bounds of the more demanding mission concepts. Indeed, for GeoSail to provide a simple log-linear technology trend towards the two other key missions discussed in Section 3.2 the sail assembly loading must be further reduced to approximately

20 – 25 g m⁻², while to reach the Mean Application Trend the sail assembly loading must be reduced to approximately 15 – 20 g m⁻².

5. Future advancement roadmap

The currently identified applications of solar sailing which will, due to the enabling or significantly enhancing aspects of solar sail propulsion, pull the technology development are, as seen in Fig. 4, significantly clustered about the mid to far-term technology; while the near-term remains sparsely populated. There can be little argument about the scientific value of missions such as SPO. However, the risk involved in directly attempting such a mission with solar sail propulsion would be so large as to be prohibitive.

Solar sailing is an elegant concept, however it must be pulled forward by mission applications at the same time as it is pushed by technology development. This also holds true for initial flight tests of solar sailing. As discussed in Section 3.2.1, unless such flight tests provide confidence in the technology and a clear path towards some enabling capability, they will not perform a useful function. A good example of this was the use of low cost sounding rockets by JAXA to test multiple sail deployment mechanisms during the short period of free-fall which allowed for several tests of scaled prototypes at the same cost as a single launch to orbit. By spreading the risk over several tests the inevitable unforeseen single point failures of deployment could be identified prior to launch of IKAROS in May 2010 as a full-scale demonstration mission (Mori et al, 2010; Normile, 2010; Sawada et al, 2010).

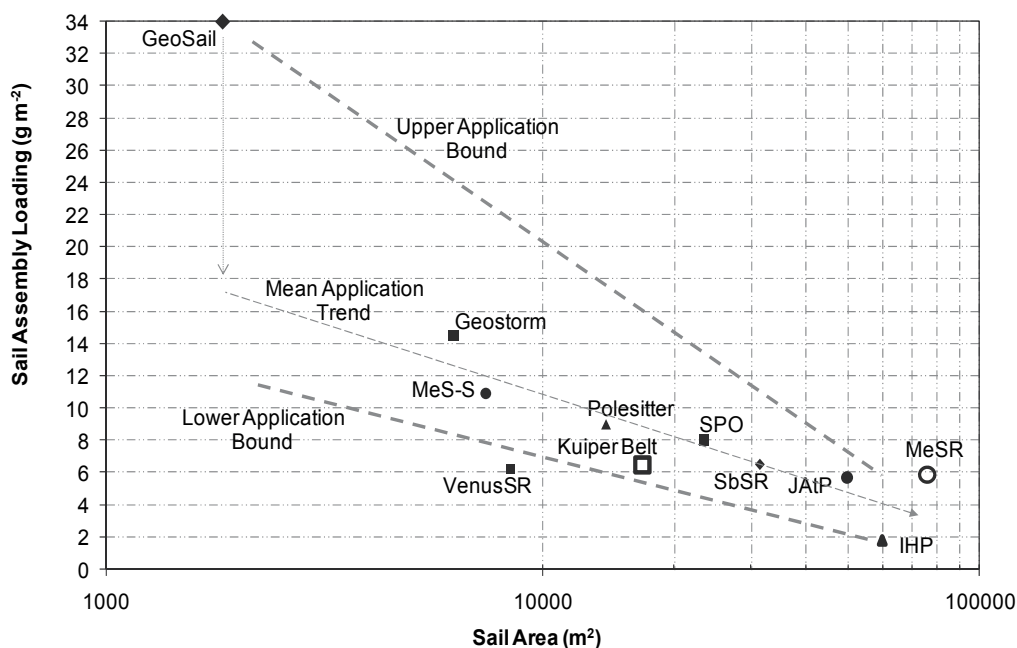


Fig. 4. Solar sail mission catalogue application technology requirements. IHP ≡ Interstellar Heliopause Probe; JAtP ≡ Jupiter Fly-by with Atmospheric Probe release; MeSR ≡ Mercury Sample Return; MeS-S ≡ Mercury Sun-Synchronous; SbSR ≡ High-Energy Small-Body Sample Return; SPO ≡ Solar Polar Orbiter; VenusSR ≡ Venus Sample Return.

With the clearly established clustering of identified enabling or significantly enhancing applications of solar sailing towards the mid to far-term a requirement exists to backfill these requirements. This can be achieved in two ways, the first of which is to develop mission concepts which are enabling or significantly enhancing by near-term solar sail propulsion in a similar way to the GeoSail concept. The alternative to this is to re-engineer the mission concepts and the vision of the future of solar sailing, such that the gap between near and mid-term applications is removed. This can be achieved by recognising and adapting the Advancement Degree of Difficulty (AD2) scale. TRLs define the maturity, or readiness, at discrete points in a schedule. However, this is only half of the engineer's problem. TRLs provide no information on how well, or easily, the technology will move from one TRL to the next, i.e. what is the risk of the technology development program. The AD2 scale was developed to address issues of programmatic risk and to aid the incorporation of low-TRL components into larger systems, however the founding principles can be adapted to larger scale, novel or advanced concepts such as solar sailing. The AD2 scale categorises risk from the lowest AD2, Level 1 (0% risk) defined as *"Exists with no or only minor modifications being required. A single development approach is adequate."* Through to the highest AD2, level 9 (90 - 100 % risk), defined as *"Requires new development outside of any existing experience base. No viable approaches exist that can be pursued with any degree of confidence. Basic research in key areas needed before feasible approaches can be defined."* Performing a simple, top-level AD2, TRL project status analysis of solar sailing for an advanced technology demonstrator it is found that the project risk is, at best, acceptable, and that dual development approaches should be pursued to increase confidence.

To reduce the risk on the solar sail development roadmap the AD2 level must be reduced. This can be done in two ways, firstly by considering solar sailing as a primary propulsion source an extension of the use of solar sailing as an attitude control device and secondly by incorporating other low-thrust, high TRL propulsion technologies into the early solar sail technology development roadmap to bridge the gap between the near and mid-term applications, i.e. hybrid sail/SEP propulsion. The use of SRP for attitude control on large spacecraft in geostationary orbit and interplanetary space is common practise. Most notably, Mariner 10 used a small *"kite"* (31 cm × 76 cm) for manoeuvring by using the pressure of sunlight for attitude control. By using the ballast solar sail for attitude control manoeuvring the Mariner 10 project was able to extend the planned life of the mission and increase mission science returns (NASA/JPL, 1975, 1976; Shirley, 2002). A similar technique was employed by the MESSENGER mission to Mercury. Thus, the principles of solar sailing are already at a high TRL. The inherent programmatic risk in solar sailing is a direct result of the high AD2 in progressing immediately to a spacecraft using SRP as the sole primary propulsion system. The programmatic risk in solar sailing can be significantly reduced by hybridising the propulsion with a high TRL SEP system, which also offers critical advantages when considering trajectory generation due to the ability of an SEP system to thrust directly towards the Sun. The Mariner 10 and MESSENGER spacecraft both used a rather small kite, or solar sail, and there is no reason why other inner solar system missions would not similarly benefit from doing so. In this regard such missions would be primarily a SEP spacecraft which also has a small solar sail. The AD2 is then significantly reduced when incrementally reducing the size of the SEP system and increasing the size of the solar sail as its TRL is increased. Furthermore, through such a hybridisation it can be expected that the mid to far-term cluster of solar sail applications seen in Fig. 4 will shift down the sail area axis towards the near-term, therefore reducing the AD2 of concepts such as SPO.

Finally, it is of note that much of the recent solar sail technology development has focused on the CubeSat platform, including NanoSail-D (Johnson et al, 2010), the DLR led Gossamer program (Lura et al, 2010), the Planetary Societies Lightsail-1 (Bidby, 2010; Cantrell & Friedman, 2010, Nehrenz, 2010) and several others (Carroll et al, 2010; Lappas et al, 2010; Pukniel et al 2010). The low-cost nature of CubeSats allows the early risk to be spread over several low-cost missions where a failure can be tolerated much as it was with NanoSail-D. The gap between a CubeSat solar sail and, say, GeoSail is rather large and does not significantly mitigate the high AD2 of solar sailing. However, if a CubeSat based solar sail system can be successfully developed then it potentially would enable an increased solar sail kite to be incorporated onto a future SEP mission, allowing solar sailing to progress along its development roadmap.

6. Conclusions

A solar sail mission catalogue has been developed and presented. The mission catalogue was sub-divided into applications which were enabled, or significantly enhanced by solar sailing, of which solar sailing is of marginal benefit and of which solar sailing could be considered unconstructive. From this the key characteristics of solar sail enabled, or significantly enhanced, missions were detailed prior to a detailed discussion of three key applications of solar sailing and the presentation of a solar sail application pull technology development roadmap.

Considering the solar sail application pull technology development roadmap it was noted that the near-term was sparsely populated, with the significant majority of applications clustered in the mid to far term. The concept of a system level Advancement Degree of Difficulty was introduced and it was illustrated that how through, for example, hybridisation with solar electric propulsion the project risk of solar sailing could be reduced while simultaneously moving the cluster of mid to far term solar sail applications towards the near-term.

7. References

- Alexander D., Sandman A. W., McInnes C. R., Macdonald M., Ayon J., Murphy N. and Angelopoulos V., GeoSail: A Novel Magnetospheric Space Mission Utilizing Solar Sails, IAC-02-IAA.11.1.04, Electronic Proceedings of the 53rd International Astronautical Congress, Houston Texas, 10-19 October 2002.
- Bacon, R.H., Logarithmic Spiral: An Ideal Trajectory for the Interplanetary Vehicle with Engines of Low Sustained Thrust, *Journal Physics*, Vol. 27, pp. 164-165, 03-1959.
- Bidby, C., Lightsail, Proceedings of the Second International Symposium on Solar Sailing (ISSS 2010), The New York City College of Technology of the City University of New York, July 2010.
- Biggs, J.D., McInnes, C.R.: Solar sail formation-flying for deep space remote sensing, *Journal of Spacecraft and Rockets*, Vol. 46, No. 3, pp. 670-678, 2009.
- Birnbaum, M., Minimum Time Earth / Mars trajectory for Solar Sail, GGC/EE/68-3 AD-836734, Air Force Institute of Technology, USA, 1968.
- Cantrell, J., Friedman, L., Lightsail 1 - Flying on Light for Less, Proceedings of the Second International Symposium on Solar Sailing (ISSS 2010), The New York City College of Technology of the City University of New York, July 2010.

- Ciołkowski, K.E., *Extension of Man into Outer Space*, 1921. Also, Tsiolkovsky, K.E., *Symposium Jet Propulsion*, No. 2, United Scientific and Technical Presses, 1936.
- Carroll, K.A., Spencer, H., Zee, R.E., Vukovich, G., *A Nanosatellite Mission to Assess Solar Sail Performance in LEO*, Proceedings of the Second International Symposium on Solar Sailing (ISSS 2010), The New York City College of Technology of the City University of New York, July 2010.
- Chen-wan, L.Y., *Solar Sail Geostorm Warning Mission Design*, AAS 04-107, Proceedings of 14th AAS/AIAA Space Flight Mechanics Conference, Maui, Hawaii, February 2004.
- Colasurdo, G., Casalino, L., *Optimal Control Law for interplanetary Trajectories with Solar Sail*, *Advances in the Astronautical Sciences*, Vol. 109, Pt. 3, pp. 2357–2368, 2001.
- Cotter, T.P., *Solar Sailing*, Sandia Research Colloquium, SCR-78, April 1959.
- Cotter, T.P., *“An Encomium on Solar Sailing”*, Informal Report LA-5231-MS, Los Alamos Scientific Laboratory, May 1973.
- Dachwald, B., *Interplanetary Mission Analysis for Non-Perfectly Reflecting Solar Sailcraft Using Evolutionary Neurocontrol*, *Advances in the Astronautical Sciences*, Vol. 116, Suppl., pp. 1–18, 2004a.
- Dachwald, B., *Solar Sail Performance Requirements for Missions to the Outer Solar System and Beyond*, IAC-04-S.P.11, Proceedings of the 55th International Astronautical Congress of the International Astronautical Federation, the International Academy of Astronautics, and the International Institute of Space Law, Vancouver, Canada, October 2004b.
- Dachwald, B., *Optimal Solar-Sail Trajectories for Missions to the outer Solar System*, *Journal of Guidance, Control and Dynamics*, Vol. 28, No. 6, pp. 1187 – 1193, 2005.
- Driver, J. M., *Analysis of an Arctic Polesitter*, *Journal of Spacecraft and Rockets*, Vol. 17, No. 3, pp. 263-269, 1980
- Eguchi, S., Ishii, N., Matsuo, H., *Guidance Strategies for Solar Sail to the Moon*, AAS 93-653, *Advances in Astronautical Sciences*, Vol. 85, Pt. 2, pp. 1419-1433, 1993.
- Fekete, T.A., Sackett, L. L., von Flotow, A.H., *Trajectory Design for Solar Sailing from Low-Earth Orbit to the Moon*, AAS 92-184, *Advances in Astronautical Sciences*, Vol. 79, Pt. 3, pp. 1083-1094, 1992.
- Fimple, W.R., *Generalized Three-Dimensional Trajectory Analysis of Planetary Escape by Solar Sail*, *American Rocket Society Journal*, Vol. 32, pp. 883-887, June 1962.
- Forward, R. L., *Statite: A Spacecraft That Does Not Orbit*, *Journal of Spacecrafts and Rockets*, Vol. 28, No. 5, pp. 606-611, 1991
- Friedman, L., Carroll, W., Goldstein, R., Jacobson, R., Kievit, J., Landel, R., Layman, W., Marsh, E., Ploszaj, R., Rowe, W., Ruff, W., Stevens, J., Stimpson, L., Trubert, M., Varsi, G., Wright, J., MacNeal, R., *“Solar Sailing – The Concept made Realistic”*, AIAA 78-82, 16th AIAA Aerospace Sciences Meeting, Huntsville, January 1978.
- Garner, C.E., Layman, W., Gavit, S.A., Knowles, T., *A Solar Sail design For A Mission To The Interstellar Medium*, Proceedings of “Space Technology and Applications International Forum”, Edited by M. El-Genk, AIP Conference Proceedings 504, NY, pp. 947-961, 2000.
- Garner, C., Price, H., Edwards, D., Baggett, *Developments And Activities In Solar Sail Propulsion*, AIAA-2001-3234, 37th AIAA/ASME/SAE/ASEE Joint Propulsion Conference, Salt Lake City, UT, USA, July 2001.

- Garwin, R.L., *Solar Sailing – A Practical Method of Propulsion Within the Solar System*, Jet Propulsion, Vol. 28, pp. 188-190, March 1958.
- Goldstein, B., Buffington, A., Cummings, A. C., Fisher, R., Jackson, B.V., Liewer, P. C., Mewaldt, R. A., and Neugebauer, M., *ASolar Polar Sail Mission: Report of a Study to Put a Scientific Spacecraft in a Circular Polar Orbit About the Sun*, SPIE International Symposium on Optical Science, Engineering and Instrumentation, July 1998.
- Gordon, B.J., *A Study of Interplanetary Travel by Solar Sail*, M.S. Thesis, Air Force University, USAF, Wright-Patterson Air Force Base, Ohio, August 1961.
- Green, A.J., *Optimal Escape Trajectories From a High Earth Orbit by Use of Solar Radiation Pressure*, T-652, Master of Science Thesis, Massachusetts Institute of Technology, 1977.
- Grinevitskaia, L.K., Polaikhova, E.N., “Derivation of an Approximate Solution to the Equation of Geocentric Motion of a Space Vehicle with a Solar Sail”, *Vestnik, Mekhanika, Astronomiia*, Leningrad University (Now Saint-Petersburg State University), April 1973. In Russian.
- Hedgepath, J.M., Benton, M.D., “Analysis of Planetary Flyby Using the Heliogyro Solar Sailor”, *Astro Research Corporation ARC-R-296*, August 1968.
- Hughes, G.W., Macdonald, M., McInnes, C.R., Lyngvi, A., Falkner, P., Atzei, A., *Sample return from Mercury and other terrestrial planets using solar sail propulsion*. *Journal of Spacecraft and Rockets*, 43 (4). pp. 828-835. 2006.
- Jacobson, R.A., Thornton, C.L., “Elements of Solar Sail Spacecraft Navigation with Application to a 1986 Halley’s Comet Rendezvous Mission”, *AAS/AIAA Astrodynamics Conference*, Jackson Hole, WY, September 1977.
- Johnson, L., Whorton, M., Heaton, M., Pinson, R., Laue, G., Adams, C., *NanoSail-D: A solar sail demonstration mission*, *Acta Astronautica*, In-Press, doi:10.1016/j.actaastro.2010.02.008, 2010
- Irving, J.H., *Space Technology*, John Wiley & Sons Inc., New York, 1959.
- Janhunen, P, *The Electric Sail – A new propulsion method which may enable fast missions to the outer solar system*, *JBIS*, Vol. 61, August 2008.
- Kawaguchi, J., *Solar Power Sail – Hybrid Propulsion and it’s applications*, *Proceedings of the Second International Symposium on Solar Sailing (ISSS 2010)*, The New York City College of Technology of the City University of New York, July 2010.
- Lappas, V., Visagie, L., Adeli, N., Theodorou, T., Fernandez, J., Steyn, H., Le Couls, O., Perren, M, *CubeSail: A Low Cost Small Cubesat Mission for Solar Sailing and Deorbiting LEO Objects*, *Proceedings of the Second International Symposium on Solar Sailing (ISSS 2010)*, The New York City College of Technology of the City University of New York, July 2010.
- Lawden, D.F., *Optimal Escape from a Circular Orbit*, *Astronautica Acta*, Vol. 4, pp. 218-234, 1958.
- Lebedew, P., *The Physical Causes of the Deviation from Newton’s Law of Gravitation*, *Astrophysical Journal*, Vol. 10, pp 155-161, 1902.
- Leipold M., Borg, E., Lingner, S., Pabsch, A., Sachs, R., Seboldt, W., *Mercury Sun-Synchronous Polar Orbiter with a Solar Sail*, *Acta Astronautica*, Vol. 39, No. 1-4, pp. 143-151, 1996a.

- Leipold, M.E., Wagner, O., Mercury Sun-Synchronous Polar Orbits Using Solar Sail Propulsion, *J. Guidance, Control and Dynamics*, Vol. 19, No. 6, pp 1337-1341, 1996b.
- Leipold, M., Wagner, O., Solar Photonic Assist Trajectory Design for Solar Sail Missions to the Outer Solar System and Beyond, *Advances in the Astronautical Sciences*, Vol. 100, No. 2, pp. 1035-1045, 1998
- Leipold, M., Solar Sail Mission Design, Doctoral thesis, Lehrstuhl für Flugmechanik und Flugregelung; Technische Universität München, DLR-FB-2000-22, 1999.
- Leipold, M., Eiden, M., Garner, C., Herbeck, L., Kassing, D., Niederstadt, T., Krüger, T., Pagel, G., Rezazad, M., Rozemeijer, H., Sebolt, W., Schöppinger, C., Sickinger, C., Unckenbold, W., Solar Sail Technology Development and Demonstration, 4th IAA International Conference on Low-Cost Planetary Missions, Laurel, Maryland, May 2000.
- Leipold, M., Fichtner, H., Heber, B., Groepper, P., Lascar, S., Burger, F., Eiden, M., Niederstadt, T., Sickinger, C., Herbeck, L., Dachwald, B., Seboldt, W., Heliopause Explorer - A Sailcraft Mission to the Outer Boundaries of the Solar System, *Acta Astronautica*, Vol. 59, pp. 785 - 796, 2006
- Leipold, M., Macdonald, M., McInnes, C.R., Eckersley, E., Falkner, P., Agnolon, D., GeoSail System Design for Demonstration of Solar Sailing in Earth Orbit, Proceedings of the Second International Symposium on Solar Sailing (ISSS 2010), The New York City College of Technology of the City University of New York, July 2010a.
- Leipold, M., Lappas, V., Lyngvi, A., Falkner, P., Fichtner, H., Kraft, S., Interstellar Heliopause Probe - System Design of a Challenging Mission to 200 AU, Proceedings of the Second International Symposium on Solar Sailing (ISSS 2010), The New York City College of Technology of the City University of New York, July 2010b.
- Lichodziejewski, D., Derbès, B., West, J., Reinert, R., Belvin, K., Pappa, R., Bringing an Effective Solar Sail Design Towards TRL 6, AIAA 2003-4659, AIAA Joint Propulsion Conference, July 2003.
- Lippman, M., E., "In-Space Fabrication of Thin-Film Structures", NASA-CR-1969, Astro Research Corporation ARC-R-410, 1972
- Logsdon, J.M., "Missing Halley's Comet: The Politics of Big Science", *ISIS*, Vol. 80, No. 302, pp 254-280, 1989.
- London, H.S., Some Exact Solutions of the Equations of Motion of a Solar Sail with a Constant Setting, *American Rocket Society Journal*, Vol. 30, pp. 198-200, February 1960.
- Lura, F., Biering, B., Geppert, U.R.M.E, The Three-Step Gossamer Road Map to Solar Sailing, Proceedings of the Second International Symposium on Solar Sailing (ISSS 2010), The New York City College of Technology of the City University of New York, July 2010.
- Lyngvi, A., Falkner, P., Peacock, A., The Interstellar Heliopause Probe, Tools and Technologies for Future Planetary Exploration, 37th ESLAB Symposium, ESTEC, 2003.
- Lyngvi, A., Falkner, P., Kemble, S., Leipold, M., Peacock, A., The Interstellar Heliopause Probe, *Acta Astronautica*, Vol. 57, pp. 104 - 111, 2005a.

- Lyngvi, A., Falkner, P., Peacock, A., The Interstellar Heliopause Probe Technology Reference Study, *Advances in Space Research*, Vol. 35, pp. 2073 – 2077, 2005b.
- Macdonald M., McInnes, C. R. GeoSail; An Enhanced Magnetosphere Mission, Using a Small Low Cost Solar Sail, IAF-00-W.1.06, Proceedings of 51st International Astronautical Congress, Rio de Janeiro, Brazil, 2-6 October, 2000
- Macdonald M., McInnes C. R., Alexander D., Sandman A., GeoSail: Exploring the Magnetosphere Using a Low-Cost Solar Sail, *Electronic Proceedings of Fifth IAA International Conference on Low-Cost Planetary Missions*, ESA Special Publication SP-542, pp. 341-349, September 2003.
- Macdonald M., McInnes C. R., Analytical Control Laws for Planet-Centred Solar Sailing, *Journal of Guidance, Control, and Dynamics*, Vol. 28, No. 5, pp. 1038-1048, 2005a.
- Macdonald M., McInnes C. R., Realistic Earth Escape Strategies for Solar Sailing, *Journal of Guidance, Control, and Dynamics*, Vol. 28, No. 2, pp 315 – 323, 2005b.
- Macdonald, M. and McInnes, C.R., Spacecraft planetary capture using gravity assist manoeuvres. *Journal of Guidance, Control and Dynamics*, 28 (2). pp. 365-369, 2005c.
- Macdonald, M., Hughes, G.W., McInnes, C.R., Lyngvi, A., Falkner, P., Atzei, A., Solar Polar Orbiter: a Solar Sail Technology Reference Study, *Journal of Spacecraft and Rockets*, 43 (5). pp. 960-972, 2006.
- Macdonald, M., Hughes, G.W., McInnes, C. R., Lyngvi, A., Falkner, P., Atzei, A., GeoSail: An Elegant Solar Sail Demonstration Mission, *Journal Spacecraft and Rockets*, Vol. 44, No 4, pp 784 – 796, 2007a.
- Macdonald, M., McInnes, C.R., Dachwald, B., Heliocentric Solar Sail Orbit Transfers with Locally Optimal Control Laws, *Journal of Spacecraft and Rockets*, Vol. 44. No. 1, pp. 273 – 276, 2007b
- Macdonald, M., McInnes, C.R., Hughes, G.W., Technology requirements of exploration beyond Neptune by solar sail propulsion. *Journal of Spacecraft and Rockets*, 47 (3), In Press, 2010.
- MacNeal, R.H., “The Heliogyro, An Interplanetary Flying Machine”, NASA Contractor’s Report, CR 84460, June 1967.
- MacNeal, R.H., Hedgepath, J.M., Schuerch, H. U., “Heliogyro Solar Sailor Summary Report”, NASA-CR-1329, June 1969.
- MacNeal R.H., “Structural Dynamics of the Heliogyro”, NASA-CR-1745A, 1971.
- MacNeal, R.H., Comparison of the Solar Sail with Electric Propulsion Systems, NASA-CR-1986, February 1972.
- McKay, R., Macdonald, M., Biggs, J., McInnes, C.R., Highly Non-Keplerian Orbits With Low-Thrust Propulsion, Submitted to *Journal Guidance, Control and Dynamics*, 2010.
- McInnes, C.R., McDonald, A.J.C., Simmons, J.F.L. and MacDonald, E.W., Solar Sail Parking in Restricted Three-Body Systems, *Journal of Guidance, Dynamics and Control*, Vol. 17, No. 2, pp. 399-406, 1994.
- McInnes, C.R., *Solar Sailing: Technology, Dynamics and Mission Applications*, Springer-Praxis, Chichester, 1999.
- McInnes C.R., Macdonald M., Angelopolous V., Alexander D., GeoSail: Exploring the Geomagnetic Tail Using a Small Solar Sail, *J. Spacecraft and Rockets*, Vol. 38, No. 4, pp. 622-629, 2001.
- McInnes, C.R., Hughes, G.W., Macdonald, M., Payload mass fraction optimization for solar cargo missions, *Journal of Spacecraft and Rockets*, 39 (6). pp. 933-935, 2002.

- McInnes, C.R., Macdonald, M., Hughes, G., Mars Sample Return, ESTEC 16534/02/NL/NR, Technical Assistance in the Study of Science Payloads Transported Through Solar Sailing, Technical Note 1, 2003a.
- McInnes, C.R., Macdonald, M., Hughes, G., Venus Sample Return, ESTEC 16534/02/NL/NR, Technical Assistance in the Study of Science Payloads Transported Through Solar Sailing, Technical Note 2, 2003b.
- McInnes, C.R., Macdonald, M., Hughes, G., Mercury Sample Return, ESTEC 16534/02/NL/NR, Technical Assistance in the Study of Science Payloads Transported Through Solar Sailing, Technical Note 3, 2003c.
- McInnes, C.R., Macdonald, M., Hughes, G., Small Body Sample Return, ESTEC 16534/02/NL/NR, Technical Assistance in the Study of Science Payloads Transported Through Solar Sailing, Technical Note 4, 2003d.
- McInnes, C.R., Macdonald, M., Hughes, G., Jupiter Exploration Missions, ESTEC 16534/02/NL/NR, Technical Assistance in the Study of Science Payloads Transported Through Solar Sailing, Technical Note 6, 2003e.
- McInnes, C.R., Macdonald, M., Hughes, G., Jupiter Microsat Explorer Mission, ESTEC 16534/02/NL/NR, Technical Assistance in the Study of Science Payloads Transported Through Solar Sailing, Technical Note 11, 2004a.
- McInnes, C.R., Macdonald, M., Hughes, G., Interstellar Heliopause Probe, ESTEC 16534/02/NL/NR, Technical Assistance in the Study of Science Payloads Transported Through Solar Sailing, Technical Note 9, 2004b.
- McInnes, C.R., Delivering Fast and Capable Missions To The Outer Solar System, *Advances in Space Research*, Vol. 34, Iss. 1, pp. 184 - 191, 2004b
- Matloff, G. L., The Solar Photon Thruster as a Terrestrial Pole Sitter, *Annals of the New York Academy of Sciences*, Vol. 1017, pp. 468-474, 2004
- Maxwell, J. C., "Electricity and Magnetism", Oxford University Press, 1873.
- MIT Student Project, "Concepts for the Space Disposal of Nuclear Waste, Appendix B, Propulsion by Reflection of Light from the Sun", Aeronautics and Astronautics Project, Spring Term 1972.
- Morgan, T.O., The Inclination Change for Solar Sails and Low Earth Orbit, AAS 79-104, *Advances in Astronautical Sciences*, 1979.
- Mori, O., Tsuda, Y., Sawada, H., Funase, R., Yamamoto, T., Saiki, T., Yonekura, K., Hoshino, H., Minamino, H., Endo, T., Kawaguchi, J., World's First Demonstration of Solar Power Sailing by IKAROS, *Proceedings of the Second International Symposium on Solar Sailing (ISSS 2010)*, The New York City College of Technology of the City University of New York, July 2010.
- Murphy, D.M., Murphey, T.W., Gierow, P.A., Scalable Solar-Sail Subsystem Design Concept, *Journal of Spacecraft and Rockets*, Vol. 40, No. 4, 2003.
- Murphy, D.M., Macy, B.D., Gaspar, J.L., Demonstration of a 10-m Solar Sail System, AIAA-200-1576, 40th Joint Propulsion Conference, Fort Lauderdale, Florida, July 2004.
- NASA/JPL Technical Memorandum 33-734, Volume 2, Mariner Venus Mercury 1973 Project Final Report, Extended Mission-Mercury II and III Encounters, 01 December 1975.
- NASA/JPL Technical Memorandum 33-734, Volume 1, Mariner Venus Mercury 1973 Project Final Report, Venus and Mercury 1 Encounters, 15 September 1976.
- Nehrenz, Initial Design and Simulation of the LightSail-1 Attitude Determination and Control System, *Proceedings of the Second International Symposium on Solar*

- Sailing (ISSS 2010), The New York City College of Technology of the City University of New York, July 2010.
- Nichols, E.F., Hull, G.F., "A Preliminary Communication on the Pressure of Heat and Light Radiation", *Physics Review (Series I)*, Vol. 13, pp. 307-320, 1901.
- Nichols, E.F., Hull, G.F., *The Pressure Due to Radiation. (Second Paper.)*, *Physics Review (Series I)*, Vol. 17, pp. 26-50 and pp 91-104, 1903.
- Norem, R., *Interstellar Travel, A Round Trip Propulsion System with Relativistic Velocity Capabilities*, AAS Paper 69-388, June 1969.
- Normile, D, *Mission to Probe Venus's Curious Winds And Test Solar Sail for Propulsion*, *Science*, Vol. 328, No. 5979, p677, 2010. DOI: 10.1126/science.328.5979.677-a.
- Oberth, H., *Die Rakete zu den Planetenräumen*, Oldenbourg, München, 1923. In German.
- Oberth, H., *Ways to Spaceflight*, Verlag, Berlin, 1929 (also NASA TTF-622)
- Pagel, G., „Extremale Steuerstrategien für Sonnensegler am Beispiel von Bahntransferproblemen zum Erdmond“, *Doctoral Thesis, Technischen Universität Berlin*, May 2002. In German.
- Pukniel, A., Coverstone, V., Burton, R., Carroll, D., *Attitude Control of the CubeSail Solar Sailing Spacecraft in Low Earth Orbit*, *Proceedings of the Second International Symposium on Solar Sailing (ISSS 2010)*, The New York City College of Technology of the City University of New York, July 2010.
- Sackett, L.L., *Optimal Solar Sail Planetocentric Trajectories*, R-1113, The Charles Stark Draper Laboratory, Inc., JPL-NASA Contract NAS 7-100 Final Report, September 1977.
- Sackett, L.L. & Edelbaum, T.N., *Optimal Solar Sail Spiral to Escape*, *Advances in Astronautical Sciences, AAS/AIAA Astrodynamics Conference*, A78 31-901, 1978.
- Sauer, Jr., C.G., *Optimal Solar Sail Interplanetary Trajectories*, *American Institute of Aeronautics and Astronautics and American Astronautical Society, Astrodynamics Conference*, San Diego, Calif., Aug. 18-20, 1976
- Sauer, C.G., "Comparison of Solar Sail and Ion Drive Trajectories for a Halley's Comet Rendezvous Mission", *AAS/AIAA Astrodynamics Conference*, Jackson Hole, WY, September 1977.
- Sauer, Jr., C., *Solar Sail Trajectories for Solar Polar and Interstellar Probe Missions*, *Astrodynamics 1999*, edited by K. Howell, F. Hoots, and B. Kaufman, Vol. 103 of *Advances in the Astronautical Sciences*, Univelt, Inc., pp. 547-562, 2000.
- Sauer, Jr., C.G., *The L1 Diamond Affair*, AAS 04-278, *Proceedings of 14th AAS/AIAA Space Flight Mechanics Conference*, Maui, Hawaii, February 2004.
- Sands, N., *Escape from Planetary Gravitational Fields by Using Solar Sails*, *American Rocket Society Journal*, Vol. 31, pp. 527-531, April 1961.
- Sawada, H., Mori, O., Okuizumi, N., Shirasawa, Y., Sakamoto, H., Furuya, H., Matunaga, S., Miyazaki, Y., *Report on Deployment Solar Power Sail Mission of IKAROS*, *Proceedings of the Second International Symposium on Solar Sailing (ISSS 2010)*, The New York City College of Technology of the City University of New York, July 2010.
- Sebolt, W., Leipold, M., Rezazad, M., Herbeck, L., Unckenbold, W., Kassing, D., Eiden, M., "Ground-Based Demonstration of Solar Sail Technology", *IAF-00-S.6.11*, *Proceedings of 51st International Astronautical Congress*, Rio de Janeiro, Brasil, 2000.

- Sharma, D.N., Scheeres, D.J., Solar System Escape Trajectories Using Solar Sails, *Journal of Spacecraft and Rockets*, Vol. 41. No. 4, pp. 684 – 68, 2004.
- Shirley, D., The Mariner 10 Mission to Venus and Mercury, IAF-02-Q.4.1.01, Proceedings of 53rd International Astronautical Congress, Houston, Texas, 10-19 October 2002.
- Sweetser, T. H., Sauer, Jr., C. G., Advanced Propulsion Options for Missions to the Kuiper Belt, AAS/AIAA Astrodynamics Specialists Conference, Quebec City, Canada, August, 2001.
- Tsander, K., From a Scientific Heritage, NASA Technical Translation TTF-541, 1967, a translation of *Iz Nauchnogo Naslediya*, Nauca Press, Moscow, 1924.
- Vulpetti, G., Sailcraft Trajectory Options for the Interstellar Probe: Mathematical Theory and Numerical Results, Chapter IV of NASA/CR-2002-211730, “The Interstellar Probe (ISP): Pre-Perihelion Trajectories and Application of Holography”, June 2002.
- Vulpetti, G., Johnson, L., Matloff, G.L., *Solar Sail: A Novel Approach to Interplanetary Travel*, Praxis, New York, 2008.
- Tsu, T.C., Interplanetary Travel by Solar Sail, *Journal of the American Rocket Society*, Vol. 29, pp. 422-427, June 1959.
- Tsander, K., From a Scientific Heritage, NASA Technical Translation TTF-541, 1967, a translation of *Iz Nauchnogo Naslediya*, Nauca Press, Moscow, 1924.
- Uphoff, C.W., “Solar Sailing: Potential for Future Missions”, JPL Report 760-164, 25 January 1977. Revision of internal memorandum, dated 10 June 1975.
- Vulpetti, G., Sailcraft at High Speed by Orbital Angular Momentum Reversal, *Acta Astronautica*, Vol. 40, No. 10, pp. 733-758, 1997.
- Wallace, R.A., Precursor Missions to Interstellar Exploration, Proceedings of Aerospace Conference 1999, Vol. 1, pp. 413-420, ISBN: 0-7803-5425-7, 1999.
- Wallace, R.A., Ayon, J.A., Sprague, G.A., Interstellar Probe Mission/System Concept, Proceedings of Aerospace Conference 2000, Vol. 7, pp. 385 – 396, ISBN: 0-7803-5846-5, 2000.
- Waters, T., and McInnes, C.R., Periodic Orbits above the Ecliptic Plane in the Solar Sail Restricted 3-body Problem, *Journal of Guidance, Control and Dynamics*, Vol. 30, No. 3, pp. 687-693, 2007.
- West, J.L., NOAA/NASA/DOD Geostorm Warning Mission, JPL Internal Document, D-13986, October 1996.
- West, J.L., Design Issues for a Mission to Exploit the Gravitational Lensing Effect at 500 AU, 2nd IAA Symposium on Realistic Near-term Advanced Scientific Space Missions, Aosta, Italy, June 1998.
- West, J.L., Solar Sail Vehicle System Design For The Geostorm Warning Mission, AIAA-2000-5326, Proceedings of Structures, Structural Dynamics, and Materials Conference, Atlanta, April 2000.
- West, J. L., The GeoStorm Warning Mission: Enhanced Opportunities Based On New Technology, 14th AAS/AIAA Spaceflight Mechanics Conference, Paper AAS 04-102, Maui, Hawaii, Feb 8th-12th, 2004
- Wiley, C., [pseudonym Sanders, R.] *Clipper Ships of Space*, Astounding Science Fiction, p. 135, May 1951.
- Winglee, R., Slough, J., Ziemba, T., Goodson, A., Mini-Magnetospheric Plasma Propulsion (M2P2): High Speed Propulsion Sailing the Solar Wind,” Proc. STAIF 2000, M. S. Elgenk, ed. AIP 2000.

- Wright, J.L., "Solar Sailing: Evaluation of Concept and Potential", Battelle Memorial Institute Report, no. BMI-NLVP-TM-74-3, November 1974.
- Wright, J., Warmke, J., Solar Sailing Mission Applications, Paper No. 76-808, AIAA/AAS Astrodynamics Conference, San Diego, August 1976.
- Wright, J., Space Sailing, Gordon and Breach Science Publications, Amsterdam, 1992.
- Yen, C. L., Comparing Solar Sail and Solar Electric Propulsions for Propulsive Effectiveness in Deep Space Missions, American Astronautical Society, AAS Paper 01-214, Feb. 2001.
- Young, R.M., Montgomery, E.E, Montgomery, S., Adams, C.L., TRL Assessment of Solar Sail Technology Development Following the 20-Meter System Ground Demonstrator Hardware Testing, 8th Gossamer Spacecraft Forum, 23-26 Apr. 2007, Honolulu, HI, United States, 2007. NASA Technical Report Server Document ID: 20070032065.

Measurements and Characterization of Ultra Wideband Propagation within Spacecrafts- Proposal of Wireless Transmission for Replacing Wired Interface Buses

Akihisa Matsubara^{1,2}, Atsushi Tomiki²,
Tomoaki Toda² and Takehiko Kobayashi¹
¹Tokyo Denki University,
²Japan Aerospace Exploration Agency,
Japan

1. Introduction

This chapter describes measurement and characterization of radio propagation—particularly of ultra wideband (UWB) signals— within spacecrafts with a view to (at least partly) replacing onboard data buses with wireless connections. On-board equipment within spacecraft is classified into bus and mission parts. Bus parts are basic subsystems dealing with maintenance of the spacecraft system, such as Communication and Data Handling Subsystem, Attitude and Orbit Control Subsystem, Electrical Power Subsystem, Solar Array Paddle Subsystem, Temperature Control Subsystem, and Reaction Control Subsystem. Mission parts are important spacecraft subsystems vital to a mission's success, such as Scientific Instruments, Transponders, and Mission Data Processing Subsystems. Recently, due to more sophisticated spacecraft missions, mission parts have taken priority over bus parts in spacecraft design. As on-board submission equipment diversifies, wire harness used to connect subsystem components increase the weight of spacecraft. For example, about 4% (more than 20 kg) of the 500 kg of weight of Japan's Venus Climate Orbiter "AKATSUKI/Planet-C" spacecraft, launched in 2010, is signal wire-harness mass. Spacecraft manufacturing is largely a manual operation, with high costs and long lead times. Harnessing or electrical interconnections form a large part of spacecraft, contributing mass and requiring more assembly, integration, and testing as spacecraft complexity increases. Although wireless technologies have not been utilized within spacecraft as a physical layer of data buses, applying wireless technologies to a portion of signal wires could be extremely useful. Adoption of wireless technologies within spacecrafts could contribute to the following:

- Reduction of cable weight and resulting launching costs
- More flexibility in layout of spacecraft subsystems
- More reliable connections at rotary, moving, and sliding joints

To realize these benefits, multipath propagation affecting digital transmission performance must be scrutinized. Narrowband communication systems, such as conventional wireless local area networks, deteriorate due to frequency-selective fading in multipath

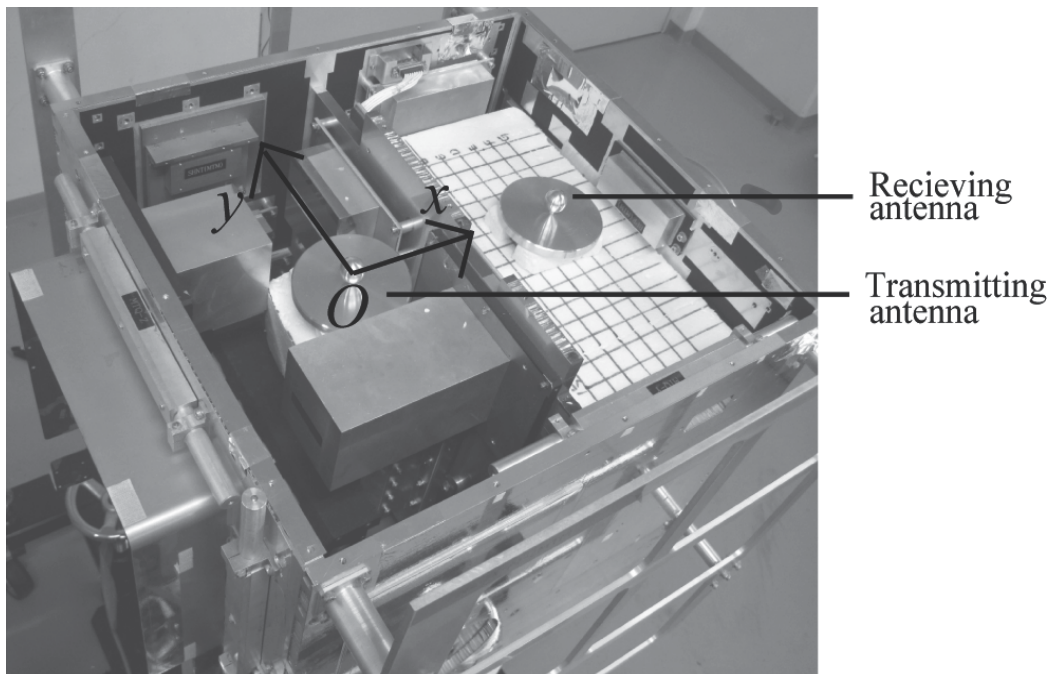
environments and hence need a substantial amount of fading margin (Kobayashi, 2006). In addition, intense long-delayed multipaths could cause inter symbol interference (ISI) and thus limit the data rate. Since UWB signals typically occupy a bandwidth of more than 500 MHz or a fractional bandwidth of more than 20%, they are expected to suffer less from multipath fading (Ghavami et al., 2007). While propagation of the UWB signals have been intensively measured and modeled in indoor and confined environments (Kobayashi, 2006; Win & Scholtz, 2002; Foerster, 2002; Haneda et al., 2006; Suzuki & Kobayashi, 2005; Gelabert et al., 2009), there has been only our study for spacecrafts. The study presented in this chapter proposes the use of UWB technology to facilitate a high data rate (e.g. maximum of 212 Mb/s per node attained with SpaceWire (European Cooperation for Space Standardization, 2003), equalling the standards of a wired onboard data bus) and to reduce fading margin.

The goal of this chapter is to measure and characterize radio propagation within a spacecraft and control it with the use of a radio absorber. In this study, UWB signal propagation (from 3.1 GHz to 10.6 GHz) in the frequency domain was measured and characterized with use of a microwave vector network analyzer. Spatial distributions of UWB and narrowband propagation gain, delay profiles (channel responses in the time domain), delay spreads (the second centered moments of the delay profiles), and the relation between fading depth and the bandwidth were derived from measurements conducted in a mechanical test model of a scientific satellite and a simulated shield box. Suppression of the delay spreads was attempted and evaluated by partially panelling a radio absorber on the inner surfaces.

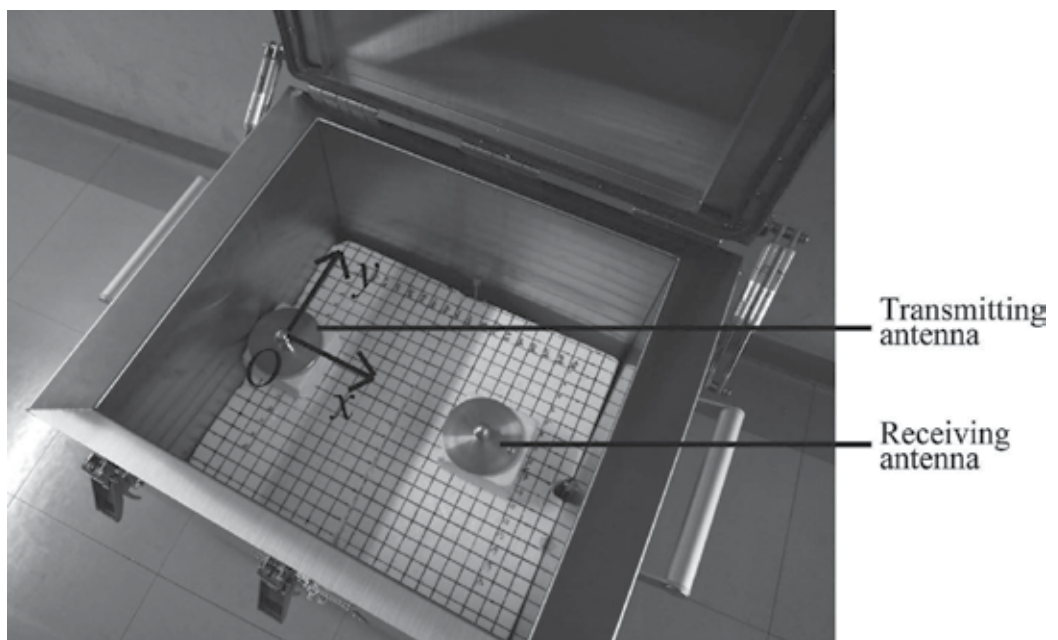
2. Measurement setup

A mechanical test model (MTM) of a small scientific satellite, which was launched in 2005, and a shield box of the same size were used for this measurement, as shown in Fig. 1. The MTM was a rectangular parallelepiped, 430 mm long \times 470 mm wide \times 435 mm high, enclosed in flat honeycomb panels made of aluminium, excluding its solar panels. Its interior was divided into two almost equal subspaces by a conductive partition having many openings, and mostly filled with mission subsystems. Hence, spatial distribution of the propagation gain would be attained only in a limited region. The shield box was employed to assess the whole inner space.

The transmitting and receiving antennas were omnidirectional, vertically polarized, low voltage-standing-wave-ratio UWB volcano-smoke antennas (Taniguchi et al., 2006), as shown in Fig. 2. Their circular ground planes were 100 mm in diameter. Within the MTM, the transmitting antenna was fixed in one subspace and the receiving antenna was scanned in another. During the measurements, the top lid was closed and the monopole elements of the two antennas were 3 mm below the lid. The x and y axes of the coordinate were parallel to the sides of the MTM, and the origin was located at the electric center of the transmitting antenna, as shown in Fig. 1(a). The receiving antenna was scanned within a region $200 \leq x$ [mm] ≤ 300 and $-140 \leq y$ [mm] ≤ 140 in 20-mm intervals on a styrofoam stage (transparent to electromagnetic waves). The feeding coaxial cables penetrated through the observation windows on the sides. Within the empty shield box, the transmitting antenna was fixed at 250 mm above the bottom and adjacent to the center of the 430-mm side, as shown in Fig. 1(b). That position was the origin of the coordinate, whose x and y axes were parallel to the sides. The receiving antenna was scanned horizontally within $0 \leq x$ [mm] ≤ 480 and $-180 \leq y$ [mm] ≤ 180 (excluding the close vicinity of the transmitting antenna) in 20-mm intervals on a styrofoam stage. During the measurements the conductive top lid was also closed. The feeding cables were relayed by coaxial connectors penetrating the wall.



(a)



(b)

Fig. 1. The measurement setup in: (a) a mechanical test model of small scientific satellite and (b) an empty shield box.



Fig. 2. Omnidirectional, low-VSWR UWB monopole antenna.

Frequency- (from 3.1 to 10.6 GHz) and time-domain propagation gains were measured with a microwave vector network analyzer. From the frequency-domain power gain data, the UWB propagation gains were calculated by integrating the power of the gains between the feeding points of the antennas over the occupied bandwidth:

$$PG_{\text{UWB}} = 10 \log \left(\frac{1}{f_H - f_L} \int_{f_L}^{f_H} 10^{\frac{PG_{\text{dB}}(f)}{10}} df \right) \quad (1)$$

where $PG_{\text{dB}}(f)$ is the propagation gain in dB measured at a frequency f , and f_L and f_H are the lowest and the highest frequencies, from 3.1 to 10.6 GHz (the full band approved in the United States) and from 7.3 to 7.9 GHz (the high band approved in Japan); and the continuous wave (CW) gain at the center frequency (= 6.85 GHz) was extracted therefrom. From the time-domain power gain data (power delay profile), the root-mean-square (rms) delay spread is the square root of the second central moment of a power delay profile. The delay spread is used to describe the average power delay profiles $P(\tau_i)$, where τ_i is the i th path delay. Average delay (D) and delay spread (S) are yielded by

$$D = \frac{\sum_{i=0}^n \tau_i P(\tau_i)}{\sum_{i=0}^n P(\tau_i)} \quad (2)$$

and

$$S = \frac{\sum_{i=0}^n (\tau_i - D)^2 P(\tau_i)}{\sum_{i=0}^n P(\tau_i)} \quad (3)$$

Delay spread estimates are sensitive to noise components having large excess delays. The usual way to cancel the effect of noise is by setting to zero the values of the power-delay profile lying below a noise threshold defined relative to the peak power in the profile. In this study, a threshold level in -20 dB below the maximum return was defined.

3. Measurement results

Examples of time- and frequency-domain propagation gains are presented in Figs. 3 and 4, measured at $(x, y) = (300, 0)$ within the MTM and the shield box. The delay spreads were computed at less than 20 ns for the MTM, and more than 100 ns for the shield box. In the frequency domain (Fig. 4), frequency selective fading occurs intensely within the MTM and the shield box. The spatial distributions of CW and UWB propagation gains within the MTM are shown in Fig. 5. Propagation gains ranged from -48 to -20 dB for CW ($= 6.85$ GHz), from -28 dB to -24 dB for the full UWB, from -28 to -21 dB for the low-band UWB, and from -30 dB to -26 dB for the high-band UWB in the MTM. Similar results were obtained within the shield box, as shown in Fig. 6. Propagation gains ranged from -41 to -6.1 dB for CW, from -15 to -12 dB for the full UWB, from -14 to -9.7 dB for the low-band UWB, and from -19 to -13 dB for the high-band UWB. The lower gains in the MTM than in the shield box were attributed to the non line-of-sight propagation paths intercepted by the conductive partition dividing the interior. The UWB propagation gains did not exhibit explicit dependence on distance, whereas the IEEE 802.15.3a (Foerster, 2002) channel model applicable to indoor environments used the path loss increasing with the square of distance. While CW resulted in up to 28 dB (in the MTM) and 35 dB (in the shield box) fading at several “dead spots” caused by multipath interference, UWB practically yielded no dead spots. The fading depth versus frequency bandwidth at the deepest dead spots $(x, y) = (300, 60)$ in the MTM and $(180, -60)$ in the shield box were derived from measured data, as shown in Fig. 7, where the center frequency was fixed at 6.85 GHz, and the 7.5-GHz-bandwidth (from 3.1 to 10.6 GHz) propagation gain was set to the 0-dB reference. A bandwidth over 400 MHz or a fractional bandwidth over 6% was capable of reducing the fading depth to approximately 2 dB for both the MTM and the shield box.

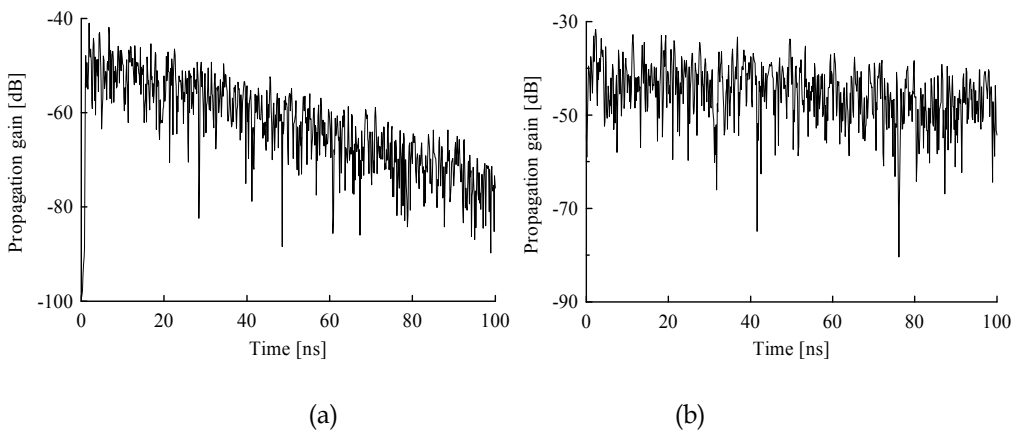


Fig. 3. Delay profiles at $(300, 0)$ in (a) the MTM and (b) the shield box.

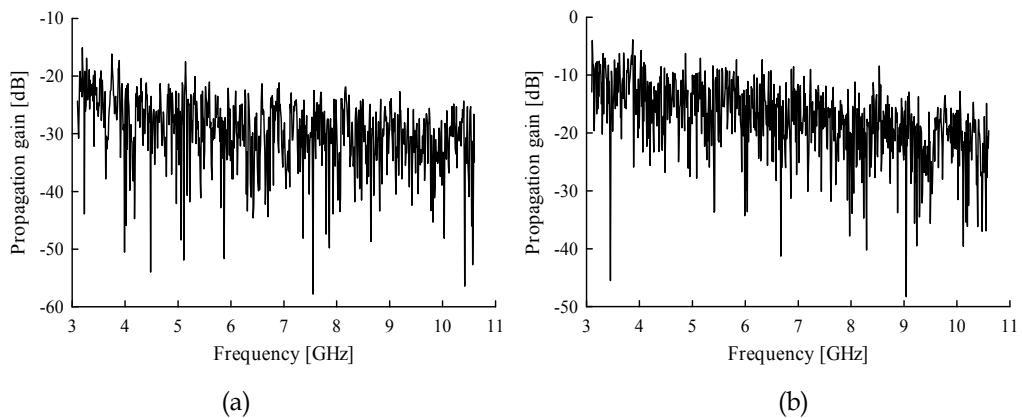


Fig. 4. Frequency responses at (300, 0) in (a) the MTM and (b) the shield box.

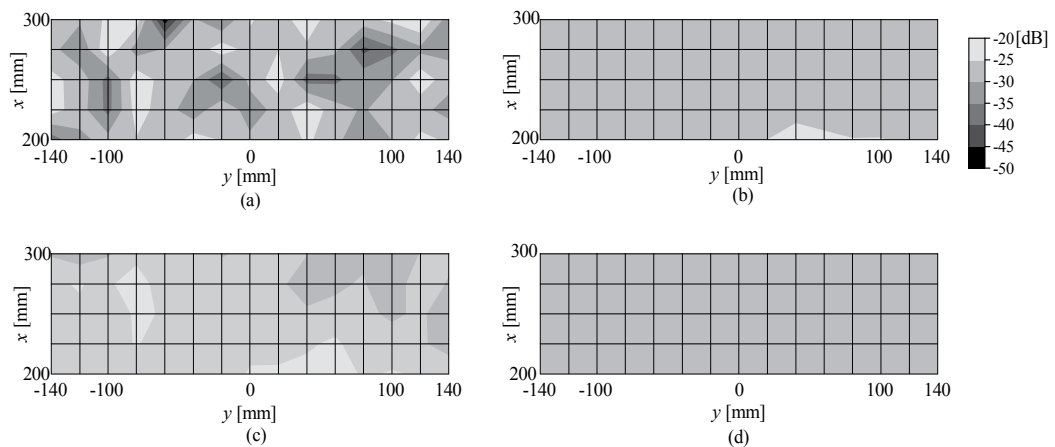


Fig. 5. Spatial distributions of propagation gain within the MTM: (a) CW (6.85 GHz), (b) fullband UWB (3.1 - 10.6 GHz), (d) low-band UWB (4.2 - 4.8 GHz), and (c) high-band UWB (7.3 - 7.9 GHz).

4. Suppression of delay spreads

The conductive enclosures yields a long delay spread, particularly when empty, which causes inter symbol interference (ISI), and hence an irreducible error floor when the modulation symbol time is on the same order as the delay spread. A patch of a thin elastic radio absorber, shown in Fig. 8, was attached at the center of the bottom of the shield box to suppress the delay spreads. The absorbers, 2.3 and 1.8 mm thick, usable in vacuum, attenuated radio wave reflection by 20 dB at 4 and 7 GHz, respectively, and by 10 dB within a 1.5-GHz bandwidth. Propagation properties were measured while the patch of the strip was $0.093 \text{ m}^2 (= 305 \text{ mm square}) \times 2^{-n}$, where $n = 0, 1, 2, \dots, 6$, corresponding $8 \times 2^{-n}\%$ against the total inner surface. Examples of delay profiles are shown in Fig. 9, when the receiving antenna was placed at $(x, y) = (300, 0)$. The conductive empty shield box caused abundant multipaths. The long delays were suppressed with use of the radio absorber. Relation

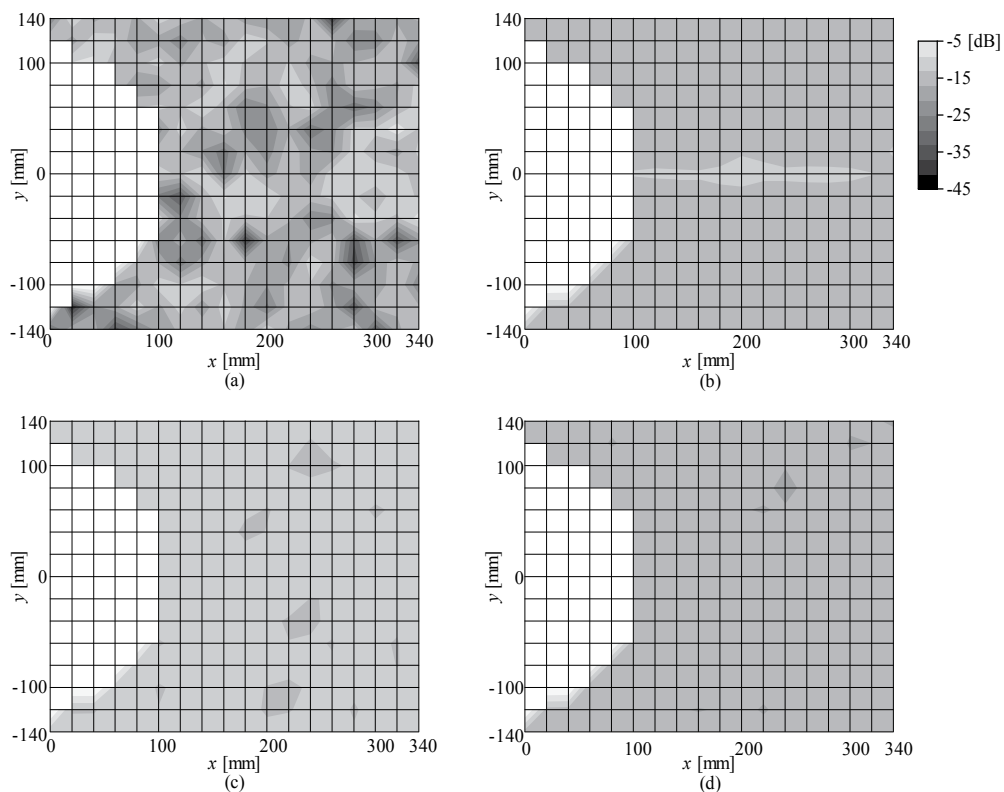


Fig. 6. Spatial distributions of propagation gain within the shield box: (a) CW (6.85 GHz), (b) full-band UWB (3.1 - 10.6 GHz), (d) low-band UWB (4.2 - 4.8 GHz), and (c) high-band UWB (7.3 - 7.9 GHz).

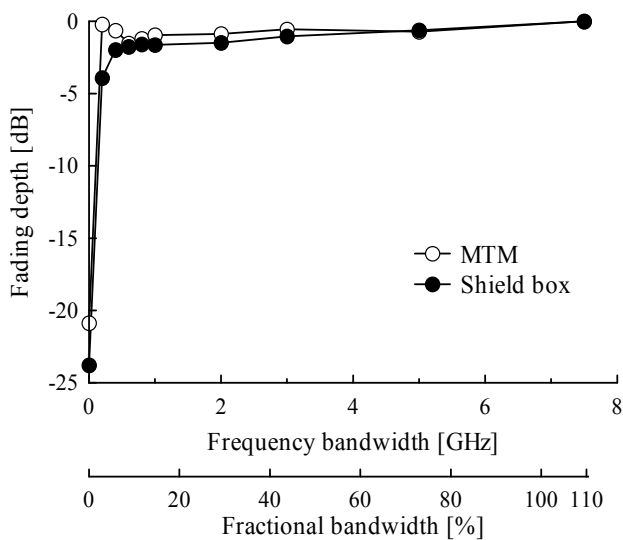


Fig. 7. Fading depth versus occupied bandwidth.

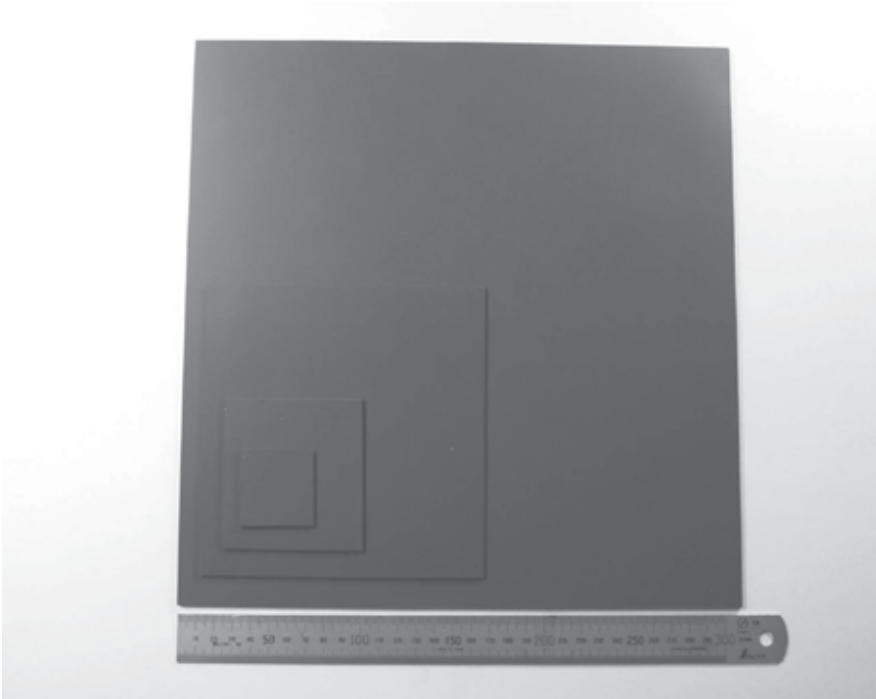


Fig. 8. Examples of radio absorber used in the experiment. The areas are 0.093, 0.023, 0.006, and 0.001 m².

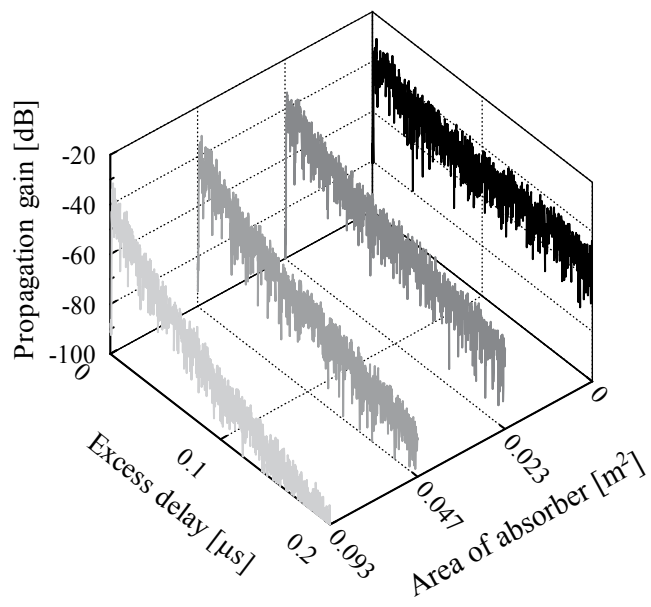


Fig. 9. Delay profiles at (300, 0) in the shield box, for various areas of radio absorber strip.

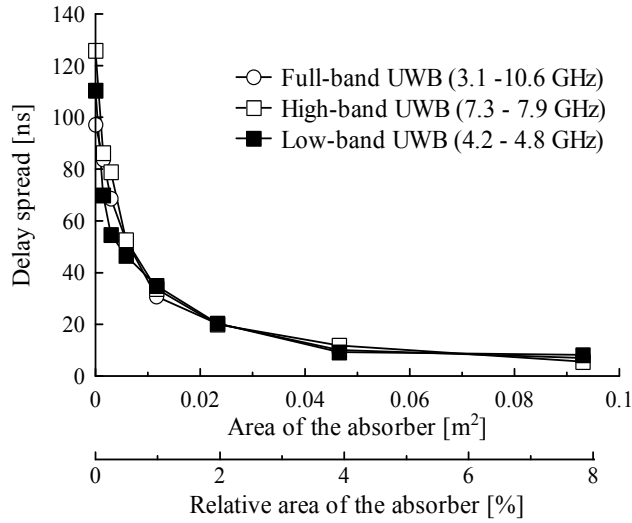


Fig. 10. Delay spread versus area of the absorber at (300, 0).

between the delay spread and the area of radio absorber is depicted in Fig. 10, where the percent area represents the ratio of the area of the radio absorber to the total inner surface area. The relatively small area of the radio absorber successfully suppressed the delay spreads in the shield box: 0.5 and 4% area of the absorber yielded 50 and 10% suppression, respectively. The spatial distributions of delay spread are shown in Fig. 11 with use of the radio absorber covering 8% of the total inner surface. Delay spread ranged from 3.7 to 9.2 ns for full UWB, from 2.3 to 16 ns for the low-band UWB, and from 2.4 to 11 ns for the high-band UWB. Cumulative distribution function (CDF) of delay spread is shown in Fig. 12, which reveals that the median (CDF = 0.5) of the delay spreads were 5.8, 6.9, 6.2 ns for the full-band, the low-band, and the high-band UWB, respectively. The smaller delay spread in the high-band UWB than the low-band UWB were attributable to higher propagation losses in the high-band than in the low-band. Received energy losses caused by the radio absorber were estimated as shown in Fig. 13: 0.5 and 4% area resulted in 2 and 5 dB in energy loss, respectively. The spatial distributions of propagation gain are shown in Fig. 14 with use of the radio absorber covering 8% of the total inner surface. Propagation gain ranged from -24 to -19 dB for full UWB, from -25 to -15 dB for the low-band UWB, and from -29 to -19 dB for the high-band UWB. The gain decreased and fluctuation of the gain increased as the area of the radio absorber increased. Including these energy losses, the relation between the fading depth and the occupied bandwidth was derived. No substantial change in the fading depth was observed as an effect of the radio absorber.

In orthogonal frequency division multiplexing (OFDM), the input data are divided into blocks of the same size, where each block is referred to as an OFDM symbol. By appending a cyclic prefix to each OFDM symbol, the ISI can be removed as long as the cyclic prefix is longer than the impulse response of the channel (typically represented by the delay spread). WiMedia (Heidari, 2008), a high-speed wireless personal area communication standard, utilized multiband OFDM, one of the UWB technologies. It employs 60.61-ns zero postfix (or zero-padded suffix as an alternative to the cyclic prefix). When the delay spreads are suppressed sufficiently shorter than the 60.61 ns, therefore, we can use the WiMedia devices, which yield the maximum data rate of 480 Mb/s, within spacecrafts.

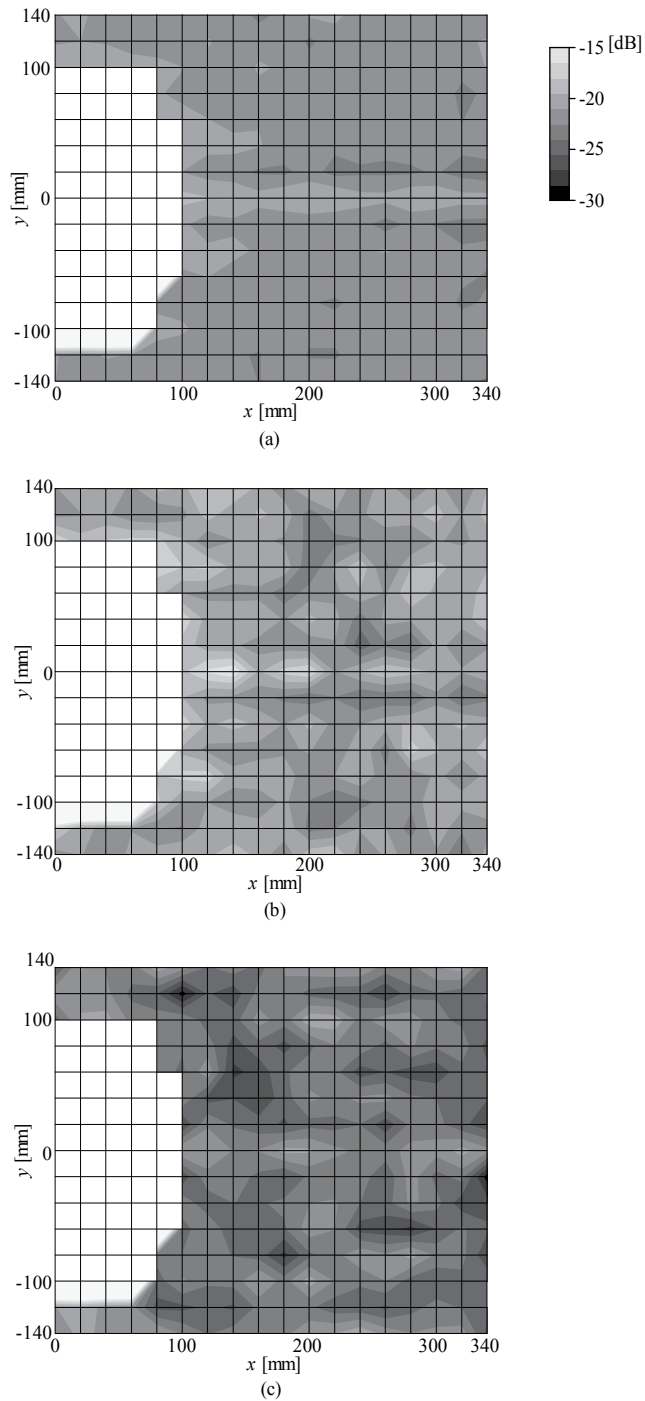


Fig. 11. Spatial distribution of delay spread with use of 0.093 m^2 area of the radio absorber, computed from: (a) full UWB (3.1 - 10.6 GHz), (b) low-band UWB (4.2 - 4.8 GHz), and (c) high-band UWB (7.3 - 7.9 GHz).

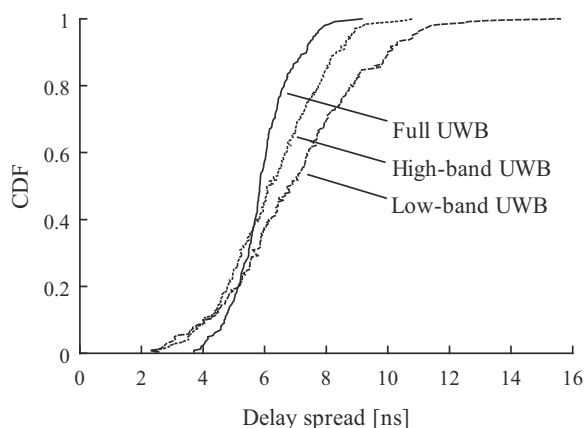


Fig. 12. Cumulative distribution function of delay spread.

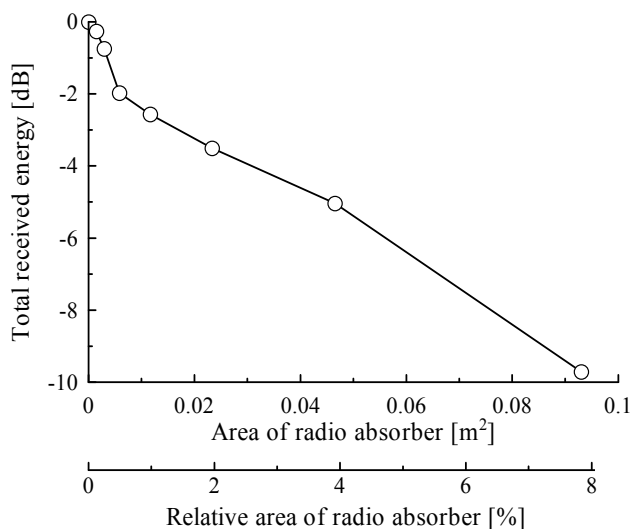


Fig. 13. Received energy loss caused by the radio absorber.

5. Conclusions

Ultra wideband (from 3.1 to 10.6 GHz, from 4.2 to 4.8 GHz, and from 7.3 to 7.9 GHz) and CW (6.85 GHz) propagation were measured and characterized inside a small spacecraft. Major findings are summarized as follows:

- While CW resulted in nearly 30-dB fading at several “dead spots” caused by multipath, UWB yielded no dead spots. The UWB systems have therefore an advantage over narrowband systems from the viewpoint of reducing fading margins.
- A bandwidth over 400 MHz or a fractional bandwidth over 6% was capable of reducing the fading depth by approximately 2 dB in conductive closed spaces like spacecraft.
- The conductive enclosures caused abundant multipaths and, as a result, long delay spreads, particularly when empty.

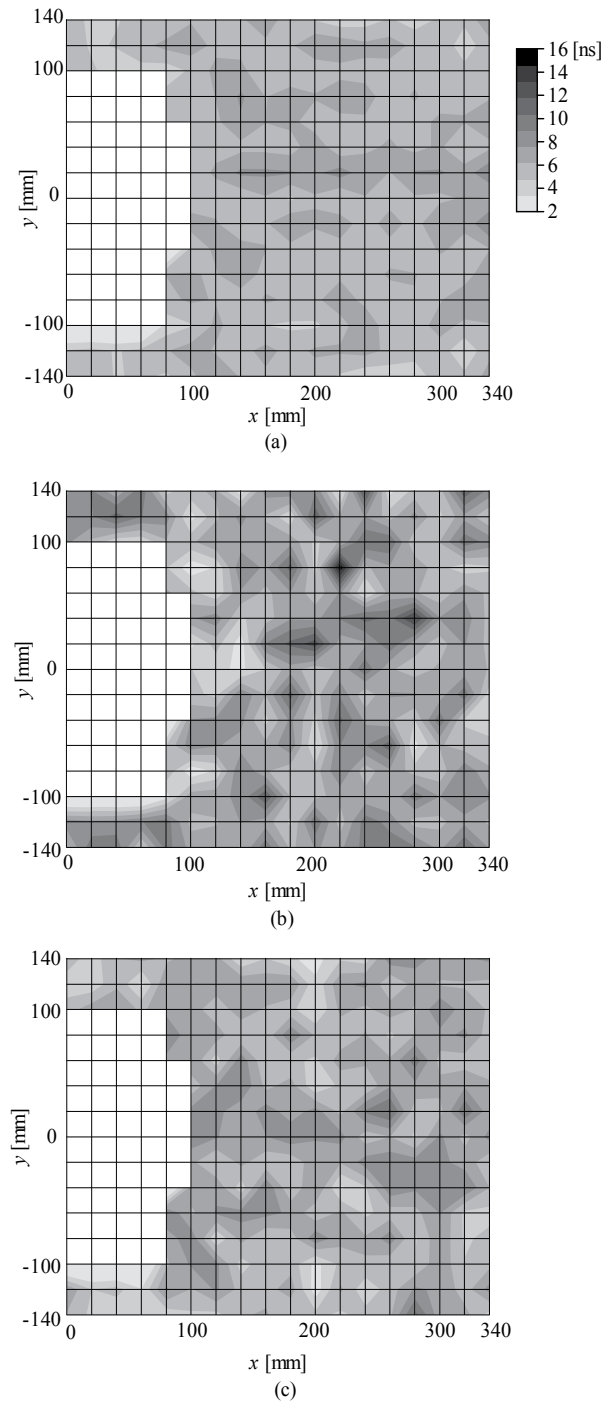


Fig. 14. Spatial distribution of propagation gain with use of 0.093 m^2 area of the radio absorber, measured from: (a) full UWB (3.1 - 10.6 GHz), (b) low-band UWB (4.2 - 4.8 GHz), and (c) high-band UWB (7.3 - 7.9 GHz).

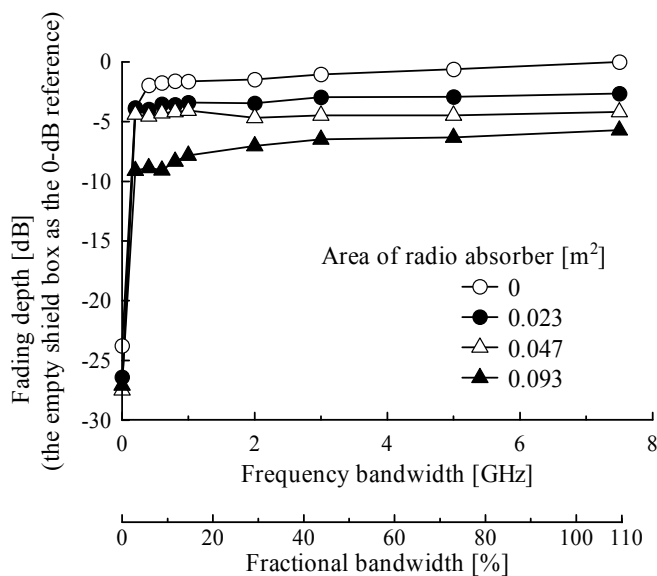


Fig. 15. Fading depth versus occupied bandwidth in the shield box with use of a radio absorber.

- Propagation gain decreased and the fluctuation range of the gain increased when increasing the area of radio absorber.
- The delay spreads can be suppressed with the use of a small patch of radio absorber. For empty enclosures, an 8% area of radio absorber can suppress the delay spreads less than 16 ns (typically 10 ns).
- Commercial, off-the-shelf WiMedia devices can be used to accommodate up to 480-Mb/s data buses within spacecraft, as long as the delay spread is suppressed far below 60 ns, from the viewpoint of propagation.

Future study and concerns include propagation measurements and characterization within larger spacecrafts and electromagnetic compatibility with the other subsystems to realize UWB wireless connection (at least partially) as a replacement for wired data buses.

6. Acknowledgment

This work has been supported in part by the Research Institute for Science and Technology, Tokyo Denki University, under the grant Q10J-07.

7. References

- T. Kobayashi. (2006). Measurements and characterization of ultra wideband propagation channels in a passenger-car compartment. *IEICE Trans. Fundamentals*, vol. E89-A, no. 11 (Nov. 2006), pp. 3089-3094.
- M. Ghavami.; L. B. Michael. & R. Kohno. (2007). *Ultra Wideband Signals and Systems in Communication Engineering*. NY: Wiley, 2nd ed. New York.

- M. Z. Win. & A. Scholtz. (2002). Characterization of ultra-wide bandwidth wireless indoor channels: a communication-theoretic view. *IEEE J. Select. Areas Commun.*, vol. 20, no. 9 (Dec. 2002), pp. 1613-1627.
- J. Foerster. (2002). Channel modelling sub-committee report final. IEEE P802.15-02/368r5-SG3a.
- K. Haneda.; J. Takada. & T. Kobayashi. (2006). Cluster properties investigated from a series of ultrawideband double directional propagation measurements in home environments. *IEEE Trans. Antennas Propag.*, vol. 54, no. 12 (Dec. 2006), pp. 3778-3788.
- Y. Suzuki. & T. Kobayashi. (2005). Ultra wideband signal propagation in desktop environments. *IEICE Trans. Fundamentals*, vol. E88-A, no. 9 (Sep. 2005), pp. 2272-2278.
- J. Gelabert.; A. Kavatzikidis.; D. J. Edwards. & C. J. Stevens. (2009) Experimental UWB channel characterisation of an electromagnetically small environment, *Proceedings of 2009 Loughborough Antennas and Propagat. Conf. (LAPC 2009)*, Loughborough, UK, Nov. 2009.
- European Cooperation for Space Standardization (2003). Standard ECSS-E-50-12A, SpaceWire—links, nodes, routers and networks.
- T. Taniguchi.; A. Maeda. & T. Kobayashi. (2006). Development of an omnidirectional and low-VSWR ultra wideband antenna. *International Journal on Wireless and Optical Communications*, vol. 3, no. 2 (Aug. 2006), pp. 145-157.
- G. Heidari. (2008). *WiMedia UWB – Technology of Choice for Wireless USB and Bluetooth*. John Wiley & Sons, New York.

Lubrication of Attitude Control Systems

Sathyan Krishnan¹, Sang-Heon Lee¹
Hung-Yao Hsu¹ and Gopinath Konchady²

¹*University of South Australia,*

²*Indian Institute of Technology Chennai,
Australia*

1. Introduction

The spacecraft attitude control system contains attitude error sensors such as gyroscopes and actuators such as momentum wheels and reaction wheels. The control moment gyro (CMG), in which the momentum wheels are mounted in gimbals, are also used in attitude control of spacecrafts. All these systems are designed to operate continuously till the end of the mission at varying speeds of several thousand rpm. The on-orbit performance of spacecrafts depends largely on the performance of the momentum/reaction wheels which in turn depends on the bearings used and its lubrication, since the only component which undergoes wear in these systems are the ball bearings. Currently, the life cycle of spacecrafts are aimed to be around 20–30 years. However, the increases in size, complexity and life expectancy of spacecrafts demand advanced technologies especially in tribology and in turn the development of more innovative lubrication systems for long-term operation.

Space tribology is a subset of the lubrication field dealing with the reliable performance of satellites and spacecraft including the space station. Lubrication of space system is still a challenging task confronting the tribologists due to the unique factors encountered in space such as near zero gravity, hard vacuum, weight restriction and unattended operation. Since the beginning of space exploration, a number of mission failures have been reported due to bearing system malfunction (Robertson & Stoneking 2003; Kingsbury, et.al., 1999; Bedingfield, et. al., 1996) and the most recent is the bearing failure in the control moment gyro (CMG) of the international space station on July 2002 (Burt and Loffi, 2003).

1.1 Momentum/reaction wheels

Momentum/reaction wheels are spacecraft actuators used for control and stabilization of spacecraft attitude to the required level. These are momentum exchange devices that works by the principle of conservation of angular momentum. The torque produced by changing angular momentum of the wheel is used to turn the satellite to the required direction. Since the inertia of the satellite is large compared to the inertia of the wheels, a very precise control of the satellite orientation is possible with these systems. A typical momentum/reaction wheel contains a flywheel which is driven by an electric motor, generally, a brushless dc motor as shown in Fig. 1 (Sathyan, 2010). Its precise rotation about a fixed axis is ensured by mounting it over a bearing unit consisting of a pair of high precision angular contact ball bearings. The flywheel and the rotor of the motor are

mounted on the bearing unit housing. The speed of the flywheel is controlled through a drive electronics circuit. All these components are enclosed in a hermetically sealed metal casing purged with an inert gas. Usually the internal pressure is less than atmospheric, typically 15 torr. There are different designs of flywheels such as single piece machined disc type wheels and built-up spoked type wheels. For larger angular momentum, spoked type flywheels are generally used since it has the advantage of low mass to inertia ratio compared to disc type flywheels. Also, built-up flywheels shows better vibration damping properties, which is highly important in spacecraft systems. The normal operating speeds of momentum wheels are in the range of 3000 to 10000 rpm and produces angular momentum 50 to 200 Nms (Briscoe & Aglietti, 2003; Sathyan, 2003). The reaction wheels are usually small in size compared to the momentum wheels and has bidirectional capability. The speed range is about 3500 rpm and angular momentum capacity upto 5 Nms.

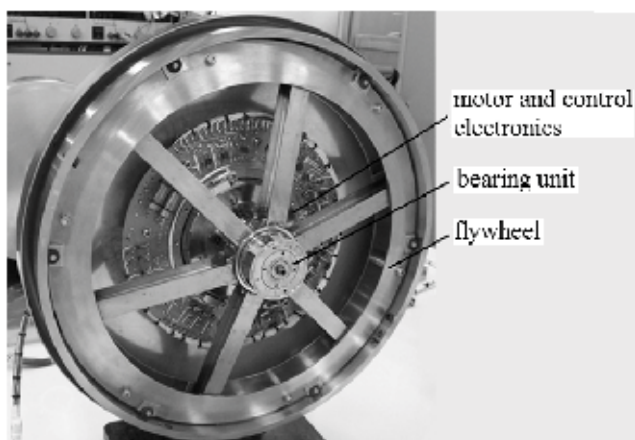


Fig. 1. Momentum wheel with top cover removed

1.2 Bearing unit

The bearing unit is the most critical subassembly of a momentum wheel. The life and performance quality of a momentum/reaction wheels to a great extent depends on the bearing unit. Unlike the electronic circuits, it is not possible to design a momentum wheel with redundant bearing units, therefore utmost care is given in the design, manufacturing and processing of bearing units. Fig. 2 shows a typical bearing unit used in a momentum wheel (Sathyan et.al., 2008). The bearing unit is generally made of high quality steel to ensure high strength and dimensional stability. AISI 440C is the most commonly used material for bearing units. Usually the bearings and the bearing unit components are made of the similar material to eliminate the effects of thermal stresses, because in service the wheels are subjected to wide ranges of temperatures. The bearings typically used in a momentum wheel are of light series high precision angular contact ball bearings (ABEC 9). The size of the bearings are determined based on the angular momentum required, typically for a 60 Nms wheel operating in a speed range 3000–6000 rpm, 20 mm bore is common (104 size). The bearings are usually arranged in back to back configuration and are separated by a set of equal length spacers.

There are two different designs of bearing units available such as rotating shaft design and rotating housing design. In rotating shaft design, the bearing housing is rigidly mounted on

the base plate of the wheel and the flywheel and the motor rotor are mounted on the shaft (Honeywell, 2003). In the rotating housing type, the bearing unit shaft is mounted on the base plate and the flywheel and motor rotor are mounted on the bearing housing (Auer, 1990; Jones and Jansen, 2005; Sathyan, 2003). Fig. 2 shows a typical rotating housing bearing unit used in a momentum wheel.

In bearing units, ball bearings with non-metallic retainers [cages] are generally used. However, retainerless bearings are also used in momentum wheel bearing units considering its advantages such as high loadability and absence of retainer instability. Retainer instability is one of the major causes of failure in high speed spacecraft bearings (Shogrin, et.al., 1999; Kannel and Snediker, 1977). Bearing retainers commonly used in momentum/reaction wheels are made from cotton based phenolic materials. The retainers made from this material can absorb certain amount of oil in its body and can act as a primary source of lubricant. Phenolic retainers are carefully and thoroughly dried to remove any absorbed moisture before they are impregnated with oil. Otherwise, the retainer will not be fully saturated and may absorb and remove oil from the bearing it is intended to lubricate (Bertrand, 1993). The lubricant stored in the retainer is sufficient to run a wheel continuously for 3–4 years with stable performance. A supplementary lubrication system is included either inside the bearing unit or inside the wheel casing to augment the life of the wheel to the required number of years.

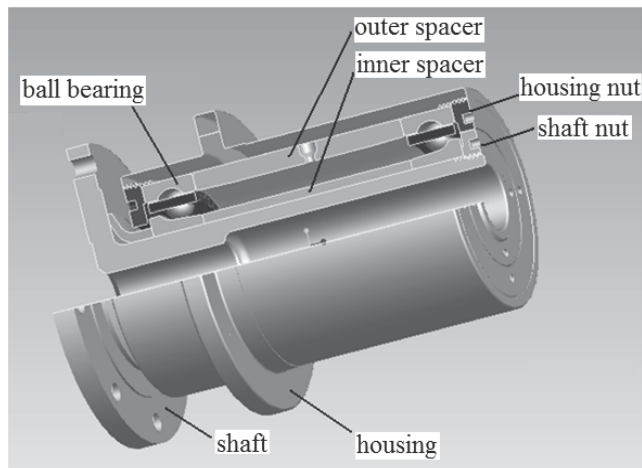


Fig. 2. Bearing unit assembly

Being a critical part, the bearing assembly needs exceptional care. The bearings in a momentum/reaction wheels are generally lubricated with specially developed liquid lubricants. A wide variety of lubricants are developed and used by different manufacturers. These lubricants possess certain important properties that are essential for successful operation in space environments.

A bearing in a momentum/reaction wheel may fail due to multiple reasons such as chemical degradation of lubricant, loss of lubricant from the working zone by surface migration and evaporation, and retainer instability. Retainer instability is the most dangerous mode of failure in spacecraft bearings. The retainer instability is related to a number of factors like geometry and mass of the retainer, operating speed, lubricant quantity, etc. The retainer instability problem can be totally eliminated by using retainerless bearings. Thus, with the

selection of proper lubricant and proven retainer design, lubrication becomes the principle life limiting problem on momentum wheels.

Generally, momentum/reaction wheels are made with high precision angular contact ball bearings having non-metallic retainers. These retainers act as a primary source of lubricant when it is impregnated with the lubricant. With this initial lubrication, the bearings can perform up to 3–4 years normally, provided the retainer is running stable. However, the current life requirement for momentum wheels and other high speed space systems are more than 20 years or even up to 30 years. This implies the need for efficient supplementary lubrication systems to achieve the mission life. Moreover, it is not possible to service the spacecrafts once it is launched. Therefore, in-situ, remote lubrication systems are employed in momentum/reaction wheels.

According to the nature of operation, the lubrication systems used in momentum wheels can be broadly classified as passive lubrication systems and active lubrication systems. The passive systems also known as continuous systems, supplies lubricant continuously to the bearings and is driven by centrifugal force or by surface migration force. The active lubrication systems, also known as positive lubrication systems, supplies a controlled amount of lubricant to the bearings when it is actuated by external commands

2. Tribology of attitude control systems

The word “tribology” was first introduced in the publication named “Department of Education and Science Report” England in 1966, and is defined as the science and technology of interacting surfaces in relative motion and of the practices related thereto (Hamrock, et.al., 1994). In other words, it is the study of friction, wear and tear, and lubrication of interacting surfaces.

At the beginning of the space explorations in 1957 when the first satellite was launched, scientists were unaware of the term tribology as a multidisciplinary subject. This is because, the spacecrafts never faced any lubrication problems for the short duration exploration. However, as the life requirement changed, especially with the development of communication satellites, spacecraft designers realised the importance of tribology in space system design. As a result, space tribology is emerged as a subset of the lubrication field dealing with the reliable performance of satellites and spacecraft including the space station. Lubrication of space system is still a challenging task before the tribologists due to the unique factors encountered in space such as near zero gravity, hard vacuum, weight restriction and unattended operation (Fusaro, 1992). Kannel and Dufrane (Kannel and Dufrane, 1986) conducted a study of tribological problems of past space systems and predicted the future tribological challenges. According to them “The development of aerospace mechanisms has required considerable advances in the science of friction, wear, and lubrication (tribology). Despite significant advances in tribology, the insatiable demands of aerospace systems seem to grow faster than the solutions.” A qualitative chart based on their study is shown in Fig. 3. This is a valid chart for the present and can be extended many more years because still there are space system failures due to tribological problems.

The main purpose of lubrication is to reduce the friction between the interacting surfaces in relative motion by introducing a third body (called lubricant) between them. The third body should have very low shear strength so that the mating surfaces do not undergo wear or damage. There are different lubricant materials available in various forms such as liquids,

gases and solids. Attitude control systems are generally lubricated with liquid lubricants. Depending upon the thickness of lubricant film present between the interacting surfaces, four well defined lubrication regimes are identified such as hydrodynamic, elastohydrodynamic (EHD), mixed and boundary lubrication regimes (Zaretsky, 1990; Jones and Jansen, 2000; Dowson, 1995; Fusaro, 2001). These four regimes are clearly understood from the Stribeck/ Hersey curve (Fig. 4), which shows the coefficient of friction as a function of dimensionless bearing parameter (ZN/P), where, Z is the lubricant viscosity, N is the velocity at the contact surface and P is the bearing load. A space bearing with liquid lubrication undergoes the last three regimes namely EHD, mixed and boundary before it fails due to lubricant starvation. Since it is not preferred to run the bearings in the hydrodynamic region due to the high viscous drag resultant from the high lubricant film thickness as seen from Fig. 4.

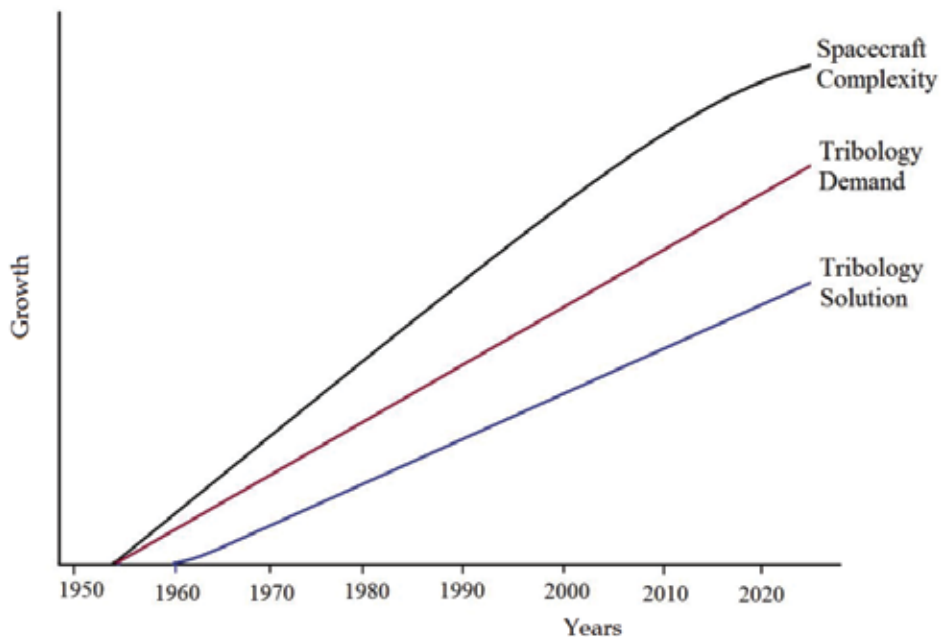


Fig. 3. Growth of spacecraft technology and tribology challenges

The concentrated research on elastohydrodynamic lubrication (EHD) resulted in the identification of three subdivisions in EHD, namely starved EHD, parched EHD and transient/non-steady state EHD (Jones and Jansen, 2005). In starved EHD lubrication, the pressure build-up at the inlet contact region is low due to restricted oil supply. As a result the lubricant film will be thinner than calculated by EHD theory (Hamrock and Dowson, 1981). In parched EHD lubrication, the lubricant films are so thin that they are immobile outside the contact zone (Kingsbury, 1985; Guangteng, et.al. 1992) and this regime is particularly important for momentum/reaction wheel bearings. In the transient/non-steady state EHD lubrication, the load, speed and contact geometry are not constant with time. The theoretical behavior of this regime in point contact bearings is not well understood (Jones and Jansen, 2005) but it was studied experimentally by Sugimura et al. (Sugimura, et.al, 1998). Generally, the momentum/reaction wheel bearings are designed to be operated in the lower boundary of EHD region because it has the advantage of the lowest coefficient of friction.

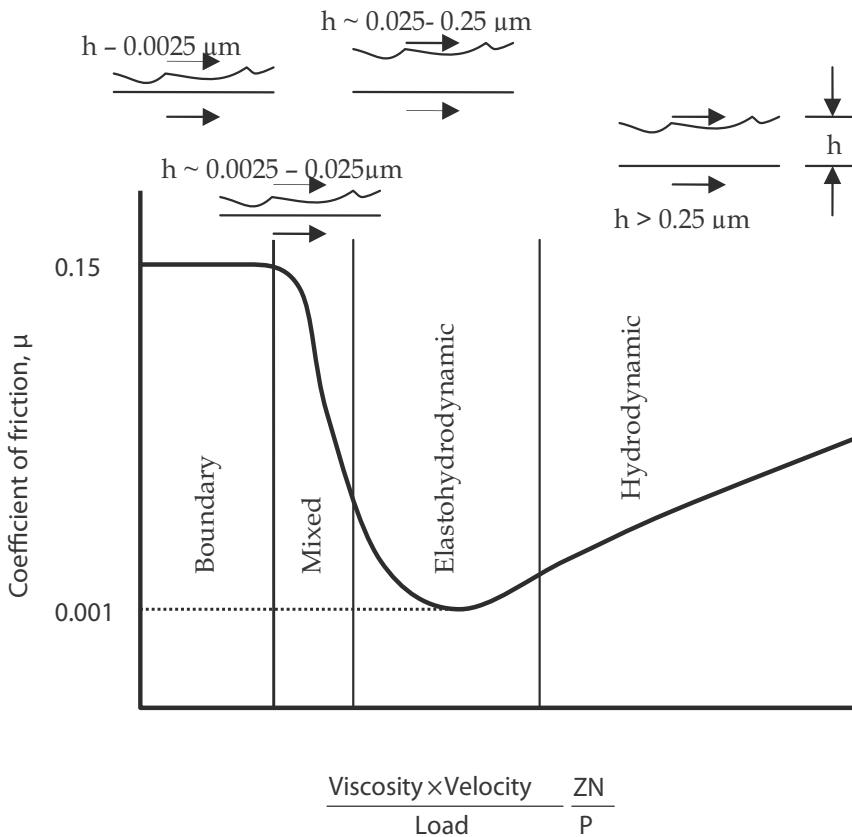


Fig. 4. Stribeck/Hersey curve (Fusaro, 2001)

In EHD lubrication, the load is carried by the elastic deformation of the bearing material together with the hydrodynamic action of the lubricant (Dowson, 1995; Hamrock and Dowson, 1981). A bearing operating in EHD region shows an indefinite life with lowest friction torque. The most interesting practical aspect of the EHD lubrication theory is the determination of lubricant film thickness which separates the ball and the races. The generally used equation for calculating the film thickness is the one developed by Hamrock and Dowson (Hamrock & Dowson, 1981):

$$H_{min} = 3.63 U_s^{0.68} G^{0.49} W^{-0.073} (1 - e^{-0.68k}) \quad (1)$$

and

$$H_{min} = \frac{h_{min}}{R_x} \quad (2)$$

where H_{min} is dimensionless minimum EHD film thickness, U_s is the dimensionless speed parameter, G is the dimensionless material parameter, W is the dimensionless load parameter, h_{min} is the minimum film thickness and R_x is the effective radius. The effectiveness of EHD lubrication is described by the λ ratio or film parameter, which is the

ratio of central film thickness at the Hertzian contact zone to the r.m.s. surface finish of the rolling element surface:

$$\lambda = \frac{h_{\min}}{\sqrt{(S_r^2 - S_b^2)}} \quad (3)$$

where S_r and S_b are the r.m.s surface finish of races and balls. The EHD regime is characterized by λ ratio between 3 and 10, which corresponds to a film thickness between 0.1 and 1 μm . It has been pointed out that a full film can be obtained with no asperity contact only when $\lambda > 3$. If the value of $\lambda < 3$, it will lead to mixed lubrication with some asperity contacts (Hamrock and Dowson, 1981). The calculated film thickness and λ ratio for a typical momentum wheel bearing (20 mm bore, 6.35 mm ball, ABEC 9P class) operating at 5400 rpm with a lubricant having pressure-viscosity coefficient $2 \times 10^{-8} \text{ m}^2/\text{N}$ and a bearing preload 50 N is 0.62 mm and 13.4 for the inner race contact and 0.76 mm and 16.3 for the outer race contact, respectively (Sathyan, 2003). Experimental verification of film thickness has been done by Coy et.al. on 20 mm bore ball bearing using the capacitance technique and the reported values ranging from 0.025 to 0.51 mm (Coy, et.al. 1979).

Tribological failures of momentum/reaction wheels are related to lubricant breakdown, loss of lubricant due to evaporation and surface migration (insufficient lubricant) and retainer instability. Lubricant breakdown failure occurs when the original liquid lubricant is chemically changed to solid friction polymer (Kingsbury, et.al., 1999). Kingsbury (Kingsbury, 1992) has shown that the rate of lubricant polymerization is determined by the thickness of the EHD film, larger rate for thinner films and negligible for thicker films. Loss of lubricant in momentum wheels occurs mainly due to evaporation, surface migration and centrifugal action. The working temperature, which is also a function of bearing friction torque, causes the lubricant to evaporate. The oil loss by migration is induced by temperature gradients and capillary forces. It was demonstrated that a small temperature gradient leads to the rapid and complete migration of thin oil films to the colder regions (Fote, et.al., 1978). The capillary migration describes the tendency of oil to flow along surface scratches and corners and is driven by pressure gradient in the radius of curvature of the oil-vapor interface.

Retainer instability is the most dangerous mode of failure in momentum wheel bearings. It has been the topic of interest for many researchers and tribologists and lot of published data are available (Taniwaki, et.al., 2007; Gupta, 1991; Kannel and Snediker, 1977; Boesiger, et.al., 1992). Generally, retainer instability is characterized by large variation in bearing friction torque associated with severe audible noise. There are three types of instabilities (Stevens, 1980) such as radial instability, axial instability and instability due to change in running position of retainer. The radial instability is characterized by high frequency radial vibration of the retainer and result in abrupt torque variation. Under marginal lubrication condition, this will cause significant torque increase and audible noise, whereas under excess lubrication it will show a sudden reduction in torque. The axial instability is characterized by high frequency axial vibration of the retainer and is mainly due to excessive clearance between the rolling element and the retainer pocket. The position instability occurs when the retainer oscillates between its mean position of running and the races. When it runs in the mean position, the friction will be nominal and occasionally the retainer moves in the radial

direction and run in that position rubbing against the race. This will result in a periodic change in friction torque as shown in Fig. 5. Uneven cage wear, lubricant degradation and insufficient lubrication are the prime causes for instabilities. It is also related to a number of factors like geometry and mass of the retainer, operating speed, lubricant quantity, etc. (Lowenthal, et.al., 1991; Boesiger and Warner, 1991; Gupta, 1988 and 1991). The retainer instability problem in attitude control wheels can be eliminated by using retainerless bearings (Shogrin, et.al., 1999; Kingsbury, et.al., 1999). Momentum/reaction wheels with retainerless ball bearings are now available (Kingsbury, et.al., 1999; Boesiger and Warner, 1991; Jones, et.al., 1997; Singer and Gelotte, 1994), which overcomes the most devastating problem observed in conventional bearings. Thus, with the selection of proper lubricant and proven retainer design, lubrication remains the principle life limiting problem on attitude control wheels.

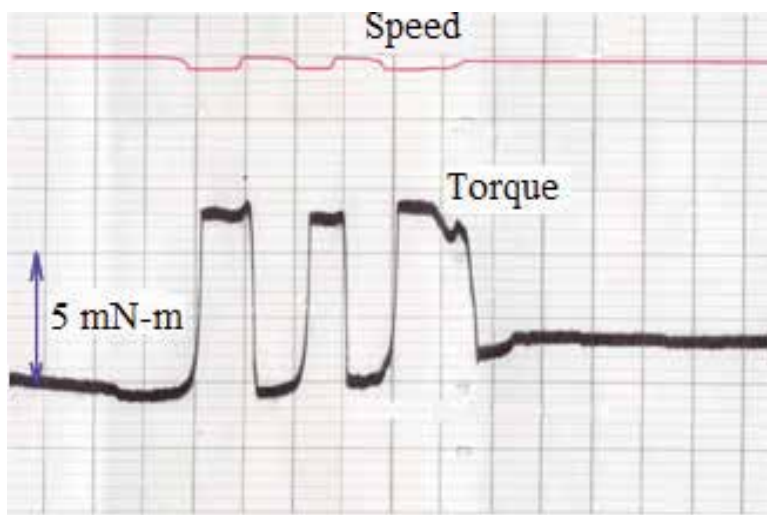


Fig. 5. Bearing friction torque variation due to retainer position change

Since the bearings are still mechanically intact when the lubricant degrades, if lubricant could be resupplied to the contact, the life of the wheels could be extended. Kingsbury (Kingsbury, 1973) has shown that only $0.2 \mu\text{g/h}$ lubricant flow rate is needed to maintain a continuous EHD film in instrument ball bearings. This is a very low value and is difficult to achieve practically, but efforts are underway to develop lubricant supply systems with the lowest possible flowrate, possibly less than $10 \mu\text{g/h}$ (Sathyan, et.al, 2010).

3. Qualities required for space lubricants

Momentum /reaction wheels are generally lubricated with liquid lubricants because of its outstanding merits over solid lubricants such as excellent torque characteristics and means of replenishment. The primary advantage obtained with liquid lubricants is that bearing surfaces separated by hydrodynamic films of liquid lubricants have virtually no wear and thereby have the potential for infinite lives. Since no single lubricant can meet the often conflicting requirements of various applications for liquids, hundreds of specialty lubricants have been developed for aerospace applications.

There are a number of factors to be considered while selecting a lubricant for attitude control wheels. Since these wheels are designed to operate in the elastohydrodynamic lubrication region, the EHL properties of the lubricant are of prime importance. Typically, a momentum wheel lubricant should have the following essential properties:

Viscosity Index: Since the attitude control wheel has to work over a wide temperature range (typically between 15 and 85°C) the change in viscosity with temperature should be minimum to maintain the EHD film. Therefore a lubricant with high viscosity index needs to be selected.

Vapor Pressure: The volatilization of lubricant contaminates the spacecraft systems and may have harmful effects; therefore the vapor pressure should be low in order to minimize losses by evaporation and to limit the pollution due to degassing. Fig. 6 shows the relative evaporation rates of various aerospace lubricants.

Pressure-viscosity Coefficient (α): The pressure-viscosity coefficient is important in determining the EHD film thickness at the ball-race contact inlet. From EHL theory, the lubricant with the largest α value should yield the thickest film at room temperature (Jones and Jansen, 2005).

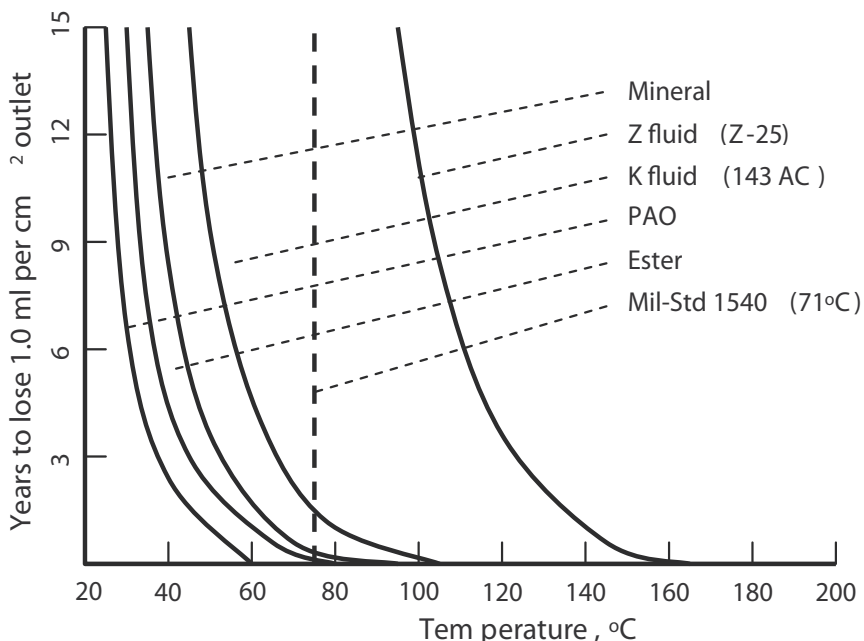


Fig. 6. Evaporation rates of various aerospace liquid lubricants (Jones and Jansen, 2005)

4. Space liquid lubricants

There are a number of liquid lubricants that have been used in attitude control wheel bearing lubrication. Most of these lubricants are formulated and developed specially for space application and some of these are not readily available in the market. These lubricants fall under different classes based on their chemical structure such as mineral oils, silicone fluids, esters, synthetic hydrocarbons, perfluoropolyethers (PFPE) and silahydrocarbons. Table 1 shows the property data of some of these lubricants.

4.1 Mineral oils

Mineral oils are natural hydrocarbons with a wide range of molecular weights. The paraffinic base oils are commonly used for space applications. Super refined mineral oils were the lubricant of choice for momentum wheels in the early periods, KG80 and Apiezon C are examples (Zaretsky, 1990). The super refined gyroscope [SRG] oils are another class of mineral oils widely used in momentum wheels. These are available in a wide viscosity ranges, for example SRG-40 [27cSt at 40°C] and SRG-60 [77.6 cSt at 40°C] (Kannel and Dufrane, 1986).

4.2 Silicon fluids

Silicon lubricants were used in the early spacecrafts. An example for silicon lubricant is GE Versilube F50, a chloroarylalkylsiloxane [CAS]. This oil has a very low vapor pressure and excellent low temperature properties. However, it degrades quickly under boundary lubrication conditions (Vernier and Casserly, 1991), which limited its application in many space systems. Silicone lubricants have a strong tendency to migrate and may adversely affect conductivity of electrical contacts.

4.3 Esters

Esters are inherently good boundary lubricants and are available in a wide range of viscosities. Diesters and triesters are the commonly used lubricants. The British Petroleum in 1970 developed a triester for space application and the European Space Tribology Laboratory [ESTL] has qualified this oil for high speed space mechanisms (Jones and Jansen, 2000), but its production was stopped and was never used in spacecrafts. A series of esters are marketed by Nye Lubricants; namely, UC4, UC7 and UC9. The ISOFLEX PDP65. A diester oil produced by Kluber Lubrication is a proven momentum wheel lubricant (Sathyan, 2003). This lubricant has very high viscosity index [235] and very low pour point [-60°C].

4.4 Synthetic hydrocarbons

Synthetic hydrocarbons are of two groups, polyalphaolefins (PAO) and multiply alkylated cyclopentanes (MACs). The PAO is typically made by oligomerization of 1-decene, for example Nye 186A, 3001A. A more detailed study of Nye 3001A and 3001(formulated) are presented in Ref. (Dube, et.al, 2003). MACs are synthesized by reacting cyclopentadiene with various alcohols in the presence of a strong base (Vernier and Casserly, 1991). The products are hydrogenated to produce the final products, which is a mixture of di-, tri-, tetra or penta alkylated cyclopentanes. These lubricants are known as Pennzanes® and the two types which currently in use are SHF X1000 and SHF X2000. It has been proved that addition of silver nano particles to MACs base oil will significantly improve its wear properties and load-carrying capacity and slight effect on its friction property (Ma, et.al., 2009).

4.5 Perfluoropolyethers (PFPE)

Perfluoropolyether is clear colorless fluorinated synthetic oil. These are nonreactive, nonflammable and long lasting lubricants. PFPE lubricants have very low outgassing properties compared to any other lubricants (Fowzy, 1998). These lubricants have been in use for over 30 years. This is a well known ball bearing lubricant for the international space

station (Mia, et.al, 2007). PFPE lubricants are made by polymerization of perfluorinated monomers. There are a number of PFPE lubricants available for space applications such as Krytox™, Fomblin™, Demnum™ etc. These are high density lubricants and due to this, yield EHD film thickness twice that of other lubricant having the same kinematic viscosity (Jones, 1993). However, it has been reported that viscosity loss both temporary and permanent occurred under EHL conditions due to high contact pressure (Mia, et.al, 2007). Also, reported that lubricant breakdown (tribo-corrosion) occurs with PFPE lubricants under boundary conditions (Jansen, et.al, 2001).

4.6 Silahydrocarbons

Silahydrocarbons are relatively new class of lubricants with great potential for use in space mechanisms. They are unimolecular species consisting of silicon, carbon and hydrogen and posses unique tribological properties. Silahydrocarbons have very low vapor pressure, high viscosity index and are available in wider viscosity ranges. These are available as tri-, tetra- and penta silahydrocarbons based on the number of silicon atoms present in their molecules. Silahydrocarbons are compatible with conventional lubricant additives. A detailed study of this class of lubricant appears in Ref. (Jones, et.al, 2001).

The EHL effectiveness of different classes of lubricant is shown in Fig. 7. The EHL performances of lubricants are improved by adding chemical additives such as extreme pressure, anti-wear and anticorrosion additives. The extreme pressure (EP) additive reacts with the bearing material to form surface films which prevent metal to metal contacts under high loads. Tricresylphosphate (TCP) is the commonly used EP additive and is usually added as 5% of the lubricant volume. The anti-wear additives are added to reduce the boundary lubrication wear, lead naphthenate (PbNp) is an example of such additives. Most lubricants mentioned above are compatible with these additives except the PFPE. Effective additives are recently developed for PFPE lubricants, but they have not yet found their application into space lubricants. A space lubricant must be thoroughly characterized before being put into real application. Various types of tribometers such as four ball tribometers, spiral orbit tribometers, pin on disk tribometers, etc. are used to evaluate the EHL properties of these lubricants. In addition to this a full scale system level life test is also recommended to evaluate actual performance.

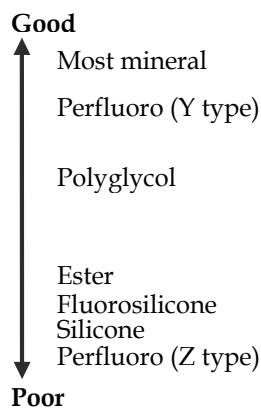


Fig. 7. EHD effectiveness of some oils (Roberts and Todd, 1990)

5. Lubrication systems

As mentioned before, the bearing unit of attitude control wheels are made with high precision angular contact ball bearings having non-metallic retainers. These retainers act as a primary source of lubricant when it is impregnated with the liquid lubricant. For example, a phenolic retainer for 104 size bearing, when properly impregnated and soaked in oil for 60 days, holds approximately 90 mg of oil in its body. This is because the retainer materials are made with phenolic resin reinforced with fine cotton fabric. During impregnation and soaking, the oil penetrates into the cotton layer and is later available for lubrication. Also, the bearing metal surface, after centrifuged to the operating speed (say 5000 rpm), hold approximately 15–20 mg of oil. Altogether, about 100 mg of oil per bearing is available initially. With this initial charge of lubrication, the bearings can perform up to 3–4 years normally, provided the retainer is running stable. However, with a retainerless bearings (full complement bearing), the retainer oil is absent and the bearing surface oil is about 20 mg (the absence of retainer facilitates addition of more balls). The current life requirement for momentum wheels and other high speed space systems are more than 20 years or even up to 30 years. According to Auer (Shapiro, et.al, 1995) “the ball bearing lubrication remains the principal life-limiting problem on momentum and reaction wheels”. This reveals the need for efficient supplementary lubrication systems to achieve the longer mission life. Moreover, it is not possible to service the spacecrafts once it is launched. Therefore, in-situ, remote lubrication systems are employed in attitude control wheels.

According to the nature of operation, the lubrication systems used in momentum/reaction wheels can be broadly classified as active lubrication systems and passive lubrication systems. The active lubrication systems, also known as positive lubrication systems, supplies a controlled amount of lubricant to the bearings when it is actuated by external commands. The positive commandable lubricators, remote in-situ systems, etc. are examples of active systems. The passive systems, also known as continuous systems, supplies lubricant continuously to the bearings and is driven by centrifugal force or by surface migration force. The centrifugal lubricators, the oozing flow lubricators, wick feed systems, porous lubricant reservoirs, etc. come under this classification.

5.1 Active lubrication systems

The active lubrication system supplies lubricant depending on the demand. Different types of active systems are currently in use and some of these systems are briefed here.

Positive Lubrication Systems: In this type of lubrication systems, a known quantity of lubricant is delivered to the bearings when the system is actuated by external commands. The command to actuate the lubricator is executed when a demand for lubricant is arise. The demand is indicated either by an increase in power consumption of the wheel or by increase in bearing temperature resultant of increased bearing friction torque. Different versions of positive lubrication systems are available with different actuators such as solenoid valves, stepper motors, etc.

The commandable oiler developed by Hughes Aircraft Company (Glassow, 1976), in which a solenoid operated piston moves inside a reservoir, one end of which acts as cylinder. A quantity of oil equal to the cylinder volume is discharged during every operation. The oil coming out of the cylinder is directed to the bearings through a 1.5 mm stainless steel tubing. The capacity of the reservoir is 6 g and the quantity delivered per stroke is 45 mg. This system had been used in the Intelsat IV satellites. The positive

lubrication system (PLUS) developed by Smith and Hooper (Smith and Hooper, 1990) is another kind of solenoid operated lubricator. In this system, the oil is stored in a metallic bellows and is pressurized by a compression spring. The high pressure oil is delivered to the bearings by actuating the solenoid valve connected to the reservoir. The amount of oil delivered is 0.2–5 mg for 125 ms opening of the valve. The amount of oil delivered depends on the reservoir pressure, oil temperature and plumbing resistance and the oil viscosity.

The positive-pressure feed system proposed by James (James, 1977) consisted of a spring loaded metallic bellows in which oil is stored under pressure, release valve, metering valve, metering bellows and lubricant feed line. When the release valve is operated, the oil flows out to the line through the metering bellows and the metering valve. The amount of oil delivered is controlled by the metering bellows. The lubricant feed line terminates near the bearing delivers oil to the bearing surface. In this case the lubricant is injected directly into the bearing balls, which transfer it to the contact surfaces. Fig. 8 shows the arrangement.

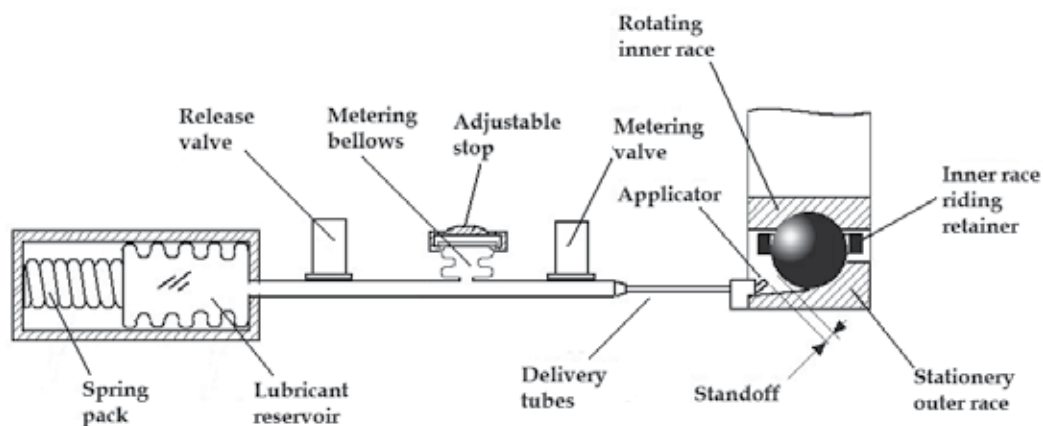


Fig. 8. Positive commandable lubricator for satellite bearing application (James, 1977)

The command lubrication system (CLS) (Sathyan, et.al., 2010) is another active lubrication system contains flexible metallic bellows, a micro stepping motor, frictionless ball screw, injection nozzle and capillary tubes. The stainless steel bellows act as the oil reservoir in which the oil is stored under ambient pressure. The pressure is usually the internal pressure of the momentum/reaction wheel or control moment gyro (CMG), if it is placed inside the system, and is usually varies between 15 torr and 350 torr. The bellows is of compression type having a swept volume of approximately 1.5 cc, i.e. the difference between the normal and fully compressed states. The micro stepping motor, which is the actuator, is a geared motor having a torque capacity of 130 mN-m and is driven through the drive electronics. The motor shaft is connected to the reservoir bellows through the precision ball screw (3 mm size). It is properly lubricated with space proven lubricant and protected from contaminants. One end of the screw is rigidly connected to the motor shaft. The housing/nut of the ball screw is attached to the bellows through the link, which houses the ball screw. The ball screw converts the rotary motion of the motor shaft into linear motion and thus actuates the bellow. On the delivery end of the bellows, a nozzle is attached which connects the capillary tubes with the bellows as shown in Fig. 9.

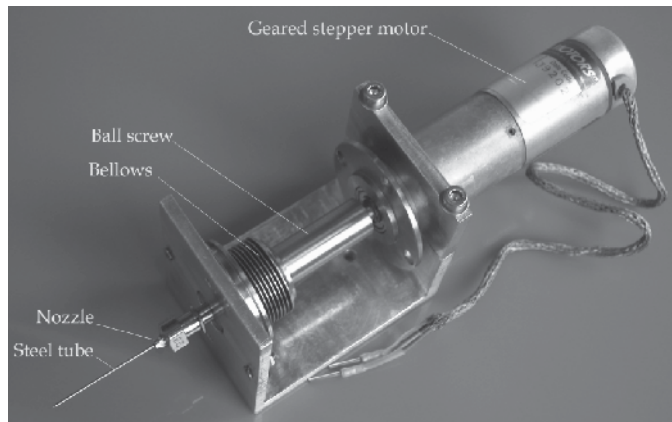


Fig. 9. Command lubrication system

The CLS is operated when a demand for lubricant arises. In spacecraft, the demand is indicated either by an increase in bearing temperature as a result of increased bearing friction torque or increased motor current to maintain the rotational speed. In such situation, the drive motor of the CLS is actuated for a predetermined period of time to deliver oil to the bearings. When the motor shaft rotates, the ball screw attached to it also rotates. The housing/nut of the ball screw which is rigidly mounted on the bellows moves linearly and presses the bellows. As a result, the pressure of oil in the bellows increases and it flows out through the capillary tubes. The delivery tip of the tube is placed adjacent of the rotating bearing. A set-off distance, i.e. the distance between the nozzle tip and the rotating element of the bearing, is provided to prevent the tip from touching the bearing. The set-off is equal to the diameter of the oil droplet. It was experimentally determined that the weight of a drop of oil (Kluber PDP-65 oil) is approximately 8 mg and the size is about 2.5 mm. therefore, the set-off distance in this case is 2 mm. At the delivery tip of the tube, oil forms droplets and when the size of the drop is sufficiently large, it touches the rotating element of the bearing and transfers to the contact surfaces. The nozzle tip can be suitably located near the bearing depending on the design of the bearing unit to ensure oil discharge to bearings.

The amount of oil delivered can be precisely controlled. Fig. 10 shows the amount of oil delivered by CLS when operated for duration of 5 s each. The bellows can hold approximately 2.5 g oil and the quantity delivered per cycle (5 s duration) as shown in figure is approximately 15 mg. Therefore, if two operations per year are planned, the CLS can lubricate the wheel bearings for more than 25 years. Also, in this system, since the oil is stored at ambient pressure, the chances of leaks are absent.

In-situ Lubrication Systems: In these systems, the lubricant is stored in a porous medium placed adjacent to the bearings. When the porous medium is heated up by some means, it ejects the oil stored in its pores due to differential thermal expansion. The in-situ on demand lubricator developed by Marchetti (Marchetti, et.al, 2001, 2001) consists of a porous material cartridge to which an electric heater is attached. The cartridge is impregnated with oil and is attached to the stationary race of the bearing. When the cartridge is heated, due to the higher thermal expansion of the oil compared to the porous material, oil flows out of the cartridge. The oil coming out of the cartridge is migrated to the bearing surfaces due to the low surface tension of oil compared to the bearing metal. It is actuated when the bearing temperature increases due to higher friction, demanding lubricant.

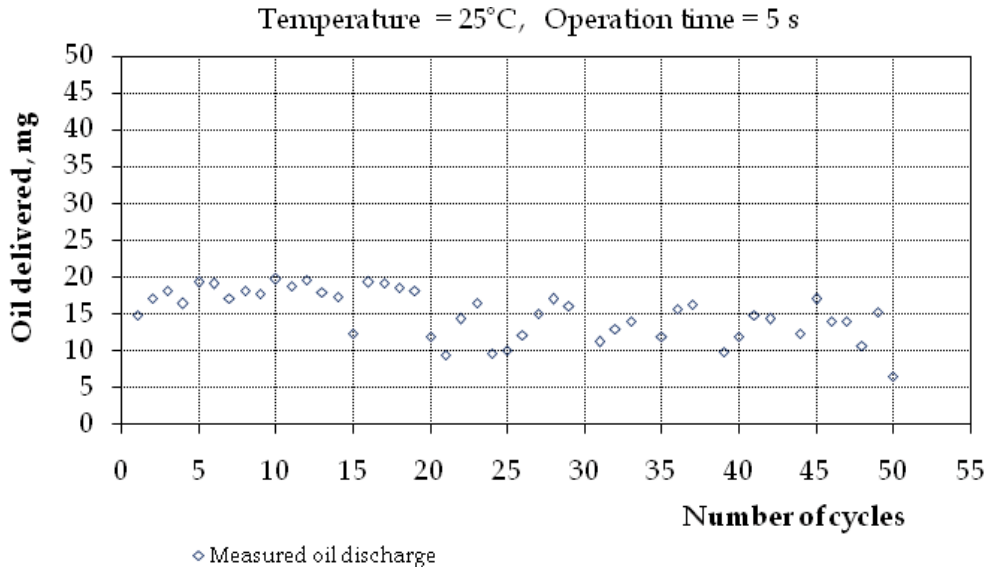


Fig. 10. Oil discharged by CLS for 50 cycles

Another type of in-situ lubrication system is the static lubricant reservoir (Sathyan, 2003), consists of a porous material reservoir of cylindrical shape mounted on an aluminum sleeve. An electric foil heater is pasted inside the aluminium sleeve. The porosity of the reservoir material is about 30% by volume so that it carries sufficient amount of lubricant to support for the entire mission period. The reservoir assembly is mounted on the static part of the bearing unit. When the heater is put on, it heats up the oil inside the reservoir and it flows out due to differential thermal expansion. The lubrication is effected by surface migration and vapor condensation. Fig. 11 illustrates the lubrication process.

The major drawback of this kind of system is the delayed lubrication process because of the delay in oil to get heated up and ejected out of the system. Moreover, the heater activation time should be progressively increased after each operation to eject the same quantity of oil.

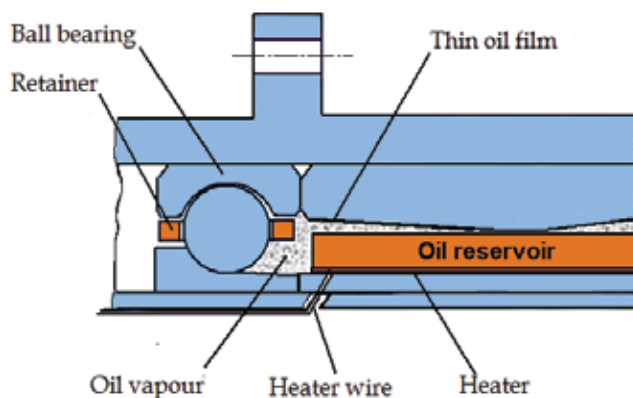


Fig. 11. Mechanism of oil transfer in static oil reservoir

5.2 Passive lubrication systems

The passive lubrication systems supplies lubricant continuously at a controlled rate irrespective of the requirement. These systems work on centrifugal force or by surface migration. Passive systems are simple in construction, but it is difficult to control the flow rate to the required amount. Different techniques are used to control the flow rate in this type of lubricators. There are a number of designs of passive lubrication systems used today by different manufacturers of attitude control wheels for spacecraft. Some of these systems are briefly discussed here.

Wick feed systems: In wick feed lubrication system (Loewenthal, et.al, 1985), a lightly spring loaded cotton wick, saturated with oil is continuously in contact with a conical sleeve adjacent to the bearings. The other end of the wick is in contact with oil in a reservoir and it absorbs and maintains its saturation level. The frictional contact causes small amount of oil to be deposited on to the contact surface. From this contact surface, oil migrates to the other end of the sleeve and then to the bearing. The oil leaving the bearing after lubrication return to the reservoir.

Rotating Lubricators: These are the most common type of lubricators currently in use and are actuated by centrifugal force due to the rotation of the lubricator. In these lubricators, the lubricant, either grease or oil, is filled in a cylindrical container and is assembled to the rotating part of the bearing unit. A lubricant bleed path is provided at the outer most layer of lubricant in the container. When the bearing unit is rotating, the lubricator attached to it also rotating at the same speed. The centrifugal force thus generated causing the lubricant to flow out through the bleed path. The oil oozing out of the lubricator is guided to the bearings mounted on either side of the lubricator. Different types of rotating lubricators are briefed under.

The ooze flow lubricator invented by Hashimoto (Hashimoto, 2001) is a novel concept. In this, the lubricator is fitted to the outer spacer of the bearing unit, the ends of which are formed as the bearing outer race. The reservoir to store the lubricant is formed by the two cylindrical components of the assembly. A set of precision turned helical grooves made at the interface of the inner and outer part of the lubricator. The helical grooves run in the axial direction and deliver lubricant to each of the bearings. The rate of flow is controlled by the dimensions of the helical groove and speed of rotation of the bearing shaft. The design life of the system is claimed as 15 years when operating at 12 000 rpm. The space cartridge bearing system presented by Kingsbury et al. (Kingsbury, et.al., 1999) and the oozing flow lubricator presented by Jones et al. (Jones, et.al., 1997) and Singer et al. (Singer, et.al., 1994) resemble the ones mentioned above. Fig. 12 shows the space bearing cartridge with oozing flow lubricator.

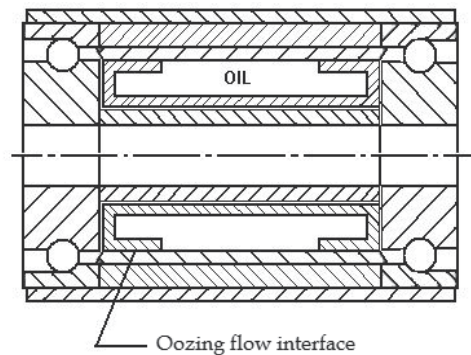


Fig. 12. Space cartridge bearing system with oozing flow lubricator (Kingsbury, et.al, 1999)

The centrifugal oil lubricator (Sathyan, et.al., 2008) contains a reservoir cup and an inner sleeve made of aluminum and machined with a high degree of accuracy. When the outer cup and inner sleeve are assembled, a cavity is formed where the lubricant is filled. The capacity of the reservoir is about 5 cc. The interfaces of the outer cup and inner sleeve are electron beam welded to make the reservoir leak proof. Two orifices of 150 μm diameter are made on the periphery of the outer cup in diametrically opposite locations. A filling hole is provided on one of the faces of the outer cup to fill oil as shown in Fig. 13 (a). The lubricator is designed to mount on the rotating outer spacer of the bearing unit, which separates the bearings. Lubrication of each bearing in the assembly is carried out by separate lubricators mounted adjacent to each bearing as shown in Fig. 13 (b).

When the bearing unit starts rotating, the centrifugal lubricator attached to the outer spacer of the bearing unit also rotates along with the bearings. The centrifugal force due to rotation of the reservoir generates pressure head in the stored oil, which is the maximum at the outer layer of oil near the orifices. The pressure thus developed forces the oil out through the orifices provided on the outer cup. The oil coming out of the orifice is directed to the bearing surface by suitably designed flow paths.

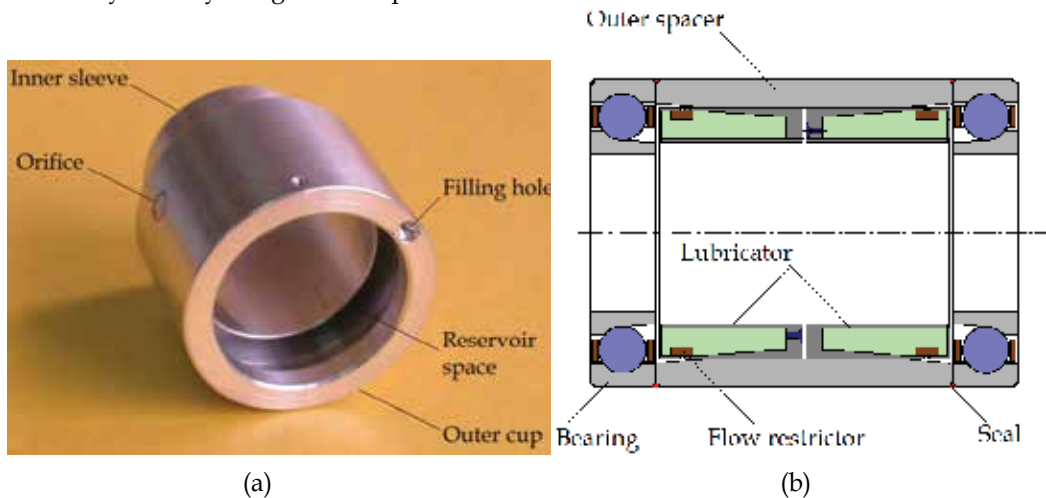


Fig. 13. Centrifugal oil lubricator components (a), schematic view of lubricator assembly (b)

It is estimated that the pressure developed at the orifice is nearly 12,000 Pa when the lubricator is running at 5000 rpm. Under this pressure, it is only a matter of hours to empty the reservoir through the 150 μm orifice. To avoid this and to control the flow rate to the lowest possible value, a flow restrictor is introduced at the orifices. Here, a piece of isotropic porous material is used to control the flow rate as shown in Fig. 13 (b). The flow area through the restrictor is further controlled to achieve the required flow rate. The material of the restrictor must be homogeneous and isotropic to ensure uniform flow rate. The particle size and porosity are the two important factors, which determine the permeability or fluid conductivity of the porous material. It is observed that sintered polyimide is an ideal material for this application. Polyimide spherical particles are available in a variety of sizes. Using graded particles sintered filter porosity can be very accurately controlled. Small pieces of branded sintered polyimide, MELDIN- 9000, is used as flow restrictor.

The rate of flow from the lubricator is given by the equation:

$$q = \frac{\alpha A \rho \omega^2}{2\mu L} (R^2 - r^2) \quad (4)$$

where, α is the permeability of the restrictor material in m^2 , A is the cross sectional area of flow through the restrictor in m^2 , ρ is the density of the lubricant in kg/m^3 , ω is the angular speed of the reservoir in rad/sec , μ is the dynamic viscosity of oil in $\text{N}\cdot\text{sec}/\text{m}^2$, L is the thickness of the restrictor in m , R is the radius of oil outer layer in m , r is the instantaneous radius of oil inner layer in m , and q is the flow rate in m^3/sec .

It is understood from Eq. 4 that the flow rate is directly proportional to the pressure of oil at the inlet to the porous restrictor. Pressure at the inlet of the restrictor is proportional to the speed of rotation and mass of liquid column above it. The pressure and thus the flow rate are the maximum when the reservoir is full and both become zero at the end of life, as shown in Fig. 14. The time to reach the zero flow rate depends on various operating parameters such as flow diameter, operating speed, temperature, and initial quantity of oil filled. Since the flow rate is proportional to the left out quantity of oil in the reservoir, the required flow rate can be obtained by filling the quantity corresponding to the flow rate as obtained from Eq. 4.

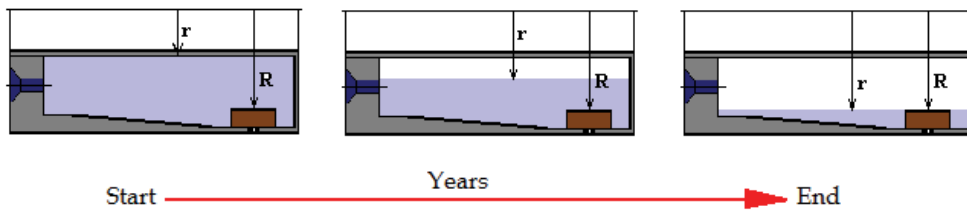


Fig. 14. Variation of oil quantity in the reservoir with time

The predicted performance of a lubricator having $150 \mu\text{m}$ flow diameter is shown in Fig. 15, obtained for operating speed and temperature 5400 rpm and 40°C respectively. It is seen that the initial flow rate is $0.037 \text{ mg}/\text{h}$ and the flow rate at the 20^{th} year is approximately $0.006 \text{ mg}/\text{h}$. The total oil expelled in 20 years is 3000 mg , which is only 60% of the total capacity of the reservoir, 5 cc .

Another version of centrifugal oil lubricator is shown in Fig. 16 (a). This design is meant to provide a delay in supplying the lubricant to the bearing during the initial stage of operation. The capacity of the reservoir is 4 cc and the initial flow rate is about $0.02 \text{ mg}/\text{h}$. It is understood from Section. 5 that the bearings are assembled with an initial charge of approximately 100 mg and with this initial oil, it can perform upto 3 years. If lubricant is supplied during this period, it may cause increased viscous drag and resultant higher power consumption of the wheel. To avoid this and maintain the frictional loss to minimum, a delay mechanism is introduced to the centrifugal lubricator. This is achieved by mounting a dry porous material sleeve in between the lubricator outlet and the bearings as shown in Fig. 16 (b). The sleeve absorbs the oil coming out of the lubricator and get saturated. Once saturated, it start giving oil to the bearings. The porosity of the sleeve material is 28% of volume and it can hold nearly 300 mg oil. Assuming a flow rate of $0.02 \text{ mg}/\text{h}$ from the lubricator, it would take about 21 months to saturate the porous sleeve with oil. The oil from the lubricator start reach the bearings only after this period and thus prevents the bearings from running with excess bearing friction due to high viscos drag.

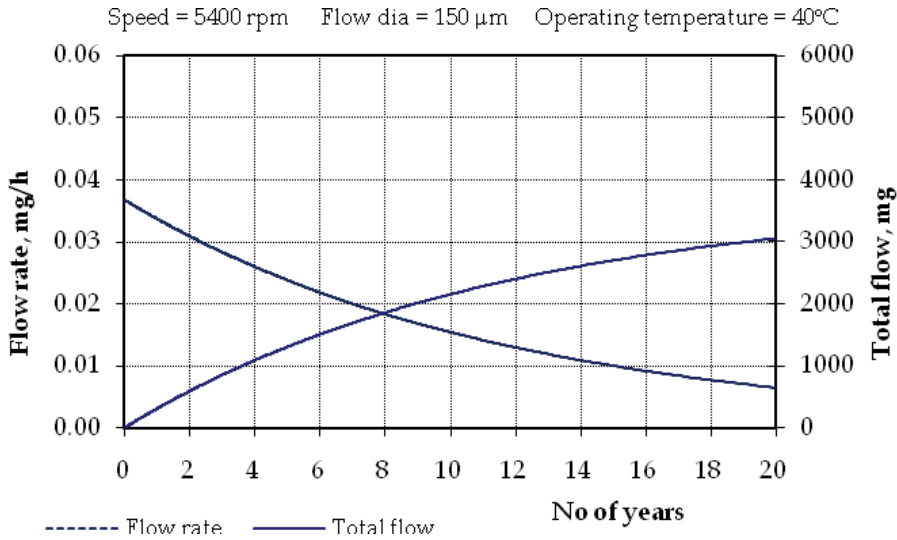


Fig. 15. Predicted performance of a lubricator with 150 μ m flow diameter at 40°C

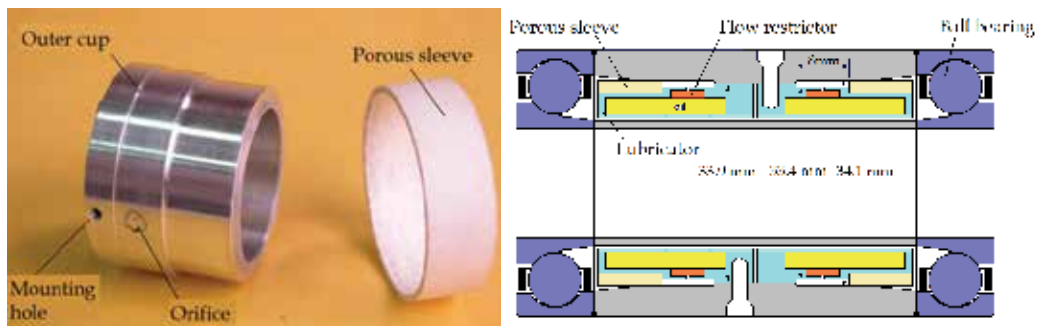


Fig. 16. Centrifugal lubricator with nylasint sleeve (a), schematic of lubricator assembly (b)

6. Conclusion

In this chapter, a brief overview of the tribological problems of the attitude control wheels is presented. The information related to momentum/reaction wheels, bearing units, lubrication requirements and various lubricants is provided. Various lubrication systems used in the past and present attitude control wheels are concisely described. A few lubrication systems developed by the authors for the future attitude control wheels requiring very long mission life are also elucidated.

7. References

- Auer, W. (1990). Test Results and Flight Experience of Ball Bearing Momentum and Reaction Wheels. Proc. the 24th Aerospace Mechanisms Symposium. 1990, pp 273-287.
- Bedingfield, K. L.; Leach, R. D.; Alexander, M. B. (1996). Spacecraft System Failures and Anomalies Attributed to the Natural Space Environment. *NASA reference publication* 1390, August 1996. Marshall Space Flight Center, MSFC, Alabama .

- Bertrand, P. A. (1993). Oil adsorption into cotton-phenolic material. *Journal of Materials Research*, 1993;8(7):1749–57, IISN: 0884-2914.
- Boesiger, E. A., Warner, M. H. Spin bearing retainer design optimization. In: *Proceedings of the 25th aerospace mechanisms symposium*, NASA conference publication, vol.3113,1991.p.161–78.
- Boesiger, E. A., Donley, A. D., Loewenthal, S. (1992). An analytical and experimental investigation of ball bearing retainer instabilities. *ASME Transactions, Journal of Tribology*, vol.14, no.3, July 1992, p. 530-539, IISN: 0742-4787.
- Briscoe, M. H.; Aglietti, G. S. (2003) Spacecraft mechanisms, In: *Spacecraft System Engineering*, Fortescue, P.; Stark, J.; Swinerd, G. 501-529, John Wiley & Sons, ISBN: 0 471 61951 5, England
- Burt, R. R.; Loffi, R. W. (2003). Failure Analysis of International Space Station Control Moment Gyro. *Proceedings, 10th European Space Mechanisms and Tribology Symposium*, pp-13 – 25, ISBN: 92-9092-834-4, Spain, September 2003, ESA Publication.
- Coy, J. J.; Rama, S. R.; Dennis, P. T. (1979). Comparison of predicted and measured elastohydrodynamic film thickness in a 20 millimeter-bore ball bearing. *NASA Technical Paper 1542*; October 1979.
- Dowson, D. (1995). Elastohydrodynamic and micro-elastohydrodynamic lubrication. *Wear* 1995; 190: 125–38.
- Dube, M. J.; Bollea, D.; Jones Jr, W.R.; Marchetti, M.; Jansen, M. J. (2003). A new synthetic hydrocarbon liquid lubricant for space application. *Tribology Letters*, 2003; 5(1).
- Fote, A. A., Slade, R. A., Feuerstein, S. (1978). The prevention of lubricant migration in spacecraft. *Wear* 1978; 51:67–75, ISSN: 0043-1648.
- Fowzy, M. A. (1998). PFPE, A unique lubricant for a unique application. Castrol Specialty Products Division, 19980624 044, ADA347666, 01 Jan 1998, Illinois.
- Fusaro, R. L. (1992). Lubrication of Space Systems—Challenges and potential solutions. *NASA technical memorandum-105560*; 1992.
- Fusaro, R. L. (2001). Preventing spacecraft failures due to tribological problems. In: *NASA technical memorandum -210806*; April 2001.
- Glassow, F. A. (1976). Assurance of lubricant supply in wet-lubricated space bearings. In: *Proceedings of the 10th aerospace mechanisms symposium*. NASA technical memorandum, vol. 33-777; April 1976. p. 90–106.
- Guangteng, G.; Cann, P. M.; Spikes, H. A. (1992). A study of parched lubrication. *Wear*, 1992, 153:91–105. ISSN: 0043-1648.
- Gupta, P. K. (1991). Cage unbalance and wear in ball bearings. *Wear* 1991; 147: 93–104. ISSN: 0043-1648.
- Gupta, P. K. (1988). Frictional instabilities in ball bearings. *TribologyTrans* 1988; 31(2): 258–68. ISSN: 0569-8197.
- Hamrock, B. J.; Schmid, S. R.; Jacobson, B. O. (2004). *Fundamentals of Fluid Film Lubrication*. Marcel Dekker, Inc., ISBN: 0-8247-5371-2, New York.
- Hamrock, B. T.; Dowson, D. (1981). *Ball bearing lubrication: the lubrication of elliptical contacts*. Wiley, ISBN: 13-9780471035534, New York.
- Hashimoto, F. (2001). Ooze flow bearing. *United State Patent*, patent no.:6290397; September 18, 2001.

- Honeywell. (2003). Product Specification Document. Model HR 0610, Defence and Space Electronics Systems, Honeywell International Inc. N61-0098-000-000, DFOISR: 03-S-1924, December 2003. www.honeywell.com.
- James, G. E. (1977). Positive commandable oiler for satellite bearing lubrication. In: *Proceedings of the 11th aerospace mechanisms symposium*. NASA CP-2038; 1977. p. 87-95.
- Jansen, M. J.; Jones Jr, W. R.; Predmore, R. E.; Loewenthal, S. L. (2001). Relative lifetimes of several space liquid lubricants using a vacuum spiral orbit tribometer (SOT). In: *NASA-TM-2001-210966*; June 2001.
- Jones, Jr, W. R.; Jansen, M. J. (2005), Lubrication for space application, in *NASA Contractor Report-2005-213424*.
- Jones, Jr, W. R.; Jansen, M. J.; Gschwender, L. J.; Snyder, C. E.; Sharma, S. K.; Predmore, R. E. (2001). The tribological properties of several silahydrocarbons for use in space mechanisms. *J Synthetic Lubrication*, 2004; 20(4).
- Jones, Jr, W. R.; Jansen, M. J. (2000). Space tribology. In: NASA technical memorandum 2000-106392; March 2000.
- Jones, Jr, W. R., Shogrin, B. A., Kingsbury, E. P. (1997). Long-term performance of a retainerless bearing cartridge with an oozing flow lubricator for space application. In: *Proceedings of the international rolling element bearing symposium*, April 1997.
- Jones, W. R. (1993). The properties of perfluoropolyethers used for space applications. In: *NASA technical memorandum 106275*; July 1993.
- Kannel, J. W., Snediker, D. (1977). Hidden Cause of Bearing Failure. *Machine Design*, April 1977, pp. 78-82.
- Kannel, J. W., Bupara, S. S. (1977). A simplified model of cage motion in angular contact ball bearings operating in the EHD region. *J Lubr Technol*, ASME Trans 1977:395-403.
- Kannel, J. W.; Dufrane, K. F. (1986). Rolling Bearings in Space. In: *Proceedings of the 20th aerospace mechanisms symposium*. NASA conference publication 2423 (revised); May 1986. p. 121-32.
- Kingsbury, E. P.; Hanson, R. A.; Jones, W. R.; Mohr, T. W. (1999). Cartridge bearing system for space applications. Proc. 33rd Aerospace Mechanisms Symposium, *NASA Conf. Publ.* 1999, 209259, 137-143.
- Kingsbury, E. P. (1985). Parched elastohydrodynamic lubrication. *ASME Journal of Tribology* 1985;107:229, IISN: 0742-4787.
- Kingsbury, E. (1992). Influences on polymer formation rate in instrument ball bearings. *Tribology Trans* 1992; 35:184-8. ISSN: 0569-8197.
- Kingsbury, E. (1973). Cross flow in a starved EHD contact. *ASLE Transactions* 1973, 16, p-276-280.
- Loewenthal, S.; Boesinger, E.; Donley, A. (1991). International rolling element symposium 91. Sponsored by C.S. Draper Lab and DOD, Instrument Bearing Working Group; April 8-11, 1991.
- Loewenthal, S. H.; Scibbe, H. W.; Parker, R. J.; Zaretsky, E. V. (1985). Operating characteristics of a 0.87 kWh flywheel energy storage module. In: *NASA technical memorandum 87038*; August 1985.
- Ma, J.; Mo, Y.; Bai, M. (2009). Effect of Ag nano particles additive on the tribological behaviour of multialkylated cyclopentanes (MACs). *Wear*, 266 (2009), 627-631.

- Marchetti, M.; Jones, Jr, W. R.; Pepper, S. V.; Jansen, M. J.; Predmore, R. E. (2002). In-situ, on-demand lubrication system for space mechanisms. In: *NASA technical memorandum* 2002-211706; July 2002.
- Marchetti, M.; Meurisse, M. H.; Vergne, P.; Sicreb, J.; Durand, M. (2001). Analysis of oil supply phenomena by sintered porous reservoirs. *Tribology Letters*, 2001; 10(3).
- Mia, S.; Komiya, H.; Hayashi, S.; Morita, S.; Ohno, N.; Obara, S. (2007). Viscosity loss in PFPE lubricant for space applications under EHL conditions. *Tribology Online*, 2007; 2(2), 54–8.
- Robertson, B.; Stoneking, E. (2003). Satellite GN&C Anomaly Trends. *Proceedings, 26th annual AAS Guidance and Control Conference*, AAS 03-071. February 2003, Colorado, AAS publications, California.
- Roberts, E. W.; Todd, M. J. (1990). Space and vacuum tribology. *Wear*; 1990,136, 157–67.
- Sathyan, K. (2010). Development of a centrifugal lubricator for long-term lubrication of momentum wheels used in spacecrafts. PhD thesis, University of South Australia; March 2010.
- Sathyan, K. (2003). Long-term lubrication systems for momentum wheels used in spacecrafts. MS thesis, Indian Institute of Technology Madras; September 2003.
- Sathyan, K.; Gopinath, K.; Hsu, H. Y.; Lee S. H. (2008). Development of a Lubrication System for Momentum Wheels Used in Spacecrafts. *Tribology Letters* , 32, 2008, 99–107, IISN:1023-8883.
- Sathyan, K.; Hsu, H. Y.; Lee, S. H.; Gopinath, K. (2010). Long-term lubrication of momentum wheels used in spacecrafts—An overview. *Tribology International*, 43, pp. 259–267. ISSN: 0301-679X.
- Sathyan, K.; Gopinath, K.; Hsu, H. Y.; Lee S. H. (2010). Development of a positive lubrication system for space application. *Tribology Online*, 5, 1, 2010, 40–45. ISSN: 1881-2198.
- Shapiro, W.; Murray, F.; Howarth, R. (1995). Space mechanisms lessons learned study, Volume II—literature review. In: *NASA technical memorandum* 107047; September 1995.
- Shogrin, B. A.; Jones, W. R.Jr.; Kingsbury, E. P.; Prah J. M. (1999). Experimental Determination of Load Carrying Capacity of Point Contact at Zero Entrainment Velocity. *NASA/TM – 1999-208848*, January 1999.
- Singer, H. B., Gelotte, E. (1994). Design of a high-speed reliable ball bearing. In: *Proceedings of the 28th aerospace mechanisms symposium*. NASA conference publication, vol. 3260, May 1994. p. 279–83.
- Smith, D. W.; Hooper, F. L. (1990). Positive lubrication system. In: *Proceedings of the 24th aerospace mechanisms symposium*. NASA conference publication, vol. 3062, 1990. p. 243–58.
- Stevens, K. T. (1980). Experimental observations on torque variations caused by ball bearing cage instabilities. In: *Proceedings of Second Space Tribology Workshop*. 15-17 October 1980, ESTL Risley, UK.
- Sugimura, J.; Jones, Jr, W. R.; Spikes, H. A. (1998). EHD film thickness in non-steady state contacts. *Trans ASME J Tribology* 1998, 120:442. IISN: 0742-4787.
- Taniwaki, S.; Kudo, M.; Sato, M.; Ohkami, Y. (2007). Analysis of retainer induced disturbances of reaction wheel. *Journal of System Design and Dynamics*, vol. 1, no.2, 2007, 307-317.

Vernier, C. G.; Casserly, E. W. (1991). Multiply-alkylated cyclopentanes (MACs): a new class of synthesized hydrocarbon fluids. *Lubrication Engineering* 1991; 47(7), 586-91.

Zaretsky, E. V. (1990). Liquid lubrication in space. In: *NASA reference publication-1240*; July 1990.

Development of Optoelectronic Sensors and Transceivers for Spacecraft Applications

José M. Sánchez-Pena, Carlos Marcos, Alberto Carrasco,
Ricardo Vergaz and Ramón Zaera
*Carlos III University of Madrid
Spain*

1. Introduction

The main goal of this chapter is to show several optoelectronic systems to be applied in two different interest areas of spacecraft technologies: mechanical testing and optical communications. In the first part of this chapter, we present a simple, cost-effective and robust microcontrolled optoelectronic system that is able to measure with a reasonable accuracy a wide range of projectile velocities for impact testing of aeronautic and aerospace structures. In the second part of this chapter, we review different approaches to optimize the performance of free-space optical communications (FSOC) systems such as architecture of transceivers, pointing and tracking subsystems, wavelength tunability, diffraction limit, photodetectors' performance, among others.

A great effort was made in the last decades to design advanced shielding to protect aircraft and spacecraft structures and to evaluate the damage on structures impacted by projectiles and meteoroids. Although numerical simulation has been increasingly adopted to analyze these problems, experimental testing is still a need to validate numerical codes and to obtain reliable information. The importance of taking measurements during an impact event is evident from the vast amount of work performed in this area. Among the variables that should be measured during the impact test, an accurate determination of the velocity of the projectile is obviously of great importance, since its square is related to the kinetic energy applied to the specimen. Many different measurement techniques have been used; however, the purpose of the next section is not an exhaustive review of the literature but to provide an overview of some typical measurement methods.

Optical communication is a major issue in both guided and unguided modes of transmission. In optical fiber systems, losses can approach less than 0.15 dB/km and multi-Gbps data streams can be transmitted over tens of thousands of kilometers without electronic regeneration. In free-space systems, optical communication again has advantages. Smaller diameter transmitter and receiver apertures are needed to establish high data-rate communication links and, unlike the congested microwave bands, there is plenty of available spectrum. In addition, the narrow beam divergence of an optical system can be used to provide additional security by lowering the probability of detecting and intercepting the transmission.

The advent of technologies such as the erbium-doped fiber amplifier (EDFA) which made the implementation of nearquantum limited receiver performance achievable and the

development of high-speed modulators and detectors provided the components necessary to carry out affordable and robust free-space optical communications (FSOC) for broadband applications (Chang, 2000). Further investments in optical beam steering technology extended the capabilities and possibilities of integrating FSOC on mobile platforms such as ground vehicles, airplanes, and satellites. Because of the complexity associated with phase or frequency modulation, current FSOC systems typically use intensity modulation with direct detection (IM/DD). Atmospheric turbulence can degrade the performance of free-space optical links, particularly over distances longer than 1 km. Due to inhomogeneities in the temperature and pressure of the atmosphere, variations of the refractive index along the transmission path can be produced. This effect can deteriorate the quality of the received image and can cause fluctuations in both the intensity and the phase of the received signal. These fluctuations can lead to an increase in the link error probability, limiting the performance of communication systems.

Additionally, platform vibrations and misalignment of the transmitter and receiver telescopes can cause similar time-varying fades of received power. These fluctuations can be mitigated using different techniques (Henniger et al., 2003). Other optical correction techniques such as adaptive optics or spatial diversity can be employed to achieve a similar compensating effect (Andrews & Phillips, 2005).

2. Optoelectronic sensors: Velocity measurement methods and proposed system

2.1 Current measurement methods

A great variety of sensors were used to estimate the velocity of projectiles. The most common measurement system is the chronograph (Paulter & Larson, 2009). In this kind of systems, the velocity of the projectile is calculated by dividing the base length, or the distance between two sensor locations, by the difference of the times when the projectile arrives at these locations. The type of sensor used to detect the passage of the solid makes the difference between chronographs.

However, other kinds of systems were also used in the last decades. The simplest ones are the break-paper and the break-wire sensors. The first system leads commonly to a small number of faults, especially when the projectile is non-metallic. In the second one, more reliable than the first one, a thin wire is cut by the projectile. The main drawback of both systems is related to impacts at subsonic velocities: the pressure wave preceding the projectile causes stretching before breaking of the wire or bulging before tearing of the sheets. The base length then varies and this lead to an unknown error.

Additionally, inductive sensors, radar Doppler and photographic systems have been also used to determine the velocity of a projectile, but all of them show some important limitations in terms of reliability, robustness, velocity range, performance-cost ratio, among others (Zukas et al, 1992). Inductive sensors are based on a circular open-coil sensor that is located surrounding the path of the projectile. When the projectile approaches, eddy currents are induced and the voltage output increases reaching a peak and then decreasing as the bullet leaves the coil. The system has to be calibrated and the gain setting has to be adjusted for each projectile material, size and shape by manually positioning it in the coil before the test. On the other hand, this type of sensor could not detect these projectiles made of non-conductive material, which would be an important drawback compared to other sensors.

Doppler radar, also called continuous-wave radar, is another measurement system used for measuring the projectile speeds. Its working principle is based on an antenna that is aligned

to the projectile path and sends a continuous radio signal. The projectile reflects the pulses with a frequency shifted due to the Doppler effect, allowing it to produce a target frequency after being mixed with a sample of the transmit frequency. Doppler radar method and apparatus for measuring a projectile's muzzle velocity offers important benefits: good accuracy, simple set up, minimal risk of damage of equipment by stray bullets. An additional advantage is the possibility to measure, in some cases, the residual velocity of the projectile after perforating the target. Nevertheless, the cost of a conventional system is quite expensive as compared to chronographs.

Photographic systems have also been used to determine the velocity of a projectile (Wilde et al, 1973). Since the event takes place quickly and time exposures should be extremely short (on the order of the microsecond or even shorter), ultra high speed cameras have to be used. In these, the high speed film usually remains stationary inside of a drum and sweeps the image across it by reflection from a rotating mirror or prism (Moss et al, 1995). Facing the film-based cameras, digital ultra high speed cameras passed through a striking development in the last decade. The appearing of highly light-sensitive mega-pixel CMOS sensors allowed acquiring images with an exposure time short enough to freeze the movement of the projectile. The easy-to operate approach of these cameras and the possibility to record long time periods facilitates the synchronization and triggering operations. Anyway, the high cost of analogical or digital cameras -and sometimes that of the lighting systems needed to illumine the projectile- means currently a great drawback.

On the other hand, optical sensor applications are growing in mechanical testing. Continuous efforts for improving robustness in every step of optical sensor development recently resulted in using optical sensors in safety critical spacecraft applications.

2.2 Proposed system: configuration and working principle

This section presents a microcontrolled opto-electronic system to measure on-line the average velocity of a projectile impacting on aircraft and spacecraft structures. The projectile velocity can vary in the range from subsonic to supersonic.

The measurement optical system provides the projectile velocity by measuring the time of flight taken by the projectile passing through the three equidistant optical barriers, which are placed in a well-know position (Fig. 1). Each barrier consists of a laser beam source and a light detector. The three laser beams are parallel and placed on the same level forming a plane. The projectile velocity can only be measured when traveling through this flight plane, therefore blocking in sequence each of the three laser beams. Obviously the railgun must be positioned perpendicular to the laser barriers.

The projectile velocity is measured through the acquisition of three different electrical signals coming from the light sensors due to the interruption of the laser beams by the projectile during its flight. As the projectile passes through the optical barrier it blocks the beam from reaching the optical sensor, therefore the sensor responds with an electrical pulse. The three electrical signals are processed by a microcontroller in order to evaluate the average velocity of the projectile. The system operation is quite simple, the photodiodes sense when laser beams are blocked in sequence, so the projectile trajectory is supposed to be perpendicularly incident to the laser barriers.

When the projectile passes through the first optical barrier, the laser beam is crossed and the optical sensor circuit gives an electrical signal which is used to trigger the microcontroller time counter. As the second and third laser beams are crossed by the projectile the flight

times are also registered. Therefore, three flight times between laser barriers are stored in the memory of the microcontroller with the aim of using them in the projectile average speed calculation (Fig. 2).

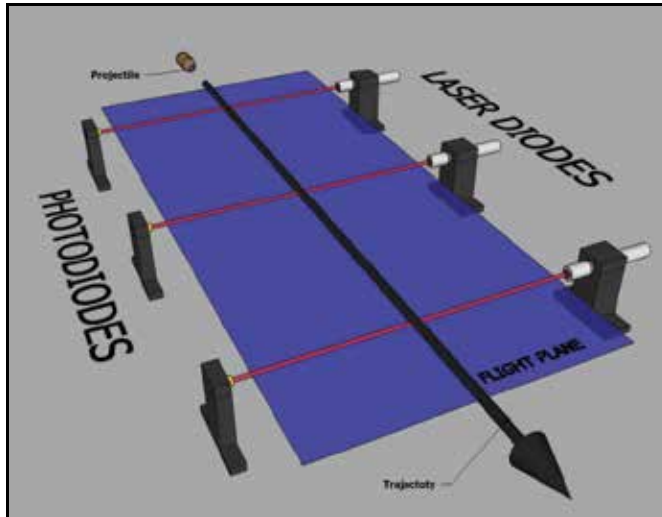


Fig. 1. Optical configuration of velocity-measuring system.

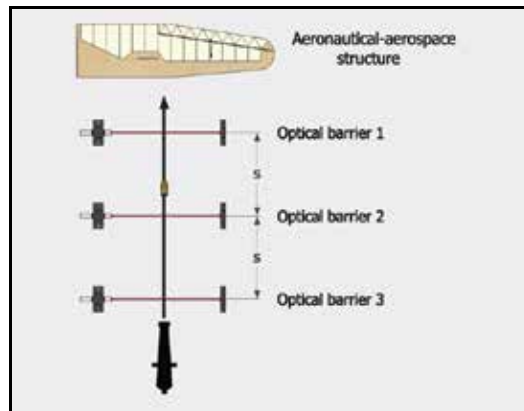


Fig. 2. System schematic showing the optical barriers, the projectile and the test structure.

The average velocity v of a projectile based on its time of flight between the optical barriers is given by the following equation:

$$v = \frac{1}{3} \left(\frac{S}{T_1} + \frac{S}{T_2} + \frac{2S}{T_3} \right) \quad (1)$$

where S is the distance between laser barriers that are equidistant, T_1 is the flight time for the projectile between the first and second optical barriers, T_2 is between the second and third barriers, and finally, T_3 is the flight time between first and third barriers. Theoretically, T_3 must be the sum of T_1 plus T_2 , but it could be different because the system is counting

microcontroller clock periods. Therefore, projectile velocity is calculated as an average, using three distances between barriers and three flight times. This simple system operation is a robust technique to avoid potential failures of either the laser sources or the photodetectors.

It is important to consider that during the flight the projectile velocity is not constant; it suffers a deceleration due to aerodynamic drag. It could be mathematically estimated by the following expression

$$m_p \frac{dv}{dt} = -\frac{1}{2} A_p C_D(v) \rho_a v^2 \quad (2)$$

where v is the velocity of the projectile, m_p is its mass, A_p is its cross-sectional area, C_D is the drag coefficient, and ρ_a is the density of the air. This equation can be modified to represent the velocity variation with the distance, after a straightforward calculation the equation leads to

$$\frac{dv}{\beta(v)v} = -dx \quad (3)$$

where β is a function of the velocity. Typical values of β vary from $5 \cdot 10^{-4}$ to $5 \cdot 10^{-2}$ in ballistic applications, considering low-density (polymers) or high-density (tungsten, uranium) projectiles; different shapes (blunt, spherical, conical, or ogival noses), cross-sectional areas; and velocities at subsonic, transonic, or fully supersonic ranges. Assuming a small variation of velocity when the projectile passes through the system, that must be confirmed afterward, we can consider C_D and β as constant. The variation of velocity Δv relative to the initial velocity v_0 as a function of the distance traveled by the projectile x could then be determined by direct integration of Eq. (3):

$$\frac{\Delta v}{v_0} = \exp(-\beta x) - 1 \quad (4)$$

Fig. 3 shows the velocity variation between the three laser barriers of the system, it has been plotted using the Eq. (4). As can be observed the variation is less than 1% in the worst situation: projectile of small density, small radius, and high aerodynamic drag.

The designed system comprises different functional blocks: electro-optical part, a sensor-signal-processing unit, a timing count block, a central processing unit and a monitoring unit with a LCD and a serial port (Fig. 4).

The three laser barriers are part of the electro-optical block; they include three red laser diodes, with low output power, pointing to high-speed silicon photodiodes. This block also includes additional hardware to verify and to notify to the central processing unit of the optical barriers status; in case of malfunction the microcontroller is able to run all the necessary actions keeping the system operative.

As can be shown in Fig. 5, the circuit integrating the sensor processing unit generates the trigger signal necessary to activate the timing count block. This unit also includes specific circuits which allow the system operation under different environmental lighting. The system evaluates the environmental lighting and sets the appropriate comparator voltage level in the sensor circuit and compares it to photodiode sensor voltage; as a result, when a projectile passes through the optical barrier and blocks the laser beam the comparator level

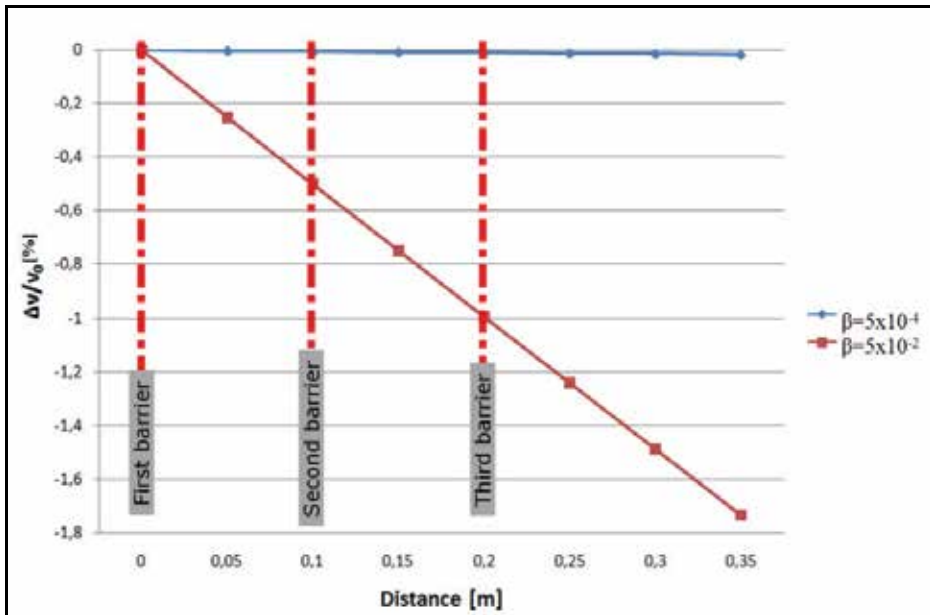


Fig. 3. Variation of velocity Δv relative to the initial velocity v_0 as a function of the distance traveled by the projectile x .

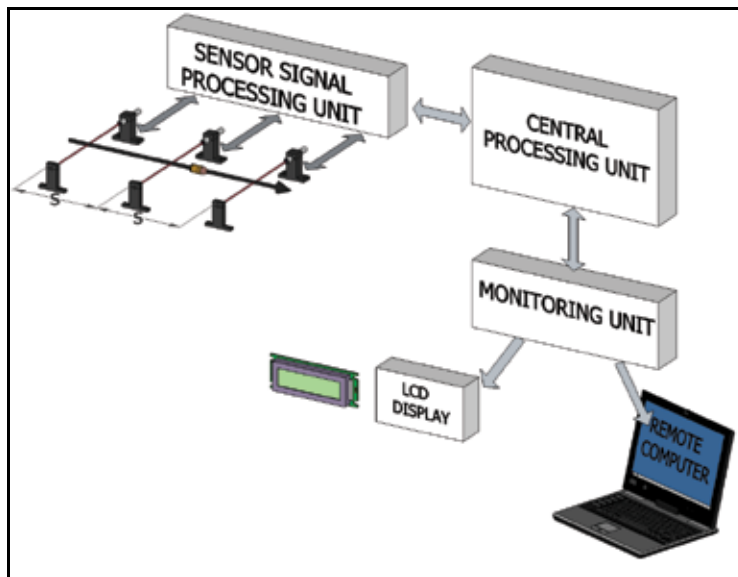


Fig. 4. Block diagram of the whole system.

changes. A customized circuit was implemented to measure the voltage level in the photodiode sensors with the lasers on and off. This circuit is based on a pulse width modulation (PWM) generator and a low-pass filter which provides a continuous voltage level that depends on the PWM duty cycle. The PWM signal is a powerful technique that is employed in a wide variety of applications, ranging from measurement and

communications, to power control and conversion. To measure the environmental lighting level it is necessary to switch the lasers off, then the continuous voltage level at the output filter is compared to the photodiode circuit voltage, registering the PWM duty cycle that changes the comparator status. The same process is followed when the lasers switch to on state, registering the new duty cycle value. Finally, the mean value of the registered duty cycles, a new PWM is generated. Therefore, this is the methodology to ensure that the sensor-signal-processing unit generates the appropriate trigger signal when the laser beam is blocked. In the case of laser or photodiode malfunction, the PWM registered values will be the same and the fault is notified to the central processing unit.

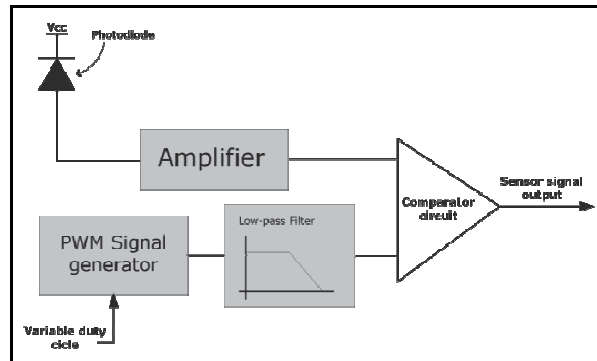


Fig. 5. Sensor-signal-processing unit.

The monitoring unit reports all the information related to the configuration process (status, failures, and parameters) and the measured average projectile velocity. All this information is not only sent to the LCD display, but also it is sent via serial bus and collected by software installed in remote computer; remote information improves the safety in the laboratory tests.

The core of the system is the central processing unit (CPU); it was implemented with the AT89C2051 Atmel microcontroller based on Intel-8051 architecture family of 8 bit microcontrollers, which provides a highly flexible and cost effective solution to many embedded control applications due to the use of the MCS-51 industry standard instruction set, and low unit cost.

With the purpose of controlling the whole velocity measure system; the CPU follows the simplified flowchart shown in Fig. 6. It must supervise the rest of the system units and properly manage trigger signals from the sensor unit. Once the system is configured, the control and processing unit waits for a trigger signal coming from the sensor-signal-processing. This trigger signal is generated once a projectile passes through the first of the three optical barriers. Once the second and third laser beams are blocked the timing count unit registers the times of flight between barriers, at this point the CPU is able to compute the average projectile velocity, sending the measurement to the LCD and the software in the remote computer.

Unlike other sophisticated systems that use light grids (Crittenden Jr., 1973) to build the target area points, beam expanders to form a light window (Hartwig, 1986) or optical doppler-radar method (Alon, 1989), the implemented system presents significant advantages such as low cost due to the reduced number of electrical and optical elements used, a high robustness against potential failures of the optical sources or detectors, simple operation, and a reasonable accuracy in the velocity measurement (Pena et al, 2007).

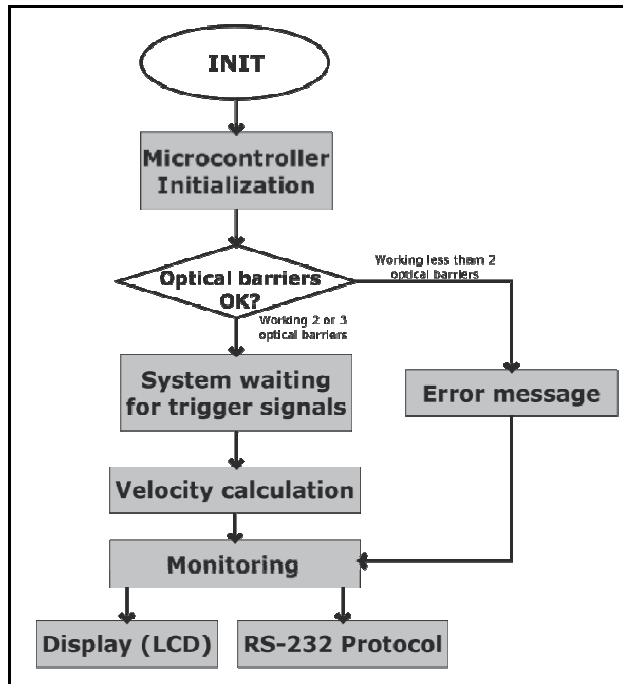


Fig. 6. Flowchart of the system performance.

2.3 Results and discussion

The performance of the velocity measurement system depends on its accuracy measuring the time of flight and the distance between barriers. Accuracy in this kind of metrology systems is a very important feature, because the kinetic energy applied to the aeronautical/aerospace structure is proportional to the square of the impact projectile velocity. To avoid potential damage of such structural elements in real working operation and to obtain the precise conclusions in high-velocity impact tests, the velocity parameter should be precisely evaluated.

The velocity of the projectile is calculated as the mean value of the ratios of the distance between the optical barriers and the registered times of flight, therefore the uncertainty in the velocity measurement depends on these two parameters. In the proposed system and in the worst situation, when only two optical barriers are working, the relative error of the projectile velocity measurement was deduced as

$$\left| \frac{\Delta v}{v} \right| \leq \frac{|\Delta S| + v|\Delta T|}{S} \quad (5)$$

where the parameters are the same as used in Eq. (1). Here Δv , ΔS , and ΔT are values of maximum error in projectile average velocity v , distance S between the two optical barriers, and the time of flight T between the barriers, respectively.

The total measurement distance error is estimated as a contribution of different physical and mechanical aspects of the optical barriers set up. Some these aspects are the following: the optical barriers distance measurement error (ΔS_1); the error because the projectile trajectory

is not normal to the laser beams (ΔS_2); the laser beams parallelism error (ΔS_3); the laser beams thickness error (ΔS_4). The maximum combined error can be calculated as $(\Delta S_1^2 + \Delta S_2^2 + \Delta S_3^2 + \Delta S_4^2)^{1/2}$, the obtained value is $\Delta S \leq 0.1$ cm.

The time measurement error is limited by the microcontroller time required to acquire the trigger signals from the optical barriers circuit; maximum microcontroller time response time is six times the microcontroller clock cycle, therefore $\Delta T \leq 32.5 \cdot 10^{-8}$ s.

Several parameters may limit the measurement accuracy in optical metrology systems (Hartwig, 1986; Schroder et al., 1999). Some of them can be avoided or minimized using more complex processing circuits for the signals coming from the optical sensors or using appropriate algorithms in experimental data processing. Fig. 7 presents accuracy as function of the projectile velocity when the system is working in the worst case, i.e., only two optical barriers are operative.

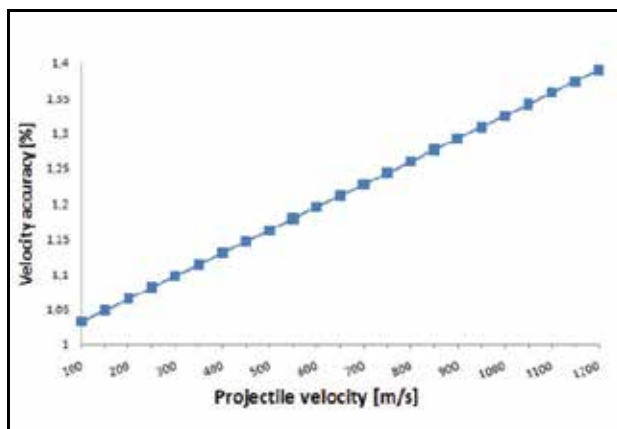


Fig. 7. Theoretical velocity accuracy of the system working in the worst case with only two optical barriers.

To evaluate the proposed system and to check the accuracy, a customized test circuit was implemented. The test circuit is necessary because simulating the high speed movement of an object is difficult to perform by mechanical methods. The implemented test circuit is based on a microcontroller circuit that can control the laser switching, making it possible to simulate a projectile crossing and blocking the laser barriers. To do that, a dwell time is programmed to generate the switching off sequence of the three lasers. Twelve different velocities were simulated from 100 to 1200 m/s, and 20 measurements for each velocity were acquired. The accuracy and the error experimentally obtained are shown in Fig. 8. Using this circuit it is possible to simulate a wide range of projectile velocities without doing expensive real tests (shoots). As we can see in Fig. 8, the measured error for the highest velocities has a slight negative deviation. Therefore, the experimental value for the projectile velocity is a bit lower than the expected value.

This biased deviation may be attributed to a systematic error in the process of acquiring and processing the experimental data. However, its influence is not relevant for the specific tests considered here. A test circuit has been implemented in the real system; it simulates a 1000 m/s projectile velocity. This feature allows checking the system before any real test (Fig. 9). The measuring system was checked under normal operation conditions (the three optical barriers were operative), and it provided an accuracy much better than in the previous case, where only two optical barriers were considered (Fig. 10).

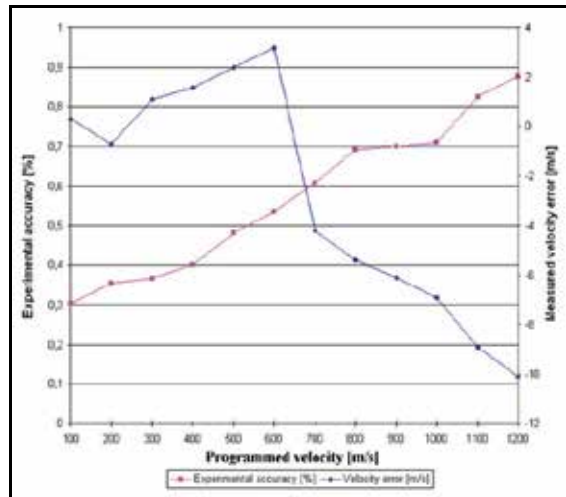


Fig. 8. Experimental accuracy and velocity error measured versus programmed velocity.



Fig. 9. Detail of the front panel of the velocity measuring system.

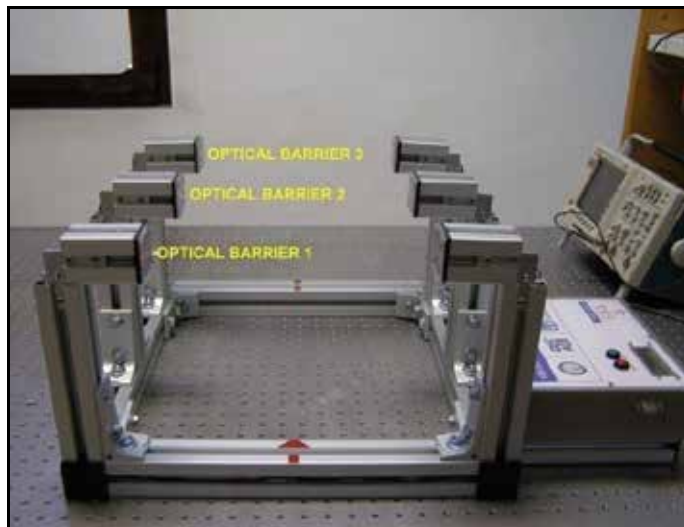


Fig. 10. Photograph of the implemented system used for high-velocity impact testing of aircraft and spacecraft structures.

3. Optical communications in space: The next generation of spacecraft transceivers

Telecommunications on future spacecraft are going to demand a paradigm shift in the way the information is transmitted. This need will be determined by the exponential increase of the amount of data to be interchanged between remote sites, together with the fact that the performance of communication links decreases with the distance.

Deep-space communications involve a bottleneck in the volume of data that can be transmitted to Earth. For instance, NASA's MRO (Mars Reconnaissance Orbiter) satellite is the probe with the largest capacity to communicate in deep-space, and its highest transmission rate in ideal conditions is below 6 Mbps (Taylor, Lee & Shambayati, 2006).

In order to satisfy the increasing demand of bandwidth, the strategy that was traditionally followed (Layland & Rauch, 1997) was to move to higher and higher carrier frequencies. That way, the L and S band (1-4 GHz), used during the 60s, gave way to the X band (7-8 GHz) in the late 70s, and to the first trials of Ka band in the 2000s, with which the best bit rates in deep-space were achieved.

The move to optical frequencies means a qualitative leap because it provides a spectrum shift from tens of GHz (Ka band) to hundreds of thousands of GHz (equivalent to a wave length of 1 μm), that is, around four orders of magnitude.

The development of optical communication technologies on board spacecraft has been slowed down by significant obstacles. Among them stands out the initial difficulty to compete with another technology which is totally consolidated and highly developed, as is the case of RF. Further difficulties to be met are those typical of the space industry, such as qualification for space environment and great resistance to new technologies. However, the development of optical communications in space will be unavoidable as future communication needs become more and more apparent, which will reveal that this new technology will be strategic for future spacecraft. The most relevant space agencies agree on that now.

The move from radio to optical frequencies involves a shift of model in the communication system design, because on the physical layer all parts of the system differ from those used with links based on microwaves. In the following sections a brief review is made of the technologies and techniques involved in this new type of telecommunication.

3.1 History of lasercom in space

Whereas a lasercom terminal on board a spaceship is completely different from an RF one, the great boom experienced by guided optical communications has brought about great progress in laser sources and optical detectors, which has enabled the necessary technology to be already available in laboratories. Besides, this technology has been used in several demonstrations in space, which have proved its feasibility.

The first test took place in December 1992 with NASA's GOPEX project. Pulses of 532 nm emitted from the earth with powers of MW were detected, with its image camera, by the Galileo probe from up to 6 million km (Wilson, Lesh & Yan, 1993).

In 1996, a second exhibition was carried out, this time with NASA's GOLD project in the form of a transmission of data at 1 Mbps between a terrestrial station and the Japanese geostationary satellite ETS6 (Jeganathan et al., 1997).

ESA's SILEX project (Fig. 11) turned out to be the first link between satellites in 2001, and in 2006 the first link between a satellite and an airship. This project involved terminals with 25 cm telescopes and 800-850 nm laser diodes with a peak power of 120 mW. Distances of



Fig. 11. ESA's SILEX project. Credits: ESA multimedia gallery.

over 45.000 km were reached with up to 50 Mbps binary rates (Fletcher, Hicks & Laurent, 1991).

Other significant projects never went beyond the design table, such as the OCDHRLF project, which in 2002 intended to load a 2.5 Gbps optical communication terminal on board the International Space Station using commercial off-the-shelf components (Ortiz et al., 1999). Or the EXPRESS project, in which a link was designed to download data from the space shuttle with a speed of up to 10 Gbps (Ceniceros, Sandusky, & Hemmati, 1999). Or the most ambitious NASA's MLCD project, which in 2009 intended to prove a link of up to 100 Mbps link from Mars by using a small low-power (5W of average power) terminal on board the MTO (Mars Telecom Orbiter), which was not launched after all due to budget pressures (Edwards et al., 2003).

3.2 Diffraction limit of a telescope and beam divergence

In fact, a telescope's primary mirror or lens can be considered a circular opening, because it produces light inside a circle described by its primary mirror. If the opening's diameter is D and the wave length is λ , the angular variation of intensity of radiation is given by the Eq. (6) (Hecht, 2002):

$$\frac{I(\theta)}{I(0)} = \left[2 \frac{J_1\left(\frac{\pi D}{\lambda} \sin(\theta)\right)}{\frac{\pi D}{\lambda} \sin(\theta)} \right]^2 \quad (6)$$

where $J_1(x)$ is the Bessel function of first order of x . The first zero refers to $(\pi D/\lambda)\sin(\theta) = 3.832$. Using the approach $\sin(\theta) \approx \theta$, we get a telescope's diffraction limit, which is given by the equation (7):

$$\theta = 1,22 \left(\frac{\lambda}{D} \right) \text{ rad} \quad (7)$$

This limit determines the lowest diffraction angle, and consequently the minimum of beam divergence with an increase in distance (Fig. 12).

Here, the diffraction limit formula has been calculated according to the criterion of the first zero in the Bessel function. If a different criterion were used, the multiplying factor of (λ/D)

would be different. For example (Franz, 2000), if one were to take the point where the power falls to a half, instead of taking the point where the first zero is, the multiplying factor would be 1.03.

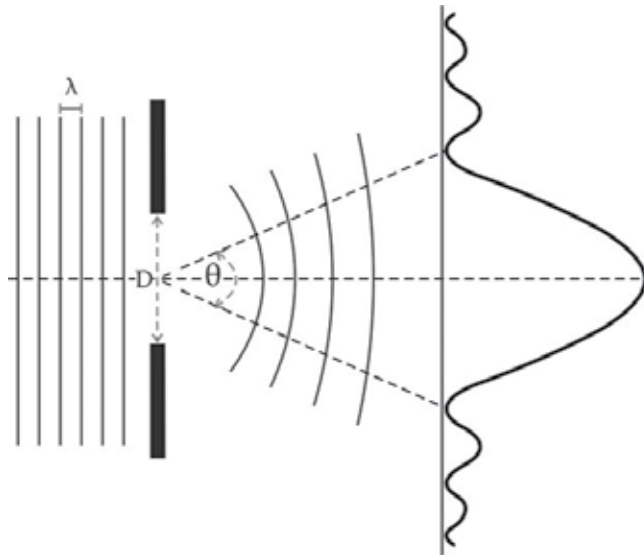


Fig. 12. Diffraction limit of a telescope.

The use of such short wavelength as the light's permits the emission of signals with a minimal diffraction. In the case of very large distances, divergence becomes a critical factor, because the wider the area that the emitted power reaches, the smaller the density of power per unit of surface area, that is, the lesser the signal that reaches the receiving antenna's surface. Since with the light's propagation, as with any electromagnetic wave, the area covered by the signal becomes squared with the distance, the loss of power is proportional to the square of the distance. This means that at great distances much more power can be delivered to the receiver compared with RF, and, since the performance of this kind of communications is limited by the signal-to-noise ratio, the use of optical wavelengths offers a great advantage to satellite communications.

Fig. 13 shows a comparison between an RF link and an optical one carried out by a space probe around Neptune transmitting with a telescope/antenna of 40 cm diameter, with a wavelength of $\sim 1 \mu\text{m}$ (IR) in the case of the optical link, and a frequency of 30 GHz (Ka band) in the case of RF. The result is that with the optical communication link the spot that is received on the earth has around one terrestrial diameter, whereas with the RF it has around 10000 times the earth's diameter. And that means that with the same emitted power the received power is 10000 times larger with the optical link. Using a large 4-meter antenna (similar to the one installed in the Cassini probe), the power received on the earth would still be 3 orders of magnitude below the one received with the lasercom terminal.

If we compare RF frequencies with optical wave lengths in terms of achievable bit rates, only potential limits can be considered, as optoelectronic technology is still very far from reaching them. The information transfer rate is limited by a fraction of the carrier frequency, so that, with such high frequencies as that of the light, bit rates far beyond Tbps could be achieved –if the technology were available– resulting in an improvement of several orders of

magnitude in relation to RF. Nowadays speeds over one Gbps have already been verified. Besides, such a large directivity permits the use of an almost infinite bandwidth, because of the absence of regulation against interferences, as is the case with RF.

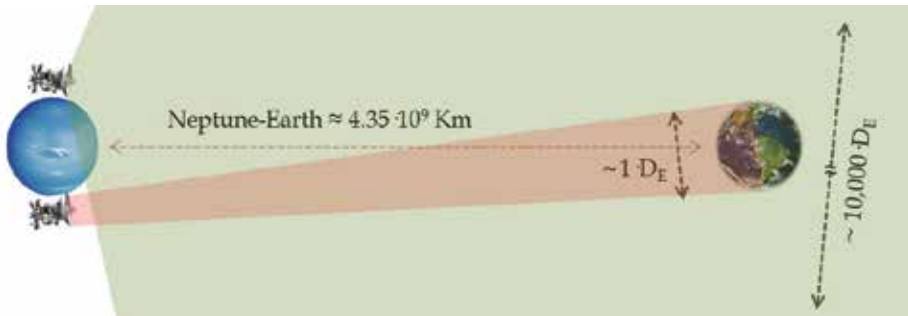


Fig. 13. Comparison between RF and optical links.

On the other hand, a great directivity demands a high pointing accuracy. After the process of pointing acquisition, in which both terminals establish the line of sight to each other, the procedure to keep the pointing is several orders of magnitude more complex than with radio frequency. In RF, the pointing accuracy is of the order of milliradians in the Ka band, which can be achieved with the spaceships' attitude control systems. By contrast, a deep-space lasercom link would typically require submicroradian accuracy (Ortiz, Lee & Alexander, 2001). In order to keep a stable line of sight, the spaceship needs to have a dedicated system in charge of isolating the optical lasercom terminal from the spaceship's platform jitter. This can be achieved by means of vibration isolators and jitter measures through a laser beacon from the ground terminal, if the probe is near the earth, and additionally celestial references and inertial sensors, if the probe is in deep-space. With a stabilized line of sight, the pointing and tracking system is responsible of pointing the beam towards the other terminal and keeping the pointing throughout the communication. This is carried out by referring the position of the laser beacon and/or the celestial references to the ground station terminal, and by maintaining it with an open loop correction.

3.3 Block diagram and main elements in a lasercom link

Any satellite optical communication link (Fig. 14) would consist of one or several ground stations, one transceptor on board each of the flight terminals, and between both ends the optical communication channel, whether it be the space in the case of an intersatellite link, or the atmosphere in the case of communication with the earth.

The flight terminal receives the information provided by the spaceship and encodes and modules it on a laser beam, which transmits it through an antenna (telescope) after the process of reception and pointing to the earth terminal. The laser beam propagates through an optical channel that causes free space losses due to the divergence in the propagation of light, background noise mainly due to the sun, and some atmospheric effects near the earth surface. Once the beam reaches the earth terminal, its job is to provide, by means of a telescope, enough of an opening to collect the received light, show an adequate photodetection sensitivity in the photons-electron conversion, and carry out the demodulation and decoding of the signal.

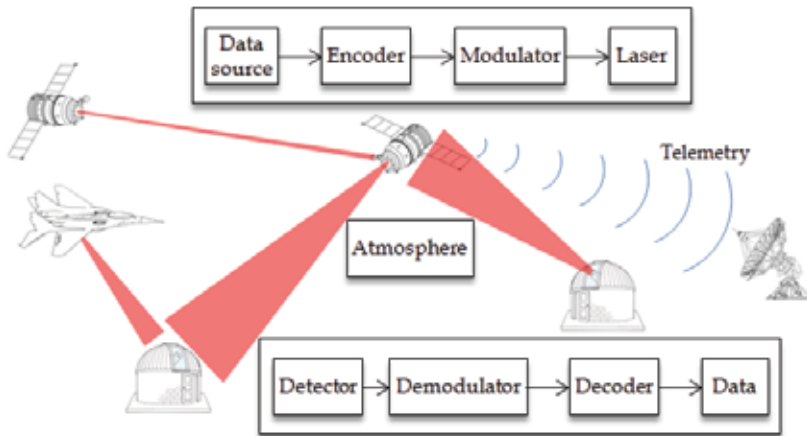


Fig. 14. Block diagram of an optical satellite communication link.

Coding schemes of information for the detection and correction of errors caused by the channel are similar to those used in RF (convolutional codes such as Reed-Solomon, and block codes such as Turbo codes), but modulation techniques vary a great deal. The most simple format consists in turning the laser on and off (OOK, On-Off Keying). However, this technique shows serious deficiencies when great distances are involved: on the one hand the peak power of the pulses needs to be high enough to compensate for the free-space losses, but on the other hand the average transmission power needs to be low enough to reduce the electricity consumption. Various modulation techniques come up here, whose common denominator is the possibility to encode more than one bit per pulse. Pulse Position Modulation (PPM) consists in dividing the duration of each sequence of n bits into $m=2^n$ slots, corresponding to the m symbols that can be encoded. Each time a pulse is sent, it is placed in one of these slots, so that its value is defined by its position within the time interval (Fig. 15).

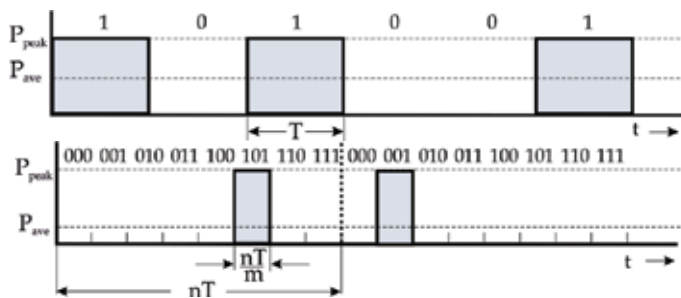


Fig. 15. Modulation of the sequence 101001 in OOK (above), and in 8-PPM (below).

That is a way (Hamkins & Moision, 2004) to get the Eq. (8), where the PPM technique is seen to help to reduce the laser’s work cycle, and improve the signal-to-noise ratio at the cost of requiring higher modulation speeds to keep the same binary rate.

$$\left(\frac{P_{peak}}{P_{ave}} \right)_{m-PPM} = \frac{m}{n} \tag{8}$$

These modulation techniques could be considered versions of encoded OOK rather than real modulations, because all of them are based on an amplitude modulation, or IM/DD (Intensity Modulation/Direct Detection), as they are known in the field of traditional optical communications. There are also coherent modulation techniques, based on the same principles as RF, consisting in placing the received signal on top of a local laser's signal, so that the surface of the photodiode receives a mixture of signals. This way the local laser acts as an amplifier of the received signal, resulting in a better signal-to-noise ratio. Unlike intensity modulation techniques, coherent modulations allow various techniques to modulate the signal, similar to the ones used in RF, like FSK (Frequency Shift Keying), PSK (Phase Shift Keying), etc.

One way to evaluate the performance of each of these types of modulation is to calculate the relation between the signal-to-noise ratios of both techniques. A comparison (Carrasco, 2005) between a coherent receptor and a direct-detection one, both being based on avalanche photodiodes (APD), would provide Eq. (9). In it, SNR_c and SNR_d symbolize the signal-to-noise ratio for coherent and non-coherent detectors respectively; P_l and P_r represent the local laser's power and the received signal's power respectively; and M , α , R_0 , I_d and N_t refer to an APD detector's traditional parameters, that is, the APD multiplication factor, the dependence on the material, the responsivity, the darkness current, and the spectral density of power of the thermal noise. Eq. (9) proves that if P_l is big enough the predominant noise is the shot, and SNR_c will always be bigger than SNR_d because the numerator increases faster than the denominator.

$$\frac{SNR_c}{SNR_d} = \left(4 \frac{P_l}{P_r} \right) \left(\frac{e M^{2+\alpha} [R_0 P_r + I_d] + N_t}{e M^{2+\alpha} [R_0 P_l + I_d] + N_t} \right) \quad (9)$$

Although in theory the coherent modulation is superior to the non-coherent one in terms of SNR, the implementation of a system based on coherent modulation involves a number of problems that prevent its ideal behavior, such as the difficulty involved in the process of mixture of signals at the photodetector's entrance in the case of very short wavelengths, or especially the effects added to the signal in its journey through the atmosphere (and the shorter the wavelength, the more pronounced those effects are). In this case, the atmospheric turbulence causes, among other things, the loss of spatial coherence by the wavefront, a crucial factor in the mixture of signals that is necessary in any coherent modulation.

Atmospheric turbulence causes the most adverse effects in optical communications in free space, due to air mass movements that cause random changes of the refraction index. The effect of the turbulence is crucial in coherent systems, but it must always be taken into account as it affects in various degrees all kinds of optical systems whose element includes the atmosphere. Besides loss of spatial coherence, turbulence also causes widening of the received beam, random wander of the beam's center, and redistribution of the beam's energy in its transversal section resulting in irradiance fluctuations, also known as scintillation.

The downlink is generally the link causing the most difficulties in the design of a satellite lasercom system. However, in the case of atmospheric turbulence, the uplink is the most seriously affected, as the effect on the beam takes place in the first kilometers, and this translates into an amplification throughout the rest of the journey, which is far longer than with the downlink. Either with uplinks or with downlinks, the effect of the turbulence can be mitigated with various techniques, among which stands out aperture averaging. This

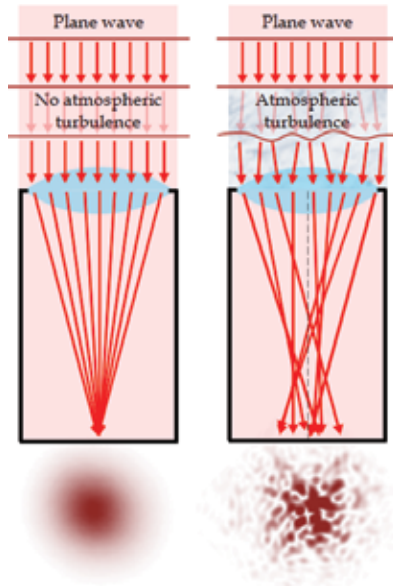


Fig. 16. Effect of turbulence on a received beam spot.

technique can be used by making the receiving opening bigger than the width of correlation of the received irradiance fluctuations. If this requirement is met, the receptor becomes bigger than a punctual one. Since the signal experiences instant fluctuations, it can be integrated into different points corresponding to the same moment, with the result that the receiver perceives several patterns of simultaneous correlations, and therefore while the signal is integrated the level of scintillation decreases on the image plane. The effect of this technique can be quantified with the aperture averaging factor (Andrews & Phillips, 2005):

$$A = \frac{\sigma_I^2(D_G)}{\sigma_I^2(0)} \quad (10)$$

where $\sigma_I^2(0)$ is the level of scintillation in the case of a punctual receiver, and $\sigma_I^2(D_G)$ is the level of scintillation averaged out for an opening with a diameter of D_G . Consequently, A provides information about the improvement achieved between $A=0$ (for no fluctuations at all) and $A=1$ (for no improvement). In the case of long-distance or deep-space links, the order of magnitude of the irradiance spatial correlation width is clearly defined: In downlinks, it is of a few centimeters, whereas in uplinks it is of tens of meters (Maseda, 2008); therefore a terminal placed in space will always act as a punctual receptor. By contrast, in ground stations it is possible to use large telescopes or separate small ones forming an array, in order to decrease scintillation fades in the downlink. The equivalent technique for the uplink is based on transmitting through multiple mutually incoherent beams, either by using various laser sources or by dividing the outgoing beam into several smaller ones. If the laser beams are separated enough, they will propagate through uncorrelated portions of the atmosphere, resulting in an effective single beam. Generally, these scintillation fades can be reduced by increasing the number of beams. Very low probability of fades can be obtained using 8–16 independent beams (Steinhoff, 2004).

As mentioned above, wavefront distortions caused by atmosphere turbulence are particularly harmful in coherent systems. This loss of spatial coherence by the wavefront can

be mitigated with adaptive optics (AO). This kind of systems, otherwise quite often used in astronomical telescopes, provides real-time wavefront control, which allows the correction of distortions caused by turbulence on a millisecond time scale. However, its application in communication systems is not direct, due to significant differences with its imaging use: in astronomical telescopes, losses in signal energy can be solved by observing longer, which is not feasible when receiving information continuously. Besides, astronomical telescopes are only used for night operation under weak turbulence. In communications, AO systems need to work in daytime too, which causes strong turbulence conditions. The classic design of an AO system is based on wavefront measurements that allow the reconstruction of distorted wavefronts and the use of the resulting information to correct the incoming beam by means of active optical elements, such as deformable mirrors based on micro-electromechanical systems (MEMS). Wavefront measurement techniques can prove difficult under strong turbulence and, to solve that, alternative designs (Weyrauch & Vorontsov, 2004) have been proposed, based on wavefront control by optimization of a performance quality metric, such as the signal strength, which is readily available in lasercom terminals.

Besides turbulence, the atmosphere causes other detrimental effects in optical communication links, although they can be mitigated through various techniques. For example, atmospheric gases, according to their composition, absorb part of the electromagnetic radiation in ways that depend on their frequency. Although in some regions the atmosphere is for all purposes opaque, there are some windows of minimal absorption in the optical area of the spectrum, such as the visible zone, from about 350 nm to around 750 nm, and those zones centered around 0.85 μm , 1.06 μm , 1.22 μm , 1.6 μm , 2.2 μm and 3.7 μm (Seinfeld & Pandis, 1998). Taking the atmospheric absorption into account is crucial because it determines the choice of the link's wavelength, although the effect of its losses in the link is negligible if the choice of wavelength is correct.

Clouds cause other detrimental atmospheric effects and can even completely block a laser's transmission if they temporarily obstruct the line of sight. The variability in their appearance and their seeming fortuitousness allow the use of only two methods to avoid their presence during communications: a correct choice in placing the earth terminals, and their replication, so that at any given moment at least one site be free of clouds, for which locations are to be chosen that show no correlation in atmospheric variability. The most adequate positionings usually coincide with those of astronomical observatories, which are placed at altitudes, normally above 2000 m, so as to prevent the effects of the first layer of the atmosphere. An availability of over 90% is possible if at least three redundant sites are used (Link, Craddock & Allis, 2005).

The first of the techniques mentioned above is also used to mitigate the scattering effect. Scattering is another of the effects that affect any optical signal propagating through the atmosphere. It is due to the presence of particles with different sizes and refraction indexes, which cause various types of light spread according to the relation between the particle size and the wavelength, and the relation between the particle's refraction index and the medium's. The most harmful effect caused by scattering over optical communications, particularly in direct-detection systems, is not on the laser signal, but on the sun light during daytime and, to a lesser degree, on the moon's and planets' light, if they come within the telescope's field of view. Solar photons are scattered by the atmospheric aerosols in all directions so that they can propagate following the line of sight, causing a background noise that is received together with the communication signal in the receiver, even if this is angularly far from the sun. The noise power N_S collected due to sky radiance is given by Eq. (11) (Hemmati, 2006).

$$N_s = L(\lambda, \theta, \varphi) \frac{\pi D^2 \Omega \Delta \lambda}{4} \quad (11)$$

where $L(\lambda, \theta, \varphi)$ is total sky radiance, a value that depends on wavelength λ , on the observer's zenith angle θ , and on the angular distance φ between observer and sun zenith angles. With a given sky radiance, the noise power depends on the aperture diameter D (cm), on the field of view Ω (srad), and on the filter width $\Delta \lambda$ (μm). The way to decrease this noise in relation to the sky radiance is that of the strategy mentioned above: a suitable location for the ground station, which in this case means low concentration of scatterers and high altitude sites. This choice is usually done according to sky radiance statistics collected by means of a network of photometers like AERONET. The technological strategies used for decreasing the sky background noise focus on the use of masks and solar rejectors, which prevent the noise not directly entering the telescope's field of view, and the use of very narrow filters, which limit the receiver's optical bandwidth, with widths below an angstrom.

The only way of completely preventing atmospheric effects is by placing all the terminals above the atmosphere. This may be done by establishing intersatellite links, which involves significant advantages and a great drawback – its cost. If the communication is carried out entirely in space, any wavelength can be chosen, as it is free from the limitations imposed by minimal absorption windows. For instance, very small wavelengths, with lesser propagation divergences, could be used, which offers the possibility to decrease the size of the telescopes on board. A rough estimate (Borosan, Bondurant & Scozzafava, 2004): in a communication between Mars and the Earth, a telescope on board a satellite around the Earth would need 2.6 meters to keep a link of the same capacity as a telescope of 8.1 meters placed on the earth's surface. Besides, sun light does not suffer scattering in space, whereas it does in the atmosphere, therefore sun background noise gets minimized. The number of necessary terminals is also greatly reduced, because direct vision lines are much wider, as the Earth does not stand in the way. For example (Edwards et al., 2003), in order to keep a continuous communication with Mars without the effects of the Earth's rotation, 2 or 3 satellites would be necessary, or between 3 and 9 ground stations. In short, the cost of a topology based on receptor satellites is still bigger than through ground stations, although at very large distances a receptor on the earth's surface could become non-viable due to the effect of the atmosphere on the very weak received signal. As an intermediate option, the use of stratospheric balloons has been proposed, which at altitudes over 40 km makes it possible to avoid 99% of the atmosphere. However, this option also meets drawbacks such as the limited duration of the flights (no more than 100 days), and the lack of a complete control of the trajectories.

3.4 Design constraints and strategies

The most basic tool to carry out a link design is the traditional equation, similar to the one used in RF. The link equation (12) relates the mean received power (P_R) and the transmitted power (P_T) in the following way (Biswas & Piazzolla, 2003):

$$P_R = P_T \cdot G_T \cdot \eta_T \cdot L_P \cdot L_S \cdot \eta_A \cdot \eta_R \cdot G_R \cdot L_M \quad (12)$$

where G_T and G_R are the gains in transmission and reception; η_T , η_R y η_A are the optical efficiency of the transmitter and the receiver, and the atmosphere's efficiency, all of which can be taken as losses; L_P , L_S y L_M are pointing losses, due to free space and other effects, like mismatch of the transmitter and receiver polarization, etc. The most significant parameters in the link equation can be easily quantified, which allows making a quick preliminary

analysis of the link. The gains in transmission and reception can be worked out with the equations (13) and (14) (Majumdar, 2005):

$$G_T = \frac{16}{\Theta_T^2} \quad (13)$$

$$G_R = \left(\frac{\pi D}{\lambda} \right)^2 \quad (14)$$

where Θ_T is the full transmitting divergence angle in radians, D is the telescope aperture diameter and λ is the wavelength. The free-space losses are shown by the equation (15) (Gowar, 1984):

$$L_s = \left(\frac{\lambda}{4\pi L} \right)^2 \quad (15)$$

where L is the distance between transmitter and receptor. Equations (13), (14) and (15) would complete the link's analysis in optical-geometric terms, which represents the most important quantitative contribution to the link equation.

In the design of a lasercom link, key parameters are the laser's transmission power, the telescope aperture, and the wavelength, among others. When making decisions about these parameters, the goal will always point to optimize the signal-to-noise ratio, which, as was shown above, is the factor that sets the limits of a system's performance.

The most direct way to optimize this parameter is by increasing the transmission power. However, the improvement in the downlink is very limited because energy available in space is also quite limited. Nevertheless the use of PPM modulation permits increasing the peak power, keeping a low average consumption, as explained above. On the other hand, by increasing the transmitting telescope's aperture the beam divergence gets reduced, so that the beam can be focused more, thereby making much better use of the transmitted energy. The drawback is the increase in volume and mass of the satellite, and the resulting greater difficulty in pointing the narrow beam. Normally, these two parameters -laser power and telescope aperture- are maximized in accordance with the satellite platform's requirements, and then they are taken as fixed parameters.

An important design aspect is the choice of wavelength. This choice is first limited by the technological availability of laser sources and optical detectors. For example, for deep-space the tendency is to choose wavelengths close to 1.064 μm or 1.55 μm due to the availability of high peak-to-average power lasers: Nd:YAG, Nd:YVO4, Nd:YKLF or erbium-doped fiber amplifier lasers (Hemati, 2006). Although limited by these requirements, equation (2) shows that the wavelength can be decreased with the same results as the increase in telescope diameter, i.e., less beam divergence without affecting the flight terminal, except in relation with the greater difficulty in pointing. However, the strength of intensity fluctuations due to atmospheric turbulence decreases as $\lambda^{-7/6}$ (Majumdar & Ricklin, 2008), in the same way as the scattering attenuation and sky radiance do as λ^{-4} (Jordan, 1985), and consequently, if the signal has to cross the atmosphere, shorter wavelengths provide a larger scintillation, which could be a limiting factor when choosing them.

The natural tendency in satellite communication links is to transfer the system's complexity to the Earth, whenever possible. The reason is that any technological effort resulting in an increase of weight, volume, consumption or complexity is more readily undertaken by a

ground station than by a satellite. Regarding this aspect, there is a number of techniques that make it possible to optimize the overall link performance, by making improvements in the ground station. The most direct ones are the increase of the receiver's collecting area and the improvement in optoelectronic efficiency of the receptors.

It is certainly possible to increase the gain in reception by building a very large telescope, although this method meets serious limitations due to the high costs and complexity of this kind of installations. Nowadays, astronomical telescopes with the largest aperture only reach 10 meters, in spite of very high costs of development and maintenance. To overcome this limitation in the ground station, a proposal has been made and tested (Vilnrotter et al., 2004) consisting of a synthesis of very large optical apertures by means of arrays of smaller telescopes. The difference between collecting light by using a large telescope and an array of smaller ones is that in the first case all the light is focused before its detection, either with one big element or an array of multiple smaller segments. By contrast, in an array of telescopes each element in the array focuses the received beam into different photodetectors, in order to later combine the signals in the electric domain. This idea offers the opportunity to rapidly implement cost-effective large apertures, otherwise unfeasible by using one single telescope that would require massive support structures, developing the necessary custom optics, complex alignment process, etc, being all of this exacerbated by the great gravitational requirements found in such heavy installations. Besides, there is a number of other significant advantages: reuse in future, more demanding missions, by making use of their great scalability through the addition of more telescopes to the array; very fast recovery in case of failure by just replacing one telescope with a spare one; the possibility of flexibly managing all the elements in the array for more than one simultaneous link; and lesser requirements over the telescopes, which makes it possible to use cheap off-the-shelf systems.

Significant improvements in detector efficiency have also been carried out. With a detector based on direct detection, the most straightforward method is by using photodetectors with inner amplification, such as avalanche photodiodes (APD), or photomultiplier tubes (PMT). The receiver's noise contribution can be ignored in some ways, such as by cooling the detector down to cryogenic temperatures; with high bias voltages, which leads to very high amplification gains; and by using error correction coding to mitigate the effect of false photon detections in the form of dark counts. This way it is possible to distinguish the entrance of a single photon, procedure called photon counting. There are two types of photon counters: linear and geiger-mode. The former can be implemented with an APD or a PMT, and provide an electrical signal that is proportional to the number of received photons. They are limited by the detector's bandwidth, which gives the greatest temporary resolution to distinguish photons. Geiger-mode photon counters work in a way similar to a Geiger counter and are implemented by taking an APD's bias voltage very close to saturation. The result is that a photon's arrival triggers a carrier's avalanche that provides a very intense pulse, which equates to an infinite gain. These devices are limited by the fact that, after each avalanche, some recovery time (in the order of μs) must go by so as to bring the APD back to below breakdown and make it ready for the next detection. During this time, the arrival of a new photon would be ignored. This can be overcome by means of a GM-APD array, so that there is an increased probability of some detector always being ready to trigger an avalanche. As in the case of arrays of telescopes, the use of arrays of detectors offer additional advantages: It is possible to use them to extract information for the tracking process, as well as information related to atmospheric conditions, because they can distinguish between pixels; and they offer a way to dynamically adapt the field of view, depending on the number of elements used. This

type of detection has proved to offer efficiency improvements of up to 40× in terms of photons per bit, compared with traditional systems (Mendenhall et al., 2007).

4. Conclusions

An optoelectronic velocity measurement system was designed, developed and implemented using discrete circuits. The system is able to measure the velocity of small projectiles, flying at speeds in the range from 30 to 1200 m/s. Velocity system is based on the noncontact measurement of the projectile times of flight between three optical barriers. The velocity data is computed by the control process unit (microcontroller) and the result is displayed on a LCD mounted in the system and sent to remote computer using a serial protocol. The velocity accuracy was theoretically calculated and experimentally evaluated. Values better than 1% were obtained for the worst case, when one of the optical barrier. This accuracy depends mainly on the projectile velocity and optical barrier distances, and it could be improved by increasing either the clock frequency of microcontroller or the distance between optical barriers. The influence of background light in the measured velocity is negligible. The implemented system is simple, cost-effective, and robust against potential failures of the optical elements and covers a wide velocity range from subsonic to supersonic.

Regarding to communication systems, a review has been made of the fundamentals on which are based free-space lasercom transceivers on board spacecraft. As it was shown, this new technology offers improvements of several orders of magnitude over present RF links, and thus it seems to have a great potential in the future. However, the leap from microwave frequencies to optical wavelengths involves a paradigm shift in how the information is transmitted, which requires the development of a new technology at all levels of the communication link. The influence of the main elements that make up a lasercom link has been studied, focusing on the techniques that are most crucial to mitigate the specific problems arising from this type of communication: atmospheric effects affecting optical signals, difficulty in controlling the pointing and tracking, etc. Finally, an analysis of the main strategies to be followed in the design of a free-space laser communication system has been presented, so that all the key parameters involved in an optical link are revised.

5. References

- Alon, Y. (1989). *Doppler Radar Method and Apparatus for Measuring a Projectile's Muzzle Velocity*, United States Patent 4837718, Lear Siegler, Inc. (Santa Monica, CA), United States.
- Andrews, L. C. & Phillips, R. L. (2005). *Laser Beam Propagation through Random Media*, SPIE Press Monograph, Volume PM152, ISBN 0819459488, Bellingham, Washington, United States.
- Biswas, A. & Piazzolla, S. (2003). Deep Space Optical Communications Downlink Budget from Mars: System Parameters. *The Interplanetary Network Progress Report*, 42-154, pp. 1-38, August, 2003.
- Boroson, D. M.; Bondurant, R. S. & Scozzafava, J. J. (2004). Overview of High Rate Deep Space Laser Communications Options, *Free-Space Laser Communications Technologies XVI, Proceedings of SPIE*, Vol. 5338, pp. 37-49, January, 2004.
- Carrasco, A. (2005). *Diseño de un Enlace de Comunicaciones Ópticas con Marte*. Engineering degree final project, University of Málaga.
- Ceniceros, J.M.; Sandusky, J. V. & Hemmati, H. (1999). 10 Gbps Shuttle-to-Ground Adjunct Communication Link Capability Experiment, *1999 Shuttle Small Payloads Project Office Symposium*, NASA/CP-1999-209476, pp. 293-295, September, 1999.

- Chan, V.W.S. (2000). Optical Space Communications, *Millennium Issue IEEE Journal on Selected Topics in Quantum Electronics*, Vol. 6, No. 6, pp. 959-975, November-December, 2000.
- Crittenden Jr., E.C.; King, R. A. & Andrews, T. C. (1973). *Target Measurement System for Precise Projectile Location*, United States Patent 3727069, Litton Systems Inc. (Beverly Hills, CA), United States.
- Edwards, B. L.; Townes, S. A.; Bondurant, R. S.; Scozzafava, J. J.; Boroson, D. M.; Roberts, W. T.; Biswas, A.; Pillsbury, A. D.; Khatri, F. I.; Burnside, J. W.; Bold, D. R.; Murphy, D. V.; McIntosh, A. K.; Caplan, D. O.; DeCew, A. E.; Sharma, J.; Parvin, B. A.; Fitzgerald, R. J.; Zingales, S. H. & De Paula, R. (2003). Overview of the Mars Laser Communications Demonstration Project, *American Institute of Aeronautics and Astronautics AIAA Space 2003 Conference*, Paper 2003-6417, pp. 1444-1454, September, 2003.
- ESA multimedia gallery. <http://www.esa.int/esa-mm/mmg/mmhome.pl>.
- Fletcher, G. D.; Hicks, T. R. & Laurent, B. (1991). The SILEX Optical Interorbit Link Experiment. *Electronics & Communication Engineering Journal*, Volume. 3, No. 6, pp. 273-279, ISSN 09540695, December, 1991.
- Franz, J. H. & Jain, V. K. (2000). *Optical Communications, Components and Systems*. Alpha Science International Ltd, ISBN 1842650556, New Delhi, India.
- Gowar, J. (1984). *Optical Communication Systems*. Prentice-Hall International Inc., ISBN 0136387276, London, United Kingdom.
- Hamkins, J. & Moision, B. (2004). Selection of Modulation and Codes for Deep Space Optical Communications. *Free-Space Laser Communication Technologies XVI, Proceedings of SPIE*, Vol. 5338, pp. 123-130, January, 2004.
- Hartwig, R. (1986). Accuracy of Velocity Measurement of Projectiles with Fins and Tracers by Means of Sky-Screens. *Journal of Ballistics*. Vol. 9, No. 3, pp. 2299-2310, 1986.
- Hecht, E. (2002). *Optics*. Addison Wesley, ISBN 0321188780, San Francisco, United States.
- Hemmati, H. (2006). *Deep Space Optical Communications*. John Wiley & Sons, ISBN 0470040025, New Jersey, United States.
- Henniger, H.; Giggenbach, D.; Florian, D. & Rapp, C. (2003). Evaluation of FEC for the Atmospheric Optical IM/DD Channel, *Free-Space Laser Communication Technologies XV, Proceedings of the SPIE*, Vol. 4975, pp. 1-11, July, 2003.
- Jeganathan, M.; Toyoshima, M.; Wilson, K.; James, J.; Xu, G. & Lesh, J. (1997). Data Analysis Results from the GOLD Experiments. *Free-Space Laser Communications Technologies IX, Proceedings of SPIE*, Vol. 2990, pp. 70-81, April, 1997.
- Jordan, E. C. (1985). *Reference Data for Engineers: Radio, Electronics, Computer & Communications*. Howard W. Sams & Co., Inc., ISBN 0672215632, Indiana, United States.
- Lambert, S. G. & Casey, W. L. (1995). *Laser Communications in Space*. Artech House, ISBN 0890067228, Boston, United States.
- Layland, J. W. & Rauch, L. L. (1997). The Evolution of Technology in the Deep Space Network: A History of the Advanced Systems Program. *The Telecommunications and Data Acquisition Progress Report*, TDA PR 42-130, pp. 1-44, August, 1997.
- Link, R. P.; Craddock, M. E. & Allis, R. J. (2005). Mitigating the Impact of Clouds on Optical Communications, *Aerospace Conference 2005 IEEE*, pp. 1258-1265, ISBN 0780388704, March, 2005.
- Majumdar, A. K. (2005). Free-space Laser Communication Performance in the Atmospheric Channel. *Journal of Optical and Fiber Communications Research*, Volume 2, No. 4, pp. 345-396, October, 2005.
- Majumdar, A. K. & Ricklin, J. C. (2008). *Free-Space Laser Communications, Principles and Advances*. Springer, ISBN 9780387286525, New York, United States.

- Maseda, R. H. (2008). *Estudio de Enlaces de Comunicaciones Ópticas a Grandes Distancias en presencia de Turbulencia Atmosférica*. Engineering degree final project, Carlos III University of Madrid.
- Mendenhall, J. A.; Candell, L. M.; Hopman, P. I.; Zogbi, G.; Boroson, D. M.; Caplan, D. O.; Digenis, C. J.; Hearn, D. R. & Shoup, R. C. (2007). Design of an Optical Photon Counting Array Receiver System for Deep-Space Communications. *Proceedings of the IEEE*, Volume 95, No. 10, pp. 2059-2069, ISSN 00189219, October, 2007.
- Moss, G.M.; Leeming, D.W. & Farrar, C.L. (1995). *Military Ballistics: a basic manual*, Brassey's New Battlefield Weapons Systems and Technology Series, ISBN 1857530845, London, United Kingdom.
- Ortiz, G. G.; Jeganathan, M.; Sandusky, J. V. & Hemmati, H. (1999). Design of a 2.5 Gbps Optical Transmitter for the International Space Station. *Free-Space Laser Communication Technologies XI, Proceedings of SPIE*, Vol. 3615, pp. 179-184, April, 1999.
- Ortiz, G. G.; Lee, S. & Alexander, J. W. (2001). Sub-microradian Pointing for Deep Space Optical Telecommunications Network. *19th AIAA International Communications Satellite Systems Conference*, 921, pp. 1-16, No. 921, April, 2001.
- Paulter, Jr. N. G. & Larson, D. R. (2009). Reference Ballistic Chronograph, *Optical Engineering*, Vol. 48, No. 4, pp. 43602-43607, April, 2009.
- Pena, J. M. S.; Marcos, C.; Fernández, M. Y. & Zaera, R.(2007). Cost-Effective Optoelectronic System to Measure the Projectile Velocity in High-Velocity Impact Testing of Aircraft and Spacecraft Structural Elements, *Optical Engineering*, Vol. 46, No. 5, pp. 510141-510146, ISSN 00913286, May, 2007.
- Schroder K.A.; Allen R.J.; Parker J.V. & Snowden P.T. (1999). In-Bore Measurements Using an Optical Data Link, *IEEE Transactions on Magnetics*, Vol. 35, pp. 95-99, ISSN 00189464, January 1999.
- Seinfeld, J. H. & Pandis, S. N. (1998). *Atmospheric Chemistry and Physics: From Air Pollution to Climate Change*. John Wiley & Sons Inc., ISBN 0471178160, New York, United States.
- Steinhoff, N. (2004). Irradiance and Fade Characteristics for the JPL MLCD Program. *The Optical Science Company*, Report No. TR-1657, California.
- Taylor, J.; Lee, D. K. & Shambayati, S. (2006). Mars Reconnaissance Orbiter Telecommunications. *DESCANSO Design and Performance Summary Series*, Article 12.
- Vilnrotter, V.; Andrews, K.; Lau, C. & Srinivasan, M. (2004). Conceptual Design of an Optical Array Receiver, with Preliminary Experimental Results. *The Interplanetary Network Progress Report*, Volume 42-156, pp. 1-9, February, 2004.
- Weyrauch, T & Vorontsov, M. A. (2004). Free-space Laser Communications with Adaptive Optics: Atmospheric Compensation Experiments. *Journal of Optical and Fiber Communications Research*, Volume 1, No. 4, pp. 355-379, ISBN 18673007, December, 2004.
- Wilde, A. F.; Roylance, D. K. & Rogers, J. M. (1973). Photographic Investigation of High-Speed Missile Impact Upon Nylon Fabric, Part I: Energy Absorption and Cone Radial Velocity in Fabric, *Textile Research Journal*, Vol. 43, No. 12, pp. 753-761, December, 1973.
- Wilson, K. E.; Lesh, J. R. & Yan, T. Y. (1993). GOPEX: A Laser Uplink to the Galileo Spacecraft on Its Way to Jupiter. *Free-Space Laser Communication Technologies V, Proceedings of SPIE*, Volume 1866, pp. 138-146, January, 1993.
- Zukas, J. A.; Nicholas, T. & Swift, H. F. (1992). *Impact Dynamics*, Krieger Publishing Company, ISBN 0894646907, Florida, United States.

Solar Electric Propulsion Subsystem Architecture for an All Electric Spacecraft

Dr. Michele Coletti, Dr. Angelo Grubisic,
Cheryl Collingwood and Prof. Stephen Gabriel
*University of Southampton,
United Kingdom*

1. Introduction

For many space missions, both a main propulsion subsystem and additional attitude control (AOCS) propulsion subsystem are required. These subsystems normally use different propellants, hence require separate tanks, different flow control units (FCU) and, in case of solar electric propulsion (SEP), separate power processing units (PPU). This leads to increases in total mass of the spacecraft and complexity while reducing system specific impulse.

One possibility to alleviate this problem would be to develop a main *and* an AOCS propulsion technology which could be integrated, sharing some of the components required for their operation, hence reducing system mass. A spacecraft employing such combined technologies as part of an SEP system is referred to as an “All-electric-spacecraft” (Wells et al., 2006).

In this chapter, the system design for an all-electric-spacecraft will be presented. A gridded ion engine (GIE) is proposed as a main propulsion subsystem with hollow cathode thrusters (HCT) considered for the AOCS propulsion subsystem. The mission considered during this study is the ESA European Student Moon Orbiter (ESMO), which the University of Southampton proposed to use SEP for both attitude control and main propulsion. During the ESMO phase-A study, a full design of the SEP subsystem was performed at QinetiQ as part of a wider study of the mission performed in conjunction with QinetiQ staff and funded by ESA. The output of this study will be here presented to explain the concept of the all-electric-spacecraft, its benefits, drawbacks and challenges.

1.1 The european student moon orbiter mission

ESMO is a student mission sponsored by the European Space Agency that started in 2006 and that, at present, is planned to be launched in early 2014 (http://www.esa.int/esaMI/Education/SEML0MPR4CF_0.html). ESMO will be completely designed, built and operated by students from across Europe resulting in the first European student built satellite reaching the moon. ESMO will be launched in a geostationary transfer orbit (GTO) as a secondary payload and from there will have to use its onboard propulsion to move to a lunar polar orbit. The payload will consist of a high resolution camera for optical imaging of the lunar surface.

3. SEP subsystem definition

As already anticipated in the introduction, the SEP subsystem proposed by Southampton University was based on the idea of an all-electric spacecraft, where a gridded ion engine provides primary propulsion and where hollow cathode thrusters are used to unload momentum from the reaction wheels. The gridded ion engine is based on the flight model hardware of the GOCE (Gravity and Ocean Open Circulation Explorer) mission T5 GIE, developed by QinetiQ (Edwards et al., 2004), whereas the HCTs to be used for AOCS will be based on the T5 discharge cathode.

The proposed SEP subsystem comprises:

- a single T5 GIE.
- eight HCTs used for AOCS functions.
- one or two (depending on the subsystem configuration) power processing units (PPU) to process and supply power to the T5 GIE and to the HCTs.
- one or two (depending on the subsystem configuration) flow control units (FCU) to regulate the propellant flow to the T5 GIE and to the HCTs.
- a tank for propellant storage.

During the course of this study, it has been assumed that the thruster to be used onboard ESMO will have the same performance as the GOCE T5 GIE (Table 1).

	GOCE T5
Thrust	1-20 mN
Specific Impulse	500-3500 s
Power	55-585 W

Table 1. T5 GOCE performance (Wells et al., 2006)

3.1 SEP subsystem design options and trade off

Three different design options were identified for the SEP subsystem, based on the level of integration between the GIE and HCTs.

Option 1 – High mass, low risk, low cost

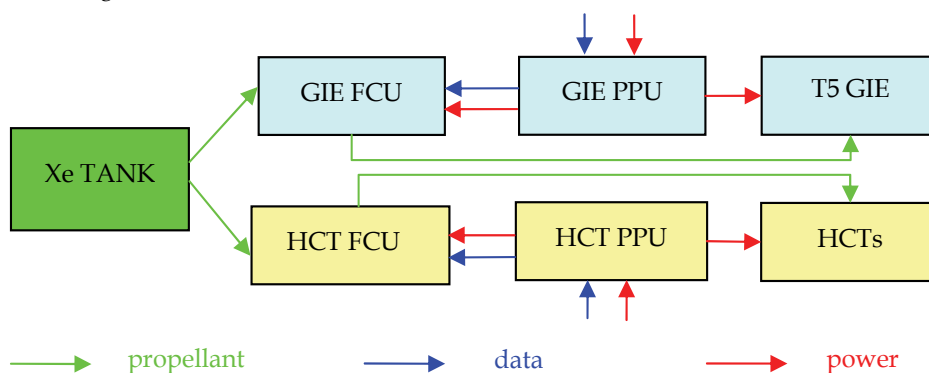


Fig. 1. First SEP subsystem architecture option: high mass, low risk, low cost

This is the option with the lowest risk and cost. Only the propellant tank is shared between the main propulsion and AOCS propulsion systems, hence leaving the more critical (and more expensive) components, such as the flow control units and the power processing units, unaltered. The low level of risk and cost is reflected in a low level of integration but results in a high system mass.

Option 2 - Medium mass, low risk, low cost

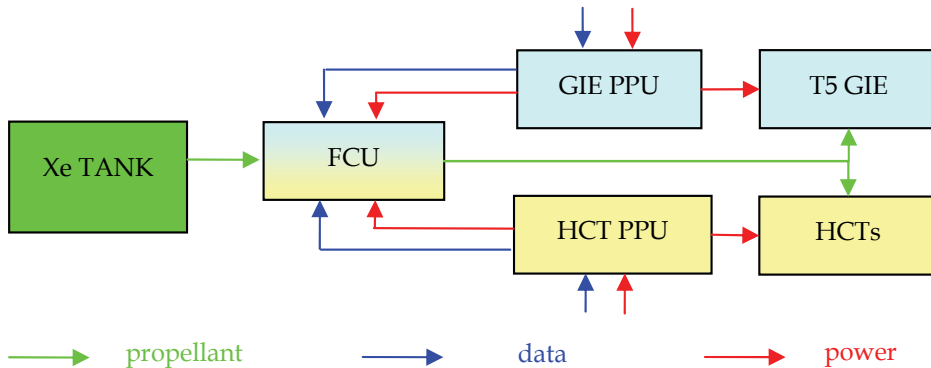


Fig. 2. Second SEP subsystem architecture option: medium mass, low risk, low cost

This option differs from the first by integrating the GIE and HCT flow control units into a single FCU. This provides a reduction of the system mass, whilst the cost and risk are kept relatively low since the PPUs (regarded as the most critical component) are left unmodified. Separate PPUs, able to supply the T5 GIE and the T5 HCTs already exist. An integrated PPU, able to supply both a GIE and several HCTs requires development and so will bring a high level of cost.

Option 3 - Low mass, high risk, high cost

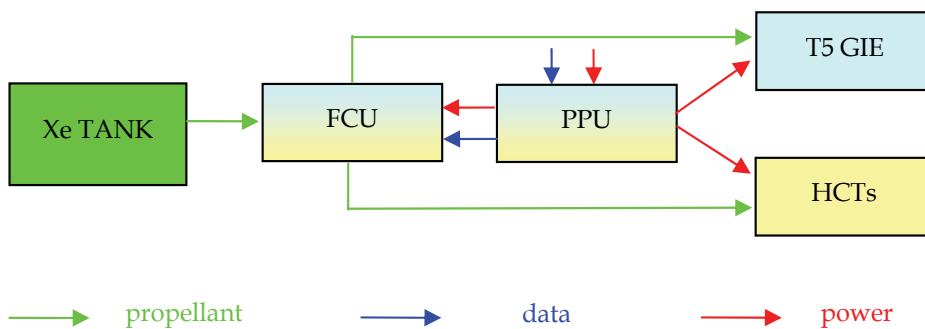


Fig. 3. SEP subsystem architecture option three: low mass, high risk, high cost

The level of integration is maximized in this final option, with the tank, PPU and FCU all being shared between the GIE and the HCTs. This leads to the lowest achievable system mass but conversely results in a high level of risk, since a new PPU must be designed able to supply both the GIE and several HCTs.

Considering that this study was carried out for a student mission with strict budget constraints, and that an EP mission to the Moon is in itself challenging, option 2 was

selected since it provides a low level of risk, whilst providing a medium level of integration and a relatively low system mass in comparison to the two non-integrated systems.

Once the general architecture has been fixed two other tradeoffs were carried out.

The first concerns compensation of the torque caused by any thrust misalignment of the main engine. Considering the long duration of the mission, associated with the long transfer time from GTO to the Moon for a SEP subsystem, the amount of propellant needed for the HCTs to compensate the torque is not negligible. Three options are available to reduce the thrust misalignment of the main engine; use of a gimbal, use of thrust vectoring or the choice to use additional propellant and accept the losses.

Thrust vectoring can be achieved using a set of movable grids on the GIE (Jameson, 2007). This technique is still experimental and hence, due to the level of risk involved, this solution was discarded. A gimbal is a relatively heavy, complex and expensive component whereas carrying additional propellant would be by far the simplest approach, though adversely affecting the overall mass budget.

The second trade-off to be carried out concerned the operation of the HCTs. Two possible options were identified: one option was to utilize a dedicated HCT PPU, able to drive as many HCTs as required whilst also driving the main propulsion system, the second option involved use of a switchbox utilizing the neutralizer cathode supply present inside the T5 GIE PPU.

Overall, four options exist for the subsystem design:

- HCTs driven by a dedicated PPU.
- HCTs driven by the neutralizer supply inside the T5 PPU via a switchbox.
- HCTs driven by a dedicated PPU plus a gimbal to reduce thrust misalignment.
- HCTs driven by the T5 PPU via a switchbox plus a gimbal to reduce thrust misalignment.

A comparison between all these options is reported in Table 2.

It is evident from Table 2 that the use of a gimbal produces a significant increase to the overall AOCS related mass. This option was therefore discarded.

The mass of the two remaining options differs by 4kg, due to the presence (or not) of a dedicated HCT PPU. These two options were traded against each other due to the cost and operational impact that the presence of a dedicated HCTs PPU would have.

The cost related to the development of a dedicated HCTs PPU would be substantial, based on estimates provided by QinetiQ; the cost would be twice that for development of a switchbox.

Regarding operation of the spacecraft, it must be noted that a switchbox offers no flexibility in the operation of the GIE and HCTs, since each time the HCTs must be used, the GIE must be switched off. Considering that the HCTs will be needed for a period from 1/3 to 1/6 of each orbit, the use of a switchbox would significantly reduce the average thrust produced by the GIE and consequently increase the transfer phase length and propellant required. The use of a dedicated PPU will instead allow both the main thruster and the HCTs to operate at the same time though, due to the limited power availability, the T5 GIE will have to be throttled down to free enough power for the HCT operations. More importantly, not having to switch off the main thruster each time the HCTs are used and perform a GIE shut-down and start-up procedure, management of the thruster subsystem is simplified.

Following the trade off studies, the use of a dedicated HCT PPU was chosen as the baseline option.

	Dedicated HCTs PPU without gimbal		Dedicated HCT PPU with gimbal		Switchbox without gimbal		Switchbox with gimbal	
	Mass	Margin	Mass	Margin	Mass	Margin	Mass	Margin
Thrust misalignment propellant mass	3 Kg	20%	0 Kg	20%	3 Kg	20%	0 Kg	20%
Solar pressure, safe manoeuvres and initial despin	1 Kg	20%	1 Kg	20%	1 Kg	20%	2 Kg	20%
HCT PPU	4 Kg	15%	4 Kg	15%				
gimbal			7 Kg	5%			7 Kg	5%
Switchbox					0.5 Kg	20%	0.5 Kg	20%
Total AOCS related mass	9.4 Kg		13 Kg		5.4 Kg		10.35 Kg	

Table 2. Comparison between a dedicated HCTs PPU and a switchbox with or without a gimbal

4. SEP baseline design description

The baseline design comprises:

- A single flight spare T5 GOCE GIT
- Eight HCTs (to provide some level of redundancy)
- A T5 PPU
- A HCT PPU
- A FCU able to supply both the HCTs and the T5 GIT
- A pressurized Xenon tank

4.1 T5 gridded ion thruster

The QinetiQ T5 Ion Thruster is a conventional electron bombardment, Kaufman-type GIE (a schematic of which is shown in Fig. 4).

In this kind of thruster a DC discharge is established between a hollow cathode (HC) and a cylindrical anode. The energetic electrons emitted from the HC collide with neutral propellant atoms injected upstream, resulting in ionization. The efficiency of the ionization is enhanced by the application of an axial magnetic field to constrain the electron motion. The ions produced are then extracted and accelerated by a system formed of two perforated disks (called grids), across which a potential difference of about 1.5 kV is applied. An external HC, referred to as the neutraliser, emits the electrons necessary to neutralise the space charge of the emerging ion beam.

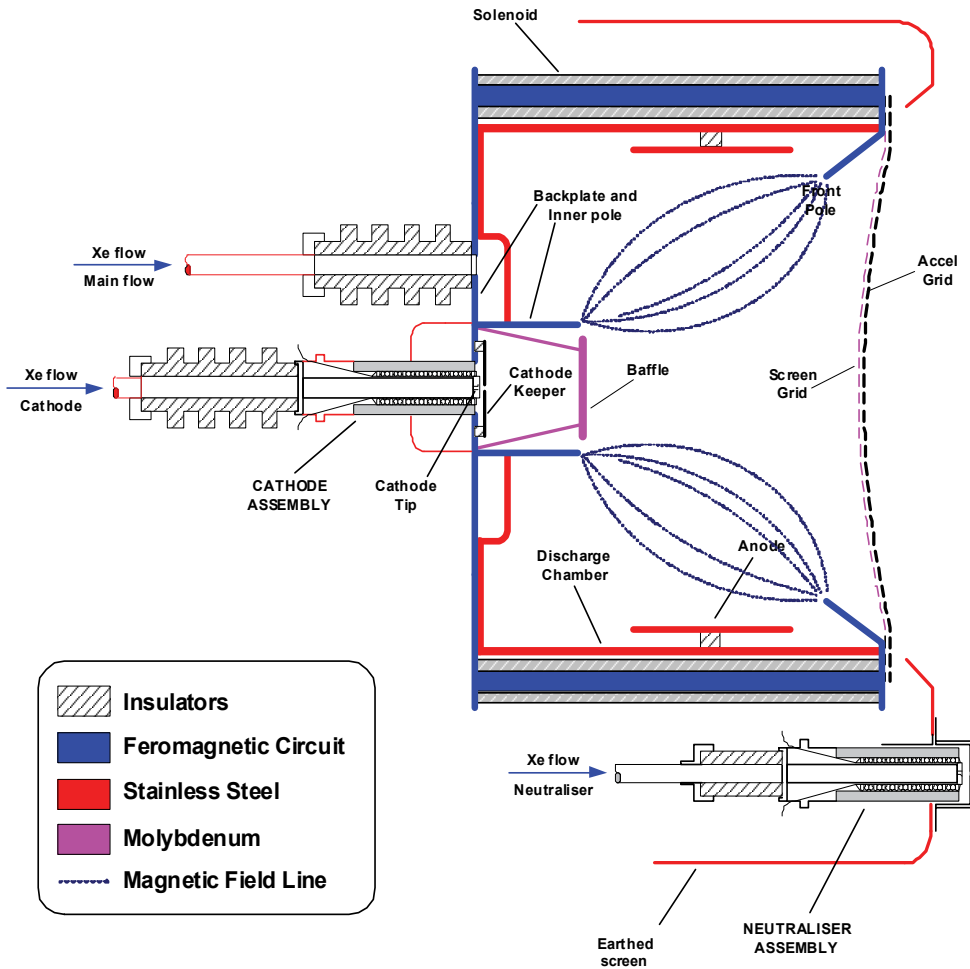


Fig. 4. A Kaufmann type gridded ion thruster schematic (T5) (image courtesy of QinetiQ)
 The T5 GIT specifications for the GOCE application are reported in Table 3

Mass	1.7 kg
Dimensions	Ø 170 mm x 200 mm long
Mean Power Consumption	up to 600 W @ 20mN
Thrust Range	1 to 20 mN
Specific Impulse	500 s to 3500 s (across thrust range)
Total Impulse	> 1.5 x 10 ⁶ Ns (under GOCE continuous throttling conditions)
T5 capability	> 8500 On/Off cycles

Table 3. T5 GIT specification (GOCE)

4.2 T5 Power processing unit

The power processing unit will be used to drive the T5 GIE and the T5 FCU will be similar to the EADS Astrium Crisa GOCE PPU (Tato, de la Cruz, 2007). The PPU includes both a high voltage and a low voltage supply with the associated telemetry. The high voltage supply will be used to apply the required potential for the first of the two grids, whereas the low voltage supply will be used to operate the neutralizer and apply the potential for the second of the thruster grids. A schematic of the PPU is displayed in Fig. 5 whilst specifications are reported in Table 4.

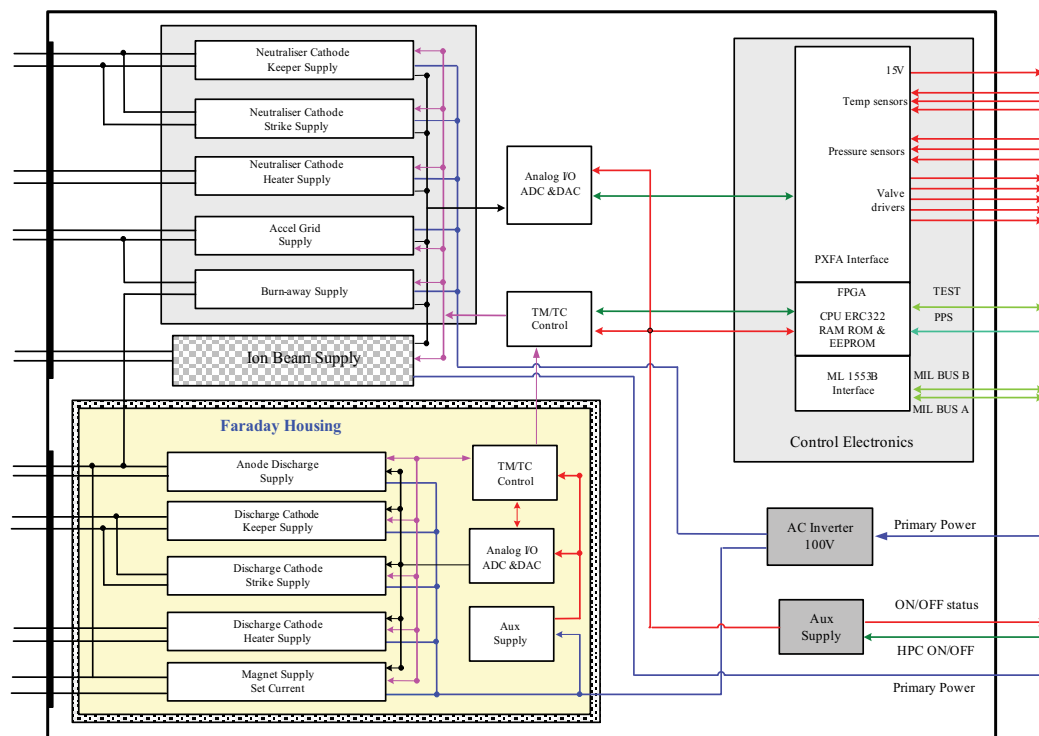


Fig. 5. GOCE PPU schematic (image courtesy of EADS Astrium Crisa)

Mass	16 kg
Dimensions	300 x 250 x 150 mm
Operating temperature	-20 °C to +50 °C
Operating lifetime	15 years in orbit (GOCE PPU qualification to mission duration of 2 years)
Nominal input voltage	22 - 37 V extended input range to 20 V without degradation
Maximum input current	37 A @ 22 V
Power	55-585 W
Electrical efficiency	Beam supply 92 - 95% other supplies \geq 92%

Table 4. T5 GOCE PPU specification

4.3 Hollow cathode thruster

The thrust generated by a hollow cathode thruster in open-diode configuration (HC and a single anode) has been extensively characterized at the University of Southampton (Grubisic, 2009).

The basic feasibility of a HCT has been demonstrated and thrust levels up to several mN have been measured with specific impulse of the order of hundreds of seconds. More recently in light of its beneficial electrical characteristics, a T5 hollow cathode has undergone preliminary thrust characterization for application on ESMO. The experiment used a T5 STRV-A1 (Space Technology Research Vehicle) DRA (Defence Research Agency) flight-spare cathode launched in June 1994. This included an experiment to allow the hollow cathode assembly to demonstrate spacecraft electrostatic discharging. The cathode is rated at a maximum DC current of 3.2A at flow rates typically $0.04 - 1\text{mgs}^{-1}$ operating below 90W. The T5 cathode was originally designed for the main discharge cathode in the UK-10 ion engine and has been extensively characterized (Crofton, 1996). The cathode assembly contains a tungsten dispenser, 1.0mm ID \times 2.8mm OD \times 11mm, impregnated with a mixture of barium-oxide, calcium oxide and aluminates ($\text{BaO} : \text{CaO} : \text{Al}_2\text{O}_3$), which lowers the insert's work function for thermionic emission and maintains a working temperature of $\sim 1000^\circ\text{C}$. A solid tantalum tip welded to the cathode body contains an axial orifice 0.2mm in diameter and 1mm long. The face of the T5 cathode is shown in Fig.6.



Fig. 6. T5 Hollow Cathode Thruster

The open keeper has a 3mm diameter aperture and is mounted 3mm downstream of the cathode tip, with the whole assembly mounted on a UK-25 ion thruster back-plate. In typical hollow cathodes a keeper electrode usually draws approximately 1A of current, however in this study the cathode is operated in an open-diode configuration with the full discharge current being drawn to the keeper, which is now termed the anode. Previous studies on this type of hollow cathode have incorporated a much larger anode disk and a secondary discharge between the keeper and the anode and applied magnetic fields to simulate a Kaufman ion engine environment.

Open-diode configuration is more representative of a standalone microthruster configuration with no need for a coupled discharge. Results for the various current conditions are shown in Fig. 7.

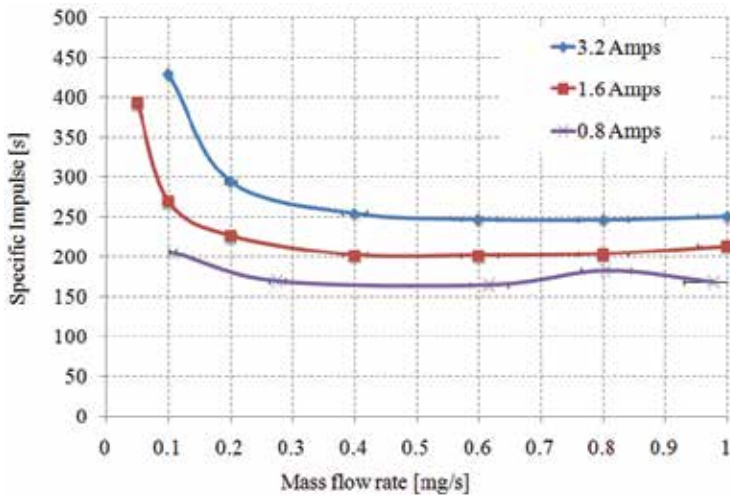


Fig. 7. Measurements of specific impulse with mass flowrate

Results show near monotonic dependence of specific impulse on discharge current with rapidly increasing performance below 0.4 mg/s^{-1} for the 3.2 and 1.6 Amp throttle settings with a less pronounced increase at 0.8 Amps. Since a change in flow rate results in a change in operating voltage it is seen that specific impulse can be correlated with specific power of the flow (J/mg) and a product of the discharge current and operating voltage, shown in Fig. 8. Operation at low powers ($<13\text{W}$) in the low current condition (0.8Amp) brings relatively high specific impulse of up to 165 seconds. At the high current condition operation at powers below 30W give specific impulse in the region of 250s. Further reduction in flow rate increases operating voltage and power invested in the flow. This results in a quadratic increase in specific impulse with declining thrust efficiency as convective and radiative losses begin to dominate.

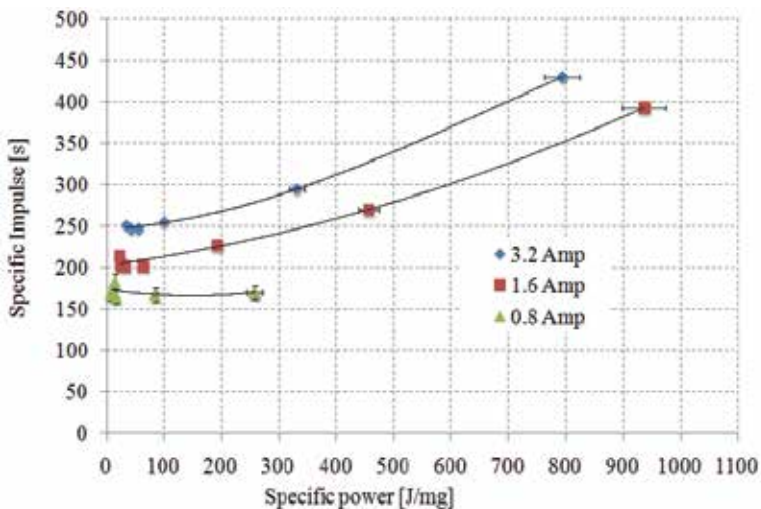


Fig. 8. Dependence of specific impulse on specific power at the various current levels with argon for the T5FO cathode

The highest specific impulse of 429s was attained at 3.2 Amps, with 1.1% thrust efficiency, 79W discharge power. Specific impulse can be traded for higher thrust to power ratios by increasing propellant flow rates or decreasing discharge current (however higher thrust efficiencies are obtained at higher discharge currents) generating thrust efficiencies of 14% ($200\mu\text{N/W}$) and specific impulse of 167s at 0.8Amps, and over 8% at the maximum rated current capacity of 3.2 Amps, with specific impulse $\sim 250\text{s}$ ($77\mu\text{N/W}$, 35W discharge power). Thrust production with respect to specific impulse is shown in Fig. 9. Up to 2.4mN could be generated at higher currents, with the maximum flow rate of $1\text{mg}\cdot\text{s}^{-1}$ with specific impulse over 250s.

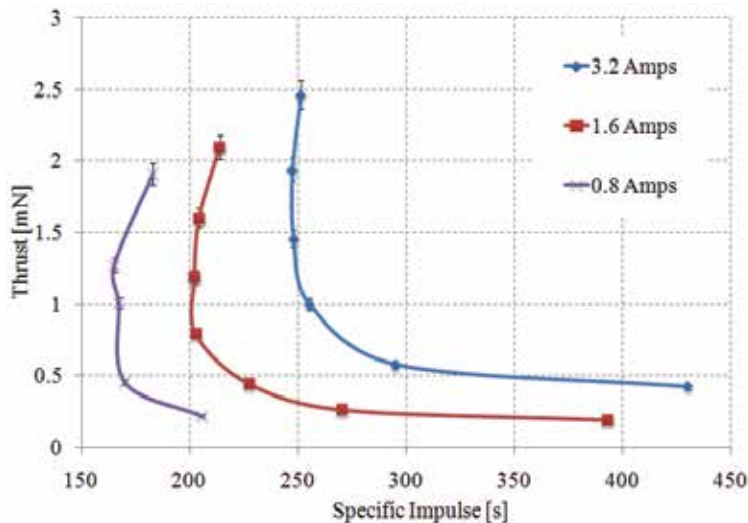


Fig. 9. Thrust and specific impulse attained at various current conditions in the T5 cathode

4.4 Hollow cathodes thruster PPU

The HCT PPU is sketched in 10.

The HCTs PPU consists of two anode and heater supplies and of a high voltage strike supply. The anode and heater supply is used to power the cathode heater during the start up phase and then, once the cathode is started using the HV strike supply, to power the cathode keeper to sustain its discharge. Two anode and heater supplies are present to allow the use of two HCTs at the same time that can be selected thanks to a system of switches. A mass estimate for this HCT PPU is 4 kg.

The anode and heater power supply is taken from the T6 neutralizer cathode PPU and is able to provide $3\text{A}@90\text{W}$. Such a supply is over-sized for a T5 hollow cathode (as can be seen from the data in Section 4.3) hence further study will be carried out to verify the possibility of powering two hollow cathodes in series (in this case with the PPU here presented we will be able to power four HCTs or alternatively we can use only one keeper heater supply saving mass).

4.5 Flow Control Unit

A suitable design for the FCU has been developed in collaboration with Thales Alenia Space (Matticari et al., 2005; Matticari et al., 2006; Van Put et al., 2004; van der List et al., 2006).

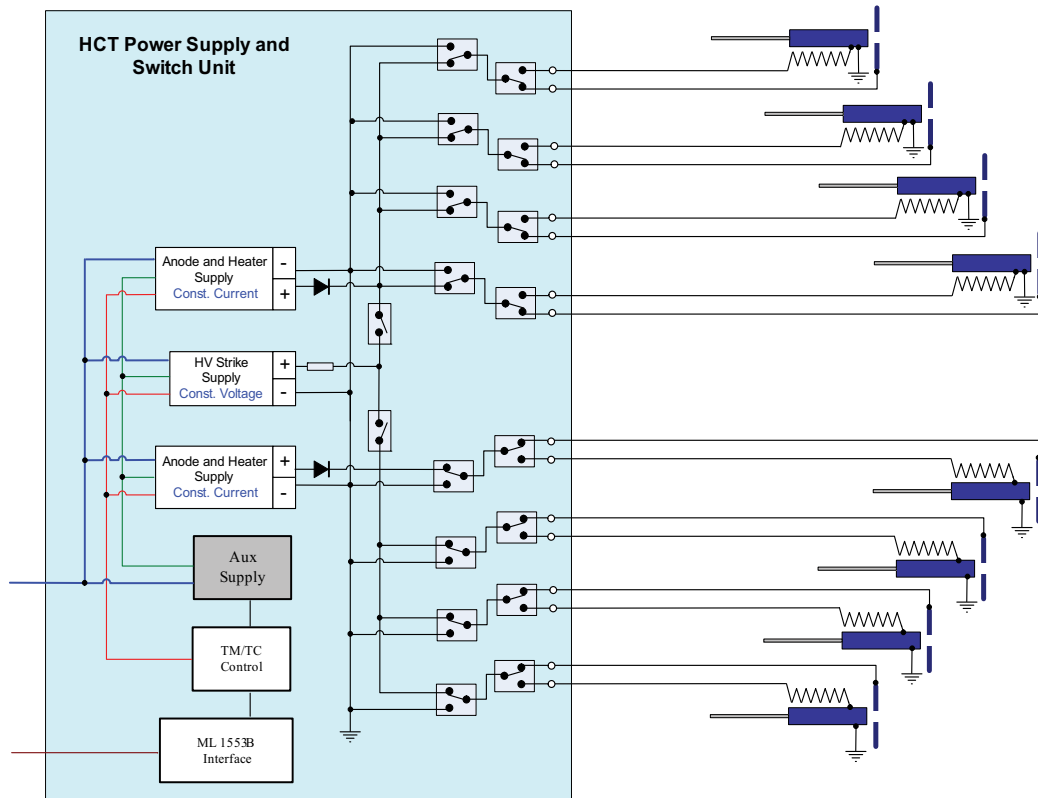


Fig. 10. HCT PPU schematic

Component	Mass flow rate [mg/s]	Pressure
T5 GIT	$0.07 - 0.53 \pm 0.007$	13 mbar (gas flow only) 20 mbar (gas flow & discharge)
T5 discharge cathode	0.1 ± 0.007	10 mbar (gas flow only) 100 mbar (gas flow & discharge)
T5 neutralizer	0.041 ± 0.006	10 mbar (gas flow only) 100 mbar (gas flow & discharge)
HCT	0.5 - 1.5	100 mbar ~ 1 bar (cold gas mode)

Table 5. Pressure and mass flow requirements

The design of the FCU, able to supply propellant to both the T5 GIE and to the HCTs, assumes that the HCTs will always be operated in pairs. Pressure and mass flow requirements are reported in Table 5.

The FCU is designed with a mass of 4 kg and a volume of approximately 300x200x100 mm. A schematic of the PPU is reported in 11.

The first element of the FCU is a gas purifier (F) needed to remove any impurities present in the Xenon gas supplied from the tank. After the filter, two high pressure solenoid valves (HPPV) used in closed loop with a low pressure transducer (LPT) and a mass flow sensor (MFS), regulate the pressure and mass flow rate to the value required for the HC. Two HPPV are used to provide redundancy in the high pressure branch of the FCU.

After MFS1 the flow is divided between the HCTs and the T5 thruster system. When the HCTs are off the flow is routed to the T5 thruster system. The HPPV is used to regulate the pressure required for the discharge/neutralizer HC and the T5 thruster according to system demands, hence there is no need to use LPPV1 and MFS2. LPPV2 and MFS3 are then used to fix the pressure and mass flow for the T5 GIT while LPC1 and LPC2 are used to regulate the mass flow rate to the neutralizer and discharge cathodes. If the HCTs are turned on, the relative on/off valves are opened. HPPV will be used to regulate pressure according to the HCT requirements and the mass flow rate according to the whole system's needs. LPPV1 and MFS2 will regulate the pressure and mass flow according to the T5 thruster system, hence LPPV2, MF3, LPC1 and LPC2 will work as if the HCTs are off. The LPCs will work such that the mass flow rates in two HCTs relative to the same axis are equal.

4.6 Propellant tank

The baseline propellant budget for the ESMO mission is shown in Table 6.

Propellant requirement	Xenon (Kg)	System margin	Xe with all margins
Transfer from GEO to low moon orbit	18.9 Kg	2%	19.8 Kg
Attitude control and initial despun	4 Kg	20%	4.8 Kg
Residuals		1.5%	0.4 Kg
Total mass			25 Kg

Table 6. Baseline ESMO propellant budget

The budget comprises the propellant processed by the T5 GIE needed for the transfer from GTO to lunar orbit, the propellant needed for the AOCS manoeuvres that is to be used by the HCTs and also any residual propellant that cannot be extracted from the tank (where 1.5% is a typical figure for this type of system). The propellant tank must be able to hold a minimum of 25 kg of Xenon. The Xenon storage pressure will be chosen from the Xenon isotherm curves reported in Fig 12. As it can be seen from Fig 12, the use of storage pressures higher than 100-150 bar does not produce any sensible reduction in volume, whilst it would produce a significant increase in mass, due to the higher pressure loads of the tank structure.

A 100 bar tank pressure was chosen as a baseline assuming room temperature (worst case); this results in 18 litres volume for 25 kg of Xenon whereas at 150 bar the tank volume is 15.3 litres. After performing a market search, a suitable tank was identified with the characteristics given in Table 7.

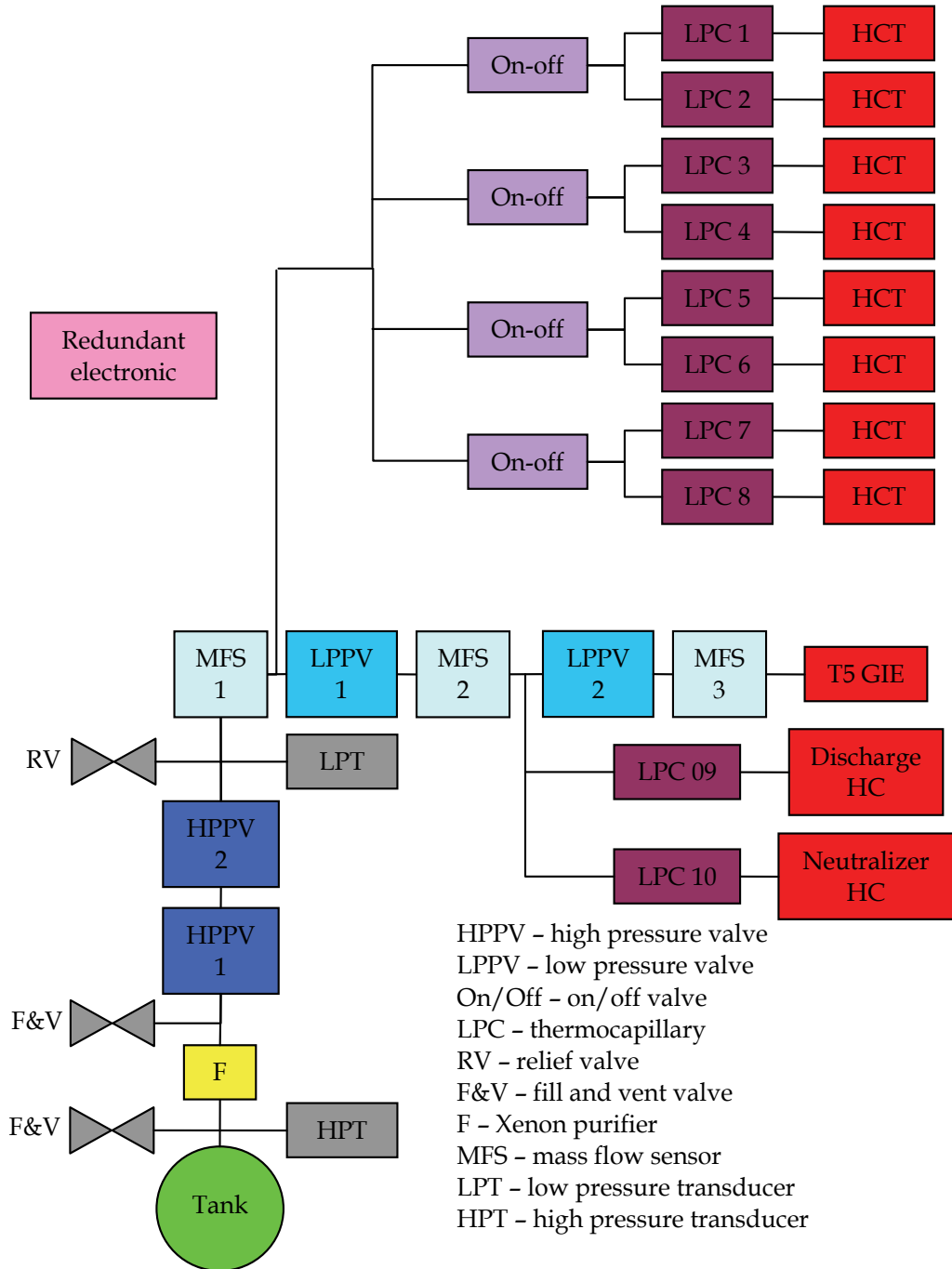


Fig. 11. Flow Controller Unit schematic

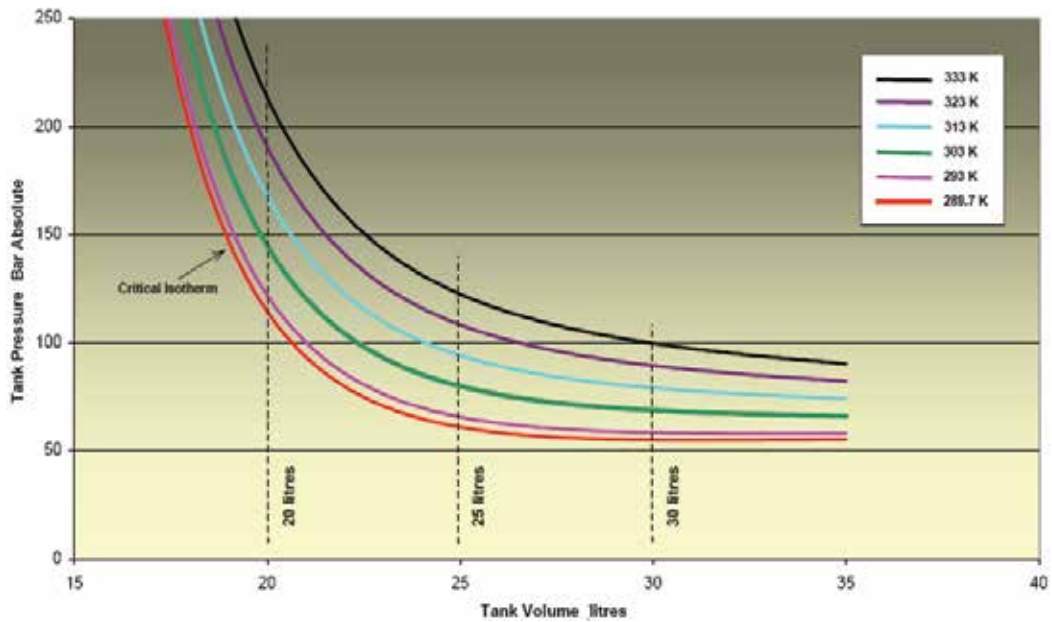


Fig. 12. Xenon isotherms for 30 Kg of Xenon

Shape	Cylindrical
Volume	19 litres
Mass	5 Kg
Maximum operating pressure (MEOP)	150 bar
Proof pressure	1.2 MEOP
Burst Pressure	1.5 MEOP
Material	Titanium T1000 liner with carbon fibre filament winding

Table 7. Thales Alenia Space Italia tank specifications

5. Conclusions

The full design of a solar electric propulsion subsystem for an all electric spacecraft has been presented which is applicable for the ESA ESMO mission.

The proposed propulsion subsystem is able to satisfy all mission requirements and achieves a medium level of integration between components providing non negligible mass savings. Table 9 displays a breakdown of the total subsystem mass.

Component	Mass
T5 GIT	1.7 Kg
GOCE-like PPU	16 Kg
FCU	4 Kg
8 x HCTs	0.8 Kg
HCT PPU	4 Kg
Tank	5 Kg
Propellant	31 Kg
Total Subsystem Mass	62.5 Kg

Table 8. ESMO Subsystem mass

The dry mass of the proposed SEP subsystem (31 kg) in this study can be compared to that of the SMART-1 electric propulsion subsystem of 29 kg (Kugelberg et al., 2004). The SMART-1 SEP subsystem comprises only a primary propulsion system, whereas the SEP subsystem in this study comprises both main and AOCS propulsion at a cost of only two extra kilograms.

6. Acknowledgments

The authors would like to thank Nigel Wells, Neil Wallace, Dave Mundy, Chris Dorn and Bill Levett from QinetiQ, Roger Walker from ESA (ESMO project manager) and Piero Siciliano and Mario Pessana from Thales Alenia Space for all their help and advice.

7. Appendix A. nomenclature

AOCS	=	attitude orbit and control subsystem
ESOC	=	European Space Operations Centre
F	=	Xenon purifier
FCU	=	flow control unit
F&V	=	fill and vent valve
GIT	=	gridded ion thruster
HCT	=	hollow cathode thruster
HPPV	=	high pressure valve
HPT	=	high pressure transducer
ID	=	internal diameter
LPC	=	thermocapillary
LPPV	=	low pressure valve
LPT	=	low pressure transducer
MFS	=	mass flow sensor
OD	=	outer diameter
On/Off	=	on/off valve
PPU	=	power processing unit
RV	=	relief valve
SEP	=	solar electric propulsion

8. References

- M. Crofton, "Evaluation of the United Kingdom Ion Thruster" *J. Spacecraft and Rockets*, Vol. 33, No. 5, 1996, pp. 739-747
- A. Grubisic, "Microthrusters Based on the T5 and T6 Hollow Cathodes", PhD Thesis, Aeronautics and Astronautics, University of Southampton, Southampton, 2009
- C. Tato and F. de la Cruz, "Power Control Unit for Ion Propulsion Assembly in GOCE Program," IEPC-2007-295, International Electric Propulsion Conference, Florence, Italy, September, 2007
- G. Matticari, G.E. Noci, P. Siciliano, G. Colangelo, R. Schmidt, "*Cold Gas Micro Propulsion Prototype for Very Fine Spacecraft Attitude/Position Control*", AIAA-2006-4872, 42nd AIAA/ASME/SAE/ASEE Joint Propulsion Conference and Exhibit, Sacramento, California, July 9-12, 2006
- G. Matticari, G.E. Noci, P. Siciliano, G. Martini, A. Rivetti, N. Kutufa, "*New Generation Propellant Flow Control Components: Status of Achievement at Alcatel Alenia Space Italia/Laben-Proel*", IEPC-2005-23, 29th International Electric Propulsion Conference, Princeton University, New Jersey, October 31 - November 4, 2005
- N. Wells, R. Walker, S. Green, A. Ball, "*SIMONE: Interplanetary Microsatellites for NEO Rendezvous Missions*", *Acta Astronautica* 59(8-11), 700-709, 2006.
- P. van Put, M. van der List, V. Yuce, "Development of an Advanced Proportional Xenon Feed Assembly for the GOCE Spacecraft", 4th International Spacecraft Propulsion Conference, Chia Laguna (Cagliari), Italy, 2-9 June, 2004.
- M. van der List, P. van Put, V. Yuce, J. Kuiper, "Next Generation Electrical Propulsion Feed Systems and Spin-off Micro-Propulsion Components ", ISU 2006 Conference, Strasbourg, France, 3-6 August 2006.
- N. Wells, R. Walker, S. Green, A. Ball, SIMONE: interplanetarymicrosatellites for NEO rendezvous missions, *Acta Astronautica*, 59 (8-11) (2006) 700-709.

Green Propellants Based on Ammonium Dinitramide (ADN)

Anders Larsson and Niklas Wingborg
*FOI – Swedish Defence Research Agency,
Sweden*

1. Introduction

Ammonium perchlorate (AP) and hydrazine are today widely used as propellants. AP as oxidizer in solid propellants and hydrazine as liquid monopropellant (Brown, 1995; Sutton and Biblarz, 2001). These propellants are well known for their good performance characteristics, but their limitations and liabilities regarding toxicity, operational handling and environmental impact are also well documented.

Perchlorate contamination is becoming a more widespread concern in the United States (EPA, 2005). In 2009, a workshop organised by the US Department of Defence identified AP as one of the key environmental, safety and occupational health issues (DoD, 2009). Perchlorate anions (ClO_4^-) has been found in drinking water supplies throughout the south-western United States, and perchlorate may be a problem for water supplies in some regions of the USA (Urbansky, 2002). At high concentrations, perchlorate can affect thyroid gland functions, where it is mistakenly taken up in place of iodide. Apart from impacting the thyroid activity in humans, AP forms vast amount of hydrochloric acid on combustion. For instance the space shuttle and the Ariane 5, generates 580 and 270 tons of concentrated hydrochloric acid, respectively, per launch (Wingborg et al., 2008).

Hydrazine is highly toxic and carcinogenic (ATSDR, 1997; Ritz et al., 2006), and handling it requires costly safety measures. A less toxic monopropellant is expected to offer substantial cost savings (Bombelli et al., 2003; Palaszewski et al., 1998; Hurlbert et al., 1998). These economic benefits were analysed and quantified in a study funded by the European Space Agency (ESA) and were considered sufficiently large to support interest in the development of hydrazine substitutes and related propulsion hardware (Bombelli et al., 2004).

Propellants of the future must not present major hazards to the crew or ground handling personnel. The use of green propellants would greatly reduce the risks associated with toxicity, operational handling complexity, spacecraft contamination, and hazardous contamination of the environment. Green propellants have also shown promise from a system performance and total life cycle cost perspective. One material that has the potential to replace AP as well as hydrazine is ammonium dinitramide (ADN), $\text{NH}_4\text{N}(\text{NO}_2)_2$.

2. Ammonium dinitramide, ADN

ADN is a high-energy inorganic salt, mainly intended as oxidizer in solid rocket propellants (Bottaro et al., 1997; Christie et al., 1996; Östmark et al., 2000). ADN was first synthesized in

1971 at the Zelinsky Institute of Organic Chemistry in Moscow, USSR, and is one of the most significant discoveries in the field of energetic materials (Agrawal and Hodgson, 2006). It is claimed that ADN-based solid propellants are in operational use in Russian Topol intercontinental ballistic missiles (Talawar et al., 2007) and that ADN previously was produced in ton-size quantities in the former USSR (Teipel, 2004). The USSR's dinitramide technology was strictly classified and unknown to the rest of the world until 1988 when it was "re-invented" at SRI (Bottaro et al., 1997) in the USA. In the beginning of the 1990s, FOI in Sweden started research on ADN in order to develop high performance solid propellants. During this development work, it was found that ADN was highly soluble in polar solvents, which led to the realization that it also could be used as an oxidizer in liquid propellants.

2.1 Basic properties of ADN

ADN (cas nr. 140456-78-6) is a solid white salt of the ammonia cation (NH_4^+) and the dinitramide anion ($\text{N}(\text{NO}_2)_2^-$), Fig. 1. It has a high oxygen balance, +25.79 %, melts at 93 °C and starts to decompose at approximately 150 °C at a heating rate of 10 K per minute, as seen in Fig. 2. Similarly to ammonium nitrate, ADN is hygroscopic and readily soluble in water and other polar solvents but scarcely soluble in non-polar solvents. The solubility of ADN in different solvents is shown in Table 1 (Wingborg et al., 2008), and the phase diagram for the system ADN-water is shown in Fig. 3 (Wingborg, 2006). The critical relative humidity for ADN is 55.2 % at 25.0 °C (Wingborg, 2006). This means that the relative humidity must be below 55.2 % to prevent ADN from absorbing moisture from the atmosphere. The density of ADN in the solid state is 1.81 g/cm³ (Östmark et al., 2000). Its molar volume and corresponding density in the liquid state at 25.0 °C is 74.08 g/mol and 1.675 g/cm³ respectively (Wingborg, 2006). Some of the physical properties of ADN are summarized in Table 2, and information concerning its toxicological properties are shown in Table 3.

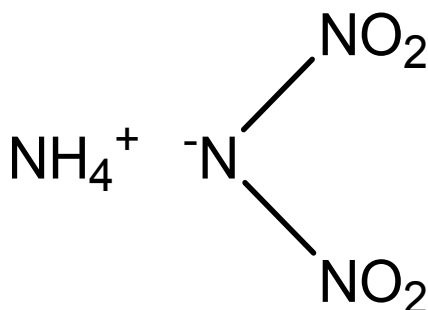


Fig. 1. The structure of ADN.

Solvent	Solubility in 100 g solvent (g)
Water	357
Methanol	86.9
Butyl acetate	0.18
N-heptane	0.005
Dichloromethane	0.003

Table 1. ADN solubility at 20.0 °C (Wingborg et al., 2008).

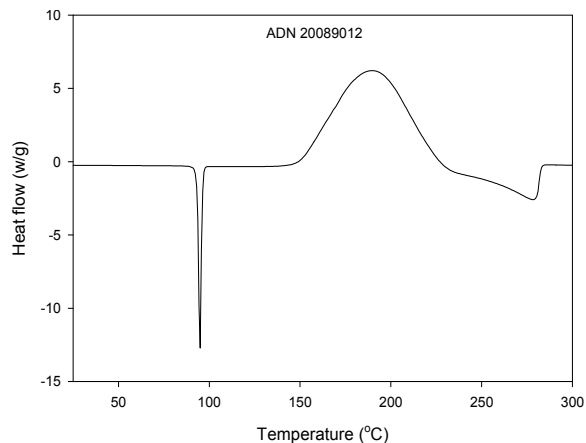


Fig. 2. Differential Scanning Calorimetry (DSC) thermogram of ADN. Heating rat 10 K/min.

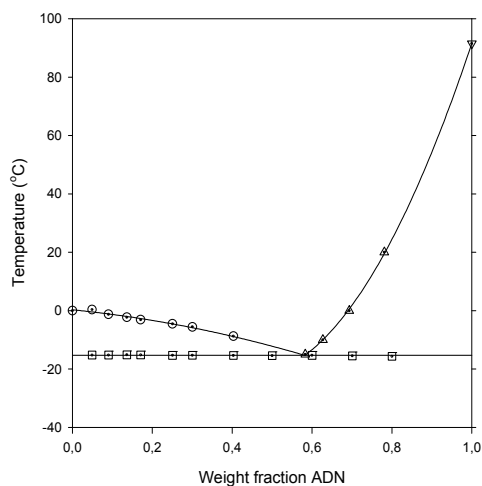


Fig. 3. Solid-liquid phase diagram for the system ADN-water (Wingborg, 2006).

Property	Value	Reference
Molecular weight	124.07 g/mol	
Mass density (solid)	1.81 g/cm ³	(Östmark et al., 2000)
Mass density (liquid)	1.675 g/cm ³	(Wingborg, 2006)
Melting point	93 °C	
Heat of melting	142 J/g	
Heat of formation	-148 kJ/mol	(Östmark et al., 2000)
Heat of combustion	424 kJ/mol	(Wingborg, 2006)
Heat of solution	35.7 kJ/mol	(Wingborg and de Flon, 2010)
Oxygen balance	+25.79 %	(Wingborg, 2006)
Molar volume (liquid)	74.08 g/mol	(Wingborg, 2006)
Critical relative humidity	55.2 %	(Wingborg, 2006)

Table 2. Properties of ADN at 25.0 °C unless otherwise stated.

Acute inhalation toxicity	Inhalation of dust may cause irritation to mucous membrane of the respiratory organ. Long-time exposure may cause problems as feeling of weakness, dizziness, indisposition and sleeping problems
Ingestion	Can cause the same symptoms as inhalation. Risk also for blood damage (anaemia), epileptic convulsion and to become unconscious
Sensitisation	Non-sensitizing
Irritant effect on skin	Rabbit test: non-irritant
Irritant effect on eyes	Rabbit test: non-irritant
LD ₅₀ (oral rat)	823 mg/kg (Kinkead et al., 1994)
LD ₅₀ (dermal rabbit)	>2000 mg/kg (Kinkead et al., 1994)
LC ₅₀	Not applicable ^b
Cancer/mutation/unborn child damage/reproduction	Toxicity study: Salmonella typhimurium: positive In vitro mammalian cell gene mutation test: negative

Table 3. ADN toxicological information^a.

a) Data from Pettersson (Pettersson, 2007) unless otherwise stated.

b) ADN is a salt and is thus not present in the gas phase.

2.2 Production of ADN

ADN can be synthesized by different methods and an overview of these has been described by Venkatachalam, et. al. (Venkatachalam et al., 2004). One viable method is based on direct nitration of salts of sulfamic acid by ordinary mixed acids (sulfuric and nitric), followed by neutralization and separation of the ADN formed, Fig. 4. This method was developed and patented by FOI in the mid 1990s (Langlet et al., 1997). The method was then scaled up and the technology was transferred to EURENCO Bofors in Sweden, which has been producing dinitramides in a pilot plant scale since 1996, on license from FOI. All chemicals involved in the method are standard industrial chemicals and thus no strategic materials are needed. Sulfamic acid is, for instance, used to produce sweeteners and as an ingredient in cleaning agents. Through the years, EURENCO Bofors has delivered samples to more than fifty research establishments and companies worldwide. By providing samples to a large community, a broader range of potential applications has emerged. Dinitramides are currently used in gas generators for automotive airbags, which is their first full scale application. For this application guanylurea dinitramide, GUDN (FOX-12) (Östmark et al., 2002), is used and EURENCO Bofors has produced GUDN in industrial scale since 2000.

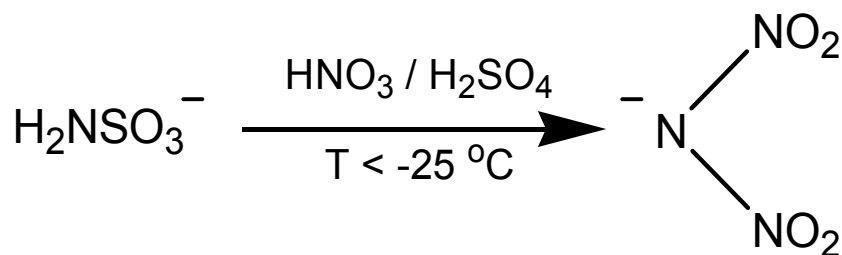


Fig. 4. Synthesis of dinitramide from sulfamic acid.

3. Solid propellants based on ADN

Solid propellants for space applications are today widely used in large boosters for launchers and, to some extent, for in-space propulsion. Propellants for these applications are based on the oxidizer ammonium perchlorate (AP), NH_4ClO_4 , and aluminium powder embedded in a polymer binder matrix. AP is in many ways an excellent oxidizer due to its relative low hazardness and the possibility to tailor its ballistic properties. However, AP has negative impacts on the environment and on personal health. By substituting AP with ADN there will be no hydrochloric emission since ADN only contains hydrogen, nitrogen and oxygen. Calculations show that ADN-based solid propellants can achieve performance equal to or higher than that of the conventional AP-based propellants (Wingborg et al., 2008).

Due to their large size, launcher boosters may not be the first application for a newly developed propellant. Smaller and less cost-sensitive applications seem to be a better choice. ADN-based solid propellants are thus more likely to initially be used for in-space propulsion applications. Today the majority of spacecrafts use liquid propulsion systems. Liquid rockets provide high performance and adjustable thrust, but they are complex, costly and use toxic propellants such as hydrazine, mono-methyl hydrazine (MMH) and nitrogen tetroxide (NTO).

When adjustable thrust is not required, solid propellants possess benefits such as storability, compactness and simplicity. No propellant delivery system is required which enables a huge improvement in reliability and cost. One disadvantage is however their relatively low specific impulse. Despite this, solid propellant rocket motors have been used to propel spacecrafts in numerous missions since first used in the upper stage of the first U.S. Satellite Explorer I in 1958. More recently solid propellant rocket motors are considered to be used for the ascend module in the Mars sample return mission (Stephenson and Willenberg, 2006). Replacing the AP-based propellants with ADN will provide higher performance and lower environmental impact.

3.1 Specific impulse

To perform a correct performance comparison between different propellants the complete propulsion system must be taken into account. This is a complex task and requires a specific spacecraft to be studied. In this case only the theoretical vacuum specific impulses were calculated for different ADN-based solid propellants and for the liquid bi-propellant combination NTO/MMH. The calculations were performed using the NASA CEA 600 computer program (Gordon and McBride, 1994; McBride and Gordon, 1996). An infinite area combustor and shifted equilibrium during expansion were assumed. Typical combustion chamber pressure for solid rocket motors (7 MPa) and liquid rocket engines (1 MPa) were used and the nozzle area expansion ratio were in all cases equal to 50.

The binder considered in combination with ADN was polyglycidylazide (GAP). GAP was chosen because it:

- is compatible with ADN
- improves performance
- provides good ballistic properties in combination with ADN.

The thermochemical inputs used in the calculations are shown in Tabela 4. The maximum solid loading in a propellant is generally limited by the viscosity of the uncured propellant slurry and must be low enough to allow casting. To obtain realistic results the maximum

solid loading was in this case limited to 80 %. The mixing ratio for the liquid bi-propellant combination NTO/MMH was two to one, similarly as used in the AESTUS rocket engine (ASTRIUM, 2007). The results from the thermochemical calculations are shown in Table 5. The results show that the theoretical specific impulse for ADN/Al/GAP with 20 % Al approaches that of NTO/MMH. At a solid loading of 80 %, the ADN-based propellants have densities 40 to 50 % higher compared to NTO/MMH. This implies that the density specific impulses ($\rho \cdot I_{sp}$) are about 30 to almost 50 % higher for the ADN-based propellants compared to NTO/MMH. Propellants with high Al-content is known to have lower performance than predicted due to Al particle agglomeration and two phase flow. Taking this into account ADN-based propellants still seems competitive due to their high densities.

Material	Formula	ρ (g/cm ³)	ΔH_f (kJ/mol)
ADN ^b	NH ₄ N(NO ₂) ₂	1.81	-148
Al	Al	2.70	0
GAP	C ₃ H ₅ N ₃ O	1.29	+114
MMH	CH ₆ N ₂	0.87	+54
NTO	N ₂ O ₄	1.45	-20

Table 4. Input for the thermochemical calculations^a.

a) all data from the ICT - Database (Bathelt et al., 2004) unless otherwise stated.

b) data from Östmark et al. (Östmark et al., 2000).

Propellant	Mixture	I_{sp} (s)	ρ (g/cm ³)	$\rho \cdot I_{sp}$ (gs/cm ³)
ADN/GAP	70/30	301	1.61	485
ADN/GAP	80/20	313	1.67	523
ADN/Al/GAP	70/10/20	327	1.73	566
ADN/Al/GAP	65/15/20	332	1.76	584
ADN/Al/GAP	60/20/20	335	1.78	596
NTO/MMH	2/1	340	1.19	405

Table 5. Results from the thermochemical calculations.

3.2 ADN prilling

A high solid loading is required to obtain high specific impulse. However, high solid loading increases the viscosity of the uncured propellant slurry. Thus, the maximum solid loading and impulse is limited by processing constraints. To obtain a castable propellant formulation with reasonable viscosity and high solid loading, particles with minimum spatial extension are required. For this reason the particles should have a low aspect ratio or more preferably spherical shape. The particle shape of ADN received from EURENCO is needle shaped and thus not suitable for formulation. Controlling the shape and size of ADN crystals is one of the most critical problems that have hampered the development of ADN-based propellants until now. At FOI, a method to produce spherical ADN particles, prills, have been developed (Johansson et al., 2006). The prills are produced by spraying molten ADN through a nozzle. In the nozzle the molten ADN is atomized to form droplets which then solidify to the desired prills seen in Fig. 5. The particle size can be controlled to some extent by varying spray nozzle size and pressure. Typical particle size distributions for the fine and coarse prills produced are shown in Table 6 and Fig. 6.

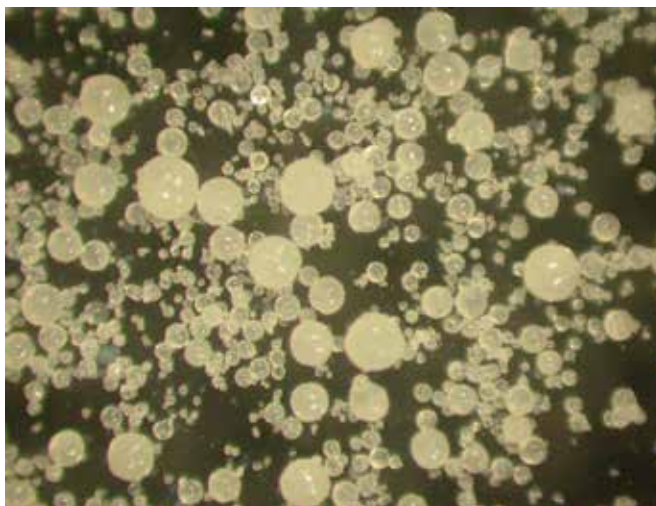


Fig. 5. Spray-prilled ADN.

Currently the prills are produced using up to 250 g ADN per batch. However, with modifications the method can be run continuously making the technology suitable for industrial production. Fumed silica (Cab-O-Sil) is added to the prilled material as an anti-caking agent. Without any anti-caking agent, the prilled ADN cakes after a short time of storage, even at dry conditions. The prills were characterized with respect to particle density, tap density, melting point and purity. The results are shown in Table 7. Properties of as-received ADN are shown for comparison. From the results in Table 7 it can be seen that the particle density decreases by 1 %, but the tap density of the prilled material increases by 30 %, which is important to obtain high solid loading. The decrease in particle density might be due to inclusions formed during the spraying. The somewhat higher nitrate content in the prilled material is due to degradation of ADN during the prilling and is probably responsible for the change in melting point.

Grade	d_{10} (μm)	d_{50} (μm)	d_{90} (μm)
Fine	30	60	120
Coarse	30	200	400

Table 6. Typical particle size distributions of prilled ADN.

	As received	Prilled
Amount Cab-O-Sil (%)	-	0.5
Particle density (g/cm^3)	1.81	1.79
Tap density (g/cm^3)	0.86	1.11
Volumetric loading (%)	47.5	62.0
Melting point ($^{\circ}\text{C}$)	93.2	92.5
Nitrate content (%)	0.03	0.08

Table 7. Typical properties of as-received ADN and coarse prills (Eldsäter et al., 2009).

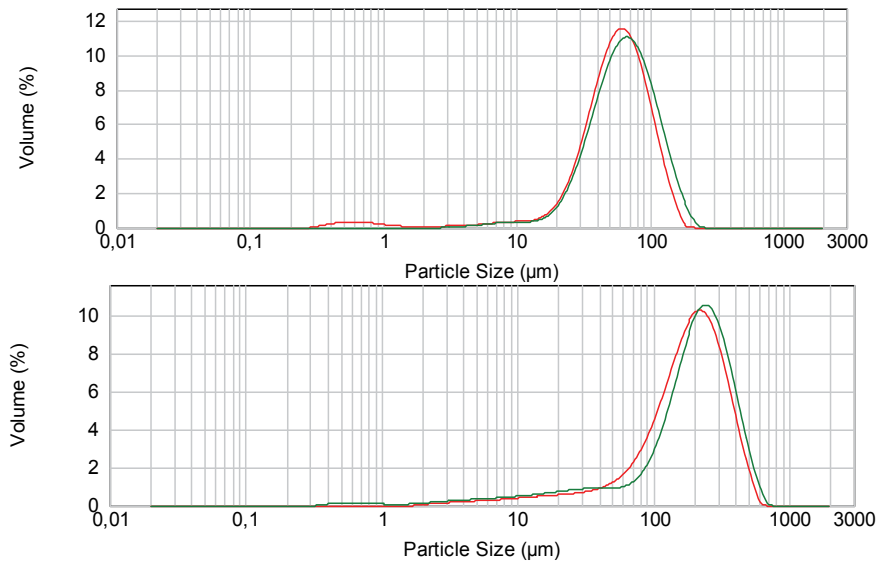


Fig. 6. Particle size distribution of fine (upper graph) and coarse (lower graph) ADN prills. Two measurements on each grade.

3.3 Formulation

An ADN-based solid propellant with a GAP-based binder has been formulated containing 70 % bimodal prilled ADN. The GAP used was obtained from EURENCO France (Lot: 76S04 (Perez, 2007)). The relatively low solid loading was chosen to ensure low viscosity and hence good quality of the casted propellant. Based on our experience, it is now clear that the solid loading can be increased. Batches up to 3.75 kg have been mixed using an IKA HKV 5 high performance kneader and samples for characterization and motor testing have successfully been cast and cured. The thermal stability of the propellants was measured using a heat flow calorimeter. According to STANAG 4582 (STANAG, 2002), the heat flow should not exceed 63.1 $\mu\text{W/g}$ at 75 °C during 19 days. Fig. 7 shows that the propellant has an excellent thermal stability with a heat flow well below the acceptance limit.

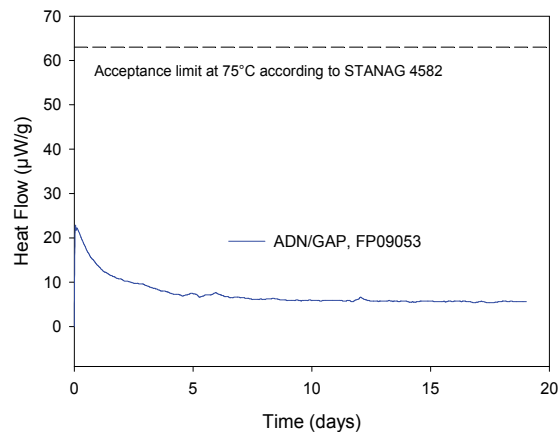


Fig. 7. Thermal stability at 75 °C of ADN/GAP propellant containing 70 % ADN.

3.4 Burning rate measurements

The burning rate was determined using a strand burner. The results were evaluated using the interpolation formula $r = ap^n$, where p is the combustion pressure, in MPa, and r is the measured burning rate in mm/s. The pressure exponent, n , and the burning rate constant, a , were determined by linear regression analysis of the data in a log-log diagram. The results from testing of four propellant batches are shown in Fig. 8 and Table 8. The data correlates well with the interpolation formula, as shown with a linear correlations coefficient, R , close to unity. The propellant has a high burning rate, 24 mm/s at 7 MPa, and a pressure exponent below 0.5 in the pressure interval examined.

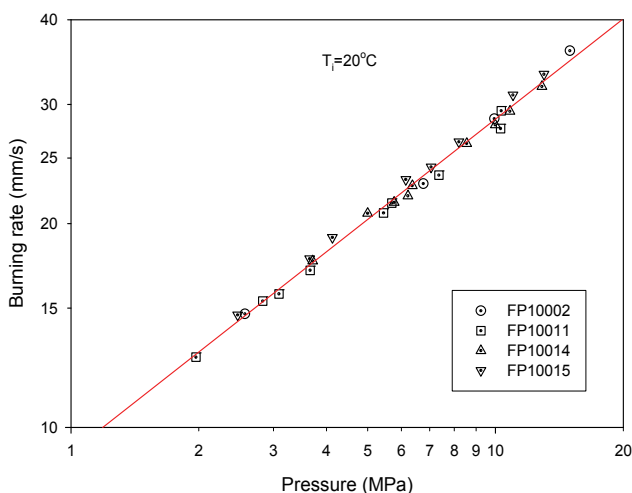


Fig. 8. Burning rate for ADN/GAP 70/30 for four different batches.

a	n	R ^{2 a}	r ₇ (mm/s)
9.2	0.49	0.993	24

Table 8. Coefficients in the interpolation formula $r = ap^n$ and burning rate at 7 MPa.

a) R^2 is the linear correlations coefficient.

3.5 Motor testing

Rocket motor firings were performed to verify the calculated specific impulse. Three 3 kg case bonded grains were cast in steel cartridges as shown in Fig. 9. A liner based on HTPB was used. Some minor machining was needed after casting. The propellant was easy to machine yielding a smooth surface. Figure 10 shows the motor during firing. The red curve in Fig. 11 shows the recorded pressure as a function of time, and the black is the calculated pressure using the strand burner data in Fig. 8. Some characteristics of the grain and the test motor, as well as some evaluated parameters from the motor firing, are shown in Table 9. The results from the test show that the burning rate was 14 % higher in the rocket motor compared to the strand burner data and the shape of the pressure curve reasonably agreed with the calculations. The measured specific impulse was a few percents lower than predicted, as is usually the case, confirming the high performance potential of ADN/GAP.



Fig. 9. Case bonded 3 kg ADN/GAP (70/30) grain cartridges for motor testing.



Fig. 10. Test firing of ADN/GAP rocket motor.

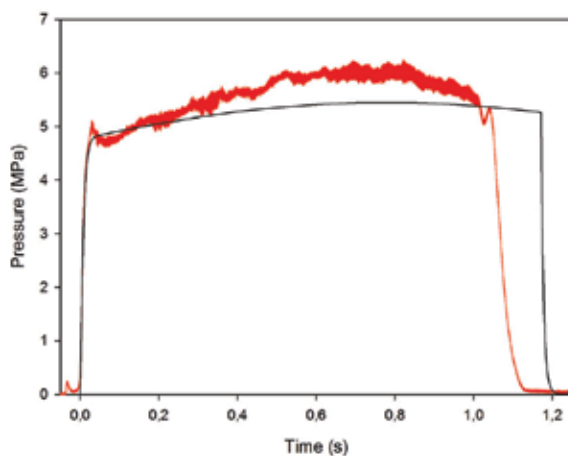


Fig. 11. Combustion pressure as a function of time. Red curve experimental, black curve calculated.

Propellant	ADN/GAP 70/30 batch no FP10015
Grain internal diameter	73.0 mm
Grain external diameter	123.2 mm
Propellant weight	3025 g
Mean pressure	5.55 MPa
Burning rate	24 mm/s (calc. 21 mm/s)
Nozzle throat diameter	31 mm
Nozzle area expansion ratio	5.0 (under-expanded)
Specific impulse	233 s

Table 9. Grain and nozzle characteristics and evaluated parameters.

3.6 Sensitivity and mechanical properties

The propellant used in this work did not contain any plasticizer or bonding agent and its mechanical properties needs to be improved to obtain the desired elasticity. The sensitivity is one of the most important issues to consider when developing new propellants. ADN/GAP-propellants with high solid loading are expected to be hazard class 1.1 materials. However, at low solid loading the sensitivity is expected to be reduced. The calculations presented in Section 3.1 show that the highest specific impulse is obtained using an aluminized formulation containing only 60 % ADN. Due to the low amount ADN needed it is feasible that future high performance solid propellants based on ADN will have an acceptable sensitivity.

4. Liquid Monopropellants based on ADN

One of the most promising alternatives to monopropellant hydrazine is blends based on an oxidizer salt dissolved in a fuel/water mixture. Hydroxylammonium nitrates (HAN) has been studied for this purpose (Meinhardt et al., 1998; Meinhardt et al., 1999; Mittendorf et al., 1997; Wucherer and Christofferson, 2000; Zube et al., 2003). Due to its high solubility, ADN can be used in the same way as HAN. The development of ADN-based monopropellants started at FOI in 1997 on a contract from the Swedish Space Corporation, SSC, and several different propellant formulations have been developed and tested.

4.1 Formulation

When formulating an ADN-based liquid monopropellant, the minimum service temperature allowed for the monopropellant when used in a spacecraft must be considered. In order to use the same thermal management system as for hydrazine (freezing point +2 °C (Schmidt, 2001)), a new monopropellant should have a similar minimum temperature limit. The solubility of the oxidizer salt must therefore be taken into account to determine which formulation that actually can be prepared at this minimum temperature. A reasonable and convenient minimum temperature limit is 0 °C, since this is close to the freezing point of hydrazine and it is easy to obtain in the laboratory by the use of ice water.

The first fuels considered in the development of ADN/fuel/water mixtures were acetone, ethanol and methanol respectively. Figure 12 shows how to optimize the composition with respect to specific impulse. The solubility curve defines the maximum amount of ADN that can be dissolved in a methanol/water mixture at 0 °C. By performance calculations, the optimum formulation is found for a methanol/water mixture containing 30.6 % methanol. The final composition is 63.4 % ADN, 25.4 % water and 11.2 % methanol.

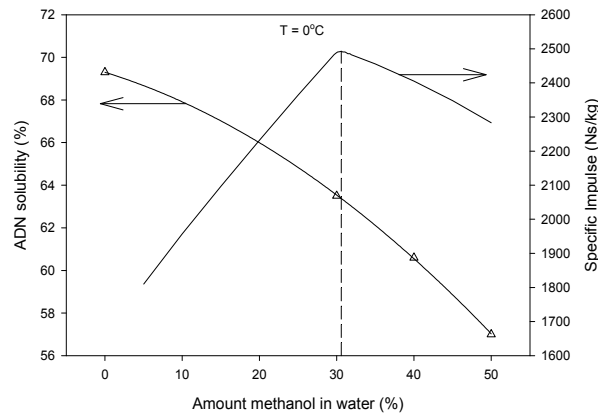


Fig. 12. Specific impulse and ADN solubility in water/methanol mixtures at 0°C. $p_c = 2.0$ MPa, $\epsilon = 50$.

Low volatile fuels such as 1,4-butanediol, glycerol, ethylene glycol and trimethylol propane were studied to minimize the amount of ignitable and/or toxic fumes. First glycerol was chosen due to the superior thermal ignition properties of the ADN/glycerol/water-blend. This monopropellant formulation was called LMP-101 (Anflo et al., 2000). However, it was discovered that LMP-101 suffered from poor thermal stability, and as a consequence it was rejected from further development. During the years, several different ADN-based monopropellants have been developed (Wingborg et al., 2004; Wingborg and Tryman, 2003). Two formulations, LMP-103S and FLP-106 have received particular attention. LMP-103S has been selected by SSC and FLP-106 has been selected by FOI as the main monopropellant candidate for further development efforts.

4.2 Properties of ADN liquid monopropellant formulation FLP-106

FLP-106 is a low-viscous yellowish liquid, as seen in Fig. 13, with high performance, low vapour pressure and low sensitivity. It is based on a low volatile fuel, water and 64.6 % ADN. The development, characterization and selection of FLP-106 are reported elsewhere (Wingborg and de Flon, 2010; Wingborg et al., 2004; Wingborg et al., 2006; Wingborg et al., 2005). Some of the properties of FLP-106 are shown in Tables 10 and 11, and its mass density as function of temperature is shown in Fig. 14.



Fig. 13. Monopropellant FLP-106.

	Hydrazine	FLP-106
Specific impulse ^b (s)	230 (Brown, 1995)	259
Density (g/cm ³)	1.0037	1.357
Temp. in chamber (°C)	1120	1880
T _{min} ^c (°C)	2.01	0.0
Viscosity (cP, mPas)	0.913	3.7
Thermal expansion coefficient (1/K)	9.538 · 10 ⁻⁴	6.04 · 10 ⁻⁴
Heat capacity (J/gK)	3.0778	2.41

Table 10. Properties of hydrazine and FLP-106^a.

a) All properties at 25 °C. Hydrazine data from Schmidt (Schmidt, 2001) and FLP-106 data from Wingborg et al. (Wingborg and de Flon, 2010; Wingborg et al., 2004; Wingborg et al., 2006; Wingborg et al., 2005).

b) Calculated Isp. Pc = 2.0 MPa, Pa = 0.0 MPa, ε = 50.

c) Minimum storage temperature determined by freezing (hydrazine) or precipitation (FLP-106).

A _e /A _t	50	100	150	200
I _{sp} (s) ^a	259	264	266	268

Table 11. Vacuum specific impulse at different nozzle area expansion ratios.

a) Pc = 2.0 MPa

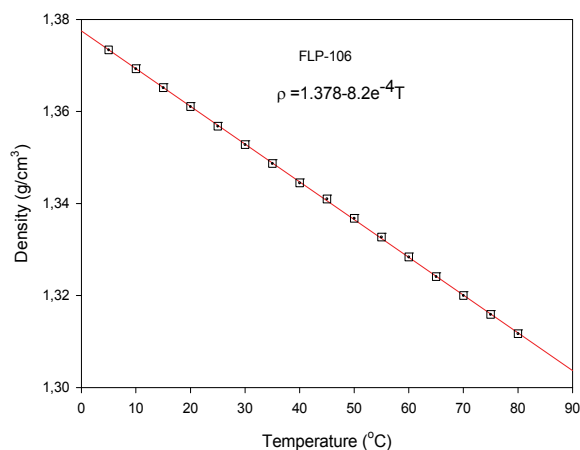


Fig. 14. Mass density of FLP-106 as a function of temperature.

4.3 FLP-106 manufacturing and batch control

FLP-106 is manufactured in two steps; first the fuel is dissolved in water and secondly ADN is mixed in the fuel/water blend. The temperature drops substantially during the dissolution of ADN and thus it takes some time before all ADN has dissolved. To speed up the dissolution, the mixture can be heated using a warm water bath. The ADN used was procured from EURENCO Bofors in Sweden. The purity of the material is above 99%. However, small amounts of insoluble impurities are present, which is clearly seen when dissolving ADN. The purity can be improved by recrystallization. In this way insoluble

impurities are removed, but the content of ammonium nitrate increases due to ADN degradation. To prevent this, the prepared propellant is instead purified *in-situ* by filtration using a 0.45 μm PTFE filter, and a completely clear liquid propellant of high purity is formed.

When manufacturing batches of FLP-106 it is important to verify it has been prepared correctly and conforms to the specification. Apart from visual examination, each batch of propellant is analysed with respect to density using a Mettler Toledo DE40 density meter. It is estimated that the ADN content in this way can be determined within $\pm 0.05\%$. The high precision is possible due to the low volatility of FLP-106.

4.3 FLP-106 material compatibility

The compatibility between the propellant and different construction materials used in propulsion systems have been assessed (Wingborg and de Flon, 2010). The materials considered are shown in Table 12. The tests were performed using a Thermometric TAM 2277 heat flow calorimeter. Pieces of respective test material were immersed in approximately 0.2 g FLP-106 in 3 cm^3 glass ampoules. The measurements were performed at 75 $^\circ\text{C}$ for 19 days. All the tested materials were supplied by Astrium GmbH, Bremen, except sample no. 13, which was cut out from a Nalgene bottle.

Sample no.	Materials
1	Metal, AISI 304L
2	Metal, AISI 321
3	Metal, AISI 347
4	Metal, Inconel 600
5	Metal, AMS 4902
6	Metal, AMS 4906
7	Metal, Nimonic 75
8	Polymer, PTFE
9	Rubber, EPDM
10	O-ring, Kalrez 4079, Du Pont
11	O-ring, Kalrez 1050LF, Du Pont
12	O-ring, 58-00391, Parker Hannifin GmbH
13	Polymer, PETG, Nalgene

Table 12. Materials used in the compatibility assessment.

In all cases the heat flow induced by the tested materials were below 0.1 $\mu\text{W}/\text{mm}^2$ (Wingborg and de Flon, 2010). Based on the heat flow measurements all materials tested are considered to be compatible with FLP-106. However, EPDM and PETG samples both showed a slight colour shift. This might be due to thermal degradation of the materials. Since the tests were performed at substantially harsher conditions than, for instance the NASA Test 15 (test time 48 h, test temp 71 $^\circ\text{C}$) (NASA, 1998), it is not clear that the colour shift detected is an issue.

4.4 Ignition of FLP-106

One important aspect in the development of a new monopropellant is the ignition. State of the art hydrazine thrusters use catalytic ignition, which is simple and reliable. To replace

hydrazine, ADN-based monopropellants must be as easy to ignite. However, a disadvantage of the ADN-based monopropellants is the high combustion temperature, which is approximately 800°C higher than hydrazine, as seen in Table 10. The combustion temperature is in the same range as for HAN-based monopropellants, and it has been reported that the current state of the art hydrazine catalyst (Shell 405) cannot withstand such high temperatures (Reed, 2003; Zube et al., 2003). This and the fact that hydrazine and ADN-based liquid propellants are very different, both physically and chemically, require development of new ignition methods, or new catalysts. When dripping the FLP-106 on a hot plate, with a temperature in the range of 200 to 250°C, it ignites and burns fast. This clearly shows that thermal ignition is possible and thermal ignition might thus be a feasible ignition method. Three different methods of heating the propellant to the ignition temperature have been identified:

- Pyrotechnic (by forming hot gases using a solid energetic material which in turn will heat the propellant)
 - Thermal conduction (by spraying the propellant on a hot object which in turn is heated by electric means)
 - Resistive (ADN is a salt and the propellants thereby possess a relatively high electric conductivity. This means that an ADN-based monopropellant can be resistively heated)
- Development of catalytic (Scharlemann, 2010), thermal (Wingborg et al., 2006), and resistive (Wingborg et al., 2005) ignition methods is ongoing.

4.5 FLP-106 compared to LMP-103S

Both FLP-106 and LMP-103S are compatible with materials currently used in propulsion systems. They both also have similar *oral* toxicity and should be considered as harmful, but not toxic. However, FLP-106 has a substantial lower vapour pressure and requires no respiratory protection during handling. They are not sensitive to shock initiation and should, from this point of view, not be considered as hazard class 1.1 materials (ECAPS, 2010; Wingborg and de Flon, 2010). The advantage using FLP-106, apart from its lower volatility, is its higher performance and higher density as shown in Table 13. The specific impulse for FLP-106 is 7 s higher compared to LMP-103S, and the density-impulse ($\rho \cdot I_{sp}$) is 13 % higher.

Propellant	FLP-106	LMP-103S
I_{sp} (s) ^a	259	252 (ECAPS, 2009)
ρ (g/cm ³) ^b	1.362	1.240 (ECAPS, 2010)
$\rho \cdot I_{sp}$ (gs/cm ³)	353	312

Table 13. Properties of ADN-based monopropellants.

a) at a nozzle area expansion ratio of 50.

b) at 20 °C.

5. Concluding remarks

Ammonium dinitramide, ADN, seems promising as a green substitute for both ammonium perchlorate, AP, and for monopropellant hydrazine. A solid ADN propellant has been formulated and test fired successfully and a high performance liquid ADN-based monopropellant has been developed.

Future work concerning solid ADN-based propellants will focus on improving the mechanical properties and to characterize the sensitivity.

Future work concerning liquid ADN-based monopropellants will focus on ignition and thruster development.

6. Acknowledgements

The authors like to acknowledge all colleagues at FOI involved in the ADN development and the Swedish Armed Forces for financial support.

7. References

- Agrawal, J. P. & Hodgson, R. D. (2006). *Organic Chemistry of Explosives*, Wiley, Chichester.
- Anflo, K., Grönland, T. A. & Wingborg, N. (2000). Development and Testing of ADN-Based Monopropellants in Small Rocket Engines. *36th AIAA/ASME/SAE/ASEE Joint Propulsion Conference*, 16-19 July 2000, Huntsville, AL, USA.
- ASTRIUM. (2007). *Aestus Rocket Engine*.
<http://cs.astrium.eads.net/sp/LauncherPropulsion/Aestus-Rocket-Engine.html>
[Accessed 2010-08-25].
- ATSDR. (1997). *Hydrazine cas # 302-01-2; 1,1-dimethylhydrazine cas # 57-14-7; 1,2-dimethylhydrazine cas # 540-73-8*. Agency for Toxic Substances and Disease Registry, USA. <http://www.atsdr.cdc.gov/tfacts100.pdf> [Accessed 2010-08-25].
- Bathelt, H., Volk, F. & Weindel, M. (2004). ICT - Database of Thermochemical Values. Version 7.0 ed.: Fraunhofer-Institut für Chemische Technologie (ICT).
- Bombelli, V., Ford, M. & Marée, T. (2004). Road Map for the Demonstration of the Use of Reduced-Hazard Monopropellants for Spacecraft. *2nd International Conference on Green Propellants for Space Propulsion*, 7-8 June 2004, Chia Laguna, Sardinia, Italy.
- Bombelli, V., Simon, D. & Marée, T. (2003). Economic Benefits of the use of Non-Toxic Monopropellants for Spacecraft Applications. *39th AIAA/ASME/SAE/ASEE Joint Propulsion Conference*, 20-23 July 2003, Huntsville, AL, USA.
- Bottaro, J. C., Penwell, P. E. & Schmitt, R. J. (1997). 1,1,3,3-Tetraoxy-1,2,3-triazapropene Anion, a New Oxy Anion of Nitrogen: The Dinitramide Anion and Its Salts. *Journal of the American Chemical Society*, 119, 9405-9410.
- Brown, C. D. (1995). *Spacecraft Propulsion*, AIAA, Washington.
- Christe, K. O., Wilson, W. W., Petrie, M. A., Michels, H. H., Bottaro, J. C. & Gilardi, R. (1996). The Dinitramide Anion, N(NO₂)₂-. *Inorganic Chemistry*, 35, 5068-5071.
- DoD (2009). *DoD Workshop Advanced Strategy for Environmentally Sustainable Energetics*, 24-25 March 2009, Rockaway, NJ, USA.
- ECAPS. (2009). *Green Propellant Technology on the Prisma Satellite*. Swedish Space Corporation Group. <http://www.nordicspace.net/PDF/NSA233.pdf> [Accessed 2010-08-25].
- ECAPS. (2010). *Monopropellant LMP-103S*. Swedish Space Corporation Group. <http://www.ecaps.se/filearchive/1/14685/LMP-103S%20Monopropellant.pdf> [Accessed 2010-08-25].
- Eldsäter, C., de Flon, J., Holmgren, E., Liljedahl, M., Pettersson, Å., Wanhatalo, M. & Wingborg, N. (2009). ADN Prills: Production, Characterisation and Formulation. *40th International Annual Conference of ICT*, 23-26 June 2009, Karlsruhe, Germany.

- EPA. (2005). *Perchlorate Treatment Technology Update*. United States Environmental Protection Agency, USA. <http://www.epa.gov/tio/download/remed/542-r-05-015.pdf> [Accessed 2010-08-25].
- Gordon, S. & McBride, B. J. (1994). Computer program for calculation of complex chemical equilibrium compositions and applications. I. Analysis. NASA.
- Hurlbert, E., Applewhite, J., Nguyen, T., Reed, B., Baojiong, Z. & Yue, W. (1998). Nontoxic Orbital Maneuvering and Reaction Control Systems for Reusable Spacecraft. *Journal of Propulsion and Power*, 14, 676-687.
- Johansson, M., de Flon, J., Pettersson, Å., Wanhatalo, M. & Wingborg, N. (2006). Spray Prilling of ADN, and Testing of ADN-Based Solid Propellants. *3rd International Conference on Green Propellants for Space Propulsion*, 17-20 September 2006, Poitiers, France.
- Kinkead, E. R., Salins, S. A., Wolfe, R. E. & Marit, G. B. (1994). Acute and Subacute Toxicity Evaluation of Ammonium Dinitramide. *Mantech Environmental Technology*.
- Langlet, A., Östmark, H. & Wingborg, N. 1997. *Method of Preparing Dinitramidic Acid and Salts Thereof*. Patent No: WO 97/06099.
- McBride, B. J. & Gordon, S. (1996). Computer program for calculation of complex chemical equilibrium compositions and applications. II. Users manual and program description. NASA.
- Meinhardt, D., Brewster, G., Christofferson, S. & Wucherer, E. J. (1998). Development and Testing of New, HAN-based Monopropellants in Small Rocket Thrusters. *34th AIAA/ASME/SAE/ASEE Joint Propulsion Conference*, 13-15 July 1998, Cleveland, OH, USA.
- Meinhardt, D., Christofferson, S. & Wucherer, E. (1999). Performance and Life Testing of Small HAN Thrusters. *35th AIAA/ASME/SAE/ASEE Joint Propulsion Conference*, 20-24 June 1999, Los Angeles, CA, USA.
- Mittendorf, D., Facinelli, W. & Sarpolus, R. (1997). Experimental Development of a Monopropellant for Space Propulsion Systems. *33rd AIAA/ASME/SAE/ASEE Joint Propulsion Conference*, 6-9 July 1997, Seattle, WA, USA.
- NASA (1998). Flammability, odor, offgassing, and compatibility requirements and test procedures for materials in environments that support combustion. NASA, USA.
- Östmark, H., Bemm, U., Bergman, H. & Langlet, A. (2002). N-Guanylurea-dinitramide: A New Energetic Material with Low Sensitivity for Propellants and Explosives Applications. *Thermochimica Acta*, 384, 253-259.
- Östmark, H., Bemm, U., Langlet, A., Sandén, R. & Wingborg, N. (2000). The Properties of Ammonium Dinitramide (ADN): Part 1, Basic Properties and Spectroscopic Data. *Journal of Energetic Materials*, 18, 123-128.
- Palaszewski, B., Ianovski, L. S. & Carrick, P. (1998). Propellant Technologies: Far-Reaching Benefits for Aeronautical and Space-Vehicle Propulsion. *Journal of Propulsion and Power*, 14, 641-648.
- Perez, M. (2007). *Bulletin de Analyses. Produit: PAG (polyazoture de glycidyle). Lots: 76S04*. EURENCO France.
- Pettersson, B. (2007). ADN Safety Data Sheet. EURENCO Bofors.
- Reed, B. D. (2003). On-Board Chemical Propulsion Technology. *10th International Workshop on Combustion and Propulsion*, 21-25 September 2003, Lerici, La Spezia, Italy.
- Ritz, B., Zhao, Y. X., Krishnadasan, A., Kennedy, N. & Morgenstern, H. (2006). Estimated effects of hydrazine exposure on cancer incidence and mortality in aerospace workers. *Epidemiology*, 17, 154-161.

- Scharlemann, C. (2010). GRASP- A European Effort to Investigate Green Propellants for Space Application. *Space Propulsion 2010*, 3-6 May 2010, San Sebastian, Spain.
- Schmidt, E. W. (2001). *Hydrazine and its Derivatives*, Wiley-Interscience.
- STANAG (2002). Explosives, Nitrocellulose Based Propellants, Stability Test Procedure and Requirements Using Heat Flow Calorimetry. NATO Standardisation Agreement STANAG 4582 (First Draft)
- Stephenson, D. D. & Willenberg, H. J. (2006). Mars ascent vehicle key elements of a Mars Sample Return mission. *IEEE Aerospace Conference*, 4-11 March 2006, Big Sky, MT, USA.
- Sutton, G. P. & Biblarz, O. (2001). *Rocket Propulsion Elements*, John Wiley & Sons, New York.
- Talawar, M. B., Sivabalan, R., Anniyappan, M., Gore, G. M., Asthana, S. N. & Gandhe, B. R. (2007). Emerging Trends in Advanced High Energy Materials. *Combustion, Explosion, and Shock Waves*, 43, 62-72.
- Teipel, U. (2004). *Energetic Materials: Particle Processing and Characterization*, Wiley-VCH, Weinheim.
- Urbansky, E. T. (2002). Perchlorate as an Environmental Contaminant. *Environ Sci & Pollut Res*, 9, 187-192.
- Venkatachalam, S., Santhosh, G. & Ninan, K. N. (2004). An Overview on the Synthetic Routes and Properties of Ammonium Dinitramide (ADN) and Other Dinitramide Salts. *Propellants, Explosives, Pyrotechnics*, 29, 178-187.
- Wingborg, N. (2006). Ammonium Dinitramide-Water: Interaction and Properties. *J. Chem. Eng. Data*, 51, 1582-1586.
- Wingborg, N. & de Flon, J. (2010). Characterization of the ADN-based liquid monopropellant FLP-106. *Space Propulsion 2010*, 3-6 May 2010, San Sebastian, Spain.
- Wingborg, N., de Flon, J., Johnson, C. & Whitlow, W. (2008). Green Propellants Based on ADN. *Space Propulsion 2008*, 5-8 May 2008, Heraklion, Crete, Greece. ESA, 3AF, SNPE.
- Wingborg, N., Eldsäter, C. & Skifs, H. (2004). Formulation and Characterization of ADN-Based Liquid Monopropellants. *2nd International Conference on Green Propellants for Space Propulsion*, 7-8 June 2004, Chia Laguna, Sardinia, Italy.
- Wingborg, N., Johansson, M. & Bodin, L. (2006). ADN-Based Liquid Monopropellants: Propellant Selection and Initial Thruster Development. *3rd International Conference on Green Propellants for Space Propulsion*, 17-20 September 2006, Poitiers, France.
- Wingborg, N., Larsson, A., Elfsberg, M. & Appelgren, P. (2005). Characterization and Ignition of ADN-Based Liquid Monopropellants. *41st AIAA/ASME/SAE/ASEE Joint Propulsion Conference*, 10-13 July 2005, Tucson, AZ, USA.
- Wingborg, N. & Tryman, R. (2003). ADN-Based Monopropellants for Spacecraft Propulsion. *10th International Workshop on Combustion and Propulsion*, 21-25 September 2003, Lercici, La Spezia, Italy.
- Wucherer, E. J. & Christofferson, S. (2000). Assessment of High Performance HAN-Monopropellants. *36th AIAA/ASME/SAE/ASEE Joint Propulsion Conference*, 16-19 July 2000, Huntsville, AL, USA.
- Zube, D. M., Wucherer, E. J. & Reed, B. (2003). Evaluation of HAN-Based Propellant Blends. *39th AIAA/ASME/SAE/ASEE Joint Propulsion Conference*, 20-23 July 2003, Huntsville, AL, USA.

Use of Space Thermal Factors by Spacecraft

N. Semena
*Space Research Institute RAS,
Russia*

1. Introduction

All the equipment used by the man can work in the limited temperature range. The necessary ambient temperature and the intensive convective mechanism help to solve a thermostabilization problem on the Earth. But in the space the decision of this problem is much more difficult by reason of the extreme thermal conditions and vacuum. Now thermostabilization of space devices is provided with special thermoregulation systems, which failure leads to emergency end of mission. These systems depend from spacecraft (Sc) electrical system which supplies energy heaters and from Sc orientation system, which doesn't allow to heat up a radiator solar or planetary irradiance.

In article it will be shown that using of very simple technical decisions allows to make Sc thermoregulation systems independent of other Sc systems and from variation of space thermal factors. In addition it is shown how Sc thermal systems can be used for determine of its orientation.

2. Analysis of shortcomings of the conventional system for ensuring the thermal regime

To solve the problem of thermal stabilization of space equipment sufficiently efficient systems of thermal regulation were developed whose basic elements are the radiator–emitter, which is a surface emitting the excessive heat flux to space, and the electric heater – the element heating the equipment if necessary.

The process for maintaining the temperature of an equipment used in space generally consists of the maintenance of a necessary temperature level of the heat balance between the heat flux irradiated from the radiator surface and the integral heat capacity of the device including heat release of the equipment, heat release of the heater and the heat flux absorbed by the external surface of the radiator-emitter. The scheme of the simplest system of thermal regulation is presented in Fig. 1.

To investigate the influence of external and internal thermal factors on the temperature regime of such a system one can use an assessment thermal model which does not account for secondary factors: the non-isothermicity of thermal nodes, heat flux across the external thermal insulation, the difference from zero of the effective temperature of space, and a possible shielding of the radiator-emitter by the structure external elements. The above factors do not affect the qualitative result of modelling but complicate the solution. Thus, the

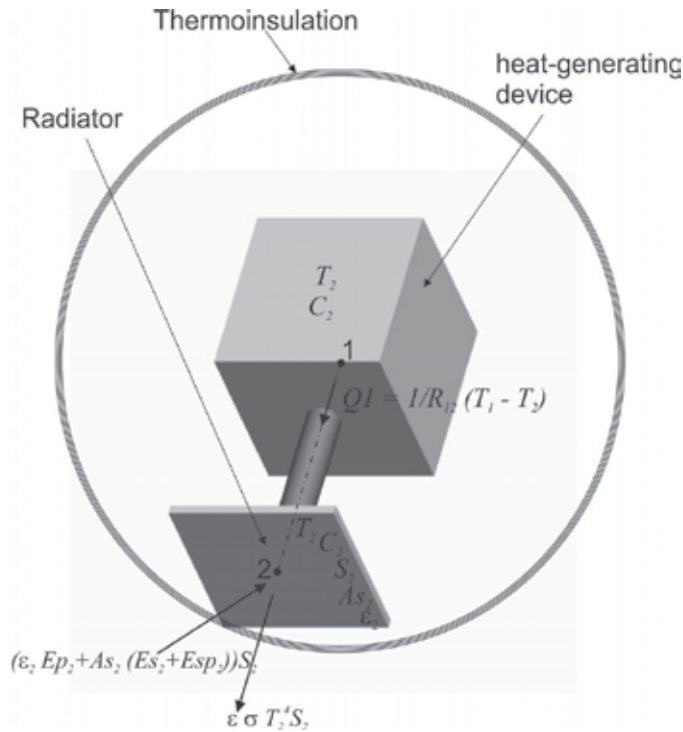


Fig. 1. Scheme of a conventional system for thermal regulation of the devices for space application.

assessment thermal model of the presented system includes two thermal nodes (node No. 1 is the heat releasing equipment, including the heater, nodes No. 2 is the radiator-emitter) and is governed by the system of two equations:

$$C_1 \frac{dT_1}{d\tau} = (Q_1 + Q_H) - \frac{1}{R_{12}}(T_2 - T_1)$$

$$C_2 \frac{dT_2}{d\tau} = (\varepsilon_2 Ep_2 + As_2(Es_2 + Esp_2))S_2 + \frac{1}{R_{21}}(T_1 - T_2) - \varepsilon_2 \sigma T_2^4 S_2,$$

where C_1 , C_2 , T_1 , and T_2 are the heat capacities and temperatures of the device and the radiator, τ is the time, Q_1 and Q_H are the heat releases of the device and the heater, S_2 , ε_2 and As_2 are the area, emissivity factor, the coefficient of absorption of solar radiation and the external surface of the radiator-emitter, Ep_2 and $Es_2 + Esp_2$ are the infrared and solar radiant fluxes incident onto the external surface of the radiator-emitter, R_{12} and R_{21} are the thermal resistance of the heat-conducting duct from the equipment to radiator and from the radiator to the equipment (usually $R_{12} = R_{21}$), σ is the Stefan – Boltzmann constant.

An analysis of the presented thermal model shows the shortcomings of the conventional system for ensuring the thermal regime, which is employed in present-day devices of space application.

1. Such a system is very sensitive to external heat fluxes falling onto the radiator-emitter surface. The reason for this is that the only model element, at the expense of

which the heat is removed is $\varepsilon_2\sigma T_2^4 S_2$, therefore, the system can function efficiently only at such a level of external heat fluxes ($E_p, E_s + E_{sp}$), which ensure, for a given temperature of the equipment (T_1), the satisfaction of inequality $(\varepsilon_2 E_p^2 + A_s^2 (E_s^2 + E_{sp}^2)) S_2 \ll$ At the equality of these two elements, the radiator-emitter stops functioning, and at a sign change of the inequality to the opposite sign the radiator-emitter reverts into a heater and stabilizes the system at a higher temperature as compared to the one, which is required for the equipment operation. This indeed means that the spacecraft must not be oriented in such a way that a highly intense external flux from the sun and a planet falls during a long time onto the radiator-emitter. The orientation constraints in their turn lead to a restriction of the spacecraft functional capabilities.

2. The system is sensitive to the internal heat release of the equipment because a small oscillation of temperature around the mean value is ensured only under the condition $Q_I + Q_H \approx \text{const}$. This means that at a reduction of the useful power consumption of equipment the freed power must be directed to the heater feeding to maintain a constant level of the total heat release. This leads, in its turn, to the fact that the power supply system of spacecraft must always be tuned to a peak power consumption, which is very wasteful under the conditions of an electric power shortage on the spacecraft.

A seeming possibility of the first factor compensation at the expense of the second one leads to an even higher loading on the power supply system, which must compensate in this case both for a non-uniformity of the internal heat release of the equipment and non-uniformity of the external radiant flux absorbed by the radiator-emitter. Thus, if a spacecraft is composed of several independent devices each of which is equipped with an autonomous system for ensuring the thermal regime and the given devices are switched on at different times, then one can ensure, at first glance, the electric power saving by directing it only to those devices, which must be switched on. However, this is impossible when using the conventional systems for ensuring the thermal regime because the specified temperature of the equipment is ensured only at a constant maximum power supply to each device.

3. Universal mechanism of self-regulation

The self-regulation mechanism of a passive system for ensuring the thermal regime must ensure the temperature independence of thermally stabilized equipment of the external heat flux variability and of its internal heat release variability in the absence of active elements. At first sight, these are mutually exclusive conditions. If one considers, however, the spacecraft as an element included in the entire thermal balance of the Solar system, then one can conclude that the presence of a stable heating source, the sun, and a stable cooling source, the open space, enables the given problem solution.

If the radiator is partitioned into six parts oriented at the right angle with respect to one another (Fig. 2), then independently of the direction in which the sun or a planet lies the integral heat flux absorbed by six radiators will vary weakly:

$$\sum_{i=2}^{i=7} (\varepsilon_i E_{p_i} + A_{s_i} (E_{s_i} + E_{sp_i})) S_i \approx \text{Const} ,$$

where i is the radiator number. This leads in its turn to that the external radiant flux absorbed by radiators is taken into account at the choice of the radiator areas as a constant heat addition, which does not lead to oscillations of temperatures of the thermal model nodes.

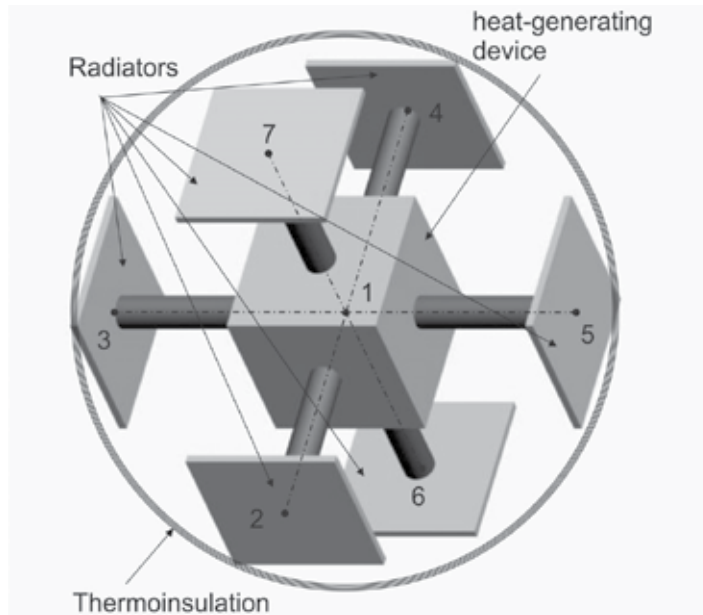


Fig. 2. Six-radiator system for ensuring equipment the thermal regime.

The given method is very efficient for compensation of the variability of radiant flux onto the spacecraft external surface under its arbitrary variable orientation.

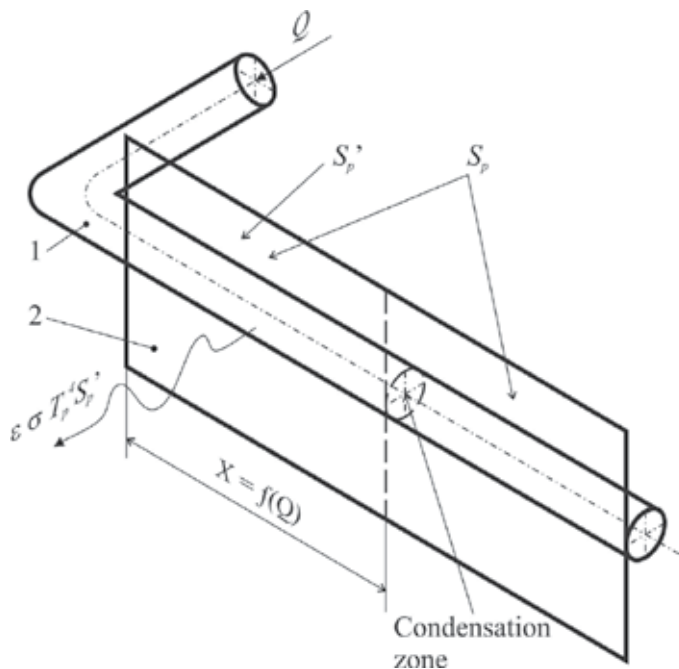
This method also enables a partial compensation of the internal heat release variability. A constant external heat inflow into the system will enable the maintenance of the equipment temperature at a minimally allowed level even at its switch-off and a non- functioning heater, that is at $Q_I + Q_H = 0$. The necessary heat balance may be ensured at the expense of choosing the optical characteristics (As_i, ε_i) of the external surface of radiators-emitters. The use of a many-radiator system enables one in some cases to refuse completely the use of heater.

As a rule, it is impossible to mount six radiators on a device because of a limited angular coefficient of the space survey and design constraints. Such a system may be used with a lesser number of radiators, but also with a lower efficiency.

4. Special mechanisms of self-regulation

The above presented mechanism of self-regulation is universal, it enables the maintenance of temperature of the heat-stabilized equipment within the given limits under the spacecraft orientation variation and under a drop of internal heat release, for example, at an accident switch-off of the equipment. There is, however, an equipment, which operates under specific thermal conditions, for example, under considerable single increases in heat release or at a very low level of temperatures. A simple solution using the separation and different orientation of radiators-emitters is insufficient for thermal stabilization of such an equipment. The advanced adjustable passive heat pipes, the gas- regulated heat pipes (GRHP) and thermal diodes (TD) [5], must be used within the system for ensuring the thermal regime of such an equipment. In the heat pipe, the heat transport occurs at the expense of the motion of evaporated heat-transfer agent from evaporation zone to

condensation zone. The return of condensed heat-transfer agent to evaporation zone occurs at the expense of capillary forces. The heat pipe edge to which the heat flux is supplied is usually the evaporation zone, and the opposite edge is the condensation zone. The condensation zone may, however, shift in GRHP along the heat pipe length depending on the value of a heat flux fed to the evaporation zone. Since effective heat transport is performed in the heat pipe only between the zones of evaporation and condensation, the GRHP represents a heat pipe of variable length. Thus, a radiator-emitter with a variable effective emissive area depending on the supplied heat flux value may be constructed based on a heat pipe and a plate with limited thermal conductivity (Fig. 3). The thermal diode is a heat pipe with a unidirectional conductivity. The given element may be used for a low-temperature system of ensuring the heat regime, if there is a need in minimizing the reverse heat inflow from the radiator-emitter.



1 – GRHP, 2 – a plate with limited longitudinal thermal conductivity, S'_p – the effective emissive area of the radiator (the active area), S_p is the radiator maximum area, T_p is the temperature of the radiator active zone, X is the GRHP active part length

Fig. 3. Radiator with an adjustable effective emissive area.

5. Efficiency of self-regulation mechanisms

With regard for the partition of the radiator-emitter into separate differently directed elements, the introduction in the system for ensuring the thermal regime of adjustable radiators based on GRHP and the plates with limited thermal conductivity as well as the use of the TD, the assessment mathematical model of a passive system for ensuring the thermal regime with introduced self-regulation mechanisms will be as follows:

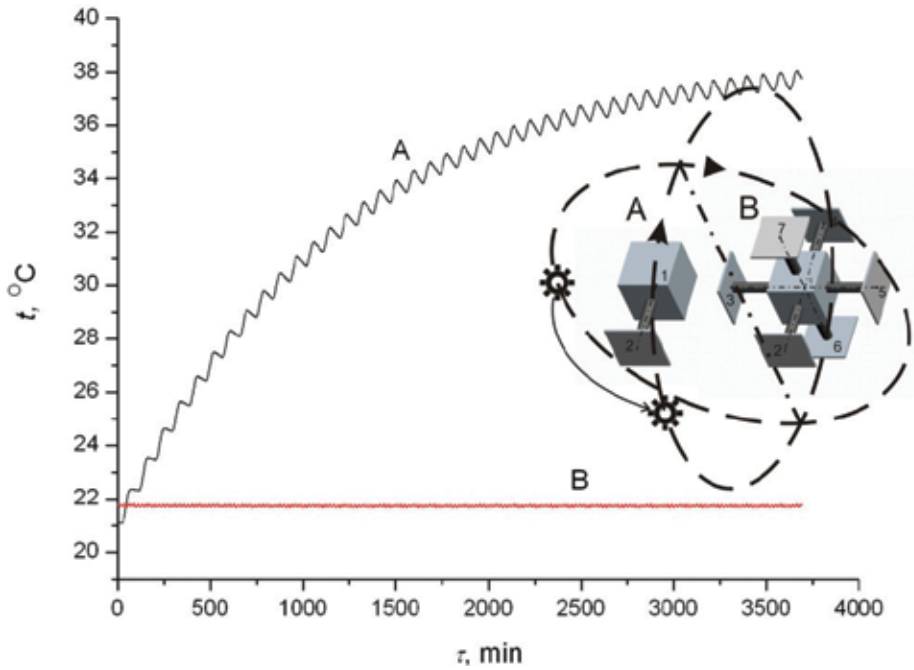
$$\begin{aligned}
C_1 \frac{dT_1}{d\tau} &= Q_1 - \sum_{i=2}^n \frac{1}{R_{1i}(\Delta T_{i1})} \cdot (T_i - T_1) \\
C_2 \frac{dT_2}{d\tau} &= (\varepsilon_2 \cdot Ep_2 + As_2 \cdot (Es_2 + Esp_2)) \cdot S_2(\Delta T_{21}) + \frac{1}{R_{21}(\Delta T_{12})} \cdot (T_1 - T_2) - \\
&\quad - \varepsilon_2 \cdot \sigma \cdot T_2^4 \cdot S_2(\Delta T_{21}) \\
&\quad \dots \\
C_n \frac{dT_n}{d\tau} &= (\varepsilon_n \cdot Ep_n + As_n \cdot (Es_n + Esp_n)) \cdot S_n(\Delta T_{n1}) + \frac{1}{R_{n1}(\Delta T_{1n})} \cdot (T_1 - T_n) - \\
&\quad - \varepsilon_n \cdot \sigma \cdot T_n^4 \cdot S_n(\Delta T_{n1}),
\end{aligned}$$

where C_i , T_i , and Q_i are the heat capacity, the temperature, and heat release of the equipment, τ is the time, $i = 2 \dots n$ is the number of radiators, C_i and T_i are the heat capacity and the temperature of the i -th radiator, $S_i(\Delta T_{i1})$ is the effective emissive area of the i -th radiator, which is a function of the heat flux to it or, what is the same, of the difference $T_i - T_1$, ε_i and As_i are the emissivity factor, the coefficient of the solar radiation absorption by the external surface of the i -th radiator, Ep_i and $Es_i + Esp_i$ are the infrared and solar radiant fluxes falling onto the external surface of the i -th radiator, $R_{1i}(\Delta T_{i1})$ and $R_{ni}(\Delta T_{i1})$ are the thermal resistance of the heat-conducting duct from the equipment to the i -th radiator and from the radiator to the equipment, what in the case of using a thermal diode depends on the heat flux direction, or, what is the same, on the sign of the difference $T_i - T_1$.

All the self-regulation mechanisms are presented in the given model. It is enough to use in real systems one of the proposed techniques, which will be in terms of its characteristics the closest one to the requirements made by the thermally stabilized equipment.

The model was used for determining the efficiency of techniques proposed for self-regulation. To this end the real situations were modeled, which are critical for the conventional system of ensuring the thermal regime. An electronic block with the parameters typical of the present-day equipment was the thermal regulation object: its mass was 10 kg ($C1 \approx 900$ J/K) and heat release $Q = 10$ W. The conventional system of ensuring the thermal regime for such a block must have a radiator with area $S_2 = 0.03$ m with optical characteristics $As_2 = 0.2$, $\varepsilon_2 = 0.9$, provided that the solar radiation does not fall on the radiator. While using the universal self-regulation mechanism it is necessary to employ six radiators, each of which must have the following characteristics: $S_i = 0.015$, $As_i = 0.9$, $\varepsilon_i = 0.9$, $i = 2 \dots 7$.

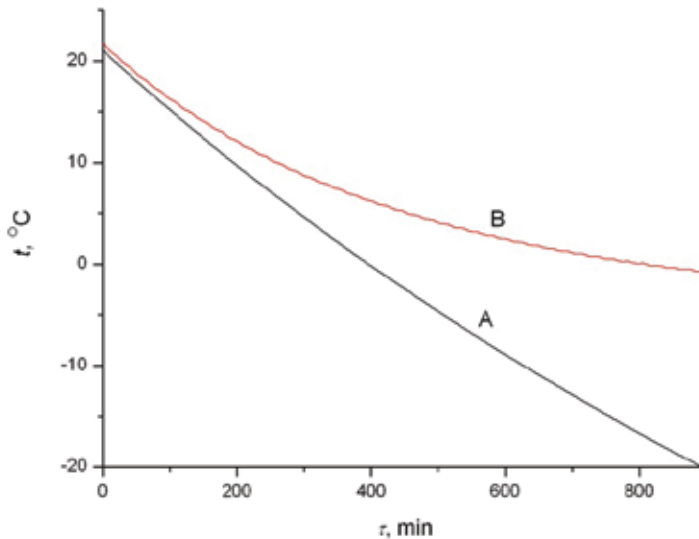
Figure 4 shows the temperature variation of the thermal regulation object mounted on an orbital spacecraft (the time of a single revolution is 90 mm) at an orbit turn of 90° with respect to the direction to the sun (it occurs at the expense of the orbit precession). The application of six radiators in this situation is seen in Fig. 4 to enable the preservation of the thermal regulation object temperature within the range $21.7 \pm 0.1^\circ\text{C}$, whereas in the case of using a single radiator the temperature increases from 21 to 38°C .



The systems supplied with radiators: one radiator (A), six radiators (B).

Fig. 4. Temperature variation of the thermal regulation object at an orbit rotation of the spacecraft.

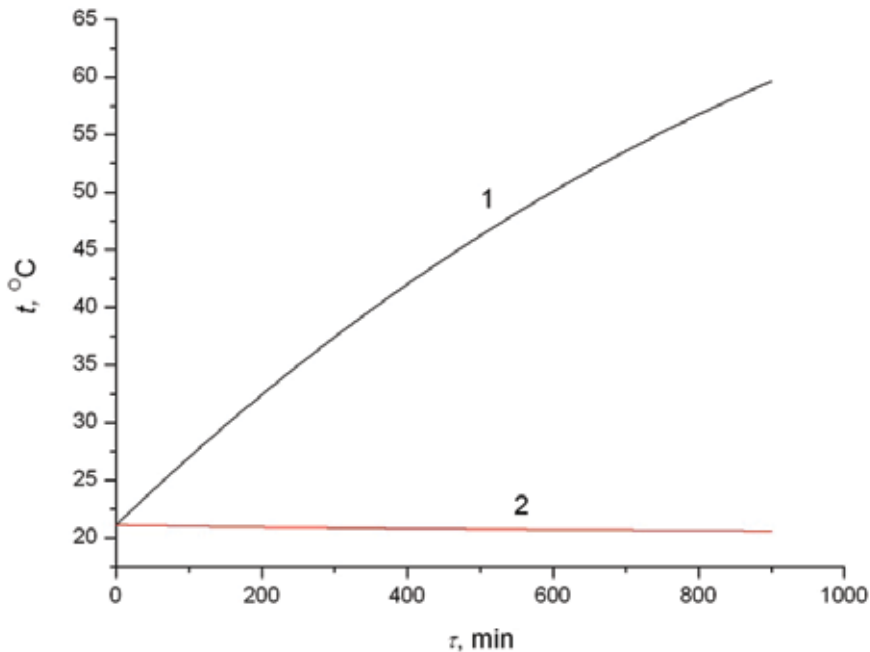
Figure 5 shows the temperature drop of the same object at a switch-off of the electric power during 900 min (a possible situation at the electric power shortage).



The systems supplied with radiators: one radiator (A), six radiators (B).

Fig. 5. Temperature drop of the thermal regulation object at a switch-off of electric power.

The presented dependence shows that at an electric power switch-off the object temperature will drop from 21 to -0.7°C when using six radiators and to -20°C when using a single radiator. At the operation of space equipment, a periodic considerable increase in power consumption by the equipment is also possible. In this case, it is necessary to use a radiator with an adjustable effective radiating area. Figure 6 shows the temperature variation of the regulation object at an increase in heat release from 10 to 20 W during 900 min while using a conventional system for ensuring the thermal regime and a system with an adjustable radiator.



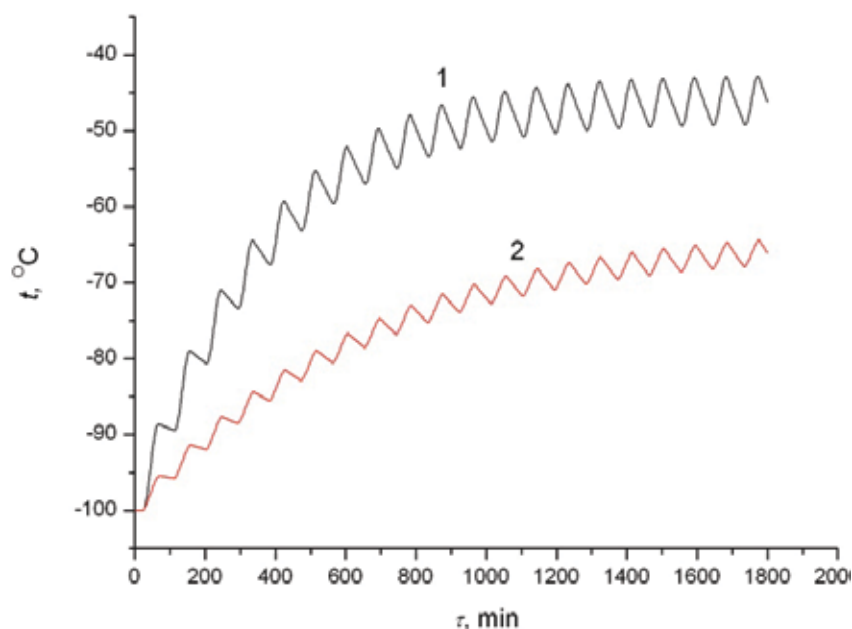
The systems supplied with radiators with constant (1) and adjustable (2) emissive areas.

Fig. 6. Temperature variation of the thermal regulation object with increasing power consumption.

It is seen from the presented dependence that the adjustable radiator is capable in this case of ensuring a nearly constant temperature of the equipment, whereas at the use of the conventional system the temperature increases from 21 to 60°C .

Figure 7, which presents the temperature increase of a thermal regulation object cooled to -100°C (the temperature typical of infrared and X-ray detectors) and mounted on the orbital spacecraft, demonstrates the efficiency of using thermal diodes in a low-temperature system at a turn by 90° of the orbit plane with respect to the direction to the sun similarly to the turn shown in Fig. 4.

The given dependence shows that when the radiator-emitter orientation changes the temperature of the thermal regulation object cooled to -100°C increases up to -43°C during 1800 min at the use of a standard system of thermal regulation and up to -64°C at the introduction of a thermal diode into the system.



The systems supplied with radiators: with one radiator (1), one radiator and thermal diode (2).

Fig. 7. Temperature variation of the thermal regulation object cooled down to -100 °C at a rotation of the spacecraft orbit.

6. Use of space thermal factors for determination of the space vehicle orbit orientation

In the previous sections the decisions have been shown, allowing to make Sc thermoregulation system the tolerant to anisotropy of a space thermal factors. But this anisotropy contains the information about a direction on external heat sources – the sun and a planet and hence, can be used for definition of Sc orientation.

As an example consider parameters of radiant flows in near-earth space. Specificity of the direct solar radiation is conditioned by significant remoteness of the Sun from Sc. In practical calculations the Sun can be considered as an infinitely distant radiation source. Therefore, its radiant flow over the near-earth orbit has characteristics that do not depend on the orbit parameters: constant small local divergence ($32'$); similar direction at a specific moment (solar radiation is parallel in volumes commensurable with Sc dimensions); constant irradiance $E_s \sim 1400 \text{ W/m}^2$, with weak seasonal variations or zero intensity at Sc approaching the Earth shadow.

Self-radiation of the Earth, on the contrary, due to its proximity to Sc has characteristics depending on the actual height over the Earth: significant (up to 150°) angle of radiation divergence and irradiance up to 230 W/m^2 . The Sun radiation reflected from the Earth also depends on the orbit height and, besides, on the time since intensity of such radiation depends on the variable in time positional relationship of the Sun, the Earth and the Sc.

Irradiance of Sc frame elements by direct solar radiation reflected from the Earth can vary in time at the orientation of the Sc to the Earth or its constant orientation to the Sun. Irradiance of various Sc frame elements by the Sun radiation reflected from the Earth is, vice versa,

constant in time at Sc orientation to the Earth and variable at its orientation to the Sun. Spectrum distribution of direct and reflected from the Earth solar radiation lies mostly in the visible area. Self-radiation of the Earth is infrared.

The following shall be noted. If on the ground temperature of the external surface of any body is conditioned by a large number of random factors (wind velocity, air humidity, present nearby objects, soil temperature, etc.) in outer space the body orientation in relation to the Sun appears to be the principal external factor forming its surface field temperature.

To identify interdependence of orientation and thermal mode of Sc surface its thermal mathematical model can be used that is demonstrated by an example of the simplest located on the Earth orbit Sc being the cube with known conductive bounds between the facets (fig. 8).

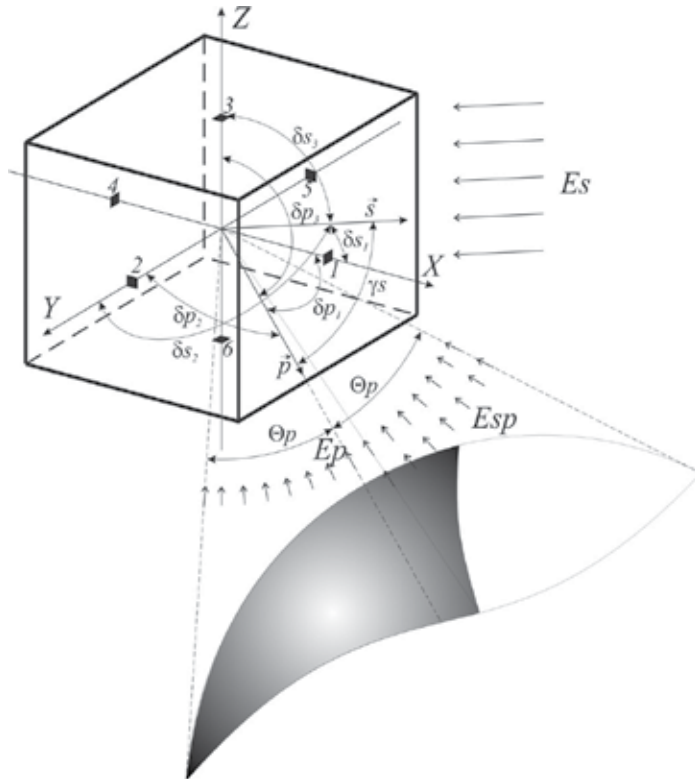


Fig. 8. Scheme of outer radiant flow effect on the near-earth cubical Sc.

Considering the cube facets as the thermal elements of Sc and assuming that Sc lacks internal heat generation and reradiation between the facets (more complex configuration and structure of the device would complicate the model having no impact on general results of the analysis), its thermal model will be described by the following six equations:

$$C_i \cdot \frac{dT_i}{d\tau} = (\varepsilon_i \cdot Ep_i + As_i \cdot (Es_i + Esp_i)) \cdot S_i + \sum_{j=1(i \neq j)}^6 \frac{T_i - T_j}{R_{ij}} - \varepsilon_i \cdot \sigma \cdot T_i^4 \cdot S_i; \\ i = 1...6,$$

where C_i , T_i — values of heat capacity and temperature of six elements (cube facets), R_{ij} — heat resistance between i - and j - heat elements (cube facets), A_{S_i} , ε_i , S_i — values of the coefficients of solar radiation absorption and degree of blackness and area of six cube facets, Es_i , Esp_i , Ep_i — momentary values of irradiation by direct solar radiation, reflected from the Earth the solar radiation and self-radiation of the Earth of six cube facets, τ — time, σ — Stefan-Boltzmann constant.

Directions to the principal heat sources – the Sun and the Earth – can be determined on the basis of eighteen values of the outer radiant flows (Es_i , Esp_i , Ep_i , $i = 1...6$). However, six equations of thermal model for their determination are not sufficient. Therefore, the thermal model shall be supplemented by no less than twelve equations. These equations can be obtained under the condition of all cube facets radiation by two sources (the Sun and the Earth) and constant mutual orientation of the facets in relation to each other.

Due to the specificity of direct solar radiation for the description of values Es_i the simplest mathematical model can be applied. Choosing directions coinciding with normals to the first, second and third cube facets (see fig. 1) as axes X , Y , Z of the coordinates system bound with Sc , we can draw up the following equations:

$$Es_i = Es \cdot \cos(\delta s_i);$$

$$i = 1...6,$$

where Es — normal irradiation by the solar radiation on the Earth orbit (the solar constant), δs_1 , δs_2 , δs_3 — angles between the positive directions of axes X , Y , Z of the coordinates system bound with Sc and the direction to the Sun, δs_4 , δs_5 , δs_6 — angles between negative directions of axes X , Y , Z of the coordinates system bound with Sc and the direction to the Sun.

Value Es has seasonal variations from 1396 to 1444 W/m², but at that, it is known with high degree of certainty for any day for a year.

Cube facets irradiation by self-radiation of the Earth (Ep_1 , ... Ep_6) is described in a more complex way:

$$Ep_i = \frac{1 - Ap}{4} \cdot Es \cdot \phi_i;$$

$$\phi_i = \cos \delta p_i \cdot \sin^2 \theta p \quad npu \quad 0 \leq \delta p_i < \frac{\pi}{2} - \theta p;$$

$$\phi_i = \frac{1}{\pi} \cdot (\cos \delta p_i \cdot \sin^2 \theta p \cdot (\frac{\pi}{2} - \arcsin(\operatorname{ctg} \theta p \cdot \operatorname{ctg} \delta p_i))) +$$

$$+ \arcsin \frac{\sqrt{\sin^2 \theta p - \cos^2 \delta p_i}}{\sin \delta p_i} - \cos \theta p \cdot \sqrt{\sin^2 \theta p - \cos^2 \delta p_i}$$

$$npu \quad \frac{\pi}{2} - \theta p \leq \delta p_i < \frac{\pi}{2} + \theta p;$$

$$\phi_i = 0 \quad npu \quad \frac{\pi}{2} + \theta p \leq \delta p_i \leq \pi;$$

$$i = 1...6,$$

where Ap — average albedo of the Earth, φ_i — angular coefficient of irradiation of the i -facet of Sc by the planet, $\delta p_1, \delta p_2, \delta p_3$ — angles between positive directions X, Y, Z of the coordinates system bound with Sc and the direction to the Earth center, $\delta p_4, \delta p_5, \delta p_6$ — angles between negative directions of axes X, Y, Z of the coordinates system bound with Sc and the direction to the center of the Earth, θp — angle of view of the planet from the center of Sc.

The most complex model serves to describe cube facets irradiation by the solar radiation reflected from the Earth.

$$\begin{aligned} Esp_i &= Ap \cdot Es \cdot \phi'_i; \\ \phi'_i &= f_2 \cdot \cos \delta p_i \cdot \cos \gamma_s + f_3 \cdot \sin \delta p_i \cdot \sin \gamma_s \cdot \cos \beta s_i; \\ i &= 1..6, \end{aligned}$$

where φ'_i — angular coefficient of irradiation of the part of the planet of i -facet of Sc, f_2 radiated by the Sun, f_3 — auxiliary functions, γ_s — angle between directions to the Sun and to Sc from the planet center, βs_i — two-facet angle with the vertex coinciding with the straight going through the planet center and Sc, in one plane of which lies the normal to i -facet of Sc and in another one — direction to the Sun.

Functions f_2, f_3 are determined as follows.

If the plane of i -facet of Sc does not cross the planet:

$$\begin{aligned} f_2(\theta p) &= \frac{1}{4} \cdot (1 + \sin^2 \theta p + 2 \cdot \sin^3 \theta p + \frac{\cos^4 \theta p}{2 \cdot \sin \theta p} \cdot \ln \frac{1 - \sin \theta p}{1 + \sin \theta p}); \\ f_3(\theta p) &= \frac{\cos^2 \theta p \cdot (3 + \sin^2 \theta p)}{16 \cdot \sin \theta p} \cdot \ln \frac{1 + \sin \theta p}{1 - \sin \theta p} - \\ &\quad - \frac{(1 - \sin \theta p) \cdot (3 + 3 \sin \theta p + 2 \cdot \sin^2 \theta p)}{8}; \end{aligned}$$

If the plane of i -facet of Sc crosses the planet:

$$\begin{aligned} f_2(\theta p, \delta p_i) &= \frac{f_2(\theta p)}{\sin^2 \theta p} \cdot \phi_i; \\ f_3(\theta p, \delta p_i) &= f_3(\theta p) \quad \text{npu} \quad 0 \leq \delta p_i \leq \frac{\pi}{2} - \theta p; \\ f_3(\theta p, \delta p_i) &= f_3(\theta p) \cdot \frac{\theta p + \frac{\pi}{2} - \delta p_i}{2 \cdot \theta p} \quad \text{npu} \quad \frac{\pi}{2} - \theta p \leq \delta p_i \leq \frac{\pi}{2} + \theta p; \end{aligned}$$

Missing equations can be obtained from the vector productions of unit vectors directed to the Sun — $\vec{s}(\cos \delta s_1, \cos \delta s_2, \cos \delta s_3)$, to the Earth — $\vec{p}(\cos \delta p_1, \cos \delta p_2, \cos \delta p_3)$, and ors — $\vec{e}_x(1, 0, 0)$, $\vec{e}_y(0, 1, 0)$, $\vec{e}_z(0, 0, 1)$:

$$\begin{aligned} \left[\bar{s} \cdot \left[\bar{e}_x \cdot \bar{e}_y \right] \right] &= \bar{s} \cdot \left(\bar{e}_x \cdot \bar{e}_y \right) - \bar{e}_x \cdot \left(\bar{s} \cdot \bar{e}_y \right); \\ \left[\bar{p} \cdot \left[\bar{e}_x \cdot \bar{e}_y \right] \right] &= \bar{p} \cdot \left(\bar{e}_x \cdot \bar{e}_y \right) - \bar{e}_x \cdot \left(\bar{p} \cdot \bar{e}_y \right); \\ \left[\bar{e}_x \cdot \bar{e}_y \right] &= \bar{e}_z. \end{aligned}$$

Thus, on the basis of the thermal mathematical model, the model that serves to calculate angles between the axes of the coordinates system bound with Sc and directions to the Sun — δ_{si} , and the planet — δ_{pi} , i. e. to determine orientation of Sc.

Thermal model shows, that general measurement system of external Sc surface can use for determination of Sc orientation. This is possible at the condition of present plane multidirectional zones with the following properties:

- these zones shall have constant orientation in relation to the coordinates system bound with Sc;
- optical characteristics of these zones shall be known;
- there shall be no screening of these zones from the space by other structural elements;
- there shall be no less than six such zones, they shall be oriented so that each axis of the coordinates system bound with Sc form with the normal to the surface at least one angle less than 30 (theoretically less than 90) degrees in positive and negative directions;
- it is desirable that thermal sensitivity of these zones to the spatial external factors be much higher than to the internal heat factors of Sc;
- thermal capacity of these zones shall be minimum.

In some Sc such zones already exist. In the devices where such zones are difficult to part they can be created artificially as separate external elements set on the surface of the spacecraft [3].

In the Space Research Institute (SRI) RAS the model of such device has been developed and called a thermosensitive element (TSE). Orientation determination system based on thermosensitive elements is called thermodynamical system of orientation determination (TDSOD). The model of TSE has extremely reliable simple and inexpensive design. It consists of (fig. 9):

- heat receiving plate (1) from highly thermoconductive metal with special coating with calibrated optical characteristics;
- resistance thermometer (2), set in the center of the plate (1) so that thermal resistance between them be minimum;
- four-beam base (3), made of thin wall plate with low thermal conductivity (material — stainless steel or titanium), at the same time being a thermal bypass between the thermosensitive plate and Sc frame;
- fiber-glass plastic base (4) with electric outputs connected with the resistance thermometer;
- thermoinsulating screen (5), decreasing radiation flow from the structural elements to the heat receiving plate.

Thermosensitive elements of two types have been developed: solar and planetary (fig. 10), differing by optical characteristics of the heat receiving plate coating. Solar TSE was especially sensitive to the visible solar radiation for the account of the coating of “black nickel” type with $A_s = 0,9$ and $\varepsilon = 0,3$. Planetary TSE had heightened sensitivity to infrared radiation of the Earth for the account of the coating of AK-573 type with $A_s = 0,2$ and $\varepsilon = 0,8$.

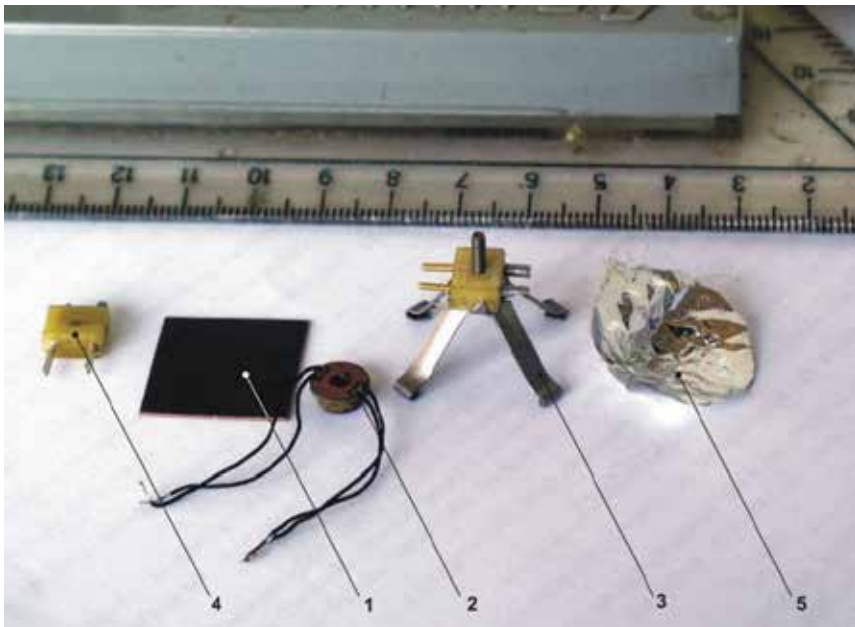


Fig. 9. TSE elements.



Fig. 10. General view of the solar (1) and planetary (2) TSE.

Thermodynamical system for orientation determination shall include not less than 12 such elements, one planetary and one solar perpendicular to each axis bound with S_c of the coordinates system in the positive and negative directions.

To assess the possibility of TSE use as an element sensitive to the changing direction to the Sun eight models of TSE differing by the parameters of thermosensitive plates which characteristics given in the table experimental research has been carried out.

The TSE models were put into the vacuum chamber where main space thermal factors were imitated: "cold", "blackness", solar and planetary radiation. The models were placed on the rotary-support that served to turn TSE so that the angle between the normal to heat receiving plate and the direction to the Sun change in the range from -90 to $+90^\circ$. The device at the same time appeared to be an imitator of the Sc frame coated with screen-vacuum thermoinsolation.

Initial angle between the normals to the heat receiving plates and the direction to the Sun was equal to -90° . TSE turn from -90 to $+90^\circ$ was performed with different angular velocities imitating possible rotation of Sc.

Dependence of the temperature of the heat receiving plates (for basic TSE № 1 and № 2) from an angle between the normal to them and the direction to the Sun is presented in fig. 11: for rotation velocity 1,5 (a), 4 (b), 10 (c), 20 (d), 30 (e) ang.deg./min.

TSE №	Characteristics of the heat receiving plate					TSE type
	Size, mm	Thickness, mm	Material	Optical characteristics of the coating		
				A_s	ε	
1	20×20	0,3	Alloy Д16	0,9	0,3	Solar
2	20×20	0,3	Alloy Д16	0,2	0,8	Planetary
3	20×20	0,5	Alloy Д16	0,9	0,3	Solar
4	20×20	0,5	Alloy Д16	0,2	0,8	Planetary
5	20×20	0,25	Cuprum	0,9	0,3	Solar
6	20×20	0,25	Cuprum	0,9	0,3	Solar
7	40×40	0,3	Alloy Д16	0,9	0,3	Solar
8	40×40	0,3	Alloy Д16	0,2	0,8	Planetary

Table 1. Characteristics of heat receiving plates of the studied TSE

Analysis of the presented experimental data shows that, first, the proposed TSE design appears to be rather sensitive for orientation determination in relation to the Sun, second, sensitivity of this method for orientation determination decreases at the increase of the velocity of Sc rotation in relation to the Sun due to the increase of thermal inertia of heat receiving plate.

To assess the possibility of orientation determination in relation to the Sun with the use of TSE it is expedient to introduce the parameter binding differential temperature and angular characteristics of TSE. Such parameter can be sensitivity K , showing temperature change of the heat receiving plate of the thermosensitive elements at their turn in relation to the Sun for one angular degree.

Dependence of TSE sensitivity K on the angle α between the normal to the heat receiving plate and the direction to the Sun obtained on the basis of the experimental data is presented in fig. 12.

Thus, at the average TSE sensitivity equal to $1,2^\circ\text{C}/\text{ang.deg.}$, determination accuracy of the direction to the Sun can be 5 arc min. at the measurement accuracy of the temperature of $0,1^\circ\text{C}$, that can be attained at the use of standard resistance thermometers and individual calibration of each TSE.

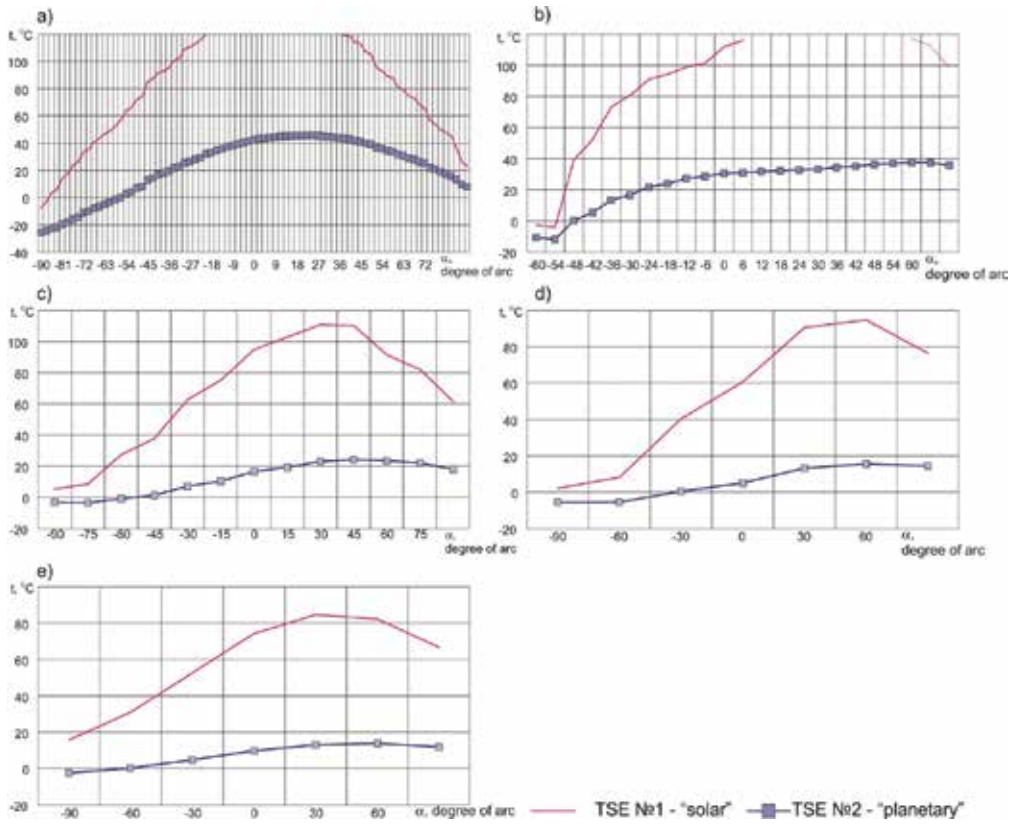


Fig. 11. Temperature dependence of the receiving plates of TSE No 1 and No 2 on the angle between the normal to them and the direction to the Sun.

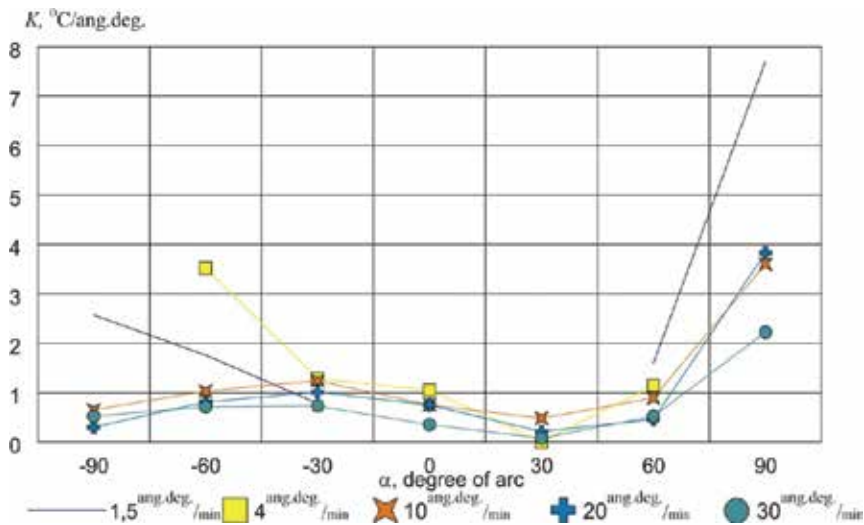


Fig. 12. Dependence of TSE sensitivity on the angle between the normal and heat receiving plate and the direction to the Sun.

During the experiment we have also studied influence of the material, thickness and area of thermoconductive plate on its sensitivity. It has been found out that replacement of the aluminum alloy by cuprum at the production of the heat receiving plate practically has no impact on TSE sensitivity (fig. 13).

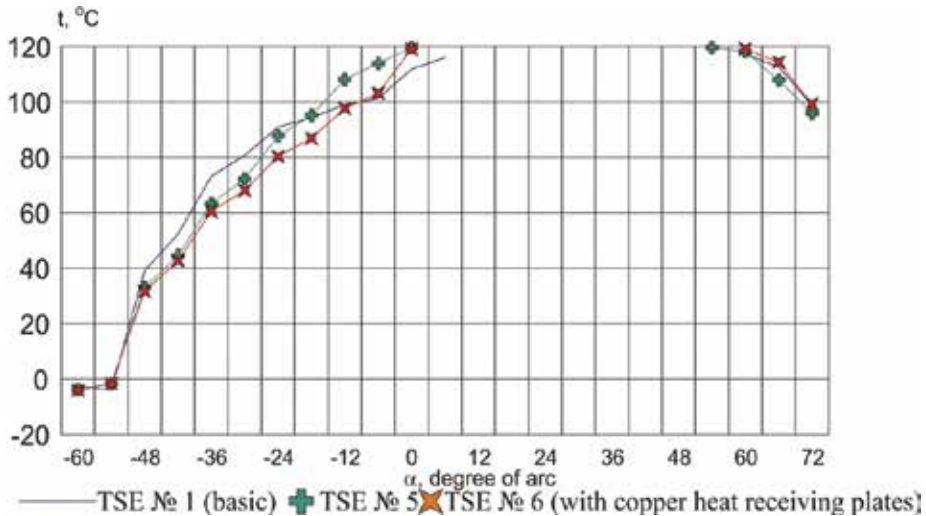


Fig. 13. Temperature dependence of aluminum and copper heat receiving plates on the angle between the normal to them and the direction to the Sun.

Increase of the area of heat receiving plate enlarges TSE sensitivity at the angle between the normal to the plate and the direction to the Sun of less than 45° (fig. 14). Increase of the thickness of the heat receiving plate significantly reduces its reaction on the changing direction of the solar radiation (fig. 15).

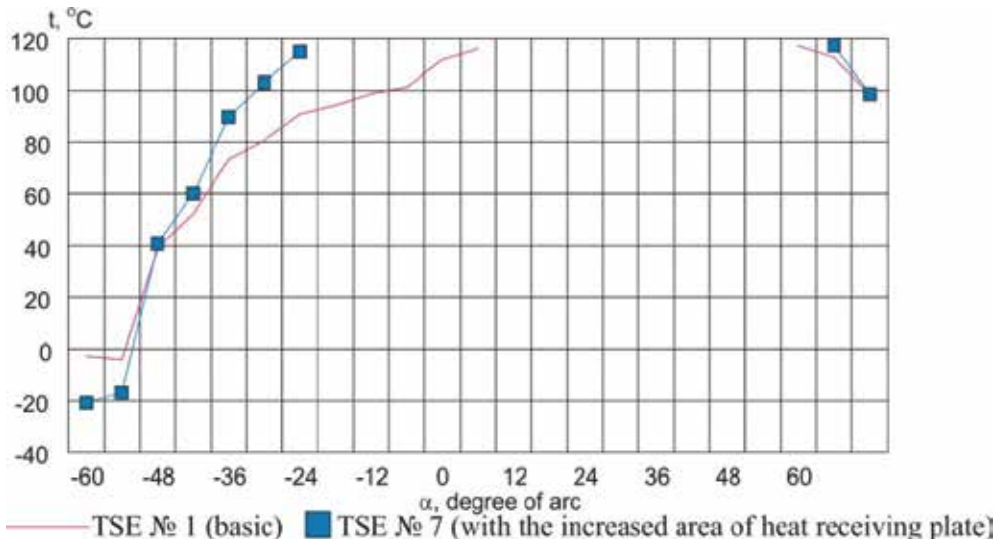


Fig. 14. Dependence of the temperature of heat receiving plates with the dimensions 20x20 and 40x40 mm on the angle between the normal to them and the direction to the Sun.

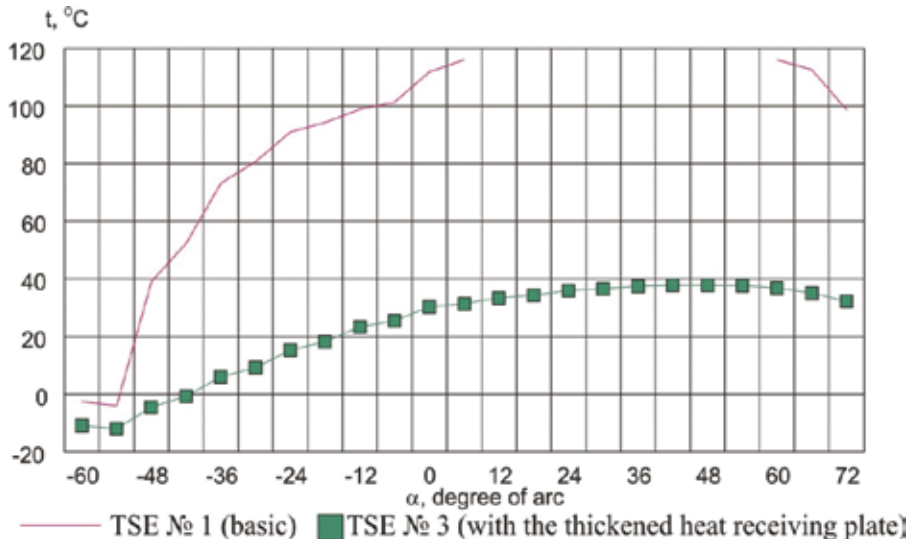


Fig. 15. Temperature dependence of heat receiving plates with the thickness of 0,3 and 0,5 mm on the angle between the normal to them and the direction to the Sun.

7. Conclusion

Usually the spacecraft have heat insulation from a space as much as possible. Heat, generated in the spacecraft, irradiate in the space through radiators – small open zone of an external surface. For additional heating of the spacecraft the heaters are provided.

However in Solar system is as heating sources (the sun and planets), so cooling sources (space). Use of several differently oriented radiators allows creating self-regulated thermal system of spacecraft on the balance between the absorbed irradiance from external heat source and the radiated thermal flux. Such system doesn't need energy and works at any spacecraft orientation. Besides, this system allows defining a direction on the Sun and the Earth and therefore can be used for definition of spacecraft orientation.

8. References

- [1] Semena N.P., Konovalov A.A. Methods for creating the self-regulating mechanisms of passive systems for ensuring thermal regime of devices for space application, *Thermophysics and Aeromechanics*, 2007, Vol. 14, No. 1, p.81-91.
- [2] Semena N.P. Determination of spacecraft orientation by the temperature field analysis of its outer surface, *Thermophysics and Aeromechanics*, 2009, Vol. 16, No 1, p.135-143.
- [3] Semena N.P., Kostenko V.I., Logvinenko S.P. Determination of the Spacecraft Angular Position by Temperature Measurements of Thermosensitive Plates, RF Patent № 2126137, 10 February 1999.

The Mechanics Analysis of Desquamation for Thermal Protection System (TPS) Tiles of Spacecraft

Zhang Taihua^{1,2}, Meng Xianhong² and Zhang Xing²

¹*Academy of Opto-Electronics, Chinese Academy of Sciences, Beijing 100080*

²*The Institute of Solid Mechanics, Beihang University, Beijing 100083
China*

1. Introduction

On the basis of solid mechanics, the “Peeling off” problem of TPS tiles on space craft surface is investigated. After considering the existence of peeling stress along the interface between the TPS tiles and the frame of space shuttle, a new model of mechanics is established to satisfy the boundary conditions of shear stress, which cannot be satisfied by the traditional shear-lag model. According to these new solutions, the reasonable explanation can be made about the failure of glued joint for TPS tiles. The stress distributions are studied when TPS tiles working in high temperature condition have different length, thickness, and material, and some advices can be provided to the design of TPS tiles.

2. Background

Various spacecrafts have their own characteristics. For example, as for as the Thermal Protection System (TPS) is concerned, their protection programs and materials are not identical. As the main material of spacecraft structure is aluminium, the temperature of the crucial structure could not be higher than 177°C to ensure that the connection between the spacecraft internal structure and the TPS tiles with sufficient strength.

Ceramic TPS tiles plays a great role of protecting the internal structure while spacecraft is re-entering the atmosphere. But in recent years, there have been many accidents and potential dangers, even tragic plane crash tragedy without any survivals during the spacecraft re-entry. For example, in 2003 the Space Shuttle *Columbia* Accident Investigation Board determined that a hole was punctured in the leading edge on one of *Columbia*'s wings, made of TPS tiles with carbon-carbon composite. The hole had formed when a piece of insulating foam from the external fuel tank peeled off during the launch 16 days earlier and struck the shuttle's wing. During the intense heat of re-entry, hot gases penetrated the interior of the wing, destroying the support structure and causing the rest of the shuttle to break apart (XING, 2003).

Of course, the desquamation of the TPS may be induced by many reasons, such as spacecraft vibration, engine noise, external rain, hail impact and so on. In the paper, the characteristics of the working TPS tiles are studied, the effects on the peeling stress by the

feature of TPS tile's working leading stress and the different levels of aerodynamic heating are analyzed too. And then, the influence of the TPS tile's size, thickness and material designing on the peeling stress are further analyzed. Then an explanation for TPS tiles desquamation is made, and some available mechanical reference frame and recommendations during the TPS tiles designing process are attempted to provide.

A sketch of glue joint with TPS tiles is shown as Figure 1.

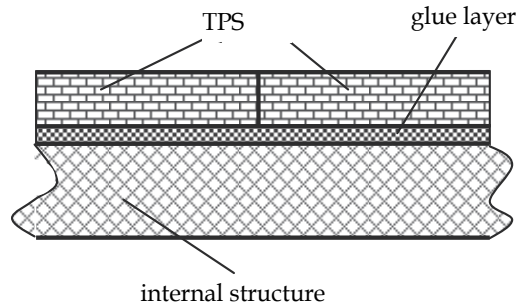


Fig. 1. A sketch of glue joint with TPS tiles

3. The mechanics analysis of desquamation for TPS tiles

3.1 The method of analysis

Based on the analysis above, it can be seen from mechanical perspective that the problem of the desquamation for TPS tiles can be solved by analyzing the stress situation of tiles, glue layer and internal structure, as well as the relation between the internal stress and the exterior aerodynamic heating or the tiles size designing and so on. Because the TPS tiles and the internal structure are connected by the glue layer, the peeling stress, one potential factor of the peeling off of the tiles, can be obtained by analyzing the stress situation of glue layer.

For this connection, to analyze glue layer stresses and confirm the strength of the joint, one can usually adopt the traditional Shear - lag Theory (Kuhn P., 1956), in which the glue layer can only suffer the shearing force while tiles and the internal structure body are only imposed on pulling force, obtaining the maximum of the glue layer shearing at its two ends. However, it is clear that this kind of analysis results can not satisfy the boundary conditions at both ends of the glue layer according to the the shear stresses reciprocal theorem, which states that the shear stresses at the ends must vanish. This article tries to provide some

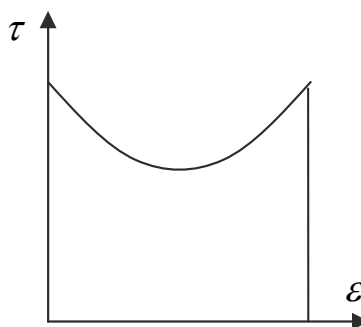


Fig. 2. Shear stress distribution along the semi-glue layer of right hand side

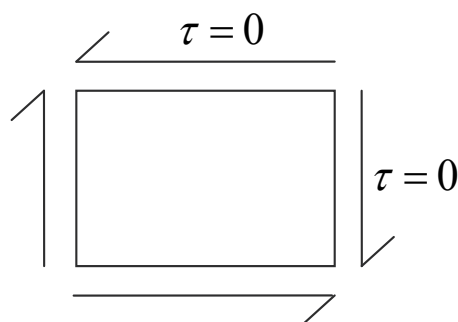


Fig. 3. Boundary condition at glue layer terminal of right hand side

reliable and advantageous mechanics basics for TPS tiles designing by studying the effects of the outside aerodynamic heating and the tiles size design on the glue layer stress but under the satisfactory of these boundary conditions.

Further, structure model shown in Figure 1 can be simplified to that shown in Figure 4(a), because the glue layer thickness is much smaller than that of tiles and structure. For the clarity, TPS tiles are marked by 1 and the internal structure by 2. In order to ensure that the layer shown Figure 4(a) could meet the boundary conditions of stress distribution, we established the following mechanical model (ZANG., 2006):

1. As shown in Figure 4(b), on the TPS tiles and the internal structure cross-sections, there is not only tension, but also bending moment and shear.
2. The glue layer thickness is ignored; however, it is assumed that the normal stress and shear stress both exists in the glue layer, as shown Figure 4(c);
3. In the connection of the TPS tiles and the structure, the longitudinal normal stress due to the tensile force and bending moment is calculated by the engineering beam theory, while the shear stress due to the elasticity of shear by the generic elasticity theory.

On this basis, we can solve the problem by force method :

1. Regard the tile's pulling stress and bending moment as generalized internal force, which is utilized to express the other internal force and stress by the equilibrium equations including tensile structure and the bending moment and glue layer's shear stresses and direct stress.
2. Establish the compatible equations which should be satisfied by the above two generalized internal force, two second order differential Eulerian equations satisfied by pulling force and bending moment, according to the complementary virtual work principle.
3. Obtain the closed analytical solution of generalized internal force and the glue layer stress by solving these two Eulerian equations under the boundary conditions.

3.2 Equilibrium equations

First, consider a cross-section having a distance x from the symmetry plane of the TPS tile, as shown in Figure 4(a), and regard the right part as one free body as shown in Figure 4(b). Obviously, the axial force N_1 and bending moment M_1 of the TPS tiles can be considered as the redundant internal forces of constrains for the equilibrium equations, which are both the function of x .

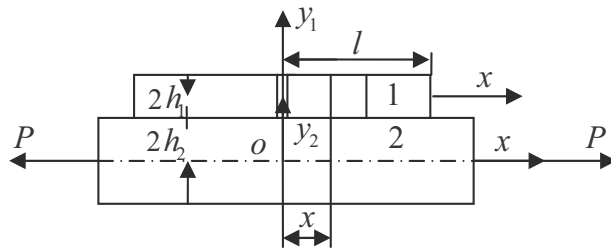


Fig. 4. (a) Coordinate systems of glue joint with mono-lateral connecting plate

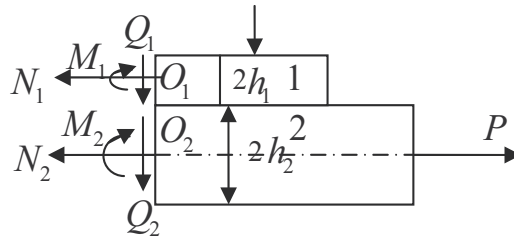


Fig. 4(b) Force state at cross section x of glue joint

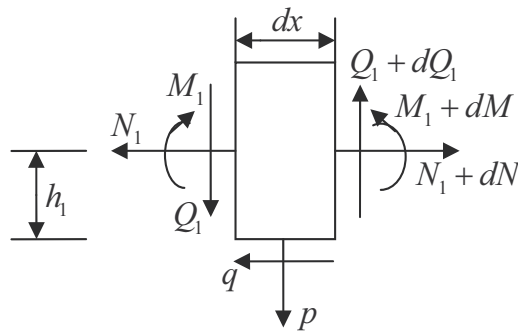


Fig. 4. (c) Free body diagram of infinitesimal segment dx along the connecting plate

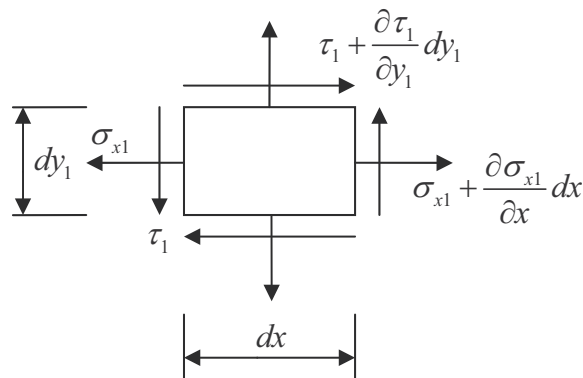


Fig. 4. (d) Free body diagram of infinitesimal element $dx \times dy$ within the connecting plate

$$N_1 = N(x) = N \quad (1)$$

$$M_1 = M(x) = M \quad (2)$$

It can be seen by applying equilibrium equations to the free body that the axial force N_2 and bending moment M_2 are respectively equal to

$$N_2 = P - N \quad (3)$$

$$M_2 = N(h_1 + h_2) - M \quad (4)$$

Then the shear layer flow q in TPS tile 1 can be obtained by applying the equilibrium equations to the free body, as shown in Figure 4(c).

$$q = \frac{dN}{dx} \quad (5)$$

It should be noted that q shall be recessed shear stress for the plate that has a unit width. Further, taking into account formula (5), the shear Q_1 in the TPS tiles equals to

$$Q_1 = qh_1 - \frac{dM}{dx} = h_1 \frac{dN}{dx} - \frac{dM}{dx} \quad (6)$$

According to equilibrium equations for the free body shown in Figure 4(b) and formula (6), the shear Q_2 in the structure is

$$Q_2 = -Q_1 = \frac{dM}{dx} - h_1 \frac{dN}{dx} \quad (7)$$

The normal stress p in the TPS tile layer can be obtain by the equilibrium equation for the free body, as shown in Figure 4(c).

$$p = \frac{dQ_1}{dx} = h_1 \frac{d^2N}{dx^2} - \frac{d^2M}{dx^2} \quad (8)$$

The normal stress σ_{x1} and shear stress τ_1 of the plate 1 should satisfy the following equation by the equilibrium conditions of an infinitesimal element that has a dx width and dy length.

$$\frac{\partial \sigma_{x1}}{\partial x} + \frac{\partial \tau_1}{\partial y_1} = 0 \quad (9)$$

According to the theory of beam (HU, 1980), we have

$$\sigma_{x1} = \frac{N_1}{A_1} - \frac{M_1}{I_1} y_1 = \frac{N}{A_1} - \frac{M}{I_1} y_1 \quad (10)$$

Inserting equation (10) into equation (9) and taking into account the following boundary conditions results in

$$y_1 = h_1 \quad , \quad \tau_1 = 0 \quad (11)$$

The integration is available

$$\tau_1 = \frac{1}{A_1} \frac{dN}{dx} (h_1 - y_1) - \frac{1}{2I_1} \frac{dM}{dx} (h_1^2 - y_1^2) \quad (12)$$

where A_1 and I_1 are the cross-sectional area and axial inertia moment of the TPS tile 1 respectively.

Similarly, for the structure 2, we have

$$\frac{\partial \sigma_{x2}}{\partial x} + \frac{\partial \tau_2}{\partial y_2} = 0 \quad (13)$$

$$\sigma_{x2} = \frac{N_2}{A_2} - \frac{M_2}{I_2} y_2 = \frac{1}{A_2} (P - N) - \frac{1}{I_2} \{N(h_1 + h_2) - M\} y_2 \quad (14)$$

$$y_2 = -h_2 \quad , \quad \tau_2 = 0 \quad (15)$$

$$\tau_2 = \frac{1}{A_2} \frac{dN}{dx} (h_2 + y_2) - \frac{1}{I_2} \left\{ \frac{dN}{dx} (h_1 + h_2) - \frac{dM}{dx} \right\} \frac{1}{2} (h_2^2 - y_2^2) \quad (16)$$

In summary, according to the balance equation and the beam theory, the stress in glued pieces can be written in the following form:

$$\sigma_{x1} = \eta_{1n} N + \eta_{1m} M + \eta_{1p} P \quad (17)$$

$$\tau_1 = \zeta_{1n} \frac{dN}{dx} + \zeta_{1m} \frac{dM}{dx} \quad (18)$$

$$\sigma_{x2} = \eta_{2n} N + \eta_{2m} M + \eta_{2p} P \quad (19)$$

$$\tau_2 = \zeta_{2n} \frac{dN}{dx} + \zeta_{2m} \frac{dM}{dx} \quad (20)$$

$$q = \frac{dN}{dx} \quad (21)$$

$$p = h_1 \frac{d^2 N}{dx^2} - \frac{d^2 M}{dx^2} \quad (22)$$

In the equations above

$$\eta_{1n} = \frac{1}{A_1} \quad , \quad \eta_{1m} = -\frac{y_1}{I_1} \quad , \quad \eta_{1p} = 0 \quad (23)$$

$$\zeta_{1n} = \frac{1}{A_1} (h_1 - y_1) \quad , \quad \zeta_{1m} = -\frac{1}{2I_1} (h_1^2 - y_1^2) \quad (24)$$

$$\left. \begin{aligned} \eta_{2n} &= -\frac{1}{A_2} - \frac{1}{I_2}(h_1 + h_2)y_2 \\ \eta_{2m} &= \frac{y_2}{I_2}, \quad \eta_{2p} = \frac{1}{A_2} \end{aligned} \right\} \quad (25)$$

$$\left. \begin{aligned} \zeta_{2n} &= \frac{1}{A_2}(h_2 + y_2) - \frac{1}{2I_2}(h_1 + h_2)(h_2^2 - y_2^2) \\ \zeta_{2m} &= \frac{1}{2I_1}(h_2^2 - y_2^2) \end{aligned} \right\} \quad (26)$$

3.3 Aerodynamic heating load equivalent strain

When space craft return to the atmosphere at a high speed , it will happen that a fierce friction with the dense atmosphere produces a lot of pneumatic hot. To ensure the normal work of the interior structure of spacecraft, the tiles internal structure temperature must below 177 °C. Thus, the external tiles suffers a high-temperature heat and deforms, while the internal architecture suffers a low temperature heat and then deforms, and the deviation of the internal and external displacement caused by aerodynamic heating leads to a potential impetus to the desquamation of the tiles.

Here, we analyze the additional load generated by aerodynamic heating.

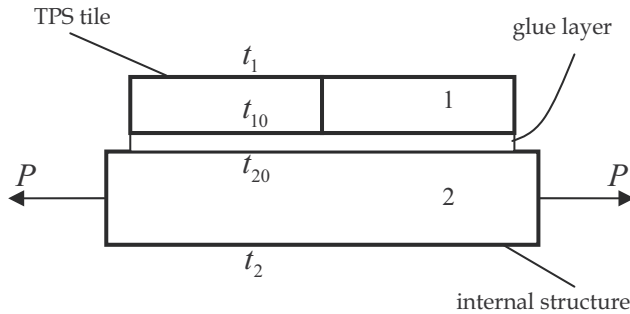


Fig. 5. The sketch of temperature between TPS tiles and structure

Let t_0 denote the initial temperature while the spacecraft begins working, t_{j0} the temperature of the connection of the plate j at working state and the layer. Specifically, as shown in Figure 5, t_1 is the local aerodynamic heating temperature of the outer surface of the TPS tiles and t_2 is the internal temperature of the structure. For a homogeneous material, the temperature can be assumed to change approximately linearly in the thickness direction. Therefore, the local temperature can be expressed by:

$$t_j = t_{j0} + \frac{dt_j}{dy_j} y_j \quad (27)$$

Furthermore, the strain caused by the temperature should be

$$\varepsilon_{t_j} = \alpha_j (t_j - t_0) \quad (28)$$

Where, α_j is the thermal expansion coefficient of board j . Inserting equation (27) into equation (28) results in

$$\varepsilon_{t_j} = \alpha_j (t_{j0} - t_0) + \alpha_j \frac{dt_j}{dy_j} y_j \quad (29)$$

Due to the linear change of the internal material temperature,

$$k_j = \alpha_j \frac{dt_j}{dy_j}, \quad \varphi_j = \alpha_j (t_{j0} - t_0) \quad (30)$$

k_j , the temperature gradient of the structure j , should be a constant. Then equation (29) can be written as:

$$\varepsilon_{t_j} = \varphi_j + k_j y_j \quad (31)$$

Which the additional strain of board j is caused by aerodynamic heating.

Since the main material of the internal structure is aluminium, which has a high thermal conductivity, the temperature of the internal layer can be assumed to be the same everywhere, i.e. the temperature gradient is 0, that is

$$t_2 = t_{20}, \quad k_2 = 0 \quad (32)$$

As the layer of tiles is much thinner than the protective layer and internal structure, the temperature at the joint of the protective layer and the TPS tiles can be thought to be the same as that at the joint of the protective layer and the internal structure. Thus

$$t_{10} = t_{20} \quad (33)$$

3.4 Compatibility equation

The stress of TPS tiles, structure and the glue layer are all determined by the axial force and bending moment. Thus, to build expression between the former and the latter, the compatibility equations is needed, which is derived according to complementary virtual work principle due to the complexity of the deformation (Timoshenko S., 1958; HU, 1980; ZHANG, 1995; QIAN, 1980).

It can be found from (17) and (22) that the stress of the protection tiles, the structure and the layer is all depend on N and M . The compatibility equation must be introduced here in order to determine these two functions. We established the compatibility equation based on the complementary virtual work principle to deal with the complexity of deformation. Let ε_j and γ_j denote respectively the normal and shear strain of board j . Then the complementary virtual work principle can be expressed as

$$\delta W_c = \sum_{j=1}^2 \int_0^l \int_{-h_j}^{h_j} \{ \varepsilon_j \delta \sigma_j + \gamma_j \delta \tau_j \} dy_j dx = 0 \quad (34)$$

Where δW_c represents the virtual work variation of W_c ; $\delta \sigma_j$ and $\delta \tau_j$ representing the stress and shear stress variation of board j .

It can be seen from (17) and (20) that

$$\left. \begin{aligned} \delta\sigma_1 &= \delta\sigma_{x1} = \eta_{1n}\delta N + \eta_{1m}\delta M \\ \delta\tau_1 &= \zeta_{1n} \frac{d\delta N}{dx} + \zeta_{1m} \frac{d\delta M}{dx} \end{aligned} \right\} \quad (35)$$

$$\left. \begin{aligned} \delta\sigma_2 &= \delta\sigma_{x2} = \eta_{2n}\delta N + \eta_{2m}\delta M \\ \delta\tau_2 &= \zeta_{2n} \frac{d\delta N}{dx} + \zeta_{2m} \frac{d\delta M}{dx} \end{aligned} \right\} \quad (36)$$

Equation (34), taking into account equations (35) and (36), can be written as:

$$\begin{aligned} \delta W_c &= \sum_{j=1}^2 \int_0^l \left\{ \int_{-h_j}^{h_j} \varepsilon_j \eta_{jn} dy_j \right\} \delta N dx + \sum_{j=1}^2 \int_0^l \left\{ \int_{-h_j}^{h_j} \varepsilon_j \eta_{jm} dy_j \right\} \delta M dx \\ &+ \sum_{j=1}^2 \int_0^l \left\{ \int_{-h_j}^{h_j} \gamma_j \zeta_{jn} dy_j \right\} \frac{d\delta N}{dx} dx + \sum_{j=1}^2 \int_0^l \left\{ \int_{-h_j}^{h_j} \gamma_j \zeta_{jm} dy_j \right\} \frac{d\delta M}{dx} dx = 0 \end{aligned} \quad (37)$$

Integrating the third and fourth term by parts and taking into account

$$x = 0, \quad \delta N = 0, \quad \delta M = 0 \quad (38)$$

$$x = l, \quad \delta N = 0, \quad \delta M = 0 \quad (39)$$

And the arbitrariness and independence of δN and δM in interval $0 < x < l$, one can obtain the following compatibility equation, which is expressed by the strain:

$$\frac{d}{dx} \left\{ \sum_{j=1}^2 \int_{-h_j}^{h_j} \gamma_j \zeta_{jn} dy_j \right\} - \sum_{j=1}^2 \int_{-h_j}^{h_j} \varepsilon_j \eta_{jn} dy_j = 0 \quad (40)$$

$$\frac{d}{dx} \left\{ \sum_{j=1}^2 \int_{-h_j}^{h_j} \gamma_j \zeta_{jm} dy_j \right\} - \sum_{j=1}^2 \int_{-h_j}^{h_j} \varepsilon_j \eta_{jm} dy_j = 0 \quad (41)$$

where ε_{t_j} is the additional strain by aerodynamic heating.

In the case of aerodynamic heating, when the TPS tiles and structure work in the elastic range, from (17) to (20) with (31), we have

$$\varepsilon_j = \frac{1}{E_j} (\eta_{jn} N + \eta_{jm} M + \eta_{jp} P) + \varepsilon_{t_j} \quad (42)$$

$$\gamma_j = \frac{\tau_j}{G_j} = \frac{1}{G_j} (\zeta_{jn} \frac{dN}{dx} + \zeta_{jm} \frac{dM}{dx}) \quad (43)$$

Inserting (42) and (43) into (40) and (41) will result in the two compatibility equations, which are expressed by the axial force N and bending moment of the protective layer:

$$\alpha_{nn} \frac{d^2 N}{dx^2} + \alpha_{nm} \frac{d^2 M}{dx^2} - \beta_{nn} N - \beta_{nm} M = \beta_{np} P + \beta_{nt} = \beta_{np} \left(P + \frac{\beta_{nt}}{\beta_{np}} \right) \quad (44)$$

$$\alpha_{mn} \frac{d^2 N}{dx^2} + \alpha_{mm} \frac{d^2 M}{dx^2} - \beta_{mn} N - \beta_{mm} M = \beta_{mp} P + \beta_{mt} = \beta_{mp} \left(P + \frac{\beta_{mt}}{\beta_{mp}} \right) \quad (45)$$

In equation (44) and type (45), β_{nt} / β_{np} and β_{mt} / β_{mp} can be considered as additional loads caused by aerodynamic heating.

$$\left. \begin{aligned} \alpha_{nn} &= \sum_{j=1}^2 \frac{1}{G_j} \left\{ \int_{-h_j}^{h_j} \zeta_{jn} \zeta_{jn} dy_j \right\} \\ \alpha_{nm} &= \sum_{j=1}^2 \frac{1}{G_j} \left\{ \int_{-h_j}^{h_j} \zeta_{jn} \zeta_{jm} dy_j \right\} \\ \beta_{nn} &= \sum_{j=1}^2 \frac{1}{E_j} \left\{ \int_{-h_j}^{h_j} \eta_{jn} \eta_{jn} dy_j \right\} \\ \beta_{nm} &= \sum_{j=1}^2 \frac{1}{E_j} \left\{ \int_{-h_j}^{h_j} \eta_{jn} \eta_{jm} dy_j \right\} \\ \beta_{np} &= \sum_{j=1}^2 \frac{1}{E_j} \left\{ \int_{-h_j}^{h_j} \eta_{jn} \eta_{jp} dy_j \right\} \\ \beta_{nt} &= \sum_{j=1}^2 \int_{-h_j}^{h_j} (\varphi_j + k_j y_j) \eta_{jn} dy_j \end{aligned} \right\} \quad (46)$$

$$\left. \begin{aligned} \alpha_{mn} &= \sum_{j=1}^2 \frac{1}{G_j} \left\{ \int_{-h_j}^{h_j} \zeta_{jm} \zeta_{jn} dy_j \right\} \\ \alpha_{mm} &= \sum_{j=1}^2 \frac{1}{G_j} \left\{ \int_{-h_j}^{h_j} \zeta_{jm} \zeta_{jm} dy_j \right\} \\ \beta_{mn} &= \sum_{j=1}^2 \frac{1}{E_j} \left\{ \int_{-h_j}^{h_j} \eta_{jm} \eta_{jn} dy_j \right\} \\ \beta_{mm} &= \sum_{j=1}^2 \frac{1}{E_j} \left\{ \int_{-h_j}^{h_j} \eta_{jm} \eta_{jm} dy_j \right\} \\ \beta_{mp} &= \sum_{j=1}^2 \frac{1}{E_j} \left\{ \int_{-h_j}^{h_j} \eta_{jm} \eta_{jp} dy_j \right\} \\ \beta_{mt} &= \sum_{j=1}^2 \int_{-h_j}^{h_j} (\varphi_j + k_j y_j) \eta_{jm} dy_j \end{aligned} \right\} \quad (47)$$

From (46) and type (47), we can see

$$\alpha_{mn} = \alpha_{nm} \quad (48)$$

$$\beta_{mn} = \beta_{nm} \quad (49)$$

3.5 Solve the governing equations

Dominant equations (44) and (45) are second order non-homogeneous differential equations, whose solution has the following forms:

$$N = N_0 + N' \quad (50)$$

$$M = M_0 + M' \quad (51)$$

where N_0 and M_0 are the generic solution of the homogeneous equations with N' and M' being the special solution of the non-homogeneous equations

N_0 and M_0 may be exponential function:

$$N_0 = Ae^{kx} \quad (52)$$

$$M_0 = Be^{kx} \quad (53)$$

Inserting (44) and (45) into the corresponding homogeneous equation, we have

$$(\alpha_{nn}k^2 - \beta_{nn})A + (\alpha_{nm}k^2 - \beta_{nm})B = 0 \quad (54)$$

$$(\alpha_{mn}k^2 - \beta_{mn})A + (\alpha_{mm}k^2 - \beta_{mm})B = 0 \quad (55)$$

The condition for the existence of non-zero solution to these equations is that the coefficient determinant of A and B is zero.

$$\begin{vmatrix} \alpha_{nn}k^2 - \beta_{nn} & \alpha_{nm}k^2 - \beta_{nm} \\ \alpha_{mn}k^2 - \beta_{mn} & \alpha_{mm}k^2 - \beta_{mm} \end{vmatrix} = 0 \quad (56)$$

Expanding the above determinant and letting

$$a = \alpha_{nn}\alpha_{mm} - \alpha_{nm}^2 \quad (57)$$

$$b = -\alpha_{nn}\beta_{mm} - \alpha_{mm}\beta_{nn} + 2\alpha_{nm}\beta_{mn} \quad (58)$$

$$c = \beta_{nn}\beta_{mm} - \beta_{nm}^2 \quad (59)$$

We can get the following algebraic equation on k^2 :

$$ak^4 + bk^2 + c = 0 \quad (60)$$

The two square roots of k^2 are

$$k^2 = \frac{1}{2a} \left\{ -b \pm \sqrt{b^2 - 4ac} \right\} \quad (61)$$

For the studied spacecraft protection system tiles, the two square roots of k^2 should be both real number greater than 0.

$$\kappa_1 = \mu \quad , \quad \kappa_2 = -\mu \quad (62)$$

$$\kappa_1 = \nu \quad , \quad \kappa_2 = -\nu \quad (63)$$

Where

$$\mu^2 = \frac{1}{2a} \left\{ -b + \sqrt{b^2 - 4ac} \right\} > 0 \quad (64)$$

$$\nu^2 = \frac{1}{2a} \left\{ -b - \sqrt{b^2 - 4ac} \right\} > 0 \quad (65)$$

Thus, N_0 and M_0 can be written in the form

$$N_0 = A_1 e^{\mu x} + A_2 e^{-\mu x} + A_3 e^{\nu x} + A_4 e^{-\nu x} \quad (66)$$

$$M_0 = B_1 e^{\mu x} + B_2 e^{-\mu x} + B_3 e^{\nu x} + B_4 e^{-\nu x} \quad (67)$$

The specific solutions for (44) and (45) of the particular solution N' and M' can be modified as

$$N' = CP \quad (68)$$

$$M' = DP \quad (69)$$

Inserting (68) and (69) into (44) and (45), one can get two algebraic equations on C and D :

$$\beta_{nn}C + \beta_{nm}D = -\beta_{np} - \frac{\beta_{nt}}{P} \quad (70)$$

$$\beta_{mn}C + \beta_{mm}D = -\beta_{mp} - \frac{\beta_{mt}}{P} \quad (71)$$

Taking into account both (70) and (71) leads to

$$C = \frac{\beta_{mn} \left(\beta_{mp} + \frac{\beta_{mt}}{P} \right) - \beta_{mm} \left(\beta_{np} + \frac{\beta_{nt}}{P} \right)}{\beta_{nn}\beta_{mm} - \beta_{mn}^2} \quad (72)$$

$$D = \frac{\beta_{nn} \left(\beta_{mp} + \frac{\beta_{mt}}{P} \right) - \beta_{mn} \left(\beta_{np} + \frac{\beta_{nt}}{P} \right)}{\beta_{mn}^2 - \beta_{nn}\beta_{mm}} \quad (73)$$

The eight undetermined coefficients depend on the following eight boundary conditions.

$$x = 0 \quad , \quad N = 0 \quad (74)$$

$$x = 0 \quad , \quad q = 0 \quad (75)$$

$$x = l , N = 0 \quad (76)$$

$$x = l , q = 0 \quad (77)$$

$$x = 0 , M = 0 \quad (78)$$

$$x = 0 , Q_1 = h_1 q - \frac{dM}{dx} = -\frac{dM}{dx} = 0 \quad (79)$$

$$x = l , M = 0 \quad (80)$$

$$x = l , Q_1 = h_1 q - \frac{dM}{dx} = -\frac{dM}{dx} = 0 \quad (81)$$

Inserting (66) and (68) into (50) and then inserting the obtained results into (74)~(77) will results in

$$A_1 + A_2 + A_3 + A_4 = -CP \quad (82)$$

$$\mu A_1 - \mu A_2 + \nu A_3 - \nu A_4 = 0 \quad (83)$$

$$e^{\mu l} A_1 + e^{-\mu l} A_2 + e^{\nu l} A_3 + e^{-\nu l} A_4 = -CP \quad (84)$$

$$\mu e^{\mu l} A_1 - \mu e^{-\mu l} A_2 + \nu e^{\nu l} A_3 - \nu e^{-\nu l} A_4 = 0 \quad (85)$$

Inserting (67) and (69) into (51) and then inserting the obtained results into (78)~(81), we have

$$B_1 + B_2 + B_3 + B_4 = -DP \quad (86)$$

$$\mu B_1 - \mu B_2 + \nu B_3 - \nu B_4 = 0 \quad (87)$$

$$e^{\mu l} B_1 + e^{-\mu l} B_2 + e^{\nu l} B_3 + e^{-\nu l} B_4 = -DP \quad (88)$$

$$\mu e^{\mu l} B_1 - \mu e^{-\mu l} B_2 + \nu e^{\nu l} B_3 - \nu e^{-\nu l} B_4 = 0 \quad (89)$$

Clearly, the generalized force N and M of TPS tiles, and the stress q and p of the layer can be calculated with the eight undetermined coefficients, which can be obtained by solving the two sets of algebraic equations.

Inserting (66), (68), (67) and (69) respectively into (50) and (51), we have

$$N = A_1 e^{\mu x} + A_2 e^{-\mu x} + A_3 e^{\nu x} + A_4 e^{-\nu x} + CP \quad (90)$$

$$M = B_1 e^{\mu x} + B_2 e^{-\mu x} + B_3 e^{\nu x} + B_4 e^{-\nu x} + DP \quad (91)$$

Further, inserting (90) and (91) into (5) and (8), we have

$$q = A_1 \mu e^{\mu x} - A_2 \mu e^{-\mu x} + A_3 \nu e^{\nu x} - A_4 \nu e^{-\nu x} \quad (92)$$

$$p = h_1 \left\{ \mu^2 (A_1 e^{\mu x} + A_2 e^{-\mu x}) + \nu^2 (A_3 e^{\nu x} + A_4 e^{-\nu x}) \right\} - \left\{ \mu^2 (B_1 e^{\mu x} + B_2 e^{-\mu x}) + \nu^2 (B_3 e^{\nu x} + B_4 e^{-\nu x}) \right\} \quad (93)$$

which are the closed solution for the stress of the layer.

4. Consequence analyses

By this analysis, solving layer stress can be summarized in the following procedure:

- i. Based on (23)~(26), write (17) and (20).
- ii. Calculate the coefficients in (60) with (57), (58) and (59).
- iii. Get (76) and (77) based on (64) and (65).
- iv. According to (70) and (71), particular solutions of inhomogeneous equation are shown as the coefficient of (68) and (69).
- v. Calculate every coefficients of generic solution for the homogeneous equation to get the distribution of stress of the layer.

From the mechanical point of view, based on the above theoretical derivation, in order to have more detailed understanding of the "Peeling off" problem for TPS tiles on space craft surfacethe, the maximum potential peeling stress was analyzed in its working condition, the effects of the outside aerodynamic heating and the tiles size design on the peeling stress are investigated.

As we all know, the material of spacecraft structure is mainly aluminium and its alloy materials. The mechanical properties of aluminium alloy can be found from "mechanical Dictionary" (The editorial department of Mechanical dictionary., 1990): $E=70\sim 79\text{GPa}$, $G=26\sim 30\text{GPa}$, $\sigma_s=35\sim 500\text{MPa}$, $\sigma_b=100\sim 550\text{MPa}$, thermal expansion coefficient $\alpha = 2.3 \times 10^{-5} / ^\circ\text{C}$. The material of rigid TPS tiles shown in Figure 2 is mainly the ceramic or ceramic-based materials. From (Davis., 2003), TPS tiles is mainly made of SiC and SiO_2 , whose mechanical properties are that $E=95\sim 402\text{GPa}$, thermal expansion coefficient $\alpha = 3.8 \sim 7.4 \times 10^{-6} / ^\circ\text{C}$. In the following stress distribution, the dimensionless coordinates are established based on Figure 6, where $x'' = x' / h_2$, $q' = qh_2 / P$, $p' = ph_2 / P$.

4.1 Different aerodynamic heating temperature on the peeling stress

The external TPS of re-entering body will have a high temperature during the spacecraft re-entering atmosphere with high aerodynamic heating, resulting thermal deformation of TPS tiles. Hence it is necessary that the effects of the outside aerodynamic heating on the peeling stress are investigated by theoretical analysis discussed above.

When the spacecraft returns to the atmosphere at high speed, the aerodynamic heating will lead to high temperature of the spacecraft re-entry body's external thermal protection system, thereby enabling protection watt thermal deformation. To study the effect of aerodynamic heating on the TPS tiles peeling stress by the above theory, we let the working stress of the structure $P=20\text{MPa}$ and take $E_1=E_2$, $h_1= 0.5h_2$, $t_0 = 20 ^\circ\text{C}$, $t_{j0}= 177 ^\circ\text{C}$, when the outside temperature of TPS tiles with aerodynamic heating $t_1 = 177 ^\circ\text{C}$, $300 ^\circ\text{C}$, $500 ^\circ\text{C}$, $700 ^\circ\text{C}$, $1000 ^\circ\text{C}$, and then get the distribution of the shear and normal stress of the adhesive layer, as shown in Figures 6, 7 and 8.

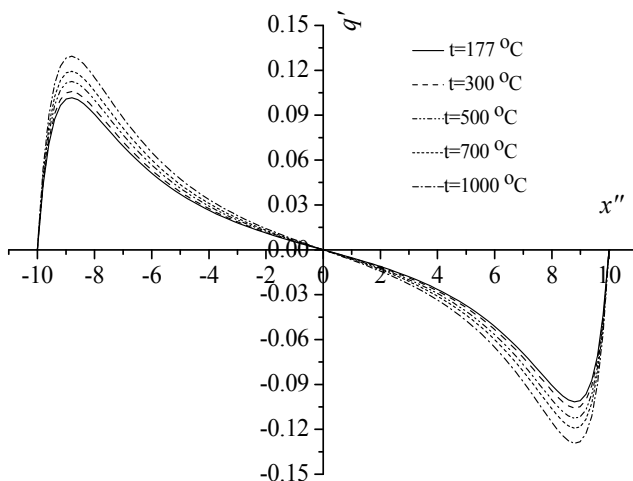


Fig. 6. Distribution of shearing stress q' along the glue layer with different t_1

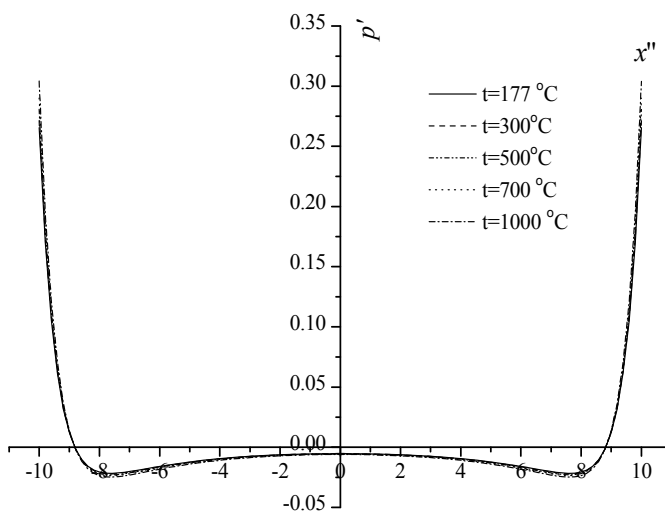


Fig. 7. Distribution of shearing stress p' along the glue layer with different t_1

4.2 The effects of the length of TPS tiles on peeling stress

Here, the effects of the length of the TPS tiles on the glue layer stress were investigated. Here, we examine the effect of the length of TPS tiles on stress distribution of the adhesive layer. Let the working stress of the structure $P=20\text{MPa}$, and $E_1 = 2E_2$, $h_1 = 0.5h_2$, $t_0 = 20^\circ\text{C}$, $t_{j0} = 177^\circ\text{C}$, $t_1 = 500^\circ\text{C}$. When $L/h_2 = 4, 6, 10, 15,$ and 20 , by the above theory, we get the distribution of shear and normal stress, as shown in Figures 9 and 10.

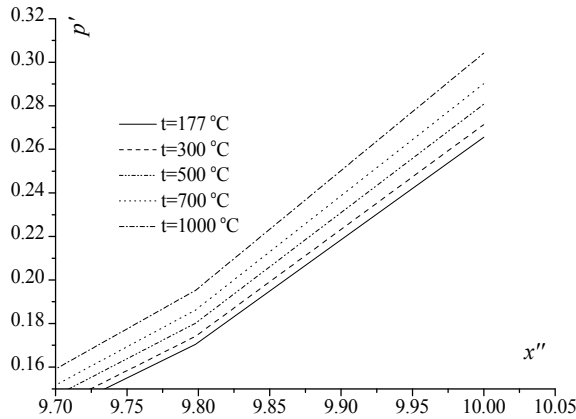


Fig. 8. Distribution of shearing stress p' along the glue layer with different t_1 (part curve)

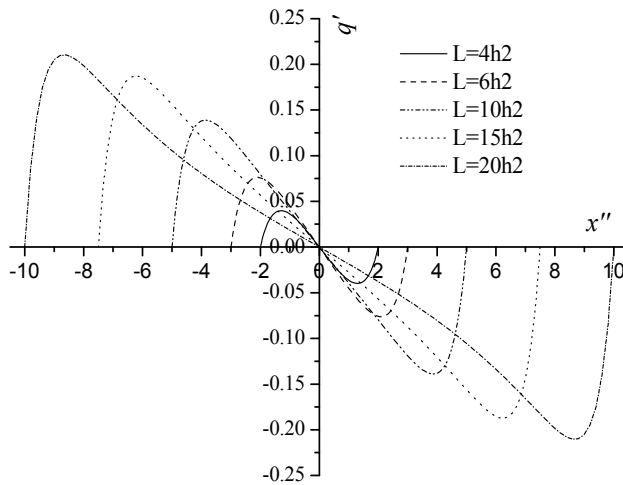


Fig. 9. Distribution of shearing stress q' along the glue layer with different length for TPS tiles

4.3 The effects of the thickness of TPS tiles on peeling stress

The thickness of the tiles in TPS design was also a very important consideration. The thickness of TPS tile thermal protection system in the design is also a very important consideration. We should analyze the effect of the TPS tiles thickness on the shear and normal stress of the layer. Let the working stress of the structure $P=20\text{MPa}$, and $E_1=2E_2$, $L=10 h_2$, $t_0=20^\circ\text{C}$, $t_{j0}=177^\circ\text{C}$, $t_1=500^\circ\text{C}$. When $h_1/h_2= 1/2, 1/3, 1/5, 1/8$, by the above theory, we also get the distribution of shear and normal stress, as shown Figures 11 and 12 respectively.

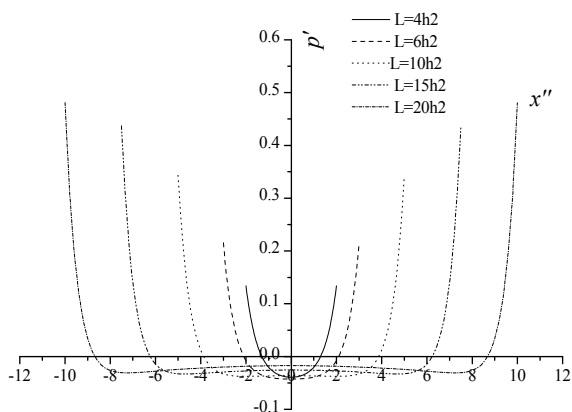


Fig. 10. Distribution of shearing stress p' along the glue layer with different length for TPS tiles

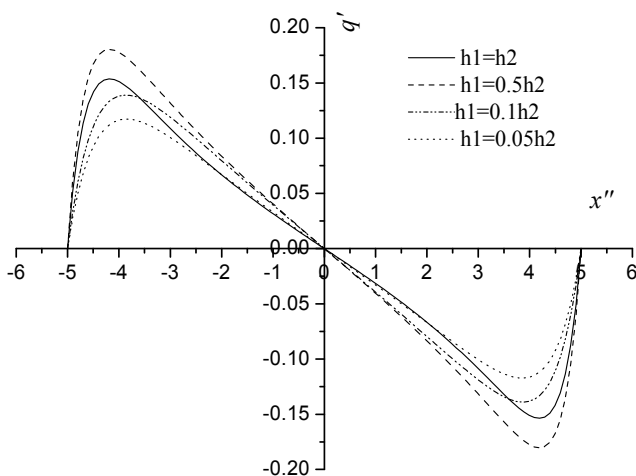


Fig. 11. Distribution of shearing stress q' along the glue layer with different thickness for TPS tiles

4.4 The effects of the material of TPS tiles on peeling stress

The selected material is different in different spacecraft TPS.

For different thermal systems of spacecraft, the selection of protection tile material is also different. Here, from a mechanical point of view, we study the effects of different material on the thermal protection tiles peeling off, i.e. the adhesive layer stress, mainly considering the effect of elastic modulus. Let the working stress of the structure $P=20\text{MPa}$, and $h_1/h_2=0.5$, $L=10 h_2$, $t_0=20^\circ\text{C}$, $t_j=177^\circ\text{C}$, $t_1=500^\circ\text{C}$. When $E_1/E_2=0.5, 1, 2,$ and 3 , by the above theory, we also get the distribution of shear and normal stress, as shown Figures 13, 14 and 15 respectively.

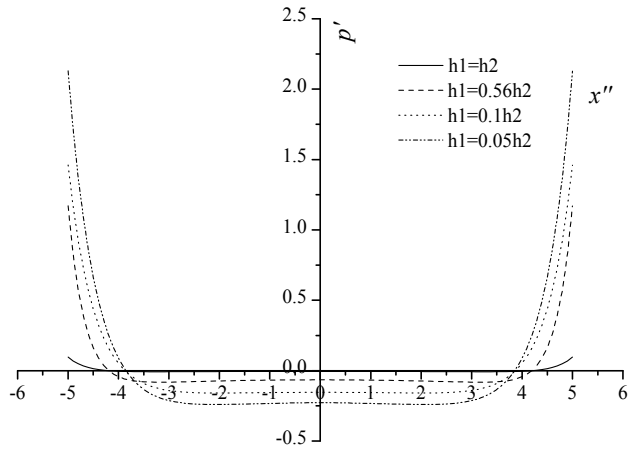


Fig. 12. Distribution of shearing stress p' along the glue layer with different thickness for TPS tiles

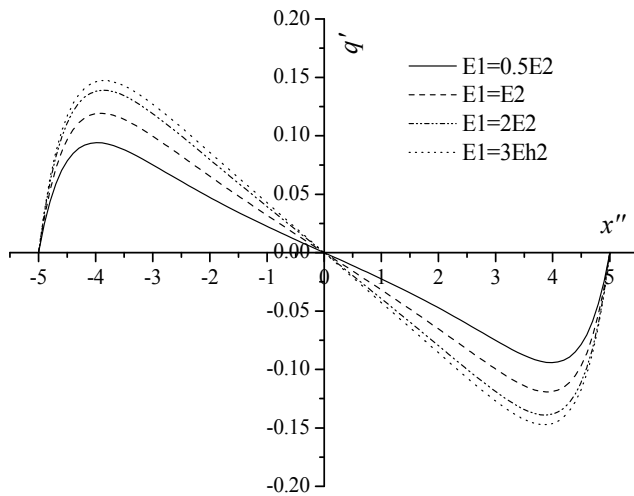


Fig. 13. Distribution of shearing stress q' along the glue layer with different materials for TPS tiles

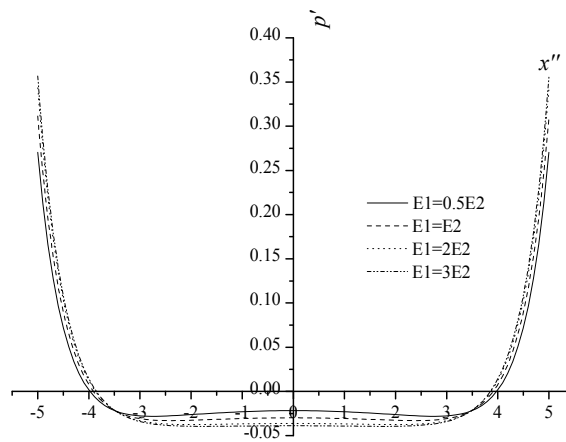


Fig. 14. Distribution of shearing stress p' along the glue layer with different materials for TPS tiles

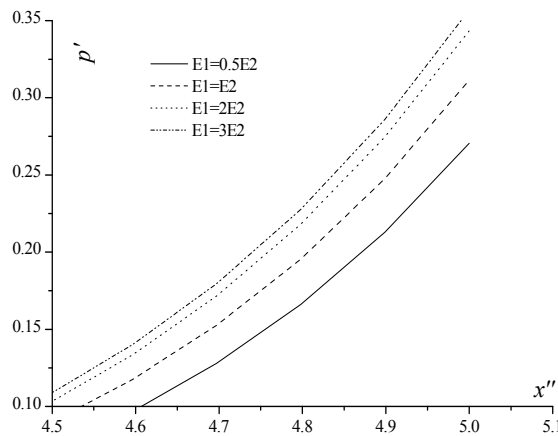


Fig. 16. Distribution of shearing stress p' along the glue layer with different materials for TPS tiles (part curve)

5. Conclusions

By analyzing the glue layer stress between TPS tiles and structures, and the influence of the size and material of TPS tiles, we concludes:

1. In the connection between TPS tiles and internal structure, the normal stress on the glue layer end reaches the max value with naught shear stress. Hence, it can be indicated that potential factors of the peeling off of the tiles are mainly contributed by peeling normal stress and influenced little by shear stress.

2. Glue layer stress concentrates near the edge of the tiles and almost naught in other areas. The fact that the ratios of glue layer shear stress and normal stress to working stress decreases with increasing working stress in the inner structure indicates that the increasing rate of glue layer stress is less than that of working stress.
3. Glue layer shear stress and normal stress both increases with temperature increasing, however, the increasing magnitude is not very large compared to influence of working stress's increasing on peeling stress, which also illustrates that the more aerodynamic heating is, the larger peeling stress of tiles is, quickening the desquamation of tiles.
4. Glue layer shear stress and normal stress concentrates much more near the end of tiles and their extremum get larger as the length of TPS tile increases; furthermore, the shear stress varies much more. This fact indicates that larger size of TPS tiles leads to peeling stress of glue larger and the influence of the length of the TPS tiles on the extremum of glue layer stress is obvious.
5. However, glue layer stress does not decrease (or increase) as the thickness of TPS tiles decreases (or increases). The thickness of TPS tiles does not influence the extremum of glue layer shear stress obviously, but much glue layer normal stress.
6. The influence of material Elastic modulus on peeling stress of glue layer is not strong, however, as a whole, the larger material Elastic modulus (i.e. Stiffness) is, the larger peeling stress of glue layer is.

6. References

- XING Yu-zhe., 2003. The final investigation report of columbia disaster[J].*Spece Exploration*, pp. 12:18-19.
- Kuhn P., 1956. *Stress in Aircraft and Structures*[M].McCraw-HIHLL BOOK COMPANY,
- ZANG Qing-lai, ZHANG Xing, WU Guo-xun. (2006). New model and new method of stress analysis about glued joints[J].*Chinese Journal of Aeronautics*, pp.6:1051-1057.
- Timoshenko S., 1958. *Strength of Materials*[M].Van Nostrand Reinhold Company.
- HU Hai-chang., 1980. Variational Principle and Application in Theory of Elasticity[M]. Beijing:Science Press.
- ZHANG Xing (editor in chief)., 1995. *Advanced Theory of Elas-ticity* [M]. Beijing:Beijing University of Aeronautics and Astronautics Press.
- QIAN Wei-chang., 1980. *Variational Method and finite Element*[M].Beijing:Sci-enee Press.
- The editorial department of Mechanical dic-tionary., 1990. *Mechanical Dietinary* [M]. Beijing:Encyclopedia of China Publishing House, pp.197-597.
- Davis J,Green, translated by Gong Jiang-hong., 2003. *The Mechanical Properties Introduction of Ceramic Materials*[M].Beijing:Tsinghua University Press, pp.21-35.]

Part 2

Cutting Edge State Estimation Techniques

Unscented Kalman Filtering for Hybrid Estimation of Spacecraft Attitude Dynamics and Rate Sensor Alignment

Hyun-Sam Myung¹, Ki-Kyuk Yong² and Hyochoong Bang¹

¹*Korea Advanced Institute of Science and Technology,*

²*Korea Aerospace Research Institute,
Republic of Korea*

1. Introduction

Requirements of highly precise pointing performance have been imposed on recently developed spacecrafts for a variety of missions. The stringent requirements have called on on-orbit estimation of spacecraft dynamics parameters and calibration of on-board sensors as indispensable practices.

Consequently, on-orbit estimation of the mass moment of inertia of spacecraft has been a major issue mostly due to the changes by solar panel deployment and a large portion of fuel consumption (Creamer et al., 1996; Ahmed et al., 1998; Bordany et al., 2000; VanDyke et al., 2004; Myung et al., 2007; Myung & Bang, 2008; Sekhavat et al., 2009).

As for measurement sensors, on-board calibration of alignment and bias errors of attitude and rate sensors is one of the main concerns of attitude sensor calibration researches (Pittelkau, 2001 & 2002, Lai et al., 2003). Pittelkau (2002) proposed an attitude estimator based on the Kalman filter (Kalman, 1960), in which spacecraft attitude quaternion, rate sensor misalignment and bias, and star tracker misalignments are taken into consideration as states, whereas the body rate is dealt as a synthesized signal by the estimates. Lai et al. (2003) derived a method for alignment estimation of attitude and rate sensors based on the unscented Kalman filter (UKF) (Julier and Uhlmann, 1997). Ma and Jiang (2005) presented spacecraft attitude estimation and calibration based only magnetometer measurements using an UKF.

An interesting point is that we need predesigned 3-axis excitation manoeuvres of spacecraft for both dynamics parameter estimation and sensor calibration. Therefore, this study is motivated to merge above estimation and calibration processes into a single filtering problem. It is noteworthy that poor information of moments of inertia is to be treated as a system uncertainty while the rate sensor model errors are to be incorporated into the measurement process.

As a filtering algorithm, this study employs a UKF. Extended Kalman filters (EKF) have been successfully applied to the nonlinear attitude estimation problem (Crassidis et al., 2007). Hybrid estimation using the EKF has been reported by Myung et al. (2007). However, the EKF estimates using the first order linearization, which may lead to instability of the filter (VanDyke et al., 2004). The UKF approximates the nonlinear model to the second order by spreading points 1 sigma apart from the *a priori* mean. Performing nonlinear

transformation of sigma points produces the *posterior* mean and covariance. Despite the computational burden of the UKF, extension of convergence region and numerical stability greatly outperform the EKF.

Parameter estimation by a dual UKF was proposed by VanDyke et al. (2004). Since UKF has more computational burden compared to EKF, a numerically efficient UKF was also developed for state and parameter estimation (van der Merwe & Wan, 2001).

In this paper, the UKF is applied to simultaneous spacecraft dynamics estimation and rate sensor alignment calibration using star tracker measurements. The spacecraft attitude and the body angular velocity are the state vectors. Estimation parameters are the six components of moment of inertia, and the bias, scale factor errors and misalignments of a rate sensor. Numerical simulations compare the results to those using the EKF.

2. Equation of motion of spacecraft

2.1 Attitude representation

Spacecraft attitude parameter is the unit quaternion defined by

$$\begin{aligned} \mathbf{q} &= \left[\mathbf{n}^T \sin\left(\frac{\phi}{2}\right) \quad \cos\left(\frac{\phi}{2}\right) \right]^T \\ &= [q_1 \quad q_2 \quad q_3 \quad q_4]^T \\ &= [q_{13} \quad q_4]^T \end{aligned} \quad (1)$$

where \mathbf{n} is the Euler axis and ϕ is the Euler angle. q_{13} is the vector part and q_4 is the scalar part in quaternion representation. Quaternion multiplication represents successive rotation (Wertz, 1978)

$$\begin{aligned} \mathbf{q}'' &= \mathbf{q}' \otimes \mathbf{q} \\ &= \begin{bmatrix} q'_4 & q'_3 & -q'_2 & q'_1 \\ -q'_3 & q'_4 & q'_1 & q'_2 \\ q'_2 & -q'_1 & q'_4 & q'_3 \\ -q'_1 & -q'_2 & -q'_3 & q'_4 \end{bmatrix} \begin{bmatrix} q_1 \\ q_2 \\ q_3 \\ q_4 \end{bmatrix} \end{aligned} \quad (2)$$

And inverse of quaternion

$$\mathbf{q}^{-1} = [-q_1 \quad -q_2 \quad -q_3 \quad q_4]^T \quad (3)$$

implies the opposite rotation of \mathbf{q} . By combining Eq. (2) and (3) residual rotation of \mathbf{q}'' with respect to \mathbf{q}' , or error quaternion $\delta\mathbf{q}$, is obtained such as

$$\delta\mathbf{q} = \mathbf{q}'' \otimes (\mathbf{q}')^{-1} \quad (4)$$

2.2 Spacecraft attitude equation of motion

The equation of motion of spacecraft is given as

$$\mathbf{J}\dot{\boldsymbol{\omega}} + \boldsymbol{\omega} \times \mathbf{J}\boldsymbol{\omega} = \mathbf{u} \quad (5)$$

where $\omega \in R^3$ is the body angular velocity, J is the mass moment of inertia matrix, and $u \in R^3$ is the external control input torque. The attitude kinematics is expressed by attitude quaternion such as (Crassidis et al., 1997)

$$\dot{q} = \frac{1}{2}\Omega(\omega)q = \frac{1}{2}\Xi(q)\omega \quad (6)$$

where

$$\Omega(\omega) \equiv \left[\begin{array}{c|c} -[\omega \times] & \omega \\ \hline -\omega^T & 0 \end{array} \right], \quad \Xi(q) \equiv \left[\begin{array}{c} q_4 I_3 + [q_{13} \times] \\ \hline -q_{13}^T \end{array} \right] \quad (7)$$

Due to the unity constraint on the attitude quaternion, only the vector component is utilized as states, and q_4 is calculated from the constraint. Choosing the body angular rate as one of the states, we rewrite Eq. (5) as

$$\dot{\omega} = -J^{-1}\omega \times J\omega + J^{-1}u \quad (8)$$

The six components of the moment of inertia are defined as

$$J = \begin{bmatrix} J_{11} & J_{12} & J_{13} \\ J_{12} & J_{22} & J_{23} \\ J_{13} & J_{23} & J_{33} \end{bmatrix} \quad (9)$$

In the form of vector notation, we define

$$p = [J_{11} \quad J_{22} \quad J_{33} \quad J_{12} \quad J_{13} \quad J_{23}]^T \quad (10)$$

2.3 Measurement model

The body angular velocity measurement equation at time $t = t_k$ is expressed as

$$\tilde{\omega}_k = (I + M)\omega_k + b + v_{\omega k} \quad (11)$$

where ω is the true body angular velocity, $\tilde{\omega}$ is the angular velocity measurement vector, M is a matrix combined by the scale factor errors and the misalignments such as

$$M = \begin{bmatrix} \lambda_1 & \delta_{12} & \delta_{13} \\ \delta_{21} & \lambda_2 & \delta_{23} \\ \delta_{31} & \delta_{32} & \lambda_3 \end{bmatrix} \quad (12)$$

where $b \in R^3$ is the bias error vector. The scale factor and the misalignment are written in vector form as

$$\lambda = [\lambda_1 \quad \lambda_2 \quad \lambda_3]^T \quad (13)$$

$$\delta = [\delta_{12} \quad \delta_{13} \quad \delta_{21} \quad \delta_{23} \quad \delta_{31} \quad \delta_{32}]^T$$

In this article, misalignment and bias error of the attitude sensor, usually given as a star tracker, are not assumed because those of the star trackers are usually less than those of the rate sensors.

3. Unscented Kalman filter

In this section, the unscented Kalman filter algorithm is presented. Ever since Julier and Uhlmann have proposed the algorithm, numerous modifications and enhancements have been reported. For estimation of parameters as well as state variables two methodologies are mainly employed – joint and dual filtering techniques. Between the two methods, the joint approach is easier and more intuitive to implement. Joint filters augment the original state variables with parameters to be estimated. Since parameters are usually assumed to be constant, time update of the filter model does not change the expanded parameter variables except its process noise if assumed. On the contrary, the dual method set up another filter for parameters so that two filters run sequentially in every step. The state estimator first propagates and updates for given measurements, and then the parameter estimator updates considering the updated output of the state variables as measurements. It is argued that the primary benefit of the dual UKF is being able to prevent erratic behaviour by decoupling the parameter filter from the state filter (VanDyke et al., 2004). However, the UKF in this problem converges only with the joint method as shown later. This section summarizes the UKF algorithm. This summary of the UKF equations follows the descriptions by Wan and van der Merwe (2000) and VanDyke et al. (2004).

3.1 Joint estimation

The state variable and the parameter are noted by $s \in \mathbb{R}^n$ and $d \in \mathbb{R}^m$, respectively. The augmented state variable of the joint filter is defined by

$$x = \begin{bmatrix} s^T & d^T \end{bmatrix}^T \quad (14)$$

The filter initialization is conducted with assumed mean and covariance of the augmented state vector.

$$\begin{aligned} \hat{x}(t_0) &= E\{\hat{x}_0\} \\ P_{x0} &= E\{(x(t_0) - \hat{x}_0)(x(t_0) - \hat{x}_0)^T\} \end{aligned} \quad (15)$$

Denoting $L = n + m$, the sigma points of L are generated using the *a priori* mean and covariance of the state as

$$\chi_{k-1} = \left[\hat{x}_{k-1}^T \quad \hat{x}_{k-1}^T + \sqrt{(L + \gamma)P_{xk-1}} \quad \hat{x}_{k-1}^T - \sqrt{(L + \gamma)P_{xk-1}} \right]^T \quad (16)$$

where $\gamma = \alpha^2(L + \kappa) - L$ is a scaling parameter. α is usually set to a small positive value. κ is a secondary scaling parameter usually set to 0. The set of singular points, χ_k , is $L \times (2L + 1)$ matrix. Defining $\chi_{i,k}$ as *i*th column of χ_k , each sigma point is propagated through the nonlinear system

$$\chi_{i,k|k-1} = F(\chi_{i,k-1}, u_{k-1})^T \quad (17)$$

The posterior mean, $\hat{\mathbf{x}}_k^-$, and the covariance, \mathbf{P}_{sk}^- , are determined from the statistics of the propagated sigma points as follows:

$$\begin{aligned}\hat{\mathbf{x}}_k^- &= \sum_{i=0}^{2L} \mathbf{W}_i^m \chi_{i,k|k-1} \\ \mathbf{P}_{\text{sk}}^- &= \sum_{i=0}^{2L} \mathbf{W}_i^c (\chi_{i,k|k-1} - \hat{\mathbf{x}}_k^-)(\chi_{i,k|k-1} - \hat{\mathbf{x}}_k^-)^T + \mathbf{Q}_{\text{sk}}\end{aligned}\quad (18)$$

\mathbf{Q}_{sk} is the process noise covariance of the system. The weights, \mathbf{W}_i^m and \mathbf{W}_i^c , are calculated by

$$\begin{aligned}\mathbf{W}_0^m &= \frac{\gamma}{L + \gamma} \\ \mathbf{W}_0^c &= \frac{\gamma}{L + \gamma} + 1 - \alpha^2 + \beta \\ \mathbf{W}_i^c &= \mathbf{W}_i^m = \frac{1}{2(L + \gamma)}, \quad i = 1, \dots, 2L\end{aligned}\quad (19)$$

β is used to incorporate prior knowledge. For Gaussian distributions, $\beta = 2$ is optimal. The estimated measurement vector $\Upsilon_{i,k|k-1}$, i th column of matrix $\Upsilon_{k|k-1}$ ($\in R^{l \times (2L+1)}$) is calculated by transforming the sigma points using the nonlinear measurement model,

$$\Upsilon_{i,k|k-1} = \mathbf{H}(\chi_{i,k|k-1}) \quad (20)$$

The mean measurement, $\hat{\mathbf{y}}_k$, and the measurement covariance, \mathbf{P}_{ykyk} , are calculated based on the statistics of the transformed sigma points.

$$\begin{aligned}\hat{\mathbf{y}}_k &= \sum_{i=0}^{2L} \mathbf{W}_i^m \Upsilon_{i,k|k-1} \\ \mathbf{P}_{\text{ykyk}} &= \sum_{i=0}^{2L} \mathbf{W}_i^c (\Upsilon_{i,k|k-1} - \hat{\mathbf{y}}_k)(\Upsilon_{i,k|k-1} - \hat{\mathbf{y}}_k)^T + \mathbf{R}_{\text{yk}}\end{aligned}\quad (21)$$

\mathbf{R}_{yk} is the measurement noise covariance matrix. The cross-correlation covariance, \mathbf{P}_{xkyk} , is calculated using

$$\mathbf{P}_{\text{xkyk}} = \sum_{i=0}^{2L} \mathbf{W}_i^c (\chi_{i,k|k-1} - \hat{\mathbf{x}}_k^-)(\Upsilon_{i,k|k-1} - \hat{\mathbf{y}}_k)^T \quad (22)$$

The Kalman gain matrix is approximated from the cross-correlation and measurement covariances using

$$\mathbf{K}_{\text{sk}} = \mathbf{P}_{\text{xkyk}} \mathbf{P}_{\text{ykyk}}^{-1} \quad (23)$$

The measurement update equations used to determine the mean, $\hat{\mathbf{x}}_k$, and covariance, \mathbf{P}_{sk} , of the filtered state are

$$\begin{aligned}\hat{\mathbf{x}}_k &= \hat{\mathbf{x}}_k^- + \mathbf{K}_k (\mathbf{y}_k - \hat{\mathbf{y}}_k^-) \\ \mathbf{P}_{xk} &= \mathbf{P}_{xk}^- - \mathbf{K}_{xk} \mathbf{P}_{ykyk} \mathbf{K}_{xk}^T\end{aligned}\quad (24)$$

3.2 Joint UKF state variables

In this paper, the state vector of the original system consists of the attitude quaternion and the angular rate. The attitude quaternion is a unique non-singular parameterization. However, quaternion has to satisfy unity constraint of the magnitude, which may result in covariance singularity if all the four elements are used. Therefore, only the vector components will be used in the UKF implementation.

Parameters of to be estimated is six components of the moment of inertia, the scale factor error, six elements of misalignment, and the bias of the rate sensor as in Eqs. (10), (12), and (13). Therefore,

$$\mathbf{x} = [\delta \mathbf{q}_{13}^T \quad \boldsymbol{\omega}^T \quad \mathbf{p}^T \quad \boldsymbol{\lambda}^T \quad \boldsymbol{\delta}^T \quad \mathbf{b}^T]^T \quad (25)$$

where

$$\delta \mathbf{q} = \bar{\mathbf{q}} \otimes \hat{\mathbf{q}}^{-1} \quad (26)$$

Since the error quaternion is utilized, the state is initialized with

$$\hat{\mathbf{x}}_{k-1} = [0_{3 \times 1}^T \quad \boldsymbol{\omega}_{k-1}^T \quad \mathbf{p}_{k-1}^T \quad \boldsymbol{\lambda}_{k-1}^T \quad \boldsymbol{\delta}_{k-1}^T \quad \mathbf{b}_{k-1}^T]^T \quad (27)$$

Once the sigma points are calculated, quaternion component $\delta \mathbf{q}_{13,i}^z$ is used to obtain the four-element sigma point quaternion \mathbf{q}_i^z to propagate the nonlinear model.

$$\mathbf{q}_i^z = \left[\delta \mathbf{q}_{13,i}^z \quad \sqrt{1 - \delta \mathbf{q}_{13,i}^z{}^T \delta \mathbf{q}_{13,i}^z} \right]^T \otimes \hat{\mathbf{q}}_{k-1} \quad (28)$$

The parameters are assumed to be constant.

$$\begin{aligned}\dot{\mathbf{p}} &= 0 \\ \dot{\boldsymbol{\lambda}} &= 0 \\ \dot{\boldsymbol{\delta}} &= 0 \\ \dot{\mathbf{b}} &= 0\end{aligned}\quad (29)$$

Now, Eqs. (6), (8) and (29) constitute the nonlinear system model of the UKF. And, lastly the following is the measurement equation.

$$\begin{aligned}\tilde{\delta \mathbf{q}}_{13,k} &= \delta \mathbf{q}_{13,k} + \mathbf{v}_{qk} \\ \tilde{\boldsymbol{\omega}}_k &= (\mathbf{I} + \mathbf{M})\boldsymbol{\omega}_k + \mathbf{b} + \mathbf{v}_{\omega k}\end{aligned}\quad (30)$$

After model propagation, three component of error quaternion is calculated again. After measurement update of Eq. (24), four-element quaternion can be determined using

$$\hat{\mathbf{q}}_k = \left[\delta \hat{\mathbf{q}}_{13,k}^T \quad \sqrt{1 - \delta \hat{\mathbf{q}}_{13,k}^T \delta \hat{\mathbf{q}}_{13,k}} \right]^T \otimes \hat{\mathbf{q}}_{k-1} \quad (31)$$

More detailed and helpful discussion on quaternion-based computation can refer (Kraft, 2003).

4. Numerical simulation results

In this section, simulation results for hybrid estimation of states, the moment of inertia and the rate sensor calibration will be presented. The joint UKF will be compared to the results using EKF (Myung et al., 2007).

4.1 Simulation conditions

In order to estimate the inertia matrix and the gyro calibration parameters, 'persistent excitation' of motion should be guaranteed. A constant body angular velocity vector or one with constant direction will not satisfy this requirement.

As one of the reference trajectories satisfying the 'persistent excitation' condition (Pittelkau, 2001), the following rate trajectory is proposed (Myung et al., 2007).

$$\omega_r = \phi \dot{l} - (1 - \cos \phi) \dot{l} \times \dot{l} + \dot{l} \sin \phi$$

where

$$\begin{aligned} \phi &= 50\pi t (\text{rad}) \\ I &= \begin{bmatrix} \sin \omega_1 t \sin \omega_2 t \\ \cos \omega_1 t \sin \omega_2 t \\ \cos \omega_2 t \end{bmatrix} \\ \omega_1 &= 0.01 \text{ rad/s} \\ \omega_2 &= 0.004 \text{ rad/s} \end{aligned}$$

For simulation purposes, a predictive controller (Crassidis et al., 1997) is applied to the spacecraft attitude control. Given reference trajectories to follow, the predictive control synthesizes control command based on nonlinear state prediction strategy using the Taylor series expansion. The reference trajectories are shown in Fig. 1 and Fig. 2.

4.2 Simulation results

The following true system and alignment parameters are assumed (Myung et al., 2007):

$$\begin{aligned} J &= \begin{bmatrix} 200 & 50 & -30 \\ 50 & 240 & 10 \\ -30 & 10 & 100 \end{bmatrix} \text{ kgm} / \text{s}^2 \\ \lambda &= [5000, -1000, -2000]^T \text{ ppm} \\ \delta &= [648, 1296, 972, 648, -648, 1296]^T \text{ arcs} \\ b &= [5, 3, 2]^T \times 10^{-4} \text{ rad} / \text{s} \end{aligned}$$

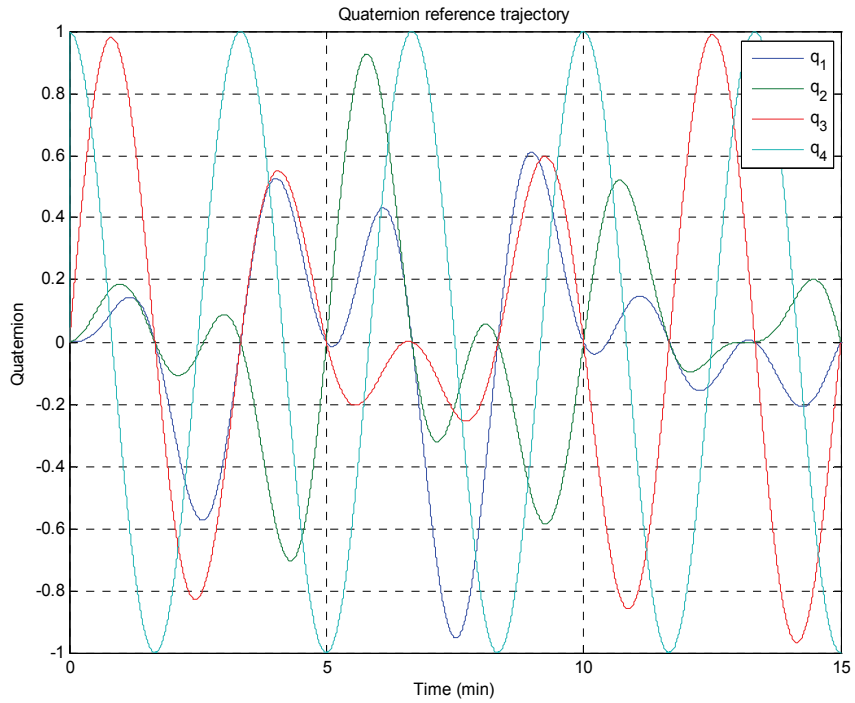


Fig. 1. Quaternion reference trajectory

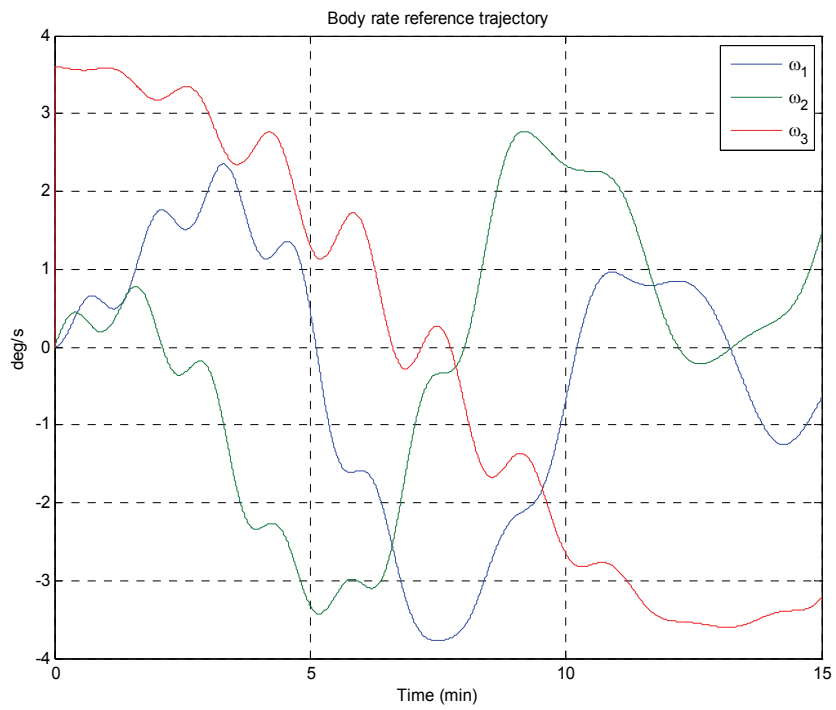


Fig. 2. Body angular rate reference trajectory

Nominal values of the parameters are given as

$$J = \begin{bmatrix} 160 & 20 & -20 \\ 20 & 160 & -20 \\ -20 & -20 & 160 \end{bmatrix} \text{kgm} / \text{s}^2$$

$$\lambda = [0 \ 0 \ 0]^T \text{ppm}$$

$$\delta = [0 \ 0 \ 0 \ 0 \ 0 \ 0]^T \text{arcs}$$

$$b = [0 \ 0 \ 0]^T \text{rad} / \text{s}$$

The process and the measurement noise covariance matrices are designated as

$$Q = 10^{-8} I_{3 \times 3} \text{rad}^2 / \text{s}^4$$

$$R_q = 10^{-6} I_{3 \times 3} \text{rad}^2$$

$$R_\omega = 10^{-5} I_{3 \times 3} \text{rad}^2 / \text{s}^2$$

Simulation is performed for 15 min. The star tracker and the rate sensor measurements are assumed to be given every 0.2 s. Table 1 – 4 present estimation error comparison of the EKF and UKF by Monte-Carlo simulation of 20 runs. The upper data in each cell of the tables are percentage error with respect to own value. The lower data are normalized values of the final covariances. Therefore, smaller values are more accurate regardless of magnitude of the nominal parameter values. The moment of inertia estimation is very accurate for both EKF and UKF in Table 1. However, rate sensor calibration results of the UKF are much more accurate than those of EKF. If the reference trajectory is designed considering excitation optimality, estimation results will be even more accurate (Sekhavat, 2009).

	units	J ₁₁ (1σ)	J ₂₂ (1σ)	J ₃₃ (1σ)	J ₁₂ (1σ)	J ₁₃ (1σ)	J ₂₃ (1σ)
EKF	% error	0.140	0.163	0.527	0.137	0.319	0.548
	%	(0.106)	(0.096)	(0.250)	(0.279)	(0.310)	(0.847)
UKF	% error	0.080	0.073	0.185	0.072	0.023	0.063
	%	(0.879)	(0.788)	(1.793)	(0.832)	(1.577)	(4.495)

Table 1. Moment of inertia estimation results of EKF and UKF by Monte-Carlo Simulation

	units	λ ₁ (1σ)	λ ₂ (1σ)	λ ₃ (1σ)
EKF	% error	53.9	56.3	13.7
	%	(82.4)	(205.6)	(117.0)
UKF	% error	1.17	61.8	18.8
	%	(32.0)	(138.0)	(55.3)

Table 2. Rate sensor scale factor error estimation results of EKF and UKF by Monte-Carlo Simulation

	units	δ_{12} (1 σ)	δ_{13} (1 σ)	δ_{21} (1 σ)	δ_{23} (1 σ)	δ_{31} (1 σ)	δ_{32} (1 σ)
EKF	% error	91.2	121.9	72.0	103.8	59.6	14.0
	%	(87.1)	(47.6)	(75.0)	(72.9)	(85.0)	(64.1)
UKF	% error	28.3	6.81	13.5	7.74	6.51	10.9
	%	(49.3)	(18.3)	(32.9)	(34.3)	(46.2)	(26.9)

Table 3. Rate sensor misalignment estimation results of EKF and UKF by Monte-Carlo Simulation

	units	b_1 (1 σ)	b_2 (1 σ)	b_3 (1 σ)
EKF	% error	267.1	166.1	37.7
	%	(29.6)	(47.6)	(67.9)
UKF	% error	2.46	11.6	1.93
	%	(9.63)	(16.0)	(23.8)

Table 4. Rate sensor bias estimation results of EKF and UKF by Monte-Carlo Simulation

Fig. 3 to Fig. 10 illustrates one of the UKF simulation results with time. Each variable has different convergence time constant. The attitude and the rate converge very fast as in Fig. 3 and Fig. 4. And then the moment of inertia components converge. And finally calibration parameters converge.

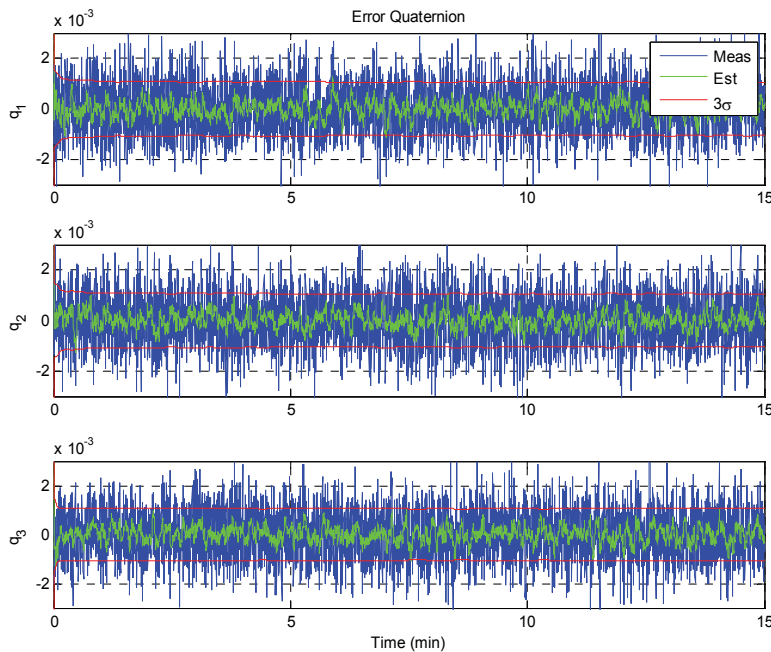


Fig. 3. Attitude estimation error with 3 σ bounds

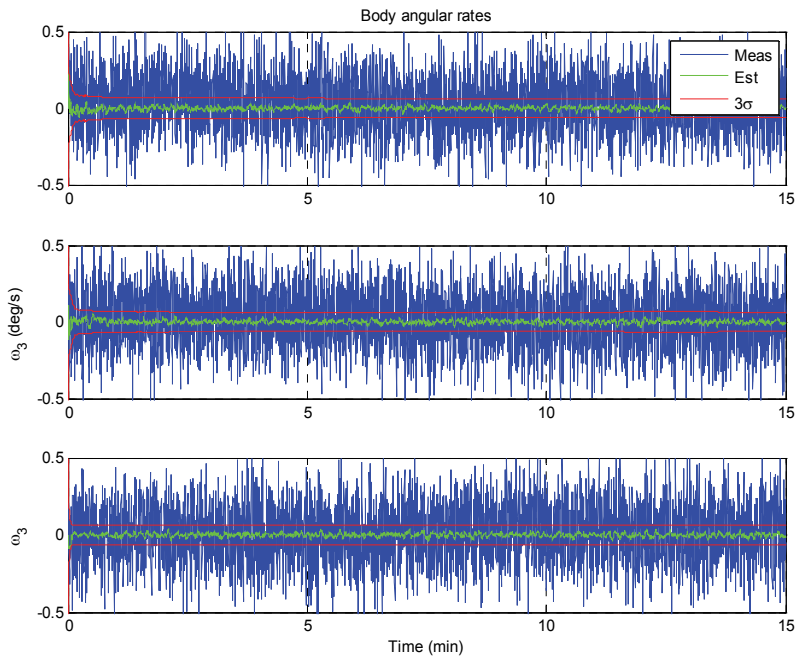


Fig. 4. Angular velocity estimation error with 3σ bounds

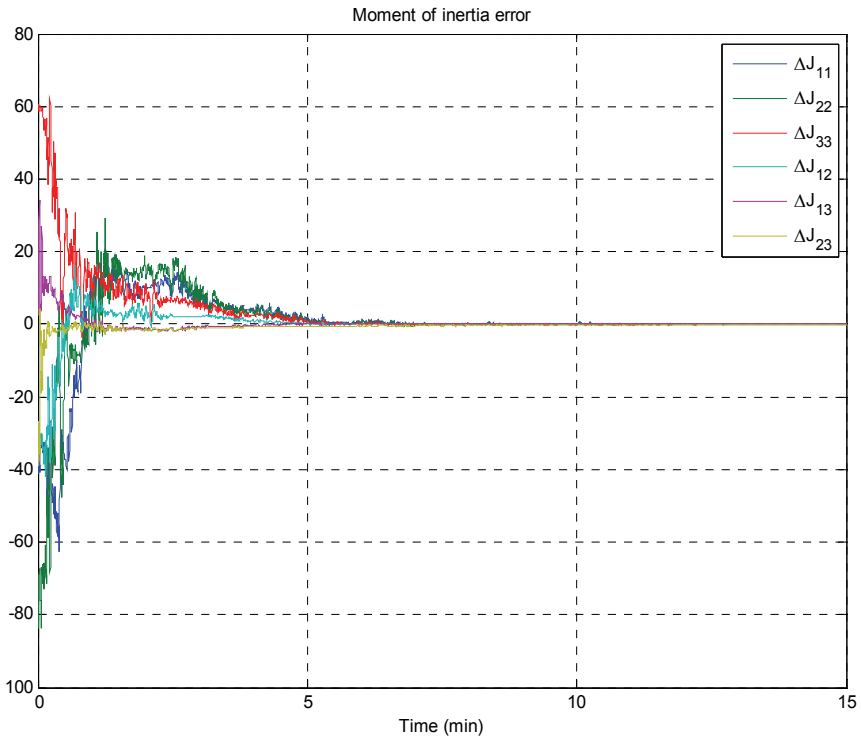


Fig. 5. Moment of inertia estimation error

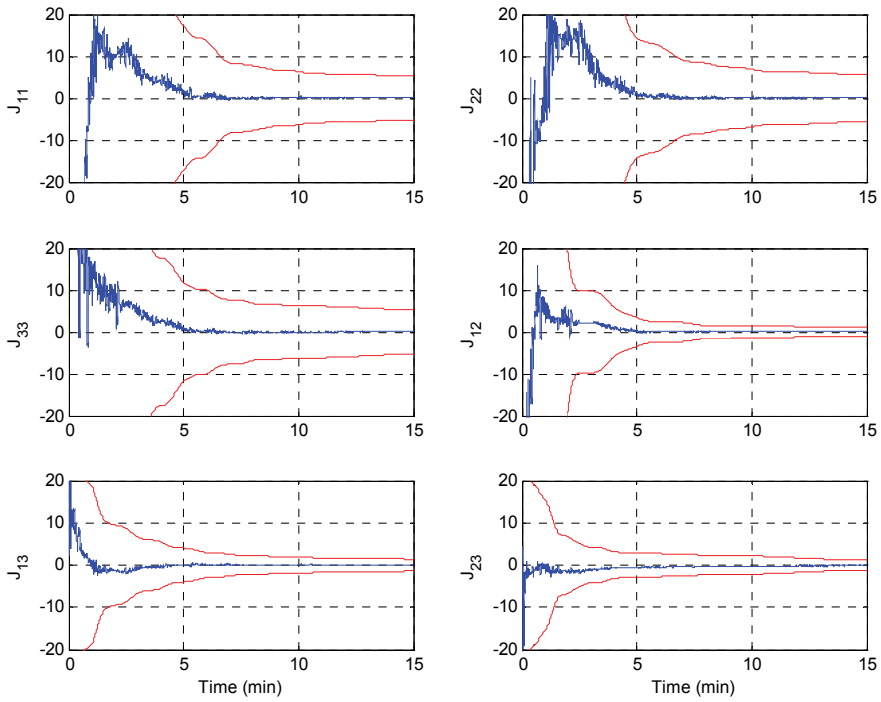


Fig. 6. Moment of inertia estimation error with 3σ bounds

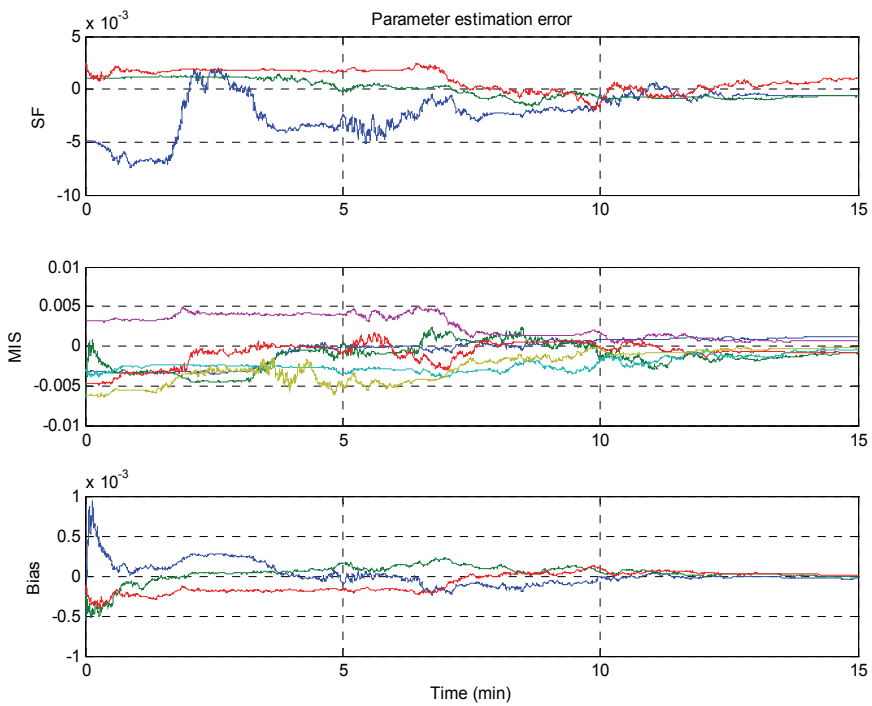


Fig. 7. Rate sensor calibration error

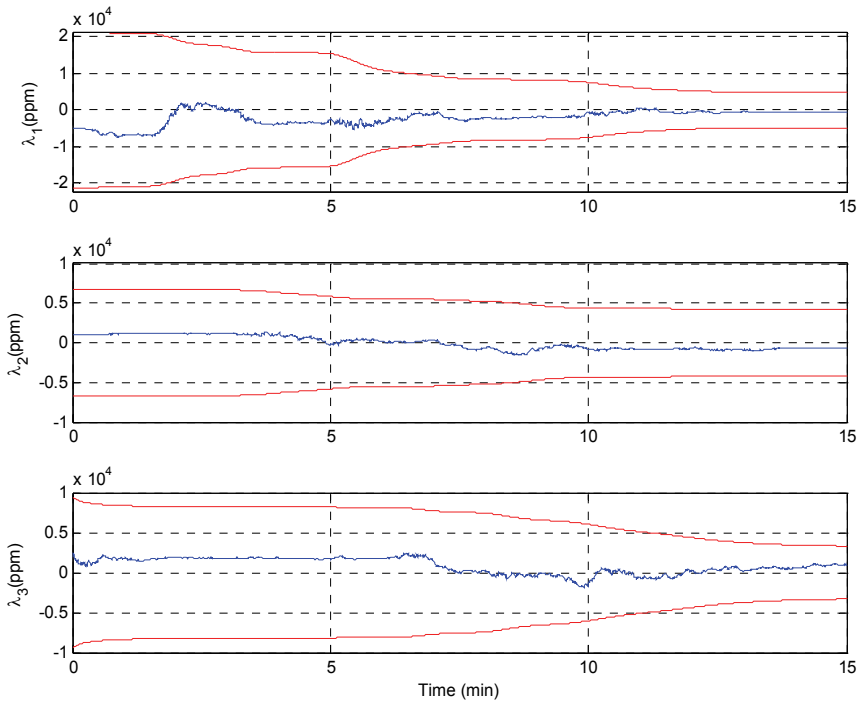


Fig. 8. Rate gyro scale factor estimation error with 3σ bounds

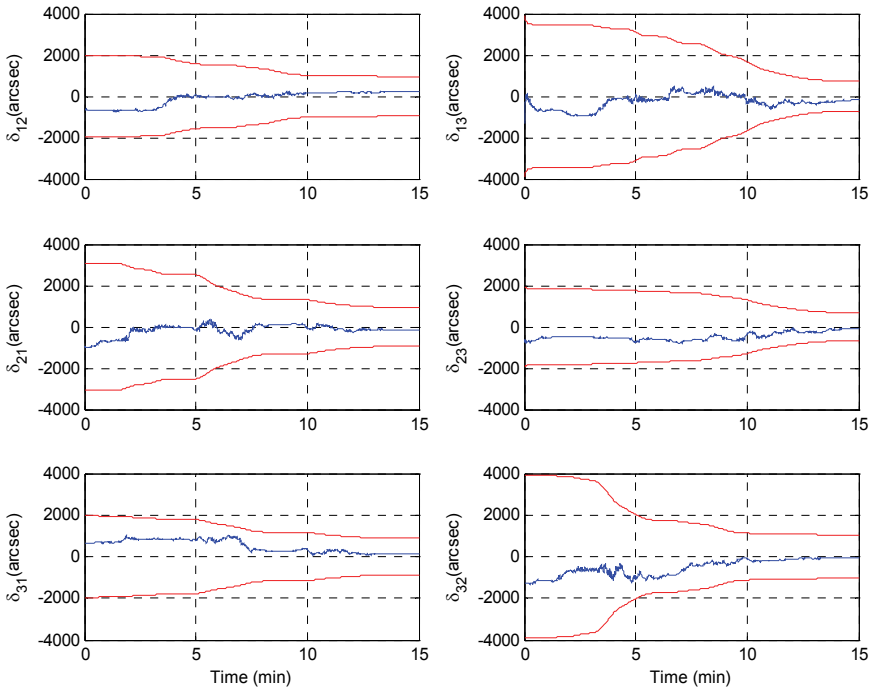


Fig. 9. Rate gyro misalignment estimation error with 3σ bounds

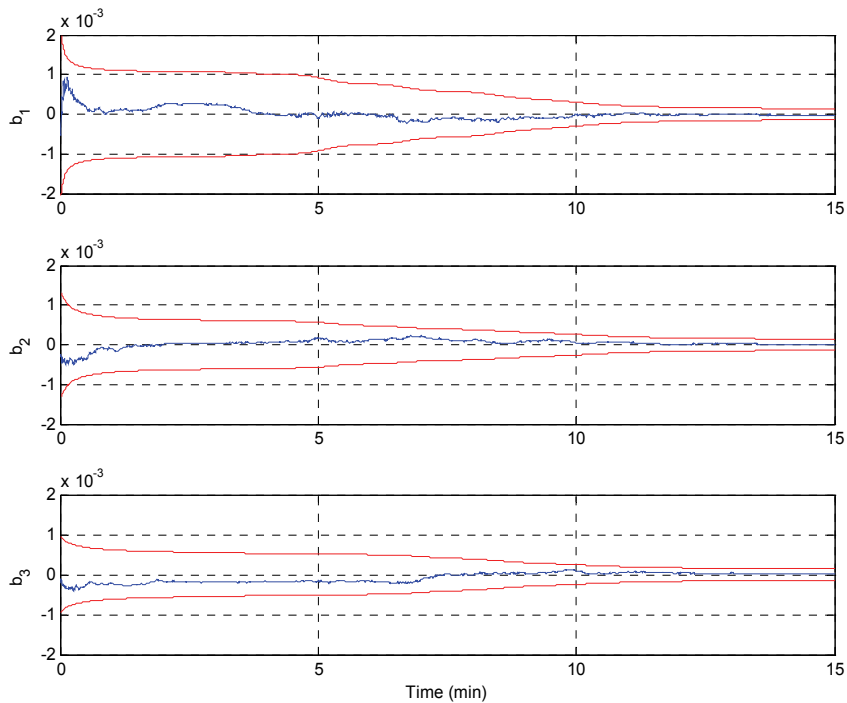


Fig. 10. Rate gyro bias estimation error with 3σ bounds

5. Conclusions

This study presented hybrid estimation of the moment of inertia of spacecraft and calibration parameters of the rate sensor such as the scale factor error, six elements of misalignment and the gyro bias error during a single estimation maneuver. For this purpose, a joint unscented Kalman filter (UKF) algorithm was successfully applied and the performance was compared to the results using the extended Kalman filter (EKF). While the components of the moment of inertia were estimated very accurately by both the EKF and the UKF, the rate sensor calibration parameters – scale factor, misalignment, and bias error – were filtered much better by the UKF than the EKF. Simulation results demonstrated applicability and performance for spacecraft system identification and the gyro calibration simultaneously.

This concept of estimation procedure can reduce efforts and costs for periodic parameter estimation and gyro calibration of spacecraft in-orbit. Also, proposed method can be extended to calibration maneuvers of other equipments such as star trackers and optical payloads.

6. References

- Ahmed, J.; Coppola, V. T. & Bernstein, D. S. (1998). Adaptive asymptotic tracking of spacecraft attitude motion with inertia matrix identification, *Journal of Guidance, Control and Dynamics*, Vol. 21, No. 5, pp. 684-691

- Bordany, R. E.; Steyn, W. H. & Crawford, M. (2000). In-orbit estimation of the inertia matrix and thruster parameters of UoSAT-12, *Proceedings of the 14th AIAA/USU Conference on Small Satellites*, Logan, Utah, USA, August 2000
- Crassidis, J. L.; Markley, F. L., Anthony, T. C. & Andrews, S. F. (1997). Nonlinear predictive control of spacecraft, *Journal of Guidance, Control and Dynamics*, Vol. 20, No. 6, pp. 1096-1103
- Crassidis, J. L.; Markley, F. L. & Cheng, Y. (2007). Survey of nonlinear attitude estimation methods, *Journal of Guidance, Control and Dynamics*, Vol. 30, No. 1, pp. 12-28
- Creamer, G.; DeLaHunt, P., Gates, S. & Leyenson, M. (1996). Attitude determination and control of Clementine during lunar mapping, *Journal of Guidance, Control and Dynamics*, Vol. 19, No. 3, pp. 505-511
- Julier, S. J. & Uhlmann, J. K. (1997). A new extension of the kalman filter to nonlinear systems, *Proceedings of the SPIE AeroSense International Symposium on Aerospace/Defence Sensing, Simulation and Controls*, Orlando, Florida, USA, April 1997
- Kalman, R. E. (1960). A new approach to linear filtering and prediction problems, *Transactions of the ASME-Journal of Basic Engineering, D*, Vol. 82, pp. 35-45
- Kraft, E. (2003). A quaternion-based unscented Kalman filter for orientation tracking, *Proceedings of IEEE 6th Conference of Information Fusion*, pp. 47-54
- Lai, K. L.; Crassidis, J. L. & Harman, R. R. (2003). In-space spacecraft alignment calibration using the unscented filter, *Proceedings of AIAA Guidance, Navigation, and Control Conference Exhibit*, Austin, Texas, USA, August 2003
- Ma, G. -F. & Jiang, X. -Y. (2005). Unscented Kalman filter for spacecraft attitude estimation and calibration using magnetometer measurements, *Proceedings of the 4th International Conference on Machine Learning and Cybernetics*, Guanzhou, August 2005
- Myung, H.; Yong, K. -L. & Bang, H. (2007). Hybrid estimation of spacecraft attitude dynamics and rate sensor alignment parameters, *Proceedings of International Conference on Control, Automation and Systems*, Seoul, Korea, October 2007
- Myung, H. & Bang, H. (2008). Spacecraft parameter estimation by using predictive filter algorithm, *Proceedings of IFAC World Congress*, Seoul, Korea, July 2008
- Pittelkau, M. E. (2001). Kalman filtering for spacecraft system alignment calibration, *Journal of Guidance, Control and Dynamics*, Vol. 24, No. 6, pp. 1187-1195
- Pittelkau, M. E. (2002), Everything is relative in spacecraft system alignment calibration, *Journal of Spacecraft and Rockets*, Vol. 39, No. 3, pp. 460-466
- Sekhavat, P. ; Karpenko, M. & Ross, I. M. (2009). UKF-based spacecraft parameter estimation using optimal excitation, *AIAA Guidance, Navigation, and Control Conference*, Chicago, Illinois, USA, August 2009
- Van der Merwe, R. & Wan, E. A. (2001). The square-root unscented Kalman filter for state and parameter-estimation, *Proceedings of IEEE International Conference on Acoustics, Speech, and Signal Processing*, Vol. 6, pp. 3461-3464
- VanDyke, M. C.; Schwartz, J. L. & Hall, C. D. (2004). Unscented Kalman filtering for spacecraft attitude state and parameter estimation, *Advances in the Astronautical Sciences*, Vol. 118, No. 1, pp. 217-228

Wan, E. A. & van der Merwe, R. (2000). The unscented Kalman filter for nonlinear estimation, *Proceedings of IEEE Symposium 2000 (AS-SPCC)*, Lake Louise, Alberta, Canada, October 2000

Wertz, J. R. (Ed.) (1978). *Spacecraft Attitude Determination and Control*, pp. 414-416, Kluwer

Fault-Tolerant Attitude Estimation for Satellite using Federated Unscented Kalman Filter

Jonghee Bae, Seungho Yoon, and Youdan Kim
*School of Mechanical and Aerospace Engineering, Seoul National University,
Republic of Korea*

1. Introduction

Satellites provide various services essential to the modern life of human being. For example, satellite images are used for many applications such as reconnaissance, geographic information system, etc. Therefore, design and operation requirements of the satellite system have become more severe, and also the system reliability during the operation is required. Satellite attitude control systems including sensors and actuators are critical subsystems, and any fault in the satellite control system can result in serious problems. To deal with this problem, various attitude estimation algorithms using multiple sensors have been actively studied for fault tolerant satellite system (Edelmayer & Miranda, 2007; Jiancheng & Ali, 2005; Karlgaard & Schaub, 2008; Kerr, 1987; Xu, 2009).

Satellites use various attitude sensors such as gyroscopes, sun sensors, star sensors, magnetometers, and so on. With these sensors, satellite attitude information can be obtained using the estimation algorithms including Kalman filter, extended Kalman filter (EKF), unscented Kalman filter (UKF), and particle filter. Agrawal et al. and Nagendra et al. presented the attitude estimation algorithm based on Kalman filter for satellite system (Agrawal & Palermo, 2002; Nagendra et al., 2002). Mehra and Bayard dealt with the problems of satellite attitude estimation based on the EKF algorithm using the gyroscope and star tracker as attitude sensors (Mehra & Bayard, 1995). In the EKF algorithm, the nonlinearities of the satellite system are approximated by the first-order Taylor series expansion, and therefore it sometimes provides undesired estimates when the system has severe nonlinearities. Recently, researches on UKF have been performed because the UKF can capture the posterior mean and covariance to the third order of nonlinear system. It is known that the UKF can provide better results for the estimation of highly nonlinear systems than EKF (Crassidis & Markley, 2003; Jin et al., 2008; Julier & Uhlmann, 2004). Crassidis and Markley proposed the attitude estimation algorithm based on unscented filter, and showed that the fast convergence can be obtained even with inaccurate initial conditions. The UKF was used to solve the relative attitude estimation problem using the modified Rodriguez parameter (MRP), where the gyroscope, star tracker, and laser rendezvous radar were employed as the attitude sensors (Jin et al., 2008).

For multi-sensor systems, there are two different filter schemes for the measured sensor data process: centralized Kalman filter (CKF) and decentralized Kalman filter (DKF) (Kim & Hong, 2003). In the CKF, all measured sensor data are processed in the center site, and

therefore information loss can be minimized. However, it causes severe computational problem and may provide unreliable results, when the CKF is overloaded with more data than it can handle. In the DKF, the local estimators of each sensor can generate the global optimal or suboptimal state estimates according to the data fusion criterion. Wei and Schwarz presented a decentralized Kalman filter strategy and applied to GSP/INS integration (Wei & Schwarz, 1990). Edelmayer and Miranda applied the decentralized extended Kalman filter to the fault tolerant estimation (Edelmayer & Miranda, 2007). A decentralized unscented Kalman filter in federated configuration was developed for multi-sensor navigation data fusion (Jiancheng & Ali, 2005). Jiancheng and Ali used the inertial navigation system (INS) integrated with astronavigation system and global positioning system (GPS). In (Kim & Hong, 2003; Lee, 2008), a decentralized information filter was proposed by combining unscented transformation method with the extended information filtering architecture, and the algorithm was extended to perform the decentralized estimation for sensor networks. The decentralized scheme has advantages in the sense that (i) much more data can be treated because of the parallel structure, and (ii) the fault can be easily detected and isolated due to the decentralized scheme (Bae & Kim, 2010; Edelmayer & Miranda, 2007).

In this study, the decentralized Kalman filter scheme in a federated configuration is adopted for satellite attitude estimation. The federated UKF can be employed to detect and isolate the sensor fault effectively (Jiancheng & Ali, 2005; Edelmayer & Miranda, 2007). Using the fault detection and isolation (FDI) algorithm, the accurate attitude information can be provided despite sensor fault occurrence, and therefore satellite can perform its mission continuously. There exist various FDI algorithms (Hwang et al., 2010). Fault can be detected and identified by (i) monitoring the measurement residual, or (ii) using sensitivity factor. In this study, sensitivity factor is used to detect and identify the sensor failure. To verify the performance of the proposed algorithm, numerical simulations are performed for a satellite with gyroscope and star tracker as attitude sensor. The numerical simulation shows that the federated UKF with FDI algorithm detects and isolates the sensor faults effectively, and therefore it provides accurate and robust attitude estimation results when the attitude sensor has a fault.

This paper is organized as follows. In Section 2, the attitude kinematics, dynamics, and sensor modeling are described. The attitude estimation algorithms using UKF and the federated configuration, and FDI algorithm are derived in Section 3. Numerical simulation and analysis to verify the proposed algorithm are shown in Section 4. Finally, conclusions are presented in Section 5.

2. Attitude kinematics, dynamics, and sensor modeling

2.1 Attitude kinematics and dynamics

In this study, quaternion is used for describing attitude dynamics of satellite (Schaub & Junkins, 2003). The quaternion is a four-dimensional vector, defined as

$$q = [q_1 \quad q_2 \quad q_3 \quad q_4]^T \equiv [\hat{q} \quad q_4]^T \quad (1)$$

where

$$\hat{q} = [q_1 \quad q_2 \quad q_3]^T = \hat{e} \sin\left(\frac{\vartheta}{2}\right) \quad (2)$$

$$q_4 = \cos\left(\frac{\vartheta}{2}\right) \quad (3)$$

where \hat{e} is the unit Euler axis, and ϑ is the rotation angle. The quaternion satisfies the following constraint.

$$q^T q = q_1^2 + q_2^2 + q_3^2 + q_4^2 = 1 \quad (4)$$

The direction cosine matrix can be written in terms of quaternion as

$$A(q) = \left(q_4^2 - \|\hat{q}\|^2\right) I_{3 \times 3} + 2\hat{q}\hat{q}^T - 2q_4\hat{q}^\times = \Xi^T(q)\Psi(q) \quad (5)$$

where $I_{3 \times 3}$ is a 3×3 identity matrix and

$$\Xi(q) = \begin{bmatrix} q_4 I_{3 \times 3} + \hat{q}^\times \\ -\hat{q}^T \end{bmatrix} \quad (6)$$

$$\Psi(q) = \begin{bmatrix} q_4 I_{3 \times 3} - \hat{q}^\times \\ -\hat{q}^T \end{bmatrix} \quad (7)$$

Also, \hat{q}^\times is the cross-product matrix defined by

$$\hat{q}^\times = \begin{bmatrix} 0 & -q_3 & q_2 \\ q_3 & 0 & -q_1 \\ -q_2 & q_1 & 0 \end{bmatrix} \quad (8)$$

The kinematic differential equation for the quaternion is given by

$$\dot{q} = \frac{1}{2}\Xi(q)\omega = \frac{1}{2}\Omega(\omega)q \quad (9)$$

where ω is the three-dimensional angular rate vector and

$$\Omega(\omega) = \begin{bmatrix} -\omega^\times & \omega \\ -\omega^T & 0 \end{bmatrix} \quad (10)$$

Quaternion provides successive rotation using quaternion multiplication as

$$A(q(t_1))A(q(t_2)) = A(q(t_1) \otimes q(t_2)) \quad (11)$$

The composition of the quaternion is defined by

$$q(t_1) \otimes q(t_2) = [\Psi(q(t_1)) \quad q(t_1)]q(t_2) = [\Xi(q(t_2)) \quad q(t_2)]q(t_1) \quad (12)$$

Also, the inverse quaternion is defined by

$$q^{-1} = \begin{bmatrix} -\hat{q} \\ q_4 \end{bmatrix} \quad (13)$$

Note that $q \otimes q^{-1} = [0 \ 0 \ 0 \ 1]^T$, which is the identity quaternion.

The attitude dynamics of a spacecraft can be represented from the Euler's momentum equation as follows (Schaub & Junkins, 2003).

$$J\dot{\omega} = -\omega^\times J\omega + \tau \quad (14)$$

where J is a 3×3 moment of inertia matrix, and $\tau \in R^3$ is a control torque vector.

2.2 Sensor modeling

2.2.1 Gyroscope model

A gyroscope is a general sensor that measures the angular rate of the satellite. The gyroscope system can be expressed mathematically by Frarrenkopf's model (Karlgaard & Schaub, 2008). In this model, the measured angular velocity is represented by the sum of the true angular velocity, an additive bias, and Gaussian white-noise. The bias dynamics are considered to be driven by a Gaussian white-noise process. Also, in this model, it is assumed that the bias term can be regarded as the net effect of several systematic error sources such as scale factor errors, non-orthogonality, misalignment, and so on. The gyroscope model can be represented as

$$\tilde{\omega} = \omega + \beta + \eta_v \quad (15)$$

$$\dot{\beta} = \eta_u \quad (16)$$

where $\tilde{\omega}$ is the measured angular velocity, ω is the true angular velocity, β is the drift, and η_v and η_u are independent zero-mean Gaussian white-noise processes with

$$E[\eta_v(t)\eta_v^T(\tau)] = \sigma_v^2 \delta(t-\tau) I_{3 \times 3} \quad (17)$$

$$E[\eta_u(t)\eta_u^T(\tau)] = \sigma_u^2 \delta(t-\tau) I_{3 \times 3} \quad (18)$$

where $E[\]$ denotes expectation, and $\delta(t-\tau)$ is the Dirac-delta function.

2.2.2 Star tracker model

The rate signal from the gyroscope is integrated to estimate the attitude of the satellite, and therefore it causes a drift of the estimates away from the true value. For this reason, it is necessary to use additional sensors such as a star tracker for the compensation of the drift error. A star tracker is an optimal device, which recognizes the star pattern and provides the attitude information of a spacecraft (Jayaraman et al., 2006). The output of the star tracker is an estimated quaternion that relates the orientation of the body with respect to the inertial

frame. The quaternion estimates are assumed to be unbiased, but it contains a random measurement noise. A star tracker model can be represented as (Karlgaard & Schaub, 2008)

$$q_s = \delta q_s \otimes q \quad (19)$$

where q_s is a star tracker output vector which is a continuously measured quaternion vector, q is the quaternion representing the true orientation, and δq_s is an independent zero-mean Gaussian white-noise process with

$$E[\delta q_s(t)] = 0 \quad (20)$$

$$E[\delta q_s(t) \delta q_s^T(\tau)] = \sigma_s^2 \delta(t - \tau) I_{4 \times 4}. \quad (21)$$

3. Fault-tolerant attitude estimation

To incorporate the various sensor data of the multi-sensor system, there are two schemes which provide accurate and robust state estimation: CKF and DKF. The decentralized scheme in a federated configuration has the benefit of detecting a fault in a local sensor during the process. Therefore, a federated UKF is adopted to detect and isolate the sensor faults, in this study. Federated UKF algorithm can prevent mission failures because an effective FDI algorithm is employed in the federated configuration.

3.1 Federated configuration filter

Federated filtering consists of two parts: local filters and master filter. The local filters are parallel processed and independent of each other, and the estimated results of the local filters are fused in the master filter. In each local filter, local estimate is obtained using the measurements of the local sensors. The master filter uses the estimates of the local filters to update the global state estimate in a fusion process, and this result is used for the initialization of the local filters. Federated filtering scheme has an advantage; it can detect and isolate the fault of the local sensor during the process. The master filter is not affected by the failure of the local sensor (Edelmayer & Miranda, 2007; Jiancheng & Ali, 2005). The structure of the federated configuration filter is shown in Fig. 1. The filtering algorithm based on UKF in the local filter and the data fusion in the master filter are explained in the subsequent sections, respectively.

3.2 Local filter: unscented Kalman filter

For the satellite attitude estimation, several algorithms have been studied: Kalman filter, EKF, UKF, and particle filter. The EKF is widely used for the state estimation of the nonlinear systems. The EKF is based on approximating the nonlinearities by the first-order Taylor series expansion, and therefore this filter may sometimes provide unreliable estimates if the system has severe nonlinearities. On the other hand, the UKF is the extension of the Kalman filter to reduce the linearization errors of the EKF. It is known that the UKF provides good estimation results not only for linear systems but also for nonlinear systems. In this study, the UKF is considered to estimate the attitude of the satellite.

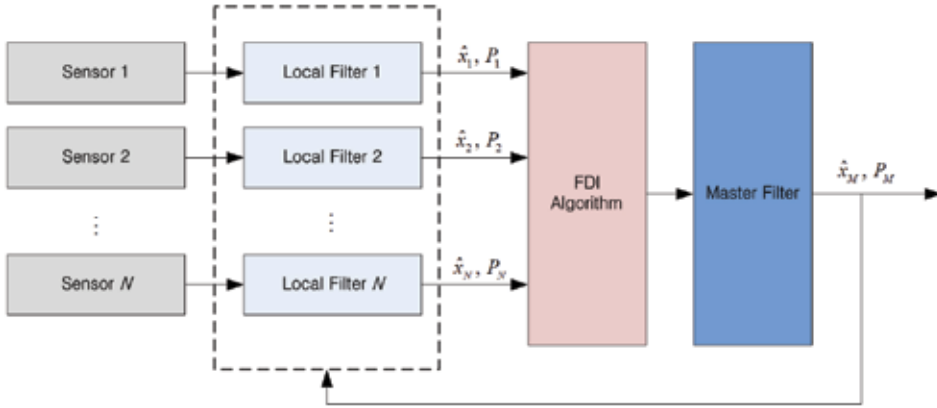


Fig. 1. The structure of the federated filter

Consider the n -state nonlinear system for UKF algorithm (Simon, 2006).

$$\begin{aligned} x_{k+1} &= f(x_k, u_k, t_k) + w_k, & w_k &\sim N(0, Q_k) \\ z_k &= h(x_k, t_k) + v_k, & v_k &\sim N(0, R_k) \end{aligned} \quad (22)$$

where $x_k \in \mathfrak{R}^n$ is the state vector, $z_k \in \mathfrak{R}^m$ is the measurement vector, $w_k \in \mathfrak{R}^n$ is the process noise vector, and $v_k \in \mathfrak{R}^m$ is the measurement noise vector. It is assumed that the noise vectors are uncorrelated white Gaussian process. The UKF is initialized as follows.

$$\begin{aligned} \hat{x}_0^+ &= E[x_0] \\ P_0^+ &= E\left[(x_0 - \hat{x}_0^+)(x_0 - \hat{x}_0^+)^T\right] \end{aligned} \quad (23)$$

The UKF is derived based on the unscented transformation which is simpler to approximate a Gaussian distribution than to approximate an arbitrary nonlinear function. A set of sigma points is first chosen which are selected to express the probability distribution, and the mean and covariance of the set of sigma points are \bar{x} and P . The nonlinear function is then applied to each sigma point, and the results provide a set of transformed points with the mean and covariance. Now, time update is performed to propagate the state estimate and covariance from on measurement time to the next. To propagate from time step $(k-1)$ to k , the set of sigma points is chosen using the current best guess of the mean and covariance as follows.

$$\begin{aligned} \hat{x}_{k-1}^i &= \hat{x}_{k-1}^+ + \tilde{x}^i \\ \tilde{x}^i &= \left(\sqrt{nP_{k-1}^+}\right)_i^T & i &= 1, \dots, n \\ \tilde{x}^{n+i} &= -\left(\sqrt{nP_{k-1}^+}\right)_i^T & i &= 1, \dots, n \end{aligned} \quad (24)$$

For the state propagation, *a priori* state estimate \hat{x}_k^- and error covariance P_k^- are computed using the propagated sigma point vectors as

$$\hat{x}_k^i = f(\hat{x}_{k-1}^i, u_k, t_k) \quad (25)$$

$$\hat{x}_k^- = \frac{1}{2n} \sum_{i=1}^{2n} \hat{x}_k^i \quad (26)$$

$$P_k^- = \frac{1}{2n} \sum_{i=1}^{2n} (\hat{x}_k^i - \hat{x}_k^-)(\hat{x}_k^i - \hat{x}_k^-)^T + Q_{k-1} \quad (27)$$

where \hat{x}_k^i denotes the transformed sigma points using the nonlinear function.

Then, the measurement update is performed using the time propagation results. Sigma points are again chosen with the appropriate changes using the current best guess of the mean and covariance.

$$\begin{aligned} \hat{x}_k^i &= \hat{x}_k^- + \tilde{x}^i \\ \tilde{x}^i &= \left(\sqrt{n P_k^-} \right)_i^T \quad i = 1, \dots, n \\ \tilde{x}^{n+i} &= -\left(\sqrt{n P_k^-} \right)_i^T \quad i = 1, \dots, n \end{aligned} \quad (28)$$

Each predicted measurement vector \hat{z}_k^i is obtained through the measurement model, and the predicted measurement \hat{z}_k is calculated as follows.

$$\hat{z}_k^i = h(\hat{x}_k^i, t_k) \quad (29)$$

$$\hat{z}_k = \frac{1}{2n} \sum_{i=1}^{2n} \hat{z}_k^i \quad (30)$$

The innovation covariance P_{zz} and the cross correlation P_{xz} are obtained with the assumption that the measurement noise is additive and independent as follows.

$$P_{zz} = \frac{1}{2n} \sum_{i=1}^{2n} (\hat{z}_k^i - \hat{z}_k)(\hat{z}_k^i - \hat{z}_k)^T + R_k \quad (31)$$

$$P_{xz} = \frac{1}{2n} \sum_{i=1}^{2n} (\hat{x}_k^i - \hat{x}_k^-)(\hat{z}_k^i - \hat{z}_k)^T \quad (32)$$

Finally, *a posteriori* state and covariance estimates can be performed using the predicted values as

$$\hat{x}_k^+ = \hat{x}_k^- + K_k(z_k - \hat{z}_k) \quad (33)$$

$$P_k^+ = P_k^- - K_k P_{zz} K_k^T \quad (34)$$

where K_k is the filter gain selected to minimize the mean squared error of the estimate as

$$K_k = P_{xz} P_{zz}^{-1} \quad (35)$$

This completes the UKF algorithms. Note that the EKF algorithm is based on the linearization while the UKF algorithm is based on the unscented transformations which are more accurate than the linearization for propagating mean and covariance.

3.3 Master filter: data fusion

The master filter is processed at the same rate of the local filter. If all local estimates are uncorrelated, the global estimate from the master filter is given by

$$\hat{x}_M = P_M \left\{ P_1^{-1} \hat{x}_1 + P_2^{-1} \hat{x}_2 + \dots + P_N^{-1} \hat{x}_N \right\} \quad (36)$$

$$P_M^{-1} = P_1^{-1} + P_2^{-1} + \dots + P_N^{-1} \quad (37)$$

where \hat{x}_i and P_i are the local estimate and its covariance of the i -th local filter, and P_M^{-1} is called the information matrix. Note that the global estimate is the sum of local estimates and linear weighted combination with weighting matrices, P_i^{-1} ($i = 1, 2, \dots, N$), and P_M^{-1} . The federated UKF scheme has two operating modes according to initializing the local filter of the fused data: reset mode and no-reset mode. In the reset mode, the local filters are initiated by the global estimate as follows:

$$\begin{aligned} \hat{x}_i &= \hat{x}_M \\ P_i &= \beta_i^{-1} P_M \end{aligned} \quad (38)$$

where β_i is the information sharing coefficient satisfying $\beta_1 + \beta_2 + \dots + \beta_N + \beta_M = 1$. This mode provides a continuous information feedback from the master filter to the local filters. In the no-reset mode, on the other hand, information is not feedback, and thereby the global fused data does not have an effect on the local filters. Also, local filters retain their information which is given locally. It is known that the reset mode can provide accurate estimates, while the no-reset mode gives the tolerance of sensor failure. In this study, the reset mode in the federated configuration filter is used to obtain better and more accurate estimation values. Instead, the FDI algorithm is adopted for the fault tolerance as described in the next subsection.

3.4 Fault detection and isolation algorithm

The federated UKF provides accurate and robust state estimation values, when all attitude sensors normally operate during the maneuver. However, if one of the attitude sensors has a problem, the performance of the federated UKF is degraded. To overcome this problem, the FDI algorithm is employed in the federated configuration.

Fault detection usually requires the careful monitoring of the measured output data. In normal situation, the output data follow the known patterns of evolution under the condition of the limited random disturbance and measurement noise. However, the measured output data change their nominal evolution pattern, when sensor failures occur. Fault detection algorithms are generally based on considering the differences between the evolution patterns and the measured output data (Bae & Kim, 2010).

General fault detection algorithms are monitoring the measurement residual and utilizing the sensitivity factor. In this study, the sensitivity factor is used to detect the sensor failure. The sensitivity factor is defined as follows.

$$S_i = (\hat{x}_i - \hat{x}_M)^T (P_i + P_M)^{-1} (\hat{x}_i - \hat{x}_M) \tag{39}$$

When S_i is smaller than a threshold value, then i -th sensor is considered as a healthy one, and therefore the sensor output can be used to calculate the global estimates \hat{x}_M and P_M . However, if S_i is larger than a threshold value, then i -th sensor might have some problems. In this case, the global estimates \hat{x}_M and P_M should be computed without using the output of i -th sensor, that is a faulty one. The threshold value can be selected based on Chi-square distribution and optimized by the experiment for the particular application. Figure 2 shows the time histories of the sensitivity factor for the sensor normal case and the sensor failure case.

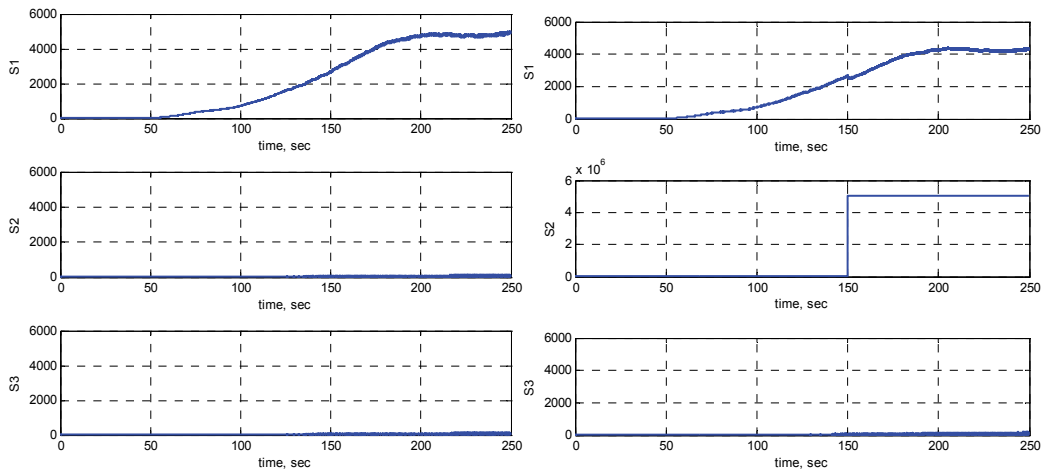


Fig. 2. Time histories of sensitivity factor: (a) normal case (left), (b) failure case (right)

Figure 2 (a) illustrates the sensitivity factor histories for normal sensors. The sensitivity factor of the first sensor is larger than others. This is because the less accuracy of the first sensor leads to provide less reliable state estimate and covariance. Therefore the corresponding first sensitivity factor is large compared with others. Figure 2 (b) shows the sensitivity factor histories when the fault of the second sensor occurs at 150 seconds. This failure causes a significantly large sensitivity factor after 150 seconds compared with Fig. 2 (a). The change of the sensitivity factor is larger than the threshold value, and the fault of the second sensor can be detected and isolated.

4. Numerical simulation and analysis

Numerical simulations are performed to verify the performance of the proposed attitude estimation algorithm based on the federated UKF. In the simulation, two types of attitude sensors are considered to estimate the attitude of the satellite: one gyroscope and two star trackers. The integrated system of the gyroscope and the star tracker provides accurate

estimates in spite of the sensor uncertainties such as drift, scale factor errors, shutting off the power, etc.

Two failure cases in each attitude sensor are considered: (i) the fault in the gyroscope, and (ii) the fault in the star tracker. The fault detection index is defined as summarized in Table 1. Note that the fault detection index is 0 when all sensors are normal. The fault detection index 1 indicates the fault of the gyroscope, the index 2 indicates the fault of the star tracker A, and the index 3 indicates the fault of the star tracker B, respectively.

Sensor fault type	Fault detection index
No sensor fault	0
Gyroscope fault	1
Star tracker A fault	2
Star tracker B fault	3

Table 1. Fault detection index

The quaternion history in a normal condition is considered as a reference. Sensor fault is not included in the normal condition. The time histories of the reference quaternion are shown in Fig. 3. Initial quaternion of all simulations is chosen as

$$q(t_0) = [0 \ 0 \ 0 \ 1]^T.$$

The local estimates and the global estimate are shown in Fig. 4. The quaternion estimates in the local and master filters are perfectly matched to the true values shown in Fig. 3, because all sensors are healthy. The attitude errors between true quaternion and the estimated quaternion are shown in Fig. 5. The first three windows from the top present the estimated attitude in three local filters, and the last window presents the global estimate in the master filter. The magnitude of the error is less than 0.05 between true quaternion and the estimated quaternion in the gyroscope. The magnitude of the error in the star tracker A and B is less than 0.02. In the master filter, the magnitude of the error between true quaternion and the global estimate is less than 0.02 since three sensor signals are fused as described in Eqs. (36)-(38).

4.1 Failure in the gyroscope

In this section, a sudden failure in the gyroscope is considered to verify the fault-tolerant performance. A failure of the gyroscope occurs at 100 seconds, and the output signals from the gyroscope to the corresponding local filter are zero after 100 seconds. The time histories of quaternion measured by the gyroscope, the star tracker A, and the star tracker B are shown in Fig. 6. The estimation results without the FDI algorithm are shown in Figs. 7 and 8. The local and global estimates are shown in Fig. 7, and the attitude errors between true quaternion and the estimated quaternion are shown in Fig. 8. The estimation results with the FDI algorithm are shown in Figs. 9 and 10. The local and global estimates are shown in Fig. 9, and the attitude errors are shown in Fig. 10. Fault detection and isolation result is presented in Fig. 11 with the fault detection index defined in Table 1.

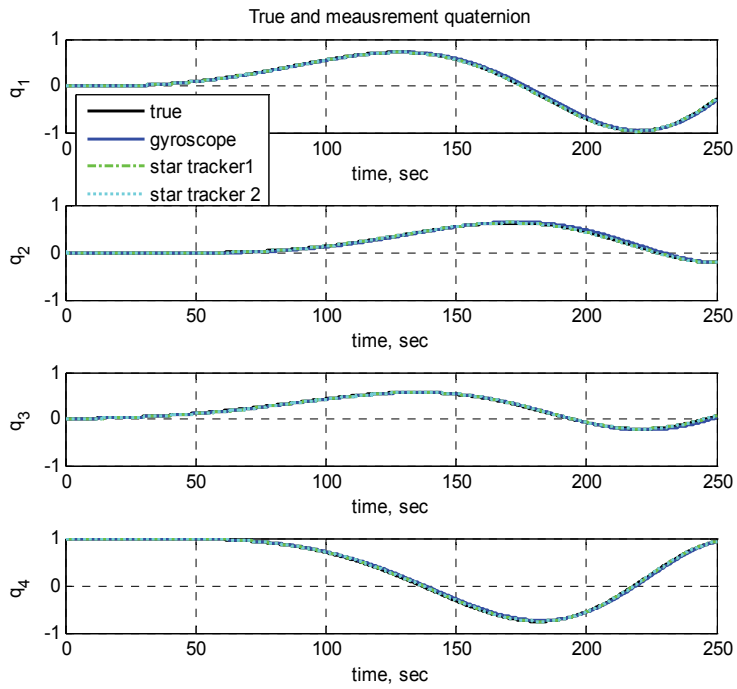


Fig. 3. Quaternion history (normal condition)

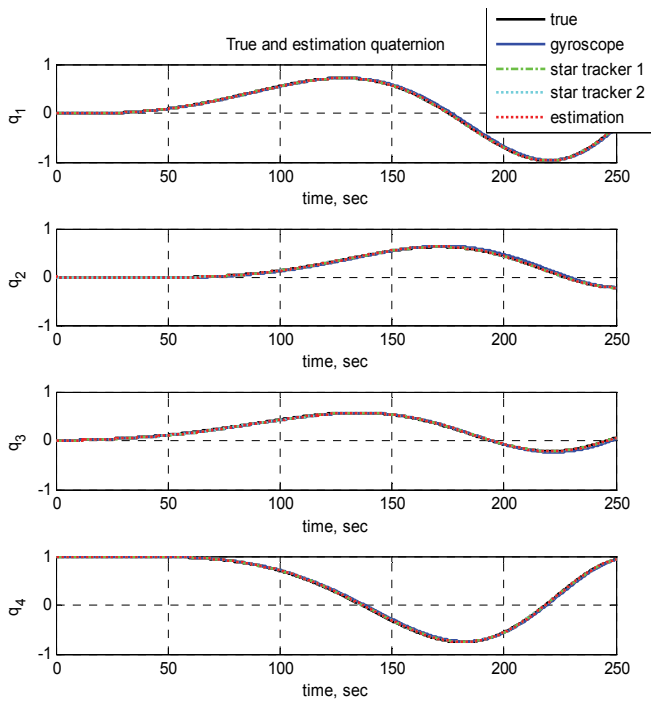


Fig. 4. Local and global estimates (normal condition)

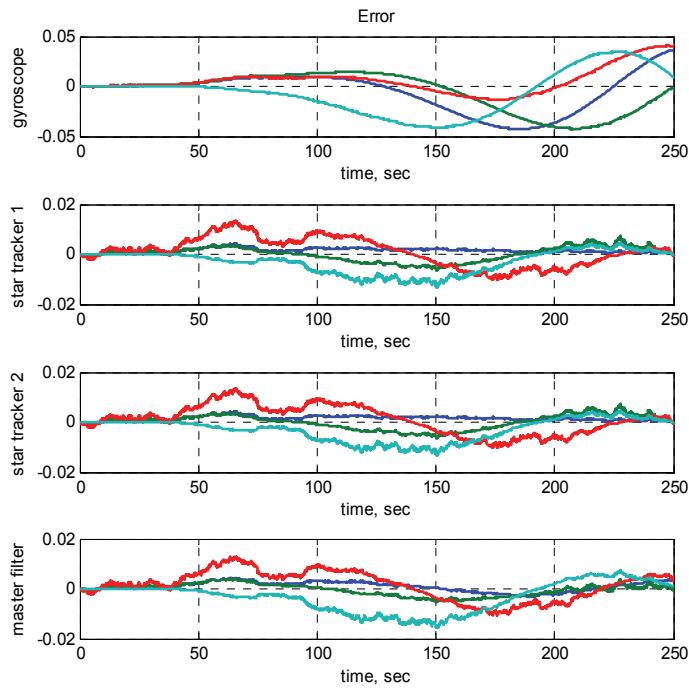


Fig. 5. Error between true quaternion and estimates (normal condition)

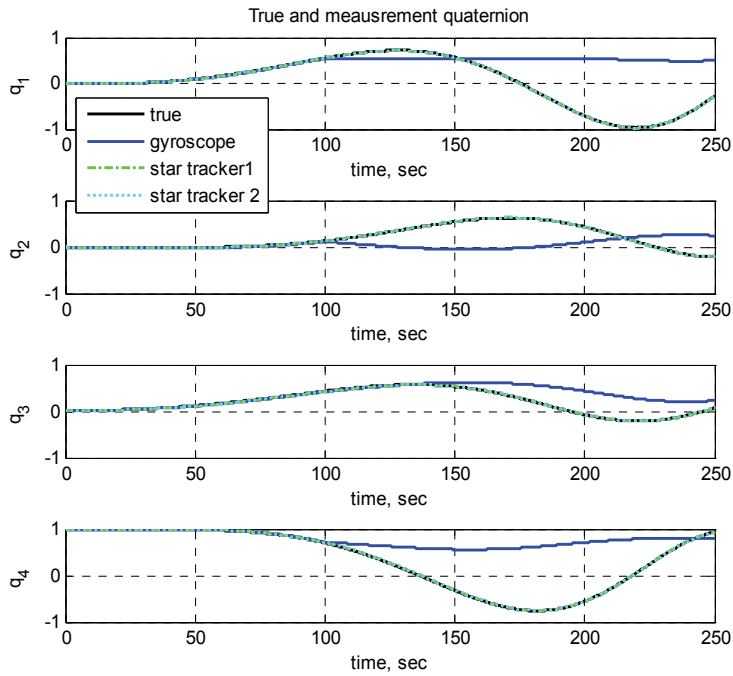


Fig. 6. Quaternion history (gyroscope fault)

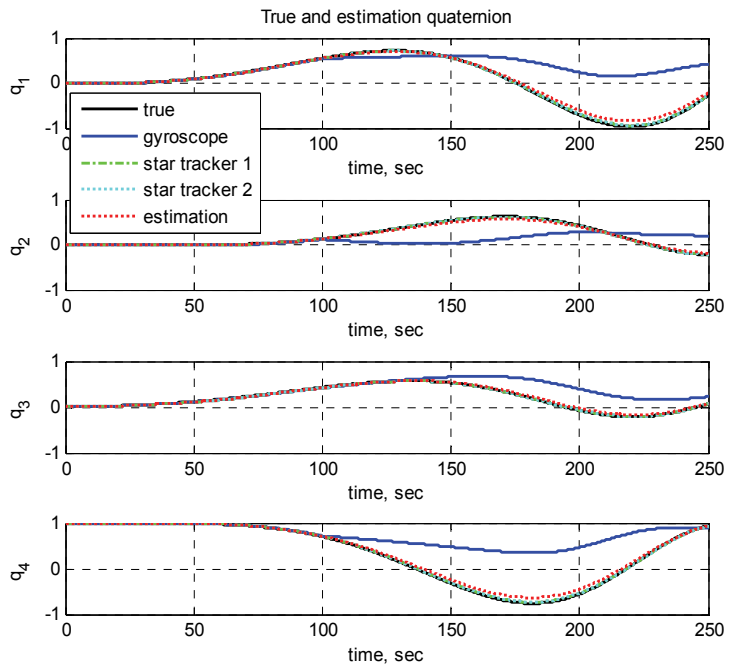


Fig. 7. Local and global estimates without FDI algorithm (gyroscope fault)

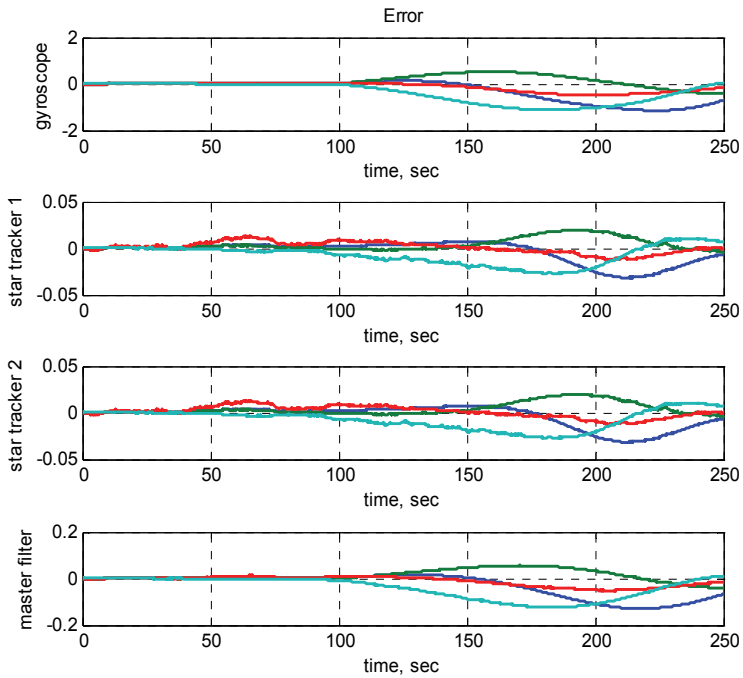


Fig. 8. Error between true quaternion and estimates without FDI algorithm (gyroscope fault)

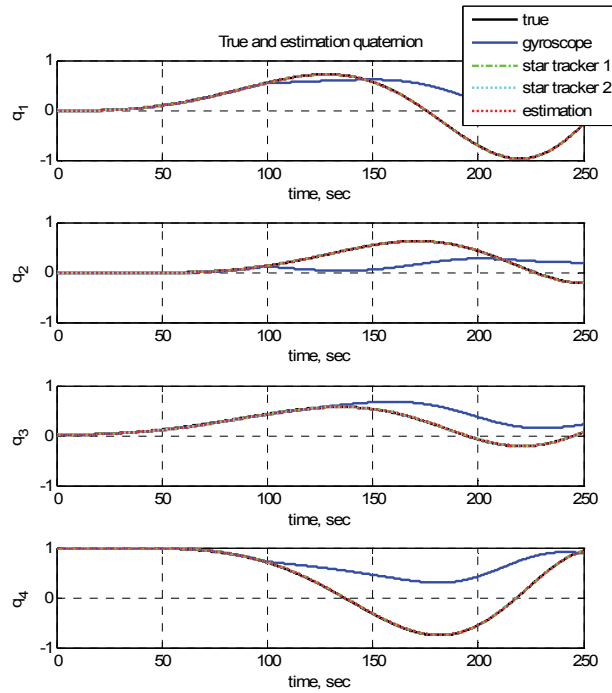


Fig. 9. Local and global estimates with FDI algorithm (gyroscope fault)

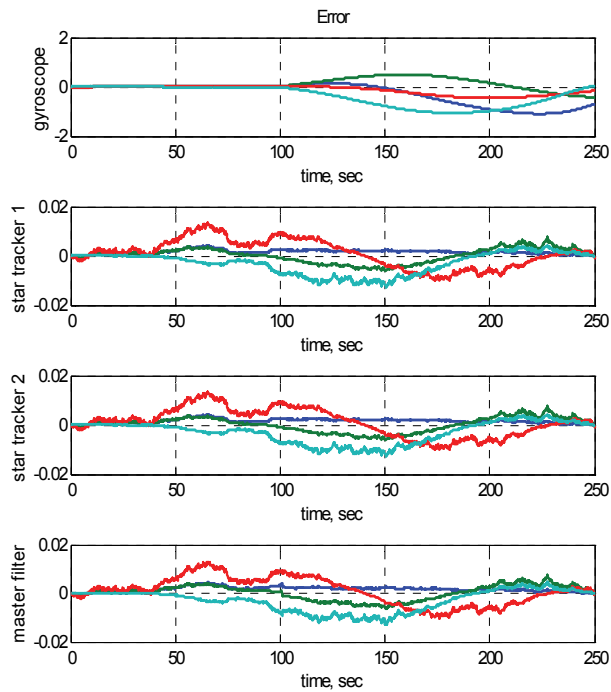


Fig. 10. Error between true quaternion and estimates with FDI algorithm (gyroscope fault)

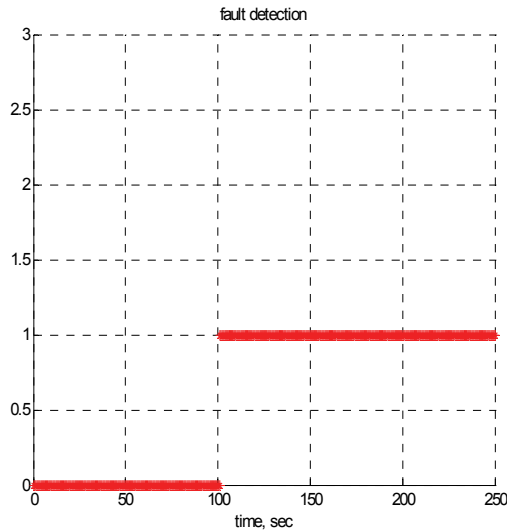


Fig. 11. Fault detection index (gyroscope fault)

As shown in Fig. 8, the maximum magnitude of the error between true quaternion and the local estimate in the gyroscope increases from 0.05 to 1.21 due to the sudden fault in the gyroscope at 100 seconds. At the same time, the maximum magnitude of the error in the master filter increases from 0.02 to 0.2. This error increase in the master filter is because the global estimate is calculated using not only healthy sensors but also the faulty sensor. Although the fault detection and isolation is not performed, the magnitude of the global estimate in the master filter is less than 0.2 as shown in Fig. 8. This result comes from the federated configuration. As shown in Fig. 10, the magnitude of the global estimate in the master filter becomes less than 0.02 when the fault detection and isolation is applied. Note that, when all sensors are normal, the maximum magnitude of the error in the gyroscope is less than 0.05 and the maximum magnitude of the error in the master filter is less than 0.02 as illustrated in Fig. 5. Consequently, the federated UKF reduces the attitude error from 1.21 (in the gyroscope) to 0.2 (in the master filter), and the FDI algorithm in the federated configuration reduces the attitude error of the master filter from 0.2 to 0.02.

4.2 Failure in the star tracker A

In this section, a sudden failure in the star tracker A is considered to verify the fault-tolerant performance. A failure of the star tracker A occurs at 100 seconds, and the output signals from the star tracker A are zero after 100 seconds. The time histories of quaternion measured by the gyroscope, the star tracker A, and the star tracker B are shown in Fig. 12. The estimation results without the FDI algorithm are shown in Figs. 13 and 14. The local and global estimates are shown in Fig. 13, and the attitude errors between true quaternion and the estimated quaternion are shown in Fig. 14. The estimation results with the FDI algorithm are shown in Figs. 15 and 16. The local and global estimates are shown in Fig. 15, and the attitude errors are shown in Fig. 16. Fault detection and isolation result is presented in Fig. 17 with the fault detection index defined in Table 1.

As shown in Fig. 14, the maximum magnitude of the error between true quaternion and the local estimates in all sensors is suddenly increased due to the sudden fault in the star tracker

A at 100 seconds: the errors in the gyroscope and the star tracker B exceed 0.1, and the error in the star tracker A exceeds 0.8. The maximum magnitude of the error in the master filter increases from 0.02 to 0.48. Similar to the gyroscope fault case described in Section 4.1, the federated UKF reduces the attitude error from 0.8 (in the star tracker A) to 0.48 (in the master filter), and the FDI algorithm in the federated filter reduces the attitude error in the master filter from 0.48 to 0.02.

The performance of the proposed algorithm is summarized in Table 2. Each failure in the gyroscope and the star tracker A is considered to verify the fault-tolerant performance of the federated UKF. The errors between true quaternion and the global estimate in the master filter are integrated regardless of the fault isolation. A single UKF is additionally simulated for comparison with the federated UKF. The federated UKF is beneficial in two respects. First, compared with the single UKF, the error sum of the federated UKF is significantly decreased from 145.21 to 12.69 in the gyroscope failure case, and from 89.40 to 40.96 in the star tracker A failure case, respectively. As shown in Figs. 8 and 14, the federated filter accommodates the fault effect in the local sensors even though any FDI logic is not included. Second, the error sum of the federated UKF including fault detection and isolation is remarkably decreased from 12.69 to 1.00 in the gyroscope failure case, and from 40.96 to 1.28 in the star tracker A failure case, respectively. As shown in Figs. 10 and 16, the FDI algorithm enhances the estimation performance by providing robust and accurate global estimate of the satellite attitude. Note that the error sum of the star tracker failure is larger than the error sum of the gyroscope failure because the star tracker provides more accurate measurement than the gyroscope.

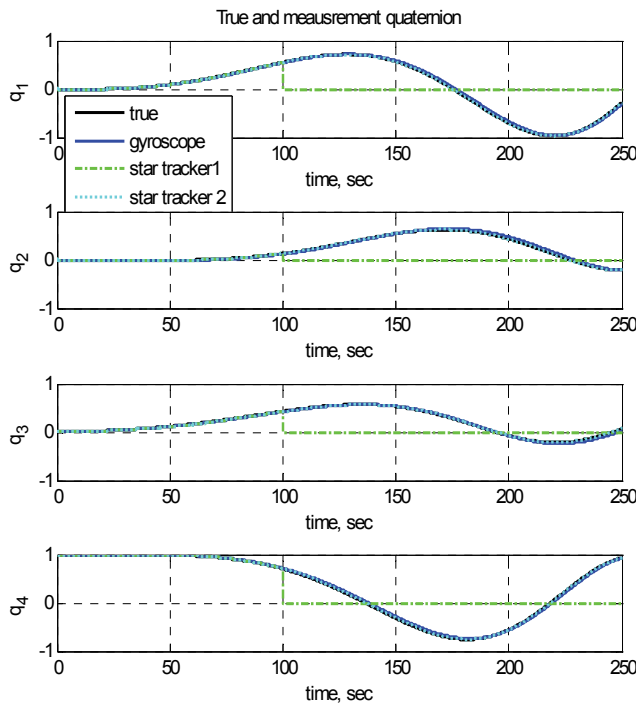


Fig. 12. Quaternion history (star tracker fault)

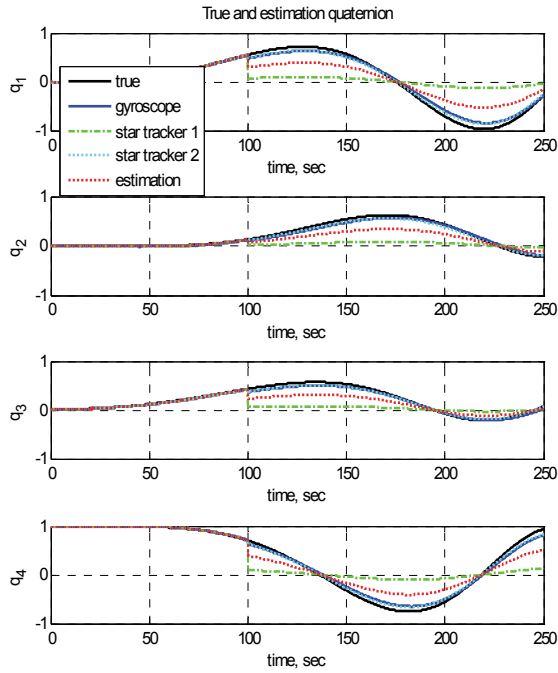


Fig. 13. Local and global estimates without FDI algorithm (star tracker fault)

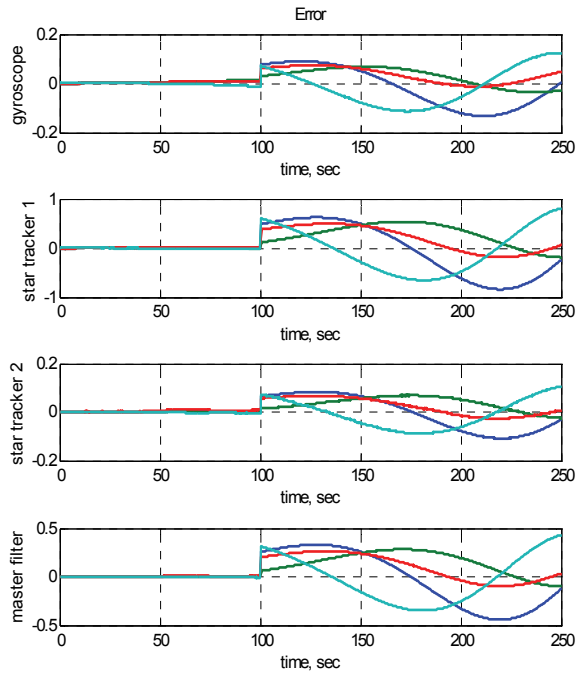


Fig. 14. Error between true quaternion and estimates without FDI algorithm (star tracker fault)

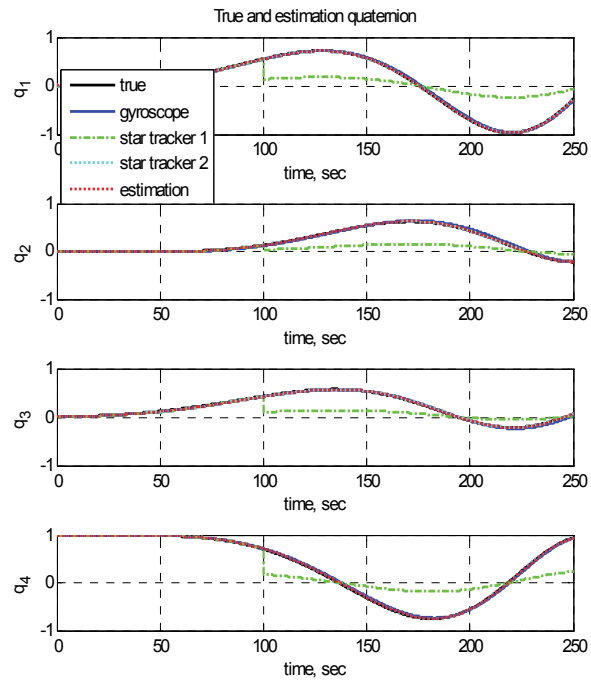


Fig. 15. Local and global estimates with FDI algorithm (star tracker fault)

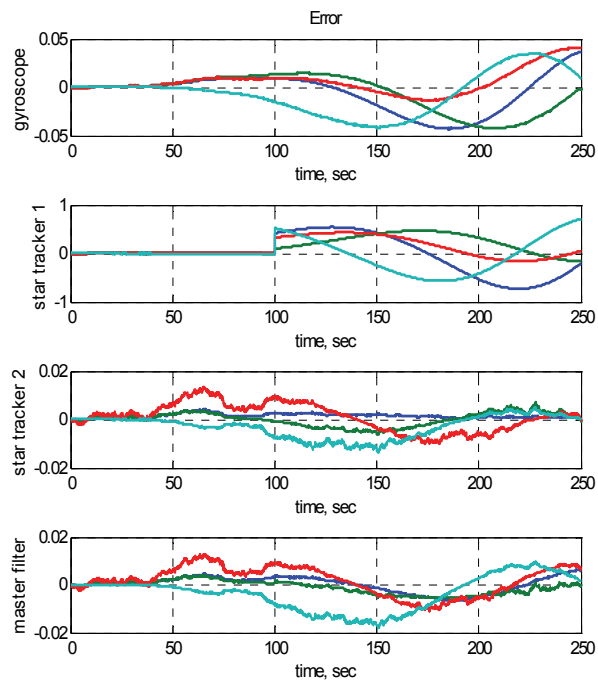


Fig. 16. Error between true quaternion and estimates with FDI algorithm (star tracker fault)

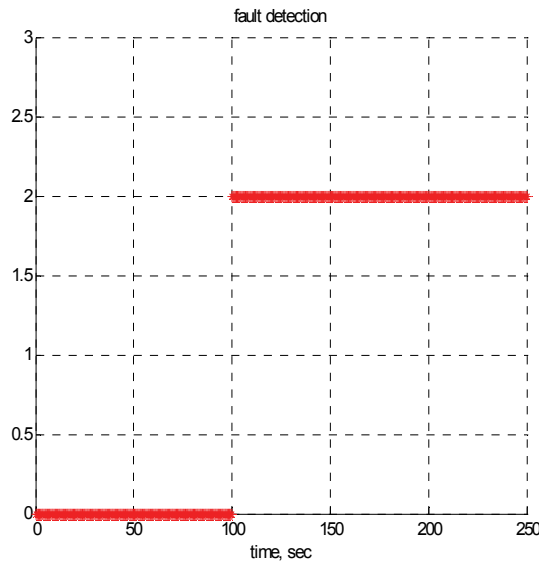


Fig. 17. Fault detection index (star tracker fault)

Sensor Fault Type	Single UKF	Federated UKF	
		Without FDI	With FDI
Gyroscope failure	145.2083	12.6870	1.0022
Star tracker failure	89.4021	40.9636	1.2780

Table 2. Error sum of attitude estimates

5. Conclusion

In this study, the federated UKF with the FDI algorithm is proposed for the estimation of the satellite attitude. The UKF gives the accurate estimates for nonlinear systems, and the federated UKF makes the system fault-tolerant and reliable. Since the FDI algorithm can detect and isolate the sensor failure immediately, the global estimate is not affected by the poor local estimate due to the faulty sensor. In this respect, the error of the global estimate using the federated UKF and the FDI algorithm is smaller than that using the federated UKF only. Numerical simulation results show that the proposed algorithm provides efficient and accurate attitude estimation of the satellite despite the fault of the attitude sensors. The proposed algorithm can be applied not only for the satellite systems but also for the ground mobile robots and aerial robot systems.

6. References

Agrawal, B. N. & Palermo, W. J. (2002). Angular Rate Estimation For Gyroless Satellite Attitude Control. *AIAA Guidance, Navigation, and Control Conference*, Monterey, CA, Aug. 2002.

- Bae, J. & Kim, Y. (2010). Attitude Estimation for Satellite Fault Tolerant System using Federated Unscented Kalman Filter. *International Journal of Aeronautical and Space Science*, Vol. 11, No. 2, 2010, pp. 80-86, ISSN: 1229-9626.
- Crassidis, J. L. & Markley, F. L. (2003). Unscented Filtering for Spacecraft Attitude Estimation. *Journal of Guidance, Control, and Dynamics*, Vol. 25, No. 4, 2003, pp. 536-542, ISSN: 0731-5090.
- Edelmayer, A. & Miranda, M. (2007). Federated Filtering for Fault Tolerant Estimation and Sensor Redundancy Management in Coupled Dynamics Distributed Systems. *Mediterranean Conference on Control and Automation*, Athens, Greece, July 2007.
- Hwang, I.; Kim, S.; Kim, Y. & Seah, C.E. (2010). A Survey of Fault Detection, Isolation, and Reconfiguration Methods. *IEEE Transactions on Control Systems Technology*, Vol. 18, No. 3, May 2010, pp.636-653, ISSN: 1063-6536.
- Jayaraman, P.; Fischer, J.; Moorhouse, A. & Lauer, M. (2006). Star Tracker Operational Usage in Different Phases of the Mars Express Mission. *SpaceOps 2006 Conference*, Rome, Italy, June 2006.
- Jiancheng, F. & Ali, J. (2005). Multisensor Data Synthesis using Federated Form of Unscented Kalman Filtering. *IEEE International Conference on Industrial Technology*, Hong Kong, Dec. 2005.
- Jin, Y.; Liu, X. & Hou, C. (2008). Relative Attitude Determination for Fly-Around Based on UKF. *7th World Congress on Intelligent Control and Automation*, Chongqing, China, Jun. 2008.
- Julier, S. J. & Uhlmann, J. K. (2004). Unscented Filtering and Nonlinear Estimation. *Proceedings of the IEEE*, Vol. 92, No. 3, 2004, pp. 401-422, ISSN: 0018-9219.
- Karlgard, C. D. & Schaub, H. (2008). Adaptive Huber-Based Filtering Using Projection Statistics: Application to Spacecraft Attitude Estimation. *AIAA Guidance, Navigation, and Control Conference*, Honolulu, HI, Aug. 2008.
- Kerr, T. (1987). Decentralized Filtering and Redundancy Management for Multisensor Navigation. *IEEE Transactions on Aerospace and Electronic Systems*, Vol. 20, No. 1, 1987, pp. 83-119, ISSN: 0018-9251.
- Kim, Y. S. & Hong, K. S. (2003). Decentralized Information Filter in Federated Form. *SICE Annual Conference*, Fukui, Japan, Aug. 2003.
- Lee, D. (2008). Unscented Information Filtering for Distributed Estimation and Multiple Sensor Fusion. *AIAA Guidance, Navigation, and Control Conference*, Honolulu, HI, Aug. 2008.
- Mehra, R. & Bayard, D. (1995). Adaptive Kalman Filtering, Failure Detection and Identification for Spacecraft Attitude Estimation. *4th IEEE Conference on Control Application*, Albany, NY, Sep. 1995.
- Nagendra, R. G.; Alex, T. K. & Seetharama, B. M. (2002). Incremental-Angle and Angular Velocity Estimation Using a Star Sensor. *Journal of Guidance, Control, and Dynamics*, Vol. 25, No. 3, 2002, pp. 433-441, ISSN: 0731-5090.
- Schaub, H. & Junkins, J. L. (2003). *Analytical Mechanics of Space Systems*, American Institute of Aeronautics and Astronautics, ISBN: 1-60086-721-9, Reston, VA.
- Simon, D. (2006). *Optimal State Estimation*, Wiley-Interscience, ISBN: 0471708585, Malden, MA.
- Wei, M. & Schwarz, K. P. (1990). Testing a Decentralized Filter for GPS/INS Integration. *Position Location and Navigation Symposium*, Las Vegas, NV, Mar. 1990.
- Xu, Y. (2009). Nonlinear Robust Stochastic Control for Unmanned Aerial Vehicles. *Journal of Guidance, Control, and Dynamics*, Vol. 32, No. 4, 2009, pp. 1308-1319, ISSN: 0731-5090.

Nonlinear Electrodynamics: Alternative Field Theory for Featuring Photon Propagation Over Weak Background Electromagnetic Fields and what Earth Receivers Read off Radio Signals from Interplanetary Spacecraft Transponders

Herman J. Mosquera Cuesta^{1,2,3}

¹*Departamento de Física Universidade Estadual Vale do Acaraú
Avenida da Universidade 850, Campus da Betânia, CEP 62.040-370, Sobral, Ceará*

²*Instituto de Cosmologia, Relatividade e Astrofísica (ICRA-BR)
Centro Brasileiro de Pesquisas Físicas, Rua Dr. Xavier Sigaud 150,
CEP 22290-180, Urca Rio de Janeiro, RJ*

³*International Center for Relativistic Astrophysics Network (ICRANet)
International Coordinating Center, Piazzalle della Repubblica 10, 065112, Pescara*

^{1,2}Brazil

³Italy

1. Introduction

A few observational and/or experimental results have dramatically pushed forward the research program on gravity as those from the radio-metric Doppler tracking received from the Pioneer 10 and 11 spacecrafts when the space vehicles were at heliocentric distances between 20 and 70 Astronomical Units (AU). These data have conclusively demonstrated the presence of an anomalous, tiny and blue-shifted frequency drift that changes smoothly at a rate of $\sim 6 \times 10^{-9} \text{ Hz s}^{-1}$. Those signals, if interpreted as a gravitational pull of the Sun on each Pioneer vehicle, translates into a deceleration of $a_p = (8.74 \pm 1.33) \times 10^{-10} \text{ m s}^{-2}$. This sunward acceleration appears to be a violation of Newton's inverse-square law of gravitation, and is referred to as the Pioneer anomaly, the nature of which remains still elusive to unveil. Within the theoretical framework of nonlinear electrodynamics (NLED) in what follows we will address this astrodynamical puzzle, which over the last fifteen years has challenged in a fundamental basis our understanding of gravitational physics. To this goal we will first, and briefly, review the history of the Pioneers 10 and 11 missions. Then a synopsis of currently available Lagrangian formulations of NLED is given. And finally, we present our solution of this enigma by invoking a special class of NLED theories featuring a proper description of electromagnetic phenomena taking place in environments where the strength of the (electro)magnetic fields in the background is decidedly low.

2 What is the problem: The Pioneer anomaly

In this short voyage to the Pioneer 10 and 11 missions our main guide will be the comprehensive and richly documented recent review on the Pioneer Anomaly by [Turyshev, S. G. & Toth, V. T. (2010). *Living Rev. Rel.* 13 (2010) 4. arXiv:1001.3686, v2, gr-qc] from which we retake some ideas and references. (The attentive readers are kindly addressed to this invaluable article).

The Pioneer 10 and 11 spacecrafts were the first two man-made space vehicles designed to explore the outer solar system. The trajectories of the spaceships were projected to passage nearby Jupiter during 1972-1973 having as objectives to conduct exploratory investigation of the interplanetary medium beyond the orbit of Mars, the nature of the asteroid belt, the environmental and atmospheric characteristics of Jupiter and Saturn (for Pioneer 11), and to investigate the solar system beyond the orbit of the Jovian planet.¹

The Pioneer missions were the first space probes to adventure over the asteroid belt, heading for close-up observations of the gaseous giant planets, and for performing in situ studies of the physical properties of the interplanetary medium in the outer solar system. The design of their missions was guided by the simplicity, having a powerful rocket-launching system to push the spacecrafts on an hyperbolic trajectory aimed directly at Jupiter, which the spacecrafts were expected to fly-by approximately 21 months after launch (see Fig. 1).

By the late 1960's, the aerospace engineering technology available to the designers of the Pioneer missions made it no longer practical to use solar panels for operating a spacecraft at large distances, as for instance that of Jupiter. A cause of this, a built-in nuclear power system, in the form of radioisotope thermoelectric generators (RTGs) powered by ²³⁸Pu, was chosen as the means to provide electrical power to the spaceship. As even this was relatively new technology at the time the missions were designed, the power subsystem was suitably over-engineered, being the unique design requirement to have a completely functional space probe capable of performing all planned scientific tasks by running only three (out of four) RTGs.

The entire design of these spacecrafts and their science missions was characterized by such conservative engineering, and for sure it was responsible for both the exceptional longevity of the two spacecrafts and their ability to deliver science results which by far exceeded the expectations of their designers.

The original plan envisioned a primary mission of two to three years in duration. Nevertheless, following its encounter with Jupiter, Pioneer 10 remained functional for over 30 years. Meanwhile, Pioneer 11, though not as long lived as its engineering-copy craft, successfully navigated a path across the solar system for another encounter with Saturn, offering the first close-up observations of the ringed planet. After the encounters with Jupiter and Saturn (for Pioneer 11, see Fig. 1), the space ships followed, near the plane of the ecliptic, hyperbolic orbits of escape heading to opposite sides of the solar system, continuing their extended missions. The spacecrafts explored the outer regions of the solar system, studying energetic particles from the Sun (solar wind), and cosmic rays entering our neighborhood in the Milky Way. (Their cousin spacecrafts, the Voyager1 and 2, that where launched contemporarily, studied in the beginning of their mission, the interplanetary space, what resulted in a very accurate mapping of the interplanetary magnetic field and its strength, as one can see in Fig. 2 below).

¹See details on the Pioneer missions at <http://www.nasa.gov/centers/ames/missions/archive/pioneer.html>. Be aware that another member of Pioneer spacecrafts family, Pioneer 6, remained operational for more than 35 years after launch.

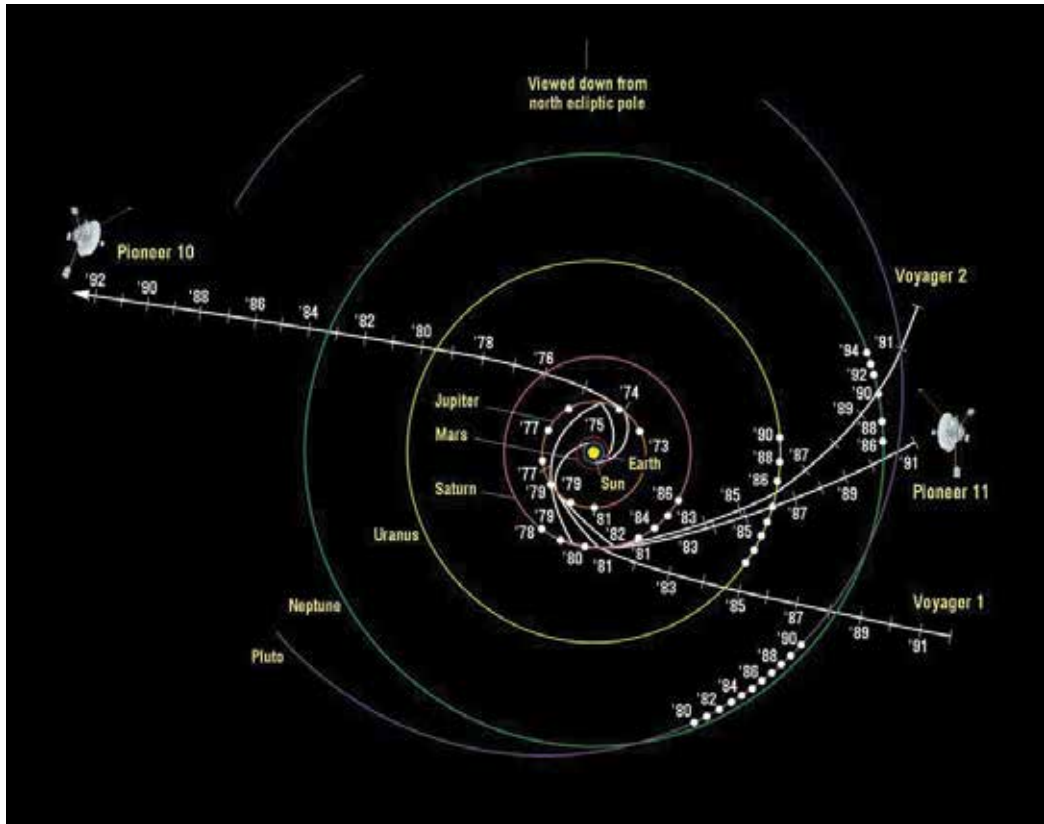


Fig. 1. Ecliptic pole view of the spacecrafts Pioneer 10 and 11 interplanetary trajectories (see also the trajectories of the vehicles Voyager 1 and 2). Credit:

<http://www.nasa.gov/centers/ames/missions/archive/pioneer.html>

In virtue of a combination of many factors, the Pioneers were excellent space sondes for pursuing experiments of high precision celestial mechanics. This includes the presence of a coherent mode transceiver on board, the attitude control (spin-stabilized, with a minimum number of attitude correction maneuvers using thrusters), the design of the power system (the RTGs being on extended booms aided the stability of the craft and also helped in reducing thermal effects), and Doppler tracking of high precision (with the accuracy of post-fit Doppler residuals at the level of mHz). The exceptional built-in sensitivity to acceleration of the Pioneer 10 and 11 spacecrafts naturally allowed them to reach a level of accuracy of $\sim 10^{-10}$ m/s². The result was one of the most precise spacecraft navigations in deep space since the early days of space exploration. That is the great legacy of the Pioneer missions.

After having had a brief accounting of the Pioneers missions, one can proceed to review our current understanding of nonlinear electrodynamics and to settle down the foundations for its use in the search for a solution to the Pioneer anomaly. In this Section we shall briefly review the theoretical foundations of some theories of NLED, focusing essentially on the fundamental prediction concerning the way photons propagate through a vacuum space permeated by electromagnetic (EM) fields: The fact that photons travel along the *effective metric*, and not over the geometry in the background. It is this peculiar feature what makes the photon to

“feel” itself being acted upon by a force, and consequently to undergo acceleration.² In our understanding, such effect is responsible for the drift in frequency undergone by the photon. Next we will show that any NLED, independently of the specific form of its Lagrangian, brings in such a frequency shift. And in our view, it is such acceleration what can account for the Pioneer anomaly.

3. Some Lagrangian formulations of nonlinear electrodynamics

To start with, it is worth to recall that according to quantum electrodynamics (QED: see Delphenich (2003; 2006) for a complete review on NLED and QED) a vacuum has nonlinear properties (Heisenberg & Euler 1936; Schwinger 1951) which affect the photon propagation. A noticeable advance in the realization of this theoretical prediction has been provided by [Burke, Field, Horton-Smith, et al., 1997], who demonstrated experimentally that the inelastic scattering of laser photons by gamma-rays in a background magnetic field is definitely a nonlinear phenomenon. The propagation of photons in NLED has been examined by several authors [Bialynicka-Birula & Bialynicki-Birula, 1970; Garcia & Plebanski, 1989; Dittrich & Gies, 1998; De Lorenci, Klippert, Novello, et al., 2000; Denisov, Denisova & Svertilov, 2001a, 2001b, Denisov & Svertilov, 2003]. In the geometric optics approximation, it was shown by [Novello, De Lorenci, Salim & et al., 2000; Novello & Salim, 2001], that when the photon propagation is identified with the propagation of discontinuities of the EM field in a nonlinear regime, a remarkable feature appears: The discontinuities propagate along null geodesics of an *effective* geometry which depends on the EM field on the background. This means that the NLED interaction can be geometrized. An immediate consequence of this NLED property is the prediction of the phenomenon dubbed as photon acceleration, which is nothing else than a shift in the frequency of any photon traveling over background electromagnetic fields. The consequences of this formalism are examined next.

3.1 Heisenberg-Euler approach

The Heisenberg-Euler Lagrangian for nonlinear electrodynamics (up to order 2 in the truncated infinite series of terms involving F) has the form Heisenberg & Euler (1936)

$$L_{\text{H-E}} = -\frac{1}{4}F + \bar{\alpha}F^2 + \bar{\beta}G^2, \quad (1)$$

where $F = F_{\mu\nu}F^{\mu\nu}$, with $F_{\mu\nu} = \partial_\mu A_\nu - \partial_\nu A_\mu$, and $G = \frac{1}{2}\eta_{\alpha\beta\gamma\delta}F^{\alpha\beta}F^{\gamma\delta} = -4\vec{E} \cdot \vec{B}$, with greek index running (0, 1, 2, 3), while $\bar{\alpha}$ and $\bar{\beta}$ are arbitrary constants.

When this Lagrangian is used to describe the photon dynamics the equations for the EM field in vacuum coincide in their form with the equations for a continuum medium in which the electric permittivity and magnetic permeability tensors $\epsilon_{\alpha\beta}$ and $\mu_{\alpha\beta}$ are functions of the electric and magnetic fields determined by some observer represented by its 4-vector velocity V^μ [Denisov, Denisova & Svertilov, 2001a, 2001b; Denisov & Svertilov, 2003; Mosquera Cuesta & Salim, 2004a, 2004b]. The attentive reader must notice that this first order approximation is valid only for B -fields smaller than $B_q = \frac{m^2 c^3}{e\hbar} = 4.41 \times 10^{13}$ G (Schwinger's critical B -field Schwinger (1951)). In curved spacetime, these equations are written as

²Because of the special theory of relativity constraints regarding the propagation of any perturbation, it becomes clear that such effect must manifest itself as a change in one or both of their physical properties: its frequency or its wavelength. Hence, through the Pioneer spacecrafts radio Doppler tracking we might be observing the effect on the photon frequency.

$$D_{||\alpha}^\alpha = 0, \quad B_{||\alpha}^\alpha = 0, \quad (2)$$

$$D_{||\beta}^\alpha \frac{V^\beta}{c} + \eta^{\alpha\beta\rho\sigma} V_\rho H_{\sigma||\beta} = 0, \quad (3)$$

$$B_{||\beta}^\alpha \frac{V^\beta}{c} - \eta^{\alpha\beta\rho\sigma} V_\rho E_{\sigma||\beta} = 0. \quad (4)$$

Here, the vertical bars subscript “||” stands for covariant derivative and $\eta^{\alpha\beta\rho\sigma}$ is the antisymmetric Levi-Civita tensor.

The 4-vectors representing the electric and magnetic fields are defined as usual in terms of the electric and magnetic fields tensor $F_{\mu\nu}$ and polarization tensor $P_{\mu\nu}$

$$E_\mu = F_{\mu\nu} \frac{V^\nu}{c}, \quad B_\mu = F_{\mu\nu}^* \frac{V^\nu}{c}, \quad (5)$$

$$D_\mu = P_{\mu\nu} \frac{V^\nu}{c}, \quad H_\mu = P_{\mu\nu}^* \frac{V^\nu}{c}, \quad (6)$$

where the dual tensor $X_{\mu\nu}^*$ is defined as $X_{\mu\nu}^* = \frac{1}{2} \eta_{\mu\nu\alpha\beta} X^{\alpha\beta}$, for any antisymmetric second-order tensor $X_{\alpha\beta}$.

The meaning of the vectors D^μ and H^μ comes from the Lagrangian of the EM field, and in the vacuum case they are given by

$$H_\mu = \mu_{\mu\nu} B^\nu, \quad D_\mu = \epsilon_{\mu\nu} E^\nu, \quad (7)$$

where the permeability and tensors are given as

$$\mu_{\mu\nu} = \left[1 + \frac{2\alpha}{45\pi B_q^2} (B^2 - E^2) \right] h_{\mu\nu} - \frac{7\alpha}{45\pi B_q^2} E_\mu E_\nu, \quad (8)$$

$$\epsilon_{\mu\nu} = \left[1 + \frac{2\alpha}{45\pi B_q^2} (B^2 - E^2) \right] h_{\mu\nu} + \frac{7\alpha}{45\pi B_q^2} B_\mu B_\nu. \quad (9)$$

In these expressions α is the EM coupling constant ($\alpha = \frac{e^2}{\hbar c} = \frac{1}{137}$). The tensor $h_{\mu\nu}$ is the metric induced in the reference frame perpendicular to the observers determined by the vector field V^μ .

Meanwhile, as we are assuming that $E^\alpha = 0$, then one gets

$$\epsilon_\beta^\alpha = \epsilon h_\beta^\alpha + \frac{7\alpha}{45\pi B_q^2} B^\alpha B_\beta \quad (10)$$

and $\mu_{\alpha\beta} = \mu h_{\alpha\beta}$. The scalars ϵ and μ can be read directly from Eqs.(8, 9) as

$$\epsilon \equiv \mu = 1 + \frac{2\alpha}{45\pi B_q^2} B^2. \quad (11)$$

Applying conditions (62) and (63) (derived in the Appendix) to the field equations when $E^\alpha = 0$, we obtain the constraints $e^\mu \epsilon_{\mu\nu} k^\nu = 0$ and $b^\mu k_\mu = 0$ and the following equations for the discontinuity fields e_α and b_α :

$$\epsilon^{\lambda\gamma} e_\gamma k_\alpha \frac{V^\alpha}{c} + \eta^{\lambda\mu\rho\nu} \frac{V_\rho}{c} (\mu b_\nu k_\mu - \mu' \lambda_\alpha B_\nu k_\mu) = 0, \quad (12)$$

$$b^\lambda k_\alpha \frac{V^\alpha}{c} - \eta^{\lambda\mu\rho\nu} \frac{V_\rho}{c} (e_\nu k_\mu) = 0. \quad (13)$$

Isolating the discontinuity field from (12), substituting in equation (13), and expressing the products of the completely anti-symmetric tensors $\eta_{\nu\zeta\gamma\beta}\eta^{\lambda\alpha\rho\mu}$ in terms of delta functions Stephani (2004), we obtain

$$b^\lambda (k_\alpha k^\alpha)^2 + \left(\frac{\mu'}{\mu} l_\beta b^\beta k_\alpha B^\alpha + \frac{\beta B_\beta b^\beta B_\alpha k^\alpha}{\mu - \beta B^2} \right) k^\lambda + \left(\frac{\mu'}{\mu l_\alpha b^\alpha} (k_\beta V^\beta)^2 (k_\alpha k^\alpha)^2 - \frac{\beta B_\alpha b^\alpha (k_\beta k^\beta)^2}{\mu - \beta B^2} \right) B^\lambda - \left(\frac{\mu'}{\mu} l_\mu b^\mu k_\alpha B^\alpha k_\beta V^\beta \right) V^\lambda = 0. \quad (14)$$

This expression is already squared in k_μ but still has an unknown b_α term. To get rid of it, one multiplies by B_λ , to take advantage of the EM wave polarization dependence. By noting that if $B^\alpha b_\alpha = 0$ one obtains the *dispersion relation* by separating out the $k^\mu k^\nu$ term, what remains is the (-) effective metric. Similarly, if $B_\alpha b^\alpha \neq 0$, one simply divides by $B_\gamma b^\gamma$ so that by factoring out $k^\mu k^\nu$, what results is the (+) effective metric. For the case $B_\alpha b^\alpha = 0$, one obtains the standard dispersion relation

$$g^{\alpha\beta} k_\alpha k_\beta = 0. \quad (15)$$

whereas for the case $B_\alpha b^\alpha \neq 0$, the result is

$$\left[\left(1 + \frac{\mu' B}{\mu} + \frac{\tilde{\beta} B^2}{\mu - \tilde{\beta} B^2} \right) g^{\alpha\beta} - \frac{\mu' B}{\mu} \frac{V^\alpha V^\beta}{c^2} + \left(\frac{\mu' B}{\mu} + \frac{\tilde{\beta} B^2}{\mu - \tilde{\beta} B^2} \right) l^\alpha l^\beta \right] k_\alpha k_\beta = 0, \quad (16)$$

where (') stands for $\frac{d}{dB}$, and we have defined

$$\tilde{\beta} = \frac{7\alpha}{45\pi B_q^2}, \quad \text{and} \quad l^\mu \equiv \frac{B^\mu}{|B^\gamma B_\gamma|^{1/2}} \quad (17)$$

as the unit 4-vector along the B -field direction.

From the above expressions we can read the effective metric $g_+^{\alpha\beta}$ and $g_-^{\alpha\beta}$, where the labels "+" and "-" refers to extraordinary and ordinary polarized rays, respectively. Then, we need the covariant form of the metric tensor, which is obtained from the expression defining the inverse metric $g_{\mu\nu} g^{\nu\alpha} = \delta_\mu^\alpha$. So that one gets from one side

$$g_{\mu\nu}^- = g_{\mu\nu} \quad (18)$$

and from the other

$$g_{\mu\nu}^+ = \left(1 + \frac{\mu' B}{\mu} + \frac{\beta B^2}{\mu - \beta B^2} \right)^{-1} g_{\mu\nu} + \left[\frac{\mu' B}{\mu \left(1 + \frac{\mu' B}{\mu} + \frac{\beta B^2}{\mu - \beta B^2} \right) \left(1 + \frac{\beta B^2}{\mu - \beta B^2} \right)} \right] \frac{V_\mu V_\nu}{c^2} + \left(\frac{\frac{\mu' B}{\mu} + \frac{\beta B^2}{\mu - \beta B^2}}{1 + \frac{\mu' B}{\mu} + \frac{\beta B^2}{\mu - \beta B^2}} \right) l_\mu l_\nu. \quad (19)$$

The function $\frac{\mu' B}{\mu}$ can be expressed in terms of the magnetic permeability of the vacuum, and is given as

$$\frac{\mu' B}{\mu} = 2 \left(1 - \frac{1}{\mu} \right). \tag{20}$$

Thus equation (19) indicates that the photon propagates on an effective metric.

3.2 Born-Infeld theory

The propagation of light can also be viewed within the framework of the Born-Infeld Lagrangian. Such theory is inspired in the special theory of relativity, and indeed it incorporates the principle of relativity in its construction, since the fact that nothing can travel faster than light in a vacuum is used as a guide to establishing the existence of an upper limit for the strength of electric fields around an isolated charge, an electron for instance. Such charge is then forced to have a characteristic size Born & Infeld (1934). The Lagrangian then reads

$$L = -\frac{b^2}{2} \left[\left(1 + \frac{F}{b^2} \right)^{1/2} - 1 \right]. \tag{21}$$

As in this particular case, the this Lagrangian is a functional of the invariant F , i.e., $L = L(F)$, but not of the invariant $G \equiv B_\mu E^\mu$, the study of the NLED effects turns out to be simpler (here again we suppose $E = 0$). In the equation above, $b = \frac{e}{R_0^2} = \frac{e}{\frac{e^4}{m_0^2 c^8}} = 9.8 \times 10^{15}$ e.s.u.

In order to derive the effective metric that can be deduced from the B-I Lagrangian, one has therefore to work out, as suggested in the Appendix, the derivatives of the Lagrangian with respect to the invariant F . The first and second derivatives then reads

$$L_F = \frac{-1}{4 \left(1 + \frac{F}{b^2} \right)^{1/2}} \quad \text{and} \quad L_{FF} = \frac{1}{8b^2 \left(1 + \frac{F}{b^2} \right)^{3/2}}. \tag{22}$$

The $L(F)$ B-I Lagrangian produces, according to Eq.(70) in the Appendix, an *effective* contravariant metric given as

$$g_{\text{eff}}^{\mu\nu} = \frac{-1}{4 \left(1 + \frac{F}{b^2} \right)^{1/2}} g^{\mu\nu} + \frac{B^2}{2b^2 \left(1 + \frac{F}{b^2} \right)^{3/2}} [h^{\mu\nu} + l^\mu l^\nu]. \tag{23}$$

Both the tensor $h_{\mu\nu}$ and the vector l^μ in this equation were defined earlier (see Eqs.(9) and (16) above).

Because the geodesic equation of the discontinuity (that defines the effective metric, see the Appendix) is conformal invariant, one can multiply this last equation by the conformal factor $-4 \left(1 + \frac{F}{b^2} \right)^{3/2}$ to obtain

$$g_{\text{eff}}^{\mu\nu} = \left(1 + \frac{F}{b^2} \right) g^{\mu\nu} - \frac{2B^2}{b^2} [h^{\mu\nu} + l^\mu l^\nu]. \tag{24}$$

Then, by noting that

$$F = F_{\mu\nu} F^{\mu\nu} = -2(E^2 - B^2), \tag{25}$$

and recalling our assumption $E = 0$, then one obtains $F = 2B^2$. Therefore, the effective metric reads

$$g_{\text{eff}}^{\mu\nu} = \left(1 + \frac{2B^2}{b^2}\right) g^{\mu\nu} - \frac{2B^2}{b^2} [h^{\mu\nu} + l^\mu l^\nu], \quad (26)$$

or equivalently

$$g_{\text{eff}}^{\mu\nu} = g^{\mu\nu} + \frac{2B^2}{b^2} V^\mu V^\nu - \frac{2B^2}{b^2} l^\mu l^\nu. \quad (27)$$

As one can check, this effective metric is a functional of the background metric $g^{\mu\nu}$, the 4-vector velocity field of the inertial observers V^ν , and the spatial configuration (orientation l^μ) and strength of the B -field.

Thus the covariant form of the background metric can be obtained by computing the inverse of the effective metric $g_{\text{eff}}^{\mu\nu}$ just derived. With the definition of the inverse metric $g_{\text{eff}}^{\mu\nu} g_{\text{eff}\nu\alpha}^{\text{eff}} = \delta^\mu_\alpha$, the covariant form of the effective metric then reads

$$g_{\mu\nu}^{\text{eff}} = g_{\mu\nu} - \frac{2B^2/b^2}{(2B^2/b^2 + 1)} V_\mu V_\nu + \frac{2B^2/b^2}{(2B^2/b^2 + 1)} l_\mu l_\nu, \quad (28)$$

which is the result that we were looking for. The terms additional to the background metric $g_{\mu\nu}$ characterize any effective metric.

3.3 Pagels-Tomboulis Abelian theory

In 1978, the Pagels-Tomboulis nonlinear Lagrangian for electrodynamics appeared as an effective model of an Abelian theory introduced to describe a perturbative gluodynamics model. It was intended to investigate the non trivial aspects of quantum-chromodynamics (QCD) like the asymptotic freedom and quark confinement Pagels & Tomboulis (1978). In fact, Pagels and Tomboulis argued that:

“since in asymptotically free Yang-Mills theories the quantum ground state is not controlled by perturbation theory, there is no a priori reason to believe that individual orbits corresponding to minima of the classical action dominate the Euclidean functional integral.”

In view of this drawback, of the at the time understanding of ground states in quantum theory, they decided to examine and classify the vacua of the quantum gauge theory. To this goal, they introduced an effective action in which the gauge field coupling constant g is replaced by the effective coupling $\bar{g}(t) \cdot T = \ln \left[\frac{F_{\mu\nu}^a F^{a\mu\nu}}{\mu^4} \right]$. The vacua of this model correspond to paramagnetism and perfect paramagnetism, for which the gauge field is $F_{\mu\nu}^a = 0$, and ferromagnetism, for which $F_{\mu\nu}^a F^{a\mu\nu} = \lambda^2$, which implies the occurrence of spontaneous magnetization of the vacuum.³ They also found no evidence for instanton solutions to the quantum effective action. They solved the equations for a point classical source of color spin, which indicates that in the limit of spontaneous magnetization the infrared energy of the field becomes linearly divergent. This leads to bag formation, and to an electric Meissner effect confining the bag contents.

This effective model for the low energy (3+1) QCD reduces, in the Abelian sector, to a nonlinear theory of electrodynamics whose density Lagrangian $L(X, Y)$ is a functional of the invariants $X = F_{\mu\nu} F^{\mu\nu}$ and their dual $Y = (F_{\mu\nu} F^{\mu\nu})^*$, having their equations of motion given by

³This is the imprint that such theory describes nonlinear electrodynamics.

$$\nabla_{\mu} (-L_X F^{\mu\nu} - L_Y {}^*F^{\mu\nu}) = 0, \tag{29}$$

where $L_X = \partial L / \partial X$ and $L_Y = \partial L / \partial Y$. This equation is supplemented by the Faraday equation, i. e., the electromagnetic field tensor cyclic identity (which remains unchanged)

$$\nabla_{\mu} F_{\nu\lambda} + \nabla_{\nu} F_{\lambda\mu} + \nabla_{\lambda} F_{\mu\nu} = 0. \tag{30}$$

In the case of a simple dependence on X , the equations of motion turn out to be Kunze (2008) (here we put $C = 0$ and $4\gamma = -(\Lambda^8)^{(\delta-1)/2}$ in the original Lagrangian given in Pagels & Tomboulis (1978))

$$L_{\delta} = -\frac{1}{4} \left(\frac{X^2}{\Lambda^8} \right)^{(\delta-1)/2} X, \tag{31}$$

where δ is an dimensionless parameter and $[\Lambda] = (\text{anenergyscale})$. The value $\delta = 1$ yields the standard Maxwell electrodynamics.

The energy-momentum tensor for this Lagrangian $L(X)$ can be computed by following the standard recipe, which then gives

$$T_{\mu\nu} = \frac{1}{4\pi} \left(L_X g^{ab} F_{\mu a} F_{\nu b} + g_{\mu\nu} L \right) \tag{32}$$

while its trace turns out to be

$$T = -\frac{1-\delta}{\pi} \left(\frac{X^2}{\Lambda^8} \right)^{(\delta-1)/2} X. \tag{33}$$

It can be shown Kunze (2008) that the positivity of the $T_0^0 \equiv \rho$ component implies that $\delta \geq 1/2$. The Lagrangian (31) has been studied by Kunze (2008) for explaining the amplification of the primordial magnetic field in the Universe, being the analysis focused on three different regimes: 1) $B^2 \gg E^2$, 2) $B^2 \simeq \mathcal{O}(E^2)$, 3) $E^2 \ll B^2$. It has also been used by Mosquera Cuesta & Lambiase (2009) to discuss both the origin of the baryon asymmetry in the universe and the origin of primordial magnetic fields. More recently it has also been discussed in the review on "Primordial magneto-genesis" by Kandus (2010).

Because the equation of motion (29) above, exhibits similar mathematical aspect as eq. (35) (reproduced in the Section), it appears clear that the Pagels and Tomboulis Lagrangian (31) leads also to an effective metric identical to that one given in equation (40), below.

3.4 Novello-Pérez Bergliaffa-Salim NLED

More recently, Novello et al. (2004) (NPS) revisited the several general properties of nonlinear electrodynamics by assuming that the action for the electromagnetic field is that of Maxwell with an extra term, namely⁴

$$S = \int \sqrt{-g} \left(-\frac{F}{4} + \frac{\gamma}{F} \right) d^4x, \tag{34}$$

where $F \equiv F_{\mu\nu} F^{\mu\nu}$.

⁴Notice that this Lagrangian is gauge invariant, and that hence charge conservation is guaranteed in this theory.

Physical motivations for bringing in this theory have been provided in Novello et al. (2004). Besides of those arguments, an equally unavoidable motivation comes from the introduction in the 1920's of both the Heisenberg-Euler and Born-Infeld nonlinear electrodynamics discussed above, which are valid in the regime of extremely high magnetic field strengths, i.e. near the Schwinger's limit. Both theories have been extensively investigated in the literature (see for instance Mosquera Cuesta & Salim (2004a;b); Mosquera Cuesta et al. (2006) and the long list of references therein). Since in nature non only such very strong magnetic fields exist, then it appears to be promising to investigate also those super weak field frontiers. From the conceptual point of view, this phenomenological action has the advantage that it involves only the electromagnetic field, and does not invoke entities that have not been observed (like scalar fields) and/or speculative ideas (like higher-dimensions and brane worlds).

At first, one notices that for high values of the field F , the dynamics resembles Maxwell's one except for small corrections associate to the parameter γ , while at low strengths of F it is the $1/F$ term that dominates. (Clearly, this term should dramatically affect, for instance, the photon- \vec{B} field interaction in intergalactic space, which is relevant to understand the solution to the Pioneer anomaly using NLED.). The consistency of this theory with observations, including the recovery of the well-stablished Coulomb law, was shown in Novello et al. (2004) using the cosmic microwave radiation bound, and also after discussing the anomaly in the dynamics of Pioneer 10 spacecraft Mbelek et al. (2007). Both analysis provide small enough values for the coupling constant γ Mosquera Cuesta (2010).

3.4.1 Photon dynamics in NPS NLED: Effective geometry

Next we investigate the effects of nonlinearities in the evolution of EM waves in the vacuum permeated by background \vec{B} -fields. An EM wave is described onwards as the surface of discontinuity of the EM field. Extremizing the Lagrangian $L(F)$, with $F(A_\mu)$, with respect to the potentials A_μ yields the following field equation Plebanski (1970)

$$\nabla_\nu(L_F F^{\mu\nu}) = 0, \quad (35)$$

where ∇_ν defines the covariant derivative. Besides this, we have the EM field cyclic identity

$$\nabla_\nu F^{*\mu\nu} = 0 \Leftrightarrow F_{\mu\nu|\alpha} + F_{\alpha\mu|\nu} + F_{\nu\alpha|\mu} = 0. \quad (36)$$

Taking the discontinuities of the field Eq.(35) one gets (all the definitions introduced here are given in Hadamard (1903))⁵

$$L_F f_\lambda{}^\mu k^\lambda + 2L_{FF} F^{\alpha\beta} f_{\alpha\beta} F^{\mu\lambda} k_\lambda = 0, \quad (37)$$

which together with the discontinuity of the Bianchi identity yields

$$f_{\alpha\beta} k_\gamma + f_{\gamma\alpha} k_\beta + f_{\beta\gamma} k_\alpha = 0. \quad (38)$$

A scalar relation can be obtained if we contract this equation with $k^\gamma F^{\alpha\beta}$, which yields

⁵Following Hadamard's method Hadamard (1903), the surface of discontinuity of the EM field is denoted by Σ . The field is continuous when crossing Σ , while its first derivative presents a finite discontinuity. These properties are specified as follows: $[F_{\mu\nu}]_\Sigma = 0$, $[F_{\mu\nu|\lambda}]_\Sigma = f_{\mu\nu} k_\lambda$, where the symbol $[F_{\mu\nu}]_\Sigma = \lim_{\delta \rightarrow 0^+} (J|_{\Sigma+\delta} - J|_{\Sigma-\delta})$ represents the discontinuity of the arbitrary function J through the surface Σ . The tensor $f_{\mu\nu}$ is called the discontinuity of the field, $k_\lambda = \partial_\lambda \Sigma$ is the propagation vector, and the symbols " $|$ " and " $||$ " stand for partial and covariant derivatives.

$$(F^{\alpha\beta} f_{\alpha\beta} g^{\mu\nu} + 2F^{\mu\lambda} f_{\lambda}{}^{\nu}) k_{\mu} k_{\nu} = 0. \tag{39}$$

It is straightforward to see that here we find two distinct solutions: a) when $F^{\alpha\beta} f_{\alpha\beta} = 0$, case in which such mode propagates along standard null geodesics, and b) when $F^{\alpha\beta} f_{\alpha\beta} = \chi$. In the case a) it is important to notice that in the absence of charge currents, this discontinuity describe the propagation of the wave front as determined by the field equation (35), above. Thence, following Lichnerowicz. (1962) the quantity $f^{\alpha\beta}$ can be decomposed in terms of the propagation vector k_{α} and a space-like vector a_{β} (orthogonal to k_{α}) that describes the wave polarization. Thus, only the light-ray having polarization and direction of propagation such that $F^{\alpha\beta} k_{\alpha} a_{\beta} = 0$ will follow geodesics in $g_{\mu\nu}$. Any other light-ray will propagate on the effective metric (40). Meanwhile, in this last case, we obtain from equations (37) and (39) the propagation equation for the field discontinuities being given by Novello et al. (2000)

$$\underbrace{\left(g^{\mu\nu} - 4 \frac{L_{FF}}{L_F} F^{\mu\alpha} F_{\alpha}{}^{\nu} \right)}_{\text{effective metric}} k_{\mu} k_{\nu} = 0. \tag{40}$$

This equation proves that photons propagate following a geodesic that is not that one on the background space-time, $g^{\mu\nu}$, but rather they follow the *effective metric* given by Eq.(40), which depends on the background field $F^{\mu\alpha}$, i. e., on the \vec{B} -field.

4. Understanding the Pioneer anomaly within NLED

4.1 Astrodynamics of Pioneer 10 and 11: Input facts

As pointed out above, since 1998 the JPL group have continuously reported an anomalous frequency shift derived from about ten years study of radio-metric data from Pioneer 10: 03/01/1987-22/07/1998 Anderson et al. (1998), Pioneer 11: 05/01/1987-01/10/1990 Anderson et al. (1995). The group has also found a similar feature in the data from of Ulysses and Galileo spacecrafts Anderson et al. (1998; 2002). The observed effect mimics a constant sunward acceleration acting on the spacecraft with magnitude

$$a_P = (8.74 \pm 1.33) \times 10^{-8} \text{ cm s}^{-2} \tag{41}$$

and a steady frequency (ν) drift

$$\frac{d\Delta\nu}{dt} \simeq 6 \times 10^{-9} \text{ Hz/s} \tag{42}$$

which equates to a "clock acceleration":

$$\frac{d\Delta\nu}{dt} = \frac{a_P}{c} \nu, \tag{43}$$

where c represents the speed of light in a vacuum, and t is the one way signal travel time. An independent analysis of the radio-metric Doppler tracking data from the Pioneer 10 spacecraft for the period 1987 - 1994 confirms the previous observations Markwardt (2002). In addition, by removing the spin-rate change contribution yields an apparent anomalous acceleration $a_P = (7.84 \pm 0.01) \times 10^{-8} \text{ cm s}^{-2}$, of the same amount for both Pioneer 10/11 Anderson et al. (2002); Abramovici & Vager (1986). Besides, it has been noted that the magnitude of a_P compares nicely to cH_0 , where H_0 is the Hubble parameter today.

As stressed above, unlike other spacecrafts like the Voyagers and Cassini which are three-axis stabilized (hence, not well-suited for a precise reconstitution of trajectory because of numerous attitude controls), the Pioneer 10/11, Ulysses and the by-now destroyed Galileo are attitude-stabilized by spinning about an axis (parallel to the axis of the high-gain antenna) which permits precise acceleration estimations to the level of $10^{-8} \text{ cm s}^{-2}$ (single measurement accuracy averaged over 5 days). Besides, because of the proximity of Ulysses and Galileo to the Sun, the data from both spacecrafts were strongly correlated to the solar radiation pressure unlike the data from the remote Pioneer 10/11. Let us point out that the motions of the four spacecrafts are modelled by general relativistic equations (see Anderson et al. (2002), section *IV*) including the perturbations from heavenly bodies as small as the large main-belt asteroids (the Sun, the Moon and the nine planets are treated as point masses). Nonetheless, the observed frequency shift remains unexplained Turyshev & Toth (2010). Thenceforth, several proposals for dedicated missions to test the Pioneer anomaly are now under consideration Pioneer Collaboration (2005), in virtue of the dramatic implications of the Pioneer puzzle for the understanding of gravity.

4.2 What has been done by other researchers

In search for a possible origin of the anomalous blueshift, a number of gravitational and non-gravitational potential causes have been ruled out by Anderson et al. (2002). According to the authors, none of these effects may explain a_P and some are 3 orders of magnitude or more too small. The addition of a Yukawa force to the Newtonian law does not work ease. An additional acceleration is predicted by taking into account the Solar quadrupole moment Mbelek & Michalski (2002). Although this entails a blueshift, it decreases like the inverse of the power four of the heliocentric radius, being of the order of a_P only below 2.1 AU. Meanwhile, the claim that the Modified Newtonian Dynamics (MOND) may explain a_P in the strongly Newtonian limit of MOND Quevedo (2005); Milgron (2001; 2002) is not obvious at all. First, the fits to the rotational curves of spiral galaxies yield for the MOND acceleration constant a_0 a value eight times smaller than cH_0 Quevedo (2005). Second, the gravitational pulling of the Sun up to 100 AU still yields an acceleration greater than a_0 by at least three orders of magnitude, equating a_0 only at about 3000 AU. Hence, Newtonian dynamics up to general relativity corrections should apply to the spacecrafts. Otherwise, one would be inclined to conclude that MOND is ruled out by a laboratory experiment Milgron (2001; 2002). Now, any true Doppler shift would involve an accompanying acceleration, which would be in conflict with both the motions of planets and long-period comets Anderson et al. (1995); Iorio (2006a;b;c).

Heretofore what we have learnt is that based on Einstein-Maxwell equations, the only other photon frequency shift that can be misinterpreted, at the solar system scale, with the Doppler shift is the gravitational frequency shift. In the weak field and low velocity limit, this would involve a time dependent gravitational potential instead of a spatial dependent one. Such proposals invoking the dark energy as the source of the time dependent gravitational potential have been suggested Iorio (2006a;b;c); Tangen (2006). However, quintessence, like other fundamental scalar fields, has not yet been observed.

In summary, prosaic explanations, non-gravitational forces and modified dynamics or new interaction (long or short range) force terms do not work Mbelek & Michalski (2002); Quevedo (2005); Milgron (2001; 2002); Rañada (2003; 2005). Gravitational origin of the anomaly is ruled out by the precision of the planetary ephemeris (see Anderson et al. (1998), Iorio (2006a;b;c),

and others Tangen (2006)) and the known bounds on dark matter within the orbital radius of Uranus or Neptune Rañada (2003; 2005); Whitmire & Matese (2003).

4.3 What we are proposing to tackle the Pioneer anomaly

By gathering together all the arguments reviewed above, one is led to the conclusion that the Pioneer anomaly does not seem to be related to the gravitational interaction Anderson et al. (1998); Iorio (2006a;b;c); Tangen (2006). If this is the case, what other of the currently known interactions in nature could afford a consistent understanding for the radio-metric Doppler tracking data from Pioneer spacecrafts?

The right answer could be related to the fact that there are only two long range interactions known today: Gravity and electromagnetism. Therefore, what remains is the EM sector.⁶ Meanwhile, the possibility of an interaction of the EM signal with the solar wind leading to a change of the frequency of the EM signal is now ruled out (see Anderson et al. (2002)).

Indeed, it appears to be unescapable to conclude that what we are observing (measuring through the receivers) could be related to the equation of motion of the photon. In other words, the mounting evidence seems to converge to what could be happening to the photon during its propagation through the interplanetary space from the Pioneer 10/11 antennas to the receivers on Earth.

It is timely, then, to recall that classical (Maxwell theory) or quantized (QED) linear electrodynamics does not allow for a change of the frequency of a photon during its propagation in a linear medium without invoking diffusion due to the interaction with the surrounding matter (hence a smear out of the image of the source). Moreover, for such a phenomenon to occur, one needs to consider a general and non trivial Lagrangian density $L = L(F)$ for which its second derivative w.r.t. F : $d^2L/dF^2 = L_{FF} \neq 0$. Therefore, the Pioneer anomaly, if not an artifact, may be a result of NLED as we show below. Indeed, relation (43) above translates, in covariant notation, into

$$\frac{dx^{\nu}}{dl} \nabla_{\nu} k^{\mu} = \frac{a_P}{c^2} k^{\mu}, \quad (44)$$

where l is some affine parameter along a ray defined by $k^{\mu} = \frac{dx^{\mu}}{dl}$ (see Fujii & Sasaki (2006)). The latter equation departs from the classical electrodynamics one (see Landau & Lifchiftz (1970), section 87)

$$\frac{dx^{\nu}}{dl} \nabla_{\nu} k^{\mu} = 0 \quad (45)$$

and suggests the occurrence of the NLED effect dubbed photon acceleration.

The concept of photon acceleration, which follows from the description of photon propagation in NLED, was discussed by Novello & Salim (2001), see also the book by Mendonça et al. (2006). Next we explain why the anomaly shows up in some situations and not others. (For experimental tests of NLED and further theoretical predictions see Mosquera Cuesta et al. (2006); Burke et al. (1997); Lundstrom et al. (2006); Lundin et al. (2006); Marklund & Shukla (2006)).

Therefore, the alternative that the Pioneer anomaly is not consequence of an actual change in the spacecraft velocity (see Anderson et al. (2002), Section X) deserves to be investigated. Indeed, a direct interpretation of the observational data from the spacecrafts implies merely an anomalous time-dependent blueshift of the photons of the communication signals. On the

⁶Non-metric fields can also be regarded as gravitational fields and there is a lot of space for speculation.

other hand, in using a time dependent potential Iorio (2006a;b;c); Tangen (2006) to explain the Pioneer 10/11 data one may be pointing out to the need of an *effective metric* for the photons. In fact, what is needed is just a time variation of the 4-momentum of the photon along its path. Thus the atomic energy levels would not be affected. Rather, only the motion of the photon being concerned.

4.4 NLED at all distance scales: From cosmology down to astrodynamics in the Solar System

Upon the collection of arguments presented above, it appears that all these requirements are achieved by considering that NLED is based on a Lagrangian density $L(F)$ which includes terms depending nonlinearly on the invariant $F = F_{\mu\nu} F^{\mu\nu}$, with $F = 2(B^2c^2 - E^2)$ Novello et al. (2000); Novello & Salim (2001); Plebanski (1970), instead of the usual Lagrangian density $L = -\frac{1}{4}F$ of classical electromagnetism in a vacuum. As stated above, we shall explore the effects of nonlinearities in the evolution of EM waves, which are envisioned onwards as the surface of discontinuity of the EM field. Therefore, as shown above, by extremizing the Lagrangian with respect to the potentials A_μ one obtains the EM field equation of motion Plebanski (1970)⁷

$$\nabla_\nu(L_F F^{\mu\nu}) = 0, \quad (46)$$

in which ∇_ν represents the covariant derivative, and $L_F = dL/dF$.

Recalling the discussion above, the dynamics of the photon propagation follows the equation

$$\left(g^{\mu\nu} - 4 \frac{L_{FF}}{L_F} F^{\mu\alpha} F_\alpha^\nu \right) k_\mu k_\nu = 0. \quad (47)$$

which exhibits the fundamental feature of NLED, i.e., the effective metric.

Then, by taking the derivative of the last expression, one arrives to

$$k^\nu \nabla_\nu k_\alpha = 4 \left(\frac{L_{FF}}{L_F} F^{\mu\beta} F_\beta^\nu k_\mu k_\nu \right)_{|\alpha}. \quad (48)$$

Eq.(48) shows that the nonlinear Lagrangian introduces a term acting as a force accelerating the photon. This acceleration of any photon which is traversing over weak background electromagnetic fields in a vacuum is the new physical element that we argue hereafter would be responsible for the Pioneer anomaly.

4.4.1 NLED photon acceleration: What Earth receivers are reading off radio signals from interplanetary spacecraft transponders - The case Pioneer anomaly

If NLED is to play a significant role at the macroscopic scale, this should occur at the intermediary scales of clusters of galaxies or the interclusters medium, wherein most observations show that the magnetic fields are almost uniform (and of the same order of magnitude⁸), unlike the dipolar magnetic fields of the Sun and planets. However, galaxies are gravitationally bound systems, whereas the cosmic expansion is acting at the cluster of galaxies scale. Thus, the magnetic field (\mathbf{B}) in clusters of galaxies (IGMF) depends on the cosmic time ($B = B_0 a^{-2}$). So, the \mathbf{B} that is relevant to this study is that of the local cluster

⁷Next we show that the "acceleration" of photons predicted by NLED may account for the anomalous blueshift indicated by the Pioneer 10/11, Ulysses and Galileo spacecrafts. This will manifest itself as a new frequency shift for the EM waves, in addition to the Doppler shift (special relativity) and the gravitational and cosmological redshift (general relativity), when both of them apply.

⁸Fujii & Sasaki (2006)

of galaxies Beck (2000). (As regard to the contribution of the CMB radiation see Riess et al. (2004)).⁹ Recently, Vallée (2002) has speculated that the 2 μ G magnetic field he has observed within the local supercluster of galaxies in cells of sizes of about 100 kpc may extend all the way down to the Sun. We explore further this idea in the framework of NLED and show that it is capable to provide an explanation of the Pioneer anomaly from first principles.

Relation (40) can be cast in the form

$$g_{\mu\nu}k^\mu k^\nu = 4 \frac{L_{FF}}{L_F} b^2, \tag{49}$$

where $b^\mu = F^{\mu\nu}k_\nu$ and $b^2 = b^\mu b_\mu$.

As $E = 0$, one can write, after averaging over the angular-dependence Bialynicka-Birula & Bialynicki-Birula (1970):

$$b^2 = -\frac{1}{2}||\vec{k}||^2 B^2 c^2 = -\frac{1}{4}||\vec{k}||^2 F \tag{50}$$

with $||\vec{k}|| = \omega/c = 2\pi\nu/c$. By inserting this relation in (49) yields

$$g_{\mu\nu}k^\mu k^\nu = -\frac{\omega^2}{c^2} F \frac{L_{FF}}{L_F}. \tag{51}$$

Taking the (x^α) derivative of Eq.(51) we obtain

$$2g_{\mu\nu}k^\mu (k^\nu)_{|\alpha} + k^\mu k^\nu (g_{\mu\nu})_{|\alpha} = -\left(\frac{\omega^2}{c^2} F \frac{L_{FF}}{L_F}\right)_{|\alpha}. \tag{52}$$

The cosmological expansion will be represented by $g_{\mu\nu} = a^2(\eta)g_{\mu\nu}^{(local)}$, with a the scale factor, η the conformal time, and $g_{\mu\nu}^{(local)}$ the local metric. So, Eq.(52) yields:

$$2g_{\mu\nu}k^\mu (k^\nu)_{|0} + 2\left(\frac{\dot{a}}{a}\right) g_{\mu\nu}k^\mu k^\nu = -\left(\frac{\omega^2}{c^2} F \frac{L_{FF}}{L_F}\right)_{|0}, \tag{53}$$

where the dot stands for partial derivative w.r.t. η . Using Eqs.(51) and (53) we obtain¹⁰

$$k_\mu (k^\mu)_{|0} = \left(\frac{\dot{a}}{a}\right) \frac{\omega^2}{c^2} F \frac{L_{FF}}{L_F} - \frac{1}{2} \left(\frac{\omega^2}{c^2} F \frac{L_{FF}}{L_F}\right)_{|0}. \tag{54}$$

Now, $\dot{F} = -4\left(\frac{\dot{a}}{a}\right) F$, by recalling that $B^2 \propto a^{-4}$. Moreover, from the method of the effective metric, it can be shown that k^0 does not vary with time in the first order approximation unlike $||\vec{k}||$.¹¹ Hence

⁹The interclusters magnetic field is in any case by far small (10^{-9} G) to add a measurable correction even to the cosmological redshift. As for the contribution of the cosmic microwave background (CMB), not only it is too weak but also, the CMB is pure radiation ($F = 0$), whereas we are interested in the case of a background magnetic field with no significant electric field counter-part, i.e., $E = 0$.

¹⁰By removing the NLED extra term from Eq.(49), this reduces it to $g_{\mu\nu}^{(local)}k^\mu k^\nu = 0$ so that the photons would just see the local background metric.

¹¹Given a background metric $g_{\mu\nu}$, as a result of NLED effects photons follow geodesic paths with respect to the effective metric (or any one conformal to it) $g_{\mu\nu}^{(eff)} = g_{\mu\nu} - 4\frac{L_{FF}}{L_F}F_\mu^\alpha F_{\alpha\nu}$ (see Novello et al. (2000),Novello & Salim (2001)). Thus, following the usual analysis on the gravitational frequency shift

$$k_\mu(k^\mu)|_0 = -\frac{\omega}{c} \left(\frac{\dot{\omega}}{c} \right). \quad (55)$$

By inserting relation (55) in (54), and then expanding and arranging, one finds

$$\left(\frac{\dot{\nu}}{\nu} \right) = - \left(\frac{\dot{a}}{a} \right) \frac{Q + 2FQ_F}{1 - Q}. \quad (56)$$

where we have set $Q = F \frac{L_{FF}}{L_F}$ and $Q_F = \partial Q / \partial F$.

At present cosmological time (t), and for a duration very short as compared to the universe age, Eq.(56) reduces to

$$\left(\frac{\dot{\nu}}{\nu} \right) \simeq -H_0 \frac{Q + 2FQ_F}{1 - Q} \quad (57)$$

where ($\dot{\nu}$ is the photon frequency t -derivative). $\dot{\nu} \neq 0$ if and only if a) the NLED contribution is non-null, i.e., $L_{FF} \neq 0$, and b) F depends on time.

4.4.2 NLED *alla* NPS as explanation of the Pioneer puzzle

The explicit form of this general nonlinear Lagrangian (which simulates the effect of dark energy in Novello et al. (2004)) reads

$$L = -\frac{1}{4}F + \frac{\gamma}{F}, \quad \text{or} \quad L = -\frac{1}{4}F + \frac{\gamma_n}{F^n}, \quad (58)$$

where n is a strictly positive integer. From Eqs.(56,58), the time variation of the photon frequency, due to interaction with very weak $\mathbf{B}(t)$ fields, reads

$$\left(\frac{\dot{\nu}}{\nu} \right) = A_n \gamma_n \frac{4n\gamma_n - (2n+1)F^{n+1}}{(F^{n+1} + 4n\gamma_n) [F^{n+1} + 4n(n+2)\gamma_n]}. \quad (59)$$

with $A_n = 4H_0 n(n+1)$. Notice that γ_n should be negative in order to guarantee that the Lagrangian is bound from below (see Landau & Lifchitz (1970), sections 27 and 93), $\gamma_n = -(B_n c)^{2(n+1)}$. Also, it is worth noticing that Eq.(59) in the nearly-zero field limit ($B \rightarrow 0$) would reduce to

$$\left(\frac{\dot{\nu}}{\nu} \right) = H_0 \left(\frac{n+1}{n+2} \right), \quad (60)$$

which implies a blueshift.

4.5 Discussion and conclusion

We stress that the NLED is a universal theory for the electromagnetic field, with $\gamma_{n=1} = \gamma$ in Eq.(58) being a universal constant. The value of γ was fixed in Novello et al. (2004) by using

but with $g_{\mu\nu}^{(eff)}$ replacing $g_{\mu\nu}$, one gets $k^0 c = \omega_0 / \sqrt{g_{00}^{(eff)}}$ (see Landau & Lifchitz (1970), section 88), where $\nu_0 = \omega_0 / 2\pi$ denotes the photon frequency in flat Minkowski spacetime. Thus, discarding the cosmological redshift (subsequent to the time dependence of the curvature), the variation of k^0 with time can be neglected in the first order approximation, since $F^{0\alpha} F_\alpha^0 = F_0^\alpha F_{\alpha 0} = 0$ in the case of a zero electric field.

the CMB constraint.¹² Indeed, in the standard model of cosmology the CMB is well described by Maxwell theory, which is likely to give a good account of the magnetic fields in galaxies too. Notwithstanding, the processes at the origin of both the seed magnetic field in the interclusters medium and clusters of galaxies are not yet clearly understood. Hence, if NLED is to play a significant role at the macroscopic scale, this should occur at the intermediary scales of clusters of galaxies or the interclusters medium.

Then, considering the possibility that the NLED correction terms described above come into play at these scales, one gets the following ordering of strengths: $B_{\text{Universe}} \ll B_{\text{Intercluster}} \ll B_1 \lesssim B_{\text{Cluster}} \lesssim B_{\text{Galaxy}}$. Turning back to the Pioneer anomaly, a good accordance is obtained with $B_{\text{LSC}} = 1.77 B_1$ (case $n = 1$) Riess et al. (2004). Thus, setting $B_1 = \frac{1}{c} |\gamma|^{1/4}$, one finds $B_1 = 0.008 \pm 0.002 \mu\text{G}$ Riess et al. (2004).¹³

Thence, to compute the effect (drift) on the Pioneer communication signal frequencies (uplink and downlink), we need only to introduce the value of the strength of the local supercluster **B**-field: $B_{\text{LSC}} \sim 10^{-8} - 10^{-7} \text{ G}$ Blasi & Olinto (1999). This involves $Q > 0$. But then, since relation (51) implies $Q < 1$, and the NLED theory must be such that $L_F < 0$ (hence, $F^{n+1} + 4n\gamma_n > 0$) for the energy density of the EM field to be positive definite [see Novello et al. (2000), appendix B], which entails $\mathbf{B} > B_1$, one can verify that the equation (59) implies a blueshift.

Meanwhile, the impressive accordance of the data from Voyager 1 and 2 magnetometers with Parker's theory (see Fig. 2) constraints B_{LSC} to be less than $0.022 \mu\text{G}$ within the solar system up to the heliopause. Hence, we may conclude that $0.01 \mu\text{G} < B_{\text{LSC}} < 0.022 \mu\text{G}$ within the solar system. By recalling that the uplink frequency of Pioneer 10 and 11 spacecrafts is $\nu = 2.2 \text{ GHz}$, one obtains for the median value $B_{\text{LSC}} = 0.018 \mu\text{G}$ (both expressions are normalized by $\left[\frac{H_0}{70 \text{ km s}^{-1} \text{ Mpc}^{-1}} \right]$). Then Eq.(60) renders

$$\left(\frac{\dot{\nu}}{\nu} \right) = 2.8 \times 10^{-18} \text{ s}^{-1}, \quad \text{or equivalently} \quad \frac{d\Delta\nu}{dt} = 6 \times 10^{-9} \frac{\text{Hz}}{\text{s}}, \quad (61)$$

with $\Delta\nu$ being the frequency drift pointed out earlier.

A digression on interplanetary magnetic field and NLED effects:

It has been pointed out that the strength of the IPMF could severely minimize the NLED effects because it will overrun the interstellar or intergalactic magnetic fields at heliocentric distances. Notwithstanding, the actual data from Voyager 1/2 spacecrafts of the IPMF average strength (see Fig. 2) are both consistent with a non-zero local supercluster magnetic field (LSCMF) amounting up to $0.022 \mu\text{G}$ NASA Voyager 1 (1978); NASA Voyager 2 (1978) (the accuracy of the measurements performed by Pioneer 10/11 magnetometers is at best $0.15 \mu\text{G}$, and

¹²Nonetheless, we stress that a conclusive method of fixing γ should benefit of a dedicated laboratory experiment, in the same spirit that it was done, for instance, to fix the electron charge through Millikan's experiment.

¹³ A clean estimate of B_1 from our definition of $\gamma_n \equiv -(B_{nc})^{2(n+1)}$, below Eq.(59), and the one in Novello et al. (2004): $\gamma \equiv -\hbar^2 \mu^8$. On account that $a_c = (1 + z_c)^{-1}$ and $\gamma = -\hbar^2 \mu^8 = -(B_1 c)^4$, Eq.(13) of Novello et al. (2004) rewrites $B_1^4 / \mu_0 B_0^2 = 1.40 \rho_c c^2$ (A1). Thus $a_c = (B_0^4 c^4 / 3 \hbar^2 \mu^8)^{1/8}$ yields $B_1 = 3^{-1/4} (1 + z_c)^2 B_0$ (A2). Then, combining both relations (A1) and (A2) one gets : $B_0 = 0.02 (1 + z_c)^{-4} \mu\text{G}$ (A3), $B_1 = 0.016 (1 + z_c)^{-2} \mu\text{G}$ (A4). Now, Riess et al. found evidence for a transition from cosmic deceleration to acceleration at redshift $z_c = 0.46 \pm 0.13$ [A. G. Riess et al., *ApJ* 607, 665 (2004)]. Inserting the latter figures in relations (A3) and (A4) yields : $B_0 = (0.005 \pm 0.002) \mu\text{G}$ (A5), $B_1 = (0.008 \pm 0.002) \mu\text{G}$ (A6). Since CMB is pure radiation (i. e., $E = Bc$ not equal to zero on average), we consider that relations (A4) and (A6) give a better estimate of B_1 than the one put forward in Novello et al. (2004).

0.022 μG for the low field system of Voyager 1/2 magnetometers Solar Wind (1980)). Besides, it is just beyond the Saturn orbit, ~ 10 Astronomical Units (AU), that the anomaly begins to be clearly observed. Surprisingly, it is just after passing the Saturn orbit that the strength of the interstellar and intergalactic magnetic fields, as one can verify by perusing on Fig. 2 (see Refs. NASA Voyager 1 (1978); NASA Voyager 2 (1978)). Thus, since a magnetic field cannot shield (or block) any another magnetic field (the stronger field can only reroute the weaker field, otherwise it would violate Maxwell's laws), then it follows that the LSCMF has its magnetic influence extended upto nearly the location of the Saturn orbit, and in this way it forces the photons being emitted by the Pioneer spacecrafts from larger heliocentric distances to get accelerated due to the NLED effects. Besides, notice that Mitra et al. (2003) also shows that the local cloud of interstellar gas in HII regions does not keep out the Galactic magnetic field.

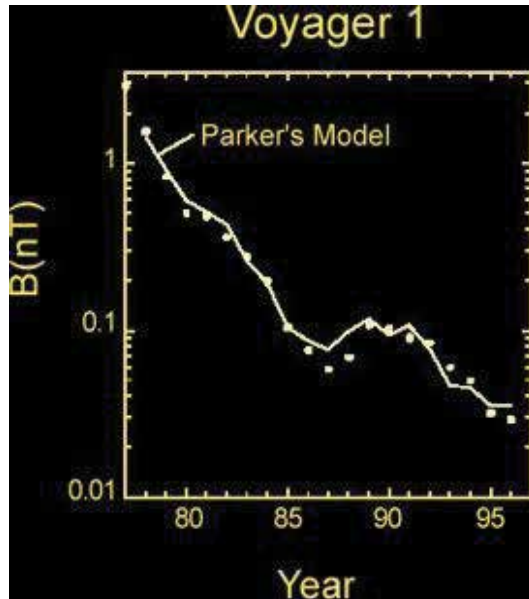
"En passant", we call to the reader's attention the fact that some workers in the field have claimed that the effect should have shown up already at the small distance corresponding to Mars, Jupiter or Saturn orbits, because of the high technology involved in the tracking of planet orbiting spacecrafts as Galileo and Cassini or the Mars' nonroving landers, which would allow to single out the anomaly at those heliocentric distances. However, as those spacecrafts are inside the region where the solar wind dominates, this definitely precludes the NLED photon acceleration effect to show up at those distances since the much higher magnetic field there would introduce a negligible NLED effect, and as stated below the solar pressure influence on the signal frequency is still large.

On the other hand, although one can use the time of flight of photons during tracking of planets with orbiting spacecrafts (by combining range and Doppler data over a spacecraft orbit) to tightly determine the range from Earth to that given planet's center of mass, the impediment to single out the radio-signal frequency shift remains the same pictured above: from one side the strength of both the host planet magnetic field and the solar magnetic field at those distances are still large, what blocks the nonlinear action of the LSCMF, and from the large up to 20 AU so as to allow the show up of the NLED frequency shift which is much smaller. Moreover, within a heliocentric distance ~ 100 AU the IPMF keeps stronger. Thus, it reduces for all practical purposes the IPMF contribution to the effects of NLED (see further arguments from our direct estimate of B_1 in Footnote 13 above, and in Riess et al. (2004)), leaving room for the sole contribution of the residual IGMF in the solar system.

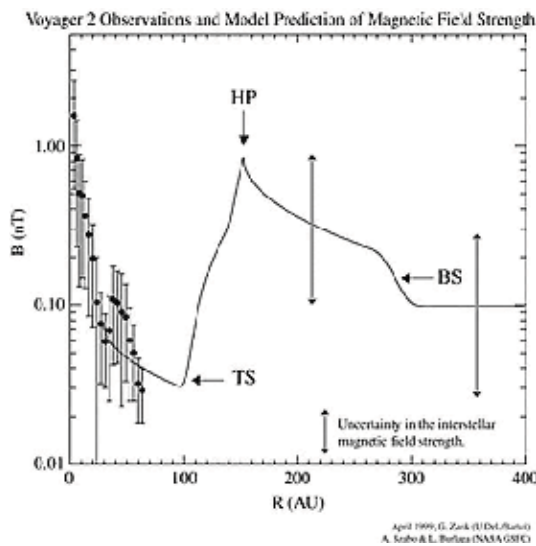
Finally, the new frequency shift that is predicted by NLED is not seen yet in the laboratory because of some of the following reasons: a) the most important, the strength of the Earth magnetic field is much larger than the one required in the NLED explanation of the anomaly for the effect to show up, and b) the coherence time $\tau = 1/\Delta\nu$ of EM waves in present atomic clocks (frequency width $\Delta\nu > 0.01$ Hz, or otherwise stated $c\tau < 0.2$ AU) is too short as compared to the time of flight of photons from Pioneer 10/11 spacecrafts past 20 AU. Nonetheless, if the conditions demanded by our model were satisfied this effect will certainly be disentangled in a dedicated experiment where, for instance, the Earth magnetic field is kept outside the case containing an experimental set up where a very weak magnetic field is maintained inside, a source of photons set to travel and a receiver data-collecting.

5. Acknowledgements

The author would like to sincerely thank Jean-Paul Mbelek (Service d'Astrophysique, C. E. Saclay, 91191 Gif-sur-Yvette Cedex, France), Mário Novello (Instituto de Cosmologia,



(a) Subfigure 1



(b) Subfigure 2

Fig. 2. Data from Voyager 1/2 spacecrafts of the interplanetary magnetic field (IPMF) average strength. Subfigure 1 presents measurements by Voyager 1 of the strength of the IPMF [nT] as a function of time [Yr]. The continuous line represents the predictions of Parker's model, and the dots the Voyager 1 data. Subfigure 2 shows the dependence with the distance [AU] of the IPMF [nT], as detected by Voyager 2, against the theoretical prediction. Credit: <http://spacephysics.ucr.edu/images/swq2-04.jpg>, and <http://interstellar.jpl.nasa.gov/interstellar/probe/interstellar/images/07BupstrmSuess-251g.gif>

Relatividade e Astrofísica (ICRA-BR), Centro Brasileiro de Pesquisas Físicas (CBPF)), and José Martins Salim (Instituto de Cosmologia, Relatividade e Astrofísica (ICRA-BR), Centro Brasileiro de Pesquisas Físicas (CBPF)) for the former collaboration in this direction of research. Also Prof. Remo Ruffini, Director General of the International Center for Relativistic Astrophysics Network (ICRANet), and the International Coordinating Centre, Pescara, Italy are thanked for the hospitality given during the final preparation of this work (September 2010).

6. References

- Abramovici, A. & Vager, Z. (1986). Phys. Rev. D 34, 3240
- Anderson, J. D., et al. (1995). Astrophys. J. 448, 885
- Anderson, J. D., et al. (1998). Phys. Rev. Lett. 81, 2858
- Anderson, J. D., et al. (2002). Phys. Rev. D 65, 082004
- Beck, R. (2001). Astrophys. Sp. Sc. Rev. 99, 243, in Proceedings of *The Astrophysics of Galactic Cosmic Rays Conference*, eds. R. Diehl et al., Kluwer, Dordrecht
- Bialynicka-Birula, Z. Bialynicki-Birula, I. (1970). Phys. Rev. D 2, 2341
- Blasi, P. & Olinto, A. V. (1999). Phys. Rev. D 59, 023001
- Burke, D. L., et al. (1997). Phys. Rev. Lett. 79, 1626
- Born, M. & Infeld, L. (1934). Proc. Roy. Soc. Lond. A 144, 425
- De Lorenci, V. A., Klippert, R., Novello, M. & Salim, M., (2002). Phys. Lett. B 482, 134
- Delphenich, D. H. (2003). Nonlinear electrodynamics and QED. arXiv: hep-th/0309108
- Delphenich, D. H. (2006). Nonlinear optical analogies in quantum electrodynamics. arXiv: hep-th/0610088
- Denisov, V. I., Denisova, I. P. & Svertilov, S. I. (2001a). Doklady Physics, Vol. 46, 705.
- Denisov, V. I., Denisova, I. P., Svertilov, S. I. (2001b). Dokl. Akad. Nauk Serv. Fiz. 380, 435
- Denisov, V. I., Svertilov, S. I. (2003). Astron. Astrophys. 399, L39
- Dittrich, W. & Gies, H. (1998). Phys Rev.D 58, 025004
- Dolag, K., Bartelmann, M. & Lesch, H. (1999). Astron. Astrophys. 348, 351
- Einstein, A.. (1936). Lens-Like Action of a Star by the Deviation of Light in the Gravitational Field. Science, New Series, Vol. 84, No. 2188, 506-507
- Einstein, A.. (1911). On The influence of gravitation on the propagation of light. Annalen Phys. 35, 898-908
- Einstein, A.. (1912). The Speed of Light and the Statics of the Gravitational Field. Annalen Phys. 38, 355-359
- Einstein, A.. (1912). On the Theory of the Static Gravitational Field. Annalen Phys.38, 443-458
- Fujii, Y. & Sasaki, M. (2006). report astro-ph/0608508
- The value of the magnetic field measured in the Galaxy is $B_{\text{Galaxy}} = 6 \pm 2 \times 10^{-6}$ G Beck (2000) and that of the local cluster of galaxies is $B_{\text{Cluster}} \sim 2 - 3 \times 10^{-6}$ G Beck (2000), and for extragalactic clusters as Abell 400, Hydra A measurements provide $B_{\text{EG-C}} \sim 3 - 20 \times 10^{-6}$ G Vogt & Ensslin (2003).
- Garcia, A.. & Plebanski, J. (1989). J. Math. Phys. 30, 2689
- Hadamard, J. (1903) Leçons sur la propagation des ondes et les equations de l'Hydrodynamique (Hermann, Paris, 1903)
- Following Hadamard Hadamard (1903), the surface of discontinuity of the EM field is denoted by Σ . The field is continuous when crossing Σ , while its first derivative presents a finite discontinuity. These properties are specified as follows: $[F_{\mu\nu}]_{\Sigma} = 0$,

$[F_{\mu\nu|\lambda}]_{\Sigma} = f_{\mu\nu}k_{\lambda}$, where the symbol $[F_{\mu\nu}]_{\Sigma} = \lim_{\delta \rightarrow 0^+} (J|_{\Sigma+\delta} - J|_{\Sigma-\delta})$ represents the discontinuity of the arbitrary function J through the surface Σ . The tensor $f_{\mu\nu}$ is called the discontinuity of the field, $k_{\lambda} = \partial_{\lambda}\Sigma$ is the propagation vector, and symbols " $|$ " and " $||$ " stand for partial and covariant derivatives.

Heisenberg, W. & Euler, H., (1936). *Zeit. Phys.* 98, 714

Iorio, L. (2006a). e-print gr-qc/0601055.

Iorio, L. (2006b). e-print gr-qc/0608068.

Iorio, L. (2006c). e-print gr-qc/0608101

Kandus, A., Kerstin, K. E. & Tsagas, C. (2010). Primordial magneto-genesis. arXiv: 1007.3891 [astro-ph.CO]

Kunze, K. E. (2008). *Phys. Rev. D* 77, 023530. arXiv:0710.2435 [astro-ph]

Landau, L. D. & Lifchitz, E. (1970). *Théorie des Champs*. (Editions MIR, Moscou)

Lichnerowicz, A., (1962). *Elements of Tensor Calculus*, (John Wiley and Sons, New York).
See also *Relativistic Hydrodynamics and Magnetohydrodynamics* (W. A. Benjamin, 1967), and *Magnetohydrodynamics: Waves and Shock Waves in Curved Space-Time* (Kluwer, Springer, 1994)

Lundstrom, E., et al. (2006). *Phys. Rev. Lett.* 96: 083602

Lundin, J., Brodin, G., & Marklund, M. (2006). *PHYSICS OF PLASMAS* 13: 102102. e-Print Archive: hep-ph/0606136; V. A. De Lorenci et al., *Phys. Lett. B* 482: 134-140 (2000);

Marklund, M. & Shukla, P. K. (2006). *Rev. Mod. Phys.* 78: 591-640

Markwardt, C. B. (2002). preprint gr-qc/0208046.

Mbelek, J. P. & Michalski, M. (2004). *Int. J. Mod. Phys. D* 13, 865

Mbelek, J. P. (2005). *Int. J. Mod. Phys. A* 20, 2304

Mbelek, J. P., Mosquera Cuesta, H. J., Novello, M. & Salim, J. M. (2007). Nonlinear electrodynamics and the Pioneer 10/11 spacecraft anomaly. *Europhys. Lett.* 77, 19001

Mendonça, J. T., (2000). *Theory of photon acceleration*. (Taylor & Francis 2000). Print ISBN: 978-0-7503-0711-6. eBook ISBN: 978-1-4200-3327-4 See also Mendonca et al. (2006). e-Print Archive: hep-ph/0607195

Milgrom, M. (2001). *Acta Phys. Polon. B* 32, 3613.

Milgrom, M. (2002). *New Astron. Rev.* 46, 741

Mitra, D., et al. (2003). *Astron. Astrophys.* 398, 993

Mosquera Cuesta, H. J., Salim, J. M., (2004). *Mon. Not. Roy. Astron. Soc.* 354, L55-L59

Mosquera Cuesta, H. J., Salim, J. M. (2004). *Astrophys. J.* 608, 925. e-print astro-ph/0307519 (2003).

Mosquera Cuesta, H. J., de Freitas Pacheco, J. A., & Salim, J. M. (2006). *Int. J. Mod. Phys. A* 21: 43-55

Mosquera Cuesta, H. J. & Lambiase, G. (2009). *Phys. Rev. D* 80:023013. e-Print: arXiv:0907.3678 [astro-ph.CO]

Mosquera Cuesta, H. J. (2010). *L'énergie sombre: Un mirage cosmique? Luminosity distance \neq proper distance: A cosmological dissimilitude induced by nonlinear electrodynamics*. *INVISIBLE UNIVERSE: Proceedings of the Conference*. AIP Conference Proceedings, Volume 1241, 1083-1092

Novello, M., De Lorenci, V. A., Salim, J. M., and Klippert, R. (2000). *Phys. Rev. D* 61, 045001

Novello, M., Salim, J. M., *Phys. Rev. D* 63, 083511 (2001)

Novello, M., Pérez Bergliaffa, S. E. & Salim, J. M. (2004). *Phys. Rev. D* 69, 127301

Pagels, H. & Tomboulis, E. (1978). *Nuc. Phys. B* 143, issue 3, 485

Pérez Martínez, A., Pérez Rojas, H., & Mosquera Cuesta, H. J. (2003). *Eur. Phys. Journ. C*, 29,

111

- Plebanski, J. (1970). Lectures on nonlinear electrodynamics. (Nordita, Copenhagen, 1970)
- Pioneer Explorer Collaboration. (2005). e-print gr-qc/0506139
- Quevedo, H. B. (2005). e-print gr-qc/0501006
- Rañada, A. F. (2003). Europhys. Lett. 63, 653
- Rañada, A. F. (2005). Found. Phys. 34, 1955
- Riess, A. G., etal. (2004). ApJ 607, 665
- Schwinger, J. (1951). Phys. Rev. 82, 664
- Solar Wind: Detection Methods and Long-term Fluctuations, at <http://herkules.oulu.fi/isbn9514271955/isbn9514271955.pdf>
- Stephani, H. (2004). Relativity. Cambridge University Press, Cambridge, UK, Third Edition, pp 44
- Tangen, K. (2006). Could the Pioneer anomaly have a gravitational origin? gr-qc/0602089:
- Tolman, R. C. (1934). Effect of Inhomogeneity on Cosmological Models. Proc. Nat. Ac. Sc. 20, 169. See also Tolman, R. C. & Ehrenfest, P. (1930). Temperature Equilibrium in a Static Gravitational Field. Phys. Rev. 36, 1791
- Turyshev, S. G. & Toth, V. T. (2010). Living Rev. Rel. 13, 4
- Vallée, J. P. (2002). Astronom. J., 124, 1322
- Vogt, C. & Ensslin, T. A.. (2003). Astron. Astrophys. 412, 373.
- Voyager 1 Observations and Parker's Model of Interplanetary Magnetic Field (IPMF) Strength, <http://spacephysics.ucr.edu/images/swq2-04.jpg>, <http://www.phy6.org/Education/wtermin.html>
- Voyager 2 Observations and Model Prediction of IPMF Strength, at <http://interstellar.jpl.nasa.gov/interstellar/probe/interstellar/images/07BupstrmSuess-251g.gif>
- Whitmire, D. P. & Matese, J. J. (2003). Icarus 165, 219

7. APPENDIX: The method of effective geometry

Following Hadamard (1903), the surface of discontinuity¹⁴ of the EM field is denoted by Σ . The field is continuous when crossing Σ , while its first derivative presents a finite discontinuity. These properties are specified as follows

$$\begin{aligned}
 [B^\mu]_\Sigma &= 0, \quad [\partial_\alpha B^\mu]_\Sigma = b^\mu k_\alpha, \quad [\partial_\alpha E^\mu]_\Sigma = e^\mu k_\alpha \\
 [F_{\mu\nu}]_\Sigma &= 0, \quad [F_{\mu\nu|\lambda}]_\Sigma = f_{\mu\nu} k_\lambda,
 \end{aligned}
 \tag{62}$$

where the symbol

$$[F_{\mu\nu}]_\Sigma \equiv \lim_{\delta \rightarrow 0^+} (J|_{\Sigma+\delta} - J|_{\Sigma-\delta})
 \tag{63}$$

represents the discontinuity of the arbitrary function J through the surface Σ . The tensor $f_{\mu\nu}$ is called the discontinuity of the field, and $k_\lambda = \partial_\lambda \Sigma$ is the propagation vector. In Eq. (62), the symbol “|” stands for partial derivative;

¹⁴Of course, the entire discussion onwards could alternatively be rephrased in terms of concepts more familiar to the astronomy community as that of light rays used for describing the propagation of electromagnetic waves in the geometric optics approximation.

Here-after we want to investigate the effects of nonlinearities of very strong magnetic fields in the evolution of electromagnetic waves described onwards as the surface of discontinuity of the electromagnetic field (represented here-to-fore by $F_{\mu\nu}$). For this reason we will restrict our analysis to the simple class of gauge invariant Lagrangians defined by $L = L(F)$. From the least action principle we obtain the following field equation

$$(L_F F^{\mu\nu})_{||\mu} = 0. \tag{64}$$

Applying the Hadamard conditions (62) and (63) to the discontinuity of the field in Eq.(64) we obtain

$$L_F f^{\mu\nu} k_\nu + 2L_{FF} \zeta F^{\mu\nu} k_\nu = 0, \tag{65}$$

where ζ is defined by $\zeta \doteq F^{\alpha\delta} f_{\alpha\delta}$. Both, the discontinuity conditions and the electromagnetic field tensor cyclic identity lead to the following dynamical relation

$$f_{\mu\nu} k_\lambda + f_{\nu\lambda} k_\mu + f_{\lambda\mu} k_\nu = 0. \tag{66}$$

In the particular case of a polarization such that $\zeta = 0$, it follows from Eq.(64) that $f^{\mu\nu} k_\nu = 0$. Thus using this result, and multiplying Eq.(66) by k^λ we obtain

$$f_{\mu\nu} k^\mu k^\nu = 0. \tag{67}$$

This equation states that for this particular polarization the discontinuity propagates with the metric $f_{\mu\nu}$ of the background space-time. For the general case, when $\zeta \neq 0$, we multiply Eq.(66) by $k_\alpha g^{\alpha\lambda} F^{\mu\nu}$ to obtain

$$\zeta k_\nu k_\mu g^{\mu\nu} + 2F^{\mu\nu} f_\nu^\lambda k_\lambda k_\mu = 0. \tag{68}$$

From this relation and Eq.(65) we obtain the propagation law for the field discontinuities, in this case given as

$$(L_F g^{\mu\nu} - 4L_{FF} F_\alpha^\mu F^{\alpha\nu}) k_\mu k_\nu = 0, \tag{69}$$

where $F_\alpha^\mu F^{\alpha\nu} = -B^2 h^{\mu\nu} - B^\mu B^\nu$. Eq.(69) allows to interpret the term inside the parenthesis multiplying $k^\mu k^\nu$ as an effective geometry

$$g_{\text{eff}}^{\mu\nu} = L_F g^{\mu\nu} - 4L_{FF} F_\alpha^\mu F^{\alpha\nu}. \tag{70}$$

Hence, one concludes that the discontinuities will follow geodesics in this effective metric.

8. APPENDIX-1: NPS theory applied to cosmology

To discuss the evolution of a universe model driven by the NPS NLED, the electromagnetic (EM) field described by Eq.(34) can be taken as source in Einstein equations to obtain a toy model for the evolution of the universe which displays accelerate expansion. Such phase of acceleration runs into action when the nonlinear EM term takes over the term describing other matter fields. This NLED theory yields ordinary radiation plus a dark energy component with $w < -1$ (phantom-like dynamics). Introducing the notation¹⁵, the EM field can act as

¹⁵Due to the isotropy of the spatial sections of the Friedman-Robertson-Walker (FRW) model, an average procedure is needed if electromagnetic fields are to act as a source of gravity Tolman (1934).

a source for the FRW model if $\langle E_i \rangle|_V = 0$, $\langle B_i \rangle|_V = 0$, $\langle E_i B_j \rangle|_V = 0$, $\langle E_i E_j \rangle|_V = -\frac{1}{3} E^2 g_{ij}$, and $\langle B_i B_j \rangle|_V = -\frac{1}{3} B^2 g_{ij}$.¹⁶ When these conditions are fulfilled, a general nonlinear Lagrangian $L(F)$ yields the energy-momentum tensor ($L_F = dL/dF$, $L_{FF} = d^2L/dF^2$)¹⁷

$$\langle T_{\mu\nu} \rangle|_V = (\rho + p)v_\mu v_\nu - p g_{\mu\nu}, \quad (71)$$

$$\rho = -L - 4E^2 L_F, \quad p = L + \frac{4}{3}(E^2 - 2B^2)L_F,$$

Hence, when there is only a magnetic field, the fluid can be thought of as composed of a collection of non-interacting fluids indexed by k , each of which obeys the equation of state $p_k = \left(\frac{4k}{3} - 1\right)\rho_k$, composed of ordinary radiation with $p_1 = \frac{1}{3}\rho_1$ and of another fluid with equation of state $p_2 = -\frac{7}{3}\rho_2$. It is precisely this component with negative pressure that may drive accelerate expansion through Friedmann equations, as was shown in Novello et al. (2004).

Thus a volumetric spatial average of a quantity X at the time t by $\langle X \rangle|_V \equiv \lim_{V \rightarrow V_0} \frac{1}{V} \int X \sqrt{-g} d^3x$, where $V = \int \sqrt{-g} d^3x$, and V_0 is a sufficiently large time-dependent three-volume. (Here the metric sign convention (+ - - -) applies).

¹⁶Let us remark that since we are assuming that $\langle B_i \rangle|_V = 0$, the background magnetic fields induce no directional effects in the sky, in accordance with the symmetries of the standard cosmological model.

¹⁷Under the same assumptions, the EM field associate to Maxwell Lagrangian generates the stress-energy tensor defined by Eq.(71) but now $\rho = 3p = \frac{1}{2}(E^2 + B^2)$.

Detection and Estimation of Satellite Attitude Jitter Using Remote Sensing Imagery

Akira Iwasaki
The University of Tokyo
Japan

1. Introduction

Most satellite remote-sensing images are obtained using pushbroom or whiskbroom scans by the coupling of line scans in one dimension and satellite movements in another dimension. Since satellite imagery should be consistent with maps when used as geospatial data, good geometric performance is a challenge for satellite data processing (Lee et al., 2004; Storey et al., 2004). Accurate attitude estimation is essential for this purpose because satellites suffer from mechanical vibration, originating from solar paddles, wheels and high-gain antennas, during line scans. In most satellites, attitude is estimated by interpolating measurement data obtained from star sensors and gyros, which are sampled at low frequency. When the sampling rate of attitude information is low compared with the frequency of attitude, images processed by geometric correction suffer from distortion. Therefore, additional information is necessary to estimate attitude accurately. One solution is to estimate the correct attitude of spacecraft using ground control points (GCPs), which requires the preparation of GCPs in the target scene and depends on their accuracy (Shin et al., 1997). Landsat adopts angular displacement sensor (ADS) to detect and compensate high-frequency jitter (Barker & Seiferth, 1996). Another possible solution is to add an image sensor on the focal plane, which tracks the displacement of ground targets (Janschek et al., 2005). A sensor system with parallax observation enables the detection of the effect of pointing fluctuation, which can be rapidly measured by attitude sensors, such as star sensors and gyros, without additional high-performance sensors. A software methodology based on image processing and optimization techniques to accurately estimate the attitude information of spacecraft under operation is important for obtaining geometrically accurate images (Iwasaki & Fujisada, 2003; Bayard, 2004; Liu & Morgan, 2006; Teshima & Iwasaki, 2008). When optical sensors on satellites suffer from pointing fluctuation, images obtained at two different times cannot be co-registered by a parallel shift. Figure 1 shows the displacement between two remote-sensing images before and after the large earthquake in Pakistan on October 8, 2005, with a magnitude of 7.6 clarified by normalized cross-correlation and the difference in digital elevation models (DEMs). Wavy patterns are observed in Figs. 1(b), (c) and (d), which correspond to horizontal displacements in the cross- and along-track directions and vertical displacement, respectively. Owing to this artifact, the fault running from upper left to lower right is difficult to trace.

Assuming that the displacement occurred only around the fault zone, the wavy patterns are destriped in Figs. 1 (e), (f) and (g), which correspond to horizontal displacements in the cross and along track directions and vertical displacement, respectively. The displacement

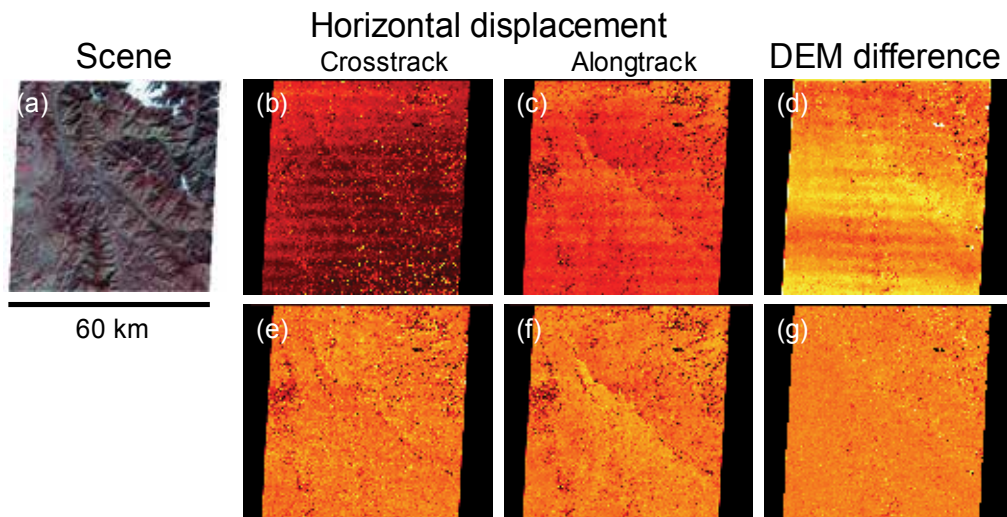


Fig. 1. Optical sensor image and displacement analysis. (a) Scene of Pakistan, displacements in (b) cross- and (c) along-track directions, (d) difference in DEMs. Displacements after satellite attitude correction in (e) cross- and (f) along-track directions, (g) difference in DEMs.

around the fault zone that runs from upper left to lower right is clearly observed, which was caused by the earthquake (Avouac et al., 2006). The upper-right portion moved toward the lower-left direction relative to the lower-left portion. Using the subpixel measurement technique, although the ground sampling distance (GSD) is 15 m, it was found that the fault offset was 4 m on average and 7 m at maximum. The analysis of ground deformation can be achieved as soon as a post-earthquake image is obtained. Note that since the fault runs in a diagonal direction, the displacement is recovered (Koga & Iwasaki, 2008, 2011). Furthermore, this type of analysis is also useful for investigating glacier flow, debris flow and sand dune migration. However, what should be done when the fault runs in the cross-track direction, that is, the same direction as the attitude jitter?

This article introduces a methodology for detecting the sign of pointing jitter using the geometric consistency of line of sight (LOS) vectors. Although our investigation starts from the analysis of large platform satellites, small satellites that do not have good pointing stability are a target of our research, for which satellite mission instruments can help bus instruments to achieve a better geometric performance. The Landsat 7 Science Data Users Handbook states that geometrically corrected products should have multispectral bands registered to 0.17 pixels (1 sigma for 30 m GSD) and that geometrically corrected images from multiple dates should be capable of being registered to an accuracy of 7.3 m (1 sigma) to meet the requirements of Landsat 7 (NASA Goddard Space Flight Center, 1998). Our methodology using a sensor system with parallax observation makes it possible to satisfy these two criteria simultaneously.

2. Sensor configuration

2.1 Layout of sensor with parallax observation

Figure 2 shows the concept of the sensor with parallax observation, which observes the specified ground target from slightly different angles, which means that time differences

exist between the observation time of each line scan. Although the parallax effect due to the terrain error in the along-track direction must be considered, many optical sensor systems on-board satellites adopt this configuration, such as QuickBird, FORMOSAT-2 and so forth (Jacobsen, 2006; Liu, 2006). Since the line sensors are arranged on the focal plane, simple optical systems using band-pass filters are realized without a prism spectrometer, which are suitable for compact optics of recent high-resolution satellite sensors.

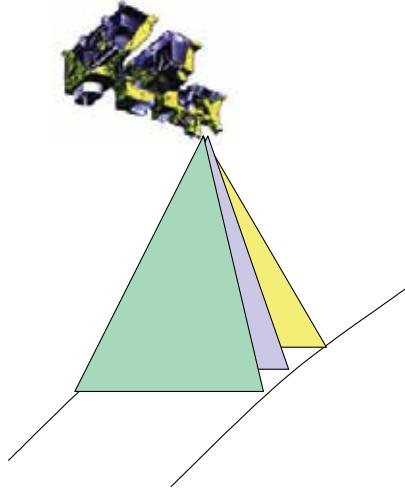


Fig. 2. Sensor system with parallax observation.

Owing to the time difference in the observation time of the specified ground target, band-to-band registration is affected by satellite attitude. In this chapter, using the Advanced Spaceborne Thermal Emission and Reflection Radiometer (ASTER) as an example, we discuss the detection and estimation of the attitude fluctuation of satellites utilizing the disadvantage of the sensor configuration to obtain satellite-based images with improved geometric performance.

2.2 ASTER sensor

The ASTER sensor is a multispectral imager on-board the Terra (EOS-AM1) spacecraft, which was launched in December 1999 (Neeck et al., 1994; Kudva & Throckmorton, 1996). The Terra spacecraft is in a sun-synchronous orbit at an altitude of 705 km with a local equatorial crossing time of 10:30. The repeat cycle is 16 days and the distance between neighboring orbits is 172 km, i.e., a similar orbit to Landsat 7 except for the local equatorial crossing time. The ASTER sensor is composed of three subsystems: visible and near infrared (VNIR), shortwave infrared (SWIR) and thermal infrared (TIR) radiometers. Table 1 shows the spectral passband of each subsystem. The VNIR subsystem has two telescopes, one at the nadir and the other with backward viewing, to construct a DEM. The VNIR subsystem is free from parallax error because a dichroic filter divides incident light into each VNIR band. Since the ASTER sensor is a complex system consisting of three subsystems with four telescopes, a Level-1 data processing system based on the configuration of the ASTER sensor has been constructed and validated (Fujisada, 1998; Iwasaki & Fujisada, 2005). The SWIR radiometer is a sensor with six narrow bands in the shortwave infrared region (1.6-2.43 μm) for discriminating rock and minerals using the specific absorption signatures.

Sub system	Band No.	Spectral range (μm)	Ground Sampling Distance
VNIR	1	0.52 - 0.60	15 m
	2	0.63 - 0.69	
	3N	0.76 - 0.86	
	3B	0.76 - 0.86	
SWIR	4	1.600 - 1.700	30 m
	5	2.145 - 2.185	
	6	2.185 - 2.225	
	7	2.235 - 2.285	
	8	2.295 - 2.365	
	9	2.360 - 2.430	
TIR	10	8.125 - 8.475	90 m
	11	8.475 - 8.825	
	12	8.925 - 9.275	
	13	10.25 - 10.95	
	14	10.95 - 11.65	

Table 1. ASTER pass band.

The SWIR images are obtained by means of a pushbroom system consisting of 2048 PtSi-CCD linear-array detectors with a pixel size of $16.5 \mu\text{m}$ that operate at liquid nitrogen temperature, which must be cooled mechanically. Therefore, the array detectors are arranged in parallel on the focal plane, as shown in Fig. 3(a). Since the distance between neighboring bands is 1.33 mm , each line scans the same ground target with a time difference of about 356.238 ms (nominal) from the nominal altitude, as shown in Fig. 3(b). The registration performance between bands deteriorates when pointing fluctuation occurs during the time lag between the observations.

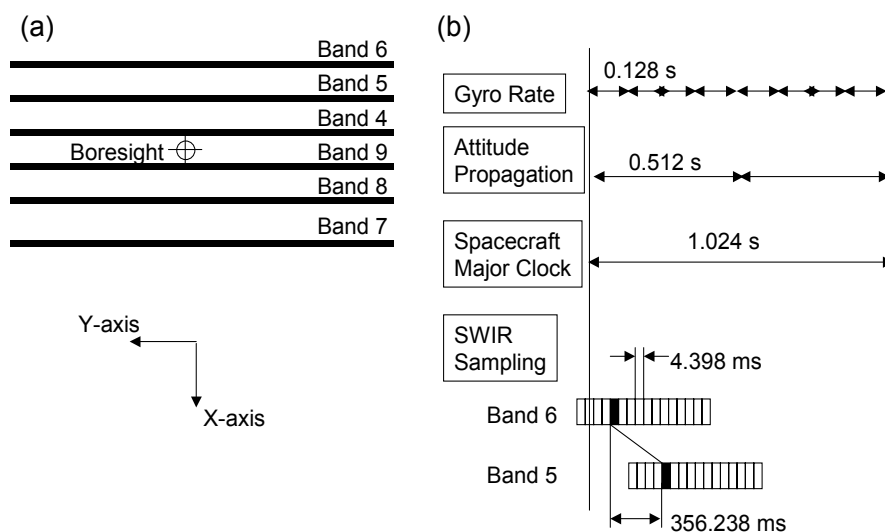


Fig. 3. ASTER sensor design. (a) Configuration of SWIR sensor and (b) timetable of attitude and image data sampling.

The Terra spacecraft provides attitude data with a resolution of 1 arcsecond and attitude rate data with a resolution of 0.5 arcseconds/s every 1.024 s, which is the major clock on which spacecraft information is based. Images are corrected geometrically using attitude and navigation data, which are interpolated using third-order polynomials. Therefore, we cannot accommodate the attitude data with high accuracy when fluctuation occurs at a higher frequency. The angular error of 1 arcsecond corresponds to about 3.4 m on the ground for the Terra spacecraft. Since the GSD of the SWIR radiometer is 30 m, the angular error of 1 arcsecond leads to a registration error between bands of 0.1 pixels or less. The sampling interval of each line of the SWIR sensor is 4.398 ms to obtain the GSD of 30 m, and the time resolution is considerably higher than that of the spacecraft attitude data. Using the registration error between bands of the SWIR images, attitude information can be corrected with a higher sampling rate of up to 220 Hz.

3. Detection and correction of satellite attitude jitter

3.1 Formulation of jitter detection by sensor with parallax observation

To reduce the registration error between bands and the internal distortion in images, the true attitude information should be estimated from the relative registration error obtained from the analysis of two images obtained with a time difference. Figure 4 shows the sequence of the image acquisition process with a time lag. Using the deviation from the correct attitude of the master data $f(t)$ at time t , the relative registration error $g(t)$ of the slave data with the deviation from the correct attitude with time lag τ , $f(t+\tau)$, is expressed as follows.

$$g(t) = f(t + \tau) - f(t) \tag{1}$$

The relative registration error is obtained from the analysis of one scene in the range $0 \leq t \leq t_e$ s. When the deviation from the correct attitude during the observation time lag, that is, $f(t; 0 \leq t \leq \tau)$, is estimated, the satellite attitude data are obtained from the relative registration error using Eq. (1). However, since there are many $f(t)$ that satisfy the above relationship, another constraint should be introduced.

Since the attitude is interpolated using third-order polynomials in Level-1 data processing, we can assume that the deviation from the correct attitude is also smooth. On the basis of this idea, the deviation from the correct attitude during the observation time lag should be obtained that minimizes the following evaluation function.

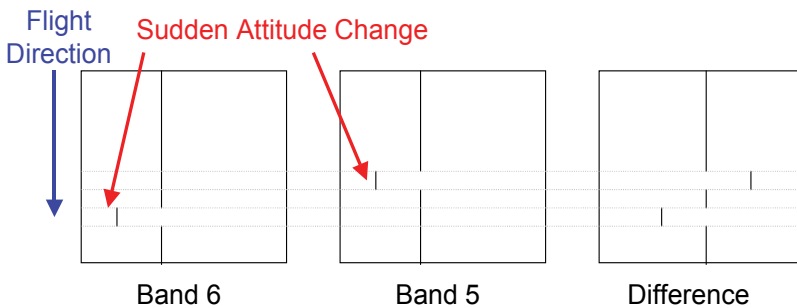


Fig. 4. Sequence of image acquisition for small parallax sensor.

$$J(f(t)) = \int \{f(t+\tau) - f(t) - g(t)\}^2 dt + \alpha \int \{f(t+\Delta t) - f(t)\}^2 dt \quad (2)$$

Here, Δt denotes the line sampling time of a line sensor. The first term on the right side corresponds to Eq. (1) and the second term is related to the smoothness using a regularization coefficient α .

The Fourier transform of Eq. (1) leads to the following equation.

$$F(\omega) = \frac{G(\omega)}{\exp(j\omega\tau) - 1} \quad (3)$$

The denominator on the right side becomes zero when $\omega\tau$ is an integer, which corresponds to the situation that the frequency is an integer multiple of the reciprocal of the time lag. This means that the satellite attitude jitter with this frequency cannot be identified because the clockwise motion of a line sensor and the anticlockwise motion of another line sensor cannot be distinguished.

3.2 Similarity measures to obtain displacement

Two similarity measures are used for the block matching of two images in this work. Zero-mean normalized cross-correlation (NCC) is widely used as the criterion of the registration error between images (Iwasaki & Fujisada, 2003 & 2005; Liu, 2006). The covariance $C(m, n)$ obtained using Eq. (4) has a maximum value when two images match each other.

$$C(m, n) = \frac{\sum_j \sum_i^{L_y L_x} \{M(i, j) - \bar{M}\} \times \{S(i-m, j-n) - \bar{S}\}}{\left[\sum_j \sum_i^{L_y L_x} \{M(i, j) - \bar{M}\}^2 \times \sum_j \sum_i^{L_y L_x} \{S(i-m, j-n) - \bar{S}\}^2 \right]^{\frac{1}{2}}} \quad (4)$$

Here, $M(i, j)$ and $S(i, j)$, respectively, denote the pixel values of the master and slave images for the pixel coordinates (i, j) . L_x and L_y denote the sizes of the correlation window in the cross-track and along-track directions, respectively. \bar{M} and \bar{S} denote the average pixel values within the correlation window in the master and slave images, respectively. The registration error is obtained by the following steps. The integer set with the maximum value of correlation is first selected as the candidate for displacement between two images. Next, the point with the highest correlation is obtained at a subpixel level by parabola fitting to the neighboring correlation values and determining the vertex value.

Phase correlation (PC) is also used as a similarity measure (Hoge, 2003; Leprince et al., 2007; Morgan et al., 2010). Consider two $N_1 \times N_2$ images $s(n_1, n_2)$ and $s'(n_1, n_2) = s(n_1 - \delta_1, n_2 - \delta_2)$ that differ by the displacement (δ_1, δ_2) . The cross-phase spectrum is expressed by Eq. (1) using the shift theorem.

$$R(\omega_1, \omega_2) = \frac{S(\omega_1, \omega_2) S'^*(\omega_1, \omega_2)}{|S(\omega_1, \omega_2) S'^*(\omega_1, \omega_2)|} = \exp \left\{ -2\pi j \left(\frac{\omega_1}{N_1} \delta_1 + \frac{\omega_2}{N_2} \delta_2 \right) \right\} \quad (5)$$

The phase correlation function $r(n_1, n_2)$ is defined as the inverse discrete Fourier transform of $R(\omega_1, \omega_2)$.

$$r(n_1, n_2) = \frac{\sin \pi(n_1 + \delta_1)}{\pi(n_1 + \delta_1)} \frac{\sin \pi(n_2 + \delta_2)}{\pi(n_2 + \delta_2)} \tag{6}$$

The peak position of the phase correlation function corresponds to the misregistration between two images. To reduce the image boundary effect in the frequency domain, a two-dimensional Hanning window is applied to the input image. A low-pass filter is also applied in the frequency domain to eliminate the high-frequency components of each image. The subpixel displacement between the images is obtained by sinc function fitting to the neighboring correlation values (Nagashima et al., 2006). Although the size of the correlation window must be larger than that of NCC, the peak of PC is much steeper than that of NCC, and thus the accuracy of PC surpasses that of NCC and reaches 1/50 pixels (Leprince et al., 2007). Therefore, we use NCC to obtain a flexible-size correlation window and PC for accurate displacement measurement in this chapter.

3.3 Using map-projected data product

Figure 5(a) shows the nadir-looking SWIR image of the Level-1B data products analyzed in this study, which was acquired on June 07, 2002, above Tokyo. Level-1B data products are map-projected images, which are projected using radiometric calibration and geometric correction coefficients for resampling that are oriented to the satellite path but not orthorectified. Thus, the line of Level-1B data products in the horizontal direction is almost equal to the scan line. The acquisition duration of one scene is about 9 s, which corresponds to 2100 lines of data. We used band 5 and band 6 images because they are placed at neighboring positions on the focal plane and because their spectral characteristics are sufficiently similar to be suitable for correlation. Furthermore, band 6 represents the SWIR subsystem and the geometric calibration relative to VNIR is performed intensively.

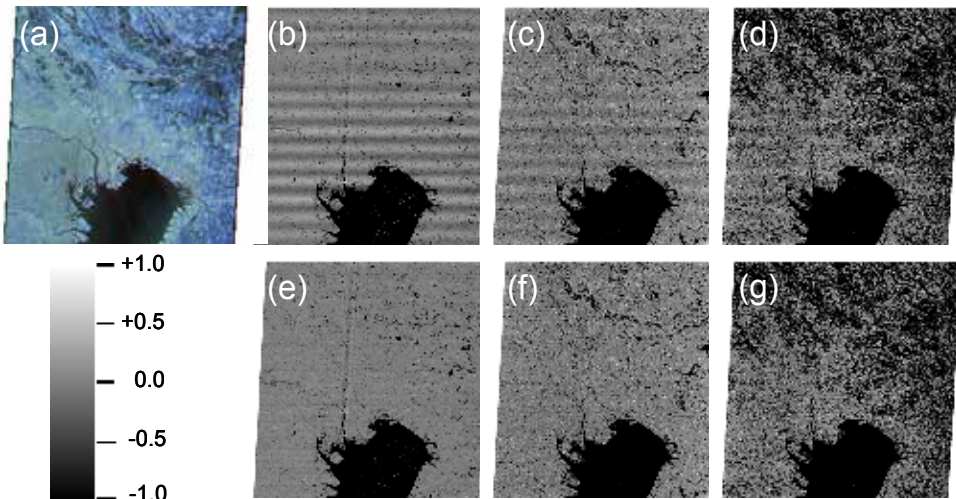


Fig. 5. (a) ASTER/SWIR scene on 06/07/2002, Tokyo, Japan. Relative registration error maps of band 5 before correction in the cross-track direction relative to (b) band 6 and (c) band 5 on 06/04/2001 and (d) Landsat 7/ETM+ band 7 on 03/29/2000. Relative registration error maps after correction relative to (e) band 6 and (f) band 5 on 06/04/2001 and (g) Landsat 7/ETM+ band 7 on 03/29/2000.

Figure 5(b) shows the registration error map of band 5 relative to band 6 in the cross-track direction. The relative registration error is plotted on the center pixel of the correlation window, the size of which is set to 7 (cross-track) by 7 (along-track), which is used only to evaluate the registration error in this scene. A bright pixel denotes that the band 5 pixel deviates to the right in the image. A black pixel denotes a point at which good correlation is not obtained, such as a pixel representing water. It can be seen that a periodic displacement pattern occurs in the error map. The relative registration error between bands is due to the time dependence of jitter on the line of sight, which is attributable to attitude variation. This means that an absolute registration error of the acquired image relative to the actual geographical position exists. The frequency and amplitude of the jitter are about 1.5 Hz and 0.2-0.3 pixels, which corresponds to 6-9 m on the ground, respectively. This jitter corresponds to the roll fluctuation of the Terra spacecraft. Since the attitude sensors of the Terra spacecraft cannot follow the vibration at this frequency, the relative deviation between bands still remains.

Comparisons with the images obtained by ASTER on a different day (Fig. 5(c)) and by Landsat 7/ETM+ (Fig. 5 (d)), which are free from pointing jitter, show a similar performance for each image. Since the master images are not disturbed by the pointing fluctuation, the jitter corresponds to the absolute pointing fluctuation of the slave image. Note that the Landsat 7/ETM+ image (2.08 μm - 2.35 μm) on 06/07/2002 is affected by some jitters, which might be related to a malfunction in the scanning mirror (Lee et al., 2004).

The time course of the relative deviation between bands in the cross-track direction is calculated for jitter analysis using a window size of 501 (cross-track) by 1 (along-track), and is averaged in the cross-track direction of a path-oriented image, which is an effective and robust method for detecting the jitter with high time resolution. Areas of water are eliminated owing to their low standard deviation of digital numbers in the window. The relative registration error is averaged in the cross-track direction with a 3σ limits. The solution of Eq. (2) is obtained by the following method. Considering that the relative registration is obtained with high accuracy, the first term on the right side in Eq. (2) is set to zero and the optimum solution that minimizes the second term is obtained, which expresses the smoothness of the deviation from the true amplitude.

$$J(\tau, f(t: -\tau \leq t \leq 0)) = \alpha \int \{f(t + \Delta t) - f(t)\}^2 dt \quad (7)$$

When the smoothest solution $f(t; -\tau \leq t \leq 0)$ that minimizes the evaluation function is obtained, $f(t; 0 \leq t \leq 9)$ is calculated using Eq. (2). We used the downhill simplex method to find the $f(t; -\tau \leq t \leq 0)$ that minimizes the evaluation function.

The relative registration error has not only an alternating current (AC) component but also a direct current (DC) component, which means that the moving average of the relative registration error in the cross-track direction is not zero but has an offset of about 0.008 pixels. This offset originates from the relative error in the LOS vector between bands. Thus, we should subtract the offset from the relative registration error. Otherwise, monotonically increasing behavior is observed.

Since τ varies with changes in the spacecraft altitude, a representative value of a scene is determined so as to minimize the relative registration error between the corrected images. The estimated pointing fluctuation that minimizes the evaluation function J is obtained, provided that the time lag τ is 80.9 lines, which is close to the nominal value of 81 lines. The deviation from the correct attitude $f(t)$ is estimated simultaneously using the relative

registration error of band 5 relative to band 6. Images are rearranged by bilinear interpolation in the cross-track direction on the basis of the corrected attitude data. Figure 5(e) shows the registration error map of band 5 relative to band 6 in the cross-track direction after correction. The primary periodic deviation observed in Fig. 5(b) disappears. The RMS value and the amplitude of the relative registration error between uncorrected images are 0.130 and 0.292 pixels, whereas those between corrected images are 0.024 and 0.074 pixels, respectively. As a result, the average registration error between bands is reduced to less than 0.1 pixels, which is a good band-to-band registration performance and will be effective for discriminating type of rock and minerals using SWIR data.

Since band-to-band registration is improved by correcting attitude data consistently, absolute distortion can be also compensated. Figure 5(f) shows the registration error map of the band 6 image taken on 06/07/2002 above Tokyo relative to that on 06/04/2001 after correction. The primary periodic deviation observed in Fig. 5(c) disappears. The RMS value and the amplitude of the average relative registration error before correction are 0.068 and 0.191 pixels, whereas those after correction are 0.027 and 0.078 pixels, respectively, showing that the internal distortion in the scene is reduced. This result shows that the method corrects the absolute distortion. Comparison with Landsat 7/ETM+ images, which are corrected using attitude information with markedly high time and angular resolutions using an ADS with a frequency of up to 250 Hz with an angular resolution of 0.025 arcseconds, shows that the periodic misregistration pattern disappears.

A limitation of the present correction method exists in the accuracy of image registration. The relative registration error is average in the correlation window. Furthermore, the peak value of the averaged relative registration error decreases owing to the undulation of the LOS vector and the parallax correction in Level-1B data processing. Thus, the relative registration error is underestimated and jitter cannot be fully corrected.

3.4 Using sensor based data product

Although the attitude jitter correction method using the Level-1B data products works well, the pointing angle from the nadir is limited. An influence of the elevation of the earth's surface exists because the earth's rotation causes a parallax in the cross-track direction. Furthermore, the time lag between band observations should be estimated. Therefore, these problems are considered using the sensor-based data products, Level-1A, which are the original raw images associated with the radiometric calibration and geometric correction coefficients used for resampling. Thus, the line of Level-1A data products in the horizontal direction is equal to the scan line.

To obtain tie points between bands 5 and 6 of ASTER by the parallax observation, we developed software to generate DEMs similar to that in previous studies (Fujisada et al., 2005; Koga & Iwasaki, 2010). First, bands 5 and 6 of Level-1A images with a radiometric correction are input, which include supplementary data and ancillary data. Second, the corresponding points between two images are detected and a disparity value is calculated using a subpixel image-matching technique. This procedure is repeated over several multiscale steps with a coarse-to-fine approach, which enables us to reduce the computational cost. In addition, we select the operation parameters in each step, such as those in the interpolation method, matching method or filtering model. Since the parallax is sufficiently small, a phase correlation that obtains the disparity accurately is available. The warping of band 5 images obtained by image matching is effective for avoiding a pixel-

locking effect in the next matching process because the disparity is distributed around zero pixels.

Third, the three-dimensional position of each pixel is calculated by bundle adjustment using the LOS vector. The ASTER LOS vector is the vector between the satellite position and ground pixel's position on the World Geodetic System 1984 (WGS84) ellipsoid obtained by interpolating the geometric correction table. Note that the ground pixel position is corrected using the parallax correction of Level-1 data processing that removes the terrain effect using image matching or coarse DEM data (Iwasaki & Fujisada, 2005), which is restored using the parallax offset in Level-1A data products. For band 6, the LOS vector \vec{e}_6 multiplied by p extends from the satellite position \vec{s}_6 to the point \vec{x}_6 , which is expressed by Eq. (8).

$$\vec{x}_6 = p\vec{e}_6 + \vec{s}_6 \quad (8)$$

Similarly, for band 5, the LOS vector \vec{e}_5 multiplied by q extends from the satellite position \vec{s}_5 to the point \vec{x}_5 , which is expressed by Eq. (9).

$$\vec{x}_5 = q\vec{e}_5 + \vec{s}_5 \quad (9)$$

Owing to the error in the LOS vectors and satellite attitude jitter, the two vectors are skew vectors and do not intersect. Minimization of the distance between \vec{x}_6 and \vec{x}_5 using the least-squares method leads to the pierce point, giving by the parameters expressed in Eq. (10).

$$\begin{aligned} p &= \frac{(\vec{e}_6, \vec{x}_6 - \vec{x}_5) - (\vec{e}_6, \vec{e}_5)(\vec{e}_5, \vec{x}_6 - \vec{x}_5)}{1 - (\vec{e}_6, \vec{e}_5)^2} \\ q &= \frac{(\vec{e}_5, \vec{x}_5 - \vec{x}_6) - (\vec{e}_6, \vec{e}_5)(\vec{e}_6, \vec{x}_5 - \vec{x}_6)}{1 - (\vec{e}_6, \vec{e}_5)^2} \end{aligned} \quad (10)$$

The bundle error is the minimum distance between two LOS vectors. Since the sensors scan the same target by bands 5 and 6 line detectors with a time interval, the bundle error between the two views includes the jitter of both scans. Since most of the fluctuation in the bundle error is related to the jitter in the roll component, the rotation angle of the LOS vectors that minimizes the bundle error is obtained. The orbital coordinate system is centered on the satellite and the orientation is determined relative to the spacecraft position. The yaw axis is parallel to the vector between the satellite and the earth's center, the pitch axis is normal to the flight vector and the yaw axis, and the roll axis is normal to the yaw and pitch axes. The bundle error of any pixel in a Level-1A image is decomposed in the cross-track direction and converted to the attitude error around the roll axis.

The measured surface position is obtained in Cartesian coordinates and is converted to the earth-centered reference (ECR), and elevation is obtained as the height on the WGS84 ellipsoid. Finally, the image and the elevation data are projected onto an orthorectified image with path-oriented Universal Transverse Mercator (UTM) coordinates.

The time difference between the two bands is not equal to the nominal time lag but differs depending on the elevation, the off-nadir angle and the pointing angle. Considering that the variation due to the elevation is about one line and the deviation from the correct attitude $f(t)$ is sufficiently smooth, this effect is small. Furthermore, since we can iteratively revise the

deviation from the correct attitude using the newly obtained $f(t)$, this problem is not discussed further. Note that the correct time lag is directly obtained when the tie points of two LOS vectors are calculated.

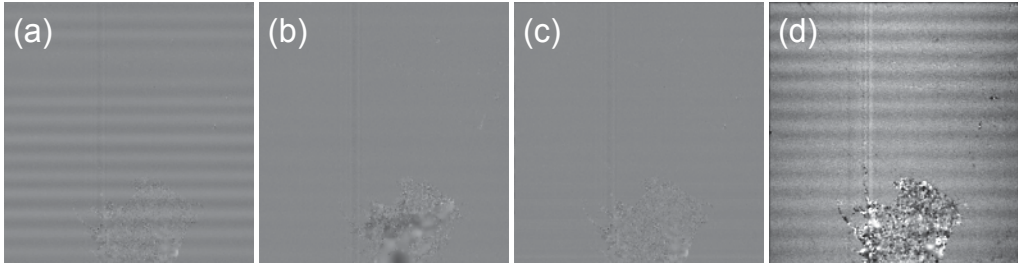


Fig. 6. Relative bundle error maps of band 5 relative to band 6 on (a) 06/07/2002 and (b) 06/04/2001. (c) Corrected bundle error map for 06/07/2002. (d) Along-track disparity obtained using bands 5 and 6 images.

Figures 6(a) and (b) show the bundle error between bands 5 and 6 in the roll direction on 06/07/2002 and 06/04/2001, respectively. The former suffers from attitude jitter, whereas the latter is almost free from vibration. The method in the previous section is next improved to make it robust and simple. First, an appropriate value of $f(t; 0 \leq t \leq \tau)$ is input and $f(t; \tau \leq t \leq t_e + \tau)$ is obtained from Eq. (1). Since $f(t)$ at this stage has many discontinuities, it is filtered using median and average filters. Next, $f(t; 0 \leq t \leq \tau)$ is obtained using Eq. (1) and the average of $f(t)$ is set to zero. Using the newly obtained $f(t; 0 \leq t \leq \tau)$, these steps are repeated several times to obtain a continuous curve that approximates Eq.(1). We obtained improved band-to-band registration compared with the former case, as shown in Fig. 6(c), which shows that most of the jitter is corrected. However, since the DEM that is obtained from the tie points of the two LOS vectors fluctuates owing to the pitch jitter, as shown in Fig. 6(d), the orthorectified products are also affected. Therefore, the correction of the pitch component is also considered at the same time, which is discussed in the next section. Another problem is the smoothing of the response curve because a square correlation window with a relatively large size is required in image matching by PC. Averaging of the measurements and exclusion of the false correlation over areas of water are also necessary in the procedure.

3.5 Detection of pitch component

Although correction of the roll component fluctuation is achieved, another task remains, detection of the pitch component. The importance of pitch control is recognized in along-track stereo vision, such as that in ASTER, SPOT-5 and ALOS/PRISM (Takaku & Tadono, 2009). Since the parallax in the along-track direction is added to the band-to-band displacement, the problem is more complicated than the detection of the roll component. Figures 7(a) and (e) show the target scenes used for this study, Tokyo on 06/07/2002 and Mt. Everest on 11/10/2004, respectively. The disparities of bands 7 and 9 relative to band 8 show a periodic pattern, as shown in Figs. 7(b) and (c), respectively. Although the scene is flat, the displacement is larger at the edge in Fig. 7(b) owing to the sphericity of the earth. The disparities of bands 7 and 9 relative to band 8 produce an elevation pattern, as shown in Figs. 7(f) and (g), respectively, where Mt. Everest is located at the upper right of the scene and the river flows from the scene center to the bottom center. Attitude fluctuation is also observed in the figures.

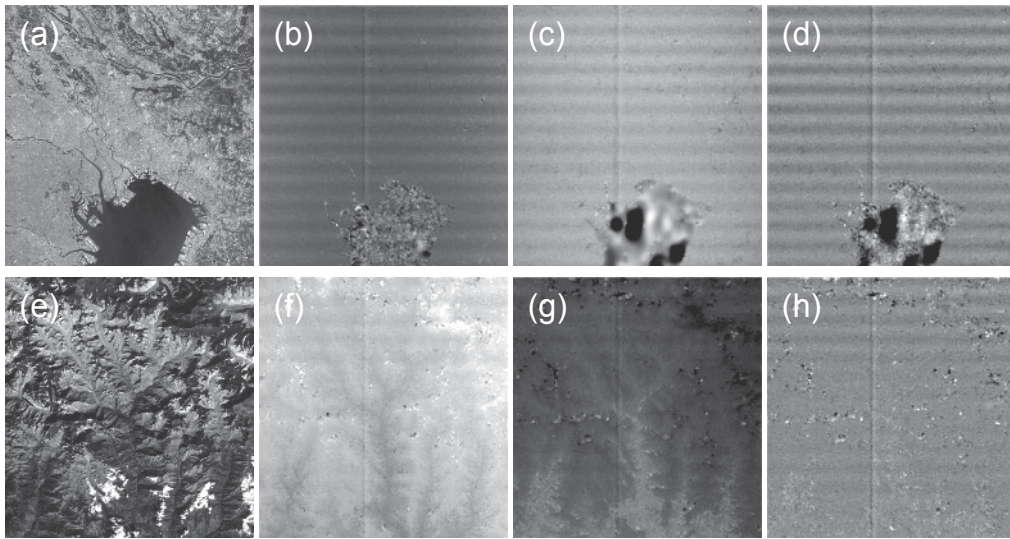


Fig. 7. (a) ASTER/SWIR scene on 06/07/2002, Tokyo, Japan. Relative registration error maps of (b) band 7 and (c) band 9 relative to band 8. (d) after canceling the elevation effect. (e) ASTER/SWIR scene on 11/10/2004, Mt. Everest. Relative registration error maps of (f) band 7 and (g) band 9 relative to band 8. (h) after canceling the elevation effect.

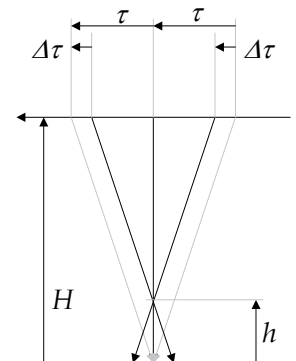


Fig. 8. Schematics of three-line data acquisition.

It is interesting that the DEM is obtained using a small-parallax configuration, which is mentioned as the small baseline stereo vision because the patterns in the two stereo images are similar (Morgan et al., 2010). Furthermore, occlusion due to steep mountains and clouds, which is critical in stereo vision, is mitigated. The base-to-height (B/H) ratio of ASTER/SWIR is $(81 \text{ lines} \times 30 \text{ m}) / 705 \text{ km} \approx 0.0034$, which is much smaller than that of the VNIR stereo system of 0.6 (Fujisada et al., 2005). Therefore, image matching using PC with high accuracy is essential for this purpose. Since the pointing jitter is critical in the stereo system, we must remove the elevation effect to detect the pointing fluctuation. The introduction of a three-line sensor configuration solves this problem, as shown in Fig. 8. With such a configuration, more accurate DEM without pointing jitter is obtained. The displacement of band 7 relative to band 8, $g'(t)$, is written as follows in terms of the effect of the elevation, *disparity*(*h*), (Okuda & Iwasaki, 2010) and the change in data

acquisition time due to the elevation, $\Delta\tau$, as shown in Fig. 8 (Schowengerdt, 2007). The contribution of $\Delta\tau$ is sufficiently small to be neglected, as was assumed in the analysis in the previous section.

$$g'(t) = f'(t + \tau - \Delta\tau) - f'(t) + \text{disparity}(h) \quad (11)$$

The displacement of band 9 relative to band 8, $g''(t)$, is written as follows.

$$g''(t) = f'(t - \tau + \Delta\tau) - f'(t) - \text{disparity}(h) \quad (12)$$

By adding Eqs. (11) and (12), we can obtain an equation free from $\text{disparity}(h)$.

$$g'(t) + g''(t) = f'(t + \tau - \Delta\tau) + f'(t - \tau + \Delta\tau) - 2f'(t) \quad (13)$$

Figure. 7(d) and (h) show the results of this operation, indicating that the affect of the elevation is canceled as shown by Eq. (13). The Fourier transform of Eq. (13) is written as follows using the shift theorem.

$$F'(\omega) = \frac{G'(\omega) + G''(\omega)}{\exp[j\omega(\tau - \Delta\tau)] + \exp[-j\omega(\tau - \Delta\tau)]} - 2 \quad (14)$$

The attitude is estimated in a similar way to the estimation of the roll component. The frequency of the pitch component jitter is the same as that of the roll component jitter. After canceling the pitch jitter, we can extract the correct elevation.

4. Conclusion and future works

To realize the good geometric performance of images obtained by earth observation sensors, accurate estimation of the spacecraft position and attitude is required. As the spatial resolution of remote-sensing missions is increased, the requirement of attitude stability will become increasingly severe, reaching to as small as 0.1 arcseconds with a frequency of more than 10 Hz. Furthermore, to meet users' data requirements, a high agility enabling multipoint observations, which cause frequent changes in satellite attitude, is needed. At the same time, the spatial resolution of small satellites is also increasing, however, their pointing stability is much lower owing to dynamic disturbances, such as solar pressure, atmospheric drag and magnetic torque (Wertz & Larson, 1999).

In this chapter, the detection and estimation of satellite jitter using remote-sensing imagery is described. Instead of requiring the very high pointing stability, mission instruments can help the satellite bus to deliver information on the pointing jitter. Consistent geometric restoration using the tie points of LOS vectors of sensors is the key to innovation. As an example, an image correction methodology using sensors arranged in parallel on the focal plane, which is necessary to fabricate a compact optical system, is proposed. An observation time lag arises between bands owing to this configuration. The relative deviation between several line sensors during the observation time lag is calculated from the image correlation. The deviation from the correct spacecraft attitude is estimated using the band-to-band displacement. The attitude data are improved using the estimated deviation from the correct spacecraft attitude. Then, the image is corrected using the revised satellite attitude information. This method improves not only the registration accuracy but also the absolute

satellite attitude. As a result, the internal distortion in the scene is reduced. At present, this technique is applicable to observation sensors with a similar parallel configuration on the focal plane, such as EO-1/ALI, QuickBird and FORMOSAT-2, although their observation bands exist in the visible wavelength. To increase the validity of the present work, the following issues must be resolved: the accuracy of tie point analysis, the similarity measures between multi-modal images and the robustness of correction methods. Implementation into time delay integration (TDI) sensors is also important.

The present method has been applied to investigate the pointing stability of the Terra spacecraft, which has five scientific instruments. Although these instruments have a large rotating mirror and mechanical coolers, analysis over ten years with sub-arcsecond accuracy has proved that the characteristic frequency of these instruments are not the source of the dynamic disturbance. What, then, is the source of the dynamic disturbance? It is difficult to discuss this for the case of the satellites in orbit. The Terra weekly report stated on January 6, 2000, "The first of several planned attitude sensor calibration slews was successfully performed. Initial data indicates that the spacecraft jitter induced by the high-gain antenna is significantly reduced by the feedforward capability."

5. Acknowledgements

This work was inspired by the ASTER science team and was developed by Y. Teshima, M. Koga, H. Kanno and T. Okuda, students at the University of Tokyo, under the support of Grants-in-Aid for Scientific Research (B), 17360405 (2005) and 21360414 (2009) from the Ministry of Education, Culture, Sports, Science and Technology. The ASTER project is promoted by ERSDAC/METI and NASA. The application to small satellites is investigated under the support of the Cabinet Office, Government of Japan for funding under the "FIRST" (Funding Program for World-Leading Innovative R&D on Science and Technology) program.

6. References

- Avouac, J. P.; Ayoub, F.; Leprince, S.; Konca, O. & Helmberger, D. V. (2006). The 2005 Mw 7.6 Kashmir Earthquake: Sub-pixel Correlation of ASTER Images and Seismic Waveforms Analysis, *Earth Planet. Sci. Lett.*, Vol. 249, pp.514-528.
- Barker, J. L. & Seiferth, J. C. (1996). Landsat Thematic Mapper Band-to-Band Registration, in *IEEE Int. Geoscience and Remote Sensing Symp.*, Lincoln, Nebraska, 27-31 May.
- Bayard, D. S. (2004). State-Space Approach to Computing Spacecraft Pointing Jitter, *J. Guidance, Control, Dynamics*, Vol. 27, No. 3, pp.426-433.
- Fujisada, H. (1998). ASTER Level-1 Data Processing Algorithm, *IEEE Trans. Geosci. Remote Sens.*, Vol. 36, No. 4, pp. 1101-1112.
- Fujisada, H.; Bailey, G. B.; Kelly, G. G.; Hara, S. & Abrams, M. J. (2005). ASTER DEM Performance, *IEEE Trans. Geosci. Remote Sens.*, Vol. 43, pp.2707-2714.
- Hoge, W. S. (2003). Subspace Identification Extension to the Phase Correlation Method, *IEEE Trans. Med. Imag.*, Vol. 22, pp.277-280.
- Iwasaki, A. & Fujisada, H. (2003). Image Correlation Tool for ASTER Geometric Validation, in *Proc. SPIE*, Agia Pelagia, Crete, Vol. 4881, pp.111-120.
- Iwasaki, A. & Fujisada, H. (2005). ASTER Geometric Performance, *IEEE Trans. Geosci. Remote Sens.*, Vol. 43, No. 12, pp.2700-2706.

- Jacobsen, K. (2006). Calibration of Imaging Satellite Sensors. *Int. Arch. Photogramm. Remote Sens.*, Band XXXVI 1/ W41, Ankara.
- Janschek, K.; Tchernykh, V. & Dyblenko, S. (2005). Integrated Camera Motion Compensation by Real-Time Image Motion Tracking and Image Deconvolution, in *Proc. IEEE/ASME International Conference on Advanced Intelligent Mechatronics*, Monterey, California, USA, 24-28 July, pp. 1437-1444.
- Koga, M. & Iwasaki, A. (2008). Three-Dimensional Displacement Measurement in Sub-pixel Accuracy for Seismic Phenomena from Optical Satellite Sensor Image, in *26th International Symposium on Space Technology and Science*, Hamamatsu, Japan, 1-8 June 1-8, 2008-n-21. (Available online at http://archive.ists.or.jp/upload_pdf/2008-n-21.pdf)
- Koga, M. & Iwasaki, A. (2011). Improving the Measurement Accuracy of Three-Dimensional Topography Changes Using Optical Satellite Stereo Image Data, submitted to *IEEE Trans. Geosci. Remote Sens.*
- Kudva, P. & Throckmorton, A. (1996). Attitude Determination Studies for the Earth Observation System AM1 (EOS-AM-1) Mission, *J. Guidance, Control, Dynamics*, Vol. 19, No. 6, pp.1326-1331.
- Lee, D. S.; Storey, J. C.; Choate, M. J. & Hayes, R. W. (2004). Four Years of Landsat 7 On-Orbit Geometric Calibration and Performance, *IEEE Trans. Geosci. Remote Sens.*, Vol. 42, No. 12, pp. 2786-2795.
- Leprince, S.; Barbot, S.; Ayoub, F. & Avouac, J. P. (2007). Automatic and Precise Orthorectification, Coregistration, and Subpixel Correlation of Satellite Images, Application to Ground Deformation Measurements, *IEEE Trans. Geosci. Remote Sens.*, Vol. 45, pp.1529-1558.
- Liu, C.-C. (2006). "Processing of FORMOSAT-2 Daily Revisit Imagery for Site Surveillance," *IEEE Trans. Geosci. Remote Sens.*, Vol. 44, No. 11, pp. 3206-3214.
- Liu, J. G. & Morgan, G. L. K. (2006). FFT Selective and Adaptive Filtering for Removal of Systematic Noise in ETM+Imageodesy Images, *IEEE Trans. Geosci. Remote Sens.*, Vol. 44, No. 12, pp. 3716-3724.
- Morgan, G. L. K.; Liu, J. G. & Yan, H. (2010). Precise Subpixel Disparity Measurement from Very Narrow Baseline Stereo, *IEEE Trans. Geosci. Remote Sens.*, Vol. 48, in press.
- Nagashima, S.; Aoki, T.; Higuchi, T. & Kobayashi, K. (2006). A Subpixel Image Matching Technique Using Phase-only Correlation," in *Proc. Int. Symp. Intelligent Signal Processing and Communication Systems*, pp. 701-704.
- NASA Goddard Space Flight Center (1998). *Landsat 7 Science Data Users Handbook*, available on <http://landsathandbook.gsfc.nasa.gov/handbook.html>.
- Neeck, S. P.; Venator, T. J. & Bolek, J. T. (1994) Jitter and Stability Calculation for the ASTER Instrument, in *Proc. SPIE*, Rome, Vol. 2317, pp.70-80.
- Okuda, T. & Iwasaki, A. (2010). Estimation of satellite pitch attitude from ASTER image data, in *IEEE Int. Geoscience and Remote Sensing Symp.*, Honolulu, Hawaii, 25-30 July, pp. 1070-1073.
- Schowengerdt, R. A. (2007). *Remote Sensing: Models and Methods for Image Processing*, Academic Press, ISBN: 0123694078, United States.
- Shin, D.; Pollard, J. K. & Muller, J.-P. (1997). Accurate Geometric Correction of ATSR Images, *IEEE Trans. Geosci. Remote Sens.*, Vol. 35, No. 4, pp. 997-1006.

- Storey, J. C.; Choate, M. J. & Meyer, D. J. (2004). A Geometric Performance Assessment of the EO-1 Advanced Land Imager, *IEEE Trans. Geosci. Remote Sens.*, Vol. 42, No. 3, pp. 602-607.
- Takaku, J. & Tadono, T. (2009). PRISM on-orbit Geometric Calibration and DSM Performance, *IEEE Trans. Geosci. Remote Sens.*, Vol. 47, No. 12, pp. 4060-4073.
- Teshima, Y. & Iwasaki, A. (2008). Correction of Attitude Fluctuation of Terra Spacecraft Using ASTER/SWIR Imagery With Parallax Observation, *IEEE Trans. Geosci. Remote Sens.*, Vol. 46, pp.222-227.
- Wertz, J. R. & Larson, W. J. (1999). *Space Mission Analysis and Design* 3rd edition, Kluwer Academic Pub, ISBN: 9780792359012, United States.

Gas-Kinetic Unified Algorithm for Re-Entering Complex Flows Covering Various Flow Regimes by Solving Boltzmann Model Equation

Zhi-Hui Li^{1,2}

¹*National Laboratory for Computational Fluid Dynamics,*

²*Hypervelocity Aerodynamics Institute,*

²*China Aerodynamics Research and Development Center,
China*

1. Introduction

Complex flow problems involving atmosphere re-entry have been one of the principal subjects of gas dynamics with the development of spaceflight. To study the aerodynamics of spacecraft re-entering Earth's atmosphere, Tsien (1946) early presented an interesting way in terms of the degree of gas rarefaction, that the gas flows can be approximately divided into four flow regimes based on the order of the Knudsen number (Kn), that is, continuum flow, slip flow, transition flow, and free molecular flow. In fact, the aerothermodynamics around space vehicles is totally different in various flow regimes and takes on the complex characteristics of many scales. In the continuum flow regime with a very small Knudsen number, the molecular mean free path is so small and the mean collision frequency per molecule is so sizeable that the gas flow can be considered as an absolute continuous model. Contrarily in the rarefied gas free-molecule flow regime with a large Knudsen number, the gas molecules are so rare with the lack of intermolecular collisions that the gas flow can but be controlled by the theory of the collisionless or near free molecular flow. Especially, the gas flow in the rarefied transition regime between the continuum regime and free molecular regime is difficult to treat either experimentally or theoretically and it has been a challenge how to effectively solve the complex problems covering various flow regimes. To simulate the gas flows from various regimes, the traditional way is to deal with them with different methods. On the one hand, the methods related to high rarefied flow have been developed, such as the microscopic molecular-based Direct Simulation Monte Carlo (DSMC) method. On the other hand, also the methods adapted to continuum flow have been well developed, such as the solvers of macroscopic fluid dynamics in which the Euler, Navier-Stokes or Burnett-like equations are numerically solved. However, both the methods are totally different in nature, and the computational results are difficult to link up smoothly with various flow regimes. Engineering development of current and intending spaceflight projects is closely concerned with complex gas dynamic problems of low-density flows (Koppenwallner & Legge 1985, Celenligil, Moss & Blanchard 1991, Ivanov & Gimelshein 1998, and Sharipov 2003), especially in the rarefied transition and near-continuum flow regimes.

The Boltzmann equation (Boltzmann 1872 and Chapman & Cowling 1970) can describe the molecular transport phenomena for the full spectrum of flow regimes and act as the main foundation for the study of complex gas dynamics. However, the difficulties encountered in solving the full Boltzmann equation are mainly associated with the nonlinear multidimensional integral nature of the collision term (Chapman & Cowling 1970, Cercignani 1984, and Bird 1994), and exact solutions of the Boltzmann equation are almost impractical for the analysis of practical complex flow problems up to this day. Therefore, several methods for approximate solutions of the Boltzmann equation have been proposed to simulate only the simple flow (Tcheremissine 1989, Roger & Schneider 1994, Tan & Varghese 1994, and Aristov 2001). The Boltzmann equation is still very difficult to solve numerically due to binary collisions, in particular, the unknown character of the intermolecular counteractions. Furthermore, this leads to a very high cost with respect to velocity discretization and the computation of the five-dimensional collision integral.

From the kinetic-molecular theory of gases, numerous statistical or relaxation kinetic model equations resembling to the original Boltzmann equation concerning the various order of moments have been put forward. The BGK collision model equation presented by Bhatnagar, Gross & Krook (1954) provides an effective and tractable way to deal with gas flows, which (Bhatnagar et al. 1954, Welander 1954, and Kogan 1958) supposes that the effect of collisions is roughly proportional to the departure of the true velocity distribution function from a Maxwellian equilibrium distribution. Subsequently, several kinds of nonlinear Boltzmann model equations have been developed, such as the ellipsoidal statistical (ES) model by Holway (1963), Cercignani & Tironi (1967), and Andries et al. (2000), the generalization of the BGK model by Shakhov (1968), the polynomial model by Segal and Ferziger (1972), and the hierarchy kinetic model equation similar to the Shakhov model proposed by Abe & Oguchi (1977). Among the main features of these high-order generalizations of the BGK model, the Boltzmann model equations give the correct Prandtl number and possess the essential and average properties of the original and physical realistic equation. Once the distribution function can be directly solved, the macroscopic physical quantities of gas dynamics can be obtained by the moments of the distribution function multiplied by some functions of the molecular velocity over the entire velocity space. Thus, instead of solving the full Boltzmann equation, one solves the nonlinear kinetic model equations and probably finds a more economical and efficient numerical method for complex gas flows over a wide range of Knudsen numbers.

Based on the main idea from the kinetic theory of gases in which the Maxwellian velocity distribution function can be translated into the macroscopic physical variables of the gas flow in normal equilibrium state, some gas-kinetic numerical methods, see Reitz (1981) and Moschetta & Pullin (1997), have been developed to solve inviscid gas dynamics. Since the 1990s, applying the asymptotic expansion of the velocity distribution function to the standard Maxwellian distribution based on the flux conservation at the cell interface, the kinetic BGK-type schemes adapting to compressible continuum flow or near continuum slip flow, see Prendergast & Xu (1993), Macrossan & Oliver (1993), Xu (1998), Kim & Jameson (1998), Xu (2001) and Xu & Li (2004), have been presented on the basis of the BGK model. Recently, the BGK scheme has also been extended to study three-dimensional flow using general unstructured meshes (Xu et al. (2005) and May et al. (2007). On the other hand, the computations of rarefied gas flows using the so-called kinetic models of the original Boltzmann equation have been advanced commendably with the development of powerful computers and numerical methods since the 1960s, see Chu (1965), Shakhov (1984), Yang &

Huang (1995a,b), Aoki, Kanba & Takata (1997) and Titarev & Shakhov (2002). The high resolution explicit or implicit finite difference methods for solving the two-dimensional BGK-Boltzmann model equations have been set forth on the basis of the introduction of the reduced velocity distribution functions and the application of the discrete ordinate technique. In particular, the discrete-velocity model of the BGK equation which satisfies conservation laws and dissipation of entropy has been developed, see Mieussens (2000). The reliability and efficiency of these methods has been demonstrated in applications to one- and two-dimensional rarefied gas dynamical problems with higher Mach numbers in a monatomic gas, see Kolobov et al.(2007).

In this work, we are essentially concerned with developing the gas-kinetic numerical method for the direct solution of the Boltzmann kinetic relaxation model, in which the single velocity distribution function equation can be translated into hyperbolic conservation systems with nonlinear source terms in physical space and time by first developing the discrete velocity ordinate method in the gas kinetic theory. Then the gas-kinetic numerical schemes are constructed by using the time-splitting method for unsteady equation and the finite difference technique in computational fluid dynamics. In the earlier papers, the gas-kinetic numerical method has been successively presented and applied to one-dimensional, two-dimensional and three-dimensional flows covering various flow regimes, see Li & Zhang (2000,2003,2004,2007,2009a,b). By now, the gas-kinetic algorithm has been extended and generalized to investigate the complex hypersonic flow problems covering various flow regimes, particularly in the rarefied transition and near-continuum flow regimes, for possible engineering applications. At the start of the gas-kinetic numerical study in complex hypersonic flows, the fluid medium is taken as the perfect gas. In the next section, the Boltzmann model equation for various flow regimes is presented. Then, the discrete velocity ordinate techniques and numerical quadrature methods are developed and applied to simulate different Mach number flows. In the fourth section, the gas-kinetic numerical algorithm solving the velocity distribution function is presented for one-, two- and three-dimensional flows, respectively. The gas-kinetic boundary condition and numerical methods for the velocity distribution function are studied in the fifth section. Then, the parallel strategy suitable for the gas-kinetic numerical algorithm is investigated to solve three-dimensional complex flows, and then the parallel program software capable of effectively simulating the gas dynamical problems covering the full spectrum of flow regimes will be developed for the unified algorithm. In the seventh section, the efficiency and convergence of the gas-kinetic algorithm will be discussed. After constructing the gas-kinetic numerical algorithm, it is used to study the complex aerodynamic problems and gas transfer phenomena including the one-dimensional shock-tube problems and shock wave inner flows at different Mach numbers, the supersonic flows past circular cylinder, and the gas flows around three-dimensional sphere and spacecraft shape with various Knudsen numbers covering various flow regimes. Finally, some concluding remarks and perspectives are given in the ninth section.

2. Description of the Boltzmann simplified velocity distribution function equation for various flow regimes

The Boltzmann equation (Boltzmann 1872; Chapman & Cowling 1970; Cercignani 1984) can describe the molecular transport phenomena from full spectrum of flow regimes in the view of micromechanics and act as the basic equation to study the gas dynamical problems.

It represents the relationships between the velocity distribution function which provides a statistical description of a gas at the molecular level and the variables on which it depends. The gas transport properties and the governing equations describing macroscopic gas flows can be obtained from the Boltzmann or its model equations by using the Chapman-Enskog asymptotic expansion method. Based on the investigation to the molecular colliding relaxation from Bhatnagar, Gross and Krook 1954, the BGK collision model equation (Bhatnagar, Gross & Krook 1954; Kogan 1958; Welander 1954) was proposed by replacing the collision integral term of the Boltzmann equation with simple colliding relaxation model.

$$\frac{\partial f}{\partial t} + \vec{V} \cdot \frac{\partial f}{\partial \vec{r}} = -\nu_m (f - f_M) , \quad (1)$$

where f is the molecular velocity distribution function which depends on space \vec{r} , molecular velocity \vec{V} and time t , f_M is the Maxwellian equilibrium distribution function, and ν_m is the proportion coefficient of the BGK equation, which is also named as the collision frequency.

$$f_M = n / (2\pi RT)^{3/2} \exp[-c^2 / (2RT)] . \quad (2)$$

Here, n and T respectively denote the number density and temperature of gas flow, R is the gas constant, c represents the magnitude of the thermal (peculiar) velocity \vec{c} of the molecule, that is $\vec{c} = \vec{V} - \vec{U}$ and $c^2 = c_x^2 + c_y^2 + c_z^2$. The \vec{c} consists of $c_x = V_x - U$, $c_y = V_y - V$ and $c_z = V_z - W$ along the x -, y - and, z - directions, where (U, V, W) corresponds to three components of the mean velocity \vec{U} .

The BGK equation is an ideal simplified form of the full Boltzmann equation. According to the BGK approximation, the velocity distribution function relaxes towards the Maxwellian distribution with a time constant of $\tau = 1/\nu_m$. The BGK equation can provide the correct collisionless or free-molecule solution, in which the form of the collision term is immaterial, however, the approximate collision term would lead to an indeterminate error in the transition regime. In the Chapman-Enskog expansion, the BGK model correspond to the Prandtl number, as the ratio of the coefficient of viscosity μ and heat conduction K obtained at the Navier-Stokes level, is equal to unity (Vincenti & Kruger 1965), unlike the Boltzmann equation which agrees with experimental data in making it approximately $2/3$. Nevertheless, the BGK model has the same basic properties as the Boltzmann collision integral. It is considered that the BGK equation can describe the gas flows in equilibrium or near-equilibrium state, see Chapmann & Cowling (1970); Bird (1994); Park (1981) and Cercignani (2000).

The BGK model is the simplest model based on relaxation towards Maxwellian. It has been shown from Park (1981) and Cercignani (2000) that the BGK equation can be improved to better model the flow states far from equilibrium. In order to have a correct value for the Prandtl number, the local Maxwellian f_M in the BGK equation can be replaced by the Eq.(1.9.7) from Cercignani (2000), as leads to the ellipsoidal statistical (ES) model equation (Holway 1966; Cercignani & Tironi 1967 and Andries & Perthame 2000). In this study, the f_M in Eq.(1) is replaced by the local equilibrium distribution function f^N from the

Shakhov model (Shakhov 1968; Morinishi & Oguchi 1984; Yang & Huang 1995 and Shakhov 1984). The function f^N is taken as the asymptotic expansion in Hermite polynomials with local Maxwellian f_M as the weighting function.

$$f^N = f_M \cdot \left[1 + (1 - \text{Pr}) \bar{c} \cdot \bar{q} \left(c^2 / (RT) - 5 \right) / (5PRT) \right] . \quad (3)$$

Here, Pr is the Prandtl number with $\text{Pr} = \mu C_p / K$ and is equal to $2/3$ for a monatomic gas, C_p is the specific heat at constant pressure, and \bar{q} and P respectively denote the heat flux vector and gas pressure. It can be shown that if $\text{Pr} = 1$ is set in Eq.(3), the BGK model is just recovered with $f^N = f_M$.

According to the relaxation time approximation (Chapmann & Cowling 1970), the collision frequency ν_m in Eq.(1) can be extended and related to the kinetic temperature as a measure of the variance of all thermal velocities in conditions far from equilibrium by using the temperature dependence of the coefficient of viscosity. The nominal collision frequency (inverse relaxation time) can be taken in the form

$$\nu = nkT / \mu , \quad (4)$$

where n is the number density, k is Boltzmann's constant, and $\mu = \mu(T)$ is the coefficient of the viscosity. Since the macroscopic flow parameters at any time at each point of the physical space are derived from moments of f over the velocity space in the kinetic theory of gases, the collision frequency ν is variable along with the space \vec{r} , time t , and thermal velocity $\bar{c} = \vec{V} - \vec{U}$. Consequently, this collision frequency relationship can be extended and applied to regions of extreme non-equilibrium, see Bird (1994); Park (1981) and Cercignani (2000).

The power law temperature dependence of the coefficient of viscosity can be obtained (Bird 1994 and Vincenti & Kruger 1965) from the Chapman-Enskog theory, which is appropriate for the inverse power law intermolecular force model and the VHS (Variable Hard Sphere) molecular model.

$$\mu / \mu_\infty = (T / T_\infty)^\chi , \quad (5)$$

where χ is the temperature exponent of the coefficient of viscosity, that can also be denoted as $\chi = (\zeta + 3) / (2(\zeta - 1))$ for the Chapman-Enskog gas of inverse power law, ζ is the inverse power coefficient related to the power force F and the distance r between centers of molecules, that is $F = \kappa / r^\zeta$ with a constant κ .

The viscosity coefficient μ_∞ in the free stream equilibrium can be expressed in terms of the nominal freestream mean free path λ_∞ for a simple hard sphere gas.

$$\mu_\infty = \frac{5}{16} m n_\infty (2\pi RT_\infty)^{1/2} \lambda_\infty . \quad (6)$$

Here, the subscripts ∞ represent the freestream value.

The collision frequency ν of the gas molecules can be expressed as the function of density, temperature, the freestream mean free path, and the exponent of molecular power law by the combination of Eqs.(4), (5), and (6).

$$\nu = \frac{16}{5} \cdot \sqrt{\frac{R}{2\pi}} \cdot \frac{T_\infty^{\chi-1/2}}{n_\infty} \cdot \frac{n}{T^{\chi-1}} \cdot \frac{1}{\lambda_\infty} . \quad (7)$$

It is, therefore, enlightened that the Boltzmann collision integral can be replaced by a simplified collision operator which retains the essential and non-equilibrium kinetic properties of the actual collision operator. Then, however, any replacement of the collision function must satisfy the conservation of mass, momentum and energy expressed by the Boltzmann equation. We consider a class of Boltzmann model equations of the form

$$\frac{\partial f}{\partial t} + \vec{V} \cdot \frac{\partial f}{\partial \vec{r}} = \nu(f^N - f) . \quad (8)$$

Where the collision frequency ν in Eq.(7) and the local equilibrium distribution function f^N in Eq.(3) can be integrated with the macroscopic flow parameters, the molecular viscosity transport coefficient, the thermodynamic effect, the molecular power law models, and the flow state controlling parameter from various flow regimes, see Li & Zhang (2004) and Li (2003).

Actually for non-homogeneous gas flow, the interaction of gas viscosity is produced from the transfer of molecular momentum between two contiguous layers of the mass flow due to the motion of molecules. However, when the gas mass interchanges between the two layers with different temperature, the transfer of heat energy results in the thermodynamic effect. The thermodynamic effect of the real gas flow is reflected in the Eq.(3) of the f^N by using the Prandtl number to relate the coefficient of viscosity with heat conduction from the molecular transport of gas. All of the macroscopic flow variables of gas dynamics in consideration, such as the density of the gas ρ , the flow velocity \vec{U} , the temperature T , the pressure P , the viscous stress tensor τ and the heat flux vector \vec{q} , can be evaluated by the following moments of the velocity distribution function over the velocity space.

$$n(\vec{r}, t) = \int f(\vec{r}, \vec{V}, t) d\vec{V} , \quad \rho(\vec{r}, t) = mn(\vec{r}, t) , \quad (9)$$

$$n\vec{U}(\vec{r}, t) = \int \vec{V} f(\vec{r}, \vec{V}, t) d\vec{V} , \quad (10)$$

$$\frac{3}{2} nRT(\vec{r}, t) = \int \frac{1}{2} c^2 f(\vec{r}, \vec{V}, t) d\vec{V} , \quad (11)$$

$$P(\vec{r}, t) = n(\vec{r}, t)kT(\vec{r}, t) , \quad (12)$$

$$\tau_{ij}(\vec{r}, t) = m \int c_i c_j f(\vec{r}, \vec{V}, t) d\vec{V} - P\delta_{ij} , \quad (13)$$

$$\vec{q}(\vec{r}, t) = m \int \frac{1}{2} c^2 \vec{c} f(\vec{r}, \vec{V}, t) d\vec{V} . \quad (14)$$

Where m denotes the molecular mass, R is the gas constant, k is the Boltzmann's constant, and the subscripts i and j each range from 1 to 3, where the values 1, 2, and 3 may be identified with components along the x -, y -, and z - directions, respectively.

Since the formulated problem involves in the scale of the microscopic statistical distribution and the macroscale of gas flow with tremendous difference of dimension order, the nondimensionalized procedure of variables and equations is needed to unify the scale in practical computation. Generally, four independent reference variables should be set in the non-dimensional reference system of the computation of gas flows. In here, let L_{ref} , T_∞ , n_∞ , and m be, respectively, the reference length, the free-stream temperature, the free-stream number density, and molecular mass, put the reference speed and time as $c_{m\infty} = \sqrt{2RT_\infty}$ and $t_\infty = L_{ref} / c_{m\infty}$. Then, the non-dimensional variables are defined as time $\tilde{t} = t / t_\infty$, flow velocity $\tilde{U}_i = U_i / c_{m\infty}$, molecular velocity $\tilde{V}_i = V_i / c_{m\infty}$, ($i = 1, 2, 3$), number density of gas flow $\tilde{n} = n / n_\infty$, temperature $\tilde{T} = T / T_\infty$, pressure $\tilde{p} = p / (mn_\infty c_{m\infty}^2 / 2)$, stress tensor $\tilde{\tau}_{ij} = \tau_{ij} / (mn_\infty c_{m\infty}^2 / 2)$, heat flux vector $\tilde{q}_i = q_i / (mn_\infty c_{m\infty}^3 / 2)$, space position $\tilde{x} = x / L_{ref}$, $\tilde{y} = y / L_{ref}$, $\tilde{z} = z / L_{ref}$, collision frequency $\tilde{\nu} = \nu \cdot t_\infty$, velocity distribution function $\tilde{f} = f / (n_\infty / (c_{m\infty}^3))$, Maxwellian distribution $\tilde{f}_M = f_M / (n_\infty / (c_{m\infty}^3))$, local equilibrium distribution $\tilde{f}^N = f^N / (n_\infty / (c_{m\infty}^3))$. The dimensionless velocity distribution function equation can be obtained with the above non-dimensional variables,

$$\frac{\partial \tilde{f}}{\partial \tilde{t}} + \tilde{\tilde{V}} \cdot \frac{\partial \tilde{f}}{\partial \tilde{r}} = \tilde{\nu} (\tilde{f}^N - \tilde{f}), \quad (15)$$

$$\tilde{f}^N = \tilde{f}_M \cdot [1 + (1 - \text{Pr}) \tilde{c} \cdot \tilde{q} (2\tilde{c}^2 / \tilde{T} - 5) / (5\tilde{p}\tilde{T} / 2)], \quad (16)$$

$$\tilde{f}_M = \frac{\tilde{n}}{(\pi\tilde{T})^{3/2}} \exp(-\tilde{c}^2 / \tilde{T}), \quad (17)$$

$$\tilde{\nu} = \frac{8\tilde{n}\tilde{T}^{1-\chi}}{5\sqrt{\pi}Kn} \quad , \quad Kn = \frac{\lambda_\infty}{L_{ref}}. \quad (18)$$

Where Kn is the Knudsen number as an important parameter characterizing the degree of rarefaction of the gas, λ_∞ is the free-stream mean free path, and \tilde{c} represents the thermal velocity of the molecule, that is $\tilde{c} = \tilde{V} - \tilde{U}$.

Similarly, the non-dimensional macroscopic variables can be represented by non-dimensionalizing Eqs. (9)~(14). In the following computation, all of the variables will have been nondimensionalized, and the “~” sign in the equations will be dropped for the simplicity and concision without causing any confusion.

The equation (15) provides the statistical description of the gas flow in any non-equilibrium state from the level of the kinetic theory of gases. Since mass, momentum and energy are conserved during molecular collisions, the equation (15) satisfies the Boltzmann’s H-theorem and conservation conditions at each of points in physical space and time,

$$\int (f^N - f) \psi^{(m)} d\tilde{V} = 0. \quad (19)$$

Where $\psi^{(m)}$ are the components of the moments on mass, momentum and energy, that is

$$\psi^{(1)} = 1, \quad \psi^{(2)} = \tilde{V}, \quad \psi^{(3)} = |\tilde{V}|^2 / 2. \quad (20)$$

3. Development and application of the discrete velocity ordinate method in gas kinetic theory

3.1 Discrete velocity ordinate method

The focus under consideration is how the velocity distribution function can be numerically solved. The distribution function f is a probability density function of statistical distribution (Riedi 1976, Chapmann & Cowling 1970, and Park 1981) with seven independent variables (for three-dimensional cases). In order to replace the continuous dependency of f on the velocity space, the discrete ordinate technique, see Huang & Giddens (1967), can be introduced and developed from the point of view of gas kinetic theory. The discrete ordinate method (Huang & Giddens 1967) is based on the representation of functions by a set of discrete points that coincide with the evaluation points in a quadrature rule, which consists of replacing the original functional dependency on the integral variable by a set of functions with N elements $W_i p(x_i)$ ($i = 1, \dots, N$), where the points x_i are quadrature points and W_i are the corresponding weights of the integration rule.

$$\int_a^b W(x) p(x) dx = \sum_{i=1}^N W_i p(x_i) . \quad (21)$$

The interval $[a, b]$ will be either $[0, \infty]$ or $[-\infty, \infty]$ for the application considered and a different weight function $W(x)$ is chosen for each problem considered. The x_i are the roots of the N th order polynomial $R_n(x)$ of the set that satisfy,

$$\int_a^b W(x) R_n(x) R_i(x) dx = \delta_{in} , \quad (22)$$

where the set of polynomials $R_n(x)$, orthonormal with respect to the weight function $W(x)$ on the interval $[a, b]$, form a complete basis of the $L^2[a, b]$ Hilbert space. The first N of these polynomials form a subspace of this Hilbert space which is isomorphic with the \mathfrak{R}^N Euclidean space. It may be shown from the treatment of the integral over the interval $[a, b]$ with the quadrature rule Eq.(21) that the discrete ordinate representation is equivalent to the truncated polynomial representation of the N th order.

It's shown from Brittin (1967) and Riedi (1976) that, in general, the velocity distribution function f for states removed from equilibrium is proportional to $\exp(-c^2)$ just as it is for equilibrium, that f has finite bounds under the specific precision in velocity space and tends to zero as c tends to infinity. That is, the integration of the normalized distribution function over all the velocity space should yield unity, and the probability of the molecular velocities far removed from the mean velocity \bar{U} of the flow is always negligible. Thus, in order to replace the continuous dependency of the molecular velocity distribution function on the velocity space, the discrete ordinate technique can be introduced in the kinetic theory of gases to discretize the finite velocity region removed from \bar{U} . The choice of the discrete velocity ordinate points in the vicinity of \bar{U} is based only on the moments of the distribution functions over the velocity space. Consequently the numerical integration of the macroscopic flow moments in Eq.(9)–(14) of the distribution function f over velocity space can be adequately performed by the same quadrature rule, with f evaluated at only a few

discrete velocity points in the vicinity of \bar{U} . The selections of the discrete velocity points and the range of the velocity space in the discrete velocity ordinate method are somewhat determined by the problem dependent.

Applying the discrete velocity ordinate method to Eq.(15) for the (V_x, V_y, V_z) velocity space, see Li (2003) and Li & Zhang (2009a), the single velocity distribution function equation can be transformed into hyperbolic conservation equations with nonlinear source terms at each of discrete velocity grid points.

$$\frac{\partial Q}{\partial t} + \frac{\partial F^x}{\partial x} + \frac{\partial F^y}{\partial y} + \frac{\partial F^z}{\partial z} = \bar{S} \tag{23}$$

with

$$Q = f_{\sigma,\delta,\theta}, \quad F^x = V_{x\sigma}Q, \quad F^y = V_{y\delta}Q, \\ F^z = V_{z\theta}Q, \quad \bar{S} = \nu(f_{\sigma,\delta,\theta}^N - f_{\sigma,\delta,\theta}),$$

where $f_{\sigma,\delta,\theta}$ and $f_{\sigma,\delta,\theta}^N$ respectively denote values of f and f^N at the discrete velocity ordinate points $(V_{x\sigma}, V_{y\delta}, V_{z\theta})$, the subscripts σ , δ and θ represent the discrete velocity grid indexes in the V_x -, V_y - and V_z - directions, respectively.

3.2 Development of numerical integration methods for evaluating macroscopic flow moments

Once the discrete velocity distribution functions $f_{\sigma,\delta,\theta}$ are solved, the macroscopic flow moments at any time in each point of the physical space can be obtained by the appropriate discrete velocity quadrature method. In terms of the symmetric quality of the exponential function $\exp(-V^2)$ over the interval $[-\infty, \infty]$, the Gauss-Hermite half-range quadrature can be extended to evaluate of the infinite integral over all the velocity space of the velocity distribution function. The discrete velocity points and the weights corresponding to the Gauss-Hermite quadrature can be obtained using the algorithms described by Huang and Giddens (1967) and by Shizgal (1981), which can be used to approximate the integrals with the exponential type as follows:

$$\int_0^\infty e^{-V^2} p(V) dV \approx \sum_{\sigma=1}^N W_\sigma p(V_\sigma) \tag{24}$$

where V_σ ($\sigma = 1, \dots, N$) are the positive roots of the Hermite polynomial of degree N , W_σ are the corresponding weights, the subscript σ is the discrete velocity index, and $p(V)$ denotes the function which can be derived from the integrands in Eq.(9)–(14). According to Kopal's discussion (Kopal 1955), it is known that for a given number of discrete subdivisions of the interval $(0, +\infty)$, the Gauss-Hermite's choice of the discrete velocity points V_σ and the corresponding weights W_σ yields the optimal discrete approximation to the considered integration in the sense. The Gauss-Hermite's V_σ and W_σ can be tabulated in the table of

the Gauss-Hermite quadrature. However, the number of the discrete velocity points is limited in this way, as it's very difficult exactly to solve high-order Hermite polynomial. The V_σ and W_σ can also be obtained by directly solving the nonlinear Eqs.(24) and (25) in terms of the decomposing principle.

$$\int_0^\infty e^{-u^2} u^k du = \frac{1}{2} \Gamma\left(\frac{k+1}{2}\right) \quad (25)$$

It is shown from the computing practice (Li 2001) that it is difficult to ensure the numerical stability with the computation of Eq.(24) and Eq.(25) when the number of discrete velocity points is greatly increased, this indicates that farther application of the Gauss-Hermite quadrature method to high speed gas flows may be restricted. To resolve this deficiency, the specific Gauss-type integration methods, such as the Gauss quadrature formulas with the weight function $2/\pi^{1/2} \exp(-V^2)$ and the Gauss-Legendre numerical quadrature rule whose integral nodes are determined by using the roots of the k th-order Legendre polynomials, have been presented and applied to simulate hypersonic flows with a wide range of Mach numbers.

The basic idea of the Gauss-type quadrature method (Henrici 1958) is to choose the fixed evaluation points V_σ and the corresponding weight coefficients W_σ of the integration rule in a way that the following approximation is exact.

$$\int_D W(V)f(V)dV \approx \sum_{\sigma=1}^N W_\sigma f(V_\sigma) \quad (26)$$

If both limits of the integration are infinite, a weighting function must be chosen that goes to zero for both positive and negative values of V . To develop the Gaussian integration method for the supersonic flows, the bell-shaped Gauss-type distribution function is introduced

$$W(V) = \frac{2}{\pi^{1/2}} \exp(-V^2), \quad -\infty < V < \infty. \quad (27)$$

When this weighting function (27) is used over the interval $[0, \infty)$, according to Eq.(26), the resulting Gauss quadrature formula with the weight function $2/\pi^{1/2} \exp(-V^2)$ is referred to as

$$\int_0^\infty \frac{2}{\pi^{1/2}} \exp(-V^2) f(V) dV \approx \sum_{\sigma=1}^N W_\sigma f(V_\sigma). \quad (28)$$

Where V_σ ($\sigma = 1, \dots, N$) are the positive roots of the orthogonal polynomials, $p_\sigma(V)$, in which the polynomials are generated by the following recurrence relation.

$$p_\sigma(V) = (V - b_\sigma)p_{\sigma-1}(V) - g_\sigma p_{\sigma-2}(V) \quad (29)$$

with $p_0(V) = 1$ and $p_{-1}(V) = 0$. Here, b_σ and g_σ are the recurrence relation parameters (Golub & Welsch 1981) for the orthogonal polynomials associated with $\exp(-V^2)$ on $[0, \infty)$. The nodes V_σ and weights W_σ of the Gauss quadrature rule (28) can be calculated from the recurrence relation by applying the QR algorithm (Kopal 1955) to determine the eigenvalues

and the first component of the orthonormal eigenvectors of the associated $N \times N$ tridiagonal matrix eigensystem. The Gaussian quadrature will exactly integrate a polynomial of a given degree with the least number of quadrature points and weights. In particular, M -point Gaussian quadrature exactly integrates a polynomial of degree $2M - 1$. Therefore, the use of the Gaussian quadrature points and weights would seem to be the optimum choice to the considered integration in the sense, see Li & Zhang (2009a,b). Since the discrete velocity solution can be treated in terms of expansion on the basis of piecewise constant functions, the computation of the moments of the distribution function can be performed by the network in the discretized velocity space. For example, the gas density is evaluated by the Gauss quadrature formula with the weight function $2 / \pi^{1/2} \exp(-V^2)$ in the following manner.

$$n = \int_{-\infty}^{\infty} \int_{-\infty}^{\infty} \int_{-\infty}^{\infty} f dV_x dV_y dV_z \approx \frac{\pi^{3/2}}{8} \sum_{\theta=-N_3}^{N_3} \sum_{\delta=-N_2}^{N_2} \sum_{\sigma=-N_1}^{N_1} W_{\theta} W_{\delta} W_{\sigma} f_{\sigma, \delta, \theta} e^{V_{x\sigma}^2} e^{V_{y\delta}^2} e^{V_{z\theta}^2}. \quad (30)$$

The other macroscopic flow moments, such as mean velocity, temperature, stress tensor and heat flux vector components, can be similarly evaluated according to the Gauss-type quadrature formula (28).

As the aforementioned Gauss-type quadrature rule with the weight function $2 / \pi^{1/2} \exp(-V^2)$ merely employs some finite evaluation points to integrate the flow moments over the whole of velocity space, in practical application, it is quite efficacious to evaluate the macroscopic flow variables with high precision, in particular for intermediate Mach number flows. However, for hypersonic flows with high Mach numbers, the velocity distribution severely deviates from the Maxwellian equilibrium with a long trail of the unsymmetrical bimodal distribution in the real line of the velocity space, so that the extensive region of the velocity space depended on distribution function needs to be discretized in quite a wide range, the number of discrete velocity ordinate points needed to cover the appropriate velocity range becomes quite large, and then the composite Gauss-Legendre quadrature rule is developed and applied to this study. The Gauss-Legendre quadrature formula for evaluation of definite integrals with the interval $[-1, 1]$ can be written as

$$\int_{-1}^1 f(t) dt \approx \sum_{i=1}^n A_i f(t_i), \quad (31)$$

where t_i is the evaluation point taken as the roots of a special family of polynomials called the Legendre polynomials, in which the first two Legendre polynomials are $p_0(t) = 1$ and $p_1(t) = t$, and the remaining members of the sequence are generated by the following recurrence relation.

$$(n + 1)p_{n+1}(t) = (2n + 1)tp_n(t) - np_{n-1}(t), \quad n \geq 1. \quad (32)$$

The corresponding weight coefficients A_i in Eq.(31) are defined by the differential equation with the form

$$A_i = \frac{2}{(1 - t_i^2)[p'_n(t_i)]^2}. \quad (33)$$

Generally, the abscissae and weight coefficients of the Gauss-Legendre formula can be computed and tabulated from the equations (32) and (33).

The interval $[-1,1]$ in the Eq.(31) can be transformed into a general finite interval $[V_k, V_{k+1}]$, see Li (2001) and Li & Zhang (2009a). Therefore, the extended Gauss-Legendre quadrature approximation becomes

$$\int_{V_k}^{V_{k+1}} f(V)dV \approx \frac{V_{k+1}-V_k}{2} \sum_{i=1}^n A_i f\left(\frac{V_{k+1}-V_k}{2} t_i + \frac{V_{k+1}+V_k}{2}\right). \quad (34)$$

To compute the macroscopic flow moments of the distribution function, the discrete velocity domain $[V_a, V_b]$ in consideration can be subdivided into a sum of smaller subdivisions $[V_k, V_{k+1}]$ with N parts according to the thoughts of the compound integration rule, and then the computation of the integration of the distribution function over the discrete velocity domain $[V_a, V_b]$ can be performed by applying the extended Gauss-Legendre formula (34) to each of subdivisions in the following manner.

$$\int_{V_a}^{V_b} f(V)dV = \sum_{k=1}^N \int_{V_k}^{V_{k+1}} f(V)dV. \quad (35)$$

4. Gas-kinetic numerical algorithm solving the velocity distribution function equation

4.1 Numerical scheme for one-dimensional gas flows

In order to reduce the computer storage requirement, the velocity distribution function equation can be integrated on the velocity components in some directions with appropriate weighting factors, where the components of macroscopic flow velocity are zero. Consequently, the reduced distribution functions can be introduced to cut back the number of independent variables in the distribution function f in the Eq.(15). For problems in one space dimension, say x , a great simplification is possible through the following reduction procedure. Two reduced distribution functions of the x , velocity component V_x and time t are defined, see Chu (1965):

$$g(x, V_x, t) = \int_{-\infty}^{\infty} \int_{-\infty}^{\infty} f(x, V_x, V_y, V_z, t) dV_y dV_z \quad (36)$$

$$h(x, V_x, t) = \int_{-\infty}^{\infty} \int_{-\infty}^{\infty} (V_y^2 + V_z^2) f(x, V_x, V_y, V_z, t) dV_y dV_z \quad (37)$$

Now integrating out the V_y and V_z dependence on Eq.(15) in describing one-dimensional gas flows, the following equivalent system to Eq.(15) is got:

$$\frac{\partial g}{\partial t} + V_x \frac{\partial g}{\partial x} = \nu (G^N - g) \quad (38)$$

$$\frac{\partial h}{\partial t} + V_x \frac{\partial h}{\partial x} = \nu (H^N - h) \quad (39)$$

Where,

$$G^N = G_M \left\{ 1 + (1 - \text{Pr})(V_x - U)q_x \left[2(V_x - U)^2 / T - 3 \right] / (5PT / 2) \right\} \quad (40)$$

$$G_M = n / (\pi T)^{1/2} \exp \left[-(V_x - U)^2 / T \right]$$

$$H^N = H_M \left\{ 1 + (1 - \text{Pr})(V_x - U)q_x \left[2(V_x - U)^2 / T - 1 \right] / (5PT / 2) \right\} \quad (41)$$

$$H_M = T \cdot G_M$$

The macroscopic flows parameters denoted by the reduced distribution functions can be similarly obtained by substituting Eq.(36) and Eq.(37) into Eqs.(9)~(14).

Thus, the molecular velocity distribution function equation for one-dimensional gas flows can be transformed into two simultaneous equations on the reduced distribution functions instead of one single equation and can be cast into the following conservation law form recurring to the discrete velocity ordinate method described in the Section 3.

$$\frac{\partial \mathbf{U}}{\partial t} + \frac{\partial \mathbf{F}}{\partial x} = \mathbf{S} \quad (42)$$

with

$$\mathbf{U} = \begin{pmatrix} g_\sigma \\ h_\sigma \end{pmatrix}, \quad \mathbf{F} = V_{x\sigma} \mathbf{U}, \quad \mathbf{S} = \begin{pmatrix} \nu(G_\sigma^N - g_\sigma) \\ \nu(H_\sigma^N - h_\sigma) \end{pmatrix},$$

where g_σ , h_σ , G_σ^N and H_σ^N correspond to the values of g , h , G^N and H^N at the discrete velocity grid points $V_{x\sigma}$, respectively.

Using the NND scheme (Zhang & Zhuang 1992) with the second-order Runge-Kutta method in temporal integral, the finite difference second-order scheme is constructed:

$$\begin{aligned} \delta_t \mathbf{U}^* &= R(\mathbf{U}^n) \\ \mathbf{U}^* &= \mathbf{U}^n + \Delta t \cdot \delta_t \mathbf{U}^* \\ \delta_t \mathbf{U}^{**} &= R(\mathbf{U}^*) \\ \mathbf{U}^{n+1} &= \mathbf{U}^n + \frac{\Delta t}{2} \cdot (\delta_t \mathbf{U}^* + \delta_t \mathbf{U}^{**}) \end{aligned} \quad (43)$$

The operator $R(\mathbf{U}^n)$ is defined by

$$R(\mathbf{U}^n) = -\frac{1}{\Delta x} (\mathbf{H}_{i+1/2}^n - \mathbf{H}_{i-1/2}^n) + \mathbf{S}_i^n$$

with the numerical flux defined by

$$\begin{aligned} \mathbf{H}_{i+1/2} = & \mathbf{F}_i^+ + \frac{1}{2} \min \text{mod}(\Delta \mathbf{F}_{i-1/2}^+, \Delta \mathbf{F}_{i+1/2}^+) \\ & + \mathbf{F}_{i+1}^- - \frac{1}{2} \min \text{mod}(\Delta \mathbf{F}_{i+1/2}^-, \Delta \mathbf{F}_{i+3/2}^-) \end{aligned}$$

and the min mod operator is defined by

$$\min \text{mod}(x, y) = \frac{1}{2} [\text{sgn}(x) + \text{sgn}(y)] \cdot \min(|x|, |y|)$$

The stable condition of the scheme can be written as

$$\Delta t_s = CFL / \left(\frac{v}{2} + \frac{3}{2} \frac{|V_{x\sigma}|}{\Delta x} \right)_{\max} \quad (44)$$

Where CFL is the adjusting coefficient of the time step in the scheme, that is set as $CFL = 0.95$.

Considering the basic feature of the molecular movement and colliding approaching to equilibrium, the time step size (Δt) in the computation should be controlled by coupling the stable condition (Δt_s) of the scheme with the local mean collision time (Δt_c), Bird (1994) and Li & Xie (1996).

$$\Delta t = \min(\Delta t_c, \Delta t_s) \quad (45)$$

Where $\Delta t_c = 1/v_{\max}$.

It is well-known that the Euler equations describing inviscid fluid dynamics can be derived from the moments of the Boltzmann or its model equation by setting the velocity distribution function f as a local equilibrium distribution function f_M . In fact, if we consider the Boltzmann model equation and multiply it for the so-called collision invariants of $(1, V_x, V_x^2/2)$, by integrating in V_x with the set of a Maxwellian equilibrium state $f = f_M$, we can obtain the Euler equations of the corresponding conservations laws for mass, momentum and energy of inviscid gas dynamics. To catch on the contribution of the collision term to the velocity distribution function and test the capability of the present gas-kinetic numerical method in simulating the Euler equation of inviscid fluid dynamics, it is tested by neglecting the colliding relaxation term in the right of Eq.(42) to substitute the $G_{M\sigma}$ and $H_{M\sigma}$ of the Maxwell equilibrium distribution from the Eqs.(40) and (41) for g_σ and h_σ in the matrix F from the Eq.(42), then the hyperbolic conservation equations can be obtained, as follows

$$\frac{\partial U}{\partial t} + \frac{\partial G}{\partial x} = 0, \quad (46)$$

where

$$U = \begin{pmatrix} g_\sigma(x, t) \\ h_\sigma(x, t) \end{pmatrix}, \quad G = \begin{pmatrix} V_{x\sigma} G_{M\sigma} \\ V_{x\sigma} H_{M\sigma} \end{pmatrix}.$$

The equation (46) can be numerically solved, and the numerical solution of the Eq.(46) is only the so-called Euler limit solution, see Li & Zhang (2008). Therefore, the gas-kinetic Euler-type scheme is developed for the inviscid flow simulations in the continuum flow regime, illustrated by in the Section 8.1.

4.2 Numerical algorithm for two-dimensional gas flows

For analyses of gas flows in x and y directions around two-dimensional bodies, the molecular velocity distribution function equation in the Eq.(15) can be integrated with respect to V_z with weighting factors 1 and V_z^2 so that the number of independent variables is reduced by integrating out the dependence of f on V_z . The following reduced distribution functions are introduced, see Morinishi & Oguchi (1984); Yang & Huang (1995) and Aoki, Kanba & Takata (1997).

$$g(x, y, t, V_x, V_y) = \int_{-\infty}^{\infty} f(x, y, t, V_x, V_y, V_z) dV_z \quad (47)$$

$$h(x, y, t, V_x, V_y) = \int_{-\infty}^{\infty} V_z^2 f(x, y, t, V_x, V_y, V_z) dV_z \quad (48)$$

After substituting Eq.(47) and Eq.(48) into the Eq.(15) describing two-dimensional gas flows, and applying the discrete velocity ordinate method to velocity components V_x and V_y , the single velocity distribution function equation can be become into two simultaneous equations with the hyperbolic conservation law form in the transformed coordinates (ξ, η) as follows:

$$\frac{\partial \mathbf{U}}{\partial t} + \frac{\partial \mathbf{F}}{\partial \xi} + \frac{\partial \mathbf{G}}{\partial \eta} = \mathbf{S} \quad (49)$$

with

$$\mathbf{U} = J \begin{pmatrix} g_{\sigma, \delta} \\ h_{\sigma, \delta} \end{pmatrix}, \quad \mathbf{F} = \bar{U} \mathbf{U}, \quad \mathbf{G} = \bar{V} \mathbf{U}, \quad \mathbf{S} = J \begin{pmatrix} \nu(G_{\sigma, \delta}^N - g_{\sigma, \delta}) \\ \nu(H_{\sigma, \delta}^N - h_{\sigma, \delta}) \end{pmatrix},$$

where $g_{\sigma, \delta}$, $h_{\sigma, \delta}$, $G_{\sigma, \delta}^N$ and $H_{\sigma, \delta}^N$ denote values of g , h , G^N and H^N at the discrete velocity points $(V_{x\sigma}, V_{y\sigma})$, respectively.

$$G^N = G_M \left[1 + (1 - \text{Pr})(C_i q_i) (2C^2 / T - 4) / (5PT / 2) \right] \quad (50)$$

$$G_M = \frac{n}{\pi T} \exp(-C^2 / T)$$

$$H^N = H_M \left[1 + (1 - \text{Pr})(C_i q_i) (2C^2 / T - 2) / (5PT / 2) \right] \quad (51)$$

$$H_M = TG_M / 2$$

$$C^2 = (V_x - U)^2 + (V_y - V)^2$$

$$C_i q_i = (V_x - U)q_x + (V_y - V)q_y$$

Note that \bar{U} , \bar{V} are the so-called “contravariant molecular velocity” defined as $\bar{U} = V_{x\sigma}\xi_x + V_{y\delta}\xi_y$, $\bar{V} = V_{x\sigma}\eta_x + V_{y\delta}\eta_y$, J is the Jacobian of the general transformation, that is $J = \partial(x, y) / \partial(\xi, \eta)$. The Jacobian coefficient matrices $A = \partial F / \partial U$ and $B = \partial G / \partial U$ of the transformed Eq.(49) are diagonal and have real eigenvalues $a = \bar{U}$ and $b = \bar{V}$.

In view of the unsteady characteristic of molecular convective movement and colliding relaxation, the time-splitting method is used to divide the Eq.(49) into the colliding relaxation equations with the nonlinear source terms and the convective movement equations. Considering simultaneously proceeding on the molecular movement and colliding relaxation in real gas, the computing order of the previous and hind time steps is interchanged to couple to solve them in the computation. The finite difference second-order scheme is developed by using the improved Euler method and the NND-4(a) scheme (Zhang & Zhuang 1992) which is two-stage scheme with second-order accuracy in time and space.

$$\mathbf{U}^{n+1} = L_s(\Delta t/2)L_\eta(\Delta t/2)L_\xi(\Delta t)L_\eta(\Delta t/2)L_s(\Delta t/2)\mathbf{U}^n \quad (52)$$

Where,

$$\mathbf{U}^* = L_s(\Delta t)\mathbf{U}^n = \mathbf{U}^n + \left(1 - \frac{\nu}{2}\Delta t\right)\Delta t \cdot \mathbf{S}^n \quad (53)$$

$$\mathbf{U}^{**} = L_\eta(\Delta t)\mathbf{U}^* = \left[1 - b\Delta t\delta_\eta + \frac{b^2\Delta t^2}{2}\delta_{\eta^2}\right]\mathbf{U}^* \quad (54)$$

$$\mathbf{U}^{n+1} = L_\xi(\Delta t)\mathbf{U}^{**} = \left[1 - a\Delta t\delta_\xi + \frac{a^2\Delta t^2}{2}\delta_{\xi^2}\right]\mathbf{U}^{**} \quad (55)$$

The integration operator $L_s(\Delta t)$ of the colliding relaxation source terms is done using the improved Euler method. The one-dimensional space operator $L_\eta(\Delta t)$ and $L_\xi(\Delta t)$ of the convective movement terms are approximated by the NND-4(a) scheme. The Δt in the computation can be chosen (Li 2001,2003) as

$$\Delta t = \min(\Delta t_c, \Delta t_s)$$

Here, $\Delta t_s = CFL / \max(\nu / 2, |\bar{U}| / \Delta \xi, |\bar{V}| / \Delta \eta)$.

4.3 Numerical algorithm for three-dimensional gas flows

For the three-dimensional gas flows, the molecular velocity distribution function remains to be a function of seven independent variables in the phase space. The discrete velocity ordinate method can be applied to the velocity distribution function in Eq.(15) to remove its

continuous dependency on velocity components (V_x, V_y, V_z) , as described in Section 3.1. Moreover, to treat arbitrary geometry configuration, the body fitted coordinate is introduced. By applying the general transformation technique, Eq.(23) on the discrete velocity distribution functions become in the transformed coordinates (ξ, η, ζ) (Li 2001) as follow:

$$\frac{\partial U}{\partial t} + \frac{\partial F}{\partial \xi} + \frac{\partial G}{\partial \eta} + \frac{\partial H}{\partial \zeta} = S. \quad (56)$$

with

$$U = JQ, F = \bar{U}U, G = \bar{V}U,$$

$$H = \bar{W}U, S = \bar{J}S.$$

where

$$\bar{U} = V_{x\sigma}\xi_x + V_{y\delta}\xi_y + V_{z\theta}\xi_z, \bar{V} = V_{x\sigma}\eta_x + V_{y\delta}\eta_y + V_{z\theta}\eta_z,$$

$$\bar{W} = V_{x\sigma}\zeta_x + V_{y\delta}\zeta_y + V_{z\theta}\zeta_z, J = \partial(x, y, z)/\partial(\xi, \eta, \zeta),$$

To solve the governing equation (56) at each of $(V_{x\sigma}, V_{y\delta}, V_{z\theta})$ for three-dimensional flow, the time-splitting numerical method can be adopted in the light of the unsteady characteristic of molecular convective movement and colliding relaxation, and the value of U in Eq.(56) at time $n+1$ can be expressed by second-order Taylor series expansion:

$$\begin{aligned} U^{n+1} = & \left[1 - \bar{U}\Delta t\delta_\xi + \frac{\bar{U}^2}{2}\Delta t^2\delta_{\xi^2} \right] \cdot \left[1 - \bar{V}\Delta t\delta_\eta + \frac{\bar{V}^2}{2}\Delta t^2\delta_{\eta^2} \right] \cdot \\ & \left[1 - \bar{W}\Delta t\delta_\zeta + \frac{\bar{W}^2}{2}\Delta t^2\delta_{\zeta^2} \right] \cdot \left[1 - \nu\Delta t\left(1 - \frac{\nu}{2}\Delta t\right) \right] U^n \\ & + O(\Delta t^2, \Delta \xi^2, \Delta \eta^2, \Delta \zeta^2) \end{aligned} \quad (57)$$

The above finite difference approximation can be split as the following four operators.

$$U^* = L_S(\Delta t)U^n = U^n + \left(1 - \frac{\nu}{2}\Delta t\right)\Delta t \cdot S^n, \quad (58)$$

$$U^{**} = L_\zeta(\Delta t)U^* = \left[1 - \bar{W}\Delta t\delta_\zeta + \frac{\bar{W}^2\Delta t^2}{2}\delta_{\zeta^2} \right] U^*, \quad (59)$$

$$U^{***} = L_\eta(\Delta t)U^{**} = \left[1 - \bar{V}\Delta t\delta_\eta + \frac{\bar{V}^2\Delta t^2}{2}\delta_{\eta^2} \right] U^{**}, \quad (60)$$

$$U^{n+1} = L_{\zeta}(\Delta t)U^{***} = \left[1 - \bar{U}\Delta t\delta_{\zeta} + \frac{\bar{U}^2\Delta t^2}{2}\delta_{\zeta^2} \right] U^{***}. \quad (61)$$

In fact, the finite difference Eqs.(58)~(61) are respectively consistent with four differential equations in the following,

$$\frac{\partial U}{\partial t} = S, \quad (62)$$

$$\frac{\partial U}{\partial t} + \frac{\partial H}{\partial \zeta} = 0, \quad (63)$$

$$\frac{\partial U}{\partial t} + \frac{\partial G}{\partial \eta} = 0, \quad (64)$$

$$\frac{\partial U}{\partial t} + \frac{\partial F}{\partial \xi} = 0. \quad (65)$$

According to the time-splitting method, on each time interval Δt , a solution of the Eq.(56) is substituted by a solution of a sequence of four Eqs.(62)~(65). Then, the colliding relaxation equation (62) can be numerically integrated by using the second-order Runge-Kutta method:

$$\begin{aligned} \delta_i U^* &= \left(1 - \frac{\nu}{2}\Delta t \right) \cdot S(U^n), \\ U^* &= U^n + \Delta t \cdot \delta_i U^*, \\ \delta_i U^{**} &= \left(1 - \frac{\nu}{2}\Delta t \right) \cdot S(U^*), \\ U^{n+1} &= U^n + \frac{\Delta t}{2}(\delta_i U^* + \delta_i U^{**}). \end{aligned} \quad (66)$$

The convective movement equations (63)~(65) in the (ζ, η, ξ) directions of the position space can be numerically solved by using the NND-4(a) finite-difference scheme (Zhang & Zhuang 1992) based on primitive variables, which is a two-stage scheme with second-order accuracy in time and space. For the Eq.(63), the finite-difference scheme can be expressed as

$$U^* = U^n - \frac{\Delta t}{\Delta \zeta} (Q_{i+1/2}^n - Q_{i-1/2}^n), \quad (67)$$

$$U^{n+1} = \frac{1}{2} [U^n + U^* - \frac{\Delta t}{\Delta \zeta} (Q_{i+1/2}^* - Q_{i-1/2}^*)], \quad (68)$$

$$Q_{i+1/2} = H_{i+1/2}^+(U_L) + H_{i+1/2}^-(U_R),$$

$$U_{L,i+1/2} = U_{p,i} + \frac{1}{2} \min \text{mod}(\Delta U_{p,i-1/2}, \Delta U_{p,i+1/2}),$$

$$U_{R,i+1/2} = U_{p,i+1} - \frac{1}{2} \min \text{mod}(\Delta U_{p,i+1/2}, \Delta U_{p,i+3/2}),$$

$$\Delta U_{p,i+1/2} = U_{p,i+1} - U_{p,i}.$$

Where, U_p denotes the primitive variable of the Eq.(63), and H^\pm respectively denote the flux vector splitters of H based on the positive and negative characteristic values λ^\pm with $\lambda^+ = (\lambda + |\lambda|) / 2$ and $\lambda^- = (\lambda - |\lambda|) / 2$. The flux limiter $\min \text{mod}$ operator in the above-mentioned scheme is defined by

$$\min \text{mod}(x, y) = \frac{1}{2} [\text{sgn}(x) + \text{sgn}(y)] \cdot \min(|x|, |y|) \tag{69}$$

Considering simultaneously proceeding on the molecular movement and colliding relaxation in real gas, the computing order of the previous and subsequent time steps is interchanged to couple to solve them in the computation. The second-order finite difference scheme directly solving the six-dimensional discrete velocity distribution functions is set as

$$U^{n+1} = L_S\left(\frac{\Delta t}{2}\right)L_\zeta\left(\frac{\Delta t}{2}\right)L_\eta\left(\frac{\Delta t}{2}\right)L_\xi(\Delta t)L_\eta\left(\frac{\Delta t}{2}\right)L_\zeta\left(\frac{\Delta t}{2}\right)L_S\left(\frac{\Delta t}{2}\right)U^n. \tag{70}$$

In view of the behaviour of the time evolution on the velocity distribution function and the decoupling technique (Bird 1994; Ivanov & Gimelshein 1998 and Li & Xie 1996) on molecular motion and intermolecular collisions in the DSMC method, the time step size (Δt) in the computation should be controlled by coupling the stability condition (Δt_s) of the scheme with the local mean collision time interval (Δt_c), thus we have

$$\Delta t = \min(\Delta t_s, \Delta t_c). \tag{71}$$

with

$$\Delta t_s = \frac{CFL}{\max\left(\frac{\nu}{2}, \frac{|\bar{U}|}{\Delta \xi}, \frac{|\bar{V}|}{\Delta \eta}, \frac{|\bar{W}|}{\Delta \zeta}\right)}, \Delta t_c = \frac{1}{\nu_{\max}}.$$

Where CFL is the adjusting coefficient of the time step in the scheme, that can be set as $CFL = 0.99$.

For constructing an effective numerical scheme (70) in solving three-dimensional complex flows, the finite difference scheme which approximates the velocity distribution function equation (56) must possess the properties of monotonicity and conservation. The conservative finite-difference schemes are constructed for each separate step in Eqs.(62)~(65), and then the whole scheme is conservative. In the computation of the velocity distribution function, to guarantee the positivity of the distribution function for different Mach number flows, only those discrete velocity ordinate points are considered, at which

the distribution function is greater than a prescribed lower threshold. If at each iteration the time step is fixed according to the condition (71), the scheme (70) is perfectly conservative for mass, momentum, and total energy, and the positivity of the distribution function can be preserved.

5. Gas-kinetic boundary conditions and numerical procedures for the velocity distribution function

Since the present gas-kinetic algorithm explicitly evaluates the time evolution of the molecular velocity distribution function at each of discrete grid points from the physical space and velocity space, all kinds of boundaries should be numerically implemented by directly acting on the velocity distribution function instead of using the macroscopic flow variables. The hyperbolic type of the convective part of the Boltzmann model equation controls and determines the appropriate values of the distribution function in the boundaries. The boundaries can be divided into two parts of Γ_b and Γ_w respectively corresponding to the boundary of the external free flow and to the surface of a body.

5.1 Gas-surface boundary

Thanks to the interaction of the gas molecules with the solid walls, one can trace the origin of the aerodynamics exerted by the gas upon the body and the heat transfer between the gas and the solid boundary Γ_w . The interaction depends on the surface finish, the cleanliness of the surface and its temperature (Cercignani 1994). In general, the interaction of a given molecule with the surface may also depend on the velocity distribution function of molecules impinging on a surface element. Hence it is more convenient to think in terms of a probability density $R(\vec{V} \rightarrow \vec{V}'; \vec{r})$ (Nocilla 1961.) that a molecule hitting the solid boundary at some point \vec{r} with some velocity \vec{V} reemerges practically at the same point with some other velocity \vec{V}' . If R is known, then the boundary conditions for the molecular velocity distribution function $f(\vec{r}, \vec{V}, t)$ can be easily written down. The general form of the boundary conditions can be written by the aid of the surface balance condition of the mass flux (number of molecules leaving or arriving per unit time and unit area) as

$$|\vec{c}' \cdot \vec{n}| f(\vec{r}, \vec{V}', t) = \int_{\vec{c} \cdot \vec{n} < 0} R(\vec{V} \rightarrow \vec{V}'; \vec{r}) f(\vec{r}, \vec{V}, t) |\vec{c} \cdot \vec{n}| d\vec{V}, \quad (\vec{r} \in S, \vec{c}' \cdot \vec{n} > 0). \quad (72)$$

In view of the difficulty of computing the scattering kernel $R(\vec{V} \rightarrow \vec{V}'; \vec{r})$ due to the complex physical phenomena of adsorption and evaporation which take place at the wall, mathematical models (Cercignani & Lampis 1971; Kuščer, Možina & Krizanac 1974), that satisfy the basic physical requirements of normalization, positivity and preservation of local equilibrium at the wall, have been proposed. In particular, the scattering kernel corresponding to the Maxwell-type model is used in this paper. By defining the accommodation coefficient which describes how much the molecules accommodate to the state of the wall, the scattering kernel turns out to be

$$R(\vec{V} \rightarrow \vec{V}'; \vec{r}) = \alpha f_M^w(\vec{V}', \vec{r}) |\vec{c}' \cdot \vec{n}| + (1 - \alpha) \delta(\vec{V}' - \vec{V} + 2\vec{n}(\vec{c} \cdot \vec{n})), \quad (\vec{c}' \cdot \vec{n} > 0, \vec{c} \cdot \vec{n} < 0). \quad (73)$$

According to this model for the scattering kernel, a fraction $(1 - \alpha)$ of molecules undergoes a specular reflection, while the remaining fraction α is diffused with the Maxwellian distribution f_M^w of the wall. In general, α turns out to depend on the distribution function of the impinging molecules. A complete accommodation is when the molecules are conserved in number, but otherwise forget completely their impinging distribution. The emerging distribution is then proportional to f_M^w with temperature and mass velocity equal to the temperature and mass velocity of the wall, this gas is in thermal and mechanical equilibrium with the wall. The opposite case with $\alpha = 0$ is when the gas remembers as much as possible of the impinging distribution, then the kernel is a delta function, and all the accommodation coefficients vanish so that the specular reflection is gained,

$$R(\vec{V} \rightarrow \vec{V}'; \vec{r}) = \delta(\vec{V}' - \vec{V} + 2\bar{n}(\vec{c} \cdot \bar{n})). \quad (74)$$

In this case, the gas molecules are specularly reflected with the normal component of velocity reversed, therefore the gas cannot exert any stress on the surface, except in the direction of the normal. In fact, if the boundary conditions do not contain the temperature of the wall with the case of a completely reflected gas, then they would allow the gas to stay in thermal equilibrium at any given temperature, irrespective of the surrounding bodies. It is clear that these boundary conditions are quite unrealistic.

In general, the Maxwell-type boundary conditions give satisfactory results with values of α rather close to 1, and in problems where the gas dynamics and momentum transfer are primarily reckoned for the perfect gas without regarding to internal energy transfer, $\alpha = 1$ is a rather accurate assumption. For practical applications, Maxwell's boundary conditions with $\alpha = 1$ are frequently used for the simplicity and reasonable accuracy, and they are a reasonable approximation to any kind of more complicated boundary conditions (Nocilla 1961; Cercignani & Lampis 1971; Kuščer, Možina & Krizanac 1974 and Grad 1949). In all the calculations in this paper, the aforementioned model of gas-surface interaction is implemented and used. According to the condition of the stationary solid wall that no particles penetrate the wall, all molecules striking the solid surface at any time must be reflected back to the gas. If the molecules strike on the surface, the molecular velocity distribution function, which is reflected from the surface, is considered as the form of "drifting Maxwellian" fully accommodating to the wall temperature T_w and velocity (U_w, V_w, W_w) , which is set in discretized form as follows:

$$f_{\Gamma_w \sigma, \delta, \theta} = \frac{n_w}{(\pi T_w)^{3/2}} \exp \left[-\frac{(V_{x\sigma} - U_w)^2 + (V_{y\delta} - V_w)^2 + (V_{z\theta} - W_w)^2}{T_w} \right], \vec{c} \cdot \bar{n} \geq 0. \quad (75)$$

Where \bar{n} is the unit vector normal to the wall surface, pointing to the gas.

The number density of molecules diffusing from the solid surface, n_w , which is not known previously and varied with the velocity distribution of incident molecules and the appearance of the solid surface, can be derived from the insulated condition of zero mass flux normal to the wall surface (Morinishi & Oguchi 1984; Aristov 2001; Li 2001,2003).

$$\int_{c_n > 0} c_n f_M^w d\vec{V} = \int_{c_n < 0} -c_n f d\vec{V}. \quad (76)$$

Then, substituting the Maxwellian distribution, characterized by the surface temperature T_w , into the left side of the equation (76), one has

$$\frac{n_w}{(\pi T_w)^{3/2}} \iiint_{c_n > 0} c_n \cdot e^{-\frac{V_x^2 + V_y^2 + V_z^2}{T_w}} dV_x dV_y dV_z = \iiint_{c_n < 0} -c_n \cdot f dV_x dV_y dV_z. \quad (77)$$

As a consequence, the n_w in the preceding reflected distribution function can be obtained

$$n_w = -2 \left(\frac{\pi}{T_w} \right)^{1/2} \iiint_{c_n < 0} c_n^- \cdot f dV_x dV_y dV_z. \quad (78)$$

Where $c_n^- = (c_n - |c_n|) / 2$.

If $\bar{c} \cdot \bar{n} < 0$, the discrete velocity distribution functions at the wall grid points of the boundary Γ_w are solved by using second-order upwind-difference approximations from the adjacent grids in the interior of the flow field.

5.2 Outer boundary

The distribution function is assumed to be in equilibrium at infinity. However, the outer boundary Γ_b must be in some finite distance from the body, so the outer boundary conditions are numerically treated using characteristic-based boundary conditions, see Li (2003) and Li & Zhang (2009a,b). These are in accord with the upwind nature of the interior point scheme. From this standpoint, the distribution functions for outgoing molecules through the outer boundary are numerically solved by the second-order finite difference approximation from the interior points, where $\bar{W} > 0$.

For molecules incoming from outside, the characterizing condition $\bar{W} \leq 0$ is satisfied for the outer boundary, and the following approximation conditions are used.

1. One can suppose that the condition $\bar{V}_\infty \cdot \bar{n}_b < 0$ is valid along the upstream boundary, where \bar{n}_b is the outward vector normal to the outer boundary and \bar{V}_∞ is the undisturbed free stream velocity, a function describing the undisturbed outer flow is accepted for the part Γ_{b1} of the outer boundary Γ_b ahead of the body, and the distribution functions of the ingoing molecules are set as the local equilibrium distribution with prescribed free stream properties. As a rule, the equilibrium distribution function for the molecules directed into the domain of the flow field is imposed for points of the free boundary surface Γ_{b1} in discretized form as follows

$$f_{\Gamma_{b1}, \sigma, \delta, \theta} = f_{M\sigma, \delta, \theta} \cdot \left[1 + (1 - \text{Pr}) \bar{c}_{\sigma, \delta, \theta} \cdot \bar{q} \left(2c_{\sigma, \delta, \theta}^2 / T - 5 \right) / (5PT/2) \right], \quad (79)$$

$$f_{M\sigma, \delta, \theta} = n / (\pi T)^{3/2} \exp \left[-c_{\sigma, \delta, \theta}^2 / T \right], \quad (80)$$

where n , T , P , \bar{U} are density, temperature, pressure and the vector of mean velocity of undisturbed gas flow.

2. For the other part Γ_{b2} of the free boundary surface Γ_b , where $\bar{V}_\infty \cdot \bar{n}_b \geq 0$ in the downstream boundary, it is assumed that there is no gradient along the outward ζ - direction for the distribution functions, which is, for incoming molecules,

$$\frac{\partial \Delta U}{\partial \zeta} = 0 \quad \text{for} \quad \bar{W} \leq 0, \quad \bar{V}_\infty \cdot \bar{n}_b \geq 0. \quad (81)$$

6. Parallel implementation of the gas-kinetic algorithm for three-dimensional complex flows

It can be shown from the present gas-kinetic algorithm that the discrete velocity ordinate method needs to be employed to discretize the molecular velocity space to cast the velocity distribution function equation into hyperbolic conservation equations with nonlinear source terms, and then the finite difference method from computational fluid dynamics is developed to numerically solve the velocity distribution functions at each of discrete velocity ordinate points. For the computation of three-dimensional flow problems, the six-dimensional array needs to be used to access the velocity distribution functions at all points in the discrete velocity space and physical space, so a great deal of computer memory is needed. It is impractical relying on current serial computer for the present gas-kinetic algorithm to attack three-dimensional complex hypersonic flows. On the other hand, it has been indicated from the computational procedure of the algorithm that the direct computation of time evolution of the velocity distribution function over the velocity space and physical space can be split up into two parts, one is that the discrete velocity distribution functions are solved by the gas-kinetic numerical schemes described in Section 4.3 independently and concurrently at every given discrete velocity ordinate point, the other is that macroscopic flow parameters at each point of the physical space are evaluated by the discrete velocity numerical integration methods described in Section 3.2. The essential and important feature of the above-mentioned computation strategy is that the calculations in the velocity space can be uncoupled from those in the physical space without any communication connection, which makes the gas-kinetic algorithm well suitable for parallelizing. To resolve the difficulty of the vast computer memory needed by the current method in solving three-dimensional complex flows and to well exploit massive power of parallel computers, the multi-processing strategy and parallel implementation technique suitable for the gas-kinetic numerical algorithm are investigated using the technique of domain decomposition, see Li (2003) and Li & Zhang (2009a,b).

The computing space of the gas-kinetic algorithm for three-dimensional flow problems relates to the six-dimensional phase space consisting of the discrete velocity space (σ, δ, θ) and physical space (i, j, k) , however, none but the velocity distribution function under consideration is defined in the six-dimensional space, other variables or modules of the algorithm are merely defined in the subspace of (i, j, k) or (σ, δ, θ) so that good data-parallel independency exists in the gas-kinetic algorithm. In practical computation, the bounds of the discrete velocity space are wide especially for hypersonic flow problems so that the number of discrete velocity grid points $N_\sigma \times N_\theta \times N_\delta$ needed could become quite large, as is specially suitable for the decomposing strategy of discrete velocity space Ω_v . For the decomposing strategy of Ω_v , as the computing quantity of the reduced summation spent on the moments of the distribution function is only under 1/5 of the whole computing workload of the algorithm, the number of parallel processors can reach up to the maximum number of $N_\sigma \times N_\theta \times N_\delta$ so that the parallel scalability of up to 1000 processors can be effectively realized. Considering that the computing process of the gas-kinetic

algorithm possesses good peculiarity of data parallel, the discrete velocity mesh (σ, δ, θ) will be distributed over the parallel processors in the block-layout manner. To enhance the parallel efficiency, the parallelized loops of σ, δ, θ are adjusted outside the loops of physical coordinates (i, j, k) , in this way, the data communication time arisen from the reduced summation during the calculation of macroscopic flow parameters is greatly reduced down to $i_{\max} \times j_{\max} \times k_{\max}$ times. It is found from the parallelizing implementation on the present gas-kinetic algorithm that the workload assigned to each processor for the numerical computation of the $f_{\sigma, \delta, \theta}$ is the $1/n$ of the total computation load, and the size of the distributed memory of each CPU is also the $1/n$ of the total amount of memory in handling the calculation of three-dimensional problems, as so makes it practicable that the problems unsolved under the limitation of serial computer memory can be solved by concurrent computation with high parallel efficiency and speed-up ratio. In this study, the parallel code adapted to the present method has been developed and applied to solve hypersonic flows around three-dimensional complex body under the parallel environment offered by the parallel multi-computer system from the Parallel Computing Research Center in Beijing.

7. Efficiency and convergence of the gas-kinetic unified algorithm

For the computational procedure of the present gas-kinetic algorithm, after the physical and velocity space are discretized and the initial condition of the flow field is set, the finite-difference scheme given in Section 4 is used to numerically solve the discrete velocity distribution functions with the use of the gas-kinetic boundary conditions, see Li (2003) and Li & Zhang (2004a,b). Then, the macroscopic flow parameters at each of points of the physical space are evaluated with the discrete velocity quadrature methods. After the above procedures are finished with the renewed correction of the velocity distribution function equation, the process of the computation of the distribution function for the new time level will be repeated. The iterative procedure is stopped when the quadratic global relative error of the flow quantities (e.g. density, flow velocity, temperature) between successive iteration steps is less than 10^{-5} .

It can be shown from the present gas-kinetic algorithm that the discrete velocity ordinate method needs to be employed to discretize the molecular velocity space to cast the velocity distribution function equation into hyperbolic conservation equations with nonlinear source terms, and then the finite difference method from computational fluid dynamics is developed to numerically solve the velocity distribution functions at each of discrete velocity ordinate points. The numerical accuracy of the gas-kinetic algorithm can be verified by the performance of the physical models, the accuracy of the discrete velocity ordinate method, the numerical precision of the finite difference scheme, and the grid convergence from the velocity space and physical space. As a model form of the Boltzmann equation, the simplified velocity distribution function equation relied by the algorithm is used to describe the molecular transport phenomena from various flow regimes. It is not exact as the original Boltzmann equation, but reliable to qualitatively describe gas flows from various regimes, even as is described in Li (2001); Li & Zhang (2007,2008,2009a,b). The accuracy of the discrete velocity ordinate method mostly rests with the relevant discrete velocity numerical quadrature technique and the size of the discrete velocity domain. Only when the number of the discrete velocity ordinate points goes up to infinity, the numerical integration may

exactly approach the original integral moment. However, the increase of the relevant discrete velocity ordinate points always brings about the need of more computer memory. Then, the discrete velocity numerical quadrature method consequentially has a finite truncation error. In the computation, the appropriate discrete velocity numerical quadrature and the discrete velocity domain for the velocity space should be selected for more accuracy by one order than the required precision of the global computation. In addition, the numerical accuracy in solving the discrete velocity distribution functions principally depends on the adoptive finite-difference scheme, here, the NND scheme is employed to discretize the convective terms in physical space which is second-order accurate in time and space with the fast convergence speed, and the second-order Runge-Kutta method is used to solve the colliding relaxation equations with the non-linear source terms. The characteristic-based boundary conditions which are in accord with the upwind nature of the interior point scheme are developed in the present algorithm. Since the interior scheme of the second-order accuracy is used, the characteristic-based second-order upwind boundary scheme may be accurate enough to retain the second-order global accuracy in the physical space. Generally, the grid is finer, and the numerical accuracy is better. It has been shown from the computing practice (Li 2003; Li & Zhang 2004a,b) that the results of the present method are not sensitive to the grid spacing in the physical space or the velocity space if only the required precision in the computation can be satisfied. The present method is very stable and robust without the limitation of the cell size, even when the grids are coarse, and the computation still is convergent rapidly to the required numerical precision. Figure 1 describes the convergent curve of the present unified algorithm in solving sphere flows, where the vertical-axis denotes the quadratic global residual error of the macroscopic flow quantities and the horizontal abscissa denotes the computing iterative times in the marched time. It can be shown from Fig.1 that the computation is very stable and convergent with the fast converging speed even though the coarse grid system is used with $25 \times 17 \times 21$ in the physical space.

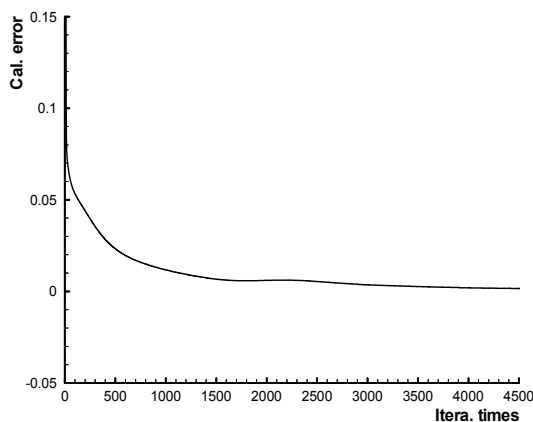


Fig. 1. Converging curve of the present algorithm

The present gas-kinetic algorithm is well competent for solving the gas flows covering various flow regimes, especially in the near-continuum and rarefied transitional flows. It has been shown from the computation that the computer time required for the present method increases as the Knudsen number decreases. In the computation of the continuum flow, as

the molecular mean collision time is generally smaller than the time step determined by the stable condition of the finite difference scheme, then the computing time step given by eq.(71) will be quite little at the magnitude of 10^{-5} , as a result, the convergent speed of the present method seems be slower than that of the Navier-Stokes solver for the continuum flow regime, especially in the computation of three-dimensional continuum flows. In addition, since a great deal of computer memory is needed to store the discrete velocity distribution functions at each of points in the discrete velocity space and physical space, the computations of the one- and two-dimensional flows can be realized in the microcomputers, however, the careful computations of three-dimensional flows with high Mach numbers have to be operated by the parallel computing on a large scale.

8. Study of gas flows covering various flow regimes

To test the accuracy and efficiency of the present numerical method in solving the gas dynamical problems from rarefied flow to continuum, the gas-kinetic numerical algorithm developed in the foregoing sections will be used to study the complex gas flows and aerodynamic phenomena with different Mach numbers including the one-dimensional shock-tube and normal shock-structure problems, the flows past two-dimensional circular cylinder and the flows past three-dimensional sphere and spacecraft shape with various Knudsen numbers, in which the one-dimensional and two-dimensional problems are studied by the serial computation, and the three-dimensional complex flows are studied by HPF parallel computing.

8.1 One-dimensional shock-tube problems with various Knudsen numbers

The unsteady shock-tube problems are usually used as one of standard examples of one-dimensional gas flows to validate the numerical methods. It can be described by the way where a diaphragm located at $x = 0.5$ divides a one-dimensional flow field into two regions, each in a constant equilibrium state at $t = 0$.

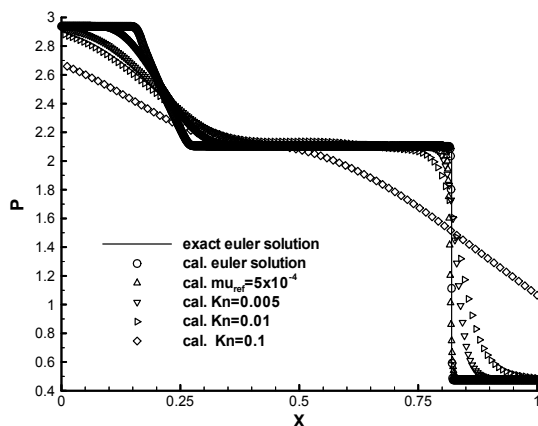
8.1.1 Unsteady Riemann shock-tube problem

The Riemann shock-tube problem, which has been numerically studied by Chu (1965); Reitz (1981); Prendergast & Xu (1993) and Xu (1998) etc. is considered with initial states:

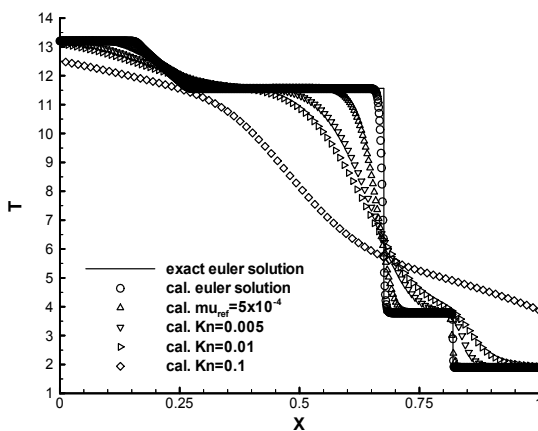
$$0.0 \leq x \leq 0.5 : \rho_L = 0.445, T_L = 13.21, U_L = 0.698,$$

$$0.5 < x \leq 1 : \rho_R = 0.5, T_R = 1.9, U_R = 0.0.$$

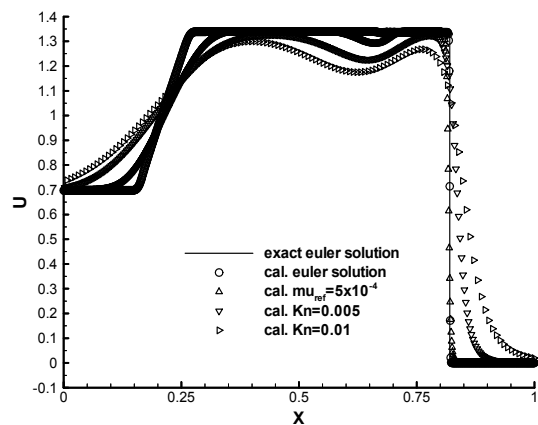
Figs.2(a)~(c) respectively show the pressure, temperature and flow velocity distribution at time $t = 0.1314$ with different Knudsen numbers from continuum to rarefied flow regimes, where the solid lines are obtained from the Riemann exact solutions of inviscid gas dynamics, the symbols (o) denote the computed Euler limit solutions of continuum flow from the gas-kinetic scheme of Eq.(46), the symbols (Δ) denote the computed results related to the continuum flow state with the viscosity coefficient of $\mu_{ref} = 0.0005$, the symbols (∇) denote the computed results related to the near-continuum flow of $Kn = 0.005$, the symbols (\triangleright) denote the computed results for the transition regime with $Kn = 0.01$, and the symbols (\diamond) denote the computed results related to the high rarefied flow of $Kn = 0.1$.



(a). Pressure



(b). Temperature



(c). Flow velocity

Fig. 2. Pressure, temperature, flow velocity distribution of Riemann shock-tube problem as a function of x with different Knudsen numbers at $t = 0.1314$.

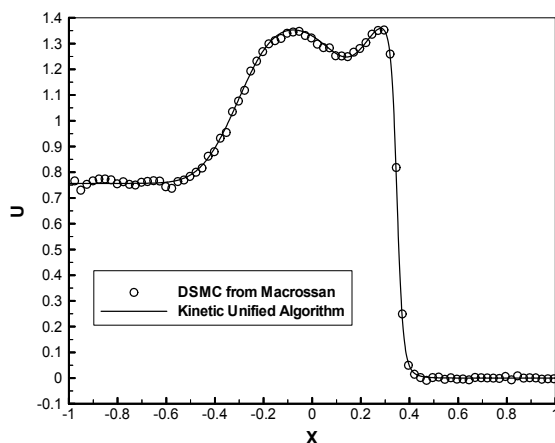


Fig. 3. Flow velocity profiles of the Riemann shock-tube flow for the case of $Kn = 0.005$ at $t = 0.13$ with the present computation and the DSMC results.

It's shown that the excellent agreement is observed between the present computed Euler limit solutions and the Riemann exact solutions. With the increase of the Knudsen number, the shock and rarefaction waves get thicker so that the rarefied flow corresponding to $Kn = 0.1$ only exists in some disturbance without the shock, contact or rarefaction waves, however, for the continuum flow related to $\mu_{ref} = 0.0005$ and the Euler limit solutions, the crisper shock and rarefaction wave profiles are given. Figs.2(a)~(c) qualitatively reveal the non-equilibrium changing process from various flow regimes that the gas flow becomes from rarefied flow to continuum along with diminishing the Knudsen number from $Kn = 0.1$ to tiny value. In particular, Fig.2(c) shows a peculiar non-equilibrium phenomenon of rarefied gas flow that the computed flow velocity near the contact discontinuity surface deviates from the exact solution of inviscid gas dynamics, the deviation becomes more prominent with the increase of Knudsen number, and the deviation gradually vanishes when the flow comes into the continuum flow. The curious and interesting deviation near the contact surface may be induced from the conservation of the total momentum in the shock tube. For rarefied flow, the molecular velocity distribution remarkably deviates from the Maxwellian distribution, and the shock and rarefaction waves become thick. To conserve the mass and momentum in the tube for any Knudsen number flow, the area under the computed velocity profiles should be the same as the area under the profiles of the exact continuum solutions, any asymmetric deviation from the continuum solutions in the shock or the expansion wave profile must necessarily appear as a deviation in the region near the contact discontinuity surface. Only when the Knudsen number becomes small and the gas comes into being the continuum flow, the velocity distribution function f approximatively or completely becomes into the Maxwellian distribution, then the velocity value should be equal in both sides of the contact discontinuity surface. To further validate this non-equilibrium phenomenon of the deviation from the equilibrium value in the flow velocity profiles, the quantitative comparison between the present computation and the DSMC results from Prof. M. Macrossan from School of Engineering in University of Queensland has been made in Fig.3. This figure presents the flow velocity distribution of the Riemann

shock-tube flow for the case of $Kn = 0.005$ at time $t = 0.13$ with two results from the present computation and the DSMC simulation, where the initial state is set as $\rho_L = 0.89$, $T_L = 6.9526$, $U_L = 0.7566$ for $-1 \leq x \leq 0$, and $\rho_R = 1$, $T_R = 1$, $U_R = 0$ for $0 < x \leq 1$. It's shown from Fig.3 that the present computation smoothly and accurately reveals the non-equilibrium deviation of rarefied gas effect in the velocity profiles, and the present computation is found in good agreement with the DSMC results.

8.1.2 SOD shock-tube problem

In order to further test the gas-kinetic numerical algorithm and show the effect of rarefaction in the shock tube flow with various Knudsen numbers, the shock-tube Sod problem is set with the initial condition,

$$0.0 \leq x \leq 0.5: \rho_L = 10.0, T_L = 1.667, U_L = 0.0,$$

$$0.5 < x \leq 1: \rho_R = 1.0, T_R = 1.333, U_R = 0.0.$$

Fig.4(a) and Fig.4(b) respectively show the computed results of density and flow velocity distribution at time $t = 0.1912$ for the cases of $Kn = 0.1, 0.01, 0.005$ and $\mu_{ref} = 0.0005$ with the comparisons between the computed Euler limit solutions from Eq.(46) and the exact solutions obtained using the Euler equations of gas dynamics of continuum flow. It can be observed that the distinct rarefaction, contact and shock wave are gradually formed along with the reduction of the Knudsen number from $Kn = 0.1$ to $Kn = 0.005$, and the computed profiles related to the continuum flow of $\mu_{ref} = 0.0005$ approach to the exact solutions of the continuum flow, especially, the computed Euler limit solutions is in excellent agreement with the Euler limit solutions of inviscid gas dynamics. There isn't shock and expansion wave, but only exists in strong disturbance for the rarefied flow related to $Kn = 0.1$.

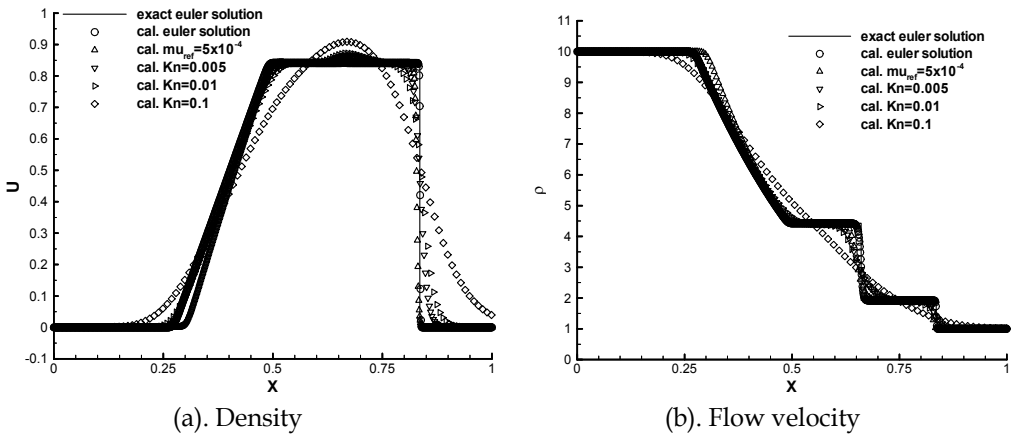


Fig. 4. Density and flow velocity distribution of shock-tube Sod problem with different Knudsen numbers at $t = 0.1912$ for the cases of the exact solution of the Euler equations (Solid line), the computed Euler limit solution (o), the computed continuum solution (Δ) related to the viscosity coefficient of $\mu_{ref} = 0.0005$, the computed results (∇) of near-continuum flow with $Kn = 0.005$, and the computed results corresponding to rarefied flow with $Kn = 0.01$ (\triangleright) and $Kn = 0.1$ (\diamond).

In Fig.4 (b), the bump phenomena of non-equilibrium deviation of rarefied gas effect can be similarly shown near the contact discontinuity surface, this bump becomes more prominent with the increase of Knudsen numbers. The above-mentioned numerical analysis demonstrates that the rarefied gas effect, viscosity and diffusivity of gas molecules are different from various flow regimes, which induces the notable difference of flow characteristic from rarefied to continuum flow regimes.

8.2 Normal shock-structure problems for different Mach numbers

The internal structure of a plane normal shock wave involves the transition from a supersonic upstream flow to a subsonic downstream flow and provides an important test case for the verification of numerical methods. Shock waves are characterized by their upstream Mach number of $M_s = U_1/a_1$, where U_1 and $a_1 = \sqrt{\gamma RT_1}$ are the flow velocity and sound speed at the upstream equilibrium state. The flow is initialized with two Maxwellian equilibrium states related by classical Rankine-Hugoniot relations. In addition, the steady state of a shock wave shows the transition between upstream and downstream flows. The profiles of shock waves take on different transport properties for strong and weak shock with different Mach numbers, in particular, the flow of shock structures with a Mach number less than two is almost in the continuum or near-continuum regime, however, the internal structure of shock waves with a higher Mach number appears as having rarefied flow character. In the following computation, the density is normalized as $(\rho - \rho_1)/(\rho_2 - \rho_1)$ in terms of the densities ρ_1 and ρ_2 in the upstream and downstream of the shock wave, and the normalized values of the temperature are defined in a similar manner. The length scale is normalized as x/λ_1 by the mean free path (λ_1) of the upstream flow, where the origin is set at the point in the profile where the density is midway between the upstream and downstream values. To describe the non-equilibrium flow properties in the interior of a normal shock wave and demonstrate the reliability of the present algorithm in solving the shock structure problems for different Mach numbers, the cases of $M_s = 1.2, 1.4, 2, 3.8, 8, 9, 10$ for argon gas have been computed with $Pr = 2/3, \gamma = 5/3$, where the properties under standard conditions for argon gas are employed from Appendix A in Bird (1994).

8.2.1 Numerical test of shock structures

Fig.5 respectively shows the computed profiles of density and temperature for the cases of $M_s = 1.2, 1.4$ and 2 corresponding to the viscosity-temperature index $\chi = 0.81$ with the comparison of the continuum Navier-Stokes solutions from Gilbarg & Paolucci (1953) and the DSMC results from Bird (1994).

As shown from Fig.5 (a), for the very weak wave of $M_s = 1.2$, the present gas-kinetic solutions are in excellent agreement with the N-S prediction and the DSMC results, however, the statistical scatter is outstanding for the DSMC method to capture such a small disturbance with the density ratio of 1.2973. It can be observed from Fig.5(b) corresponding to $M_s = 1.4$ that three sets of results generally accord well with one another, however there is a significant discrepancy in the density profiles from the predictions of the Navier-Stokes equations occurred in the downstream half of the shock wave. For the case of $M_s = 2$, two sets of results from the present algorithm and DSMC method are in good agreement, but the

N-S solutions are seriously deviated from the DSMC simulation and the present computation so that the continuum N-S predictions seem to be invalid for shock Mach numbers greater than two, which confirms studies of weak shock wave from Pham-Van-Diep, Erwin & Muntz (1991) and Bird (1984). On the other hand, it can be validated from Fig.5 that there is a prominent increase in the separation between the temperature and density profiles with the higher shock Mach numbers from $M_s = 1.2$ to $M_s = 2$, which manifests that the normal shock wave is a non-equilibrium flow with large departures from thermodynamic equilibrium.

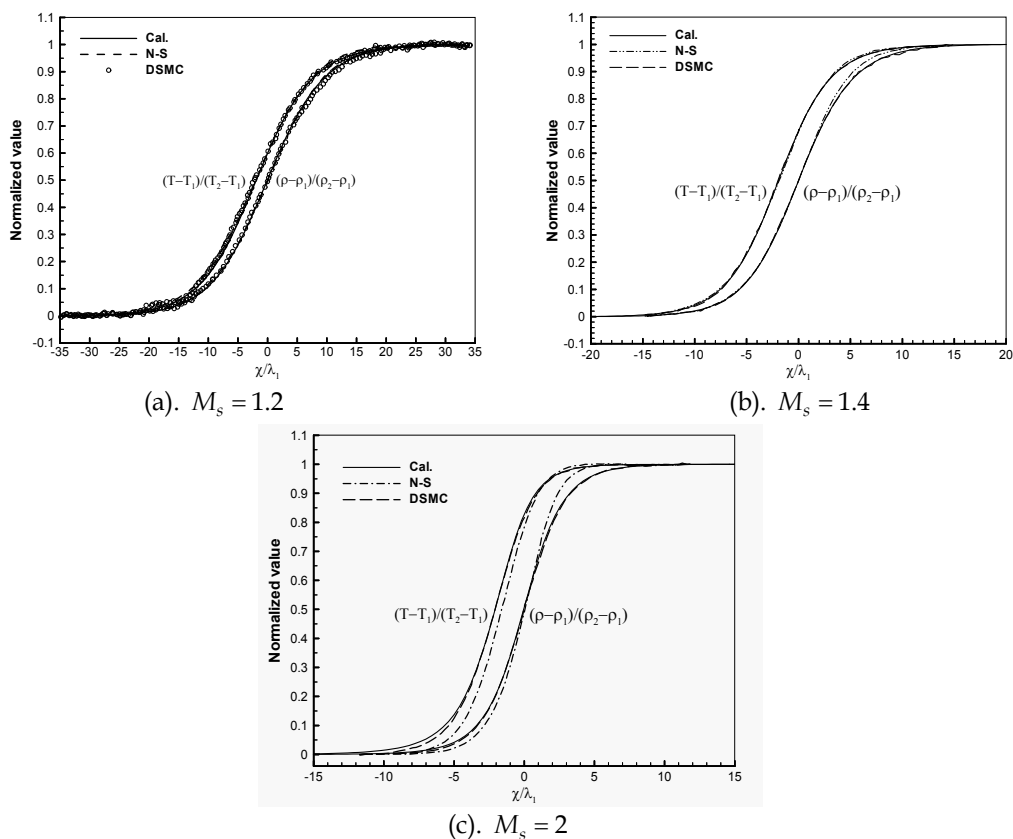


Fig. 5. Computed temperature and density profiles of shock structure with DSMC results and N-S prediction for the cases of $M_s = 1.2$, 1.4 and 2 .

Corresponding to the structures of moderate and strong shock waves for the cases of $M_s = 3.8$ and $M_s = 9$, the present computed results for $\chi = 0.72$, as well as the experiment data from Alsmeyer (1976), the DSMC simulation from Bird (1970) and the solutions of the Mott-Smith theory (Muckenfuss 1962), are shown in Fig.6, respectively.

The figure clearly shows that the present gas-kinetic solutions of the shock profiles for both the intermediate Mach number $M_s = 3.8$ and the high Mach number $M_s = 9$ are in good agreement with the experiment data and DSMC results. It can be shown that the Mott-Smith moment method fits well to describe the density distribution for the structure of shock

waves, however, it is difficult to give the temperature distribution since temperature is a more sensitive quantity as a higher moment of the velocity distribution function, and the Mott-Smith theory is better for lower than for higher Mach number flow. It can be confirmed from the present computations described in Fig.5 and Fig.6 over the whole range of Mach numbers from $M_s = 1.2$ to $M_s = 9$ that the density profiles are nearly symmetric on the point of the intermediate density between the upstream and downstream states, however, as the shock becomes stronger, some qualitative changes different from the weak shock waves appear in the strong shock profiles shown in Fig.6, that is, a marked asymmetry and overshoot phenomena has arisen in the temperature profiles. The asymmetry and prominent augment are more remarkable for higher Mach numbers from $M_s = 3.8$ to $M_s = 9$, as reveals the severe rarefied non-equilibrium effect existing in the strong shocks.

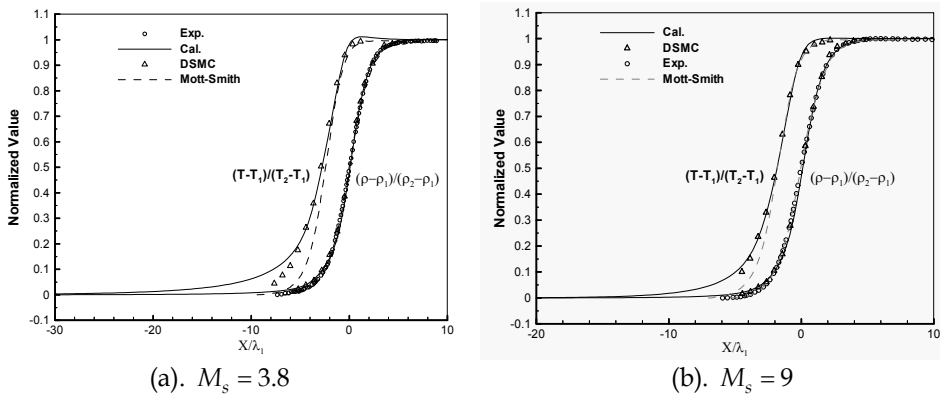


Fig. 6. Shock wave profiles of temperature and density with the comparison of the present computation and the DSMC results, Mott-Smith moments, and experimental data for the cases of $M_s = 3.8$ and 9.

8.2.2 Non-equilibrium velocity distribution in the interior of normal shock wave

In this section, the behavior of the velocity distribution function in the interior of steady normal shock wave is described by the present gas-kinetic numerical method. Figures 6~8 show the non-normalized distribution function g of Eq.(36) as the function of the velocity component of V_x/c_{mref} at different locations of $x/\lambda_1 = -20, -10, -5, 0, 10$ within the shock wave for the cases of $M_s = 1.4, 3.8$ and 8. For the inner flow of the shock wave with low Mach number of $M_s = 1.4$, it can be observed from Fig.7 that the velocity distribution almost takes on the standard form of the Maxwellian equilibrium distribution at any situations of shock structure. For the shock structure of the intermediate Mach number $M_s = 3.8$, the velocity distribution function plotted in Fig.8 is different from the velocity distribution corresponding to the weak wave of $M_s = 1.4$, especially near by the central location of $x/\lambda_1 = 0$, the velocity distribution holds a long trail of the non-equilibrium distribution in the negative direction of the axial velocity, however, when the flow is at equilibrium (upstream and downstream), the dependent relation of the velocity distribution function on the axial component of velocity almost pertains to the symmetric form of the

Maxwellian distribution, such as at locations of $x/\lambda_1 = -20, -10, -5$ closely in the front of the shock wave and $x/\lambda_1 = 10$ behind the shock wave.

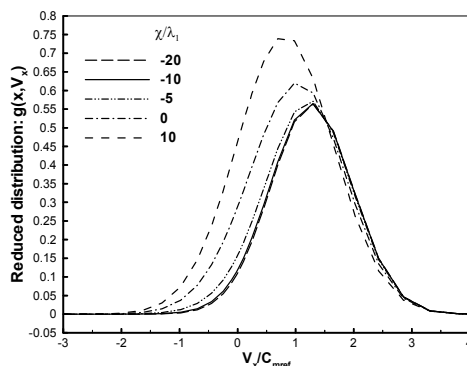


Fig. 7. Computed profiles of the axial velocity distribution function at different locations of $x/\lambda_1 = -20, -10, -5, 0, 10$ within the shock wave for $M_s = 1.4$.

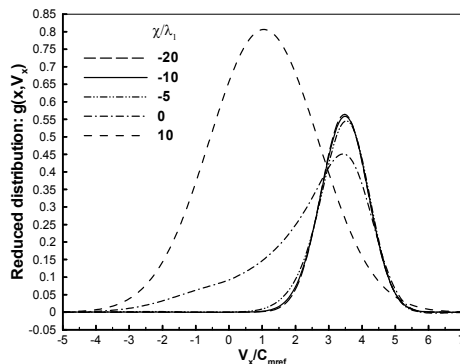


Fig. 8. Computed profiles of the axial velocity distribution function at different locations of $x/\lambda_1 = -20, -10, -5, 0, 10$ within the shock wave for $M_s = 3.8$.

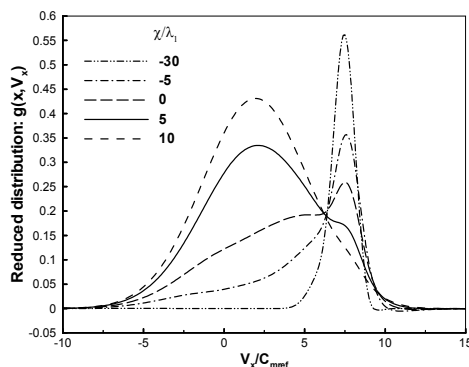


Fig. 9. Computed profiles of the axial velocity distribution function at different locations of $x/\lambda_1 = -30, -5, 0, 5, 10$ within the shock wave for $M_s = 8$.

Fig.9 exhibits the velocity distribution of g as the function of the axial component of velocity for the strong shock wave with the high Mach number of $M_s = 8$ at different locations of $x/\lambda_1 = -30, -5, 0, 5, 10$. It can be shown from Fig.9 that the molecular velocity distribution appears as the essentially non-equilibrium form across the inner flow of the shock structure, the distribution function at the center of the shock wave seems to present the complete non-equilibrium distribution with the long tail similar to bimodal distribution. The severe departure from equilibrium of the distribution function reflects the extreme non-equilibrium effect existed in the interior of the shock structure. Figs.7~9 exhibit that the gas flow becomes from the small deviation from local equilibrium to the highly non-equilibrium when the shock Mach number change from $M_s = 1.4$ to $M_s = 8$.

8.2.3 High moments of heat flux and stress within the shock structures

In order to further validate the capability of the gas-kinetic algorithm in computing the higher-order macroscopic moments of the velocity distribution function, the heat flux vector q_x and the viscous shear stress τ_{xx} from the present computation for the strong shock flow of $M_s = 8$ are shown in Figs. 10 and 11 with the comparison of the continuum Navier-Stokes prediction and the DSMC simulation in Bird (1970), where the vertical ordinate denotes the negative value of heat flux in the x -direction, the heat flux q_x has been normalized by dividing by the product of the density and the cube of the most probable velocity in the undisturbed gas, and the viscous shear stress τ_{xx} has been normalized by dividing by the product of the density and the square of the most probable velocity.

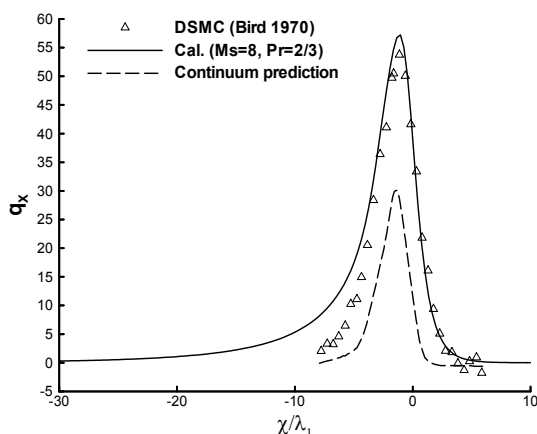


Fig. 10. Computed heat flux profiles in the interior of the shock wave with DSMC results and N-S prediction for $M_s = 8$.

From Figs.10 and 11, it can be distinctly revealed that the profiles of heat flux and viscous stress possess the remarkable asymmetric distribution based on the centre of the wave, and the agreement between the DSMC results (Symbols Δ) and the present computation (Solid line) can be obtained where some differences exist in the front of the shock wave with more prominent non-equilibrium distribution from the present computation, however, a severe deviation exists in the results of the continuum Navier-Stokes prediction (Dashed line),

especially the prediction of heat flux distribution is poor so that the macroscopic continuum theory based on the Chapman-Enskog expansion of the Maxwellian equilibrium distribution have difficulty in describing higher-order flow moments of the distribution function. To see the variation of the viscous stress and heat flux inside the shock structures at different Mach numbers, Figs.12(a) and (b) respectively illustrate the heat flux and viscous stress profiles in the x - direction for the cases of $M_s = 3.8, 9$ and 10 , where the Dash-Dot-Dot line denotes the computed results for $M_s = 3.8$, the Dashed line relates to the computed results for $M_s = 9$, and the Solid line denotes the computed results for $M_s = 10$.

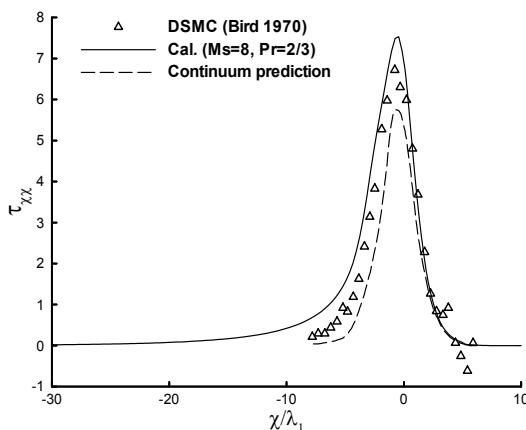


Fig. 11. Computed viscous stress profiles in the interior of the shock wave with DSMC results and N-S prediction for $M_s = 8$.

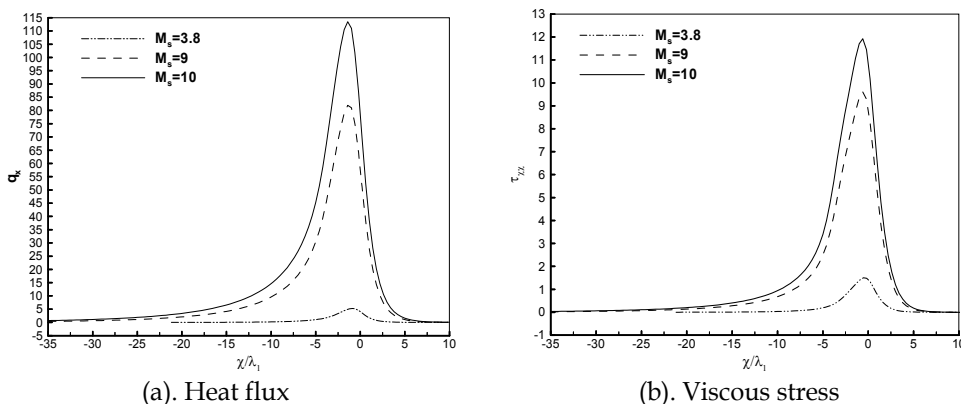


Fig. 12. Heat flux and Viscous stress distribution of the shock structure with different Mach numbers of $M_s = 3.8, 9, 10$.

It can be shown from Fig.12 that as the shock Mach number increases, the heat flux and viscous stress quantities go up rapidly, and the peak of the profiles is far from the centre of the wave with strong rarefied non-equilibrium effect. For the intermediate Mach number ($M_s = 3.8$) shock structure, the profiles of the viscous stress and heat flux only have a small deviation from the symmetric equilibrium distribution based on the center of the wave. For

the high Mach number ($M_s = 9$ and $M_s = 10$) shock flow, the prominent asymmetric distribution appears in the profiles, the significant increase in the heat flux is accentuated by a region in the front of the wave.

8.3 Two-dimensional supersonic flows past cylinder from rarefied regime to continuum

The steady supersonic flows past a circular cylinder under various free-stream Mach (M_∞) and Knudsen numbers are computed. Here, due to symmetry, only half plane on the cylinder is considered and symmetry boundary conditions were employed. The mesh system used is 71×51 (streamwise \times surface normal) in the physical space and the modified Gauss-Hermite quadrature formula with 32×32 discrete velocity ordinate points was employed. The computational results of the pressure and Mach number contours are shown in Fig.13 and Fig.14, respectively, respected to the states of $M_\infty = 1.8$, $Pr = 2/3$, $\gamma = 5/3$, the ratio $T_w / T_0 = 1$ of the wall temperature to the total temperature, $Kn = 1, 0.1, 0.03$ and $Kn = 0.001$ ($M_\infty = 4$). It's shown in Fig.13 and Fig.14 that there is no shock wave disturbing region for the fully rarefied flow related to $Kn = 1$, however, the strong disturbing domain and the dim bow shock appear in the rarefied transition flows related to $Kn = 0.1$ and $Kn = 0.01$, and for the near continuum flow of $Kn = 0.001$, the flow structures including the front bow shock, stagnation region and near wake are well captured. The smaller is the Knudsen number, the thinner and clearer is the bow shock occurring in front of the body. It's shown from Fig.13-Fig.14 that the gas flow approaches to continuum flow from rarefied transition flow while the Knudsen number is diminishing from $Kn = 1$ to $Kn = 0.001$.

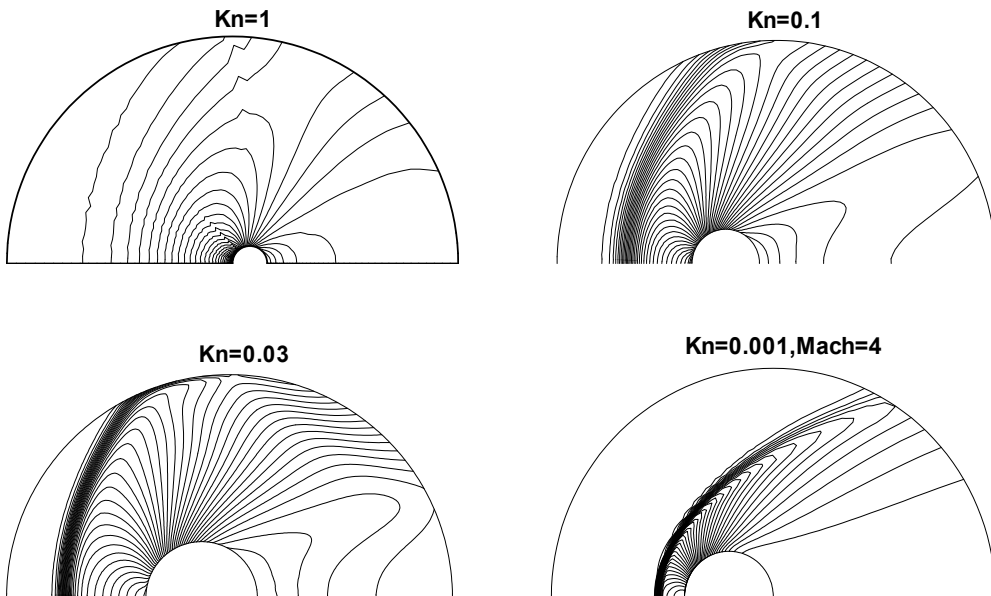


Fig. 13. Pressure contours of cylinder for supersonic flows with various Kn

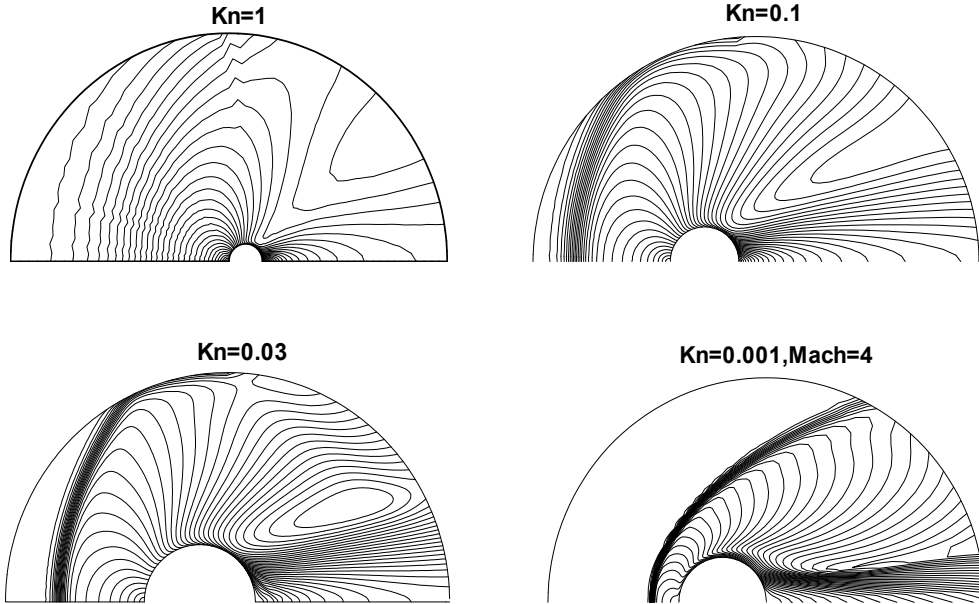


Fig. 14. Mach number contours of cylinder for supersonic flows with various Kn

To try out the computation of the present algorithm to the two-dimensional continuum flow, the case of $Kn = 0.0001$, $M_\infty = 1.8$, $Pr = 2/3$, $T_w = T_0$ and $\gamma = 5/3$ in the continuum flow regime was set with the 71×51 space cells and the modified Gauss-Hermite quadrature formula with 32×16 discrete points. The computed results of pressure, density, temperature, Mach number contours, and wake flow structures are shown in Fig.15. The flow structures including the front bow shock, the stagnation region, the recompression shock, and the wake region are captured very well. An enlarged view of the recirculation zone past the circular cylinder is scored clearly in Fig.15(e), as is only the feature of the continuum flow.

For comparison purpose, the computed results from Yang & Huang (1995b) using a Navier-Stokes solver (based on a high resolution finite-difference method) are also shown in Fig.16 for the similar flow conditions ($Re_D = 2996$, $M_\infty = 1.8$). By comparing the results shown in Fig.15 to those shown in Fig.16, it can be found that most of the flow structures are similar. The distribution of the pressure along wall surface for the state of $Kn = 0.0001$ and $M_\infty = 1.8$ is shown in Fig.17 together with the continuum theoretic data from Любимов & Русањов (1970). In Fig.17, the horizontal coordinates denote the angle along wall surface far from the stagnation line between the free-stream direction and the outward direction normal to the wall surface, the vertical coordinates denote the non-dimensional pressure, the symbols (o) indicate the continuum theoretic solutions from Любимов & Русањов (1970), the symbols (•) indicate the computed results. It's shown that the computed results agree with the continuum theoretic data. The foregoing comparisons from Fig.15-17 confirm that the present method is reliable in solving continuum gas flows.

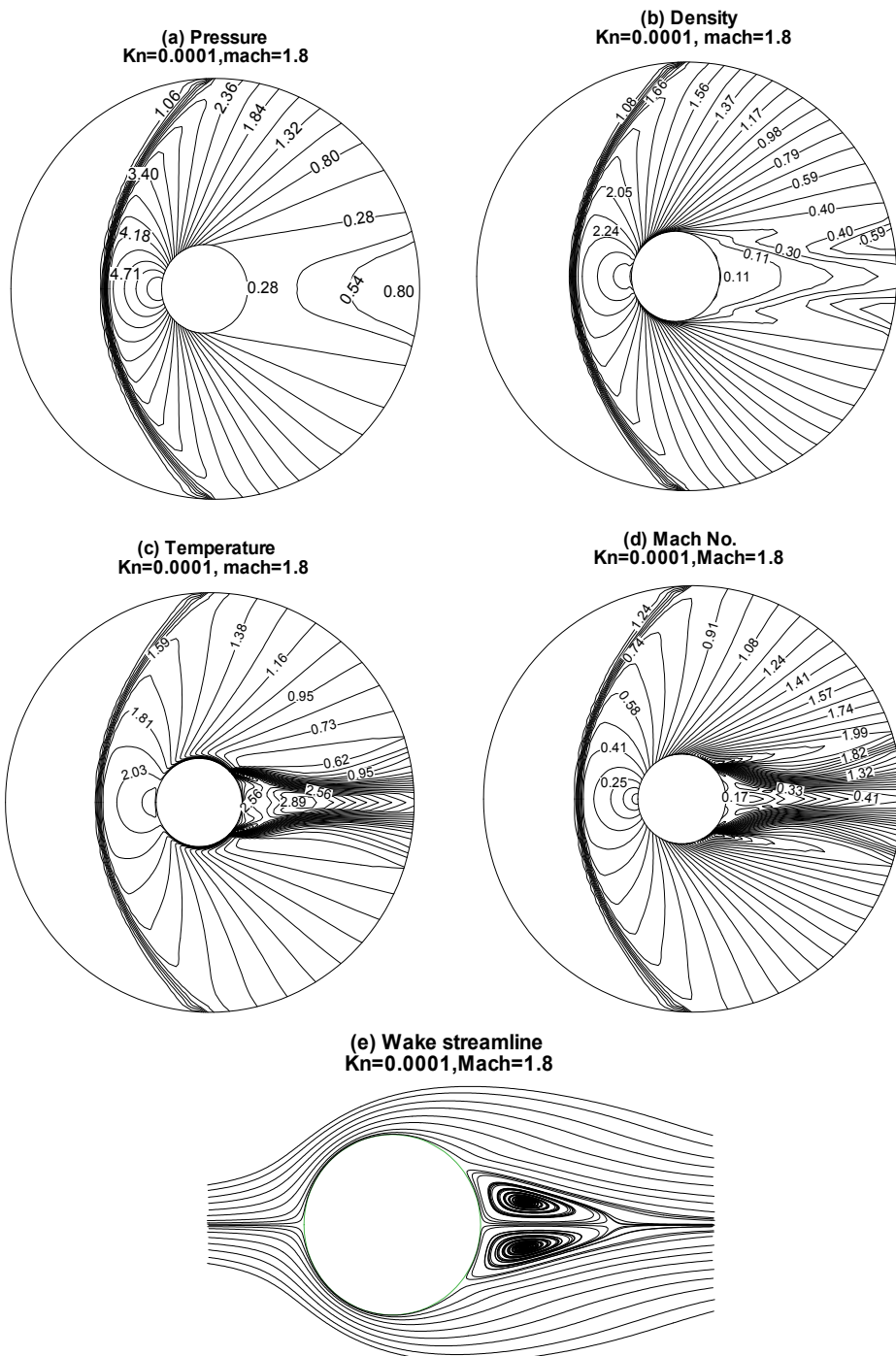


Fig. 15. Computed results of pressure, density, temperature, Mach number and wake streamline for $Kn = 10^{-4}$, $M_\infty = 1.8$.

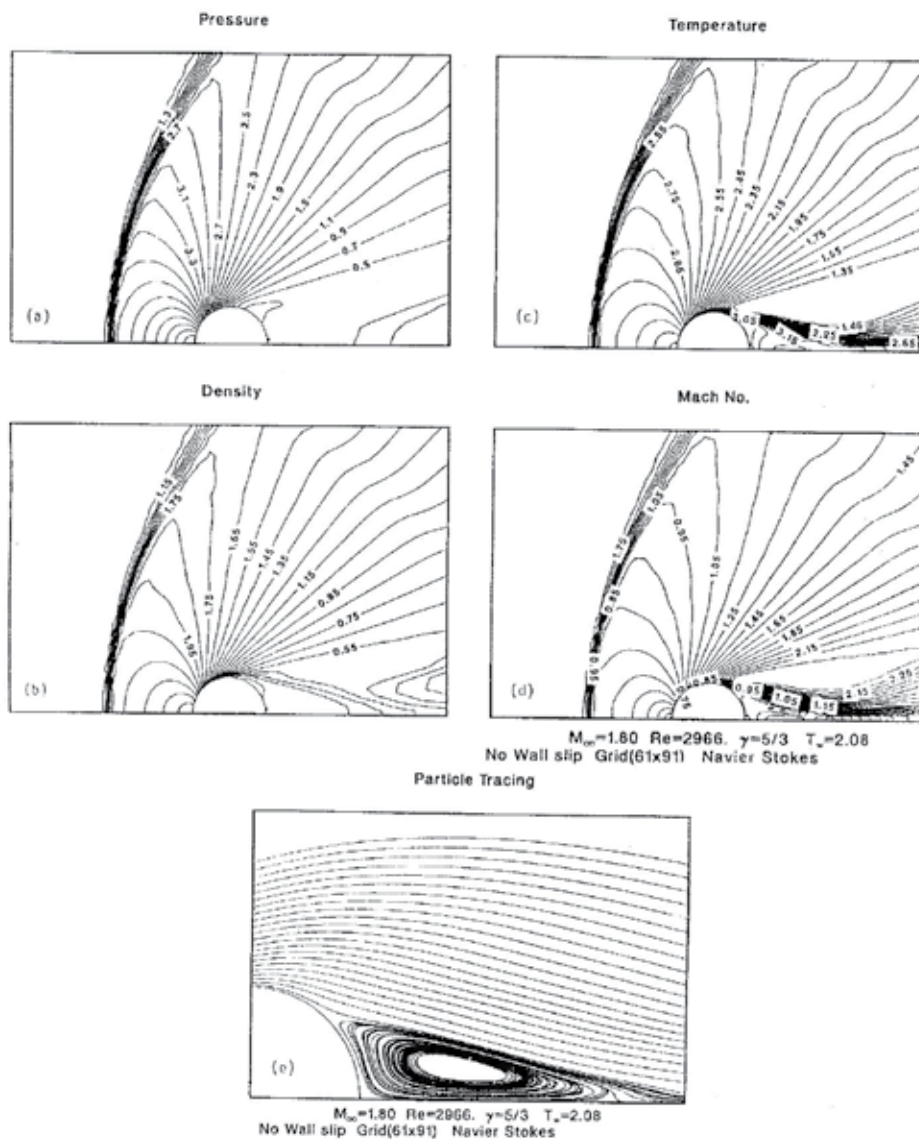


Fig. 16. Continuum Navier-Stokes solutions past cylinder for $M_\infty = 1.8$, $Re_D = 2966$ from Yang & Hsu (1992).

The stagnation line profiles of density are shown in Fig.18 together with the DSMC results from Vogenitz etc.(1968) for two Knudsen numbers ($Kn=1, 0.3$) with the states of $M_\infty = 1.8$, $Pr = 1$, $T_w/T_0 = 1$. Here, the space grid system used is 41×35 , and the modified Gauss-Hermite quadrature formula with 32×16 discrete points was employed. In Fig.18, the solid line denotes the computed $Kn=0.3$ results, the symbols (\square) denote the DSMC results of $Kn=0.3$, the dashed line denotes the computed $Kn=1$ results, and the symbols (Δ) denote the DSMC results of $Kn=1$. In general good agreement between the present computations and DSMC solutions can be observed.

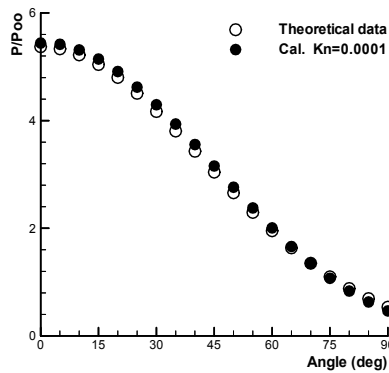


Fig. 17. Pressure distribution along surface.

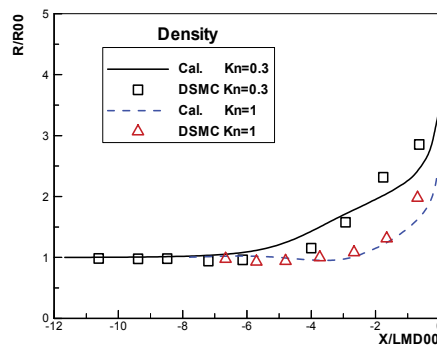


Fig. 18. Stagnation line density profiles

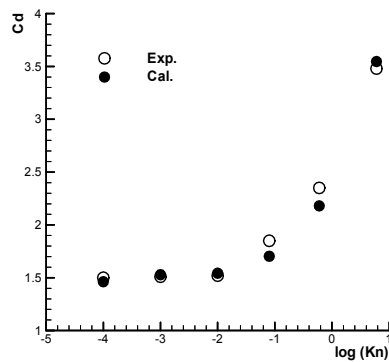


Fig. 19. Drag coefficients of cylinder

In Fig.19, the comparisons between the calculated cylinder drag coefficients and experimental data for argon gas are given for the cases of $M_\infty = 1.96$, $Pr = 2/3$, $T_w/T_0 = 0.7$, $\gamma = 5/3$, $Kn = 6, 0.6, 0.08, 0.01, 0.001$, and 0.0001 . The symbols (o) denote the experimental data from Maslach & Schaaf (1963) and the relevant continuum flow limit solution, and the symbols (●) denote the computed results. It's shown that the computed results agree with the experimental data very well.

8.4 Parallel computation of three-dimensional complex problems covering various flow regimes

It has been made out from the computation of the three-dimensional flows that the present unified algorithm requires to use six-dimensional array to access the discrete velocity distribution functions for every points in the discrete velocity space and physical space so that a great deal of computer memory needs to be occupied in solving three-dimensional flow problems. It is impractical using serial computers at the present time for the present algorithm to run the careful computation of three-dimensional complex problems. The inner concurrent peculiarity of the gas kinetic numerical method makes good opportunities for computing complex flow problems. To test the performance of the parallel program described in Section 6, the speed-up ratio and parallel efficiency are respectively shown in Fig.20 and Fig.21 from 6 to 1024 processors.

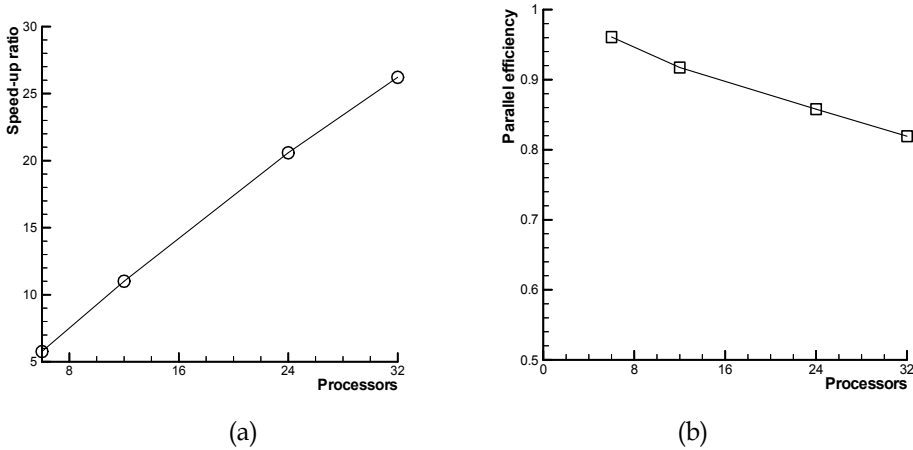


Fig. 20. (a) Speed-up ratio (b) Parallel efficiency

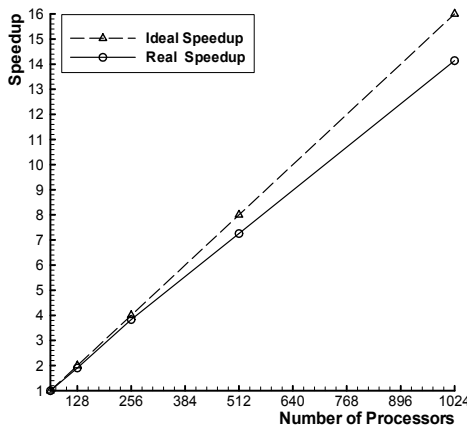


Fig. 21. Parallel speedup ratio based on 64 processors for gas-kinetic parallel algorithm

It can be shown that the unified algorithm is quite suitable for parallel calculations, and the efficiency of concurrent calculations is found rather high.

8.4.1 Three-dimensional sphere flows from rarefied to continuum regime

To investigate the nature of the three-dimensional gas flows, which covers various flow regimes, and to verify the present gas-kinetic numerical models, the basic blunt configuration exemplified by a sphere will be studied and analyzed in detail. A wide range of engineering studies associated with re-entry vehicles are concerned with the aerodynamics of low-density flows in the transitional flow regime between continuum and free-molecule flows. The determination of sphere drag has been for long time a classical problem in aerodynamics. Unfortunately, there are few reliable complete calculations, and careful comparisons between theory and experiment of sphere drag in the transitional flight regime with Reynolds numbers below about 2000. In order to resolve this state of affairs and to gain a comparison with the experimental measurements from Peter & Harry(1962), sphere flows with intermediate Mach numbers for $3.8 < M_\infty < 4.3$ are computed under the cases of ten with the sets of $Pr = 0.72$, $T_w / T_0 = 1$, $\gamma = 1.4$, $\chi = 0.75$, where the free-stream Knudsen numbers are in the range of $0.006 < Kn_\infty < 0.107$ with the corresponding free-stream Reynolds number of $50 < Re_\infty < 1000$. To save computer memory with a resource of 32 processors, the space grid points used are only $25 \times 17 \times 21$ with streamwise, circumferential and surface normal directions. The Gauss quadrature formula with the weight function $2 / \pi^{1/2} \exp(-x^2)$, described in section 3.2, is employed in the discrete velocity numerical integration method to determine macroscopic flow parameters. Table 1 illustrates the computed results of the drag coefficients of the sphere with the comparison of the experimental data from Peter & Harry(1962).

$d_s(m)^a$	0.0191	0.0381	0.0476	0.0381	0.0476	0.0476	0.0572	0.1143	0.1524	0.1523
M_∞^b	3.865	3.865	3.863	4.169	4.096	4.322	4.324	4.275	4.229	4.322
Kn_∞^c	0.1071	0.0550	0.0447	0.0350	0.0319	0.0203	0.0163	0.0094	0.0079	0.0064
$H(km)^d$	76.525	76.732	76.841	73.522	74.466	71.113	70.828	71.913	72.765	71.180
$C_{D,Exp}^e$	1.713	1.502	1.452	1.337	1.336	1.275	1.229	1.227	1.206	1.177
$C_{D,Cal}^f$	1.743	1.491	1.457	1.411	1.389	1.279	1.255	1.233	1.212	1.211
$Error(\%)^g$	1.75%	0.73%	0.34%	5.53%	3.97%	0.31%	2.12%	0.49%	0.50%	2.89%

a Diameter of sphere in meter. b Mach number of the freestream. c Knudsen number of the freestream. d Flying altitude in kilometer corresponding to d_s and Kn_∞ . e Drag coefficient from the experiment in Peter & Harry (1962). f Drag coefficient from the present computation. g The relative error.

Table 1. Drag coefficients of sphere for $3.8 < M_\infty < 4.3$, $0.006 < Kn_\infty < 0.107$ in the transition flow regime

Each column, from the second to the eleventh, respectively refers to the simulation of ten cases: the parameters including the diameter d_s of the sphere, the Mach number M_∞ and Knudsen number Kn_∞ of the freestream in the front three rows of that column are given from the experiment reference and are used as input to the simulation code, and then the values below are output. To provide physical insight concerning the flying states of transitional flows, the flying altitude $H(km)$ of the sphere relative to the given free-stream Knudsen number Kn_∞ and the diameter d_s of the sphere are deduced with the range of

$70km < H < 77km$ and also shown in the fourth row of Tab.1. It is seen from Tab.1 that the computed drag coefficients, in the sixth row, are in excellent agreement with the experimental data indicated in the fifth row with all of Knudsen numbers from $Kn_\infty = 0.1071$ to $Kn_\infty = 0.0064$. The relative differences denoted in the seventh row are of the order of 0.31%~5.53%, which indicates that the present algorithm has good capability in computing the aerodynamics of the rarefied transitional flow even though the coarse spatial mesh system is used. To analyze and compare the flow structures past the sphere with the DSMC solutions from Vogenitz etc.(1968), the flow state of $Kn_\infty = 0.03$, $M_\infty = 3.83$, $Pr = 2/3$, $T_w / T_0 = 1$, $\gamma = 5/3$, $\chi = 0.75$ from the near-continuum transitional regime is studied. Fig.22 shows the variation of temperature and flow velocity on the stagnation line in front of the body, where the vertical ordinate of $(T - T_{00}) / (T_0 - T_{00})$ and U / V_{00} respectively denote the non-dimensionalized temperature $(T - T_\infty) / (T_0 - T_\infty)$ and velocity $|\vec{U}| / V_\infty$ distribution, and the abscissa denotes the non-dimensionalized position from the stagnation point in the direction of the freestream.

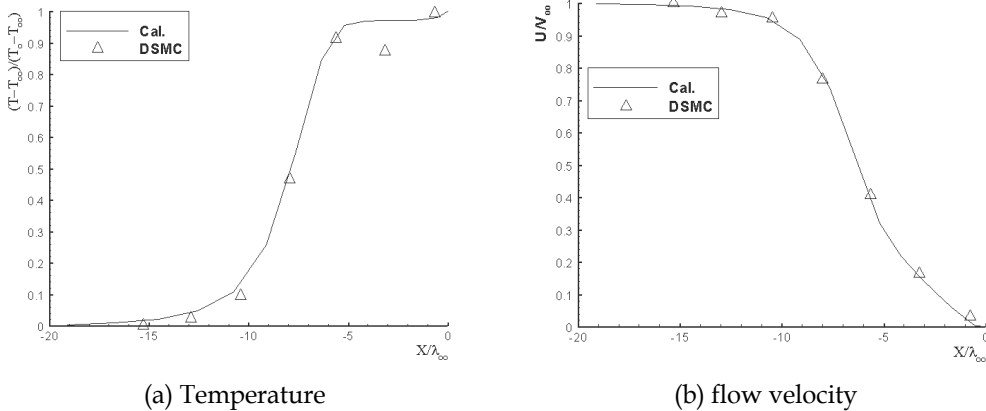


Fig. 22. Stagnation-line profiles for a sphere with $Kn_\infty = 0.03$, $M_\infty = 3.83$, where X / λ_∞ is the distance from the stagnation point of body surface. Solid line, present computations; delta, DSMC results.

As shown in Fig.22, the computed profiles agree with the DSMC results, however, some difference appears in the temperature profiles from Fig.22(a), as seems to result from the considerable statistical scatter of the DSMC results. For the comparison of the drag coefficient of the above-mentioned sphere, the present computed value of $C_{D,Cal} = 1.3749$ is in good agreement with the DSMC result of $C_{D,DSMC} = 1.4122$ with the relative deviation of 2.64%, even though the present computation is performed in quite a coarse spatial mesh system of $25 \times 19 \times 27$, as indicates that the present algorithm isn't sensitive to spatial grid division with strong and stable capability of computing convergence.

Rarefied hypersonic flows about bodies are of greatest practical interest. The hypersonic flows in the near-continuum transitional regime are difficult to treat either experimentally or theoretically over an altitude range of $40km \sim 90km$. To illustrate the capability of the present gas-kinetic numerical method for hypersonic Mach number flows and to apperceive the physical nature of hypersonic transition flows, eight cases of hypersonic flows past sphere are computed with the sets of $Pr = 0.72$, $T_w = 300k$, $\gamma = 1.4$, $\chi = 0.75$ with different

Reynolds numbers Re_2 behind the wave and Mach numbers of $M_\infty = 8.65, 8.68, 10.39, 13$ from the low-density wind tunnel test conditions of Koppenwallner & Legge (1985). Table 2 summarizes the computing parameters of the above states, where each column from the second to the ninth respectively refers to the flow state of eight cases, parameters, including the diameter d_s of the sphere, the Mach number M_∞ of the freestream and the Reynolds number Re_2 behind the normal wave in the front three rows of that column, are given from the experiment reference and are also used as input to the simulation code. The other values including the free-stream Knudsen numbers (Kn_∞), Reynolds numbers (Re_∞) and the relevant flight altitudes $H(km)$ are obtained from the computation.

$d_s(m)$ ^a	0.04	0.04	0.04	0.005	0.003	0.001	0.001	0.001
M_∞ ^b	13.00	13.00	13.00	10.39	8.68	8.65	8.65	8.65
Re_2 ^c	271.53	191.61	113.60	23.62	10.093	3.3996	0.9926	0.1985
Kn_∞ ^d	0.0050	0.0071	0.0119	0.0640	0.1616	0.4827	1.6532	8.2659
Re_∞ ^e	3943.13	2782.54	1649.69	245.32	131.11	27.07	7.90	1.58
$H(km)$ ^f	58.07	60.96	65.44	62.01	61.45	65.55	75.07	84.79

a Diameter of sphere in meters. b Mach number of the freestream. c Reynolds number behind the normal shock. d Knudsen number of the freestream related to M_∞ and Re_2 . e Reynolds number of the freestream. f Flying altitude in kilometer related to d_s and Kn_∞ .

Table 2. Computed states of hypersonic flows of $M_\infty = 8.65, 8.68, 10.39, \text{ and } 13$ past sphere for $0.005 \leq Kn_\infty \leq 8.266, 58km < H < 85km, 1.5 < Re_\infty < 3950$

It can be shown from Tab.2 that the flying altitude corresponding to the considered eight cases is in the range of $58km < H < 85km$ and the free-stream Knudsen number is in the wide range of $0.005 < Kn_\infty < 8.266$ with $1.5 < Re_\infty < 3950$ relative to the small characteristic length of sphere diameter. The computed results of the drag coefficients as a function of the free-stream Knudsen numbers are shown in Fig.23 together with the early experimental data, see Koppenwallner & Legge (1985). In this case, the abscissa (Kn) denotes the logarithm values of Kn_∞ , and the vertical ordinate denotes the drag coefficient (C_D) of sphere. In general, the agreement between the present computations and the experiments can be observed well.

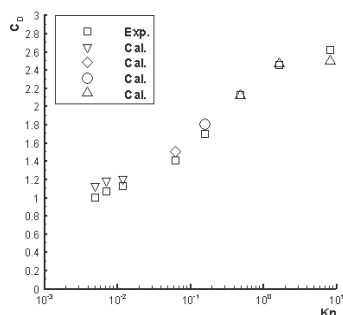


Fig. 23. Drag coefficients for hypersonic flow past a sphere. Square (\square) represents experimental data in Koppenwallner & Legge (1985); other symbols denote the present computed results, where gradient (∇) corresponds to $M_\infty = 13$, diamond (\diamond) corresponds to $M_\infty = 10.39$, circle (\circ) corresponds to $M_\infty = 8.68$, delta (Δ) corresponds to $M_\infty = 8.65$.

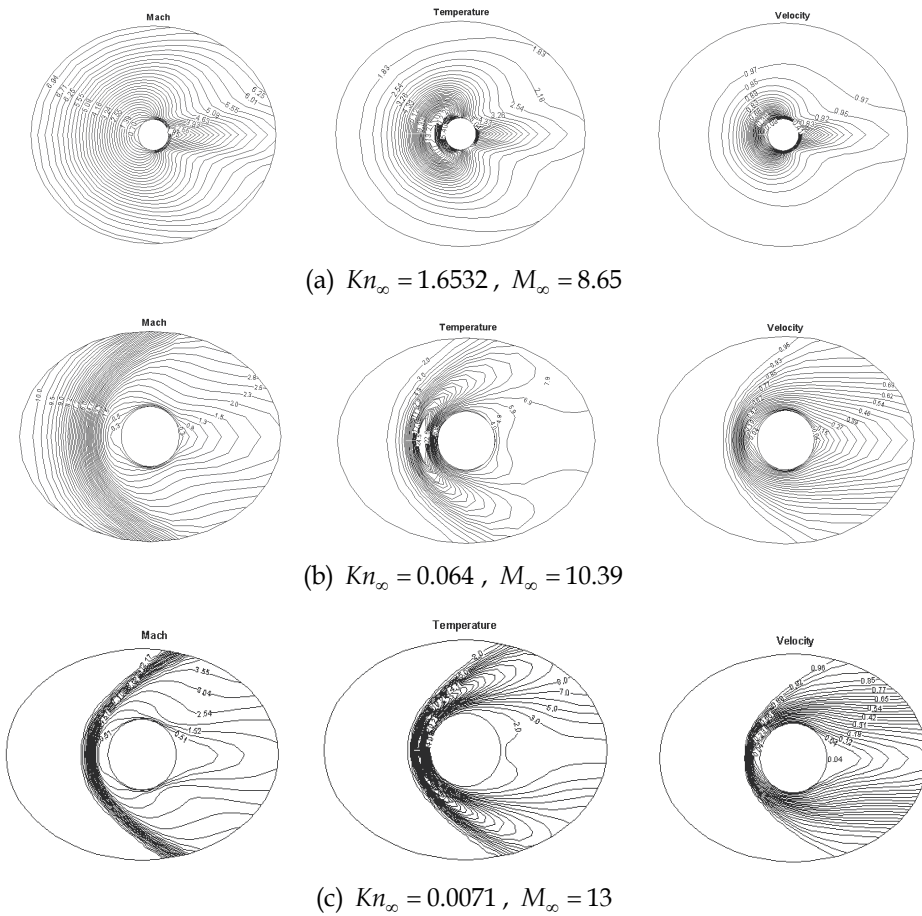


Fig. 24. Mach, temperature and flow velocity contours of hypersonic flows past sphere.

Fig.24 shows the flow field contours of Mach number, temperature and flow velocity in the symmetrical plane around the sphere corresponding to the aforementioned flow states of (a) $Kn_\infty = 1.6532, M_\infty = 8.65$, (b) $Kn_\infty = 0.064, M_\infty = 10.39$ and (c) $Kn_\infty = 0.0071, M_\infty = 13$, where the numeral on the contours including all of figures denotes the normalized magnitude of related flow parameters. It can be indicated from Fig.24 that the flow decelerates gradually as it approaches the body. The disturbed region of flow becomes wider for the full rarefied flow with higher Knudsen number of $Kn_\infty = 1.6532$. The disturbed zone of the blurry shock wave appears in front of the body for the rarefied transitional flow of $Kn_\infty = 0.064$, and in the end, a thick and explicit bow shock wave is formed so that the flow field is clearly divided into the undisturbed gas and the disturbed one in the hypersonic near-continuum flow of $Kn_\infty = 0.0071, M_\infty = 13$. Furthermore, it exists a zone of high temperature in the contours of temperature due to the cooled body with low surface temperature, the hypersonic flow around the body passes by the zenith with the supersonic expansion, and there does not form any recompression phenomena in the back of the body.

To numerically analyze the flow features and physical nature, from various flow regimes, and to test the reliability of the present gas-kinetic algorithm in solving three-dimensional flow problems from rarefied transition to continuum regime, four cases of the $M_\infty = 3$ flow past sphere with $Kn_\infty = 1, 0.1, 0.01$ and 0.0001 , $Pr = 2/3$, $T_w/T_0 = 1$, $\chi = 0.75$ are investigated by the HPF parallel computation. In this instance, the modified Gauss-type quadrature method for the discrete velocity space is employed with the $41 \times 21 \times 35$ spatial cells in the physical space. It can be shown from the flow velocity contours, in Fig.25, that for the fully rarefied flow related to $Kn_\infty = 1$, the disturbed region of flow is quite large and the flow decelerates gradually clinging to the body surface as it approaches the sphere.

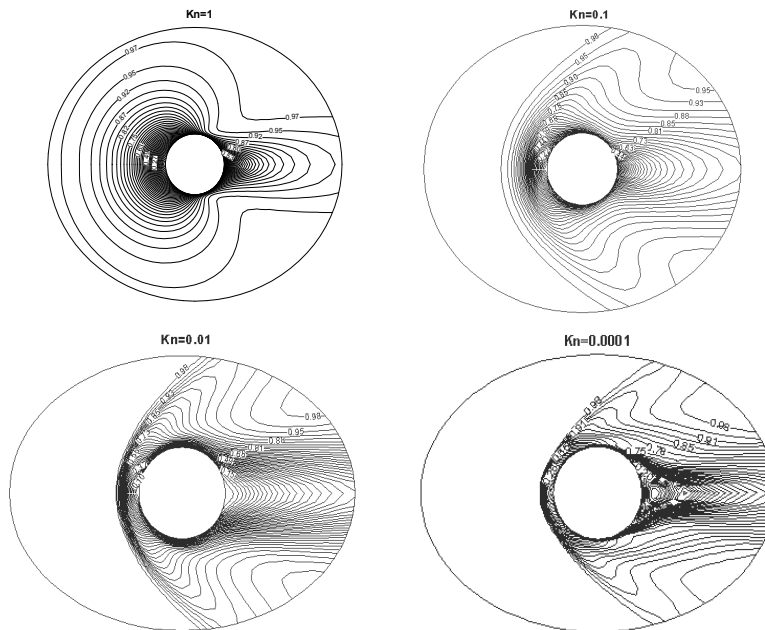


Fig. 25. Flow velocity contours in the symmetrical plane around sphere for $Kn_\infty = 1, 0.1, 0.01$ and 0.0001 with $M_\infty = 3$.

As the Knudsen number decreases from $Kn_\infty = 1$ to $Kn_\infty = 0.0001$, the disturbed region of flow becomes smaller and smaller near the body, and the strong disturbance, the dim bow shock and the recompression phenomena of the flow, appear in the rarefied transition flows related to $Kn_\infty = 0.1$ and $Kn_\infty = 0.01$. For the supersonic continuum flow of $Kn_\infty = 0.0001$, the flow structures including the thin front bow shock, the stagnation region, the accompanied weak shock wave beyond the top of sphere, the recompressing shock wave formed by the turning of the flow and the wake region are captured well. Further more, the front bow shock wave is closer to the body when the flow approaches the continuum flow from the near-continuum transition flow by diminishing the Knudsen number from $Kn_\infty = 0.1$ to $Kn_\infty = 0.0001$. The streamline structures in the symmetrical plane around sphere for the cases of $Kn_\infty = 0.1$, $Kn_\infty = 0.01$ and $Kn_\infty = 0.0001$ are shown in Fig.26, where the arrowhead on the streamline denotes the flow direction, and the symbol (Kn) in all of figures denotes the free-stream Knudsen number (Kn_∞).

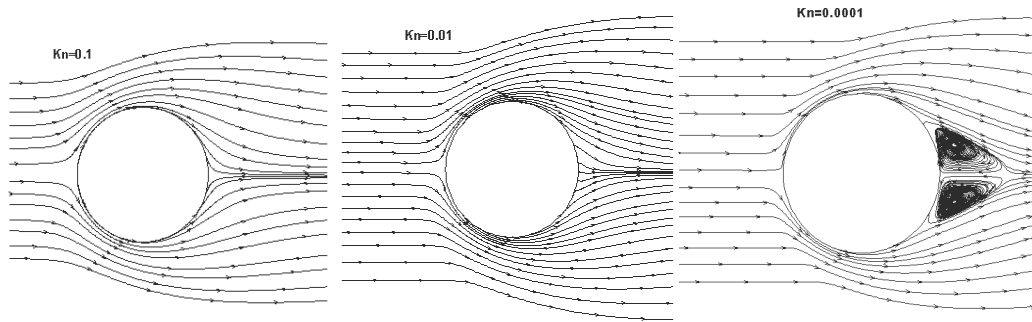


Fig. 26. Streamlines in the symmetrical plane around sphere for $Kn_\infty = 0.1, 0.01$ and 0.0001 with $M_\infty = 3$

It can be seen that for rarefied transitional flows of $Kn_\infty = 0.1$ and $Kn_\infty = 0.01$, the flow is attached to the sphere surface with strong wall slip effect of flow velocity, and there is no evidence of flow separation in the wake, as is expected for this two rarefied flow conditions of $Re_\infty = 43.67$ and $Re_\infty = 436.67$. However, for the case of $Kn_\infty = 0.0001$, the boundary layer flow separation behind the sphere is clearly visible and the separated vortices exist in the wake with well defined recirculation zones as the feature of the continuum flow. The flow details of the boundary layer separation, the separated vortex, and the near wake will be stable for this flow with the Reynolds number of $Re_\infty = 43666.96$. Fig.27 qualitatively reveals the variation of collision frequency with different position points in the interior of the flow field for various flow regimes from $Kn_\infty = 1$ to $Kn_\infty = 0.0001$. It can be illustrated that the collision frequency is entirely different with variation of spatial position in the same flow field around the body. For the completely rarefied flow of $Kn_\infty = 1$, $M_\infty = 3$, the intermolecular collisions are quite rare, the collision frequency just varies from a maximum of about 4.92 near the stagnation point to the minimum value of 10^{-3} near the back-end of the body in the wake region. However, in the rarefied transition flows of $Kn_\infty = 0.1$ and $Kn_\infty = 0.01$ or continuum flow of $Kn_\infty = 0.0001$, the gas becomes more and more dense, the collision frequency rapidly increases and the strong disturbance and bow shock wave appears. Particularly for the case of $Kn_\infty = 0.0001$, $M_\infty = 3$, the collision frequency varies from a maximum of about 71345.2 near the stagnation point to a minimum value of less than 630 in the wake. Fig.28 presents the stagnation line profiles of pressure for the cases of $Kn_\infty = 0.1$, $Kn_\infty = 0.01$ and $Kn_\infty = 0.0001$, respectively.

For the supersonic rarefied flow of $Kn_\infty = 0.1$, $M_\infty = 3$, the pressure rises smoothly and gradually and goes up to the maximum value at the sphere stagnation point as the flow approaches the sphere, which forms a quite wide region of flow disturbance. However, for the near-continuum transition flow with a low Knudsen number of $Kn_\infty = 0.01$, the region of pressure disturbances almost cuts down to half of that for the case of $Kn_\infty = 0.1$, and there exists the faint shock wave in the stagnation-line profiles. For the supersonic continuum flow of $Kn_\infty = 0.0001$, $M_\infty = 3$, the sharp variation of pressure only occurs in the very narrow disturbed domain so much as half of that in the case of $Kn_\infty = 0.01$, and a thin and clear shock wave lies in the stagnation-line near the forepart of the body. Figs.25-28 qualitatively reveal the evolving process and physical phenomena of the flows around the body from the highly rarefied to continuum flow while the Knudsen number diminishes from $Kn_\infty = 1$ to $Kn_\infty = 0.0001$.

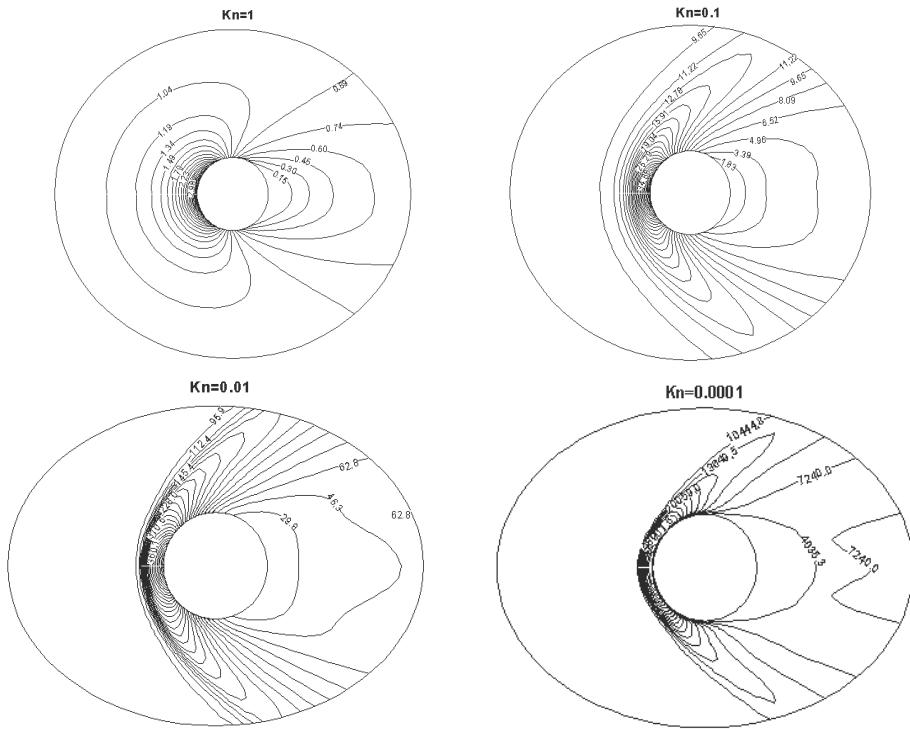


Fig. 27. Variation of collision frequency in the symmetrical plane around sphere for $Kn_\infty = 1, 0.1, 0.01$ and 0.0001 with $M_\infty = 3$.

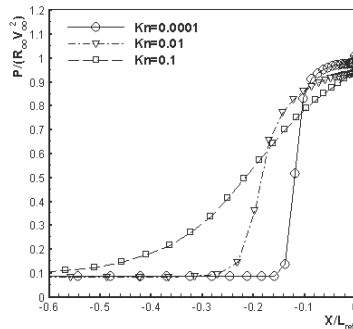


Fig. 28. Stagnation-line pressure profiles of a sphere for $Kn_\infty = 0.1, 0.01$ and 0.0001 with $M_\infty = 3$, where abscissa (X/L_{ref}) is the normalized distance from body surface based on the diameter of sphere, and coordinate ($P/(R_{00}V_{00}^2)$) denotes the normalized pressure ($p/(\rho_\infty V_\infty^2)$).

Since the present gas-kinetic algorithm explicitly evaluates the time evolution of the molecular velocity distribution function to update all the macroscopic flow variables, it is different from any other numerical approach where the macroscopic fluid equations are discretized directly, the slip boundary condition can be naturally comprised and satisfied according to the interaction model between the gas and the solid surface. To explore the

wall slip phenomena from various flow regimes and flow details along the body surface, Fig.29 illustrates the normalized tangent velocity (V_t/V_∞), that is so-called wall slip velocity, along the sphere surface in the cases of $Kn_\infty = 0.1, 0.01$ and 0.0001 .

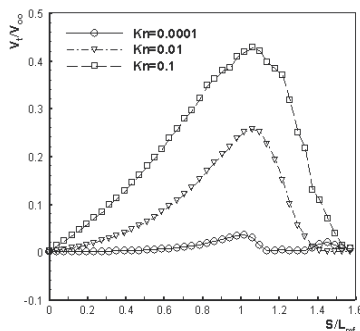


Fig. 29. Slip velocity along the tangent direction of sphere surface for $Kn_\infty = 0.1, 0.01$ and 0.0001 with $M_\infty = 3$, where abscissa (S/L_{ref}) is the normalized surface distance from the stagnation point based on the diameter of sphere, and coordinate (V_t/V_∞) denotes the normalized tangent velocity V_t/V_∞ .

For the continuum flow with the very low Knudsen number of $Kn_\infty = 0.0001$, the tangent velocity along the body surface is quite small particularly near the region of the stagnation point so that it can be neglected, which is consistent with the assumption of no slip velocity of macroscopic continuum fluid dynamics. However, even though for the case of $Kn_\infty = 0.0001$ and $M_\infty = 3$, the slip velocity still gradually goes up to the maximum value of about 0.0428 in the region far from the stagnation point, especially beyond the top of the sphere. As the free-stream Knudsen number increases along with augmentation of the effect of gas rarefaction, the magnitude of slip velocity increases rapidly. For the near-continuum flow of $Kn_\infty = 0.01$ and the rarefied transitional flow of $Kn_\infty = 0.1$, on almost all of the body surface exists wall slip phenomena except the front and back stagnation point, particularly for the case of $Kn_\infty = 0.1$, the maximum value of wall slip velocity almost reaches to half of the free-stream velocity, that is about $(V_t/V_\infty)_{max} = 0.4296$.

8.4.2 Hypersonic flow problems past spacecraft shape

In this subsection, we apply the gas-kinetic algorithm to study three-dimensional complex flows past the spacecraft shape with various Knudsen numbers and Mach numbers. Figures 30 and 31 respectively present the computed results of Mach number and pressure contours for the two cases of $Kn_\infty = 0.5$ and $Kn_\infty = 0.01$ with $M_\infty = 5$, $\alpha = 20^\circ$, $Pr = 0.72$, $T_w/T_0 = 1$, $\gamma = 1.4$. It can be shown that for the near-continuum flow of $Kn_\infty = 0.01$, the flow structures including the front bow shock, stagnation region and recompression shock are well captured, however, for the highly rarefied flow of $Kn_\infty = 0.5$, there exists the wide domain of flow disturbance around the body with no shock wave and recompression phenomena in the flow field. Figs.30 and 31 qualitatively reveal that the gas flow gradually approaches from highly rarefied flow to near-continuum flow while the Knudsen number diminishes from $Kn_\infty = 0.5$ to $Kn_\infty = 0.01$.

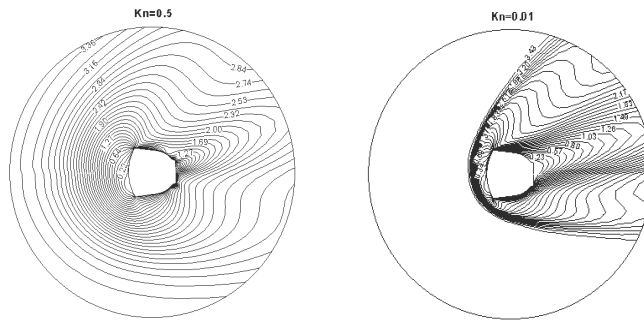


Fig. 30. Mach number contours in the symmetrical plane past spacecraft shape for $Kn_\infty = 0.5$ and $Kn_\infty = 0.01$ with $M_\infty = 5$ and $\alpha = 20^\circ$.

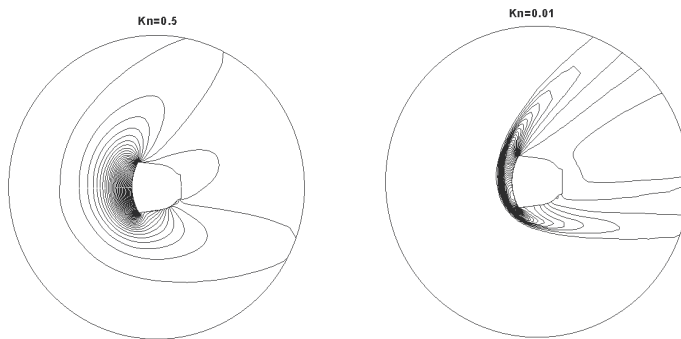


Fig. 31. Pressure contours in the symmetrical plane past spacecraft shape for $Kn_\infty = 0.5$ and $Kn_\infty = 0.01$ with $M_\infty = 5$ and $\alpha = 20^\circ$.

To reveal the variation of stagnation line profiles from various flow regimes, Fig.32 shows the flow velocity distribution past the spacecraft shape along with the stagnation line for the full rarefied flow of $Kn_\infty = 5$, $M_\infty = 4$ and the near-continuum flow of $Kn_\infty = 0.01$, $M_\infty = 4$.

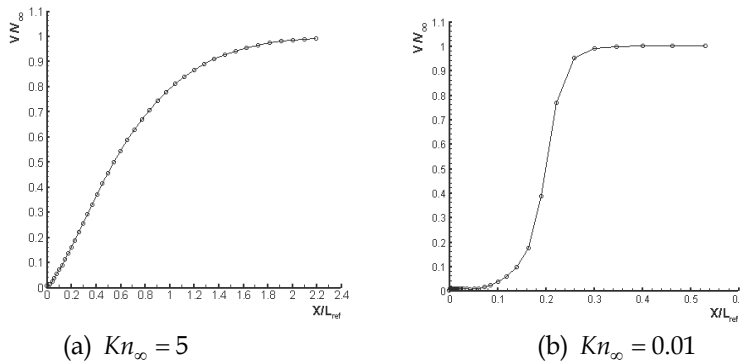


Fig. 32. Stagnation line velocity profiles from different flow regimes for $Kn_\infty = 5$ and $Kn_\infty = 0.01$ with $M_\infty = 4$, where abscissa (X / L_{ref}) is the normalized distance from the stagnation point of the body, and coordinates (V / V_∞) denote the normalized flow velocity $|\vec{u}| / V_\infty$.

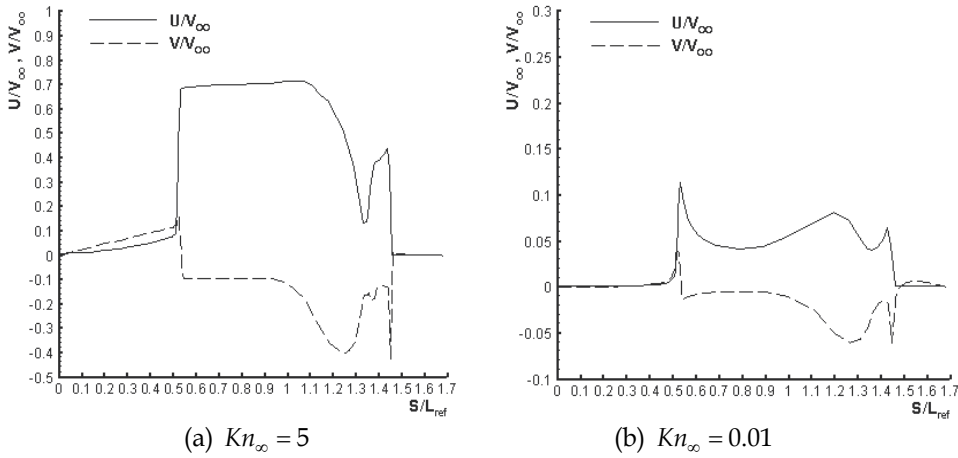


Fig. 33. Axial and lateral flow velocity distribution along the body surface in the symmetric plane around the spacecraft shape for $Kn_\infty = 5$ and $Kn_\infty = 0.01$ with $M_\infty = 4$ and $\alpha = 0^\circ$, where abscissa (S / L_{ref}) is the normalized surface distance from the forefront point of the body, and coordinates ($U / V_\infty, V / V_\infty$) denote the normalized velocity U / V_∞ and V / V_∞ in axial and lateral direction, respectively.

In the rarefied flow regime, the flow velocity smoothly and gradually increases from the zero at the stagnation point to the free-stream value near the undisturbed outer boundary for the case of $Kn_\infty = 5$, $M_\infty = 4$, which undergoes a wider region of disturbed flow up to two more times of the characteristic length of the body. However, in the near-continuum transitional flow regime, the flow velocity almost approximates to zero in the vicinity of the stagnation point, and at some distance far from the stagnation point, the flow velocity sharply goes up with distinctly jumping phenomena, then approaches the free-stream value corresponding to the near-continuum flow of $Kn_\infty = 0.01$, $M_\infty = 4$. It is indicated from Fig.32(b) that the flow phenomena of the front bow shock wave is in a very narrow disturbed domain as much as one fifth of that corresponding to the full rarefied flow of $Kn_\infty = 5$, $M_\infty = 4$. Fig.33 shows the normalized wall velocity components U/V_∞ and V/V_∞ in the symmetrical plane along the body surface from the stagnation point related to the two cases of $Kn_\infty = 5$ and $Kn_\infty = 0.01$ with $M_\infty = 4$, $\alpha = 0^\circ$. It can be revealed that the wall velocity diminishes down to zero in the vicinity of the front and back stagnation point. However, a distinct wall slip velocity exists far from the stagnation point both for the high rarefied flow of $Kn_\infty = 5$ and for the near-continuum flow of $Kn_\infty = 0.01$. While the free-stream Knudsen number increases from $Kn_\infty = 0.01$ to $Kn_\infty = 5$, the effect of gas rarefaction is greatly enhanced, which induces that the wall slip velocity increases rapidly so that the maximum value of the wall slip velocity is more than half of the free stream velocity for the case of $Kn_\infty = 5$, $M_\infty = 4$. To reveal the varying characteristic of surface heat flux covering various flow regimes, Figs.34 and 35 respectively show the distribution of heat flux $q / (\rho_\infty a_\infty^3)$ along the streamwise surface of the spacecraft for two cases of $Kn_\infty = 5$, $M_\infty = 4$, $\alpha = 0^\circ$ and $Kn_\infty = 0.001$, $M_\infty = 4$, $\alpha = 20^\circ$, where the horizontal coordinates denote the surface distance S/L_{ref} from the front end point of the body along stream direction.

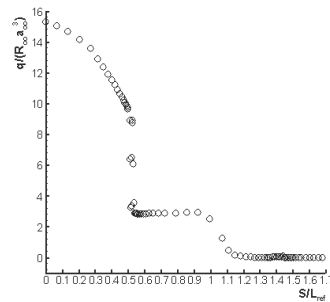


Fig. 34. Heat flux distribution along the body surface past spacecraft shape for $Kn_\infty = 5$, $M_\infty = 4$ and $\alpha = 0^\circ$, where abscissa (S / L_{ref}) is the normalized surface distance from the forefront point of the body, and coordinate $q / (R_{00} a_{00}^3)$ denotes the magnitude of normalized heat flux $q / (\rho_\infty a_\infty^3)$.

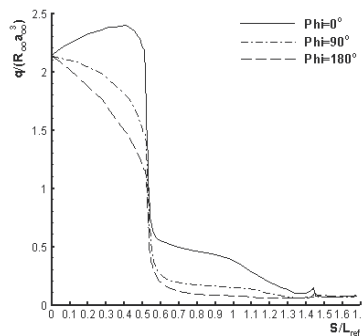


Fig. 35. Heat flux distribution along the body surface in different meridian planes of $\phi = 0^\circ, 90^\circ, 180^\circ$ past spacecraft shape for $Kn_\infty = 0.001$, $M_\infty = 4$ and $\alpha = 20^\circ$.

It can be shown from Fig.34 corresponding to the full rarefied flow of $Kn_\infty = 5$, $M_\infty = 4$, with $\alpha = 0^\circ$ that the maximum value of surface heat flux appears at the front end point of the body, the surface heat flux descends gradually along with the variation of surface curvature, and the surface heat flux goes sharply down across the top of the body, then holds the line on the whole in course of the surface of the inversion cone, ultimately drops down to zero in the leeward region of the spacecraft, which reflects the peculiarity of attaching wall flow in the high rarefied flow regime. Fig.35 shows the distribution of the surface heat flux along with the three symmetrical meridian planes of $\phi = 0^\circ, 90^\circ, 180^\circ$ related to the case of supersonic continuum flow of $Kn_\infty = 0.001$, $M_\infty = 4$, $\alpha = 20^\circ$. For the windward plane of $\phi = 0^\circ$, the surface heat flux gradually goes up and reaches the maximum value at the top of the body; however for the cross-stream plane of $\phi = 90^\circ$ and the leeward plane of $\phi = 180^\circ$ the maximum heat flux arises at the front end point of the body. In the region of the afterbody across the top of the body, the surface heat flux goes sharply down owing to the rapid expansion of the flow so that the heat flux turns to the minimum in the back end of the body. It can be validated from Figs.34 and 35 that the surface heat flux for the full rarefied flow of $Kn_\infty = 5$, $M_\infty = 4$ is six times as much as that for the near-continuum flow of $Kn_\infty = 0.001$, $M_\infty = 4$.

To numerically analyze and compare the variation of flow pattern, from rarefied to continuum regime around three-dimensional complex bodies, Fig.36 shows the vector streamline structures around the spacecraft shape for the three cases of $Kn = 5$, $Kn = 0.01$ and $Kn_\infty = 0.001$ with $M_\infty = 4$ under different angles of attack $\alpha = 0^\circ$ and $\alpha = 20^\circ$.

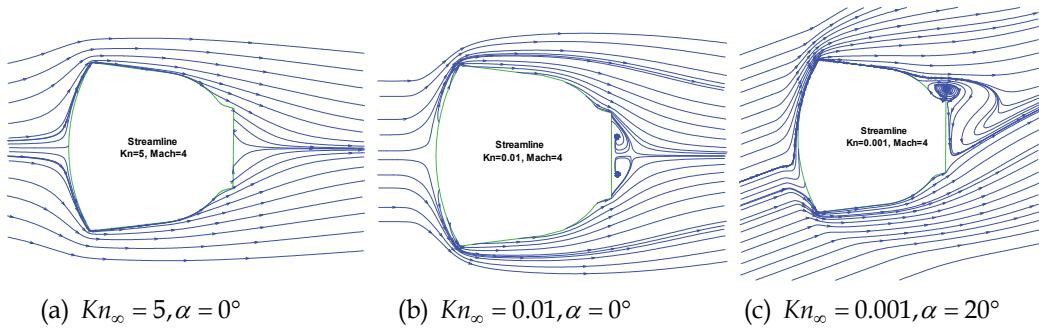
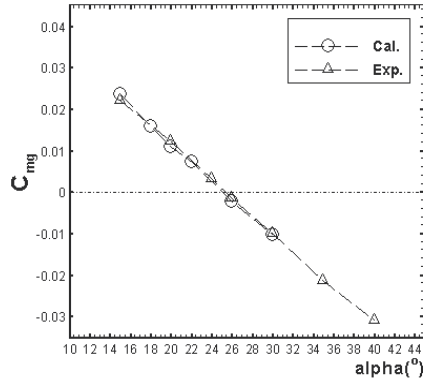
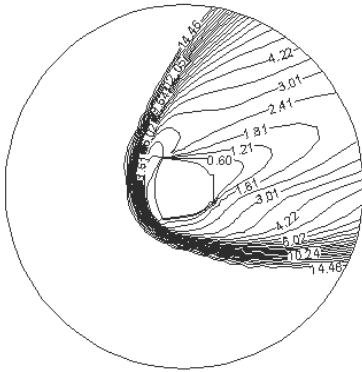


Fig. 36. Flow structures in the symmetric plane around spacecraft shape for $Kn_\infty = 5$, $Kn_\infty = 0.01$ and $Kn_\infty = 0.001$ with $M_\infty = 4$, $\alpha = 0^\circ$ and 20° .

It can be seen that for high rarefied flow of $Kn = 5$, it is completely attached to the surface with strong wall slip effect and there is no evidence of flow separation in the back of the body. However, in the near-continuum transition flow with low Knudsen number of $Kn = 0.01$, the flow separation and vortex wake structures emerge from the rearward region of the body. For the case of supersonic continuum flow with $Kn_\infty = 0.001$, $M_\infty = 4$, the boundary layer flow separation in the region of the afterbody is clearly visible and the separated vortex exists in the wake with a well defined recirculation zone, as it is only a particular feature of continuum gas flow. The above computations nicely tally with the theoretical predictions and affirm the flow phenomena and characteristic past the complex shape.

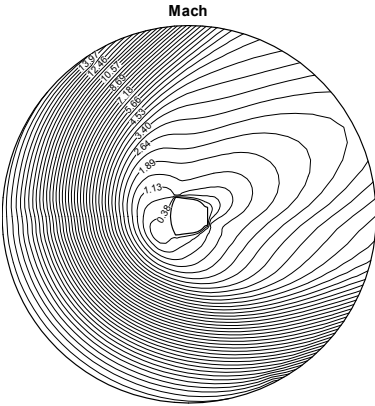
To solve the problem of the trim angle of attack of the reentry flight, we compute and study the flying states of hypersonic Mach number flow past the spacecraft shape for the flying case of $Kn_\infty = 0.0063$, $M_\infty = 15.587$, $Re_\infty = 3729.15$ and $T_w / T_0 = 0.5435$. Fig.37(a) illustrates the Mach number contours in the symmetrical plane past the body with the flying angle of attack of $\alpha = 26^\circ$. It can be observed from Fig.37(a) and the above-mentioned Fig.34, Fig.35 and Fig.30 that no recompression shock exists in the hypersonic flows around the body, which exhibits the flow characteristic remarkably different from supersonic flows, and that the hypersonic flow generally expands supersonically beyond the top of the body and remains supersonic in most of the wake region. Fig.37(b) presents the pitching moment coefficient C_{mg} relative to the centre of mass as a function of angle of attack α for the relevant flight altitude of $H = 88.34km$, where the symbols of circle (O) denote the present computed results for $\alpha = 15^\circ, 18^\circ, 20^\circ, 22^\circ, 26^\circ, 30^\circ$ and the delta (Δ) corresponds to the experimental data (Dai, Yang & Li 2004) from low-density hypervelocity wind tunnel. It can be shown from the comparison that the present computations of C_{mg} are in good agreement with the experiments, where the computed trim angle of attack is $\alpha_{Cal} = 25.06^\circ$ and the experimental measurement is about $\alpha_{Exp} = 25.39^\circ$.



(a) Mach number contours with $\alpha = 26^\circ$

(b) Pitching moment coefficient C_{mg} vs α ($^\circ$)

Fig. 37. Hypersonic flow past spacecraft shape for $Kn_\infty = 0.0063$, $M_\infty = 15.587$, $Re_\infty = 3729.15$.



9. Concluding remarks

In this study, the gas-kinetic unified algorithm is studied and developed to solve the complex flow problems in perfect gas from rarefied transition to continuum flow regimes. The present numerical method uses the non-linear Boltzmann model equation describing microscopic molecular transport phenomena as the starting point for the computation, the single velocity distribution function equation is transformed into hyperbolic conservation equations with non-linear source terms by introducing the discrete velocity ordinate method of gas kinetic theory. Based on the decoupling technique on molecular movement and collision in the DSMC method, the time-splitting method for the unsteady equation is used to split up the discrete velocity distribution function equations into the colliding relaxation equations and the convective movement equations, and then the NND finite difference scheme is employed to solve the convective equations and the second-order Runge-Kutta method is used to numerically simulate the colliding relaxation equations. The gas-kinetic boundary conditions are studied and numerically implemented by directly acting on the velocity distribution function. The discrete velocity numerical quadrature techniques for different Mach number flows are developed and applied to evaluate the macroscopic flow moments over the velocity space. After constructing the present gas-kinetic numerical scheme, the multi-processing strategy and parallel implementation technique suitable for the gas-kinetic numerical method have been studied, and then the parallel processing software has been developed for solving three-dimensional complex flow problems. To test the feasibility of the present unified algorithm in solving the gas flows from rarefied transition to continuum regime, the one-dimensional shock-tube and shock-structure problems, the flows past two-dimensional circular cylinder, and the flows around three-dimensional sphere and spacecraft shape with various Knudsen numbers and different Mach numbers are simulated. The computational results are found in high resolution of the flow fields and good agreement with the relevant theoretical, DSMC, N-S and experimental results. It has been shown from the above computations that the results of the present method aren't sensitive to the grid spacing in the physical space or the velocity space if only the computing precision be satisfied, however, the finer is the grid, the better should be the precision of the results for certain at the expense of more computing memory and time. The present method is very stable and robust without the limitation of the cell size, unlike the DSMC method which exists statistical fluctuations and requires that the grid spacing have to be less than the mean free path, in general, the computational speed of the present method seems be faster than the DSMC method in computing one- and two-dimensional problems of the rarefied flows. However, the computer time required for the present method increases as the Knudsen number decreases. In the computation of the continuum flow, as the molecular mean collision time is generally smaller than the time step determined by the stable condition of the finite difference scheme, then the convergent speed of the present method seems be slower than that of the Navier-Stokes solver for the continuum flow regime, especially in the computations of three-dimensional continuum flows.

As the possible engineering applications involving atmosphere re-entry, the gas-kinetic numerical algorithm is employed to study the three-dimensional hypersonic flows and aerodynamic phenomena around sphere and spacecraft shape covering various flow regimes by parallel computing. It's shown by the study that the parallel algorithm has not only high parallel efficiency, but also good expansibility. The concurrent calculations show that the present parallel algorithm can effectively simulate the three-dimensional complex

flows from various flow regimes. The computed results match the relevant experimental data and DSMC results well, and the peculiar flow phenomena and mechanisms from various flow regimes are explored. It can be tasted from this study that the present gas-kinetic numerical algorithm directly solving the Boltzmann simplified velocity distribution function equation may provide an important and feasible way that complex hypersonic aerothermodynamic problems and flow mechanisms from rarefied flow to continuum regimes can be effectively studied with the aid of the power of parallel computer systems. As this work is only the beginning of the study of hypersonic flows by solving the Boltzmann-type velocity distribution function, farther investigations on the kinetic models for real-gas non-equilibrium effects involving internal energy and chemical reaction, and the efficiency and improvement of the present gas-kinetic numerical method, et al. need to be studied in more detail in the future

10. References

- Abe, T. & Oguchi, H. 1977 A Hierarchy Kinetic Model and Its Applications. *Progress in Astronautics and Aeronautics*, Vol.51, edited by Potter J.I., AIAA, NewYork, 781-793.
- Alsmeyer, H. 1976 Density Profiles in Argon and Nitrogen Shock Waves Measured by the Absorption of an Electron Beam, *J. Fluid. Mech.* 74 (3), 497.
- Andries, P., Le Tallec, P., Perlat, J. & Perthame, B. 2000 The Gaussian-BGK model of Boltzmann equation with small Prandtl number, *European J. of Mechanics: B Fluids* 19 (6), 813.
- Andries, P. & Perthame, B. 2000 The ES-BGK Model Equation with Correct Prandtl Number, in *Proc. of 22nd International Symposium on Rarefied Gas Dynamics*, Sydney, Australia, edited by T. J. Bartel and M. A. Gallis (AIP Conference Proceedings, Melville, New York, 2001), Vol.585, 30-36.
- Aoki, K., Kanba, K. & Takata, S. 1997 Numerical Analysis of a Supersonic Rarefied Gas Flow past a Flat Plate. *Phys. Fluids* 9(4), 1144-1161.
- Aristov V. V. 2001 *Direct Methods for Solving the Boltzmann Equation and Study of Nonequilibrium Flows*. Fluid Mechanics and its Applications, Vol.60, Kluwer Academic Publishers.
- Bhatnagar, P. L., Gross, E. P. & Krook, M. 1954 A Model for Collision Processes in Gases. I. Small Amplitude Processes in Charged and Neutral One-Component Systems. *Phys. Rev.* 94, 511.
- Bird, G. A. 1970 Aspects of the Structure of Strong Shock Waves. *Phys. Fluids* 13(5), 1172-1177.
- Bird, G. A. 1994 *Molecular Gas Dynamics and the Direct Simulation of Gas Flows*. Clarendon Press, Oxford.
- Boltzmann L. 1872 *Sber. Akad. Wiss Wien. Abt. II* 66, 275.
- Brittin W. E. 1967 *Lectures in Theoretical Physics: Kinetic theory*, Volume IX C, Gordon and Breach, Science publishers, New York / London / Paris.
- Celenligil, M. C., Moss, J. N. & Blanchard, R. C. 1991 Three-Dimensional Rarefied Flow Simulations for the Aeroassist Flight Experiment Vehicle. *AIAA Journal* 29(1), 52-57.

- Cercignani, C. & Tironi G. 1967 Nonlinear heat transfer between two parallel plates at large temperature ratios. *Rarefied Gas Dynamics*, edited by Brundin C. L., Academic Press, New York, Vol.1, 441-453.
- Cercignani, C. & Lampis M. 1971 Kinetic models for gas-surface interactions, *Transport Theory and Stat. Phys.*, 1, 101-114.
- Cercignani, C. 1984 *Kinetic Theories and the Boltzmann Equation*. Lecture Notes in Mathematics, Springer-Verlag, Berlin.
- Cercignani C. 1994 *The Mathematical Theory of Dilute Gases*, Springer-Verlag, New York.
- Cercignani, C. 2000 *Rarefied Gas Dynamics: from Basic Concepts to Actual Calculations*. Cambridge University Press, Cambridge.
- Chapmann, S. & Cowling, T. G. 1970 *The Mathematical Theory of Non-Uniform Gases*. 3rd ed. Cambridge Univ. Press.
- Chu, C. K. 1965 Kinetic-Theoretic Description of the Formation of a Shock Wave. *Physics of Fluids* 8(1), 12-22.
- Dai, J. W., Yang, Y. G. & Li, X. G. 2004 Investigation of Rarefied Gas Aerodynamics of Spacecraft Shape in low density wind tunnel, *Tech. Rep. No. S423.15*, Hypersonic Aerodynamics Institute, China Aerodynamic Research and Development Centre.
- Gilbarg, D. & Paolucci, D. 1953 The structure of shock waves in the continuum theory of fluids. *J. Rat. Mech. Anal.* 2, 617-642.
- Grad 1949 On the kinetic theory of rarefied gases. *Commun. Pure Appl. Math.* 2, 331-407.
- Golub, G. H. & Welsch, J. 1981 Calculation of Gauss Quadrature Rules, *Tech. Rep. No. CS81*, Computer Science Dept., Stanford University.
- Henrici P. 1958 The Quotient-Difference Algorithm. *Nat. Bur. Standards Appl. Math. Series* 49, 23-46.
- Holway Jr., L. H. 1963 Approximation Procedures for Kinetic Theory. Ph.D. Thesis, Harvard.
- Holway Jr., L. H. 1966 New Statistical Models for Kinetic Theory, *Methods of Construction*. *Phys. Fluids* 9(9), 1658.
- Huang, A. B. & Giddens, D. P. 1967 The Discrete Ordinate Method for the Linearized Boundary Value Problems in Kinetic Theory of Gases. *Proc. of 5th International Symposium on Rarefied Gas Dynamics*, edited by Brundin C. L., New York, Vol.1, 481-486.
- Ivanov, M. S. & Gimelshein, S. F. 1998 Computational Hypersonic Rarefied Flows. *Annu. Rev. Fluid Mech.* 30, 469-505.
- Kim C. & Jameson, A. 1998 A Robust and Accurate LED-BGK Solver on Unstructured Adaptive Meshes. *J. Comput. Phys.* 143(2), 598.
- Kolobov, V.I., Arslanbekov, R.R., Aristov, V.V., Frolova, A.A. & Zabelok, S.A. 2007 Unified solver for rarefied and continuum flows with adaptive mesh and algorithm refinement. *J. Comput. Phys.* 223, 589-608.
- Kogan, M. N. 1958 On the Equations of Motion of a Rarefied Gas. *Appl. Math. Mech.* 22, 597.
- Kopal, Z. 1955 *Numerical Analysis*, Chapman & Hull Ltd., London
- Koppenwallner, G. & Legge, H. 1985 Drag of Bodies in Rarefied Hypersonic Flow. *AIAA Paper 85-0998*, Progress in Astronautics and Aeronautics: Thermophysical Aspects of Re-entry Flows, Vol.103, edited by Moss J.N. & Scott C.D., New York, 44-59.

- Kuščer I., Možina, Krizanac F. 1974 The Knudsen model of thermal accommodation. In Rarefied Gas Dynamics, edited by Dini et al., Vol.I, 97-108, Editrice Tecnico-Scientifica, Pisa.
- Li, Z. H. & Xie, Y. R. 1996 Technique of Molecular Indexing Applied to the Direct Simulation Monte Carlo Method. *Proc. of 20th International Symposium on Rarefied Gas Dynamics*, edited by C. Shen, Beijing: Peking University Press, 205-209.
- Li, Z.H. & Zhang, H.X. 2000 Study on Gas Kinetic Algorithm for Flows from Rarefied Transition to Continuum, *Proc. of 22nd International Symposium on Rarefied Gas Dynamics*, ed. by Bartel T.J. and Gallis M.A., Sydney, Australia, Jul. 9-14, Vol.585, 628-636.
- Li, Z. H. 2001, *Study on the Unified Algorithm from Rarefied Flow to Continuum*, Ph. D. thesis, China Aerodynamics Researchment and Development Center.
- Li, Z. H. & Zhang, H. X. 2003 Numerical Investigation from Rarefied Flow to Continuum by Solving the Boltzmann Model Equation. *Int. J. Numer. Meth. Fluids*, 42, 361-382.
- Li, Z.H. 2003 Applications of gas kinetic unified algorithm for flows from rarefied transition to continuum, Post-doctor Dissertation, Beijing: Tsinghua University.
- Li, Z. H. & Zhang, H. X. 2004a Study on Gas Kinetic Unified Algorithm for Flows from Rarefied Transition to Continuum. *J. Comput. Phys.*, 193(2), 708-738.
- Li, Z. H. & Zhang, H. X. 2004b Gas kinetic algorithm using Boltzmann model equation, *Computers and Fluids*, 33, 967-991.
- Li, Z. H. & Zhang, H. X. 2007 Gas-Kinetic Numerical Method Solving Mesoscopic Velocity Distribution Function Equation, *Acta Mechanica Sinica*, 23(3), 121-132.
- Li, Z. H. & Zhang, H. X. 2008 Gas-kinetic description of shock wave structures by Boltzmann model equation, *Inter. J. of Comput. Fluid Dyna.*, 22(9), 623-638.
- Li, Z. H. & Zhang, H. X. 2009a Gas-kinetic numerical studies of three-dimensional complex flows on spacecraft re-entry. *J. Comput. Phys.*, 228(2), 1116-1138.
- Li, Z. H. & Zhang, H. X. 2009b Study on the unified algorithm for three-dimensional complex problems covering various flow regimes using Boltzmann model equation, *Science in China (Series G)*, 52(1), 124-138.
- Macrossan, M.N. & Oliver, R. I. 1993 A kinetic theory solution method for the Navier-Stokes equations. *Int. J. Numer. Meth. Fluids*, 17, 177.
- Maslach, G. J. & Schaaf, S. A. 1963 Cylinder Drag in the Transition from Continuum to Free-Molecule Flow, *Phys. Fluids* 16(3), 315-321.
- May, G., Srinivasan, B. & Jameson, A. 2007 An improved gas-kinetic BGK finite-volume method for three-dimensional transonic flow. *J. Comput. Phys.* 220, 856-878.
- Mieussens, L. 2000 Discrete-velocity models and numerical schemes for the Boltzmann-BGK equation in plane and axisymmetric geometries. *J. Comput. Phys.* 162(2), 429-466.
- Morinishi, K. & Oguchi H. 1984 A Computational Method and its Application to Analyses of Rarefied Gas Flows. *Proc. of 14th International Symposium on Rarefied Gas Dynamics*, Tsukubva, Japan, edited by H. Oguchi, Tokyo:University of Tokyo Press, 1, 149-158.
- Moschetta, J.M. & Pullin D. 1997 A Robust Low Diffusive Kinetic Scheme for the Navier-Stokes/Euler Equations. *J. Comput. Phys.* 133, 193-204.
- Muckenfuss, C. 1962 Some Aspects of Shock Structure According to the Bimodal Model, *Phys. Fluids* 5, 1325-1336.

- Nocilla S. 1961 On the interaction between stream and body in free-molecule flow. In *Rarefied Gas Dynamics*, edited by L. Talbot, 169, Academic Press, New York.
- Park, D. C. 1981 *The Kinetic Theory of Gases with Applications in Rarefied Gas Dynamics*. University of Strathclyde, Scotland.
- Peter, P. W & Harry, A. 1962 Wind Tunnel Measurements of Sphere Drag at Supersonic Speeds and Low Reynolds. *J. of Fluid Mechanics* 10, 550-560.
- Pham-Van-Diep, G.C., Erwin, D.A. & Muntz, E.P. 1991 Testing Continuum Descriptions of Low Mach Number Shock Structures, *J. Fluid Mech.*, 232, 403-413.
- Prendergast, K. H. & Xu, K. 1993 Numerical hydrodynamics from gas-kinetic theory. *J. Comput. Phys.* 109, 53.
- Reitz, R. D. 1981 One-Dimensional Compressible Gas Dynamics Calculations Using the Boltzmann Equation. *J. Comput. Phys.* 42, 108-123.
- Riedi, P. C. 1976 *Thermal physics: An Introduction to Thermodynamics, Statistical Mechanics and Kinetic Theory*. The Macmillan Press Ltd., London.
- Roger, F. & Schneider J. 1994 Deterministic Method for Solving the Boltzmann Equation. *Rarefied Gas Dynamics: Theory and Simulations*, edited by Shizgal B. & Weaver D. P., AIAA, Vol.159, 335-343.
- Segal, B. M. & Ferziger, J. H. 1972 Shock-Waves Structure Using Nonlinear Model Boltzmann Equations. *Phys. Fluids* 15, 1233.
- Shakhov, E. M. 1968 Generalization of the Krook Kinetic Relaxation Equation. *Fluid Dynamics* 3(1), 95.
- Shakhov, E. M. 1984 Kinetic Model Equations and Numerical Results. *Proc. of 14th International Symposium on Rarefied Gas Dynamics*, edited by Oguchi H., Tokyo: University of Tokyo Press, Vol.1, 137-148.
- Sharipov F. 2003 Hypersonic Flow of Rarefied Gas Near the Brazilian Satellite During its Re-entry into Atmosphere. *Brazilian Journal of Physics* 33(2), 398-405.
- Shizgal, B. 1981 A Gaussian Quadrature Procedure for Use in the Solution of the Boltzmann Equation and Related Problems. *J. Comput. Phys.* 41, 309-328.
- Tan Z. & Varghese P. 1994 The Δ - ϵ Method for the Boltzmann Equation. *Journal of Computational Physics* 110, 327-340.
- Tcheremissine F. G. 1989 Advancement of the Method of Direct Numerical Solving of the Boltzmann Equation. *Rarefied Gas Dynamics: Theoretical and Computational Techniques*, edited by Muntz E. P. & Campbell D. H., AIAA, Vol.118, 343-358.
- Titarev V. A. & Shakhov E. M. 2002 Heat Transfer and Evaporation from a Plane Surface into a Half-Space upon a Sudden Increase in Body Temperature. *Fluid Dynamics* 37(1), 126-137.
- Tsien, H. S. 1946 Superaerodynamics, Mechanics of Rarefied Gases. *J. Aeronautical Science* 13(12), 653-664.
- Vincenti, W. G. & Kruger, C. H. 1965 *Introduction to Physical Gas Dynamics*. Wiley, New York.
- Vogenitz, F. W., Bird, G. A., Broadwell, J. E. & Rungaldier H. 1968 Theoretical and Experimental Study of Rarefied Supersonic Flows about Several Simple Shapes. *AIAA Journal* 6(12), 2388-2394.
- Welander, P. 1954 On the Temperature Jump in a Rarefied Gas. *Ark. Fys.* 7, 507.

- Xu, K. 1998 *Gas-Kinetic Schemes for Unsteady Compressible Flow Simulations*, 29th CFd Lecture Series 1998-03, Von Karman Institute for Fluid Dynamics, Lecture Series, Belgium, Feb.23-27.
- Xu, K., Mao, M. & Tang, L. 2005 A multidimensional gas-kinetic BGK schemes for hypersonic viscous flow. *J. Comput. Phys.* 203, 405-421.
- Xu K. 2001 A Gas-kinetic BGK Schemes for the Navier-Stokes Equations and Its Connection with Artificial Dissipation and Godunov Method. *J. Comput. Phys.* 171, 289-335.
- Xu, K. & Li, Z. H. 2004 Microchannel flow in the slip regime: gas-kinetic BGK-Burnett solutions. *J. Fluid Mech.* 513, 87-110.
- Yang, J.Y. & Hsu, C.A. 1992 High Resolution, Nonoscillatory Schemes for Unsteady Compressible Flows, *AIAA J.* 30, 1570-1575.
- Yang, J. Y. & Huang, J. C. 1995a Rarefied Flow Computations Using Nonlinear Model Boltzmann Equations. *J. Comput. Phys.* 120, 323-339.
- Yang, J. Y. & Huang, J. C. 1995b Numerical solution of the nonlinear model Boltzmann Equation. *Proc. R. Soc. Lond. A* 448, 55-77.
- Zhang, H. X. & Zhuang F. G. 1992 NND Schemes and Their Application to Numerical Simulation of Two- and Three-Dimensional Flows. *Advances in Applied Mechanics* 29, 193.
- Любимов, А. Н. and Русафов В. В. 1970, ТЕЧЕНИЯ ГАЗА ОКОЛО ТУПЫХ ТЕЛ, Часть II, ИЗДАТЕЛЬСТВО «НАУКА», p.32-33, МОСКВА, (1970).

Aerodynamic Disturbance Force and Torque Estimation For Spacecraft and Simple Shapes Using Finite Plate Elements – Part I: Drag Coefficient

Charles Reynerson
*The Phoenix Index Inc,
United States of America*

1. Introduction

Aerodynamic properties, such as the drag and lift coefficients (C_D & C_L), are key parameters for Low Earth Orbiting (LEO) spacecraft when determining lifetime propellant consumption, predicting deorbit maneuvers, and determining aerodynamic disturbance torque. The drag and lift coefficients for complex shapes is difficult to compute analytically, so a method was developed to determine values these coefficients using a finite plate element method. By superimposing the effect of individual elements, the drag and lift coefficients for a complex object can be determined. Characteristics of the flat plate element are modeled using either experimental data or theoretical models based on hypersonic gas-surface interactions.

It is the goal of this chapter to show examples of how the satellite drag coefficient can be determined using a finite plate element model. This information can then be used to help determine spacecraft trajectories and aerodynamic disturbance torques as a function of the spacecraft attitude. The internal workings of the modeling tools are not addressed here but instead example results for simple satellite shapes are presented ¹. A separate chapter will address results for the lift coefficient and aerodynamic force vector in the future.

This chapter describes a method for determining the drag coefficient of spacecraft in orbits significantly affected by aerodynamic forces. A spacecraft configuration and mission orbit is required for this method to be useful. An effective drag coefficient is determined that is useful for both attitude control disturbance torque and orbital mechanics perturbation force modeling. By using finite plate elements, used to approximate the shape of spacecraft in three dimensions, complex shapes can be readily modeled for high-accuracy computations. The net force created on the shape at any attitude can be readily computed along with the disturbance torque if the mass properties of the shape are also known. This model is validated using experimental data for hypersonic molecular beams and Direct Simulation Monte Carlo (DSMC) methods. Examples of spacecraft drag coefficient mapping in three dimensions are included for both simple shapes and a hypothesized spacecraft. It is the goal of this chapter to show examples of how the satellite drag coefficient can be determined using a finite plate element model and to demonstrate some results using simple shapes.

¹Reference 12 has some information on equations used for this model.

2. ThreeD, a model to determine drag and lift coefficients for complex shapes

For the results presented here in, a computer program was developed to address the drag and lift coefficients at any desired attitude for three dimensional complex shapes. Written in the Python version 2.4 language, the program uses equations within this chapter to account for a wide range of environmental conditions, allowing the user to change the plate model to use either the DSMC² method at specularities of 0%, 50%, or 100%, or the Experimental Superpositioned Molecular (ESM) model³. By changing the altitude within the ESM model, the percentage of molecular constituents in the atmosphere is calculated. The ESM model currently uses experimental data for oxygen, nitrogen, and helium. At altitudes above 1000 km there will be some errors due to the growing percentage of hydrogen by weight. The data in the following sections has been created using the ThreeD program. Perspective views in the following figures have also been created using ThreeD⁴.

3. Drag coefficients for common shapes

Using both the DSMC and ESM methods, the drag coefficient for some common shapes are explored. These shapes include a cube, a cylinder, and a cone. Each shape is first rotated about the x axis 180 degrees in 10 degree increments then rotated about the z axis 360 degrees in 10 degree increments. The view vector (velocity) is down the x axis. The altitude is assumed to be at 300 km for these computations. For the DSMC method, two data sets are determined for 0% and 50% specularity. A third specularity value of 25% is presented since it correlates well with the ESM model. This third data set is determined by interpolating the data sets for 0% and 50% specularity. The following drag coefficient analyses assume an altitude of 300 km (except where noted).

3.1 Drag coefficients for a cube

The drag coefficient profile for a cube is determined below. The side length of the cube is assumed to be 1 unit of length. The reference axes (x, y, and z) are normal to the faces of the cube. Figure 1 shows projected area of a cube based upon perspective over 2-pi steradians. Figures 2 through 7 show drag coefficient data for a cube. Figure 2, 6, and 7 display the data using the experimental plate model. Figures 3 through 5 uses DSMC data for specularity of 0%, 25%, and 50% respectively. The maximum drag coefficient occurs when perspective views are normal to the cube faces (z - rotations of 0, 90, 180, and 270 degrees when x - rotation is 0 or 90 degrees). Notice that the data for x-rotation of 0 and 90 degrees overlap. Therefore, there are 6 potential directions in which the drag coefficient can be maximized for a cube. This projected view is shown in Figure 8.

The minimum drag coefficient depends on the model assumptions. Using the DSMC method with a specularity of 0%, the minimum drag coefficient occurs when the z - rotations are at 45, 135, 225, and 315 degrees with x -rotations of 10 and 80 degrees. This projected view is shown in Figure 9. This result is counter-intuitive and occurs due to the high skin friction assumption inherent with a diffuse plate model. The remaining models have the minimum drag coefficient at the same z - rotation angles but with the x - rotation

² The DSMC plate models formulated were produced using G. Bird's software "Visual Wind Tunnel".

³ Reference 12 provides details the ESM model.

⁴For more information on the ThreeD program, see reference 11.

at 45 degrees. If another 2-pi steradians were plotted, the minimum also occurs at an x - rotation of 135 degrees (this can be seen in Figures 6 and 7). This view corresponds to a view axis that intersects 2 corners and the geometric center of mass. Therefore, there are 8 directions at which the drag coefficient can be minimized for a cube. This projected view is shown in Figure 10.

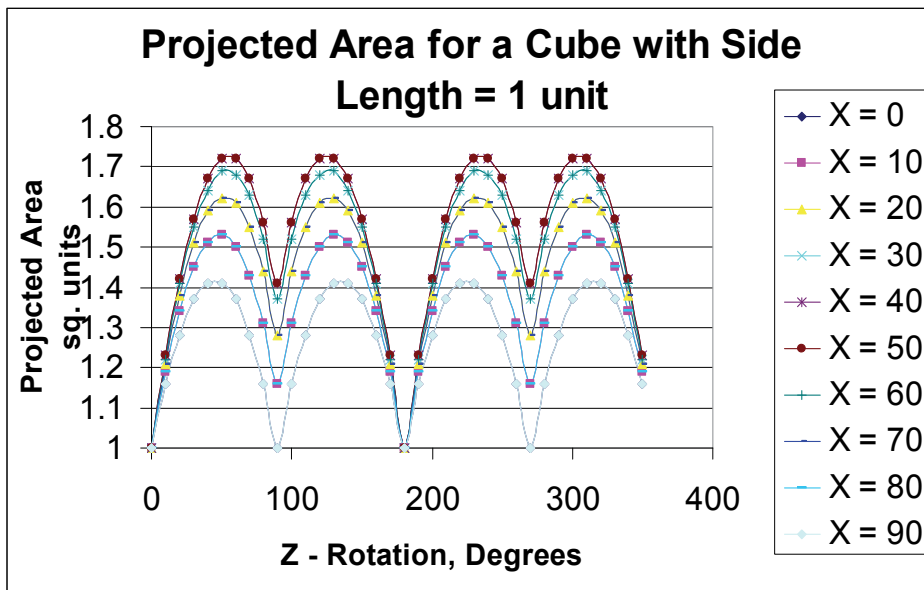


Fig. 1. Projected Area For A Cube, Side Length = 1 Unit (2-Pi Steradians)

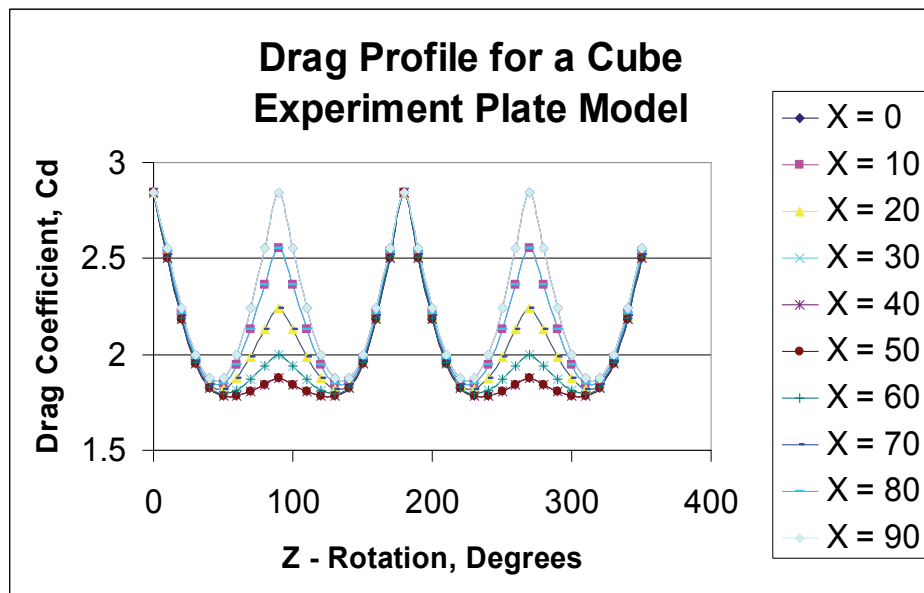


Fig. 2. Drag Profile For A Cube Using Experimental Plate Model Data (2-Pi Steradians)

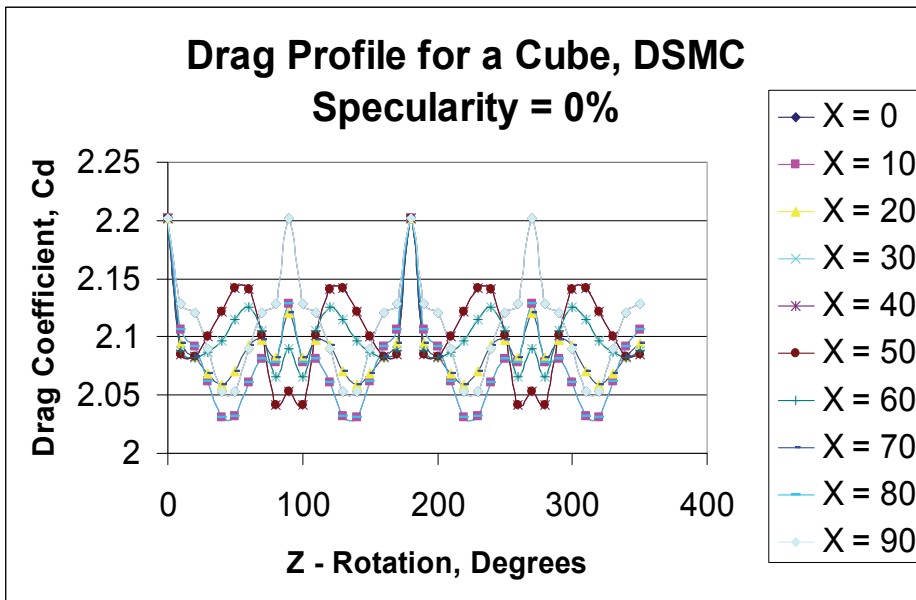


Fig. 3. Drag Profile For A Cube Using DSMC Method Data, Specularity = 0 % (2-Pi Steradians)

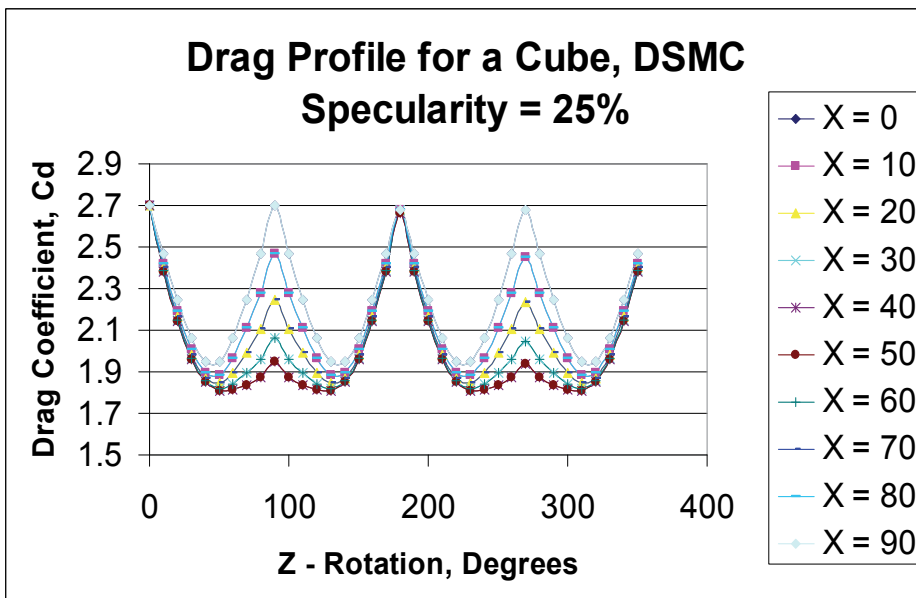


Fig. 4. Drag Profile For A Cube Using DSMC Method Data, Specularity = 25 % (2-Pi Steradians)

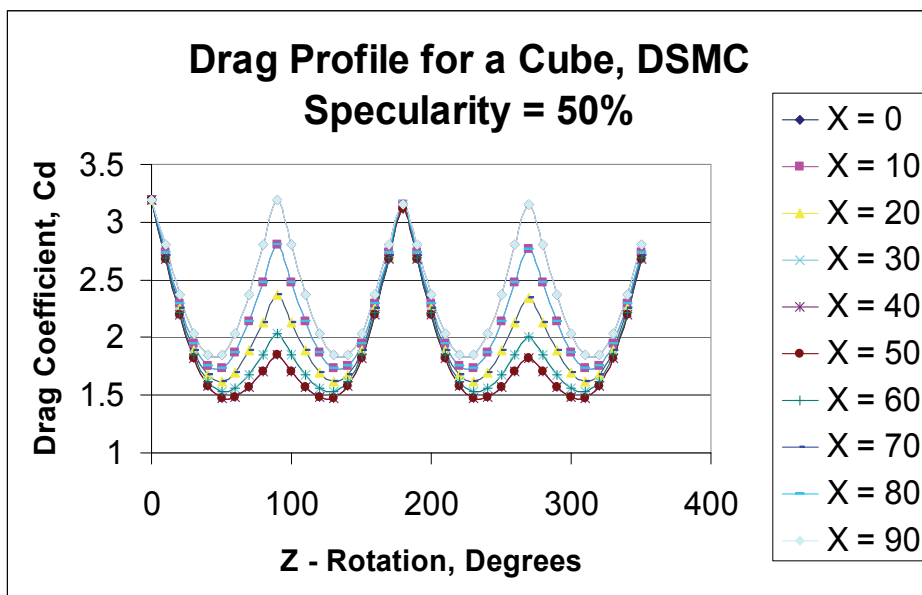


Fig. 5. Drag Profile For A Cube Using DSMC Method Data, Specularity = 50 % (2-Pi Steradians)

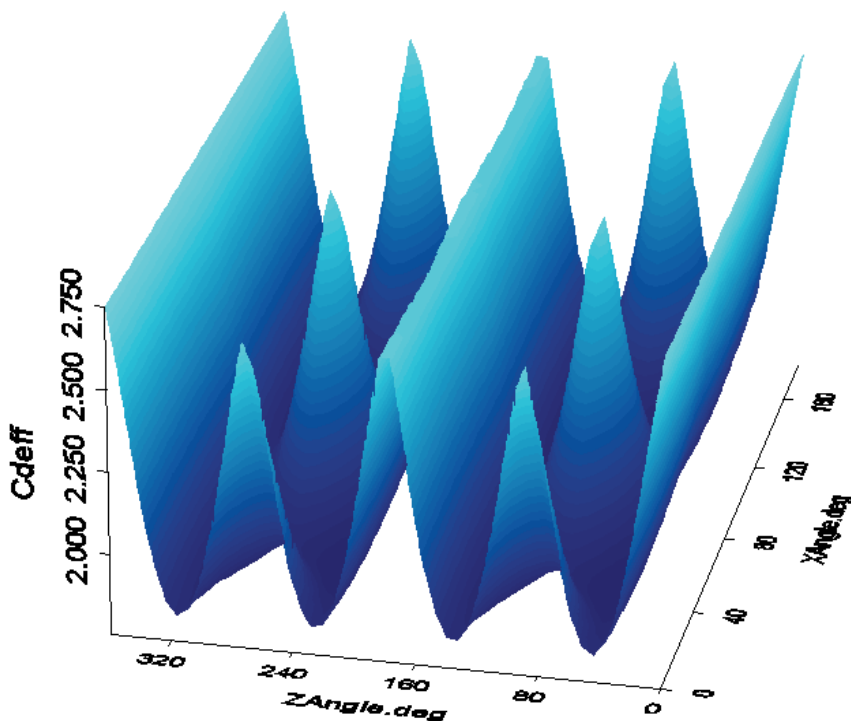


Fig. 6. Drag Profile For A Cube Using Experimental Plate Model Data – at 400 km, 3D Plot (4-Pi Steradians)

	DSMC 0	DSMC 25	DSMC 50	Experiment
Average	2.096182	2.089747	2.083312	2.1045439
Max	2.202087	2.698921	3.195754	2.842236
Min	2.031157	1.809315	1.477173	1.781762
Range	0.17093	0.889606	1.718581	1.060474

Table 1. Data Summary For Cube Drag Coefficients Using 4 Model Variations

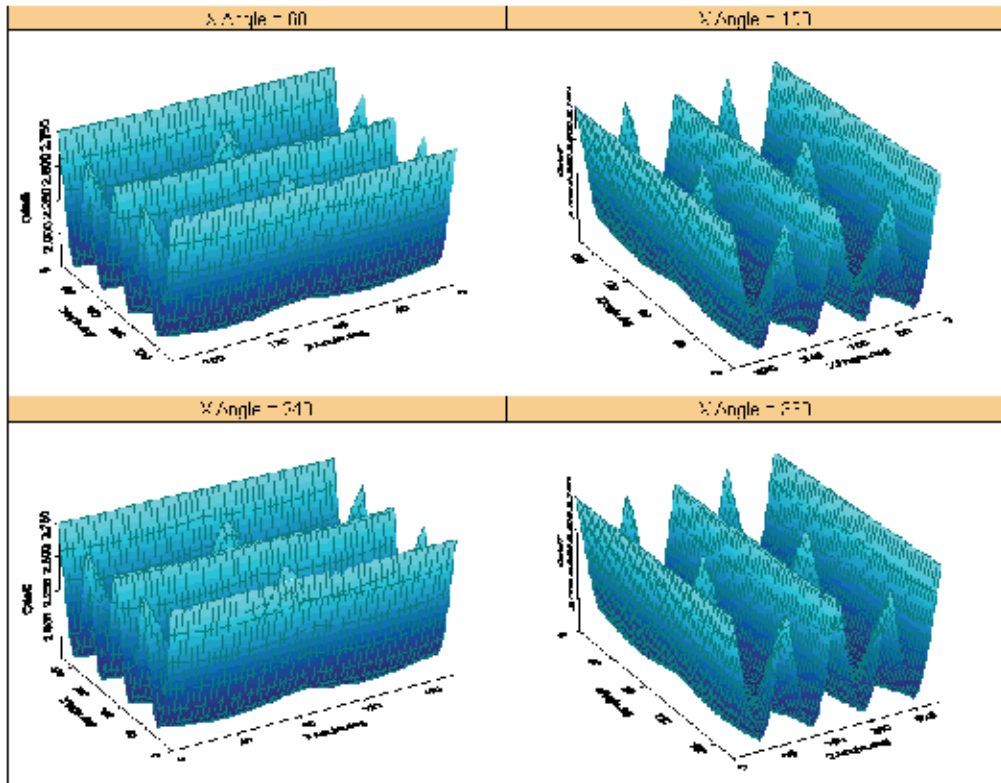


Fig. 7. Drag Profile For A Cube Using Experimental Plate Model Data - at 400 km, Rotated 3D Plot (4-Pi Steradians)



Fig. 8. Maximum Drag Coefficient Profile For A Cube (All Models)

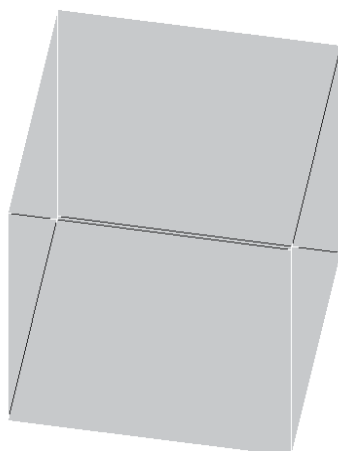


Fig. 9. Minimum Drag Coefficient Profile For A Cube (DSMC Specularity of 0%)

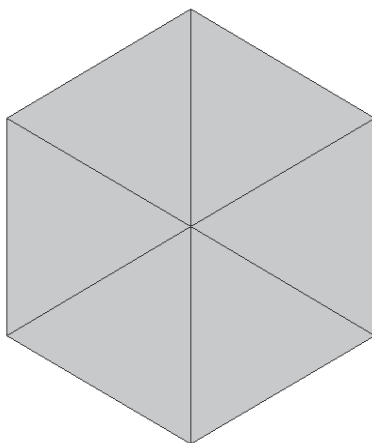


Fig. 10. Minimum Drag Coefficient Profile For A Cube (Experimental Data; DSMC Specularities 25% and 50%)

3.2 Drag coefficient profile for a cylinder

Using a length to diameter ratio of 2, the drag coefficient profile for a cylinder is determined. The z-axis is aligned with the axis of the cylinder (normal to the circular ends). Figure 11 shows the projected area of the cylinder based upon perspective over 2-pi steradians. Figures 12 through 17 show the drag coefficient data for the cylinder. Figure 12, 16, and 17 display the data using the experimental plate model. Figures 13 through 15 uses DSMC data for specularities of 0%, 25%, and 50% respectively. The maximum drag coefficient occurs with an perspective views are normal to the cylinder ends (z - rotations of 90 and 270 degrees when x - rotation 90 degrees). Therefore, there are 2 potential directions in which the drag coefficient can be maximized for a cylinder. This projected view is shown in Figure 18. Notice that for an x-rotation of 0 degrees the drag coefficient stays constant. This corresponds to the velocity vector being perpendicular to the cylinder's axis, showing it will be same from any direction perpendicular to this axis, as expected.

Similar to the cube, the minimum drag coefficient for a cylinder depends on the model assumptions. Using the DSMC method with a specularity of 0%, the minimum drag coefficient occurs when the cylinder is rotated about the x-axis by 90 degrees and with z-rotations of 80, 100, 260, or 280 degrees. This projected view is shown in Figure 19. This corresponds to the velocity vector being 10 degrees off the axis of the cylinder.

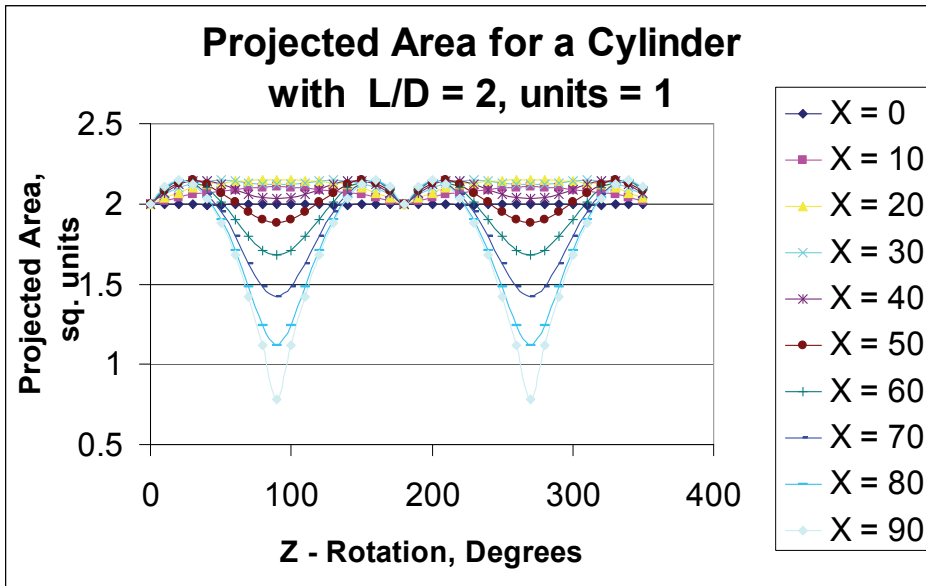


Fig. 11. Projected Area For A Cylinder, $L/D = 1$ ($2\text{-}\pi$ Steradians)

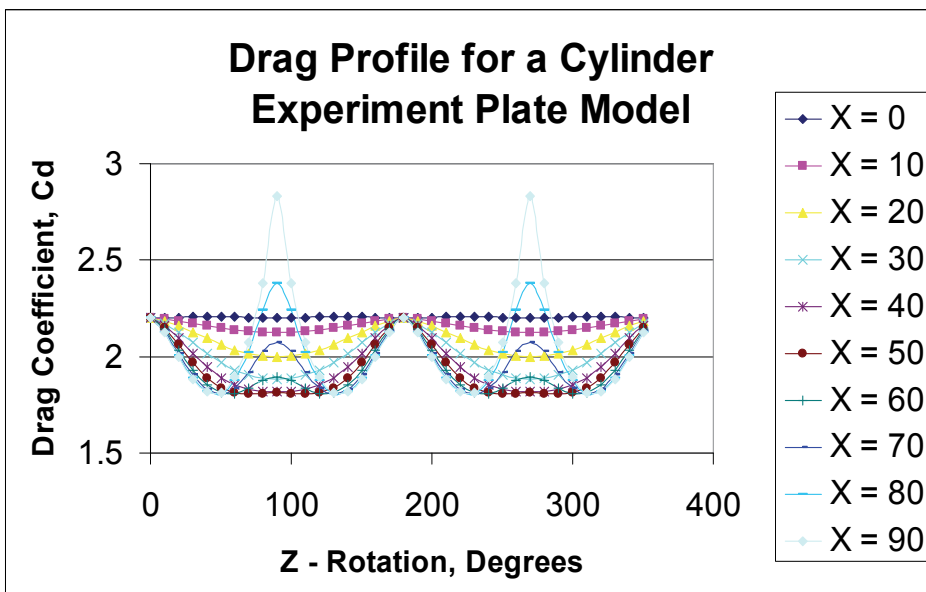


Fig. 12. Drag Profile For A Cylinder ($L/D = 2$) Using Experimental Plate Model Data ($2\text{-}\pi$ Steradians)

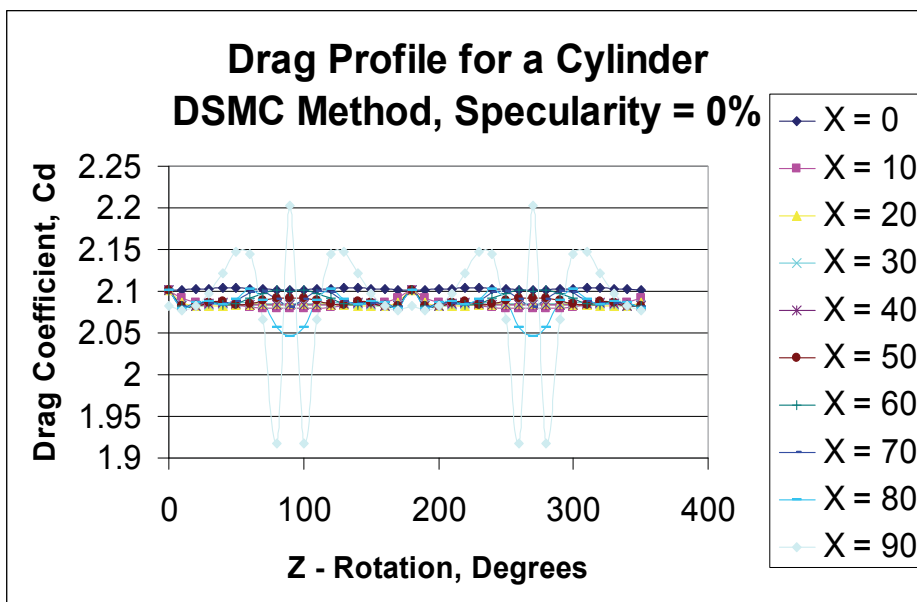


Fig. 13. Drag Profile For A Cylinder ($L/D = 2$) Using DSMC Method Data, Specularity = 0 % (2-Pi Steradians)

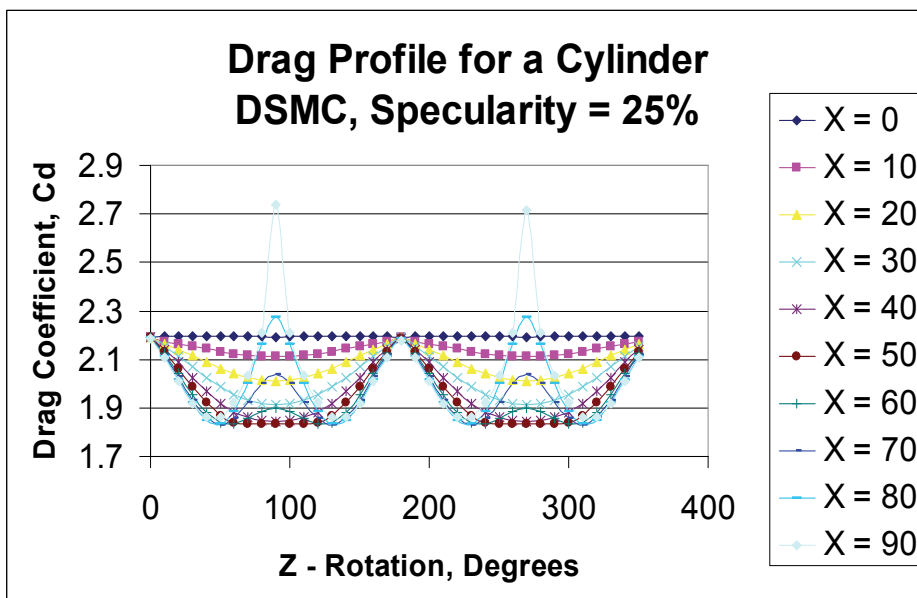


Fig. 14. Drag Profile For A Cylinder ($L/D = 2$) Using DSMC Method Data, Specularity = 25 % (2-Pi Steradians)

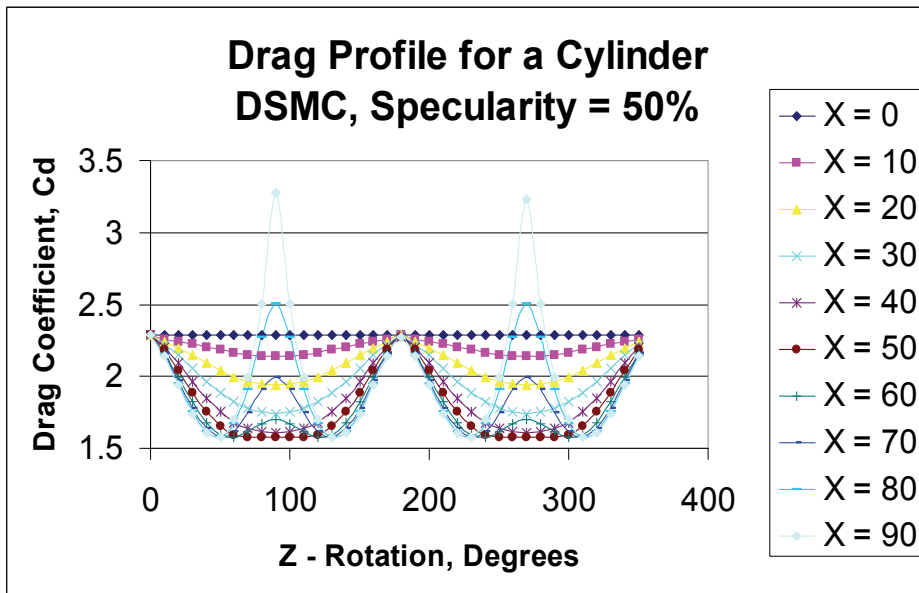


Fig. 15. Drag Profile For A Cylinder ($L/D = 2$) Using DSMC Method Data, Specularity = 50 % (2- π Steradians)

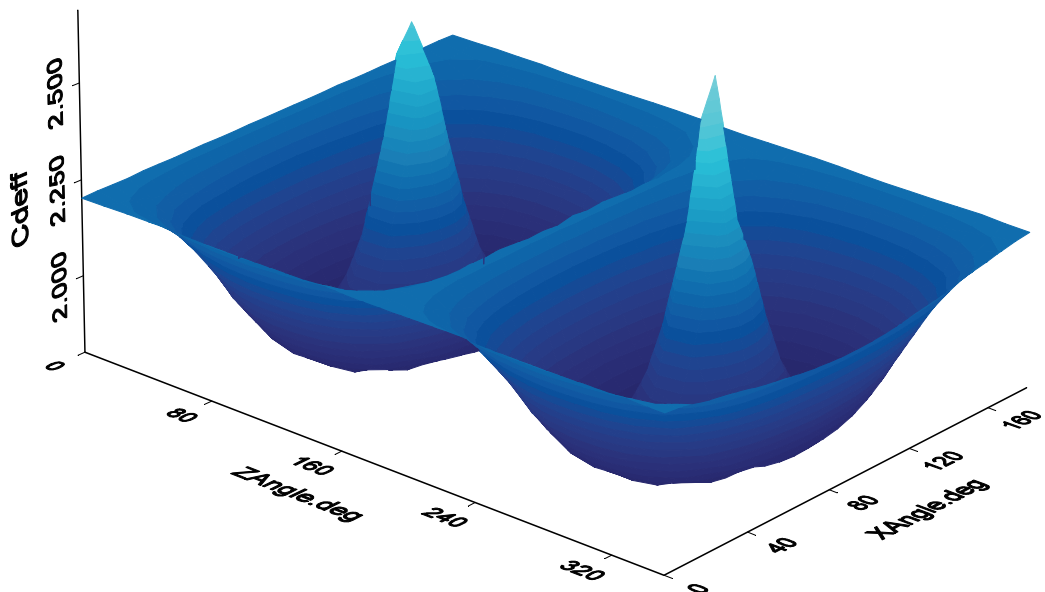


Fig. 16. Drag Profile For A Cylinder ($L/D = 2$) Using Experimental Plate Model Data, 3D Plot (4- π Steradians)

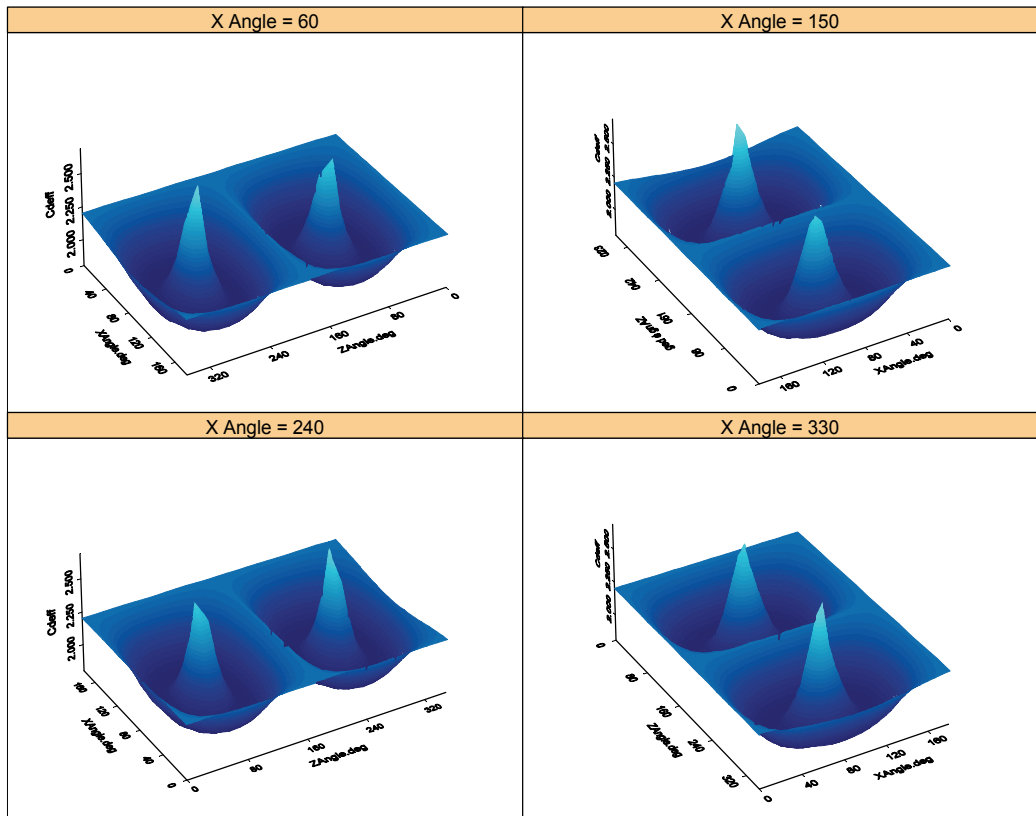


Fig. 17. Drag Profile For A Cylinder ($L/D = 2$) Using Experimental Plate Model Data, Rotated 3D Plot (4-Pi Steradians)

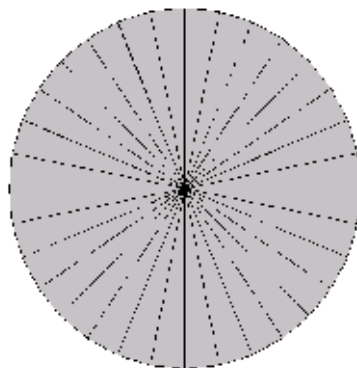


Fig. 18. Maximum Drag Coefficient Profile For A Cylinder With $L/D = 2$ (All Models)

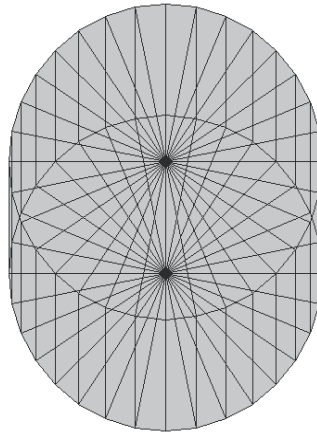


Fig. 19. Minimum Drag Coefficient Profile For A Cylinder With $L/D = 2$ (DSMC Specularity Of 0%) - 10 Degrees Off Of Cylinder Axis

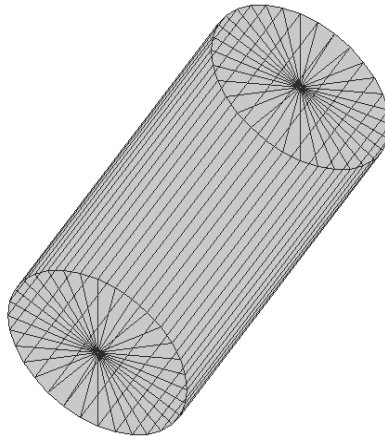


Fig. 20. Minimum Drag Coefficient Profile For A Cylinder ($L/D = 2$) (Experimental Data; DSMC Specularities 25% And 50%) - 52.8 Degrees Off Of Cylinder Axis

Using the DSMC method with a specularity of 25%, the minimum drag coefficient occurs when the cylinder is rotated about the x axis by 70 degrees then with z - rotations of 230 or 310 degrees, or when is rotated about the x axis by 110 degrees then with z - rotations of 50 or 130 degrees. For both the experimental data method and the DSMC method with a specularity of 50%, the minimum drag occurs not only at the same 4 points as the DSMC method with a specularity of 25%, but also at 4 additional points: when the cylinder is rotated about the x axis by 70 degrees then with z - rotations of 50 or 130 degrees, or when it is rotated about the x axis by 110 degrees then with z - rotations of 230 or 310 degrees. This projected view is shown in Figure 20. This corresponds to the velocity vector being 52.8 degrees off the axis of the cylinder.

Therefore, an infinite number of directions at which the drag coefficient can be minimized for a cylinder. The important aspect is to set the axis of the cylinder relative to the velocity vector at an angle depending on the surface characteristics and the length to diameter ratio of the cylinder.

The average, minimum, maximum and range for the cylinder drag coefficient is displayed in Table 2 by model type. Note that the average value of the DSMC model with a specularity of 25% is again very close the average of the experimental data model.

	DSMC 0	DSMC 25	DSMC 50	Experiment
Average	2.088085	2.029561	1.971037	2.027999
Max	2.202087	2.738893	3.275698	2.834196
Min	1.917499	1.831433	1.575661	1.804935
Range	0.284588	0.90746	1.700037	1.029261

Table 2. Data Summary For Cylinder Drag Coefficients ($L/D = 2$) Using 4 Model Variations

3.3 Drag coefficient profile for a cone

Using a height to diameter ratio of 1, the drag coefficient profile for a cone is presented. The z -axis goes through the cone apex and is normal to the circular base. When the z -rotation ranges from 0 to 180 degrees the rear face of the cone is exposed. When the z -rotation ranges from 180 to 360 degrees, the apex of the cone points against the velocity (view) vector.

Figure 21 shows projected area of the cone based upon perspective over 2π steradians. Figures 22 through 27 show drag coefficient data for the cone. Figures 22, 26, and 27 display the data using the experimental plate model. Figures 23 through 25 uses DSMC data for specularities of 0%, 25%, and 50% respectively. The maximum drag coefficient occurs when perspective views are normal to the cone end (z - rotations of 90 degrees when x - rotation is 90 degrees), with the exception of the DSMC model using a specularity of 0%. This projected view is shown in Figure 28. If only the front of the cone is considered, the maximum drag coefficient occurs when velocity vector is at an angle of 80.2 degrees off the cone axis (corresponds to z - rotations of 210 or 330 degrees when x - rotation is 60 or 120 degrees), again with the exception of the DSMC model using a specularity of 0%. This projected view is shown in Figure 29. The values of the maximum frontal drag coefficients are 2.2014, 2.1732, and 2.2446 for the experimental, DSMC 25% specularity, and DSMC 50% specularity models respectively. Notice for an x -rotation of 0 degrees, the drag coefficient stays constant. This corresponds to the velocity vector being perpendicular to the z -axis of the cone.

As with the cube and cylinder, the minimum drag coefficient for a cone depends on the model assumptions. Using the DSMC method with a specularity of 0%, the minimum drag coefficient occurs when the cone is rotated about the x -axis by 60 degrees then with z - rotations of 70 or 110 degrees. This projected view is shown in Figure 30. This corresponds to the velocity vector being 64.3 degrees off the axis of the cone. If only the front of the cone is considered, the minimum drag coefficient occurs when the cone is rotated about the x -axis by 60 or 120 degrees then with z - rotations of 250 or 290 degrees. Interestingly, the perspective view is the same as that of Figure 30, but from the reverse direction. The minimum frontal drag coefficient is 2.0599 for the DSMC 0% specularity model.

The maximum drag coefficient for a cone using the DSMC method with a specularity of 0% occurs at the same direction as the minimum drag for the other models. This is shown in Figure 28. This can be explained by the high emphasis of skin friction from this model. This perspective provides a view of the most exposed surface area for the cone.

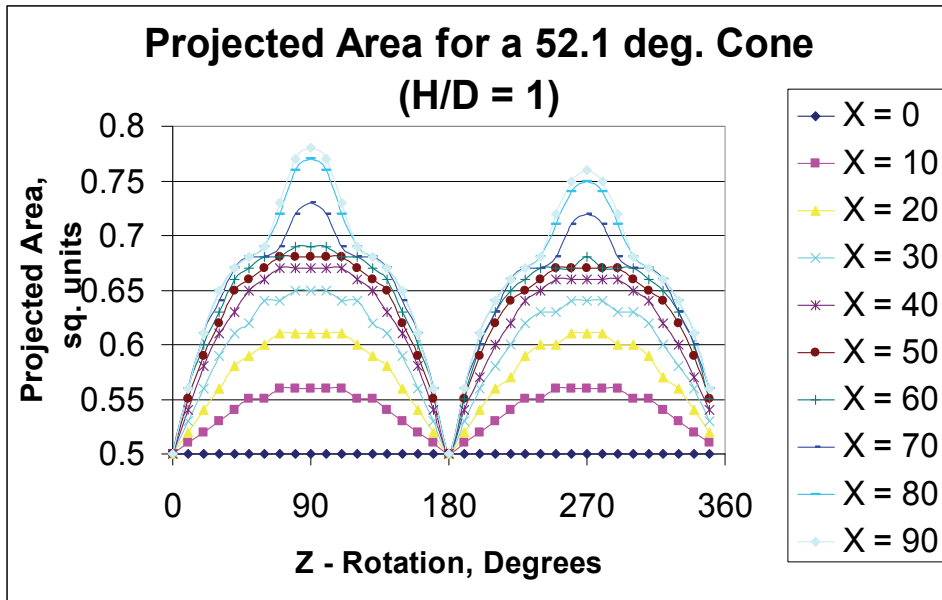


Fig. 21. Projected Area For A Cone, H/D = 1 (2-Pi Steradians)

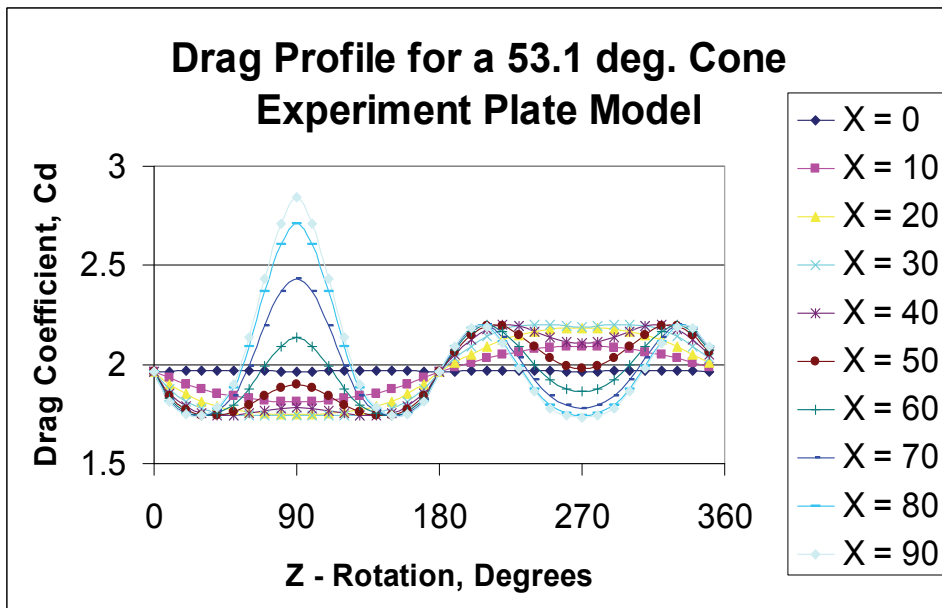


Fig. 22. Drag Profile For A Cone, H/D = 1, Using Experimental Plate Model Data (2-Pi Steradians)

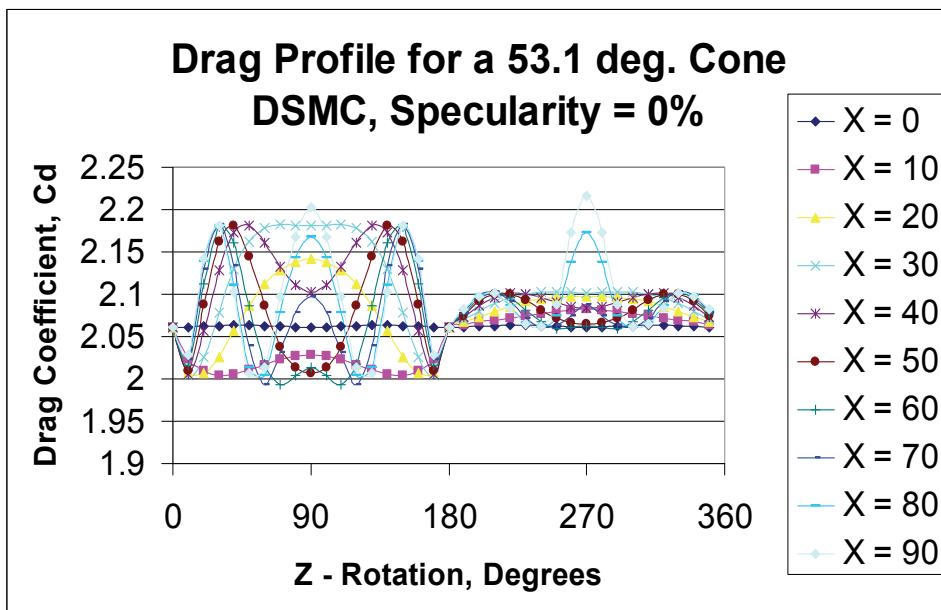


Fig. 23. Drag Profile For A Cone, $H/D = 1$, Using DSMC Method Data, Specularity = 0 % (2-Pi Steradians)

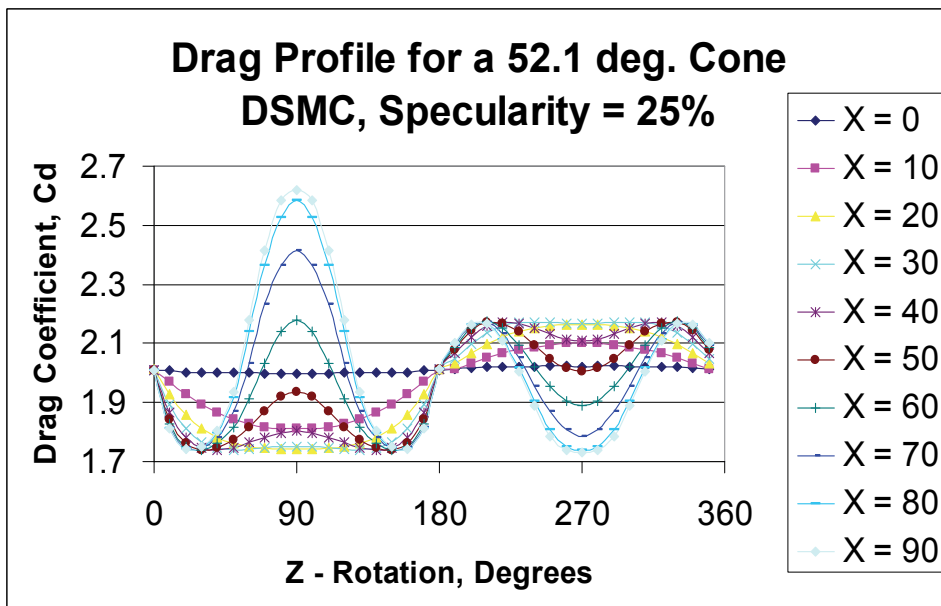


Fig. 24. Drag Profile For A Cone, $H/D = 1$, Using DSMC Method Data, Specularity = 25 % (2-Pi Steradians)

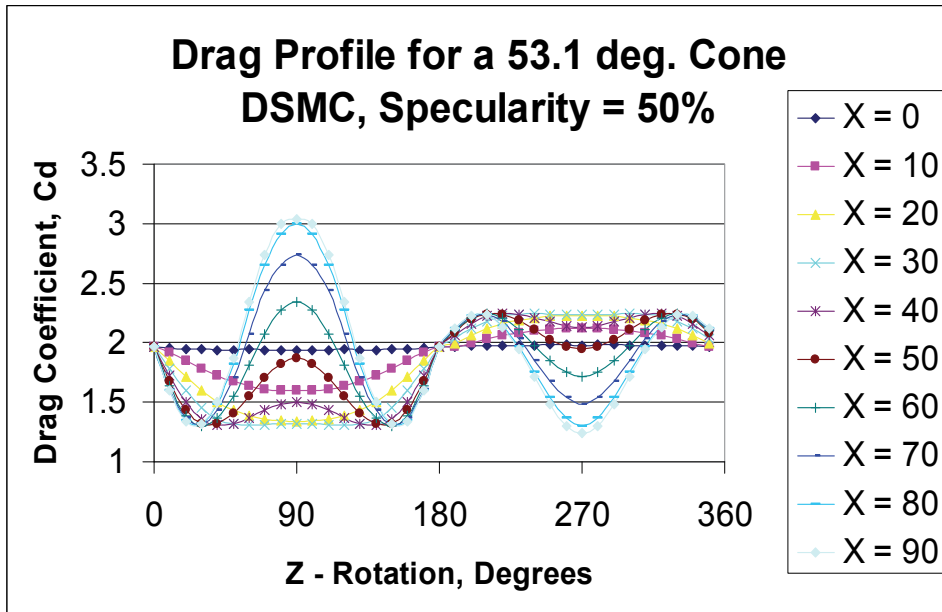


Fig. 25. Drag Profile For A Cone, $H/D = 1$, Using DSMC Method Data, Specularity = 50 % (2-Pi Steradians)

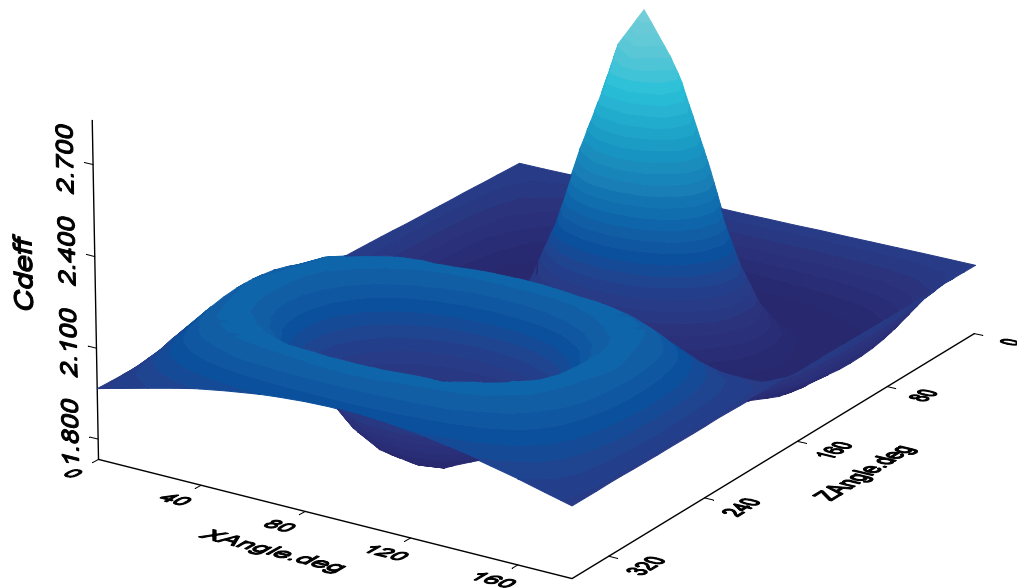


Fig. 26. Drag Profile For A Cone, $H/D = 1$, Using Experimental Plate Model Data, 3D Plot (4-Pi Steradians)

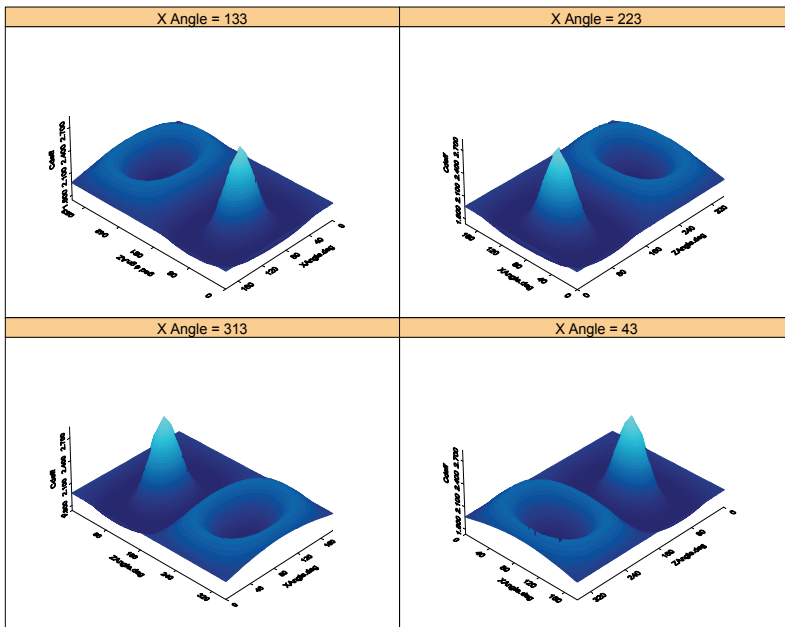


Fig. 27. Drag Profile For A Cone, ($H/D = 1$) Using Experimental Plate Model Data, Rotated 3D Plot ($4\text{-}\pi$ Steradians)

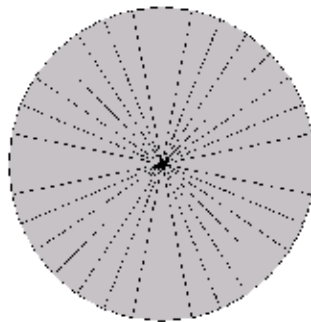


Fig. 28. Minimum And Maximum Drag Coefficient Profile For A Cone With $H/D = 1$ (All Models Except DSMC Specularity 0% For Minimum Drag Coefficient)

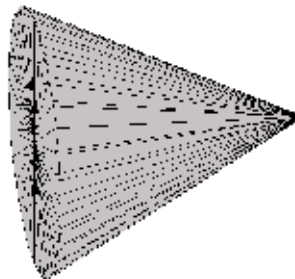


Fig. 29. Maximum Drag Coefficient Profile (Frontal Direction Only) For A Cone With $H/D = 1$ (Experimental Data; DSMC Specularities 25% And 50%) – 80.2 Degrees Off Of Cone Axis

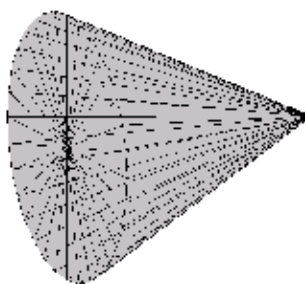


Fig. 30. Minimum Drag Coefficient Profile (Front And Rear Directions) For A Cone, $H/D = 1$, (DSMC Specularity 0%) - 64.3 Degrees Off Of Cone Axis

The average, minimum, maximum and range for the cone drag coefficient is displayed in Table 3 by model type. Notice once again that the average value of the DSMC model with a specularity of 25% is very close the average of the experimental data model. A value of 0% has proven not to be realistic as it does not correlate well with the other results.

	DSMC 0	DSMC 25	DSMC 50	Experiment
Average	2.080749	1.980765	1.880782	1.9716522
Max	2.216739	2.620121	3.038154	2.842236
Min	1.993266	1.729126	1.241512	1.732459
Range	0.223473	0.890995	1.796642	1.109777

Table 3. Data Summary For Cone Drag Coefficients ($H/D = 1$) Using 4 Model Variations

4. Drag coefficients for complex satellite shapes

The modeling program ThreeD is designed to combine an unlimited number of plate elements to create more complex shapes. A more complex satellite, designated "CubeSat", was created using some simple shapes and is shown in Figure 31. This satellite has a cube-shaped bus, four solar array panels that are articulated at an angle of 60 degrees from one of the faces of the cube, and a gravity gradient boom modeled with a tapered cylinder. The projected area for this satellite is shown in Figure 32. The drag coefficient profile is shown in Figure 33.

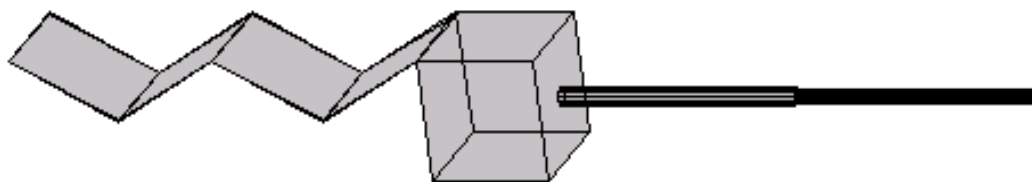


Fig. 31. Example Of A Complex Satellite For Drag Coefficient Modeling (Cubesat)

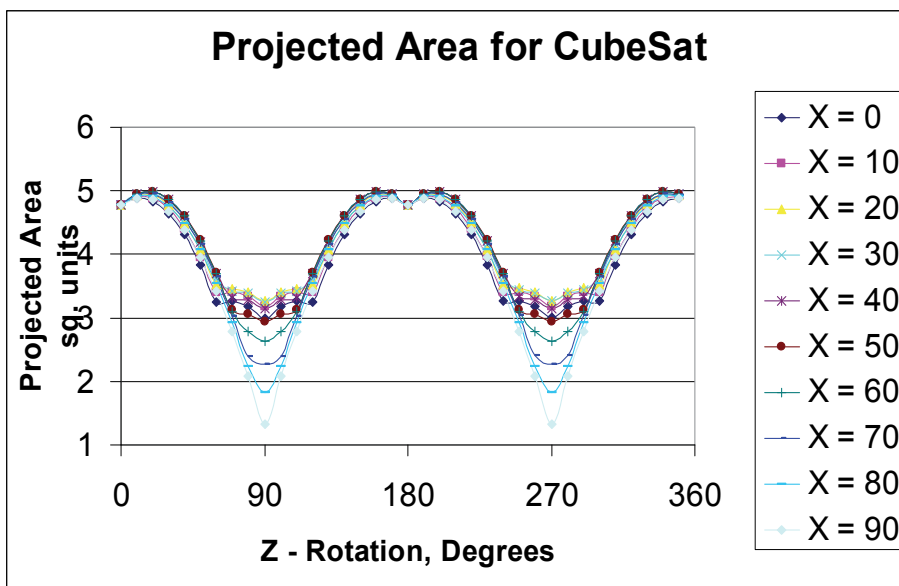


Fig. 32. Projected Area For Cubesat Example

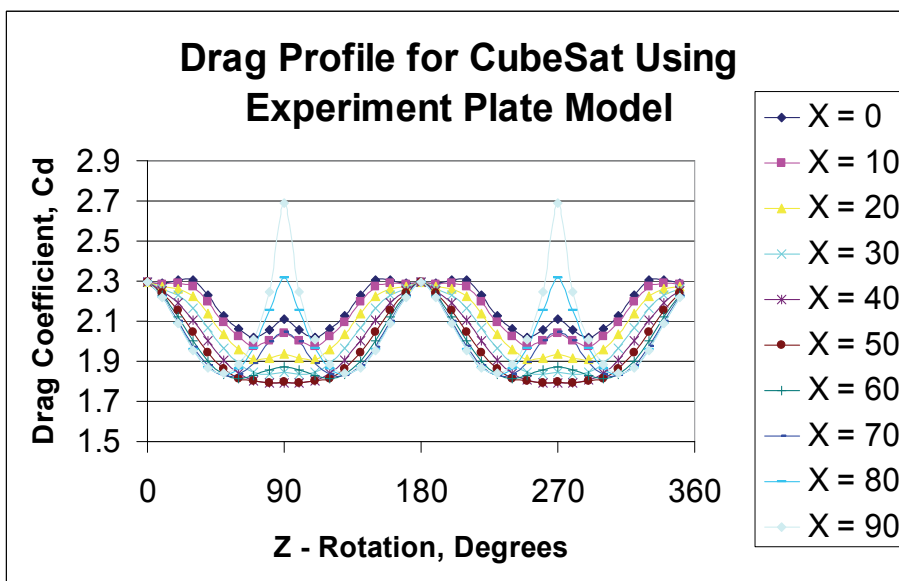


Fig. 33. Drag Profile For Cubesat Using ESM Plate Model

5. Conclusions

This chapter has shown a method for determining the drag coefficient for simple and complex objects in the rarefied conditions of low Earth orbits. Using both DSMC methods and the ESM method, a reliable estimate can be found for objects at any attitude. By looking

at the drag coefficient of common shapes at all attitudes, maximum values occur when the velocity vector is perpendicular to flat faces of the object. Minimum values tend to occur at oblique angles that depend on the geometry of the object and the gas-surface interaction model chosen. A DSMC specularity value of 0% was shown not to be realistic.

Another chapter will be written to address the lift coefficient, aerodynamic vector, and aerodynamic torque in the future. It will again incorporate the ThreeD program after sufficient modifications have been completed.

6. References

- G. A. Bird (1994). "Molecular Gas Dynamics and the Direct Simulation of Gas Flows."
- J. W. Boring, R. R. Humphris (1973). "Drag Coefficients for Spheres in Free Molecular Flow in O at Satellite Velocities," NASA CR-2233.
- G. E. Cook (1965). "Satellite Drag Coefficients," *Planetary & Space Science*, Vol 13, pp 929 - 946.
- R. Crowther, J. Stark (1989). "Determination of Momentum Accommodation from Satellite Orbits: An Alternative Set of Coefficients," from *Rarefied Gas Dynamics: Space-Related Studies*, AIAA Progress in Aeronautics and Astronautics, Vol. 116, pp 463-475.
- F. A. Herrero (1987) "Satellite Drag Coefficients and Upper Atmosphere Densities: Present Status and Future Directions," AAS Paper 87-551, pp 1607-1623.
- F. C. Hurlbut (1986) "Gas/Surface Scattering Models for Satellite Applications," from *Thermophysical Aspects of Re-entry Flows*, AIAA Progress in Aeronautics and Astronautics, Vol. 103, pp 97 - 119.
- R. R. Humphris, C. V. Nelson, J. W. Boring (1981). "Energy Accommodation of 5-50 eV Ions Within an Enclosure', from *Rarefied Gas Dynamics: Part I*, AIAA Progress in Aeronautics and Astronautics, Vol. 74, pp 198 - 205.
- J. C. Lengrand, J. Allegre, A. Chpoun, M. Raffin (1994). "Rarefied Hypersonic Flow over a Sharp Flat Plate: Numerical and Experimental Results," from *Rarefied Gas Dynamics: Space Science and Engineering*, AIAA Progress in Aeronautics and Astronautics, Vol. 160, pp 276 - 283.
- F. A. Marcos, M. J. Kendra (1999). J. N. Bass, "Recent Advances in Satellite Drag Modeling," AIAA Paper 99-0631, 37th AIAA Aerospace Sciences Meeting and Exhibit.
- K. Moe, M. M. Moe, S. D. Wallace (1996). "Drag Coefficients of Spheres in Free Molecular Flow," AAS Paper 96-126, AAS Vol. 93 part 1, pp 391-405.
- C. M. Reynerson (2002). "ThreeD User's Manual," Boeing Denver Engineering Center Document.
- C. M. Reynerson (2002). "Drag Coefficient Computation for Spacecraft in Low Earth Orbits Using Finite Plate Elements," Boeing Denver Engineering Center Document.
- R. P. Nance, Richard G. Wilmoth, etal. (1994). "Parallel DSMC Solution of Three-Dimensional Flow Over a Flat Plate," AIAA Paper, 1994.
- L. H. Sentman, S. E. Neice (1967). " Drag Coefficients for Tumbling Satellites," *Journal of Spacecraft and Rockets*, Vol. 4. No. 9, pp 1270 - 1272.
- R. Schamberg (1959). Rand Research Memorandum, RM-2313.
- P. K. Sharma (1977). "Interactions of Satellite-Speed Helium Atoms with Satellite Surfaces III: Drag Coefficients from Spatial and Energy Distributions of Reflected Helium Atoms," NASA CR-155340, N78-13862.

State Feature Extraction and Relative Navigation Algorithms for Spacecraft

Kezhao Li^{1,2}, Qin Zhang¹ and Jianping Yuan³

¹*Dept.of Geomatics, Chang'an University,*

²*Henan Polytechnic University,*

³*Northwestern Polytechnical University,
China*

1. Introduction

Since 1957 when the first manmade satellite launched, humankind has made splendid progress in space exploration. However, we must face some new problems, which have affected or will affect new space activities: (i) space debris problem. There are more than 8700 objects larger than 10~30 cm in Low Earth Orbit (LEO) and larger than 1m in Geostationary Orbit (GEO) registered in the US Space Command Satellite Catalogue (D.Mehrholz, 2002). Among these space objects, approximately 6% are operational spacecrafts, that is to say, about 94% of the catalogued objects no longer serve any useful purpose and are collectively referred to as 'space debris'. If we don't track, detect, model for these space debris, the hazards of on-orbit spacecrafts or future spacecrafts will be enhanced. Fortunately, this problem has been recognized; (ii) maintenance for disable satellites. Sometimes an operational spacecraft is out of use only due to some simple faults. If it is maintained properly, it can still work as usual. So this is an economical way to use space resource. For example, a tyre of an expensive car has been broken, we can take a few of money to maintain it, and it can work as well as before. First of all, the problem of tacking, detecting and relative posing for disable spacecrafts must be solved, and then we can capture them or do some on-orbit service; (iii)on-orbit assembling of large-scale space platform. Along with the space exploring, it is a challenge and profound space project to build a large-scale space platform through launching in batches and assembling in orbit, and this will provide a valid platform for human to explore deep space. Whereas, the key technology of on-orbit assembling of large-scale space platform is space rendezvous and docking, it is also needed tracking, detecting and relative posing space objects. To solve those above problems successfully, the problem about space detection and relative posing must be researched and solved firstly. In recent twenty years, a series of important plans for space operations, including Demonstration of Autonomous Rendezvous Technology (DART) (Ben Iannotta, 2005 ; Richard P. Kornfeld, 2002 ; LiYingju, 2006),Orbital Express (OE) (Kornfeld, 2002 ; Michael A. Dornheim, 2006 ; Joseph W. Evans, 2006 ; Richard T. Howard, 2008), HII Transfer Vehicle (HTV) (Isao Kawano, 1999 ; Yoshihiko Torano, 2010), Automated Transfer Vehicle (ATV) (Gianni Casonato, 2004) etc, are paid greatly attention to by National Aeronautics and Space Administration (NASA) and Defense Advanced Research Projects Agency of America (DARPA) or National Space Development Agency of

Japan (NASDA) or European Space Agency (ESA) etc. And the operations, such as autonomous rendezvous and docking (AR&D), capturing, maintaining, assembling and attacking etc, have been involved in the plans above. As mentioned above, autonomous relative navigation is one of key technologies in all these space activities. And autonomous relative navigation based on machine vision is a direction all over the world currently. But there are some disadvantages of some traditional algorithms, such as complicated description, huge calculation burden, and lack of real-time ability etc (Wang Guangjun, 2004; Li Guokuan, 2000 ; H. P. Xu , 2006).

In order to overcome these disadvantages above, the algorithms of shape & state feature extraction and relative navigation for spacecraft are emphatically researched in this chapter.

2. Shape & state feature extraction algorithm based-on mathematical morphology

Mathematical morphology (MM) is a new discipline for imaging analysis and processing. Based on these characters, such as the character of nonlinear, morphological analysis, fast and parallel processing, simple and apt operation etc., mathematical morphology is very suitable for automation and intelligence object detection, and make it become a hotspot in imaging processing and correlation field. Recently, some successful applications of mathematical morphology have been made at home and abroad (Richard Alan Peters II, 1995; Joonki Paik, 2002; Ulisses Braga-Neto, 2003).

2.1 Basic four operation of MM

MM is a theory for the analysis of spatial structures which is a tool for extracting image components. It is called "Morphology" since it aims at analyzing the shape and form of object. The four basic morphological set transformations are dilation, erosion, opening and closing.

2.1.1 Dilation

Let \mathbf{A} be an original image, and \mathbf{B} be a SE. The dilation of \mathbf{A} by \mathbf{B} is defined as follows,

$$\mathbf{A} \oplus \mathbf{B} = \bigcup_{b_i \in \mathbf{B}} \mathbf{A}_{b_i} \quad (1)$$

Where $\mathbf{A}_{b_i} = \{a + b_i \mid a \in \mathbf{A}\}$.

2.1.2 Erosion

The erosion of \mathbf{A} by \mathbf{B} is defined as follows,

$$\begin{aligned} \mathbf{A} \ominus \mathbf{B} &= \mathbf{A}^C \oplus \bar{\mathbf{B}}^C \\ &= \{p \mid \exists_{b_i \in \mathbf{B}} \exists_{a_j \in \mathbf{A}^C} (p = a_j - b_i)\}^C \end{aligned} \quad (2)$$

The superscript C in \mathbf{A}^C stands for the complement of \mathbf{A} such that $\mathbf{A}^C + \mathbf{A} = \text{constant}$; $\bar{\mathbf{B}}$ stands for the reflection of \mathbf{B} , that is, $\bar{\mathbf{B}} = \{-b_i \mid b_i \in \mathbf{B}\}$; The superscript C in (\dots) and $\{\dots\}$ also stand for the complements of them.

2.1.3 Opening

The opening of **A** by **B** is defined as follows,

$$A \circ B = (A \ominus B) \oplus B \tag{3}$$

2.1.4 Closing

The closing of **A** by **B** is defined as follows,

$$A \bullet B = [A \oplus (-B)] \ominus (-B) \tag{4}$$

2.2 The vital function of the structuring element (SE)

Using a probe called as SE to detect the image information is the principle idea of MM. When the probe is moving in the image, we can find and know the correlation the structure feature of the image each part. This method is similar to the human FOA (Focus of Attention) from detecting thought. As a probe, SE can be included some knowledge directly, such as shape, size, further more, the information of gray and colour, and we can use the knowledge and information to detect and study the characters of the image (Cui Yi, 2002). So how to select a convenient SE is very important.

Fig. 1 gives the different feature extraction results of the satellite according to the different SEs. From the Fig. 1, we can see that the feature extraction result from SE (b1) is better than the result from (b2). Therefore it is necessary to select SE according to the different applications. In the feature extraction of distributed spacecraft system, we can select the convenient structure element according to the character and the approximate attitude and orbital information of the spacecraft. Additionally, spacecraft move regularly in orbit, the relative position and attitude is changed every time. Thus dynamically re-structured element based-on the approximate attitude and orbital information of the spacecraft system is one of the research directions.

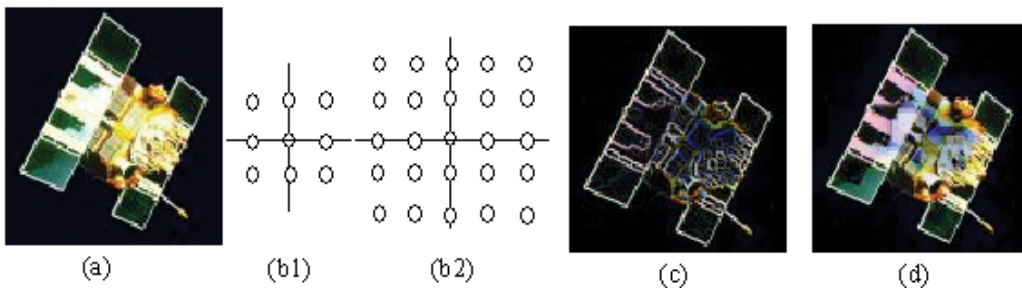


Fig. 1. The different feature extraction results of the satellite according to the different SEs. (a) The original image of satellite; (b1) and (b2) are two kind of SEs; (c) and (d) are the feature extraction results according to (b1) and (b2)

2.3 Dynamically re-structured element based-on the approximate attitude and orbital information of the spacecraft system

In the idea conditions, spacecraft move regularly in orbit according to their six basis orbital elements (semi-major axis: a ; excentricity: e ; ascending node: Ω ; inclination of orbit: i ; argument of perigee: ω ; time of perigee passage: t_p) and their relative navigation angles

(yaw angle: ψ ; roll angle: ϕ ; pitch angle: θ); As mentioned above, it is very important to select a valid SE in feature extraction of distributed spacecraft system, thus we can build the relationship between the movement rule of the spacecraft and dynamically re-structured element by using the SE database built beforehand. Considering that function $\Gamma(a, e, \Omega, i, \omega, f, \psi, \phi, \theta)$ to stand for the spacecraft transformation from time t_1 to time t_2 (see Figure 2). On the basis theory of the attitude dynamics of spacecraft (Y. L. Xiao, 2003), we will build the function Γ as follow.

Two frame must be defined when the relative attitude described. Commonly, one is the space reference frame $ox_r y_r z_r$, and the other is body frame $ox_b y_b z_b$ of the spacecraft. Thus the attitude Euler form is described as

$$\begin{cases} \psi = \arctan\left[-\frac{\mathbf{A}_{yx}}{\mathbf{A}_{yy}}\right] \\ \phi = \arcsin[\mathbf{A}_{yz}] \\ \theta = \arctan\left[-\frac{\mathbf{A}_{xz}}{\mathbf{A}_{zz}}\right] \end{cases} \quad (5)$$

$\mathbf{A}_{xz}, \mathbf{A}_{yx}, \mathbf{A}_{yy}, \mathbf{A}_{yz}, \mathbf{A}_{zz}$ stand for the cosine between $ox_r y_r z_r$ and $ox_b y_b z_b$.

The spacecraft attitude differential equation can be calculated form this equation,

$$\begin{bmatrix} \dot{\psi} \\ \dot{\phi} \\ \dot{\theta} \end{bmatrix} = \frac{1}{\cos \phi} \begin{bmatrix} -\omega_x \sin \theta + \omega_z \cos \theta \\ \omega_x \cos \theta \cos \phi + \omega_z \sin \theta \cos \phi \\ \omega_x \sin \theta \sin \phi + \omega_y \cos \phi - \omega_z \cos \theta \sin \phi \end{bmatrix} \quad (6)$$

$\omega_x, \omega_y, \omega_z$ is the angle velocity.

So the absolute attitude expression of time t_k can be deduced from eq. (5) and (6),

$$\begin{bmatrix} \psi_{t_k} \\ \phi_{t_k} \\ \theta_{t_k} \end{bmatrix} = \begin{bmatrix} \psi_{t_0} \\ \phi_{t_0} \\ \theta_{t_0} \end{bmatrix} + (t_k - t_0) \begin{bmatrix} \dot{\psi} \\ \dot{\phi} \\ \dot{\theta} \end{bmatrix} \quad (7)$$

To calculate the relative attitude of spacecraft, we always build the relationship by geocentric equatorial inertial frame, the transformation formulation can be described as follow,

$$\begin{aligned} \mathbf{R}_{oi} &= \mathbf{R}_z(\omega + f) \mathbf{R}_x(i) \mathbf{R}_z(\Omega) \\ &= \begin{bmatrix} \cos(\omega + f) & \sin(\omega + f) & 0 \\ -\sin(\omega + f) & \cos(\omega + f) & 0 \\ 0 & 0 & 1 \end{bmatrix} \begin{bmatrix} 1 & 0 & 0 \\ 0 & \cos i & \sin i \\ 0 & -\sin i & \cos i \end{bmatrix} \begin{bmatrix} \cos \Omega & \sin \Omega & 0 \\ -\sin \Omega & \cos \Omega & 0 \\ 0 & 0 & 1 \end{bmatrix} \end{aligned} \quad (8)$$

Thus the absolute attitude angle of t_k defined in geocentric equatorial inertial frame can be calculated from eq. (9),

$$\Gamma_{t_k}(a, e, \Omega, i, \omega, f, \psi, \phi, \theta) = \mathbf{R}_{oi} \begin{bmatrix} \psi_{t_k} \\ \phi_{t_k} \\ \theta_{t_k} \end{bmatrix} \tag{9}$$

When the $\Gamma(a, e, \Omega, i, \omega, f, \psi, \phi, \theta)$ is calculated, how to select the SE dynamically? As Fig. 2 shows, consider the track spacecraft attitude of time t_1 and time t_2 are orderly Λ_1 and Λ_2 , the tracked spacecraft attitude of time t_1 and time t_2 are orderly Θ_1 and Θ_2 , then we can build the expression as follows,

$$\Delta\Lambda_1\Theta_1 = \Gamma_{\Theta_1} - \Gamma_{\Lambda_1} \tag{10}$$

$$\Delta\Lambda_2\Theta_2 = \Gamma_{\Theta_2} - \Gamma_{\Lambda_2} \tag{11}$$

$$\Delta\Lambda_{1,2}\Theta_{1,2} = \Delta\Lambda_2\Theta_2 - \Delta\Lambda_1\Theta_1 \tag{12}$$

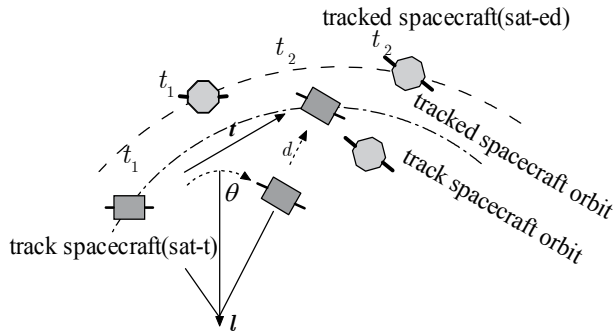


Fig. 2. Track and tracked spacecraft sketch map

$\nabla\Delta\Lambda_{1,2}\Theta_{1,2}$ stands for the relative attitude between track and tracked spacecraft from time t_1 to time t_2 . So dynamically re-structured element can be implemented from eq. (12).

2.4 Simulations and analyses

To prove the algorithm above, a simulation about a track and tracked satellites formation is studied in this section.

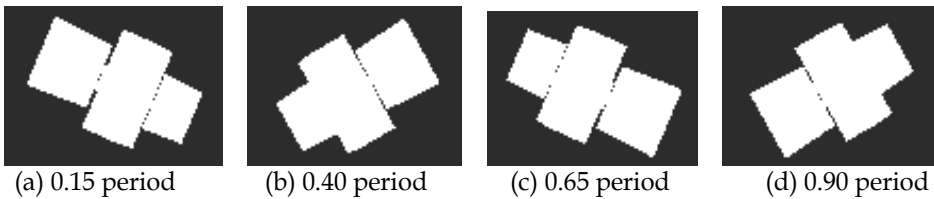


Fig. 3. The original image of tracked satellite corresponding periods

According to Fig. 3, the corresponding SEs are designed from the solar panels character of the tracked spacecraft corresponding period (see Fig. 4). On the basis of these SEs, the feature extraction results are described as Figure 5 and Figure 6.

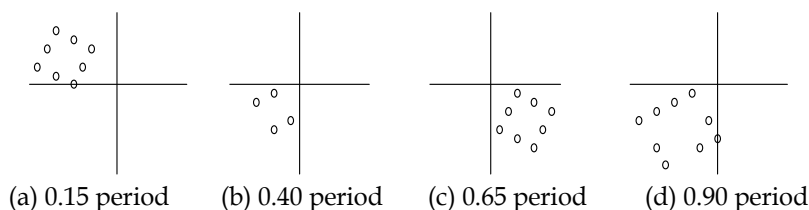


Fig. 4. SEs of corresponding periods

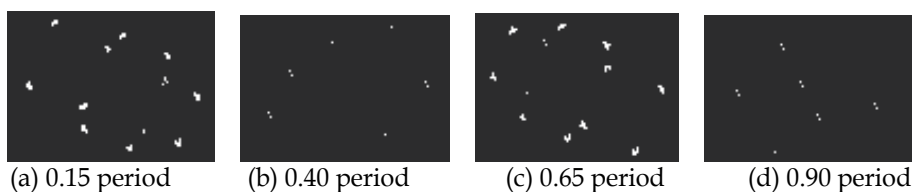


Fig. 5. The feature extraction results corresponding SE of Fig. 4 (a)

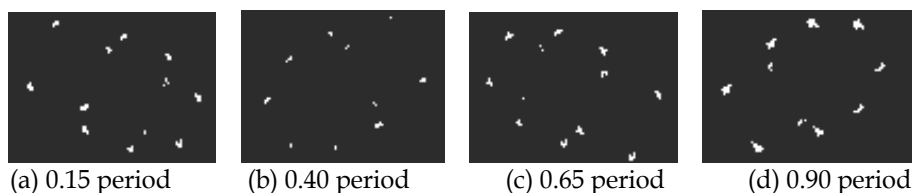


Fig. 6. The feature extraction results corresponding period SEs of Fig. 4

From Fig. 5 and Fig. 6, we can see: () the feature extraction results of Fig. 5 are worse, especially the results (b) and (d) are distorted by using the SE of Figure 4 (a), because the shape of (b) and (d) are different from the SE of Fig. 4 (a); () the feature extraction results of Fig. 6 are better because the corresponding period SEs are used in data processing.

3. Static forecast algorithms based-on quaternion and Rodrigues

3.1 Static forecast algorithm based-on quaternion

There already exists Hall algorithm for positioning and posing (Schwab A. L,2002). We now propose a new algorithm that we believe in better than Hall's. In this section, we explain in some detail our algorithm. We just add some pertinent remarks to listing the two topics of explanation. The first topic is: quaternion based method for determining position and attitude. Its two subtopics are: the quaternion based description of the rotational transformation for three dimensional bodies (subtopic 3.1.1), the camera model and the basic equation for machine vision for determining position and attitude (subtopic 3.1.2) and the quaternion based model for determining position and attitude by machine vision (subtopic 3.1.3). In subtopic 3.1.3, the initial position values are calculated by eq.(25) in this section; eq.(25) is based on Taylor expansion and least squares method. The second topic is: the algorithm for positioning and posing based on quaternion and spacecraft orbit and attitude information. Finally we give an example of numerical simulation, whose results are given in Figs. 8 through 10 in this section. These results show preliminarily that our proposed algorithm is much faster than Hall's.

3.1.1 Representation of 3D vector transformation by quaternion

Considering that \mathbf{x} stands for 3D vector, and \mathbf{x}' is a 3D vector from \mathbf{x} by transformation matrix \mathbf{R} , this transformation can be represented as

$$\mathbf{Q}_x = (0, \mathbf{x}) \tag{13}$$

$$\mathbf{Q}_{x'} = (0, \mathbf{x}') \tag{14}$$

$$\mathbf{Q} = (q_0, \mathbf{q}) = q_0 + q_1\mathbf{i} + q_2\mathbf{j} + q_3\mathbf{k} \tag{15}$$

$$\mathbf{Q}_{x'} = \mathbf{Q} \circ \mathbf{Q}_x \circ \mathbf{Q}^{-1} = \mathbf{Q} \circ \mathbf{Q}_x \circ \bar{\mathbf{Q}} \tag{16}$$

Where $\mathbf{Q}_x, \mathbf{Q}_{x'}, \mathbf{Q}$ are all quaternions, $\mathbf{Q}^{-1}, \bar{\mathbf{Q}}$ are inverse and onjugate of \mathbf{Q} , and \mathbf{Q} is the corresponding quaternion of matrix \mathbf{R} .

The relation of matrix \mathbf{R} and \mathbf{Q} can be described as

$$\mathbf{x}' = (q_0^2 - \mathbf{q} \cdot \mathbf{q})\mathbf{x} + 2q_0(\mathbf{q} \times \mathbf{x}) + 2(\mathbf{q} \cdot \mathbf{x})\mathbf{q} = \mathbf{R}\mathbf{x} \tag{17}$$

3.1.2 The camera model and the basic equation of computer vision

The process of relative position and pose based on computer vision is: first to extract and match the feature of the image; secondly to calculate the position and pose between the camera and the object. Therefore, camera model is the basis model of relative position and pose based on computer vision. And camera model is a simple style of optics imaging. This model represents the transformation from 3D to 2D object. Usually, two kinds of camera model, viz. linear and nonlinear camera model, are classified by the imaging process, whether object point, centre point and image point are co-lined or not. Nonlinear camera model is from linear camera model added by the aberration correction. In this paper we will apply linear camera model. The detail of nonlinear camera model can be see literature (Z.G. Zhu, 1995 ; S. D. Ma, 1998 ; G. J. Zhang, 2005 ; Marc Pollefeys, 2002).

Fig. 7 shows the projection relation of object point, centre point and image point. Where $O_I - uv$ stands for image frame, $O_i - x_i y_i$ stands for physical image frame, $O_c - x_c y_c z_c$ stands for camera frame, $O_w - x_w y_w z_w$ stands for object frame, this is consistent with body frame of objective spacecraft later.

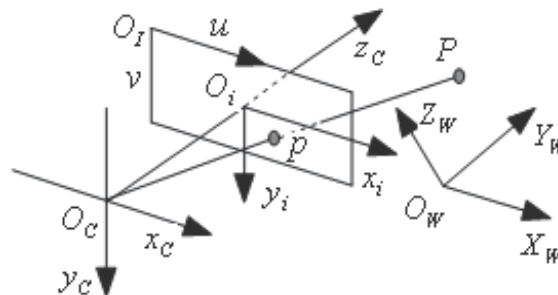


Fig. 7. Sketch of image frame, camera frame and object frame

The projection relation of object point, centre point and image point can be represented as,

$$\begin{cases} x_i = \frac{fx_C}{z_C} \\ y_i = \frac{fy_C}{z_C} \end{cases} \quad (18)$$

Where f is the focus of camera.

According to eq. (17) and (18), the relation of object frame and camera frame can be describe as

$$z_C \begin{bmatrix} x_i \\ y_i \\ 1 \end{bmatrix} = \begin{bmatrix} f & 0 & 0 & 0 \\ 0 & f & 0 & 0 \\ 0 & 0 & 1 & 0 \end{bmatrix} \begin{bmatrix} \mathbf{R} & \mathbf{t} \\ \mathbf{0}^T & 1 \end{bmatrix} \begin{bmatrix} x_W \\ y_W \\ z_W \\ 1 \end{bmatrix} = \begin{bmatrix} f & 0 & 0 & 0 \\ 0 & f & 0 & 0 \\ 0 & 0 & 1 & 0 \end{bmatrix} \begin{bmatrix} l_{11} & l_{12} & l_{13} & t_1 \\ l_{21} & l_{22} & l_{23} & t_2 \\ l_{31} & l_{32} & l_{33} & t_3 \\ 0 & 0 & 0 & 1 \end{bmatrix} \begin{bmatrix} x_W \\ y_W \\ z_W \\ 1 \end{bmatrix} \quad (19)$$

From formula (19), co-line equation is get as follows

$$\begin{cases} x_i = f \frac{l_{11}x_W + l_{12}y_W + l_{13}z_W + t_1}{l_{31}x_W + l_{32}y_W + l_{33}z_W + t_3} \\ y_i = f \frac{l_{21}x_W + l_{22}y_W + l_{23}z_W + t_2}{l_{31}x_W + l_{32}y_W + l_{33}z_W + t_3} \end{cases} \quad (20)$$

Eq. (20) is the basic equation of computer vision, $l_{ij}(i=1,2,3;j=1,2,3)$ is the relative attitude, $t_i(i=1,2,3)$ is the objective spacecraft coordinate defined in camera frame.

3.1.3 The relative position and pose model based-on quaternion

In eq. (20), there are six absolute parameters: three attitude parameters and three translation parameters. In order to reduce the calculation parameters, quaternion is applied here. Let

$$\begin{cases} \bar{X} = l_{11}x_W + l_{12}y_W + l_{13}z_W + t_1 = (q_0^2 + q_1^2 - q_2^2 - q_3^2)x_W + 2(q_1q_2 + q_0q_3)y_W + 2(q_3q_1 - q_0q_2)z_W + t_1 \\ \bar{Y} = l_{21}x_W + l_{22}y_W + l_{23}z_W + t_2 = 2(q_1q_2 - q_0q_3)x_W + (q_0^2 - q_1^2 + q_2^2 - q_3^2)y_W + 2(q_2q_3 + q_0q_1)z_W + t_2 \\ \bar{Z} = l_{31}x_W + l_{32}y_W + l_{33}z_W + t_3 = 2(q_3q_1 + q_0q_2)x_W + 2(q_2q_3 - q_0q_1)y_W + (q_0^2 - q_1^2 - q_2^2 + q_3^2)z_W + t_3 \end{cases} \quad (21)$$

Then eq. (20) can be rewritten as

$$\begin{cases} x_i = f \frac{\bar{X}}{\bar{Z}} \\ y_i = f \frac{\bar{Y}}{\bar{Z}} \end{cases} \quad (22)$$

Obviously, eq. (22) are nonlinear equations, then the linearisations are accomplished by expanding the function in a Taylor series to the first order (linear term) as,

$$\begin{cases} x_i = Fx_0 + \Delta Fx \\ y_i = Fy_0 + \Delta Fy \end{cases} \quad (23)$$

Where Fx_0, Fy_0 are the results of entered the initial value of q_0, q_1, q_2, q_3 , t_1, t_2, t_3 into eq. (22). $\Delta Fx, \Delta Fy$ are calculated as follows,

$$\left. \begin{aligned} \Delta Fx &= \frac{\partial x}{\partial q_0} \Delta q_0 + \frac{\partial x}{\partial \mathbf{q}} \Delta \mathbf{q} + \frac{\partial x}{\partial \mathbf{t}} \Delta \mathbf{t} \\ \Delta Fy &= \frac{\partial y}{\partial q_0} \Delta q_0 + \frac{\partial y}{\partial \mathbf{q}} \Delta \mathbf{q} + \frac{\partial y}{\partial \mathbf{t}} \Delta \mathbf{t} \end{aligned} \right\} \quad (24)$$

In eq. (24), $\Delta \mathbf{q} = (\Delta q_1, \Delta q_2, \Delta q_3)^T$, $\Delta \mathbf{t} = (\Delta t_1, \Delta t_2, \Delta t_3)^T$.

The iterative calculation above will be continued until the corrections less than the threshold values.

When observation point number $n > 4$, the results will be calculated by using least squares method. According to literature (Z.G. Zhu, 1995), the results of least squares method can be get from eq. (25) as follow,

$$\Delta \mathbf{X} = -(\mathbf{A}^T \mathbf{P} \mathbf{A})^{-1} \mathbf{A}^T \mathbf{P} \mathbf{I} \quad (25)$$

Where $\Delta \mathbf{X} = [\Delta q_0, \Delta q_1, \Delta q_2, \Delta q_3, \Delta t_1, \Delta t_2, \Delta t_3]^T$; \mathbf{A} is the coefficient matrix of \mathbf{X} coefficients of eq. (24). \mathbf{P} stands for weight matrix; $\mathbf{I} = [(Fx_0)_1 (Fy_0)_1 \cdots (Fx_0)_n (Fy_0)_n]^T - (x_1 \ y_1 \ \cdots \ x_n \ y_n)^T$; n is the number of observation.

3.1.4 Relative navigation based on quaternion and spacecraft orbit & attitude information

From above, we can see that the calculation speed of the relative position and pose algorithm based-on quaternion of least squares method depends on the initial value selection. In this section, we look spacecraft orbit & attitude information as initial values. And next section will introduce how to calculate the relative position and pose of spacecraft according to spacecraft orbit & attitude information.

a. Relative position calculated by using differential method

Considering there are active spacecraft A and objective spacecraft P, and their orbital elements are known, according to literature (Y. L. Xiao, 2003), the coordinates (x_A, y_A, z_A) , (x_P, y_P, z_P) of inertial frame of active spacecraft A and objective spacecraft P can be calculated. So the relative position can be described as

$$\begin{bmatrix} \Delta x_{AP} \\ \Delta y_{AP} \\ \Delta z_{AP} \end{bmatrix} = \begin{bmatrix} x_P \\ y_P \\ z_P \end{bmatrix} - \begin{bmatrix} x_A \\ y_A \\ z_A \end{bmatrix} \quad (26)$$

Finally we can transform $[\Delta x_{AP} \ \Delta y_{AP} \ \Delta z_{AP}]^T$ from inertial frame to body frame defined in active spacecraft A, and the relative position between spacecraft A and P is calculated.

b. Relative pose calculated by using quaternion

Considering S_A is the body frame of spacecraft A, S_P is the body frame of spacecraft P, the relation of S_A, S_P and inertial frame S_i can be represented by using Rodrigues as

$$\left. \begin{array}{l} S_i \quad \underline{\mathbf{Q}}_{Pi} \quad S_P \\ S_i \quad \underline{\mathbf{Q}}_{Ai} \quad S_A \\ S_P \quad \underline{\mathbf{Q}}_{AP} \quad S_A \end{array} \right\} \quad (27)$$

Thus relative attitude of spacecraft A and P can be described as

$$\mathbf{Q}_{AP} = \mathbf{Q}_{iP} \circ \mathbf{Q}_{Ai} \quad (28)$$

Where \circ is quaternion multiplication sign.

Usually, camera is fixed on the active spacecraft A, we can transform $[x_b \ y_b \ z_b]^T$ from the body frame of the active spacecraft A to the camera frame $O_C - x_C y_C z_C$ as follows

$$\begin{bmatrix} x_C \\ y_C \\ z_C \end{bmatrix} = \mathbf{M} \begin{bmatrix} x_b \\ y_b \\ z_b \end{bmatrix} + \mathbf{T} \quad (29)$$

Where \mathbf{M} is the attitude transition matrix, and \mathbf{T} is the transition matrix from body frame defined in active spacecraft A to camera frame. They can be designed or measured.

Hereto, the relative attitude and position parameters between objective spacecraft P and camera frame are calculated. Then let these parameters as the initial value of eq. (25). And then the relative attitude and position between active spacecraft A and objective spacecraft P can be determined quickly.

3.1.5 Simulations and analyses

On the basis of the algorithm above, let the camera focus $f = 350\text{mm}$, the objective spacecraft P is a $2m \times 2m \times 2m$ cube, and its body frame coordinates of feature points are respectively $\{-1,-1,1\}$, $\{-1,-1,-1\}$, $\{-1,1,1\}$, $\{-1,1,-1\}$, $\{-1,0,-1\}$, $\{0,0,1\}$, $\{1,-1,1\}$, $\{1,1,1\}$. Table 1 lists the initial parameters of the simulations. According to the parameters of table 1, calculate the relative position and pose parameters between active spacecraft A and objective spacecraft P by eq. (26) and (28). And let these relative parameters as true value $\tilde{\mathbf{X}}$. Then calculate image coordinates by eq. (22), and add one pixel white noise to the image coordinates and let them as the simulation observations. Finally, calculate the relative position and pose parameters $\hat{\mathbf{X}}$ between active spacecraft A and objective spacecraft P by eq. (23) and (25). The simulation time is 1200 seconds. Fig. 8 - Fig. 10 are the simulation results. It is not intuitionistic to represent the attitude results by quaternion, yet the attitude results are described as their Euler form. In Fig. 8 - Fig. 10, (a) stands for the results based on spacecraft orbit & attitude information, (b) stands for the results based on optional value. The results of simulation are calculated by using the computer of HP Pavilion Intel (R), Pentium (R) 4, CPU 3.06GHz, 512 MB, the consumable times of method (a) and (b) are 4662 ms and 7874 ms respectively.

	Active spacecraft A	Objective spacecraft B
ascending node/deg	0.0	0.0
inclination of orbit/deg	96.498	96.498005
argument of perigee/deg	0.0	0.0
excentricity	0.0	0.00000001
semi-major axis/km	7146.768	7146.768
time of perigee passage/s	0	0.008
yaw/deg	0.5	0.5
pitch/deg	0.2	0.2
roll/deg	0.4	0.5
yaw angle velocity/(deg/s)	5×10^{-7}	5×10^{-7}
pitch angle velocity/(deg/s)	5×10^{-7}	5×10^{-7}
roll angle velocity/(deg/s)	5×10^{-7}	5×10^{-7}

Table 1. The Initial parameters of the simulations

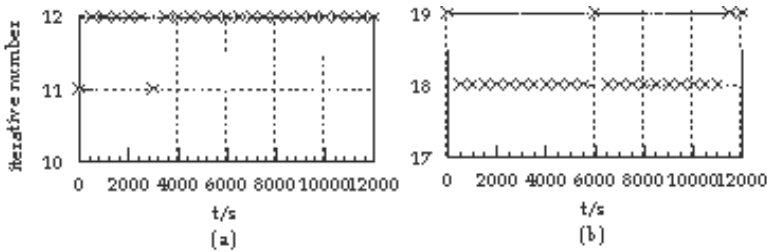


Fig. 8. Iterative number of the algorithm based-on quaternion

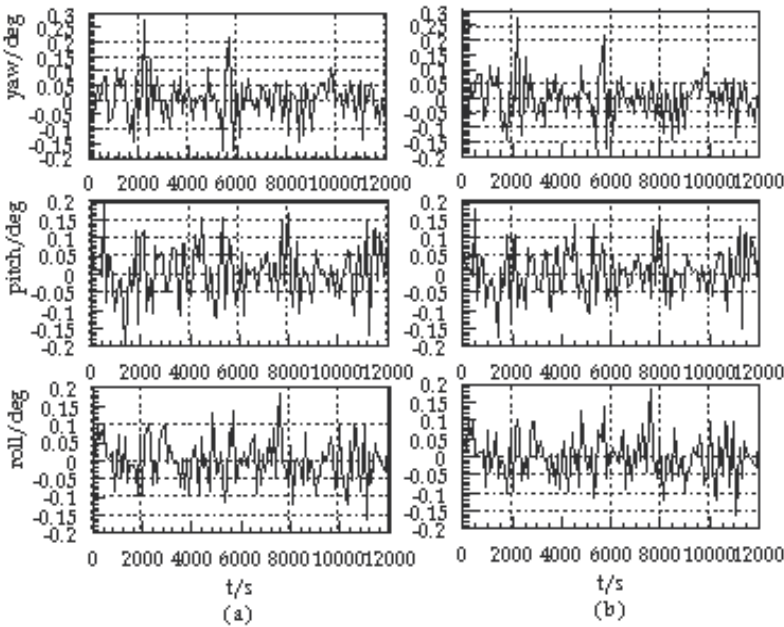


Fig. 9. Relative attitude errors of the algorithm based-on quaternion

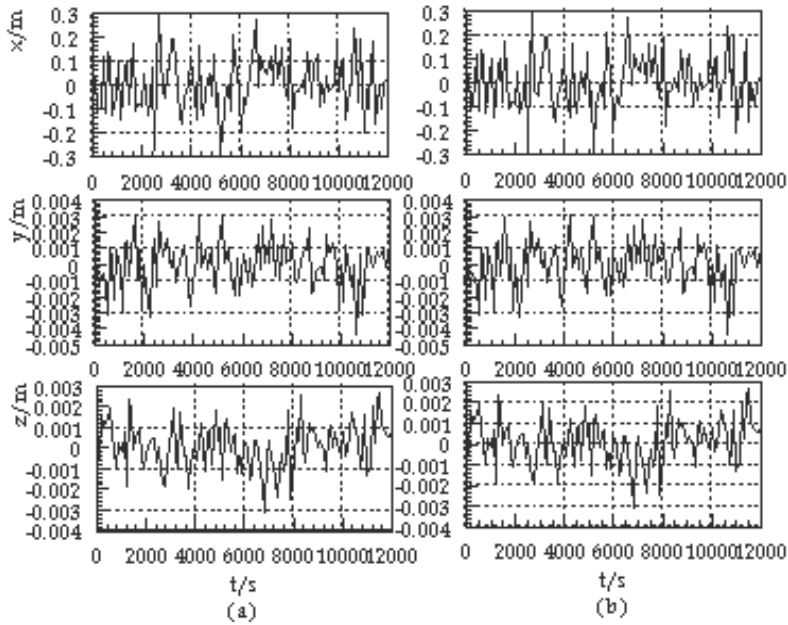


Fig. 10. Relative position errors of the algorithm based-on quaternion

From the simulation results, we can see that both two methods of (a) and (b) can get the high and similar precision results, whereas the iterative number of (a) is 11-12, and the iterative number of (b) is 18-19, moreover the consumable times of (a) is about half of the times of (b). All these show that the algorithm (a) is better than (b).

3.2 Static forecast algorithm based-on Rodrigues

As mentioned as 3.1 section, the algorithm based on quaternion is better than Hall's, because the Jacobi matrix of this method is lower than Hall's. But there is redundance value by using quaternion to represent the attitude. Rodrigues has three parameters to describe the attitude with no redundance variable. In this section we will discuss the static forecast algorithm by using Rodrigues.

3.2.1 Representation of 3D vector transformation by Rodrigues

Considering that \mathbf{x} stands for 3D vector, and \mathbf{x}' is a 3D vector from \mathbf{x} by transformation matrix \mathbf{R} , this transformation can be represented as

$$\mathbf{x}' = \mathbf{R}\mathbf{x} \tag{30}$$

$$\text{Where } \mathbf{R} = \frac{1}{\Delta} \begin{bmatrix} 1 + a^2 - b^2 - c^2 & 2(ab + c) & 2(ac - b) \\ 2(ab - c) & 1 - a^2 + b^2 - c^2 & 2(bc + a) \\ 2(ac + b) & 2(bc - a) & 1 - a^2 - b^2 + c^2 \end{bmatrix} = \begin{bmatrix} l_{11} & l_{12} & l_{13} \\ l_{21} & l_{22} & l_{23} \\ l_{31} & l_{32} & l_{33} \end{bmatrix},$$

$$\Delta = |\mathbf{I} + \mathbf{S}| = 1 + a^2 + b^2 + c^2.$$

3.2.2 The relative position and pose model based-on Rodrigues

In eq. (20), there are six absolute parameters: three attitude parameters and three translation parameters. In order to reduce the calculation parameters, Rodrigues is applied here. Let

$$\left. \begin{aligned} \bar{X} &= l_{11}x_W + l_{12}y_W + l_{13}z_W + t_1 = (1 + a^2 - b^2 - c^2)X_W + 2(ab + c)Y_W + 2(ac - b)Z_W + (1 + a^2 + b^2 + c^2)t_1 \\ \bar{Y} &= l_{21}x_W + l_{22}y_W + l_{23}z_W + t_2 = 2(ab - c)X_W + (1 - a^2 + b^2 - c^2)Y_W + 2(bc + a)Z_W + (1 + a^2 + b^2 + c^2)t_2 \\ \bar{Z} &= l_{31}x_W + l_{32}y_W + l_{33}z_W + t_3 = 2(ac + b)X_W + 2(bc - a)Y_W + (1 - a^2 - b^2 + c^2)Z_W + (1 + a^2 + b^2 + c^2)t_3 \end{aligned} \right\} \quad (31)$$

Then formula (20) can be rewritten as

$$\left. \begin{aligned} x_i &= f \frac{\bar{X}}{\bar{Z}} \\ y_i &= f \frac{\bar{Y}}{\bar{Z}} \end{aligned} \right\} \quad (32)$$

Obviously, eq. (32) are nonlinear equations, then the linearisations are accomplished by expanding the function in a Taylor series to the first order (linear term) as,

$$\left. \begin{aligned} x &= Rodrx_0 + \Delta Rodrx \\ y &= Rodry_0 + \Delta Rodry \end{aligned} \right\} \quad (33)$$

Where $Rodrx_0, Rodry_0$ are the results of entered the initial value of a, b, c into eq. (32). $\Delta Rodrx, \Delta Rodry$ are calculated as follows,

$$\Delta Rodrx = \frac{\partial x}{\partial a} \Delta a + \frac{\partial x}{\partial b} \Delta b + \frac{\partial x}{\partial c} \Delta c + \frac{\partial x}{\partial t_1} \Delta t_1 + \frac{\partial x}{\partial t_2} \Delta t_2 + \frac{\partial x}{\partial t_3} \Delta t_3 \quad (34)$$

$$\Delta Rodry = \frac{\partial y}{\partial a} \Delta a + \frac{\partial y}{\partial b} \Delta b + \frac{\partial y}{\partial c} \Delta c + \frac{\partial y}{\partial t_1} \Delta t_1 + \frac{\partial y}{\partial t_2} \Delta t_2 + \frac{\partial y}{\partial t_3} \Delta t_3 \quad (35)$$

In eq. (34) and (35), $\Delta a, \Delta b, \Delta c, \Delta t_1, \Delta t_2, \Delta t_3$ are the corrections of the initial value of a, b, c , $\frac{\partial x}{\partial a}, \frac{\partial x}{\partial b}, \frac{\partial x}{\partial c}, \frac{\partial y}{\partial a}, \frac{\partial y}{\partial b}, \frac{\partial y}{\partial c}, \frac{\partial x}{\partial t_1}, \frac{\partial x}{\partial t_2}, \frac{\partial x}{\partial t_3}, \frac{\partial y}{\partial t_1}, \frac{\partial y}{\partial t_2}, \frac{\partial y}{\partial t_3}$ are partial derivatives.

The iterative calculation above will be continued until the corrections less than the threshold values.

When observation point number $n > 4$, the results will be calculated by using least squares method. According to literature (Z.G. Zhu, 1995), the results of least squares method can be get from formula (12) as follow,

$$\Delta \mathbf{X} = -(\mathbf{A}^T \mathbf{P} \mathbf{A})^{-1} \mathbf{A}^T \mathbf{P} \mathbf{I} \quad (36)$$

Where $\Delta \mathbf{X} = [\Delta a, \Delta b, \Delta c, \Delta t_1, \Delta t_2, \Delta t_3]^T$; \mathbf{A} is the coefficient matrix of \mathbf{X} coefficients of formula (34) and (35). \mathbf{P} stands for weight matrix;

$\mathbf{I} = [((Rodrx_0)_1 \ (Rodry_0)_1 \ \cdots \ (Rodrx_0)_n \ (Rodry_0)_n)^T \ -(x_1 \ y_1 \ \cdots \ x_n \ y_n)^T]^T$; n is the number of observation.

3.2.3 Relative navigation based on Rodrigues and spacecraft orbit & attitude information

Considering S_a is the body frame of spacecraft A , S_p is the body frame of spacecraft P , the relation of S_a , S_p and inertial frame S_i can be represented by using Rodrigues as

$$\left. \begin{matrix} S_i & \text{Rodr}_{P_i} & S_p \\ S_i & \text{Rodr}_{A_i} & S_A \\ S_p & \text{Rodr}_{AP} & S_A \end{matrix} \right\} \quad (37)$$

Thus relative attitude of spacecraft A and P can be described as

$$\text{Rodr}_{AP} = \text{Rodr}_{iP} * \text{Rodr}_{Ai} \quad (38)$$

Where * is Rodrigues multiplication sign.

Hereto, as section 3.1, the relative attitude and position parameters between objective spacecraft P and camera frame are calculated. Then let these parameters as the initial value of eq. (36). And then the relative attitude and position between active spacecraft A and objective spacecraft P can be determined quickly.

3.2.4 Simulations and analyses

On the basis of the algorithm based-on Rodrigues above, considering the simulation conditions as 3.1.5 section, we can get the results as Fig. 11-Fig. 13. In Fig. 11-Fig. 13, (a) stands for the results based on spacecraft orbit & attitude information, (b) stands for the results based on optional value.

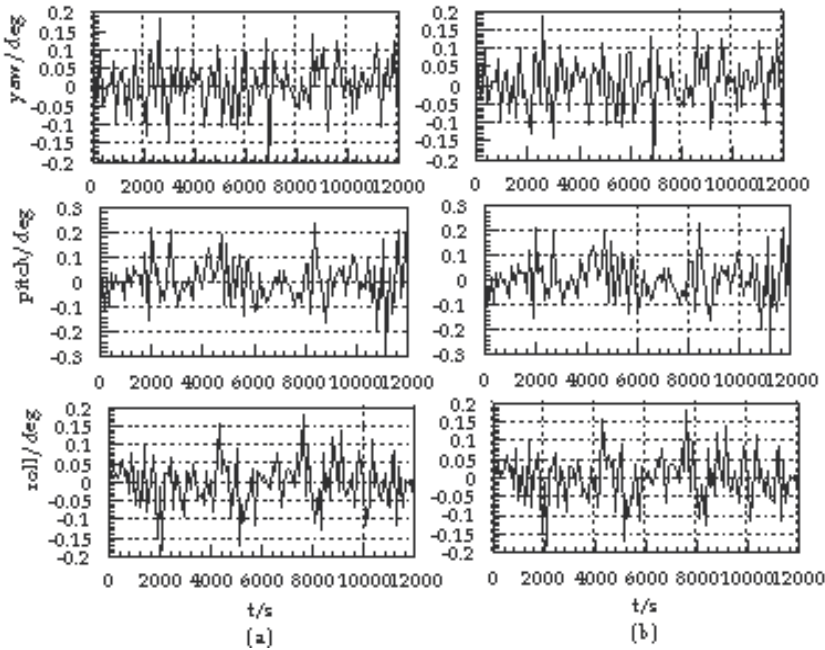


Fig. 11. Relative attitude errors of the algorithm based-on Rodrigues

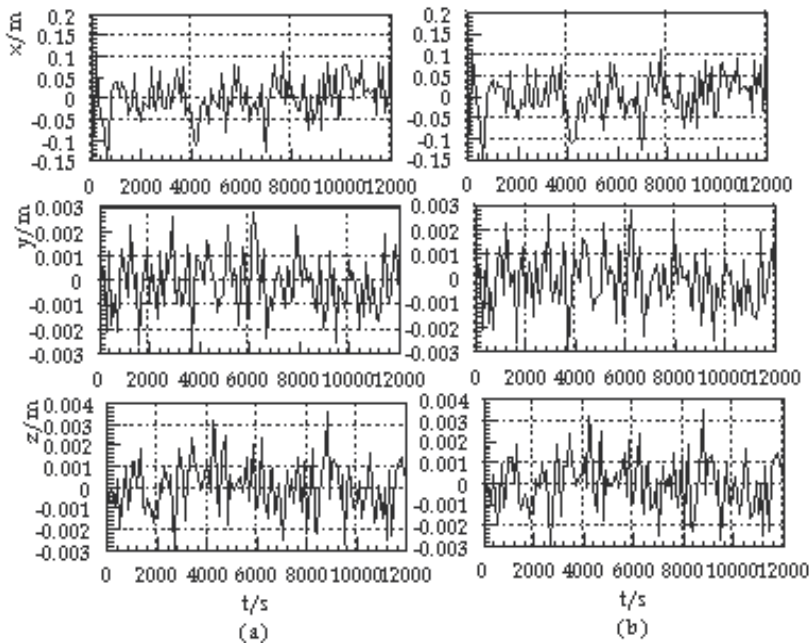


Fig. 12. Relative position errors of the algorithm based-on Rodrigues

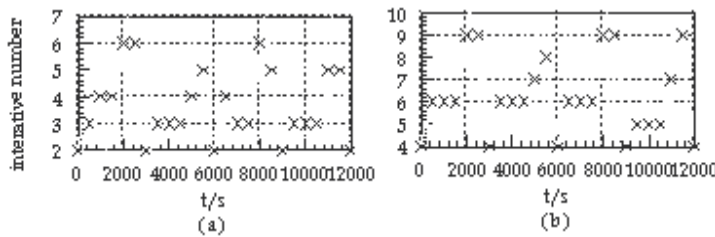


Fig. 13. Iterative number of calculation of the algorithm based-on Rodrigues

The results of simulation are calculated by using the computer of HP Pavilion Intel (R), Pentium (R) 4, CPU 3.06GHz, 512 MB, the consumable times of method (a) and (b) are 3281 ms and 6344 ms respectively.

From the simulation results, we can see that both two methods of (a) and (b) can get the high and similar precision results, whereas the iterative number of (a) is 1-5, and the iterative number of (b) is 4-9, moreover the consumable times of (a) is about half of the times of (b). All these show that the algorithm (a) is better than (b).

4. Pose and motion and estimation for spacecraft

4.1 Autonomous relative navigation for spacecraft based-on Quaternion and EKF (QEKF)

It is an innovative way to solve some difficult space problems by distributed spacecraft system, which depends on the collaboration each satellite of the system. And these difficult spacecraft problems always can not be solved by one satellite alone. Recent years, many researches about distributed spacecraft system have been developed. And considerable

progresses have been made in space exploration, earth observation and military domain etc (Graeme B. Shaw, 1998; Dr. Kim Luu, 1999; RF Antenna C. Sabol, 1999; H. P. Xu , 2006). But autonomous relative navigation, which is one of key technologies for distributed spacecraft system, and the relative theories need to be studied yet.

In this section, we first introduce how to select the state variable and build the state equations according to C-W equation and quaternion differential equation; Then how to build observation equation according to con-line equation of vision navigation and the state variable is described.

4.1.1 State equation of QEKF

To solve the dynamic estimation problem based on EKF, the state equation must be built. And how to select state variable is introduced here firstly. Since the filter computation time is proportional to the number of state variables, fewer variables are desirable. Based on the approach given by T. J. Broida (1990), J. S. Goddard (1997), Daniël François Malan (2004), thirteen variables are used. In these applications, angle velocity vector is regarded as constant. But in the application of relative navigation for spacecraft, relative angle velocity vector $(\omega_{AP})_b$ is a variable. In this chapter, we can estimate $(\omega_{AP})_b$ in advance, and look it as an input variable of time t . In this way, the number of state variables is reduced, but also the practical problem is solved well. Thus the state variables are three relative position variables $(\Delta x_{PA-O'}, \Delta y_{PA-O'}, \Delta z_{PA-O'})^T$, three relative velocity variables $(\Delta Vx, \Delta Vy, \Delta Vz)^T$ and four relative attitude variables $\Delta \mathbf{Q} = (\Delta q_0, \Delta q_1, \Delta q_2, \Delta q_3)^T$. Where the vector $(\Delta x_{PA-O'}, \Delta y_{PA-O'}, \Delta z_{PA-O'}, \Delta Vx, \Delta Vy, \Delta Vz)^T$ is defined in orbital frame of objective spacecraft, vector $\Delta \mathbf{Q}$ is defined in body frame of active spacecraft A . However, vision relative navigation is based on camera frame, and we must build the relationship of the camera frame, orbital frame and body frame each other. This will be studied in section three. As mentioned above, the state variable assignment is

$$\mathbf{S} = (\Delta x_{PA-O'}, \Delta y_{PA-O'}, \Delta z_{PA-O'}, \Delta Vx, \Delta Vy, \Delta Vz, \Delta q_0, \Delta q_1, \Delta q_2, \Delta q_3)^T \quad (39)$$

Without disturbances, according to literature (Y. L. Xiao, 2003), the nonlinear continuous equation of \mathbf{S} is

$$f(\mathbf{S}) = \frac{1}{2} \begin{bmatrix} 0 & 0 & 0 & 2 & 0 & 0 & 0 & 0 & 0 & 0 \\ 0 & 0 & 0 & 0 & 2 & 0 & 0 & 0 & 0 & 0 \\ 0 & 0 & 0 & 0 & 0 & 2 & 0 & 0 & 0 & 0 \\ 0 & 0 & 0 & 0 & 0 & 4\Omega & 0 & 0 & 0 & 0 \\ 0 & -2\Omega^2 & 0 & 0 & 0 & 0 & 0 & 0 & 0 & 0 \\ 0 & 0 & 6\Omega^2 & -4\Omega & 0 & 0 & 0 & 0 & 0 & 0 \\ 0 & 0 & 0 & 0 & 0 & 0 & 0 & -\omega_x & -\omega_y & -\omega_z \\ 0 & 0 & 0 & 0 & 0 & 0 & \omega_x & 0 & \omega_z & -\omega_y \\ 0 & 0 & 0 & 0 & 0 & 0 & \omega_y & -\omega_z & 0 & \omega_x \\ 0 & 0 & 0 & 0 & 0 & 0 & \omega_z & \omega_y & -\omega_x & 0 \end{bmatrix} \begin{bmatrix} \Delta x_{PA-O'} \\ \Delta y_{PA-O'} \\ \Delta z_{PA-O'} \\ \Delta Vx \\ \Delta Vy \\ \Delta Vz \\ \Delta q_0 \\ \Delta q_1 \\ \Delta q_2 \\ \Delta q_3 \end{bmatrix} \quad (40)$$

Where Ω is the angle velocity of objective satellite P , $(\omega_x, \omega_y, \omega_z)^T$ is the vector $(\boldsymbol{\omega}_{AP})_b$. From eq. (40), we can get the linearization matrix Φ .

4.1.2 Observation equation of QEKF

From equations (20) and (39), we can see that the state variables we selected are not related with image coordinate directly. So we must build the relationship between them before observation equation is built. Hereinafter, we will talk about the transformation of $(\Delta x_{PA-O'}, \Delta y_{PA-O'}, \Delta z_{PA-O'})^T$ firstly, and then will discuss the transformation of ΔQ .

4.1.2.1 The transformation of $(\Delta x_{PA-O'}, \Delta y_{PA-O'}, \Delta z_{PA-O'})^T$

- a. Transform $(\Delta x_{PA-O'}, \Delta y_{PA-O'}, \Delta z_{PA-O'})^T$ from orbital frame defined in objective spacecraft P to inertial frame defined in active spacecraft A as follows

$$\begin{bmatrix} \Delta x_{AP-i} \\ \Delta y_{AP-i} \\ \Delta z_{AP-i} \end{bmatrix} = - \begin{bmatrix} \Delta x_{PA-i} \\ \Delta y_{PA-i} \\ \Delta z_{PA-i} \end{bmatrix} = -\mathbf{L}_{P-iO} \mathbf{L}_{P-OO'} \begin{bmatrix} \Delta x_{PA-O'} \\ \Delta y_{PA-O'} \\ \Delta z_{PA-O'} \end{bmatrix} \quad (41)$$

Where \mathbf{L}_{P-iO} is the transition matrix from orbital frame defined in objective spacecraft P to its inertial frame; $\mathbf{L}_{P-OO'}$ is the transition matrix from second orbital frame defined in objective spacecraft P to its geocentric orbital frame.

- b. Transform $(\Delta x_{AP-i} \ \Delta y_{AP-i} \ \Delta z_{AP-i})^T$ form inertial frame defined in active spacecraft A to its body frame by the formulation

$$\begin{bmatrix} \Delta x_{AP-b} \\ \Delta y_{AP-b} \\ \Delta z_{AP-b} \end{bmatrix} = \mathbf{L}_{A-bO'} \mathbf{L}_{A-O'O} \mathbf{L}_{A-Oi} \begin{bmatrix} \Delta x_{AP-i} \\ \Delta y_{AP-i} \\ \Delta z_{AP-i} \end{bmatrix} \quad (42)$$

Where $\mathbf{L}_{A-bO'}$ is the transition matrix from second orbital frame defined in active spacecraft A to its body frame; $\mathbf{L}_{A-O'O}$ is the transition matrix from geocentric orbital frame in active spacecraft A to its second orbital frame; \mathbf{L}_{A-Oi} is the transition matrix from inertial frame defined in active spacecraft A to its geocentric orbital frame.

- c. Transform $(\Delta x_{AP-b} \ \Delta y_{AP-b} \ \Delta z_{AP-b})^T$ from body frame defined in active spacecraft A to camera frame by the formulation as follows

$$\begin{bmatrix} \Delta x_{AP-C} \\ \Delta y_{AP-C} \\ \Delta z_{AP-C} \end{bmatrix} = \mathbf{M} \begin{bmatrix} \Delta x_{AP-b} \\ \Delta y_{AP-b} \\ \Delta z_{AP-b} \end{bmatrix} + \mathbf{T} \quad (43)$$

Where \mathbf{M} is the attitude transition matrix, and \mathbf{T} is the transition matrix from body frame defined in active spacecraft A to camera frame. They can be designed or measured.

Thus the relative relationship between active spacecraft A and objective spacecraft P is built, we can described this relation by the formulation as follows

$$\begin{bmatrix} \Delta x_{AP-C} \\ \Delta y_{AP-C} \\ \Delta z_{AP-C} \end{bmatrix} = -\mathbf{M} \mathbf{L}_{A-bO'} \mathbf{L}_{A-O'} \mathbf{L}_{A-Oi} \mathbf{L}_{P-iO} \mathbf{L}_{P-OO'} \begin{bmatrix} \Delta x_{PA-O'} \\ \Delta y_{PA-O'} \\ \Delta z_{PA-O'} \end{bmatrix} + \mathbf{T} = \begin{bmatrix} r_{11} & r_{12} & r_{13} \\ r_{21} & r_{22} & r_{23} \\ r_{31} & r_{32} & r_{33} \end{bmatrix} \begin{bmatrix} \Delta x_{PA-O'} \\ \Delta y_{PA-O'} \\ \Delta z_{PA-O'} \end{bmatrix} + \begin{bmatrix} T_1 \\ T_2 \\ T_3 \end{bmatrix} \quad (44)$$

4.1.2.2 The transformation of $\Delta \mathbf{Q}$

We can translate the relative attitude \mathbf{M} into quaternion \mathbf{Q}_{Cb} form according to the transformation between cosine matrix and quaternion.

$$\mathbf{Q}_{Cb} = (q_{Cb-0} \quad q_{Cb-1} \quad q_{Cb-2} \quad q_{Cb-3})^T \quad (45)$$

And we can transform $\Delta \mathbf{Q}$ form body frame defined in active spacecraft A to camera frame by \mathbf{Q}_{Cb} as follows

$$\mathbf{Q}_{CP} = (q_{CP-0} \quad q_{CP-1} \quad q_{CP-2} \quad q_{CP-3})^T = \Delta \mathbf{Q} \circ \mathbf{Q}_{Cb} \quad (46)$$

Substitute $(\Delta x_{CP}, \Delta y_{CP}, \Delta z_{CP})^T$ of eq. (44), \mathbf{Q}_{CP} of eq. (46) for $t_i (i=1,2,3)$ and $a_{ij} (i=1,2,3; j=1,2,3)$ of eq. (20) in turn, observation equation about state variable \mathbf{S} can be represented as

$$\begin{cases} x_i = f \frac{l_{11}X_{W_i} + l_{12}Y_{W_i} + l_{13}Z_{W_i} + \Delta x_{AP-C}}{l_{31}X_{W_i} + l_{32}Y_{W_i} + l_{33}Z_{W_i} + \Delta z_{AP-C}} \\ y_i = f \frac{l_{21}X_{W_i} + l_{22}Y_{W_i} + l_{23}Z_{W_i} + \Delta y_{AP-C}}{l_{31}X_{W_i} + l_{32}Y_{W_i} + l_{33}Z_{W_i} + \Delta z_{AP-C}} \end{cases} \quad (47)$$

Where

$$\left. \begin{aligned} l_{11} &= q_{CP-0}^2 + q_{CP-1}^2 - q_{CP-2}^2 - q_{CP-3}^2 \\ l_{12} &= 2(q_{CP-1}q_{CP-2} + q_{CP-0}q_{CP-3}) \\ l_{13} &= 2(q_{CP-3}q_{CP-1} - q_{CP-0}q_{CP-2}) \\ l_{21} &= 2(q_{CP-1}q_{CP-2} - q_{CP-0}q_{CP-3}) \\ l_{22} &= q_{CP-0}^2 - q_{CP-1}^2 + q_{CP-2}^2 - q_{CP-3}^2 \\ l_{23} &= 2(q_{CP-2}q_{CP-3} + q_{CP-0}q_{CP-1}) \\ l_{31} &= 2(q_{CP-3}q_{CP-1} + q_{CP-0}q_{CP-2}) \\ l_{32} &= 2(q_{CP-2}q_{CP-3} - q_{CP-0}q_{CP-1}) \\ l_{33} &= q_{CP-0}^2 - q_{CP-1}^2 - q_{CP-2}^2 + q_{CP-3}^2 \end{aligned} \right\} \quad (48)$$

Let

$$\begin{cases} \bar{X} = l_{11}X_{W_i} + l_{12}Y_{W_i} + l_{13}Z_{W_i} + r_{11}\Delta x_{PA-O'} + r_{12}\Delta y_{PA-O'} + r_{13}\Delta z_{PA-O'} + T_1 \\ \bar{Y} = l_{21}X_{W_i} + l_{22}Y_{W_i} + l_{23}Z_{W_i} + r_{21}\Delta x_{PA-O'} + r_{22}\Delta y_{PA-O'} + r_{23}\Delta z_{PA-O'} + T_2 \\ \bar{Z} = l_{31}X_{W_i} + l_{32}Y_{W_i} + l_{33}Z_{W_i} + r_{31}\Delta x_{PA-O'} + r_{32}\Delta y_{PA-O'} + r_{33}\Delta z_{PA-O'} + T_3 \end{cases} \quad (49)$$

Then the formulation (47) can be simplified as

$$\begin{cases} x_i = f \frac{\bar{X}}{\bar{Z}} \\ y_i = f \frac{\bar{Y}}{\bar{Z}} \end{cases} \tag{50}$$

Obviously, the equations of eq. (50) are nonlinear about \mathbf{S} . And they must be linearized in visual relative navigation estimation based-on EKF. On the basis of the theory of EKF, we can get the linearization matrix \mathbf{H}_k of observation equation.

$$\mathbf{H}_k(\hat{\mathbf{S}}_k(-)) = \left. \frac{\partial h(\mathbf{S})}{\partial \mathbf{S}} \right|_{\mathbf{s}=\hat{\mathbf{S}}_k(-)} \tag{51}$$

Where \mathbf{H}_k is a $2i \times n$ matrix, i is the number of feature point, n is the number of state variable.

4.1.3 Simulations and analyses

On the basis of the algorithm above, let the camera focus $f = 50\text{mm}$, the objective spacecraft P is a $4.0\text{m} \times 4.0\text{m} \times 4.0\text{m}$ cube, and its body frame coordinates of feature points are respectively $\{-2.25,-8.5,2.25\}$, $\{-2.25,-7.8,-2.25\}$, $\{-2.25,9,2.25\}$, $\{-2.25,7.8,-2.25\}$, $\{-2.25,6.0,-2.25\}$, $\{1.25,7.6,2.25\}$, $\{2.25,-9,2.25\}$, $\{2.25,8.9,2.25\}$. Table 2 lists the initial parameters of the simulations. The initial variance covariance matrix of $[\Delta x \ \Delta y \ \Delta z]^T$ is $0.4\mathbf{I}_{3 \times 3}$, the variance covariance matrix of $[V_x \ V_y \ V_z]^T$ is $2 \times 10^{-4}\mathbf{I}_{3 \times 3}$, the variance covariance matrix of $\Delta \mathbf{Q}$ is $1 \times 10^{-7}\mathbf{I}_{4 \times 4}$ (\mathbf{I} is identity matrix).The simulation time is three periods. Fig. 14 is the simulation results.

	spacecraft A	spacecraft P	Initial parameters	
ascending node/deg	0	0	$\Delta x/\text{m}$	0.0
inclination of orbit/deg	57.5005	57.5	$\Delta y/\text{m}$	0.0
argument of perigee/deg	0	0	$\Delta z/\text{m}$	35.25502
eccentricity	0.000005	0.0	$V_x/(\text{m/s})$	0.07518633
semi-major axis/km	7051.000	7051.000	$V_y/(\text{m/s})$	-0.06561435
time of perigee passage/s	0	0	$V_z/(\text{m/s})$	0.0
yaw/deg	0.5	0.4	Δq_0	1
pitch/deg	0.2	0.2	Δq_1	0
roll/deg	0.5	0.5	Δq_2	0
yaw angle velocity/(deg/s)	5×10^{-7}	5×10^{-7}	Δq_3	0
pitch angle velocity/(deg/s)	5×10^{-7}	5×10^{-7}		
roll angle velocity/(deg/s)	5×10^{-7}	5×10^{-7}		

Table 2. The initial parameters of the simulations

It is not intuitionistic to represent the attitude results by quaternion, yet the attitude results are described as their Euler form.

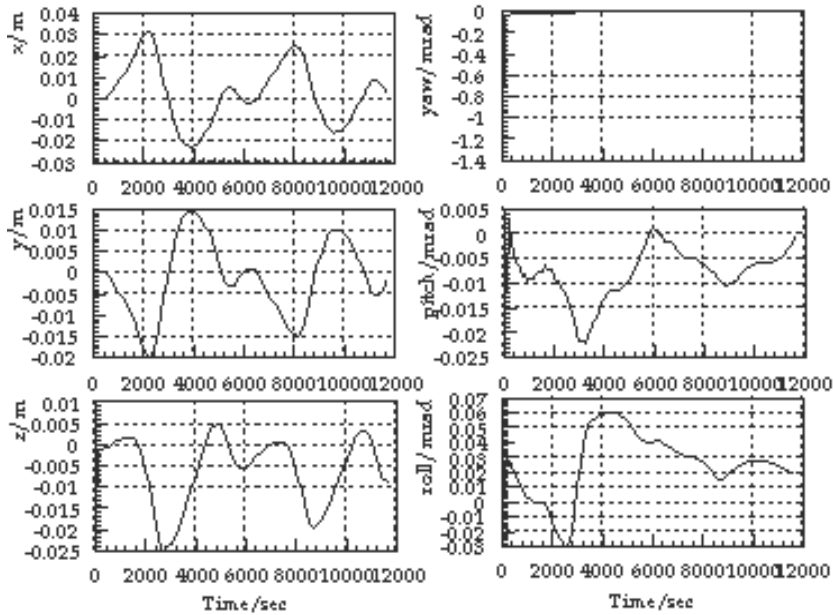


Fig. 14. Relative position and attitude errors of QEKF

From Fig. 14, we can see that this algorithm is convergent. And Fig. 14 shows the relative position x error is within $-0.03m$ to $0.04m$; y error is within $-0.02m$ to $0.015m$; z error is within $-0.025m$ to $0.01m$; relative yaw angle error is about -1.4 to zero mrad when the simulation time is about 400 seconds before, but after 400 seconds relative yaw angle error tend to zero; relative pitch error is within -0.025 to 0.005 mrad; relative roll angle error is within -0.03 mrad to 0.07 mrad.

4.2 Autonomous relative navigation for spacecraft based-on Rodrigues and EKF (REKF)

4.2.1 State equation of REKF

For Rodrigues with no redundancy valvate to represent the attitude. So here we use Rodrigues $\Phi_{AP-b} = (\Phi_{AP-b-1} \ \Phi_{AP-b-2} \ \Phi_{AP-b-3})^T$ instead of quaternion. As section 4.1, we can select the state variable assignment as eq. (52).

$$f(S) = \frac{1}{2} \begin{bmatrix} 0 & 0 & 0 & 2 & 0 & 0 & 0 & 0 & 0 \\ 0 & 0 & 0 & 0 & 2 & 0 & 0 & 0 & 0 \\ 0 & 0 & 0 & 0 & 0 & 2 & 0 & 0 & 0 \\ 0 & 0 & 0 & 0 & 0 & 4\Omega & 0 & 0 & 0 \\ 0 & -2\Omega^2 & 0 & 0 & 0 & 0 & 0 & 0 & 0 \\ 0 & 0 & 6\Omega^2 & -4\Omega & 0 & 0 & 0 & 0 & 0 \\ 0 & 0 & 0 & 0 & 0 & 0 & Rodr_{11} & Rodr_{12} & Rodr_{13} \\ 0 & 0 & 0 & 0 & 0 & 0 & Rodr_{21} & Rodr_{22} & Rodr_{23} \\ 0 & 0 & 0 & 0 & 0 & 0 & Rodr_{31} & Rodr_{32} & Rodr_{33} \end{bmatrix} \begin{bmatrix} \Delta x_{PA-O'} \\ \Delta y_{PA-O'} \\ \Delta z_{PA-O'} \\ \Delta V_x \\ \Delta V_y \\ \Delta V_z \\ \Delta a \\ \Delta b \\ \Delta c \end{bmatrix} \quad (52)$$

Where Ω is the angle velocity of objective satellite P , $Rodr_{11} = 2\Delta a\omega_x + \Delta b\omega_y + \Delta c\omega_z$, $Rodr_{12} = \Delta a\omega_y + \omega_z$, $Rodr_{13} = -\omega_y + \Delta a\omega_z$, $Rodr_{21} = \Delta b\omega_x - \omega_z$, $Rodr_{22} = \Delta a\omega_x + 2\Delta b\omega_y + \Delta c\omega_z$, $Rodr_{23} = \omega_x + \Delta b\omega_z$, $Rodr_{31} = \Delta c\omega_x + \omega_y$, $Rodr_{32} = -\omega_x + \Delta c\omega_y$, $Rodr_{33} = \Delta a\omega_x + \Delta b\omega_y + 2\Delta c\omega_z$, $(\omega_x, \omega_y, \omega_z)^T$ is the vector $(\omega_{AP})_b$.

From eq. (52), we can get the linearization matrix Φ .

4.2.2 Observation equation of REKF

The structural observation equation of REKF is similar to the QEKF's. Here we mainly discuss the transformation of $\Phi_{AP-b} = [\Phi_{AP-b-1} \ \Phi_{AP-b-2} \ \Phi_{AP-b-3}]^T$. Transform \mathbf{M} of eq. (44) into Rodrigues $\Phi_{Cb} = [\Phi_{Cb-1} \ \Phi_{Cb-2} \ \Phi_{Cb-3}]^T$, transform Φ_{AP-b} from body frame of active spacecraft to the camera frame as follows

$$\Phi_{CP} = \Phi_{AP-b} * \Phi_{Cb} \quad (53)$$

Substitute $(\Delta x_{CP}, \Delta y_{CP}, \Delta z_{CP})^T$ of eq. (44), Φ_{CP} of eq. (53) for $t_i (i=1,2,3)$ and $a_{ij} (i=1,2,3; j=1,2,3)$ of eq. (20) in turn, observation equation about state variable \mathbf{S} can be represented as

$$\begin{cases} x_i = f \frac{l_{11}X_{W_i} + l_{12}Y_{W_i} + l_{13}Z_{W_i} + \Delta x_{AP-C}}{l_{31}X_{W_i} + l_{32}Y_{W_i} + l_{33}Z_{W_i} + \Delta z_{AP-C}} \\ y_i = f \frac{l_{21}X_{W_i} + l_{22}Y_{W_i} + l_{23}Z_{W_i} + \Delta y_{AP-C}}{l_{31}X_{W_i} + l_{32}Y_{W_i} + l_{33}Z_{W_i} + \Delta z_{AP-C}} \end{cases} \quad (54)$$

$$\text{Where } \left. \begin{aligned} l_{11} &= (1 + \Phi_{CP-1}^2 - \Phi_{CP-2}^2 - \Phi_{CP-3}^2) / (1 + \Phi^2) \\ l_{12} &= 2(\Phi_{CP-1}\Phi_{CP-2} + \Phi_{CP-3}) / (1 + \Phi^2) \\ l_{13} &= 2(\Phi_{CP-1}\Phi_{CP-3} - \Phi_{CP-2}) / (1 + \Phi^2) \\ l_{21} &= 2(\Phi_{CP-1}\Phi_{CP-2} - \Phi_{CP-3}) / (1 + \Phi^2) \\ l_{22} &= (1 - \Phi_{CP-1}^2 + \Phi_{CP-2}^2 - \Phi_{CP-3}^2) / (1 + \Phi^2) \\ l_{23} &= 2(\Phi_{CP-2}\Phi_{CP-3} + \Phi_{CP-1}) / (1 + \Phi^2) \\ l_{31} &= 2(\Phi_{CP-1}\Phi_{CP-3} + \Phi_{CP-2}) / (1 + \Phi^2) \\ l_{32} &= 2(\Phi_{CP-2}\Phi_{CP-3} - \Phi_{CP-1}) / (1 + \Phi^2) \\ l_{33} &= (1 - \Phi_{CP-1}^2 - \Phi_{CP-2}^2 + \Phi_{CP-3}^2) / (1 + \Phi^2) \end{aligned} \right\} \quad (55)$$

The linear method of eq. (54) is similar to 4.1.2.2 section.

4.2.3 Simulations and analyses

On the basis of the theories of REKF, considering the simulation conditions as 4.1.3, and let $\Phi_{AP-b} = [0 \ 0 \ 0]^T$, the initial variance covariance matrix of Φ_{AP-b} is $1 \times 10^{-7} \mathbf{I}_{3 \times 3}$, we get the simulation results as Fig. 15.

From Fig. 15, we can see that this algorithm is convergent. And Fig. 15 shows the relative position x error is within -0.02m to 0.03m ; y error is within -0.015m to 0.01m ; z error is within -0.03m to 0.01m ; relative yaw angle error is about -0.7 to zero mrad when the simulation time is about 400 seconds before, but after 400 seconds relative yaw angle error tend to zero; relative pitch error is about -0.16 mrad when the simulation time is about 400 seconds before, but after 400 seconds relative pitch error is within -0.08 to 0.02 mrad; relative roll angle error is about -0.12 mrad when the simulation time is about 400 seconds before, but after 400 seconds relative roll error is within -0.04 to 0.04 mrad.

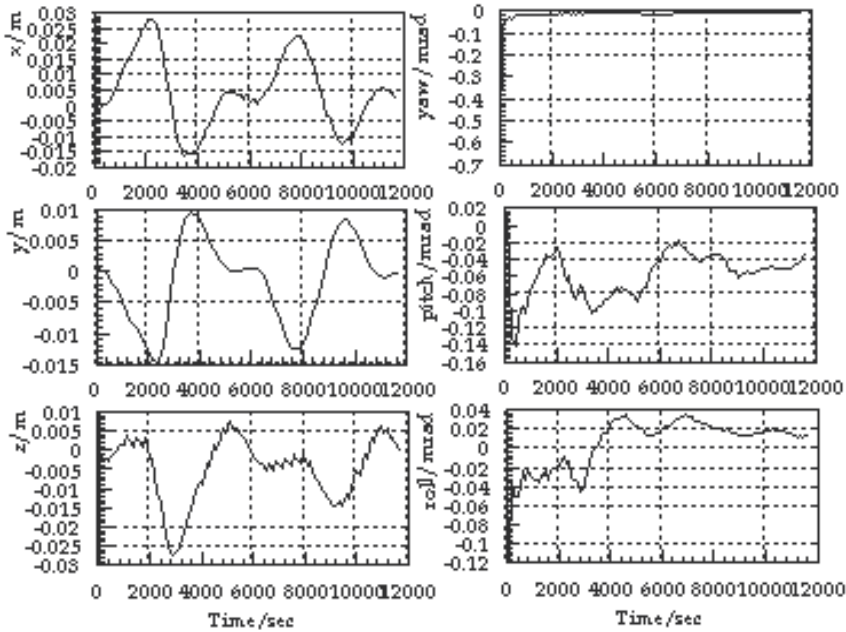


Fig. 15. Relative position and attitude errors of REKF

4.3 Autonomous relative navigation for spacecraft based-on Dual Quaternion and EKF (DQKF)

4.3.1 How to depict a 3-D line and its transformation with dual quaternion

According to geometric algebra theory (D. Hestenes, G. Sobczyk, 1984), dual quaternion can be found in special 4D even subalgebra of $\Xi_{3,0,1}$ and is spanned by the following basis

$$\underbrace{1}_{\text{scalar}} \quad \underbrace{e_2e_3, e_3e_1, e_1e_2, e_4e_1, e_4e_2, e_4e_3}_{\text{bivectors}} \quad \underbrace{I}_{\text{unit pseudoscalar}} \quad (56)$$

Since a rigid motion consists of the transformations rotation and translation according to Euler theorem, a simple rotor in its Euler representation for a rotation by an angle θ

$$\mathbf{R} = q_0 + q_1e_2e_3 + q_2e_3e_1 + q_3e_1e_2 = q_0 + \mathbf{q} = \cos(\theta/2) + \sin(\theta/2)\mathbf{n} = q_0 + q_s\mathbf{n} \quad (57)$$

Where \mathbf{n} is the unit 3D bivector of the rotation-axis spanned by the bivector basis e_2e_3, e_3e_1, e_1e_2 and $q_0, q_s (s=1,2,3) \in R$.

In $\Xi_{3,0,1}$, a translation \mathbf{t} is represented by a spinor \mathbf{T} . Thus applying \mathbf{T} from the left and its conjugated from the right to the \mathbf{R} in eq. (57), we can get the modified rotor

$$\mathbf{M} = \mathbf{TRT}^* = (1 + \mathbf{I}\frac{\mathbf{t}}{2})(q_0 + \mathbf{q})(1 - \mathbf{I}\frac{\mathbf{t}}{2}) = q_0 + \mathbf{q} + \mathbf{I}(\mathbf{q} \wedge \mathbf{t}) \tag{58}$$

As we know a 3D line \mathbf{l}_a can be represented by Plücker coordinate

$$\tilde{\mathbf{l}}_a = \mathbf{l}_a + \varepsilon \mathbf{m}_a \tag{59}$$

Hence the Euclidean transformation of the 3D line \mathbf{l}_a by the modified rotor \mathbf{M} can be represented

$$\tilde{\mathbf{l}}_b = \mathbf{l}_b + \varepsilon \mathbf{m}_b = \mathbf{M}\tilde{\mathbf{l}}_a\mathbf{M}^* \tag{60}$$

4.3.2 State equation of DQEKF

The structural state equation of DQEKF is similar similar to the QEKF's. It is unnecessary to go into details.

4.3.3 Observation equation of DQEKF

On the basis of 4.3.1, here we will build the observation equations according to the observation valuable. Fig.16 shows the relation of projective line and projective plane with space object frame.

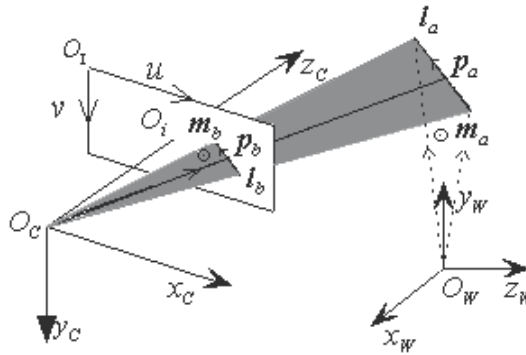


Fig. 16. Relation of projective line and projective plane with space object frame

$O_W - x_W y_W z_W$ stands for object frame, i.e. body frame of passive spacecraft in this paper; $O_C - x_C y_C z_C$ stands for camera frame; $O_i - x_i y_i$ stands for image frame. In Fig.16, \mathbf{l}_a stands for a 3D object line and its projective line is \mathbf{l}_b . We can represent the transformation between \mathbf{l}_a and \mathbf{l}_b as formulation (60). But how to calculate the translator \mathbf{M} using image coordinates and object coordinates? In order to process the data simply, first we give a definition as follow.

Definition: Feature line point is the intersection point of the projective line \mathbf{l}_b and a perpendicular line passing through the origin O_i , it is unique.

In camera frame, the projective plane, which is shown in grey, can be represented as

$$m_{bx}x_C + m_{by}y_C + m_{bz}z_C = 0 \tag{61}$$

Where $(m_{bx} \ m_{by} \ m_{bz})^T = \mathbf{m}_b$.

From Fig.16, we can see that the projective line \mathbf{l}_b lies in either projective plane or image plane. When $z_C = f$ (f is the focus of the camera), the equation of the projective line \mathbf{l}_b lies in image plane can be described as

$$m_{bx}x_i + m_{by}y_i + m_{bz}f = 0 \tag{62}$$

Thus we can get the vector \mathbf{m}_{bP} containing the feature line point of \mathbf{l}_b normal to the projective plane

$$\mathbf{m}_{bP} = \frac{f}{\sqrt{m_{bx}^2 + m_{by}^2}} [m_{bx} \ m_{by} \ m_{bz}]^T \tag{63}$$

Then the feature line point of \mathbf{l}_b coordinates is described as

$$\begin{cases} x_{iP} = -f \frac{m_{bx}m_{bz}}{m_{bx}^2 + m_{by}^2} \\ y_{iP} = -f \frac{m_{by}m_{bz}}{m_{bx}^2 + m_{by}^2} \end{cases} \tag{64}$$

\mathbf{m}_b can be calculated according to literature (LI K. Z, 2007).

Obviously, eq. (64) are nonlinear equations about \mathbf{S} . And they must be linearized in visual relative navigation estimation based-on EKF. The partial differential equations to eq. (64) about \mathbf{S} can be represented as follows

$$\left. \begin{aligned} \frac{\partial x_{iP}}{\partial \mathbf{S}} &= \frac{\partial x_{iP}}{\partial m_{bx}} \frac{\partial m_{bx}}{\partial \mathbf{S}} + \frac{\partial x_{iP}}{\partial m_{by}} \frac{\partial m_{by}}{\partial \mathbf{S}} + \frac{\partial x_{iP}}{\partial m_{bz}} \frac{\partial m_{bz}}{\partial \mathbf{S}} \\ \frac{\partial y_{iP}}{\partial \mathbf{S}} &= \frac{\partial y_{iP}}{\partial m_{bx}} \frac{\partial m_{bx}}{\partial \mathbf{S}} + \frac{\partial y_{iP}}{\partial m_{by}} \frac{\partial m_{by}}{\partial \mathbf{S}} + \frac{\partial y_{iP}}{\partial m_{bz}} \frac{\partial m_{bz}}{\partial \mathbf{S}} \end{aligned} \right\} \tag{65}$$

From eq. (57)-(60), we can get the equation as follows

$$\mathbf{l}_b + \varepsilon \mathbf{m}_b = (\mathbf{q} + \varepsilon \frac{\mathbf{t}}{2} \mathbf{q})(\mathbf{l}_a + \varepsilon \mathbf{m}_a)(\mathbf{q}^* + \varepsilon \frac{1}{2} \mathbf{q}^* \mathbf{t}^*) = \mathbf{q} \mathbf{l}_a \mathbf{q}^* + \varepsilon (\frac{1}{2} \mathbf{q} \mathbf{l}_a \mathbf{q}^* \mathbf{t}^* + \mathbf{q} \mathbf{m}_a \mathbf{q}^* + \frac{1}{2} \mathbf{t} \mathbf{q} \mathbf{l}_a \mathbf{q}^*) \tag{66}$$

And from eq. (66), we can get

$$\mathbf{m}_b = \frac{1}{2} \mathbf{q} \mathbf{l}_a \mathbf{q}^* \mathbf{t}^* + \mathbf{q} \mathbf{m}_a \mathbf{q}^* + \frac{1}{2} \mathbf{t} \mathbf{q} \mathbf{l}_a \mathbf{q}^* \tag{67}$$

According to the theories of quaternion, we can described the eq. (67) as follows

$$\mathbf{m}_b = \frac{1}{2} \mathbf{M}_t^- \mathbf{M}_q^+ \mathbf{M}_q^- \mathbf{l}_a + \mathbf{M}_q^+ \mathbf{M}_q^- \mathbf{m}_a + \frac{1}{2} \mathbf{M}_t^+ \mathbf{M}_q^+ \mathbf{M}_q^- \mathbf{l}_a \tag{68}$$

$$\text{Let } \mathbf{R}_M = \mathbf{M}_q^+ \mathbf{M}_q^- = \begin{bmatrix} 1 & 0 & 0 & 0 \\ 0 & q_0^2 + q_1^2 - q_2^2 - q_3^2 & 2(q_1q_2 + q_0q_3) & 2(q_3q_1 - q_0q_2) \\ 0 & 2(q_1q_2 - q_0q_3) & q_0^2 - q_1^2 + q_2^2 - q_3^2 & 2(q_2q_3 + q_0q_1) \\ 0 & 2(q_3q_1 + q_0q_2) & 2(q_2q_3 - q_0q_1) & q_0^2 - q_1^2 - q_2^2 + q_3^2 \end{bmatrix} \quad (69)$$

Where $[q_0 \ q_1 \ q_2 \ q_3]^T = [q_{CP-0} \ q_{CP-1} \ q_{CP-2} \ q_{CP-3}]^T$,

$$\mathbf{M}_{t,t^*} = 2 \begin{bmatrix} 0 & 0 & 0 & 0 \\ 0 & 0 & -t_3 & t_2 \\ 0 & t_3 & 0 & -t_1 \\ 0 & -t_2 & t_1 & 0 \end{bmatrix} \quad (70)$$

Eq. (68) can be simplified as follows

$$\mathbf{m}_b = \mathbf{R}_M \mathbf{m}_a + \frac{1}{2} \mathbf{M}_{t,t^*} \mathbf{R}_M \mathbf{l}_a \quad (71)$$

So the partial differential equations of \mathbf{S} can be calculated simply from eq. (71).

4.3.4 Simulations and analyses

On the basis of the theories of DQEKF, considering the simulation conditions as 4.1.3 section, we can get the results as Fig. 17.

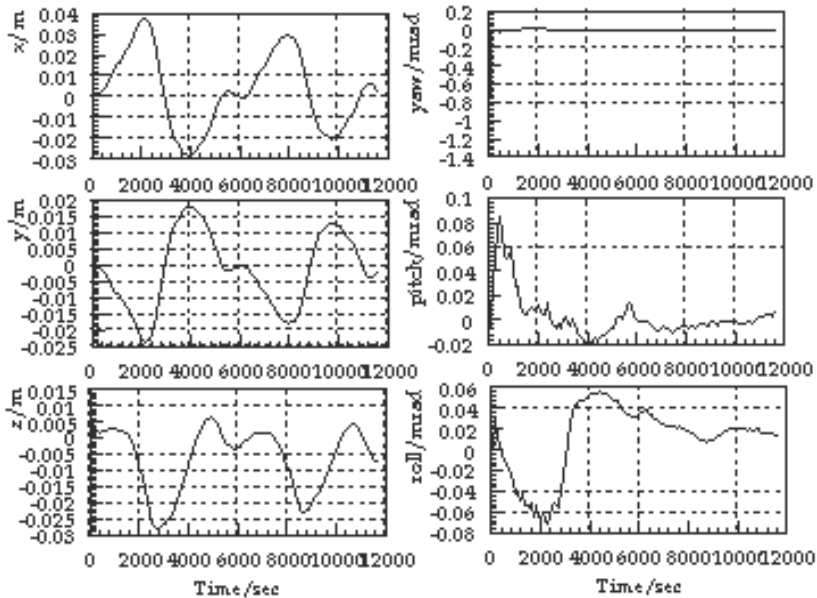


Fig. 17. Relative position and attitude errors of DQEKF

From Fig. 17, we can see that this algorithm is convergent. And Fig. 17 shows the relative position x error is within -0.03m to 0.04m; y error is within -0.025m to 0.02m; z error is within -0.03m to 0.015m; relative yaw angle error is about -1.4 to zero mrad when the simulation time is about 400 seconds before, but after 400 seconds relative yaw angle error tend to zero; relative pitch error is about 0.1 mrad when the simulation time is about 400 seconds before, but after 400 seconds relative pitch error is within -0.02 to 0.04 mrad; relative roll angle error is within -0.08 to 0.06 mrad.

4.4 Autonomous relative navigation for spacecraft based-on Dual Rodrigues-Quaternion and EKF (DRQEKF)

4.4.1 State equation of DRQEKF

Compare with section 4.3, here we use Rodrigues $\Phi_{AP-b} = (\Phi_{AP-b-1} \ \Phi_{AP-b-2} \ \Phi_{AP-b-3})^T$ instead of quaternion. Thus the structural state equation of DRQEKF is similar similar to section 4.2.1. It is unnecessary to go into details.

4.4.2 Observation equation of DRQEKF

For attitude matrix has a unique attribute, \mathbf{R}_M of eq. (69) can also be represented as

$$\mathbf{R}_M = \begin{bmatrix} 1 & 0 & 0 & 0 \\ 0 & l_{11} & l_{12} & l_{13} \\ 0 & l_{21} & l_{22} & l_{23} \\ 0 & l_{31} & l_{32} & l_{33} \end{bmatrix} \quad (72)$$

$l_{ij} (i = 1, 2, 3; j = 1, 2, 3)$ of eq. (72) equal to l_{ij} of eq. (55).

So the partial differential equations to eq. (71) about $\Phi_{AP-b-i} (i = 1, 2, 3)$ can be represented as follows

$$\frac{\partial \mathbf{m}_b}{\partial \Phi_{AP-b-i}} = \frac{\partial \mathbf{R}_M}{\partial \Phi_{AP-b-i}} \mathbf{m}_a + \frac{1}{2} \mathbf{M}_{t,t} \cdot \frac{\partial \mathbf{R}_M}{\partial \Phi_{AP-b-i}} \mathbf{1}_a, (i = 1, 2, 3) \quad (73)$$

The other partial differential of the state valuable parameters can be deduced as section 4.3.3.

4.4.3 Simulations and analyses

On the basis of the theories of DRQEKF, considering the simulation conditions as 4.1.3 and 4.1.3 sections, we can get the results as Fig. 18.

From Fig. 18, we can see that this algorithm is convergent. And Fig. 18 shows the relative position x error is within -0.02m to 0.03m; y error is within -0.02m to 0.01m; z error is within -0.03m to 0.01m; relative yaw angle error is about -0.5 to zero mrad when the simulation time is about 400 seconds before, but after 400 seconds relative yaw angle error tend to zero; relative pitch error is about -0.1 mrad when the simulation time is about 400 seconds before, but after 400 seconds relative pitch error is within -0.08 to 0.02 mrad; relative roll angle error is within -0.08 to 0.08 mrad.

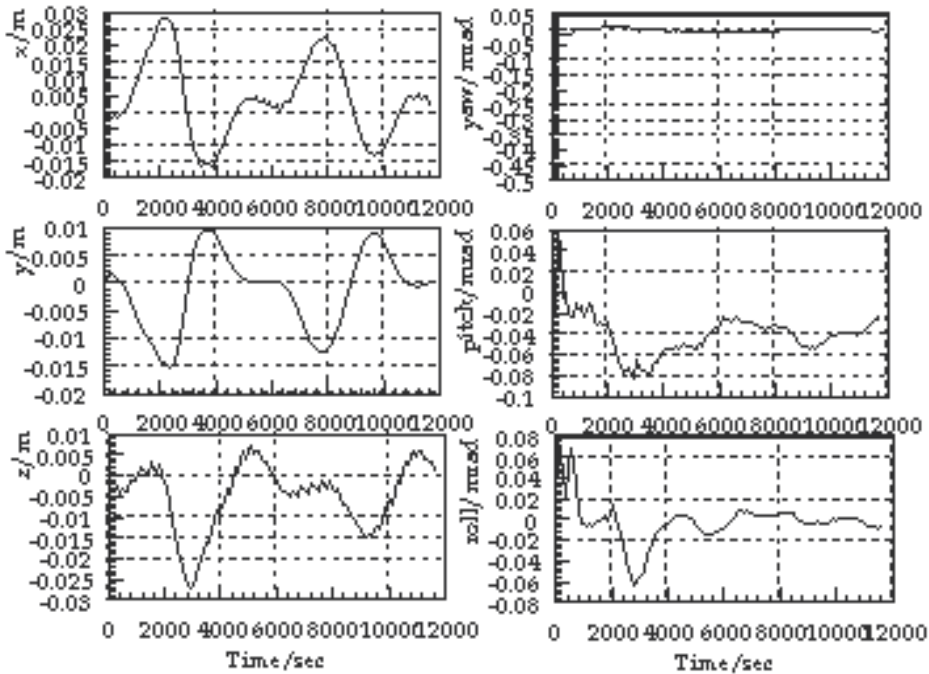


Fig. 18. Relative position and attitude errors of DRQEKF

5. Conclusion

In section 2, a feature extraction algorithm based-on dynamically structured element is proposed. The simulation results show that this algorithm is an accurate valid method in feature extraction for distributed spacecraft system.

In section 3, we propose the relative position and pose algorithms based on quaternion/Rodrigues and the orbit & attitude information of the spacecrafts. The algorithms reduces the Jacobian matrix rank by using quaternion/Rodrigues. The simulations show that the iterative numbers of this algorithm are reduced when the orbit & attitude information of the spacecrafts has been used. The algorithm based-on Rodrigues is better than quaternion's when attitude angles are smaller. This thought is valuable for the similar applications based on least squares method.

In section 4, four pose and motion estimation algorithms are proposed. And they can meet the high requirement of spacecraft. QEKF and REKF are based-on point observations, and DQEKF and DRQEKF are based-on line observations. The results of simulation are calculated by using the computer of HP Pavilion Intel (R), Pentium (R) 4, CPU 3.06GHz, 512 MB, the consumable times of method QEKF, REKF, DQEKF and DRQEKF are 6688 ms, 4187 ms, 12437 ms and 7141 ms respectively. So if the observations are points, REKF is proposed when the attitude angles are smaller; if the observations are lines, DRQEKF is proposed when the attitude angles are smaller.

In our future work, the theories in SE reconstruction and relative position and attitude combination will be further studied, and the corresponding simulations about them will be also researched. And we will consider the disturbance factor of satellites in order to improve the practicability of the static forecast and the pose and motion estimation algorithms.

6. Acknowledgment

The authors wish to thank Jikun Ou, who is a precisian and kindly professor of Institute of Geodesy and Geophysics, Chinese Academy of Sciences. This work is supported by Projects of the Ministry of Land and Resources P.R.C (Grant No. 1212010914015), Doctor Foundation of Henan Polytechnic University (Grant No. 648296) and National Natural Science Funds for Distinguished Young Scholar (Grant No 50525414).

7. References

- D.Mehrholz, L.Leushacke, W.Flury etc (2002). Detecting, tracking and imaging space debris. *ESA bulletin*, February 2002, 109, pp: 128-134
- Ben Iannotta (2002). DART Aims at Space Rendezvous. *Aerospace America*, March 2005, pp. 26-30
- Richard P. Kornfeld, Robert L (2002). Bunker, Gordy C. Cucullu, et al. New Millennium ST6 Autonomous Rendezvous Experiment (ARX). IEEEAC paper #1114, Updated September 19, 2002, pp. 1-12
- LiYingju · LiHui Feng · NingWei (2006). Rendezvous and Docking Technologies—Present and Future. *Sciencepaper Online*, <http://www.paper.edu.cn>. pp: 1-5
- Michael A. Dornheim (2006). Orbital Express to Test Full Autonomy for On-Orbit Service. http://www.aviationweek.com/aw/generic/story_generic.jsp?channel=awst&id=news/aw060506p1.xml
- Joseph W. Evans, Tom A. Mulder (2006). Autonomous Rendezvous Guidance and Navigation for Orbital Express and Beyond. *16th AAS/AIAA Space Flight Mechanics Conference*, Tampa, Florida, January 22-26, 2006, Paper AAS 06-194
- Richard T. Howard, Andrew F. Heaton, Robin M. Pinson etc (2008). The Advanced Video Guidance Sensor: Orbital Express and the Next Generation. http://ntrs.nasa.gov/archive/nasa/casi.ntrs.nasa.gov/20080015656_2008015631.pdf, pp : 1-8
- Isao Kawano, Masaaki Mokuno, Toru Kasai, Takashi Suzuki (1999). Result and Evaluation of Autonomous Rendezvous Docking Experiment of ETS-VII. AIAA-99-4073
- Yoshihiko Torano (2010). H-IIA Launch Vehicle. <http://www.jaxa.jp/pr/brochure/pdf/01/rocket03.pdf>, pp :1-4
- Gianni Casonato, Giovanni B. Palmerini (2004). Visual Techniques Applied to the ATV/ISS Rendez-Vous Monitoring. *IEEE Aerospace Conference Proceedings*, pp. 613-625
- Wang Guangjun, Tian Jinwen, Liu jian (2004). Infrared small objects detection based on local entropy method, *Infrared and laser engineering*, Vol.29 No.4, pp. 26-29
- Li Guokuan, Peng Jiexiong (2000). Infrared Imaging Dim Target Detection Based on Wavelet Transformation, *J. Huazhong Univ. of Sci. & Tech.*, 28 (5), pp. 69-71

- H. P. Xu , J. Chen, B. F. Wang , Y. Q. Zhou (2006). Quick method of distributed small satellite synthetic aperture radar single-look complex image simulation. *Journal of Beijing University of Aeronautics and Astronautics*, pp : 445-449
- Richard Alan Peters II (1995). A new algorithm for image noise reduction using mathematical morphology. *IEEE Translation on Imaging Processing*, 4 (3): pp : 554-568
- Joonki Paik, Cheolha P.Lee, and Mongi A. Abidi (2002). *Image processing-based mine detection techniques: A review. Subsurface Sensing Technologies and Applications*, 3 (3): pp :203-252
- Ulisses Braga-Neto, Manish Choudhary and Johan Goutsias (2003). Automatic target detection and tracking in forward-looking infrared image sequences using morphological connected operators. *Journal of Electronic Imaging*, 3: pp : 1-22.
- Cui Yi (2002). Imaging processing and analysis-mathematical morphology methods and applications. Beijing : *Science Press*, pp : 1-157
- Y. L. Xiao (2003). Foundation of Flight Dynamics-Modeling of Aerospace Vehicle Motion. *BeiHang University Press*, pp : 1-80
- Schwab A. L (2002). Quaternions, Finite Rotation and Euler Parameters [EB/OL]. <http://tam.cornell.edu/~als93/quaternion.pdf>, pp :1-4
- Z.G. Zhu, H. Sun, B. G. Cui (1995). Foundation of Photogrammetry. *Mapping Press of China*, 185-190 (In Chinese)
- S. D. Ma, Z. Y. Zhang (1998). Computer Vision—Foundation of Calculation and Algorithm. *Science Press*, PP : 20-36 (In Chinese)
- G. J. Zhang (2005). Machine Vision. *Science Press of China*, pp : 14-32 (In Chinese)
- Marc Pollefeys (2002). Visual 3D Modeling from Images. <http://www.cs.unc.edu/~marc/tutorial.pdf>, pp :8-100
- Graeme B. Shaw (1998). The Generalized information network analysis methodology for distributed satellite systems [Ph.D Thesis]. MIT, pp: 12-58
- Dr. Kim Luu, Mr. Maurice Martin, Dr. Mike Stallard, et al. (1999). University Nanosatellite Distributed Satellite Capabilities to support TechSat 21. *AIAA/USU SMALL SATELLITE CONFERENCE, LOGAN UT*, pp : 23-26
- RF Antenna C. Sabol, R. Burns, and C. McLaughlin (1999). Formation Flying Design and Evolution. *AAS/AIAA Spaceflight Mechanics Meeting, Breckenridge, CO*, 7-10 February 1999, AAS paper, pp : 99-121
- T. J. Broida, S.Chandrashekhar, R. Chaellappa (1990). Recursive 3-D motion estimation from a monocular image sequence. *IEEE Transactions on Aerospace and Electronic Systems*, 26 (4), pp : 639-656
- J. S. Goddard (1997). Pose and Motion Estimation from Vision Using Dual Quaternion-Based Extended Kalman Filtering [Ph. D Thesis]. *The University of Tennessee, Knoxville*, pp : 20-60
- Daniël François Malan (2004). 3D Tracking between Satellites using Monocular Computer Vision [Master Thesis]. Department of Electrical & Electronic Engineering, *University of Stellenbosch*, pp : 35-88
- D. Hestenes, G. Sobczyk (1984). Clifford Algebra to Geometric calculus. D. *Reidel Publishing Company, Holland*, pp: 45-78

LI K. Z., Yuan J. P, Yue X. K. , FANG Q. (2007). Autonomous Navigation Algorithm for Spacecrafts Based-on Dual Quaternion, *Second International Conference on Space Information Technology*, Proc. SPIE 6795, 3K1-3K6

Part 3

Novel Control Methods

Inertia-Independent Generalized Dynamic Inversion Control of Spacecraft Attitude Maneuvers

Abdulrahman Bajodah
King Abdulaziz University
Saudi Arabia

1. Introduction

Dynamic inversion (DI) is a transformation from a nonlinear system to an equivalent linear system, performed by means of a change of variables and through feedback. The theory of DI was initially formalized in (Su, 1982) and (Hunt et al., 1983), and its first reported application to spacecraft attitude control problem is due to (Dwyer III, 1984). The methodology is widely accepted among control system practitioners because it substantially facilitates control system design. Additionally, it preserves the nonlinear nature of plant's dynamics and thus it avoids limitations of linearizing approximations.

Classical DI is based on constructing inverse mapping of the controlled plant and augmenting it within the feedback control system. Therefore the linearizing transformation depends heavily on nature of the plant, and it becomes difficult or impossible as complexity of the plant increases. For this reason it may become necessary to introduce simplifying approximations to the plant's mathematical model in order to obtain the DI linearizing transformation, which adversely affects closed loop control system stability and performance characteristics in real implementations of the transformation. Additionally, DI in particular situations must be local in state space, as it is the case for spacecraft attitude dynamics (Dwyer III, 1984).

A paradigm shift was made to DI in (Paielli & Bach, 1993) in the context of spacecraft attitude control. Their approach aims to impose a prescribed dynamics on the errors of spacecraft attitude variables from their desired trajectory values. Rather than inverting the mathematical model of the spacecraft, the desired attitude error dynamics is inverted for the control variables that realize the dynamics. The transformation is global and does not involve deriving inverse equations of motion. It involves simple mathematical inversions of terms that include motion variables and control system design parameters, and therefore it is easier and more systematic than its counterpart.

Nevertheless, a common feature between the above mentioned DI approaches is that the linearizing transformation eliminates nonlinearities from the transformed closed loop system dynamics without distinguishing between types of nonlinearities. For instance, a nonlinearity may cause the spacecraft at a particular time instant to accelerate in a manner that is in favor of the control objective, e.g., in performing a desired maneuver. Yet a needless control effort is made to eliminate that nonlinearity, and an additional control effort is made to satisfy the control objective. This can be extremely disadvantageous as large control signals may cause actuator saturation and control system's failure.

It is therefore desirable to come up with a dynamic inversion control design methodology that provides a global linearizing transformation, alleviates the difficulty of plant's mathematical

model inversion, and requires less control effort to perform the inversion by avoiding blind cancelation of dynamical system's nonlinearity. These features are offered by generalized dynamic inversion (GDI) control. Some basic elements of GDI were introduced in (Bajodah et al., 2005; Bajodah, 2008; 2009), together with particular GDI control designs. Every design exhibits different characteristics in terms of closed loop system stability, performance, and control signal behavior.

The GDI control combines the flexibility of non-square inversion with the simplicity of DI by observing that the inverse system dynamics problem is in general a problem with non-unique solution, i.e., there exist infinite control strategies that realize a prescribed outer system dynamics, and infinite ways by which the system's inner states evolve in time to realize that outer dynamics. Therefore, the original philosophy of dynamic inversion is quite restrictive, and there must exist infinite inverse control laws that realize a servo-constraint dynamics, i.e., the differential equation in system's variables which has its steady state solution satisfies the control design objective.

A GDI spacecraft control design begins by defining a norm measure function of attitude error from desired attitude trajectory. An asymptotically stable linear time varying second-order differential equation in the norm function is prescribed, resembling the desired servo-constraint dynamics. The differential equation is then transformed to a relation that is linear in the control vector by differentiating the norm measure function along the trajectories defined by solution of the spacecraft's state space mathematical model. The Greville formula (Greville, 1959; Ben-Israel & Greville, 2003) is utilized thereafter to invert this relation for the control law required to realize the desired stable linear servo-constraint dynamics.

The Greville formula is capable of modeling solution nonuniqueness to problems where requirements can be satisfied in more than one course of action. For that reason, the formula had remarkable contributions towards advancements in science and engineering. In the arena of robotics, it has been extensively used in analysis and design of kinematically redundant manipulators (Siciliano & Khatib, 2008). Utilization of the formula in the field of analytical dynamics was made by deriving the Udwadia-Kalaba equations of motion for constrained dynamical systems (Udwadia & Kalaba, 1996). Other applications include the evolving subject of pointwise optimal control in the sense of Gauss' principle of least constraints (Gauss, 1829), e.g., (De Sapio et al., 2008; Udwadia, 2008; Peters et al., 2008).

The GDI control law exhibits useful geometrical features of generalized inversion. It consists of auxiliary and particular parts, residing in the nullspace of the inverted matrix and the complementary orthogonal range space of its transpose, respectively. The particular part involves the standard Moore-Penrose generalized inverse (MPGI) (Moore, 1920; Penrose, 1955), and the auxiliary part involves a free null-vector that is projected onto nullspace of the inverted matrix by means of a nullprojection matrix.

Orthogonality of the two parts composing the GDI control law makes it possible for the control system to satisfy multi-design objectives in a noninterfering manner, and makes it possible to merge dynamic inversion with other control design methodologies to enhance closed loop system design features. This is achieved through construction of the null-control vector that appears explicitly in the auxiliary part of the control law. In the present context, the null-control vector provides by its affine parametrization of controls coefficient's nullspace a convenient way to stabilize the inner dynamics of the closed loop control system without affecting servo-constraint realization.

The geometric structure of the GDI control law motivates employing the controls coefficient's

nullprojection matrix to simplify designing the null-control vector. Hence, a positive semidefinite control Lyapunov function that involves the nullprojection matrix is utilized for this purpose. It is shown in Refs. (Iqqidr et al., 1996; Bensoubaya et al., 1999) that a semi-definite Lyapunov function is usable to show stability of a dynamical system if some conditions on system trajectories in the null value of the Lyapunov function are satisfied. Applying Lyapunov direct method (Khalil, 2002) yields a controls coefficient null-projected Lyapunov equation. The equation is solved to obtain a simple control law for global asymptotic stability of inner spacecraft dynamics.

Generalized inversion singularity is a well-known problem in the applications of an MPGI with dynamic matrix elements, and it has been thoroughly investigated in the subject of inverse kinematics, e.g., (Baker & Wampler II, 1988). The reason for MPGI singularity is that a matrix with continuous function elements has discontinuous MPGI function elements. These discontinuities occur whenever the inverted matrix changes rank. Moreover, these discontinuous elements approach infinite values at discontinuities. Accordingly, the corresponding solutions provided by the Greville formula must also be discontinuous and unbounded.

The MPGI singularity forms an obstacle in the way of utilizing the Greville formula in engineering solutions. Several remedies for the problem of generalized inversion instability due to MPGI singularity have been offered in the literature of robotics and control moment gyroscopic devices, in what has become known as the singularity avoidance problem. Remedies are either nullspace parametrization-based, made by proper choices of the null-vector in the auxiliary part of the Greville formula, e.g., (Liegeois, 1977; Mayorga et al., 1995; Yoon & Tsiotras, 2004), or approximation-based, made by modifying the definition of the generalized inverse itself in the particular part of the formula, e.g., (Nakamura & Hanafusa, 1986; Wampler II, 1986; Oh & Vadali, 1991).

A series of solutions to the GDI closed loop instability due to MPGI singularity have been provided in the context of GDI control. One solution is made by deactivating the particular part of the GDI control law in the vicinity of singularity, resulting in discontinuous control laws (Bajodah, 2006). Another solution is presented in (Bajodah, 2008), made by modifying the definition of MPGI by means of a damping factor, resulting in uniformly ultimately bounded attitude trajectory tracking and a tradeoff between generalized inversion stability and closed loop system performance.

The concept of dynamically scaled generalized inversion for GDI singularity avoidance is introduced in (Bajodah, 2010). The concept is based on replacing the MPGI in the particular part of the GDI control law by a growth-controlled dynamically scaled generalized inverse (DSGI), such that the DSGI elements converge uniformly to the standard MPGI elements. The DSGI is constructed by adding a dynamic scaling factor to each denominator of MPGI's elements. The dynamic scaling factor is the p^{th} integer power of a vector p norm of the difference between spacecraft body angular velocity and reference angular velocity. The null-control vector in the auxiliary part of the control law is designed to nullify the dynamic scaling factor such that the DSGI recovers the structure of the MPGI. This causes the particular part of the control law to converge to its projection on the range space of the controls coefficient's MPGI, which drives the attitude variables to satisfy desired servo-constraint stable dynamics, resulting in global attitude trajectory tracking.

This work adopts a generalization of the concept of dynamically scaled generalized inversion, based on augmenting an integrator of the dynamic scaling factor to increase the order of the closed loop dynamics and cause a delay in the scaling factor dynamics. The augmented

stable mode is driven by the spacecraft angular velocity error's norm from reference angular velocity, and is designed to be fast compared to spacecraft dynamics. The dynamic scaling delay caused by the augmented stable mode enhances singularity avoidance performance of dynamic scaling.

The attitude error norm function reduces the order of attitude dynamics from three to one. This feature in addition to skew symmetry of the angular velocity cross product matrix makes the proposed GDI control law totally independent from the inertia matrix. Furthermore, the GDI control methodology does not involve inertia matrix identification in the control design. Two spacecraft attitude maneuvers with different desired asymptotic behaviors are used to illustrate the present GDI control methodology. The first is a rest-to-rest slew maneuver that aims to reorient the spacecraft from an initial attitude to another prescribed attitude. The second is a sinusoidal angular velocity-commanded attitude quaternion trajectory tracking maneuver. Asymptotic tracking is achieved for the first maneuver because the spacecraft angular velocity components asymptotically converge to the reference angular velocity components.

However, since the steady state reference trajectories for the second maneuver are time varying, then spacecraft angular velocity components continue to exhibit small errors from reference angular velocity components during steady state phase of closed loop response. Hence, the stable augmented mode continues to get excited, and asymptotic quaternion attitude tracking is lost. Instead, a practical ultimately bounded tracking is achieved.

This chapter reformulates the GDI spacecraft attitude control methodology in terms of multiplicative quaternion attitude errors that accommodate for spacecraft maneuvers with big changes in attitude angles. Time-varying linear attitude deviation servo-constraint is used to reduce the control load at initial stage of closed loop response. Additionally, a new nullprojection control Lyapunov design is made for constructing the null-control vector, and a modified dynamic scaling factoring is used for improved singularity-free GDI quaternion attitude trajectory tracking.

2. Spacecraft mathematical model

The unit quaternion attitude vector \mathbf{q} that represents the attitude of spacecraft body reference frame \mathcal{B} relative to the inertial reference frame \mathcal{I} is defined as (Wertz, 1980)

$$\mathbf{q} = [q^T \quad q_4]^T \quad (1)$$

where $q \in \mathbb{R}^3$ is given by

$$q = [q_1 \quad q_2 \quad q_3]^T \quad (2)$$

and $q_4 \in \mathbb{R}$. The four attitude unit quaternion scalars q_1, \dots, q_4 are constrained such that

$$\mathbf{q}^T \mathbf{q} = 1. \quad (3)$$

The skew-symmetric cross product matrix ζ^\times that corresponds to a vector $\zeta = [\zeta_1 \quad \zeta_2 \quad \zeta_3]^T$ is defined as

$$\zeta^\times = \begin{bmatrix} 0 & -\zeta_3 & \zeta_2 \\ \zeta_3 & 0 & -\zeta_1 \\ -\zeta_2 & \zeta_1 & 0 \end{bmatrix}. \quad (4)$$

The spacecraft attitude dynamics is governed by the following system of kinematical differential equations (Wertz, 1980)

$$\dot{\mathbf{q}} = \begin{bmatrix} \dot{q} \\ \dot{q}_4 \end{bmatrix} = \frac{1}{2} \begin{bmatrix} (q^\times + q_4 I_{3 \times 3}) \\ -q^T \end{bmatrix} \omega, \quad \mathbf{q}(0) = \mathbf{q}_0 \quad (5)$$

where $\omega \in \mathbb{R}^{3 \times 1}$ is the vector of angular velocity of \mathcal{B} relative to \mathcal{I} expressed in \mathcal{B} and $I_{3 \times 3}$ is the identity matrix. The spacecraft inner (angular velocity) dynamics is given by the following system of dynamical differential equations

$$\dot{\omega} = -J^{-1} \omega^\times J \omega + \tau, \quad \omega(0) = \omega_0 \quad (6)$$

where $J \in \mathbb{R}^{3 \times 3}$ is the spacecraft's body-fixed moments of inertia matrix, and $\tau := J^{-1} u \in \mathbb{R}^{3 \times 1}$ is the vector of scaled control torques, where $u \in \mathbb{R}^{3 \times 1}$ contains the applied gas jet actuator torque components about the spacecraft's body axes.

3. Attitude deviation dynamics

The orthogonal rotation transformation matrix $\mathbf{R} \in \mathbf{SO}(3)$ will be used to quantify large spacecraft attitude changes. The matrix \mathbf{R} is expressed in terms of the unit quaternion components as (Wertz, 1980)

$$\mathbf{R}(\mathbf{q}) = (q_4^2 - q^T q) I_{3 \times 3} + 2q q^T - 2q_4 q^\times. \quad (7)$$

Let $\mathbf{q}_d(t) = [q_d^T(t) \quad q_{d4}^T(t)]^T$ be a twice continuously differentiable unit quaternion vector trajectory that represents the prescribed attitude of desired spacecraft frame \mathcal{D} relative to the attitude of \mathcal{I} , where $q_d(t)$ and $q_{d4}(t)$ are such that $\mathbf{q}_d^T(t) \mathbf{q}_d(t) = 1$. The corresponding rotation transformation $\mathbf{R}(\mathbf{q}_d)$ is composed of two consecutive rotation transformations; the transformation $\mathbf{R}(\mathbf{q})$ that brings the attitude of \mathcal{I} to the current attitude of \mathcal{B} , followed by the attitude error transformation $\mathbf{R}(\mathbf{q}_e)$ that brings the attitude of \mathcal{B} to that of \mathcal{D} . Therefore, $\mathbf{R}(\mathbf{q}_d)$ is given by

$$\mathbf{R}(\mathbf{q}_d) = \mathbf{R}(\mathbf{q}_e) \mathbf{R}(\mathbf{q}). \quad (8)$$

Solving for $\mathbf{R}(\mathbf{q}_e)$ yields

$$\mathbf{R}(\mathbf{q}_e) = \mathbf{R}(\mathbf{q}_d) (\mathbf{R}(\mathbf{q}))^{-1} = \mathbf{R}(\mathbf{q}_d) \mathbf{R}^T(\mathbf{q}). \quad (9)$$

In terms of quaternion products, the attitude quaternion error vector $\mathbf{q}_e(\mathbf{q}, t)$ is equivalently given by

$$\mathbf{q}_e(\mathbf{q}, t) = \mathbf{q}^{-1} \otimes \mathbf{q}_d(t), \quad \forall t \in [0, \infty) \quad (10)$$

where \mathbf{q}^{-1} is the spacecraft conjugate attitude quaternion given by

$$\mathbf{q}^{-1} = [-q^T \quad q_4]^T. \quad (11)$$

For convenience, the quaternion product given by (10) is written in the compact form (Show & Juang, 2003)

$$\mathbf{q}_e(\mathbf{q}, t) = \begin{bmatrix} q_e \\ q_{e4} \end{bmatrix} = \begin{bmatrix} q_{d4}(t)q - q_4 q_d(t) - q_d^\times(t)q \\ q_4 q_{d4}(t) + q^T q_d(t) \end{bmatrix}. \quad (12)$$

It can be easily verified that the above expression satisfies the quaternion constraint (Show & Juang, 2003)

$$\mathbf{q}_e^T(\mathbf{q}, t) \mathbf{q}_e(\mathbf{q}, t) = (q^T q + q_4^2)(q_d^T(t) q_d(t) + q_{d4}(t)^2) = 1. \quad (13)$$

Let $\omega_r(t) : [0, \infty) \rightarrow \mathbb{R}^3$ be the prescribed angular velocity vector of \mathcal{D} relative to \mathcal{I} expressed in \mathcal{B} . The quaternion error kinematical differential equations are given by

$$\dot{\mathbf{q}}_e = \begin{bmatrix} \dot{q}_e \\ \dot{q}_{e4} \end{bmatrix} = \frac{1}{2} \begin{bmatrix} q_e^\times + q_{e4} I_{3 \times 3} \\ -q_e^T \end{bmatrix} \omega_e \quad (14)$$

where $\omega_e := \omega - \omega_r(t)$. The reference angular velocity vector $\omega_r(t)$ satisfies

$$\dot{\omega}_r(t) = -J^{-1} \omega_r^\times(t) J \omega_r(t). \quad (15)$$

Therefore,

$$\dot{\omega}_e = \dot{\omega} - \dot{\omega}_r(t) \quad (16)$$

$$= -J^{-1} \omega^\times J \omega + J^{-1} \omega_r^\times(t) J \omega_r(t) + \tau. \quad (17)$$

A scalar attitude deviation norm measure function $\phi : [-1, 1] \rightarrow [0, 1]$ is defined as

$$\phi(q_{e4}) = 1 - q_{e4}^2 \quad (18)$$

and the control objective is to enforce the servo-constraint

$$\phi(q_{e4}) \equiv 0. \quad (19)$$

From (13), the same servo-constraint requirement can also be written as

$$q_e \equiv \mathbf{0}_{3 \times 1}. \quad (20)$$

The first two time derivatives of ϕ along the spacecraft error trajectories given by the solutions of (14) and (17) are

$$\dot{\phi} = q_{e4} q_e^T \omega_e \quad (21)$$

and

$$\ddot{\phi} = \frac{1}{2} \omega_e^T \left(q_{e4}^2 I_{3 \times 3} - q_e q_e^T \right) \omega_e + q_{e4} q_e^T \left(-J^{-1} \omega^\times J \omega + J^{-1} \omega_r^\times J \omega_r + \tau \right). \quad (22)$$

Skew symmetries of the cross product matrices ω^\times and ω_r^\times imply that the corresponding terms in $\ddot{\phi}$ are zeros. Hence, the expression of (22) reduces to

$$\ddot{\phi} = \frac{1}{2} \omega_e^T \left(q_{e4}^2 I_{3 \times 3} - q_e q_e^T \right) \omega_e + q_{e4} q_e^T \tau. \quad (23)$$

A desired dynamics of ϕ that leads to asymptotic realization of the servo-constraint given by (19) is described to be stable second-order in the general functional form given by

$$\ddot{\phi} = \mathcal{L}(\phi, \dot{\phi}, t) \quad (24)$$

where \mathcal{L} is continuous in its arguments. A special choice of $\mathcal{L}(\phi, \dot{\phi}, t)$ is

$$\mathcal{L}(\phi, \dot{\phi}, t) = -c_1(t) \dot{\phi} - c_2(t) \phi \quad (25)$$

where $c_1(t)$ and $c_2(t)$ are continuous scalar functions. With this choice of $\mathcal{L}(\phi, \dot{\phi}, t)$, the stable attitude deviation servo-constraint dynamics given by (24) becomes linear in the form

$$\ddot{\phi} + c_1(t)\dot{\phi} + c_2(t)\phi = 0. \quad (26)$$

With ϕ , $\dot{\phi}$, and $\ddot{\phi}$ given by (18), (21), and (23), it is possible to write (26) in the pointwise-linear form

$$\mathcal{A}(\mathbf{q}_e)\tau = \mathcal{B}(\mathbf{q}_e, \omega_e), \quad (27)$$

where the vector valued the controls coefficient function $\mathcal{A}(\mathbf{q}_e)$ is given by

$$\mathcal{A}(\mathbf{q}_e) = q_{e4}q_e^T \quad (28)$$

and the scalar valued controls load function $\mathcal{B}(\mathbf{q}_e, \omega_e)$ is given by

$$\mathcal{B}(\mathbf{q}_e, \omega_e) = -\frac{1}{2}\omega_e^T \left(q_{e4}^2 I_{3 \times 3} - q_e q_e^T \right) \omega_e - c_1(t)q_{e4}q_e^T \omega_e - c_2(t)(1 - q_{e4}^2). \quad (29)$$

4. Generalized dynamic inversion attitude control

The MPGI-based Greville formula is used now to obtain a preliminary form of GDI spacecraft attitude control laws.

Proposition 1 (Linearly parameterized attitude control laws) *The infinite set of all control laws that globally realize the attitude deviation servo-constraint dynamics given by (26) by the spacecraft equations of motion is parameterized by an arbitrarily chosen null-control vector $y \in \mathbb{R}^{3 \times 1}$ as*

$$\tau = \mathcal{A}^+(\mathbf{q}_e)\mathcal{B}(\mathbf{q}_e, \omega_e) + \mathcal{P}(\mathbf{q}_e)y \quad (30)$$

where “ \mathcal{A}^+ ” stands for the MPGI of the controls coefficient (abbreviated as CCGI), and is given by

$$\mathcal{A}^+(\mathbf{q}_e) = \begin{cases} \frac{\mathcal{A}^T(\mathbf{q}_e)}{\mathcal{A}(\mathbf{q}_e)\mathcal{A}^T(\mathbf{q}_e)}, & \mathcal{A}(\mathbf{q}_e) \neq \mathbf{0}_{1 \times 3} \\ \mathbf{0}_{3 \times 1}, & \mathcal{A}(\mathbf{q}_e) = \mathbf{0}_{1 \times 3} \end{cases} \quad (31)$$

and $\mathcal{P}(\mathbf{q}_e)$ is the corresponding controls coefficient nullprojection matrix given by

$$\mathcal{P}(\mathbf{q}_e) = I_{3 \times 3} - \mathcal{A}^+(\mathbf{q}_e)\mathcal{A}(\mathbf{q}_e). \quad (32)$$

Proof 1 *Multiplying both sides of (30) by $\mathcal{A}(\mathbf{q}_e)$ recovers the algebraic system given by (27). Therefore, τ enforces the attitude deviation servo-constraint dynamics given by (26) for all $\mathcal{A}(\mathbf{q}_e) \neq \mathbf{0}_{1 \times 3}$.*

The controls coefficient nullprojector $\mathcal{P}(\mathbf{q}_e)$ projects the null-control vector y onto the nullspace of the controls coefficient $\mathcal{A}(\mathbf{q}_e)$. Therefore, the choice of y does not affect realizability of the linear attitude deviation norm measure dynamics given by (26). Nevertheless, the choice of y substantially affects transient state response and spacecraft inner stability, i.e., stability of the closed loop dynamical subsystem

$$\dot{\omega} = -J^{-1}\omega^\times J\omega + \mathcal{A}^+(\mathbf{q}_e)\mathcal{B}(\mathbf{q}_e, \omega_e) + \mathcal{P}(\mathbf{q}_e)y \quad (33)$$

obtained by substituting (30) in (6).

5. Generalized inverse instability

The expression given by (28) for the controls coefficient implies that if the dynamics given by (26) is realizable by spacecraft equations of motion, then

$$\lim_{\phi \rightarrow 0} \mathcal{A}(\mathbf{q}_e) = \mathbf{0}_{1 \times 3}. \quad (34)$$

Accordingly, the discontinuous expression of $\mathcal{A}^+(\mathbf{q}_e)$ given by (31) implies that for any initial condition $\mathcal{A}(\mathbf{q}_e) \neq \mathbf{0}_{1 \times 3}$, state trajectories of a continuous closed loop control system in the form given by (5) and (33) must evolve such that

$$\lim_{\phi \rightarrow 0} \mathcal{A}^+(\mathbf{q}_e) = \infty_{3 \times 1}. \quad (35)$$

That is, $\mathcal{A}^+(\mathbf{q}_e)$ must go unbounded as the spacecraft dynamics approaches steady state. This is a source of instability for the closed loop system because it causes the control law expression given by (30) to become unbounded. One solution to this problem is made by switching the value of the CCGI according to (31) to $\mathcal{A}^+(\mathbf{q}_e) = \mathbf{0}_{3 \times 1}$ when the controls coefficient $\mathcal{A}(\mathbf{q}_e)$ approaches singularity, which implies deactivating the particular part of the control law as the closed loop system reaches steady state, leading to a discontinuous control law (Bajodah, 2006).

Alternatively, a solution is made by replacing the Moore-Penrose generalized inverse in (30) by a damped generalized inverse (Bajodah, 2008), resulting in uniformly ultimately bounded trajectory tracking errors, and a tradeoff between generalized inversion stability and steady state tracking performance. A solution to this problem that avoids control law discontinuity and improves singularity avoiding trajectory tracking is presented in (Bajodah, 2010), made by replacing the MPGI in (30) by a growth-controlled dynamically scaled generalized inverse. A generalization of the dynamically scaled generalized inverse is presented in the following section.

6. Generalized inverse singularity avoidance by stable mode augmentation

The dynamically scaled generalized inverse provides the necessary generalized inversion singularity avoidance to the GDI control design.

Definition 1 (Dynamically scaled generalized inverse) *The DSGI $\mathcal{A}_s^+(\mathbf{q}_e, \nu)$ is given by*

$$\mathcal{A}_s^+(\mathbf{q}_e, \nu) = \frac{\mathcal{A}^T(\mathbf{q}_e)}{\mathcal{A}(\mathbf{q}_e)\mathcal{A}^T(\mathbf{q}_e) + \nu} \quad (36)$$

where ν satisfies the asymptotically stable dynamics

$$\dot{\nu} = -a\nu + \|\omega_e\|_p^p, \quad a > 0, \quad p \in \mathbb{Z}^+. \quad (37)$$

The positive integer p is the generalized inversion dynamic scaling index, and $\|\cdot\|_p$ is the vector p norm.

Properties of dynamically scaled generalized inverse

The following properties can be verified by direct evaluation of the CCGI $\mathcal{A}^+(\mathbf{q}_e)$ given by (31) and its dynamic scaling $\mathcal{A}_s^+(\mathbf{q}_e, \nu)$ given by (36).

1. $\mathcal{A}_s^+(\mathbf{q}_e, \nu) \mathcal{A}(\mathbf{q}_e) \mathcal{A}^+(\mathbf{q}_e) = \mathcal{A}_s^+(\mathbf{q}_e, \nu)$
2. $\mathcal{A}^+(\mathbf{q}_e) \mathcal{A}(\mathbf{q}_e) \mathcal{A}_s^+(\mathbf{q}_e, \nu) = \mathcal{A}_s^+(\mathbf{q}_e, \nu)$
3. $(\mathcal{A}_s^+(\mathbf{q}_e, \nu) \mathcal{A}(\mathbf{q}_e))^T = \mathcal{A}_s^+(\mathbf{q}_e, \nu) \mathcal{A}(\mathbf{q}_e)$
4. $\lim_{\|\omega_e\|_p \rightarrow 0} \mathcal{A}_s^+(\mathbf{q}_e, \nu) = \mathcal{A}^+(\mathbf{q}_e)$.

7. Dynamically scaled generalized inverse control

The dynamically scaled generalized inverse control law is obtained by replacing the CCGI in the particular part of the expression given by (30) by the DSGI as

$$\tau_s = \mathcal{A}_s^+(\mathbf{q}_e, \nu) \mathcal{B}(\mathbf{q}_e, \omega_e) + \mathcal{P}(\mathbf{q}_e) y \quad (38)$$

resulting in the following spacecraft closed loop dynamical equations

$$\dot{\omega} = -J^{-1} \omega^\times J \omega + \mathcal{A}_s^+(\mathbf{q}_e, \nu) \mathcal{B}(\mathbf{q}_e, \omega_e) + \mathcal{P}(\mathbf{q}_e) y. \quad (39)$$

Proposition 2 (Asymptotic Attitude Trajectory Tracking) *If the null-control vector y in the control law expression given by (38) is chosen such*

$$\lim_{t \rightarrow \infty} \omega_e = \mathbf{0}_{3 \times 1} \quad (40)$$

then

$$\lim_{t \rightarrow \infty} q_e = \mathbf{0}_{3 \times 1}. \quad (41)$$

Proof 2 *Let ϕ_s be a norm measure function of the attitude deviation obtained by applying the control law given by (38) to the spacecraft equations of motion (5) and (6), and let $\dot{\phi}_s, \ddot{\phi}_s$ be its first two time derivatives. Therefore,*

$$\phi_s := \phi_s(\mathbf{q}_e) = \phi(\mathbf{q}_e) \quad (42)$$

$$\dot{\phi}_s := \dot{\phi}_s(\mathbf{q}_e, \omega_e) = \dot{\phi}(\mathbf{q}_e, \omega_e) \quad (43)$$

$$\ddot{\phi}_s := \ddot{\phi}_s(\mathbf{q}_e, \omega_e, \tau_s) = \ddot{\phi}(\mathbf{q}_e, \omega_e, \tau) + \mathcal{A}(\mathbf{q}_e) \tau_s - \mathcal{A}(\mathbf{q}_e) \tau \quad (44)$$

where τ and τ_s are given by (30) and (38), respectively. Adding $c_1(t)\dot{\phi}_s + c_2(t)\phi_s$ to both sides of (44) yields

$$\ddot{\phi}_s + c_1(t)\dot{\phi}_s + c_2(t)\phi_s = \ddot{\phi} + c_1(t)\dot{\phi} + c_2(t)\phi + \mathcal{A}(\mathbf{q}_e) \tau_s - \mathcal{A}(\mathbf{q}_e) \tau \quad (45)$$

$$= \mathcal{A}(\mathbf{q}_e) [\tau_s - \tau]. \quad (46)$$

Therefore, boundedness of the expression of $\mathcal{A}(\mathbf{q}_e)$ given by (28) in addition to satisfaction of (40) imply that

$$\lim_{t \rightarrow \infty} [\ddot{\phi}_s + c_1(t)\dot{\phi}_s + c_2(t)\phi_s] = \lim_{t \rightarrow \infty} [\mathcal{A}(\mathbf{q}_e) [\tau_s - \tau]] = 0 \quad (47)$$

resulting in

$$\lim_{t \rightarrow \infty} \phi_s = 0 \quad (48)$$

and therefore, (41) follows for all permissible initial attitude quaternion vectors $q_0 \in \mathbb{R}^3$. The same conclusion is obtained by multiplying both sides of (38) by $\mathcal{A}(\mathbf{q}_e)$, resulting in

$$\mathcal{A}(\mathbf{q}_e) \tau_s = \mathcal{A}(\mathbf{q}_e) \mathcal{A}_s^+(\mathbf{q}_e, \nu) \mathcal{B}(\mathbf{q}_e, \omega_e) \quad (49)$$

where

$$\mathcal{A}(\mathbf{q}_e)\mathcal{A}_s^+(\mathbf{q}_e, \nu) = \frac{\mathcal{A}(\mathbf{q}_e)\mathcal{A}^T(\mathbf{q}_e)}{\mathcal{A}(\mathbf{q}_e)\mathcal{A}^T(\mathbf{q}_e) + \nu}. \quad (50)$$

Therefore,

$$0 < \mathcal{A}(\mathbf{q}_e)\mathcal{A}_s^+(\mathbf{q}_e, \nu) \leq 1 \quad (51)$$

and

$$\lim_{\omega_e \rightarrow \mathbf{0}_{3 \times 1}} \mathcal{A}(\mathbf{q}_e)\mathcal{A}_s^+(\mathbf{q}_e, \nu) = 1. \quad (52)$$

Dividing both sides of (49) by $\mathcal{A}(\mathbf{q}_e)\mathcal{A}_s^+(\mathbf{q}_e, \nu)$ yields

$$\mathcal{A}(\mathbf{q}_e)\bar{\tau} = \mathcal{B}(\mathbf{q}_e, \omega_e) \quad (53)$$

where $\mathcal{A}(\mathbf{q}_e)$ and $\mathcal{B}(\mathbf{q}_e, \omega_e)$ are the same controls coefficient and controls load in (27), and

$$\bar{\tau} = \frac{\tau_s}{\mathcal{A}(\mathbf{q}_e)\mathcal{A}_s^+(\mathbf{q}_e, \nu)}. \quad (54)$$

Furthermore, (52) implies that

$$\lim_{\omega_e \rightarrow \mathbf{0}_{3 \times 1}} \bar{\tau} = \lim_{\omega_e \rightarrow \mathbf{0}_{3 \times 1}} \tau_s = \tau. \quad (55)$$

Therefore, $\bar{\tau}$ in the algebraic system given by (53) asymptotically converges to τ , recovering the algebraic system given by (27), and resulting in asymptotic convergence of $\phi_s(t)$ to $\phi_s = \phi = 0$, and q_d to $q_d(t)$.

Proposition 2 states that using the DSGI $\mathcal{A}_s^+(\mathbf{q}_e, \nu)$ in the attitude control law yields the same attitude convergence property that is obtained by using the CCGI $\mathcal{A}^+(\mathbf{q}_e)$, provided that the condition given by (40) is satisfied. A design of the null-control vector y is made in the next section to guarantee global satisfaction of the condition given by (40).

Remark 1 It is well-known that topological obstruction of the attitude rotation matrix precludes the existence of globally stable equilibria for the attitude dynamics (Bhat & Bernstein, 2000). Therefore, although the servo-constraint attitude deviation dynamics given by (26) is globally realizable, there exists no null-control that renders the spacecraft attitude dynamics globally stable. In particular, if $q_d(t) \equiv \mathbf{0}_{3 \times 1}$ then for any null-control vector y there exists an attitude vector q_0 such that the closed loop system given by (5) and (39) is unstable in the sense of Lyapunov.

8. Nullprojection Lyapunov control design

A Lyapunov-based design of null-control vector y is introduced in this section to enforce spacecraft inner stability. Let y be chosen as

$$y = K\omega_e(t) \quad (56)$$

where $K \in \mathbb{R}^{3 \times 3}$ is a matrix gain that is to be determined. Hence, a class of control laws that realize the attitude deviation norm measure dynamics given by (26) is obtained by substituting this choice of y in (38) such that

$$\tau_s = \mathcal{A}_s^+(\mathbf{q}_e, \nu)\mathcal{B}(\mathbf{q}_e, \omega_e) + \mathcal{P}(\mathbf{q}_e)K\omega_e(t). \quad (57)$$

Consequently, a class of spacecraft closed loop dynamical subsystems that realize the servo-constraint dynamics given by (26) is obtained by substituting the control law given by (57) in (6), and it takes the form

$$\dot{\omega} = -J^{-1}\omega^\times J\omega + \mathcal{A}_s^+(\mathbf{q}_e, \nu)\mathcal{B}(\mathbf{q}_e, \omega_e) + \mathcal{P}(\mathbf{q}_e)K\omega_e(t) \tag{58}$$

and the closed loop error dynamics $\dot{\omega}_e$ is obtained from (17) as

$$\dot{\omega}_e = -J^{-1}\omega^\times J\omega + J^{-1}\omega_r^\times J\omega_r + \mathcal{A}_s^+(\mathbf{q}_e, \nu)\mathcal{B}(\mathbf{q}_e, \omega_e) + \mathcal{P}(\mathbf{q}_e)K\omega_e. \tag{59}$$

The matrix gain K is synthesized by utilizing the positive-semidefinite control Lyapunov function

$$V(\mathbf{q}_e, \omega_e) = \omega_e^T \mathcal{P}(\mathbf{q}_e) \omega_e. \tag{60}$$

Evaluating the time derivative of $V(\mathbf{q}_e, \omega_e)$ along solution trajectories of the error dynamics given by (59) yields

$$\begin{aligned} \dot{V}(\mathbf{q}_e, \omega_e) = 2\omega_e^T \mathcal{P}(\mathbf{q}_e) & \left[-J^{-1}\omega^\times J\omega + J^{-1}\omega_r^\times(t)J\omega_r(t) \right. \\ & \left. + \mathcal{A}_s^+(\mathbf{q}_e, \nu)\mathcal{B}(\mathbf{q}_e, \omega_e) \right] + 2\omega_e^T \mathcal{P}(\mathbf{q}_e)K\omega_e + \omega_e^T \dot{\mathcal{P}}(\mathbf{q}_e, \omega_e)\omega_e \end{aligned} \tag{61}$$

where $\dot{\mathcal{P}}(\mathbf{q}_e, \omega_e)$ is obtained by differentiating the elements of $\mathcal{P}(\mathbf{q}_e)$ along attitude trajectory solutions of the closed loop kinematical subsystem given by (14). Skew symmetry of the cross product matrix $[\cdot]^\times$, the nullprojection property of $\mathcal{P}(\mathbf{q}_e)$, and the second property of $\mathcal{A}_s^+(\mathbf{q}_e, \omega_e)$ imply that the first term in the above equation is zero. Therefore,

$$\dot{V}(\mathbf{q}_e, \omega_e) = 2\omega_e^T \mathcal{P}(\mathbf{q}_e)K\omega_e + \omega_e^T \dot{\mathcal{P}}(\mathbf{q}_e, \omega_e)\omega_e. \tag{62}$$

Because $V(\mathbf{q}_e, \omega_e)$ is only positive semidefinite, it is impossible to design a matrix gain K that renders $\dot{V}(\mathbf{q}_e, \omega_e)$ negative definite. Nevertheless, a matrix gain K that renders $\dot{V}(\mathbf{q}_e, \omega_e)$ negative semidefinite guarantees Lyapunov stability of $\omega_e = \mathbf{0}_{3 \times 1}$ if it asymptotically stabilizes $\omega_e = \mathbf{0}_{3 \times 1}$ over the invariant set of \mathbf{q}_e and ω_e values on which $V(\mathbf{q}_e, \omega_e) = 0$. Moreover, the same gain matrix asymptotically stabilizes $\omega_e = \mathbf{0}_{3 \times 1}$ if and only if it asymptotically stabilizes $\omega_e = \mathbf{0}_{3 \times 1}$ over the largest invariant set of \mathbf{q}_e and ω_e values on which $\dot{V}(\mathbf{q}_e, \omega_e) = 0$ (Iqdir et al., 1996).

Proposition 3 *Let $K = K(\mathbf{q}_e, \omega_e)$ be a full-rank normal matrix gain, i.e., $KK^T = K^T K$ for all $t \geq 0$. Then the equilibrium point $\omega_e = \mathbf{0}_{3 \times 1}$ of the closed loop error dynamics given by (59) is asymptotically stable over the invariant set of \mathbf{q}_e , and ω_e values on which $V(\mathbf{q}_e, \omega_e) = 0$.*

Proof 3 *Since the matrix $\mathcal{P}(\mathbf{q}_e)$ is idempotent, the function $V(\mathbf{q}_e, \omega_e)$ can be rewritten as*

$$V(\mathbf{q}_e, \omega_e) = \omega_e^T \mathcal{P}(\mathbf{q}_e) \omega_e = \omega_e^T \mathcal{P}(\mathbf{q}_e) \mathcal{P}(\mathbf{q}_e) \omega_e \tag{63}$$

which implies that

$$V(\mathbf{q}_e, \omega_e) = 0 \Leftrightarrow \mathcal{P}(\mathbf{q}_e) \omega_e = \mathbf{0}_{3 \times 1}. \tag{64}$$

Therefore,

$$V(\mathbf{q}_e, \omega_e) = 0 \Leftrightarrow \omega_e \in \mathcal{N}(\mathcal{P}(\mathbf{q}_e)) \tag{65}$$

where $\mathcal{N}(\cdot)$ refers to matrix nullspace. Since the matrix $K(\mathbf{q}_e, \omega_e)$ is normal and of full-rank, it preserves matrix range space and nullspace under multiplication. Accordingly,

$$\mathcal{N}(\mathcal{P}(\mathbf{q}_e)) = \mathcal{N}(\mathcal{P}(\mathbf{q}_e)K(\mathbf{q}_e, \omega_e)) \quad (66)$$

which implies from (64) that

$$V(\mathbf{q}_e, \omega_e) = 0 \Leftrightarrow \mathcal{P}(\mathbf{q}_e)K(\mathbf{q}_e, \omega_e)\omega_e = \mathbf{0}_{3 \times 1}. \quad (67)$$

Therefore, the last term in the closed loop error dynamics given by (59) is the zero vector, and the closed loop error dynamics becomes

$$\dot{\omega}_e = -J^{-1}\omega^\times J\omega + J^{-1}\omega_r^\times(t)J\omega_r(t) + \mathcal{A}_s^+(\mathbf{q}_e, \nu)\mathcal{B}(\mathbf{q}_e, \omega_e). \quad (68)$$

On the other hand, since

$$\mathcal{N}(\mathcal{P}(\mathbf{q}_e)) = \mathcal{R}(\mathcal{A}^T(\mathbf{q}_e)) \quad (69)$$

it follows from (65) that

$$V(\mathbf{q}_e, \omega_e) = 0 \Leftrightarrow \omega_e \in \mathcal{R}(\mathcal{A}^T(\mathbf{q}_e)). \quad (70)$$

Accordingly, $V(\mathbf{q}_e, \omega_e) = 0$ if and only if there exists a continuous scalar function $a(t)$, $t \geq 0$, satisfying

$$0 < |a(t)| < \infty \quad (71)$$

such that

$$\omega_e = a(t)\mathcal{A}^T(\mathbf{q}_e). \quad (72)$$

Since the expression of $\mathcal{A}(\mathbf{q}_e)$ given by (28) is bounded for all values of \mathbf{q}_e , it follows from (72) that ω_e is also bounded. Therefore, the trajectory of ω_e must remain in a finite region, and it follows from the Poincare-Bendixon theorem (Slotine & Li, 1991) that the trajectory goes to the equilibrium point $\omega_e = \mathbf{0}_{3 \times 1}$.

Theorem 1 (CCNP Lyapunov control design) Let the nullprojection gain matrix $K(\mathbf{q}_e, \omega_e)$ be

$$K(\mathbf{q}_e, \omega_e) = -\dot{\mathcal{P}}(\mathbf{q}_e, \omega_e) - \sigma_{\max}(\dot{\mathcal{P}}(\mathbf{q}_e, \omega_e))I_{3 \times 3} - Q \quad (73)$$

where $\sigma_{\max}(\cdot)$ denotes the maximum singular value, and $Q \in \mathbb{R}^{3 \times 3}$ is arbitrary positive definite. Then the equilibrium point $\omega_e = \mathbf{0}_{3 \times 1}$ of the closed loop error dynamics given by (59) is globally asymptotically stable, and

$$\lim_{t \rightarrow \infty} \omega_e = \mathbf{0}_{3 \times 1}. \quad (74)$$

Proof 4 Let $\mathcal{Q}(\mathbf{q}_e, \omega) : \mathbb{R}^{4 \times 1} \times \mathbb{R}^{3 \times 1} \rightarrow \mathbb{R}^{3 \times 3}$ be a positive semidefinite matrix function. Then, a matrix gain K that enforces negative semidefiniteness of $\dot{V}(\mathbf{q}_e, \omega_e)$ is obtained by setting

$$\dot{V}(\mathbf{q}_e, \omega_e) = 2\omega_e^T \mathcal{P}(\mathbf{q}_e)K\omega_e + \omega_e^T \dot{\mathcal{P}}(\mathbf{q}_e, \omega_e)\omega_e = -2\omega_e^T \mathcal{Q}(\mathbf{q}_e, \omega_e)\omega_e. \quad (75)$$

Hence, K satisfies the following Lyapunov equation

$$2\mathcal{P}(\mathbf{q}_e)K + \dot{\mathcal{P}}(\mathbf{q}_e, \omega_e) + 2\mathcal{Q}(\mathbf{q}_e, \omega_e) = \mathbf{0}_{3 \times 3}. \quad (76)$$

Consistency of the above-written nullprojection equation implies that every term maps into $\mathcal{P}(\mathbf{q}_e)$. The range space of $\dot{\mathcal{P}}(\mathbf{q}_e, \omega_e)$ is a subset of the range space of $\mathcal{P}(\mathbf{q}_e)$. This is shown by writing

$$\mathcal{P}(\mathbf{q}_e) = \mathcal{P}(\mathbf{q}_e)\mathcal{P}(\mathbf{q}_e) \Rightarrow \dot{\mathcal{P}}(\mathbf{q}_e, \omega_e) = 2\mathcal{P}(\mathbf{q}_e)\dot{\mathcal{P}}(\mathbf{q}_e, \omega_e) \quad (77)$$

so that

$$\mathcal{R}[\dot{\mathcal{P}}(\mathbf{q}_e, \omega_e)] = \mathcal{R}[\mathcal{P}(\mathbf{q}_e)\dot{\mathcal{P}}(\mathbf{q}_e, \omega_e)] \subseteq \mathcal{R}[\mathcal{P}(\mathbf{q}_e)] \quad (78)$$

where $\mathcal{R}(\cdot)$ refers to matrix range space. Moreover, for $\mathcal{Q}(\mathbf{q}_e, \omega_e)$ to map into the range space of $\mathcal{P}(\mathbf{q}_e)$, then there must exist a positive definite matrix function $\bar{\mathcal{Q}}(\mathbf{q}_e, \omega_e) : \mathbb{R}^{4 \times 1} \times \mathbb{R}^{3 \times 1} \rightarrow \mathbb{R}^{3 \times 3}$ such that a polar decomposition of $\mathcal{Q}(\mathbf{q}_e, \omega_e)$ is given by

$$\mathcal{Q}(\mathbf{q}_e, \omega_e) = \mathcal{P}(\mathbf{q}_e)\bar{\mathcal{Q}}(\mathbf{q}_e, \omega_e). \quad (79)$$

By substituting the expressions of $\dot{\mathcal{P}}(\mathbf{q}_e, \omega_e)$ and $\mathcal{Q}(\mathbf{q}_e, \omega_e)$ given by (77) and (79) in (76), a solution for K that renders $\dot{V}(\mathbf{q}_e, \omega_e)$ negative semidefinite is obtained as

$$K(\mathbf{q}_e, \omega_e) = -\dot{\mathcal{P}}(\mathbf{q}_e, \omega_e) - \bar{\mathcal{Q}}(\mathbf{q}_e, \omega_e). \quad (80)$$

Furthermore, it follows from Proposition 3 that K guarantees asymptotic stability of $\omega_e = \mathbf{0}_{3 \times 1}$ over the invariant set of \mathbf{q}_e , and ω_e values on which $V(\mathbf{q}_e, \omega_e) = 0$ if K remains nonsingular for all $t \geq 0$. This is achieved by choosing $\bar{\mathcal{Q}}(\mathbf{q}_e, \omega_e)$ as

$$\bar{\mathcal{Q}}(\mathbf{q}_e, \omega_e) = \sigma_{\max}(\dot{\mathcal{P}}(\mathbf{q}_e, \omega_e))I_{3 \times 3} + Q \quad (81)$$

so that $K(\mathbf{q}_e, \omega_e)$ remains negative definite. Substituting the above written expression for $\bar{\mathcal{Q}}(\mathbf{q}_e, \omega_e)$ in (80) results in the expression of $K(\mathbf{q}_e, \omega_e)$ given by (73). Therefore, in addition to rendering $\dot{V}(\mathbf{q}_e, \omega_e)$ negative semidefinite, $K(\mathbf{q}_e, \omega_e)$ guarantees asymptotic stability of $\omega_e = \mathbf{0}_{3 \times 1}$ over the invariant set of \mathbf{q}_e and ω_e values on which $V(\mathbf{q}_e, \omega_e) = 0$, and Lyapunov stability of $\omega_e = \mathbf{0}_{3 \times 1}$ follows (Iqqidr et al., 1996). Since $V(\mathbf{q}_e, \omega_e)$ is radially unbounded with respect to ω_e , Lyapunov stability of $\omega_e = \mathbf{0}_{3 \times 1}$ is global. Moreover, it is noticed from the expression of $\dot{V}(\mathbf{q}_e, \omega_e)$ given by (61) and from (78) that the largest invariant set of \mathbf{q}_e and ω_e on which $\dot{V}(\mathbf{q}_e, \omega_e) = 0$ is the same invariant set on which $V(\mathbf{q}_e, \omega_e) = 0$, implying global asymptotic stability of the equilibrium point $\omega_e = \mathbf{0}_{3 \times 1}$ (Iqqidr et al., 1996). Global asymptotic convergence of the attitude vector q to the desired attitude vector $q_d(t)$ follows from Proposition 2.

9. Damped controls coefficient nullprojector

Although the CCNP $\mathcal{P}(q_e)$ has bounded elements, dependency of CCNP on the unbounded vector $\mathcal{A}^+(\mathbf{q}_e)$ may cause undesirable behavior of the auxiliary part in the control law τ_s during steady state tracking response of time varying trajectories. For this reason, a damped controls coefficient nullprojector (DCCN) $\mathcal{P}_d(\mathbf{q}_e, \epsilon)$ is used in place of $\mathcal{P}(\mathbf{q}_e)$ in (57). The DCCN is defined as

$$\mathcal{P}_d(\mathbf{q}_e, \epsilon) := I_{3 \times 3} - \mathcal{A}_d^+(\mathbf{q}_e, \epsilon)\mathcal{A}(\mathbf{q}_e) \quad (82)$$

where ϵ is a small positive number, and $\mathcal{A}_d^+(\mathbf{q}_e, \epsilon)$ is given by

$$\mathcal{A}_d^+(\mathbf{q}_e, \epsilon) := \frac{\mathcal{A}^T(\mathbf{q}_e)}{\mathcal{A}(\mathbf{q}_e)\mathcal{A}^T(\mathbf{q}_e) + \epsilon}. \quad (83)$$

Therefore,

$$\lim_{\epsilon \rightarrow 0} \mathcal{A}_d^+(\mathbf{q}_e, \epsilon) = \mathbf{0}_{3 \times 1} \quad (84)$$

and consequently,

$$\lim_{\epsilon \rightarrow 0} \mathcal{P}_d(\mathbf{q}_e, \epsilon) = I_{3 \times 3}. \quad (85)$$

Hence, the DCCN maps the null-control vector to itself in steady state phase of response, during which the auxiliary part of the control law converges to the null-control vector.

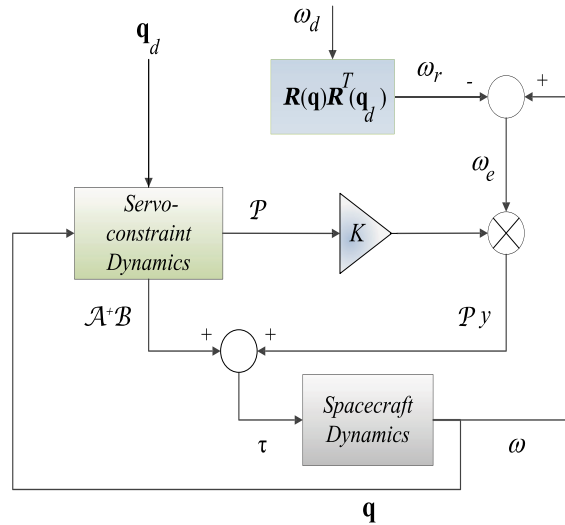


Fig. 1. Schematic of GDI spacecraft attitude control system

Independency of nullprojection on the attitude state of the spacecraft substantially eliminates unnecessary abrupt behavior of the control vector. Replacing $\mathcal{P}(\mathbf{q}_e)$ by $\mathcal{P}_d(\mathbf{q}_e, \epsilon)$ in the control expression given by (57) yields the following form of the GDI control law

$$\tau_{sd} = \mathcal{A}_s^+(\mathbf{q}_e, \nu)\mathcal{B}(\mathbf{q}_e, \omega_e) + \mathcal{P}_d(\mathbf{q}_e, \epsilon)K\omega_e(t). \tag{86}$$

A schematic of the GDI spacecraft attitude control system is shown in Fig. 1.

10. Tuning the GDI control design parameters

When the second-order deviation dynamics given by (26) is chosen to be time invariant, then increasing the value of the constant c_1 increases the damping ratio of closed loop spacecraft dynamics. Additionally, increasing the value of c_2 improves steady state trajectory tracking accuracy. Nevertheless, excessively large values of c_1 and c_2 require large control torque inputs and cause large amplitude oscillations of spacecraft body angular velocity components, particularly during the initial phase of response when the state deviation variable ϕ and its time derivative $\dot{\phi}$ are at their biggest magnitudes, i.e., when the controls load $\mathcal{B}(\mathbf{q}_e, \omega_e)$ has a large value. Accordingly, to increase damping and to improve steady state tracking with simultaneous avoidance of these drawbacks, the coefficients $c_1(t)$ and $c_2(t)$ are chosen to be of the form $c_1(t) = C_1(1 - e^{-\alpha_1 t})$ and $c_2(t) = C_2(1 - e^{-\alpha_2 t})$, where $C_1, C_2, \alpha_1,$ and α_2 are positive constants. Hence, $c_1(0) = 0$ and $c_2(0) = 0$, which substantially decreases the magnitude of $\mathcal{B}(\mathbf{q}_e, \omega_e)$.

11. Numerical simulations

The spacecraft model has inertia scalars $I_{11} = 200 \text{ Kg.m}^2, I_{22} = 150 \text{ Kg.m}^2, I_{33} = 175 \text{ Kg.m}^2, I_{12} = -100 \text{ Kg.m}^2, I_{13} = I_{23} = 0 \text{ Kg.m}^2$. The first maneuver considered is a rest-to-rest slew maneuver, aiming to reorient the spacecraft at the initial attitude given by $\mathbf{q}(0) = \mathbf{q}_0$ to a different attitude given by $\mathbf{q}_d(T)$, where T is duration of the maneuver. It is required that the spacecraft quaternion attitude variables follow the trajectories given by the following

transition functions (McInnes, 1998)

$$q_d(t) = q_d(0) + \left[10 \left(\frac{t}{T} \right)^3 - 15 \left(\frac{t}{T} \right)^4 + 6 \left(\frac{t}{T} \right)^5 \right] [q_d(T) - q_d(0)] \quad (87)$$

$$q_{4d}(t) = \sqrt{1 - q_d^T(t)q_d(t)}. \quad (88)$$

The desired quaternion attitude variables and their derivatives satisfy the differential equations

$$\dot{\mathbf{q}}_d(t) = \begin{bmatrix} \dot{q}_d(t) \\ \dot{q}_{4d}(t) \end{bmatrix} = \frac{1}{2} \begin{bmatrix} (q_d^\times(t) + q_{4d}(t)I_{3 \times 3}) \\ -q_d^T(t) \end{bmatrix} \omega_d(t) \quad (89)$$

where $\omega_d(t)$ is the angular velocity of \mathcal{D} relative to \mathcal{I} expressed in \mathcal{D} . Equations (89) can be inverted to calculate $\omega_d(t)$ as (Behal et al., 2002)

$$\omega_d(t) = 2(q_{4d}(t)\dot{q}_d(t) - q_d(t)\dot{q}_{4d}(t)) - 2q_d^\times(t)\dot{q}_d(t). \quad (90)$$

Accordingly, $\omega_r(t)$ is obtained as

$$\omega_r(t) = \mathbf{R}(\mathbf{q})\mathbf{R}^T(\mathbf{q}_d)\omega_d(t) \quad (91)$$

and is used in the control expression τ_{sd} given by (86). Values of second-order attitude deviation dynamics functions are chosen to be $c_1(t) = 20(1 - e^{-0.07t})$ and $c_2(t) = 10(1 - e^{-0.07t})$. With $q_d(0) = [0.7 \ 0.4 \ 0.5]^T$, $q_d(T) = [0 \ 0 \ 0]^T$, $T = 60$ sec., $Q = 0.1 \times I_{3 \times 3}$, $a = 100$, $p = 2$, $\epsilon = 10^{-4}$ and an arbitrary initial attitude, Fig. 2 shows the excellent asymptotic tracking of attitude quaternion variables q_1, \dots, q_4 trajectories. Figs. 3 and 4 show the corresponding time histories of spacecraft's angular velocity components $\omega_1, \omega_2, \omega_3$ and the GDI control variables u_1, u_2, u_3 .

The second maneuver considered is a trajectory tracking maneuver. The reference trajectory is determined via a sinusoidal trajectory generator at the angular velocity level that is given by

$$\omega_d(t) = [\cos(0.1t) \quad -\cos(0.2t) \quad \sin(0.3t)]. \quad (92)$$

Values of second-order attitude deviation dynamics functions are chosen to be $c_1(t) = 45(1 - e^{-0.40t})$ and $c_2(t) = 40(1 - e^{-0.02t})$. With $Q = 0.1 \times I_{3 \times 3}$, $a = 200$, $p = 2$, $\epsilon = 10^{-4}$ and arbitrary initial conditions, Fig. 5 shows the attitude quaternion error variables q_{e1}, \dots, q_{e4} trajectories. Figs. 6 and 7 show the corresponding time histories of spacecraft's angular velocity components $\omega_1, \omega_2, \omega_3$ and the GDI control variables u_1, u_2, u_3 .

12 Conclusion

Despite that the attitude parametrization provided by quaternion attitude variables is nonminimal, quaternion algebraic properties and multiplicative attitude quaternion error dynamics simplify the expressions of controls coefficient and controls load functions, and therefore simplify the GDI control law. Lyapunov control system design is well-known to consume less energy than classical DI design. The geometric properties of the GDI control law makes it possible to combine DI with Lyapunov control to reduce the control energy required to perform DI.

The choice of desired stable servo-constraint dynamics has its tangible effect on closed loop system response. For instance, choosing the linear servo-constraint dynamics coefficients to

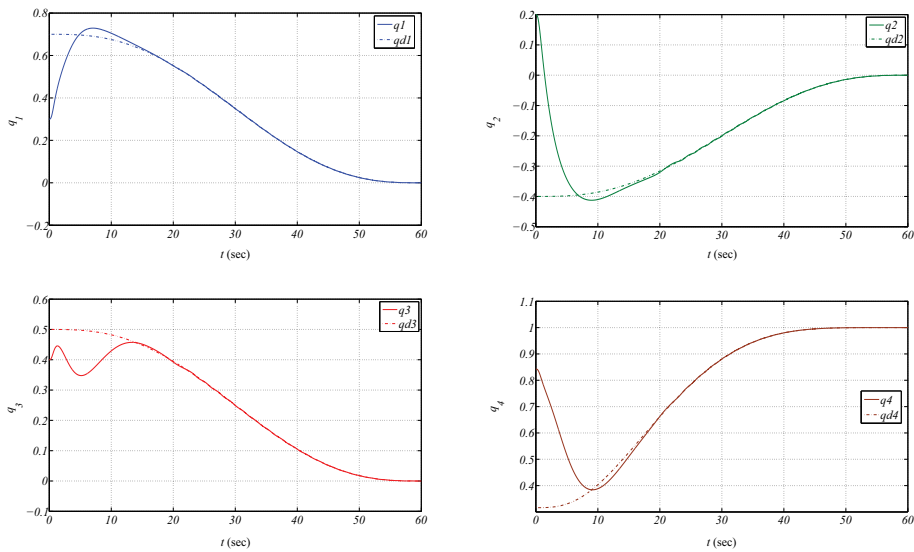


Fig. 2. Quaternion attitude parameters vs. Time: rest-to-rest slew maneuver

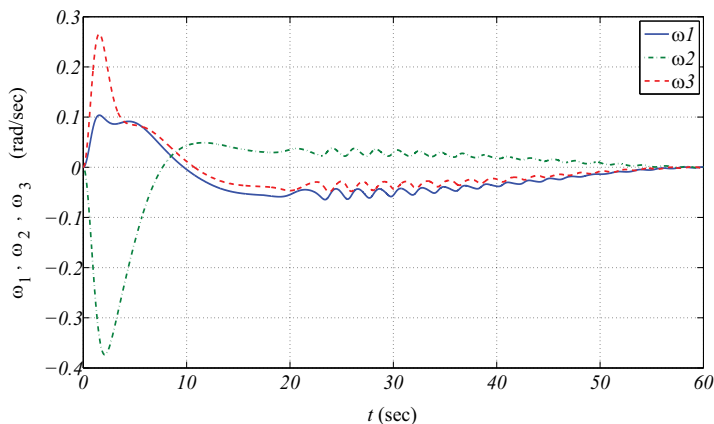


Fig. 3. Angular velocity components vs. Time: rest-to-rest slew maneuver

be time varying with vanishing values at initial time substantially reduces the magnitude of controls load function, and hence substantially reduces initial control signal magnitude.

The null-control vector in the auxiliary part of the control law is designed to be linear in angular velocity's error vector. A novel construction of the state dependent linearity gain matrix is made by means of positive semidefinite control Lyapunov function and nullprojected control Lyapunov equation that utilize geometric features of the GDI control law's structure. The generalized inversion stable mode augmentation generalizes the concept of dynamic scaling, and it effectively overcomes controls coefficient generalized inversion singularity. If the augmented mode is designed to be very fast, then the delayed DSGI closely approximates the instantaneous DSGI. For problems involving time invariant steady state trajectory

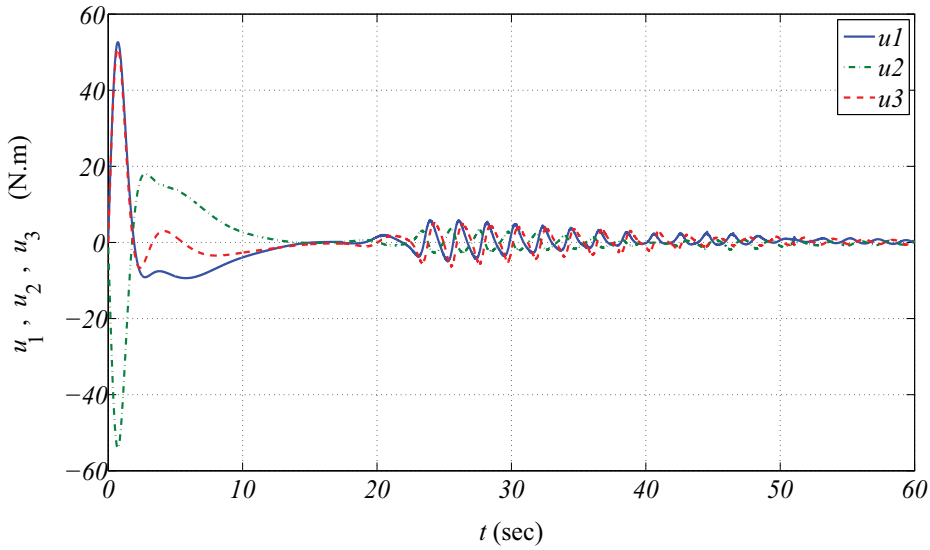


Fig. 4. Control variables vs. Time: rest-to-rest slew maneuver

tracking, the particular part of the control law asymptotically converges to its projection on the range space of the controls coefficient's MPGI, leading to asymptotic realization of desired servo-constraint stable dynamics. Practically stable trajectory tracking control is achieved otherwise.

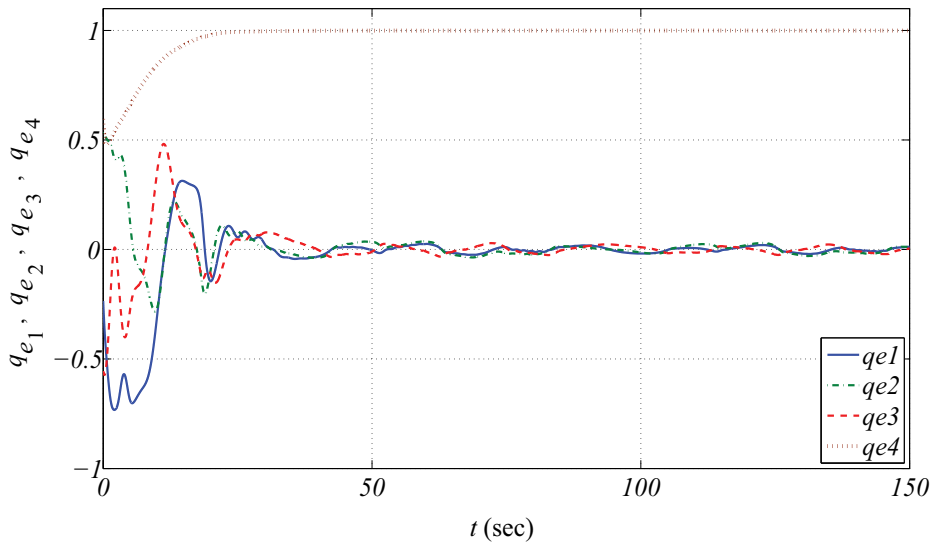


Fig. 5. Quaternion attitude parameters errors vs. Time: trajectory tracking maneuver

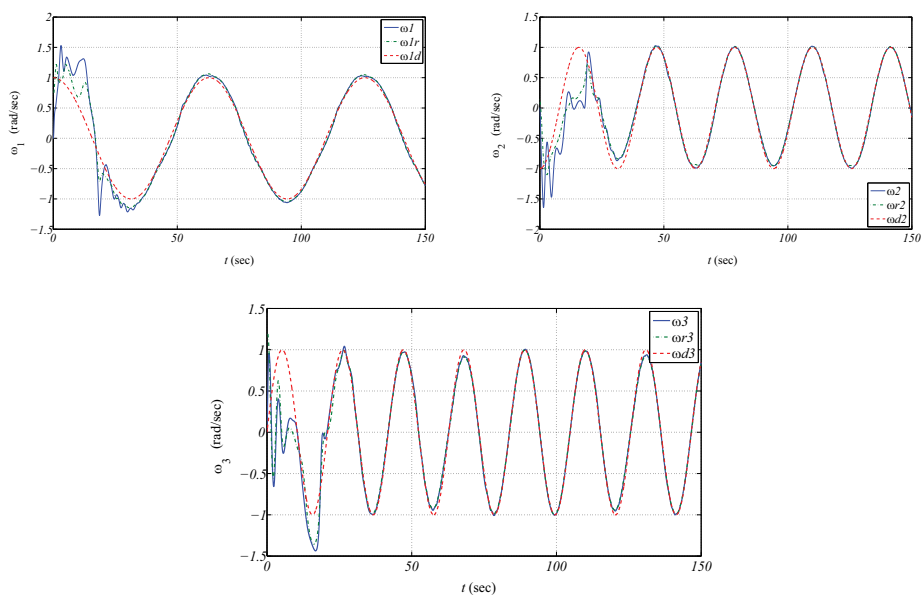


Fig. 6. Angular velocity components vs. Time: trajectory tracking maneuver

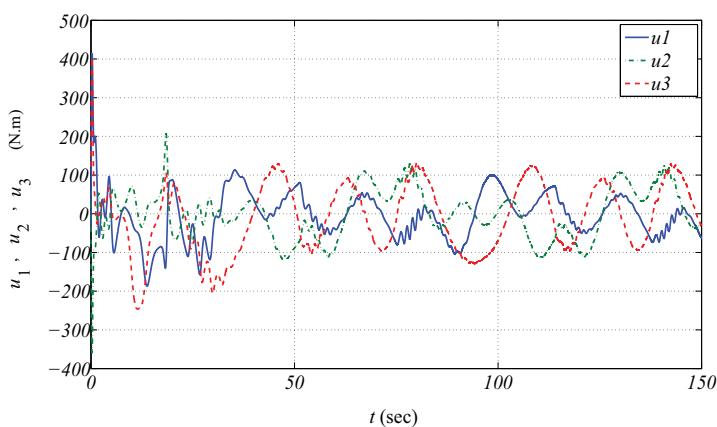


Fig. 7. Control variables vs. Time: trajectory tracking maneuver

13. References

- Bajodah, A. H. (2006). Stabilization of underactuated spacecraft dynamics via singularly perturbed feedback linearization, *Journal of King Abdulaziz University: Engineering Sciences* 16(2): 35–53.
- Bajodah, A. H. (2008). Singularly perturbed feedback linearization with linear attitude deviation dynamics realization, *Nonlinear Dynamics* 53(4): 321–343.
- Bajodah, A. H. (2009). Generalized dynamic inversion spacecraft control design methodologies, *IET Control Theory & Applications* 3(2): 239–251.
- Bajodah, A. H. (2010). Asymptotic generalized inversion attitude control, *IET Control Theory*

- & Applications* 4(5): 827–840.
- Bajodah, A. H., Hodges, D. H. & Chen, Y. H. (2005). Inverse dynamics of servo-constraints based on the generalized inverse, *Nonlinear Dynamics* 39(1-2): 179–196.
- Baker, D. R. & Wampler II, C. W. (1988). On inverse kinematics of redundant manipulators, *International Journal of Robotics Research* 7(2): 3–21.
- Behal, A., Dawson, D., Zergeroglu, E. & Fang, Y. (2002). Nonlinear tracking control of an underactuated spacecraft, *Journal of Guidance, Control, and Dynamics* 25(5): 979–985.
- Ben-Israel, A. & Greville, T. N. E. (2003). *Generalized Inverses, Theory and Applications*, second edn, Springer-Verlag New York, Inc.
- Bensoubaya, M., Ferfera, A. & Iqqidr, A. (1999). Stabilization of nonlinear systems by use of semidefinite Lyapunov functions, *Applied Mathematics Letters* 12(7): 11–17.
- Bhat, S. & Bernstein, D. (2000). A topological obstruction to continuous global stabilization of rotational motion and the unwinding phenomenon, *Systems & Control Letters* 39(1): 63–70.
- De Sapio, V., Khatib, O. & Delp, S. (2008). Least action principles and their application to constrained and task-level problems in robotics and biomechanics, *Multibody System Dynamics* 19(3): 303–322.
- Dwyer III, T. (1984). Exact nonlinear control of large angle rotational maneuvers, *IEEE Transactions on Automatic Control* 29(9): 769–774.
- Gauss, C. F. (1829). Ueber ein neues allgemeines grundgesetz der mechanik, *Zeitschrift Fuer die reine und angewandte Mathematik* 4: 232–235.
- Greville, T. N. E. (1959). The pseudoinverse of a rectangular or singular matrix and its applications to the solutions of systems of linear equations, *SIAM Review* 1(1): 38–43.
- Hunt, L., Su, R. & Meyer, G. (1983). Global transformations of nonlinear systems, *IEEE Transactions on Automatic Control* AC-28: 24–31.
- Iqqidr, A., Kalitine, B. & Outbib, R. (1996). Semidefinite Lyapunov functions stability and stabilization, *Mathematics of Control, Signals and Systems* 9(2): 95–106.
- Khalil, H. K. (2002). *Nonlinear Systems*, 3rd edn, Prentice-Hall, Inc.
- Liegeois, A. (1977). Automatic supervisory control of the configuration and behavior of multi-body mechanisms, *IEEE Transactions on Systems, Man, and Cybernetics* 7(12): 868–871.
- Mayorga, R. V., Janabi-Sharifi, F. & Wong, A. K. C. (1995). A fast approach for the robust trajectory planning of redundant robot manipulators, *Journal of Robotic Systems* 12(2): 147–161.
- McInnes, C. R. (1998). Satellite attitude slew manoeuvres using inverse control, *Aeronautical Journal* 102: 259–265.
- Moore, E. H. (1920). On the reciprocal of the general algebraic matrix, *Bulletin of the American Mathematical Society* 26: 394–395.
- Nakamura, Y. & Hanafusa, H. (1986). Inverse kinematic solutions with singularity robustness for robot manipulator control, *Journal of Dynamic Systems, Measurements, and Control* 10(8): 163–171.
- Oh, H. S. & Vadali, S. R. (1991). Feedback control and steering laws for spacecraft using single gimbal control moment gyros, *Journal of the Astronautical Sciences* 39(2): 183–203.
- Paielli, R. A. & Bach, R. E. (1993). Attitude control with realization of linear error dynamics, *Journal of Guidance, Control, and Dynamics* 16(1): 182–189.
- Penrose, R. (1955). A generalized inverse for matrices, *Proceedings of the Cambridge Philosophical Society* 51: 406–413.

- Peters, J., Mistry, M., Udwadia, F., Nakanishi, J. & Schaal, S. (2008). A unifying framework for robot control with redundant DOFs, *Autonomous Robots* 24(1): 1–12.
- Show, L.-L. & Juang, J.-C. (2003). Satellite large angle tracking control design: Thruster control approach, *Proceedings of the American Control Conference*, Denver, Colorado, pp. 1098–1103.
- Siciliano, B. & Khatib, O. (2008). *Springer Handbook of Robotics*, Springer.
- Slotine, J. E. & Li, W. (1991). *Applied Nonlinear Control*, Prentice-Hall.
- Su, R. (1982). On the linear equivalents of nonlinear systems, *Systems and Control Letters* 2: 48–52.
- Udwadia, F. E. (2008). Optimal tracking control of nonlinear dynamical systems, *Proceedings of the Royal Society of London. Series A* 464: 2341–2363.
- Udwadia, F. E. & Kalaba, R. E. (1996). *Analytical Dynamics, A New Approach*, Cambridge University Press, New York, NY.
- Wampler II, C. W. (1986). Manipulator inverse kinematic solutions based on vector formulations and damped least-squares methods, *IEEE Transactions on Systems, Man, and Cybernetics* SMC-16: 93–101.
- Wertz, J. W. (1980). *Spacecraft Attitude Determination and Control*, D. Reidel Publishing Co., Dordrecht, Holland.
- Yoon, H. & Tsiotras, P. (2004). Singularity analysis of variable-speed control moment gyros, *Journal of Guidance, Control, and Dynamics* 27(3): 374–386.

Tracking Control of Spacecraft by Dynamic Output Feedback - Passivity- Based Approach -

Yuichi Ikeda¹, Takashi Kida² and Tomoyuki Nagashio²

¹*Shinshu University,*

²*The University of Electro-Communications,
Japan*

1. Introduction

In this study, we investigate the possibility of capturing an inoperative spacecraft using an orbital servicing vehicle or a space robot in future space infrastructure. These missions involve problems related to the tracking control of a target spacecraft; therefore, a control system design that takes into account the interference with the nonlinear motion of the spacecraft is required because the equations of motion of such a spacecraft are nonlinear system in which the six-degree-of-freedom (six-dof) translational motion and the rotational motion are coupled.

They have been many studies on the six-dof tracking control problem related to spacecrafts (Ahmed et al., 1998; Terui, 1998; Dalsmo & Egeland, 1999; Bošković et al., 2004; Ikeda et al., 2008; Seo & Akella, 2008). The control methods proposed by these researches are state feedback control methods and involve measurements of the linear and angular velocities of the spacecraft. It is necessary to develop an output feedback control method, which does not require velocity measurements in cases where a velocity sensor cannot be mounted on the spacecraft because of the limitations on the cost and weight of the spacecraft, or as a backup controller to ensure spacecraft stability when the velocity sensor breaks down.

For the output feedback tracking control problem, a control method that eliminate the velocity measurement via the filtering of the position and attitude information (Costic et al., 2000; Costic et al., 2001; Pan et al., 2004) or the estimation of the velocity by the observer (McDuffie & Shtessel, 1997; Seo & Akella, 2007) has previously been proposed. However, these methods cannot be used for tracking a spacecraft with an arbitrary trajectory since the attitude controller has a singular point at which the control input diverges; another instance where the method cannot be used is when the initial state of the control system is restricted.

In this paper, we propose a new passivity-based control method that involves the use of output feedback for solving the tracking control problem. Although the proposed method has a filter as well as (Costic et al., 2000), (Costic et al., 2001), and (Pan et al., 2004), and is implemented by using the conventional methods, it can track a spacecraft with an arbitrary trajectory because the controller does not have a singular point. Thus, the proposed method has characteristics that are better than those of conventional methods.

This paper is organized as follows: Section 2 describes the tracking control problem and the derivation of the relative equation of motion; the equation is then used for transforming the tracking control problem to a regulation problem. In section 3, we construct the dynamic

output feedback controller that is based on passivity. Concretely speaking, the relative equation of motion is transformed into a passive system by a coordinate and feedback transformation, and a controller based on the passive system is designed. In addition, the controller obtained can be considered to be an observer. In section 4, we provide the guidelines for obtaining the controller parameters and show that the controller can be made to be similar to a proportional-derivative (PD) controller by appropriately setting the parameters. The effectiveness of the control methods is verified by performing numerical simulations in section 5. Finally, the conclusion is given in section 6.

2. Relative equation of motion of spacecraft

In this paper, we consider the tracking control problem in which the chaser spacecraft tracks to the target spacecraft that has a broken down actuator and moves in space freely. The definition of the coordinate systems and the position vectors are shown in Fig. 1. $\{i\}$, $\{c\}$, and $\{t\}$ represent the inertial, chaser, and target frame, respectively. Here, the position of the chaser conforms to a constant vector $p_t \in R^3$ fixed at $\{t\}$. In addition, the attitude of the chaser and target represent the quaternion (Hughes, 1986).

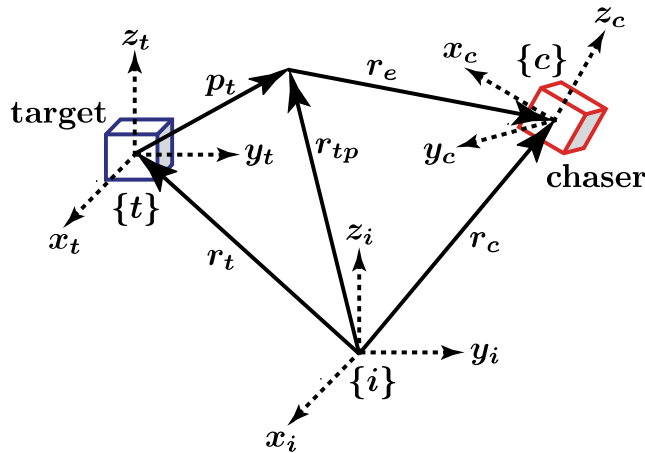


Fig. 1. Definition of the coordinate system and the position vector.

The equation of motion of the target and the chaser can be described as follows (Terui, 1998):

Target:

$$\dot{r}_t = v_t - \omega_t^\times r_t, \quad (1)$$

$$\dot{q}_t = \frac{1}{2} \begin{bmatrix} \varepsilon_t^\times + \eta_t I_3 \\ -\varepsilon_t^T \end{bmatrix} \omega_t = E(q_t) \omega_t, \quad \|q_t\| = 1, \quad (2)$$

$$m_t \dot{v}_t = -m_t \omega_t^\times v_t, \quad (3)$$

$$J_t \dot{\omega}_t = -\omega_t^\times J_t \omega_t. \quad (4)$$

Chaser:

$$\dot{r}_c = v_c - \omega_c^\times r_c, \quad (5)$$

$$\dot{q}_c = \frac{1}{2} \begin{bmatrix} \varepsilon_c^\times + \eta_c I_3 \\ -\varepsilon_c^T \end{bmatrix} \omega_c = E(q_c) \omega_c, \quad \|q_c\| = 1, \quad (6)$$

$$m_c \dot{v}_c = -m_c \omega_c^\times v_c + f_c, \quad (7)$$

$$J_c \dot{\omega}_c = -\omega_c^\times J_c \omega_c + \tau_c + \rho_c^\times f_c, \quad (8)$$

where $r_i \in R^3$ ($i = t, c$) is the position from the origin of the inertial frame $\{i\}$ to the center of mass of each frame, $v_i \in R^3$ is the linear velocity of the body-fixed frame with respect to $\{i\}$, $\omega_i \in R^3$ is the angular velocity of the body-fixed frame with respect to $\{i\}$, $q_i = [\varepsilon_i^T \quad \eta_i]^T \in S^3$ is the quaternion, $f_c \in R^3$ is the control force, $\tau_c \in R^3$ is the control torque, $m_i \in R$ is the mass, $J_i \in R^{3 \times 3}$ is the inertia matrix, $\rho_c \in R^3$ is the vector of the point of application of control force, I_n is an $n \times n$ identity matrix, and a^\times is the skew symmetric matrix,

$$a^\times = \begin{bmatrix} 0 & -a_3 & a_2 \\ a_3 & 0 & -a_1 \\ -a_2 & a_1 & 0 \end{bmatrix} \quad (9)$$

which is induced from vector $a = [a_1 \quad a_2 \quad a_3]^T$. In addition, S^3 is the hypersphere of dimension three and is defined as follows:

$$S^3 = \{q_i \in R^4 \mid \|q_i\| = 1\} \quad (i = t, c).$$

Our tracking control problem is to find a controller such that

$$r_c = r_{tp}, \varepsilon_c = \varepsilon_t, \eta_c = \eta_t, v_c = v_{tp}, \omega_c = \omega_t$$

when $t \rightarrow \infty$. The position and the velocity of the tip of vector p_t fixed at $\{t\}$ are given by

$$r_{tp} = r_t + p_t, \quad v_{tp} = v_t + \omega_t^\times p_t. \quad (10)$$

To this end, an error system in $\{c\}$ is described as follows: Let the direction cosine matrix from $\{t\}$ to $\{c\}$ be

$$C = (\eta_e^2 - \varepsilon_e^T \varepsilon_e) I_3 + 2\varepsilon_e \varepsilon_e^T - 2\eta_e \varepsilon_e^\times \quad (11)$$

using the quaternion of relative attitude $q_e = [\varepsilon_e^T \quad \eta_e]^T$, where ε_e and η_e are defined as

$$\varepsilon_e = \eta_t \varepsilon_c - \eta_c \varepsilon_t + \varepsilon_c^\times \varepsilon_t, \quad \eta_e = \eta_c \eta_t + \varepsilon_c^T \varepsilon_t. \quad (12)$$

The relative position, linear velocity, and angular velocity are given in the same $\{c\}$ frame as

$$r_e = r_c - Cr_{tp}, \quad v_e = v_c - Cv_{tp}, \quad \omega_e = \omega_c - C\omega_t. \quad (13)$$

From (12) and (13), using the identity $\dot{C} = -\omega_e^\times C$, we obtain the relative equations of motion as

$$\dot{r}_e = v_e - (\omega_e + C\omega_t)^\times r_e, \quad (14)$$

$$\dot{q}_e = \frac{1}{2} \begin{bmatrix} \varepsilon_e^\times + \eta_e I_e \\ -\varepsilon_e^T \end{bmatrix} \omega_e = E(q_e) \omega_e, \quad \|q_e\| = 1, \quad (15)$$

$$m_c \dot{v}_e = -m_c \left[(\omega_e + C\omega_t)^\times v_e + C\dot{v}_{tp} + (C\omega_t)^\times Cv_{tp} \right] + f_c, \quad (16)$$

$$J_c \dot{\omega}_e = -(\omega_e + C\omega_t)^\times J_c (\omega_e + C\omega_t) - J_c (C\dot{\omega}_t - \omega_e^\times C\omega_t) + \tau_c + \rho_c^\times f_c. \quad (17)$$

After the transform, the tracking control problem is reduced to a regulation problem to design a controller such that

$$r_e = 0, \varepsilon_e = 0, v_e = 0, \omega_e = 0$$

when $t \rightarrow \infty$ according to (14)-(17).

Hereafter, in order to simplify the derivation of the controller, the control force and torque are as follows:

$$\hat{f}_c = f_c, \hat{\tau}_c = \tau_c + \rho_c^\times f_c. \quad (18)$$

The controller is derived using (18) in the sequel. Since the inverse transform from $\hat{f}_c, \hat{\tau}_c$ to f_c, τ_c obviously exists, f_c, τ_c can be uniquely determined after $\hat{f}_c, \hat{\tau}_c$ is derived.

Remark 1: η_e at $\varepsilon_e = 0$ exists as $\eta_e \pm 1$ because of the constraint of the quaternion $\|q_e\| = 1$. In this paper, η_e , which should be asymptotically stabilized, is set to $\eta_e = 1$.

3. Dynamic output feedback control

3.1 Passivation of relative equation of motion

Since the relative equation of motion (14)-(17) is a complicated nonlinear time-varying system, it is difficult to design a controller based on (14)-(17). Therefore, in order to facilitate a controller, the relative equation of motion (14)-(17) is transformed into a passive system by a coordinate and feedback transformation, and a controller design based on the passive system is designed. Further, in this paper, we consider the output feedback control problem - the linear velocity v_c and the angular velocity ω_c of the chaser, in other words, the relative linear velocity v_e and the angular velocity ω_e , cannot be measured. We suppose that the states r_t, q_t, v_t, ω_t of the target can be measured in some way, for example, the target

motion estimation method using image information (Lichter & Dubowsky, 2004; Tanaka et al., 2007).

Let us consider the following coordinate and feedback transformation.

$$\bar{v}_e = v_e - (C\omega_t)^\times r_e, \quad (19)$$

$$\hat{f}_c = \bar{f}_c + m_c \delta_r, \quad \hat{\tau}_c = \bar{\tau}_c + \delta_q, \quad (20)$$

where $\bar{f}_c, \bar{\tau}_c \in R^3$ are the new control inputs, and

$$\delta_r = (C\dot{\omega}_t)^\times r_e + (C\omega_t)^\times (C\omega_t)^\times r_e + C\dot{v}_{tp} + (C\omega_t)^\times C v_{tp},$$

$$\delta_q = (C\omega_t)^\times J_c (C\omega_t) + J_c C\dot{\omega}_t.$$

From (19) and (20), the relative equation of motion (14)-(17) is transformed into the following system:

$$\dot{r}_e = \bar{v}_e - \omega_e^\times r_e, \quad (21)$$

$$\dot{q}_e = E(q_e)\omega_e, \quad (22)$$

$$m_c \dot{\bar{v}}_e = -m_c (\omega_e + 2C\omega_t)^\times \bar{v}_e + \bar{f}_c, \quad (23)$$

$$J_c \dot{\omega}_e = -\omega_e^\times J_c (\omega_e + C\omega_t) - H\omega_e + \bar{\tau}_c, \quad (24)$$

where $H = (C\omega_t)^\times J_c + J_c (C\omega_t)^\times$ and H is a skew-symmetric matrix. If we can find a controller such that

$$r_e = 0, \varepsilon_e = 0, \bar{v}_e = 0, \omega_e = 0$$

when $t \rightarrow \infty$ according to (21)-(24), then the tracking control is achieved since $\bar{v}_e = 0$ implies $v_e = 0$ from (19). Therefore, the tracking control problem is reduced to a regulation problem of $(r_e, \varepsilon_e, \bar{v}_e, \omega_e)$.

At the end of this subsection, it is shown that the system (21)-(24) is passive. Let us consider the following storage function:

$$E = \frac{1}{2} m_c \bar{v}_e^T \bar{v}_e + \frac{1}{2} \omega_e^T J_c \omega_e. \quad (25)$$

By using the skew symmetric matrix properties $a^T b^\times a = 0$, $a^T a^\times = 0$, $\forall a, b \in R^3$, we can express the time derivative of (25) along with the trajectories as

$$\begin{aligned}
\dot{E} &= \bar{v}_e^T \left[-m_c (\omega_e + 2C\omega_t)^\times \bar{v}_e + \bar{f}_c \right] + \omega_e^T \left[-\omega_e^\times J_c (\omega_e + C\omega_t) - H\omega_e + \bar{\tau}_c \right] \\
&= \bar{v}_e^T \bar{f}_c + \omega_e^T \bar{\tau}_c \\
&= \bar{y}^T \bar{u}, \quad \bar{y} = \begin{bmatrix} \bar{v}_e^T & \omega_e^T \end{bmatrix}^T, \quad \bar{u} = \begin{bmatrix} \bar{f}_c^T & \bar{\tau}_c^T \end{bmatrix}.
\end{aligned} \tag{26}$$

Therefore, the system (21)-(24) is passive with respect to input \bar{u} and output \bar{y} .

Remark 2: In feedback transformation (20), although the acceleration \dot{v}_{ip} and $\dot{\omega}_t$ are needed, this information can be calculated algebraically from (3), (4), and (10) if v_t and ω_t can be measured. In addition, we suppose that the inertia matrix J_t is known hereafter.

3.2 Controller design

In this subsection, the dynamic output feedback controller that asymptotically stabilizes the relative position and attitude is designed on the basis of the passivity of the system (21)-(24). With respect to the target states, the following assumption is made.

Assumption 1: The target states r_t , q_t , v_t , ω_t , \dot{v}_t , and $\dot{\omega}_t$ are uniformly continuous and bounded.

Then, the following theorem can be obtained.

Theorem 1: Consider the following dynamic output controller

$$\begin{cases} \dot{z}_1 = A_1 z_1 + B_1 r_e \\ y_1 = C_1 \dot{z}_1 = C_1 (A_1 z_1 + B_1 r_e), \\ \bar{f}_c = -k_{p1} r_e - k_1 y_1 \end{cases} \tag{27}$$

$A_1 \in R^{n_1 \times n_1}$, $B_1 \in R^{n_1 \times 3}$, $C_1 \in R^{3 \times n_1}$, $n_1 \geq 3$,

$$\begin{cases} \dot{z}_2 = A_2 z_2 + B_2 q_e \\ y_2 = C_2 \dot{z}_2 = C_2 (A_2 z_2 + B_2 q_e) \\ \bar{\tau}_c = -K(q_e) \varepsilon_e + k_1 r_e^\times y_1 - k_2 E(q_e)^T y_2 \end{cases}, \tag{28}$$

$K(q_e) = T(q_e)^T K_{p2} - k_{p3} (\eta_e - 1) I_3$, $T(q_e) = \eta_e I_3 + \varepsilon_e^\times$,
 $A_2 \in R^{n_2 \times n_2}$, $B_2 \in R^{n_2 \times 4}$, $C_2 \in R^{4 \times n_2}$, $n_2 \geq 4$,

where k_{p1} , k_{p3} , k_1 , $k_2 > 0$ are scalar feedback gains; $K_{p2} = K_{p2}^T > 0$, $K_{p2} \in R^{3 \times 3}$ is the matrix feedback gain; A_i , B_i , and C_i are design parameters (A_i is stable, and B_i is a full column rank matrix). Furthermore, A_i , B_i , and C_i must be designed such that there exists a matrix $P_i = P_i^T > 0$ that satisfies the following matrix algebraic equations (a strictly positive real condition):

$$A_i^T P_i + P_i A_i = -Q_i, \quad P_i B_i = C_i^T \tag{29}$$

for an arbitrary matrix $Q_i = Q_i^T > 0$. Then, the state variable of the closed-loop system of (21)-(24) with (27) and (28) becomes

$$\begin{aligned} (r_e, \varepsilon_e, \eta_e, \bar{v}_e, \omega_e, z_1, z_2) &\rightarrow (0, 0, 1, 0, 0, 0, z_2^*) \\ z_2^* &= -A_2^{-1}B_2q_e^*, q_e^* = [0 \ 0 \ 0 \ 1]^T \end{aligned} \quad (30)$$

when $t \rightarrow \infty$ for an arbitrary initial state.

Proof: Consider the following candidate of a Lyapunov function:

$$\begin{aligned} V(x) &= E + \frac{k_{p1}}{2} r_e^T r_e + \varepsilon_e^T K_{p2} \varepsilon_e + k_{p3} (\eta_e - 1)^2 + \frac{k_1}{2} (A_1 z_1 + B_1 r_e)^T P_1 (A_1 z_1 + B_1 r_e) \\ &\quad + \frac{k_2}{2} (A_2 z_2 + B_2 q_e)^T P_2 (A_2 z_2 + B_2 q_e), \\ x &= [r_e^T \ \varepsilon_e^T \ \eta_e \ \bar{v}_e^T \ \omega_e^T \ z_1^T \ z_2^T]^T. \end{aligned} \quad (31)$$

In (31), V equals to zero only when x is (30), $V > 0$ with the exception of (30). By using the skew symmetric matrix properties $a^T b^x a = 0$, $a^T \dot{a}^x = 0$, $(\dot{a}^x)^T = -a^x$, $\forall a, b \in R^3$ and (29), we can express the time derivative of (31) along with the trajectories as

$$\begin{aligned} \dot{V} &= \bar{v}_e^T \dot{\bar{f}}_c + \omega_e^T \dot{\bar{\tau}}_c + k_{p1} \bar{v}_e^T \dot{r}_e + \omega_e^T T (q_e)^T K_{p2} \dot{\varepsilon}_e - k_{p3} (\eta_e - 1) \omega_e^T \dot{\varepsilon}_e + \sum_{i=1}^2 \frac{k_i}{2} \dot{z}_i^T (A_i^T P_i + P_i A_i) \dot{z}_i \\ &\quad + k_1 \dot{r}_e^T B_1^T P_1 \dot{z}_1 + k_2 \dot{q}_e^T B_2^T P_2 \dot{z}_2 \\ &= -\sum_{i=1}^2 \frac{k_i}{2} \dot{z}_i^T Q_i \dot{z}_i + \bar{v}_e^T (\dot{\bar{f}}_c + k_{p1} \dot{r}_e + C_1 \dot{z}_1) + \omega_e^T [\dot{\bar{\tau}}_c + K(q_e) \dot{\varepsilon}_e - k_1 r_e^x C_1 \dot{z}_1 + k_2 E(q_e)^T C_2 \dot{z}_2] \\ &= -\sum_{i=1}^2 \frac{k_i}{2} \dot{z}_i^T Q_i \dot{z}_i \leq 0. \end{aligned} \quad (32)$$

Therefore, x is bounded since

$$V(x(t)) \leq V(x(0)), \quad \forall t \geq 0 \quad (33)$$

and V is radially unbounded in the state space $\Omega := R^{(9+n_1+n_2)} \times S^3$. Then, \dot{x} is also bounded because the control inputs \bar{f}_c , $\bar{\tau}_c$ are bounded by Assumption 1. It follows that

$$\ddot{V} = -\sum_{i=1}^2 k_i \dot{z}_i^T Q_i \ddot{z}_i$$

is bounded, and \dot{V} is uniformly continuous with respect to t . Therefore, it is shown that

$$\dot{V} \rightarrow 0 \Rightarrow \dot{z}_i \rightarrow 0$$

when $t \rightarrow \infty$ from the Lyapunov-like lemma (Slotine & Li, 1991), and then

$$\dot{z}_i = 0, z_i = \text{const.} \Rightarrow r_e = q_e = \text{const.} \Rightarrow \dot{r}_e = 0, \dot{q}_e = 0$$

when $t \rightarrow \infty$ from (27) and (28) since B_i is a full column rank matrix, and

$$\bar{v}_e = 0, \omega_e = 0$$

from (21) and (22). Furthermore, the closed-loop system becomes

$$k_{p1}I_3r_e = 0, K(q_e)\varepsilon_e = 0, A_1z_1 + B_1r_e, A_2z_2 + B_2q_e = 0. \quad (34)$$

From (34), $r_e = 0$, $\varepsilon_e = 0$ since $k_{p1} > 0$ and $\det K(q_e) \neq 0, \forall q_e$, and $\eta_e = 1$ from $V = 0$. In addition, since A_i is stable and B_i is a full column rank matrix, it follows that

$$z_1 = 0, z_2 = -A_2^{-1}B_2q_e^* = 0.$$

It is known that a controller, as (27) and (28), based on the strictly positive real condition (29) is a type of observer. The controllers (27) and (28) are the observers, and the estimate errors are

$$\bar{z}_1 = z_1 + A_1^{-1}B_1r_e, \bar{z}_2 = z_2 + A_2^{-1}B_2q_e. \quad (35)$$

Then, the following corollary can be obtained.

Corollary 1: Dynamic compensators of dynamic output feedback controllers (27) and (28) are the observers; the estimate errors are (35), and

$$z_1 \rightarrow -A_1^{-1}B_1r_e, z_2 \rightarrow -A_2^{-1}B_2q_e$$

when $t \rightarrow \infty$.

Proof: By using the estimate error (35), we can represent the dynamic output feedback controllers (27) and (28) as

$$\begin{cases} \dot{\bar{z}}_1 = A_1\bar{z}_1 + A_1^{-1}B_1\dot{r}_e \\ y_1 = C_1A_1\bar{z}_1 \\ \bar{f}_c = -k_{p1}r_e - k_1y_1 \end{cases}, \quad (36)$$

$$\begin{cases} \dot{\bar{z}}_2 = A_2\bar{z}_2 + A_2^{-1}B_2\dot{q}_e \\ y_2 = C_2A_2\bar{z}_2 \\ \bar{v}_c = -K(q_e)\varepsilon_e + k_1r_e \times y_1 - k_2E(q_e)^T y_2 \end{cases}. \quad (37)$$

Consider the following candidate of a Lyapunov function:

$$V(x) = E + \frac{k_{p1}}{2}r_e^T r_e + \varepsilon_e^T K_{p2}\varepsilon_e + k_{p3}(\eta_e - 1)^2 + \sum_{i=1}^2 \frac{k_1}{2} \bar{z}_i^T A_i^T P_i A_i \bar{z}_i. \quad (38)$$

From the calculations (32), we obtain the time derivative of (38) along with the trajectories as

$$\begin{aligned}
\dot{V} &= \bar{v}_e^T \bar{f}_c + \omega_e^T \bar{r}_c + k_{p1} \bar{v}_e^T r_e + \omega_e^T T(q_e)^T K_{p2} \varepsilon_e - k_{p3} (\eta_e - 1) \omega_e^T \varepsilon_e \\
&\quad + \sum_{i=1}^2 \frac{k_i}{2} \bar{z}_i^T A_i^T (A_i^T P_i + P_i A_i) A_i z_i + k_1 \bar{z}_1^T A_1^T P_1 B_1 (\bar{v}_e - \omega_e^\times r_e) + k_2 \bar{z}_2^T A_2^T P_2 B_2 E(q_e) \omega_e \\
&= -\sum_{i=1}^2 \frac{k_i}{2} \bar{z}_i^T A_i^T Q_i A_i \bar{z}_i + \bar{v}_e^T (\bar{f}_c + k_{p1} r_e + k_1 C_1 A_1 \bar{z}_1) \\
&\quad + \omega_e^T \left[\bar{r}_c + K(q_e) \varepsilon_e - k_1 r_e^\times C_1 A_1 \bar{z}_1 + k_2 E(q_e)^T C_2 A_1 \bar{z}_2 \right] \\
&= -\sum_{i=1}^2 \frac{k_i}{2} \bar{z}_i^T A_i^T Q_i A_i \bar{z}_i.
\end{aligned} \tag{39}$$

Since $A_i^T P_i A_i > 0$, $A_i^T Q_i A_i > 0$ from P_i and Q_i are positive definite matrices and A_i is a stable matrix, $V > 0$ and $\dot{V} \leq 0$ hold. Hereafter, in the same way as in the case of Theorem 1, the state variable of the closed-loop system of (21)-(24) with (36) and (37) becomes

$$(r_e, \varepsilon_e, \eta_e, \bar{v}_e, \omega_e, \bar{z}_1, \bar{z}_2) \rightarrow (0, 0, 1, 0, 0, 0, 0) \tag{40}$$

when $t \rightarrow \infty$ for an arbitrary initial state in the state space Ω .

Remark 3: In the conventional methods (Costic et al., 2000; Costic et al., 2001; Pan et al., 2004), the relative equation of motion with respect to the attitude is transformed into an Euler-Lagrange form by $(1/2)(\varepsilon_e^\times + \eta_e I_3) := S(q_e)$ of (15) as the coordinate transform matrix, and a controller based on the Euler-Lagrange form is designed. However, $\eta_e = 0$ is a singular point because $\det S(q_e) = 0$ when $\eta_e = 0$. In contrast, the proposed method does not exist a singular point since a controller based on the relative equation of motion is designed.

4. Guidelines of controller parameter setting

It is difficult for dynamic output feedback controllers (27) and (28) to find a clear meaning for the design parameters A_i , B_i , and C_i (or Q_i) as the state feedback control (e.g., PD control). Therefore, the control performance deteriorates according to the value of the design parameters as the convergence of the relative error is slow or the response of the relative error vibrates. In this section, we discuss a guideline for the design parameters.

In order to simply the argument, the design parameters A_i , B_i , and Q_i ($i=1,2$) are set as follows:

$$\begin{aligned}
A_1 &= -a_1 I_3, \quad B_1 = -A_1 = a_1 I_3, \quad Q_1 = q_1 I_3, \\
A_2 &= -a_2 I_4, \quad B_2 = -A_2 = a_2 I_4, \quad Q_2 = q_2 I_4,
\end{aligned}$$

where $a_i, q_i > 0$. In addition, P_i and C_i are

$$P_1 = \frac{q_1}{2a_1} I_3, \quad C_1 = B_1^T P_1 = \frac{q_1}{2} I_3,$$

$$P_2 = \frac{q_2}{2a_2} I_4, \quad C_2 = B_2^T P_2 = \frac{q_2}{2} I_4$$

from (29). Then, the output y_i ($i=1,2$) of the dynamic compensator of (27) and (28) becomes

$$y_1 = -\frac{a_1 q_1}{2} e^{-a_1 t} I_3 \cdot z_1(0) + \frac{q_1}{2} L^{-1} \left[\left\{ \frac{s}{(1/a_1)s + 1} \right\} I_3 \cdot r_e(s) \right], \quad (41)$$

$$y_2 = -\frac{a_2 q_2}{2} e^{-a_2 t} I_4 \cdot z_2(0) + \frac{q_2}{2} L^{-1} \left[\left\{ \frac{s}{(1/a_2)s + 1} \right\} I_4 \cdot q_e(s) \right], \quad (42)$$

where $z_i(0)$ is the initial value of the dynamic compensator, $r_e(s)$ and $q_e(s)$ are the Laplace transformation of $r_e(t)$ and $q_e(t)$, and $L^{-1}[\bullet]$ is the inverse Laplace transformation. Moreover, the first term of (41) and (42) reveals the effect of the initial value of the dynamic compensator, and the second term of (41) and (42) reveals the effect of the input ($r_e(t), q_e(t)$) to the dynamic compensator.

From (41) and (42), we can conclude that the transfer function of the second term is an approximation differentiator. Therefore, when the value of a_i is large, the output y_i can be approximated as

$$y_1 \approx \frac{q_1}{2} L^{-1} \left[\left\{ \frac{s}{(1/a_1)s + 1} \right\} I_3 \cdot r_e(s) \right], \quad (42)$$

$$y_2 \approx \frac{q_2}{2} L^{-1} \left[\left\{ \frac{s}{(1/a_2)s + 1} \right\} I_4 \cdot q_e(s) \right], \quad (43)$$

and the terms of $-k_1 y_1$ and $-k_2 E(q_2)^T y_2$ of control law approximately become the velocity feedback with respect to \dot{r}_e and \dot{q}_e (Note that $\dot{r}_e \neq \bar{v}_e$, $\dot{q}_e \neq \omega_e$ from (21) and (22)). Further, parameter q_i is considered to be the feedback gain. Therefore, by setting a_i to a large value, the dynamic output feedback controllers (27) and (28) approximately become the PD controllers and k_j, q_j ($j=1,2$) become the derivative gain. However, the value of k_1 must be determined carefully because the control torque $\bar{\tau}_c$ may become excessive at a certain value of k_1 since the control law of (28) includes the term $k_1 r_e^\times y_1$. Moreover, although the control inputs \bar{f}_c and $\bar{\tau}_c$ become large when a_i becomes large since \bar{f}_c and $\bar{\tau}_c$ are represented as

$$\bar{f}_c = -\left(k_{p1} + \frac{k_1 a_1 q_1}{2} \right) r_e + \frac{k_1 a_1 q_1}{2} z_1, \quad (44)$$

$$\bar{\tau}_c = -K(q_e)\varepsilon_e + \frac{k_2 a_2 q_2}{2} E(q_e)^T z_2 - \frac{k_1 a_1 q_1}{2} r_e^\times z_1, \quad (45)$$

by setting the initial state $z_i(0)$ as

$$z_1(0) = r_e(0), z_2(0) = q_e(0), \quad (46)$$

the amplitude of the control inputs at an early stage can be reduced without changing the feedback gains. This reason can be expounded as follows: Since the controllers (27) and (28) are the observers and the estimate errors are (35) from Corollary 1, by setting the initial state $z_i(0)$ as (46), we find that $z_i(t)$ becomes

$$z_1(t) = r_e(t), z_2(t) = q_e(t), \quad \forall t \geq 0. \quad (47)$$

Therefore, since control inputs \bar{f}_c and $\bar{\tau}_c$ become

$$\bar{f}_c = -k_{p1} r_e, \quad \bar{\tau}_c = -K(q_e)\varepsilon_e \quad (48)$$

by using the skew symmetric matrix property $a^\times a = 0, \forall a \in R^3$, the amplitude of the control inputs at an early stage can be reduced. The aforementioned results lead to the numerical simulation in the next section.

5. Numerical simulation

The simulation conditions are given in Table 1. The results of the numerical simulation are shown in Figs. 2 and 3. Fig. 2 is the result of Case1, and Fig. 3 is the result of Case2; further θ_e is the relative attitude Euler angle that transforms the relative quaternion q_e into 3-2-1 Euler angle.

From the simulation results, we conclude that the chaser tracks the target and state variables z_1 and z_2 correspond with r_e and q_e as shown by Corollary 1, that is, the dynamic compensator of the controllers (27) and (28) are the observers and the estimate errors are (35). Although the response of Euler angle θ_e deteriorates by approximately 50 [s], this is assumed to be due to the effect of the position feedback term ($k_1 r_e^\times y_1$) of the attitude control law. In addition, the maximum values of the control input f_c and τ_c of Case1 and Case2 are

$$\text{Case1} : f_{c,\max} = [-44.9 \quad -14.3 \quad -45.9]^T [N], \quad \tau_{c,\max} = [70.9 \quad 65.1 \quad -66.7]^T [Nm],$$

$$\text{Case2} : f_{c,\max} = [-0.969 \quad -0.241 \quad -1.30]^T \times 10^4 [N], \quad \tau_{c,\max} = [53.7 \quad 51.2 \quad -53.1]^T [Nm],$$

and the control force f_c of Case2 is relatively large at an early stage as compared to that of Case1 (Figs. 2(f) and 3(e)-(f) have an expanded vertical axis in order to show the change in input). Therefore, by setting the initial state $z_i(0)$ as (46) as described in the previous section, the amplitude of the control inputs at an early stage can be reduced without changing the feedback gains. On the other hand, the amplitude of the control torque τ_c

does not change. This could be attributed to the fact that the effect of the position feedback term (the third term) of (45) is cancelled out by the attitude feedback term (the first and the second terms). As a result, the performance of the attitude control deteriorates, and the undershoot of θ_{e1} becomes large. Therefore, it can be concluded that the effect of the position feedback term in the attitude control is suppressed by setting the initial state $z_i(0)$ as (46).

Then, we compare the proposed method to a conventional method (Cotic et al., 2000; Cotic et al., 2001); we consider the case where the relative attitude η_e falls into the singular point $\eta_e = 0$. The output feedback controller of the conventional method is given as follows:

$$\begin{cases} \dot{z} = -(k+1)z + k^2\varepsilon_e + \frac{\varepsilon_e}{(1-\varepsilon_e^T\varepsilon_e)^2}, z(0) = k\varepsilon_e(0) \\ \tau_c = S(q_e)^T \left(ke_f - W_d - \frac{\varepsilon_e}{(1-\varepsilon_e^T\varepsilon_e)^2} \right) \\ e_f = -k\varepsilon_e + z, W_d = -J_c\dot{\omega}_t - \frac{1}{2}\omega_t^\times J_c\omega_t, \end{cases} \quad (49)$$

where $k > 0$ is a design parameter. The simulation results of the proposed method are shown in Fig. 4, and those of the conventional method are shown in Fig. 5. In this simulation, the initial state $\eta_e(0)$ sets the singular point (that is, $\eta_e(0) = 0$), and we consider the attitude control only because the conventional method addresses the attitude control problem. Further, from (49) and the norm constraint of the quaternion $\|q_e\| = 1$, since division by zero accrues and the control input cannot be calculated in the conventional method when $\eta_e = 0$, $\eta_e(0)$ sets $\eta_e = 8.73 \times 10^{-3}$ in Fig. 5. From the simulation results, it is apparent that in the conventional method, the relative quaternion fluctuates in the neighborhood of the singular point (when $\eta_e(0) \rightarrow 0$, the relative quaternion fluctuates more) and the control torque is considerably large, while in the proposed method, the tracking control is achieved even if the relative quaternion fall into the singular point. These results show that the proposed method can track a spacecraft with an arbitrary trajectory.

6. Conclusion

In this paper, we propose a new passivity-based control method that involves the use of output feedback for solving the tracking control problem. The proposed method has an advantage that it can track a spacecraft with an arbitrary trajectory because the controller does not have a singular point as compared to a conventional method. Furthermore, we show that the controller can be made to be similar to a PD controller by appropriately setting the controller parameters. The effectiveness of the proposed methods is verified by performing numerical simulations. Future works, include an extension to the case in which the physical parameter error exists and the robustness against a disturbance can be achieved.

Physical parameters
$m_t = 300[\text{kg}], J_t = \text{diag}\{50, 275, 275\}[\text{kgm}^2], m_c = 200[\text{kg}], J_c = \begin{bmatrix} 75 & -28 & -28 \\ -28 & 75 & -28 \\ -28 & -28 & 75 \end{bmatrix}[\text{kgm}^2]$ $p_t = [0 \ 5 \ 0]^T [\text{m}], \rho_c = [0 \ 0 \ 0]^T [\text{m}]$
Initial state of the target
$r_t(0) = [0 \ 0 \ 0]^T [\text{m}], v_t(0) = [0.005 \ 0.005 \ 0.005]^T [\text{m/s}],$ $q_t(0) = [0 \ 0 \ 0 \ 1]^T [-], \omega_t(0) = [0.005 \ 0.005 \ 0.005]^T [\text{rad/s}]$
Initial state of the chaser
$r_c(0) = [8 \ 9 \ 10]^T [\text{m}], v_c(0) = [0 \ 0 \ 0]^T [\text{m/s}],$ $q_c(0) = [0.19 \ 0.51 \ 0.19 \ 0.82]^T [-], \omega_c(0) = [0 \ 0 \ 0]^T [\text{rad/s}]$
Initial state of the dynamic compensator
$\text{Case1} : z_1(0) = r_e(0), z_2(0) = q_e(0),$ $\text{Case2} : z_1(0) = 0.5r_e(0), z_2(0) = 0.5q_e(0),$ $r_e(0) = [6.44 \ 1.60 \ 8.66]^T [\text{m}], q_t(0) = [0.19 \ 0.51 \ 0.19 \ 0.82]^T [-]$
Feedback gains and design parameters
$k_{p1} = 3, k_1 = 150, K_{p2} = 30I_3, k_{p3} = 12, k_2 = 1400,$ $A_1 = -20I_3, B_1 = -A_1 = 20I_3, C_1 = I_3,$ $A_2 = -20I_3, B_2 = -A_2 = 20I_3, C_2 = I_3$

Table 1. Simulation conditions.

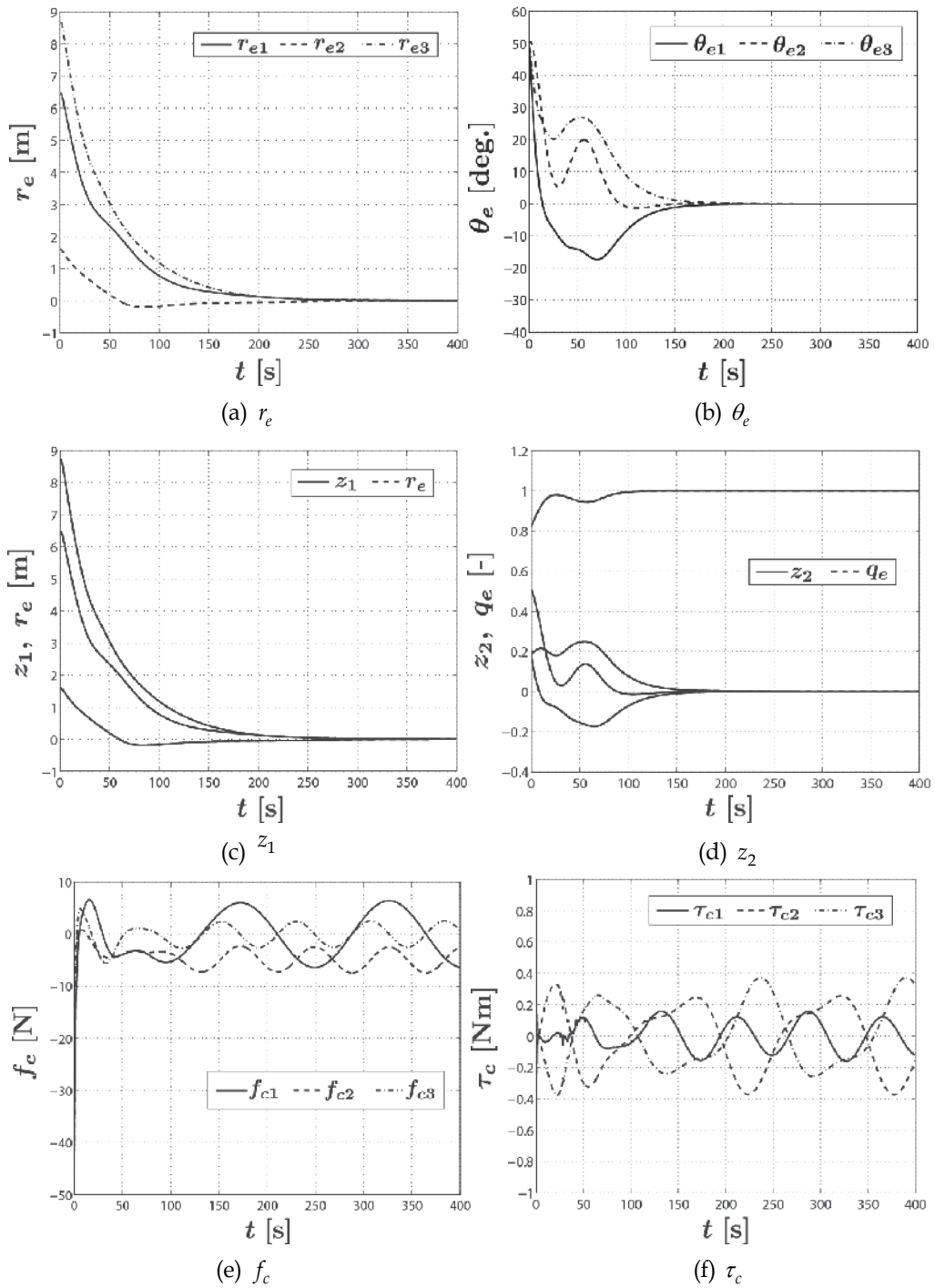


Fig. 2. Simulation results (Case1).

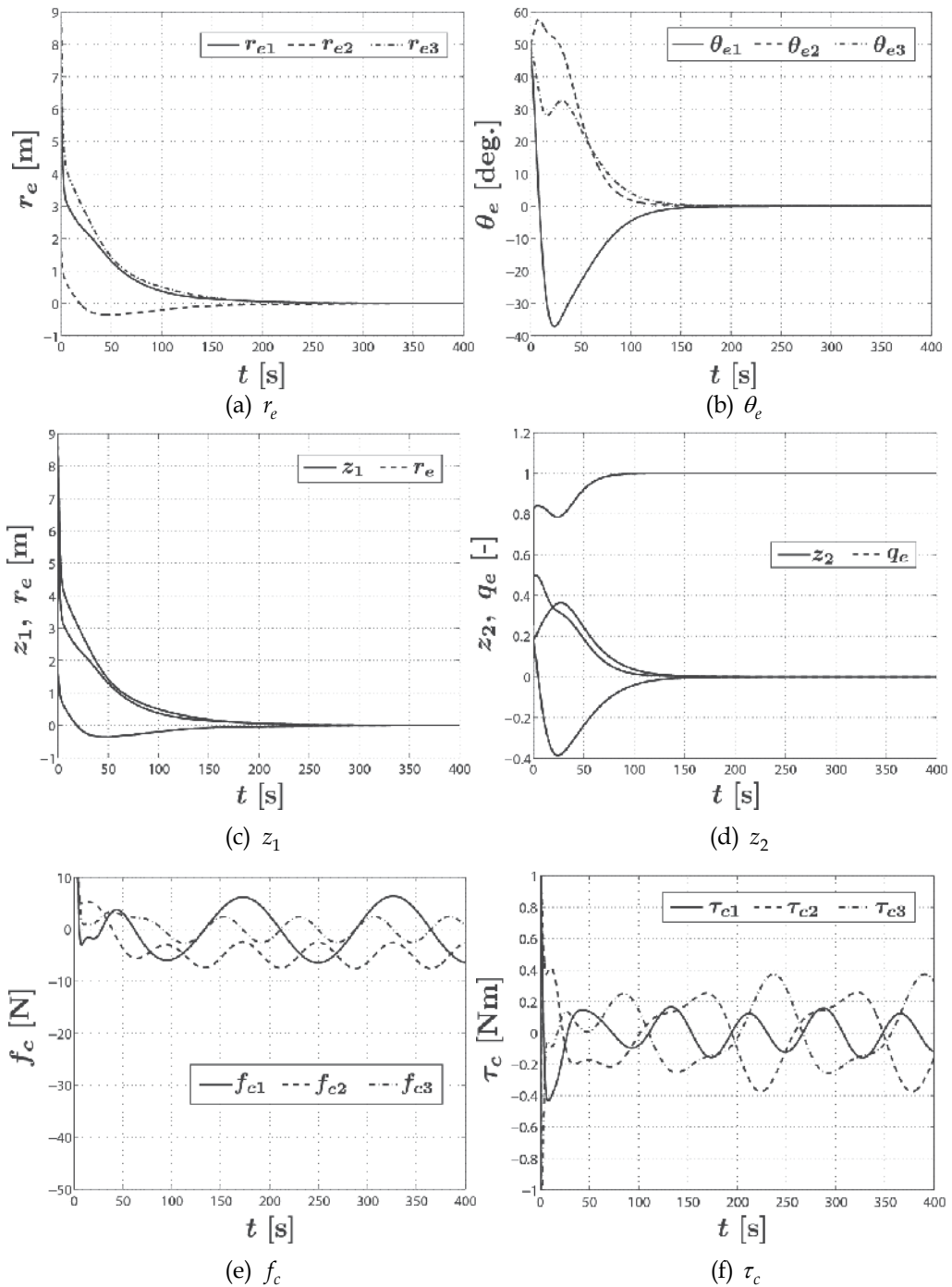


Fig. 3. Simulation results (Case2).

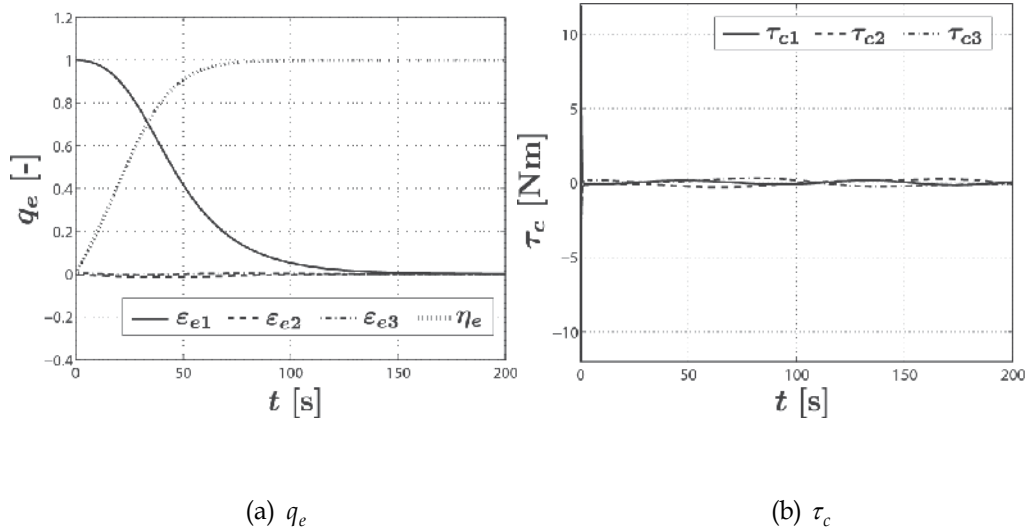


Fig. 4. Simulation results at singular point (proposed method).

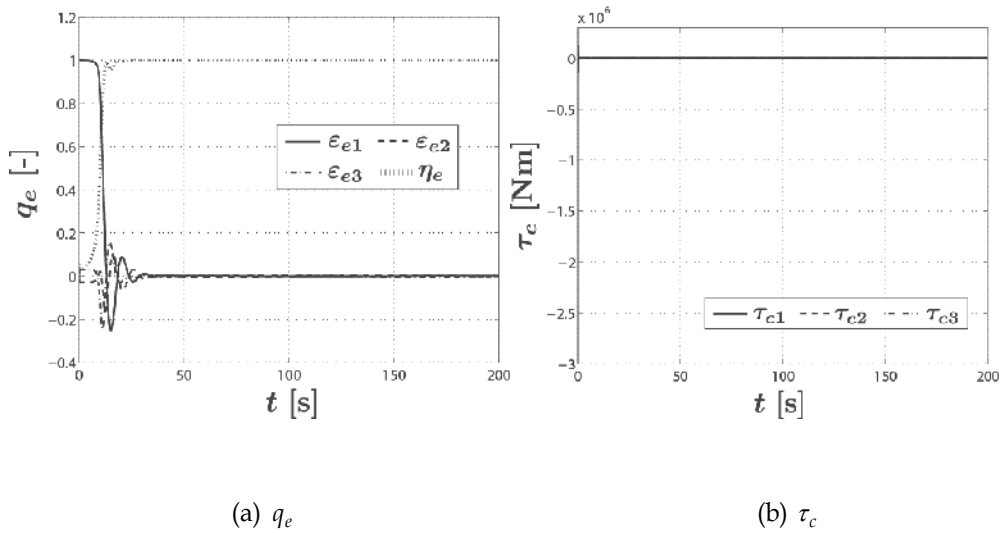


Fig. 5. Simulation results at singular point (Cotic's method).

7. References

- Ahmed, J.; Coppola, V. & Bernstein, D. (1998). Adaptive Asymptotic Tracking of Spacecraft Attitude Motion with Inertia Matrix Identification. *AIAA Journal of Guidance, Control, and Dynamics*, Vol.21, No.5, 684-691.
- Arimoto, S. (1996). Control theory of non-linear mechanical systems: A passivity-based and circuit-theoretic approach. *Oxford Univ. Press*.
- Bošković, J.; Li, S. & Mehra, R. (2004). Robust Tracking Control Design for Spacecraft Under Control Input Saturation. *AIAA Journal of Guidance, Control, and Dynamics*, Vol.27, No.4, 627-633.
- Costic, B.; Dawson, D.; Queiroz, M. & Kapila, V. (2000) A Quaternion-Based Adaptive Attitude Tracking Controller Without Velocity Measurements. *Proceedings of the 39th IEEE Conference on Decision and Control*, 2424-2429.
- Costic, B.; Dawson, D.; Queiroz, M. & Kapila, V. (2001). Quaternion-Based Adaptive Attitude Tracking Controller Without Velocity Measurements, *AIAA Journal of Guidance, Control, and Dynamics*, Vol.24, No.6, 1214-1222.
- Dalsmo, M. & Egeland, O. (1999). Tracking of Rigid Body Motion via Nonlinear H_∞ Control. *13th IFAC Triennial World Congress*, 395-400.
- Hughes, P. (1986). Spacecraft Attitude Dynamics. *John Wiley, New York*.
- Ikeda, Y.; Kida, T. & Nagashio, T. (2008) Stabilizing Nonlinear Adaptive PID State Feedback Control for Spacecraft Capturing. *17th IFAC Triennial World Congress*, 15040-15045.
- McDuffie, J. & Shtessel, Y. (1997). A De-coupled Sliding Mode Controller and Observer for Satellite Attitude Control, *Proceedings of the American Control Conference*, 564-565.
- Lichter, M. & Dubowsky, S. (2004). State, Shape, and Parameter Estimation of Space Objects From Range Images. *Proceedings of the 2004 IEEE International Conference on Robotics and Automation*, 2974-2979.
- Pan, H.; Wong, H. & Kapila, V. (2004). Output Feedback Control for Spacecraft with Coupled Translation and Attitude Dynamics, *Proceedings of the 43th IEEE Conference on Decision and Control*, 4453-4458.
- Tanaka, H.; Yairi, T & Machida, K. (2007). Attitude-Motion Estimation of Tumbling Objects Using Radio Frequency Identification. *AIAA Journal of Guidance, Control, and Dynamics*, Vol.30, No.5, 1557-1563.
- Terui, F. (1998). Position and Attitude Control of a Spacecraft by Sliding Mode Control. *Proceedings of American Control Conference*, 217-221.
- Seo, D. & Akella, M. R. (2007). Separation Property for the Rigid-Body Attitude Tracking Control Problem, *AIAA Journal of Guidance, Control, and Dynamics*, Vol.30, No.6, 1569-1576.

Seo, D. & Akella, M. (2008). High-Performance Spacecraft Adaptive Attitude-Tracking Control Through Attracting-Manifold Design. *AIAA Journal of Guidance, Control, and Dynamics*, Vol.31, No.4, 884-891.

Slotine, J. & Li, W. (1991). *Applied Nonlinear Control*. Prentice Hall, 127.

Linear Differential Games and High Precision Attitude Stabilization of Spacecrafts With Large Flexible Elements

Georgi V. Smirnov¹, Anna D. Guerman² and Susana Dias³

¹*University of Minho*

²*University of Beira Interior*

³*University of Porto
Portugal*

1. Introduction

Space mission success depends on adequate attitude control system performance. High precision pointing control design for flexible spacecraft with large appendages requires special care (Yamada & Yoshikawa, 1996; Nagashio, 2010). Many linear control schemes such as LQR, LQG, QFT, H_∞ , and μ -synthesis have been used to guarantee robust stability against both vibrations and parameter uncertainties. Future advanced space missions will involve control system design techniques with novel architectures, technologies, and algorithms. Next generation of microcomputers will allow one to use more sophisticated control algorithms. Pontryagin's theory of linear differential games (Pontryagin, 1981) is a natural tool to solve local stabilization problems under conditions of uncertainty. The corresponding mathematical model involves a linear differential equation

$$\dot{x} = Ax - u + v, \quad (1)$$

with two control parameters $u \in P$ and $v \in Q$ belonging to bounded sets. One can choose the control u so as to bring the point x into the terminal set S , while the term v represents the disturbances caused by the model uncertainties, vibration of flexible elements, and state estimation errors. Differential games of stabilization (Smirnov, 2002) have some characteristic features that distinguish them from other differential games. Namely, the terminal set S should be invariant (see Sec. 3). Moreover, the zero equilibrium position of the linear differential equation

$$\dot{x} = Ax, \quad (2)$$

is assumed to be asymptotically stable. Equation (2) can be obtained applying standard linear stabilization techniques to the control system under consideration. The trajectories of the closed-loop system

$$\dot{x} = Ax + v, \quad (3)$$

subject to the disturbance v , approach a limit set Ω and not tend to zero. The aim of the differential game approach is to construct a smaller invariant set $S \subset \Omega$, to bring the trajectory $x(t)$ into S , and to maintain it there.

The idea to use differential game methods to solve stabilization problems with uncertainties is not new (see (Gutman & Leitmann, 1975a; Gutman & Leitmann, 1975b), for example). However, the previous studies are based on Lyapunov functions (Gutman, 1979) or solutions to the Hamilton-Jacobi-Isaacs-Bellman equation (Isaacs, 1965; Kurzhanski & Varaiya, 2002; Mitchell et al., 2005). In this chapter we discuss theoretical and computational aspects of differential games of stabilization considered in the framework of Pontryagin's approach. Theoretically both approaches are equivalent (Kurzhanski & Melnikov, 2000). But, from the computational point of view, the geometric language of Pontryagin's method (alternating integral, support functions, etc.) proves more efficient in constructing the stabilizing control than the approach based on Lyapunov functions or the solution to Hamilton-Jacobi-Isaacs-Bellman equation. Since a local stabilization problem is considered, linear model (1) suffices to adequately describe the system behaviour. Although the dynamics is linear, the approach itself is based on the usage of nonlinear methods such as convex analysis and nonlinear programming.

This chapter is organized in the following way. First we give a short introduction to the theory of linear differential games and describe numerical methods developed for the alternating integral approximation. We also address the problem of construction of a minimal invariant set. Next, we apply the developed techniques to the problem of high precision attitude stabilization of spacecrafts with large flexible elements.

2. Mathematical background

Throughout this chapter we denote the set of real numbers by R and the usual n -dimensional space of vectors $x = (x_1, \dots, x_n)$, where $x_i \in R$, $i = \overline{1, n}$, by R^n . The inner product of two vectors x and y in R^n is expressed by

$$\langle x, y \rangle = x_1 y_1 + \dots + x_n y_n.$$

The norm of a vector $x \in R^n$ is defined by $\|x\| = \langle x, x \rangle^{1/2}$. Let A be a linear operator from R^n to R^m . If A is an $m \times n$ real matrix corresponding to the linear operator A (we use the same symbol), then the transposed matrix A^* corresponds to the adjoint operator. The unit linear operator from R^n to R^n will be denoted by I_n . We denote the unit ball in R^n by B_n :

$$B_n = \{x \in R^n \mid \|x\| \leq 1\}.$$

Let $C \subset R^n$. The distance function $d(\cdot, C) : R^n \rightarrow R$ is defined by

$$d(x, C) = \inf\{\|x - c\| \mid c \in C\}, \quad x \in R^n.$$

Let $\lambda \in R$. Then put by definition

$$\lambda C = \{\lambda c \mid c \in C\}.$$

For two sets C_1 and C_2 in R^n their sum is defined by

$$C_1 + C_2 = \{c_1 + c_2 \mid c_1 \in C_1, c_2 \in C_2\}.$$

A set $C \subset R^n$ is said to be convex if $\lambda x + (1 - \lambda)y \in C$ whenever $x \in C$, $y \in C$, and $\lambda \in [0, 1]$. From definition it follows that an intersection of any number of convex sets is a convex set, and if $C_1 \subset R^n$, $C_2 \subset R^n$ are convex, and α_1 and α_2 are real numbers, then the set $\alpha_1 C_1 + \alpha_2 C_2$ is convex. Let $C \subset R^n$. The intersection of all convex sets containing C is called the convex hull of C and is denoted by $\text{co}A$.

All convex sets $C \subset R^n$ considered in this chapter are assumed to be symmetric, i.e., $C = -C$. This family is enough for our goals. The function $S(\cdot, C) : R^n \rightarrow R$ defined by

$$S(\varphi, C) = \sup\{\langle x, \varphi \rangle \mid x \in C\}$$

is called the support function of C . The distance function can be expressed via support function:

$$d(x, C) = \sup\{\langle x, \varphi \rangle - S(\varphi, C) \mid \varphi \in B_n\}. \quad (4)$$

Moreover, the support function allows one to express the inclusion $x \in C$ in an analytical form. Namely, $x \in C$ if and only if $\langle x, \varphi \rangle \leq S(\varphi, C)$ for all $\varphi \in B_n$.

Another description of a compact convex set C can be obtained in terms of the Minkowski function. A point $x \in C$ if and only if $\mu(x, C) \leq 1$, where

$$\mu(x, C) = \inf\{t > 0 \mid t^{-1}x \in C\}$$

is the Minkowski function of the set C .

Let C_1 and C_2 be convex sets in R^n . The Minkowski difference of these sets is defined by

$$C_1 \overset{*}{-} C_2 = \{c \mid c + C_2 \subset C_1\}.$$

If C_1 is convex and closed and C_2 is compact, then $C_1 \overset{*}{-} C_2$ is closed and convex. It is easy to see that the following relations hold

$$(C_1 \overset{*}{-} C_2) + C_2 \subset C_1,$$

and

$$(C_1 + C_2) \overset{*}{-} C_2 = C_1.$$

Moreover if C_3 is compact and convex, then we have

$$(C_1 \overset{*}{-} C_2) + C_3 \subset (C_1 + C_3) \overset{*}{-} C_2.$$

The Hausdorff distance between two sets $C_1, C_2 \subset R^n$ is defined as

$$h(C_1, C_2) = \min\{h \geq 0 \mid C_1 \subset C_2 + hB_n, C_2 \subset C_1 + hB_n\}.$$

A set-valued map $F : R^n \rightarrow R^m$ with compact values is called continuous at $x_0 \in R^n$ if for any $\epsilon > 0$ there exists $\delta > 0$ such that $h(F(x), F(x_0)) < \epsilon$, whenever $x \in x_0 + \delta B_n$.

Let $F : [a, b] \rightarrow R^n$ be a set-valued map with compact convex values. Its Riemann integral $\int_a^b F(t)dt$ is defined as a limit in the sense of the Hausdorff distance of the integral sums $\sum_k F(\xi_k)(t_{k+1} - t_k)$, where $a = t_0 < t_1 < \dots < t_N = b$, is a partition of the interval $[a, b]$ and $\xi_k \in [t_k, t_{k+1}]$. The integral exists whenever F is continuous at all points of the interval. Moreover, it coincides with the set of all integrals of integrable selections $f(t) \in F(t)$

$$\int_a^b F(t)dt = \left\{ \int_a^b f(t)dt \mid f(t) \in F(t), t \in [0, T] \right\}$$

(see (Castaing & Valadier, 1977)) and

$$S\left(\varphi, \int_a^b F(t)dt\right) = \int_a^b S(\varphi, F(t))dt$$

for all $\varphi \in R^n$. This equality allows one to compute integrals of set-valued maps.

3. Linear differential games of pursuit

Differential games are control problems in a conflict situation. For example, if one aircraft pursues another one we have such a situation. The dynamics of the system is described by a differential equation depending on two control parameters

$$\dot{x} = f(x, u, v), \quad u \in P, \quad v \in Q.$$

One player controls the parameter u and the other one controls the parameter v . The aim of the first player is to drive the system to a terminal set \mathcal{S} while the aim of the second player is to avoid this event. The solution to this problem consists in determination of functions $u = u(x)$ and $v = v(x)$, known as strategies (Krasovski & Subbotin, 1987), guaranteeing

1. the fastest arrival to the terminal set \mathcal{S} for the first player;
2. the latest arrival to the terminal set \mathcal{S} for the second player.

In this form the problem is extremely involved because the functions $u(x)$ and $v(x)$ can be discontinuous and the differential equation $\dot{x} = f(x, u(x), v(x))$ may have no solution in the classical sense. This difficulty can be overcome introducing the concept of Pontryagin's ϵ -strategy. The differential game is considered as a pursuit game or an evasion game.

In the first case we identify ourselves with the first player. At the initial moment of time t_0 the second player communicates to the first player a number $\epsilon_0 > 0$ and his control $v(t)$ defined in the time interval $[t_0, t_0 + \epsilon_0]$. The first player uses this information to choose his own control $u(t)$, $t \in [t_0, t_0 + \epsilon_0]$. Next, at the moment of time $t_1 = t_0 + \epsilon_0$ the second player communicates to the first player a number $\epsilon_1 > 0$ and his control $v(t)$ defined in the time interval $[t_1, t_1 + \epsilon_1]$. The first player uses this information to choose his control $u(t)$, $t \in [t_1, t_1 + \epsilon_1]$, and so on. In the case of evasion games we identify ourselves with the second player and the first one communicates us numbers $\epsilon_k > 0$ and controls $u(t)$, $t \in [t_k, t_k + \epsilon_k]$.

Here we study only pursuit games for linear control systems

$$\dot{x} = Ax - u + v \tag{5}$$

and without the objective to reach the terminal set \mathcal{S} in an optimal time. Our aim is to finish the game in a time T not necessarily optimal. The sets P and Q are assumed to be compact and convex. The terminal set \mathcal{S} is closed and convex. Moreover, the number ϵ from the definition of the ϵ -strategy is assumed to be fixed.

Differential games of stabilization have some characteristic features that distinguish them from other differential games. Namely, the terminal set \mathcal{S} should be invariant, i.e., if $x_0 \in \mathcal{S}$, then for any control $v(t) \in Q$ there should exist a control $u(t) \in P$ such that it maintains the trajectory $x(t, x_0, u(\cdot), v(\cdot))$ in the set \mathcal{S} . There are many possibilities to formalize the concept of invariance. We say that a set \mathcal{S} is ϵ -invariant if the following inclusion holds

$$\Lambda_\epsilon \mathcal{S} + \mathcal{Q}_\epsilon \subset \mathcal{S} + \mathcal{P}_\epsilon. \tag{6}$$

Here we use the notations

$$\Lambda_\epsilon = e^{\epsilon A}, \quad \mathcal{P}_\epsilon = \int_0^\epsilon e^{tA} P dt, \quad \text{and} \quad \mathcal{Q}_\epsilon = \int_0^\epsilon e^{tA} Q dt. \tag{7}$$

Let $x \in \mathcal{S}$ and $v(t) \in Q, t \in [0, \epsilon]$, be an admissible disturbance. After a change of variable in integrals (7) we obtain

$$\mathcal{P}_\epsilon = \int_0^\epsilon e^{(\epsilon-t)A} P dt \text{ and } \mathcal{Q}_\epsilon = \int_0^\epsilon e^{(\epsilon-t)A} Q dt \quad (8)$$

From (6) and (8) we see that there exists an admissible control $u(t) \in Q, t \in [0, \epsilon]$ such that

$$x(\epsilon) = e^{\epsilon A} x - \int_0^\epsilon e^{(\epsilon-t)A} u(t) dt + \int_0^\epsilon e^{(\epsilon-t)A} v(t) dt \in \mathcal{S},$$

i.e., starting at \mathcal{S} we always return to it after time ϵ .

The zero equilibrium position of the linear differential equation

$$\dot{x} = Ax, \quad (9)$$

is assumed to be asymptotically stable. This implies that there exists a positive definite symmetric matrix V satisfying the Lyapunov equation

$$VA + A^*V = -I_n.$$

If $\alpha > 0$ is sufficiently large and ϵ is sufficiently small, then the ellipsoid αE , where

$$E = \{x \mid \langle x, Vx \rangle \leq 1\} \quad (10)$$

is ϵ -invariant.

Consider the sets $\mathcal{I}_k \subset R^n$ defined by $\mathcal{I}_0 = \mathcal{S}$,

$$\mathcal{I}_{k+1} = (\mathcal{I}_k + \mathcal{P}_\epsilon) - \mathcal{Q}_\epsilon, \quad k = \overline{0, N-1}.$$

The sets \mathcal{I}_k are known as Pontryagin alternating sums. Fix $T > 0$ and set $\epsilon = T/N$. The limit of the Pontryagin alternating sums as N goes to infinity,

$$\mathcal{I}_T = \lim_{N \rightarrow \infty} \mathcal{I}_N,$$

is called Pontryagin alternating integral. The inclusion $\Lambda_\epsilon x \in \mathcal{I}_{k+1}$ implies that for any admissible disturbance $v(t) \in Q, t \in [0, \epsilon]$, there exists an admissible control $u(t) \in Q, t \in [0, \epsilon]$ such that

$$x(\epsilon) = e^{\epsilon A} x - \int_0^\epsilon e^{(\epsilon-t)A} u(t) dt + \int_0^\epsilon e^{(\epsilon-t)A} v(t) dt \in \mathcal{I}_k.$$

By induction we see that if $\Lambda_\epsilon^N x \in \mathcal{I}_N$, then the game can be finished in time $N\epsilon$, i.e., that the first player can choose an ϵ -strategy in order to guarantee the inclusion $x(N\epsilon) \in \mathcal{I}_0 = \mathcal{S}$. The set

$$\mathcal{F}_T = e^{-TA} \mathcal{I}_T$$

is known as Pontryagin-Pshenichnyj pursuit operator and consists of all initial points x_0 such that the game starting from x_0 can be finished in time less than or equal to T independently on the ϵ -strategy of the second player. Instead of the Pontryagin alternating sums we shall use the Pontryagin-Pshenichnyj pursuit ϵ -operators defined by $\mathcal{F}_0 = \mathcal{S}$,

$$\mathcal{F}_k = \mathcal{F}_\epsilon^k(\mathcal{S}), \quad k = \overline{0, N}, \quad (11)$$

where

$$\mathcal{F}_\epsilon(\mathcal{C}) = \Lambda_\epsilon^{-1} \left((\mathcal{C} + \mathcal{P}_\epsilon)^* - \mathcal{Q}_\epsilon \right).$$

If the set \mathcal{F}_k is ϵ -invariant (see (6)), then the set \mathcal{F}_{k+1} is also invariant. Indeed, from the inclusion

$$\Lambda_\epsilon \mathcal{F}_k + \mathcal{Q}_\epsilon \subset \mathcal{F}_k + \mathcal{P}_\epsilon,$$

we have

$$\mathcal{F}_k \subset \Lambda_\epsilon^{-1} \left((\mathcal{F}_k + \mathcal{P}_\epsilon)^* - \mathcal{Q}_\epsilon \right) = \mathcal{F}_{k+1}. \quad (12)$$

This implies

$$\Lambda_\epsilon \mathcal{F}_{k+1} + \mathcal{Q}_\epsilon = \left((\mathcal{F}_k + \mathcal{P}_\epsilon)^* - \mathcal{Q}_\epsilon \right) + \mathcal{Q}_\epsilon \subset \mathcal{F}_k + \mathcal{P}_\epsilon \subset \mathcal{F}_{k+1} + \mathcal{P}_\epsilon.$$

Therefore the operators \mathcal{F}_k form a monotone family, provided that the terminal set \mathcal{S} is ϵ -invariant.

To construct an absorbing family of Pontryagin-Pshenichnyj operators, suppose that the terminal set is strictly invariant, i.e.,

$$\Lambda_\epsilon(\mathcal{S} + E) + \mathcal{Q}_\epsilon \subset \mathcal{S} + \mathcal{P}_\epsilon,$$

where the ellipsoid E satisfies the inclusion $\Lambda_\epsilon E \subset E$ (see (10)). The strict invariance of \mathcal{S} implies the inclusion $\mathcal{S} + E \subset \mathcal{F}_\epsilon(\mathcal{S})$. Observe that

$$\Lambda_\epsilon(\mathcal{F}_\epsilon(\mathcal{S}) + E) + \mathcal{Q}_\epsilon = ((\mathcal{S} + \mathcal{P}_\epsilon)^* - \mathcal{Q}_\epsilon) + \Lambda_\epsilon E + \mathcal{Q}_\epsilon \subset \mathcal{S} + \mathcal{P}_\epsilon + E \subset \mathcal{F}_\epsilon(\mathcal{S}) + \mathcal{P}_\epsilon.$$

From this we obtain

$$\mathcal{S} + 2E \subset \mathcal{F}_\epsilon(\mathcal{S}) + E \subset \mathcal{F}_\epsilon^2(\mathcal{S}).$$

By induction we have $\mathcal{S} + kE \subset \mathcal{F}_\epsilon^k(\mathcal{S})$. Therefore $\bigcup_{k \geq 0} \mathcal{F}_\epsilon^k(\mathcal{S}) = R^n$.

4. Computational aspects

To numerically compute the pursuit operator and the stabilizing control, the considered sets should be approximated by polyhedrons. In this section we briefly present the computational geometry tools necessary for this purpose.

Fix two sets of unit vectors $\{\varphi_m\}_{m=1}^M$ and $\{\zeta_l\}_{l=1}^L$. An exterior polyhedral approximation, \overline{C} , of a convex compact set $C \subset R^n$ is given by

$$C \subset \overline{C} = \{x \mid \langle \varphi_m, x \rangle \leq S(\varphi_m, C), m = \overline{1, M}\},$$

and an interior polyhedral approximation, \underline{C} , of a convex compact set $C \subset R^n$ is given by

$$C \supset \underline{C} = \text{co} \left\{ (\mu(\zeta_l, C))^{-1} \zeta_l \mid l = \overline{1, L} \right\}.$$

We shall use the notations $\sigma_m = S(\varphi_m, C)$ and $\mu_l = \mu(\zeta_l, C)$ for the values of the support function and of the Minkowski function, respectively. The vectors $\sigma = (\sigma_1, \dots, \sigma_M)$ and $\mu = (\mu_1, \dots, \mu_L)$ define the exterior and interior approximations of a compact convex set C . We say that the exterior and interior approximations are consistent if the following conditions are satisfied:

1. $\langle \xi_l, \varphi_m \rangle \leq \mu_l \sigma_m$, for all $l = \overline{1, L}$ and $m = \overline{1, M}$,
2. for any $l = \overline{1, L}$ there exists $m(l)$ such that $\langle \xi_l, \varphi_{m(l)} \rangle = \mu_l \sigma_{m(l)}$,
3. for any $m = \overline{1, M}$ there exists $l(m)$ such that $\langle \xi_{l(m)}, \varphi_m \rangle = \mu_{l(m)} \sigma_m$.

If exterior and interior descriptions $\sigma = (\sigma_1, \dots, \sigma_M)$ and $\mu = (\mu_1, \dots, \mu_L)$ are not consistent, they can be made consistent using one of adjustment operators $\mu \rightarrow \mathcal{A}^\sigma(\mu)$ and $\sigma \rightarrow \mathcal{A}^\mu(\sigma)$ defined by

$$\mathcal{A}^\sigma(\mu) = (\sigma_1(\mu), \dots, \sigma_M(\mu)), \quad \sigma_m(\mu) = \max_{l=\overline{1, L}} \mu_l^{-1} \langle \xi_l, \varphi_m \rangle$$

and

$$\mathcal{A}^\mu(\sigma) = (\mu_1(\sigma), \dots, \mu_L(\sigma)), \quad \mu_l(\sigma) = \left(\min_{\substack{m=\overline{1, M} \\ \langle \xi_l, \varphi_m \rangle > 0}} \frac{\sigma_m}{\langle \xi_l, \varphi_m \rangle} \right)^{-1}.$$

Let C_1 and C_2 be two convex compact sets, and let $\sigma(C_1)$ and $\sigma(C_2)$ be the vectors defining their exterior approximations. Since $S(\varphi, C_1 + C_2) = S(\varphi, C_1) + S(\varphi, C_2)$, it is natural to define the exterior approximation vector $\sigma(C_1 + C_2)$ for the sum as

$$\sigma(C_1 + C_2) = \sigma(C_1) + \sigma(C_2).$$

The evaluation of the approximation for the Minkowski difference $C_1 -^* C_2$ is more involved. The point is that the difference of support functions $S(\varphi, C_1) - S(\varphi, C_2)$ may be not a support function of a convex set and some correction is needed. This correction is done using the interior description. Namely, we set

$$\sigma(C_1 -^* C_2) = \mathcal{A}^\sigma(\mathcal{A}^\mu(\sigma(C_1) - \sigma(C_2))).$$

If the vectors $\{\varphi_m\}_{m=1}^M$ and $\{\xi_l\}_{l=1}^L$ form rather fine meshes in the unite sphere, the above exterior approximations of the sum and the Minkowski difference given by

$$\{x \mid \langle x, \varphi_m \rangle \leq \sigma_m(C_1 + C_2), m = \overline{1, M}\}$$

and

$$\{x \mid \langle x, \varphi_m \rangle \leq \sigma_m(C_1 -^* C_2), m = \overline{1, M}\}$$

tend to $C_1 + C_2$ and $C_1 -^* C_2$, respectively, as M and L go to infinity. Some estimates for the precision of the approximations can be found in (Polovinkin et al., 2001).

The approximation of the set ΛC , where $\Lambda : R^n \rightarrow R^n$ is a linear operator, is based on the following property of support functions:

$$S(\varphi, \Lambda C) = S(\Lambda^* \varphi, C) = \|\Lambda^* \varphi\| S\left(\frac{\Lambda^* \varphi}{\|\Lambda^* \varphi\|}, C\right)$$

and is computed as

$$S(\varphi_m, \Lambda C) = \|\Lambda^* \varphi_m\| S\left(\varphi_{\lambda(m)}, C\right),$$

where the vector $\varphi_{\lambda(m)}$ satisfies the condition

$$\left\| \varphi_{\lambda(m)} - \frac{\Lambda^* \varphi_m}{\|\Lambda^* \varphi_m\|} \right\| = \min_{m'=\overline{1, M}} \left\| \varphi_{m'} - \frac{\Lambda^* \varphi_m}{\|\Lambda^* \varphi_m\|} \right\|.$$

Now, consider the problem of a minimal invariant set construction. Let $\mathcal{P} \subset R^n$ and $\mathcal{Q} \subset R^n$ be convex compact sets, and let $\Lambda : R^n \rightarrow R^n$ be a linear operator. The condition of a convex set \mathcal{S} invariance,

$$\Lambda\mathcal{S} + \mathcal{Q} \subset \mathcal{S} + \mathcal{P}, \tag{13}$$

in terms of support functions takes the form

$$S(\varphi, \Lambda\mathcal{S}) + S(\varphi, \mathcal{Q}) \leq S(\varphi, \mathcal{S}) + S(\varphi, \mathcal{P}), \text{ for all } \varphi, \|\varphi\| = 1. \tag{14}$$

We say that an invariant set \mathcal{S} is minimal, if for any $\mathcal{S}' \subset \mathcal{S}$, $\mathcal{S}' \neq \mathcal{S}$, we have $\Lambda\mathcal{S}' + \mathcal{Q} \not\subset \mathcal{S}' + \mathcal{P}$. Note that the minimal invariant set may be not unique and that the intersection of two invariant sets may be not invariant. Indeed, consider the following example in R^2 . Let $\Lambda = \frac{1}{2}I_2$, $\mathcal{P} = \text{co}\{(0,2), (0,-2)\}$, and $\mathcal{Q} = \text{co}\{(1,1), (1,-1), (-1,1), (-1,-1)\}$. It is easy to see that any set $\mathcal{S}_a = \{(x, ax) \mid x \in [-2,2]\}$, $a \in [-1,1]$, is minimal invariant. The intersection $\mathcal{S}_{a_1} \cap \mathcal{S}_{a_2} = \{0\}$, $a_1 \neq a_2$, is not invariant.

To restrict the set of invariant sets, we introduce the following definition. Put

$$r(\mathcal{S}) = \min\{r > 0 \mid \mathcal{S} \subset rB_n\}.$$

An invariant set \mathcal{S} is said to be r -minimal, if for any \mathcal{S}' satisfying $r(\mathcal{S}') < r(\mathcal{S})$, we have $\Lambda\mathcal{S}' + \mathcal{Q} \not\subset \mathcal{S}' + \mathcal{P}$. In the previous example a unique r -minimal invariant set is $\text{co}\{(1,0), (-1,0)\}$. Note that in general the r -minimality does not define a unique invariant set, as it is clear from the following example. Set

$$\Lambda = \frac{1}{2} \begin{pmatrix} 0 & 1 \\ -1 & 0 \end{pmatrix},$$

$\mathcal{P} = \text{co}\{(0,1), (0,-1)\}$, and $\mathcal{Q} = \text{co}\{(1,1), (1,-1), (-1,1), (-1,-1), (0,2), (0,-2)\}$. It is easy to see that the sets $\mathcal{S}_1 = 2B_2$ and $\mathcal{S}_1 = \text{co}\{(1,0), (-1,0), (0,1), (0,-1)\}$ are both r -minimal invariant.

Although the property of r -minimality does not define a unique invariant set, it is quite suitable from the practical point of view.

We developed the following algorithm to compute a minimal invariant set. Let \mathcal{S}_0 be an invariant set. (Recall that in the case of a differential game of stabilization there always exists an invariant ellipsoid (see Sec. 3).) Then we obtain an interior approximation of \mathcal{S}_0 described by a vector $\mu^{(0)} = (\mu_1^{(0)}, \dots, \mu_L^{(0)})$ and set $\mathcal{S}_0 = \text{co}\{\pm(\mu_1^{(0)})^{-1}\xi_1, \dots, \pm(\mu_L^{(0)})^{-1}\xi_L\}$. Let $\delta > 0$.

The current invariant set \mathcal{S}_k is successively shrunk going through the vectors ξ_l , $l = \overline{1, L}$, and considering the sets

$$\mathcal{S}_k^l = \text{co}\{\pm(\mu_1^{(0)})^{-1}\xi_1, \dots, \pm(\mu_l^{(0)} + \delta)^{-1}\xi_l, \dots, \pm(\mu_L^{(0)})^{-1}\xi_L\}.$$

If the set \mathcal{S}_k^l is invariant, we put $\mathcal{S}_{k+1} = \mathcal{S}_k^l$. After passing through all vectors ξ_l , $l = \overline{1, L}$, the algorithm turns to the vector ξ_1 . The algorithm stops if none of the modified sets \mathcal{S}_k^l , $l = \overline{1, L}$, is invariant. This algorithm is very simple and efficient. However, in general, it does not lead to a r -minimal invariant sets.

The problem of r -minimal invariant set construction is more involved and can be solved using nonlinear programming techniques. The invariance condition (14) implies that the vector $\sigma^r = (\sigma_1^r, \dots, \sigma_M^r)$ giving the external description of a r -minimal invariant set has to be a solution to

the following linear programming problem

$$\begin{aligned} r &\rightarrow \min, \\ \|\Lambda^* \varphi_m\|_{\sigma_{\lambda(m)}} + q_m &\leq \sigma_m + p_m, \quad m = \overline{1, M}, \\ 0 &\leq \sigma_m \leq r, \quad m = \overline{1, M}, \end{aligned}$$

where $p_m = S(\varphi_m, \mathcal{P})$, $q_m = S(\varphi_m, \mathcal{Q})$, and σ_m , $m = \overline{1, M}$, and r are the unknown variables. Unfortunately the solution to this problem is not unique and a vector σ , solving the problem, may be not a vector of a support function values. For this reason it is necessary to use inner approximations for the invariant set and solve the following nonlinear programming problem

$$\begin{aligned} r &\rightarrow \min, \\ \max_{l=\overline{1, L}} \langle \mu_l^{-1} \Lambda \xi_l, \varphi_m \rangle + q_m &\leq \max_{l=\overline{1, L}} \langle \mu_l^{-1} \xi_l, \varphi_m \rangle + p_m, \quad m = \overline{1, M}, \\ 0 &\leq \mu_l^{-1} \leq r, \quad l = \overline{1, L}, \end{aligned}$$

with the variables μ_l , $l = \overline{1, L}$, and r .

A very important issue is the stabilizing control u construction. Assume that the current position of the system x_k belongs to the set \mathcal{F}_{N-k} . To determine the stabilizing control $u(t)$ defined on the interval $[k\epsilon, (k+1)\epsilon]$ we numerically solve the optimal control problem

$$\begin{aligned} d \left(e^{\epsilon A} x_k - \int_0^\epsilon e^{(\epsilon-t)A} u(k\epsilon + t) dt + \int_0^\epsilon e^{(\epsilon-t)A} v(k\epsilon + t) dt, \mathcal{F}_{N-k-1} \right) &\rightarrow \min, \\ u(k\epsilon + t) &\in P. \end{aligned}$$

The distance function is calculated using representation (4) and the control $u(t)$, $t \in [k\epsilon, (k+1)\epsilon]$, is considered to be a piece-wise constant function, $u(t) = u_j$, $t \in [(k-j/J)\epsilon, (k-(j+1)/J)\epsilon]$, $j = \overline{0, J-1}$. Approximating the set P by a polyhedron, we get the linear programming problem

$$\begin{aligned} r &\rightarrow \min \\ \left\langle e^{\epsilon A} - \frac{\epsilon}{J} \sum_{j=1}^J e^{\epsilon(1-j/J)A} u_j + \int_0^\epsilon e^{(\epsilon-t)A} v(k\epsilon + t) dt, \varphi_m \right\rangle - S(\varphi_m, \mathcal{F}_{N-k-1}) &\leq r, \quad m = \overline{1, M} \\ \langle u_j, \varphi_m \rangle &\leq S(\varphi_m, P), \quad m = \overline{1, M}, \quad j = \overline{1, J}. \end{aligned}$$

Here u_j , $j = \overline{1, J}$, and r are the unknown variables. This problem can be solved using the simplex-method or an interior-point method. Since the difference between the problems on the adjacent time intervals is rather small, the solution u_j , $j = \overline{1, J}$, obtained at the moment $t = k\epsilon$ can be used as an initial point to solve the linear programming problem on the next time interval.

5. Robust Pontryagin-Pshenichnyj operator

At the instant $t = k\epsilon$ the disturbance $v(t)$ defined on the interval $[k\epsilon, (k+1)\epsilon]$, needed to construct the control $u(t)$, $t \in [k\epsilon, (k+1)\epsilon]$, is not available. For this reason we use the disturbance $v(t)$ defined on the interval $[(k-1)\epsilon, k\epsilon]$. It turns out that this can cause serious problems and the construction of the Pontryagin-Pshenichnyj operator should be modified in order to overcome them. To clarify this issue we need some notations. Let $T(x_0)$ be such that

$x_0 \in \mathcal{F}_{T(x_0)}$ and $x_0 \notin \mathcal{F}_t, t < T(x_0)$. By $u(t, v(t - \epsilon), x_0)$ denote the control $u(t), t \in [k\epsilon, (k + 1)\epsilon]$, computed using the disturbance $v(t)$ defined on the interval $[(k - 1)\epsilon, k\epsilon]$, and by $u(t, v(t), x_0)$ denote the control $u(t), t \in [k\epsilon, (k + 1)\epsilon]$, computed using the disturbance $v(t)$ defined on the interval $[k\epsilon, (k + 1)\epsilon]$. The corresponding solutions of system (5) we denote by

$$X_{-\epsilon}(x_0) = e^{\epsilon A} x_0 - \int_0^\epsilon e^{(\epsilon-t)A} u(t, v(t - \epsilon), x_0) dt + \int_0^\epsilon e^{(\epsilon-t)A} v(t) dt$$

and

$$X_\epsilon(x_0) = e^{\epsilon A} x_0 - \int_0^\epsilon e^{(\epsilon-t)A} u(t, v(t), x_0) dt + \int_0^\epsilon e^{(\epsilon-t)A} v(t) dt.$$

The controls $u(t, v(t - \epsilon), x_0)$ and $u(t, v(t), x_0), t \in [k\epsilon, (k + 1)\epsilon]$, are constructed to minimize the distances $d(X_{-\epsilon}(x_0), \mathcal{F}_{T(x_0)-\epsilon})$ and $d(X_\epsilon(x_0), \mathcal{F}_{T(x_0)-\epsilon})$, respectively. It turns out that, in general, in the first case the trajectory rapidly zigzags in the vicinity of the equilibrium position and in the second case its behaviour is more regular.

Consider the following example. The control system

$$\ddot{x} = -\beta\dot{x} - \alpha x - u + v, \quad |u| \leq u_{\max}, \quad |v| \leq v_{\max} \tag{15}$$

describes the motion of a harmonic oscillator with friction. The control resource of the first player is enough to compensate any disturbance. The control $v(t)$ takes alternating values $\pm v_{\max}$ on the intervals $[k\epsilon, (k + 1)\epsilon]$. The influence of the delay can be seen comparing Figures 1 and 2. It is clear that the presence of delay causes violent oscillations of the trajectories.

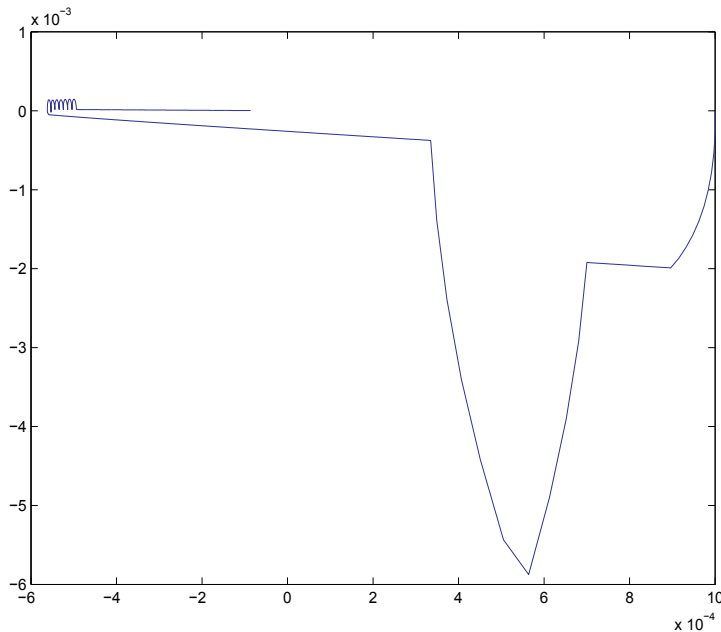


Fig. 1. Trajectory (x, \dot{x}) : motion without delay.

To overcome this difficulty we introduce a robust Pontryagin-Pshenichnyj ϵ -operator. The definition of ϵ -invariant set also should be revised. We say that a convex set \mathcal{S} is robustly ϵ -invariant if $\mathcal{S} = \mathcal{S}_0 + 2\mathcal{Q}_\epsilon$ and

$$\Lambda_\epsilon \mathcal{S}_0 + 2\Lambda_\epsilon \mathcal{Q}_\epsilon + \mathcal{Q}_\epsilon \subset \mathcal{S}_0 + \mathcal{P}_\epsilon. \tag{16}$$

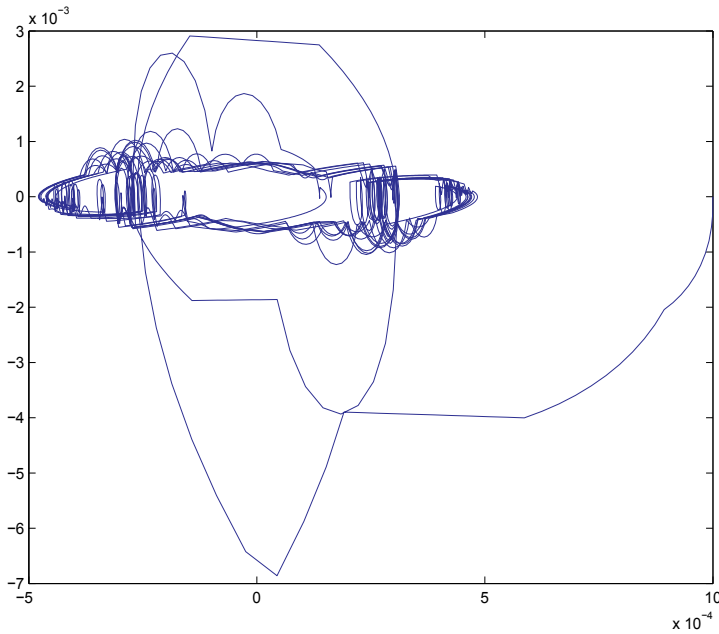


Fig. 2. Trajectory (x, \dot{x}) : motion with delay.

This definition implies the inclusion

$$\Lambda_\epsilon \mathcal{S} + \mathcal{Q}_\epsilon \subset (\mathcal{S} - 2\mathcal{Q}_\epsilon)^* + \mathcal{P}_\epsilon. \quad (17)$$

The robust Pontryagin-Pshenichnyj ϵ -operator is defined by $\mathcal{G}_0 = \mathcal{S}$,

$$\mathcal{G}_k = \mathcal{G}_\epsilon^k(\mathcal{S}), \quad k = \overline{0, N}, \quad (18)$$

where

$$\mathcal{G}_\epsilon(\mathcal{C}) = \Lambda_\epsilon^{-1} \left(\left(\left(\mathcal{C} - 2\mathcal{Q}_\epsilon \right)^* + \mathcal{P}_\epsilon \right)^* - \mathcal{Q}_\epsilon \right).$$

If $x_0 \in \mathcal{G}_{k+1}$ and we choose the control $u(t, v(t - \epsilon), x_0)$ to guarantee the inclusions $X_-(\epsilon, x_0) \in \mathcal{G}_k - 2\mathcal{Q}_\epsilon$, then we have

$$\begin{aligned} X_\epsilon(x_0) &= e^{\epsilon A} x_0 - \int_0^\epsilon e^{(\epsilon-t)A} u(t, v(t - \epsilon), x_0) dt + \int_0^\epsilon e^{(\epsilon-t)A} v(t - \epsilon) dt \\ &- \int_0^\epsilon e^{(\epsilon-t)A} v(t - \epsilon) dt + \int_0^\epsilon e^{(\epsilon-t)A} v(t) dt \in \left(\mathcal{G}_k - 2\mathcal{Q}_\epsilon \right)^* + 2\mathcal{Q}_\epsilon \subset \mathcal{G}_k. \end{aligned} \quad (19)$$

A trajectory generated by the robust Pontryagin-Pshenichnyj ϵ -operator for the above example can be seen in Fig. 3. It is more regular although the limit set is larger. The latter can be reduced diminishing the parameter ϵ . From the qualitative point of view, the difference between the behaviours of the trajectories generated by the usual Pontryagin-Pshenichnyj ϵ -operator and the robust one can be explained as follows. The inclusion $x_0 \in \mathcal{F}_{k+1}$ does not imply the inclusion $X_\epsilon(x_0) \in \mathcal{F}_k$. In general, we need much time than ϵ to achieve the set \mathcal{F}_k and the search of the way to the set \mathcal{F}_k results in zigzags of the trajectories. On the other hand, the inclusion $x_0 \in \mathcal{G}_{k+1}$ always imply (19).

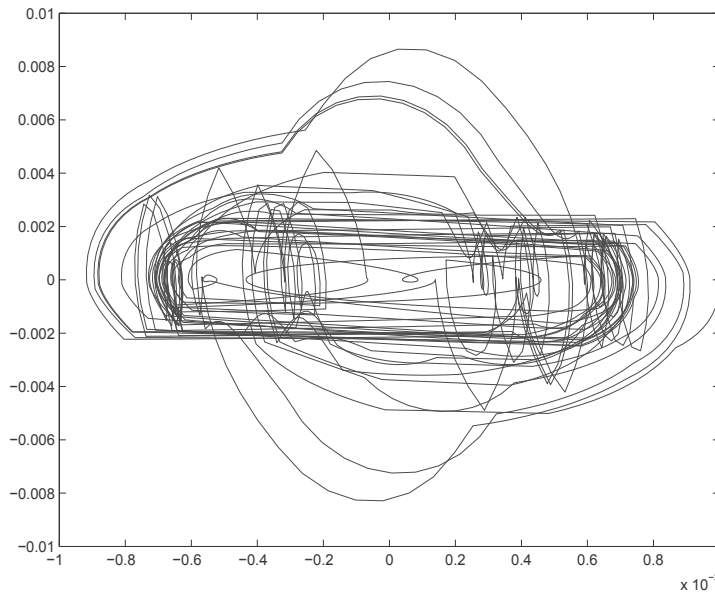


Fig. 3. Trajectory (x, \dot{x}) : motion generated by the robust Pontryagin-Pshenichnyj ϵ -operator.

6. High precision attitude stabilization of spacecrafts with large flexible elements

Satellites with flexible appendages are modelled by hybrid systems of differential equations

$$\dot{x} = f(x, g(y, \dot{y}, \ddot{y}), u), \quad (20)$$

$$\ddot{y} = G(x, \dot{x}, \ddot{x}, y), \quad (21)$$

where $x \in R^n$, $y \in Y$ is vector in a Hilbert space, and $g : Y^3 \rightarrow R^m$ is an integral operator (Junkins & Kim, 1993). Equation (20) is an ordinary differential equation describing the motion of the satellite and depending on the control $u \in U$, while (21) is a partial differential equation modelling the dynamics of flexible appendages. We illustrate the stabilization techniques based on the differential game approach by a model example.

Consider a spacecraft composed of a rigid body with a flexible appendage (a beam, see Fig. 4). The satellite is modelled as a cylinder. The distance between its longitudinal axis and the point c where the beam is cantilevered is denoted by r_0 . The length of the beam is denoted by l . We use two systems of coordinates: the inertial one denoted by $OXYZ$ and the system $oxyz$ rigidly connected to the satellite. The axis oz is directed along the satellite longitudinal axis, and the axis ox passes through the point c . The position of the point o is described by the coordinates (X_0, Y_0) , and the position of the axis ox relatively to the inertial coordinate system is defined by the angle θ . The deflection of the beam from the axis ox is described by the function $y(t, x)$ (see Fig. 5). We assume that the oscillations of the flexible appendage are small and can be described in the framework of linear theory of elasticity. We consider only a rotation of the satellite around its longitudinal axis.

To obtain the Lagrange equations for this system we write down the Lagrangian function

$$L = \frac{1}{2}m(\dot{X}_0^2 + \dot{Y}_0^2) + \frac{1}{2}I\dot{\theta}^2 + \frac{\rho}{2} \int_{r_0}^{r_0+l} \left((\dot{X}_0 - (\dot{y} + x\dot{\theta}) \sin \theta)^2 + (\dot{Y}_0 + (\dot{y} + x\dot{\theta}) \cos \theta)^2 \right) dx$$

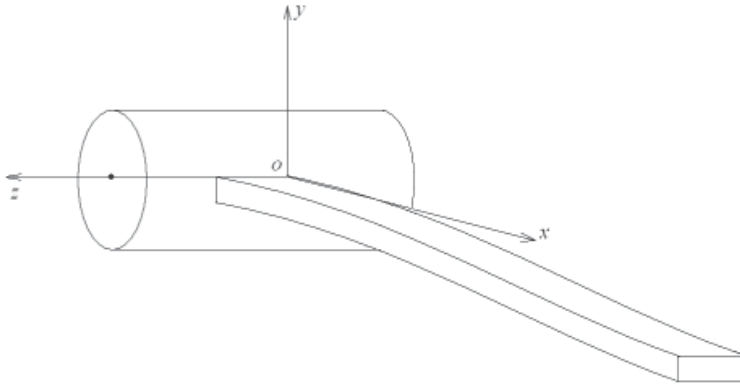


Fig. 4. Satellite with a flexible appendage.

$$-\frac{1}{2}EI \int_{r_0}^{r_0+l} (y'')^2 dx.$$

Here m is the mass of the satellite, I is its moment of inertia about the longitudinal axis, ρ is the mass/unit length of the beam, EI is the bending stiffness of the beam. 'Dot' is used to denote the derivatives with respect to time, while 'prime' stands for the derivative with respect to x . The Lagrangian equations of free oscillations of the system have the form

$$\begin{aligned} & (m + l\rho)\ddot{X}_0 - \frac{\rho}{2}((r_0 + l)^2 - r_0^2)(\ddot{\theta} \sin \theta + \dot{\theta} \cos \theta) \\ & - \rho \int_{r_0}^{r_0+l} (\ddot{y} \sin \theta + \dot{\theta} \dot{y} \cos \theta) dx = 0, \\ & (m + l\rho)\ddot{Y}_0 + \frac{\rho}{2}((r_0 + l)^2 - r_0^2)(\ddot{\theta} \cos \theta - \dot{\theta} \sin \theta) \\ & + \rho \int_{r_0}^{r_0+l} (\ddot{y} \cos \theta - \dot{\theta} \dot{y} \sin \theta) dx = 0, \\ & I\ddot{\theta} - \frac{\rho}{2}((r_0 + l)^2 - r_0^2)(\dot{X}_0 \sin \theta - \dot{Y}_0 \cos \theta) \\ & + \rho \int_{r_0}^{r_0+l} x(\ddot{y} + x\ddot{\theta}) dx + \rho \int_{r_0}^{r_0+l} (\dot{X}_0 \dot{y} \cos \theta + \dot{Y}_0 \dot{y} \sin \theta) dx = 0, \\ & \rho(-\ddot{X}_0 \sin \theta + \ddot{Y}_0 \cos \theta - \dot{X}_0 \dot{\theta} \cos \theta - \dot{Y}_0 \dot{\theta} \sin \theta + \ddot{y} + x\ddot{\theta}) + EIy'''' = 0. \end{aligned}$$

Linearizing these equations in the vicinity of the zero equilibrium position $X_0 = Y_0 = \theta = 0$, $y(\cdot, \cdot) \equiv 0$, we get

$$\begin{aligned} & (m + l\rho)\ddot{X}_0 = 0, \\ & (m + l\rho)\ddot{Y}_0 + \frac{\rho}{2}((r_0 + l)^2 - r_0^2)\ddot{\theta} + \rho \int_{r_0}^{r_0+l} \ddot{y} dx = 0, \\ & \left(I + \frac{\rho}{3}((r_0 + l)^3 - r_0^3) \right) \ddot{\theta} + \frac{\rho}{2}((r_0 + l)^2 - r_0^2)\ddot{Y}_0 + \rho \int_{r_0}^{r_0+l} x \ddot{y} dx = 0, \\ & \rho x \ddot{\theta} + \rho \ddot{y} + \rho \ddot{Y}_0 + EIy'''' = 0. \end{aligned}$$

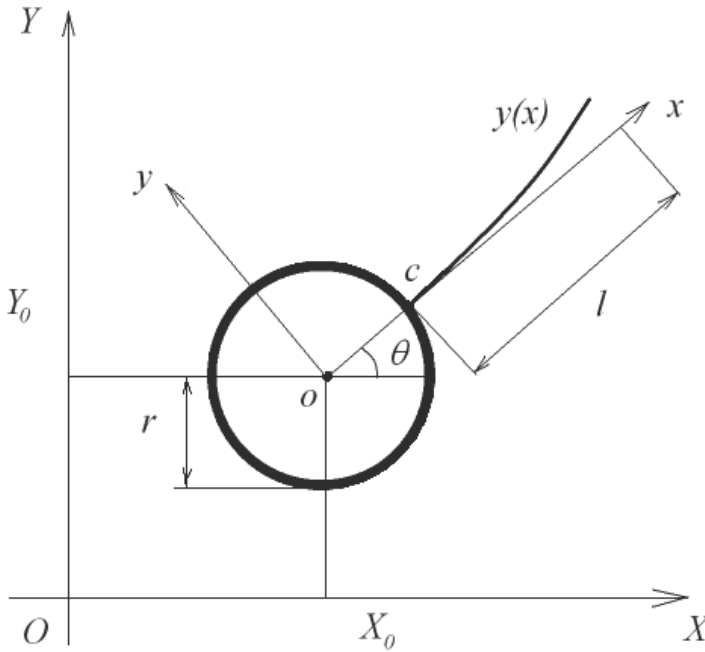


Fig. 5. Transversal section of the satellite with a flexible appendage.

The function $y = y(t, x)$ satisfies the following boundary conditions:

$$y(r_0, t) = y'(r_0, t) = y''(r_0 + l, t) = y'''(r_0 + l, t) = 0.$$

Adding the control moment M , $|M| \leq M_{\max}$, and the internal viscous friction, we obtain the following system of differential equations:

$$(m + l\rho)\ddot{X}_0 = 0, \tag{22}$$

$$(m + l\rho)\ddot{Y}_0 + \frac{\rho}{2}((r_0 + l)^2 - r_0^2)\ddot{\theta} + \rho \int_{r_0}^{r_0+l} \ddot{y} dx = 0, \tag{23}$$

$$\frac{\rho}{2}((r_0 + l)^2 - r_0^2)\ddot{Y}_0 + \left(I + \frac{\rho}{3}((r_0 + l)^3 - r_0^3)\right)\ddot{\theta} + \rho \int_{r_0}^{r_0+l} x \ddot{y} dx = M, \tag{24}$$

$$\rho\ddot{Y}_0 + \rho x \ddot{\theta} + \rho \ddot{y} + EI y'''' + EI \chi \dot{y}'''' = 0, \tag{25}$$

where χ is the coefficient of internal viscous friction.

Using the Galerkin method we approximate $y(t, x)$ by a linear combination

$$y(t, x) = \sum q_i(t) \Phi_i(x - r_0) \tag{26}$$

of eigenfunctions $\Phi_i(x)$ of the differential operator d^4/dx^4 with the boundary conditions $\Phi(0) = \Phi'(0) = \Phi''(l) = \Phi'''(l) = 0$. Substituting (26) to system (23) - (25), multiplying (25) by

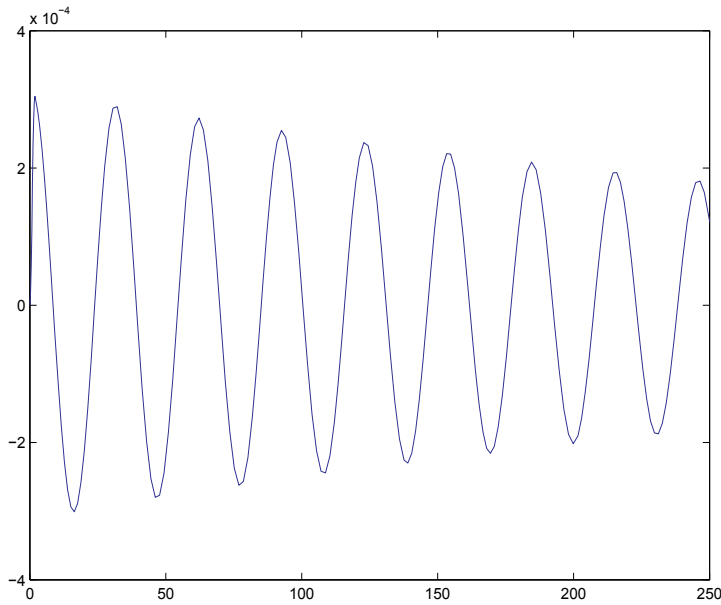


Fig. 6. The disturbance $v(t)$ caused by the flexible appendage.

$\Phi_i(x)$ and integrating in $x \in [r_0, r_0 + l]$, we get a system of ordinary differential equations for the variables X_0, Y_0, θ , and q_i .

For simplicity consider the approximation involving the first natural mode only:

$$y(t) = q(t)\Phi(x - r_0),$$

where

$$\Phi(x) = \cosh(\beta x) - \cos(\beta x) - \frac{\cosh(\beta l) + \cos(\beta l)}{\sinh(\beta l) + \sin(\beta l)} (\sinh(\beta x) - \sin(\beta x)),$$

and $\beta \approx 1.875/l$. Then from system (22) - (25) we obtain

$$(m + l\rho)\ddot{X}_0 = 0, \tag{27}$$

$$(m + l\rho)\ddot{Y}_0 + \frac{\rho}{2}((r_0 + l)^2 - r_0^2)\ddot{\theta} + \rho J_1 l \dot{q} = 0, \tag{28}$$

$$\frac{\rho}{2}((r_0 + l)^2 - r_0^2)\ddot{Y}_0 + \left(I + \frac{\rho}{3}((r_0 + l)^3 - r_0^3)\right)\ddot{\theta} + \rho(J_2 l^2 + J_1 l r_0)\dot{q} = M, \tag{29}$$

$$\rho J_1 l \ddot{Y}_0 + \rho(J_2 l^2 + J_1 l r_0)\ddot{\theta} + \rho J_3 l \dot{q} + EI\beta^4 J_3 l q + EI\chi\beta^4 J_3 l \dot{q} = 0, \tag{30}$$

where $J_1 = 0.7829, J_2 = 0.5688, J_3 = 0.9998$. System (28) - (30) can be written in the matrix form as

$$\frac{d^2}{dt^2} \begin{pmatrix} Y_0 \\ \theta \\ q \end{pmatrix} = \begin{pmatrix} a_{11} & a_{12} & a_{13} \\ a_{21} & a_{22} & a_{23} \\ a_{31} & a_{32} & a_{33} \end{pmatrix}^{-1} \begin{pmatrix} 0 \\ M \\ -EI\beta^4 J_3 l (q + \chi \dot{q}) \end{pmatrix},$$

where

$$\begin{pmatrix} a_{11} & a_{12} & a_{13} \\ a_{21} & a_{22} & a_{23} \\ a_{31} & a_{32} & a_{33} \end{pmatrix} = \begin{pmatrix} (m + l\rho) & 0 & 0 \\ \frac{\rho}{2}((r_0 + l)^2 - r_0^2) & (I + \frac{\rho}{3}((r_0 + l)^3 - r_0^3)) & \rho(J_2 l^2 + J_1 l r_0) \\ \rho J_1 l & \rho(J_2 l^2 + J_1 l r_0) & \rho J_3 l \end{pmatrix}.$$

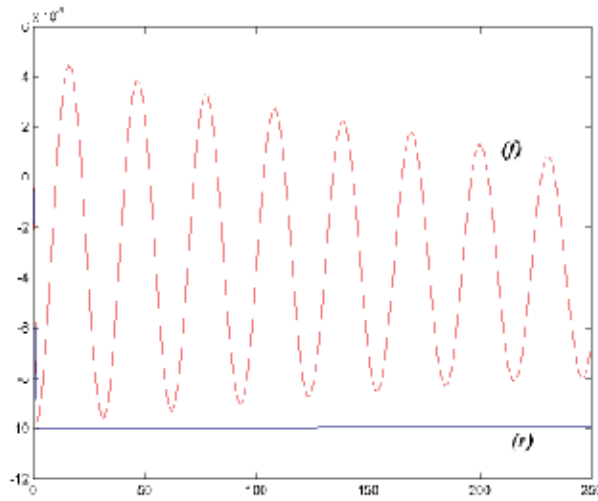


Fig. 7. Rest-to-rest manoeuvre: the discrepancy of the attitudes $\theta_r(t)$ and $\theta_f(t)$ between the motion of the rigid system and the flexible one.

Denote this matrix by \mathcal{A} . Thus, the angular dynamics of the satellite near the zero equilibrium position is described by the linear control system

$$\ddot{\theta} = \left(\mathcal{A}^{-1}\right)_{22} M - D \left(\mathcal{A}^{-1}\right)_{23} (q + \chi \dot{q}), \quad (31)$$

$$\ddot{q} = \left(\mathcal{A}^{-1}\right)_{32} M - D \left(\mathcal{A}^{-1}\right)_{33} (q + \chi \dot{q}), \quad (32)$$

where $D = EI\beta^4 J_3 l$.

In our numerical simulations we use a model example with the following values of parameters: $m = 10$, $l = 10$, $r_0 = 3$, $\rho = 0.5$, $I = 45$, $EI = 3.5$, and $\chi = 0.1$ (SI units).

The influence of the flexible appendages can be rather significant. Consider a rest-to-rest manoeuvre for the model under study. We apply the moment $+M$ and then $-M$ during the same time and compare the motion of the configuration considering the appendage as flexible with low stiffness ($EI = 3.5$) and as rigid. The disturbance caused by the appendage is shown in Fig. 6, while the difference between the angular positions of the satellite with flexible and rigid appendages is shown in Fig. 7. It is quite large. Therefore a high-precision attitude stabilization system should take into account the flexibility.

To stabilize system (31) and (32) we use the linear stabilizer

$$M = a\theta + b\dot{\theta} \quad (33)$$

with the coefficients a and b determined from the condition of the maximum degree of stability of the closed-loop system

$$\ddot{\theta} = \left(\mathcal{A}^{-1}\right)_{22} (a\theta + b\dot{\theta}) - D \left(\mathcal{A}^{-1}\right)_{23} (q + \chi \dot{q}),$$

$$\ddot{q} = \left(\mathcal{A}^{-1}\right)_{32} (a\theta + b\dot{\theta}) - D \left(\mathcal{A}^{-1}\right)_{33} (q + \chi \dot{q}).$$

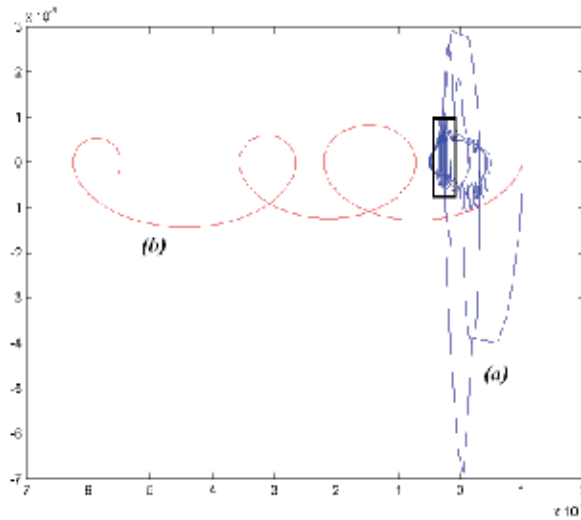


Fig. 8. Trajectories $(\theta, \dot{\theta})$ with high precision stabilizer (a) and without it (b).

If the angular position θ and the angular velocity $\dot{\theta}$ are known with some errors $\delta\theta$ and $\delta\dot{\theta}$, respectively, we obtain the following differential game:

$$\ddot{\Theta} = (\mathcal{A}^{-1})_{22} (a\Theta + b\dot{\Theta}) - u + v,$$

where $\Theta = \theta + \delta\theta$, $v = -(\mathcal{A}^{-1})_{22} (a\delta\theta + b\delta\dot{\theta}) - D(\mathcal{A}^{-1})_{23} (q + \chi\dot{q})$, and q is governed by the differential equation

$$\ddot{q} = (\mathcal{A}^{-1})_{32} \left((a\theta + b\dot{\theta}) - (\mathcal{A}^{-1})_{22}^{-1} u \right) - D(\mathcal{A}^{-1})_{33} (q + \chi\dot{q}).$$

The differential game approach to the stabilizer design problem presumes that the controls u and v satisfy the restrictions $|u| \leq u_{\max}$ and $|v| \leq v_{\max}$, respectively. To determine the values u_{\max} and v_{\max} and the neighborhood of the equilibrium position where the differential game stabilizer works we use the following method. Consider the vector $x = (\theta, \dot{\theta}, q, \dot{q})^T$. Its behaviour is described by the differential equation

$$\dot{x} = \mathcal{B}x + b, \tag{34}$$

where

$$\mathcal{B} = \begin{pmatrix} 0 & 1 & 0 & 0 \\ (\mathcal{A}^{-1})_{22} a & (\mathcal{A}^{-1})_{22} b & -D(\mathcal{A}^{-1})_{23} & (\mathcal{A}^{-1})_{23} \chi \\ 0 & 0 & 0 & 1 \\ (\mathcal{A}^{-1})_{32} a & (\mathcal{A}^{-1})_{32} b & -D(\mathcal{A}^{-1})_{33} & (\mathcal{A}^{-1})_{33} \chi \end{pmatrix}$$

and

$$b = (0, -u + (\mathcal{A}^{-1})_{22} a\delta\theta + (\mathcal{A}^{-1})_{22} b\delta\dot{\theta}, 0, -(\mathcal{A}^{-1})_{32} u_{\max} / ((\mathcal{A}^{-1})_{22})^T)^T.$$

If $|\delta\theta| \leq \delta\theta_{\max}$ and $|\delta\dot{\theta}| \leq \delta\dot{\theta}_{\max}$, then the estimate

$$\|b\| \leq b(u_{\max})$$

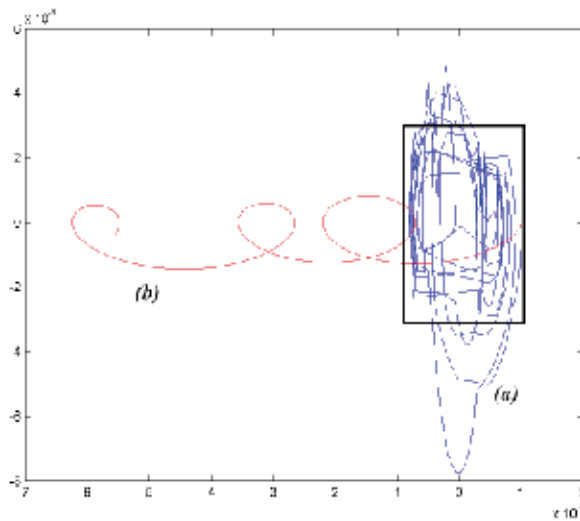


Fig. 9. Trajectories $(\theta, \dot{\theta})$ with high precision stabilizer (a) and without it (b): the robust Pontryagin-Pshenichnyj stabilizer.

$$= \left(\left(u_{\max} + \left| (\mathcal{A}^{-1})_{22} \right| (|a|\delta\theta_{\max} + |b|\delta\dot{\theta}_{\max}) \right)^2 + \left((\mathcal{A}^{-1})_{32} (\mathcal{A}^{-1})_{22}^{-1} u_{\max} \right)^2 \right)^{1/2}$$

holds. Let V be a symmetric (4×4) matrix satisfying the Lyapunov equation

$$B^T V + V B = -I_4.$$

The solution $x(t)$ to differential equation (34) satisfies the following differential inequality:

$$\frac{d}{dt} \langle x(t), Vx(t) \rangle = -\|x(t)\|^2 + 2 \langle Vx(t), b(t) \rangle \leq -\|x(t)\|^2 + 2 \|V\| \|x(t)\| b(u_{\max}) \leq 0,$$

whenever $2 \|V\| b(u_{\max}) \leq \|x(t)\|$. Define the family of ellipsoids

$$E_c = \{x \mid \langle x, Vx \rangle \leq c\}$$

and put

$$c(u_{\max}) = \min\{c \mid 2 \|V\| b(u_{\max}) B_4 \subset E_c\}.$$

Obviously $x(t) \in E_{c(u_{\max})}$, whenever t is large enough. Thus, the differential game of stabilization is playable if the Pontryagin-Pshenichnyj ϵ -operators are contained in $E_{c(u_{\max})}$ and the following conditions are satisfied:

$$v_{\max} < u_{\max},$$

$$v_{\max} \leq \left| (\mathcal{A}^{-1})_{22} \right| (|a|\delta\theta_{\max} + |b|\delta\dot{\theta}_{\max}) + \max \left\{ \left| D (\mathcal{A}^{-1})_{23} \right| |q + \chi\dot{q}| \mid (\theta, \dot{\theta}, q, \dot{q}) \in E_{c(u_{\max})} \right\},$$

and

$$\max \{ |a\theta + b\dot{\theta}| \mid (\theta, \dot{\theta}, q, \dot{q}) \in E_{c(u_{\max})} \} + u_{\max} \leq M_{\max}.$$

Typical trajectories generated by a linear feed-back and by a high-precision stabilizer with the Pontryagin-Pshenichnyj ϵ -operator and the robust Pontryagin-Pshenichnyj ϵ -operator, respectively, are shown in Fig. 8 and 9. (The disturbance v in the numerical simulations is a periodic function.) The differential game method of stabilization yields significantly smaller limit set (marked by box) than the simple linear stabilizer (33).

7. Conclusion

We present here a new approach to stabilization of mechanical systems with uncertainties in parameters and/or state data. This approach considers the perturbations caused by these uncertainties as an evader control in a linear pursuit differential game. We describe the general theoretical basis and the numerical algorithms for implementation of the described differential game stabilizer. Estimates for the amplitude of the evader control should be obtained for any specific case of control system using its mechanical properties.

We consider here an application of the suggested method to the stabilization problem for a satellite with large flexible appendages. The estimates for the evader control caused by uncertainties are deduced applying the method of Lyapunov functions. We construct a high-precision stabilizer using the differential game approach and the above estimates for the evader control.

The principal advantage of the suggested method is that, to achieve a high-precision stabilization, it requires only the satellite attitude data and does not need any estimation for the flexible elements' state and/or unknown system parameters.

8. Acknowledgments

This research is supported by the Portuguese Foundation for Science and Technologies (FCT), the Portuguese Operational Programme for Competitiveness Factors (COMPETE), the Portuguese National Strategic Reference Framework (QREN), and the European Regional Development Fund (FEDER).

9. References

- [Castaing & Valadier, 1977] Castaing, C. & Valadier, M. (1977). *Convex Analysis and Measurable Multifunctions*, Lect. Notes in Math., n. 580, Springer-Verlag.
- [Gutman, 1979] Gutman, S. (1979). Uncertain Dynamical Systems: A Lyapunov Min-Max Approach, *IEEE Transactions on Automatic Control*, Vol. 24, No. 3, 437-443.
- [Gutman & Leitmann, 1975a] Gutman, S. & Leitmann, G. (1975). On a Class of Linear Differential Games, *Journal of Optimization Theory and Applications*, Vol. 17, No. 5-6, 511-522.
- [Gutman & Leitmann, 1975b] Gutman, S. & Leitmann, G. (1975). Stabilizing Control for Linear Systems with Bounded Parameter and Input Uncertainty, *Proceedings of the 7th IFIP Conference on Optimization Techniques*, Nice, France, Springer-Verlag, Berlin.
- [Isaacs, 1965] Isaacs, R. (1965). *Differential Games*, John Wiley and Sons, New York.
- [Junkins & Kim, 1993] Junkins, J. L. & Kim, Y. (1993). *Introduction to dynamics and control of flexible structures*, American Institute of Aeronautics and Astronautics, Washington DC.
- [Krasovski & Subbotin, 1987] Krasovski, N.N. & Subbotin, A.I. (1987). *Game-Theoretical Control Problems*, Springer-Verlag, New York.
- [Kurzanski & Melnikov, 2000] Kurzanski, A. & Melnikov, N. (2000). On the Problem

- of Control Synthesis: the Pontryagin Alternating Integral and the Hamilton-Jacobi Equation, *Sbornik: Mathematics*, Vol. 191, 849-881.
- [Kurzshanski & Varaiya, 2002] Kurzshanski, A. & Varaiya, P. (2002). On Reachability under Uncertainty, *SIAM J. Control optimization*, Vol. 41, No. 1, 181-216.
- [Mitchell et al., 2005] Mitchell, I. M.; & Bayen, A. & Tomlin, C. (2005). Time-Dependent Hamilton-Jacobi Formulation of Reachable Sets for Continuous Dynamic Games, *IEEE Transactions on Automatic Control*, Vol. 50, No. 7, 947-957.
- [Nagashio, 2010] Nagashio, T.; Kida, T.; Ohtani, T. & Hamada, Y. Design and Implementation of Robust Symmetric Attitude Controller for ETS-VIII Spacecraft, *Control Engineering Practice* (in press).
- [Polovinkin et al., 2001] Polovinkin, E.; Ivanov, G.; Balashov, M.; Konstantinov, R.; & Khorev, A. (2001). An Algorithm for the Numerical Solution of Linear Differential Games, *Sbornik: Mathematics*, Vol. 192, 1515-1542.
- [Pontryagin, 1981] Pontryagin, L. (1981). Linear Differential Games of Pursuit, *Mathematics of the USSR-Sbornik*, Vol. 40, 285-303.
- [Pshenichnyj, 1969] Pshenichnyj, B. (1969). The structure of differential games, *Sov. Math. Dokl.* Vol. 10, 70-72.
- [Smirnov, 2002] Smirnov, G. (2002) *Introduction to the Theory of Differential Inclusions*, Graduate Studies in Mathematics, vol. 41, American Mathematical Society, Providence.
- [Yamada & Yoshikawa, 1996] Yamada, K. & Yoshikawa, S. (1996). Adaptive Attitude Control for an Artificial Satellite with Mobile Bodies, *Journal of Guidance, Control and Dynamics*, Vol. 19, No. 4, 948-953.

Advanced Attitude and Position MIMO Robust Control Strategies for Telescope-Type Spacecraft with Large Flexible Appendages

Mario Garcia-Sanz^{1,2}, Irene Eguinoa² and Marta Barreras²

¹*Case Western Reserve University,*

²*Public University of Navarra,*

¹*USA*

²*Spain*

1. Introduction

With extraordinary high priority science objectives to break the current barriers of our knowledge of the universe, and dealing with significant weight limitations of launch vehicle for cost-effective access to space, several NASA and ESA missions will involve both formation flying technology and satellites with large flexible structures in the next few decades: Terrestrial Planet Finder, Stellar and Planet Imager, Life Finder, Darwin and Lisa missions, etc. This chapter deals with the design of multi-input multi-output (MIMO) robust control strategies to regulate simultaneously the position and attitude of a telescope-type spacecraft with large flexible appendages. Section 2 describes the main control challenges and dynamic characteristics of a MIMO system in general, and a spacecraft in particular; Section 3 presents advanced techniques to design MIMO robust controllers based on the quantitative feedback theory (QFT); and Section 4 shows some illustrative results achieved when applying the MIMO QFT control methodology to one of the telescope-type spacecraft (a 6-inputs/6-outputs MIMO system) of a multiple formation flying constellation of a European Space Agency (ESA) cornerstone mission (Fig. 1).

Control of spacecraft with large flexible structures and very demanding astronomical performance specifications, as the telescope-type satellite mission, involves significant difficulties due to the combination of a large number of flexible modes with small damping, model uncertainty and coupling among the inputs and outputs. The scientific objectives of such missions require very demanding control specifications, as micrometer accuracy for position and milli-arc-second precision for attitude, high disturbance rejection properties, loop-coupling attenuation and low controller complexity and order. The dynamics of such spacecraft usually present a complex 6-inputs/6-outputs MIMO plant, with 36 transfer functions with high order dynamics (50th order models in our example), large model uncertainty and high loop interactions introduced by the flexible modes of the low-stiffness appendages.

This chapter presents advanced tools and techniques to analyse and design MIMO robust control systems to regulate simultaneously the position and attitude of telescope-type spacecraft with large flexible appendages.

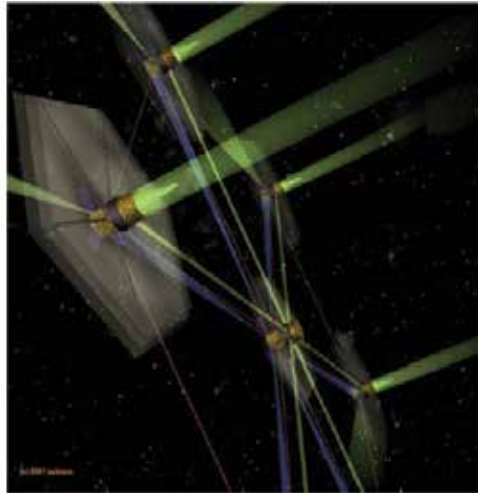


Fig. 1. Telescope-type spacecraft with large flexible appendages flying in formation (ESA courtesy)

2. MIMO systems – description and characteristics

Control of multivariable systems (multiple-input-multiple-output, MIMO) with model uncertainty are still one of the most difficult problems the control engineer has to face in real-world applications. Two of the main characteristics that define a MIMO system are the input and output directionality -different vectors to actuate \mathbf{U} and to measure \mathbf{Y} -; and the coupling among control loops -each input u_i can affect some outputs y_i , and each output can be affected by one or several inputs. This problem, which is known as interaction or coupling, makes the control system design less intuitive since any change in one loop interferes with the rest of the plant loops.

The systems considered from now on are supposed to be linearizable, at least within a range of operating conditions, as we used to do with most of physical real problems. This type of systems can be described by means of an $n \times m$ matrix of transfer functions $\mathbf{P}(s) = [p_{ij}(s)]$, also called as the plant transfer function matrix (TFM), which relates the m input variables - manipulated variables- $[u_j(s)$ with $j = 1, \dots, m]$ with the n output variables -controlled variables- $[y_i(s)$ with $i = 1, \dots, n]$, so that $[y_i(s)] = \mathbf{P}(s) [u_j(s)]$.

In general, the MIMO transfer function matrix $\mathbf{P}(s)$ can be rectangular. However, most of the related literature deals with square systems -i.e., with the same number of inputs and outputs-. If it is not the case for the plant under study, there exist different procedures that can be followed, such as using weighting matrices which reduce the system to a square effective plant matrix (Houpis, Rasmussen & Garcia-Sanz, 2006), leaving some outputs (inputs) uncontrolled (not used), or looking for independent extra inputs or outputs, depending on which one is in excess (Dutton *et al.*, 1997).

Multivariable systems have aroused great interest within the control community and many design techniques have been developed. This is not only because of their mathematical and computational challenge -derived from the matrix representation-, but also due to inherent features that do not appear in SISO systems. The particular nature of MIMO systems poses additional difficulties to control design such as directionality, coupling, transmission zeros, etc.; and all with the intrinsic uncertainty of real-world applications.

2.1 Loops-Coupling and controller structure

The most distinctive aspect of MIMO plants is the existence of coupling among the different control loops. Thus, one input (manipulated variable) can affect various outputs (controlled variables), and the other way around, i.e., an output can be affected by one or several inputs. Consequently, applying a control signal to one of the plant inputs will cause responses at more than one output, which hampers the controller design. Then, it becomes hard to predict the type and amount of control action simultaneously needed at several inputs in order to get outputs to behave as desired.

The first and easiest way that comes to mind for dealing with a MIMO system is to reduce it to a set of SISO problems ignoring the system interactions, which is the so-called decentralized control (Skogestad & Postlethwaite, 2005). Then, each input is responsible for only one output and the resulting controller is diagonal. Finding a suitable input-output pairing becomes therefore essential for decentralized control. However, this approach is only valid provided the coupling among variables is not important, which unfortunately is not the case for many real applications, including our 6x6 spacecraft. In other approaches the goal is to remove, or at least greatly reduce, the effects of the interaction before performing a decentralized control of the somehow decoupled plant as if there were independent input-output pairs.

In any case, it is necessary to quantify the amount of coupling present in the system. Many of the MIMO design techniques, particularly the sequential ones, strongly depend on the correct selection and pairing of inputs and outputs at the beginning of the design procedure. Determining the controller structure is also crucial. This means deciding whether the multivariable system can be divided into several SISO or smaller MIMO subsystems, and establishing the off-diagonal compensators needed if a populated matrix controller is to be designed, avoiding non required extra controllers. This issue becomes extremely complex in the presence of large coupling and has generated great interest within the control community, as show the numerous related references, e.g. (Campo & Morari, 1994; Chiu & Arkun, 1990; Grosdidier *et al.*, 1985; Grosdidier & Morari, 1986; Manousiouthakis *et al.*, 1986; Mijares *et al.*, 1986; Morari & Zafiriou, 1989; Van de Wal & de Jager, 1995). Nevertheless, as (Nett & Spang, 1987) pointed out, too often only the extreme controller structures -the fully centralised (fully-populated matrix) and the fully decentralized (set of SISO loops)- are discussed.

2.1.1 Interaction analysis

An extensive amount of work on the way of quantifying the system interaction can be found in the literature (Maciejowski, 1989; Skogestad & Postlethwaite, 2005). One of the most popular techniques is the *Relative Gain Array* (RGA) defined by Bristol as a matrix of relative gains Λ based on the steady-state gains of the plant (Bristol, 1966):

$$\Lambda = \begin{bmatrix} \lambda_{11} & \lambda_{12} & \cdots & \lambda_{1n} \\ \lambda_{21} & \lambda_{22} & \cdots & \lambda_{2n} \\ \vdots & \vdots & \cdots & \vdots \\ \lambda_{n1} & \lambda_{n2} & \cdots & \lambda_{nn} \end{bmatrix} \quad (1)$$

The elements λ_{ij} which constitute this matrix are dimensionless and represent the relation between the following gains of the system:

$$\lambda_{ij} = \frac{K_{OFF}}{K_{ON}} \quad (2)$$

where K_{OFF} is the open-loop gain between the output i and the input j when the rest of loops are open, while K_{ON} is the open-loop gain between the same output i and input j when the remaining loops are working in automatic mode, i.e. they are closed.

Another way of computing the RGA is through the following matrix expression:

$$\Lambda = P_0 \otimes (P_0^{-1})^T \quad (3)$$

where P_0 is an $n \times n$ matrix representing the steady-state process. Its elements are determined by applying the final value theorem to the transfer functions describing the system dynamics. The operator $[\otimes]$ denotes element-by-element multiplication (Hadamard or Schur product).

The RGA provides a scaling independent measure of the coupling among loops and useful information on how to achieve the best possible pairing of variables (McAvoy, 1983). Its elements λ_{ij} are closely related to the interaction among the different control loops. This is the meaning of the several possible values:

1. $\lambda_{ij} = 1 \Rightarrow$ The closure of the rest of loops does not change the influence of the input j on the output i . Hence the ij loop is decoupled from the rest of the system and can be treated as a SISO subsystem.
2. $\lambda_{ij} = 0 \Rightarrow$ There is no influence of the manipulated variable j over the control variable i .
3. $0 < \lambda_{ij} < 1 \Rightarrow$ When the rest of loops are closed, the gain between the input j and the output i increases, i.e., $K_{ON} > K_{OFF}$.
4. $\lambda_{ij} < 0 \Rightarrow$ At the closure of the remaining loops, the system gain changes its sign. Providing a controller with negative gain for the normal situation (all the loops closed and working), the system will react in the opposite direction if some of the remaining loops are open for any reason. Then, integrity is lost.
5. $\lambda_{ij} > 1 \Rightarrow$ When all the loops are closed, higher gains are required. The interaction reduces the gain in the ij control loop: $K_{OFF} > K_{ON}$.
6. $\lambda_{ij} > 10 \Rightarrow$ Pairings of variables with large RGA values are undesirable. They are sensitive to modelling errors and to small variations in the loop gain.

Given its importance, the RGA method has been the subject of multiple revisions and research. For instance, although originally defined for the steady-state gain, the RGA was extended to a frequency-dependent definition and used to assess the interaction at frequencies other than zero (McAvoy, 1983; Skogestad & Postlethwaite, 2005; Slaby & Rinard, 1986; Witcher & McAvoy, 1977). In most cases, it is the value of RGA at frequencies close to crossover which is the most important one, and both the gain and the phase are to be taken into account. For a detailed analysis of the plant we consider RGA as a function of frequency:

$$RGA(\omega) = P(\omega) \otimes (P^{-1}(\omega))^T \quad (4)$$

where $P(\omega)$ is a frequency-dependent matrix.

According to the meaning of the RGA elements outlined above, it is desired to pair variables so that λ_{ij} is positive and close to one, because this means that the gain from the input u_j to output y_i is not very much affected by closing the other loops. On the other hand, a pairing

corresponding to $0 < \lambda_{ij} < 1$ values means that the other loops reinforce the gain of our given loop; corresponding to $1 < \lambda_{ij}$ values means that the other loops reduce the gain of our given loop; and negative values of λ_{ij} are undesirable because it means that the steady-state gain in our given loop changes sign when the other loops are closed.

As a conclusion, to avoid instability caused by interactions, in the crossover region one should prefer pairings for which the RGA-matrix in this frequency range is close to identity. In the same way, to avoid instability caused by poor integrity, one should avoid pairings with negative steady-state RGA elements.

Further information on how to perform the pairing is available in (McAvoy, 1983). And different properties of the RGA can be consulted at (Bristol, 1966; McAvoy, 1983; Grosdidier *et al.*, 1985; Skogestad & Morari, 1987 a & b; Skogestad & Postlethwaite, 2005; Hovd & Skogestad, 1992, Skogestad & Havre, 1996).

Other measures of interaction that exist in the literature are: the *Block Relative Gain* (Manousiouthakis *et al.*, 1986; Grosdidier & Morari, 1987; Yu & Fan, 1990); the *Relative Disturbance Gain* (Stanley *et al.*, 1985; Marino-Galarraga *et al.*, 1985; Skogestad & Morari, 1987 a & b); or the *Generalized Relative Disturbance Gain* (Chang & Yu, 1992).

2.2 Multivariable poles and zeros

Due to the abovementioned interaction among loops, the poles and zeros of a multivariable system may differ from what could be deduced from observation of the elements of the plant transfer function matrix -TFM- (Maciejowski, 1989). In fact, the pole positions can be inferred from the matrix elements $p_{ij}(s)$, but not their multiplicity, which is of great importance when applying Nyquist-like stability theorems in the presence of right-half plane (RHP) poles. Regarding the multivariable zeros -also known as transmission zeros-, neither the position nor the multiplicity can be derived from direct observation of $p_{ij}(s)$. These multivariable zeros present a transmission-blocking property, since they provoke the loss of rank of the plant TFM.

Thus, it is necessary to determine the effective poles and zeros of a MIMO system, e.g., by using the so-called Smith-McMillan form (McMillan, 1952), as Rosenbrock first suggested (Rosenbrock, 1970; 1973; 1974). Alternative definitions for transmission zeros can be found in (Davison & Wang, 1974; Desoer & Schulman, 1974; MacFarlane & Karcianas, 1976; MacFarlane & Karcianas, 1978; Wolovich, 1974). Further information on this issue is available in (Hsu & Chen, 1968; Kailath, 1980; Maciejowski, 1989; Rosenbrock, 1970).

2.3 Directionality

Among the main reasons why SISO analysis and design tools are difficult to translate to the MIMO case is the existence of directionality, which is one of the most important differences between MIMO and SISO plants (Freudenberg & Looze, 1988; Skogestad & Postlethwaite, 2005). A given direction is a combination of input signal values: for instance $[u_1, u_2, u_3] = [4 \ 1 \ 3]$ has the same direction as $[u_1, u_2, u_3] = [8 \ 2 \ 6]$, which is $2 \times [4 \ 1 \ 3]$. Inherently, MIMO systems present spatial -directional- and frequency dependency. Basically, such systems respond differently to input signals lying in distinct directions. As a result, the relationship between the open-loop and closed-loop properties of the feedback system is less obvious. This directionality is completely in accordance with the TFM representation for MIMO systems.

2.3.1 Gain and phase

The concept of gain of a system is somehow easy to translate to MIMO plants through the *Singular Value Decomposition* (SVD) of the TFM (Deshpande, 1989; Doyle, 1978; MacFarlane & Scott-Jones, 1979; Skogestad & Postlethwaite, 2005), which provides the plant gain at each particular frequency with respect to the main directions –determined by the corresponding singular vectors–.

However, the extension of the notion of phase, as understood in scalar systems, is not so straightforward. Several attempts have been made to define a multivariable phase, such as (Freudenberg & Looze, 1988; Hung & MacFarlane, 1982; MacFarlane & Hung, 1981; Postlethwaite *et al.*, 1981). On the other hand, as (Wall *et al.*, 1980) showed, transmission zeros contribute with extra phase lag in some directions, but not in others. Generally speaking, the change imposed by a MIMO system upon a vector signal can be observed in the magnitude, the direction and the phase (Freudenberg & Looze, 1988).

2.3.2 Effect of poles and zeros

The effect of multivariable poles and zeros –see Section 2.2– strongly depends on directionality as well. That is, their nature is only perceptible for particular directions. So, the TFM transmittance gets unbounded when the matrix is evaluated at a pole, but only in the directions determined by the residue matrix at the pole. Likewise, transmission zeros exert their blocking influence provided the TFM is evaluated at the zero, and the input signal lies in the corresponding null-space (Freudenberg & Looze, 1988).

2.3.3 Disturbance and noise signals

Because of directionality, disturbance and noise signals generally do not equally affect all the loops. In general, they have more influence on some loops than on others. Depending on the disturbance direction –i.e., the direction of the system output vector resulting from a specific disturbance–, some disturbances may be easily rejected, while others may not. The disturbance direction can influence in two ways: through the magnitude of the manipulated variables needed to cancel the effect of the disturbance at steady-state, independently of the designed controllers, and through its effect on closed-loop performance of the controlled outputs (Skogestad & Morari, 1987 a & b). To address this issue, Skogestad and Morari defined the *Disturbance Condition Number*. It measures the magnitude of the manipulated variables needed to counteract a disturbance acting in a particular direction relative to the “best” possible direction.

2.4 Uncertainty

Uncertainty, present in all real-world systems, adds a bigger complexity to MIMO systems, especially in the crossover frequency region. Indeed, uncertainty is one of the reasons – together with the presence of disturbances, and the original instability of the plant if that is the case– why feedback is necessary in control systems.

There exist multiple sources of uncertainty (model/plant mismatch), for instance:

- The model is known only approximately or have been inaccurately identified,
- The model varies because of a change in the operating conditions (experimental models are accurate for a limited range of operating conditions), wear of components, non-linearities, etc.
- Measurement devices are not perfect and their resolution range may be limited.

- The structure or order of the system are unknown at high frequencies.
- The plant model is sometimes simplified to carry out the controller design, being the neglected dynamics considered as uncertainty.
- Other events such as sensor and actuator failures, changes in the control objectives, the switch from automatic to manual –or the other way around- in any loop, inaccuracy in the implementation of the control laws, etc.

The uncertainty can be characterised as *unstructured* when the only available knowledge is the loop location, the stability and a frequency-dependent magnitude of the uncertainty. The weights used for that magnitude (or bound) are generally stable and minimum-phase to avoid additional problems, and multiplicative –relative- weights are usually preferred. This description is useful for representing unmodeled dynamics, particularly in the high frequency range, and small nonlinearities. Different ways of expressing the unstructured uncertainty mathematically and their corresponding properties are available in (Skogestad & Postlethwaite, 2005).

Nevertheless, unstructured uncertainty is often a poor assumption for MIMO plants. It can sometimes lead to highly conservative designs since the controller has to face events that, in fact, are not likely to exist. On the one hand, errors on particular model parameters, such as mode shapes, natural frequencies, damping values, etc., are highly structured. This is the so-called *parametric uncertainty*. Likewise, parameters errors arising in linearised models are correlated, i.e., they are not independent. On the other hand, uncertainty that is unstructured at a component level becomes structured when analysed at a system level.

Thus, in all those cases, it is more convenient to use *structured uncertainty*. Several approaches can be followed to represent this type of uncertainty. For example, a diagonal block can be utilised (Doyle, 1982; Doyle *et al.*, 1982), or a straightforward and accurate representation of the uncertain elements can be performed by means of the plant templates – which are particularly useful for parametric uncertainty-. Introduced by Horowitz in the Quantitative Feedback Theory (QFT) framework (Houpis, Rasmussen & Garcia-Sanz, 2006), the templates describe the set of possible frequency responses of a plant at each frequency. Indeed, the QFT robust control theory can quantitatively handle both types of uncertainty, structured and unstructured.

Alternative approaches for describing uncertainty are also available, but so far its practicality is somehow limited for controller design. An example is the assumption of a probabilistic distribution (e.g. normal, uniform) for parametric uncertainty.

As for the rest of system features, uncertainty in MIMO systems also displays directionality properties. One loop may contain substantially more uncertainty due to unmodeled dynamics or parameter variations than do other loops. Added to this, and again because of directionality, uncertainty at the plant input or output has a different effect –see Section 2.3-. Primarily, input uncertainty is usually a diagonal perturbation, since in principle there is no reason to assume that the perturbations in the manipulated variables are correlated. This uncertainty represents errors on the change rather than on the absolute value (Skogestad & Morari, 1987 a & b).

2.5 Stability

Stability of MIMO systems is also a crucial point in the design process. In the literature, and depending on the design methodology applied, there exist different ways of assessing the feedback system stability.

One of the main approaches is the *generalized Nyquist stability criterion*, in its direct and inverse version (Postlethwaite, 1977; Rosenbrock, 1970). It places an encirclement condition on the Nyquist plot of the determinant of the return difference matrix (Rosenbrock, 1974). However, it is necessary to get a diagonally dominant system for this criterion to be practical because of loop interaction. This is achieved by means of pre-compensation. The designer is helped in this task by the Gershgorin and Ostrowski bands –see (Maciejowski, 1989; Rosenbrock, 1970; Rosenbrock, 1974)–, or by Mees’ theorem (Mees, 1981). This stability criterion is mainly used in non-sequential classical methodologies –e.g. the Inverse Nyquist Array (Rosenbrock, 1969) and Direct Nyquist Array (Rosenbrock, 1970; 1974). By contrast, sequential classical techniques do not make a direct use of it. Proofs of the multivariable Nyquist stability criterion have been given from different viewpoints, e.g. (Barman & Katzenelson, 1974; Desoer & Wang, 1980; MacFarlane & Postlethwaite, 1977; Postlethwaite & MacFarlane, 1979).

An alternative way of checking stability is by means of the *Smith-McMillan poles* (McMillan, 1952). This approach is applied in classical sequential methodologies through stability conditions such as those defined by De Bedout and Franchek (De Bedout & Franchek, 2002) for non-diagonal sequential techniques.

A completely different strategy is adopted by synthesis techniques, which make use of stability robustness results such as the *small-gain theorem* (Desoer, C.A. & Vidyasagar, 1975). This states that a feedback loop composed of stable operators will remain stable if the product of all the operator gains is smaller than unity. The theorem is applied to systems with unstructured uncertainty. When the phases of perturbations, rather than their gains, can be bounded, the *small-phase theorem* (Postlethwaite *et al.*, 1981) can be used. However, the main drawback of this approach is the highly conservative results it may provide. In the presence of structured uncertainty, results based on the *structured singular value SSV* (Doyle *et al.*, 1982) can be used instead.

3. MIMO QFT control

3.1 Overview

The Quantitative Feedback Theory (QFT), first introduced by Prof. Isaac Horowitz in 1959, is an engineering control design methodology, which explicitly emphasizes the use of feedback to simultaneously reduce the effects of plant uncertainty and satisfy performance specifications (Horowitz, 1993; Yaniv, 1999; Sidi, 2002; Houppis, Rasmussen & Garcia-Sanz, 2006). Horowitz’s work is deeply rooted in classical frequency response analysis involving Bode diagrams, template manipulations and Nichols Charts. It relies on the observation that the feedback is needed principally when the plant presents model uncertainty or when there are uncertain disturbances acting on the plant.

Model uncertainty, frequency domain specifications and desired time-domain responses translated into frequency domain tolerances, lead to the so-called Horowitz-Sidi bounds (or constraints). These bounds serve as a guide for shaping the nominal loop transfer function $L(s) = G(s) P(s)$, which involves the selection of gain, poles and zeros to design the appropriate controller $G(s)$. On the whole, the QFT main objective is to synthesize (loop-shape) a simple, low-order controller with minimum bandwidth, which satisfies the desired performance specifications for all the possible plants due to the model uncertainty. The use of CAD tools have made the QFT controller design much simpler –see for instance the QFT Control MATLAB Toolbox developed by (Garcia-Sanz, Mauch & Philippe, 2009) for the

European Space Agency; the popular QFT Control Design MATLAB Toolbox developed by (Borghesani, Chait, & Yaniv, 2002); the pioneer AFIT CAD tool developed by (Sating, 1992; Houpis & Sating, 1997; also at Houpis, Rasmussen & Garcia-Sanz, 2006); and the Qsyn CAD tool developed by (Gutman, 1996).

The first proposal for MIMO QFT design was made by Horowitz in his first book (Horowitz, 1963), where he pointed out the possibility of using diagonal controllers for quantitative design. This was divided into different frequency ranges: for the low-frequency interval the controller gain generally needs to be high and is easily determined. As for the medium and high-frequency bands, he suggested the progressive tuning loop by loop sorted in increasing order. A more systematic and precise approach was later introduced by (Shaked *et al.*, 1976). However, no proof of convergence to a solution was provided.

The first rigorous MIMO QFT methodology was again developed by Horowitz (Horowitz, 1979). This non-sequential technique translates the original $n \times n$ MIMO problem with uncertainty into n MISO systems with uncertainty, disturbances and specifications derived from the initial problem. The coupling is then treated as a disturbance at the plant input, and the individual solutions guarantee the whole multivariable solution. This is assured by the application of the Schauder's fixed point theorem (Kantorovich & Akilov, 1964). This theory maps the desired fixed point on the basis of unit impulse functions.

As before, there exist differentiated frequency ranges in the design procedure. Loops are designed as basically non-interacting (BNI) at low frequency, whereas in the middle and high-frequency range attention must be paid to the effect of the noise at the plant input, especially in problems with significant uncertainty.

On the whole, first Horowitz's method is a direct technique oriented towards MIMO plants with uncertainty. It also allows the trade-off among loops in the ranges of frequency. Nevertheless, the type of plant which can be dealt with is constrained in several ways, and the method places necessary conditions depending on the system size, which hampers its application to high-order systems. In addition, it presents potential overdesign and may generate highly conservative designs. Additional references on this methodology and its applications are available in (Horowitz & Sidi, 1980; Horowitz & Loecher, 1981; Horowitz *et al.*, 1981; Horowitz *et al.*, 1982).

An improvement of the preceding technique was also provided by Horowitz with a sequential procedure (Horowitz, 1982), also called *Second Method* in (Houpis, Rasmussen & Garcia-Sanz, 2006). There exist some similarities between this technique and the SRD method from Mayne (Mayne, 1973; 1979), such as the fact that the resulting controller is diagonal or that they proceed as if each input-output pair was a standard SISO system with loop interaction behaving as an external disturbance. Besides, both methods incorporate the effects of each loop once it is designed into the subsequent loop designs.

Nevertheless, the main difference is that Horowitz's methodology relies on a factorisation of the return difference matrix which is based on the inverse of the plant TFM. By using the inverse plant, a much simpler relationship between the closed-loop and the open-loop TFMs is obtained. One of Horowitz's major contributions with this technique is that he dealt with the problem of robust stability by considering parametric uncertainty.

The stability proof for Horowitz's Second Method was provided in (Yaniv & Horowitz, 1986) and (De Bedout & Franchek, 2002). By and large, the method constituted a great step forward in MIMO QFT design techniques. First, as abovementioned, parametric uncertainty was considered. Second, the Schauder's fixed point theorem was no longer needed. Third, the limitation related to the system size from the first method was avoided. Finally, it

reduced the conservativeness of the former method by using the concept of equivalent plant –which takes into account the controllers previously designed-. All in all, the second method is a much more powerful technique –although obviously more complicated than other classical approaches-, and the physical sense is kept all along the procedure.

Different authors made some improvements of these first two MIMO QFT design methods by Horowitz in subsequent works (Nwokah, 1984; 1988; Yaniv & Horowitz, 1986). A detailed compilation of the above techniques is presented in (Houpis, Rasmussen & Garcia-Sanz, 2006).

An alternative approach to MIMO QFT methodologies was presented by (Park *et al.*, 1994), who developed a direct technique. In other words, the inversion of the plant matrix was not required anymore, which therefore simplified the design process to some extent.

The methodologies outlined so far only deal with the problem of designing a diagonal controller. Nevertheless, there exist potential benefits in the use of full-matrix compensators. Horowitz (Horowitz, 1979) already commented that the use of diagonal controllers was established just to simplify the theoretical development, but that in practice it could be convenient to consider the off-diagonal elements as well. These terms could then be used to reduce the level of coupling in open loop, and therefore reduce the amount of feedback needed in the diagonal compensators to fulfil the required specifications (Horowitz, 1982).

Furthermore, as (Franchek *et al.*, 1997) demonstrated, non-diagonal compensators can be used for ensuring that no SISO loop introduces extra unstable poles into the subsequent loops in sequential procedures based on the inverse plant domain, e.g. Horowitz's second method (Horowitz, 1982), –accordingly, this is not possible in Mayne's (Mayne, 1973; 1979), or Park's (Park *et al.*, 1994) framework-. As a result, it can be reduced the minimum cross-over frequency needed to achieve closed-loop stability in these succeeding loops. In other words, the actuation bandwidth requirements can be relaxed. Additionally, specific integrity objectives can be achieved, allowing the design of fault-tolerant MIMO systems. In the case of Horowitz's diagonal sequential method (Horowitz, 1982), however, it is not possible to remove the unstable poles originally present in those subsequent loops, but a more general design technique could be developed for that purpose (De Bedout & Franchek, 2002). On the other hand, diagonal compensators are limited for the correction of the plant directionality when needed. There even exist cases where a diagonal or triangular controller cannot stabilise the system (De Bedout & Franchek, 2002).

On balance, the designer has greater flexibility to design the MIMO feedback control system when using fully populated controllers. But the introduction of such non-diagonal controllers poses two main issues: the way of determining the off-diagonal compensators and the need for suitable stability conditions. In systems controlled by a full-matrix compensator, the property of diagonal dominance is not assured. The Gershgorin circles become too conservative in that case and the stability test gets more complicated. As a result, different stability results are needed. Sufficient stability conditions for non-diagonal sequential procedures have been defined by (De Bedout & Franchek, 2002).

Regarding the determination of the needed off-diagonal compensators, different techniques have arisen to deal with. The first attempt in non-diagonal MIMO QFT was proposed by Horowitz and co-workers (Horowitz *et al.*, 1981; Horowitz, 1991), who suggested the pre-multiplication of the plant by a full matrix. Yaniv (Yaniv, 1995) presented a procedure where a non-diagonal decoupler is applied as a pre-compensator and a classical diagonal controller is designed afterwards. Therein, the main objective becomes the improvement of the system bandwidth.

A different approach was adopted by Boje and Nwokah (Boje & Nwokah, 1999; 2001). They used the Perron-Frobenius root as a measure of interaction and of the level of triangularization of the uncertain plant. The full-matrix pre-compensator is accordingly designed to reduce the coupling before designing a diagonal QFT controller.

On the other hand, Franchek and collaborators (Franchek *et al.*, 1995), (Franchek *et al.*, 1997) introduced a non-diagonal sequential procedure. They made use of the Gauss elimination technique (Bryant, 1985) to introduce the effects of the controllers previously designed by means of a recursive expression. Integrity considerations are also included. The controller is then divided into three parts with differentiated roles in the design process. The technique achieves the reduction of the required bandwidth with respect to previous classical sequential techniques. Additionally, De Bedout and Franchek established sufficient stability conditions for non-diagonal sequential procedures (De Bedout & Franchek, 2002).

Another important sequential technique to be considered is the one presented by Garcia-Sanz and collaborators (Garcia-Sanz & Egana, 2002; Garcia-Sanz *et al.*, 2005; Garcia-Sanz & Eguinoa, 2005; Garcia-Sanz & Barreras, 2006; Garcia-Sanz *et al.*, 2006; Garcia-Sanz & Hadaegh, 2007; Garcia-Sanz *et al.*, 2008; Houppis, Rasmussen & Garcia-Sanz, 2006). Following Horowitz's ideas, they extended Horowitz's sequential methodology (Horowitz, 1982) to the design of fully populated MIMO controllers. The role of the non-diagonal terms is simultaneously analysed for the fundamental cases of reference tracking, disturbance rejection at plant input and disturbance rejection at plant output. The compensators are aimed at the reduction of the coupling on the basis of defined coupling matrices, which are accordingly minimised. This method has proved to be a convincing design tool in real applications from different fields (Barreras & Garcia-Sanz, 2004; Garcia-Sanz *et al.*, 2005; Barreras, 2005; Barreras *et al.*, 2006; Garcia-Sanz & Barreras, 2006; Garcia-Sanz *et al.*, 2006), including control of spacecraft flying in formation (Garcia-Sanz & Hadaegh, 2007) or spacecraft with flexible appendages (Garcia-Sanz *et al.*, 2008) at NASA and ESA respectively. In 2009, Garcia-Sanz and Eguinoa (Garcia-Sanz *et al.*, 2009) introduced a reformulation of the full-matrix QFT robust control methodology for MIMO plants with uncertainty. The methodology includes a generalization of their previous non-diagonal MIMO QFT techniques; avoiding former hypotheses of diagonal dominance; simplifying the calculations for the off-diagonal elements, and then the method itself; reformulating the classical matrix definition of MIMO specifications by designing a new set of loop-by-loop QFT bounds on the Nichols Chart which establish necessary and sufficient conditions; giving explicit expressions to share the load among the loops of the MIMO system to achieve the matrix specifications; and all for stability, reference tracking, disturbance rejection at plant input and output, and noise attenuation problems. The new methodology was also applied to the design of a MIMO controller for a spacecraft flying in formation in a low Earth orbit.

Regarding the field of non-sequential MIMO QFT techniques, it is to be remarked the approach by Kerr, Jayasuriya and co-workers in (Kerr, 2004; Kerr *et al.*, 2005b; Kerr & Jayasuriya, 2006; Kerr *et al.*, 2007; Lan *et al.*, 2004). Stability conditions have also been established within this framework (Kerr & Jayasuriya, 2003; Kerr *et al.*, 2005a).

Other approaches have also been introduced for particular types of MIMO systems. For example, there are results on NMP MIMO plants (Horowitz *et al.*, 1986). It is noted that not all the $n \times n$ transfer functions have to suffer the limitations imposed by the NMP behaviour (Horowitz & Liao, 1984). The MIMO system has the capacity to relocate the RHP zeros in those outputs which are not so determining, while the critical outputs are kept as minimum-phase loops. Likewise, some research has been done for unstable and strongly NMP MIMO

systems, e.g. the X-29 aircraft (Horowitz, 1986; Kerr *et al.*, 2007; Walke et al, 1984). One interesting suggestion is the *singular-G method* (Horowitz, 1986; Walke et al, 1984), which makes use of a singular compensator -i.e., with a determinant equal to zero, which implies that one output is dependent from the rest of outputs-. In this way, the technique allows easing the NMP problem and the instability in the MIMO system, and simultaneously achieving good performance.

3.2 Non-diagonal MIMO QFT Technique

This section describes the main characteristics of the non-diagonal MIMO QFT technique introduced by (Garcia-Sanz & Egaña, 2002; Garcia-Sanz *et al.*, 2005; and Garcia-Sanz & Eguinoa, 2005; Houppis, Rasmussen & Garcia-Sanz, 2006).

3.2.1 System definition

Let us consider the generic $n \times n$ linear multivariable system shown in Fig. 2. The plant is represented by the matrix $P(s) = [p_{ij}(s)]$, $[y_i(s)] = P(s) [u_i(s)]$, where $P \in P$, and P is the set of possible plants due to uncertainty. The compensator matrix is $G(s) = [g_{ij}(s)]$ and $F(s) = [f_{ij}(s)]$ is the prefilter. All these matrices are of dimension $n \times n$. The transfer function matrices of disturbances at plant input and plant output are represented by $P_{di}(s)$ and $P_{do}(s)$ respectively. The reference vector $r'(s)$, the external disturbance vectors at plant input $d_i'(s)$ and plant output $d_o'(s)$, and the noise $n(s)$ are the inputs of the system. The output vector $y(s)$ represents the variables to be controlled.

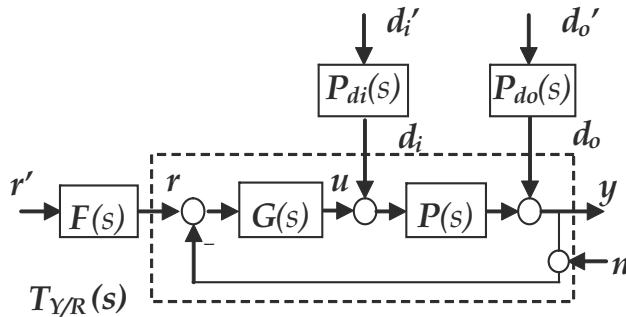


Fig. 2. Two degree of freedom MIMO control system

The plant inverse, denoted by $P^*(s)$, and the compensator $G(s)$ can be respectively expressed as the sum of their diagonal part and their balance:

$$P^{-1} = P^* = [p_{ij}^*] = A + B = \begin{bmatrix} p_{11}^* & 0 & 0 \\ 0 & \dots & 0 \\ 0 & 0 & p_{nn}^* \end{bmatrix} + \begin{bmatrix} 0 & \dots & p_{1n}^* \\ \dots & 0 & \dots \\ p_{n1}^* & \dots & 0 \end{bmatrix} \tag{5}$$

$$G = G_d + G_b = \begin{bmatrix} g_{11} & 0 & 0 \\ 0 & \dots & 0 \\ 0 & 0 & g_{nn} \end{bmatrix} + \begin{bmatrix} 0 & \dots & g_{1n} \\ \dots & 0 & \dots \\ g_{n1} & \dots & 0 \end{bmatrix} \tag{6}$$

3.2.2 Hypothesis

Given the transfer function t_{ij} , an element of the Transfer matrix $T_{Y/R} = y/r'$, the sole necessary hypothesis that the compensator design methodology needs to meet is:

$$\left| (p_{ij}^* + g_{ij}) t_{jj} \right| \gg \left| (p_{ik}^* + g_{ik}) t_{kj} \right| \quad (7)$$

for $k \neq j$ and in the bandwidth of t_{ij} , which is usually satisfied once the matrix is ordered with the RGA procedure -Relative Gain Analysis (Bristol, 1966)-.

3.2.3 Methodology steps

The design methodology consists in four steps. Step A arranges the system to apply afterwards the sequential procedure closing n loops with steps B and C, which are repeated for every column of the compensator matrix $G(s)$ (Fig. 3). Step D designs the prefilter.

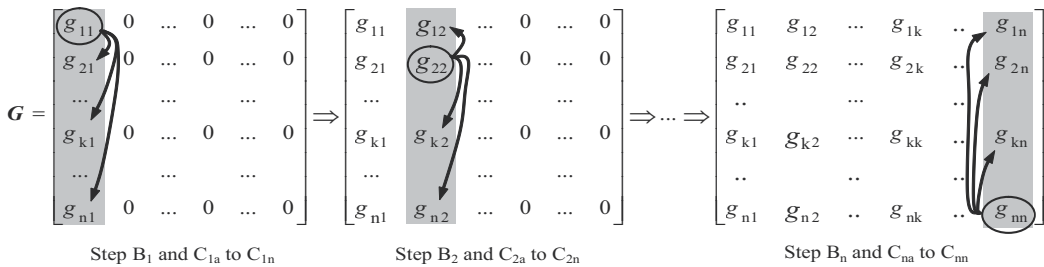


Fig. 3. Sequential steps for $G(s)$ controller design

Step 1. *Input-Output pairing and loop ordering.* First, the methodology identifies input-output pairings by using the RGA (Bristol, 1966). Then, the matrix P^* is reorganized so that $(p_{11}^*)^{-1}$ has the smallest bandwidth, $(p_{22}^*)^{-1}$ the next smallest bandwidth, and so on (Houpis, Rasmussen & Garcia-Sanz, 2006).

Step 2. *Design of the diagonal compensator g_{kk} .* The diagonal element g_{kk} is calculated through standard QFT loop-shaping (Horowitz, 1982; Houpis, Rasmussen & Garcia-Sanz, 2006) for the inverse of the equivalent plant $(p_{kk}^{*e})^{-1}$ in order to achieve robust stability and robust performance specifications (Franchek *et al.*, 1997; De Bedout and Franchek, 2002). The equivalent plant satisfies the recursive relationship of Eq. (8) (Franchek *et al.*, 1997), which is an extension for the non-diagonal case of the recursive expression proposed by (Horowitz, 1982).

$$\left[p_{ii}^{*e} \right]_k = \left[p_{ii}^* \right]_{k-1} - \frac{\left(\left[p_{i(i-1)}^* \right]_{k-1} + \left[g_{i(i-1)} \right]_{k-1} \right) \left(\left[p_{(i-1)i}^* \right]_{k-1} + \left[g_{(i-1)i} \right]_{k-1} \right)}{\left[p_{(i-1)(i-1)}^* \right]_{k-1} + \left[g_{(i-1)(i-1)} \right]_{k-1}} \quad (8)$$

$$i \geq k; \quad \left[P^* \right]_{k=1} = P^*$$

Step 3. *Design of the $(n-1)$ non-diagonal elements g_{ik} ($i \neq k, i = 1, 2, \dots, n$).* These elements are designed to minimize the cross-coupling terms c_{ik} according to the type problem case: for reference tracking (Eq. 9), for disturbance rejection at plant input (Eq. 10) or at plant output (Eq. 11).

$$c_{1ik} = g_{ik} - \frac{g_{kk} (p_{ik}^* + g_{ik})}{(p_{kk}^* + g_{kk})} ; \quad i \neq k \quad (9)$$

$$c_{2ik} = \frac{(p_{ik}^* + g_{ik})}{(p_{kk}^* + g_{kk})} ; \quad i \neq k \quad (10)$$

$$c_{3ik} = p_{ik}^* - \frac{p_{kk}^* (p_{ik}^* + g_{ik})}{(p_{kk}^* + g_{kk})} ; \quad i \neq k \quad (11)$$

Step 4. *Design of the prefilter.* The final $T_{y/r}(s)$ function shows less loop interaction thanks to the fully populated compensator design. Therefore, the prefilter $F(s)$ can generally be a diagonal matrix.

3.2.4 Stability conditions

Closed-loop stability of a MIMO system with a non-diagonal controller, designed by using a sequential procedure as the one presented above, is guaranteed by the following sufficient conditions (De Bedout and Franchek, 2002):

1. each $L_i(s) = g_{ii}(s) (p_{ii}^*)^{-1}$, $i=1, \dots, n$, satisfies the Nyquist encirclement condition,
2. no RHP pole-zero cancellations occur between $g_{ii}(s)$ and $(p_{ii}^*)^{-1}$, $i=1, \dots, n$,
3. no Smith-McMillan pole-zero cancellations occur between $P(s)$ and $G(s)$, and
4. no Smith-McMillan pole-zero cancellations occur in $|P^*(s) + G(s)|$

3.2.5 Non-minimum phase aspects

Although it is very remote, theoretically there exists the possibility of introducing right-half plane (RHP) transmission zeros in the controller design procedure. This undesirable situation cannot be detected until the multivariable system design is completed. To avoid it, the proposed methodology –Steps A, B and C– is inserted in an additional procedure (Garcia-Sanz & Eguinoa, 2005). Once the matrix compensator $G(s)$ is designed, the transmission zeros of $P(s)G(s)$ are determined using the Smith-McMillan form and over the set of possible plants P due to uncertainty. If there exist new RHP zeros apart from those initially present in $P(s)$, they can be removed by using the non-diagonal elements of the last column of the $G(s)$ matrix.

4. Application to control a telescope-type spacecraft

4.1 System description

This Section shows some illustrative results achieved when applying the non-diagonal MIMO QFT control methodology introduced in Section 3 to one of the telescope-type spacecraft (a 6-inputs/6-outputs MIMO system) of a multiple formation flying constellation of a European Space Agency (ESA) cornerstone mission: the Darwin mission (Garcia-Sanz *et al.*, 2008). It consists of one master satellite (central hub) and three to six telescopes arranged in a symmetric configuration flying in formation (Fig. 1). They will operate together to analyze the atmosphere of remote planets through appropriate spectroscopy techniques. The mission will employ nulling interferometry to detect dim planets close to bright stars. The infrared light

collected by the free flying telescopes will be recombined inside the hub-satellite in such a way that the light from the central star will suffer destructive interference and will be cancelled out, allowing the much fainter planet to stand out. That interferometry technology requires very accurate and stable positioning of the spacecraft in the constellation, which puts high demands on the attitude and position control system. Instead of an orbit around the Earth, the mission will be placed further away, at a distance of 1.5 million kilometers from Earth, in the opposite direction from the Sun (Earth-Sun Lagrangian Point L2).

The present Section shows the control of one of the telescope flyers. Each telescope flyer is cylindrically shaped (2 m diameter, 2 m height) and weighs 500 kg. In order to protect the instrument from the sunlight, it is equipped with a sunshield modeled with 6 large flexible beams (4 m long and 7 kg) attached to the rigid structure (see Fig. 3; beam end-point coordinates in brackets).

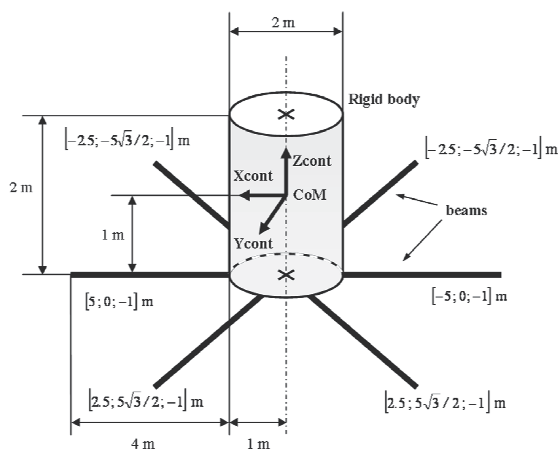


Fig. 3. Spacecraft description

For every beam, two different frequencies for the first modes along Y and Z beam axes are considered. Their frequency can vary from 0.05 Hz to 0.5 Hz, with a nominal value of 0.1 Hz, and their damping can vary from 0.1% to 1%, with a nominal value of 0.5%. As regards spacecraft mass and inertia, the corresponding uncertainty around their nominal value is of 5%.

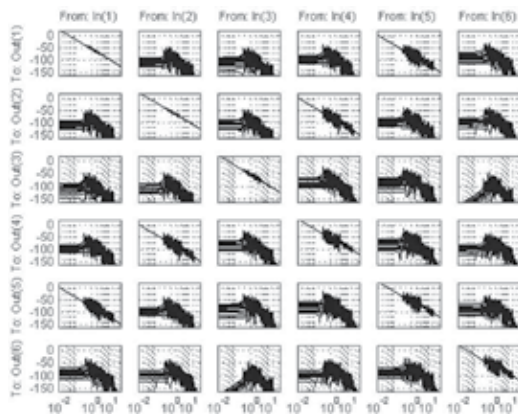


Fig. 4. Spacecraft model dynamics

Based on that description, and using a mechanical modeling formulation for multiple flexible appendages of a rigid body spacecraft, the open-loop transfer function matrix representation of the Flyer is given in (12) and Fig. 4, where x, y, z are the position coordinates; ϕ, θ, ψ are the corresponding attitude angles; F_x, F_y, F_z are the force inputs; T_ϕ, T_θ, T_ψ are the torque inputs; and where each $p_{ij}(s), i, j = 1, \dots, 6$, is a 50th order Laplace transfer function with uncertainty.

$$\begin{bmatrix} x(s) \\ y(s) \\ z(s) \\ \phi(s) \\ \theta(s) \\ \psi(s) \end{bmatrix} = \mathbf{P}(s) \mathbf{U}(s) = \begin{bmatrix} p_{11}(s) & p_{12}(s) & p_{13}(s) & p_{14}(s) & p_{15}(s) & p_{16}(s) \\ p_{21}(s) & p_{22}(s) & p_{23}(s) & p_{24}(s) & p_{25}(s) & p_{26}(s) \\ p_{31}(s) & p_{32}(s) & p_{33}(s) & p_{34}(s) & p_{35}(s) & p_{36}(s) \\ p_{41}(s) & p_{42}(s) & p_{43}(s) & p_{44}(s) & p_{45}(s) & p_{46}(s) \\ p_{51}(s) & p_{52}(s) & p_{53}(s) & p_{54}(s) & p_{55}(s) & p_{56}(s) \\ p_{61}(s) & p_{62}(s) & p_{63}(s) & p_{64}(s) & p_{65}(s) & p_{66}(s) \end{bmatrix} \begin{bmatrix} F_x(s) \\ F_y(s) \\ F_z(s) \\ T_\phi(s) \\ T_\theta(s) \\ T_\psi(s) \end{bmatrix} \quad (12)$$

The Bode diagram of the plant (Fig. 4) shows the dynamics of the 36 matrix elements. Each of them and the MIMO system (matrix) itself are minimum phase. The flexible modes introduced by the appendages (second-order dipoles) affect all the elements around the frequencies $\omega = [0.19, 10]$ rad/sec. The diagonal elements $p_{ii}(s), i = 1, \dots, 6$, and the elements $p_{15}(s), p_{51}(s), p_{24}(s)$ and $p_{42}(s)$ are mainly double integrators plus the flexible modes.

4.2 Performance specifications

The main objective of the spacecraft control system is to fulfill some astronomical requirements that demand to keep the flying telescope pointing at both the observed space target and the central hub-satellite. This set of specifications leads to some additional engineering requirements (bandwidth, saturation limits, noise rejection, etc.) and also needs some complementary control requirements (stability, low loop interaction, low controller complexity and order, etc.). In other words, the requirements are:

- A. *Astronomical specifications:*
 - A1. Position accuracy: maximum absolute value: 1 μm (micro-meter) for all axes, and standard deviation: 0.33 μm for all axes.
 - A2. Pointing accuracy: maximum absolute value: 25 mas (milli-arc-second) for all axes, and standard deviation: 8.5 mas for all axes.
- C. *Engineering specifications:*
 - B1. Bandwidth: ~ 0.01 Hz for all axes.
 - B2. Saturation limits: maximum force: 150 μN , maximum torque: 150 μNm .
 - B3. High frequency noise rejection: high roll-off after the bandwidth.
- D. *Control specifications:*
 - C1. Loop interaction: minimum.
 - C2. Rejection of flexible modes: maximum.
 - C3. Controller complexity and order: minimum.

To achieve these goals, the astronomical, engineering and control specifications are translated into frequency domain requirements (see some examples at D'Azzo, Houpis, & Sheldon, 2003), defined as shown in Table I, where $(p_{ii}^*)^{-1}$ is the inverse of the equivalent plant, which corresponds to $p_{ii}(s)$ in the SISO case (Garcia-Sanz *et al.*, 2008).

		Value ($\forall \omega$)	Loops
1	$\left \frac{(p_{ii}^{*e})^{-1} g_{ii}(s)}{1 + (p_{ii}^{*e})^{-1} g_{ii}(s)} \right = \left \frac{y_i(s)}{r_i(s)} \right = \left \frac{y_i(s)}{n_i(s)} \right = \left \frac{u_i(s)}{v_i(s)} \right \leq \delta_1(\omega)$	$\delta_1(\omega) = 1.85$ (14)	1,2,3
		$\delta_1(\omega) = \left \frac{0.1687}{s^2 + 0.4s + 0.0912} \right $ (15)	4,5,6
2	$\left \frac{1}{1 + (p_{ii}^{*e})^{-1} g_{ii}(s)} \right = \left \frac{e_i(s)}{n_i(s)} \right = \left \frac{y_i(s)}{d_i(s)} \right \leq \delta_2(\omega)$	$\delta_2(\omega) = 2$ (17)	1,2,3, 4,5,6
3	$\left \frac{(p_{ii}^{*e})^{-1}}{1 + (p_{ii}^{*e})^{-1} g_{ii}(s)} \right \leq \delta_3(\omega)$	$\delta_3(\omega) = \left \frac{0.21553(s + 0.385)}{(s + 0.307)(s + 6.18)(s^2 + 0.4s + 0.0912)} \right $ (19)	1,2
		$\delta_3(\omega) = \left \frac{0.313(s - 0.01705)(s^2 + 0.009974s + 5.104 \cdot 10^{-5})}{(s - 0.01813)(s^2 + 0.02554s + 0.0004754)} \right $ (20)	3
	$\delta_3(\omega) = \left \frac{(s + 0.2)(s + 0.186)(s + 0.2044)(s + 0.003892)(s^2 + 0.06014s + 0.02736)}{(s + 0.007333)(s + 0.445)(s^2 + 0.07904s + 0.00326)(s^2 + 0.2352s + 0.0981)} \right $ (21)	4,5,6	
4	$\left \frac{g_{ii}(s)}{1 + (p_{ii}^{*e})^{-1} g_{ii}(s)} \right \leq \delta_4(\omega)$	$\delta_4(\omega) = \left \frac{557.1(s + 5)}{(s^2 + 3.23s + 6.5)} \right $ (23)	1,2
		$\delta_4(\omega) = \left \frac{106.9210(s + 0.55)(s^2 + 0.04s + 0.13)}{(s + 1.4)^2(s^2 + 0.1227s + 0.097)} \right $ (24)	3
		$\delta_4(\omega) = \left \frac{4.026(s^2 - 0.1854s + 0.203)(s^2 + 0.04s + 0.504)}{(s^2 + 0.305s + 0.056)(s^2 + 0.115s + 0.095)} \right $ (25)	4,5,6

Table I. Transfer function for Frequency Domain Specifications

4.3 Applying the non-diagonal MIMO QFT control methodology

The MIMO QFT methodology explained in Section 3.2 is applied here to design the 6x6 robust control system for the telescope-type spacecraft described in Section 4.1, and with the performance specifications defined in Section 4.2.

Step A. *Input-Output pairing and loop ordering.*

An illustrative result of the Relative Gain Array for all the uncertainty, at low frequency (steady state), and up to 0.19 rad/sec, is shown in Eq. (26). According to it, the pairing should be done through the main diagonal of the matrix, which contains positive RGA elements, and the elements $g_{15}(s)$, $g_{24}(s)$, $g_{42}(s)$, $g_{51}(s)$ should also be considered relevant.

$$\mathbf{RGA}_{(\omega=6.28 \cdot 10^{-4} \text{ rad/sec})} = \begin{bmatrix} 1.0064 & 0 & 0 & 0 & 0.0064 & 0 \\ 0 & 1.0064 & 0 & 0.0064 & 0 & 0 \\ 0 & 0 & 1 & 0 & 0 & 0 \\ 0 & 0.0064 & 0 & 1.0064 & 0 & 0 \\ 0.0064 & 0 & 0 & 0 & 1.0064 & 0 \\ 0 & 0 & 0 & 0 & 0 & 1 \end{bmatrix} \quad (26)$$

In accordance with the above RGA results and taking into account the requirement of minimum controller complexity and order (Section 4.2, Specification C3), the compensator structure consisting of six diagonal elements and four off-diagonal elements is chosen as the most suitable one (27).

$$\mathbf{G}(s) = \begin{bmatrix} g_{11}(s) & 0 & 0 & 0 & g_{15}(s) & 0 \\ 0 & g_{22}(s) & 0 & g_{24}(s) & 0 & 0 \\ 0 & 0 & g_{33}(s) & 0 & 0 & 0 \\ 0 & g_{42}(s) & 0 & g_{44}(s) & 0 & 0 \\ g_{51}(s) & 0 & 0 & 0 & g_{55}(s) & 0 \\ 0 & 0 & 0 & 0 & 0 & g_{66}(s) \end{bmatrix} \quad (27)$$

From this, four independent compensator design problems have been adopted, two SISO - $[g_{33}(s)]$ and $[g_{66}(s)]$ - and two 2x2 MIMO - $[g_{11}(s) \ g_{15}(s) ; g_{51}(s) \ g_{55}(s)]$ and $[g_{22}(s) \ g_{24}(s) ; g_{42}(s) \ g_{44}(s)]$ - problems. The SISO problems are considered as a classical SISO QFT problem, while the two 2x2 MIMO subsystems are studied through the non-diagonal MIMO QFT methodology.

Step B0. *Design of the diagonal compensator $g_{kk}(s)$, $k = 3, 6$. SISO cases.*

Compensators $g_{33}(s)$ and $g_{66}(s)$ are independently designed by using classical single-input single-output SISO QFT (Houpis, Rasmussen & Garcia-Sanz, 2006) to satisfy the performance specifications stated in Table I for every plant within the uncertainty. The corresponding QFT bounds and the nominal open-loop transfer functions $L_{ii}(s) = p_{ii}(s) g_{ii}(s)$, $i = 3, 6$, are plotted on the Nichols Charts shown in Fig. 5.

Step B1. *Design of the diagonal compensator $g_{11}(s)$. First MIMO problem.*

The compensator $g_{11}(s)$ is designed according to the non-diagonal MIMO QFT methodology explained in Section 3.2, for the inverse of the equivalent plant $[p_{11}^*e(s)]_1 = p_{11}^*(s)$. See Fig. 6a.

Step C1. *Design of the non-diagonal compensator $g_{51}(s)$. First MIMO problem.*

The non-diagonal compensator $g_{51}(s)$ is designed to minimize the (5,1) element of the coupling matrix in the case of disturbance rejection at plant input, which gives the following expression:

$$g_{51}^{opt}(s) = -p_{51}^{*N}(s) \quad (28)$$

where N denotes the middle plant that interpolates the expression $[-p_{51}^*(s)]$ from 0 to 10^{-1} rad/s, as shown in Fig. 7, (Garcia-Sanz *et al.*, 2008).

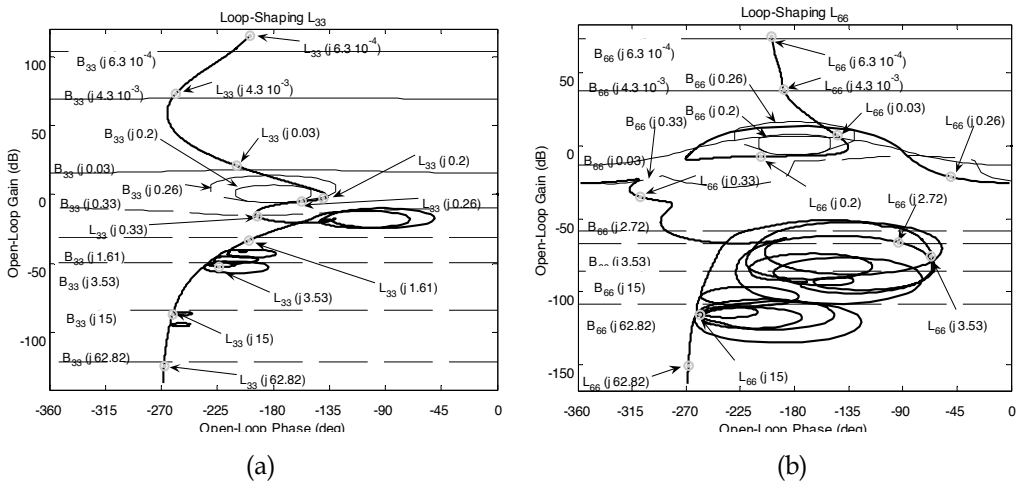


Fig. 5. Loop-shaping: (a) $L_{33}(s) = p_{33}(s) g_{33}(s)$, (b) $L_{66}(s) = p_{66}(s) g_{66}(s)$

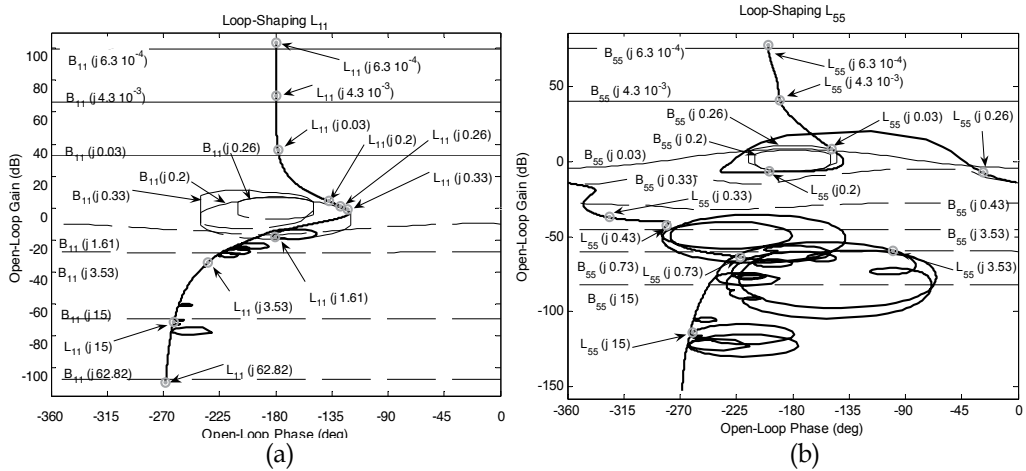


Fig. 6. Loop-shaping (a) $L_{11}(s) = [p_{11}^{*e}(s)]_1^{-1} g_{11}(s)$. (b) $L_{55}(s) = [p_{55}^{*e}(s)]_2^{-1} g_{55}(s)$

Step B2. Design of the diagonal compensator $g_{55}(s)$. First MIMO problem.

The compensator $g_{55}(s)$ is designed according to the non-diagonal MIMO QFT methodology explained in Section 3.2, for the inverse of the equivalent plant $[p_{55}^{*e}(s)]_2$, which is:

$$[p_{55}^{*e}(s)]_2 = [p_{55}^{*e}(s)]_1 - \left([p_{51}^{*e}(s)]_1 + [g_{51}(s)]_1 \right) \left([p_{15}^{*e}(s)]_1 \right) / \left([p_{11}^{*e}(s)]_1 + [g_{11}(s)]_1 \right). \text{ See Fig. 6b.}$$

Step C2. Design of the non-diagonal compensator $g_{15}(s)$. First MIMO problem.

The non-diagonal compensator $g_{15}(s)$ is designed to minimize the (1,5) element of the coupling matrix in the case of disturbance rejection at plant input which, taking the 4.2-C3 performance specification also into account gives the following expression:

$$g_{15}^{opt}(s) = -p_{15}^{*N}(s) = 0 \tag{29}$$

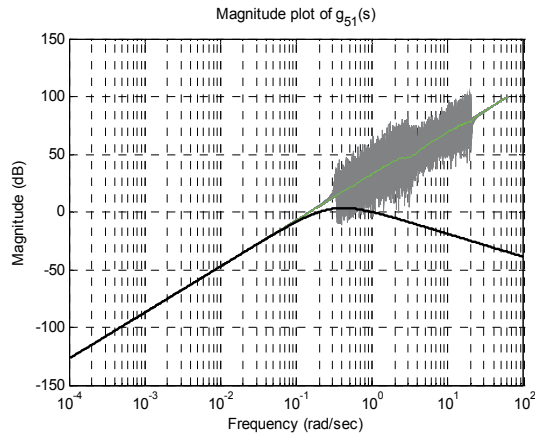


Fig. 7. Magnitude plot of $[-p_{51}^*(s)]$ with uncertainty and $g_{51}(s)$ -bold solid line-

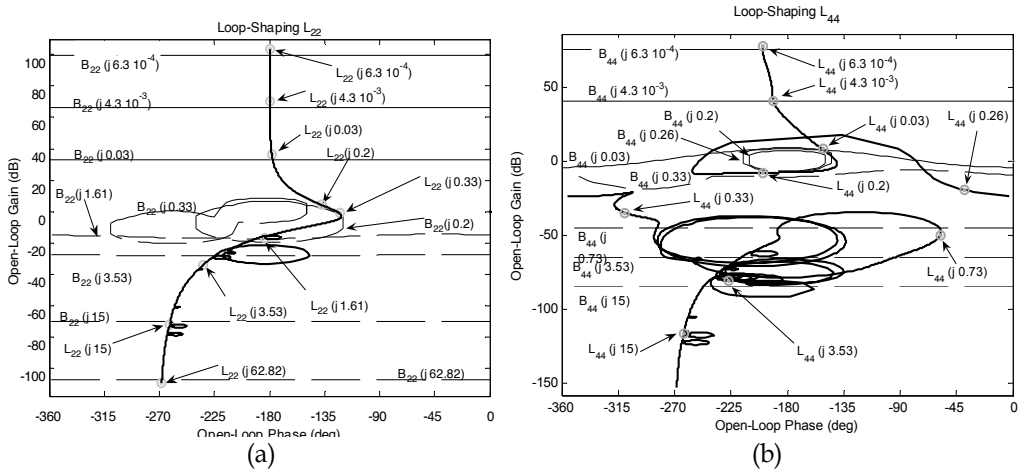


Fig. 8. Loop-shaping (a) $L_{22}(s) = [p_{22}^{*e}(s)]_1^{-1} g_{22}(s)$. (b) $L_{44}(s) = [p_{44}^{*e}(s)]_2^{-1} g_{44}(s)$

The second MIMO problem is shown in the following Steps. It consists of the design of the elements $g_{22}(s)$, $g_{42}(s)$, $g_{44}(s)$ and $g_{24}(s)$, which are equivalently performed as in the previous Steps B1, C1, B2 and C2 respectively.

Step B3. Design of the diagonal compensator $g_{22}(s)$. Second MIMO problem.

The compensator $g_{22}(s)$ is designed according to the non-diagonal MIMO QFT methodology explained in Section 3.2, for the inverse of the equivalent plant $[p_{22}^{*e}(s)]_1 = p_{22}^*(s)$. See Fig. 8a.

Step C3. Design of the non-diagonal compensator $g_{42}(s)$. Second MIMO problem.

The non-diagonal compensator $g_{42}(s)$ is designed to minimize the (4,2) element of the coupling matrix in the case of disturbance rejection at plant input, which gives the following expression:

$$g_{42}^{opt}(s) = -p_{42}^{*N}(s) \tag{30}$$

where N denotes the middle plant that interpolates the expression $[-p_{42}^*(s)]$ from 0 to 10^{-1} rad/s, as shown in Fig. 9, (Garcia-Sanz *et al.*, 2008).

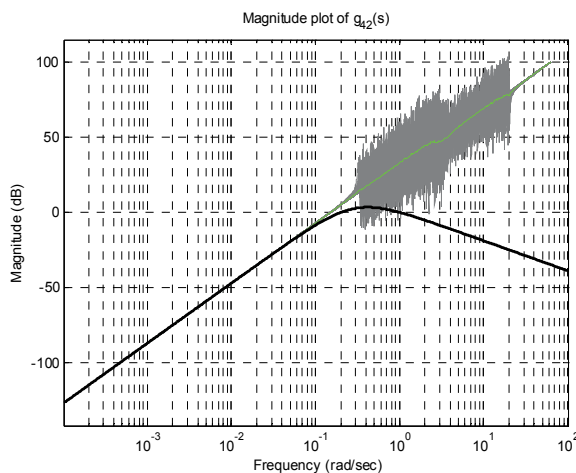


Fig. 9. Magnitude plot of $[-p_{42}^*(s)]$ with uncertainty and $g_{42}(s)$ -bold solid line-

Step B4. Design of the diagonal compensator $g_{44}(s)$. Second MIMO problem.

The compensator $g_{44}(s)$ is designed according to the non-diagonal MIMO QFT methodology explained in Section 3.2, for the inverse of the equivalent plant $[p_{44}^{*e}(s)]_2$, which is:

$$[p_{44}^{*e}(s)]_2 = [p_{44}^{*e}(s)]_1 - \left([p_{42}^{*e}(s)]_1 + [g_{42}(s)]_1 \right) \left([p_{24}^{*e}(s)]_1 \right) / \left([p_{22}^{*e}(s)]_1 + [g_{22}(s)]_1 \right).$$

See Fig. 8b.

Step C4. Design of the non-diagonal compensator $g_{24}(s)$. Second MIMO problem.

The non-diagonal compensator $g_{24}(s)$ is designed to minimize the (2,4) element of the coupling matrix in the case of disturbance rejection at plant input which, taking the 4.2-C3 performance specification also into account gives the following expression:

$$g_{24}^{opt}(s) = -p_{24}^{*N}(s) = 0 \quad (31)$$

Step D. Design of the prefilter $f_{kk}(s)$, $k = 1, 2, \dots, 6$.

There is not prefilter required in this example, because we do not have reference tracking specifications (See Section 4.2).

4.4 Validation

Time domain simulations were performed for 300 random mode dynamics within the uncertainty range (MonteCarlo analysis) in the ESA telescope-type benchmark simulator (Fig. 10).

The position and attitude performance obtained by the non-diagonal MIMO QFT was excellent, fulfilling easily all the required specifications (Section 4.2, A, B and C), improving also by two order of magnitude the results obtained by other robust control techniques on the maximum and standard deviation error results. At the same time, while these other robust control techniques (H-infinity type) required controller structures with full-matrices of 36 elements of 42nd order, the non-diagonal MIMO QFT design consists of only eight compensators going from 3rd to 14th order, dividing by more than 20 the number of operations per second needed (see Table II).

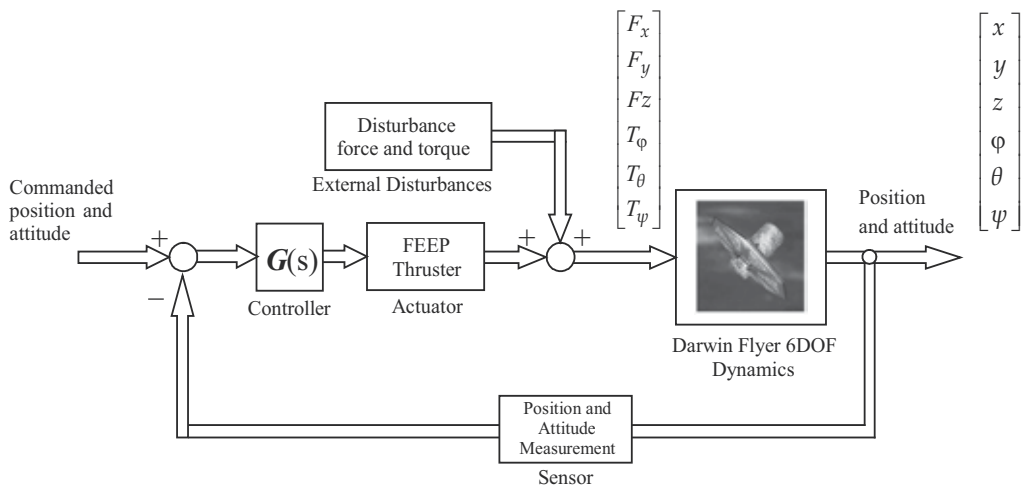


Fig. 10. ESA Telescope-type Spacecraft Simulator

<i>Controller</i>	<i>Number of Multiplications</i>	<i>Number of Sums</i>
Non-diagonal MIMO QFT	130	124
Other robust control technique	2994	2988

Table II. Number of operations per second required by the controllers

5. Conclusions

This chapter demonstrated the feasibility of sequential non-diagonal multi-input multi-output -MIMO- robust QFT control strategies to regulate simultaneously the position and attitude of a telescope-type spacecraft with large flexible appendages. The chapter described: 1) the main control challenges and dynamic characteristics of MIMO systems in general; 2) advanced MIMO techniques to design robust controllers based on the quantitative feedback theory -QFT-; and 3) some illustrative results achieved when applying the MIMO QFT control methodology to one of the telescope-type spacecraft of a multiple formation flying constellation of a European Space Agency cornerstone mission, fulfilling satisfactory the astronomical, engineering and control requirements of the spacecraft.

6. References

- Barman, J.F. and Katzenelson, J., "A generalized Nyquist-type stability criterion for multivariable feedback systems," *International Journal of Control*, 20(4): pp. 593-622, 1974.
- Barreras, M., "Control robusto QFT multivariable mediante métodos secuenciales no-diagonales. Aplicación al gobierno de procesos térmicos.," *Universidad Pública de Navarra*, Pamplona, Spain, PhD Thesis, 2005.

- Barreras, M. and Garcia-Sanz, M., "Multivariable QFT controllers design for heat exchangers of solar systems," *International Conference on Renewable Energy and Power Quality*, Barcelona (Spain), 2004.
- Barreras, M., Villegas, C., Garcia-Sanz, M. and Kalkkuhl, J., "Robust QFT tracking controller design for a car equipped with 4-wheel steer-by-wire," *2006 IEEE Conference on Computer Aided Control System Design, 2006 IEEE International Conference on Control Applications, 2006 IEEE International Symposium on Intelligent Control*, 4-6 Oct. 2006, Munich, Germany, 2006.
- Boje, E. and Nwokah, O.D.I., "Quantitative multivariable feedback design for a turbofan engine with forward path decoupling," *International Journal of Robust and Nonlinear Control*, 9(12): pp. 857-882, 1999.
- Boje, E. and Nwokah, O.D.I., "Quantitative feedback design using forward path decoupling," *Transactions of the ASME. Journal of Dynamic Systems, Measurement and Control*, 123(1): pp. 129-32, 2001.
- Borghesani, C., Chait, Y. and Yaniv, O., *Quantitative Feedback Theory Toolbox. For use with Matlab*. 2nd Ed. *Terasoft*, 2002.
- Bristol, E.H., "On a new measure of interaction for multi-variable process control," *IEEE Transactions on Automatic Control*, AC-11(1): pp. 133-134, 1966.
- Bryant, G.F., "Direct methods in multivariable control. I. Gauss elimination revisited," *International Conference - Control 85 (Conf. Publ. No. 252)*, 9-11 July 1985, Cambridge, UK, 1985.
- Campo, P.J. and Morari, M., "Achievable closed-loop properties of systems under decentralized control: conditions involving the steady-state gain," *IEEE Transactions on Automatic Control*, 39(5): pp. 932-943, 1994.
- Chang, J.-W. and Yu, C.-C., "Relative disturbance gain array," *AIChE Journal*, 38(4): pp. 521-534, 1992.
- Chiu, M.-S. and Arkun, Y., "Decentralized control structure selection based on integrity considerations," *Industrial & Engineering Chemistry Research*, 29(3): pp. 369-373, 1990.
- Davison, E. and Wang, S.H., "Properties and calculation of transmission zeros of linear multivariable systems," *Automatica*, 10(6): pp. 643-58, 1974.
- D'Azzo, J.J., Houpis, C.H., and Sheldon, S.N., "Linear Control System Analysis and Design with Matlab", 5th ed., *Marcel Dekker*, New York, 2003.
- De Bedout, J.M. and Franchek, M.A., "Stability conditions for the sequential design of non-diagonal multivariable feedback controllers," *International Journal of Control*, 75(12): pp. 910-922, 2002.
- Deshpande, P.B., "Multivariable process control." *Research Triangle Park, NC: Instrument Society of America*, 1989.
- Desoer, C.A. and Schulman, J.D., "Zeros and poles of matrix transfer functions and their dynamical interpretation," *IEEE Transactions on Circuits and Systems*, CAS-21(1): pp. 3-8, 1974.
- Desoer, C.A. and Vidyasagar, M., "Feedback Systems: Input-Output Properties". New York [etc.]: *Academic Press*, 1975.
- Desoer, C. and Wang, Y.-T., "On the generalized nyquist stability criterion," *Automatic Control, IEEE Transactions on*, 25(2): pp. 187-196, 1980.
- Doyle, J.C., "Robustness of multiloop linear feedback systems," *IEEE Conference on Decision and Control, 17th Symposium on Adaptive Processes*, 1978.

- Doyle, J., "Analysis of feedback systems with structured uncertainties," *IEE Proceedings D (Control Theory and Applications)*, 129(6): pp. 242-50, 1982.
- Doyle, J.C., Wall, J.E. and Stein, G., "Performance and robustness analysis for structured uncertainty," *21st IEEE Conference on Decision and Control*, 1982.
- Dutton, K., Thompson, S. and Barraclough, B., "The art of control engineering". Great Britain: *Pearson. Prentice-Hall*, 1997.
- Franchek, M.A., Herman, P.A. and Nwokah, O.D.I., "Robust multivariable control of distillation columns using a non-diagonal controller matrix," *1995 ASME International Mechanical Engineering Congress and Exposition. Part 1 (of 2)*, Nov 12-17 1995, San Francisco, CA, USA, 1995.
- Franchek, M.A., Herman, P. and Nwokah, O.D.I., "Robust nondiagonal controller design for uncertain multivariable regulating systems," *Transactions of the ASME. Journal of Dynamic Systems, Measurement and Control*, 119(1): pp. 80-85, 1997.
- Freudenberg, J.S. and Looze, D.P., "Frequency Domain Properties of Scalar and Multivariable Feedback Systems". Heiderberg (Germany): *Springer-Verlag Berlin*, 1988.
- Garcia-Sanz, M. and Barreras, M., "Nondiagonal QFT controller design for a three-input three-output industrial furnace," *Transactions of the ASME. Journal of Dynamic Systems, Measurement and Control*, 128(2): pp. 319-29, 2006.
- Garcia-Sanz, M. and Egana, I., "Quantitative non-diagonal controller design for multivariable systems with uncertainty," *International Journal of Robust and Nonlinear Control*, 12(4): pp. 321-333, 2002.
- Garcia-Sanz, M. and Eguinoa, I., "Improved non-diagonal MIMO QFT design technique considering non-minimum phase aspects". *7th International Symposium on Quantitative Feedback Theory QFT and Robust Frequency Domain Methods*, Lawrence, Kansas, USA, August 2005.
- Garcia-Sanz, M., Egana, I. and Barreras, M., "Design of Quantitative Feedback Theory non-diagonal controllers for use in uncertain multiple-input multiple-output systems," *IEE Proceedings-Control Theory and Applications*, 152(2): pp. 177-187, 2005.
- Garcia-Sanz, M., Eguinoa, I., Ayesa, E. and Martin, C., "Non-diagonal multivariable robust QFT control of a wastewater treatment plant for simultaneous nitrogen and phosphorus removal," *5th IFAC Symposium on Robust Control Design*, Toulouse, France, 2006.
- Garcia-Sanz, M., Eguinoa, I., Barreras, M. and Bennani, S., "Nondiagonal MIMO QFT Controller Design for Darwin-Type Spacecraft With Large Flimsy Appendages," *Journal of Dynamic Systems, Measurement, and Control*, 130(1): pp. 011006-1 - 15, 2008.
- Garcia-Sanz, M., Eguinoa I. and Bennani S., "Non-diagonal MIMO QFT controller design reformulation", *International Journal of Robust and Non-Linear Control*, 19 (9): pp. 1036-1064, June 2009.
- Garcia-Sanz, M. and Hadaegh, F.Y., "Load-sharing robust control of spacecraft formations: deep space and low Earth elliptic orbits," *IET Control Theory & Applications*, 1(2): pp. 475-484, 2007.
- Garcia-Sanz, M, A. Mauch and C. Philippe, "QFT Control Toolbox: an Interactive Object-Oriented Matlab CAD tool for Quantitative Feedback Theory," *6th IFAC Symposium on Robust Control Design, ROCOND'09*, Haifa, Israel, June 2009.

- Grosdidier, P., Morari, M. and Holt, B.R., "Closed-loop properties from steady-state gain information," *Industrial and Engineering Chemistry, Fundamentals*, 24(2): pp. 221-235, 1985.
- Grosdidier, P. and Morari, M., "Interaction measures for systems under decentralized control," *Automatica*, 22(3): pp. 309-319, 1986.
- Grosdidier, P. and Morari, M., "A computer aided methodology for the design of decentralized controllers," *Computers & Chemical Engineering*, 11(4): pp. 423-33, 1987.
- Gutman, P.O., "Qsyn – The Toolbox for Robust Control Systems Design for use with Matlab, User's Guide", *El-Op Electro-Optics Industries Ltd, Rehovot*, 1996.
- Horowitz, I., "Synthesis of Feedback Systems". New York, *Academic Press*, 1963.
- Horowitz, I., "Quantitative synthesis of uncertain multiple input-output feedback system," *International Journal of Control*, 30(1): pp. 81-106, 1979.
- Horowitz, I., "Improved design technique for uncertain multiple-input-multiple-output feedback systems," *International Journal of Control*, 36(6): pp. 977-988, 1982.
- Horowitz, I., "Singular-G method for unstable non-minimum-phase plants.," *International Journal of Control*, 44(2): pp. 533-541, 1986.
- Horowitz, I., "Survey of quantitative feedback theory (QFT)," *International Journal of Control*, 53(2): pp. 255-291, 1991.
- Horowitz I., "Quantitative Feedback Design Theory (QFT)". *QFT Publishing*, 660 South Monaco Parkway, Denver, Colorado, 1993.
- Horowitz, I., Kopelman, Z., Yaniv, O., Neumann, L. and Golubev, B., "Multivariable Flight Control Design with Uncertain Parameters (YF16CCV)," *Air Force Wright Aeronautical Laboratories, Wright-Patterson AFB, OH*, Final scientific rept. 1 Jan 81-31 Aug 82. Contract number AFOSR-80-0213 AFWALTR-83-3036, Sep 1982, 1982.
- Horowitz, I. and Liao, Y.-K., "Limitations of non-minimum-phase feedback systems," *International Journal of Control*, 40(5): pp. 1003-1013, 1984.
- Horowitz, I. and Loecher, C., "Design of a 3x3 multivariable feedback system with large plant uncertainty," *International Journal of Control*, 33(4): pp. 677-99, 1981.
- Horowitz, I., Neumann, L. and Yaniv, O., "A synthesis technique for highly uncertain interacting multivariable flight control system (TYF16CCV)," *Naecon Conf.*, Dayton, OH, 1981.
- Horowitz, I., Oldak, S. and Yaniv, O., "An important property of non-minimum-phase multiple-input-multiple-output feedback systems," *International Journal of Control*, 44(3): pp. 677-688, 1986.
- Horowitz, I. and Sidi, M., "Practical design of feedback systems with uncertain multivariable plants," *International Journal of Systems Science*, 11(7): pp. 851-75, 1980.
- Houpis, C.H., Rasmussen, S.J. and Garcia-Sanz, M., "Quantitative Feedback Theory Fundamentals and Applications", 2nd edition ed. Florida, USA: a CRC Press Book. *Taylor and Francis*, 2006.
- Houpis, C.H. and Sating, R.R., "MIMO QFT CAD package (Version 3)," *International Journal of Robust and Nonlinear Control*, 7(6): pp. 533-49, 1997.
- Hovd, M. and Skogestad, S., "Simple frequency-dependent tools for control system analysis, structure selection and design," *Automatica*, 28(5): pp. 989-96, 1992.
- Hsu, C.-H. and Chen, C.-T., "A proof of the stability of multivariable feedback systems," *Proceedings of the IEEE*, 56(11): pp. 2061-2062, 1968.

- Hung, Y.S. and MacFarlane, A.G.J., "Multivariable Feedback: a Quasi-classical approach", vol. 40. Berlin, Germany: Springer-Verlag, 1982.
- Kailath, T., "Linear Systems". Englewood Cliffs (NJ): Prentice-Hall, 1980.
- Kantorovich, L.V. and Akilov, G.P., "Functional analysis in normed spaces", vol. 46. Oxford [etc.]: Pergamon Press, 1964.
- Kerr, M., "Robust control of an articulating flexible structure using MIMO QFT," *University of Queensland*, Queensland, Australia, Doctor of Philosophy, 2004.
- Kerr, M. and Jayasuriya, S., "Sufficient conditions for robust stability in non-sequential MIMO QFT," presented at 42nd IEEE International Conference on Decision and Control, 9-12 Dec. 2003, Maui, HI, USA, 2003.
- Kerr, M.L., Jayasuriya, S. and Asokanthan, S.F., "On stability in Non-sequential MIMO QFT Designs," *ASME Journal of Dynamic Systems Measurement and Control*, 127(1): pp. 98-104, 2005a.
- Kerr, M.L., Lan, C.-Y. and Jayasuriya, S., "Non-sequential MIMO QFT control of the X-29 aircraft," *7th International Symposium on Quantitative Feedback Theory QFT and Robust Frequency Domain Methods*, Lawrence, Kansas, USA, 2005b.
- Kerr, M.L. and Jayasuriya, S., "An improved non-sequential multi-input multi-output quantitative feedback theory design methodology," *International Journal of Robust and Nonlinear Control*, 16(8): pp. 379-95, 2006.
- Kerr, M.L., Lan, C.-Y. and Jayasuriya, S., "Non-sequential MIMO QFT control of the X-29 aircraft using a generalized formulation," *International Journal of Robust and Nonlinear Control*, 17(2-3): pp. 107-134, 2007.
- Lan, C.-Y., Kerr, M.L. and Jayasuriya, S., "Synthesis of controllers for non-minimum phase and unstable systems using non-sequential MIMO quantitative feedback theory," *2004 American Control Conference (AAC)*, Jun 30-Jul 2 2004, Boston, MA, United States, 2004.
- MacFarlane, A.G.J. and Hung, Y.S., "Use of parameter groups in the analysis and design of multivariable feedback systems," *20th IEEE Conference on Decision and Control including the Symposium on Adaptive Processes*, 16-18 Dec. 1981, San Diego, CA, USA, 1981.
- MacFarlane, A.G.J. and Karcnias, N., "Poles and zeros of linear multivariable systems: a survey of the algebraic, geometric and complex-variable theory," *International Journal of Control*, 24(1): pp. 33-74, 1976.
- MacFarlane, A.G.J. and Karcnias, N., "Relationships between state space and frequency response concepts," *Proc. 7th IFAC Congress*: pp. 1771-1779, 1978.
- MacFarlane, A.G.J. and Postlethwaite, I., "The generalized Nyquist stability criterion and multivariable root loci," *International Journal of Control*, 25(1): pp. 81-127, 1977.
- MacFarlane, A.G.J. and Scott-Jones, D.F.A., "Vector gain," *International Journal of Control*, 29(1): pp. 65-91, 1979.
- Maciejowski, J.M., "Multivariable Feedback Design". Reading, MA: Addison-Wesley Publishing Company, 1989.
- Manousiouthakis, V., Savage, R. and Arkun, Y., "Synthesis of decentralized process control structures using the concept of block relative gain," *AIChE Journal*, 32(6): pp. 991-1003, 1986.

- Marino-Galarraga, M., Marlin, T.E. and McAvoy, T.J., "Using the relative disturbance gain to analyse process operability," *1985 American Control Conference* (Cat. No. 85CH2119-6), 19-21 June 1985, Boston, MA, USA, 1985.
- Mayne, D.Q., "The design of linear multivariable systems," *Automatica*, 9(2): pp. 201-207, 1973.
- Mayne, D.Q., "Sequential design of linear multivariable systems," *Proceedings of the Institution of Electrical Engineers*, 126(6): pp. 568-572, 1979.
- McAvoy, T.J., "Interaction Analysis - Principles and Applications": *Instrument Society of America*, 1983.
- McMillan, B., "Introduction to formal realizability theory - I, II," *Bell System Technical Journal*, 31(2, 3): pp. 217-79, 541-600, 1952.
- Mees, A.I., "Achieving diagonal dominance," *Systems & Control Letters*, 1(3): pp. 155-8, 1981.
- Mijares, G., Cole, J.D., Naugle, N.W., Preisig, H.A. and Holland, C.D., "New criterion for the pairing of control and manipulated variables.," *AIChE Journal*, 32(9): pp. 1439-1449, 1986.
- Morari, M. and Zafiriou, E., "Robust process control". Englewood Cliffs, NJ, USA: *Prentice-Hall International*, 1989.
- Nett, C.N. and Spang, H.A., "Control structure design: A missing link in the evolution of modern control theories," *Amer. Contr. Conf.*, Minneapolis, MN, 1987.
- Nwokah, O.D.I., "Synthesis of controllers for uncertain multivariable plants for prescribed time-domain tolerances," *International Journal of Control*, 40(6): pp. 1189-1206, 1984.
- Nwokah, O.D.I., "Strong robustness in uncertain multivariable systems," *27th IEEE Conference on Decision and Control*, 1988.
- Park, M.S., Chait, Y. and Steinbuch, M., "A new approach to multivariable quantitative feedback theory: theoretical and experimental results," *1994 American Control Conference - ACC '94*, 29 June - 1 July 1994, Baltimore, MD, USA, 1994.
- Postlethwaite, I., "A generalized inverse Nyquist stability criterion," *International Journal of Control*, 26(3): pp. 325-40, 1977.
- Postlethwaite, I., Edmunds, J. and MacFarlane, A., "Principal gains and principal phases in the analysis of linear multivariable feedback systems," *Automatic Control, IEEE Transactions on*, 26(1): pp. 32-46, 1981.
- Postlethwaite, I. and MacFarlane, A.G.J., "A Complex variable approach to the analysis of linear multivariable feedback systems", vol. 12. Berlin, Germany: *Springer-Verlag*, 1979.
- Rosenbrock, H.H., "Design of multivariable control systems using the inverse Nyquist array," *Instn Elec Engrs-Proc, Nov 1969*, 116(11): pp. 1929-36, 1969.
- Rosenbrock, H.H., "State-space and Multivariable Theory": *Thomas Nelson and Sons LTD*, 1970.
- Rosenbrock, H.H., "The zeros of a system," *International Journal of Control*, 18(2): pp. 297-99, 1973.
- Rosenbrock, H.H., "Corrections to 'the zeros of a system'," *International Journal of Control*, 20(3): pp. 525-527, 1974.
- Rosenbrock, H.H., "Computer-aided control system design". London, UK: *Academic Press*, 1974.

- Sating, R.R., "Development of an analog MIMO Quantitative Feedback Theory (QFT) CAD Package," *Air Force Institute of Technology*, Wright Patterson AFB, OH, AFIT/GE/ENG/92J-04, Ms Thesis, 1992.
- Shaked, U., Horowitz, I. and Golde, S., "Synthesis of multivariable, basically non-interacting systems with significant plant uncertainty.," *Automatica*, 12(1): pp. 61-71, 1976
- Sidi M., "Design of Robust Control Systems: From classical to modern practical approaches". *Krieger Publishing*, 2002.
- Skogestad, S. and Havre, K., "The use of RGA and condition number as robustness measures," *Computers & Chemical Engineering*, 20: pp. S1005-S1010, 1996.
- Skogestad, S. and Morari, M., "Implications of large RGA elements on control performance," *Industrial & Engineering Chemistry Research*, 26(11): pp. 2323-2330, 1987a.
- Skogestad, S. and Morari, M., "Effect of disturbance directions on closed-loop performance.," *Industrial & Engineering Chemistry Research*, 26(10): pp. 2029-2035, 1987b.
- Skogestad, S. and Postlethwaite, I., "Multivariable feedback control. Analysis and design", 2nd Edition ed. Chichester, West Sussex, England: *John Wiley & Sons Ltd.*, 2005.
- Slaby, J. and Rinard, I.H., "Complete interpretation of the dynamic relative gain array.," *American Institute of Chemical Engineers, 1986 Annual Meeting.*, Miami, FL, USA, 1986.
- Stanley, G., Marino-Galarraga, M. and McAvoy, T.J., "Shortcut operability analysis. I. The relative disturbance gain," *Industrial and Engineering Chemistry, Process Design and Development*, 24(4): pp. 1181-8, 1985.
- Van de Wal, M. and de Jager, B., "Control structure design: a survey," *American Control Conference*, 1995.
- Walke, J.G., Horowitz, I.M. and Houppis, C.H., "Quantitative synthesis of highly uncertain, multiple input-output, flight control system for the forward swept wing X-29 aircraft," *IEEE 1984 National Aerospace and Electronics Conference. NAECON 1984* (IEEE Cat. No. 84CH2029-7), 21-25 May 1984, Dayton, OH, USA, 1984.
- Wall, J.E., Doyle, J.C. and Harvey, C.A., "Tradeoffs in the design of multivariable feedback systems," *18th Allerton Conference*, 1980.
- Witcher, M.F. and McAvoy, T.J., "Interacting control systems: steady state and dynamic measurement of interaction," *ISA Transactions*, 16(3): pp. 35-41, 1977.
- Wolovich, W.A., "Linear multivariable systems", vol. 11. New York [etc.]: *Springer-Verlag*, 1974.
- Yu, C.-C. and Fan, M.K.H., "Decentralized integral controllability and D-stability," *Chemical Engineering Science*, 45(11): pp. 3299-3309, 1990.
- Yaniv, O., "MIMO QFT using non-diagonal controllers," *International Journal of Control*, 61(1): pp. 245-253, 1995.
- Yaniv O., "Quantitative Feedback Design of Linear and Non-linear Control Systems". *Kluwer Academic Publishing*, 1999.
- Yaniv, O. and Horowitz, I.M., "A quantitative design method for MIMO linear feedback systems having uncertain plants," *International Journal of Control*, 43(2): pp. 401-421, 1986.

Fuzzy Attitude Control of Flexible Multi-Body Spacecraft

Siliang Yang and Jianli Qin
*Beijing University of Aeronautics and Astronautics,
China*

1. Introduction

In order to complete the flexible multi-body spacecraft attitude control, this chapter will research on the dynamics and attitude control problems of flexible multi-body spacecraft which will be used in the future space missions.

Through investigating plentiful literatures, it is known that some important progress has been obtained in the research of flexible multi-body spacecraft dynamic modeling and fuzzy attitude control technologies. In the aspect of dynamic modeling, most models were founded according to spacecrafts with some special structures. In order to satisfy the requirement of modern project design and optimization, acquire higher efficiency and lower cost, researching on the dynamic modeling problem of flexible multi-body spacecraft with general structures and founding universal and programmable dynamic models are needed.

In the aspect of attitude control system design, the issues encountered in flexible spacecraft have increased the difficulties in attitude control system design, including the high stability and accuracy requirements of orientation, attitude control and vibration suppression, high robustness against the different kinds of uncertain disturbances. At the present time, classical control theory and modern control theory are often used in flexible multi-body spacecraft attitude control. These two methods have one common characteristic which is basing on mathematics models, including control object model and external disturbance model. It is usually considered that the models are already known or could be obtained by identification. But those two methods which are based on accurate math models both have unavoidable defects for large flexible multi-body spacecraft. Until this time, the most advanced and effective control system is the human itself. Therefore, researching on the control theory of human being and simulating the control process is an important domain of intelligent control. If we consider the brain and the nerve center system as a black box, we only investigate the relationship between the inputs and the outputs and the behavior represented from this process, that is called fuzzy control. The fuzzy control doesn't depend on the accurate math models of the original system. It controls the complicated, nonlinear, uncertainty original system through the qualitative cognition of the system dynamic characteristics, intuitional consequence, online determination or changing the control strategies. This control method could more easily be realized and ensured its real time characteristic. It is especially becoming to the control problem of math models unknown, complicated, uncertainty nonlinear system. Accordingly, large flexible multi-body spacecraft attitude control using fuzzy control theory is a problem which is worth researching.

2. Attitude dynamic modeling of flexible multi-body spacecraft

Mathematics model is the basement of most control system design. Dynamic modelling is to describe the real system in physics world using models in mathematics world. Mathematics model provide the mapping from input to response, the coincidence extent between the response and the real object being controlled represent the quality of the model. Mathematics model world is totally different from physics system world, so a real physics object being controlled can not be constructed exactly by mathematics models. Therefore, engineers intend to establish a model which can reflect dynamic characteristics of spacecraft system, as well as the controller design based on the model can be applied into the real system.

In this section, the attitude dynamic equations of flexible multi-body spacecraft with topological tree configuration have been derived based on the Lagrange equations in terms of quasi-coordinates. The dynamic equations are universal and programmable due to the information of system configuration being introduced into the modelling process.

2.1 Description of system configuration

2.1.1 Coordinate system definition

The movement of spacecraft is always described in a reference coordinate, several coordinate systems used in the attitude dynamic modeling process are as follows:

1. Inertial coordinate system $f_i(o_i x_i y_i z_i)$

This inertial frame is defined as its origin at the mass center of the earth, the third axis z_i perpendicular to the Earth's equatorial plane pointing to the arctic, axis x_i and y_i lying in the Earth's equatorial plane, axis x_i pointing to the direction of the vernal equinox, axis y_i forms this coordinate system as a right-handed one.

2. Orbit coordinate system $f_o(o_o x_o y_o z_o)$

Its origin at the mass center of the spacecraft, axis z_o pointing to the geocenter, axis x_o lying in the orbit plane perpendicular to axis z_o , pointing along the direction of spacecraft velocity, axis y_o forms this coordinate system as a right-handed one.

3. Central body coordinate system $f_b(o_b x_b y_b z_b)$

Its origin at the mass center of the spacecraft which has not been deformed, axis x_b pointing along the direction of spacecraft velocity, axis z_b pointing to the geocenter, axis y_b forms this coordinate system as a right-handed one.

4. Floating coordinate system $f_{ai}(o_{ai} x_{ai} y_{ai} z_{ai}), i = 2, 3, \dots, n$

Floating coordinate system is the body frame of the flexible body i , its origin usually at the mass center of the flexible body i which has not been deformed.

5. Gemel coordinate system $f_{ck}(o_{ck} x_{ck} y_{ck} z_{ck})$

Gemel coordinate system is the body frame of the gemel k between the flexible bodies, its origin usually at the connection point between the gemel k and its inboard connected flexible body.

2.1.2 Description of spacecraft system

Considering a flexible multi-body spacecraft with topological tree configuration which contains a central body and $n - 1$ flexible appendages, there are several accesses, objects are connected by gemels, ignoring collision and friction at gemels, access 1 of the system can be shown in figure 1:

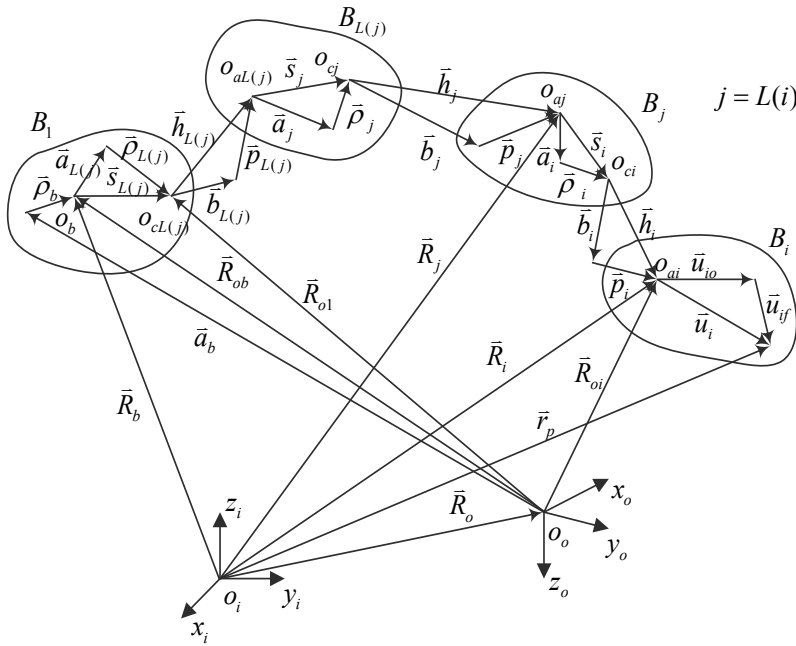


Fig. 1. Access I of flexible multi-body spacecraft system

In this figure, $o_i x_i y_i z_i$ is the inertial frame, $o_o x_o y_o z_o$ is the orbit frame. B_1 is the central body, origin of $o_b x_b y_b z_b$ is at the mass center of the spacecraft which has not been deformed, as well as axes are parallel to the principle axes of inertia. Radius vector \bar{a}_b and $\bar{\rho}_b$ respectively are rigid and flexible displacement of mass center o_b , \bar{R}_{ob} is the radius vector of mass center o_b in orbit coordinate system, $\bar{R}_{ob} = \bar{a}_b + \bar{\rho}_b$. Gemel frames are founded at each gemel h_k , o_{ck} is the origin of gemel coordinate system of h_k , its radius vector in flexible body $B_{L(k)}$ is \bar{s}_k , $\bar{s}_k = \bar{a}_k + \bar{\rho}_k$, \bar{a}_k and $\bar{\rho}_k$ respectively are rigid and flexible displacement of h_k in flexible body $B_{L(k)}$. o_{ak} is the origin of floating coordinate system of object B_k , its radius vector in gemel coordinate system of h_k is \bar{h}_k , $\bar{h}_k = \bar{b}_k + \bar{p}_k$, \bar{b}_k and \bar{p}_k respectively are rigid and flexible displacement of origin o_{ak} in gemel coordinate system of h_k , $k = 2, \dots, n$.

If the central body of the spacecraft system is rigid, the origin of orbit coordinate system is coincident with the origin of central body coordinate system, according to the analysis result of mass matrix (Lu, 1996), choosing frames like this can eliminate the coupling term of rigid body translation and rotation, as well as $\bar{R}_{ob} = \bar{a}_b = \bar{\rho}_b = 0$.

2.2 Description of flexible multi-body system using graph theory

Graph theory (Wittenburg & Roberson, 1977) is a useful tool to describe topological configuration, here several relative concept were given before we using it to do more research.

Oriented graph description: multi-body system can be described using gemel and its adjacent objects, if we express the objects in system using the vertex, express gemels using arc, then topological configuration of multi-body can be expressed as a oriented graph $D = \langle V, A \rangle$. There is a bijection between the collection of vertex V and the collection of objects and also a bijection between the collection of arc A and the collection of gemels. A

description of multi-body system with topological tree configuration using oriented graph is shown in figure 2. H_i represent Gemels, and B_i represent objects.

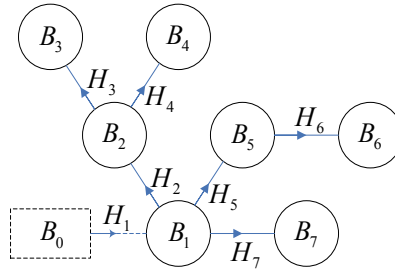


Fig. 2. Description of multi-body system using oriented graph

Regular labelling: Regular labelling approach is specified as follows:

1. The adjacency object of the root object B_0 is defined as B_1 , relative gemel defined as H_1 ;
2. Each object has the same serial number with its inboard connected gemel;
3. Each object has a bigger serial number than its inboard connected object;
4. Each gemel has a deviated direction from the root object B_0 .

Multi-body system shown in figure 2 is numbered in accordance with rules

Inboard connected object array: according to the regular labelling approach, label the N objects of spacecraft system. Define a N order one dimension integer array $L(i)$, $i = 1, \dots, N$, i is the subscript of object B_i , $L(i)$ is the subscript of the inboard connected object of B_i . System topological configuration can be described by array $L(i)$ which is called inboard connected object array of system.

A graph can be conveniently expressed by matrix, its advantage is that structural features and character can be studied using of kinds of operation in matrix algebra.

Access matrix: Supposed that $D = \langle V, A \rangle$ is an oriented graph, $V = \{u_1, u_2, \dots, u_n\}$, name matrix $T = (t_{ij})$ is the access matrix of the oriented graph D , if:

$$t_{ij} = \begin{cases} 1, & \text{when there is a connectivity between } u_j \text{ and } u_i \\ 0, & \text{otherwise} \end{cases} \tag{1}$$

Access matrix of the system with topological tree configuration shown in figure 2 can be written as:

$$T = \begin{bmatrix} 1 & 0 & 0 & 0 & 0 & 0 & 0 \\ 1 & 1 & 0 & 0 & 0 & 0 & 0 \\ 1 & 1 & 1 & 0 & 0 & 0 & 0 \\ 1 & 1 & 0 & 1 & 0 & 0 & 0 \\ 1 & 0 & 0 & 0 & 1 & 0 & 0 \\ 1 & 0 & 0 & 0 & 1 & 1 & 0 \\ 1 & 0 & 0 & 0 & 0 & 0 & 1 \end{bmatrix} \tag{2}$$

2.3 Recursion relationship of adjacency bodies kinematics

Considering the kinematics relationship between flexible body i and flexible body j , $j = L(i)$. According to figure 2, we know that :

$$\vec{R}_i = \vec{R}_j + \vec{s}_i + \vec{h}_i \tag{3}$$

where $\vec{s}_i = \vec{a}_i + \vec{\rho}_i$, $\vec{h}_i = \vec{b}_i + \vec{p}_i$.

The time derivative of equation (3) in inertial coordinate system is obtained as follows :

$$\frac{D\vec{R}_i}{Dt} = \dot{\vec{R}}_i = \dot{\vec{R}}_j + \vec{\omega}_{aj} \times \vec{s}_i + \dot{\vec{\rho}}_i + \vec{\omega}_{ci} \times \vec{h}_i + \dot{\vec{p}}_i, \quad i = 2, 3, \dots, N \tag{4}$$

where $\frac{D(\bullet)}{Dt}$ expresses the time derivative of vector “•” in inertial coordinate system, the “•” and “••” above vectors respectively express the 1-order and 2-order time derivative in their own body coordinate systems. $\vec{\omega}_{aj}$ is the angular velocity vector of the floating coordinate system of flexible body B_j , $\vec{\omega}_{ci}$ is the angular velocity vector of the gemel coordinate system of gemel h_i .

Suppose that the deformation of flexible bodies is always in the range of elastic deformation, translation and rotation modal matrix of gemel h_i respectively are ϕ_{ci} and ψ_{ci} , corresponding modal coordinate is q_{ci} , translation modal matrix of flexible body B_i is ϕ_{ai} , coresponding modal coordinate is q_i , we have:

$$\vec{\rho}_i = \phi_{ci} \vec{q}_{ci}, \quad \vec{p}_i = \phi_{ai} \vec{q}_i, \quad \vec{\omega}_{ci} = \vec{\omega}_{aj} + \psi_{ci} \vec{q}_{ci} \tag{5}$$

Write equation 4 in form of matrix for convenience like:

$$\dot{\vec{R}}_i = \mathbf{i}^T \dot{\vec{R}}_j - \mathbf{a}_j^T \mathbf{s}_i^\times \boldsymbol{\omega}_{aj} + \mathbf{a}_j^T \dot{\vec{\rho}}_i - \mathbf{c}_i^T \mathbf{h}_i^\times \boldsymbol{\omega}_{ci} + \mathbf{c}_i^T \dot{\vec{p}}_i \tag{6}$$

where $\mathbf{i}^T = [\vec{i}_x \quad \vec{i}_y \quad \vec{i}_z]$ is the unit base vector of \mathbf{f}_i ; $\mathbf{a}_j^T = [\vec{a}_{xj} \quad \vec{a}_{yj} \quad \vec{a}_{zj}]$, $j = 2, 3, \dots, N$, is the unit base vector of \mathbf{f}_{aj} ; $\mathbf{c}_i^T = [\vec{c}_{xi} \quad \vec{c}_{yi} \quad \vec{c}_{zi}]$, is the unit base vector of \mathbf{f}_{ci} , $\boldsymbol{\omega}_{aj}$, \mathbf{s}_i and $\dot{\vec{\rho}}_i$ respectively are component column arrays of corresponding vector in \mathbf{f}_{aj} , $\boldsymbol{\omega}_{ci}$, \mathbf{h}_i and \mathbf{p}_i respectively are component column arrays of corresponding vector in \mathbf{f}_{ci} .

Vector equation (5) can be written in form of matrix as follows:

$$\vec{\rho}_i = \mathbf{c}_i^T \phi_{ci} \mathbf{q}_{ci}, \quad \vec{p}_i = \mathbf{a}_i^T \phi_{ai} \mathbf{q}_i, \quad \vec{\omega}_{ci} = \mathbf{a}_j^T (\boldsymbol{\omega}_{aj} + \mathbf{A}_{ajci} \psi_{ci} \mathbf{q}_{ci}) \tag{7}$$

From Eq. (6) and Eq. (7), we obtain

$$\dot{\vec{R}}_i = \mathbf{i}^T \dot{\vec{R}}_j - (\mathbf{a}_j^T \mathbf{s}_i^\times + \mathbf{c}_i^T \mathbf{h}_i^\times \mathbf{A}_{ajci}) \boldsymbol{\omega}_{aj} + \mathbf{c}_i^T \phi_{ci} \dot{\mathbf{q}}_{ci} - \mathbf{c}_i^T \mathbf{h}_i^\times \psi_{ci} \mathbf{q}_{ci} + \mathbf{a}_i^T \phi_{ai} \dot{\mathbf{q}}_i \tag{8}$$

where \mathbf{q}_{ci} is the component column array of corresponding vector in \mathbf{f}_{ci} ; \mathbf{q}_i is the component column array of corresponding vector in \mathbf{f}_{ai} ; \mathbf{A}_{ciaj} is the coordinate conversion matrix from \mathbf{f}_{aj} to \mathbf{f}_{ci} , besides $\mathbf{A}_{ciaj} = \mathbf{A}_{ajci}^T$. For central body B_1 , we have

$$\bar{\mathbf{R}}_b = \bar{\mathbf{R}}_o + \bar{\mathbf{R}}_{ob} = \bar{\mathbf{R}}_o + \bar{\mathbf{a}}_b + \bar{\boldsymbol{\rho}}_b \tag{9}$$

where $\bar{\boldsymbol{\omega}}_o$ is the angular velocity of orbit coordinate system; $\dot{\bar{\boldsymbol{\rho}}}_b = \boldsymbol{\phi}_b^T \dot{\bar{\mathbf{q}}}_b$, $\boldsymbol{\phi}_b$ is the translation modal matrix of the central body, \mathbf{q}_b is the corresponding modal coordinate. Upon that matrix form of absolute velocity vector of the spacecraft can be written as

$$\dot{\bar{\mathbf{R}}}_b = \mathbf{i}^T \dot{\mathbf{R}}_o - \mathbf{i}_o^T \mathbf{R}_{ob}^\times \boldsymbol{\omega}_o + \mathbf{b}^T \boldsymbol{\phi}_b \dot{\mathbf{q}}_b = \mathbf{i}^T \mathbf{v}_o - \mathbf{i}_o^T \mathbf{R}_{ob}^\times \boldsymbol{\omega}_o + \mathbf{b}^T \boldsymbol{\phi}_b \dot{\mathbf{q}}_b \tag{10}$$

where $\mathbf{i}_o^T = [\bar{i}_{ox} \quad \bar{i}_{oy} \quad \bar{i}_{oz}]$ is the unit base vector of orbit coordinate system \mathbf{f}_o ; $\mathbf{b}^T = [\bar{b}_x \quad \bar{b}_y \quad \bar{b}_z]$ is the unit base vector of central body coordinate system \mathbf{f}_b .

From Eq.(8) and Eq. (10), we get

$$\begin{aligned} \dot{\bar{\mathbf{R}}}_i &= \mathbf{i}^T \mathbf{v}_o - \mathbf{i}_o^T \mathbf{R}_{ob}^\times \boldsymbol{\omega}_o + \mathbf{b}^T \boldsymbol{\phi}_b \dot{\mathbf{q}}_b - (\mathbf{b}^T \mathbf{s}_k^\times + \mathbf{c}_k^T \mathbf{h}_k^\times \mathbf{A}_{ckb}) \boldsymbol{\omega}_b + \mathbf{c}_k^T \boldsymbol{\phi}_{ck} \dot{\mathbf{q}}_{ck} - \mathbf{c}_k^T \mathbf{h}_k^\times \boldsymbol{\psi}_{ck} \mathbf{q}_{ck} + \mathbf{a}_k^T \boldsymbol{\phi}_{ak} \dot{\mathbf{q}}_k \\ &+ \sum_{i \in D} \left[-(\mathbf{a}_j^T \mathbf{s}_i^\times + \mathbf{c}_i^T \mathbf{h}_i^\times \mathbf{A}_{ciaj}) \boldsymbol{\omega}_{aj} + \mathbf{c}_i^T \boldsymbol{\phi}_{ci} \dot{\mathbf{q}}_{ci} - \mathbf{c}_i^T \mathbf{h}_i^\times \boldsymbol{\psi}_{ci} \mathbf{q}_{ci} + \mathbf{a}_i^T \boldsymbol{\phi}_{ai} \dot{\mathbf{q}}_i \right] \end{aligned} \tag{11}$$

where k is the serial number of the outboard connected object of the central body B_1 in the access from object B_1 to B_i ; D is the serial number collection of the objects in the access from object B_1 to B_i except for B_1 and its outboard connected object; $j = L(i)$; $\boldsymbol{\omega}_b$ is the component column array of angular velocity of the central body B_1 in \mathbf{f}_b .

If we define that $\mathbf{b}^T = \mathbf{a}_1^T$, $\mathbf{A}_{cib} = \mathbf{A}_{cia1}$, $\boldsymbol{\omega}_b = \boldsymbol{\omega}_{a1}$, then the Eq.(11) can be written in more concise form like:

$$\begin{aligned} \dot{\bar{\mathbf{R}}}_i &= \mathbf{i}^T \mathbf{v}_o - \mathbf{i}_o^T \mathbf{R}_{ob}^\times \boldsymbol{\omega}_o + \mathbf{b}^T \boldsymbol{\phi}_b \dot{\mathbf{q}}_b \\ &+ \sum_{i \in E} \left[-(\mathbf{a}_j^T \mathbf{s}_i^\times + \mathbf{c}_i^T \mathbf{h}_i^\times \mathbf{A}_{ciaj}) \boldsymbol{\omega}_{aj} + \mathbf{c}_i^T \boldsymbol{\phi}_{ci} \dot{\mathbf{q}}_{ci} - \mathbf{c}_i^T \mathbf{h}_i^\times \boldsymbol{\psi}_{ci} \mathbf{q}_{ci} + \mathbf{a}_i^T \boldsymbol{\phi}_{ai} \dot{\mathbf{q}}_i \right] \end{aligned} \tag{12}$$

where i is the serial number collection of objects in the access from object B_1 to B_i except for the central body B_1 .

The projection of the vector $\dot{\bar{\mathbf{R}}}_i$ in the central body coordinate system can be written as:

$$\begin{aligned} (\dot{\bar{\mathbf{R}}}_i)_b &= \mathbf{A}_{bi} \mathbf{v}_o - \mathbf{A}_{bo} \mathbf{R}_{ob}^\times \boldsymbol{\omega}_o + \boldsymbol{\phi}_b \dot{\mathbf{q}}_b \\ &+ \sum_{i \in E} \left[-(\mathbf{A}_{baj} \mathbf{s}_i^\times + \mathbf{A}_{bci} \mathbf{h}_i^\times \mathbf{A}_{ciaj}) \boldsymbol{\omega}_{aj} + \mathbf{A}_{bci} \boldsymbol{\phi}_{ci} \dot{\mathbf{q}}_{ci} - \mathbf{A}_{bci} \mathbf{h}_i^\times \boldsymbol{\psi}_{ci} \mathbf{q}_{ci} + \mathbf{A}_{bai} \boldsymbol{\phi}_{ai} \dot{\mathbf{q}}_i \right] \end{aligned} \tag{13}$$

where \mathbf{A}_{bi} is the coordinate conversion matrix from \mathbf{f}_i to \mathbf{f}_b , besides, $\mathbf{A}_{bi} = \mathbf{A}_{ib}^T$; \mathbf{A}_{bo} is the coordinate conversion matrix from \mathbf{f}_o to \mathbf{f}_b , besides, $\mathbf{A}_{bo} = \mathbf{A}_{ob}^T$; \mathbf{A}_{baj} is the coordinate conversion matrix from \mathbf{f}_{aj} to \mathbf{f}_b , besides, $\mathbf{A}_{baj} = \mathbf{A}_{ajb}^T$; \mathbf{A}_{bci} is the coordinate conversion

matrix from f_{ci} to f_b , besides, $A_{bci} = A_{cib}^T$; A_{bai} is the coordinate conversion matrix from f_{ai} to f_b , besides, $A_{bai} = A_{aib}^T$. We make several definitions as follows:

$$\begin{aligned}
 E_1 &= A_{bi} v_o - A_{bo} R_{ob}^\times \omega_o + \phi \dot{q}_b \\
 E_2 &= [-(A_{baj} s_i^\times + A_{bci} h_i^\times A_{ciaj}) \omega_{aj} + A_{bci} \phi \dot{q}_{ci} - A_{bci} h_i^\times \psi_{ci} q_{ci} + A_{bai} \phi \dot{q}_{ai}]_{i=2} \\
 &\vdots \\
 E_n &= [-(A_{baj} s_i^\times + A_{bci} h_i^\times A_{ciaj}) \omega_{aj} + A_{bci} \phi \dot{q}_{ci} - A_{bci} h_i^\times \psi_{ci} q_{ci} + A_{bai} \phi \dot{q}_{ai}]_{i=n}
 \end{aligned}
 \tag{14}$$

$$E = [E_1 \quad E_2 \quad \dots \quad E_n]^T
 \tag{15}$$

Upon that the origin velocity of arbitrary flexible body coordinate system can be expressed using access matrix as follows:

$$(\dot{R}_i)_b = (T)_i E
 \tag{16}$$

where $(T)_i$ represents the i row of access matrix T .

2.4 Dynamics modeling based on quasi-Lagrange equations

2.4.1 Quasi-Lagrange equations

Quasi-Lagrange equations is a kind of improvement of classical Lagrange equations, on one hand they have the advantage of normalized derivation, on the other hand they can reserve the presentation form of dynamics equations of rigid body. Therefore they are applicable for researching the dynamics problem of large spacecraft. Using quasi-Lagrange equations system dynamics can be expressed as follows:

$$\left\{ \begin{aligned}
 \frac{d}{dt} \left(\frac{\partial L}{\partial v_b} \right) + \omega_b^\times \frac{\partial L}{\partial v_b} &= Q_{bt} \\
 \frac{d}{dt} \left(\frac{\partial L}{\partial \omega_b} \right) + v_b^\times \frac{\partial L}{\partial v_b} + \omega_b^\times \frac{\partial L}{\partial \omega_b} &= Q_{br} \\
 \frac{d}{dt} \left(\frac{\partial L}{\partial \omega_{ai}} \right) + A_{aib} v_i^\times \frac{\partial L}{\partial v_i} + (A_{aib} \omega_b^\times A_{aib}^T + \omega_{ai}^\times) \frac{\partial L}{\partial \omega_{ai}} &= Q_{air} \\
 \frac{d}{dt} \left(\frac{\partial L}{\partial \dot{q}_b} \right) + \frac{d\Phi}{dq_b} - \frac{dL}{dq_b} &= Q_{vb} \\
 \frac{d}{dt} \left(\frac{\partial L}{\partial \dot{q}_i} \right) + \frac{d\Phi}{dq_i} - \frac{dL}{dq_i} &= Q_{vi}
 \end{aligned} \right.
 \tag{17}$$

where L is the Lagrange function of system, $L = T - U$, T is the kinetic energy of system, U is the potential energy of system, Φ is the dissipated energy of system; v_b, ω_b respectively are

the spacecraft central body coordinate system velocity and angular velocity coordinates in $o_b x_b y_b z_b$ relative to the inertial coordinate system; \mathbf{v}_{ai} is the velocity coordinate in $o_b x_b y_b z_b$ of the floating coordinate system of flexible body i relative to the inertial coordinate system; $\boldsymbol{\omega}_{ai}$ is the angular velocity coordinate in $o_b x_b y_b z_b$ of the floating coordinate system of flexible body i relative to the inertial coordinate system; \mathbf{q}_b is the modal coordinate of the central body B_1 ; \mathbf{q}_i is the modal coordinate of the flexible body B_i ; \mathbf{Q}_{bt} is the generalized force corresponding to the translation of spacecraft central body; \mathbf{Q}_{br} is the generalized moment corresponding to the rotation of spacecraft central body; \mathbf{Q}_{air} is the generalized moment corresponding to the rotation of flexible body B_i ; \mathbf{Q}_{vb} is the generalized force corresponding to the modal coordinate \mathbf{q}_b ; \mathbf{Q}_{vi} is the generalized force corresponding to the modal coordinate \mathbf{q}_i ; \mathbf{A}_{aib} is the conversion matrix from $o_b x_b y_b z_b$ to $o_{ai} x_{ai} y_{ai} z_{ai}$; for an arbitrary 3×1 column array $\mathbf{x} = [x_1 \ x_2 \ x_3]^T$, \mathbf{x}^\times represents the skew symmetric matrix as follows:

$$\mathbf{x}^\times = \begin{bmatrix} 0 & -x_3 & x_2 \\ x_3 & 0 & -x_1 \\ -x_2 & x_1 & 0 \end{bmatrix} \quad (18)$$

2.4.2 Lagrange function

Using Lagrange equations to found the system dynamics model, firstly, we should calculate the kinetic energy and potential energy of each body in the system, then add them together in order to get the total kinetic and potential energy of the system, finally obtain the Lagrange function.

2.4.2.1 Kinetic energy of system

The kinetic energy of flexible body i expressed by generalized velocity is as follows:

$$T_i = \frac{1}{2} \mathbf{v}_i^T \mathbf{M}_i \mathbf{v}_i \quad (19)$$

The generalized velocity \mathbf{v}_i in the above formula is defined as:

$$\mathbf{v}_i = \left(\dot{\mathbf{R}}_i^T \quad \boldsymbol{\omega}_{ai}^T \quad \dot{\mathbf{q}}_i \right)^T \quad (20)$$

where $\dot{\mathbf{R}}_i$ is the floating coordinate system origin velocity of the flexible body i ; $\boldsymbol{\omega}_{ai}$ is the floating coordinate system origin angular velocity of the flexible body i ; \mathbf{q}_i is the deformation modal coordinate of the flexible body i . \mathbf{M}_i is the mass matrix of the flexible body i , which is defined as:

$$\mathbf{M}_i = \begin{bmatrix} \mathbf{m}_{RR}^i & \mathbf{m}_{R\omega}^i & \mathbf{m}_{Rf}^i \\ \mathbf{m}_{R\omega}^i & \mathbf{m}_{\omega\omega}^i & \mathbf{m}_{\omega f}^i \\ \mathbf{m}_{Rf}^i & \mathbf{m}_{\omega f}^i & \mathbf{m}_{ff}^i \end{bmatrix} \quad (21)$$

The specific expression of each sub-matrix can be found in reference written by Lu. Upon that the kinetic energy of the flexible body i can be written as follows:

$$T_i = \frac{1}{2} (\dot{\mathbf{R}}_i^T \mathbf{m}_i^i \dot{\mathbf{R}}_i + 2\dot{\mathbf{R}}_i^T \mathbf{m}_{R\omega}^i \boldsymbol{\omega}_{ai} + 2\dot{\mathbf{R}}_i^T \mathbf{m}_{Rf}^i \dot{\mathbf{q}}_i + \boldsymbol{\omega}_{ai}^T \mathbf{m}_{\omega\omega}^i \boldsymbol{\omega}_{ai} + 2\boldsymbol{\omega}_{ai}^T \mathbf{m}_{\omega f}^i \dot{\mathbf{q}}_i + \dot{\mathbf{q}}_i^T \mathbf{m}_{ff}^i \dot{\mathbf{q}}_i) \quad (22)$$

The entire kinetic energy of the system can be expressed as:

$$\begin{aligned} T &= \frac{1}{2} \sum_{i=1}^n (\dot{\mathbf{R}}_i^T \mathbf{m}_i^i \dot{\mathbf{R}}_i + 2\dot{\mathbf{R}}_i^T \mathbf{m}_{R\omega}^i \boldsymbol{\omega}_{ai} + 2\dot{\mathbf{R}}_i^T \mathbf{m}_{Rf}^i \dot{\mathbf{q}}_i + \boldsymbol{\omega}_{ai}^T \mathbf{m}_{\omega\omega}^i \boldsymbol{\omega}_{ai} + 2\boldsymbol{\omega}_{ai}^T \mathbf{m}_{\omega f}^i \dot{\mathbf{q}}_i + \dot{\mathbf{q}}_i^T \mathbf{m}_{ff}^i \dot{\mathbf{q}}_i) \\ &= \frac{1}{2} (\dot{\mathbf{R}}_b^T \mathbf{m}_{RR}^b \dot{\mathbf{R}}_b + 2\dot{\mathbf{R}}_b^T \mathbf{m}_{R\omega}^b \boldsymbol{\omega}_b + 2\dot{\mathbf{R}}_b^T \mathbf{m}_{Rf}^b \dot{\mathbf{q}}_b + \boldsymbol{\omega}_b^T \mathbf{m}_{\omega\omega}^b \boldsymbol{\omega}_b + 2\boldsymbol{\omega}_b^T \mathbf{m}_{\omega f}^b \dot{\mathbf{q}}_b + \dot{\mathbf{q}}_b^T \mathbf{m}_{ff}^b \dot{\mathbf{q}}_b) \\ &\quad + \frac{1}{2} \sum_{i=2}^n (\dot{\mathbf{R}}_i^T \mathbf{m}_i^i \dot{\mathbf{R}}_i + 2\dot{\mathbf{R}}_i^T \mathbf{m}_{R\omega}^i \boldsymbol{\omega}_{ai} + 2\dot{\mathbf{R}}_i^T \mathbf{m}_{Rf}^i \dot{\mathbf{q}}_i + \boldsymbol{\omega}_{ai}^T \mathbf{m}_{\omega\omega}^i \boldsymbol{\omega}_{ai} + 2\boldsymbol{\omega}_{ai}^T \mathbf{m}_{\omega f}^i \dot{\mathbf{q}}_i + \dot{\mathbf{q}}_i^T \mathbf{m}_{ff}^i \dot{\mathbf{q}}_i) \end{aligned} \quad (23)$$

2.4.2.2 Potential and dissipated energy of system

Define p_{bm} is the m^{th} order natural frequency of the central body, then the elastic energy of the central body can be expressed as:

$$U_b = \frac{1}{2} \mathbf{q}_b^T \mathbf{K}_b \mathbf{q}_b \quad (24)$$

where \mathbf{K}_b is the rigidity matrix of the central body, $\mathbf{K}_b = \text{diag}(p_{b1}^2, p_{b2}^2, \dots, p_{bm}^2)$.

Define p_{im} is the m^{th} order natural frequency of the flexible body B_i , then the elastic energy of the flexible body i can be expressed as:

$$U_i = \frac{1}{2} \mathbf{q}_i^T \mathbf{K}_i \mathbf{q}_i \quad (25)$$

where \mathbf{K}_i is the rigidity matrix of the flexible body i , $\mathbf{K}_i = \text{diag}(p_{i1}^2, p_{i2}^2, \dots, p_{im}^2)$.

If we only consider about the deformation energy of the spacecraft structure, the potential energy of the system can be expressed as:

$$U = \frac{1}{2} \mathbf{q}_b^T \mathbf{K}_b \mathbf{q}_b + \sum_{i=2}^n \frac{1}{2} \mathbf{q}_i^T \mathbf{K}_i \mathbf{q}_i = \frac{1}{2} \mathbf{q}_b^T \mathbf{K}_b \mathbf{q}_b + \frac{1}{2} \mathbf{q}_a^T \mathbf{K}_a \mathbf{q}_a \quad (26)$$

where

$$\mathbf{K}_a = \begin{bmatrix} \mathbf{K}_2 & \cdots & \mathbf{0} & \cdots & \mathbf{0} \\ \vdots & \ddots & \vdots & \cdots & \vdots \\ \mathbf{0} & \cdots & \mathbf{K}_i & \cdots & \mathbf{0} \\ \vdots & \cdots & \vdots & \ddots & \vdots \\ \mathbf{0} & \cdots & \mathbf{0} & \cdots & \mathbf{K}_n \end{bmatrix} \quad (27)$$

$$\mathbf{q}_a = \left[\mathbf{q}_2^T \quad \mathbf{q}_3^T \quad \cdots \quad \mathbf{q}_n^T \right]^T \quad (28)$$

Define ξ_{bm} is the damping coefficient corresponding to p_{bm} of the central body B_1 , then the dissipated energy of the central body can be expressed as:

$$\Phi_b = \frac{1}{2} \dot{\mathbf{q}}_b^T \mathbf{D}_b \dot{\mathbf{q}}_b \quad (29)$$

where \mathbf{D}_b is the damping matrix of the central body, $\mathbf{D}_b = \text{diag}(2\xi_{b1}p_{b1}, 2\xi_{b2}p_{b2}, \dots, 2\xi_{bm}p_{bm})$.

Define ξ_{im} is the damping coefficient corresponding to p_{im} of the flexible body B_i , then the dissipated energy of the flexible body B_i can be expressed as:

$$\Phi_i = \frac{1}{2} \dot{\mathbf{q}}_i^T \mathbf{D}_i \dot{\mathbf{q}}_i \quad (30)$$

where \mathbf{D}_i is the damping matrix of the flexible body B_i , $\mathbf{D}_i = \text{diag}(2\xi_{i1}p_{i1}, 2\xi_{i2}p_{i2}, \dots, 2\xi_{im}p_{im})$.

Upon that the dissipated energy of the system can be expressed as:

$$\Phi = \frac{1}{2} \dot{\mathbf{q}}_b^T \mathbf{D}_b \dot{\mathbf{q}}_b + \sum_{i=2}^n \frac{1}{2} \dot{\mathbf{q}}_i^T \mathbf{D}_i \dot{\mathbf{q}}_i = \frac{1}{2} \dot{\mathbf{q}}_b^T \mathbf{D}_b \dot{\mathbf{q}}_b + \frac{1}{2} \dot{\mathbf{q}}_a^T \mathbf{D}_a \dot{\mathbf{q}}_a \quad (31)$$

where

$$\mathbf{D}_a = \begin{bmatrix} \mathbf{D}_2 & \cdots & \mathbf{0} & \cdots & \mathbf{0} \\ \vdots & \ddots & \vdots & \cdots & \vdots \\ \mathbf{0} & \cdots & \mathbf{D}_i & \cdots & \mathbf{0} \\ \vdots & \cdots & \vdots & \ddots & \vdots \\ \mathbf{0} & \cdots & \mathbf{0} & \cdots & \mathbf{D}_n \end{bmatrix} \quad (32)$$

2.4.3 Dynamics equations of the system

2.4.3.1 Translation equations of the central body

$$\frac{\partial L}{\partial \mathbf{v}_b} = (\mathbf{m}_{RR}^b + \sum_{i=2}^n \mathbf{m}_{RR}^i) \mathbf{v}_b + \mathbf{m}_{R\omega}^b \boldsymbol{\omega}_b + \mathbf{m}_{Rf}^b \dot{\mathbf{q}}_b + \sum_{i=2}^n (\mathbf{m}_{R\omega}^i \mathbf{A}_{bai} \boldsymbol{\omega}_i + \mathbf{m}_{Rf}^i \mathbf{A}_{bai} \dot{\mathbf{q}}_i) \quad (33)$$

$$\boldsymbol{\omega}_b^x \frac{\partial L}{\partial \mathbf{v}_b} = \boldsymbol{\omega}_b^x \left[(\mathbf{m}_{RR}^b + \sum_{i=2}^n \mathbf{m}_{RR}^i) \mathbf{v}_b + \mathbf{m}_{R\omega}^b \boldsymbol{\omega}_b + \mathbf{m}_{Rf}^b \dot{\mathbf{q}}_b + \sum_{i=2}^n (\mathbf{m}_{R\omega}^i \mathbf{A}_{bai} \boldsymbol{\omega}_i + \mathbf{m}_{Rf}^i \mathbf{A}_{bai} \dot{\mathbf{q}}_i) \right] \quad (34)$$

$$\begin{aligned} \frac{d}{dt} \left(\frac{\partial L}{\partial \mathbf{v}_b} \right) &= (\mathbf{m}_{RR}^b + \sum_{i=2}^n \mathbf{m}_{RR}^i) \dot{\mathbf{v}}_b + \mathbf{m}_{R\omega}^b \dot{\boldsymbol{\omega}}_b + \mathbf{m}_{Rf}^b \ddot{\mathbf{q}}_b \\ &+ \sum_{i=2}^n \left(\mathbf{m}_{R\omega}^i \dot{\mathbf{A}}_{bai} \boldsymbol{\omega}_{ai} + \mathbf{m}_{R\omega}^i \mathbf{A}_{bai} \dot{\boldsymbol{\omega}}_{ai} + \mathbf{m}_{Rf}^i \dot{\mathbf{A}}_{bai} \dot{\mathbf{q}}_i + \mathbf{m}_{Rf}^i \mathbf{A}_{bai} \ddot{\mathbf{q}}_i \right) \end{aligned} \quad (35)$$

Substitute Eq. (33)-Eq. (35) into the first formula of Eq. (17), the translation equations of the central body is obtained as follows:

$$\begin{aligned} &(\mathbf{m}_{RR}^b + \sum_{i=2}^n \mathbf{m}_{RR}^i) \dot{\mathbf{v}}_b + \mathbf{m}_{R\omega}^b \dot{\boldsymbol{\omega}}_b + \mathbf{m}_{Rf}^b \ddot{\mathbf{q}}_b \\ &+ \sum_{i=2}^n \left(\mathbf{m}_{R\omega}^i \dot{\mathbf{A}}_{bai} \boldsymbol{\omega}_{ai} + \mathbf{m}_{R\omega}^i \mathbf{A}_{bai} \dot{\boldsymbol{\omega}}_{ai} + \mathbf{m}_{Rf}^i \dot{\mathbf{A}}_{bai} \dot{\mathbf{q}}_i + \mathbf{m}_{Rf}^i \mathbf{A}_{bai} \ddot{\mathbf{q}}_i \right) \\ &+ \boldsymbol{\omega}_b^\times \left[(\mathbf{m}_{RR}^b + \sum_{i=2}^n \mathbf{m}_{RR}^i) \mathbf{v}_b + \mathbf{m}_{R\omega}^b \boldsymbol{\omega}_b + \mathbf{m}_{Rf}^b \dot{\mathbf{q}}_b + \sum_{i=2}^n \left(\mathbf{m}_{R\omega}^i \mathbf{A}_{bai} \boldsymbol{\omega}_{ai} + \mathbf{m}_{Rf}^i \mathbf{A}_{bai} \dot{\mathbf{q}}_i \right) \right] = \mathbf{F}_b \end{aligned} \quad (36)$$

2.4.3.2 Rotation equations of the central body

$$\begin{aligned} \frac{\partial L}{\partial \boldsymbol{\omega}_b} &= (\mathbf{A}_{bi} \mathbf{v}_o - \mathbf{A}_{bo} \mathbf{R}_{ob}^\times \boldsymbol{\omega}_o + \boldsymbol{\phi} \dot{\mathbf{q}}_b)^\top \mathbf{m}_{R\omega}^b + \mathbf{m}_{\omega\omega}^b \boldsymbol{\omega}_b + \mathbf{m}_{\omega f}^b \dot{\mathbf{q}}_b \\ &+ \sum_{i=2}^N \left[\mathbf{m}_{RR}^i (\mathbf{T})_i \mathbf{E}(\mathbf{T})_i \frac{\partial \mathbf{E}}{\partial \boldsymbol{\omega}_b} + \mathbf{m}_{R\omega}^i \mathbf{A}_{bai} \boldsymbol{\omega}_{ai} (\mathbf{T})_i \frac{\partial \mathbf{E}}{\partial \boldsymbol{\omega}_b} + \mathbf{m}_{Rf}^i \mathbf{A}_{bai} \dot{\mathbf{q}}_i (\mathbf{T})_i \frac{\partial \mathbf{E}}{\partial \boldsymbol{\omega}_b} \right] \end{aligned} \quad (37)$$

$$\mathbf{v}_b^\times \frac{\partial L}{\partial \mathbf{v}_b} = \mathbf{v}_b^\times \left[(\mathbf{m}_{RR}^b + \sum_{i=2}^n \mathbf{m}_{RR}^i) \mathbf{v}_b + \mathbf{m}_{R\omega}^b \boldsymbol{\omega}_b + \mathbf{m}_{Rf}^b \dot{\mathbf{q}}_b + \sum_{i=2}^n \left(\mathbf{m}_{R\omega}^i \mathbf{A}_{bai} \boldsymbol{\omega}_{ai} + \mathbf{m}_{Rf}^i \mathbf{A}_{bai} \dot{\mathbf{q}}_i \right) \right] \quad (38)$$

$$\begin{aligned} \boldsymbol{\omega}_b^\times \frac{\partial L}{\partial \boldsymbol{\omega}_b} &= \boldsymbol{\omega}_b^\times \left[(\mathbf{A}_{bi} \mathbf{v}_o - \mathbf{A}_{bo} \mathbf{R}_{ob}^\times \boldsymbol{\omega}_o + \boldsymbol{\phi} \dot{\mathbf{q}}_b)^\top \mathbf{m}_{R\omega}^b + \mathbf{m}_{\omega\omega}^b \boldsymbol{\omega}_b + \mathbf{m}_{\omega f}^b \dot{\mathbf{q}}_b \right] \\ &+ \boldsymbol{\omega}_b^\times \left\{ \sum_{i=2}^N \left[\mathbf{m}_{RR}^i (\mathbf{T})_i \mathbf{E}(\mathbf{T})_i \frac{\partial \mathbf{E}}{\partial \boldsymbol{\omega}_b} + \mathbf{m}_{R\omega}^i \mathbf{A}_{bai} \boldsymbol{\omega}_{ai} (\mathbf{T})_i \frac{\partial \mathbf{E}}{\partial \boldsymbol{\omega}_b} + \mathbf{m}_{Rf}^i \mathbf{A}_{bai} \dot{\mathbf{q}}_i (\mathbf{T})_i \frac{\partial \mathbf{E}}{\partial \boldsymbol{\omega}_b} \right] \right\} \end{aligned} \quad (39)$$

$$\begin{aligned} \frac{d}{dt} \left(\frac{\partial L}{\partial \boldsymbol{\omega}_b} \right) &= (\dot{\mathbf{A}}_{bi} \mathbf{v}_o + \mathbf{A}_{bi} \dot{\mathbf{v}}_o - \dot{\mathbf{A}}_{bo} \mathbf{R}_{ob}^\times \boldsymbol{\omega}_o - \mathbf{A}_{bo} \dot{\mathbf{R}}_{ob}^\times \boldsymbol{\omega}_o - \mathbf{A}_{bo} \mathbf{R}_{ob}^\times \dot{\boldsymbol{\omega}}_o + \boldsymbol{\phi} \dot{\mathbf{q}}_b)^\top \mathbf{m}_{R\omega}^b \\ &+ \mathbf{m}_{\omega\omega}^b \dot{\boldsymbol{\omega}}_b + \mathbf{m}_{\omega f}^b \ddot{\mathbf{q}}_b \end{aligned} \quad (40a)$$

$$\begin{aligned}
 & \left[\begin{aligned}
 & m_{RR}^i(T)_i \dot{E}(T)_i \frac{\partial E}{\partial \omega_b} + m_{RR}^i(T)_i E(T)_i \frac{d}{dt} \left(\frac{\partial E}{\partial \omega_b} \right) + m_{R\omega}^i \dot{A}_{bai} \omega_{ai}(T)_i \frac{\partial E}{\partial \omega_b} \\
 & + \sum_{i=2}^N \left[m_{R\omega}^i A_{bai} \dot{\omega}_{ai}(T)_i \frac{\partial E}{\partial \omega_b} + m_{R\omega}^i A_{bai} \omega_{ai}(T)_i \frac{d}{dt} \left(\frac{\partial E}{\partial \omega_b} \right) + m_{Rf}^i \dot{A}_{bai} \dot{q}_i(T)_i \frac{\partial E}{\partial \omega_b} \right. \\
 & \left. + m_{Rf}^i A_{bai} \ddot{q}_i(T)_i \frac{\partial E}{\partial \omega_b} + m_{Rf}^i A_{bai} \dot{q}_i(T)_i \frac{d}{dt} \left(\frac{\partial E}{\partial \omega_b} \right) \right]
 \end{aligned} \right] \quad (40b)
 \end{aligned}$$

Substitute Eq. (37)-Eq. (40) into the second formula of Eq. (17), the rotation equations of the central body is obtained as follows:

$$\begin{aligned}
 & \left(\dot{A}_{bi} v_o + A_{bi} \dot{v}_o - \dot{A}_{bo} R_{ob}^\times \omega_o - A_{bo} \dot{R}_{ob}^\times \omega_o - A_{bo} R_{ob}^\times \dot{\omega}_o + \phi_b \ddot{q}_b \right)^T m_{R\omega}^b + m_{\omega\omega}^b \dot{\omega}_b + m_{\omega f}^b \ddot{q}_b \\
 & + \sum_{i=2}^N \left[\begin{aligned}
 & m_{RR}^i(T)_i \dot{E}(T)_i \frac{\partial E}{\partial \omega_b} + m_{RR}^i(T)_i E(T)_i \frac{d}{dt} \left(\frac{\partial E}{\partial \omega_b} \right) + m_{R\omega}^i \dot{A}_{bai} \omega_{ai}(T)_i \frac{\partial E}{\partial \omega_b} \\
 & + m_{R\omega}^i A_{bai} \dot{\omega}_{ai}(T)_i \frac{\partial E}{\partial \omega_b} + m_{R\omega}^i A_{bai} \omega_{ai}(T)_i \frac{d}{dt} \left(\frac{\partial E}{\partial \omega_b} \right) + m_{Rf}^i \dot{A}_{bai} \dot{q}_i(T)_i \frac{\partial E}{\partial \omega_b} \\
 & + m_{Rf}^i A_{bai} \ddot{q}_i(T)_i \frac{\partial E}{\partial \omega_b} + m_{Rf}^i A_{bai} \dot{q}_i(T)_i \frac{d}{dt} \left(\frac{\partial E}{\partial \omega_b} \right)
 \end{aligned} \right] \\
 & + v_b^\times \left[\left(m_{RR}^b + \sum_{i=2}^n m_{RR}^i \right) v_b + m_{R\omega}^b \omega_b + m_{Rf}^b \dot{q}_b + \sum_{i=2}^n \left(m_{R\omega}^i A_{bai} \omega_{ai} + m_{Rf}^i A_{bai} \dot{q}_i \right) \right] \\
 & + \omega_b^\times \left[\left(A_{bi} v_o - A_{bo} R_{ob}^\times \omega_o + \phi_b \dot{q}_b \right)^T m_{R\omega}^b + m_{\omega\omega}^b \omega_b + m_{\omega f}^b \dot{q}_b \right] \\
 & + \omega_b^\times \left\{ \sum_{i=2}^N \left[m_{RR}^i(T)_i E(T)_i \frac{\partial E}{\partial \omega_b} + m_{R\omega}^i A_{bai} \omega_{ai}(T)_i \frac{\partial E}{\partial \omega_b} + m_{Rf}^i A_{bai} \dot{q}_i(T)_i \frac{\partial E}{\partial \omega_b} \right] \right\} = Q_{br} \quad (41)
 \end{aligned}$$

2.4.3.3 Rotation equations of the flexible body i

$$\begin{aligned}
 \frac{\partial L}{\partial \omega_{ai}} &= A_{aib} [(T)_i E]^T m_{R\omega}^i + m_{\omega\omega}^i \omega_{ai} + m_{\omega f}^i \dot{q}_i \\
 & + A_{aib} \sum_{j=2}^n \left[m_{RR}^j(T)_j E(T)_j \frac{\partial E}{\partial \omega_{ai}} + m_{R\omega}^j A_{baj} \omega_{aj}(T)_j \frac{\partial E}{\partial \omega_{ai}} + m_{Rf}^j A_{baj} \dot{q}_j(T)_j \frac{\partial E}{\partial \omega_{ai}} \right] \quad (42)
 \end{aligned}$$

$$\frac{\partial L}{\partial v_i} = A_{aib} m_{RR}^i(T)_i E + m_{R\omega}^i \omega_{ai} + m_{Rf}^i \dot{q}_i \quad (43)$$

$$\begin{aligned}
 \frac{d}{dt} \left(\frac{\partial L}{\partial \omega_{ai}} \right) &= \dot{A}_{aib} [(T)_i E]^T m_{R\omega}^i + A_{aib} [(T)_i \dot{E}]^T m_{R\omega}^i + m_{\omega\omega}^i \dot{\omega}_{ai} + m_{\omega f}^i \ddot{q}_i \\
 &+ \dot{A}_{aib} \sum_{j=2}^n \left[m_{RR}^j (T)_j E(T)_j \frac{\partial E}{\partial \omega_{ai}} + m_{R\omega}^j A_{baj} \omega_{aj} (T)_j \frac{\partial E}{\partial \omega_{ai}} + m_{Rf}^j A_{baj} \dot{q}_j (T)_j \frac{\partial E}{\partial \omega_{ai}} \right] \\
 &+ A_{aib} \sum_{j=2}^n \left[m_{RR}^j (T)_j \dot{E}(T)_j \frac{\partial E}{\partial \omega_{ai}} + m_{RR}^j (T)_j E(T)_j \frac{d}{dt} \left(\frac{\partial E}{\partial \omega_{ai}} \right) + m_{R\omega}^j \dot{A}_{baj} \omega_{aj} (T)_j \frac{\partial E}{\partial \omega_{ai}} \right. \\
 &\quad \left. + m_{R\omega}^j A_{baj} \dot{\omega}_{aj} (T)_j \frac{\partial E}{\partial \omega_{ai}} + m_{R\omega}^j A_{baj} \omega_{aj} (T)_j \frac{d}{dt} \left(\frac{\partial E}{\partial \omega_{ai}} \right) + m_{Rf}^j \dot{A}_{baj} \dot{q}_j (T)_j \frac{\partial E}{\partial \omega_{ai}} \right. \\
 &\quad \left. + m_{Rf}^j A_{baj} \ddot{q}_j (T)_j \frac{\partial E}{\partial \omega_{ai}} + m_{Rf}^j A_{baj} \dot{q}_j (T)_j \frac{d}{dt} \left(\frac{\partial E}{\partial \omega_{ai}} \right) \right] \tag{44}
 \end{aligned}$$

Substitute Eq. (42)-Eq. (44) into the third formula of Eq. (17), the rotation equations of the flexible body i is obtained as follows:

$$\begin{aligned}
 &\dot{A}_{aib} [(T)_i E]^T m_{R\omega}^i + A_{aib} [(T)_i \dot{E}]^T m_{R\omega}^i + m_{\omega\omega}^i \dot{\omega}_{ai} + m_{\omega f}^i \ddot{q}_i \\
 &+ \dot{A}_{aib} \sum_{j=2}^n \left[m_{RR}^j (T)_j E(T)_j \frac{\partial E}{\partial \omega_{ai}} + m_{R\omega}^j A_{baj} \omega_{aj} (T)_j \frac{\partial E}{\partial \omega_{ai}} + m_{Rf}^j A_{baj} \dot{q}_j (T)_j \frac{\partial E}{\partial \omega_{ai}} \right] \\
 &+ A_{aib} \sum_{j=2}^n \left[m_{RR}^j (T)_j \dot{E}(T)_j \frac{\partial E}{\partial \omega_{ai}} + m_{RR}^j (T)_j E(T)_j \frac{d}{dt} \left(\frac{\partial E}{\partial \omega_{ai}} \right) + m_{R\omega}^j \dot{A}_{baj} \omega_{aj} (T)_j \frac{\partial E}{\partial \omega_{ai}} \right. \\
 &\quad \left. + m_{R\omega}^j A_{baj} \dot{\omega}_{aj} (T)_j \frac{\partial E}{\partial \omega_{ai}} + m_{R\omega}^j A_{baj} \omega_{aj} (T)_j \frac{d}{dt} \left(\frac{\partial E}{\partial \omega_{ai}} \right) + m_{Rf}^j \dot{A}_{baj} \dot{q}_j (T)_j \frac{\partial E}{\partial \omega_{ai}} \right. \\
 &\quad \left. + m_{Rf}^j A_{baj} \ddot{q}_j (T)_j \frac{\partial E}{\partial \omega_{ai}} + m_{Rf}^j A_{baj} \dot{q}_j (T)_j \frac{d}{dt} \left(\frac{\partial E}{\partial \omega_{ai}} \right) \right] \tag{45} \\
 &+ A_{aib} v_i^x \left\{ m_{RR}^i (T)_i E + m_{R\omega}^i A_{bai} \omega_{ai} + m_{Rf}^i A_{bai} \dot{q}_i \right\} \\
 &+ \left(A_{aib} \omega_b^x A_{aib}^T + \omega_{ai}^x \right) \left\{ A_{aib} [(T)_i E]^T m_{R\omega}^i + m_{\omega\omega}^i \omega_{ai} + m_{\omega f}^i \dot{q}_i \right. \\
 &\quad \left. + A_{aib} \sum_{j=2}^n \left[m_{RR}^j (T)_j E(T)_j \frac{\partial E}{\partial \omega_{ai}} + m_{R\omega}^j A_{baj} \omega_{aj} (T)_j \frac{\partial E}{\partial \omega_{ai}} \right. \right. \\
 &\quad \left. \left. + m_{Rf}^j A_{baj} \dot{q}_j (T)_j \frac{\partial E}{\partial \omega_{ai}} \right] \right\} = Q_{air}
 \end{aligned}$$

2.4.3.4 Vibration equations of the central body

$$\begin{aligned} \frac{\partial L}{\partial \dot{\mathbf{q}}_b} &= \mathbf{m}_{RR}^b (\mathbf{A}_{bi} \mathbf{v}_o - \mathbf{A}_{bo} \mathbf{R}_{ob}^\times \boldsymbol{\omega}_o + \boldsymbol{\phi} \dot{\mathbf{q}}_b) \boldsymbol{\phi} + \mathbf{m}_{R\omega}^b \boldsymbol{\omega}_b \boldsymbol{\phi} + \mathbf{m}_{Rf}^b \dot{\mathbf{q}}_b \boldsymbol{\phi} \\ &+ (\mathbf{A}_{bi} \mathbf{v}_o - \mathbf{A}_{bo} \mathbf{R}_{ob}^\times \boldsymbol{\omega}_o + \boldsymbol{\phi} \dot{\mathbf{q}}_b)^\top \mathbf{m}_{Rf}^b + \boldsymbol{\omega}_b^\top \mathbf{m}_{\omega f}^b + \mathbf{m}_{ff}^b \dot{\mathbf{q}}_b \\ &+ \sum_{i=2}^n \left[\mathbf{m}_{RR}^i (\mathbf{T})_i \mathbf{E} \boldsymbol{\phi} + \mathbf{m}_{R\omega}^i \mathbf{A}_{bai} \boldsymbol{\omega}_{ai} \boldsymbol{\phi} + \mathbf{m}_{Rf}^i \mathbf{A}_{bai} \dot{\mathbf{q}}_i \boldsymbol{\phi} \right] \end{aligned} \quad (46)$$

$$\begin{aligned} \frac{d}{dt} \left(\frac{\partial L}{\partial \dot{\mathbf{q}}_b} \right) &= \mathbf{m}_{RR}^b (\dot{\mathbf{A}}_{bi} \mathbf{v}_o + \mathbf{A}_{bi} \dot{\mathbf{v}}_o - \dot{\mathbf{A}}_{bo} \mathbf{R}_{ob}^\times \boldsymbol{\omega}_o - \mathbf{A}_{bo} \dot{\mathbf{R}}_{ob}^\times \boldsymbol{\omega}_o - \mathbf{A}_{bo} \mathbf{R}_{ob}^\times \dot{\boldsymbol{\omega}}_o + \boldsymbol{\phi} \ddot{\mathbf{q}}_b) \boldsymbol{\phi} \\ &+ (\dot{\mathbf{A}}_{bi} \mathbf{v}_o + \mathbf{A}_{bi} \dot{\mathbf{v}}_o - \dot{\mathbf{A}}_{bo} \mathbf{R}_{ob}^\times \boldsymbol{\omega}_o - \mathbf{A}_{bo} \dot{\mathbf{R}}_{ob}^\times \boldsymbol{\omega}_o - \mathbf{A}_{bo} \mathbf{R}_{ob}^\times \dot{\boldsymbol{\omega}}_o + \boldsymbol{\phi} \ddot{\mathbf{q}}_b)^\top \mathbf{m}_{Rf}^b \\ &+ \sum_{i=2}^n \left[\mathbf{m}_{RR}^i (\mathbf{T})_i \dot{\mathbf{E}} \boldsymbol{\phi} + \mathbf{m}_{R\omega}^i \dot{\mathbf{A}}_{bai} \boldsymbol{\omega}_{ai} \boldsymbol{\phi} + \mathbf{m}_{R\omega}^i \mathbf{A}_{bai} \dot{\boldsymbol{\omega}}_{ai} \boldsymbol{\phi} + \mathbf{m}_{Rf}^i \dot{\mathbf{A}}_{bai} \dot{\mathbf{q}}_i \boldsymbol{\phi} + \mathbf{m}_{Rf}^i \mathbf{A}_{bai} \ddot{\mathbf{q}}_i \boldsymbol{\phi} \right] \\ &+ \mathbf{m}_{R\omega}^b \dot{\boldsymbol{\omega}}_b \boldsymbol{\phi} + \mathbf{m}_{Rf}^b \ddot{\mathbf{q}}_b \boldsymbol{\phi} + \dot{\boldsymbol{\omega}}_b^\top \mathbf{m}_{\omega f}^b + \mathbf{m}_{ff}^b \ddot{\mathbf{q}}_b \end{aligned} \quad (47)$$

$$\frac{d\Phi}{d\dot{\mathbf{q}}_b} = \mathbf{D}_b \dot{\mathbf{q}}_b \quad (48)$$

$$\frac{dL}{dq_b} = -\mathbf{K}_b q_b \quad (49)$$

Substitute Eq. (46)-Eq. (49) into the fourth formula of Eq. (17), the vibration equations of the central body is obtained as follows:

$$\begin{aligned} &\mathbf{m}_{RR}^b (\dot{\mathbf{A}}_{bi} \mathbf{v}_o + \mathbf{A}_{bi} \dot{\mathbf{v}}_o - \dot{\mathbf{A}}_{bo} \mathbf{R}_{ob}^\times \boldsymbol{\omega}_o - \mathbf{A}_{bo} \dot{\mathbf{R}}_{ob}^\times \boldsymbol{\omega}_o - \mathbf{A}_{bo} \mathbf{R}_{ob}^\times \dot{\boldsymbol{\omega}}_o + \boldsymbol{\phi} \ddot{\mathbf{q}}_b) \boldsymbol{\phi} \\ &+ (\dot{\mathbf{A}}_{bi} \mathbf{v}_o + \mathbf{A}_{bi} \dot{\mathbf{v}}_o - \dot{\mathbf{A}}_{bo} \mathbf{R}_{ob}^\times \boldsymbol{\omega}_o - \mathbf{A}_{bo} \dot{\mathbf{R}}_{ob}^\times \boldsymbol{\omega}_o - \mathbf{A}_{bo} \mathbf{R}_{ob}^\times \dot{\boldsymbol{\omega}}_o + \boldsymbol{\phi} \ddot{\mathbf{q}}_b)^\top \mathbf{m}_{Rf}^b \\ &+ \sum_{i=2}^n \left[\mathbf{m}_{RR}^i (\mathbf{T})_i \dot{\mathbf{E}} \boldsymbol{\phi} + \mathbf{m}_{R\omega}^i \dot{\mathbf{A}}_{bai} \boldsymbol{\omega}_{ai} \boldsymbol{\phi} + \mathbf{m}_{R\omega}^i \mathbf{A}_{bai} \dot{\boldsymbol{\omega}}_{ai} \boldsymbol{\phi} + \mathbf{m}_{Rf}^i \dot{\mathbf{A}}_{bai} \dot{\mathbf{q}}_i \boldsymbol{\phi} + \mathbf{m}_{Rf}^i \mathbf{A}_{bai} \ddot{\mathbf{q}}_i \boldsymbol{\phi} \right] \\ &+ \mathbf{m}_{R\omega}^b \dot{\boldsymbol{\omega}}_b \boldsymbol{\phi} + \mathbf{m}_{Rf}^b \ddot{\mathbf{q}}_b \boldsymbol{\phi} + \dot{\boldsymbol{\omega}}_b^\top \mathbf{m}_{\omega f}^b + \mathbf{m}_{ff}^b \ddot{\mathbf{q}}_b + \mathbf{D}_b \dot{\mathbf{q}}_b + \mathbf{K}_b q_b = \mathbf{Q}_{vb} \end{aligned} \quad (50)$$

2.4.3.5 Vibration equations of the flexible body i

$$\begin{aligned} \frac{\partial L}{\partial \dot{\mathbf{q}}_i} &= \mathbf{A}_{aib} \sum_{j=2}^n \left[\mathbf{m}_{RR}^j (\mathbf{T})_j \mathbf{E} (\mathbf{T})_j \frac{\partial \mathbf{E}}{\partial \dot{\mathbf{q}}_i} + \mathbf{m}_{R\omega}^j \mathbf{A}_{baj} \boldsymbol{\omega}_{aj} (\mathbf{T})_j \frac{\partial \mathbf{E}}{\partial \dot{\mathbf{q}}_i} + \mathbf{m}_{Rf}^j \mathbf{A}_{baj} \dot{\mathbf{q}}_j (\mathbf{T})_j \frac{\partial \mathbf{E}}{\partial \dot{\mathbf{q}}_i} \right] \\ &+ \mathbf{A}_{aib} [(\mathbf{T})_i \mathbf{E}]^\top \mathbf{m}_{Rf}^i + \boldsymbol{\omega}_{ai}^\top \mathbf{m}_{\omega f}^i + \mathbf{m}_{ff}^i \dot{\mathbf{q}}_i \end{aligned} \quad (51)$$

$$\begin{aligned}
\frac{d}{dt} \left(\frac{\partial L}{\partial \dot{q}_i} \right) &= \dot{A}_{aib} \sum_{j=2}^n \left[m_{RR}^j(T)_j E(T)_j \frac{\partial E}{\partial \dot{q}_i} + m_{R\omega}^j A_{baj} \omega_{aj}(T)_j \frac{\partial E}{\partial \dot{q}_i} + m_{Rf}^j A_{baj} \dot{q}_j(T)_j \frac{\partial E}{\partial \dot{q}_i} \right] \\
&+ A_{aib} \sum_{j=2}^n \left[m_{RR}^j(T)_j \dot{E}(T)_j \frac{\partial E}{\partial \dot{q}_i} + m_{RR}^j(T)_j E(T)_j \frac{d}{dt} \left(\frac{\partial E}{\partial \dot{q}_i} \right) + m_{R\omega}^j \dot{A}_{baj} \omega_{aj}(T)_j \frac{\partial E}{\partial \dot{q}_i} \right. \\
&+ m_{R\omega}^j A_{baj} \dot{\omega}_{aj}(T)_j \frac{\partial E}{\partial \dot{q}_i} + m_{R\omega}^j A_{baj} \omega_{aj}(T)_j \frac{d}{dt} \left(\frac{\partial E}{\partial \dot{q}_i} \right) + m_{Rf}^j \dot{A}_{baj} \dot{q}_j(T)_j \frac{\partial E}{\partial \dot{q}_i} \\
&\left. + m_{Rf}^j A_{baj} \ddot{q}_j(T)_j \frac{\partial E}{\partial \dot{q}_i} + m_{Rf}^j A_{baj} \dot{q}_j(T)_j \frac{d}{dt} \left(\frac{\partial E}{\partial \dot{q}_i} \right) \right] \\
&+ \dot{A}_{aib} [(T)_i E]^T m_{Rf}^i + A_{aib} [(T)_i \dot{E}]^T m_{Rf}^i + \dot{\omega}_{ai}^T m_{\omega f}^i + m_{ff}^i \ddot{q}_i
\end{aligned} \tag{52}$$

$$\frac{d\Phi}{d\dot{q}_i} = D_i \dot{q}_i \tag{53}$$

$$\frac{dL}{dq_i} = -K_i q_i \tag{54}$$

Substitute Eq. (51)-Eq. (54) into the fifth formula of Eq. (17), the vibration equations of the flexible body i is obtained as follows:

$$\begin{aligned}
&\dot{A}_{aib} \sum_{j=2}^n \left[m_{RR}^j(T)_j E(T)_j \frac{\partial E}{\partial \dot{q}_i} + m_{R\omega}^j A_{baj} \omega_{aj}(T)_j \frac{\partial E}{\partial \dot{q}_i} + m_{Rf}^j A_{baj} \dot{q}_j(T)_j \frac{\partial E}{\partial \dot{q}_i} \right] \\
&+ A_{aib} \sum_{j=2}^n \left[m_{RR}^j(T)_j \dot{E}(T)_j \frac{\partial E}{\partial \dot{q}_i} + m_{RR}^j(T)_j E(T)_j \frac{d}{dt} \left(\frac{\partial E}{\partial \dot{q}_i} \right) + m_{R\omega}^j \dot{A}_{baj} \omega_{aj}(T)_j \frac{\partial E}{\partial \dot{q}_i} \right. \\
&+ m_{R\omega}^j A_{baj} \dot{\omega}_{aj}(T)_j \frac{\partial E}{\partial \dot{q}_i} + m_{R\omega}^j A_{baj} \omega_{aj}(T)_j \frac{d}{dt} \left(\frac{\partial E}{\partial \dot{q}_i} \right) + m_{Rf}^j \dot{A}_{baj} \dot{q}_j(T)_j \frac{\partial E}{\partial \dot{q}_i} \\
&\left. + m_{Rf}^j A_{baj} \ddot{q}_j(T)_j \frac{\partial E}{\partial \dot{q}_i} + m_{Rf}^j A_{baj} \dot{q}_j(T)_j \frac{d}{dt} \left(\frac{\partial E}{\partial \dot{q}_i} \right) \right] \\
&+ \dot{A}_{aib} [(T)_i E]^T m_{Rf}^i + A_{aib} [(T)_i \dot{E}]^T m_{Rf}^i + \dot{\omega}_{ai}^T m_{\omega f}^i + m_{ff}^i \ddot{q}_i + D_i \dot{q}_i + K_i q_i = Q_{vi}
\end{aligned} \tag{55}$$

2.4.4 Acquisition of generalized extraneous force

In order to acquire the explicit equations of the system dynamics, we need to express the generalized force in Lagrange equations (17) by actual force and moment. Assuming that the column array in f_b of actual force and moment on the central body respectively are F_b and T_b , the column array in f_{ai} of the driving moment on the gemel is T_{ai} , the column array

in f_{ai} of the distributed force on the flexible appendages is F_{ai} . Calculate the generalized extraneous force according to the principle of virtual work, we firstly obtain the virtual displacement in f_b of an arbitrary volum differential element dV_{ai} in flexible body B_i as follows:

$$\begin{aligned} \delta R_{ai} &= A_{bi} \delta R_b - (R_{bai}^\times + A_{bai} R_{ai}^\times A_{aib} + A_{bai} u_{ai}^\times A_{aib}) \delta \varphi_b \\ &\quad - A_{bai} (R_{ai}^\times + u_{ai}^\times) \delta \varphi_{ai} + \phi_b \delta q_b + A_{bak} \phi_{ak} \delta q_{ak} \end{aligned} \tag{56}$$

where R_{bai} is the component column array in f_b of the position vector from o_b to o_{ai} ; R_{ai} is the component column array in f_{ai} of the position vector from o_{ai} when the flexible body B_i has not been deformed to the mass differential element dm_{ai} ; u_{ai} is the component column array in f_{ak} of the elastic displacement vector of the mass differential element dm_{ai} ; $\delta R_b, \delta \varphi_b, \delta \varphi_{ai}, \delta q_b$ and δq_{ai} are the virtual displacements of the generalized coordinates. The virtual work of the system expressed by actual force and moment can be written as:

$$\begin{aligned} \delta W &= F_b^\top A_{bi} \delta R_b + T_b^\top \delta \varphi_b + \sum_{i=2}^n T_{ai}^\top \delta \varphi_{ai} + F_b^\top \phi_b \delta q_b + \sum_{i=2}^n \int_{ai} (A_{bai} F_{ai})^\top \delta R_{ai} dV_{ai} \\ &= F_b^\top A_{bi} \delta R_b + T_b^\top \delta \varphi_b + \sum_{i=2}^n T_{ai}^\top \delta \varphi_{ai} + F_b^\top \phi_b \delta q_b + \sum_{i=2}^n \int_{ai} (A_{bai} F_{ai})^\top [A_{bi} \delta R_b \\ &\quad - (R_{bai}^\times + A_{bai} R_{ai}^\times A_{aib} + A_{bai} u_{ai}^\times A_{aib}) \delta \varphi_b - A_{bai} (R_{ai}^\times + u_{ai}^\times) \delta \varphi_{ai} + \phi_b \delta q_b + A_{bai} \phi_{ai} \delta q_{ai}] dV_{ai} \\ &= Q_{bt}^\top \delta R_b + Q_{br}^\top \delta \varphi_b + \sum_{i=1}^N Q_{air}^\top \delta \varphi_{ai} + Q_{vb}^\top \delta q_b + \sum_{i=1}^N Q_{vi}^\top \delta q_{ai} \end{aligned} \tag{57}$$

From Eq. (57), we can obtain the expression of the generalized extraneous force as follows:

$$Q_{bt} = A_{ib} F_b + \sum_{i=2}^n \int_{ai} A_{lai} F_{ai} dV_{ai} \tag{58}$$

$$Q_{br} = T_b + \sum_{i=2}^n \int_{ai} (R_{bai}^\times A_{bai} + A_{bai} R_{ai}^\times + A_{bai} u_{ai}^\times) F_{ai} dV_{ai} \tag{59}$$

$$Q_{air} = T_{ai} + \int_{ai} (R_{ai}^\times + u_{ai}^\times) F_{ai} dV_{ai} \tag{60}$$

$$Q_{vb} = F_b^\top \phi_b + \sum_{i=2}^n \int_{ai} \phi_b^\top F_{ai} dV_{ai} \tag{61}$$

$$Q_{vi} = \int_{ai} \phi_{ai}^\top F_{ai} dV_{ai} \tag{62}$$

3. Design and analysis of variable universe fractal fuzzy controller

After several decades of effort, we have achieved great success in terms of the research on the attitude control of flexible multi-body spacecraft. However, it still need to base on the precise mathematical model. On one hand, this kind of spacecraft has complicated dynamics characteristics including low rigidity, high flexibility, weak damping, low first order and intensive modal due to the launch weight limit and the configuration symmetry; On the other hand, it is difficult to establish the precise mathematical of flexible multi-body spacecraft. All about these factors challenge the classical and modern control theory which depends on precise mathematical model. However, the fuzzy control theory does not need the accurate model of system, which is suitable for the control problem of complicated large system. Nevertheless, the main disadvantages of general fuzzy control are the limited control accuracy and adaptive ability. Upon that, fuzzy control theory only has a few applications in astrospace fields.

Variable universe fuzzy control is a primary method for improving the performance of the fuzzy controller (Li, 1995). Input and output variables values change in rationally in the variable universe fuzzy control system. Adaptive variable universe fuzzy control problems have already been researched on (Si & Li, 2007). In that research real-time calculating shrinkage parameters are applied. However, real-time calculation of the shrinkage parameters will lead to the real-time shrinkage of the universe, consequently it can not constrain the future input signals by rules, which practicality requires future research.

Aiming at this problem, variable universe fractal fuzzy control method is introduced into the fuzzy control system, which could avoid the real-time calculating of the shrinkage parameters, make the contracted universe practical.

3.1 Attitude dynamics simulation model of spacecraft system

The dynamics equations of flexible multi-body spacecraft with topological tree configuration obtained in section 2 is strongly nonlinear. In this section we only research on the spacecraft attitude control problems. In order to design the attitude controller conveniently, we usually form such hypotheses as follows:

1. Consider the central body of large complicated configuration flexible spacecraft as rigid.
2. The central body coordinate system has its origin at the mass centre, so the displacement and velocity of the mass centre has little effect on attitude of spacecraft.
3. There is not any distributed control force on the flexible appendages usually in project.
4. The angular velocity of the central body, the angular velocity of the flexible appendages relative to the central body and the vibration velocity of the flexible appendages usually are very small, so we could ignore the high order nonlinear coupling item caused by them.

Through all above simplification, we obtain the finally spacecraft dynamics equations with uncertain moment of inertial as follows:

$$\begin{aligned} (I + \Delta I) \dot{\omega} + \omega^\times [(I + \Delta I) \omega + C\dot{\eta}] + C\ddot{\eta} &= u + w \\ \ddot{\eta} + D\dot{\eta} + K\eta + C^T \dot{\omega} &= 0 \end{aligned} \quad (63)$$

where I is the moment of inertial matrix of spacecraft; ΔI is the uncertain increment of moment of inertial caused by rotation of the solar panel; C is the coupling coefficient

between the central body and the flexible appendages; u is the control torque of three axes; η is the disturbing torque; ξ is the flexible modal coordinate; $D = 2\xi\Lambda$, $K = \Lambda^2$, ξ is the modal damping coefficient matrix of flexible appendages, Λ is the modal frequency matrix of flexible appendages, assume that D and K are both positive.

In order to avoid the large angle singular problem caused by using Euler angle, we adopt Modified Rodrigues Parameters (Crassidis & Markley, 1996) to describe the spacecraft kinematics as follows:

$$\dot{p} = \frac{1}{4} \left\{ (1 - p^T p) I_{3 \times 3} + 2(p^\times + pp^T) \right\} \omega = F(p)\omega \tag{64}$$

where $\omega = [\omega_1 \ \omega_2 \ \omega_3]^T$ is the angular velocity of spacecraft; $p = [p_1 \ p_2 \ p_3]^T$ is Modified Rodrigues Parameters of spacecraft relative to inertial space, p^\times represent the skew-symmetric matrix of vector p .

From the flexible spacecraft dynamics and kinematics equations we know that the rigid attitude motion and the flexible vibration interact with each other. On one hand, extraneous force makes the attitude changed, at the same time, it also cause the flexible deformation. On the other hand, any deformation of the flexible body could cause the attitude angular changes. Otherwise, there is also some disturbing torque directly influence the rigid attitude motion, such as gravity gradient moments, atmosphere resistance moments, solar pressure moments and geomagnetic moments. Upon that, in order to ensure the attitude control accuracy, the designed controller is supposed to have the ability to suppress the disturbance efficiently and have the adaptation in the interaction between the rigid and flexible bodies.

3.2 Variable universe fractal attitude fuzzy controller

3.2.1 Variable universe fuzzy controller

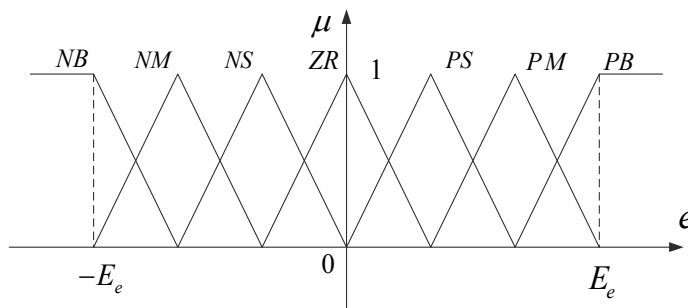


Fig. 3. Initial universe and fuzzy division

Variable universe ideology is proposed by Professor Li H. X. firstly. The control effect could be improved by changing the input and output universe values reasonably. Take the two inputs and one output fuzzy control system as an example. Assuming that the input variable is $\vec{e} = [e \ \dot{e}]^T$, which has the initial universe as $[-E_e, E_e]$ and $[-E_{ec}, E_{ec}]$, E_e, E_{ec} are real numbers. Usually we use seven rules to divide the universe as figure 3, variable universe means that the input universe $\vec{E} = (E_e, E_{ec})$ and the output universe U of the fuzzy controller could adjust reasonably with the changing of the input \vec{e} and the

output u . Among recent researches, this kind of universe adjustment is realised by using shrinkage parameters:

$$\begin{aligned} E_i(\bar{e}) &= [-\alpha_i(\bar{e})E_i^0, \alpha_i(\bar{e})E_i^0] \\ U(u) &= [-\beta(u)U_0, \beta(u)U_0] \end{aligned} \tag{65}$$

where $\alpha_i(\bar{e})$ and $\beta(u)$ are called shrinkage parameters. By the effect of the shrinkage parameters, the expansion and compression of the universe can be shown as figure 4:

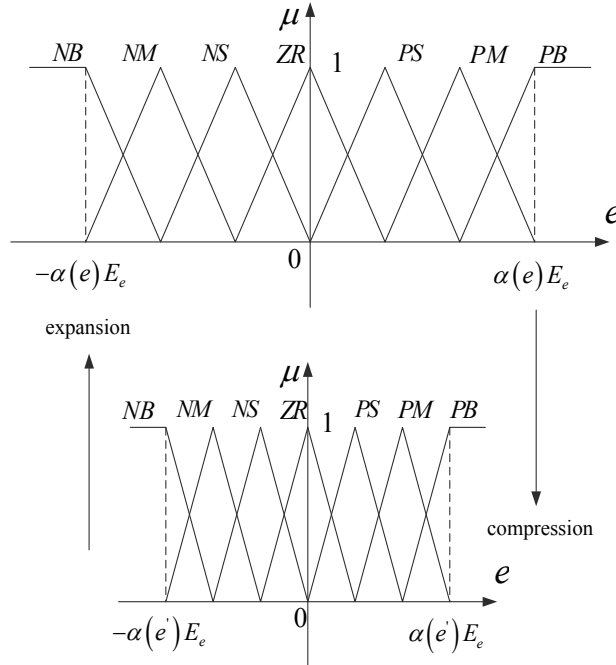


Fig. 4. The expansion and compression of the universe

Several common shrinkage parameters of variable universe control are given as follows:

1. Proportion index form

$$\begin{aligned} \alpha(e) &= (|e| / E_e)^\tau, (0 < \tau < 1) \\ \beta(e, \dot{e}) &= \left(\frac{|e|}{E_e}\right)^{\tau_1} \left(\frac{|\dot{e}|}{E_{ec}}\right)^{\tau_2} \text{ 或 } \beta(e, \dot{e}) = \frac{1}{2} \left[\left(\frac{|e|}{E_e}\right)^{\tau_1} + \left(\frac{|\dot{e}|}{E_{ec}}\right)^{\tau_2} \right], (0 < \tau_1, \tau_2 < 1) \end{aligned} \tag{66}$$

2. Natural index form

$$\begin{aligned} \alpha(e) &= 1 - \exp(-k_1 e^2) \\ \beta(\dot{e}) &= 1 - \exp(-k_2 \dot{e}^2) \end{aligned} \tag{67}$$

3. Modified natural index form

$$\begin{aligned}\alpha(e) &= 1 - c_1 \exp(-k_1 e^2), (0 < c_1 < 1) \\ \beta(\dot{e}) &= 1 - c_2 \exp(-k_2 \dot{e}^2), (0 < c_2 < 1)\end{aligned}\quad (68)$$

There is some research on the efficiency of several kinds of shrinkage parameters in the literature written by Pan X. F. The conclusion is that these several kinds of common shrinkage parameters can not improve the fuzzy controller performance efficiently. In order to avoid the real-time contracting problem of universe, we try to introduce the fractal control strategy into the variable universe fuzzy control system.

3.2.2 Fractal control strategy

A kind of fractal control strategy has been proposed by literature written by Xu J. B., which is formulated beforehand, and has only finite times fractal. Therefore, it can not obtain high interpolation accuracy.

The improved fractal control strategy in our research is proposed as follows:

First of all, define the initial universe of the inputs e, \dot{e} and output u as $[-E_{e0}, E_{e0}]$, $[-E_{\dot{e}0}, E_{\dot{e}0}]$ and $[-U_0, U_0]$ according to experience. Through the process of the program operation, when $\dot{e} = 0$, namely when the error e achieves extreme value, system has one time fractal automatically, make the absolute value of present error e_1 as the present universe of input variable e , written as:

$$[-E_{e1}, E_{e1}] = [-|e_1|, |e_1|] \quad (69)$$

The universe of error derivation can be written as:

$$[-E_{\dot{e}1}, E_{\dot{e}1}] = \left[-\frac{c_{ec} |e_1| E_{\dot{e}0}}{E_{e0}}, \frac{c_{ec} |e_1| E_{\dot{e}0}}{E_{e0}} \right] \quad (70)$$

The universe of output variable can be written as:

$$[-U_1, U_1] = \left[-\frac{c_u |e_1| U_0}{E_{e0}}, \frac{c_u |e_1| U_0}{E_{e0}} \right] \quad (71)$$

The subscript 1 in above formulas represent the first time fractal, c_{ec} and c_u are adjustable design parameters. After the fractal the program continue running until $\dot{e} = 0$ happens again, system has the second time fractal. Write the present error as e_2 , the universe of input and output variable respectively adjust as follows:

$$[-E_{e_2}, E_{e_2}] = [-|e_2|, |e_2|] \quad (72)$$

$$[-E_{ec_2}, E_{ec_2}] = \left[-\frac{c_{ec} |e_2| E_{ec1}}{E_{e1}}, \frac{c_{ec} |e_2| E_{ec1}}{E_{e1}} \right] \quad (73)$$

$$[-U_2, U_2] = \left[-\frac{c_u |e_2| U_1}{E_{e1}}, \frac{c_u |e_2| U_1}{E_{e1}} \right] \quad (74)$$

To this analogize, through the process of the program operation, system will has infinite times fractal until the accuracy satisfies the requirement.

This fractal strategy has advantages in following aspects:

1. The time to have a fractal and the expansion and compression scale of universe are determined according to the variation of input error value, not chosen beforehand by person, so it has a certain degree of universality to different control systems.
2. Infinite times of fratal makes the distance between the interpolation points of the interpolator as the mathematical essence of fuzzy controller enough small, therefore the interpolation precision could meet an arbitrary given $\varepsilon > 0$, achieve the effect of dynamic pointwise convergent interpolator, suitable for any high precision control problems.
3. The universe variation of the error derivation and the output variable are related to the universe expansion and compression of the error. Under the same control rules, multistage microform of the overall control information is realised, truly achieve the effect of combining the multistage coarse control with the fine control. Avoiding the complicated derivation of adaptive law and provement of stability in adaptive controllers, the stable high precision control with a certain degree of robustness can also be accomplished by using this approach.

3.3 Numerical simulation

In order to demonstrate the effectiveness of the proposed control strategy, we discuss a large angle attitude maneuver problem of a flexible multi-body spacecraft. We supposed that the spacecraft initial attitude is $p_0 = [0.020 \quad 0.322 \quad 0.288]^T$, and the target attitude is $p_t = [0 \quad 0 \quad 0]^T$. If the attitude is expressed by Euler angles with the transform order as 3-2-1, the initial roll is $\varphi_0 = 35^\circ$, the initial pitch is $\theta_0 = 60^\circ$, the initial yaw is $\psi_0 = 50^\circ$, the target attitude is $\varphi_t = \theta_t = \psi_t = 0^\circ$. The initial angular velocity is chosen as $\omega_0 = [0.03 \quad 0.02 \quad 0.04]^T / s$. The initial modal coordinate and its derivation are supposed to be zero. Spacefrat moment of inertial I , coupling coefficient matrix between the central body and the flexible appendages C , modal damping coefficient matrix of flexible appendages ξ , modal frequency matrix of flexible appendages Λ are given in Table 1 as below:

Moment of inertial I ($kg \cdot m^2$)	$\begin{bmatrix} 1070000 & -25000 & -1700 \\ -25000 & 29200 & -3100 \\ -1700 & -3100 & 1080000 \end{bmatrix}$
Coupling parameter C ($kg \cdot m^2$) ^{1/2}	$\begin{bmatrix} 64.8 & 0 & -0.007 \\ 0 & -69.7 & 0 \\ -1.3 & -1.7 & -22.3 \end{bmatrix}$
Modal damping ratio ξ	$\begin{bmatrix} 0.046 & 0 & 0 \\ 0 & 0.031 & 0 \\ 0 & 0 & 0.019 \end{bmatrix}$
Modal frequency Λ (rad / s)	$\begin{bmatrix} 0.542 & 0 & 0 \\ 0 & 0.798 & 0 \\ 0 & 0 & 1.3 \end{bmatrix}$

Table 1. Related parameters in the spacecraft system simulation

The input and output of the controller both has 7 fuzzy subsets, respectively expressed by NB, NM, NS, ZR, PS, PM, PB. Because choosing linear or nonlinear membership functions has little influence on the fuzzy control effect, meanwhile using triangle has advantage of convenient and quick for calculating (Kruse, 1994), we adapt triangle membership function in our simulation, coincidence degree of neighbour fuzzy subsets is 0.5, Table 2 is the classical fuzzy control rule base used in the system.

input		Derivation of error						
		NB	NM	NS	ZR	PS	PM	PB
error	NB	PB	PB	PB	PB	PM	ZR	ZR
	NM	PB	PB	PB	PB	PM	ZR	ZR
	NS	PM	PM	PM	PM	ZR	NS	NS
	ZR	PM	PM	PS	ZR	NS	NM	NM
	PS	PS	PS	ZR	NM	NM	NM	NM
	PM	ZR	ZR	NM	NB	NB	NB	NB
	PB	ZR	ZR	NM	NB	NB	NB	NB

Table 2. Fuzzy control rule base

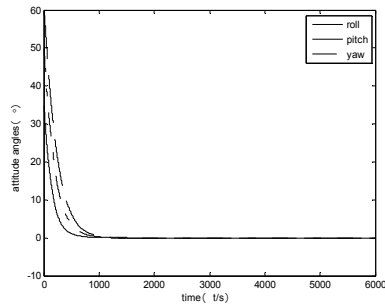
Simulation results are shown in follow figures, in order to make a comparison, the control effect of the fixed universe controller is given at the same time. Fig. 5 and Fig. 6 give the variation of the spacecraft attitude angles and modal coordinates of flexible appendages with time, and the control effect when the spacecraft moment of inertial increases 20 percent under the action of variable universe fractal fuzzy controller. Fig. 7 and Fig. 8 give the variation of the spacecraft attitude angles and modal coordinates of flexible appendages with time, and the control effect when the spacecraft moment of inertial increases 20 percent under the action of fixed universe fuzzy controller.

Take the actual attitude angles and attitude angular velocity of 2000-6000 seconds when the system has been stable as statistical data, calculate the 3σ value of attitude control accuracy and attitude stability under the action of two kinds of fuzzy controller both in the normal condition and in the condition when the moment of inertial increases 20 percent as shown in Table 3.

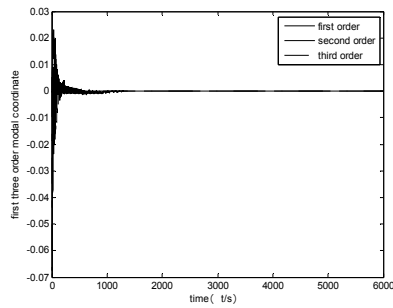
(3σ)		Variable universe fractal fuzzy control	General fuzzy control
I	<i>e</i>	$[0.0032 \quad 0.0404 \quad 0.0543]^\circ$	$[0.5309 \quad 0.0311 \quad 1.1964]^\circ$
	<i>ec</i>	$[0.0141 \quad 0.1335 \quad 0.0982] \times 10^{-4} \text{ }^\circ/s$	$[1.5028 \quad 0.0553 \quad 1.2592] \times 10^{-3} \text{ }^\circ/s$
	<i>eta</i>	$[0.1271 \quad 0.0399 \quad 0.0034] \times 10^{-4}$	$[0.4487 \quad 0.0458 \quad 0.0182] \times 10^{-4}$
II	<i>e</i>	$[0.0030 \quad 0.0476 \quad 0.0452]^\circ$	$[1.4163 \quad 0.0652 \quad 2.1949]^\circ$
	<i>ec</i>	$[0.0157 \quad 0.1210 \quad 0.0859] \times 10^{-4} \text{ }^\circ/s$	$[7.1558 \quad 0.1637 \quad 3.0126] \times 10^{-3} \text{ }^\circ/s$
	<i>eta</i>	$[0.0947 \quad 0.0502 \quad 0.0031] \times 10^{-4}$	$[1.1131 \quad 0.0647 \quad 0.0512] \times 10^{-4}$

Table 3. The control accuracy of the attitude angle, attitude angular velocity and vibration modal (I represent the normal condition, II represent the condition of moment of inertial increasing 20 percent)

From the simulation results, we know that the variable universe fractal fuzzy control has shorter dynamic adjusting time, faster response, smaller overshoot and higher static precision compared to the fixed universe fuzzy control. Meanwhile, it is insensitive to the variation of moment of inertial parameters, in other words, it has good robustness and adaptability to the model uncertainty of spacecraft. Besides, it could suppress the vibration of flexible appendages due to the attitude maneuver efficiently, then assure the attitude control precision of spacecraft.

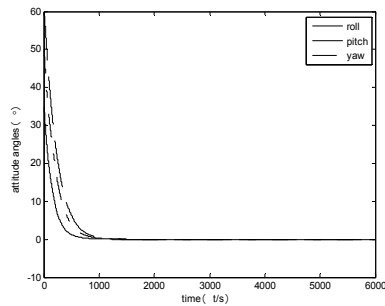


(a) Simulation results of the attitude angles

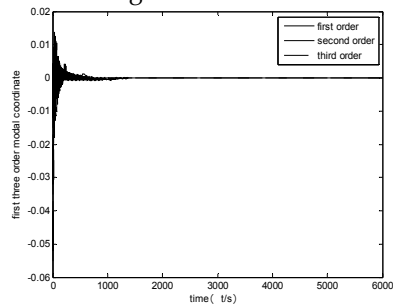


(b) Simulation results of the modal coordinates

Fig. 5. The control effect of the variable universe fractal controller

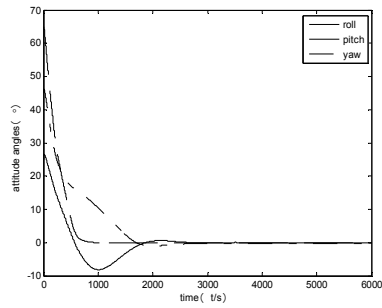


(a) Simulation results of the attitude angles

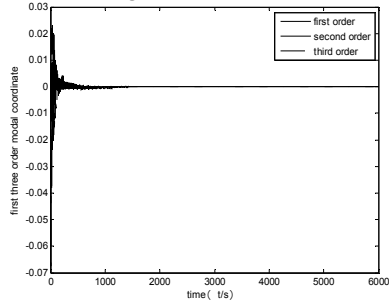


(b) Simulation results of the modal coordinates

Fig. 6. The control effect of the variable universe fractal controller when the moment of inertia of the spacecraft increases 20 percent

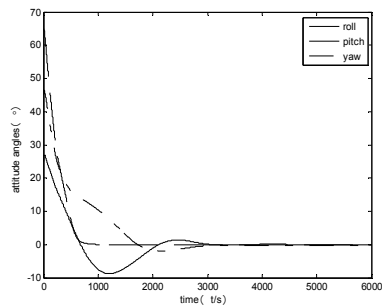


(a) Simulation results of the attitude angles

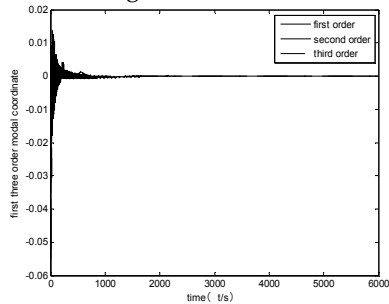


(b) Simulation results of the modal coordinates

Fig. 7. The control effect of the fixed universe controller



(a) Simulation results of the attitude angles



(b) Simulation results of the modal coordinates

Fig. 8. The control effect of the fixed universe controller when the moment of inertia of the spacecraft increases 20 percent

4. Conclusion

In this chapter, we research on the flexible multi-body spacecraft attitude dynamics and control problem. By using quasi-Lagrange equations, we have established the attitude dynamic equations of flexible multi-body spacecraft with topological tree configuration in section 2. The information of the system configuration has been introduced into the process of modelling, therefore the proposed attitude dynamic equations are universal and programmable. Then variable universe fractal fuzzy control method is developed in section 3. The strongly nonlinear attitude dynamics equations are simplified under several reasonable hypotheses. In order to avoid the disadvantage of using shrinkage factor, fractal control strategy is introduced into variable universe fuzzy control system. Finally we have demonstrated the effectiveness of the proposed control method through numerical simulation. The simulation results show that variable universe fractal fuzzy controller could accomplish the flexible multi-body spacecraft attitude control mission with good dynamic performance and high static precision.

5. References

- Crassidis J. L. , Markley F. L.(1996) *Sliding Mode Control Using Modified Rodrigues Parameters*, Journal of Guidance , Control and Dynamics, Vol.19(No.6):1381-1383.
- Kruse R. (1994) *Foundation of Fuzzy System*. John Wiley&Sons, UK.
- Li H. X. (1995). *See the Success of Fuzzy Logic from Mathematical Essence of Fuzzy Control*. Fuzzy system and mathematics, Vol.9(No.4):1-13.
- Lu Y. F. (1996). *Dynamics of Flexible Multi-body System*, Higher education press, Beijing.
- Pan X. F., Song L. Z.(2008) *Effectiveness of Several Shrinkage Factors of Variable Universe Fuzzy Control*, Control Engineering of China, Vol.15(No.s1):106-108.
- Si H. W. (2007.) *Adaptive Fuzzy Control Based on Scaling Universe of Discourse for Rigid-flexible Coupling Spacecrafts*, Aerospace control, Vol.25(No.5):28-32.

Applications of Optimal Trajectory Planning and Invariant Manifold Based Control for Robotic Systems in Space

Ka Wai Lee¹, Hirohisa Kojima² and Pavel M. Trivailo³

¹*RMIT University, Melbourne*

²*Tokyo Metropolitan University*

³*RMIT University, Melbourne*

^{1,3}*Australia*

²*Japan*

1. Optimal trajectory planning for robotic manipulators

1.1 Introduction

Complex space missions require high precision control of sophisticated robotic system to perform variety of difficult tasks. Robotic arm manipulator plays an important role and is widely used in modern space mission due to its reliability and versatility of application. It is capable to perform specific tasks such as payloads transportation and capturing, stabilizing a tumbling satellite, space station construction and monitoring.

Heavy lifting, payload transportation and capturing are the most common and frequently used applications of robotic system. The Canadarm is a classic example of payload manoeuvring robotic system in space. Modern space robot such as The Japanese Experiment Module Remote Manipulator System (JEMRMS) was also developed to support Japanese Experiment Module (JEM) maintenance tasks. Due to the new challenges of space missions to date, there is a need for developing new and robust technology to increase the efficiency of operation as well as reduce the likelihood of mission failure in performing complex tasks. Panfeng Huang proposed a Particle Swarm Optimization (PSO) to search the global time optimal trajectory for space manipulator. (Huang & Xu, 2006) SongHua Hu also applied PSO to optimize the trajectory of robotic manipulator for the reorientation of satellite after capturing. (Hu et al., 2008) Similar research and simulation was developed by Wenfu Xu. (Xu et al., 2009)

The increasing complexity of missions tends to increase the likelihood of collision between robotic arms and wandering obstacles in the surrounding environment. Such undesirable collision should be avoided to prevent causing damage to the robotic arm and payloads during operation. Therefore, collision free optimal path planning of robotic arm manipulators becomes critical to successful mission completion. An example of the two staged collision free path planning for the space manipular was illustrated by using virtual robotic test-bed (VRT). (Yoshida et al., 2008) The development of Real-time adaptive motion planning (RAMP) also provides optimal trajectory planning for robotic arm control in different dynamic environments and for various scenarios. (Vannoy & Xiao, 2008)

Previous publications of the authors have successfully demonstrated the methodology of collision free trajectory planning for two-link robotic arm manipulators in the presence of morphing mobile obstacles by minimizing the actuation efforts and performing payload capture in two-dimensional formulation. (Williams et al., 2009) It has been further extended to the optimal control system, which continuously evaluates the change of the position, velocity and shape of tumbling objects in the three-dimensional space.

1.2 Mathematical model of the three-dimensional rigid robotic manipulators

Fig. 1 shows the model of a three-dimensional two-link robotic manipulators with three rotational joints (RRR) and an end effector with a payload. θ_1 , θ_2 and θ_3 represent the positive orientation of the three joints. L_1 , L_2 and L_3 define the length of each link with the center of mass m_1 , m_2 and m_3 at the position r_1 , r_2 and r_3 , respectively.

The equation of motion of the robotic manipulators is obtained by using the Lagrange equation

$$L = E_k - E_p \quad (1)$$

where E_k is the kinetic energy and E_p is the potential energy of the system. Using the above equation, the Lagrange Equation for each link is expressed as follows:

$$\eta_i = \frac{d}{dt} \left(\frac{\partial L}{\partial \dot{\theta}_i} \right) - \left(\frac{\partial L}{\partial \theta_i} \right), (i = 1, 2, 3, \dots) \quad (2)$$

By substituting Equation 1 into Equation 2, the second-order differential equation in terms of the manipulator joint variables can be expressed in the following form

$$\tau = M(\Theta) \ddot{\Theta} + V(\Theta, \dot{\Theta}) \quad (3)$$

where $M(\Theta)$ is mass matrix of the manipulator and $V(\Theta, \dot{\Theta})$ is the vector of centrifugal, Coriolis forces and $\Theta = (\theta_1, \theta_2, \theta_3)$.

The final Lagrange Equation for each link of motion can be expressed as follows

$$\eta_1 = (\ddot{\theta}_1 \cos^2 \theta_2 - 2\dot{\theta}_1 \dot{\theta}_2 \cos \theta_2 \sin \theta_2) \times (L_2^2 m_3 + L_2^2 m_4 + L_3^2 m_4 + m_2 r_2^2 + m_3 r_3^2 + 2L_2 L_3 m_4 + 2L_2 m_3 r_3) \quad (4)$$

$$\begin{aligned} \eta_2 = & (L_2^2 m_3 \dot{\theta}_1^2 \sin(2\theta_2))/2 - (L_2^2 m_3 \dot{\theta}_2^2 \sin(2\theta_2))/2 \\ & + (L_2^2 m_4 \dot{\theta}_1^2 \sin(2\theta_2))/2 - (L_2^2 m_4 \dot{\theta}_2^2 \sin(2\theta_2))/2 \\ & + (L_3^2 m_4 \dot{\theta}_1^2 \sin(2\theta_2))/2 + (L_3^2 m_4 \dot{\theta}_3^2 \sin(2\theta_3))/2 \\ & + (m_2 r_2^2 \dot{\theta}_1^2 \sin(2\theta_2))/2 - (m_2 r_2^2 \dot{\theta}_2^2 \sin(2\theta_2))/2 \\ & + (m_3 r_3^2 \dot{\theta}_1^2 \sin(2\theta_2))/2 + (m_3 r_3^2 \dot{\theta}_3^2 \sin(2\theta_3))/2 \\ & + L_2 L_3 m_4 \dot{\theta}_1^2 \sin(2\theta_2) + L_2 m_3 r_3 \dot{\theta}_1^2 \sin(2\theta_2) \\ & + L_2 L_3 m_4 \dot{\theta}_2 \dot{\theta}_3 \sin(\theta_2 - \theta_3) + L_2 m_3 r_3 \dot{\theta}_2 \dot{\theta}_3 \sin(\theta_2 - \theta_3) \end{aligned} \quad (5)$$

$$\begin{aligned}
 \eta_3 = & \dot{\theta}_3 \cos \theta_3 (m_4 \dot{\theta}_3 \sin \theta_3 L_3^2 + L_2 m_4 \dot{\theta}_2 \sin \theta_2 L_3 \\
 & + m_3 \dot{\theta}_3 \sin \theta_3 r_3^2 + L_2 m_3 \dot{\theta}_2 \sin \theta_2 r_3) \\
 & - (m_3 (2r_3 \dot{\theta}_3 \cos \theta_1 \cos \theta_3 (r_3 \dot{\theta}_1 \cos \theta_2 \sin \theta_1 + r_3 \dot{\theta}_3 \cos \theta_1 \sin \theta_3 \\
 & + 2r_3 \dot{\theta}_3 \cos \theta_3 \sin \theta_1 (L_2 \dot{\theta}_2 \sin \theta_1 \sin \theta_2 + r_3 \dot{\theta}_3 \sin \theta_1 \sin \theta_3 \\
 & - L_2 \dot{\theta}_1 \cos \theta_1 \cos \theta_2 - r_3 \dot{\theta}_1 \cos \theta_1 \cos \theta_2))) / 2 \\
 & - (m_4 (2L_3 \dot{\theta}_3 \cos \theta_1 \cos \theta_3 (L_2 \dot{\theta}_1 \cos \theta_2 \sin \theta_1 \\
 & + L_2 \dot{\theta}_2 \cos \theta_1 \sin \theta_2 + L_3 \dot{\theta}_1 \cos \theta_2 \sin \theta_1 \\
 & + L_3 \dot{\theta}_3 \cos \theta_1 \sin \theta_3) + 2L_3 \dot{\theta}_3 \cos \theta_3 \sin \theta_1 (L_2 \dot{\theta}_2 \sin \theta_1 \sin \theta_2 \\
 & + L_3 \dot{\theta}_3 \sin \theta_1 \sin \theta_3 - L_2 \dot{\theta}_1 \cos \theta_1 \cos \theta_2 - L_3 \dot{\theta}_1 \cos \theta_1 \cos \theta_2))) / 2
 \end{aligned} \tag{6}$$

1.3 Formulation of the path constraints for collision avoidance

Previous research of a two-dimensional collision avoidance modelling was developed by Paul Williams et al. (Williams et al., 2009) and (Trivailo, 2007) An extension of this method to the three-dimensional cases is presented below. Fig. 2 illustrates the model of collision avoidance constraints for the i th link. The wandering obstacle is assumed to be rotating at the center of mass, P_{ob} , with an unknown orientation. It is modeled as a spheroid with a radius of R_{ob} . Which also represents the distance from the center of mass to the edge of the obstacle at the very end point. The length of the i th link is denoted by L_i along the two joints at point P_i and point P_{i+1} .

In order to prevent collision, it is required to find the shortest distance between the obstacle and the robotic arms. Consider the three displacement vectors $\vec{P}_{i,i+1}$, $\vec{P}_{i,ob}$ and $\vec{P}_{i+1,ob}$ are given by

$$\vec{P}_{i,i+1} = P_{i+1} - P_i \tag{7}$$

$$\vec{P}_{i,ob} = P_{ob} - P_i \tag{8}$$

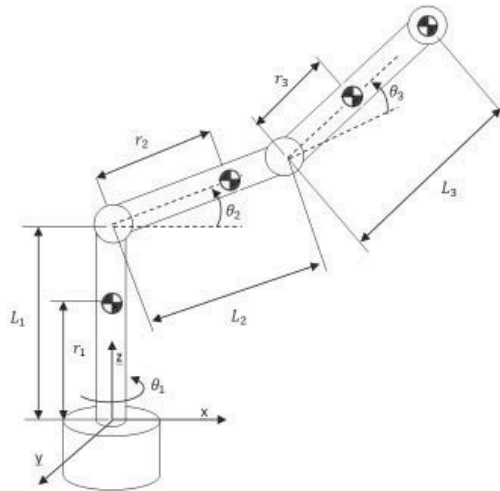


Fig. 1. Coordinate system of the 3D robotic manipulator

$$\vec{P}_{i+1,ob} = P_{ob} - P_{i+1} \quad (9)$$

The projection from the center of mass of the obstacle normal to the link is given by

$$l_i = \vec{P}_{i,ob} \cdot \vec{P}_{i,i+1} / \left| \vec{P}_{i,i+1} \right| \quad (10)$$

The distance between the center of mass of the obstacle and the link can then be determined by

$$d_i = \left| \vec{P}_{i,ob} - l_i \vec{P}_{i,i+1} \right| \quad (11)$$

The path constraint of the i th is defined by g_i which is subject to three conditions that are expressed in Equation 12. If the projected length l_i is last than zero or larger than the length of the i th link L_i , the path constraint is set to avoid the obstacle collide with the particular joint. Otherwise the distance from the obstacle to the i th link should always be larger than the radius of spheroid. The path constraints are always forced to be larger than zero preventing collision.

$$g_i := \begin{cases} \left| \vec{P}_{i,ob} \right|^2 - R_{ob}^2 \geq 0, & l_i \leq 0 \\ \left| \vec{P}_{i+1,ob} \right|^2 - R_{ob}^2 \geq 0, & l_i \geq L_i \\ d_i^2 - R_{ob}^2 \geq 0, & \text{otherwise} \end{cases} \quad (12)$$

1.4 Direct transcription method

In order to find the optimal control trajectory of the robotic manipulators, minimization of the following performance index is required

$$\mathcal{J} = \mathcal{M}[x(t_f), t_f] + \int_{t_0}^{t_f} \mathcal{L}[x(t), u(t), t] dt \quad (13)$$

subject to the dynamical constraints

$$\dot{x}(t) = f[x(t), u(t), t] \quad (14)$$

where $t \in \mathbb{R}$, $x \in \mathbb{R}^N$ and $u \in \mathbb{R}^M$, and boundary conditions

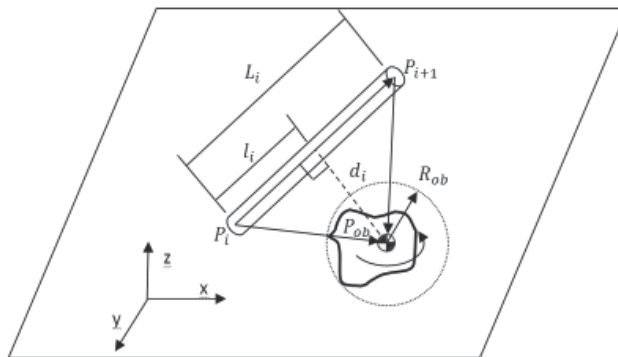


Fig. 2. Representation of Wandering Obstacle Relative to i th Link

$$\begin{aligned}\psi_0[x(t_0), u(t_0), t_0] &= 0 \\ \psi_f[x(t_f), u(t_f), t_f] &= 0\end{aligned}\tag{15}$$

where $\psi_0 \in \mathbb{R}^p$ and $\psi_f \in \mathbb{R}^q$ with $p \leq n$ and $q \leq n$, and the state and control box constraints

$$\begin{aligned}x_{i(\min)} &\leq x_i(t) \leq x_{i(\max)} \\ \dot{x}_{i(\min)} &\leq \dot{x}_i(t) \leq \dot{x}_{i(\max)} \\ u_{j(\min)} &\leq u_j(t) \leq u_{j(\max)}\end{aligned}\tag{16}$$

where $i = 1, \dots, N$ and $j = 1, \dots, M$

In this work, we applied Chebyshev polynomials for the interpolation. The Chebyshev-Gauss-Lobatto (CGL) points lie in the interval $[-1, 1]$ and are located at the extrema of the N th-order Chebyshev polynomial $T_N(\zeta)$. The j th-order Chebyshev polynomial of the first kind $T_j(\zeta)$ is expressed as

$$T_j(\zeta) = \cos(j \cos^{-1} \zeta)\tag{17}$$

where the extreme values occur at the points ζ_j is

$$\zeta_j = -\cos\left(\frac{\pi j}{N}\right)\tag{18}$$

The Lagrange interpolating polynomials

$$\mu_j(\zeta) = \frac{(-1)^{j+1}(1-\zeta^2)\dot{T}_N(\zeta)}{c_j N^2(\zeta - \zeta_j)}\tag{19}$$

where $c_j = 1$ for $1 \leq j \leq N-1$ and $c_0 = c_N = 2$ for $j = 0, N$.

The states and controls are approximated by using Lagrange interpolating polynomials function

$$x_N(\zeta) = \sum_{j=0}^N x(\zeta_j) \mu_j(\zeta)\tag{20}$$

$$u_N(\zeta) = \sum_{j=0}^N u(\zeta_j) \mu_j(\zeta)\tag{21}$$

The Chebyshev differentiation matrices can be obtained by finding the derivatives of the approximating functions in Equation 20 at the CGL node

$$d_k = \dot{x}(\zeta_k) = \sum_{j=0}^N D_{k,j} x(\zeta_j)\tag{22}$$

$$d_k^{(2)} = \ddot{x}(\zeta_k) = \sum_{j=0}^N D_{k,j}^{(2)} x(\zeta_j)\tag{23}$$

where $D_{k,j}$ represents the differentiation matrix.

Since the Chebyshev polynomials are defined over the interval $[-1,1]$, it is required to perform a linear transformation for the expression in physical time domain t .

$$t = [(t_f - t_0)\zeta + t_f + t_0]/2 \quad (24)$$

The derivatives with respect to physical time t is then given by

$$\dot{x}(t) = \frac{2}{t_f - t_0} \dot{x}(\zeta) \quad (25)$$

$$\ddot{x}(t) = \frac{2}{t_f - t_0} \ddot{x}(\zeta) \quad (26)$$

The control problem can then be formulated as a nonlinear programming problem that aims to minimize the performance index

$$\mathcal{J}_N = \mathcal{M} \left[\frac{4}{(t_f - t_0)^2} d_N^{(2)}, \frac{2}{t_f - t_0}, x_N, t_f \right] + \sum_{k=0}^N \mathcal{L} \left[\frac{4}{(t_f - t_0)^2} d_k^{(2)}, \frac{2}{t_f - t_0} d_k, x_k, u_k, t \right] \omega_k \quad (27)$$

where ω_k is the Legendre-Gauss-Lobatto weights.

The direct discretization method has been developed and implemented in Matlab known as DIRECT by Paul Williams at RMIT University. (Williams, 2005) It is capable of discretizing constrained nonlinear programming problem and search for the numerical solution by employing SNOPT as a solver. (Gil et al., 2002)

1.5 Optimal trajectory planning

Point-to-point optimal trajectory planning is usually classified into two main categories: minimum travelling time and actuation effort. Optimization tasks are generally aimed to minimize the performance index that is defined in the cost function. Variety of research has been done using different techniques and strategies. Xiong Luo deployed evolutionary programming algorithms to search for the optimal solution. (Luo et al., 2004) Minimum travelling time path planning was also developed by using polytope method with penalty function. (Cao et al., 1997) Other work involved collision avoidance and minimum-energy path planning (MEPP) or minimum-fuel path planning (MFPP) was undertaken by using method of local variations (MLV). (Seshadri & Ghosh, 1993)

In this work, we consider minimization of the energy consumption which is more critical in space applications. Therefore, the actuation effort should be minimized with the cost function \mathcal{J} defined by

$$\mathcal{J} = \sum_{i=1}^3 \int_0^{t_f} u_i^2(t) dt \quad (28)$$

where u_i represents the input of i th actuator and t_f is the pre-defined non-dimensional time constant for finishing the particular task.

1.5.1 Case study and results

Fig. 3 shows the optimized trajectory motion of the robotic arms which aims to deliver a mass payload from the bottom point to the top while an obstacle is wandering along the straight line between the start and end position. The robotic arm has been chosen to pass around the obstacle from behind because the obstacle travel path and speed is predicted. It can be noted

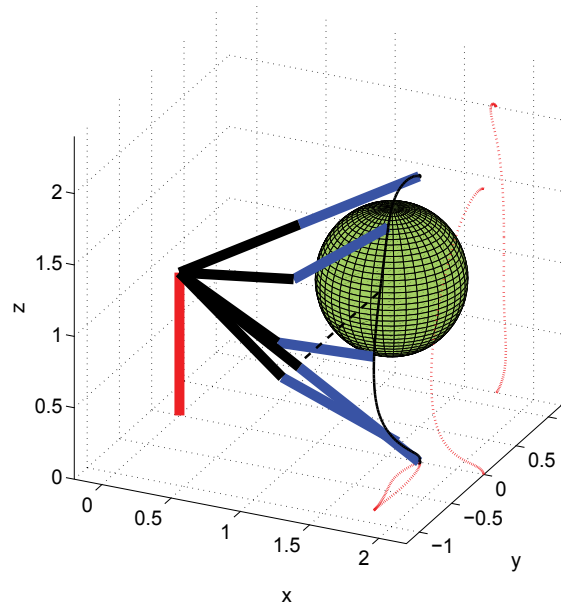


Fig. 3. Optimal Trajectory and the final position of the robotic manipular and obstacle

that the total end effector travelling trajectory should not necessary be the shortest path to minimize the actuator efforts.

Fig. 4 shows the time history of the position angles θ_j and angular velocities $\dot{\theta}_j$ of the robotic manipulators, respectively. Fig. 4(a) also shows the initial conditions of the position angle as $\theta_1 = 0$ deg, $\theta_2 = -30$ deg and $\theta_3 = -30$ deg at time $t_0 = 0$ while $\theta_1 = 0$ deg, $\theta_2 = 30$ deg and $\theta_3 = 30$ deg at time $t_f = 1$. It is interesting to note that the angular velocity constraints have been ensured: as Fig. 4(b) clearly shows, θ_2 and $\dot{\theta}_3$ hit the upper bound of 90 deg per unit time and did not exceed this imposed limit.

Fig. 5 shows the time history of control inputs u_j . Similar to the angular velocities, the control inputs u_1 and u_3 were limited by the pre-defined constraints $|u_j| \leq 45$ and have always remained within these limits, as shown in Fig. 5(a). Maximum power consumption should also be considered as an important factor. Fig. 5(b) shows the time history of the summation of squared inputs which represents the combined effort of the system during its operation. The two peak consumption values can be found when the manipulator begins to accelerate at the beginning and decelerates near the end. Finally, the time history of the minimized cost function \mathcal{J} , which was defined in Equation 13, is shown in Fig. 6

2 Invariant manifold based control for space robotic system

2.1 Introduction

A planar space robot is a nonholonomic system, and the problem of the reorientation of a planar space robot has attracted the interest of many researchers. There exist no smooth time-invariant control methods that can stabilize nonholonomic systems, even if the system is controllable. This negative fact is well known as Brockett's theorem. (Brockett,

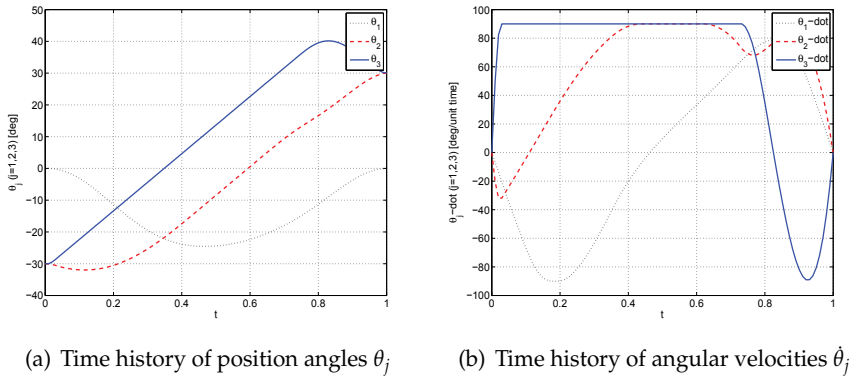


Fig. 4. Time history of position angles and angular velocities

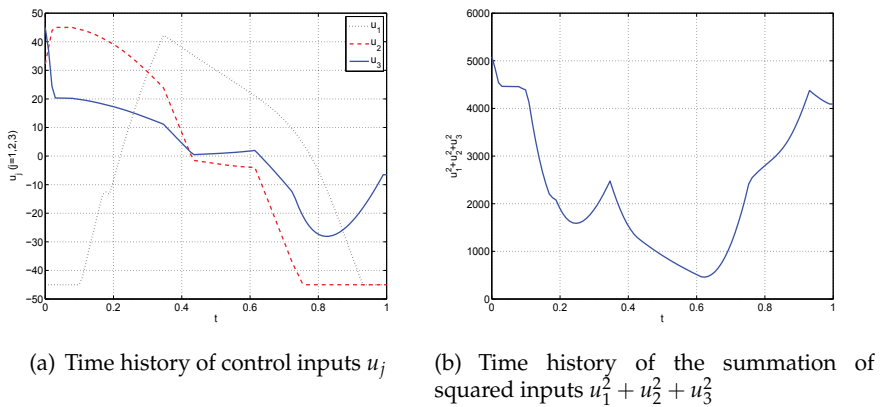


Fig. 5. Time history of control inputs

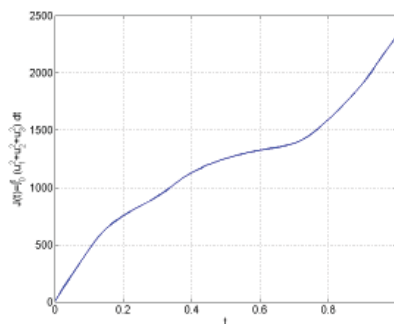


Fig. 6. Time history of the minimized cost function \mathcal{J}

1983) Reyhanoglu et al. (Reyhanoglu & McClamroch, 1992) have proposed a feed-forward control method that defines the trajectory of the joint angles before controlling. Yamada (Yamada, 1994) proposed a method which involves prescribing the arm path first and then determining the quasi-optimal path that causes the desired attitude change with minimal arm movement. In order to get around Brockett's theorem and stabilize nonholonomic systems, some advanced nonlinear control techniques have been proposed, and these can be classified into various classes, such as canonical form based methods (Sordalen & Egeland, 1995) (Samson, 1995) (Luo & Tsiotras, 1998), smooth time-varying feedback control methods (Luo & Tsiotras, 1998) (Pomet, 1992) (Teel & Walsh, 1995), discontinuous methods, time-varying and discontinuous combining methods, sliding-mode control, and center-manifold based control methods. Although the canonical form based method is useful, a space robot reorientation system cannot be transformed to canonical form, because it has singularities. In order to handle this situation, Cerven et al. (Cerven & Coverstone, 2001) have proposed optimal control theory, using averaging theory, and Hashimoto, et al. (Hashimoto & Amemiya, 2006) have proposed a feedback controller by approximating the system with a first order chained system. In some studies of the reorientation problem for a planar space robot, an invariant manifold has been utilized. Mukherjee et al. (Mukherjee & Kamon, 1999) have proposed the concept of a "radially isometric orientation", and have established a smooth time-invariant feedback control method based on this concept.

However, their method suffers from a slow rate of convergence if the desired attitude and joint angles are near zero holonomy curves, which are defined as curves in the joint space for which the first-order Lie bracket becomes zero, that is, when the attitude of the main body of a space robot cannot be changed by controlling the joint angles.

In order to overcome this disadvantage of the radially isometric orientation based control method, Hokamoto and Funasako (Hokamoto & Funasako, 2007) have proposed a modified version of the smooth time-invariant feedback method by introducing a moving manifold that has a virtual desired point. However, time delay for the planar space robot has apparently not yet been considered.

In this section, an "invariant-based switching control" method is proposed. This is a discontinuous control method, consisting of two steps: firstly, the link angles are controlled periodically to reach the invariant manifold by feedback control, and secondly, the ratio between the angular velocities of joint angles is controlled constantly so that the state slides on the invariant manifold until reaching the goal state. The proposed method is useful for estimating the time delay in the system because the manifold depends on the system parameters but is independent of time; it can estimate the time delay by comparing the predicted trajectories of arm angles and the actual ones. The difference between them is caused by the time delay. In addition, after estimating the time delay, modeling errors, which are assumed to be related to the moment of inertia of the main body in this study, can also be estimated by comparing the predicted attitude change of the main body with the actual one. The effectiveness of the proposed control scheme's functions, that is, the reduction in the convergence time, the estimation of not only the time delay, but also modeling errors, is verified experimentally.

2.2 Modelling of the system

2.2.1 Two-link planar space robot

Fig. 7 shows a schematic model of a planar space robot, which has a two-link manipulator, connected by revolution joints.

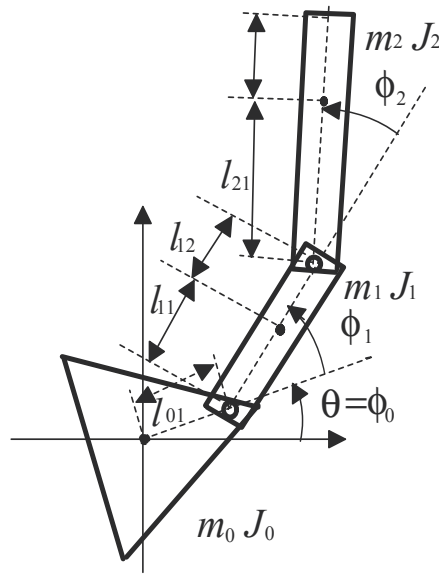


Fig. 7. Model of a Planar Two-Link Space Robot

Suppose that the orientation of the main body is θ , the first link angle 1, ϕ_1 , and the second link angle 2, ϕ_2 . The masses of the main body, the first arm, and the second arm are denoted by m_0 , m_1 , and m_2 , respectively and correspondingly, J_0 , J_1 , and J_2 are the moments of inertia of the main body, and that of the first and second arms, respectively.

Distances between the mass center of each body and the angle joints are denoted as in Fig. 7. Given that the initial total angular momentum is zero, and that no external torque and force affects the system, the angular momentum conservation law holds, and then the angular velocity of the main body of the space robot is represented by functions of the two-link angles ϕ_1 and ϕ_2 , and their angular velocities as follows:

$$\dot{\theta} = h_1(\phi_1, \phi_2) \dot{\phi}_1 + h_2(\phi_1, \phi_2) \dot{\phi}_2 \quad (29)$$

Now suppose that the state vector \vec{x} , and the control input \vec{u} are, respectively, given as $\vec{x} = [\phi_1, \phi_2, \theta]^T$, and $\vec{u} = [u_1, u_2]^T = [\dot{\phi}_1, \dot{\phi}_2]^T$. Then Equation 29 can be rewritten in the following affine form:

$$\begin{bmatrix} \dot{\phi}_1 \\ \dot{\phi}_2 \\ \dot{\theta} \end{bmatrix} = \begin{bmatrix} 1 & 0 \\ 0 & 1 \\ h_1(\phi_1, \phi_2) & h_2(\phi_1, \phi_2) \end{bmatrix} \begin{bmatrix} u_1 \\ u_2 \end{bmatrix} \quad (30)$$

2.2.2 Equations of motion

Here, we derive the equations of motion for a planar two-link space robot. Let the mass, moment of inertia, center of mass, and velocity of mass center of the i link be denoted respectively by m_i , J_i , (x_i, y_i) , and (\dot{x}_i, \dot{y}_i) . The angular momentum P_g is given by

$$P_g = \sum_{i=0}^2 J_i \dot{\theta}_i + \frac{1}{M} \sum_{i=0}^1 \sum_{j=i+1}^2 m_i m_j (\bar{x}_{ji} \dot{y}_{ji} - \dot{x}_{ji} \bar{y}_{ji}) \quad (31)$$

where

$$\begin{aligned}\theta_i &= \sum_{j=0}^i \phi_j \\ \bar{x}_{ji} &= x_j - x_i, \quad \bar{y}_{ji} = y_j - y_i \\ x_i &= \sum_{j=1}^i l_{(j-1)j} \cos \theta_{j-1} + \sum_{j=1}^i l_{jj} \cos \theta_j \\ y_i &= \sum_{j=1}^i l_{(j-1)j} \sin \theta_{j-1} + \sum_{j=1}^i l_{jj} \sin \theta_j \\ M &= \sum_{i=0}^2 m_i\end{aligned}$$

For the case of zero angular momentum, that is, $P_g = 0$, we have

$$a(\phi_1, \phi_2) \dot{\theta}_0 + b(\phi_1, \phi_2) \dot{\phi}_1 + c(\phi_1, \phi_2) \dot{\phi}_2 = 0 \quad (32)$$

where

$$\begin{aligned}a(\phi_1, \phi_2) &= J_0 + J_1 + J_2 \\ &+ \left\{ m_0 m_1 (l_{01}^2 + l_{11}^2) \right. \\ &+ m_2 \left(m_0 (l_{01}^2 + (l_{11} + l_{12})^2 \right. \\ &+ l_{21}^2 + 2l_{01} l_{21} \cos(\phi_1 + \phi_2)) \\ &+ m_1 (l_{12}^2 + l_{21}^2) \\ &+ 2(m_0 (l_{11} + l_{12}) + m_1 l_{12}) l_{21} \cos \phi_2 \\ &\left. \left. + 2m_0 l_{01} (m_1 l_{11} + m_2 (l_{11} + l_{12})) \cos \phi_1 \right\} / M \\ b(\phi_1, \phi_2) &= J_1 + J_2 \\ &+ \left\{ m_0 m_1 l_{11}^2 + m_2 \left(m_0 \left((l_{11} + l_{12})^2 + l_{21}^2 \right. \right. \right. \\ &+ l_{01} l_{21} \cos(\phi_1 + \phi_2)) + m_1 (l_{12}^2 + l_{21}^2) \\ &+ 2l_{21} \cos \phi_2 (m_0 (l_{11} + l_{12}) + m_1 l_{12}) \\ &\left. \left. \left. + m_0 l_{01} \cos \phi_1 (m_1 l_{11} + m_2 (l_{11} + l_{12})) \right\} / M \\ c(\phi_1, \phi_2) &= J_2 + \left\{ m_2 l_{21} \left((l_{21} + (l_{11} + l_{12}) \cos \phi_2 \right. \right. \right. \\ &\left. \left. \left. + m_0 l_{01} \cos(\phi_1 + \phi_2) \right) + m_1 (l_{21} + l_{12} \cos \phi_2) \right\} / M\end{aligned}$$

h_1 and h_2 in Equation 30 are, respectively, as follows:

$$h_1(\phi_1, \phi_2) = -b(\phi_1, \phi_2) / a(\phi_1, \phi_2) \quad (33)$$

$$h_2(\phi_1, \phi_2) = -c(\phi_1, \phi_2) / a(\phi_1, \phi_2) \quad (34)$$

2.2.3 First-order lie bracket and zero-holonomy curves

The attitude deviation of the main body due to the arm motion is determined by integrating the third term of Equation 30, or Equation 29. Now suppose that the trajectory of arm motion is a closed curve in the link angle space (ϕ_1, ϕ_2) . Then the attitude deviation of the main body is given by

$$\Delta\theta = \oint h_1(\phi_1, \phi_2) d\phi_1 + h_2(\phi_1, \phi_2) d\phi_2 \quad (35)$$

Using Stokes's theorem, Equation 35 can be rewritten from path integral form to surface integral form as follows:

$$\Delta\theta = \oint \left(\frac{\partial h_1}{\partial \phi_2} - \frac{\partial h_2}{\partial \phi_1} \right) d\phi_1 \wedge d\phi_2 \quad (36)$$

where $h_3 := \partial h_1 / \partial \phi_2 - \partial h_2 / \partial \phi_1$ is the first-order Lie bracket, and $d\phi_1 \wedge d\phi_2$ is the exterior derivative, in which the direction of the path integral is defined so that the closed surface is seen on the left side of the path.

Equation 36 implies that, even if the link angles return to the initial angles after moving along a closed path in link angle space, the main body does change its attitude. This phenomenon is called "Lie bracket motion."

Fig. 8 shows a contour map for h_3 . Note that the main body does not change its attitude when the link angles move along a contour line of $h_3 = 0$. This special contour line of $h_3 = 0$ is referred to as a "zero holonomy curve."

Link motion along a zero holonomy curve is desirable in the case where the link motion must not affect the attitude of the main body. On the other hand, link motion along the zero holonomy curve is undesirable in the case where the main body is required to change its attitude by means of the link motion. In this sense, the zero holonomy curve is regarded as being representative of uncontrollable motion with respect to the attitude of the main body. In addition, h_3 changes sign across the zero holonomy curve. This implies that the attitude of the main body increases or decreases on opposite sides of the zero holonomy curve. (Mukherjee & Kamon, 1999)

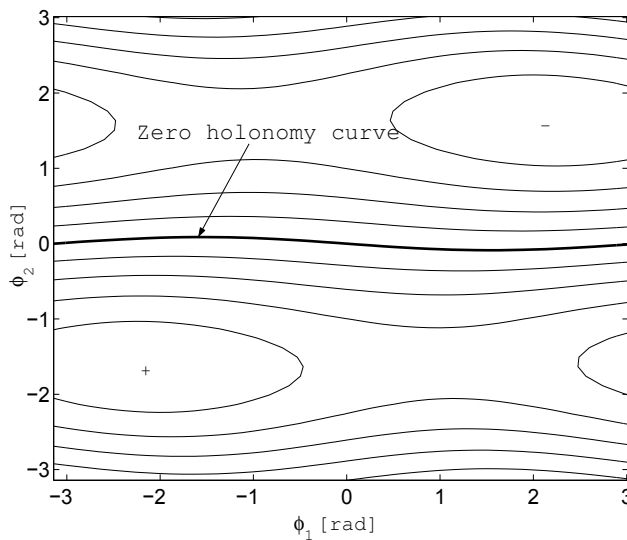


Fig. 8. Contour map of h_3 , and the zero holonomy curve

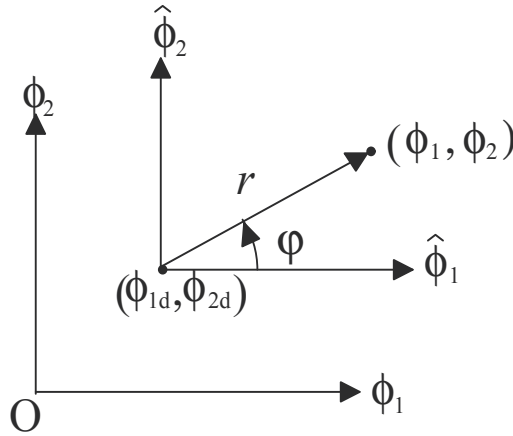


Fig. 9. Coordinates in link angle space.

2.2.4 The radially isometric orientation(invariant manifold) and its approximation

As mentioned above, the attitude variation of the main body is not determined directly from the link angles, but depends on the path in link angle space. Here, by referring to (Mukherjee & Kamon, 1999) we explain the definition of the “radially isometric orientation,” or, hereinafter, the invariant manifold.

Let the difference between the goal link angles (ϕ_{1d}, ϕ_{2d}) and the current link angle (ϕ_1, ϕ_2) be parameterized in polar coordinates (r, φ) , as shown in Fig. 9

$$\hat{\phi}_1 = \phi_1 - \phi_{1d} = r \cos \varphi \quad (37)$$

$$\hat{\phi}_2 = \phi_2 - \phi_{2d} = r \sin \varphi \quad (38)$$

where

$$r = \sqrt{\hat{\phi}_1^2 + \hat{\phi}_2^2} \quad (39)$$

$$\varphi = \tan^{-1}(\hat{\phi}_2/\hat{\phi}_1) \quad (40)$$

Suppose that the phase argument φ , which indicates the direction from the goal link angles to the current link angles, is kept constant, or that link angles are moved [along the straight line from the current angles to the goal angles] in Cartesian coordinates (ϕ_1, ϕ_2) . In this case, the attitude variation of the main body is obtained as

$$\Delta\theta = \int_{\varphi=\text{const}} h_1(r, \varphi) d\phi_1(r, \varphi) + h_2(r, \varphi) d\phi_2(r, \varphi) \quad (41)$$

In order to change the integral variables from (ϕ_1, ϕ_2) to (r, φ) the following relation is taken into consideration.

$$d\hat{\phi}_1(r, \varphi) = dr \cos \varphi - r \sin \varphi d\varphi \quad (42)$$

$$d\hat{\phi}_2(r, \varphi) = dr \sin \varphi + r \cos \varphi d\varphi \quad (43)$$

Because the phase argument is assumed to be constant, Equation 41 can be rewritten as

$$\Delta\theta^* = \int_0^r \left[h_1(r, \varphi) \cos \varphi + h_2(r, \varphi) \sin \varphi \right]_{\varphi=\text{const}} dr \quad (44)$$

The difference between the goal attitude of the main body and that after moving the link angle directly to the goal link angles is given by

$$\beta := \hat{\theta} - \Delta\theta^* \quad (45)$$

The condition of $\beta = 0$ is presented to show that if the link angles move [along the straight line from the current angles to their goals in Cartesian coordinates (ϕ_1, ϕ_2)], the attitude of the main body reaches its goal attitude also. The parameter β is referred to as the “radially isometric orientation” in (Mukherjee & Kamon, 1999).

Fig. 10 shows an example of a “radially isometric orientation” where parameters of the robot as listed in Table 1 are used.

For the controller that will be described later, the control input is determined using the value of the radially isometric orientation, β . As shown in Equation 44, an integral is needed to obtain the value of β . This implies that a controller using the value of β needs an integral calculation every control cycle to obtain the value of β . This control scheme is thus undesirable for a spacecraft equipped with limited on-board computational resources.

In order to reduce the effect of such limited on-board computation resources, we consider an approximation of the “radially isometric orientation,” or simply, manifold.

Although it depends on the mass and the moment of inertia of the space robot, as shown in Fig. 10, the invariant manifold can be approximated by a plane surface around the goal link angles.

Any set of link angles around the goal link angles, $\hat{x} = [\hat{\phi}_1, \hat{\phi}_2, \hat{\theta}]^T$, can be approximated by a linear combination of $h_1(\phi_{1d}, \phi_{2d})$ and $h_2(\phi_{1d}, \phi_{2d})$

$$\begin{bmatrix} \hat{\phi}_1 \\ \hat{\phi}_2 \\ h_1(\phi_{1d}, \phi_{2d}) \hat{\phi}_1 + h_2(\phi_{1d}, \phi_{2d}) \hat{\phi}_2 \end{bmatrix} \quad (46)$$

Fig. 11 shows a manifold approximated by a plane surface. It should be noted that if a set of link angles is far away from the goal link angles, the difference between the approximating manifold and the exact manifold, of course, becomes larger. Therefore, if a more accurate approximate manifold is required, types of surfaces other than plane surfaces, such as spline surfaces, should be used. However, we need a trade off between accuracy and computational cost. In this chapter, taking into consideration experiments that will be discussed later, we use an approximating manifold that is a plane surface.

2.3 Invariant manifold based control

2.3.1 Smooth time invariant feedback control

The control method proposed in (Mukherjee & Kamon, 1999) is given by

$$\dot{r} = \alpha r \left[\rho^2 \tanh(n_1 \beta^2) - r^2 \right] \quad (47)$$

$$\dot{\phi} = -n_2 \text{sgn}(h_3(\phi_{1d}, \phi_{2d})) \tanh(n_3 \beta) \quad (48)$$

where α, n_1, n_2, n_3 , and ρ are positive scalar constants, and the link angle velocities are driven by Equations 42 and 43.

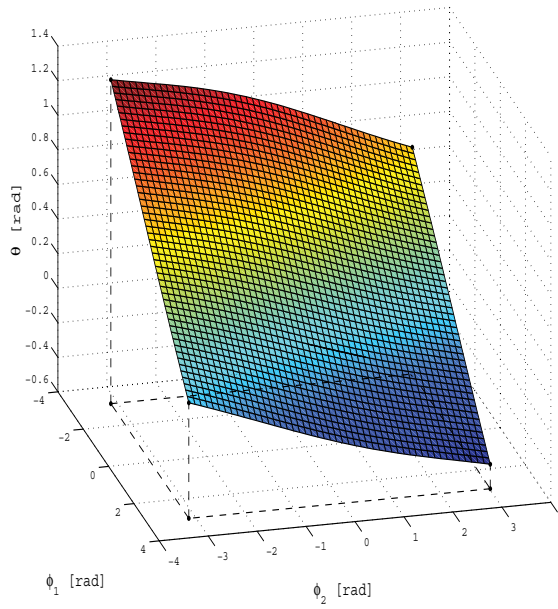


Fig. 10. Invariant manifold.

This control method is asymptotically stable, because as the value of β approaches zero, the radius r , and the phase argument φ driven by the above control method approach zero. This

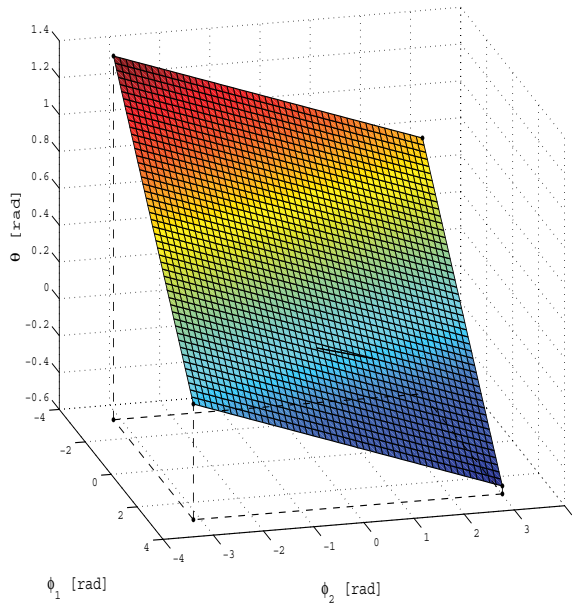


Fig. 11. Plane surface approximation of the invariant manifold.

control method, however, suffers from slow convergence, and we now explain the reason for this.

When β approaches zero, the control method (47) is equivalent to

$$\dot{r} = -\alpha r^3 \quad (49)$$

This implies that the radius r does not converge to zero at a first-order convergence rate. In addition, as β approaches zero, the change of phase argumentation, that is, the Lie bracket motion, also becomes slower. As a result, the rate of convergence to approach the goal state becomes very slow.

Furthermore, modeling errors were not considered in (Mukherjee & Kamon, 1999). The time invariant feedback control method cannot stabilize the state to the goal state in the presence of modeling errors, because the actual manifold is different from the manifold based on the mathematical model.

2.3.2 Adaptive manifold based switching control

To overcome the disadvantages of the time invariant feedback controller, an adaptive manifold based switching control is proposed here. (Kojima & Kasahara, 2010)

Firstly, the control method in the absence of modeling errors and time delay is explained as a basic controller; then advanced functions are introduced. The basic control method consists of two steps.

In the first step, in order to change the attitude of the main body as much as possible, Lie bracket motion is actively utilized. For this purpose, until the state reaches the invariant manifold, the radius r and the phase argument velocity $\dot{\phi}$ are controlled to be constant:

$$\dot{r} = 0, \quad (50)$$

$$\dot{\phi} = -n_4 \text{sgn}(h_3(\phi_{1d}, \phi_{2d})) \text{sgn}(\beta). \quad (51)$$

If a trajectory of the link angles crosses the zero holonomy curve under the condition of constant radius, as presented in (Hokamoto & Funasako, 2007), virtual goal link angles, which asymptotically reach the goal angles, are set for the link trajectory not to cross the zero holonomy curve.

In the second step, the state variables slide along the manifold until they reach the goal states. In this step, in order for the radius r to converge to zero at a first-order convergence rate, the radius is controlled by

$$\dot{r} = -dr \quad (52)$$

We can expect a fast convergence rate from Equations 50, 51 and 52, compared with the smooth time invariant feedback control. This expectation will be verified experimentally.

The control input determined by the smooth invariant feedback control (Mukherjee & Kamon, 1999) is smooth, whereas the proposed control method is a switching control. This proposed switching control, therefore, may induce undesirable oscillations on flexible appendages attached to the main body or links.

Undesirable oscillations could be avoided by controlling the phase argument velocity $\dot{\phi}$ so that the connection from Equation 51 to Equation 48 becomes smooth as β approaches the manifold. In this study, a smooth connection has not yet been investigated, and thus it remains a future topic for study.

Next, let us consider an adaptive law to estimate the modeling error in the absence of a time delay. In this study, we assume that there exists only a difference between the mathematical

moment of inertia of the main body and the correct one, which is treated as a modeling error. If an angular acceleration sensor is installed on the main body, and the link angles are driven by the torque motors, then the moment of inertia of the main body can be directly estimated from the relation between the torques and the angular acceleration. However, the link angles of the model treated in this study are controlled in terms of the angular velocity. This implies that the moment of inertia of the main body cannot be directly estimated using the relation between the torque and the angular acceleration.

We are assuming here that the attitude of the main body can be measured by an attitude sensor such as a magnetometer. We consider an adaptive law to estimate the moment of inertia of the main body from the difference between the predicted attitude change and the actual one. Let the error of the moment of inertia of the main body be given by

$$\Delta J_0 = J_0 - \hat{J}_0, \quad (53)$$

where J_0 and \hat{J}_0 are the correct and estimated moments of inertia of the main body, respectively. The attitude change of the main body per one period of $\delta\varphi = 2\pi$ is given by

$$\Delta\theta = \oint_{r=const} h_1(r, \varphi, J_0) d\phi_1(r, \varphi) + h_2(r, \varphi, J_0) d\phi_2(r, \varphi) \quad (54)$$

The above path integral can be converted into a surface integral using Stokes's theorem, Recall that the modeling error given by Equation 53, Equation 54 can be approximated as follows:

$$\begin{aligned} \Delta\theta &= \oint_{r=const} h_3(r, \varphi, J_0) d\phi_1 \wedge d\phi_2 \\ &\simeq \oint_{r=const} h_3(r, \varphi, \hat{J}_0) d\phi_1 \wedge d\phi_2 \\ &+ \oint_{r=const} \left. \frac{\partial h_3(r, \varphi, J_0)}{\partial J_0} \right|_{J_0=\hat{J}_0} \Delta J_0 d\phi_1 \wedge d\phi_2 \end{aligned} \quad (55)$$

The attitude change of the main body corresponding to the assumed moment of inertia of the main body \hat{J}_0 is given by

$$\Delta\hat{\theta} := \oint_{r=const} h_3(r, \varphi, \hat{J}_0) d\phi_1 \wedge d\phi_2 \quad (56)$$

By comparing Equation 55 with Equation 56, the difference between the predicted and actual attitude changes can be approximately represented by

$$\Delta\theta - \Delta\hat{\theta} \simeq \oint_{r=const} \left. \frac{\partial h_3(r, \varphi, J_0)}{\partial J_0} \right|_{J_0=\hat{J}_0} \Delta J_0 d\phi_1 \wedge d\phi_2 \quad (57)$$

Because the radius r is restricted to be constant during the first step in the proposed control method, the surface area $d\phi_1 \wedge d\phi_2$ during one periodic motion of the phase argument $\delta\varphi = 2\pi$ is always the same. Therefore, by solving Equation 57 with respect to the modeling error, we have

$$\Delta\hat{J}_0 \simeq \frac{\Delta\theta - \Delta\hat{\theta}}{\oint_{r=const} \left. \frac{\partial h_3(r, \varphi, J_0)}{\partial J_0} \right|_{J_0=\hat{J}_0} d\phi_1 \wedge d\phi_2} \quad (58)$$

Using this relation, the actual moment of inertia of the main body can be estimated as

$$J_0 = \hat{J}_0 + \Delta\hat{J}_0 \quad (59)$$

The denominator of Equation 58 is, however, based on the estimated moment of inertia of the main body, which is not yet equivalent to the actual one. Therefore, if the moment of inertia of the main body is simply updated, based on Equation 59, the estimated moment of inertia might become a meaningless (e.g., negative) value in a physical sense. In order to avoid such a situation, Equation 59 is replaced with

$$J_0 = \hat{J}_0 + \gamma\Delta\hat{J}_0 \quad (0 < \gamma < 1) \quad (60)$$

to update the estimated moment of inertia.

We explain the value that is selected for γ in this study. In general, the smaller the value of γ and the greater the number of estimations chosen, then the more accurate the estimation could be, whereas a long time is required to obtain an accurate moment of inertia.

Suppose that the estimated moment of inertia approaches the actual moment after ten estimations. In this case, it may be natural to set γ to $0.1 (= 1/10)$. For greater safety, half this value, i.e., 0.05 , is chosen for γ .

In addition, a value, which is surely less than the actual one, is chosen as the initial guess for the moment of inertia so that the estimated moment of inertia is unlikely to decrease or become negative, but instead increases during updates.

Next, we consider a case where a time delay exists. In this study, we assume that a time delay exists only for the output, but not in the control input, and that this time delay does not vary, but instead, is always constant.

Because the control method tries to control the link angles so that the radius r and the phase argument velocity $\dot{\phi}$ are kept constant during the first step, if no time delay exists in the output, the vector of the link angle motion is always tangential to the vector from the goal angles to the current link angles, and thus the radius r never changes.

On the other hand, if a time delay τ exists, a phase argument difference $\tau\dot{\phi}$ occurs between the measured link angles $B(\hat{\phi}_1(t - \tau), \hat{\phi}_2(t - \tau))$ and the actual link angles $A(\hat{\phi}_1(t), \hat{\phi}_2(t))$, which corresponds to the time delay τ , as shown in Fig. 12. In this case, the vector of link angles velocity is determined as \vec{b} , based on the measured link angles B. This vector differs from the desired velocity vector \vec{a} which is determined in the absence of time delay. The phase argument difference results in a radius increase Δr . Taking this fact into consideration, we introduce here a method for estimating the time delay from radius changes.

Suppose that the radius at link angles A is the same as that of B. In this case, both vectors \vec{a} and \vec{b} have the same length $r\dot{\phi}$, as shown in Fig. 12. Taking into account that the angle between these two vectors corresponds to $\tau\dot{\phi}$, the radius increase can be approximately expressed as

$$\dot{r} = r\dot{\phi} \tan(\tau\dot{\phi}) \quad (61)$$

From this relation, using the radius increase Δr during a specified time duration Δt , the time delay τ can be estimated as

$$\tau = (1/\dot{\phi}) \tan^{-1}(\Delta r/r\dot{\phi}\Delta t) \quad (62)$$

Note that the radius r at the link angles A is not always the same as that at the measured link angles B due to the effect of the past control input, thus, the estimation of the time delay should be updated using Equation 62 several times. In this study, the time delay was estimated every phase argument change of $\delta\phi = \pi/4$ during the first step.

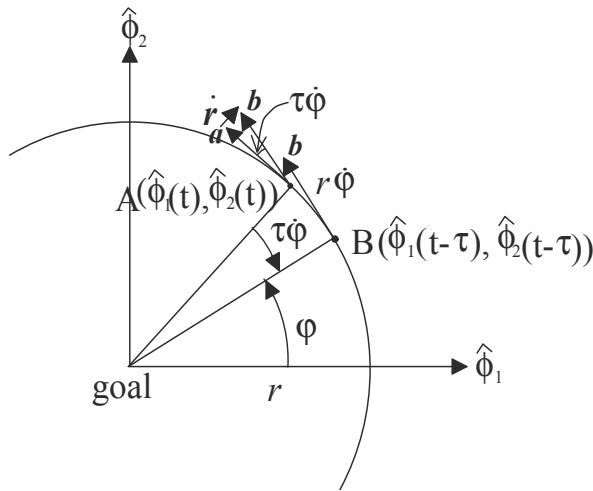


Fig. 12. Schematic representation of relation between the time delay and the radius change.

Until the next estimation of the time delay, the current attitude of the main body, the link angles (A in Fig. 12), and the radius r are predicted using the history of the past control input corresponding to the estimated time delay.

Then the new value for the control input is determined using the predicted current state. At the next estimation of the time delay, it is updated by inspecting the difference between the predicted radius and the actual one.

2.4 Experimental verification

2.4.1 Experimental setup

Fig. 13 shows the experimental setup of a planar two-link space robot. This robot was equipped with a magnetometer to sense the attitude of the main body, two stepper motors to drive each link angle, and two encoders to sense each link angle. Note that operational angle of each link was restricted within ± 110 deg due to structural limitations.

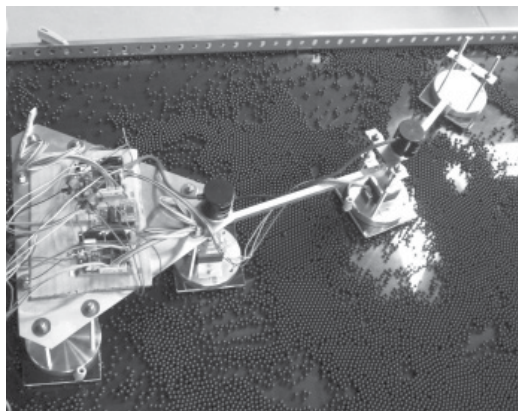


Fig. 13. Experimental apparatus for the planar two-link robot.

m_0	2.280 kg
m_1	0.922 kg
m_2	0.493 kg
l_{01}	0.125 m
l_{11}	0.283 m
l_{12}	0.017 m
l_{21}	0.270 m
J_0	0.03585 kgm ²
J_1	0.00410 kgm ²
J_2	0.00324 kgm ²

Table 1. Robot parameters.

A large glass board, called a flight-bed, was horizontally placed. To imitate microgravity, the surface of the board was paved with a number of ball bearings to decrease frictional drag. Note that friction due to the ball bearings was about 0.019 G, which is much greater than that of air bearings. The ball bearings, therefore, will have to be replaced with air bearings in the near future.

Because noise was included in the attitude output from the magnetometer, a low-pass filter, whose time-lag does not have an impact on the attitude measurement, was implemented, to cut off the noise. A personal desktop computer (PC) equipped with a digital board was placed next to the board. The PC measured the state of the robot via the board, determined the control input (link angular velocities) based on the control law implemented in the C language, and drove the stepper motors situated on the link joints. The sampling and control cycle is 100 msec.

The mass of each link was measured by an electro balance, and the moment of inertia of each link was measured by a moment of inertia measurement device, MOI-005-104 from the Inertia Dynamics and the LLC Co.

The moment of inertia of the main body was measured around the center of mass, while the moment of inertia of each link was measured around the joint part, and then converted to one around the mass center. The parameters of the experimental setup are as listed in Table 1.

2.4.2 Experimental results

Experiments were carried out on smooth invariant feedback control and the proposed adaptive invariant manifold based switching control using the parameters listed in Table 2. Then their convergence rates as they approached the goal state were compared in the presence of both modeling error and time delay.

Gains	$\alpha = 0.2, 0.4, n_1 = 1.0, n_2 = 2.0, n_3 = 1.0$ $n_4 = \pi/5, d = 0.2, \gamma = 0.05$
Initial state	$\phi_1 = \phi_2 = \theta = 0.3$ rad
Goal state	$\phi_{1d} = \phi_{2d} = 0.6$ rad, $\theta_d = 0.2$ rad
Initial estimated moment of inertia	$\hat{J}_0 = 0.015$ kgm ²

Table 2. Experimental conditions.

Taking into consideration that the magnetometric sensor output included noise of approximately 2 deg, the tolerance of the judgment of attainment with regard to the invariant manifold and the convergence criterion to the goal value were set to 2 deg in the mean square root of the second power of angle errors. The time delay was set to 0.5 sec, and implemented by feeding the controller the output measured five sampling cycles previously. The initial guess for the moment of inertia was set to 0.015 kgm², which is surely less than the actual value. We explain the results below.

Two results for the smooth invariant feedback control are shown in Figs. 14(a) and 14(b). These correspond to the results for control gains of $\alpha = 0.4$, and $\alpha = 0.2$, respectively. The results of the proposed control method are shown in Figs. 15 to 17. Figs. 15, 16, and 17 show the time responses of the state variables, the estimated time delay, and the estimated moment of inertia of the main body, respectively.

The link angle ϕ_1 controlled by the smooth invariant feedback control exceeded the link angle limitation around 4 sec for the case of a control gain with $\alpha = 0.4$. This is because the phase argument velocity $\dot{\phi}$ was very large, and the phase argument error due to time delay was also very large, thus leading to radius divergence, as explained in Fig. 12.

Contrary to the above case, for the case of the control gain $\alpha = 0.2$, which is less than that of the above case, the phase argument velocity $\dot{\phi}$ became smaller, the phase argument error due to time delay became smaller, which led to a smaller divergence rate of the link angles. As the result, the link angles did not exceed the angle limitation. Although the link angles reached the goal link angles, the attitude of the main body did not converge to the goal attitude. This is because β based on the mathematical model was incorrect, due to the error in the moment of inertia, and after determining that β approached zero, the link angles, which were controlled by the controller without any adaptive law to compensate for the error, moved to the goal angles (ϕ_{1d}, ϕ_{2d}) directly, and finally converged to other state. In addition, it took a long time for the link angles to move directly to the goal link angles (ϕ_{1d}, ϕ_{2d}) in the second step, because the control law almost became $\dot{r} = -\alpha r^3$, for which the convergence rate was not of first order as β approached zero.

On the other hand, the proposed control method succeeded in controlling so as to move the states to the goal states, and the estimated time delay and moment of inertia converged to 0.77 sec, and 0.0244 kgm², respectively.

The estimated moment of inertia of the main body was slightly less than the actual one. This may be because additional torque was generated due to friction between the ball bearings and the arms, which prevented the links from moving in the ideal motion, and in turn induced greater than the ideal attitude reaction of the main body, which resulted in an interpretation of the moment of inertia to be less than the actual one.

As shown in Fig. 16, the estimated time delay, 0.77 sec, was slightly greater than the actual time delay, that is, 0.5 sec. However, from Fig. 15, we can justify the estimated time delay because after the time delay was estimated, the magnitude of sinuous motion of the link angle ϕ_1 around the goal angle was the same as that of ϕ_2 for the period between 8 and 14 sec. In other words, it can be said that the radius r did not change; thus the states were almost correctly predicted.

After the time delay was estimated, the link angles changed their sinuous motion to straight line motion at a time of around 14 sec, in order to approach the goal angles at a first-order convergence rate, as shown in Fig. 15. This implies that the state approached the invariant manifold around the above time, and at that time the control logic changed from the first step to the second step.

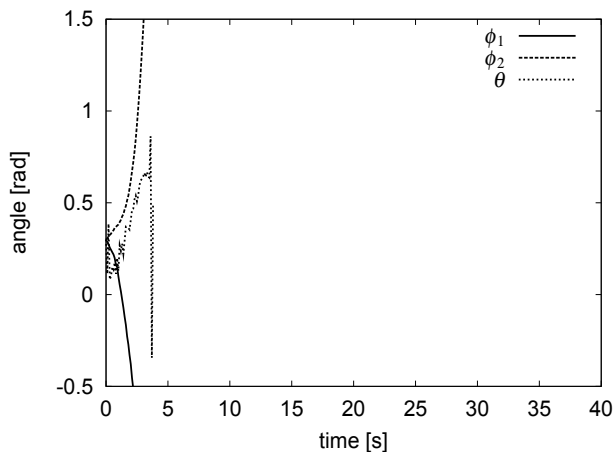
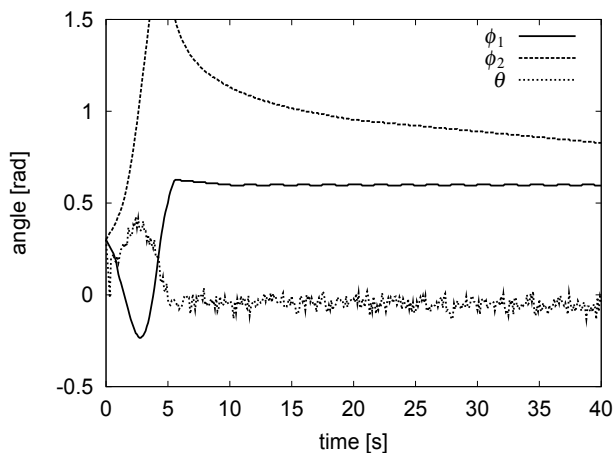
(a) $\alpha = 0.4$ (b) $\alpha = 0.2$

Fig. 14. Time responses of the state variables resulting from smooth invariant feedback control

In addition, Fig. 15 shows that the link motion returned to a sinuous motion at around 25 sec. This implies that even as the link angles were controlled to slide on the manifold, β left the convergence tolerance due to the moment of inertia error of the main body, and then the control logic returned to the first step.

We can observe in Fig. 17 that since the control logic returned to the first step, the adaptive law to estimate the moment of inertia of the main body re-functioned, the moment of inertia was updated towards the correct value at around 30 sec, and this update contributed to the state convergence to the goal state.

Consequently, the effectiveness of the proposed control method was validated by comparing the results of the smooth invariant feedback control method with those of the proposed control method.

3. Conclusion

This Chapter presents two main topics related to the space robotic systems: (1) Optimal trajectory planning for two-link robotic arm manipulators in the presence of chaotic wandering obstacles and (2) Invariant manifold based control methods for spacecraft attitude control problems.

The first Section describes mathematical modeling of a two-link robotic manipulator in three-dimensional space using Lagrange equations. The system includes three rotational joints (RRR) and a point mass payload at the end effector. To ensure collision avoidance, the path constraints are formulated based on the projected obstacle's position along the arms of the robot. The associated non-linear optimization problems were formulated and solved using the Chebyshev-pseudospectral method. It should be stressed out that, the method presented in the current work allows not only to minimize the specified arbitrary non-linear cost function, but also allows to solve the optimization task in view of multiple additional non-linear constraints that the user of the robotic systems may choose to impose based on mission requirements or considerations. In the current work a procedure of optimal path planning for rigid manipulators performing operations in presence of the wandering obstacles, changing their positions and shapes, has been successfully implemented. The optimal scenarios enable to perform deployment of the payloads avoiding their collision with the non-statioary obstacles. It has been demonstrated that the actuator efforts required to perform the task is higher than for the similar cases without the obstructing obstacles. Examples of additional constraints may involve path constraints on the system, prohibiting the members to enter a specified space area or, on the contrary, prescribing the system to follow the desired trajectory or prescribing for the members of the robotic system not to leave the allowed bandwidth corridors. The method is generic and is not restricted to the listed examples of the cost functions and additional constraints.

In the second Section, an adaptive invariant manifold based switching control has been proposed for controlling a planar two-link space robot. The proposed control method is a kind of invariant manifold based control, and has two advanced functions: estimation of the time delay in the system, and estimation of the moment of inertia of the main body. The proposed

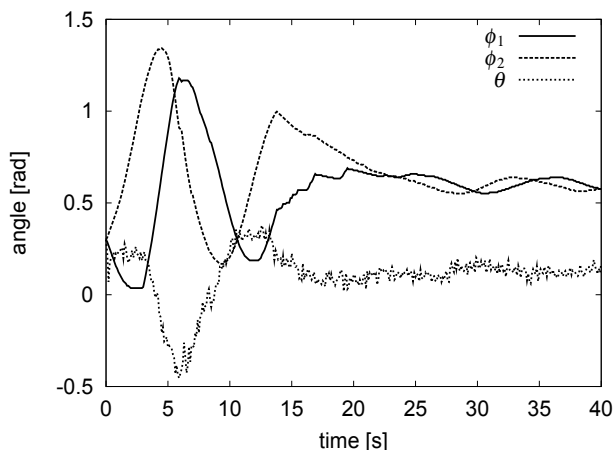


Fig. 15. Time responses of the state variables for the case of adaptive invariant manifold switching control.

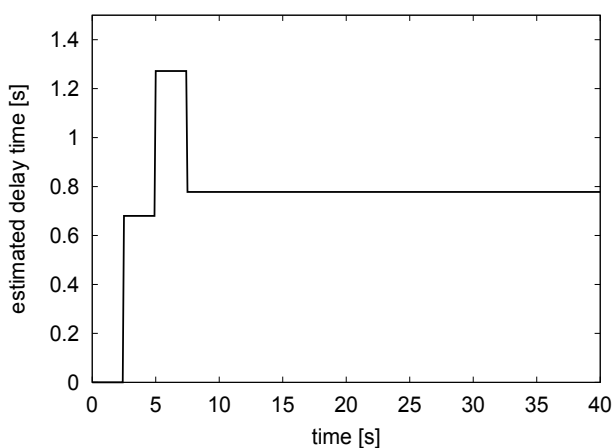


Fig. 16. Time response of the estimated time delay.

control method consists of two steps. In the first step, link angles are controlled to carry out Lie bracket motion so that the attitude of the main body approaches the invariant manifold as much as possible. In addition, the time delay and the modeling error due to the moment of inertia are estimated. During the first step, provided that a time delay does not exist, the control method manages to control the link angles so that the distance between the current link angles and goal link angles, that is, the radius, is kept constant. The radius does however change, due to the time delay. Taking into consideration the relation between the change of radius and the time delay, the time delay is estimated from the change in the radius. After estimating the time delay, a modeling error, which is taken to be the difference between the accurate and the estimated moments of inertia of the main body, is estimated by comparing the predicted attitude change of the main body and the actual one, and then the mathematical moment of inertia is updated. In the second step, the link angles are controlled to slide on the invariant manifold until it converges to the goal state. The effectiveness of the functions of the proposed control scheme method, the reduction in convergence time compared to the smooth

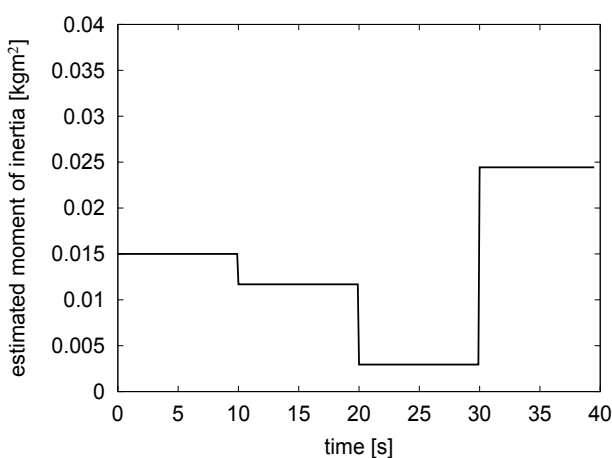


Fig. 17. Time response of the estimated moment of inertia of the main body.

invariant feedback control, and estimation of not only the time delay, but also the modeling errors, were successfully verified experimentally.

4. References

- Brockett, R. (1983). *Differential Geometric Control Theory, Asymptotic Stability and Feedback Stabilization*, Birkhauser, Boston.
- Cao, B., Dodds, G. & Irwin, G. (1997). Constrained time-efficient and smooth cubic spline trajectory generation for industrial robots, *Control Theory and Applications, IEE Proceedings - 144(5)*: 467–475.
- Cerven, W. T. & Coverstone, V. L. (2001). Optimal reorientation of a multibody spacecraft through joint motion using averaging theory, *Journal of Guidance, Control and Dynamics* 24(4): 788–795.
- Gil, P., Murray, W. & Saunders, M. (2002). *User's Guide for SNOPT, Version 6: A FORTRAN Package for Large-Scale Nonlinear Programming*, University of California, San Diego, CA.
- Hashimoto, T., F. A. H. & Amemiya, T. (2006). Simultaneous feedback stabilization of space robot attitude, *J. Japan Soc. Aero. Space Sci.* 54(635): 549–554.
- Hokamoto, S. & Funasako, T. (2007). Feedback control of a planar space robot using a moving manifold, *Journal of Robotic Society of Japan* 25(5): 95–101.
- Hu, S., Xue, L., Xu, W., Qiang, W. & Liang, B. (2008). Trajectory planning of space robot system for reorientation after capturing target, *Systems and Control in Aerospace and Astronautics, 2008. ISSCAA 2008. 2nd International Symposium on*, pp. 1–6.
- Huang, P. & Xu, Y. (2006). Pso-based time-optimal trajectory planning for space robot with dynamic constraints, *Robotics and Biomimetics, 2006. ROBIO '06. IEEE International Conference on*, Kunming, China, pp. 1402–1407.
- Kojima, H. & Kasahara, S. (2010). Adaptive invariant manifold based switching control for planar two-link space robot(2nd report), *J. Japan Soc. Aero. Space Sci.* 58(679): 233–238.
- Luo, J. & Tsiotras, P. (1998). Exponentially convergent control laws for nonholonomic systems in power form, *Systems & Control Letters* 35(2): 87–95.
- Luo, X., Fan, X., Zhang, H. & Chen, T. (2004). Integrated optimization of trajectory planning for robot manipulators based on intensified evolutionary programming, *Robotics and Biomimetics, 2004. ROBIO 2004. IEEE International Conference on*, pp. 546–551.
- Mukherjee, R. & Kamon, M. (1999). Almost smooth time-invariant control of planar space multibody systems, *Robotics and Automation, IEEE Transactions on* 15(2): 268–280.
- Pomet, J. B. (1992). Explicit design of time-varying stabilization control law for a class of controllable systems without drift, *Systems & Control Letters* 18(2): 147–158.
- Reyhanoglu, M. & McClamroch, H. H. (1992). Planar reorientation maneuvers of space multibody systems using internal controls, *Journal of Guidance, Control, and Dynamics* 15(6): 1475–1480.
- Samson, C. (1995). Control of chained systems application to path following and time-varying point- stabilization of mobile robots, *Automatic Control, IEEE Transactions on* 40(1): 64–77.
- Seshadri, C. & Ghosh, A. (1993). Optimum path planning for robot manipulators amid static and dynamic obstacles, *Systems, Man and Cybernetics, IEEE Transactions on* 23(2): 576–584.
- Sordalen, O. & Egeland, O. (1995). Exponential stabilization of nonholonomic chained systems, *Automatic Control, IEEE Transactions on* 40(1): 35–49.

- Teel, A. R., M. R. M. & Walsh, G. C. (1995). Nonholonomic control systems: From steering to stabilization with sinusoids, *International Journal of Control* 62(4): 849–870.
- Trivailo, P. M. (2007). Collision-free trajectory planning for 2d and 3d robotic arm manipulators in the presence of mobile wandering obstacles - paper iac-07-c2.3.02., 58th International Astronautical Federation Congress, Hyderabad, India, pp. 4952–4960.
- Vannoy, J. & Xiao, J. (2008). Real-time adaptive motion planning (ramp) of mobile manipulators in dynamic environments with unforeseen changes, *Robotics, IEEE Transactions on* 24(5): 1199–1212.
- Williams, P. (2005). *User's Guide to DIRECT, Version 1.17*, RMIT Technical Report, Melbourne, Australia.
- Williams, P., Trivailo, P. M. & Lee, K. W. (2009). Real-time optimal collision-free control for robotic arm manipulators in the presence of wandering obstacles, *60th International Astronautical Congress*, Vol. 7, pp. 5500–5508.
- Xu, W., Li, C., Liang, B., Xu, Y., Liu, Y. & Qiang, W. (2009). Target berthing and base reorientation of free-floating space robotic system after capturing, *ACTA ASTRONAUTICA* 64(2-3): 109–126.
- Yamada, K. (1994). Attitude control of space robot by arm motion, *Journal of Guidance, Control, and Dynamics* 17(5): 1050–1054.
- Yoshida, E., Esteves, C., Belousov, I., Laumond, J.-P., Sakaguchi, T. & Yokoi, K. (2008). Planning 3-d collision-free dynamic robotic motion through iterative reshaping, *Robotics, IEEE Transactions on* 24(5): 1186–1198.

Optimal Control Techniques for Spacecraft Attitude Maneuvers

Shifeng Zhang, Shan Qian and Lijun Zhang
*National University of Defense Technology,
P. R. China*

1. Introduction

The capability of attitude maneuvers and attitude tracking for spacecrafts is required in the current sophisticated space missions. In short, it is to obtain command requirements and attitude orientation after some form of control. With the development of space missions, the ability of rapid and energy-saved large-angle attitude maneuvers is actively expected. And the high requirements for the attitude control design system are increasingly demanded. Consequently, optimal control for attitude maneuvers has become an important research direction in the aerospace control area.

From control aspect, spacecraft attitude maneuvers mainly involve trajectory planning (Guidance), attitude determination (Navigation), and attitude control (Control). Further researches about these three key technologies are necessary to achieve optimal control for attitude maneuvers. In this chapter, the necessary background on optimal control for attitude maneuvers of three-axis stabilized spacecraft is provided, and the recent work about guidance and navigation as well as control is summarized, which is presented from three parts as follows:

1. The optimal trajectory planning method for minimal energy maneuvering control problem (MEMCP) of a rigid spacecraft;
2. Attitude determination algorithm based on the improved gyro-drift model;
3. Attitude control of three-axis stabilized spacecraft with momentum wheel system.

2. Optimal trajectory planning method for MEMCP of a rigid spacecraft

The trajectory planning for attitude maneuvers is to determine the standard trajectory for spacecraft attitude maneuvers with multi-constraints using optimization algorithm, which makes the spacecraft move from the initial state to the anticipated state within the specified period and optimizes the given performance index. At present, the optimal trajectory planning problems for spacecraft attitude maneuver mainly focus on the time-optimal and fuel-optimal control. A fuel-optimal reorientation attitude control scheme for symmetrical spacecraft with independent three-axis controls is derived in (Li & Bainum, 1994). Based on the low-thrust gas jet model and Euler's rotational equation of motion, Junkins and Turner (Junkins & Turner, 1980) investigate the optimal attitude control problem with multi-axis maneuvers. They use the closed-form solution of the single-axis maneuver as an initial value and minimize the quadratic sum of the integral of the control torques. Vadali and Junkins (Vadali & Junkins, 1984) have addressed the large-angle reorientation optimal attitude

control problem for asymmetric rigid spacecraft with multiple reaction wheels by using an integral of a weighted quadratic function associated with controlled variables as loss function. Further more, Vadali and Junkins (Vadali & Junkins, 1983) also investigate the optimal attitude maneuvering control problem of rigid vehicles.

The complete optimal attitude control problem is essentially a two-point boundary value problem. Since the input variables of the control system are restricted, Pontryagin's Minimum Principle (PMP) is usually used to solve the optimal attitude control problem of the symmetric or asymmetric rigid spacecraft with constraints. The optimal attitude control problem with fixed maneuvering period has been solved in (Vadali & Junkins, 1984; Vadali & Junkins, 1983; Dwyer, 1982; Schaub & Junkins, 1997). In practice, numerical methods are generally used to solve the highly nonlinear and close coupling differential equations derived from PMP. However, the method falls short to deal with dynamic optimization problem with uncertain terminal time, and the shooting method is commonly adopted whereas it will increase the iterations and computational burden. Therefore, the satisfied development has not yet been achieved for large-angle attitude reorientation of asymmetric rigid spacecraft up to now.

Recently, (Chung & Wu, 1992) presents a nonlinear programming (NLP) method to solve time-optimal control problem for linear system. Different from the conventional shooting method which sets the time step as a fixed value, the NLP method considers the time step as a variable and obtains the optimal solution on the premise of ensuring sufficient discretization precision of the model. (Yang et al., 2007) further discusses MEMCP of a rigid spacecraft, which introduces two aspects of research on the three-axis spacecraft with limited output torque, including: 1) the description of MEMCP using NLP method, and 2) the construction method for initial feasible solution of the NLP. However, the derivation in that paper has some errors and the initial feasible solution does not conform to the actual motion of the spacecraft. Moreover, the method augments the optimizing time and the randomness of the variation between the adjacent attitude commands. Consequently, this section (Zhang et al., 2009) further improves the proposed method and presents a new construction method for initial feasible solution of the NLP, and obtains the optimal control period and torques by the energy-optimal criterion. Simulation results demonstrate the feasibility and advantages of the improved method.

2.1 Dynamical and kinematical equations of a rigid spacecraft

The attitude motion of a spacecraft can be described by its dynamical and kinematical equations. In general, the dynamic equation of motion can be represented as

$$\begin{bmatrix} \dot{\omega}_x \\ \dot{\omega}_y \\ \dot{\omega}_z \end{bmatrix} = - \begin{bmatrix} 1/I_x & 0 & 0 \\ 0 & 1/I_y & 0 \\ 0 & 0 & 1/I_z \end{bmatrix} \begin{bmatrix} 0 & -\omega_z & \omega_y \\ \omega_z & 0 & -\omega_x \\ -\omega_y & \omega_x & 0 \end{bmatrix} \times \left\{ \begin{bmatrix} (I_x + I_1)\omega_x \\ (I_y + I_2)\omega_y \\ (I_z + I_3)\omega_z \end{bmatrix} + \begin{bmatrix} I_1\omega_1 \\ I_2\omega_2 \\ I_3\omega_3 \end{bmatrix} \right\} - \begin{bmatrix} T_1 / I_x \\ T_2 / I_y \\ T_3 / I_z \end{bmatrix} \quad (1)$$

where I_x, I_y, I_z and I_1, I_2, I_3 denote the moment of inertia of rigid spacecraft about the principal axis and the three reaction wheels, respectively. $\omega_x, \omega_y, \omega_z$ are the components of spacecraft's angular velocity expressed in its body-fixed frame, and $\omega_1, \omega_2, \omega_3$ are the components of the reaction wheel's angular velocity. T_1, T_2, T_3 are the control torques provided by the perpendicular momentum wheels along the principal axis.

The equation of angular motion of the momentum wheels can be obtained from Eq.(1)

$$\begin{bmatrix} \dot{\omega}_1 \\ \dot{\omega}_2 \\ \dot{\omega}_3 \end{bmatrix} = \begin{bmatrix} 1/I_x & 0 & 0 \\ 0 & 1/I_y & 0 \\ 0 & 0 & 1/I_z \end{bmatrix} \begin{bmatrix} 0 & -\omega_z & \omega_y \\ \omega_z & 0 & -\omega_x \\ -\omega_y & \omega_x & 0 \end{bmatrix} \times \left\{ \begin{bmatrix} (I_x + I_1)\omega_x \\ (I_y + I_2)\omega_y \\ (I_z + I_3)\omega_z \end{bmatrix} + \begin{bmatrix} I_1\omega_1 \\ I_2\omega_2 \\ I_3\omega_3 \end{bmatrix} \right\} + \begin{bmatrix} (1/I_x + 1/I_1)T_1 \\ (1/I_y + 1/I_2)T_2 \\ (1/I_z + 1/I_3)T_3 \end{bmatrix} \quad (2)$$

Considering the 1-2-3 sequence of rotations, the kinematic equation of motion using Euler angle representation is given by

$$\begin{bmatrix} \dot{\phi} \\ \dot{\theta} \\ \dot{\psi} \end{bmatrix} = \begin{bmatrix} \sec \theta \cos \psi & -\sec \theta \sin \psi & 0 \\ \sin \psi & \cos \psi & 0 \\ -\tan \theta \cos \psi & \tan \theta \sin \psi & 1 \end{bmatrix} \begin{bmatrix} \omega_x \\ \omega_y \\ \omega_z \end{bmatrix} \quad (3)$$

where ϕ is roll angle, θ is pitch angle and ψ is yaw angle.

2.2 Modeling and analysis of MEMCP

The MEMCP of the rigid spacecraft between two attitudes can be described as an optimizing problem as follows.

The initial attitude is given by

$$\begin{cases} (\phi(0), \theta(0), \psi(0)) = (\phi_{\text{initial}}, \theta_{\text{initial}}, \psi_{\text{initial}}) \\ (\omega_x(0), \omega_y(0), \omega_z(0)) = (0, 0, 0) \\ (\omega_1(0), \omega_2(0), \omega_3(0)) = (\omega_{1,\text{initial}}, \omega_{2,\text{initial}}, \omega_{3,\text{initial}}) \end{cases} \quad (4)$$

The goal is to determine the control inputs $\mathbf{T}(t) = [T_1(t), T_2(t), T_3(t)]^T$ for some $t \in [0, t_f]$ to minimize the following objective function

$$J = \int_0^{t_f} (T_1^2(t) + T_2^2(t) + T_3^2(t)) dt = \int_0^{t_f} \sum_{k=1}^3 T_k^2(t) dt$$

subject to

$$\begin{cases} (\phi(t_f), \theta(t_f), \psi(t_f)) = (\phi_{\text{final}}, \theta_{\text{final}}, \psi_{\text{final}}) \\ (\omega_x(t_f), \omega_y(t_f), \omega_z(t_f)) = (0, 0, 0) \\ T_{i,\text{min}} \leq T_i(t) \leq T_{i,\text{max}}, \text{ for } t \in [0, t_f], \quad i = 1, 2, 3 \end{cases} \quad (5)$$

where $(\phi_{\text{initial}}, \theta_{\text{initial}}, \psi_{\text{initial}})$ and $(\phi_{\text{final}}, \theta_{\text{final}}, \psi_{\text{final}})$ represent the initial and desired final attitudes of the spacecraft, respectively. t_f is determined by the optimization process.

Due to the characteristics of highly nonlinear and close coupling of the problem, it will be solved in the discrete-time domain using numerical method. First, we divide the interval $t \in [0, t_f]$ into N equidistant subinterval and assume that the angular acceleration is constant in each subinterval. Therefore, from Eq.(1) and Eq.(2), we can obtain

$$\begin{aligned} \begin{bmatrix} \omega_x(i) \\ \omega_y(i) \\ \omega_z(i) \end{bmatrix} &= \begin{bmatrix} \omega_x(0) \\ \omega_y(0) \\ \omega_z(0) \end{bmatrix} - \begin{bmatrix} 1/I_x & 0 & 0 \\ 0 & 1/I_y & 0 \\ 0 & 0 & 1/I_z \end{bmatrix} \sum_{k=0}^{i-1} \left\{ \begin{bmatrix} 0 & -\omega_z(k) & \omega_y(k) \\ \omega_z(k) & 0 & -\omega_x(k) \\ -\omega_y(k) & \omega_x(k) & 0 \end{bmatrix} \times \right. \\ &\quad \left. \begin{bmatrix} (I_x + I_1)\omega_x(k) + I_1\omega_1(k) \\ (I_y + I_2)\omega_y(k) + I_2\omega_2(k) \\ (I_z + I_3)\omega_z(k) + I_3\omega_3(k) \end{bmatrix} + \begin{bmatrix} T_1(k) / I_x \\ T_2(k) / I_y \\ T_3(k) / I_z \end{bmatrix} \right\} \Delta t \end{aligned} \tag{6}$$

$$\begin{aligned} \begin{bmatrix} \omega_1(i) \\ \omega_2(i) \\ \omega_3(i) \end{bmatrix} &= \begin{bmatrix} \omega_1(0) \\ \omega_2(0) \\ \omega_3(0) \end{bmatrix} + \begin{bmatrix} 1/I_x & 0 & 0 \\ 0 & 1/I_y & 0 \\ 0 & 0 & 1/I_z \end{bmatrix} \sum_{k=0}^{i-1} \left\{ \begin{bmatrix} 0 & -\omega_z(k) & \omega_y(k) \\ \omega_z(k) & 0 & -\omega_x(k) \\ -\omega_y(k) & \omega_x(k) & 0 \end{bmatrix} \times \right. \\ &\quad \left. \begin{bmatrix} (I_x + I_1)\omega_x(k) + I_1\omega_1(k) \\ (I_y + I_2)\omega_y(k) + I_2\omega_2(k) \\ (I_z + I_3)\omega_z(k) + I_3\omega_3(k) \end{bmatrix} + \begin{bmatrix} (1/I_x + 1/I_1)T_1(k) \\ (1/I_y + 1/I_2)T_2(k) \\ (1/I_z + 1/I_3)T_3(k) \end{bmatrix} \right\} \Delta t \end{aligned} \tag{7}$$

where $\Delta t = t_i - t_{i-1} = t_f / N$, $i = 1, 2, \dots, N$.

Suppose that the time derivative of ϕ, θ, ψ are constant during each subinterval, then we have

$$\begin{bmatrix} \phi(i) \\ \theta(i) \\ \psi(i) \end{bmatrix} = \begin{bmatrix} \phi(0) \\ \theta(0) \\ \psi(0) \end{bmatrix} + \sum_{k=0}^{i-1} \begin{bmatrix} \sec \theta(k) \cos \psi(k) & -\sec \theta(k) \sin \psi(k) & 0 \\ \sin \psi(k) & \cos \psi(k) & 0 \\ -\tan \theta(k) \cos \psi(k) & \tan \theta(k) \sin \psi(k) & 1 \end{bmatrix} \begin{bmatrix} \omega_x(k) \\ \omega_y(k) \\ \omega_z(k) \end{bmatrix} \Delta t \tag{8}$$

Therefore, the previous MEMCP can be described as a constrained NLP problem. Given the initial attitudes, determine the values of $T(0), \dots, T(N-1)$ and Δt to minimize

$$J = \sum_{k=1}^3 \sum_{i=0}^{N-1} T_k^2(i) \Delta t$$

subject to

$$\begin{cases} 0 < \varepsilon < \Delta t < \Delta t_{\text{upper}} \\ (\phi(N), \theta(N), \psi(N)) = (\phi_{\text{final}}, \theta_{\text{final}}, \psi_{\text{final}}) \\ (\omega_x(N), \omega_y(N), \omega_z(N)) = (0, 0, 0) \\ T_{i,\text{min}} \leq T_i(j) \leq T_{i,\text{max}}, \quad i = 1, 2, 3; \quad j = 0, 1, \dots, N-1 \end{cases} \tag{9}$$

where ε is a small positive number to ensure the computation time is not excessively long. The question is how to select the value of N to solve the discrete NLP problem mentioned above. For the unconstrained linear programming problem, (Chung & Wu, 1992) points out the initial value of N must be greater than the dimensions of the state variables, which is adopted in this paper.

2.3 Construction of initial feasible solution of NLP problem

The NLP problem usually requires the initial feasible solution to start the optimization process. The initial feasible solution is a set of optimization variables $T(0), \dots, T(N-1)$ and Δt which satisfy Eq.(9). Different initial feasible solutions will yield different local optimal solutions, and the deviation of the initial feasible solution from the optimal solution will affect the iteration times and computation time. (Yang et al., 2007) presents a construction method of the initial feasible solution. However, the solution does not agree well with the actual motion of the spacecraft, and the randomness of variation between the adjacent attitude commands is excessively large. To solve this problem, a new construction of the initial feasible is presented in this section.

The first step is to determine a maneuvering trajectory satisfying the boundary conditions without the constraints of the control torques. Then, the set of control torques computed in the above trajectory is checked. If it satisfies all the constraints, the set of control torques and Δt is the initial feasible solution. Otherwise, we need to adjust the velocity and acceleration until finding a set of initial feasible solution.

With the given N , the attitude trajectories satisfying the boundary conditions can be determined by

$$\phi(i) = \begin{cases} \phi_{\text{initial}} & i = 0, 1 \\ \gamma_i \phi(i-1) + \frac{i-2}{N-2} \gamma_i (\phi_{\text{final}} - \phi(i-1)) & i = 2, \dots, N-1 \\ \phi_{\text{final}} & i = N, N+1 \end{cases} \quad \theta(i) = \begin{cases} \theta_{\text{initial}} & i = 0, 1 \\ \theta(i-1) + \frac{i-2}{N-2} \gamma_i (\theta_{\text{final}} - \theta(i-1)) & i = 2, \dots, N-1 \\ \theta_{\text{final}} & i = N, N+1 \end{cases} \quad (10)$$

$$\psi(i) = \begin{cases} \psi_{\text{initial}} & i = 0, 1 \\ \psi(i-1) + \frac{i-2}{N-2} \gamma_i (\psi_{\text{final}} - \psi(i-1)) & i = 2, \dots, N-1 \\ \psi_{\text{final}} & i = N, N+1 \end{cases}$$

where γ_i is a random number obeying the uniform distribution in the interval $[0, 1]$. Euler angle vector is defined as $\lambda = [\phi, \theta, \psi]^T$, and it is obvious that $\lambda(i)$ satisfies the initial constraints in Eq.(4) and final constraints in Eq.(9).

Take the roll angle ϕ for example, we can easily obtain the inequalities $\phi(i-1) \leq \phi(i) \leq \phi_{\text{final}}$ or $\phi(i-1) \geq \phi(i) \geq \phi_{\text{final}}$. It is shown that the attitude trajectory $\phi(i)$ constructed by the previous model approaches the value of ϕ_{final} all along. The process is not reciprocating and in well agreement with the optimal maneuvering process.

Choose the appropriate value of Δt to satisfy the constraint $0 < \varepsilon < \Delta t < \Delta t_{\text{upper}}$, so that

$$\begin{bmatrix} \dot{\phi}(i) \\ \dot{\theta}(i) \\ \dot{\psi}(i) \end{bmatrix} = \begin{bmatrix} \frac{\phi(i+1) - \phi(i)}{\Delta t} \\ \frac{\theta(i+1) - \theta(i)}{\Delta t} \\ \frac{\psi(i+1) - \psi(i)}{\Delta t} \end{bmatrix} \quad i = 0, 1, \dots, N \quad (11)$$

where $[\dot{\phi}(0) \ \dot{\theta}(0) \ \dot{\psi}(0)] = [0 \ 0 \ 0]$ and $[\dot{\phi}(N) \ \dot{\theta}(N) \ \dot{\psi}(N)] = [0 \ 0 \ 0]$. We can obtain from Eq.(3) that

$$\begin{bmatrix} \omega_x(i) \\ \omega_y(i) \\ \omega_z(i) \end{bmatrix} = \begin{bmatrix} \sec\theta(i)\cos\psi(i) & -\sec\theta(i)\sin\psi(i) & 0 \\ \sin\psi(i) & \cos\psi(i) & 0 \\ -\tan\theta(i)\cos\psi(i) & \tan\theta(i)\sin\psi(i) & 1 \end{bmatrix}^{-1} \begin{bmatrix} \dot{\phi}(i) \\ \dot{\theta}(i) \\ \dot{\psi}(i) \end{bmatrix} \quad (12)$$

Obviously, the angular velocity ω also satisfies the boundary constraints in Eq.(4) and Eq.(9).

Then let us check whether the maneuvering trajectory satisfies the torque constraints or not. After determining $(\omega_x(i), \omega_y(i), \omega_z(i))$ and $(\dot{\omega}_x(i), \dot{\omega}_y(i), \dot{\omega}_z(i))$, the corresponding values of $T(0), \dots, T(N-1)$ can be sequentially calculated. The calculation flow is summarized as follows:

1. Substituting $(\omega_1(0), \omega_2(0), \omega_3(0))$ and $(\omega_x(0), \omega_y(0), \omega_z(0))$ into Eq.(6) to calculate $(T_1(0), T_2(0), T_3(0))$.
2. Substituting $(\omega_1(0), \omega_2(0), \omega_3(0))$, $(\omega_x(0), \omega_y(0), \omega_z(0))$ and $(T_1(0), T_2(0), T_3(0))$ into Eq.(7) to determine $(\omega_1(1), \omega_2(1), \omega_3(1))$.
3. Repeat the step 1 and step 2, and determine the values of $T(0), \dots, T(N-1)$ sequentially.

If the obtained control torques satisfy the constraints, the set of $T(0), \dots, T(N-1)$ and Δt is the initial feasible solution. Otherwise, Δt is increased to decrease the maneuvering velocity and acceleration until the control torques satisfy the constraints. Since the initial feasible solution is stochastically yielded via Eq.(10), the final optimal control scheme is derived from the multiple initial feasible solutions separately.

2.4 NLP solution process of MEMCP

On the basis of the previous sections, the NLP solution process of MEMCP can be described as follows:

- Step 1.** Choose an integer N and iteration number n_f ;
- Step 2.** Set $i = 0$;
- Step 3.** Describe the MEMCP using NLP model;
- Step 4.** $i = i + 1$;
- Step 5.** Determine the NLP initial feasible solution of MEMCP;
- Step 6.** Solve the MEMCP using NLP with the given initial values;
- Step 7.** If $i \leq n_f$, then go to step 5, if not, continue;
- Step 8.** Choose the smallest local optimal solution as the solution of MEMCP;
- Step 9.** End.

In the above algorithm, the computation time and nonlinear degree should be considered to choose n_f , it is generally set as 20. In addition, the value of Δt is required smaller to obtain the high discretization accuracy, while it is also required as larger as possible to minimize the energy consumption. By the tradeoff, we can determine the upper limit denoted as Δt_{limit} . If $\Delta t(N)$ is greater than Δt_{limit} , the value of N needs to be adjusted. (Chung & Wu, 1992) provides a selection and adjustment approach about the values of Δt_{limit} and N .

2.5 Simulation results

In this section, the feasibility and validity of the above approach are verified. The following parameters are used for simulations. The initial conditions are $(\omega_x(0), \omega_y(0), \omega_z(0)) = (0, 0, 0)$, $(\phi(0), \theta(0), \psi(0)) = (0, 0, 0)$, $(\omega_1(0), \omega_2(0), \omega_3(0)) = (0, 0, 0)$, and the final conditions are:

$(\omega_x(t_f), \omega_y(t_f), \omega_z(t_f)) = (0, 0, 0)$, $(\phi(t_f), \theta(t_f), \psi(t_f)) = (30, 45, 0)$. The boundary conditions of control torques are :

$(T_{1,max}, T_{2,max}, T_{3,max}) = (0.56, 0.53, 0.24)(Nm)$, $(T_{1,min}, T_{2,min}, T_{3,min}) = (-0.56, -0.53, -0.24)(Nm)$. The moment of inertia of spacecraft are $(I_x, I_y, I_z) = (182, 329, 336)(kgm^2)$, and the moment of inertia of momentum wheels are $I_1 = I_2 = I_3 = 0.041(kgm^2)$.

2.5.1 Case 1

The case is used to verify the construction of initial feasible solution of NLP. When Δt is small (e.g., $\Delta t = 6s$), the initial set of control torques $T(0), \dots, T(N-1)$ is large. The control torques obtained will be easy to exceed the constraints, as shown in Table 1. It is necessary to increase the value of Δt (e.g., $\Delta t = 10s$) to decrease the maneuvering velocity and acceleration. Thus, the control torques can satisfy the constraints, as illustrated in Table 2.

	ϕ	θ	ψ	T_1	T_2	T_3
1	0	0	0	-0.272	-0.737	0
2	3.080	0	0	0.009	0.021	-0.039
3	6.073	4.620	0	-0.218	-0.605	-0.103
4	11.60	9.110	0	-0.133	-0.423	-0.213
5	18.88	17.39	0	0.116	0.211	-0.140
6	25.29	28.32	0	0.316	0.908	0.234
7	27.90	37.93	0	0.160	0.547	0.226
8	28.22	41.85	0	-0.026	-0.095	-0.044
9	28.94	42.33	0	-0.021	-0.080	-0.040
10	30	43.41	0	0.068	0.253	0.118
11	30	45	0	--	--	--

Table 1. A set of infeasible solution to $\Delta t = 6s$ and $N = 10$

	ϕ	θ	ψ	T_1	T_2	T_3
1	0	0	0	-0.113	-0.307	0
2	0	0	0	0.065	0.175	-0.008
3	3.563	5.345	0	-0.130	-0.357	-0.036
4	5.091	7.636	0	0.036	0.086	-0.032
5	10.76	16.14	0	-0.094	-0.296	-0.111
6	15.44	23.15	0	0.141	0.381	0.062
7	23.55	35.32	0	0.069	0.223	0.083
8	27.24	40.85	0	0.026	0.092	0.041
9	28.34	42.51	0	-0.037	-0.138	-0.063
10	28.37	42.56	0	0.038	0.140	0.065
11	30	45	0	--	--	--

Table 2. A set of feasible solution to $\Delta t = 10s$ and $N = 10$

2.5.2 Case 2

Fig. 1 illustrates the performance index J with respect to different values of Δt_{upper} in the cases of $N = 10$ and $N = 20$. When the maneuvering times N is fixed, we can find that a larger value of Δt_{upper} will result in a smaller value of J ; when Δt_{upper} is fixed, the greater value of N will result in the smaller value of performance index J . It is shown that the longer maneuvering period will require the smaller energy consumption which agrees well with the actual situation.

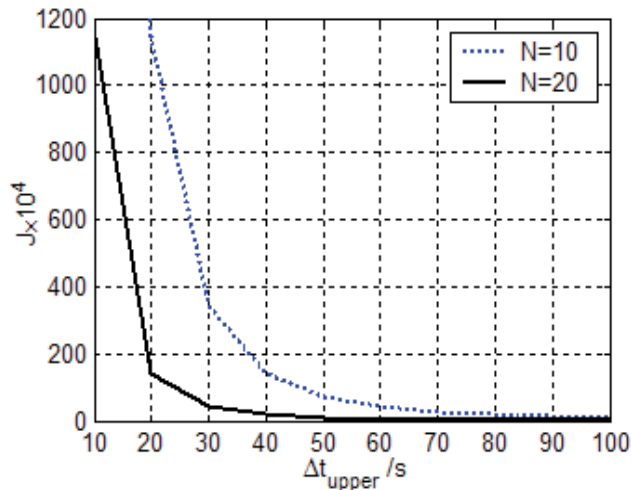


Fig. 1. Performance index J with respect to Δt_{upper}

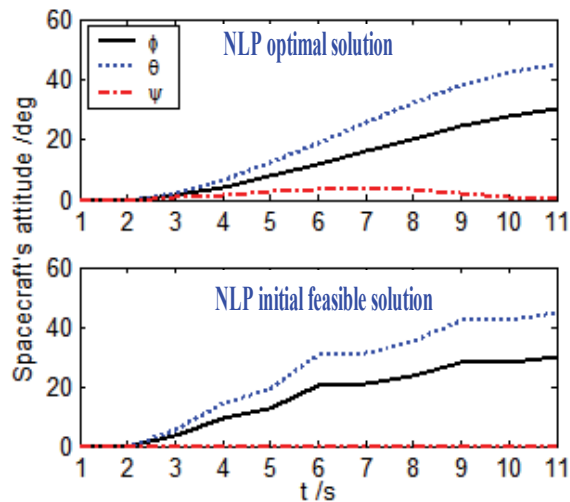


Fig. 2. Spacecraft's attitude

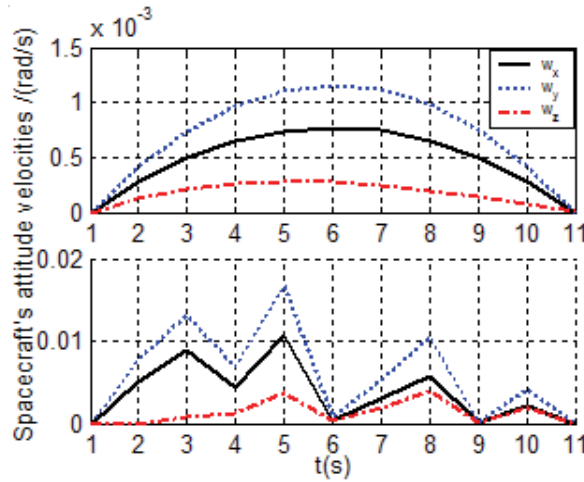


Fig. 3. Spacecraft's angular velocities

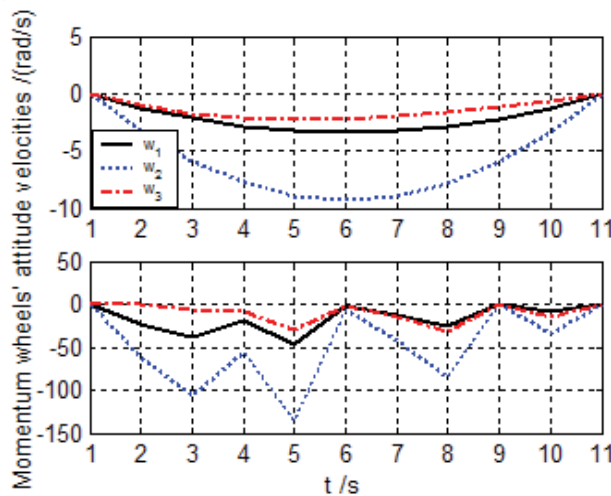


Fig. 4. Momentum wheels' angular velocities

2.5.3 Case 3

In this simulation case, we choose the parameters $N = 10$ and $\Delta t_{upper} = 100s$. Figs. 2-4 show the responses of attitude angle λ and angular velocities of spacecraft ω as well as angular velocity of momentum wheels ω_w , respectively. In each figure, we compared the results in the case of NLP initial feasible solution (top) and NLP optimal solution (bottom). Obviously, in the initial feasible solution of NLP, the Euler angles λ tend to the final attitude angle all the time while the variation curve is not smooth. The curve of ω_w is oscillating and unstable, which means that the control inputs vary severely during the attitude maneuvers. After a period of the NLP optimizing, Euler angle λ approaches the desired states gradually, control curve ω_w is steady and smooth, and the energy function of the control decreases from 7.3217 to 9.1401×10^{-4} .

3. Attitude determination algorithm based on the improved gyro-drift model

Attitude determination is the process of computing the orientation of the spacecraft relative to an inertial reference frame or some reference objects in space (e.g., Earth, Sun, Star) using attitude sensors. It is prerequisite of attitude maneuvering control for spacecraft.

For a three-axis stabilized spacecraft, the attitude measurement system consisting of gyroscopes and star sensors is the typical composition of attitude determination. Based on the attitude kinematical equations of spacecraft, combined with Extend Kalman Filter (EKF) algorithm, the attitude can be estimated and the accumulated errors of gyroscopes can be eliminated using star sensor data. Modeling the gyro drift is required for the process and zero-order or one-order Markovian model is usually adopted. When adopting the above gyro drift model, the filter has good performance and fast rate of convergence. However, the estimated error curves of attitude and angular velocity are not smooth with various noises and the maximum relative error can reach to 10%. Since attitude and angular velocity are the feedback signals in the attitude control system (ACS), the unstable estimated errors may affect the stability and precision of the control system. For this problem, two types of improved gyro drift models are presented to decrease the steady state deviation of estimated errors and improve the estimated accuracy (Qian et al., 2009).

3.1 Gyro-based attitude determination scheme

3.1.1 Fundamental principle

In the gyro-based attitude determination system, the gyro data provide a continuous attitude reference through attitude propagation, but the estimated attitude errors accumulate due to the gyro drift. Star sensor data provide high-precision attitude information to eliminate the errors at some sampling rate, thereby data processing is indispensable owing to the measurement errors. Therefore, the attitude filter can be established using the gyroscope and star sensor data, where the Extended Kalman filter algorithm is used to estimate and correct the attitude.

3.1.2 State equation of attitude determination system

The gyro-based determination scheme includes prediction estimation and observation correction. Corresponding attitude estimation model includes the state prediction model and state-error estimation model.

The orbital coordinate system is selected as the reference frame of the attitude motion of the spacecraft, and the state equations of the attitude determination system can be represented as (Wertz, 1998)

$$\dot{\mathbf{q}} = \frac{1}{2} \Omega(\boldsymbol{\omega}_{ob}^b) \mathbf{q} \quad (13)$$

$$\dot{\mathbf{b}} = \mathbf{v}_b \quad (14)$$

where $\mathbf{q} \equiv [q_1 \ q_{24}^T]^T$ denotes orbital-to-body attitude quaternion, $\boldsymbol{\omega}_{ob}^b$ denotes the angular velocity in the orbital coordinate system determined by $\boldsymbol{\omega}_{ob}^b = \boldsymbol{\omega} - R_o^b(\mathbf{q}) \cdot \boldsymbol{\omega}_{io}^o$, $\boldsymbol{\omega}$ denotes the inertial angular velocity measured by the gyroscope, $\boldsymbol{\omega} = \mathbf{U} - \mathbf{b} - \mathbf{v}_g$; R_o^b is the orbital-to-

body attitude matrix, ω_{io}^o denotes the orbital angular velocity with respect to inertial space. \mathbf{b} is the drift-rate bias and \mathbf{v}_g is the drift-rate noise.

1. State prediction model

Integrating the Eq.(13) the attitude quaternion estimates in the interval $[t - \Delta t_g, t]$ can be obtained, and the prediction model of state estimation is given by

$$\hat{\mathbf{q}}(t) = \hat{\mathbf{q}}(t - \Delta t_g) + \frac{1}{2} \Omega(\hat{\boldsymbol{\omega}}_{ob}^b \cdot \Delta t_g) \hat{\mathbf{q}}(t - \Delta t_g) \tag{15}$$

$$\hat{\mathbf{b}}(t) = \hat{\mathbf{b}}(t - \Delta t_g) \tag{16}$$

where superscript “ ^ ” denotes the estimates of the corresponding value.

2. Error state equation

The error state equation of the error quaternion can be given by (Wang, 2004)

$$\begin{cases} \Delta \dot{\mathbf{q}}_1 = 0 \\ \Delta \dot{\mathbf{q}}_{24} = -[\hat{\boldsymbol{\omega}} \times] \Delta \mathbf{q}_{24} - \frac{1}{2} \Delta \mathbf{b} - \frac{1}{2} \mathbf{v}_g \\ \Delta \dot{\mathbf{b}} = \mathbf{v}_b \end{cases} \tag{17}$$

where $\Delta \mathbf{q} \equiv [\Delta q_1 \ \Delta \mathbf{q}_{24}^T]^T$ denotes the attitude error quaternion, and $\Delta \mathbf{b} = \mathbf{b} - \hat{\mathbf{b}}$.

3.1.3 Observation model

Observation model 1: When gyroscope and star sensor are adopted as the sensors for the attitude determination system, the error state vector is defined as $\delta \mathbf{X} \equiv [\Delta q_2 \ \Delta q_3 \ \Delta q_4 \ \Delta q_1 \ \Delta b_1 \ \Delta b_2 \ \Delta b_3]^T$, and the observation vector is observation residuals of the star sensor defined as $\mathbf{z} \equiv [\Delta \varphi \ \Delta \theta \ \Delta \psi]^T$. With the small angle approximations, the observation equation can be given by

$$\mathbf{z}_k = \mathbf{H}_k \cdot \delta \mathbf{X}_k + \mathbf{v}_k \tag{18}$$

with

$$\begin{bmatrix} \Delta \varphi \\ \Delta \theta \\ \Delta \psi \end{bmatrix} = \begin{bmatrix} \varphi_m \\ \theta_m \\ \psi_m \end{bmatrix} - \begin{bmatrix} \hat{\varphi} \\ \hat{\theta} \\ \hat{\psi} \end{bmatrix}$$

where $[\hat{\varphi} \ \hat{\theta} \ \hat{\psi}]^T$ is the attitude estimate derived from the prediction model, and the observation matrix is $\mathbf{H}_k = [2\mathbf{I}_{3 \times 3} \ \mathbf{0}_{3 \times 3}]$.

Observation model 2: When the attitude sensors for the attitude determination system are chosen as gyroscope and sun sensor as well as infrared horizon sensor, the constant biases along roll axis and pitch axis of the infrared horizon sensor are generally augmented into the state variable. Therefore, we choose the state vector as $\mathbf{X} \equiv [\mathbf{q}^T(t) \ \mathbf{b}^T(t) \ \varphi_{bias} \ \theta_{bias}]^T$ and

error state vector as $\delta X \equiv [\Delta q_2 \ \Delta q_3 \ \Delta q_4 \ \Delta q_1 \ \Delta b_1 \ \Delta b_2 \ \Delta b_3 \ \Delta \varphi_{bias} \ \Delta \theta_{bias}]^T$. Observation vector is the observation residuals between infrared horizon sensor and sun sensor, denoted as $Z_k \equiv [\Delta \varphi \ \Delta \theta \ \Delta D_\xi \ \Delta D_\eta]^T$. Similarly, the observation equation is given by

$$Z_k = \mathbf{H}_k \cdot \delta X_k + v_k \quad (19)$$

with

$$\begin{bmatrix} \Delta \varphi \\ \Delta \theta \end{bmatrix} = \left(\begin{bmatrix} \varphi_m \\ \theta_m \end{bmatrix} - \begin{bmatrix} \hat{\varphi}_{bias} \\ \hat{\theta}_{bias} \end{bmatrix} \right) - \begin{bmatrix} \hat{\varphi} \\ \hat{\theta} \end{bmatrix}$$

$$\begin{bmatrix} \Delta D_\xi \\ \Delta D_\eta \end{bmatrix} = \begin{bmatrix} D_{\xi m} \\ D_{\eta m} \end{bmatrix} - \begin{bmatrix} \hat{D}_\xi \\ \hat{D}_\eta \end{bmatrix}$$

where $\hat{\varphi}_{bias}$ and $\hat{\theta}_{bias}$ represent the bias error estimates along the roll and pitch axes of the infrared horizon sensor, respectively. $[D_{\xi m} \ D_{\eta m}]^T$ and $[\hat{D}_\xi \ \hat{D}_\eta]^T$ represent the measurements from Sun sensor and corresponding estimates, respectively.

3.2 Improved gyro drift model

Improved gyro model 1: Error quaternion Δq is introduced into the gyro drift model (Thienel, 2004), that is

$$\Delta \dot{\mathbf{b}} = \frac{\alpha}{2} \cdot \Delta q_{24} \cdot \text{sign}(\Delta q_1) + v_b \quad (20)$$

where α is a positive scale factor, $\text{sign}(\cdot)$ is sign function.

The above gyro drift model makes good use of the observability of Δq and associates Δq with gyro drift $\Delta \mathbf{b}$. Hence, Δq is fed back to $\Delta \mathbf{b}$ thus $\Delta \dot{\mathbf{b}}$ is adaptive. This can improve the estimated precision of \mathbf{b} and decrease the steady state error of $\Delta \mathbf{b}$. The analysis is as follows.

At time t , let the quaternion q represent the actual orientation of the rigid body with respect to the reference system, and corresponding rotation angle is Φ . Simultaneously, \hat{q} is the estimated quaternion and $\hat{\Phi}$ is the rotation angle. If the attitude is referred as a rotation, then attitude error is the rotation from actual attitude to estimated attitude, defined by

$$\Delta q = \left[\cos \frac{\Delta \Phi}{2} \ E_x \sin \frac{\Delta \Phi}{2} \ E_y \sin \frac{\Delta \Phi}{2} \ E_z \sin \frac{\Delta \Phi}{2} \right]^T \quad (21)$$

where $\Delta \Phi$ is the rotation angle derived from the rotation from q to \hat{q} about \mathbb{E} axis, $\Delta \Phi \in [0, 2\pi)$; E_x, E_y, E_z are the components of unit vector of \mathbb{E} expressed in the $Oxyz$ coordinate system.

If $\Delta q_1 = \cos \frac{\Delta \Phi}{2} > 0$, $\Delta \Phi \in (0, \pi)$, it is seen that \hat{q} advances q , that is, $\hat{\Phi} > \Phi$. The rotation is illustrated in Fig. 5(a).

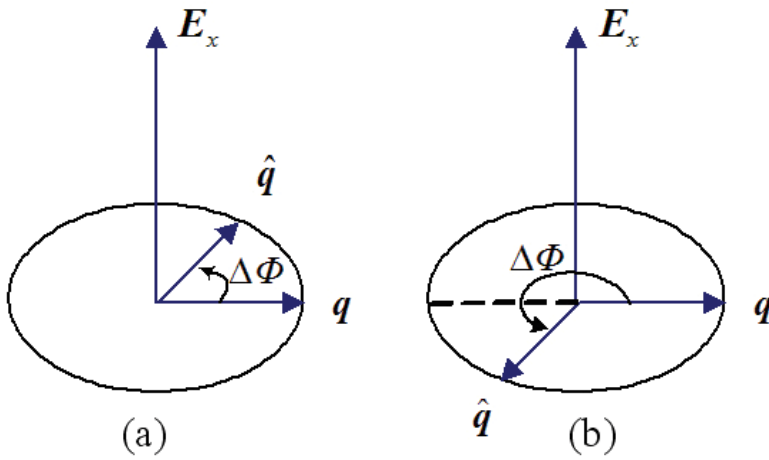


Fig. 5. The rotation of the error quaternion

We have $sign(\Delta q_1) = 1 > 0$, and the magnitude of $\Delta \hat{b}$ can be given by the product of scale factor $\frac{\alpha}{2}$ and $\Delta \alpha_{24}$. If $\Delta q_1 = \cos \frac{\Delta \Phi}{2} < 0$, the results can be analogously analyzed.

Improved gyro model 2: The statistic mean of drift error Δb can be used for its estimate value, that is

$$\Delta b = E[\Delta b(t_i)] \quad t_i \in [t - \Delta T, t] \tag{22}$$

This model makes use of the noise distribution property of Δb in steady state and decreases the estimated error by the data processing. In this chapter, this model is applied in the Mode II of the following attitude determination scheme.

3.3 Filter implement

Based on the previous derivation, attitude determination scheme using EKF algorithm consists of state prediction and observation correction with the flow chart illustrated in Fig. 6.

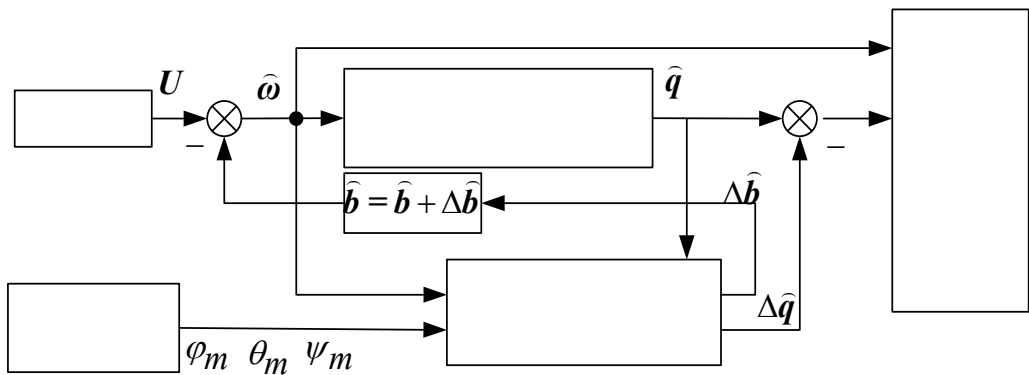


Fig. 6. The flow chart of attitude determination scheme

3.4 Simulation results

In this section, two types of mode of attitude determination system are used to estimate attitude. In each mode, we adopt different gyro drift model previously discussed. The following parameters are used for simulation.

The gyro "measurements" are simulated with a gyro noise standard deviation 0.1 deg/hr, a constant drift of 5 deg/hr, and measurement frequency of 50 HZ. The measurement error of star sensor is Gaussian white noise of 0.1 arcsec and measurement frequency is 5HZ. The measurements of infrared horizon sensor are simulated with a constant bias of 0.1 deg, and Gaussian white noise of 0.05 deg and measurement frequency is 1 HZ.

3.4.1 Mode I

For the observation model 1 previous described, two types of gyro drift model are used in simulations. They are $\Delta \dot{b} = v_b$ (Traditional gyro model) and $\Delta \dot{b} = \frac{\alpha}{2} \cdot \Delta q_{24} \cdot \text{sign}(\Delta q_1) + v_b$ (Improved gyro model 1). The simulation results are shown as follows.

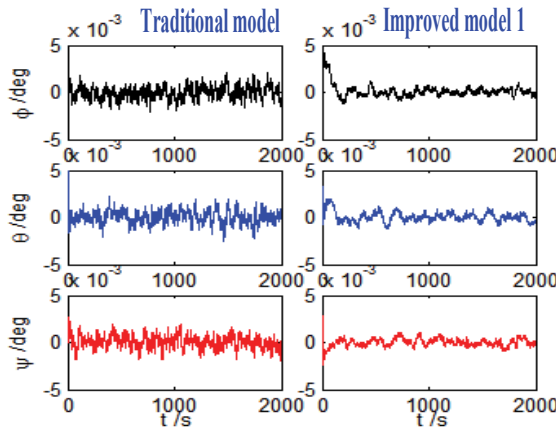


Fig. 7. Comparison of the attitude estimated error.

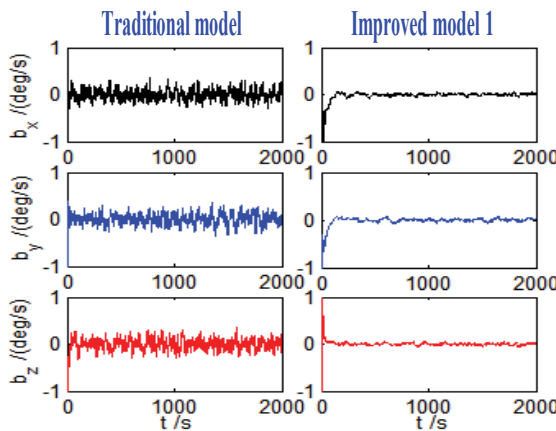


Fig. 8. Comparison of the gyro random drift estimated error.

		λ	b	ω
Traditional gyro model	Max	0.0024	0.4831	2.140e-4
	RMSx	7.251e-4	0.1089	4.109e-5
	RMSy	6.962e-4	0.1134	4.191e-5
	RMSz	6.498e-4	0.1027	3.983e-5
Improved gyro Model 1	Max	0.0018	0.2067	1.413e-4
	RMSx	4.147e-4	0.0238	2.849e-5
	RMSy	3.846e-4	0.0219	2.848e-5
	RMSz	4.304e-4	0.0249	2.860e-5

Table 3. Max and RMS of the stabilization estimate error(attitude unit: deg)

It is shown that the precision of the estimate of attitude and gyro drift increased dramatically when adopting improved gyro model 1. The attitude angular estimated error curves are smooth and the stability is enhanced. When adopting traditional gyro model, the attitude filter converged in 50 sec, but the estimated error is not stable; when adopting improved gyro model 1, the filter converged after a gap of 200 sec, but the estimated error is stable. Therefore, two types of gyro model can be integrated in use.

3.4.2 Mode II

For the observation model 2 previous described, two types of gyro drift model are used in simulations. They are $\Delta b = v_b$ (Traditional gyro model) and $\Delta b = E[\Delta b(t_i)]$ (Improved gyro model 2). The simulation results are shown as follows.

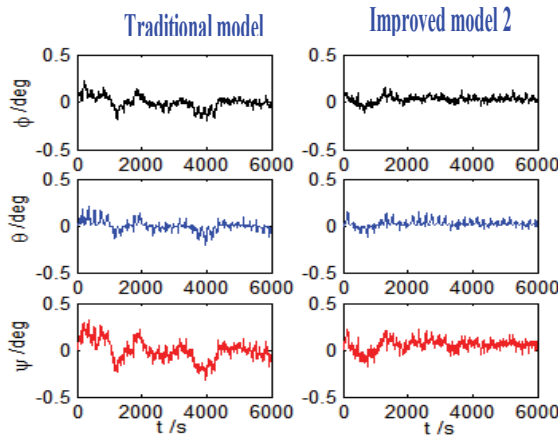


Fig. 9. Comparison of the attitude estimated error

From the Figs. 9-10 and Table 4, we can see that the precision of the estimate of attitude and gyro drift increased and the stability is enhanced when adopting improved gyro model 2. Theoretical analysis and simulation results indicate that the attitude determination system satisfies the design requirement and the improved gyro drift models are feasible and efficient.

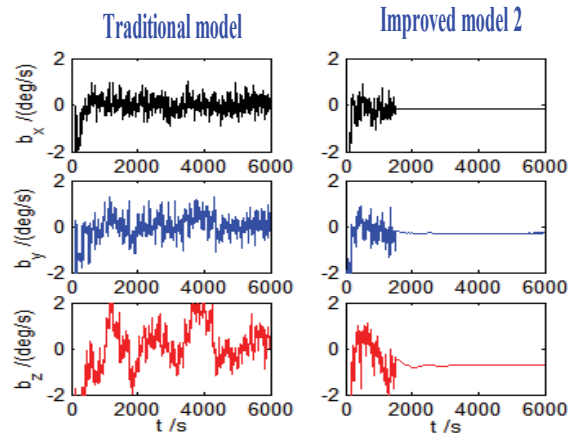


Fig. 10. Comparison of the gyro random drift estimated error

		λ	b	ω	$\varphi_{bias}, \theta_{bias}$
Traditional gyro model	Max	0.3033	2.3769	7.280e-4	0.2825
	RMSx	0.0516	0.3759	1.080e-4	0.0587
	RMSy	0.0423	0.4179	1.194e-4	0.0533
	RMSz	0.0887	0.7534	2.112e-4	/
Improved gyro Model 2	Max	0.1527	0.1575	1.556e-4	0.0295
	RMSx	0.0219	0.1096	4.125e-5	0.0113
	RMSy	0.0202	0.0112	2.784e-5	0.0101
	RMSz	0.0393	0.0463	3.057e-5	/

Table 4. Max and RMS of the stabilization estimate error (attitude unit: deg)

4. Attitude control of three-axis stabilized spacecraft with momentum wheel system

Attitude control is the process of orienting the spacecraft in a specified or predetermined direction, which makes the spacecraft obtain the desired attitude angle and angular velocity. Attitude control in the large angle attitude maneuvers of spacecraft belongs to the tracking control area, and many mature control methods can be referred, e.g., classical control, adaptive control, robust control, prediction control, multimode control and intelligent control, et al. In this section, a key problem above control decoupling and precession inhibition for zero-bias-momentum spacecraft is discussed.

Although the angular momentum exchange device such as momentum wheel is widely applied to attitude control for three-axis stabilized spacecraft, further studies about control decoupling and precession inhibition are deficient. For example, when the satellite is controlled by the momentum wheel operated only in rate mode, it is known to decouple the roll and yaw channels for bias-momentum satellite. However, the decoupling is not usually carried out for zero-bias-momentum satellite, since three axes of it are usually assumed independent. In fact, if the momentum wheel operated only in rate mode, whatever the bias-momentum scheme or zero-bias-momentum scheme, the decoupling along roll and yaw channel must be carried out. Otherwise, there exists precession in both roll and yaw

directions. But in the actual practice, the decoupling is dispensable since the control scheme includes magnetic control besides wheel control (Stickler & Alfriend, 1974). (Tian et al., 2001; Qian, 2002) analyze the ACS stability of spacecraft with angular momentum exchange device as actuator, and demonstrate that the introduction of magnetic unloading control can damp precession motion of the spacecraft effectively, which is the main reason why it is dispensable to decouple along roll and yaw channel. But in this way, the magnetic torque actuator is always required in work mode against the original design intention of the magnetic unloading system. Therefore, some researchers (Li et al., 2009) present a method to adjust the magnetic dipole moments along pitch axis to eliminate the precession and nutation, which is proved to be effective.

In this section, the principle which is used to eliminate precession and nutation for bias-momentum spacecraft is introduced to solve the attitude control problem for zero-bias-momentum spacecraft. Moreover, according to the differences between zero-bias-momentum scheme and bias-momentum scheme, the magnetic control command law has been improved to solve the precession inhibition problem effectively for zero-bias-momentum spacecraft.

4.1 Kinematic and dynamic model of attitude motion

4.1.1 Kinematic equation of motion

Based on the small-angle approximations, the linearized kinematic equation of motion of spacecraft can be given by (Wertz, 1998)

$$\boldsymbol{\omega} = \begin{bmatrix} \dot{\varphi} - \omega_0 \psi \\ \dot{\theta} - \omega_0 \\ \dot{\psi} + \omega_0 \varphi \end{bmatrix} \quad (23)$$

where $\boldsymbol{\omega}$ is the angular velocity of spacecraft with respect to inertial frame, ω_0 denotes the orbital angular velocity.

4.1.2 Dynamic equation of motion

Considering the rigid body model of spacecraft, the dynamic equation of motion of spacecraft equipped with momentum wheels as actuators is given by

$$\mathbf{I}\dot{\boldsymbol{\omega}} + [\boldsymbol{\omega} \times](\mathbf{I}\boldsymbol{\omega} + \mathbf{h}) = -\dot{\mathbf{h}} + \mathbf{T}_c + \mathbf{T}_d \quad (24)$$

Note that $\mathbf{H} = \mathbf{I}\boldsymbol{\omega}$ represents the angular momentum vector of spacecraft. \mathbf{I} is the moment-of-inertia tensor; $\dot{\mathbf{h}}$ is the wheel control torque. \mathbf{T}_c is the control torque which is not provided by the wheels and \mathbf{T}_d is disturbance torque.

Substituting Eq.(23) into Eq.(24) yields the dynamic equations of motion with Euler angle representation given by

$$\begin{aligned} M_{dx} &= I_x \ddot{\varphi} + (I_y - I_x - I_z) \omega_0 \dot{\psi} + (I_y - I_z) \omega_0^2 \varphi + \\ &\quad I \dot{\Omega}_x + I \Omega_z (\dot{\theta} - \omega_0) - I \Omega_y (\dot{\psi} + \omega_0 \varphi) \\ M_{dy} &= I_y \ddot{\theta} + I \dot{\Omega}_y + I \Omega_x (\dot{\psi} + \omega_0 \varphi) - I \Omega_z (\dot{\varphi} - \omega_0 \psi) \\ M_{dz} &= I_z \ddot{\psi} - (I_y - I_x - I_z) \omega_0 \dot{\varphi} + (I_y - I_x) \omega_0^2 \psi + \\ &\quad I \dot{\Omega}_z + I \Omega_y (\dot{\varphi} - \omega_0 \psi) - I \Omega_x (\dot{\theta} - \omega_0) \end{aligned} \quad (25)$$

4.1.3 Disturbance torque

Since the environmental torques are not only related to the orbit, shape, and mass distribution of the spacecraft, but also solar activity, season, date and diurnal fluctuation, the calculations of environmental torques are very complicated. In the preliminary design, a Fourier expansion is usually used for disturbance torques expressed in the body frame of spacecraft with the consideration of the zero-order and one-order term. The orbital frequency ω_0 is chosen as the basic frequency of the harmonic term. Therefore, the disturbance torque model used in this chapter can be written as

$$\mathbf{T}_d = 10^{-3} \begin{bmatrix} 3 \cos \omega_0 t + 1 \\ 1.5 \sin \omega_0 t + 3 \cos \omega_0 t \\ -3 \sin \omega_0 t + 1 \end{bmatrix} \text{ (Nm)} \quad (26)$$

It is seen that the accumulated torque impulse arising from disturbance torque along pitch axis is zero. For small attitude angle, when the spacecraft orbits one circle, the accumulated impulse generated by the constant components of disturbance torque in the roll and yaw directions is approximately zero, while the accumulated impulse generated by the harmonic components are $\Delta H_X^I = 3T$ and $\Delta H_Z^I = 0$, respectively, where T is the orbital period.

4.2 Analysis of stability

Since the values of φ, θ, ψ and $\dot{\varphi}, \dot{\theta}, \dot{\psi}$ are very small, the linearization of the dynamic model can be given by

$$I_y \ddot{\theta} = -\dot{h}_y + T_{dy} \quad (27)$$

$$\begin{bmatrix} I_x s^2 + g_z \omega_0 & g_0 s \\ -g_0 s & I_z s^2 + g_x \omega_0 \end{bmatrix} \begin{bmatrix} \varphi \\ \psi \end{bmatrix} = - \begin{bmatrix} s & -\omega_0 \\ \omega_0 & s \end{bmatrix} \begin{bmatrix} h_x \\ h_z \end{bmatrix} + \begin{bmatrix} T_{cx} + T_{dx} \\ T_{cz} + T_{dz} \end{bmatrix} \quad (28)$$

It follows that

$$g_x = (I_y - I_x) \omega_0 - h_y,$$

$$g_z = (I_y - I_z) \omega_0 - h_y,$$

$$g_0 = (I_y - I_x - I_z) \omega_0 - h_y$$

From the above equations, we can see that the pitch axis loop is independent of roll and yaw axes and can be designed separately. There exists a close coupling along roll and pitch axis, and the coupling are different owing to the different control schemes. Consequently, the above attitude control is a nonlinear control problem which can be solved using two kinds of methods. One is to design the nonlinear control law for nonlinear problem, the other is to consider the coupling terms arising from the orbital frequency and angular momentum of wheels are small and assume the three channels are independent, so the control law can be designed separately.

In fact, if the spacecraft is controlled only by reaction wheels, whether the reaction wheels are operated in moment mode or momentum mode, the roll and yaw channels must be decoupled. Otherwise, the closed loop response of the system is a pure oscillation at an angular frequency of ω_0 . The analysis is as follows.

Consider the spacecraft is controlled with the wheels operated in rate mode and ignore the constant external disturbances. The linearized feedback control law along x axis and z axis is given by

$$\begin{bmatrix} V_X(s) \\ V_Z(s) \end{bmatrix} = \mathbf{G}_c(s) \begin{bmatrix} \varphi \\ \psi \end{bmatrix} \quad (29)$$

where $\mathbf{G}_c \in F^{2 \times 2}$ is the transfer function, V_X and V_Z represent the control voltage of the reaction wheels along x axis and z axis, respectively.

Assume the initial attitude angle and angular velocity are zero, so we have

$$\begin{bmatrix} h_x \\ h_z \end{bmatrix} = \begin{bmatrix} \frac{K_r}{1+T_r} & 0 \\ 0 & \frac{K_r}{1+T_r} \end{bmatrix} \begin{bmatrix} V_x \\ V_z \end{bmatrix} \quad (30)$$

Substitute Eq.(30) into Eq.(24) and consider the spacecraft is controlled only by wheels, that is, $T_{cx} = T_{cz} = 0$, so we can obtain

$$\begin{bmatrix} I_x s^2 + g_z \omega_0 & g_0 s \\ -g_0 s & I_z s^2 + g_x \omega_0 \end{bmatrix} \begin{bmatrix} \varphi \\ \psi \end{bmatrix} = \begin{bmatrix} T_{dx} \\ T_{dz} \end{bmatrix} - \frac{K_r}{1+T_r s} \begin{bmatrix} s & -\omega_0 \\ \omega_0 & s \end{bmatrix} \mathbf{G}_c \begin{bmatrix} \varphi \\ \psi \end{bmatrix} \quad (31)$$

$$\begin{bmatrix} s & -\omega_0 \\ \omega_0 & s \end{bmatrix} \begin{bmatrix} I_x s & g_x \\ -g_z & I_z s \end{bmatrix} \begin{bmatrix} \varphi \\ \psi \end{bmatrix} = \begin{bmatrix} T_{dx} \\ T_{dz} \end{bmatrix} - \frac{K_r}{1+T_r s} \begin{bmatrix} s & -\omega_0 \\ \omega_0 & s \end{bmatrix} \mathbf{G}_c \begin{bmatrix} \varphi \\ \psi \end{bmatrix} \quad (32)$$

$$\begin{bmatrix} \varphi \\ \psi \end{bmatrix} = \frac{1}{s^2 + \omega_0^2} \left(\begin{bmatrix} I_x s & g_x \\ -g_z & I_z s \end{bmatrix} + \mathbf{G}_c \frac{K_r}{1+T_r s} \right)^{-1} \begin{bmatrix} s & \omega_0 \\ -\omega_0 & s \end{bmatrix} \begin{bmatrix} \varphi \\ \psi \end{bmatrix} \begin{bmatrix} T_{dx} \\ T_{dz} \end{bmatrix} \quad (33)$$

It is obvious that no matter what the forms of \mathbf{G}_c is, $s = \pm j\omega_0$ are always a couple of poles of the closed loop system. However, $s = \pm j\omega_0$ are the uncontrolled modality of the system, and the system always oscillate with the angular frequency ω_0 , that is, there exists precession in both roll and yaw directions. Therefore, it is imperative to introduce some other controls to eliminate the above precession for the zero-bias-momentum spacecraft.

4.3 Principle of magnetic control

For the precession inhibition problem without decoupling, (Tian et al., 2001; Qian, 2002) demonstrated that the introduction of magnetic unloading control can damp spacecraft precession effectively. But the magnetic actuator is always required in work mode against the original design intention of the magnetic unloading system. (Li et al., 2009) presents a method to adjust the magnetic dipole moments along pitch axis to eliminate the precession

and nutation for three-axis stabilized spacecraft. In this section, we introduce the principle that how to eliminate precession and nutation used in bias-momentum wheel spacecraft and improve the magnetic control law.

Precession control and nutation damping are provided by driving the pitch dipole according to

$$M_y = -K_1 B_x \varphi - K_2 B_z \psi + m_y - K_3 \dot{B}_y \quad (34)$$

where φ and ψ represent the corresponding deviation of roll and yaw angle from the command attitude, respectively; B represents magnetic field intensity; \dot{B}_y is derived from the differential of the magnetometer aligned along y axis; m_y is the magnetic moment used to eliminate precession, and K_1, K_2, K_3 are the gains. The discussion below demonstrated that the prior three terms provide precession control and the last one nutation damping.

4.3.1 Nutation damping

For small attitude errors, we have

$$\dot{B}_y = B_z \dot{\varphi} - B_x \dot{\psi} \quad (35)$$

Control torques caused by the nutation damping term ($-K_3 \dot{B}_y$) in Eq.(34) are given by

$$\begin{aligned} T_{Mx} &= -K_3 \dot{B}_y B_z = -K_3 B_z^2 \dot{\varphi} + K_3 B_x B_z \dot{\psi} \\ T_{Mz} &= -K_3 \dot{B}_y B_x = -K_3 B_x^2 \dot{\psi} + K_3 B_x B_z \dot{\varphi} \end{aligned} \quad (36)$$

The first term on the right-hand-side indicates the damping torque is proportional to the nutational amplitude. The pitch component of the magnetic field intensity generally varies small, whereas the value of \dot{B}_y is somewhat larger when the spacecraft performs the nutational cone motion, which can generate the damping torques together with geomagnetic field.

4.3.2 Precession control

Ignore the related term associated with the moment of inertia and consider the coupling term associated with orbital motion solely. The precession equations of motion are given by

$$\begin{aligned} \omega_0 h_y \varphi + h_y \dot{\psi} - h_z \omega_0 &= T_{cx} \\ -h_y \dot{\varphi} + \omega_0 h_y \psi + h_x \omega_0 &= T_{cz} \end{aligned} \quad (37)$$

For bias-momentum spacecraft, we have inequalities $h_y \gg h_x$ and $h_y \gg h_z$, so the precessional effects generated by h_x and h_z with respect to by h_y are small quantity, which can be ignored. However, h_x, h_y, h_z are all small quantities for zero-bias-momentum spacecraft. The method used in bias-momentum spacecraft can be used in zero-bias-momentum spacecraft to eliminate the precession results from quantity h_y , but falls short in the precession arising from $h_x \omega_0$ and $h_z \omega_0$. It can be further seen from the simulation results below that the magnetic actuator can weaken the precession amplitude dramatically but there still exists precession. Accordingly, momentum moment of reaction wheels referred as feedback signal is introduced to magnetic torque, which eliminates the precession arising from h_x and h_z effectively. Simulation results verify the feasibility of the scheme.

1. Elimination of precession caused by h_y

Assume the magnetic dipole moment is adopted in the similar form used in bias-momentum spacecraft, that is

$$M_{y1} = -K_1 B_x \varphi - K_2 B_z \psi \quad (38)$$

and the generated magnetic torque can be given by

$$T_1 = M_1 \times B = \begin{bmatrix} 0 \\ M_{y1} \\ 0 \end{bmatrix} \times \begin{bmatrix} B_x \\ B_y \\ B_z \end{bmatrix} = \begin{bmatrix} -K_1 B_x B_z \varphi - K_2 B_z^2 \psi \\ 0 \\ K_1 B_x^2 \varphi + K_2 B_x B_z \psi \end{bmatrix} \quad (39)$$

it can be changed to

$$\begin{bmatrix} T_{cx1} \\ T_{cz1} \end{bmatrix} = \begin{bmatrix} -K_1 B_x B_z & -K_2 B_z^2 \\ K_1 B_x^2 & K_2 B_x B_z \end{bmatrix} \begin{bmatrix} \varphi \\ \psi \end{bmatrix} = \begin{bmatrix} -k_1 & -k_2 \\ k_3 & k_4 \end{bmatrix} \begin{bmatrix} \varphi \\ \psi \end{bmatrix} \quad (40)$$

with

$$\begin{aligned} k_1 &= K_1 B_x B_z & k_2 &= K_2 B_z^2 \\ k_3 &= K_1 B_x^2 & k_4 &= K_2 B_x B_z \end{aligned} \quad (41)$$

The precession equations of motion results from h_y via Eq.(37) can be given by

$$\begin{aligned} -h_y (\dot{\psi} + \omega_0 \varphi) &= T_{cx1} \\ h_y (\dot{\varphi} - \omega_0 \psi) &= T_{cz1} \end{aligned} \quad (42)$$

which can be rewritten as

$$\begin{bmatrix} -\omega_0 h_y & -s h_y \\ s h_y & -\omega_0 h_y \end{bmatrix} \begin{bmatrix} \varphi \\ \psi \end{bmatrix} = \begin{bmatrix} T_{cx1} \\ T_{cz1} \end{bmatrix} \quad (43)$$

Combining Eq.(40) gives

$$\begin{bmatrix} \omega_0 h_y - k_1 & s h_y - k_2 \\ -s h_y + k_3 & \omega_0 h_y + k_4 \end{bmatrix} \begin{bmatrix} \varphi \\ \psi \end{bmatrix} = 0 \quad (44)$$

The characteristic equation of the system is given by

$$C(s) = s^2 h_y^2 - h_y (k_2 + k_3) s + k_2 k_3 - k_1 k_4 + (k_4 - k_1) \omega_0 h_y + \omega_0^2 h_y^2 = 0 \quad (45)$$

For bias-momentum spacecraft, we have $h_y < 0$, but for zero-bias-momentum spacecraft the value of h_y can be a positive or negative, different from the one of bias-momentum spacecraft. By the Routh criterion, one finds that the stability requirements are

$$-h_y(k_2 + k_3) > 0 \quad (46)$$

$$k_2k_3 - k_1k_4 + (k_4 - k_1)\omega_0 h_y + \omega_0^2 h_y^2 > 0 \quad (47)$$

We can find the identity $k_2k_3 = k_1k_4$ via Eq.(41). If we set $K_1 = K_2$ in Eq.(41), thus we can obtain $k_1 = k_4$ and Eq.(47) can be reduced to $\omega_0^2 h_y^2 > 0$, which satisfies the stability condition. Furthermore, substituting k_2 and k_3 into Eq.(46) gives

$$-h_y(K_1 B_x^2 + K_2 B_z^2) > 0 \quad (48)$$

Together with the equality $K_1 = K_2$ leads to

$$-h_y K_1 (B_x^2 + B_z^2) > 0 \quad (49)$$

so

$$h_y K_1 < 0 \quad (50)$$

Therefore, the sign of K_1 can be determined by $-\text{sign}(h_y)$ and the magnitude of it can be computed by the performance indices of second-order system $C(s)$, where $\text{sign}(\cdot)$ is sign function.

2. Elimination of precession caused by h_x and h_z

It is known from the previous analysis that the method used in bias-momentum spacecraft to eliminate precession can't weaken the precession terms of $-h_z\omega_0$ and $h_x\omega_0$. To solve this problem, the approach that adding the additional magnetic dipole moment along pitch axis is presented. Suppose m_y is that magnetic moment, and using the relation $T_{m1} = m_y \times B$ we can obtain

$$\begin{aligned} T_{mx1} &= m_y B_z \\ T_{mz1} &= -m_y B_x \end{aligned} \quad (51)$$

The value of m_y can be determined by minimizing the following function

$$J = [m_y B_z - (-h_z\omega_0)]^2 + [-m_y B_x - (h_x\omega_0)]^2 \quad (52)$$

Setting $\frac{\partial J}{\partial m_y} = 0$ leads to

$$2m_y B_z^2 + 2B_z h_z \omega_0 + 2m_y B_x^2 + 2B_x h_x \omega_0 = 0 \quad (53)$$

from which we have

$$m_y = -\frac{(B_x h_x + B_z h_z)}{B_x^2 + B_z^2} \omega_0 \quad (54)$$

4.3.3 Magnetic dipole moment

According to the previous analysis, the control torque to eliminate the precession can be given by

$$T = T_1 + T_{m1} = \begin{bmatrix} -K_1 B_x B_z \varphi - K_2 B_z^2 \psi + m_y B_z \\ K_1 B_x^2 \varphi + K_2 B_x B_z \psi - m_y B_x \end{bmatrix} \quad (55)$$

and the corresponding command acting on the pitch axis is

$$M_y = M_{y1} + m_y = -K_1 (B_x \varphi + B_z \psi) + m_y \quad (56)$$

So the magnetic dipole moment along pitch axis can be obtained by

$$M_y = -K_1 (B_x \varphi + B_z \psi) - K_3 \dot{B}_y + m_y \quad (57)$$

which is in agreement with Eq.(34).

4.4 Simulation results

The feasibility of the proposed scheme is verified by the numerical simulations. The PID control law is adopted in the zero-bias-momentum spacecraft and the following parameters are used in simulations.

In accord with the previously stated assumptions regarding the geomagnetic field and orbit, we have

$$\begin{cases} B_x = B_0 \cos u \\ B_y = 0 \\ B_z = 2B_0 \sin u \end{cases}$$

where $B_0 = 10^{-2}$ (T) is the equatorial magnetic field intensity, and $u = \omega_0 t$ is the orbit argument, measured from ascending node. The spacecraft's moment of inertia tensor is

$$\mathbf{I} = \begin{bmatrix} 4229.8 & 48.9 & 1.1 \\ 48.9 & 1458.2 & 252.6 \\ 1.1 & 252.6 & 4450.6 \end{bmatrix} (\text{kg} \cdot \text{m}^2)$$

The parameters of PID control law are $\mathbf{K}_p = 3 \times 10^{-3} \cdot \text{diag}(\mathbf{I})$, $\mathbf{K}_d = 7.36 \times 10^{-2} \cdot \text{diag}(\mathbf{I})$ and $\mathbf{K}_I = 1 \times 10^{-5} \cdot \text{diag}(\mathbf{I})$, respectively. The orbital angular velocity is $\omega_0 = 0.001$ (rad / s). The initial states are set as $\varphi_0 = \theta_0 = \psi_0 = 0.5^\circ$, and $\boldsymbol{\omega} = [0.04 \quad -0.08 \quad 0.04]^T$ (rad / s). The gains are chosen as $K_1 = K_2 = 8.2 \times 10^4$ and $K_4 = 10$.

4.4.1 Case 1

Consider the PID control law is solely adopted for the zero-bias-momentum spacecraft. The simulation results are shown as Fig. 11. It is shown that the attitude and wheel speed oscillate with frequency ω_0 , which agrees well with the preceding stability analysis. The amplitude of attitude is 0.5° , and the curves of attitude and wheel speed in both roll and yaw directions diverge. Therefore, the additional control torque is required to eliminate precession and nutation for the ACS since PID control law doesn't work well.

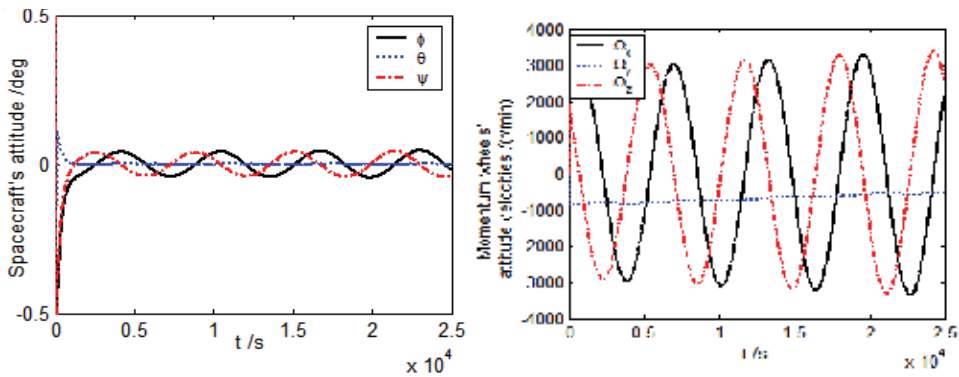


Fig. 11. Spacecraft's attitude and wheel speed versus time (PID)

4.4.2 Case 2

On the basis of Case 1, the method for eliminating precession and nutation used in the bias-momentum system is introduced to zero-bias-momentum system, that is, we use the magnetic dipole moment along pitch axis, $M_y = -K_1 B_x \dot{\phi} - K_2 B_z - K_3 \dot{B}_y$. As can be seen in Fig. 12, the attitude can converge quickly and the precession effect is weakened. But from the wheel speed curve, we can see that the precession is not wholly eliminated and still oscillates periodically.

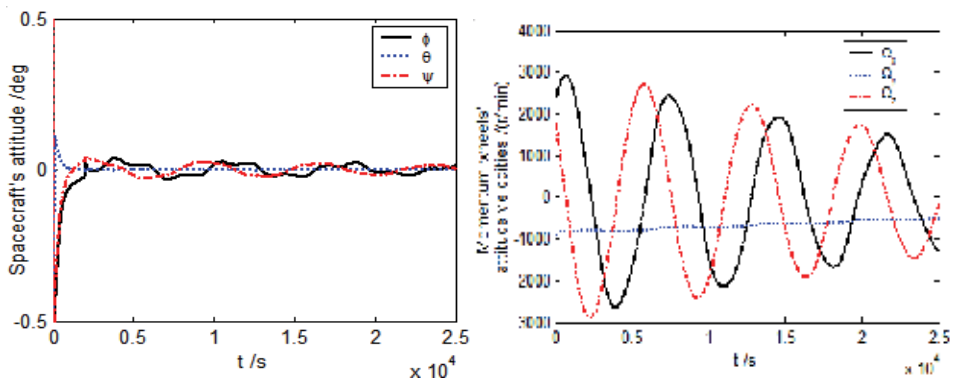


Fig. 12. Spacecraft's attitude and wheel speed versus time (Magnetic Unloading Control)

4.4.3 Case 3

The precession caused by h_x and h_z is further studied in this case. m_y is introduced into the pitch magnetic dipole moment, that is, $M_y = -K_1 B_x \dot{\phi} - K_2 B_z \psi + m_y - K_3 \dot{B}_y$. The simulation results are given in Fig.13. Compared with the previous cases, the convergence of attitude is better and attitude accuracy in steady state is higher. From the wheel speed curve we can see the effect of precession is basically eliminated, and the wheel speeds in three axes are stabilized at the neighborhood of corresponding fixed value. It is shown that the selected magnetic torque can be used to eliminate precession effectively, satisfying the attitude stabilization requirements of zero-bias-momentum system.

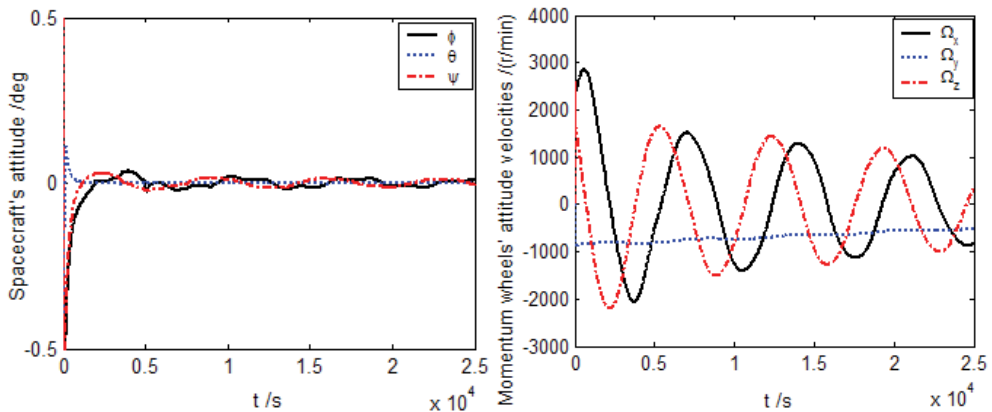


Fig. 13. Spacecraft's attitude and wheel speed versus time (Precession Control)

5. Conclusion

In this chapter, the three key techniques involved guidance, navigation and control are investigated. The method using NLP method to solve MEMCP is improved and a new construction method for initial feasible solution of the NLP is presented. The improved approach makes the initial attitude trajectory approach the actual one and improves the computational efficiency. For the attitude determination system, two types of improved gyro-drift models are presented. Simulation results show that the improved models can decrease the steady state deviation of estimated errors and improve the estimated accuracy. In the section 4, a key problem above control decoupling and precession inhibition for zero-bias-momentum spacecraft is discussed. The principle used to eliminate precession and nutation for bias-momentum spacecraft is introduced to solve the attitude control problem for zero-bias-momentum spacecraft. According to the differences between zero-bias-momentum scheme and bias-momentum scheme, the magnetic control command law has been improved to solve the precession inhibition problem effectively for zero-bias-momentum spacecraft.

6. Reference

- Chung, T. S. & Wu, C. J. (1992). A computationally efficient numerical algorithm for the minimum-time control problem of continuous systems. *Automatica*, Vol.28, pp. 841-847
- Dwyer, T. A. W. (1982). The control of angular momentum for asymmetric rigid bodies. *IEEE Trans. Autom. Control*, Vol.3, pp.686-688
- Junkins, J. L & Turner, J. D. (1980). Optimal continuous torque attitude maneuvers. *Journals of Guidance, Control, Dynamics*, Vol 3(3), pp. 210-217
- Li, P.K., Qian, S., Guo, C.F. & Cai, H. (2009). Research on satellite attitude control problems of zero-momentum reaction wheel system, *Chinese Space Science and Technology*, Vol.29(2), pp.25-32
- Li, F. & Bainum, P.M. (1994). Numerical approach for solving rigid spacecraft minimum time attitude maneuvers. *Journals of Guidance, Control, Dynamics*, Vol 13 (1), pp. 38-45

- Qian, Y. (2002). High accuracy attitude determination and control system for the three-axis stabilized satellite. Northwestern Polytechnical University, Dr Thesis
- Qian, S., Li, P. K., Zhang, S. F. & Cai, H. (2009). Satellite attitude estimation based on improved model of the gyro random drift, *Journal of Astronautics*, Vol.30(2), pp.585-589
- Schaub, H. & Junkins, J. L. (1997). New penalty functions and optimal control formulation for spacecraft attitude control problems. *Guidance Control Dyn*, Vol.20(3), pp.428-434
- Stickler, A. C. & Alfriend, K. T. (1974). An Elementary Magnetic Attitude Control System. *AIAA paper*, No.74-923
- Tian, C. H., Ma, G. F., Li, C. J., et al. (2001). General problems of satellite attitude control. *Techniques of Automation and Applications*, No.1, pp.9-12
- Thienel, J. K. (2004). Nonlinear observer/controller designs for spacecraft attitude control systems with uncalibrated gyros. Department of Aerospace Engineering, *Dr Thesis*
- Vadali, S. R. & Junkins, J. L. (1984). Optimal open-loop and stable feedback control of rigid spacecraft attitude maneuvers. *Astronaut Sci*, Vol.32:pp.105-122
- Vadali, S. R. & Junkins, J. L. (1983). Spacecraft large angle rotational maneuvers with optimal momentum transfer. *Astronaut Sci*, Vol.31, pp. 217-235
- Wertz, J. R. ed. (1998). *Spacecraft Attitude Determination and Control*, Kluwer Academic, Dordrecht, The Netherlands
- Wang, J. Q. (2004). Research for satellite autonomous navigation and fusion attitude determination algorithm based on attitude sensors. Harbin Institute of Technology, *Dr Thesis*, pp.90-96
- Yang, C. C., Li, C. L. & Wu, C. J. (2007). Minimal energy maneuvering control of a rigid spacecraft with momentum transfer. *Journal of the Franklin Institute, ScienceDirect*, pp.991-1005
- Zhang, S. F., Qian, S. & Li, P. K. (2009). Study on the minimal energy maneuvering control of a rigid spacecraft with momentum transfer, *Journal of Astronautics*, Vol.30(4), pp.1504-1509

Modeling and Control of Space Vehicles with Fuel Slosh Dynamics

Mahmut Reyhanoglu
Embry-Riddle Aeronautical University
USA

1. Introduction

In April of 1957, a Jupiter Intermediate Range Ballistic Missile was terminated 90 seconds after launch due to propellant slosh. Ever since the launch of the early high-efficiency rockets, controlling liquid fuel slosh within a launch vehicle has been a major design concern. Moreover, with today's large and complex spacecraft, a substantial mass of fuel is necessary to place them into orbit and to perform orbital maneuvers. The mass of fuel contained in the tanks of a geosynchronous satellite amounts to approximately 40% of its total mass (Sidi, 1997). When the fuel tanks are only partially filled, large quantities of fuel move inside the tanks under translational and rotational accelerations and generate the fuel slosh dynamics.

The traditional treatment of liquid slosh control began with the inclusion of physical barriers, such as baffles and complete compartmentalization, meant to limit the movement of liquid fuel to small amplitudes of high, negligible frequencies. Later, bladders were added to the list of ways to limit these motions. These techniques, although helpful in some cases, do not completely succeed in canceling the sloshing effects. Moreover, these suppression methods involve adding to the spacecraft structural mass, thereby increasing mission cost.

The effects of baffle positions (and quantities) on sloshing frequency have been studied in the literature (Biswal et al., 2004). The mathematical techniques used in these studies are based on the velocity potential function solved using finite-element analysis. Results show that baffles are more effective when near the free-surface of the fluid. In (Venugopal & Bernstein, 1996), surface pressure control and surface flap actuators have been proposed for controlling slosh in rectangular tanks. The feedback controllers are designed using a Linear-Quadratic-Gaussian (LQG) synthesis. Fluid is assumed to be incompressible, inviscid, and irrotational. Results show a steady-state slosh amplitude lower than the no-actuator case.

The effect of liquid fuel slosh on spinning spacecraft has also been explored in the literature (Hubert, 2003, 2004). Different slosh motion types - surface waves, bulk fluid motion, and vortices - as well as fluid configurations during spinning are defined (Hubert, 2003). The design of control strategies for a launch vehicle with propellant sloshing has been a topic of extensive research in several works (Blackburn & Vaughan, 1971; Freudenberg & Morton, 1992; Hubert, 2004). In (Blackburn & Vaughan, 1971), an advanced linear model of the Saturn V launch vehicle is developed and a linear optimal control law is proposed to control the vehicle. The work in (Freudenberg & Morton, 1992) studies the problem of robust control of a launch vehicle subject to aerodynamic, flexible, and slosh mode instabilities.

It has been demonstrated that pendulum and mass-spring models can approximate complicated fluid and structural dynamics; such models have formed the basis for many studies on dynamics and control of space vehicles with fuel slosh (Peterson et al., 1989). There is an extensive body of literature on the interaction of vehicle dynamics and slosh dynamics and their control, but this literature treats only the case of small perturbations to the vehicle dynamics. However, in this chapter the control laws are designed by incorporating the complete nonlinear translational and rotational vehicle dynamics.

For accelerating space vehicles, several thrust vector control design approaches have been developed to suppress the fuel slosh dynamics. These approaches have commonly employed methods of linear control design (Sidi, 1997; Bryson, 1994; Wie, 2008) and adaptive control (Adler et al., 1991). A number of related papers following a similar approach are motivated by robotic systems moving liquid filled containers (Feddemma et al., 1997; Grundelius, 2000; Grundelius & Bernhardsson, 1999; Yano, Toda & Terashima, 2001; Yano, Higashikawa & Terashima, 2001; Yano & Terashima, 2001; Terashima & Schmidt, 1994). In most of these approaches, suppression of the slosh dynamics inevitably leads to excitation of the transverse vehicle motion through coupling effects; this is a major drawback which has not been adequately addressed in the published literature.

In this chapter, a spacecraft with a partially filled spherical fuel tank is considered, and the lowest frequency slosh mode is included in the dynamic model using pendulum and mass-spring analogies. A complete set of spacecraft control forces and moments is assumed to be available to accomplish planar maneuvers. Aerodynamic effects are ignored here, although they can be easily included in the spacecraft dynamics assuming that they are canceled by the spacecraft controls. It is also assumed that the spacecraft is in a zero gravity environment, but this assumption is for convenience only. These simplifying assumptions render the problem tractable, while still reflecting the important coupling between the unactuated slosh dynamics and the actuated rigid body motion of the spacecraft. The control objective, as is typical for spacecraft orbital maneuvering problems, is to control the translational velocity vector and the attitude of the spacecraft, while attenuating the slosh mode. Subsequently, mathematical models that reflect all of these assumptions are constructed. These problems are interesting examples of underactuated control problems for multibody systems. In particular, the objective is to simultaneously control the rigid body degrees of freedom and the fuel slosh degree of freedom using only controls that act on the rigid body. Control of the unactuated fuel slosh degree of freedom must be achieved through the system coupling. Finally, linear and nonlinear feedback control laws are designed to achieve this control objective.

It is shown that a linear controller, while successful in stabilizing the pitch and slosh dynamics, fails to control the transverse dynamics of a spacecraft. A Lypunov-based nonlinear feedback control law is designed to achieve stabilization of the pitch and transverse dynamics as well as suppression of the slosh mode while the spacecraft accelerates in the axial direction. The results of this chapter are illustrated through simulation examples.

2. Mathematical model

In this section, we formulate the dynamics of a spacecraft with a spherical fuel tank and include the lowest frequency slosh mode. We represent the spacecraft as a rigid body (base body) and the sloshing fuel mass as an internal body, and follow the development in our previous work (Cho et al., 2000a) to express the equations of motion in terms of the spacecraft translational velocity vector, the angular velocity, and the internal (shape) coordinate representing the slosh mode.

To summarize the formulation in (Cho et al., 2000a), let $\mathbf{v} \in \mathbb{R}^3$, $\boldsymbol{\omega} \in \mathbb{R}^3$, and $\eta \in \mathbb{R}$ denote the base body translational velocity vector, the base body angular velocity vector, and the internal coordinate, respectively. In these coordinates, the Lagrangian has the form $L = L(\mathbf{v}, \boldsymbol{\omega}, \eta, \dot{\eta})$, which is $SE(3)$ -invariant in the sense that it does not depend on the base body position and attitude. The generalized forces and moments on the spacecraft are assumed to consist of control inputs which can be partitioned into two parts: $\boldsymbol{\tau}_t \in \mathbb{R}^3$ (typically from thrusters) is the vector of generalized control forces that act on the base body and $\boldsymbol{\tau}_r \in \mathbb{R}^3$ (typically from symmetric rotors, reaction wheels, and thrusters) is the vector of generalized control torques that act on the base body. We also assume that the internal dissipative forces are derivable from a Rayleigh dissipation function R . Then, the equations of motion of the spacecraft with internal dynamics are shown to be given by:

$$\frac{d}{dt} \frac{\partial L}{\partial \mathbf{v}} + \hat{\boldsymbol{\omega}} \frac{\partial L}{\partial \mathbf{v}} = \boldsymbol{\tau}_t, \quad (1)$$

$$\frac{d}{dt} \frac{\partial L}{\partial \boldsymbol{\omega}} + \hat{\boldsymbol{\omega}} \frac{\partial L}{\partial \boldsymbol{\omega}} + \hat{\mathbf{v}} \frac{\partial L}{\partial \mathbf{v}} = \boldsymbol{\tau}_r, \quad (2)$$

$$\frac{d}{dt} \frac{\partial L}{\partial \dot{\eta}} - \frac{\partial L}{\partial \eta} + \frac{\partial R}{\partial \dot{\eta}} = 0, \quad (3)$$

where $\hat{\mathbf{a}}$ denotes a 3×3 skew-symmetric matrix formed from $\mathbf{a} = [a_1, a_2, a_3]^T \in \mathbb{R}^3$:

$$\hat{\mathbf{a}} = \begin{bmatrix} 0 & -a_3 & a_2 \\ a_3 & 0 & -a_1 \\ -a_2 & a_1 & 0 \end{bmatrix}.$$

Note that equations (1)-(2) are identical to Kirchhoff's equations (Meirovitch & Kwak, 1989), which can also be expressed in the form of Euler-Poincaré equations. It must be pointed out that in the above formulation it is assumed that no control forces or torques exist that directly control the internal dynamics. The objective is to simultaneously control the rigid body dynamics and the internal dynamics using only control effectors that act on the rigid body; the control of internal dynamics must be achieved through the system coupling. In this regard, equations (1)-(3) model interesting examples of underactuated mechanical systems. In our previous research (Reyhanoglu et al., 1996, 1999), we have developed theoretical controllability and stabilizability results for a large class of underactuated mechanical systems using tools from nonlinear control theory. We have also developed effective nonlinear control design methodologies (Reyhanoglu et al., 2000) that we applied to several examples of underactuated mechanical systems, including underactuated space vehicles (Reyhanoglu, 2003; Cho et al., 2000b).

2.1 Pendulum analogy

2.1.1 Spacecraft with throtttable side thrusters

The formulation using a pendulum analogy can be summarized as follows. Consider a rigid spacecraft moving in a fixed plane as indicated in Fig. 1. The important variables are the axial and transverse components of the velocity of the center of the fuel tank, v_x, v_z , the attitude angle θ of the spacecraft with respect to a fixed reference, and the angle ψ of the pendulum with respect to the spacecraft longitudinal axis, representing the fuel slosh. A thrust F , which is assumed to act through the spacecraft center of mass along the spacecraft's longitudinal axis, a transverse force f , and a pitching moment M are available for control purposes. The constants in the problem are the spacecraft mass m and moment of inertia I (without fuel), the

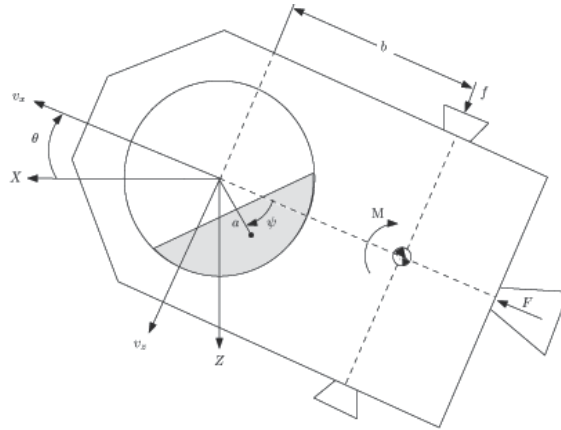


Fig. 1. A single slosh pendulum model for a spacecraft with throttlable side thrusters.

fuel mass m_f and moment of inertia I_f (assumed constant), the length $a > 0$ of the pendulum, and the distance b between the pendulum point of attachment and the spacecraft center of mass location along the longitudinal axis; if the pendulum point of attachment is in front of the spacecraft center of mass then $b > 0$. The parameters m_f , I_f and a depend on the shape of the fuel tank, the characteristics of the fuel and the fill ratio of the fuel tank.

Let \hat{i} and \hat{k} denote unit vectors along the spacecraft-fixed longitudinal and transverse axes, respectively, and denote by (x, z) the inertial position of the center of the fuel tank. The position vector of the center of mass of the vehicle can then be expressed in the spacecraft-fixed coordinate frame as

$$\vec{r} = (x - b)\hat{i} + z\hat{k}.$$

Clearly, the inertial velocity of the vehicle can be computed as

$$\begin{aligned}\dot{\vec{r}} &= (\dot{x} + z\dot{\theta})\hat{i} + (\dot{z} - x\dot{\theta} + b\dot{\theta})\hat{k} \\ &= v_x\hat{i} + (v_z + b\dot{\theta})\hat{k},\end{aligned}\quad (4)$$

where we have used the fact that $v_x = \dot{x} + z\dot{\theta}$ and $v_z = \dot{z} - x\dot{\theta}$.

Similarly, the position vector of the center of mass of the fuel lump in the spacecraft-fixed coordinate frame is given by

$$\vec{r}_f = (x - a\cos\psi)\hat{i} + (z + a\sin\psi)\hat{k},$$

and the inertial velocity of the fuel lump can be computed as

$$\begin{aligned}\dot{\vec{r}}_f &= [\dot{x} + a\dot{\psi}\sin\psi + \dot{\theta}(z + a\sin\psi)]\hat{i} + [\dot{z} + a\dot{\psi}\cos\psi - \dot{\theta}(x - a\cos\psi)]\hat{k} \\ &= [v_x + a(\dot{\theta} + \dot{\psi})\sin\psi]\hat{i} + [v_z + a(\dot{\theta} + \dot{\psi})\cos\psi]\hat{k}.\end{aligned}\quad (5)$$

The total kinetic energy can now be expressed as

$$\begin{aligned}T &= \frac{1}{2}m\dot{\vec{r}}^2 + \frac{1}{2}m_f\dot{\vec{r}}_f^2 + \frac{1}{2}I\dot{\theta}^2 + \frac{1}{2}I_f(\dot{\theta} + \dot{\psi})^2 \\ &= \frac{1}{2}m[v_x^2 + (v_z + b\dot{\theta})^2] + \frac{1}{2}m_f[(v_x + a(\dot{\theta} + \dot{\psi})\sin\psi)^2 + (v_z + a(\dot{\theta} + \dot{\psi})\cos\psi)^2] \\ &\quad + \frac{1}{2}I\dot{\theta}^2 + \frac{1}{2}I_f(\dot{\theta} + \dot{\psi})^2.\end{aligned}\quad (6)$$

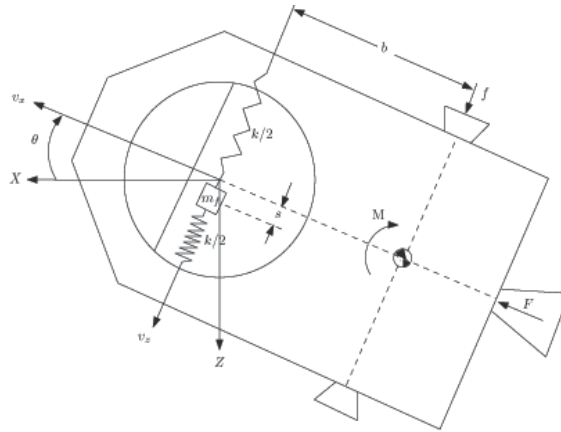


Fig. 3. A single slosh mass-spring model for a spacecraft with throtttable side thrusters.

The control objective is to design feedback controllers so that the controlled spacecraft accomplishes a given planar maneuver, that is a change in the translational velocity vector and the attitude of the spacecraft, while attenuating the slosh mode. The work in (Cho et al., 2000b) considers a constant thrust $F > 0$ and develops a feedback law (using a backstepping approach) to stabilize the system (7)-(10) to a relative equilibrium defined by a constant acceleration in the axial direction. A slightly modified and relatively simpler feedback controller that uses a Lyapunov approach (without resorting to backstepping) can be found in (Reyhanoğlu, 2003). In the subsequent development, we will develop feedback controllers to achieve the same control objective using the system (11)-(14).

2.2 Mass-spring analogy

The mass-spring analogy is related to the pendulum analogy, in which the oscillation frequency of the mass-spring element represents the lowest frequency sloshing mode (Sidi, 1997).

Consider a rigid spacecraft moving on a plane as indicated in Fig. 3, where v_x, v_z are the axial and transverse components, respectively, of the velocity of the center of the fuel tank, and θ denotes the attitude angle of the spacecraft with respect to a fixed reference. The slosh mode is modeled by a point mass m_f whose relative position along the body z -axis is denoted by s ; a restoring force $-ks$ acts on the mass whenever the mass is displaced from its neutral position $s = 0$. As in the previous model, a thrust F , which is assumed to act through the spacecraft center of mass along the spacecraft's longitudinal axis, a transverse force f , and a pitching moment M are available for control purposes. The constants in the problem are the spacecraft mass m and moment of inertia I , the fuel mass m_f , and the distance b between the body z -axis and the spacecraft center of mass location along the longitudinal axis. The parameters m_f, k and b depend on the shape of the fuel tank, the characteristics of the fuel and the fill ratio of the fuel tank.

The position vector of the fuel mass m_f in the spacecraft-fixed coordinate frame is given by

$$\vec{r}_f = x\hat{i} + (z + s)\hat{k},$$

and the inertial velocity of the fuel can be computed as

$$\begin{aligned}\dot{\vec{r}}_f &= [\dot{x} + (z + s)\dot{\theta}] \hat{i} + [\dot{z} - x\dot{\theta} + \dot{s}] \hat{k} \\ &= (v_x + s\dot{\theta}) \hat{i} + (v_z + \dot{s}) \hat{k}.\end{aligned}\quad (15)$$

Thus, under the indicated assumptions, the Lagrangian can be found as

$$\begin{aligned}L &= \frac{1}{2}m\dot{r}^2 + \frac{1}{2}m_f\dot{\vec{r}}_f^2 + \frac{1}{2}I\dot{\theta}^2 - \frac{1}{2}ks^2 \\ &= \frac{1}{2}m[v_x^2 + (v_z + b\dot{\theta})^2] + \frac{1}{2}m_f[(v_x + s\dot{\theta})^2 + (v_z + \dot{s})^2] + \frac{1}{2}I\dot{\theta}^2 - \frac{1}{2}ks^2.\end{aligned}\quad (16)$$

Applying equations (1)-(3) with

$$\eta = s, R = \frac{1}{2}cs^2, \mathbf{v} = \begin{pmatrix} v_x \\ 0 \\ v_z \end{pmatrix}, \boldsymbol{\omega} = \begin{pmatrix} 0 \\ \dot{\theta} \\ 0 \end{pmatrix}, \boldsymbol{\tau}_t = \begin{pmatrix} F \\ 0 \\ f \end{pmatrix}, \boldsymbol{\tau}_r = \begin{pmatrix} 0 \\ M + fb \\ 0 \end{pmatrix},$$

the equations of motion can be obtained as

$$(m + m_f)(\dot{v}_x + \dot{\theta}v_z) + m_f s \ddot{\theta} + mb\dot{\theta}^2 + 2m_f s \dot{\theta} = F, \quad (17)$$

$$(m + m_f)(\dot{v}_z - \dot{\theta}v_x) + mb\ddot{\theta} + m_f \ddot{s} - m_f s \dot{\theta}^2 = f, \quad (18)$$

$$(I + mb^2 + m_f s^2)\ddot{\theta} + m_f s(\dot{v}_x + \dot{\theta}v_z) + 2m_f s \dot{\theta} + mb(\dot{v}_z - \dot{\theta}v_x) = M + bf, \quad (19)$$

$$m_f(\ddot{s} + \dot{v}_z - \dot{\theta}v_x - s\dot{\theta}^2) + ks + c\dot{s} = 0. \quad (20)$$

The control objective is again to design feedback controllers so that the controlled spacecraft accomplishes a given planar maneuver, that is a change in the translational velocity vector and the attitude of the spacecraft, while suppressing the slosh mode.

3. Feedback control design

In this section, we restrict the development to the single slosh pendulum model of a spacecraft with a gimballed thrust engine, i.e. we design feedback controllers for the system (11)-(14) only. In particular, we study the problem of controlling the system to a relative equilibrium defined by a constant acceleration in the axial direction.

3.1 Linearization-based controller design

To obtain the linearized equations of motion, assume small gimbal deflection so that $\cos \delta \approx 1$ and $\sin \delta \approx \delta$, and we rewrite (11)-(14) as:

$$(m + m_f)a_x + m_f a(\ddot{\theta} + \ddot{\psi}) \sin \psi + mb\dot{\theta}^2 + m_f a(\dot{\theta} + \dot{\psi})^2 \cos \psi = F, \quad (21)$$

$$(m + m_f)a_z + m_f a(\ddot{\theta} + \ddot{\psi}) \cos \psi + mb\ddot{\theta} - m_f a(\dot{\theta} + \dot{\psi})^2 \sin \psi = F\delta, \quad (22)$$

$$(I + mb^2)\ddot{\theta} + mba_z - \epsilon\dot{\psi} = M + Fl\delta, \quad (23)$$

$$(I_f + m_f a^2)(\ddot{\theta} + \ddot{\psi}) + m_f a(a_x \sin \psi + a_z \cos \psi) + \epsilon\dot{\psi} = 0, \quad (24)$$

where $l = b + p$ and $(a_x, a_z) = (\dot{v}_x + \dot{\theta}v_z, \dot{v}_z - \dot{\theta}v_x)$ are the axial and transverse components of the acceleration of the center of the fuel tank. The number of equations of motion can

be reduced to two by solving equations (21) and (22) for a_x and a_z , and eliminating these accelerations from equations (23) and (24).

$$[I + m^*(b^2 - ab \cos \psi)]\ddot{\theta} - m^*ab\ddot{\psi} \cos \psi + m^*ab(\dot{\theta} + \dot{\psi})^2 \sin \psi - \epsilon\dot{\psi} = M + b^*F\delta, \quad (25)$$

$$[I_f + m^*(a^2 - ab \cos \psi)]\ddot{\theta} + (I_f + m^*a^2)\ddot{\psi} + (a^*F - m^*ab\dot{\theta}^2) \sin \psi + \epsilon\dot{\psi} = -a^*F\delta \cos \psi, \quad (26)$$

where

$$m^* = \frac{mm_f}{m + m_f}, \quad a^* = \frac{m_f a}{m + m_f}, \quad b^* = \frac{m_f b}{m + m_f} + d.$$

As mentioned previously, without loss of generality, we will assume that the desired equilibrium is given by:

$$(\theta^*, \dot{\theta}^*, \psi^*, \dot{\psi}^*) = (0, 0, 0, 0).$$

Assuming that θ , $\dot{\theta}$, ψ , and $\dot{\psi}$ are small, the following linearized equations can be obtained:

$$I_1\ddot{\theta} - I_2\ddot{\psi} - \epsilon\dot{\psi} = M + b^*F\delta, \quad (27)$$

$$I_3\ddot{\theta} + I_4\ddot{\psi} + a^*F\dot{\psi} + \epsilon\dot{\psi} = -a^*F\delta. \quad (28)$$

where

$$I_1 = I + m^*(b^2 - ab), \quad I_2 = m^*ab,$$

$$I_3 = I_f + m^*(a^2 - ab), \quad I_4 = I_f + m^*a^2.$$

For the linearized system (27)-(28), the state variables are the attitude angle θ , the slosh angle ψ , and their time derivatives. The collection of these state variables is defined as the partial state vector given by

$$\mathbf{x} = [\theta, \dot{\theta}, \psi, \dot{\psi}]^T.$$

Let $\mathbf{u} = [\delta, M]^T$ denote the control input vector. Then, the state space equations can be written as:

$$\dot{\mathbf{x}} = \mathbf{A}\mathbf{x} + \mathbf{B}\mathbf{u}, \quad (29)$$

where

$$\mathbf{A} = \begin{bmatrix} 0 & 1 & 0 & 0 \\ 0 & 0 & -\frac{a^*I_2F}{\Delta} & -\frac{(I_2 - I_4)\epsilon}{\Delta} \\ 0 & 0 & 0 & 1 \\ 0 & 0 & -\frac{a^*I_1F}{\Delta} & -\frac{(I_1 + I_3)\epsilon}{\Delta} \end{bmatrix}, \quad \mathbf{B} = \begin{bmatrix} 0 & 0 \\ -\frac{(I_2a^* - I_4b^*)F}{\Delta} & \frac{I_4}{\Delta} \\ 0 & 0 \\ -\frac{(I_1a^* + I_3b^*)F}{\Delta} & -\frac{I_3}{\Delta} \end{bmatrix}. \quad (30)$$

and

$$\Delta = I_1I_4 + I_2I_3.$$

We consider an LQR (Linear Quadratic Regulator) controller of the form

$$\mathbf{u} = -\mathbf{K}\mathbf{x} \quad (31)$$

that minimizes the quadratic cost function

$$J = \int_0^{\infty} (\mathbf{x}^T \mathbf{Q}\mathbf{x} + \mathbf{u}^T \mathbf{R}\mathbf{u}) dt, \quad (32)$$

where \mathbf{Q} is a symmetric positive-semidefinite weighting matrix and \mathbf{R} is a positive-definite weighting matrix.

The optimal control gain matrix \mathbf{K} is found by solving the corresponding matrix Riccati equation (or using MATLAB's *lqr* function). This controller is then applied to the actual nonlinear system (11)-(14). The simulation results show that the linear controller (31) results in undesirable steady-state errors in transverse velocity (see Figure 4).

3.2 Lyapunov-based controller design

Consider the single slosh pendulum model of a spacecraft with a gimballed thrust engine shown in Fig. 2. If the thrust F is a positive constant, and if the gimbal deflection angle and pitching moment are zero, $\delta = M = 0$, then the spacecraft and fuel slosh dynamics have a relative equilibrium defined by

$$v_x^*(t) = \frac{F}{m + m_f} t + v_{x0}, v_z = v_z^*,$$

$$\theta = \theta^*, \dot{\theta} = 0, \psi = 0, \dot{\psi} = 0,$$

where v_z^* and θ^* are arbitrary constants, and v_{x0} is the initial axial velocity of the spacecraft. Note that θ^* and v_z^* are the desired attitude angle and transverse velocity, chosen as zero here. Now assume the axial acceleration term a_x is not significantly affected by small gimbal deflections, pitch changes and fuel motion (an assumption verified in simulations). Consequently, equation (11) becomes:

$$\dot{v}_x + \dot{\theta} v_z = \frac{F}{m + m_f}. \quad (33)$$

Substituting this approximation leads to the following equations of motion for the transverse, pitch and slosh dynamics:

$$(m + m_f)(\dot{v}_z - \dot{\theta} v_x(t)) + m_f a(\ddot{\theta} + \ddot{\psi}) \cos \psi + mb\ddot{\theta} - m_f a(\dot{\theta} + \dot{\psi})^2 \sin \psi = F\delta, \quad (34)$$

$$(I + mb^2)\ddot{\theta} + mb(\dot{v}_z - \dot{\theta} v_x(t)) - \epsilon \dot{\psi} = M + Fl\delta, \quad (35)$$

$$(I_f + m_f a^2)(\ddot{\theta} + \ddot{\psi}) + m_f a \frac{F}{m + m_f} \sin \psi + m_f a(\dot{v}_z - \dot{\theta} v_x(t)) \cos \psi + \epsilon \dot{\psi} = 0, \quad (36)$$

where $v_x(t)$ is considered as an exogenous input.

Define the error variable

$$\tilde{v}_x = v_x(t) - v_x^*(t).$$

Then, the equations of motion can be written in the following form

$$\dot{\tilde{v}}_x = -\dot{\theta} v_z, \quad (37)$$

$$\dot{v}_z = u_1 + \dot{\theta}(\tilde{v}_x + v_x^*(t)), \quad (38)$$

$$\ddot{\theta} = u_2, \quad (39)$$

$$\ddot{\psi} = -u_1 c \cos \psi - u_2 - d \sin \psi - e \dot{\psi}, \quad (40)$$

where

$$c = \frac{m_f a}{I_f + m_f a^2}, d = \frac{F c}{m + m_f}, e = \frac{\epsilon}{I_f + m_f a^2},$$

and (u_1, u_2) are new control inputs defined as

$$\begin{bmatrix} u_1 \\ u_2 \end{bmatrix} = \mathbf{M}^{-1}(\psi) \begin{bmatrix} F \sin \delta - m_f a \ddot{\psi} \cos \psi + m_f a (\dot{\theta} + \dot{\psi})^2 \sin \psi \\ M + Fl \sin \delta + \epsilon \dot{\psi} \end{bmatrix}, \quad (41)$$

where

$$\mathbf{M}(\psi) = \begin{bmatrix} m_f a \cos \psi + mb & m + m_f \\ I + mb^2 & mb \end{bmatrix}. \quad (42)$$

Now, we consider the following candidate Lyapunov function for the system (37)-(40):

$$V = \frac{r_1}{2} (\tilde{v}_x^2 + v_z^2) + \frac{r_2}{2} \theta^2 + \frac{r_3}{2} \dot{\theta}^2 + r_4 d (1 - \cos \psi) + \frac{r_4}{2} (\dot{\theta} + \dot{\psi})^2, \quad (43)$$

where $r_1, r_2, r_3,$ and r_4 are positive constants. The function V is positive definite in the domain

$$D = \{(\tilde{v}_x, v_z, \theta, \dot{\theta}, \psi, \dot{\psi}) \mid -\pi < \psi < \pi\}.$$

The time derivative of V along the trajectories of (37)-(40) is

$$\begin{aligned} \dot{V} = & [r_1 v_z - r_4 c(\dot{\theta} + \dot{\psi}) \cos \psi] u_1 + [r_1 v_x^*(t) v_z + r_2 \theta + r_3 u_2 + r_4 e(\dot{\theta} + \dot{\psi}) - r_4 d \sin \psi] \dot{\theta} \\ & - r_4 e(\dot{\theta} + \dot{\psi})^2. \end{aligned} \quad (44)$$

Clearly, the feedback laws

$$u_1 = -l_1 [r_1 v_z - r_4 c(\dot{\theta} + \dot{\psi}) \cos \psi], \quad (45)$$

$$u_2 = -l_2 \dot{\theta} - \left[\frac{r_1}{r_3} v_x^*(t) v_z + \frac{r_2}{r_3} \theta \right] - \frac{r_4}{r_3} [e(\dot{\theta} + \dot{\psi}) - d \sin \psi], \quad (46)$$

where l_1 and l_2 are positive constants, yield

$$\dot{V} = -l_1 [r_1 v_z - r_4 c(\dot{\theta} + \dot{\psi}) \cos \psi]^2 - l_2 \dot{\theta}^2 - r_4 e(\dot{\theta} + \dot{\psi})^2,$$

which satisfies $\dot{V} \leq 0$ in D . Using LaSalle's principle, it is easy to prove asymptotic stability of the origin of the closed loop defined by the equations (37)-(40) and the feedback control laws (45)-(46). Note that the positive gains $r_i, i = 1, 2, 3, 4$ and $l_j, j = 1, 2$, can be chosen arbitrarily to achieve good closed loop responses.

4. Simulations

The feedback control laws developed in the previous sections are implemented here for a spacecraft. The physical parameters used in the simulations are $m = 600 \text{ kg}$, $I = 720 \text{ kg/m}^2$, $m_f = 100 \text{ kg}$, $I_f = 90 \text{ kg/m}^2$, $a = 0.2 \text{ m}$, $b = 0.3 \text{ m}$, $p = 0.2 \text{ m}$, $F = 2300 \text{ N}$ and $\epsilon = 0.19 \text{ kg} \cdot \text{m}^2/\text{s}$. We consider stabilization of the spacecraft in orbital transfer, suppressing the transverse and pitching motion of the spacecraft and sloshing of fuel while the spacecraft is accelerating. In other words, the control objective is to stabilize the relative equilibrium corresponding to a constant axial spacecraft acceleration of 3.286 m/s^2 and $v_z = \theta = \dot{\theta} = \psi = \dot{\psi} = 0$.

4.1 Linearization-based controller

In this section, an LQR controller of the form (31) is applied to the complete nonlinear system (11)-(14). Using the physical parameters given above, the \mathbf{A} and \mathbf{B} matrices defined by equation (30) were computed as

$$\mathbf{A} = \begin{bmatrix} 0 & 1 & 0 & 0 \\ 0 & 0 & -0.005 & 0.0002 \\ 0 & 0 & 0 & 1 \\ 0 & 0 & -0.6987 & -0.0023 \end{bmatrix},$$

$$\mathbf{B} = \begin{bmatrix} 0 & 0 \\ 0.7629 & 0.0014 \\ 0 & 0 \\ -1.4243 & -0.0013 \end{bmatrix}.$$

Choosing the weighting matrices as

$$\mathbf{Q} = \begin{bmatrix} 1 & 0 & 0 & 0 \\ 0 & 1 & 0 & 0 \\ 0 & 0 & 1 & 0 \\ 0 & 0 & 0 & 1 \end{bmatrix},$$

$$\mathbf{R} = \begin{bmatrix} 10 & 0 \\ 0 & 0.01 \end{bmatrix},$$

the LQR gain matrix for the linear system (29) was found as

$$\mathbf{K} = \begin{bmatrix} 0.3153 & 1.2214 & -0.3496 & -0.2696 \\ 0.7627 & 2.8027 & 0.6462 & 0.0764 \end{bmatrix}.$$

This gain matrix yields the following eigenvalues for the closed-loop system matrix $\mathbf{A} - \mathbf{BK}$: $(-0.3312 \pm 0.8233i, -0.3297 \pm 0.3294i)$.

Time responses shown in Fig. 4 and Fig. 5 correspond to the initial conditions $v_{x0} = 10000 \text{ m/s}$, $v_{z0} = 0$, $\theta_0 = 2^\circ$, $\dot{\theta}_0 = 0.57^\circ/\text{s}$, $\psi_0 = 15^\circ$, and $\dot{\psi}_0 = 0$. As can be seen in the figures, the LQR controller stabilizes the pitch and slosh dynamics, but fails to stabilize the transverse velocity to zero. The controller results in a steady-state error of $v_z = -349.1 \text{ m/s}$.

4.2 Lyapunov-based controller

In this section, we demonstrate the effectiveness of the Lyapunov-based controller (45)-(46) by applying to the complete nonlinear system (11)-(14).

Time responses shown in Fig. 6 and Fig. 7 correspond to the initial conditions $v_{x0} = 10000 \text{ m/s}$, $v_{z0} = 350 \text{ m/s}$, $\theta_0 = 2^\circ$, $\dot{\theta}_0 = 0.57^\circ/\text{s}$, $\psi_0 = 30^\circ$, and $\dot{\psi}_0 = 0$. As can be seen in the figures, the transverse velocity, attitude angle and the slosh angle converge to the relative equilibrium at zero while the axial velocity v_x increases and \dot{v}_x tends asymptotically to 3.286 m/s^2 . Note that there is a trade-off between good responses for the directly actuated degrees of freedom (the transverse and pitch dynamics) and good responses for the unactuated degree of freedom (the slosh dynamics); the controller given by (45)-(46) with parameters $r_1 = 10^{-7}$, $r_2 = 10$, $r_3 = 10^2$, $r_4 = 10^{-2}$, $l_1 = 10^3$, $l_2 = 1$ represents one example of this balance.

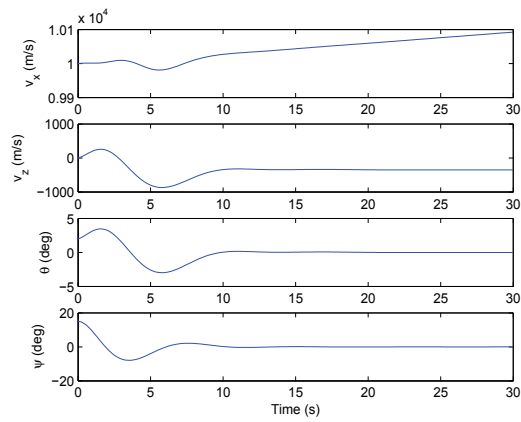


Fig. 4. Time responses of state variables v_x , v_z , θ , and ψ (LQR controller).

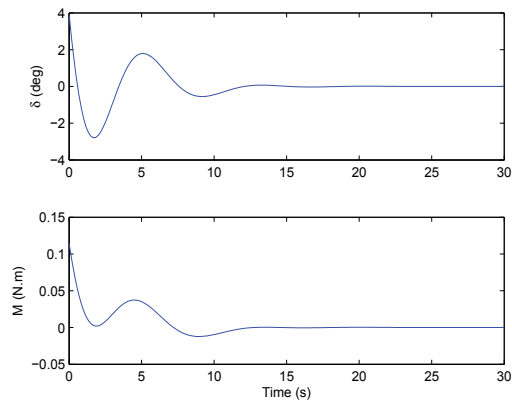


Fig. 5. Gimbal deflection angle δ and pitching moment M (LQR controller).

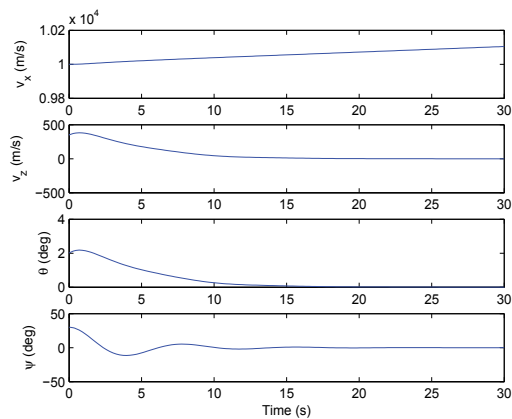


Fig. 6. Time responses of state variables v_x , v_z , θ , and ψ (Lyapunov-based controller).

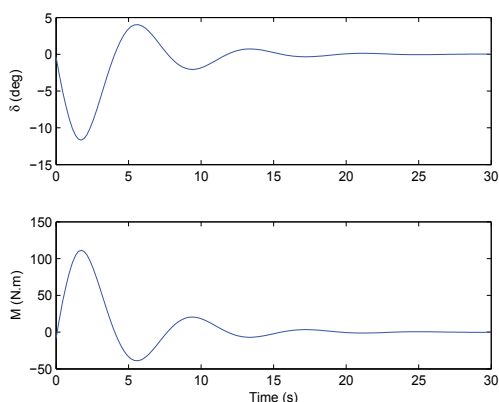


Fig. 7. Gimbal deflection angle δ and pitching moment M (Lyapunov-based controller).

5. Conclusions

We have shown that a linear controller, while successful in stabilizing the pitch and slosh dynamics, fails to control the transverse dynamics of a spacecraft. We have designed a Lyapunov-based nonlinear feedback control law that achieves stabilization of the pitch and transverse dynamics as well as suppression of the slosh mode, while the spacecraft accelerates in the axial direction. The effectiveness of this control feedback law has been illustrated through a simulation example.

The many avenues considered for future research include problems involving higher-frequency slosh modes, multiple propellant tanks, and three dimensional maneuvers. Future research also includes designing nonlinear control laws that achieve robustness, insensitivity to system and control parameters, and improved disturbance rejection. In particular, we plan to explore the use of sliding mode controllers to accomplish this.

6. References

- Adler, J. M., Lee, M. S. & Saugen, J. D. (1991). Adaptive control of propellant slosh for launch vehicles, *SPIE Sensors and Sensor Integration* 1480: 11–22.
- Biswal, K. C., Bhattacharyya, S. K. & Sinha, P. K. (2004). Dynamic characteristics of liquid filled rectangular tank with baffles, *IE (I) Journal-CV* 84: 145–148.
- Blackburn, T. R. & Vaughan, D. R. (1971). Application of linear optimal control and filtering theory to the saturn v launch vehicle, *IEEE Transactions on Automatic Control* 16(6): 799–806.
- Bryson, A. E. (1994). *Control of Spacecraft and Aircraft*, Princeton University Press.
- Cho, S., McClamroch, N. H. & Reyhanoglu, M. (2000a). Dynamics of multibody vehicles and their formulation as nonlinear control systems, *Proceedings of American Control Conference*, pp. 3908–3912.
- Cho, S., McClamroch, N. H. & Reyhanoglu, M. (2000b). Feedback control of a space vehicle with unactuated fuel slosh dynamics, *Proceedings of AIAA Guidance, Navigation, and Control Conference*, pp. 354–359.
- Feddema, J. T., Dohrmann, C. R., Parker, G. G., Robinett, R. D., Romero, V. J. & Schmitt, D. J. (1997). Control for slosh-free motion of an open container, *IEEE Control Systems*

- Magazine* pp. 29–36.
- Freudenberg, J. & Morton, B. (1992). Robust control of a booster vehicle using h_∞ and ssv techniques, *Proceedings of the 31st IEEE Conference on Decision and Control*, pp. 2448–2453.
- Grundelius, M. (2000). Iterative optimal control of liquid slosh in an industrial packaging machine, *Proceedings of the 39th IEEE Conference on Decision and Control*, pp. 3427–3432.
- Grundelius, M. & Bernhardsson, B. (1999). Control of liquid slosh in an industrial packaging machine, *Proceedings of IEEE International Conference on Control Applications*, pp. 1654–1659.
- Hubert, C. (2003). *Behavior of Spinning Space Vehicles with Onboard Liquids*, NASA/KSC Contract NAS10-02016.
- Hubert, C. (2004). Design and flight performance of a system for rapid attitude maneuvers by a spinning vehicle, *Proceedings of the 27th Annual AAS Guidance and Control Conference*.
- Meirovitch, L. & Kwak, M. K. (1989). State equations for a spacecraft with maneuvering flexible appendages in terms of quasi-coordinates, *Applied Mechanics Reviews* 42(11): 161–170.
- Peterson, L. D., Crawley, E. F. & Hansman, R. J. (1989). Nonlinear fluid slosh coupled to the dynamics of a spacecraft, *AIAA Journal* 27(9): 1230–1240.
- Reyhanoglu, M. (2003). Maneuvering control problems for a spacecraft with unactuated fuel slosh dynamics, *Proceedings of IEEE Conference on Control Applications*, pp. 695–699.
- Reyhanoglu, M., Cho, S. & McClamroch, N. H. (2000). Discontinuous feedback control of a special class of underactuated mechanical systems, *International Journal of Robust and Nonlinear Control* 10(4): 265–281.
- Reyhanoglu, M., van der Schaft, A. J., McClamroch, N. & Kolmanovsky, I. (1996). Nonlinear control of a class of underactuated systems, *Proceedings of IEEE Conference on Decision and Control*, pp. 1682–1687.
- Reyhanoglu, M., van der Schaft, A. J., McClamroch, N. & Kolmanovsky, I. (1999). Dynamics and control of a class of underactuated mechanical systems, *IEEE Transactions on Automatic Control* 44(9): 1663–1671.
- Sidi, M. J. (1997). *Spacecraft Dynamics and Control*, Cambridge University Press, New York.
- Terashima, K. & Schmidt, G. (1994). Motion control of a cart-based container considering suppression of liquid oscillations, *Proceedings of IEEE International Symposium on Industrial Electronics*, pp. 275–280.
- Venugopal, R. & Bernstein, D. S. (1996). State space modeling and active control of slosh, *Proceedings of IEEE International Conference on Control Applications*, pp. 1072–1077.
- Wie, B. (2008). *Space Vehicle Dynamics and Control*, AIAA Education Series.
- Yano, K., Higashikawa, S. & Terashima, K. (2001). Liquid container transfer control on 3d transfer path by hybrid shaped approach, *Proceedings of IEEE International Conference on Control Applications*, pp. 1168–1173.
- Yano, K. & Terashima, K. (2001). Robust liquid container transfer control for complete sloshing suppression, *IEEE Transactions on Control Systems Technology* 9(3): 483–493.
- Yano, K., Toda, T. & Terashima, K. (2001). Sloshing suppression control of automatic pouring robot by hybrid shape approach, *Proceedings of the 40th IEEE Conference on Decision and Control*, pp. 1328–1333.

Synchronization of Target Tracking Cascaded Leader-Follower Spacecraft Formation

Rune Schlanbusch and Per Johan Nicklasson

*Department of Technology, Narvik University College, PB 385, AN-8505 Narvik
Norway*

1. Introduction

In recent years, formation flying has become an increasingly popular subject of study. This is a new method of performing space operations, by replacing large and complex spacecraft with an array of simpler micro-spacecraft bringing out new possibilities and opportunities of cost reduction, redundancy and improved resolution aspects of onboard payload. One of the main challenges is the requirement of synchronization between spacecraft; robust and reliable control of relative position and attitude are necessary to make the spacecraft cooperate to gain the possible advantages made feasible by spacecraft formations. For fully autonomous spacecraft formations both path- and attitude-planning must be performed on-line which introduces challenges like collision avoidance and restrictions on pointing instruments towards required targets, with the lowest possible fuel expenditure. The system model is a key element to achieve a reliable and robust controller.

1.1 Previous work

The simplest Cartesian model of relative motion between two spacecraft is linear and known as the Hill (Hill, 1878) or Clohessy-Wiltshire (Clohessy & Wiltshire, 1960) equations; a linear model based on assumptions of circular orbits, no orbital perturbations and small relative distance between spacecraft compared with the distance from the formation to the center of the Earth. As the visions for tighter spacecraft formations in highly elliptic orbits appeared, the need for more detailed models arose, especially regarding orbital perturbations. This resulted in nonlinear models as presented in *e.g.* (McInnes, 1995; Wang & Hadaegh, 1996), and later in (Yan et al., 2000a) and (Kristiansen, 2008), derived for arbitrary orbital eccentricity and with added terms for orbital perturbations. Most previous work on reference generation are concerned with translational trajectory generation for fuel optimal reconfiguration and formation keeping such as in (Wong & Kapila, 2005) where a formation located at the Sun-Earth L_2 Langrange Point is considered, while (Yan et al., 2009) proposed two approaches to design perturbed satellite formation relative motion orbits using least-square techniques. Trajectory optimization for satellite reconfiguration maneuvers coupled with attitude constraints have been investigated in (Garcia & How, 2005) where a path planner based on rapidly-exploring random tree is used in addition to a smoother function. Coupling between the position and attitude is introduced by the pointing constrains, and thus the trajectory design must be solved as a single $6N$ Degrees of Freedom (DOF) problem instead of N separate 6 DOF problems.

Ground target tracking for spacecraft has been addressed by several other researchers, such as (Goerre & Shucker, 1999; Chen et al., 2000; Tsiotras et al., 2001) and (Steyn, 2006) where only one spacecraft is considered. The usual way to generate target tracking reference is to find a vector pointing from the spacecraft towards a point on the planet surface where the instrument is supposed to be pointing, and then the desired quaternions and angular velocities are generated to ensure high accuracy tracking of the specified target point.

Due to the parameterization of the attitude for both Euler angles and the unit quaternion we obtain a set of two equilibria of the closed-loop system of a rigid body, and possibilities of the unwinding phenomenon. One approach to solve the problem of multiple equilibria is the use of hybrid control (*cf.* (Liberzon, 2003), (Goebel et al., 2009)), and different solutions have been presented, as in (Casagrande, 2008) for an underactuated non-symmetric rigid body, and by (Mayhew et al., 2009) using quaternion-based hybrid feedback where the choice of rotational direction is performed by a switching control law.

The nonlinear nature of the tracking control problem has been a challenging task in robotics and control research. The so called *passivity-based approach* to robot control have gained much attention, which, contrary to computed torque control, couple with the robot control problem by exploiting the robots' physical structure (Berghuis & Nijmeijer, 1993). A simple solution to the closed-loop passivity approach was proposed by (Takegaki & Arimoto, 1981) on the robot position control problem. The natural extension the motion control task was solved in (Paden & Panja, 1988), where the controller was called *PD+*, and in (Slotine & Li, 1987) where the controller was called *passivity-based sliding surface*. The control structure was later applied for spacecraft formation control in (Kristiansen, 2008).

For large systems, *e.g.* complex dynamical systems such as spacecraft formations, the expression *divide and conquer* may seem appealing, and for good reasons; by dividing a system into smaller parts, the difficulties of stability analysis and control design can be greatly reduced. A particular case of such systems is cascaded structure which consists of a *driving* system which is an input to the *driven* system through an *interconnection* (see (Loría & Panteley, 2005) and references therein).

The topic of cascaded systems have received a great deal of attention and has successfully been applied to a wide number of applications. In (Fossen & Fjellstad, 1993) a cascaded adaptive control scheme for marine vehicles including actuator dynamics was introduced, while (Loría et al., 1998) solved the problem of synchronization of two pendula through use of cascades. The authors of (Janković et al., 1996) studied the problem of global stabilisability of feedforward systems by a systematic recursive design procedure for autonomous systems, while time-varying systems were considered in (Jiang & Mareels, 1997) for stabilization of robust control, while (Panteley & Loría, 1998) established sufficient conditions for Uniform Global Asymptotical Stability (UGAS) for cascaded nonlinear time-varying systems. The aspects of practical and semi-global stability for nonlinear time-varying systems in cascade were pursued in (Chaillet, 2006) and (Chaillet & Loría, 2008). A stability analysis of spacecraft formations including both leader and follower using relative coordinates was presented in (Grötli, 2010), where the controller-observer scheme was proven input-to-state-stable.

1.2 Contribution

In this paper we present a solution for real-time generation of attitude references for a leader-follower spacecraft formation with target tracking leader and followers complementing the measurement by pointing their instruments at a common target on the Earth surface. The solution is based on a 6DOF model where each follower generates the

attitude references in real-time based on relative translational motion between the leader and its followers, which also ensures that the spacecraft are pointing at the target during formation reconfiguration. We are utilizing a passivity-based sliding surface controller for relative position and Uniform Global Practical Asymptotic Stability (UGPAS) is proven for the equilibrium point of the closed-loop system. The control law is also adapted for hybrid switching control with hysteresis for attitude tracking spacecraft in formation to ensure robust stability when measurement noise is considered, and avoid unwinding, thus achieving Uniform Practical Asymptotic Stability (UPAS) in the large on the set $\mathcal{S}^3 \times \mathbb{R}^3$ for the equilibrium point of the closed-loop system. Simulation results are presented to show how the attitude references are generated during a formation reconfiguration using the derived control laws.

The rest of the paper is organized as follows. In Section 2 we describe the modeling of relative translation and rotation for spacecraft formations; in Section 3 we present a scheme where the attitude reference for the leader and follower spacecraft is generated based on relative coordinates; in Section 4 we present continuous control of relative translation and hybrid control of relative rotation where stability of the overall system is proved through use of cascades; in Section 5 we present simulation results and we conclude with some remarks in Section 6.

2 Modeling

In the following, we denote by $\dot{\mathbf{x}}$ the time derivative of a vector \mathbf{x} , *i.e.* $\dot{\mathbf{x}} = d\mathbf{x}/dt$, and moreover, $\ddot{\mathbf{x}} = d^2\mathbf{x}/dt^2$. We denote by $\|\cdot\|$ the Euclidian norm of a vector and the induced \mathcal{L}_2 norm of a matrix. The cross-product operator is denoted $\mathbf{S}(\cdot)$, such that $\mathbf{S}(\mathbf{x})\mathbf{y} = \mathbf{x} \times \mathbf{y}$. Reference frames are denoted by $\mathcal{F}^{(\cdot)}$, and in particular, the standard Earth-Centered Inertial (ECI) frame is denoted \mathcal{F}^i and The Earth-Centered Earth-Fixed (ECEF) frame is denoted \mathcal{F}^e . We denote by $\boldsymbol{\omega}_{b,a}^c$ the angular velocity of frame \mathcal{F}^a relative to frame \mathcal{F}^b , referenced in frame \mathcal{F}^c . Matrices representing rotation or coordinate transformation from frame \mathcal{F}^a to frame \mathcal{F}^b are denoted $\mathbf{R}_{a,b}^b$. When the context is sufficiently explicit, we may omit to write arguments of a function, vector or matrix.

2.1 Cartesian coordinate frames

Basically there are two different approaches for modeling spacecraft formations: Cartesian coordinates and orbital elements, which both have their pros and cons. The orbital element method is often used to design formations concerning low fuel expenditure because of the relationship towards natural orbits, while Cartesian models often are used where an orbit with fixed dimensions are studied, which is the case in this paper.

The coordinate reference frames used throughout the paper are shown in Figure 1, and defined as follows:

Leader orbit reference frame: The leader orbit frame, denoted \mathcal{F}^l , has its origin located in the center of mass of the leader spacecraft. The \mathbf{e}_r axis in the frame coincide with the vector $\mathbf{r}_l \in \mathbb{R}^3$ from the center of the Earth to the spacecraft, and the \mathbf{e}_h axis is parallel to the orbital angular momentum vector, pointing in the orbit normal direction. The \mathbf{e}_θ axis completes the right-handed orthonormal frame. The basis vectors of the frame can be defined as

$$\mathbf{e}_r := \frac{\mathbf{r}_l}{\|\mathbf{r}_l\|}, \quad \mathbf{e}_\theta := \mathbf{S}(\mathbf{e}_h)\mathbf{e}_r \quad \text{and} \quad \mathbf{e}_h := \frac{\mathbf{h}}{\|\mathbf{h}\|}, \quad (1)$$

where $\mathbf{h} = \mathbf{S}(\mathbf{r}_l)\dot{\mathbf{r}}_l$ is the angular momentum vector of the orbit.

Follower orbit reference frame: The follower orbit frame has its origin in the center of mass of the follower spacecraft, and is denoted \mathcal{F}^f . The vector pointing from the center of the Earth to the frame origin is denoted $\mathbf{r}_f \in \mathbb{R}^3$, and the frame is specified by a relative orbit position vector $\mathbf{p} = [x, y, z]^\top$ expressed in \mathcal{F}^l components, and its unit vectors align with the basis vectors of \mathcal{F}^l . Accordingly,

$$\mathbf{p} = \mathbf{R}_i^l(\mathbf{r}_f - \mathbf{r}_l) = x\mathbf{e}_r + y\mathbf{e}_\theta + z\mathbf{e}_h \Rightarrow \mathbf{r}_f = \mathbf{R}_i^l\mathbf{p} + \mathbf{r}_l. \tag{2}$$

2.2 Quaternions and kinematics

The attitude of a rigid body is often represented by a rotation matrix $\mathbf{R} \in SO(3)$ fulfilling

$$SO(3) = \{\mathbf{R} \in \mathbb{R}^{3 \times 3} : \mathbf{R}^\top \mathbf{R} = \mathbf{I}, \det \mathbf{R} = 1\}, \tag{3}$$

which is the special orthogonal group of order three, where \mathbf{I} denotes the identity matrix. A rotation matrix for a rotation θ about an arbitrary unit vector $\mathbf{k} \in \mathbb{R}^3$ can be angle-axis parameterized as *-cf.* (Egeland & Gravdahl, 2002),

$$\mathbf{R}_{\mathbf{k},\theta} = \mathbf{I} + \mathbf{S}(\mathbf{k})\sin\theta + \mathbf{S}^2(\mathbf{k})(1 - \cos\theta), \tag{4}$$

and coordinate transformation of a vector \mathbf{r} from frame a to frame b is written as $\mathbf{r}^b = \mathbf{R}_a^b\mathbf{r}^a$. The rotation matrix in (4) can be expressed by an Euler parameter representation as

$$\mathbf{R} = \mathbf{I} + 2\eta\mathbf{S}(\boldsymbol{\epsilon}) + 2\mathbf{S}^2(\boldsymbol{\epsilon}), \tag{5}$$

where the matrix $\mathbf{S}(\cdot)$ is the cross product operator

$$\mathbf{S}(\boldsymbol{\epsilon}) = \boldsymbol{\epsilon} \times = \begin{bmatrix} 0 & -\epsilon_z & \epsilon_y \\ \epsilon_z & 0 & -\epsilon_x \\ -\epsilon_y & \epsilon_x & 0 \end{bmatrix}, \quad \boldsymbol{\epsilon} = \begin{bmatrix} \epsilon_x \\ \epsilon_y \\ \epsilon_z \end{bmatrix}. \tag{6}$$

Quaternions are often used to parameterize members of $SO(3)$ where the unit quaternion is defined as $\mathbf{q} = [\eta, \boldsymbol{\epsilon}^\top]^\top \in \mathcal{S}^3 = \{\mathbf{x} \in \mathbb{R}^4 : \mathbf{x}^\top \mathbf{x} = 1\}$, where $\eta = \cos(\theta/2) \in \mathbb{R}$ is the scalar

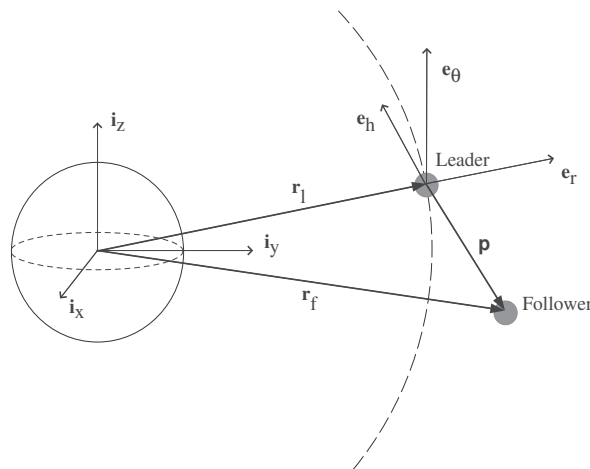


Fig. 1. Reference coordinate frames.

part and $\boldsymbol{\epsilon} = \mathbf{k} \sin(\theta/2) \in \mathbb{R}^3$ is the vector part. The set \mathcal{S}^3 forms a group with quaternion multiplication, which is distributive and associative, but not commutative, and the quaternion product is defined as

$$\mathbf{q}_1 \otimes \mathbf{q}_2 = \begin{bmatrix} \eta_1 \eta_2 - \boldsymbol{\epsilon}_1^\top \boldsymbol{\epsilon}_2 \\ \eta_1 \boldsymbol{\epsilon}_2 + \eta_2 \boldsymbol{\epsilon}_1 + \mathbf{S}(\boldsymbol{\epsilon}_1) \boldsymbol{\epsilon}_2 \end{bmatrix}. \quad (7)$$

The inverse rotation can be performed by using the inverse conjugate of \mathbf{q} given by $\bar{\mathbf{q}} = [\eta, -\boldsymbol{\epsilon}^\top]^\top$. The time derivative of the rotation matrix is

$$\dot{\mathbf{R}}_b^a = \mathbf{S}(\boldsymbol{\omega}_{a,b}^a) \mathbf{R}_b^a = \mathbf{R}_b^a \mathbf{S}(\boldsymbol{\omega}_{a,b}^b), \quad (8)$$

and the kinematic differential equations may be expressed as

$$\dot{\mathbf{q}} = \mathbf{T}(\mathbf{q}) \boldsymbol{\omega}, \quad \mathbf{T}(\mathbf{q}) = \frac{1}{2} \begin{bmatrix} -\boldsymbol{\epsilon}^\top \\ \eta \mathbf{I} + \mathbf{S}(\boldsymbol{\epsilon}) \end{bmatrix} \in \mathbb{R}^{4 \times 3}. \quad (9)$$

2.2.1 Relative translation

The fundamental differential equation of the two-body problem can be expressed as (cf. (Battin, 1999))

$$\ddot{\mathbf{r}}_s = -\frac{\mu}{r_s^3} \mathbf{r}_s + \frac{\mathbf{f}_{sd}}{m_s} + \frac{\mathbf{f}_{sa}}{m_s}, \quad (10)$$

where $\mathbf{f}_{sd} \in \mathbb{R}^3$ is the perturbation term due to external effects, $\mathbf{f}_{sa} \in \mathbb{R}^3$ is the actuator force, m_s is the mass of the spacecraft, and super-/sub-script s denotes the spacecraft in question, so $s = l, f$ for the leader and follower spacecraft respectively. The spacecraft masses are assumed to be small relative to the mass of the Earth M_e , so $\mu \approx GM_e$, where G is the gravitational constant. According to (2) the relative position between the leader and follower spacecraft may be expressed as

$$\mathbf{R}_l^i \mathbf{p} = \mathbf{r}_f - \mathbf{r}_l, \quad (11)$$

and by differentiating twice we obtain

$$\mathbf{R}_l^i \ddot{\mathbf{p}} + 2\mathbf{R}_l^i \mathbf{S}(\boldsymbol{\omega}_{i,l}^l) \dot{\mathbf{p}} + \mathbf{R}_l^i \left(\mathbf{S}^2(\boldsymbol{\omega}_{i,l}^l) + \mathbf{S}(\dot{\boldsymbol{\omega}}_{i,l}^l) \right) \mathbf{p} = \ddot{\mathbf{r}}_f - \ddot{\mathbf{r}}_l. \quad (12)$$

By inserting (10), the right hand side of (12) may be written as

$$\ddot{\mathbf{r}}_f - \ddot{\mathbf{r}}_l = -\frac{\mu}{r_f^3} \mathbf{r}_f + \frac{\mathbf{f}_{fd}}{m_f} + \frac{\mathbf{f}_{fa}}{m_f} + \frac{\mu}{r_l^3} \mathbf{r}_l - \frac{\mathbf{f}_{ld}}{m_l} - \frac{\mathbf{f}_{la}}{m_l}, \quad (13)$$

and by inserting (2) into (13), we find that

$$m_f (\ddot{\mathbf{r}}_f - \ddot{\mathbf{r}}_l) = -m_f \mu \left[\left(\frac{1}{r_f^3} - \frac{1}{r_l^3} \right) \mathbf{r}_l + \frac{\mathbf{R}_l^i \mathbf{p}}{r_f^3} \right] + \mathbf{f}_{fa} + \mathbf{f}_{fd} - \frac{m_f}{m_l} (\mathbf{f}_{la} + \mathbf{f}_{ld}). \quad (14)$$

Moreover, by inserting (14) into (12), and rearranging the terms we obtain

$$m_f \ddot{\mathbf{p}} + \mathbf{C}_t(\boldsymbol{\omega}_{i,l}^l) \dot{\mathbf{p}} + \mathbf{D}_t(\boldsymbol{\omega}_{i,l}^l, \boldsymbol{\omega}_{i,l}^l, r_f) \mathbf{p} + \mathbf{n}_t(\mathbf{r}_l, r_f) = \mathbf{F}_a + \mathbf{F}_d, \quad (15)$$

where

$$\mathbf{C}_t(\boldsymbol{\omega}_{i,l}^l) = 2m_f \mathbf{S}(\boldsymbol{\omega}_{i,l}^l) \quad (16)$$

is a skew-symmetric matrix,

$$\mathbf{D}_t(\dot{\boldsymbol{\omega}}_{i,l}^l, \boldsymbol{\omega}_{i,l}^l, r_f) = m_f \left[\mathbf{S}^2(\boldsymbol{\omega}_{i,l}^l) + \mathbf{S}(\dot{\boldsymbol{\omega}}_{i,l}^l) + \frac{\mu}{r_f^3} \mathbf{I} \right] \quad (17)$$

may be viewed as a time-varying potential force, and

$$\mathbf{n}_t(\mathbf{r}_l, r_f) = \mu m_f \mathbf{R}_i^l \left[\frac{1}{r_f^3} - \frac{1}{r_l^3} \right] \mathbf{r}_l \quad (18)$$

is a nonlinear term. The composite perturbation force \mathbf{F}_d and the composite relative control force \mathbf{F}_a are respectively written as

$$\mathbf{F}_d = \mathbf{R}_i^l \left(\mathbf{f}_{fd} - \frac{m_f}{m_l} \mathbf{f}_{ld} \right) \quad \text{and} \quad \mathbf{F}_a = \mathbf{R}_i^l \left(\mathbf{f}_{fa} - \frac{m_f}{m_l} \mathbf{f}_{la} \right). \quad (19)$$

Note that all forces \mathbf{f} are presented in the inertial frame. If the forces are computed in another frame, the rotation matrix should be replaced accordingly. The orbital angular velocity and angular acceleration can be expressed as $\boldsymbol{\omega}_{i,l}^i = \mathbf{S}(\mathbf{r}_l) \mathbf{v}_l / \mathbf{r}_l^\top \mathbf{r}_l$, and

$$\dot{\boldsymbol{\omega}}_{i,l}^i = \frac{\mathbf{r}_l^\top \mathbf{r}_l \mathbf{S}(\mathbf{r}_l) \mathbf{a}_l - 2 \mathbf{v}_l^\top \mathbf{r}_l \mathbf{S}(\mathbf{r}_l^\top) \mathbf{v}_l}{(\mathbf{r}_l^\top \mathbf{r}_l)^2}, \quad (20)$$

respectively.

5.2.2 Relative rotation

With the assumptions of rigid body movement, the dynamical model of a spacecraft can be found from Euler's momentum equations as (Sidi, 1997)

$$\mathbf{J}_s \dot{\boldsymbol{\omega}}_{i,sb}^{sb} = -\mathbf{S}(\boldsymbol{\omega}_{i,sb}^{sb}) \mathbf{J}_s \boldsymbol{\omega}_{i,sb}^{sb} + \boldsymbol{\tau}_{sd}^{sb} + \boldsymbol{\tau}_{sa}^{sb} \quad (21)$$

$$\boldsymbol{\omega}_{s,sb}^{sb} = \boldsymbol{\omega}_{i,sb}^{sb} - \mathbf{R}_i^{sb} \boldsymbol{\omega}_{i,s}^i \quad (22)$$

where $\mathbf{J}_s = \text{diag}\{J_{sx}, J_{sy}, J_{sz}\} \in \mathbb{R}^{3 \times 3}$ is the spacecraft moment of inertia matrix, $\boldsymbol{\tau}_{sd}^{sb} \in \mathbb{R}^3$ is the total disturbance torque, $\boldsymbol{\tau}_{sa}^{sb} \in \mathbb{R}^3$ is the total actuator torque and $\boldsymbol{\omega}_{i,s}^i = \mathbf{S}(\mathbf{r}_s) \mathbf{v}_s / \mathbf{r}_s^\top \mathbf{r}_s$ is the orbital angular velocity. Rotation from the leader body frame to the inertial frame are denoted \mathbf{q}_{lb}^i , while rotation from the follower body frame to the inertial frame are denoted \mathbf{q}_{fb}^i . Relative rotation between the follower and leader body frame is found by applying the quaternion product (cf. (7)) expressed as

$$\mathbf{q}_{fb}^{lb} = \mathbf{q}_{fb}^i \otimes \bar{\mathbf{q}}_{lb}^i, \quad (23)$$

and with a slightly abuse of notation we denote $\mathbf{q}_l = \mathbf{q}_{lb}^i$ and $\mathbf{q}_f = \mathbf{q}_{fb}^{lb}$. The relative attitude dynamics may be expressed as (cf. (Yan et al., 2000b; Kristiansen, 2008))

$$\begin{aligned} \mathbf{J}_f \dot{\boldsymbol{\omega}} + \mathbf{J}_f \mathbf{S}(\mathbf{R}_{lb}^{fb} \boldsymbol{\omega}_{i,lb}^{lb}) \boldsymbol{\omega} - \mathbf{J}_f \mathbf{R}_{lb}^{fb} \mathbf{J}_l^{-1} \mathbf{S}(\boldsymbol{\omega}_{i,lb}^{lb}) \mathbf{J}_l \boldsymbol{\omega}_{i,lb}^{lb} \\ + \mathbf{S}(\boldsymbol{\omega} + \mathbf{R}_{lb}^{fb} \boldsymbol{\omega}_{i,lb}^{lb}) \mathbf{J}_f (\boldsymbol{\omega} + \mathbf{R}_{lb}^{fb} \boldsymbol{\omega}_{i,lb}^{lb}) = \mathbf{Y}_d + \mathbf{Y}_a, \end{aligned} \quad (24)$$

where

$$\boldsymbol{\omega} = \boldsymbol{\omega}_{i,fb}^{fb} - \mathbf{R}_{lb}^{fb} \boldsymbol{\omega}_{i,lb}^{lb} \quad (25)$$

is the relative angular velocity between the follower body reference frame and the leader body reference frame expressed in the follower body reference frame,

$$\mathbf{Y}_d = \boldsymbol{\tau}_{fd}^{fb} - \mathbf{J}_f \mathbf{R}_{lb}^{fb} \mathbf{J}_l^{-1} \boldsymbol{\tau}_{ld}^{lb}, \quad \mathbf{Y}_a = \boldsymbol{\tau}_{fa}^{fb} - \mathbf{J}_f \mathbf{R}_{lb}^{fb} \mathbf{J}_l^{-1} \boldsymbol{\tau}_{la}^{lb} \quad (26)$$

are the relative perturbation torque and actuator torque, respectively. For simplicity (24) may be rewritten as

$$\mathbf{J}_f \dot{\boldsymbol{\omega}} + \mathbf{C}_r(\boldsymbol{\omega}) \boldsymbol{\omega} + \mathbf{n}_r(\boldsymbol{\omega}) = \mathbf{Y}_d + \mathbf{Y}_a, \quad (27)$$

where

$$\mathbf{C}_r(\boldsymbol{\omega}) = \mathbf{J}_f \mathbf{S}(\mathbf{R}_{lb}^{fb} \boldsymbol{\omega}_{i,lb}^{lb}) + \mathbf{S}(\mathbf{R}_{lb}^{fb} \boldsymbol{\omega}_{i,lb}^{lb}) \mathbf{J}_f - \mathbf{S}(\mathbf{J}_f(\boldsymbol{\omega} + \mathbf{R}_{lb}^{fb} \boldsymbol{\omega}_{i,lb}^{lb})) \quad (28)$$

is a skew-symmetric matrix, and

$$\mathbf{n}_r(\boldsymbol{\omega}) = \mathbf{S}(\mathbf{R}_{lb}^{fb} \boldsymbol{\omega}_{i,lb}^{lb}) \mathbf{J}_f \mathbf{R}_{lb}^{fb} \boldsymbol{\omega}_{i,lb}^{lb} - \mathbf{J}_f \mathbf{R}_{lb}^{fb} \mathbf{J}_l^{-1} \mathbf{S}(\boldsymbol{\omega}_{i,lb}^{lb}) \mathbf{J}_l \boldsymbol{\omega}_{i,lb}^{lb} \quad (29)$$

is a nonlinear term.

3. Reference generation

Our objective for the spacecraft formation is to have each spacecraft, including the leader, tracking a fixed point located at the surface of *e.g.* the Earth by specifying a tracking direction of the selected pointing axis where a measurement instrument is mounted such as *e.g.* a camera or antenna. The target is chosen by the spacecraft operator as a given set of coordinates such as latitude (ϕ) and longitude (λ). The vector pointing from the center of Earth to the target in an Earth Centered Earth Fixed (ECEF) frame is obtained by applying

$$\mathbf{r}_t^e = \begin{bmatrix} \cos(\phi) \cos(\lambda) \\ \cos(\phi) \sin(\lambda) \\ \sin(\phi) \end{bmatrix} r_e \quad (30)$$

where $r_e = 6378.137 \times 10^3$ m is the Earth radii. It is assumed a perfect spherical Earth; alternatively a function of the Earth radii may be used as $r_e(\lambda, \phi)$ with longitude and latitude as arguments. If we assume that the Earth has a constant angular rate $\omega_e = 7.292115 \times 10^{-5}$ rad/s around its rotation axis we can rotate the target vector to ECI coordinates by utilizing

$$\mathbf{r}_t = \mathbf{R}_e^i \mathbf{r}_t^e \quad (31)$$

where the rotation matrix from ECEF to ECI coordinates is denoted

$$\mathbf{R}_e^i = \begin{bmatrix} \cos(\omega_e t + \alpha) & -\sin(\omega_e t + \alpha) & 0 \\ \sin(\omega_e t + \alpha) & \cos(\omega_e t + \alpha) & 0 \\ 0 & 0 & 1 \end{bmatrix}, \quad (32)$$

where t is time scalar and α is an initial phase between the x -axis of the ECEF and EIC coordinates at $t = 0$.

3.1 Leader reference

For the leader spacecraft we start by defining a target pointing vector in inertial coordinates as

$$\mathbf{l}_{ld} = \mathbf{r}_t - \mathbf{r}_l, \quad (33)$$

which is used to construct a leader desired frame called \mathcal{F}^{ld} as

$$\mathbf{x}_{ld} = -\frac{\mathbf{l}_{ld}}{\|\mathbf{l}_{ld}\|}, \quad \mathbf{y}_{ld} = \frac{\mathbf{S}(\mathbf{x}_{ld})(-\mathbf{h}_l)}{\|\mathbf{S}(\mathbf{x}_{ld})(-\mathbf{h}_l)\|} \quad \text{and} \quad \mathbf{z}_{ld} = \mathbf{S}(\mathbf{x}_{ld})\mathbf{y}_{ld}, \quad (34)$$

and thus we can obtain a desired quaternion vector by transforming the constructed rotation matrix and require continuity of solution to ensure a smooth vector over time. By differentiating (33) twice we obtain

$$\dot{\mathbf{l}}_{ld} = \dot{\mathbf{r}}_t - \dot{\mathbf{r}}_l, \quad (35)$$

$$\ddot{\mathbf{l}}_{ld} = \ddot{\mathbf{r}}_t - \ddot{\mathbf{r}}_l, \quad (36)$$

where

$$\dot{\mathbf{r}}_t = \mathbf{S}(\boldsymbol{\omega}_{i,e}^i)\mathbf{R}_e^i\dot{\mathbf{r}}_t^e, \quad (37)$$

$$\ddot{\mathbf{r}}_t = \mathbf{S}^2(\boldsymbol{\omega}_{i,e}^i)\mathbf{R}_e^i\ddot{\mathbf{r}}_t^e, \quad (38)$$

and $\boldsymbol{\omega}_{i,e}^i = [0, 0, \omega_e]^T$. According to (Wertz, 1978) the relationship between the desired angular velocity and the normalized target vector is

$$\dot{\boldsymbol{\ell}}_{ld} = \mathbf{S}(\boldsymbol{\omega}_{i,ld}^i)\boldsymbol{\ell}_{ld}, \quad (39)$$

where

$$\boldsymbol{\ell}_{ld} = \mathbf{l}_{ld} / \|\mathbf{l}_{ld}\|. \quad (40)$$

Equ. (39) is linearly dependent, thus the desired angular velocity is not uniquely specified. On component form (39) is written as

$$\dot{\ell}_{ldx} = -\omega_{ldz}\ell_{ldy} + \omega_{ldy}\ell_{ldz}, \quad (41a)$$

$$\dot{\ell}_{ldy} = \omega_{ldz}\ell_{ldx} - \omega_{ldx}\ell_{ldz}, \quad (41b)$$

$$\dot{\ell}_{ldz} = -\omega_{ldy}\ell_{ldx} + \omega_{ldx}\ell_{ldy}, \quad (41c)$$

where $\boldsymbol{\omega}_{i,ld}^i = [\omega_{ldx}, \omega_{ldy}, \omega_{ldz}]^T$ and $\boldsymbol{\ell}_{ld} = [\ell_{ldx}, \ell_{ldy}, \ell_{ldz}]^T$. This particular problem was solved in (Chen et al., 2000) by adding a cost constraint to minimize the amplitude of $\boldsymbol{\omega}_{i,ld}^i$ such as

$$J = \frac{1}{2}k\boldsymbol{\omega}_{i,ld}^{i,\top}\boldsymbol{\omega}_{i,ld}^i, \quad (42)$$

where k is a positive cost scalar. We then define a Hamiltonian function based on (41b) and (41c) leading to

$$\mathcal{H} = \frac{1}{2}k\boldsymbol{\omega}_{i,ld}^{i,\top}\boldsymbol{\omega}_{i,ld}^i + \lambda_1(\dot{\ell}_{ldy} - \omega_{ldz}\ell_{ldx} + \omega_{ldx}\ell_{ldz}) + \lambda_2(\dot{\ell}_{ldz} - \omega_{ldy}\ell_{ldx} + \omega_{ldx}\ell_{ldy}), \quad (43)$$

where λ_1, λ_2 are constant adjoint scalars. By differentiating (43) with respect to $\boldsymbol{\omega}_{i,ld}^i$ and setting the result to zero, we obtain

$$k\omega_{ldx} + \lambda_1 \ell_{ldz} - \lambda_2 \ell_{ldy} = 0, \quad (44a)$$

$$k\omega_{ldy} + \lambda_2 \ell_{ldx} = 0, \quad (44b)$$

$$k\omega_{ldz} - \lambda_1 \ell_{ldx} = 0. \quad (44c)$$

By inserting (44b) and (44c) into (44a) we obtain the relation

$$\boldsymbol{\omega}_{i,ld}^i \cdot \boldsymbol{\ell}_{ld} = 0, \quad (45)$$

which implies that the desired angular velocity will be orthogonal to the desired tracking direction. By solving (39) and (45) for the angular velocity, we obtain

$$\boldsymbol{\omega}_{i,ld}^i = \mathbf{S}(\boldsymbol{\ell}_{ld}) \dot{\boldsymbol{\ell}}_{ld}, \quad (46)$$

which is a solution resulting in no rotation about the desired pointing direction during tracking maneuvers. By inserting (40) and its differentiated into (46), it can be shown that

$$\boldsymbol{\omega}_{i,ld}^i = \frac{\mathbf{S}(\mathbf{1}_{ld}) \dot{\mathbf{1}}_{ld}}{\|\mathbf{1}_{ld}\|^2}. \quad (47)$$

To obtain the desired angular acceleration we differentiate (47), which leads to the expression

$$\dot{\boldsymbol{\omega}}_{i,ld}^i = \frac{\mathbf{S}(\mathbf{1}_{ld}) \ddot{\mathbf{1}}_{ld} \|\mathbf{1}_{ld}\|^2 - 2\mathbf{1}_{ld}^\top \mathbf{S}(\mathbf{1}_{ld}) \dot{\mathbf{1}}_{ld}}{\|\mathbf{1}_{ld}\|^2}. \quad (48)$$

Since the leader body frame is utilized in the dynamic equations (21), we simply rotate (47) and (48), obtaining

$$\boldsymbol{\omega}_{i,ld}^{lb} = \mathbf{R}_i^{lb} \boldsymbol{\omega}_{i,ld}^i, \quad (49)$$

$$\dot{\boldsymbol{\omega}}_{i,ld}^{lb} = -\mathbf{S}(\boldsymbol{\omega}_{i,ld}^{lb}) \mathbf{R}_i^{lb} \boldsymbol{\omega}_{i,ld}^i + \mathbf{R}_i^{lb} \dot{\boldsymbol{\omega}}_{i,ld}^i. \quad (50)$$

3.2 Follower reference

The procedure to generate a follower reference is similar to the one presented in Section 3.1. We start by defining a target pointing vector in the inertial frame as

$$\mathbf{1}_{fd} = \mathbf{r}_t - \mathbf{r}_l - \mathbf{R}_{l_0}^i \mathbf{p}, \quad (51)$$

which is used to construct a follower desired reference frame called \mathcal{F}^{fd} as

$$\mathbf{x}_{fd} = -\frac{\mathbf{1}_{fd}}{\|\mathbf{1}_{fd}\|}, \quad \mathbf{y}_{fd} = \frac{\mathbf{S}(\mathbf{x}_{fd})(-\mathbf{h}_l)}{\|\mathbf{S}(\mathbf{x}_{fd})(-\mathbf{h}_l)\|} \quad \text{and} \quad \mathbf{z}_{fd} = \mathbf{S}(\mathbf{x}_{fd}) \mathbf{y}_{fd}. \quad (52)$$

We can now construct a rotation matrix between \mathcal{F}^{fd} and \mathcal{F}^i , and because the relative rotation is between \mathcal{F}^{fb} and \mathcal{F}^{lb} we apply composite rotation, thus obtaining

$$\mathbf{R}_{fd}^{lb} = \mathbf{R}_i^{lb} \mathbf{R}_{fd}^i, \quad (53)$$

and transform the rotation matrix (53) to desired quaternion. By differentiating (51) twice, we obtain

$$\dot{\mathbf{1}}_{fd} = \dot{\mathbf{r}}_t - \dot{\mathbf{r}}_l - \mathbf{S}(\boldsymbol{\omega}_{i,lo}^i) \mathbf{R}_{lo}^i \mathbf{p} - \mathbf{R}_{lo}^i \dot{\mathbf{p}}, \quad (54)$$

$$\ddot{\mathbf{1}}_{fd} = \ddot{\mathbf{r}}_t - \ddot{\mathbf{r}}_l - (\mathbf{S}(\dot{\boldsymbol{\omega}}_{i,lo}^i) + \mathbf{S}^2(\boldsymbol{\omega}_{i,lo}^i)) \mathbf{R}_{lo}^i \mathbf{p} - 2\mathbf{S}(\boldsymbol{\omega}_{i,lo}^i) \mathbf{R}_{lo}^i \dot{\mathbf{p}} - \mathbf{R}_{lo}^i \ddot{\mathbf{p}}. \quad (55)$$

The same optimization technique as presented in Section 3.1 can then be applied, leading to

$$\boldsymbol{\omega}_{i,fd}^i = \frac{\mathbf{S}(\mathbf{1}_{fd}) \dot{\mathbf{1}}_{fd}}{\|\mathbf{1}_{fd}\|^2}, \quad (56)$$

$$\dot{\boldsymbol{\omega}}_{i,fd}^i = \frac{\mathbf{S}(\mathbf{1}_{fd}) \ddot{\mathbf{1}}_{fd} \|\mathbf{1}_{fd}\|^2 - 2\mathbf{1}_{fd}^\top \mathbf{S}(\mathbf{1}_{fd}) \dot{\mathbf{1}}_{fd}}{\|\mathbf{1}_{fd}\|^2}. \quad (57)$$

The desired angular rotation and acceleration vectors have to be transformed according to the relative dynamics of (24), resulting in

$$\boldsymbol{\omega}_{lb,fd}^{fb} = \mathbf{R}_i^{fb} \boldsymbol{\omega}_{i,fd}^i - \mathbf{R}_{lb}^{fb} \boldsymbol{\omega}_{i,lb}^{lb}, \quad (58)$$

$$\dot{\boldsymbol{\omega}}_{lb,fd}^{fb} = -\mathbf{S}(\boldsymbol{\omega}_{i,fb}^{fb}) \mathbf{R}_i^{fb} \boldsymbol{\omega}_{i,fd}^i + \mathbf{R}_i^{fb} \dot{\boldsymbol{\omega}}_{i,fd}^i + \mathbf{S}(\boldsymbol{\omega}_{lb,fb}^{fb}) \mathbf{R}_{lb}^{fb} \boldsymbol{\omega}_{i,lb}^{lb} - \mathbf{R}_{lb}^{fb} \dot{\boldsymbol{\omega}}_{i,lb}^{lb}. \quad (59)$$

4. Controller design

In this section we present a control law for relative translation and switching control laws for attitude control of the leader spacecraft and relative attitude control for the follower spacecraft. All controllers are reminiscent of the so-called Slotine and Li controller for robot manipulators –*cf.* (Slotine & Li, 1987). For all control laws it is assumed that all disturbances are unknown but upper bounded.

4.1 Translational control

We assume that disturbances for both the leader and follower spacecraft are unknown but bounded such that $\|\mathbf{f}_{ld}\| \leq \alpha_{ld}$ and $\|\mathbf{f}_{fd}\| \leq \alpha_{fd}$. In addition we also assume that control force of the leader spacecraft is upper bounded such that $\|\mathbf{f}_{la}\| \leq \alpha_{la}$. Reference trajectories are defined as

$$\dot{\mathbf{p}}_r = \dot{\mathbf{p}}_d - \gamma \tilde{\mathbf{p}}, \quad \ddot{\mathbf{p}}_r = \ddot{\mathbf{p}}_d - \gamma \dot{\tilde{\mathbf{p}}}, \quad (60)$$

where \mathbf{p}_d is the desired position, $\gamma > 0$ is a constant gain, and $\tilde{\mathbf{p}} = \mathbf{p} - \mathbf{p}_d$ is the position error. The reference vector $\dot{\mathbf{p}}_r$ represent a notational manipulation that allows translation of energy-related properties expressed in terms of the actual velocity vector $\dot{\mathbf{p}}$ into trajectory control properties expressed in terms of the virtual velocity error vector \mathbf{s} . This is performed by shifting the desired velocities $\dot{\mathbf{p}}_d$ according to the position error $\tilde{\mathbf{p}}$ (*cf.* (Slotine & Li, 1987; Berghuis & Nijmeijer, 1993)). The sliding surface is defined as

$$\mathbf{s} = \dot{\mathbf{p}} - \dot{\mathbf{p}}_r = \dot{\tilde{\mathbf{p}}} + \gamma \tilde{\mathbf{p}}. \quad (61)$$

A model based control law is derived based on (15) as

$$\mathbf{f}_{fa} = m_f \ddot{\mathbf{p}}_r + \mathbf{C}_t(\boldsymbol{\omega}_{i,l}^l) \dot{\mathbf{p}}_r + \mathbf{D}_t(\boldsymbol{\omega}_{i,l}^l, \boldsymbol{\omega}_{i,l}^l, r_f) \mathbf{p} + \mathbf{n}_t(\mathbf{r}_l, r_f) - \mathbf{K}_p \tilde{\mathbf{p}} - \mathbf{K}_d \mathbf{s} \quad (62)$$

where \mathbf{K}_p and \mathbf{K}_d are both symmetric positive definite constant matrices such that $\mathbf{K}_p = \mathbf{K}_p^\top > 0$ and $\mathbf{K}_d = \mathbf{K}_d^\top > 0$. By inserting (62) and (61) into (15), the closed-loop dynamics may be written as

$$m_f \dot{\mathbf{s}} + (\mathbf{C}_t + \mathbf{K}_d) \mathbf{s} + \mathbf{K}_p \tilde{\mathbf{p}} - \mathbf{f}_{fd} + \frac{m_f}{m_l} (\mathbf{f}_{ld} + \mathbf{f}_{la}) = \mathbf{0}. \quad (63)$$

A suitable Lyapunov Function Candidate (LFC) is chosen as

$$V_t = \frac{1}{2} \mathbf{s}^\top m_f \mathbf{s} + \frac{1}{2} \tilde{\mathbf{p}}^\top \mathbf{K}_p \tilde{\mathbf{p}} > 0 \quad \forall \mathbf{s} \neq \mathbf{0}, \tilde{\mathbf{p}} \neq \mathbf{0}, \quad (64)$$

and by differentiation and insertion of (63), we obtain

$$\dot{V}_t = -\mathbf{s}^\top \mathbf{C}_t \mathbf{s} - \mathbf{s}^\top \mathbf{K}_p \tilde{\mathbf{p}} - \mathbf{s}^\top \mathbf{K}_d \mathbf{s} + \tilde{\mathbf{p}}^\top \mathbf{K}_p \dot{\tilde{\mathbf{p}}} + \mathbf{s}^\top \left(\mathbf{f}_{fd} - \frac{m_f}{m_l} (\mathbf{f}_{ld} + \mathbf{f}_{la}) \right). \quad (65)$$

Using the fact that $\mathbf{C}_t(\boldsymbol{\omega}_{i,l}^l)$ is skew-symmetric, we further obtain

$$\dot{V}_t = -(\mathbf{s}^\top - \dot{\tilde{\mathbf{p}}}^\top) \mathbf{K}_p \tilde{\mathbf{p}} - \mathbf{s}^\top \mathbf{K}_d \mathbf{s} + \mathbf{s}^\top \left(\mathbf{f}_{fd} - \frac{m_f}{m_l} (\mathbf{f}_{ld} + \mathbf{f}_{la}) \right) \quad (66)$$

$$= -\mathbf{x}_t^\top \mathbf{P} \mathbf{x}_t + \mathbf{s}^\top \left(\mathbf{f}_{fd} - \frac{m_f}{m_l} (\mathbf{f}_{ld} + \mathbf{f}_{la}) \right) \quad (67)$$

$$\leq -p_m \|\mathbf{x}_t\|^2 + \left(\alpha_{fd} + \frac{m_f}{m_l} (\alpha_{ld} + \alpha_{la}) \right) \|\mathbf{x}_t\| \quad (68)$$

where $\mathbf{x}_t = [\mathbf{s}^\top, \tilde{\mathbf{p}}^\top]^\top$, $\mathbf{P} = \text{diag}\{\mathbf{K}_d, \gamma \mathbf{K}_p\}$ and $p_m > 0$ is the smallest eigenvalue of \mathbf{P} . Thus $\dot{V}_t < 0$ when $\|\mathbf{x}_t\| > \delta_t = [\alpha_{fd} + (\alpha_{ld} + \alpha_{la} m_f / m_l)] / p_m$ and δ_t can be diminished by increasing p_m which is done by increasing the controller gains, and we can conclude that equilibrium point of the closed-loop system is Uniformly Globally Practically Exponentially Stable (UGPES) (cf. (Grøtli, 2010)).

Remark 1. *If some of the unknown forces are assumed to be known, they can be removed by the control law thus putting less constraint on the controller gains.*

Remark 2. *We would also like to remark that even if we state global stability, this is not precise since when $\mathbf{R}_l^i \mathbf{p} = -\mathbf{r}_l$, which means that the follower is located at the center of the orbit, there is a singularity in (15) and according to (Hahn, 1967) the adjective global pertains to the case and only to the case when the state space is \mathbb{R}^n .*

4.2 Rotational control

For attitude control, the system's solutions are defined using Teel's framework (cf. (Goebel et al., 2009)) for hybrid systems and incorporates a switching law with hysteresis to cope with the well known problem of dual equilibrium points when working with quaternion attitude representation. We assume that disturbances for both the leader and follower spacecraft are unknown but bounded such that $\|\boldsymbol{\tau}_{ld}^{lb}\| \leq \beta_{ld}$ and $\|\boldsymbol{\tau}_{fd}\| \leq \beta_{fd}$. The leader-follower dynamical system is looked upon as a cascaded system on the form

$$\Sigma_1 : \dot{x}_1 = f_1(t, x_1) + g(t, x) \quad (69)$$

$$\Sigma_2 : \dot{x}_2 = f_2(t, x_2), \quad (70)$$

where $x_1 \in \mathbb{R}^n$, $x_2 \in \mathbb{R}^m$, $x = [x_1^\top, x_2^\top]^\top$ and the functions $f_1(\cdot, \cdot)$, $f_2(\cdot, \cdot)$ and $g(\cdot, \cdot)$ are continuous in their arguments, locally Lipschitz in x , uniformly in t , and $f_1(\cdot, \cdot)$ is continuously differentiable in both arguments. Equation (70) is said to be the *driving* system,

$$\dot{x}_1 = f_1(t, x_1) \quad (71)$$

is said to be the *driven* system, while the *interconnection* is the term $g(t, x)$. In our case the leader spacecraft is the driving system while the follower spacecraft represents the driven system.

The spacecraft error quaternion $\tilde{\mathbf{q}}_s = [\tilde{\eta}_s, \tilde{\boldsymbol{\epsilon}}_s^\top]^\top$ is given by the quaternion product (cf. (7))

$$\tilde{\mathbf{q}}_s = \mathbf{q}_s \otimes \bar{\mathbf{q}}_{sd} = \begin{bmatrix} \eta_s \eta_{sd} + \boldsymbol{\epsilon}_s^\top \boldsymbol{\epsilon}_{sd}^\top \\ \eta_{sd} \boldsymbol{\epsilon}_s - \eta_s \boldsymbol{\epsilon}_{sd} - \mathbf{S}(\boldsymbol{\epsilon}_s) \boldsymbol{\epsilon}_{sd} \end{bmatrix}, \quad (72)$$

and the error kinematics may be presented analogous to (9) as

$$\dot{\tilde{\mathbf{q}}}_s = \mathbf{T}_{se}(\tilde{\mathbf{q}}_s) \mathbf{e}_{s\omega}, \quad (73)$$

where

$$\mathbf{e}_{l\omega} = \boldsymbol{\omega}_{i,lb}^{lb} - \boldsymbol{\omega}_{i,ld}^{lb}, \quad \mathbf{e}_{f\omega} = \boldsymbol{\omega}_{lb,fb}^{fb} - \boldsymbol{\omega}_{lb,fd}^{fb}. \quad (74)$$

We perform coordinate transformation of the attitude error such that $\mathbf{e}_{sq} = [1 - h_s \tilde{\eta}_s, \tilde{\boldsymbol{\epsilon}}_s^\top]^\top$ which satisfies the kinematic equation

$$\dot{\mathbf{e}}_{sq} = \mathbf{T}_{se}^\top(\mathbf{e}_{sq}) \mathbf{e}_{s\omega}, \quad (75)$$

where

$$\mathbf{T}_{se}^\top(\mathbf{e}_{sq}) = \begin{bmatrix} h_s \tilde{\boldsymbol{\epsilon}}_s^\top \\ \tilde{\eta}_s \mathbf{I} + \mathbf{S}(\tilde{\boldsymbol{\epsilon}}_s) \end{bmatrix}, \quad (76)$$

and the *state* variables $h_s \in H = \{-1, 1\}$ determines the choice of goal equilibrium point.

4.2.1 Control of leader

The controller is given by

$$\boldsymbol{\tau}_{la}^{lb} = \mathbf{J}_l \dot{\boldsymbol{\omega}}_{lr} - \mathbf{S}(\mathbf{J}_l \boldsymbol{\omega}_{i,lb}^{lb}) \boldsymbol{\omega}_{lr} - k_{lq} \mathbf{T}_{le}^\top \mathbf{e}_{lq} - k_{l\omega} \mathbf{s}_l, \quad (77a)$$

$$\boldsymbol{\omega}_{lr} = \boldsymbol{\omega}_{i,ld}^{lb} - \gamma_l \mathbf{T}_{le}^\top(\mathbf{e}_{lq}) \mathbf{e}_{lq}, \quad (77b)$$

$$\mathbf{s}_l = \boldsymbol{\omega}_{i,lb}^{lb} - \boldsymbol{\omega}_{lr} = \mathbf{e}_{l\omega} + \gamma_l \mathbf{T}_{le}^\top(\mathbf{e}_{lq}) \mathbf{e}_{lq}. \quad (77c)$$

where $k_{lq} > 0$, $k_{l\omega} > 0$ and $\gamma_l > 0$ are constant feedback gains. Next, let $\mathbf{x}_2 = [\mathbf{e}_{lq}^\top, \mathbf{e}_{l\omega}^\top, h_l]^\top$, and for a given hysteresis margin $\sigma_l > 0$ define the flow and jump sets, respectively as

$$C_l = \{(\mathbf{e}_{lq}, \mathbf{e}_{l\omega}, h_l) : h_l(k_{lq} \tilde{\eta}_l - \frac{1}{4} \gamma_l \tilde{\boldsymbol{\epsilon}}_l^\top \mathbf{J}_l \mathbf{e}_{l\omega}) \geq -\sigma_l\}, \quad (78a)$$

$$D_l = \{(\mathbf{e}_{lq}, \mathbf{e}_{l\omega}, h_l) : h_l(k_{lq} \tilde{\eta}_l - \frac{1}{4} \gamma_l \tilde{\boldsymbol{\epsilon}}_l^\top \mathbf{J}_l \mathbf{e}_{l\omega}) \leq -\sigma_l\}. \quad (78b)$$

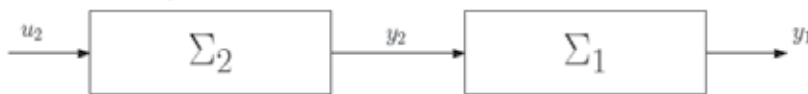


Fig. 2. Cascade interconnection of two dynamical systems.

Then, the switching law is defined by

$$\dot{h}_l = 0 \quad \mathbf{x}_2 \in C_l \quad (79a)$$

$$\mathbf{x}_2^+ = G_l(\mathbf{x}_2) = [\mathbf{e}_{lq}^\top, \mathbf{e}_{l\omega}^\top, -h_l]^\top \quad \mathbf{x}_2 \in D_l. \quad (79b)$$

We have the following.

Proposition 1. Consider the system defined by (21) and (75)–(76) in closed-loop with the hybrid controller (77)–(79). Then, the set

$$A_l = \{(\mathbf{e}_{lq}, \mathbf{e}_{l\omega}, h_l) : (\mathbf{e}_{lq}, \mathbf{e}_{l\omega}) \in \mathcal{B}_{\delta_l}\} \quad (80)$$

where $\mathcal{B}_{\delta_l} = \{\mathbf{x}^n \in \mathbb{R}^n : \|\mathbf{x}\| \leq \delta_l\}$ and δ_l is to be defined, is Uniformly Asymptotically Stable (UAS) in the large on the set $\mathcal{S}^3 \times \mathbb{R}^3$. That is, the equilibrium point $(\mathbf{e}_{lq}, \mathbf{e}_{l\omega}) = (\mathbf{0}, \mathbf{0})$ of the closed-loop system is Uniformly Practically Asymptotically Stable (UPAS) for all initial conditions in $\mathcal{S}^3 \times \mathbb{R}^3$.

Proof: Define the LFC as

$$V_l(\mathbf{x}_2) = \frac{1}{2}(\mathbf{s}_l^\top \mathbf{J}_l \mathbf{s}_l + \mathbf{e}_{lq}^\top k_{lq} \mathbf{e}_{lq}) > 0 \quad \forall \mathbf{s}_l \neq \mathbf{0}, \mathbf{e}_{lq} \neq \mathbf{0}. \quad (81)$$

Its total time derivative along the trajectories of the closed-loop system (21), (75)–(76) with the controller (77) and the switching law (79) yields

$$\begin{aligned} \dot{V}_l(\mathbf{x}_2) = & \mathbf{s}_l^\top \mathbf{S}(\mathbf{J}_l \boldsymbol{\omega}_{i,lb}^{lb}) \mathbf{s}_l - \mathbf{s}_l^\top k_{l\omega} \mathbf{s}_l - \mathbf{s}_l^\top k_{lq} \mathbf{T}_{le}^\top \mathbf{e}_{lq} \\ & + \mathbf{e}_{lq}^\top k_{lq} \mathbf{T}_{le} \mathbf{s}_l - \mathbf{e}_{lq}^\top k_{lq} \mathbf{T}_{le} \gamma_l \mathbf{T}_{le}^\top \mathbf{e}_{lq} + \mathbf{s}_l^\top \boldsymbol{\tau}_{ld}^{lb} \end{aligned} \quad (82)$$

and by inserting (77c) and applying the fact that $\mathbf{S}(\mathbf{J}_l \boldsymbol{\omega}_{i,lb}^{lb})$ is skew-symmetric, we obtain

$$\dot{V}_l = -\boldsymbol{\chi}_2^\top \mathbf{Q}_l \boldsymbol{\chi}_2 + (\mathbf{e}_{l\omega} + \gamma_l \mathbf{T}_{le}^\top \mathbf{e}_{lq})^\top \boldsymbol{\tau}_{ld}^{lb}, \quad (83)$$

where

$$\mathbf{Q}_l = \begin{bmatrix} \gamma_l \mathbf{T}_{le} \mathbf{T}_{le}^\top (k_{lq} + \gamma_l k_{l\omega}) & \gamma_l k_{l\omega} \mathbf{T}_{le} \\ \gamma_l k_{l\omega} \mathbf{T}_{le}^\top & k_{l\omega} \mathbf{I} \end{bmatrix} = [\mathbf{q}_{ij}], \quad i, j = 1, 2, \quad (84)$$

and $\boldsymbol{\chi}_2 = [\mathbf{e}_{lq}^\top, \mathbf{e}_{l\omega}^\top]^\top$. According to (Horn & Johnson, 1985) \mathbf{Q}_l is positive definite if

$$\mathbf{q}_{22} = k_{l\omega} \mathbf{I} \succ \mathbf{q}_{21} \mathbf{q}_{11}^{-1} \mathbf{q}_{12} = k_{l\omega}^2 \gamma_l^2 \mathbf{T}_{le}^\top \left(\gamma_l \mathbf{T}_{le} \mathbf{T}_{le}^\top (k_{lq} + \gamma_l k_{l\omega}) \right)^{-1} \mathbf{T}_{le} \quad (85)$$

$$= \frac{k_{l\omega}^2 \gamma_l}{k_{lq} + \gamma_l k_{l\omega}} \mathbf{I} \quad (86)$$

$$k_{lq} + \gamma_l k_{l\omega} > k_{l\omega} \gamma_l \rightarrow k_{lq} > 0, \quad (87)$$

with the additional conservative condition that $k_{l\omega} \geq k_{lq}$, thus yielding

$$\dot{V}_l \leq -q_{lm} \|\boldsymbol{\chi}_2\|^2 + \beta_{ld} \left(1 + \frac{\gamma_l}{2}\right) \|\boldsymbol{\chi}_2\|, \quad (88)$$

and $q_{lm} > 0$ is the smallest eigenvalue of \mathbf{Q}_l . Thus $\dot{V}_l < 0$ when $\|\boldsymbol{\chi}_2\| > \delta_l = \beta_{ld}(1 + \gamma_l/2)/q_{lm}$ and δ_l can be diminished by increasing q_{lm} which is done by increasing the controller gains. The change in V_l during jumps is expressed as

$$V_l(G_l(\mathbf{x}_2)) - V_l(\mathbf{x}_2) = 2h_l(k_{lq} \tilde{\eta}_l - \frac{1}{4} \gamma_l \tilde{\mathbf{e}}_l^\top \mathbf{J}_l \mathbf{e}_{l\omega}), \quad (89)$$

and by defining the flow and jump sets as in (78) we ensure that $V_l(G_l(\mathbf{x}_2)) - V_l(\mathbf{x}_2) < -2\sigma_l$ when $\mathbf{x}_2 \in D_l$, thus V_l is strictly decreasing over jumps, and then

$$\dot{V}_l(\mathbf{x}_2) \leq 0 \quad \forall \mathbf{x}_2 \in C_l / \mathcal{B}_{\delta_l}, \quad (90a)$$

$$V_l(G_l(\mathbf{x}_2)) - V_l(\mathbf{x}_2) < 0 \quad \forall \mathbf{x}_2 \in D_l. \quad (90b)$$

Since the projection $\text{Proj}_{\mathcal{S}^3 \times \mathbb{R}^3} \mathcal{A}_l = \{(\mathbf{e}_{lq}, \mathbf{e}_{l\omega}, h_l) : (\mathbf{e}_{lq}, \mathbf{e}_{l\omega}) \in \mathcal{B}_{\delta_l}\}$, according to (Sanfelice et al., 2007) renders the set \mathcal{A}_l UAS with the basin of attraction $\mathcal{B}_{\mathcal{A}_l} = C_l \cup D_l$, thus UPAS in the large on the set $\mathcal{S}^3 \times \mathbb{R}^3$ of the equilibrium point $(\mathbf{e}_{lq}, \mathbf{e}_{l\omega}) = (\mathbf{0}, \mathbf{0})$ of the closed-loop system follows. \square

Proposition 2. *The interconnection term between the leader and follower spacecraft in (26), denoted as*

$$g(t, \mathbf{x}) = -\mathbf{J}_f \mathbf{R}_{lb}^{fb} \mathbf{J}_l^{-1} (\boldsymbol{\tau}_{ld}^{lb} + \boldsymbol{\tau}_{la}^{lb}), \quad (91)$$

is uniformly bounded.

Proof: Since V_l is positive definite and proper for $\|\boldsymbol{\chi}_2\| > \delta_l$ we obtain that $\|\boldsymbol{\chi}_2\|$ is bounded that is, for any $r > 0$ there exists $\Delta(r) > 0$ such that $\sup_{t \geq t_0} \|\boldsymbol{\chi}_2(t)\| \leq \Delta$ for all initial conditions $\|\boldsymbol{\chi}_2(t_0)\| < r$, $t_0 \geq 0$. Both $\|\boldsymbol{\omega}_{i,ld}^{lb}\| \leq \beta_{\boldsymbol{\omega}_{i,ld}^{lb}}$ and $\|\dot{\boldsymbol{\omega}}_{i,ld}^{lb}\| \leq \beta_{\dot{\boldsymbol{\omega}}_{i,ld}^{lb}}$, derived in Section 3 are continuous and bounded functions for some positive constants $\beta_{\boldsymbol{\omega}_{i,ld}^{lb}}$ and $\beta_{\dot{\boldsymbol{\omega}}_{i,ld}^{lb}}$. Thus it follows from (74) that $\|\boldsymbol{\omega}_{i,lb}^{lb}\| \leq \beta_{\boldsymbol{\omega}_{i,lb}^{lb}}$ is bounded by a positive constant $\beta_{\boldsymbol{\omega}_{i,lb}^{lb}}$ for all $t \geq t_0 \geq 0$. The derivative of (77b) can be denoted as

$$\dot{\boldsymbol{\omega}}_{lr} = \dot{\boldsymbol{\omega}}_{i,ld}^{lb} - \gamma_l (\mathbf{T}_{le}^\top \mathbf{e}_{lq} + \mathbf{T}_{le}^\top \dot{\mathbf{e}}_{lq}), \quad (92)$$

where

$$\mathbf{T}_{le}^\top \mathbf{e}_{lq} = \frac{1}{2} \dot{\boldsymbol{\epsilon}}_l - \mathbf{T}_{le}^\top \dot{\mathbf{e}}_{lq} = \left(\frac{1}{2} [\tilde{\eta}_l \mathbf{I} + \mathbf{S}(\frac{1}{2} \dot{\boldsymbol{\epsilon}}_l)] - \frac{1}{4} \right) \mathbf{e}_{l\omega}, \quad (93)$$

and by inserting (93) and (75) into (92) we obtain

$$\dot{\boldsymbol{\omega}}_{lr} = \dot{\boldsymbol{\omega}}_{i,ld}^{lb} - \frac{\gamma_l}{2} [\tilde{\eta}_l \mathbf{I} + \mathbf{S}(\tilde{\boldsymbol{\epsilon}}_l)] \mathbf{e}_{l\omega}. \quad (94)$$

Then by inserting (77b), (94) and (77c) into (77a) we obtain

$$\begin{aligned} \boldsymbol{\tau}_{la}^{lb} = & \mathbf{J}_l \left(\dot{\boldsymbol{\omega}}_{i,ld}^{lb} - \frac{\gamma_l}{2} [\tilde{\eta}_l \mathbf{I} + \mathbf{S}(\tilde{\boldsymbol{\epsilon}}_l)] \mathbf{e}_{l\omega} \right) \\ & - \mathbf{S}(\mathbf{J}_l \boldsymbol{\omega}_{i,lb}^{lb}) [\boldsymbol{\omega}_{i,ld}^{lb} - \gamma_l \mathbf{T}_{le}^\top \mathbf{e}_{lq}] - k_{lq} \mathbf{T}_{le}^\top \mathbf{e}_{lq} - k_{l\omega} (\mathbf{e}_{l\omega} + \gamma_l \mathbf{T}_{le}^\top \mathbf{e}_{lq}). \end{aligned} \quad (95)$$

Note that h_l is removed from the calculations since it won't have any impact on (96). Since all terms in (95) are either constant or upper bounded we have that $\|\boldsymbol{\tau}_{la}^{lb}\| \leq \beta_{la}$, where β_{la} is a positive constant, for all $t \geq t_0 \geq 0$. The interconnection term (91) can thus be written as

$$\|g(t, \mathbf{x})\| \leq j_{lm} j_{lm} (\beta_{ld} + \beta_{la}), \quad (96)$$

where $j_{lm} \leq \|\mathbf{J}_l\| \leq j_{lM}$, and we conclude that the interconnection term is uniformly bounded. \square

4.2.2 Control of leader-follower formation

This section follows the line of Section 4.2.1 but we now talk of relative attitude and stress the point that the relative rotation and angular velocity is denoted \mathbf{q}_f and $\boldsymbol{\omega}$, respectively. We define the control law as

$$\boldsymbol{\tau}_{fa}^{fb} = \mathbf{J}_f \dot{\boldsymbol{\omega}}_{fr} + \mathbf{C}_r(\boldsymbol{\omega}) \boldsymbol{\omega}_{fr} + \mathbf{n}_r(\boldsymbol{\omega}) - k_{fq} \mathbf{T}_{fe}^\top(\mathbf{e}_{fq}) \mathbf{e}_{fq} - k_{f\omega} \mathbf{s}_f, \quad (97a)$$

$$\boldsymbol{\omega}_{fr} = \boldsymbol{\omega}_{lb,fd}^{fb} - \gamma_f \mathbf{T}_{fe}^\top(\mathbf{e}_{fq}) \mathbf{e}_{fq}, \quad (97b)$$

$$\mathbf{s}_f = \boldsymbol{\omega}_{lb,fb}^{fb} - \boldsymbol{\omega}_{fr} = \mathbf{e}_{f\omega} + \gamma_f \mathbf{T}_{fe}^\top(\mathbf{e}_{fq}) \mathbf{e}_{fq}. \quad (97c)$$

where $k_{fq} > 0$, $k_{f\omega} > 0$ and $\gamma_f > 0$ are constant gains. Next, let $\mathbf{x}_1 = [\mathbf{e}_{fq}^\top, \mathbf{e}_{f\omega}^\top, h_f]^\top$ and, for a given hysteresis margin $\sigma_f > 0$ define the flow and jump sets, respectively as

$$C_f = \{(\mathbf{e}_{fq}, \mathbf{e}_{f\omega}, h_f) : h_f(k_{fq} \tilde{\eta}_f - \frac{1}{4} \gamma_f \tilde{\mathbf{e}}_f^\top \mathbf{J}_f \mathbf{e}_{f\omega}) \geq -\sigma_f\}, \quad (98a)$$

$$D_f = \{(\mathbf{e}_{fq}, \mathbf{e}_{f\omega}, h_f) : h_f(k_{fq} \tilde{\eta}_f - \frac{1}{4} \gamma_f \tilde{\mathbf{e}}_f^\top \mathbf{J}_f \mathbf{e}_{f\omega}) \leq -\sigma_f\}. \quad (98b)$$

Then, the switching law is defined by

$$\dot{h}_f = 0 \quad \mathbf{x}_1 \in C_f, \quad (99a)$$

$$\mathbf{x}_1^+ = G_f(\mathbf{x}_1) = [\mathbf{e}_{fq}^\top, \mathbf{e}_{f\omega}^\top, -h_f]^\top \quad \mathbf{x}_1 \in D_f. \quad (99b)$$

We have the following.

Proposition 3. Consider the system defined by (27) and (75)–(76) in closed-loop with the hybrid controller (97)–(99). Then, the set

$$\mathcal{A}_f = \{(\mathbf{e}_{fq}, \mathbf{e}_{f\omega}, h_f) : (\mathbf{e}_{fq}, \mathbf{e}_{f\omega}) \in \mathcal{B}_{\delta_f}\} \quad (100)$$

where $\mathcal{B}_{\delta_f} = \{\mathbf{x}^n \in \mathbb{R}^n : \|\mathbf{x}\| \leq \delta_f\}$ and δ_f is to be defined, is UAS in the large on the set $\mathcal{S}^3 \times \mathbb{R}^3$. That is, the equilibrium point $(\mathbf{e}_{fq}, \mathbf{e}_{f\omega}) = (\mathbf{0}, \mathbf{0})$ of the closed-loop system is UPAS for all initial conditions in $\mathcal{S}^3 \times \mathbb{R}^3$.

Proof: Define the LFC as

$$V_f(\mathbf{x}_1) = \frac{1}{2} (\mathbf{s}_f^\top \mathbf{J}_f \mathbf{s}_f + \mathbf{e}_{fq}^\top k_{fq} \mathbf{e}_{fq}) > 0 \quad \forall \mathbf{s}_f \neq \mathbf{0}, \mathbf{e}_{fq} \neq \mathbf{0}. \quad (101)$$

Its total time derivative along the trajectories of the closed-loop system (27), (75)–(76) with the controller (97a)–(97c) and the switching law (99) yields

$$\begin{aligned} \dot{V}_f(\mathbf{x}_1) = & \mathbf{s}_f^\top \mathbf{C}_r(\boldsymbol{\omega}) \mathbf{s}_f - \mathbf{s}_f^\top k_{f\omega} \mathbf{s}_f - \mathbf{s}_f^\top k_{fq} \mathbf{T}_{fe}^\top \mathbf{e}_{fq} + \mathbf{e}_{fq}^\top k_{fq} \mathbf{T}_{fe} \mathbf{s}_f \\ & - \mathbf{e}_{fq}^\top k_{fq} \mathbf{T}_{fe} \gamma_f \mathbf{T}_{fe}^\top \mathbf{e}_{fq} + \mathbf{s}_f^\top \left[\boldsymbol{\tau}_{fd}^{fb} - \mathbf{J}_l \mathbf{R}_{lb}^{fb} \mathbf{J}_l^{-1} (\boldsymbol{\tau}_{ld}^{lb} + \boldsymbol{\tau}_{la}^{lb}) \right] \end{aligned} \quad (102)$$

and by inserting (97c) and applying the fact that $\mathbf{C}(\boldsymbol{\omega})$ is skew-symmetric, we obtain

$$\dot{V}_f(\mathbf{x}_1) = -\boldsymbol{\chi}_1^\top \mathbf{Q}_f \boldsymbol{\chi}_1 + (\mathbf{e}_{f\omega} + \gamma_f \mathbf{T}_{fe}^\top \mathbf{e}_{fq})^\top \left[\boldsymbol{\tau}_{fd}^{fb} - \mathbf{J}_l \mathbf{R}_{lb}^{fb} \mathbf{J}_l^{-1} (\boldsymbol{\tau}_{ld}^{lb} + \boldsymbol{\tau}_{la}^{lb}) \right], \quad (103)$$

where \mathbf{Q}_f is similar to (84), and thus positive definite, and $\boldsymbol{\chi}_1 = [\mathbf{e}_{lq}^\top, \mathbf{e}_{l\omega}^\top]^\top$. Eq. (103) can now be written as

$$\dot{V}_f(\mathbf{x}_1) \leq -q_{fm} \|\boldsymbol{\chi}_1\|^2 + \beta_f \|\boldsymbol{\chi}_1\|, \quad (104)$$

where $\beta_f = \beta_{fd}(1 + \gamma_f/2) + j_{lM}j_{lm}(\beta_{ld} + \beta_{la})$ and $q_{fm} > 0$ is the smallest eigenvalue of \mathbf{Q}_f . Thus $\dot{V}_f < 0$ when $\|\boldsymbol{\chi}_1\| > \delta_f = \beta_f/q_{fm}$ and δ_f can be diminished by increasing q_{fm} which is done by increasing the controller gains. The change in V_f during jumps is expressed as

$$V_f(G_f(\mathbf{x}_1)) - V_f(\mathbf{x}_1) = 2h_f(k_{fq}\tilde{\eta}_f - \frac{1}{4}\gamma_f\tilde{\mathbf{e}}_f^\top \mathbf{J}_f \mathbf{e}_{f\omega}), \quad (105)$$

and by defining the flow and jump sets as in (98) we ensure that $V_f(G_f(\mathbf{x}_1)) - V_f(\mathbf{x}_2) < -2\sigma_f$ when $\mathbf{x}_1 \in D_f$, thus V_f is strictly decreasing over jumps, and then

$$\dot{V}_f(\mathbf{x}_1) \leq 0 \quad \forall \mathbf{x}_1 \in C_f/\mathcal{B}_{\delta_f}, \quad (106a)$$

$$V_f(G_f(\mathbf{x}_1)) - V_f(\mathbf{x}_1) < 0 \quad \forall \mathbf{x}_1 \in D_f. \quad (106b)$$

Thus we conclude that the set \mathcal{A}_f is UAS with the basin of attraction $\mathcal{B}_{\mathcal{A}_f} = C_f \cup D_f$, and UPAS in the large on the set $\mathcal{S}^3 \times \mathbb{R}^3$ of the equilibrium points $(\mathbf{e}_{\pm fq}, \mathbf{e}_{f\omega}) = (\mathbf{0}, \mathbf{0})$ of the closed-loop system follows. \square

It follows that since both the equilibrium point of the *driving* system and the equilibrium point of the *driven* system are UPAS in the large on the set $\mathcal{S}^3 \times \mathbb{R}^3$ and the *interconnection* term is uniformly bounded, the equilibrium point of the closed-loop system of the total cascaded system on the form (69)–(70) is UPAS in the large on the set $\mathcal{S}^3 \times \mathbb{R}^3$ (cf. Loría & Panteley (2005)).

5. Simulation results

In this section we present simulation results where one leader and one follower spacecraft were tracking a common point on the Earth surface. The simulation was performed in Simulink using a fixed sample-time Runge-Kutta ODE4 solver, with sampling period equal to 0.1 s. The leader spacecraft was flying in an elliptic Low Earth Orbit (LEO) with perigee at 600 km, apogee at 750 km, inclination (i) at 79° and the argument of perigee (ω) and the right ascension of the ascending node (Ω) at 0° . The tracking point was located on the Earth surface at zero degrees latitude and longitude, and both spacecraft continued tracking the point even if it was outside field of view. The spacecraft moments of inertia were $\mathbf{J}_l = \mathbf{J}_f = \text{diag}\{4.350, 4.337, 3.664\}$ kgm² and spacecraft masses $m_l = m_f = 100$ kg. The initial conditions were set to $\mathbf{p}(t_0) = [0, -100, 0]^\top$ m, $\dot{\mathbf{p}}(t_0) = \ddot{\mathbf{p}}(t_0) = \mathbf{0}$, $\mathbf{q}_l(t_0) = \mathbf{q}_f(t_0) = [0.9437, 0.1277, 0.1449, -0.2685]^\top$, $\boldsymbol{\omega}_{i,lb}^{lb}(t_0) = [1.745 \quad -3.491 \quad 0.873]^\top \times 10^{-3}$ rad/s and $\boldsymbol{\omega}_{i,fb}^{fb}(t_0) = [0, 0, 0]^\top$ rad/s. The desired conditions for relative translation were set to $\mathbf{p}_d = [0, -1000, 500]^\top$ m, $\dot{\mathbf{p}}_d = \ddot{\mathbf{p}}_d = \mathbf{0}$, while the desired values for relative rotation were calculated based on the results presented in Section 3. The controller gains were set to $\mathbf{K}_p = \mathbf{K}_d = \{0.5\}\mathbf{I}$ for control of relative translation, and $k_{lq} = k_{fq} = 5$, $k_{l\omega} = k_{f\omega} = 10$ and $\gamma_l = \gamma_f = 1$ for control of relative rotation.

Since we are considering a slightly elliptic LEO, we only consider the disturbance torques which are the major contributors to these kind of orbits; namely, gravity gradient torque (Sidi, 1997), and forces and torques caused by atmospheric drag (Wertz, 1978) and J_2 effect (Montenbruck & Gill, 2001). The J_2 effect is caused by non-homogeneous mass distribution

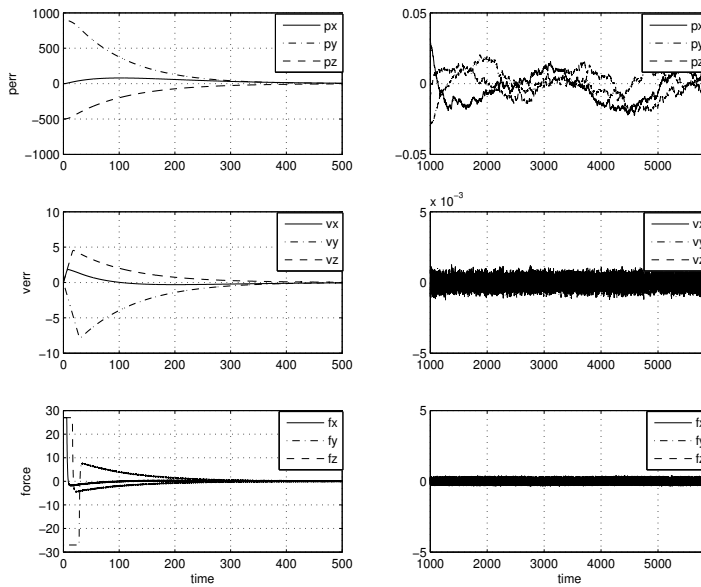


Fig. 3. Relative position error, relative velocity error and control force with uncompensated disturbances and unfiltered sensor noise.

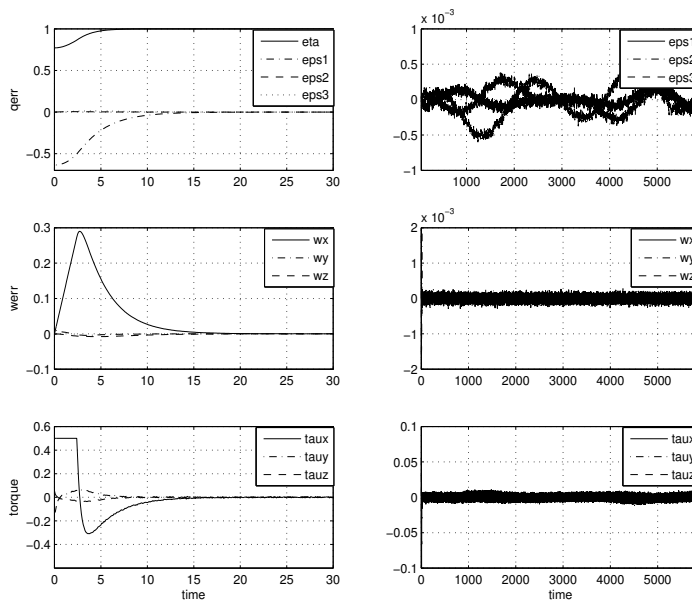


Fig. 4. Relative attitude error, relative angular velocity error and control torque with uncompensated disturbances and unfiltered sensor noise.

of a planet. The torques generated by atmospheric drag and J_2 are induced because of a 10 cm displacement of the center of mass. All disturbances were considered continuous and bounded. The noise was considered to be contained in a compact $\sigma\mathbb{B}^n = \{x \in \mathbb{R}^n : \|x\| \leq \sigma\}$ and a suitable amount were added to the measured vectors such that $\mathbf{r}_{ln} = \mathbf{r}_l + 0.01\mathbb{B}^3$, $\mathbf{p}_n = \mathbf{p} + 0.01\mathbb{B}^3$, $\mathbf{p}_{ln} = \mathbf{p}_l + 5 \times 10^{-3}\mathbb{B}^3$, $\dot{\mathbf{p}}_n = \dot{\mathbf{p}} + 5 \times 10^{-3}\mathbb{B}^3$. The measured states \mathbf{q}_{ln} and \mathbf{q}_n satisfies $\mathbf{q}_{ln} \in (\mathbf{q}_l + [0, (0.001\mathbb{B}^3)^\top]^\top) \cap \mathcal{S}^3$ and $\mathbf{q}_n \in (\mathbf{q} + [0, (0.001\mathbb{B}^3)^\top]^\top) \cap \mathcal{S}^3$, and $\boldsymbol{\omega}_{ln} = \boldsymbol{\omega}_{i,lb}^{lb} + 2 \times 10^{-3}\mathbb{B}^3$ and $\boldsymbol{\omega}_n = \boldsymbol{\omega} + 2 \times 10^{-3}\mathbb{B}^3$. The simulation time is set to one orbital period (5896 s) to show the performance of the reference generation scheme.

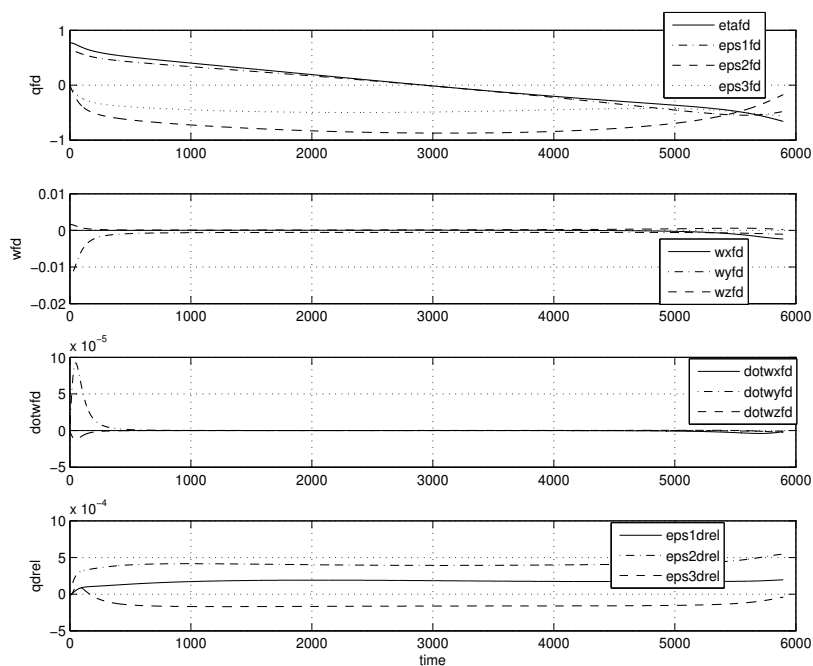


Fig. 5. Follower desired attitude, angular velocity, angular acceleration and relative desired attitude with uncompensated disturbances and unfiltered sensor noise.

Figure 3 shows the relative position, velocity and control force during both settling and station keeping phase. As can be seen the position of the follower spacecraft converged toward the desired position and was then stationed there within a few centimeters during the orbital period. Figure 4 shows the relative attitude, angular velocity and control torque during settling and station keeping phase, and results similar to the relative translation can be observed for relative rotation as well. It can further be shown that the fluctuations caused by the disturbances can be diminished by increasing the controller gains. The states are converging towards the equilibrium point and kept close during the following orbit. The three topmost plots in Figure 5 shows the desired attitude, angular velocity and angular acceleration for the leader spacecraft during one orbit. What can be seen is that there is no rotation about the x -axis during the orbital period. It should also be mentioned that the desired angular velocity and acceleration are smaller during the second pass compared to the

first. This is because the Earth is rotating, thus the distance between the spacecraft and target is longer, causing less fluctuation on the components. The bottommost plot in Figure 5 shows the epsilon components of the difference in attitude between desired leader and follower, defined as $\tilde{\epsilon}_d = \eta_{ld}\epsilon_{fd} - \eta_{fd}\epsilon_{ld} - \mathbf{S}(\epsilon_{fd})\epsilon_{ld}$. It can be seen that since the follower spacecraft was moving away from the leader spacecraft during the first 500 seconds, the difference in desired relative attitude increased during the same period.

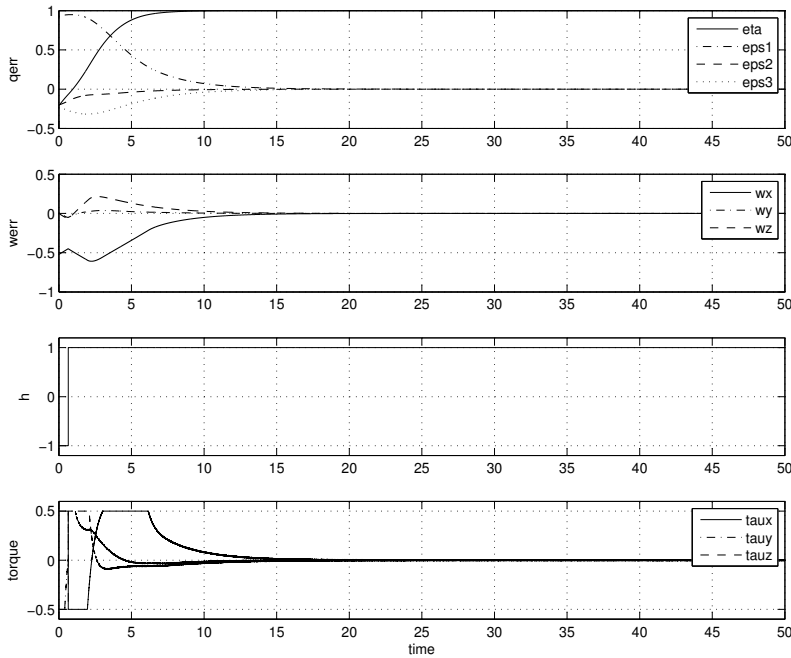


Fig. 6. Relative attitude error, relative angular velocity error, switching value and control torque with uncompensated disturbances and unfiltered sensor noise.

Figure 6 shows simulation results where the follower spacecraft starts with an initial attitude of $\mathbf{q}_f(t_0) = [-0.866, 0.5, 0, 0]^\top$ and $\boldsymbol{\omega}_{i,fb}^{fb}(t_0) = [-0.5236, 0, 0]^\top$ rad/s. As can be seen, the negative equilibrium point is the closest one, thus $h_f = -1$, but a switch occurs because of the initial angular velocity, driving the states towards the positive equilibrium.

6. Conclusions

In this paper we have presented a scheme for calculating the desired attitude, angular velocity and angular acceleration for a leader spacecraft and relative attitude, angular velocity and angular acceleration for a leader-follower spacecraft formation. Sliding surface tracking control laws were presented for both relative translational and rotational control of a leader and follower in cascades. For relative position the equilibrium point of the closed-loop system was proven globally uniformly asymptotically stable, while for relative rotation, the equilibrium point of the cascaded closed-loop systems was proven uniformly practically asymptotically stable in the large on the set $\mathcal{S}^3 \times \mathbb{R}^3$, both control laws were considered

to be perturbed by unknown but bounded disturbances which were not compensated for. Simulation results were presented to show both the performance of the control laws, and that the presented scheme enables a leader-follower formation to perform measurements on a common point on the Earth surface even during formation reconfiguration.

7. References

- Battin, R. H. (1999). *An Introduction to the Mathematics and Methods of Astrodynamics, Revised Edition*, AIAA Education Series, American Institute of Aeronautics and Astronautics, Reston, VA. ISBN 1-56347-342-9.
- Berghuis, H. & Nijmeijer, H. (1993). A passivity approach to controller-observer design for robots, *IEEE Transactions on Robotics and Automation* 9(6): 740–754.
- Casagrande, D., A. A. P. T. (2008). Global asymptotic stabilization of the attitude and the angular rates of an underactuated non-symmetric rigid body, *Automatica* 44: 1781–1789.
- Chaillet, A. (2006). *On Stability and Robustness of Nonlinear Systems: Applications to Cascaded Systems*, PhD thesis, UFR Scientifique D'Orsay, Paris, France.
- Chaillet, A. & Loría, A. (2008). Uniform semiglobal practical asymptotic stability for non-autonomous cascaded systems and applications, *Automatica* 44: 337–347.
- Chen, X., Steyn, W. H. & Hashida, Y. (2000). Ground-target tracking control of earth-pointing satellites, *AIAA Guidance, Navigation, and Control Conference and Exhibit*, Denver, CO, pp. 1834–1844.
- Clohessy, W. H. & Wiltshire, R. S. (1960). Terminal guidance system for satellite rendezvous, *Journal of Aerospace Sciences* 27(9): 653–658.
- Egeland, O. & Gravdahl, J. T. (2002). *Modeling and Simulation for Automatic Control*, Marine Cybernetics, Trondheim, Norway. ISBN 82-92356-01-0.
- Fossen, T. I. & Fjellstad, O.-E. (1993). Cascaded adaptive control of ocean vehicles with significant actuator dynamics, *Proceedings of the IFAC World Congress*, Sydney, Australia.
- Garcia, I. & How, J. P. (2005). Trajectory optimization for satellite reconfiguration maneuvers with position and attitude constraints, *Proceedings of the American Control Conference*, Portland, OR.
- Goebel, R., Sanfelice, R. G. & Teel, A. R. (2009). Hybrid dynamical systems, *IEEE Control Systems Magazine* 29(2): 28–93.
- Gorre, B. B. & Shucker, B. (1999). Geometric attitude control of a small satellite for ground tracking maneuvers, *Proceedings of the 13th AIAA/USU Conference on Small Satellites*, Utah State University.
- Grøtli, E. I. (2010). *Robust stability and control of spacecraft formations*, PhD thesis, Norwegian University of Science and Technology.
- Hahn, W. (1967). *Stability of Motion*, Springer-Verlag, Berlin, Germany.
- Hill, G. W. (1878). Researches in the lunar theory, *American Journal of Mathematics* 1(1): 5–26.
- Horn, R. A. & Johnson, C. R. (1985). *Matrix Analysis*, Cambridge University Press. ISBN 0-521-38632-2.
- Janković, M., Sepulchre, R. & Kokotović, P. V. (1996). Constructive lyapunov stabilization of non linear cascaded systems, *IEEE Transactions on Automatic Control* 41: 1723–1736.
- Jiang, Z. P. & Mareels, I. (1997). A small gain control method for nonlinear cascaded systems with dynamic uncertainties, *IEEE Transaction on Automatic Control* 42: 1–17.
- Kristiansen, R. (2008). *Dynamic Synchronization of Spacecraft - Modeling and Coordinated Control*

- of *Leader-Follower Spacecraft Formations.*, PhD thesis, Department of Engineering Cybernetics, Norwegian University of Science and Technology, Trondheim, Norway.
- Liberzon, D. (2003). *Switching in Systems and Control*, Birkhäuser. ISBN 0-8176-4297-8.
- Loría, A., Nijmeijer, H. & O., E. (1998). Cascaded synchronization of two pendula, *Proceedings of the American Control Conference*.
- Loría, A. & Panteley, E. (2005). Cascaded nonlinear time-varying systems: Analysis and design, *Advanced Topics in Control Systems Theory*, Vol. 311 of *Lecture Notes in Control and Information Sciences*, Springer Verlag, chapter 2, pp. 23–64. ISBN 1-85233-923-3.
- Mayhew, C. G., Sanfelice, R. G. & Teel, A. R. (2009). Robust global asymptotic attitude stabilization of a rigid body by quaternion-based hybrid feedback, *Proceedings of the IEEE Conference on Decision and Control*.
- McInnes, C. R. (1995). Autonomous ring formation for a planar constellation of satellites, *AIAA Journal of Guidance, Control and Dynamics* 18(5): 1215–1217.
- Montenbruck, O. & Gill, E. (2001). *Satellite Orbits. Models, methods, applications*, Springer-Verlag, Berlin, Germany. First edition, corrected second printing, ISBN 3-540-67280-X.
- Paden, B. & Panja, R. (1988). Globally asymptotically stable 'PD+' controller for robot manipulators, *International Journal of Control* 47(6): 1697–1712.
- Panteley, E. & Loría, A. (1998). On global uniform asymptotic stability of nonlinear time-varying systems in cascade, *Systems & Control Letters* 33(2): 131–138.
- Sanfelice, R. G., Goebel, R. & Teel, A. R. (2007). Invariance principles for hybrid systems with connections to detectability and asymptotic stability, *IEEE Transactions on Automatic Control* 52(12): 2282–2297.
- Sidi, M. J. (1997). *Spacecraft Dynamics and Control*, Cambridge University Press, New York. ISBN 0-521-78780-7.
- Slotine, J. J.-E. & Li, W. (1987). On the adaptive control of robot manipulators, *International Journal of Robotics Research* 6: 49–59.
- Steyn, W. H. (2006). A view finder control system for an earth observation satellite, *Aerospace Science and Technology* 10(3): 248–255.
- Takegaki, M. & Arimoto, S. (1981). A new feedback method for dynamic control of manipulators, *ASME Journal of Dynamical Systems, Measurement and Control* 102: 119–125.
- Tsiotras, P., Shen, H. & Hall, C. (2001). Satellite attitude control and power tracking with energy/momentum wheels, *AIAA Journal of Guidance, Control and Dynamics* 24(1): 23–34.
- Wang, P. K. C. & Hadaegh, F. Y. (1996). Coordination and control of multiple microspacecraft moving in formation, *Journal of the Astronautical Sciences* 44(3): 315–355.
- Wertz, J. R. (ed.) (1978). *Spacecraft Attitude Determination and Control*, Kluwer Academic Publishers, London. ISBN 90-277-0959-9.
- Wong, H. & Kapila, V. (2005). Spacecraft formation flying near sun-earth l_2 lagrange point: Trajectory generation and adaptive output feedback control, *Proceedings of the American Control Conference*, Portland, OR.
- Yan, H., Alfriend, K. T., Vadali, S. R. & Sengupta, P. (2009). Optimal design of satellite formation relative motion orbits using least-square methods, *AIAA Journal of Guidance, Control and Dynamics* 32(2): 599–604.
- Yan, Q., Yang, G., Kapila, V. & de Queiroz, M. (2000a). Nonlinear dynamics and adaptive control of multiple spacecraft in periodic relative orbits, *Proceedings of the AAS*

Guidance and Control Conference, Breckenridge, CO.

Yan, Q., Yang, G., Kapila, V. & de Queiroz, M. (2000b). Nonlinear dynamics and output feedback control of multiple spacecraft in elliptical orbits, *Proceedings of the American Control Conference*, Chicago, Illinois.

Rendezvous Between Two Active Spacecraft with Continuous Low Thrust

Yechiel Crispin and Dongeun Seo
Embry-Riddle Aeronautical University
USA

1. Introduction

Rendezvous problems between spacecraft have attracted a major research interest due to important applications in actual space missions. Rendezvous problems may be categorized into two groups depending on how the rendezvous maneuver is performed by the participating spacecraft for a given mission: active-passive and cooperative maneuvers. In an active-passive rendezvous problem involving two vehicles, the first vehicle, known as the target vehicle, does not apply any control force while following its trajectory. The second vehicle, which serves as the active vehicle, is controlled in such a way as to meet the target vehicle at a later time. The control objective for the active vehicle is to match the position and the velocity of the target vehicle. On the other hand, in a cooperative rendezvous problem, both vehicles are controlled and guided to match the same position and velocity. Therefore, solutions to either rendezvous problem consist of a sequence of control maneuvers or guidance laws, designed to bring the vehicles to the same states, i.e., position and velocity. Based on the overall mission requirements, the control objective of the rendezvous can include additional constraints such as the total amount of propellant for each vehicle or the mission time from beginning to end.

An optimal control problem consists of finding the control sequences as a function of time, while achieving the control objectives and satisfying the given constraints. In the rendezvous problem, the performance index to be minimized can be the duration of the maneuver or the amount of fuel for each vehicle. The control objective is to match the final states of each vehicle. The vehicle dynamics are defined by a set of ordinary differential equations.

The solution methods for the optimal control problem consist of indirect and direct methods. Indirect methods are founded on the methods of the calculus of variation and its extension to the maximum principle of Pontryagin and use a Hamiltonian formulation. They require the solution of a two-point boundary value problem (TPBVP) for the system state variables and a set of adjoint variables. The state variables are subject to the initial conditions and the adjoint variables to the final conditions (constraints). The TPBVP is derived from the original optimal control problem and its dimension is higher than the dimension of the original problem. In addition, a TPBVP is more difficult to solve than an initial value problem (IVP) [Shampine & Thompson (2003)]. For this reason, direct methods have been developed in order to avoid the development of the Hamiltonian formulation from the optimal control problem.

Direct search methods include direct collocation nonlinear programming (DCNLP) [Hargraves & Paris (1987)], genetic algorithms (GA) [Goldberg (1989); Michalewicz (1994)], particle swarm optimization (PSO) [Venter & Sobieszczanski-Sobieski (2002)], simulated

annealing (SA) [Kirkpatrick & Vecchi (1983); van Laarhoven & Aarts (1987); Davis (1987)], etc. In the DCNLP method, the system of equations and the constraints are satisfied at a finite set of specific points, known as the collocation points. On the other hand, evolutionary methods such as the GA, the PSO and SA, mimic either some biological behavior or some physical phenomenon. For example, the PSO algorithm is inspired by the social behavior of a swarm of birds or insects [Crispin (2005)].

Orbital transfer problems and cooperative rendezvous problems using an optimal control formulation have been studied by many authors [Pourtakdous & Jalali (1995); Marinescu (1976); Park & Guibout (2006); Jezewski (1992); Rauwolf & Coverstone-Carroll (1996); Carpenter & Jackson (2003); Kim & Spencer (2002); Olsen & Fowler (2005)]. A Hamiltonian formulation was used as a solution searching method by Marinescu [Marinescu (1976)] and Pourtakdoust [Pourtakdous & Jalali (1995)]. Another method based on generating functions has been proposed by Park [Park & Guibout (2006)], where generating functions were used to find the optimal solution, treating the TPBVP as a canonical transformation. Rouwolf and Coverstone-Carroll [Rauwolf & Coverstone-Carroll (1996)] proposed the use of a GA for a low-thrust orbital transfer problem. A chaser-target rendezvous problem was solved by Carpenter [Carpenter & Jackson (2003)] using a GA. They used the Clohessy-Wiltshire equations as a linear approximation for preliminary mission planning. Another chaser-target type problem is studied by Kim and Spencer [Kim & Spencer (2002)] with minimum fuel consumption as the objective function. Olsen and Fowler [Olsen & Fowler (2005)] also adopted the GA to generate a near optimal solution to a rendezvous problem using elliptic orbits.

Crispin [Crispin (2006; 2007)] obtained GA based solutions to rendezvous problems as nonlinear discrete or continuous time optimal control problems with terminal constraints. Using the GA has the advantage of completely eliminating the need for a TPBVP reformulation. Instead, GA utilizes a stochastic search method that can explore a large region of the solution space. In addition, GA requires no derivatives, which simplifies the computation of the actual algorithm. However, it does not guarantee finding the global optimum, because of the stochastic behavior. Several methods have been proposed in order to prevent GA's from converging to a local optimum [Schraudolph & Belew (1992); Fogel (1995)]. In this paper, we treat the rendezvous problem using GA's and simulated annealing in order to find nearly optimal solutions. We consider a cooperative rendezvous problem where both vehicles are active and the mission time duration is taken as a terminal constraint. The spacecraft dynamics are based on a continuous low-thrust assumption and are not restricted to a specific orbital shape. This is different from the Clohessy-Wiltshire approximation, which assumes the trajectories remain in the vicinity of a given orbit, usually circular or elliptic. Furthermore, the near optimal solutions obtained by the GA or the SA are used as an initial guess in a collocation method, in order to obtain more accurate solutions.

The paper is organized as follows. In the following Section 2, a detailed problem formulation is presented and the equations of motion for both spacecraft are derived. Then, it is followed by Section 3, which contains numerical simulation results in order to demonstrate the points given in the previous section. Finally, concluding remarks and future research directions are given in Section 4.

2 Problem formulation

This section describes the formulation of the optimal control problem for the given rendezvous mission with both spacecraft active. The rendezvous mission time is prescribed

a priori. If no solution can be found for the prescribed time duration, it usually means that the time is too short to achieve rendezvous. Therefore, the mission time is increased and the optimal problem is solved again. Fig. 1 shows the frame of reference and the nomenclature for the rendezvous problem.

It is assumed that the initial orbit of each spacecraft is circular. Here ν is the true anomaly measured counter-clockwise from the $+x$ axis direction. Initially, the two spacecraft are located at different positions so that their radial locations and true anomalies values are different at the initial time $t = t_0$. Each spacecraft is equipped with a low thrust rocket engine, which is assumed to have a constant thrust force T . This assumption simplifies the optimal control problem because the steering angle θ of the thrust vector can be used as a single control variable. The measurement directions for each quantity are depicted in Fig. 1. It is also assumed that there are no gravity perturbations due to the oblateness of the main attracting body, the existence of another attracting body in the vicinity of the spacecraft and the mutual attraction between the spacecraft. We restrict our problem to two identical spacecraft with the same initial masses as well as the same constant thrust force and the same propellant mass flow rate. Therefore, the dynamics of each spacecraft are given by

$$m \left(\frac{d^2r}{dt^2} - r \left(\frac{dv}{dt} \right)^2 \right) = -\frac{m\mu}{r^2} + T \sin \theta \tag{1}$$

$$m \left(r \frac{d^2\nu}{dt^2} + 2 \left(\frac{dr}{dt} \right) \left(\frac{d\nu}{dt} \right) \right) = T \cos \theta \tag{2}$$

where $\mu = GM$ is the gravitational constant of the main attracting body, which is located at the origin O in Fig. 1, M is the corresponding mass of the attracting body, and G is the universal gravitational constant. As seen in Eq. (1) and Eq. (2), the motion of each spacecraft is decomposed into the radial and the transverse direction. Accordingly, the radial and transverse components of the velocity vector are given by

$$u = \frac{dr}{dt}, \quad v = r \frac{d\nu}{dt} \tag{3}$$

Using the velocity components given in Eq. (3), we may now rewrite Eq. (1) and Eq. (2) as first-order differential equations as follows

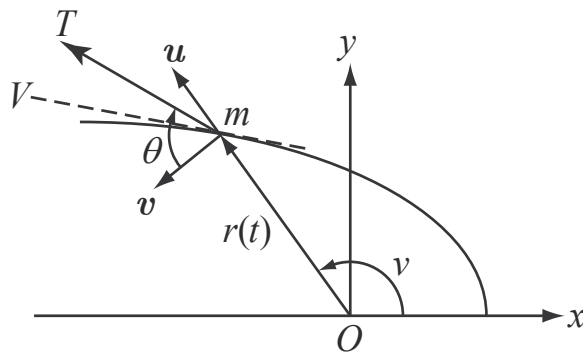


Fig. 1. Spacecraft trajectory for the rendezvous mission. The center of attraction is at the origin of the xy -frame. u and v are the components of the velocity V in polar coordinates

$$m \left(\frac{du}{dt} - \frac{v^2}{r} \right) = -\frac{m\mu}{r^2} + T \sin \theta \quad (4)$$

$$m \left(\frac{dv}{dt} + \frac{uv}{r} \right) = T \cos \theta \quad (5)$$

Therefore, the system of first-order differential equations consisting of Eq. (3), Eq. (4), and Eq. (5) describes the dynamics of the spacecraft. We now introduce the following characteristic parameters (time, speed, and thrust force) in order to non-dimensionalize the system of equations.

$$t^* = \sqrt{\frac{r_o^3}{\mu}}, \quad V_o = \sqrt{\frac{\mu}{r_o}}, \quad T_o = \frac{\mu m_o}{r_o^2} \quad (6)$$

where r_o is the radius of the initial orbit; m_o is the initial mass of each spacecraft; and V_o is the initial velocity of each spacecraft. Since each spacecraft starts its motion on a circular orbit before the start of the rendezvous mission, V_o has only a transverse velocity component, which is identical to the orbital velocity of the spacecraft in its circular orbit. The definitions of the non-dimensional variables are given by

$$\begin{aligned} \bar{r} &= r/r_o & \bar{m} &= m/m_o & \bar{t} &= t/t^* = t/\sqrt{r_o^3/\mu} \\ \bar{u} &= u/V_o = u/\sqrt{\mu/r_o} & \bar{v} &= v/V_o = v/\sqrt{\mu/r_o} & \tau &= T/T_o = T/(\mu m_o/r_o^2) \end{aligned} \quad (7)$$

where the bar denotes non-dimensional variables and the symbol τ is chosen for the non-dimensional thrust in order to avoid confusion with \bar{t} , which is the normalized time. Since the mass of the spacecraft varies during the rendezvous mission, the mass m is a function of \bar{t} and is given by

$$m(t) = m_o + \dot{m}t \quad (8)$$

where \dot{m} is negative, since the mass of the vehicle decreases as fuel is consumed. Thus, \bar{m} is obtained by

$$\bar{m} = 1 - \frac{|\dot{m}|}{m_o} \sqrt{\frac{r_o^3}{\mu}} \bar{t} = 1 - B\bar{t} \quad (9)$$

where $B = (|\dot{m}|/m_o)\sqrt{r_o^3/\mu}$ is introduced for notational simplicity. The corresponding non-dimensionalized system of equations (Eq. (3), Eq. (4), and Eq. (5)) are obtained as follows

$$\frac{d\bar{r}}{d\bar{t}} = \bar{u} \quad (10)$$

$$\frac{d\bar{v}}{d\bar{t}} = \bar{v} \quad (11)$$

$$\frac{d\bar{u}}{d\bar{t}} = \frac{\bar{v}^2}{\bar{r}} - \frac{1}{\bar{r}^2} + \frac{\tau \sin \theta}{(1 - B\bar{t})} \quad (12)$$

$$\frac{d\bar{v}}{d\bar{t}} = -\frac{\bar{u} \cdot \bar{v}}{\bar{r}} + \frac{\tau \cos \theta}{(1 - B\bar{t})} \quad (13)$$

The non-dimensional initial conditions are

$$\bar{r}(0) = 1, \quad \bar{u}(0) = 0, \quad \bar{v}(0) = 1, \quad v(0) = v_o \quad (14)$$

In order to achieve the rendezvous, the following final conditions must be satisfied by each spacecraft

$$\bar{r}(\bar{t}_f) = \bar{r}_f, \quad \bar{u}(\bar{t}_f) = 0, \quad \bar{v}(\bar{t}_f) = \bar{v}_f = \frac{1}{\sqrt{\bar{r}_f}}, \quad v(\bar{t}_f) = v_f \quad (15)$$

From Eq. (15), we see that the rendezvous point is located on the final circular orbit with an arbitrary true anomaly value. As mentioned before, \bar{r}_f and \bar{t}_f are prescribed parameters of the optimal control problem. The final \bar{t}_f can be reduced if it is required to find a shorter time for the mission duration.

The objective function to be minimized for the given rendezvous problem is chosen as

$$J = \max\{w_1 \cdot [\bar{r}(\bar{t}_f) - \bar{r}_f]^2, w_2 \cdot [\bar{u}(\bar{t}_f) - \bar{u}_f]^2, w_3 \cdot [\bar{v}(\bar{t}_f) - \bar{v}_f]^2, w_4 \cdot [v(\bar{t}_f) - v_f]^2\} \quad (16)$$

where w_i is a weight determining the contribution of each error and can be adjusted based on the mission scenario. In fact, in our simulations, w_4 is set to zero for a free final true anomaly value at the the rendezvous point. The choice of J is not unique and the reason for the choice of J in Eq. (16) is to improve the simulation speed based on several J trials. In the following section, the rendezvous between two spacecraft is considered. If we denote the objective function for the i th spacecraft as J_i from Eq. (16), the objective function for a rendezvous mission consisting of N spacecraft (e.g., $N = 2$ in our simulations) is given by

$$J_{\text{tot}} = \max \bigcup_{i=1}^N J_i \quad (17)$$

3. Numerical results

The rendezvous simulations are performed using canonical units. The characteristic distance r_o is in astronomical unit (AU) which is the average distance between the Earth and the Sun ($r_o = 1\text{AU} \approx 1.4960 \times 10^8$ km). The gravitational constant μ for the sun is about 1.3271×10^{11} km³/s². The mass of the spacecraft [Bryson (1999)] is $m_o = 4536$ kg. The characteristic time is obtained by Eq. (6) and set to $t^* = 58.13$ days. Similarly, $V_o = 29.785$ km/s and $T_o = 26.9$ N. The constant thrust force for the spacecraft [Bryson (1999)] is $T = 3.778$ N and leads to the non-dimensionalized thrust force $\tau = 0.1405$. Finally, the mass consumption rate estimated from the spacecraft model [Bryson (1999)] is $\dot{m} = 6.7564 \times 10^{-5}$ kg/s and corresponding B for Eq. (9) is about 0.0748. As a reference mission, we consider the rendezvous mission at Mars orbit ($\bar{r}_f = 1.5237$). The velocity constraints at the final position are $\bar{u}_f = 0$ and $\bar{v}_f = 0.8101$. The prescribed mission time $\bar{t}_f = 5.5$ to ensure the fast convergence to near optimal solutions by the GA and SA. In the following discussion, we drop the bar for the non-dimensional variables to simplify the notation.

3.1 Rendezvous between two spacecraft using genetic algorithms and simulated annealing

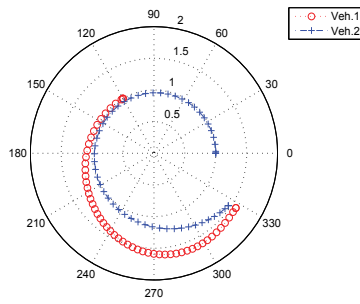
Two cases are discussed in the following simulations. First, both spacecraft start from the orbit of the Earth. However, the difference between the initial values of the true anomaly of the two spacecraft is larger than $\pi/2$, in order to study the case of relatively large initial angular differences between the locations of the two vehicles. The second case is about the

rendezvous of spacecraft starting from two different orbits such as the orbit of Mars and orbit of the Earth, meeting at an intermediate orbit. In both cases, the final value of the true anomaly of both spacecraft is free (is not prescribed a priori). In both cases, the GA and SA methods are used and the results are compared.

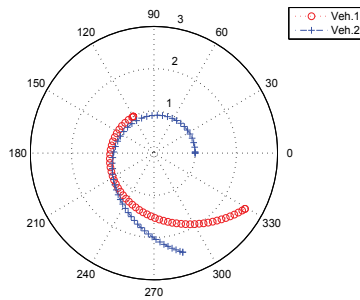
The numerical integration of the differential equations describing the spacecraft dynamics is performed using a fourth order Runge-Kutta method. The time duration $t_f = 5.5$ is divided into N_t time steps each of $\Delta t = t_f / N_t$. The discrete time is $t_i = i\Delta t$. The corresponding control function $\theta(t)$ is also discretized to $\theta^i = \theta(t_i)$ based on the number of time steps N_t . In the simulations, the number of time steps N_t is fixed. The control function $\theta(t)$ is smoothed by fitting a third order polynomial to the discrete values of θ^i from $i = 1$ to $i = 41$. A population size of 50 members was used for the GA. All the members of the initial population $\theta^i = \theta(t_i)$ are set to zero. The chosen crossover fraction is 0.8. For SA, the re-annealing interval is 100 and the initial temperature is 100. The maximum iteration number for the GA is 100 and for the SA it is 300. The objective function tolerance is set to 0.001 for both the GA and the SA.

The rate of convergence may vary dramatically when running the same case many times, because both the GA and SA operations are stochastic processes. Furthermore, the number of iterations for the same order of magnitude of the objective function is another aspect that distinguishes the GA from the SA. Fig. 2 shows the simulation results using the GA and the SA. Both methods failed to satisfy the tolerance condition (less than 0.001) for the objective function and were stopped after 100 iterations. Spacecraft 1 starts from $r_{1o} = 1$ with $\theta_{1o} = 0$ and Spacecraft 2 starts from $r_{2o} = 1$ with $\theta_{2o} = 2\pi/3$. The final radius for both spacecrafts is $r_f = 1.528$, corresponding to the orbit of Mars ($r_f = 1.528au$). The final true anomaly θ_f is free as mentioned earlier. Fig. 2(a) represents the result when the objective function value is 0.043 and Fig. 2(b) corresponds to 11.046 for the same objective function. The errors in Fig. 2(b) are due to a large value of the final radius being greater than 2. However, the calculation time for the SA is much less than that of the GA for the same number of iterations. The final true anomaly values for Spacecraft 1 and 2 are $\nu_{1f} \approx 325.5^\circ$ and $\nu_{2f} \approx 326.9^\circ$ when using the GA; $\nu_{1f} \approx 286.6^\circ$ and $\nu_{2f} \approx 329.1^\circ$ when using the SA. Fig. 2(c) and Fig. 2(d) show the control history obtained by the GA and the SA. Since we use third order polynomials to smooth the control function based on θ_1^i and θ_2^i with $i \in [1, 41]$, both $\theta_1(t)$ for Spacecraft 1 and $\theta_2(t)$ for Spacecraft 2 look similar to each other except for the direction of the curvatures.

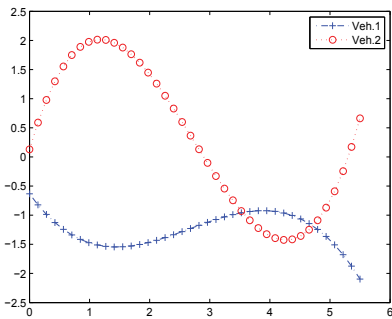
The second case we consider is when each spacecraft starts from a different orbit (the orbits of Mars and Earth, respectively) and rendezvous at an intermediate orbit. Spacecraft 1 starts from a point on the Earth orbit ($r_{1o} = 1$, $\theta_{1o} = 2\pi/3$) and Spacecraft 2 from a point located on the Mars orbit ($r_{2o} = 1.528$, $\theta_{2o} = 2\pi/3$). The rendezvous is at the intermediate orbit ($r_f = 1.2$) between Earth and Mars orbits and the final true anomaly is free (not prescribed). The final time is the same as in the previous simulations ($t_f = 5.5$). The maximum numbers of iterations for the GA and the SA are also the same as in the previous case. Fig. 3 shows the simulation results for the GA and the SA. The objective function value obtained using the SA Fig. 3(a) is about 0.06 and for the GA in Fig. 3(b) it is about 3.64. Although the number of iterations of the SA is larger than the number of generations of the GA, the actual CPU time for the SA is shorter than that of the GA. The final true anomalies obtained are $\nu_{1f} \approx 23.4^\circ$ and $\nu_{2f} = 22.2^\circ$ in the case of the GA; and $\nu_{1f} \approx 37.9^\circ$ and $\nu_{2f} \approx 44.4^\circ$ in the case of the SA. Fig. 3(c) and Fig. 3(d) show the corresponding control histories.



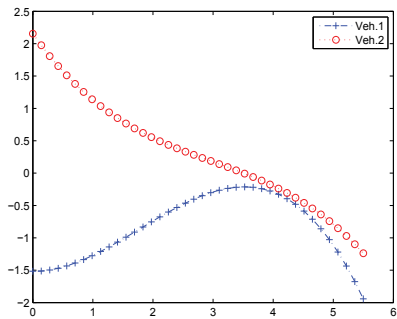
(a) Trajectories for a rendezvous between two spacecraft (circles and crosses) obtained by the GA



(b) Trajectories for a rendezvous between two spacecraft (circles and crosses) obtained by the SA

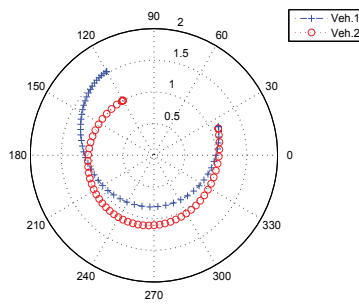


(c) Steering angles $\theta_1(t)$ (circles) and $\theta_2(t)$ (crosses) for a rendezvous between two spacecraft obtained by GA

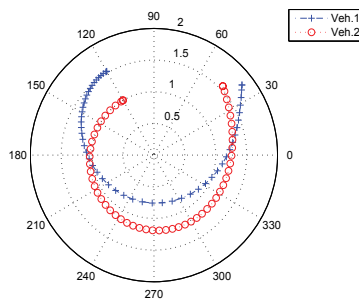


(d) Steering angles $\theta_1(t)$ (circles) and $\theta_2(t)$ (crosses) for a rendezvous between two spacecraft obtained by SA

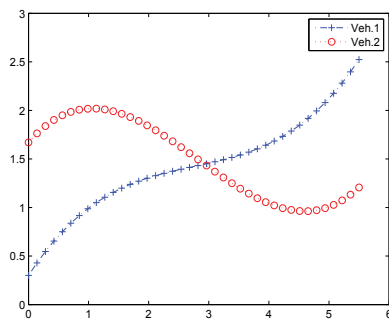
Fig. 2. Trajectories generated by the GA and the SA direct search methods. The number of iterations is 100 for the GA and 300 for the SA. The radial distances and the angles are in AU and degrees, respectively.



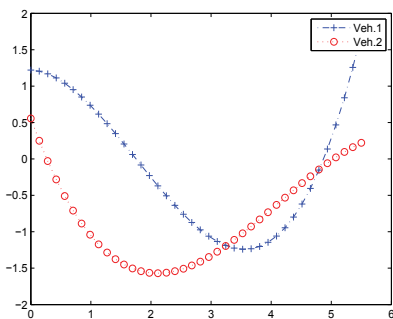
(a) Trajectories for a rendezvous between two spacecraft (circles and crosses) obtained by the GA



(b) Trajectories for a rendezvous between two spacecraft (circles and crosses) obtained by the SA



(c) Steering angles $\theta_1(t)$ (circles) and $\theta_2(t)$ (crosses) for a rendezvous between two spacecraft obtained by GA



(d) Steering angles of $\theta_1(t)$ (circles) and $\theta_2(t)$ (crosses) for a rendezvous between two spacecraft obtained by the SA

Fig. 3. Optimal control trajectories generated by the GA and the SA direct search methods. The number of iterations for the GA is 100 and 300 for the SA. The units for the radius and angles are AU and degrees, respectively

3.2 Using GA and SA near-optimal solutions as initial guesses for a collocation method

Direct search methods like the GA and the SA may not generate solutions accurate enough to satisfy the final conditions because of the stochastic behavior. On the other hand, numerical methods for the solution of TPBVP's are more accurate than stochastic methods, but they require the knowledge of initial solutions (initial guesses) for starting the solution. Noting that the GA/SA methods can provide approximate trajectories, we can use them as initial guesses in a numerical method for solving TPBVP's, based on the collocation method. In this way, we can attempt to combine the advantages of the stochastic method and of the more accurate collocation method for TPBVP's. The nearly optimal initial solutions are obtained without solving optimal control problems with adjoint variables and we solve a TPBVP of reduced dimensions without adjoint variables, which simplifies the original optimal control problem significantly. Solving optimal control problems directly by TPBVP is not easy and numerical solutions are very sensitive to the initial guesses for the solutions [Bailey & Waltman (1968); Shampine & Thompson (2003)]. For this purpose, we combine the SA method with a collocation method [Kierzenka (1998); Shampine & Thompson (2003)]. Fig. 4 shows the simulation results where SA results are used as an initial guess.

We use the solutions obtained using the SA method in Section 3.1. We parameterize the steering control as follows

$$\theta_1(t) = \sum_{i=0}^{N_1} A_i t^{N_1-i}, \quad \theta_2(t) = \sum_{i=0}^{N_2} B_i t^{N_2-i} \quad (18)$$

where the subscript i refers to the i th spacecraft in the rendezvous mission. By adopting the parametrization for the control inputs, the spacecraft dynamics become

$$\frac{d\mathbf{y}}{dt} = \mathbf{f}(t, \mathbf{y}, \mathbf{A}) \quad (19)$$

where the parameter vector \mathbf{A} for the collocation method is defined by

$$\mathbf{A} = [A_0, A_1, \dots, A_{N_1}, B_0, B_1, \dots, B_{N_2}]^T \quad (20)$$

and the state vector is

$$\mathbf{y} = [r_1, u_1, v_1, \dot{r}_1, \dot{u}_1, \dot{v}_1, r_2, u_2, v_2, \dot{r}_2, \dot{u}_2, \dot{v}_2]^T \quad (21)$$

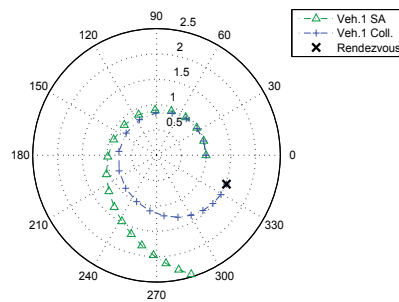
The nonlinear vector field \mathbf{f} in Eq. (19) refers to the system of equations Eq. (10), Eq. (12), Eq. (13), and Eq. (11) in an order of components in \mathbf{y} . We use polynomials of degree 3 for each spacecraft ($N_1 = N_2 = 3$). The initial value of \mathbf{A} using SA is given by

$$\mathbf{A} = [-0.0613, 0.3264, -0.0196, -1.5158, -0.0365, 0.3279, -1.3149, 2.1545]^T \quad (22)$$

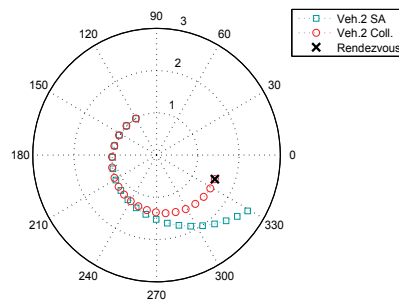
The results obtained by the collocation method for \mathbf{A} are

$$\mathbf{A} = [0.0291, -0.3704, 1.3080, -2.4064, -0.0080, -0.1863, 0.4425, 1.5668]^T \quad (23)$$

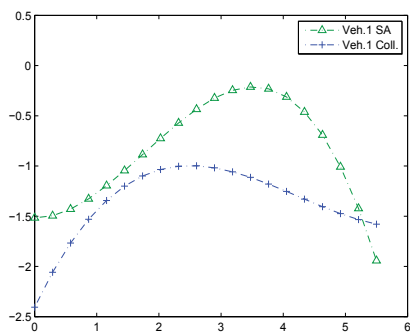
As we can see from Eq. (22) and Eq. (23), the solution of the TPBVP by the collocation method gives results which satisfy the final conditions of Eq. (15). A comparison of the control functions and the trajectories for each spacecraft is presented in Fig. 4.



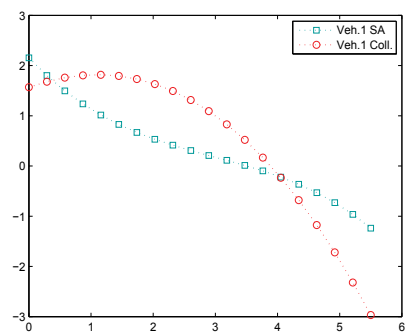
(a) Trajectories of the first spacecraft obtained by SA and the collocation method



(b) Trajectories of the second spacecraft obtained by SA and the collocation method



(c) Steering angles $\theta_1(t)$ by SA and the collocation method



(d) Steering angles $\theta_2(t)$ by SA and the collocation method

Fig. 4. Optimal trajectories generated by a combination of SA and a collocation method. The units for the radius and the angle are AU and degrees, respectively

4. Conclusion

The rendezvous problem between two spacecraft using low thrust continuous propulsion systems has been formulated as an optimal control problem. Instead of using a Hamiltonian formulation, the optimal control problem is solved by direct search methods such as GA's and SA. Since SA is faster than the GA for the same number of iterations, SA is combined with the collocation method to overcome the stochastic behavior of SA (i.e., to match the final constraints). Simulations of a rendezvous mission between two spacecraft are performed in order to demonstrate the proposed methodology. The SA and the collocation method have been used successfully as complementary methods in order to achieve improved solutions to the original optimal control problem.

5. References

- Bailey, P. B.; Shampine, L. & Waltman, P. (1968). *Nonlinear Two Point Boundary Value Problems*, Academic Press, New York.
- Bryson, A. (1999). *Dynamic Optimization*, Addison Wesley Longman.
- Carpenter, B. & Jackson, B. (2003). Stochastic optimization of spacecraft rendezvous trajectories, *Advances in the Astronautical Sciences* 113: 219–232.
- Crispin, Y. (2005). Cooperative control of a robot swarm with network communication delay, The First International Workshop on Multi-Agent Robotic Systems (MARS 2005).
- Crispin, Y. (2006). *An Evolutionary Approach to Nonlinear Discrete-Time Optimal Control With Terminal Constraints*, Informatics in Control, Automation and Robotics I, Springer, Dordrecht, Netherlands.
- Crispin, Y. (2007). *Evolutionary Computation for Discrete and Continuous Time Optimal Control Problems*, Informatics in Control, Automation and Robotics II, Springer, Dordrecht, Netherlands.
- Davis, L. (1987). Genetic algorithms and simulated annealing, research notes in artificial intelligence, hyperion books.
- Fogel, D. B. (1995). *Evolutionary Computation*, IEEE press, New York.
- Goldberg, D. E. (1989). *Genetic Algorithms in Search, Optimization and Machine Learning*, Addison-Wesley Publishing.
- Hargraves, C. R. & Paris, S. W. (1987). Direct trajectory optimization using nonlinear programming and collocation, *Journal of Guidance Control and Dynamics* 10: 338–342.
- Jezewski, D. J. (1992). Optimal rendezvous trajectories subject to arbitrary perturbations and constraints, *AIAA-92-4507-CP*, American Institute of Aeronautics and Astronautics, Washington, pp. 235–245.
- Kierzenka, J. (1998). *Studies in the Numerical Solution of Ordinary Differential Equations*, PhD thesis, Southern Methodist University, Dallas, Texas.
- Kim, Y. H. & Spencer, D. B. (2002). Optimal spacecraft rendezvous using genetic algorithms, *Journal of Spacecraft and Rockets* 39(6): 859–865.
- Kirkpatrick, S.; Gelatt, C. & Vecchi, M. (1983). Optimization by simulated annealing, *Science* 220(4598): 671.
- Marinescu, A. (1976). Optimal low-thrust orbital rendezvous, *Journal of Spacecraft* 13(7): 385–398.
- Michalewicz, Z. (1994). *Genetic Algorithms + Data Structures = Evolution Programs*, 2 edn, Springer-Verlag, Berlin, Heidelberg, New York.
- Olsen, C. & Fowler, W. (2005). Characterization of the relative motions of rendezvous between

- vehicles in proximate, highly elliptic orbits, *Advances in the Astronautical Sciences* 119: 879–895.
- Park, C.; Scheeres, D. J. & Guibout, V. (2006). Solving optimal continuous thrust rendezvous problem with generating functions, *Journal of Guidance Control and Dynamics* 29(2): 321–331.
- Pourtakdous, S. H. & Jalali, M. A. (1995). Thrust limited optimal three dimensional spacecraft trajectories, *AIAA-95-3325-CP*, American Institute of Aeronautics and Astronautics, Washington, pp. 1395–1404.
- Rauwolf, G. A. & Coverstone-Carroll, V. (1996). Near optimal low-thrust orbit transfers generated by a genetic algorithm, *Journal of Spacecraft and Rockets* 33(6): 859–862.
- Schraudolph, N. N. & Belew, R. K. (1992). Dynamic parameter encoding for genetic algorithms, *Machine Learning* 9: 9–21.
- Shampine, L. F.; Gladwell, I. & Thompson, S. (2003). *Solving ODEs With Matlab*, Cambridge University Press, Cambridge, UK.
- van Laarhoven, P. & Aarts, E. (1987). Simulated annealing: Theory and applications, *Mathematics and Its Applications, D. Reidel, Dordrecht*.
- Venter, G. & Sobieszcanski-Sobieski, J. (2002). Particle swarm optimization, *43rd AIAA/ASME/ASCE/AHS/ASC Structures, Structural Dynamics and Materials Conference*.

Edited by Jason Hall

The development and launch of the first artificial satellite Sputnik more than five decades ago propelled both the scientific and engineering communities to new heights as they worked together to develop novel solutions to the challenges of spacecraft system design. This symbiotic relationship has brought significant technological advances that have enabled the design of systems that can withstand the rigors of space while providing valuable space-based services. With its 26 chapters divided into three sections, this book brings together critical contributions from renowned international researchers to provide an outstanding survey of recent advances in spacecraft technologies. The first section includes nine chapters that focus on innovative hardware technologies while the next section is comprised of seven chapters that center on cutting-edge state estimation techniques. The final section contains eleven chapters that present a series of novel control methods for spacecraft orbit and attitude control.

Photo by viking75 / iStock

IntechOpen

